

---

ELEVENTH SYMPOSIUM ON

# turbulent shear flows

---

Grenoble, France  
September 8-10, 1997

**DISTRIBUTION STATEMENT A**

Approved for public release;  
Distribution Unlimited

**VOLUME 2**  
**SESSIONS 11-22**  
**POSTER SESSION 2**

19971209 069



INSTITUT NATIONAL  
POLYTECHNIQUE  
DE GRENOBLE



CENTRE NATIONAL  
DE LA RECHERCHE  
SCIENTIFIQUE



UNIVERSITE  
JOSEPH FOURIER  
SCIENCES, TECHNOLOGIE, MEDECINE

DTIC QUALITY INSPECTED 4

**ELEVENTH SYMPOSIUM ON TURBULENT SHEAR FLOWS**  
**Institut National Polytechnique**  
**Université Joseph Fourier**  
**Grenoble, September 8-10, 1997**

**CONTENTS OF VOLUME 2**  
**SESSSIONS 11 - 22**  
**POSTER SESSION 2**

<b>SESSION 11 - WALL FLOWS I</b>	<b>11-1</b>
On clustering of quasi-streamwise vortices in near-wall turbulence .....	11-1
<i>Y. Miyake, K. Tsujimoto, T. Yoshikawa, T. Morikawa</i>	
Scaling of the viscous wall layer .....	11-7
<i>T. J. Hanratty, D. V. Papavassiliou</i>	
Experimental study of a turbulent Couette flow at low-Reynolds number .....	11-10
<i>K. Nakabayashi, O. Kitoh, F. Nishimura</i>	
Application of oil-surface visualisation and topology principles to identify the flow patterns around wall-mounted cubes .....	11-16
<i>E. R. Meinders, R. J. Martinuzzi, K. Hanjalic</i>	
Large eddy simulation of annular duct flow .....	11-22
<i>H. Xu, A. Pollard</i>	
 <b>SESSION 12 - VARIABLE DENSITY FLOWS</b>	 <b>12-1</b>
Reaction of near wall turbulence to strong density gradients .....	12-1
<i>S. Tardu, M. Favre Marinet, J. L. Harion</i>	
Monte Carlo computations of turbulent variable density jets .....	12-6
<i>J. P. H. Sanders, I. Gokalp</i>	
Experimental determination of some characteristic scales in variable density turbulent jets .....	12-12
<i>J. Page, Y. Haidous, B. Sarh, I. Gokalp</i>	
Velocity statistics associated with scale distributions in variable density turbulent jets .....	12-18
<i>L. Pietri, J. F. Lucas, M. Amielh, F. Anselmet</i>	
Variable density mixing in kinematically homogeneous turbulence.....	12-24
<i>P. Chassaing, S. Castaldi, G. Haran, L. Joly</i>	
 <b>SESSION 13 - CLOSURES II</b>	 <b>13-1</b>
Realizability of non-linear stress-strain relationships for Reynolds-stress closures .....	13-1
<i>S.R. Fu, T. Rung, F. Thiele</i>	



Predicting non-inertial effects with algebraic stress models which account for dissipation rate anisotropies .....	13-7
<i>T. Jongen, L. Machiels, T. B. Gatski</i>	
A new explicit algebraic Reynolds stress turbulence model for 3D flow .....	13-13
<i>S. Wallin, A. V. Johansson</i>	
Nonlinear eddy viscosity modelling with a transport equation for Lumley's stress flatness parameter .....	13-18
<i>K. Suga</i>	
Development of the the k - j turbulence model .....	13-24
<i>J. Cousteix, V. Saint Martin, R. Messing, H. Beazard, B. Aupoix</i>	

## SESSION 14 - WALL FLOWS II 14-1

Comparison between directly simulated numerical and experimental data of the unsteady turbulent channel flow .....	14-1
<i>M. Hartmann, C. Völtz, D. Ronneberger</i>	
Second-moment modelling of periodic and transient pipe flow .....	14-6
<i>M. A. Cotton, A. W. Guy, B. E. Launder</i>	
Relaxation process of 2D asymmetric turbulent channel flow subjected to sudden replacement of smooth and rough walls .....	14-12
<i>M. Miyata</i>	
Turbulence Measurements in a rough wall boundary layer .....	14-18
<i>S. Young, D.J. Bergstrom</i>	
Drag reduction in turbulent MHD pipe flows .....	14-22
<i>P. Orlandi</i>	

## SESSION 15 - APPLICATIONS I 15-1

Combined P.I.V. and L.D.V. analysis of the evolution and breakdown of a compressed tumbling vortex .....	15-1
<i>D. Marc, J. Boree, R. Bazile, G. Charnay</i>	
Compression of a turbulent vortex flow .....	15-7
<i>O. Le Roy, L. Le Penven</i>	
Analytical and direct numerical study of the evolution and breakdown of a compressed tumbling vortex .....	15-13
<i>J. Boree, A. Corjon, D. Marc</i>	
Evolution of cylinder spin-down turbulence subjected to a single-stroke compression: experiments and modelling .....	15-19
<i>K. Hanjalic, S. Jakirlic, C. Tropea, J. Volkert</i>	
A model defroster flow .....	15-25
<i>K. Willenborg, J.F. Foss, R. AbdulNour, J.J. McGrath, B. AbdulNour</i>	

<b>SESSION 16 - DNS AND LARGE EDDY SIMULATION - I</b>	<b>16-1</b>
Stimulated small scale SGS model and its application to channel flow .....	16-1
<i>K. B. Shah, J. H. Ferziger</i>	
Subgrid-scale modeling based on the generalized scale-similarity models .....	16-7
<i>K. Horiuti</i>	
A subgrid-scale model for nonpremixed turbulent combustion .....	16-13
<i>A. W. Cook, J. J. Riley, S. M. deBruynKops</i>	
Large-eddy simulation of turbulent reactive flows .....	16-19
<i>F. Mathey, J.P. Chollet</i>	
A priori testing of subgrid-scale models in anisotropic homogeneous turbulence .....	16-25
<i>A. Juneja, J. G. Brasseur</i>	
 <b>SESSION 17 - INSTABILITY AND TRANSITION</b>	 <b>17-1</b>
Large-scale instability and small-scale transition in vortex pairs .....	17-1
<i>T. Leweke, C. H. K. Williamson</i>	
Transition to turbulence in the wakes of axisymmetrical objects .....	17-7
<i>M. Provansal, D. Ormieres</i>	
Distinct modes of small-scale instability in wake transition .....	17-12
<i>C. H. K. Williamson, T. Leweke</i>	
Absolute instability of round heated air jet .....	17-18
<i>A. Boguslawski, S. Drobnik</i>	
Instability induced by a roughness .....	17-24
<i>K. Ono, T. Motohashi</i>	
 <b>SESSION 18 - COMBUSTION I</b>	 <b>18-1</b>
Reynolds stress closures for strongly swirling combustng jets .....	18-1
<i>T. Landefeld, A. Kremer, E. P. Hassel, J. Janicka</i>	
A multi-scalar PDF method for SI engine combustion simulation .....	18-7
<i>R. Tatschl</i>	
Turbulence statistics and scalar transport in highly-sheared premixed flames .....	18-13
<i>D. Duarte, P. Ferrao, M. V. Heitor</i>	
An experimental study on the consecutive and competing reaction in a turbulent liquid jet by the light absorption spectrometric method .....	18-19
<i>Y. Sakai, I. Nakamura, T. Kubo</i>	
Extended self-similarity and intermittency in turbulent combustion .....	18-25
<i>D. Queiros-Conde</i>	

**SESSION 19 - APPLICATIONS II**

19-1

Vortex formation processes in open channel flows with a side discharge by using the nonlinear k- $\epsilon$  model .....

*T. Hosoda, Y. Muramoto, I. Kimura*

Numerical simulation and experimental validation of the turbulent combustion and perlite expansion processes in an industrial perlite expansion furnace .....

*A. Klipfel, M. Founti, K. Zahringer, J. P. Martin, J. P. Petit*

Generation of longitudinal vortices in internal flows with an inclined impinging jet and enhancement of target plate heat transfer .....

*K. Suzuki, K. Nakabe, A. Higashio, J. S. Acton, W. Chen*

Physical and numerical modeling of turbulent flow over complex topography .....

*A. Nakayama, H. Noda*

Experimental investigation of flow near friction screens .....

*P. Sullivan, T. Oshinowo, D. C. S. Kuhn, Z. Huang*

**SESSION 20 - STRATIFIED FLOWS**

20-1

The effect of stable density stratification on the dynamics of turbulent channel flow .....

*O. Iida, N. Kasagi, Y. Nagano*

Heat Transfer in a stably stratified shear flow .....

*T. Kanzaki, Y. Ichikawa*

Importance of third-moment modelling in horizontal, stably stratified flows .....

*T. J. Craft, J. Kidger, B. E. Launder*

Modeling of turbulent transport in PBL with third-order moments .....

*B.B. Ilyushin, A.F. Kurbatskii*

Mixing in a stably-stratified shear layer .....

*C. Staquet, K. B. Winters*

**SESSION 21 - COMBUSTION II**

21-1

Large eddy simulation of a turbulent non-premixed flame .....

*N. Branley, W. P. Jones*

Analysis of flame surface density concepts in non-premixed turbulent combustion using direct numerical simulations .....

*E. Van Kalmthout, D. Veynante*

Large eddy simulations of turbulent premixed flames based on the G-equation and a flame front wrinkling description .....

*J. Piana, F. Ducros, D. Veynante*

Modeling of turbulent convection in joint pdf equation. Applications for turbulent premixed combustion .....

*F. Galzin, T. Mantel, G. Borghi*

Effects of unstable stratification and mean shear on the chemical reaction in grid-generated turbulence .....	21-25
<i>S. Komori, K. Nagata</i>	

<b>SESSION 22 - JETS I</b>	<b>22-1</b>
----------------------------	-------------

Measured Reynolds stress distributions and energy budgets of fully pulsed round free jets and comparisons with k-e model predictions .....	22-1
<i>K. Bremhorst, P. Gehrke, S. He</i>	

Vortical structure of an acoustically forced plane jet: bi-orthogonal eddies vs. physical eddies .....	22-7
<i>D. Faghani, A. Sevrain, H.-C. Boisson</i>	

Entrainment and mixing patterns in coflowing forced jets subjected to axial and azimuthal forcing .....	22-12
<i>K. P. Prestridge, J. C. Lasheras</i>	

Sensitivity of impinging turbulent jets to the external disturbances .....	22-18
<i>S. V. Alekseenko, A. V. Bilski, D. M. Markovich, V. I. Semenov</i>	

Large eddy simulation of plane impinging jets .....	22-24
<i>M. Tsubokura, T. Kobayashi, N. Taniguchi</i>	

**POSTER SESSION 2**

P2-1

New first-order closure models for stably stratified flows ..... P2-1  
*B. Abart, J.-F. Sini*

Numerical simulation of diurnal atmospheric flow variations in a coastal complex terrain  
area and comparison of results with field observations ..... P2-7  
*K. Sada, Y. Ichikawa, K. Asakura*

Experimental study of internal waves in the stratified shear flow between two immiscible  
layers ..... P2-13  
*M. Keicher, A. M. K. P. Taylor*

Numerical prediction of performance of annular jet pump ..... P2-19  
*N. Namiki, O. Kitamura, M. Yamamoto*

Fuel-air ratio influence on mixing processes in turbulent premixed acetylene flame ..... P2-25  
*V. V. Bakic, S. N. Oka, A. A. Acanski, M. M. Stefanovic*

Role of mean strain and turbulent diffusion in early turbulent premixed flame growth ..... P2-30  
*T. Mantel, F. Galzin, R. Borghi*

Modelling of variable density effects in the second moment and dissipation equations in  
turbulent premixed flames ..... P2-36  
*R. P. Lindstedt, E. M. Vaos*

Direct numerical simulation of 2-D compressible chemically reacting mixing layer with  
compact difference scheme ..... P2-42  
*G. Cai, F. Zhuang, D. Fu*

Two-point velocity measurements in nonreacting and reacting turbulent stagnation flows P2-43  
*E. Bourguignon, Y. Michou, I. Gokalp*

Characteristics of the turbulent flow in pipes with helical turbulence promoters ..... P2-49  
*K. F. F. Vicari, S. V. Möller*

Turbulent structure of an intermittent region of the turbulent boundary layer interacting  
with controlled longitudinal vortex arrays ..... P2-55  
*C. Fukushima, H. Osaka, G. Nedelcu*

Effect of local blowing on the instability of channel flow ..... P2-61  
*Y. M. Chung, H. J. Sung, A. V. Boiko*

Turbulent velocity profiles in gravel bed rivers ..... P2-67  
*G. M. Smart*

Computation with the k- $\epsilon$  model with turbulent mass transfer in the wall-region ..... P2-71  
*B. Chaouat*

Investigation of the bursting phenomenon in transitional boundary layers ..... P2-77  
*V. Uruba, P. Jonas, O. Mazur*

Computation of turbulent flows using upwind-bias 5th order schemes ..... P2-83  
*P.G.Huang*

Development of a non-linear, strain-sensitive k- $\omega$  turbulence model ..... P2-89  
*D. Sofialidis, P. Prinos*

Proposal of a low-Reynolds-number two-equation model to predict dynamic and thermal field .....	P2-95
<i>C. B. Hwang, C. A. Lin</i>	
Near wall modellization for dissipation equation in second-moment turbulence closures .	P2-101
<i>G. B. Deng, M. Visonneau</i>	
Calibration of models for the slow pressure-strain rate using LES .....	P2-107
<i>K. Alvelius, M. Hallbäck, A. V. Johansson</i>	
L.R.N. k-e model for prediction of turbulent boundary layers, developing under strong pressure gradient conditions .....	P2-113
<i>E. V. Shishov, A. I. Leontiev, A. V. Gerasimov</i>	
Experimental and computational study of pressure effects on turbulent flow in an asymmetric plane diffuser .....	P2-114
<i>L. Brunet, J. B. Cazalbou, P. Chassaing, L. Jervase</i>	
Mixing in coaxial jets with large density differences .....	P2-120
<i>M. Favre-Marinet, E. B. Camano, J. Sarboch</i>	
Simulation of two-dimensional structures in variable density coaxial jets .....	P2-126
<i>P. Reynier, A. Kourta, H. Ha Minh</i>	

## **AUTHOR INDEX**

**VOLUME 1:   SESSIONS 1 - 10  
              POSTER SESSION 1 (P1)**

**VOLUME 2 :   SESSIONS 11 - 22  
              POSTER SESSION 2 (P2)**

**VOLUME 3 :   SESSIONS 23 - 34  
              POSTER SESSION 3 (P3)**

Abart B. , P2.1  
 Abdel Gawad A. F., P1.1  
 Abdel Latif O. E., P1.1  
 AbdulNour B., 15.25  
 AbdulNour R., 15.25  
 Acanski A. A., P2.25  
 Acton J. S., 19.13  
 Alboussiere T., 5.7  
 Alekseenko S. V., 22.18  
 Alvelius K., P2.107  
 Amano R. S., P1.18  
 Amielh M., 12.18  
 An P., P1.83  
 Andersson H. I., 34.6, 34.12  
 Anselmet F., 4.7, 12.18  
 Antonia R. A., 2.1, 4.7, 10.16, P3.117  
 Apsley D. D., 6.25  
 Arad E., P3.77  
 Arroyo G., 5.1  
 Asakura K., P1.61, P2.7  
 Aubrun S. , 30.1  
 Aupoix B., 6.1, 13.24  
 Ayrault M., P1.67  
 Bakic V. V., P2.25  
 Banerjee S., 27.24  
 Barakos G., 32.19  
 Barré C., 24.17  
 Bataille F., P3.1, P3.65  
 Bazile R., 15.1  
 Bech K. H., 34.6  
 Beguier C., P3.122  
 Beharelle S., 2.25  
 Bellettre J., P3.1  
 Benaissa A., P3.113  
 Bergstrom D. J., 14.18, 23.24  
 Bertoglio J. P., 32.13, P3.65  
 Bezard H., 13.24  
 Bilger R. W., 07.24  
 Biłski A. V., 22.18  
 Blaisdell G. A., 29.14  
 Boguslawski A., 17.18  
 Boiko A. V., P2.61  
 Boisson H.-C., 22.7, 30.1  
 Boniforti M. A., P1.106  
 Bonnet J.-P., 2.25, 5.1, 33.25, P1.55  
 Boree J., 15.1, 15.13  
 Borghi R., 7.18, 21.19, P2.30  
 Bouhadji A., P1.31  
 Bourguignon E., P2.43  
 Branley N., 21.1  
 Brasseur J. G., 16.25  
 Braza M., P1.31  
 Breard C., P1.25  
 Bremhorst K., 22.1  
 Breuer M., 26.7  
 Brun C., 25.23, P1.89  
 Brun G., 32.25  
 Brunet L., P2.114  
 Brunvoll A. S., 34.12  
 Cadiou A., 23.13  
 Cai G., P2.42  
 Calmet I., 8.24  
 Camano E. B., P2.120  
 Cambon C., 31.7  
 Carles P., 30.1  
 Carvalho I. S., 27.6  
 Castaldi S., 12.24  
 Cazalbou J. B., P2.114  
 Chaouat B., P2.71  
 Charnay G., 15.1  
 Chassaing P. , 12.24, P2.114  
 Chen J. C., P3.59  
 Chen K. H., 31.1  
 Chen W., 19.13  
 Chen W. L., 1.13  
 Choi H., P1.37, P3.107  
 Choi Y. D., P3.47  
 Chollet J. P., 16.19  
 Chun K. B., 26.13  
 Chun K. H., P3.47  
 Chung Y. M., P2.61  
 Ciliberto S., 23.19  
 Cioni S., 23.19  
 Citriniti J. H., 5.12, 5.18  
 Clancy P., 29.1  
 Coleman G. N., 33.1  
 Comte P., 1.1  
 Cook A. W., 16.13  
 Cordier L., P1.101  
 Corjon A., 15.13  
 Cotton M. A., 14.6  
 Coulomb J., 30.1  
 Cousteix J., 6.1, 13.24  
 Craft T.J., 20.13, 30.19  
 Daisaka H., P1.49  
 Davidson L., 26.1  
 De Angelis V., 27.24  
 De Chanterac L., 32.1  
 de Souza F., 33.25, P1.55  
 deBruynKops S. M., 16.13  
 deGraaff D. B., 1.19  
 Dejoan A., 30.25  
 Delcayre F., 26.24  
 Delville J., 2.25, 5.1, 33.25, P1.55, P1.101  
 Deng G. B., P2.101  
 Deniau H., 29.19  
 Deutsch E., P3.22  
 Doussinault M., 6.1  
 Dreier T. M., 24.1  
 Drikakis D., 32.19  
 Drobniak S., 17.18  
 Duarte D., 18.13



Dubief Y., 1.1  
 Ducros F., 21.13, 28.1  
 Dumont T., 10.11  
 Dupont P., 29.8  
 Durbin P. A., 6.19  
 Durst F., 2.13  
 Dussauge J. P., 29.8  
 Eaton J. K., 1.19, 8.13  
 Eifert C., 3.1  
 Elkins C. J., 8.13  
 Engel K., P1.11  
 Eulitz F., P1.11  
 Ewing D., 5.12, P3.113  
 Faghani D., 22.7  
 Fauchet G., 32.13  
 Favre Marinet M., 12.1, P2.120  
 Ferrao P., 18.13  
 Ferre J. A., 2.7, P1.95  
 Ferziger J. H., 16.1  
 Foss J. F., 15.25  
 Founti M., 19.7  
 Friedrich R., 33.19  
 Fu D., P2.42  
 Fu S., 6.7  
 Fu S. R., 13.1  
 Fujisawa N., 9.13  
 Fukushima C., P2.55  
 Fureby C., 28.13  
 Galzin F., 21.19, P2.30  
 Gareem J.-H., 5.1  
 Gatski T. B., 13.7  
 Geffroy P., 29.7  
 Gehrke P., 22.1  
 Gerasimov A. V., P2.113  
 Gibson M. M., 31.19  
 Giralt F., P1.95  
 Girimaji S. S., P1.118  
 Givi P., 24.17  
 Gleyzes C., 6.1  
 Godeferd F. S., P3.53  
 Gokalp I., 12.6, 12.12, P2.43  
 Gonzalez M., 7.18  
 Gooden J. H. M., 6.1  
 Gosman A. D., 28.13  
 Graftieaux L., 28.25  
 Guy A. W., 14.6  
 Ha Minh H., 30.1, P2.126  
 Hadjadj A., 32.1  
 Hagiwara Y., 28.19  
 Hahn S., P1.37  
 Haidous Y., 12.12  
 Hallback M., 8.1, P2.107  
 Hamba F., 32.7  
 Hana H., 28.19  
 Hanjalic K., 11.16, 15.19, 23.13  
 Hanratty T. J., 9.25, 11.7  
 Harion J. L., 12.1  
 Harper R. D., 31.19  
 Harran G., 12.24  
 Hartmann M., 14.1  
 Hassel E. P., 18.1  
 Hauville F., P1.25  
 Hayashi I., 24.11  
 He S., 22.1, P1.83  
 Heinz S., 23.13  
 Heitor M. V., 18.13, 27.6  
 Heitz D., 5.1  
 Henkes R. A. W. M., 31.13, 33.13  
 Henningson D. S., 33.13  
 Herard J. M., 32.25  
 Herbert V., 10.7  
 Higashio A., 19.13  
 Hishida K., 24.11, P1.49  
 Hopfinger E. J., 25.7, 27.1  
 Horiuti K., 16.7  
 Hosoda T., 19.1  
 Houra T., 33.7  
 Howard R. J. A., P3.29  
 Huang P. G., P2.83  
 Huang S., P3.122  
 Huang X., 23.24  
 Huang Z., 19.25  
 Huberson S., P1.25  
 Humphrey J. A. C., P3.47  
 Hwang C. B., P2.95  
 Iacovides H., 3.19  
 Ichikawa Y., 20.7, P1.61, P2.7  
 Iida O., 20.1  
 Ikeda J., 4.17, P1.77  
 Ilyushin B. B., 20.19  
 Jackson J. D., P1.83  
 Jacobitz F. G., 23.1  
 Jacquin L., 29.7  
 Jakirlic S., 15.19  
 Jan P. Y., 25.11  
 Janicka J., 3.1, 18.1, 25.17  
 Jeandel D., 32.25  
 Jervase L., P2.114  
 Johansson A. V., 8.1, 13.13, P2.107  
 Joia I. A., P3.6  
 Joly L., 12.24  
 Jonas P., P2.77  
 Jones W. P., 3.25, 21.1  
 Jongen T., 13.7  
 Jovanovic J., 2.13  
 Juneja A., 16.25  
 Kang H. S., P3.107  
 Kanzaki T., 20.7  
 Kasagi N., 9.7, 9.18, 20.1, P1.43  
 Kassinos S. C., 7.1

Kawaguchi Y., P1.49	Liu N.-S., 31.1
Kawahara G., 1.7	Lollini L., 28.25
Kawamura H., 8.7	Lombardi G., 25.1, 27.24
Keffer J. F., P1.95	Lucas J. F., 12.18
Keicher M., P2.13	Lumley J. L., 31.1
Kent J. H., 7.24	Ly T., 25.11
Khris S., P1.19	Machiels L., 4.23, 13.7
Kida S., 1.7	Maeda M., P1.49
Kidger J., 20.13	Magnaudet J., 8.24
Kim D. S., P1.71	Mantel T., 21.19, P2.30
Kim J., 33.1	Marc D., 15.1, 15.13
Kim J. H., 29.1	Marchal P., 5.1
Kimura I., 19.1	Marcillat J., P1.19
Kinselbach W., 24.1	Marcu B., 24.5
Kitamura O., P2.19	Marie J. L., P3.16
Kitoh O., 11.10	Markovich D. M., 22.18
Klipfel A., 19.7	Marquis A. J., 3.7
Kobayashi T., 22.24	Martin J. P., 19.7
Koch R., P1.7	Martinelli L., P3.77
Kohnen G., P3.23	Martinez C., 27.12
Komori S., 21.25	Martinuzzi R. J., 11.16, 26.18
Kopp G. A., P1.95	Mashayek F., 24.17
Kourta A., P2.126, P3.35, P3.71	Massah H., 9.24
Kremer A., 18.1	Mathey F., 16.19
Kronenburg A., 7.24	Mazur O., P2.77
Kubo T., 18.19	McComb W. D., 4.23
Kuhn D. C. S., 19.25	McDonough J. M., P3.89
Kurbatskii A. F., 20.19	McGrath J. J., 15.25
Lakehal D., 3.13	Meiburg E., 24.5
Lallemand A., P3.1	Meinders E. R., 11.16
Lamballais E., 28.7	Menzies K. R., 3.25
Landenfeld T., 18.1	Messing R., 13.24
Larcheveque M., 10.7	Metais O., 25.23
LaRue J. C., 25.11	Michard M., 28.25
Lasheras J. C., 22.12, 27.1, 27.12	Michelot C., P1.67
Lauder B. E., 14.6, 20.13	Michou Y., P2.43
Lavieville J., P3.22	Minier J. P., P1.112
Le Penven L., 15.7	Mito Y., 9.7
Le Roy O., 15.7	Miyake Y., 11.1
Leblanc S., P3.53	Miyata M., 14.12
Lee D. H., P1.71	Miyauchi T., 4.17
Lejeune C., P3.71	Miyazaki T., P1.102
Leontiev A. I., P2.113	Möller S. V., P2.49
Leschziner M. A., 1.13, 6.25	Moreau R., 5.7
Lesieur M., 28.7	Morel C., P3.10
Leuchter O., 31.7	Morganti M., P1.106
Lewalle J., 33.25	Morikawa T., 11.1
Leweke T., 17.1, 17.12	Moschetta J. M., 29.19
Li H., P3.101	Motohashi T., 17.24
Li J., P1.83	Muramoto Y., 19.1
Lien F. S., 1.13, 6.19	Muscat P., 29.8
Lin B., P1.18	Nagano Y., 20.1, 33.7
Lin C. A., P2.95, P3.59	Nagata K., 21.25
Lindstedt R. P., P2.36	Nakabayashi T., 9.13, 11.10
Liou W. W., 31.1	Nakabe K., 19.13

Nakagawa S., 2.19  
 Nakamura I., 18.19  
 Nakayama A., 19.19  
 Namiki N., P2.19  
 Nedelcu G., P2.55  
 Nemoda S., P3.41  
 Nguyen P. N., 5.24  
 Nicolleau F., 4.13  
 Nicoud F., 28.1  
 Nieuwstadt F. T. M., 23.7  
 Nishimura F., 11.10  
 Nitta K., 2.19  
 Noda H., 19.19  
 Nozawa K., P3.95  
 Oberlack M., 10.21  
 Ohsaka K., 8.7  
 Oka S. N., P2.25  
 Ong L. Y., 3.7  
 Ono K., 17.24  
 Orlandi P., 14.22  
 Ormieres D., 17.7  
 Ory E., 24.23  
 Osaka H., P2.55  
 Oshinowo T., 19.25  
 Ould-Rouis M., 4.7  
 Page J., 12.12  
 Papavassiliou D. V., 11.7  
 Park J., P1.37  
 Parneix S., 6.19  
 Pearson B. R., P3.117  
 Perkins R. J., 24.23, P3.6, P3.16  
 Petit J. P., 19.7  
 Pettersson B. A., 34.12  
 Pfuderer D. G., 3.1  
 Piana J., 21.13  
 Picut M., P1.89  
 Pietri L., 12.18  
 Pinheiro J., 7.18  
 Pollard A., 11.22, P3.113  
 Pomponio S., 30.7  
 Pons M. D., 2.7  
 Pozorski J., P1.112  
 Prestridge K. P., 22.12  
 Prinos P., P2.89  
 Priymak V.G., P1.102  
 Protas B., 10.1  
 Provansal M., 17.7  
 Queiros-Conde D., 18.25  
 Querzoli G., 30.7  
 Ragab S. A., P1.1  
 Rahai H., 25.11  
 Raynal L., 27.1  
 Rehab H., 25.7  
 Renouard D., 34.18  
 Rewerts J., 25.17  
 Rexroth C. H., P1.7  
 Reynier P., P2.126  
 Reynolds W. C., 7.1  
 Riley J. J., 16.13  
 Ristorcelli J.R., 7.7, 29.14  
 Robert R., 10.11  
 Rodi W., 3.13  
 Romano G. P., 30.7  
 Ronneberger D., 14.1  
 Rubinstein R., 31.25  
 Rung T., 6.7, 13.1  
 Sabelnikov V., P1.67  
 Sada K., P1.61, P2.7  
 Saint Martin V., 13.24  
 Sakai Y., 18.19  
 Sakiz M., P3.22  
 Salvetti M. V., 25.1  
 Samimy M., 29.1  
 Sanders J. P. H., 12.6  
 Sandham N., 28.13  
 Sandham N. D., P3.29  
 Santos D., 27.6  
 Sarboch J., P2.120  
 Sardi K., 8.19  
 Sarh B., 12.12  
 Sarkar S., 23.1  
 Satake S., P1.43  
 Sato Y., 24.11  
 Schiestel R., 30.25  
 Schönfeld T., 28.1  
 Sciortino G., P1.106  
 Semenov V. I., 22.18  
 Senda M., 2.19  
 Sevrain A., 22.7  
 Shaalan M. R., P1.1  
 Shah K. B., 16.1  
 Shao L., 32.13  
 Shih T.-H., 31.1  
 Shima N., 7.12  
 Shimomura Y., 34.1  
 Shin J. K., P3.47  
 Shishov E. V., P2.113  
 Sijercic M., P3.41  
 Silvestrini J. H., 28.7  
 Simoens S., P1.67  
 Simonin O., 27.18, P3.22  
 Sini J. F., P2.1  
 Sirovich L., 4.1  
 Skote M., 33.13  
 Smart G. M., P2.67  
 Sofialidis D., P2.89  
 Sommerfeld M., P3.23  
 Sommeria J., 10.11, 23.19  
 Song H. B., P1.71  
 Sotiropoulos F., 34.24

Spalart Ph. R., 30.13, 33.1  
 Squires K. D., 6.13, 27.18  
 Staquet C., 10.7, 20.25  
 Starke A. R., 31.13  
 Stefanovic M. M., P2.25  
 Strelets M. Kh., 30.13  
 Suga K., 13.18  
 Sullivan P., 19.25  
 Sung H. J., 26.13, P2.61  
 Suzuki Y., 9.18, 19.13  
 Tabor G., 28.13  
 Takashina Y., 28.19  
 Talamelli A., 25.1  
 Tamura T., P3.95  
 Tanahashi M., 4.17  
 Tanaka M., 1.7, 28.19  
 Taniguchi N., 22.24  
 Tarbouriech L., 34.18  
 Tardu S., 9.1, 12.1  
 Tarman I. H., 4.1  
 Tatschl R., 18.7  
 Taulbee D. B., 24.17  
 Taylor A. M. K. P., 8.19, P2.13  
 Tenaud C., P1.101  
 Theodoridis G. S., 3.13  
 Thiele F., 6.7, 13.1  
 Thivet F., 29.19  
 Tran-Cong S., P3.16  
 Tropea C., 15.19  
 Tsang W. K., 2.1  
 Tsubokura M., 22.24  
 Tsuji T., 33.7  
 Tsujimoto K., 11.1  
 Tummers M. J., 31.13  
 Uhlmann M., 32.25  
 Urbin G., 25.23  
 Uruba V., P2.77  
 Ushijima T., P3.6  
 Uspenski V., 5.7  
 Van Kalmthout E., 21.7  
 Vandromme D., 32.1  
 Vaos E. M., P2.36  
 Vassilicos J. C., 4.13  
 Vedy E., 30.25  
 Veldman A. E. P., P3.83  
 Ventikos Y., 34.24  
 Verstappen R. W. C. P., P3.83  
 Versteegh T. A. M., 23.7  
 Veynante D., 21.7, 21.13  
 Vicari K. F. F., P2.49  
 Villiermaux E., 25.7, 27.1  
 Virant M., 24.1  
 Visonneau M., P2.101  
 Volkert J., 15.19  
 Völtz C., 14.1  
 Voutsinas S. G., P1.25  
 Wagner C., 33.19  
 Wallin S., 13.13  
 Wang Q., 27.18  
 Warholc M., 9.24  
 Weatherly D. C., P3.89  
 Webster D. R., 1.19  
 Weinberger C., 25.17  
 Weller H. G., 28.13  
 Wesfreid J. E., 10.1  
 Wikstrom P. M., 8.1  
 Willenborg K., 15.25  
 Williamson C. H. K., 17.1, 17.12  
 Winters K. B., 20.25  
 Wittig S., P1.7  
 Wolfshtein M., 28.13  
 Wu K. C. Q., 26.18  
 Wu X., 6.13  
 Wunenburger R., 32.13  
 Xu H., 11.22  
 Yabe A., P1.49  
 Yamagami K., 2.19  
 Yamamoto K., 8.7  
 Yamamoto M., P2.19  
 Yanase S., 1.7  
 Yang T. J., 4.23  
 Yasuda R., P1.77  
 Ye Q. Y., 2.13  
 Yoo J. Y., P3.107  
 Yoon S. H., P1.71  
 Yoshikawa T., 11.1  
 Young A., 4.23  
 Young S., 14.18  
 Younis B. A., 31.25  
 Zahringer K., 19.7  
 Zhai Z., 6.7  
 Zhou T., 10.16  
 Zhou Y., 2.1, 31.25, P3.65  
 Zhu J., 31.1  
 Zhu Y., 4.7, 10.16  
 Zhuang F., P2.42

## **SESSION 11 - WALL FLOWS I**

# ON CLUSTERING OF QUASI-STREAMWISE VORTICES IN NEAR-WALL TURBULENCE

Y. Miyake, K. Tsujimoto, T. Yoshikawa

Department of Mechanical Engineering

Osaka University

2-1, Yamada-oka, Suita, 565

Japan

T. Morikawa

Yamaha Motor Co., LTD

2500, Singai, Iwata, 438

Japan

## INTRODUCTION

Coherent structure is a remarkable feature observed in near-wall turbulence as demonstrated by beautiful pictures obtained from computer graphics of a highly resolved numerical simulation (Robinson *et al.* (1991)). Today, it is well established that quasi-streamwise vortices which have their axis nearly in the flow direction play a key role there. The behavior of individual quasi-streamwise vortex such as its birth, growth, attenuation, regeneration, etc. has been investigated extensively (Smith *et al.* (1991), Brooke & Hanratty *et al.* (1993), Bernard *et al.* (1993), Miyake *et al.* (1996, 1997)). However, coherent structure is not uniquely defined but is defined in many different manners depending on point of view. That is, in addition to individual quasi-streamwise vortices, there exist coherent structures of different kinds which should attract one's attention as to be responsible for controlling near-wall turbulence. The topic mentioned in this paper is concerned with clustering or grouping of quasi-streamwise vortices which is a novel concept and has no reports thus far.

In the present paper, a fact that quasi-streamwise vortices are not distributed homogeneously but densely populated in some places and less elsewhere, in a layer close to the wall is shown at first by referring to a DNS data for a channel flow. Then, that regeneration property of quasi-streamwise vortices is one of the crucially important possible mechanisms for this clustering is shown by a simplified non-dynamical simulation. Next, a wavelet decomposition of quasi-streamwise vortices in two scale-based groups is shown. The interaction between vortices of two groups indicates that individual quasi-streamwise vortices can not survive long without assistance of surrounding large scale structure which is adapted for them. Thus, it is pointed out that large scale structure around a cluster of vortices is an important coherent structure to be investigated more in detail.

## CLUSTERING OF QUASI-STREAMWISE VORTICES

A direct numerical simulation of a channel flow was carried out using a computational volume which is long enough in streamwise direction to avoid interference of inlet

and outlet sections possibly caused by periodic condition and to allow us to observe long evolution of vortical field. The size  $h^+ = hu_\tau/\nu$  in wall unit, of the computational box in each direction is  $h_x^+ = 4608, h_y^+ = 300, h_z^+ = 576$  where  $x, y, z$  are streamwise, wall-normal and cross-stream direction, respectively and  $u_\tau$  is mean wall friction velocity and  $\nu$ , kinematic viscosity. The Reynolds number  $Re_\tau = u_\tau h_y/\nu = 300$ . The grid number is  $256 \times 64 \times 64$  in  $x, y, z$  direction, respectively. The numerical scheme used in the code is described in Kajishima *et al.* (1997).

Figs.1(a)(b) show an evolution of distribution of quasi-streamwise vortices at six consecutive time instants. That is, each long strip in the figure is a plan view at the time instant  $\Delta t^+ = 30$  after that of the one next to its left and shows a plan view of quasi-streamwise vortices of  $|\omega_x^+| \geq 0.2$ , included in the bottom half computational. Conducting smoothing operation to Fig.1(a) by

$$\bar{f} = \frac{1}{H} \int_{-\Delta\xi}^{\Delta\xi} \int_{-\Delta\zeta}^{\Delta\zeta} f(x+\xi, y, z+\zeta) d\xi d\zeta \quad (1)$$

where  $H = 4\Delta\xi\Delta\zeta$ ,  $\Delta\xi = 50, \Delta\zeta = 20$ , we obtain Fig.1(b). The shaded area in Fig.1(b) is  $|\omega_x^+| \geq 0.135$ . Obviously, the population density of quasi-streamwise vortices is not homogeneous but enhanced islands are found and as shown by rectangulars labeled A, B, C, some are growing and some others are decaying. The clusters are convected downstream, changing their configuration gradually. Compared with mean lifetime of an individual vortex which is known to be about 150 in  $t^+ = tu_\tau^2/\nu$ , clusters live longer.

The densely populated area of vortices are located in the layer close to the wall, between  $y^+ = 10 \sim 50$  and does not modify strongly the mean flow above it. For example, mean velocity distribution normal to the wall in the clustered region manifests no visible difference from that in non-clustered one. However, fluctuation of flow is enhanced significantly inside cluster region. Conducting the smoothing by eq.(1) for each  $y$ -plane and specifying threshold value of  $|\omega_x^+|$  as 0.135 as before, one obtain three dimensional volume of vortex clusters. Mean values of turbulence inside these volume and those outside are as follows :  $u'_{rms} = (2.07, 1.49), v'_{rms} = (0.87, 0.58), w'_{rms} = (1.19,$

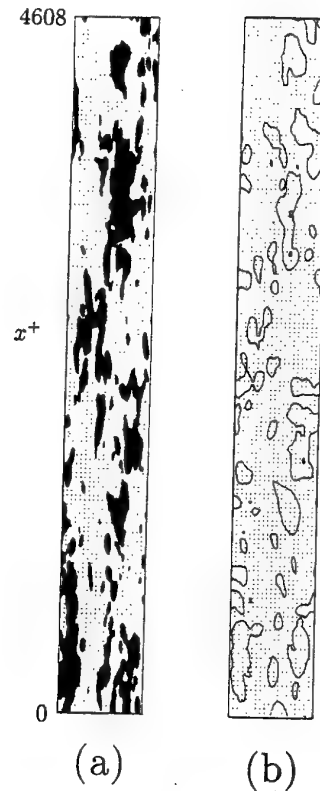
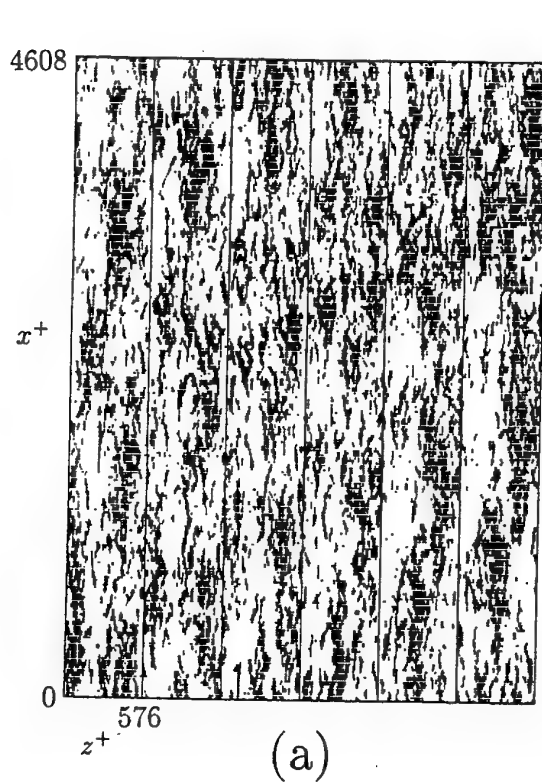


Fig.2 Similarity of distribution of fluctuating pressure on the wall and quasi-streamwise vortices, filtered by eq.(1). (a) : Quasi-streamwise vortices of  $|\omega_x^+| \geq 0.135$  (the left-end strip in Fig1(b)). (b) : Fluctuating pressure  $|p'^+| \geq 1.4$ , both at the instant of the left-end strip of Fig.1.

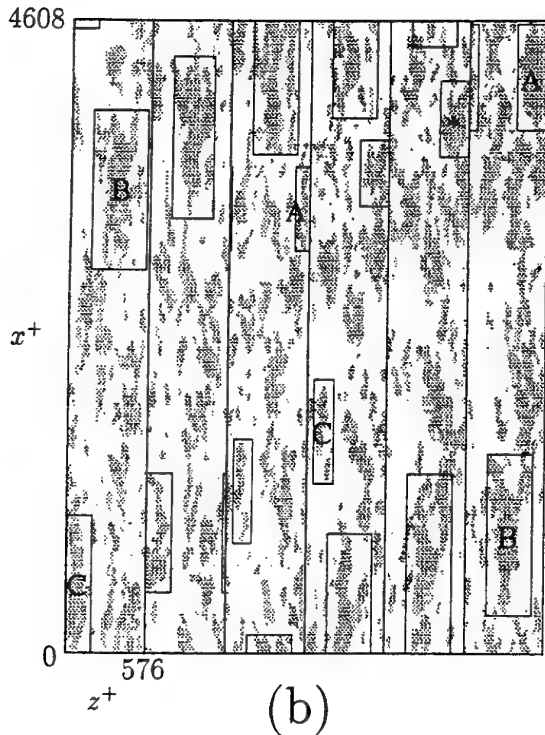


Fig.1 Evolution of distribution of quasi-streamwise vortices. Each long strip is a plan view at the time instant  $\Delta t^+ = 30$  after that of the one next to its left, (a) : quasi-streamwise vortices of  $|\omega_x^+| \geq 0.2$ , (b) : filtered quasi-streamwise vortices of  $|\omega_x^+| \geq 0.135$  by eq. (1)

0.71),  $(u'v')_{rms}^+ = (2.13, 1.00)$ ,  $P_{k,rms}^+ = (0.45, 0.14)$ ,  $\omega_{x,rms}^+ = (0.22, 0.06)$  where the first numbers in the parenthesis mean inside and the second ones, outside and  $u', v', w'$  are  $x, y, z$ -wise fluctuating velocity component, respectively, and  $P_x$ , production rate of  $\omega_x$ . The suffix  $(rms)$  means root mean square value. Obviously, turbulence activity is far stronger inside clustered region. The volume of total clustered region occupies only 2% of the whole computational volume, but 22% of total streamwise vorticity is included inside. High fraction rate of shear stress is to be noted as well.

Corresponding to the intensified turbulence inside cluster, pressure on the wall show correlated distribution with vortex cluster as in Fig.2, despite that pressure is strongly affected by far field.

## FORMATION OF VORTEX CLUSTERS

In order to find out a substantial property concerning how vortex clusters are formed, a simulation which is not based on dynamical condition but on probability condition was carried out. The simulation is done in two-dimensional plane of the same rectangular box as in Fig.1, under the following procedure and assumptions.

1. 30 pieces of straight line vortices are supplied to the flow field every  $\Delta t^+ = 20$ .
2. The locations of the supplied vortices are determined randomly, consulting for random number table.

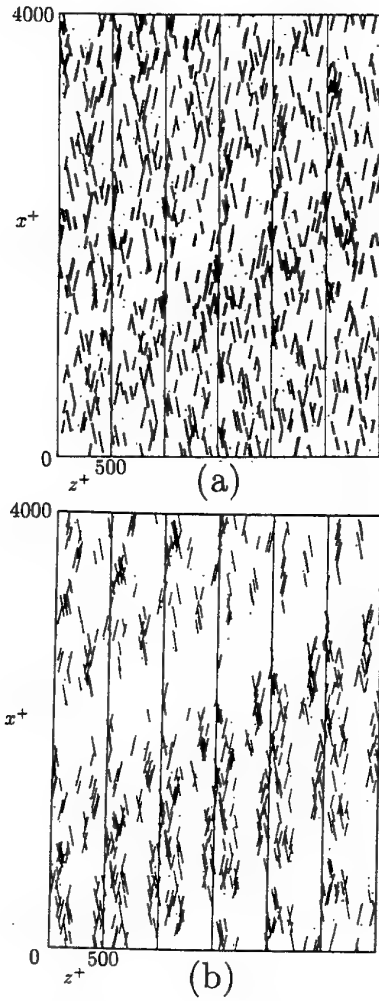


Fig.3 Cluster formation of quasi-streamwise vortices by means of simple probability model on a two-dimensional plane. (a) : Case of randomly supplied vortices, (b) : case of conditionally supplied vortices according to above-described [5].

3. The vortices are convected to downstream with speed  $u_c^+ = 15$ .
4. Each vortex has lifetime of  $\Delta t^+ = 100$  and in its first half, it grows linearly and attains the maximum length  $l^+ = 200$  at  $t^+ = 50$  from its supply and then shrinks linearly, in the latter half.
5. The supplied vortices are allowed only in a certain distance around existing vortices. That is, influential area of each vortex which is  $\Delta s^+ = 20$  from a vortex is defined, only within which a new vortex can be supplied.

Condition [3] mimics the DNS data that vortices are convected with the speed slightly lower than local mean velocity, maintaining its configuration long time. Since we are considering quasi-streamwise vortices in the layer  $y^+ = 10 \sim 35$ , most probable mean convection velocity is  $u_c^+ = 15$ . Condition [4], i.e., both mean lifetime and mean scale of quasi-streamwise vortices are also brought from the DNS data.

If we do not apply the last condition, that is, if new vortex is allowed to be born at any place, no clusterization

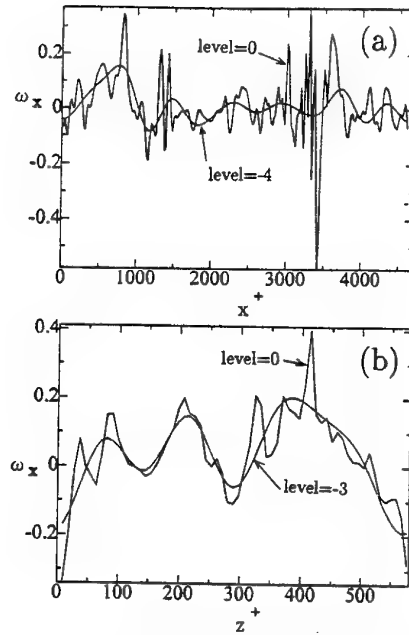


Fig.4 An example of one dimensional wavelet decomposition of  $\omega_x^+$ , in a plane  $y^+ = 15$  and for the time instant of the left-end strip of Fig.1. (a) : Streamwise (level = -4), (b) : spanwise (level = -3).

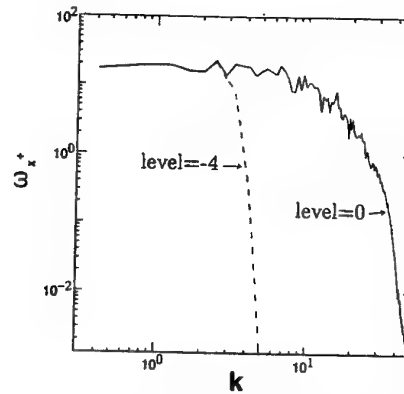


Fig.5 Decomposition of  $\omega_x^+$  in one dimensional spectrum, for the example of Fig.4.

occurs as shown in Fig.3(a) which is depicted in the same manner as Fig.1. But with the last condition, Fig.3(b) is obtained. The left-end strip of Figures 3(a)(b) is at an arbitrary time instant enough long time after the start of simulation and each strip is for  $\Delta t^+ = 20$  after the one next to its left. Fig.3(b) is quite similar to Fig.1(a) and we find that clusters grow as time marches. Since the last condition mimics the fact that new a vortex is usually born under the influence of an existing vortex, or by regeneration, the result indicates strongly that regeneration inherently generates clusterized structure of vortices. If the last condition is relaxed slightly to allow a small fraction of vortex, say 15%, to be born at any place without restriction, the result of the simulation becomes much closer to Fig.1(a).

Although cluster formation may have other mechanism, it is substantially important that commonly observed properties of behavior of quasi-streamwise vortices itemized above can reproduce the process of cluster formation.



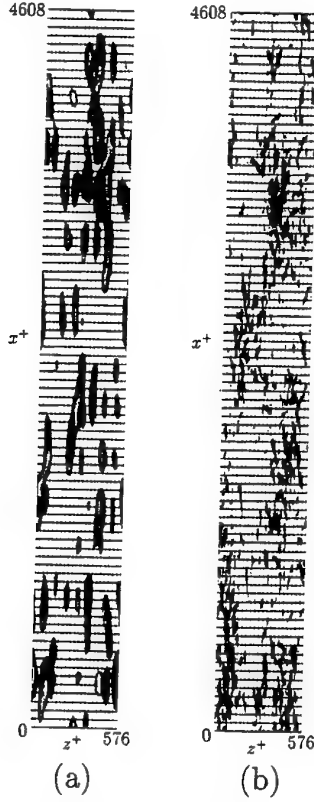


Fig.6 Plan view of decomposed larger and smaller scale quasi-streamwise vortices. (a) Larger scale vortices for the level  $j = 4$  in  $x$  and  $j = 3$  in  $z$  direction, obtained by wavelet transform.  $|\omega_x^+| \geq 0.07$ . (b) smaller scale vortices obtained by subtracting larger scale components of Fig.6(a) from total vortical field.  $|\omega_x^+| \geq 0.2$ .

## DECOMPOSITION OF QUASI - STREAMWISE VORTICES

### Wavelet Transform

In order to investigate larger scale coherent structures surrounding clusters and their role in cluster, wavelet decomposition is introduced.

One dimensional wavelet transformation based on mother function  $\psi[(x-b)/a]$  of a quasi-random function  $f(x)$  which includes local coherency embedded in a pure random function of  $x$  is denoted here  $(W_\psi f)(a, b)$  and is defined by

$$(W_\psi f)(b, a) = \int_{-\infty}^{\infty} \frac{1}{\sqrt{|a|}} \psi\left(\frac{x-b}{a}\right) f(x) dx \quad (2)$$

where  $a, b$  are constants representing scale of coherent length and  $x$ -wise location. The inverse transform of above one is

$$f(x) = \int_{-\infty}^{\infty} (W_\psi f)(b, a) \frac{1}{\sqrt{|a|}} \psi\left(\frac{x-b}{a}\right) \frac{dad b}{a^2} \quad (3)$$

A possible discretized transform and inverse one corresponding to above definition are written as

$$\begin{aligned} d_k^{(j)} &= (W_\psi f)(b, a) = (W_\psi f)\left(\frac{k}{2^j}, \frac{1}{2^j}\right) \\ &= \int_{-\infty}^{\infty} f(x) \overline{\{2^{j/2} \psi(2^j x - k)\}} dx \end{aligned} \quad (4)$$

$$f(x) \sim \sum_j \sum_k d_k^{(j)} \psi(2^j x - k) dx \quad (5)$$

where mother wavelet  $\psi(x)$  must be properly specified so as to satisfy admissible condition or  $\int_{-\infty}^{\infty} \psi(x) dx = 0$ , which is a spline wavelet in this work. Then, a function  $f(x)$  is expressed as linear series expansion of mother wavelet  $\psi$  amplified in scale by  $1/2^j$  and shifted with respect to  $x$  by  $k/2^j$ . Putting

$$g_j(x) = \sum_k d_k^{(j)} \psi(2^j x - k) \quad (6)$$

$$f_j(x) = \sum_k C_k^{(j)} \phi(2^j x - k), \quad (7)$$

above  $f_j(x)$ , are related to  $g_j(x)$  by recurrent form

$$f_j(x) = g_{j-1}(x) + f_{j-1}(x). \quad (8)$$

where scale function  $\phi$  employed here is a basic spline

$$\phi_m(x) = \frac{1}{(m-1)!} \sum_{k=0}^m (-1)^k \binom{m}{k} (x-k)_+^{m-1} \quad (9)$$

with  $m = 4$  and is related to  $\psi$  as  $\psi(x) = \sum_k p_k \phi(2x-k)$ . Consequently, the original function  $f_0(x)$  can be decomposed into large scale component greater than  $j$ -th level and that smaller than it as

$$\begin{aligned} f_0(x) &= g_{-1}(x) + f_{-1}(x) \\ &= g_{-1}(x) + g_{-2}(x) + f_{-2}(x) \\ &= \dots \end{aligned} \quad (10)$$

One dimensional  $x$ -wise decomposition of  $\omega_x^+$  field of a shot of the instant of the left-end strip of Fig.1(a) is shown in Fig.4(a) where the signal is that along constant  $z$  in a plane  $y^+ = 15$  and the level is  $j = 4$ . Quickly fluctuating line is original signal representing  $\omega_x^+$  and slowly fluctuating one corresponds to extracted large scale fluctuation. The latter one has peaks with period  $\Lambda_x^+ \simeq 600$  each of which is located at near the center of a cluster of vortices. The separation of these larger and smaller scale fluctuations in spectrum is given in Fig.5. Same operation to spanwise ( $z$ ) direction gives Fig.4(b) which is along spanwise line in a plane  $y^+ = 15$  and the level is  $j = 3$ . It is found that in the spanwise direction also peaks which indicate clusters appear.

The above transform is extended to two - dimensional space of  $x$ - $z$  plane and is applied to the  $\omega_x^+$  field of above-mentioned time instant.

Fig.6(a) is a physical space structure of larger scale structure of quasi-streamwise vortices for the level  $j = 4$  in  $x$  and  $j = 3$  in  $z$  direction, obtained by inverse transform and the threshold value for vorticity is  $|\omega_x^+| = 0.07$ . The rest of the field of quasi-streamwise vortices, or the smaller scale structure, obtained by the same operation as above is shown in Fig.6(b) where threshold is  $|\omega_x^+| = 0.2$ . It is interesting that the latter is quite similar to the original picture of Fig.1(a), which suggests that usual identification of quasi-streamwise vortices by limiting vorticity as  $|\omega_x^+| \geq 0.2$  yields small scale structure. Figures 6(a)(b) demonstrate that around a small scale structure, a larger scale structure involving the former exists.

Wall-normal distribution of rms-value of  $\langle |\omega_{x,rms}^+| \rangle$  of small and large scales averaged in a plane parallel to the wall is shown in Fig.7 where thick and fine solid lines and broken lines are for total, small scale and large scale vorticity, respectively. Other components  $\langle \omega_{y,rms}^+ \rangle$  and  $\langle \omega_{z,rms}^+ \rangle$  show similar distributions. Vorticity is mostly included in small scale vortices and in viscous sublayer,

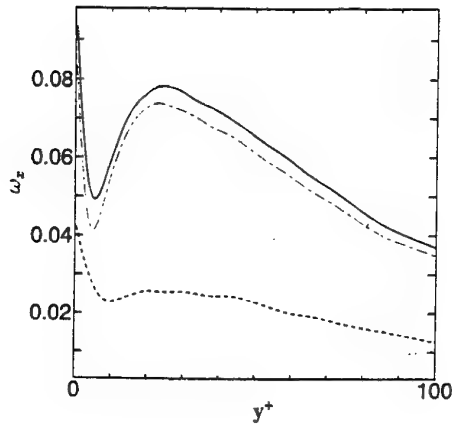


Fig.7 Wall-normal distribution of rms-value of  $\omega_x^+$  of small and large scales averaged in a plane parallel to the wall. Thick line : total, fine chained line : small scale and broken line : large scale.

large scale vortices become important since small scale fluctuation is hard to be born there because of strong viscosity effect. But in the sublayer, vorticity usually represents vortex sheet but not vortex tube.

### Sustenance of Vortices

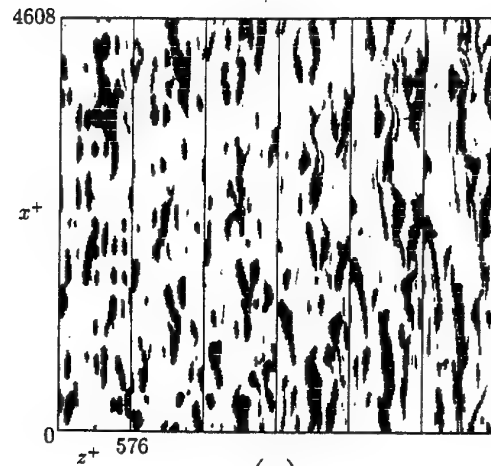
Since larger scale structure experiences slower dissipation due to viscosity, above-mentioned large scale vortical field can live long if small scale structure underneath is taken off, as shown in Fig.8(a) which shows evolution of large scale vortices by plan view of every  $\Delta t^+ = 30$  in each strip. As for the cluster of small scale vortices, it may be expected that it can survive by itself if it is embedded in a mean shear layer of any kind, since it is known that a single quasi-streamwise vortex has self-sustaining mechanism (Miyake *et al.*, 1996). A numerical experiment in which above-mentioned cluster of small scale vortices of Fig.6(b) is placed in a homogeneous mean channel flow which is uniform both in  $x$  and  $z$  direction and has turbulent velocity distribution normal to the wall was conducted. Fig.8(b) shows the result where the distribution of vortices are depicted in the same manner as in Fig.1(a). That is, the left-end strip is for the initial instant when the vortices are distributed identically with Fig.6(b) and each strip is for  $\Delta t^+ = 30$  after to that to its left. It is found that small scale structure quickly disappears, far quickly than in Fig.1(a). This indicates that mean shear of arbitrary velocity distribution is not useful in sustaining a cluster of small scale vortices. That is, small scale structure necessitates its own large scale structure around it which is inherent to itself, in order to be able to generate new vorticity to live long.

In order to get an idea how large and small scale vortices are interacting with each other, vorticity production is investigated.

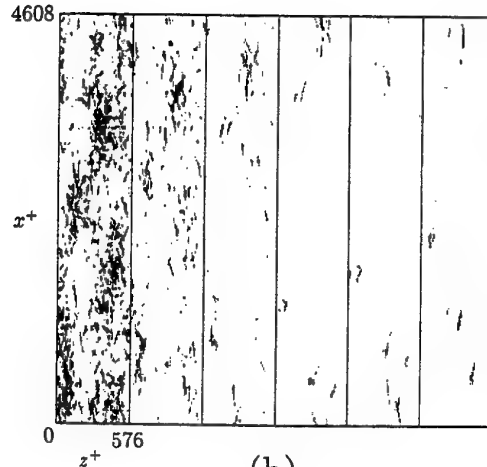
Vorticity equation is given by

$$\frac{D\omega}{Dt} = A \cdot \omega + \frac{1}{Re_\tau} \nabla^2 \omega = f_e e_\omega + f_t e_t + \frac{1}{Re_\tau} \nabla^2 \omega \quad (11)$$

where  $e_\omega = \omega/|\omega|$ ,  $A = \partial u_i / \partial x_j$  and  $D/Dt$  is material derivative (Tsujiimoto *et al.*, 1997).  $f_e$  is production rate of vorticity by stretching and  $f_t$  is that by turning or sum of tilting and yawing. Denoting the quantities of large scale vortex by over bar as  $\bar{f}$  and that of small scale vortex by prime as  $f'$ , one has four components of  $A \cdot \omega$ .



(a)



(b)

Fig.8 The time evolution of each decomposed initial large and small scale vortices embedded in mean turbulent Poiseuille flow. (a) : Large scale ( $|\omega_x^+| \geq 0.07$ ), (b) : small scale ( $|\omega_x^+| \geq 0.2$ ).

Namely, as for the stretching part of it,  $A_e: [(\bar{A} \cdot \bar{\omega}) \cdot e_\omega]$ ,  $B_e: [(A' \cdot \bar{\omega}) \cdot e_\omega]$ ,  $C_e: [(\bar{A} \cdot \omega') \cdot e_\omega]$ ,  $D_e: [(A' \cdot \omega') \cdot e_\omega]$  and for turning part,  $A_t: \bar{A} \cdot \bar{\omega} - [(\bar{A} \cdot \bar{\omega}) \cdot e_\omega] \cdot e_\omega$ ,  $B_t: A' \cdot \bar{\omega} - [(A' \cdot \bar{\omega}) \cdot e_\omega] \cdot e_\omega$ ,  $C_t: \bar{A} \cdot \omega' - [(\bar{A} \cdot \omega') \cdot e_\omega] \cdot e_\omega$ ,  $D_t: A' \cdot \omega' - [(A' \cdot \omega') \cdot e_\omega] \cdot e_\omega$ . A and D mean production rate of large scale vorticity and small scale one, by themselves, respectively, B is production rate of large scale vorticity by small scale strain rate and C, that of small scale vorticity by large scale strain rate.

Wall-normal distribution of above  $A_e$ ,  $A_t$ , etc., for  $x$ -wise vorticity component  $\omega_x$ , averaged in a plane parallel to the wall are shown in Fig.9(a) for stretching part  $f_{ex}$  and Fig.9(b) for turning part  $f_{tx}$ .

In the figures, thick solid lines are for A, broken lines, for B, thin solid lines, for C, thin dotted lines, for D and symbols are for total production rate. It is demonstrated in the figure that large scale structures are not self-sustainable since both  $A_{ex}$  and  $A_{tx}$  are negligibly small in whole section but the lines B indicate that large scale vortices produces vorticity supported by stretching of small scale vortices. However, they dissipate vorticity in buffer layer to produce small scale vorticity by turning.

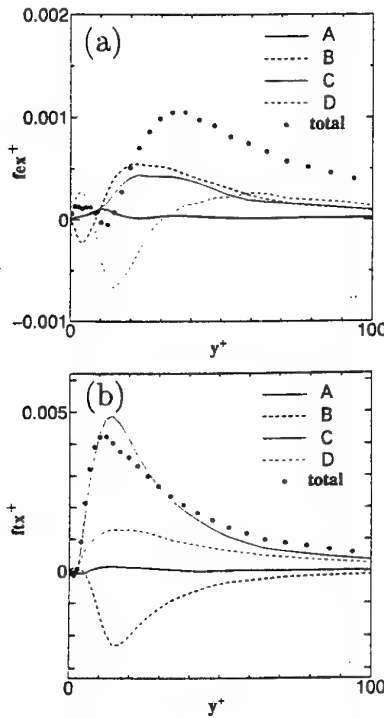


Fig. 9 Wall-normal distribution of the splitted production rate for  $x$ -wise vorticity component  $\omega_x$ , (a): stretching part  $f_{ex}$ , (b): turning part  $f_{tx}$ . Thick solid line : A, broken line : B, thin solid line : C, thin dotted line : D and symbols : total.

As for the small scale vortices, major field of production is buffer layer, as is known widely and both stretching and turning due to straining by large scale vortices contribute parallelly, though the latter is much larger than the former. The property that turning is the largest contributor is interpreted as that supply of new streamwise vorticity by tilting of wall-normal vorticity due to velocity gradient of large scale flow field is the major source of  $\omega_x$ . Stretching effect  $f_{ex}$  is known to be most important in the core region of mature quasi-streamwise vortices (Tsujiimoto et al., 1997).

But it should be noted that net production rate shown in the figure is negative in large scale vortices which is because the presented data on which the curve is based is at only one instant and long-term average is needed for more exact quantitative conclusion.

Figures 10 show the tilting angle of vortex lines of large and small scale vortices. Fig.10(a) is wall-normal distribution of tilting angle  $\alpha$  from the wall, of quasi-streamwise vortices and thin solid line is for small scale vortices and broken line is for large scale ones and thick solid line in between is for whole ones. Small scale vortices are more tilted from the wall, suggesting that many of them are underway of turning to horizontal direction. Meanwhile, large scale vortices are found to be of flat configuration, extending in horizontal direction. Fig.10(b) is similar distribution as Fig.10(a) of tilting angle  $\beta$  from the spanwise direction.

## Conclusion

1. Clustering of quasi-streamwise vortices was exemplified by a particular DNS using a long streamwise computational box.
2. The clustering is confirmed to be inherent in the near wall turbulence. Regeneration property of quasi-streamwise vortices is substantial in cluster formation.

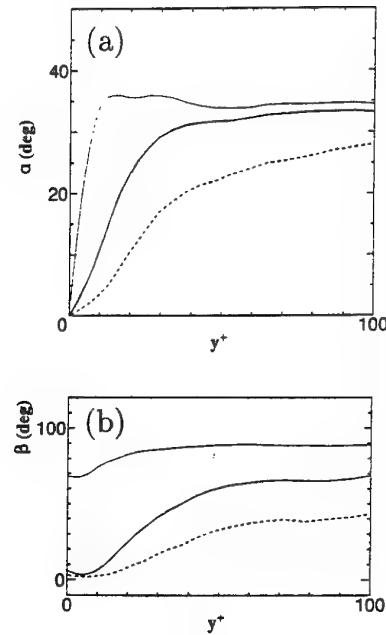


Fig.10 wall-normal distribution of the tilting angle of vortex lines of large and small scale vortices. (a) angle  $\alpha$  from the wall, (b) angle  $\beta$  from the spanwise direction. Thin solid line : small scale, broken line : large scale and thick solid line : whole.

3. By decomposition of vortical field into large scale and small scale structures, it turned out that usually observed quasi-streamwise vortices are small scale ones and are covered by large scale structure.

4. Large scale vortices can survive long if they do not interact with small scale vortices though they are not self-sustainable. But small scale vortices necessitate assistance of large scale vortices which is not arbitrary one but inherent to themselves, to sustain.

## Reference

- P. S. Bernard, J. H. Thomas, R. A. Handler (1995) "Vortex dynamics and the production of Reynolds stress", *J. Fluid Mech.*, **253**, 385-419.
- J. W. Brooke, T. J. Hanratty (1993) "Origin of turbulence-producing eddies in a channel flow", *Phys. Fluids*, **A5-4**, 1011-1022.
- T. Kajishima, T. Ohta, Y. Miyake (1997) "High-order finite difference method for incompressible flows using collocated grid system", (submitted to *Trans. JSME ser.B*)
- Y. Miyake, K. Tsujiimoto (1996) "Behavior of Quasi-Streamwise Vortices in Near-Wall Turbulence" *ASME FED*, **238-3**, 41-48
- Y. Miyake, R. Ushiro, T. Morikawa (1997) "The Regeneration of Quasi-Streamwise Vortices in the Near-Wall Region", *JSME Intern. J.*, **40-2**.
- S. K. Robinson, S. J. Kline, P. R. Spalart (1988) "Quasi-Coherent Structures in the Turbulent Boundary Layer: Part II. Verification and New Information from a Numerically Simulated Flat-Plate Layer", *Near Wall Turbulence*, eds. S. J. Kline & N. H. Afgan, 218-247, Hemisphere
- C. R. Smith, J. D. Walker, A. H. Haidari, U. Sobrun (1991), "On the dynamics of near-wall turbulence", *Phil. Trans. Roy. Soc. London - A*, **336**, 134-175.
- K. Tsujiimoto, Y. Miyake, T. Kado (1997) "Analysis of dynamics of a quasi-streamwise vortex in near-wall turbulence", (submitted to *Trans. JSME, ser.B*)

## SCALING OF THE VISCOUS WALL LAYER

Thomas J. Hanratty, Dimitri V. Papavassiliou  
Department of Chemical Engineering  
University of Illinois  
600 South Mathews Avenue  
Urbana, IL 61801  
USA

### ABSTRACT

Direct numerical simulations of turbulent flow in a channel have provided an opportunity to understand how turbulence is produced by flow over a flat wall. Elongated vortices at the wall, which regenerate themselves, are found to play a key role. Studies at two different Reynolds numbers reveal that these vortices scale with wall parameters. Wavenumber spectra for spanwise and streamwise velocity fluctuations in the viscous wall region change with Reynolds number. Wavenumber spectra for the Reynolds stress do not.

### INTRODUCTION

Fluid flowing over a smooth solid wall generates turbulence if the flow rate is large enough. A plot of the mean velocity made dimensionless with the friction velocity,  $\bar{U}$ , versus the logarithm of the dimensionless distance from the wall,  $y$ , reveals important characteristics of this flow. The region  $y^+ < 30$  is called the viscous wall region because time-mean viscous stresses are contributing to the determination of the variation of the mean velocity. For turbulent flow in a channel with a half-width of  $H$  the mean velocity in the region  $y^+ > 30$  and  $y/H < 0.15$  is described by the relation

$$\bar{U} = A \ln y + B$$

where, except for very small Reynolds numbers, the constants are not affected by Reynolds number.

Turbulence measurements reveal that there is a net production of turbulence in the viscous wall region, that production equals dissipation in the log-layer, and that there is a net dissipation in the outer flow. In this sense, the viscous wall region is the engine that drives the turbulence. Laboratory studies suggest that the viscous wall region is dominated by elongated eddies which have a lateral width of 50 wall units. These eddies create a streaky structure, with a spacing of  $\lambda=100$ , when dye is injected at the wall.

Direct numerical simulations of turbulent flow in a channel with  $H=150$  (Lyons, et al., 1991) and with  $H=190$  (Kim, et al., 1997) have provided considerable information about the

structure of the wall eddies. Recently, Papavassiliou (1996) has developed a simulation for  $H=300$ . This paper summarizes what is being discovered about the wall vortices. In particular, it uses the simulations at  $H=150$  and  $H=300$  to provide an understanding of the scaling.

### INSTANTANEOUS VECTOR FIELDS

One of the best ways of understanding this scaling is to examine the vectors in a plane perpendicular to the flow. Figures 1a and 1b show this plane for  $H=150$  and for  $H=300$ . The abscissas,  $z/H$ , and the ordinates,  $y/H$ , are normalized with the outer flow variable. Figure 1a is for a low enough Reynolds number that a log-layer hardly exists. It shows that the region close to the wall is dominated by vortices. Results presented by Brooke, et al. (1993) would suggest that these vortices should be independent of outer flow events. However, an examination of flows right at the wall shows the influence of large scale (outer flow) events on the spanwise flow. An important feature of this vector field is the existence of large scale flows, which we will call "sheets," that extend over large distances in the  $y$ -direction. These sheets could be associated with the wall vortices and their spacing in the  $y$ -direction represents the larger scales in the outer flow. A comparison of Figures 1a and 1b reveals that the wall vortices decrease in size with an increase in  $H$ .

Figures 2a and 2b present a plot of this same vector field in which the ordinate and the abscissa are normalized with the viscous length scale,  $\nu/v^+$ . It is noted that the wall vortices are the same size when plotted in this way, as are the small swirling motions in the outer flow. Vortices attached to the wall have a size of 40-50 wall units for both  $H=150$  and  $H=300$ . The vortices which have detached have been shown by Brooke, et al. (1993) to be part of a larger vortex structure which, most often, is attached to the wall upstream. These vortices increase in size with distance from the wall; they could be the dominant feature in the log-layer.

Large Reynolds stresses and large productions of turbulence in the viscous wall region are found to be associated with the attached vortices;  $q_2$  and  $q_4$  events are,

respectively, associated with the outflows and inflows of these vortices. An examination of the x-y plane reveals with the  $q_2$ - and  $q_4$ -events are parts of elongated negative and positive velocity streaks which fill the viscous wall region.

The up and down drafts of detached vortices are also associated with  $q_2$  and  $q_4$  - Reynolds stress events. Large Reynolds stresses in the outer flow are associated with the sheetlike structures shown in Figures 1 and 2. In the x-y plane these events are displayed as positive or negative surges in the streamwise velocity which extend over large distances in the y- and x-directions. Laboratory measurements with PIV (Hanratty, et al., 1993; Liu, et al., 1991) reveal the presence of such surges over a large range of Reynolds numbers.

### WAVENUMBER SPECTRA

A more quantitative definition of the scales representing the turbulence can be obtained by comparing wavenumber spectra in the z- and x-directions for  $H=150$  and for  $H=300$ . It is found that, in the viscous wall region (see Figure 3), the wavenumber spectrum of the Reynolds stress in the z-direction is independent of  $H$ . This is consistent with the idea that the turbulence producing events in the viscous wall region scale with wall parameters. This also seems to be the case for the normal velocity fluctuations. However, the spectral functions for the streamwise and spanwise velocity fluctuations at low  $k_z$  are found to be dependent on  $H$ . This indicates that the outer flow is affecting the turbulent velocity fluctuations but not turbulence production. Spectra in the outer flow are best normalized with outer flow scales. These show that the influence of viscosity becomes important at large wavenumbers, which scale with wall parameters. Because of this damping, the median wavenumber increases with increasing  $H$ .

### DISCUSSION

The picture that evolves from this study and previous works of Brooke & Hanratty (1993), Lyons, et al., (1989), Kline & Robinson (1989) and Kim, Moin & Moser (1987) is that the viscous wall region is an "active region" which is a net producer of turbulence. This production occurs through vortices attached to the wall. The wall streaks appear to be the result of a number of these vortices which line up in the direction of flow. The vortices recreate themselves and scale with viscous wall units; the outer flow appears to be exerting little influence. We speculate that Reynolds stresses in the log-layer are associated with vortical structures (created at the wall) which grow in size with distance from the wall. The importance of the viscous wall region is maintaining turbulence created at smooth walls becomes evident.

This central role of the viscous wall region is a surprising result since, at very large Reynolds numbers, a small fraction of the change in streamwise velocity occurs in the viscous wall region. As the Reynolds number increases the size of the wall vortices becomes quite small. Certainly, in the limit of very large Reynolds numbers many aspects of the process could change because wall roughness will then become an important factor.

The constant  $B$  characterizing the logarithmic behavior of the mean velocity profile outside the viscous wall region does not appear to change over a wide range of Reynolds numbers, so long as the wall may be considered to be

smooth. The magnitude of the constant is governed by processes in the viscous wall region. Even though measurements close to the wall cannot be made at very large Reynolds numbers, measurements of mean velocity profiles do support the notion that turbulence creation processes in the viscous wall region remain the same over a large range of Reynolds numbers.

### ACKNOWLEDGMENT

This work is supported by the National Science Foundation under Grants NSF CTS 95 03000 and NSF CTS 95 00518.

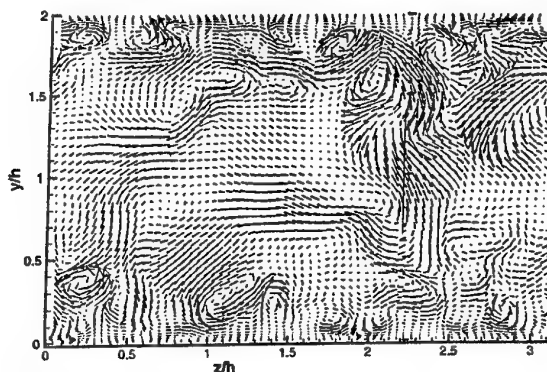


Figure 1a. Vectors in y-z plane plotted with outer flow scaling;  $H=150$ .

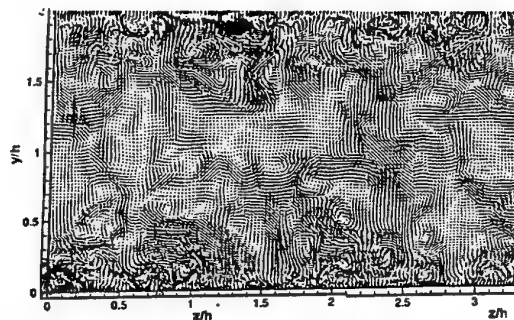


Figure 1b. Vectors in y-z plane plotted with outer flow scaling;  $H=300$ .

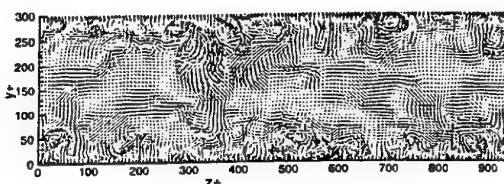


Figure 2a. Vectors in y-z plane plotted with wall scaling;  $H=150$ .

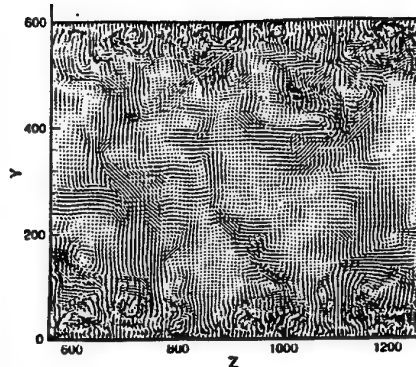


Figure 2b. Vectors in z-y plane plotted with wall scaling;  $H=300$ .

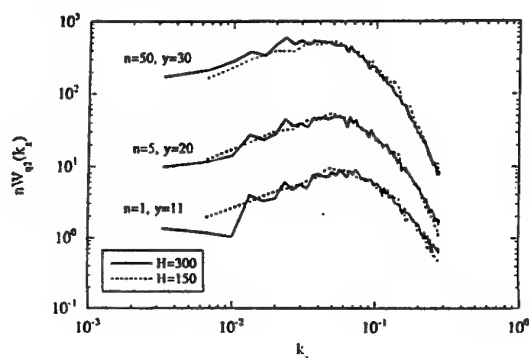


Figure 3. Wavenumber spectra of the  $q_2$  components of the Reynolds stress.

## REFERENCES

- Brooke, J. W., and Hanratty, T. J., 1993, "Origin of Turbulence-Producing Eddies in a Channel Flow," *Phy. Fluids A*, Vol. 5, pp. 1011-1022.
- Hanratty, T. J., Adrian, R. J., Liu, Z. C., Brooke, J., Papavassiliou, D. V., and McLaughlin, J. B., 1993, "Recent Results on the Structure of Wall Turbulence," *Ninth Symposium on Turbulent Shear Flows*, Kyoto.
- Kim, J., Moin, P., and Moser, R., 1987, "Turbulence Statistics in Fully Developed Channel Flow at Low Reynolds Numbers," *J. Fluid Mech.*, Vol. 177, p. 133.
- Kline, S. J. and Robinson, S. K., 1989, Progress; Status and Challenges," *Proceedings of the 2nd IUTAM Symposium on Structure of Turbulence and Drag Reduction*, Fed. Institute of Technology, Zurich, Switzerland.
- Liu, Z. C., Landreth, C. C., Adrian, R. J., and Hanratty, T. J., 1991, "High Resolution Measurement of Turbulent Structure in a Channel with Particle Image Velocimetry," *Exp. in Fluids*, Vol. 10, pp. 301-312.
- Lyons, S. L., Hanratty, T. J., and McLaughlin, J. B., 1991, "Large-scale Computer Simulations of Fully Developed Channel Flow with Heat Transfer," *Int. J. Num. Methods Fluids*, Vol. 13, p. 999.
- Lyons, S. L., Hanratty, T. J., and McLaughlin, J. B., 1989, "Turbulence Producing Eddies in Viscous Wall Region," *AIChE J.*, Vol. 15, pp. 1962-1974.
- Papavassiliou, D. V., 1996, "Structure and Transport in Wall Turbulence," Ph.D. thesis, Univ. of Illinois, Urbana.

# EXPERIMENTAL STUDY OF A TURBULENT COUETTE FLOW AT LOW-REYNOLDS NUMBER

K. Nakabayashi, O. Kitoh, F. Nishimura

Department of Mechanical Engineering

Nagoya Institute of Technology

Gokiso-cho

Showa, Nagoya, Aichi, 466

Japan

## ABSTRACT

So far, Reynolds number effects on flow have been studied with Poiseuille flow. However, since the Reynolds number and non-dimensional shear stress gradient parameter are coincidentally the same for Poiseuille flow, we can not study the Reynolds number effect separately. On the other hand, as the turbulent Couette flow has a constant shear stress and the shear stress gradient parameter does not change, the Reynolds number is only parameter of this flow. Using this feature of the Couette flow, the first objective of this work is to study the Reynolds number effects on the mean velocity and turbulent statistics of the wall turbulent flow. The second objective is to elucidate the differences between Poiseuille and Couette flows. Experiments have been performed in the range of  $3000 \leq \frac{2hU_b}{\nu} \leq 20000$  ( $U_b$ , moving belt speed;  $2h$ , channel height).

Low Reynolds number effects are shown as follows; additive constant of the law of the wall  $B$ , a coefficient of defect law  $R_s$  and the maximum turbulence intensity  $u'/u_*$  ( $u_*$ , friction velocity) decrease as the Reynolds number decreases. Compared to the Poiseuille flow, the power spectrum of streamwise velocity of the Couette flow has greater power in the low frequency range due to the fluctuating longitudinal large eddies.

## INTRODUCTION

Concerning the low Reynolds number effects on the law of the wall, Huffman & Bradshaw reported an upward shift of  $U^+ (= U/u_*)$  in the logarithmic region as the Reynolds number decreases for Poiseuille flow. Wei & Willmarth and Antonia et al. studied the effects of the Reynolds number on the inner scaling law of the turbulence intensities,  $u'^+$ ,  $v'^+$  and Reynolds stress  $-\overline{u^+v^+}$ , using plane Poiseuille flows.

Kitoh et al. studied Couette-Poiseuille flow in which the shear stress gradient can be set at any value, and showed that the law of the wall is mainly affected by the shear stress gradient rather than by the Reynolds number.

From dimensional analyses, the velocity profile near the wall in the case of Couette-Poiseuille flow can be expressed

as,

$$U^+ (= U/u_*) = f(y^+, Re^*, \mu) \quad (1)$$

where  $\mu$  is a non-dimensional shear stress gradient parameter  $\left( = \frac{u_*^2 / \frac{1}{\rho} \frac{d\tau}{dy}}{\nu/u_*} \right)$ , and  $Re^* = \frac{u_* h}{\nu}$ .

For plane Poiseuille flow, the relation of  $Re^* = -\mu$  holds, so it is not clear which parameter ( $Re^*$  or  $\mu$ ) substantially affects the velocity profile as  $Re^*$  is changed. On the other hand, Couette flow has infinite  $\mu$ , so the velocity profile is expressed as,

$$U^+ = f(y^+, Re^*). \quad (2)$$

Eq. (2) shows that the velocity profile of the Couette flow depends only on  $Re^*$ , allowing us to study the Reynolds number effects on the wall turbulent flow. This is the first objective of this work. The second objective is to show the differences in higher order moments of turbulent velocities between the Poiseuille and Couette flows.

## EXPERIMENTAL APPARATUS AND PROCEDURE

The measurement reported here is made in air in a belt-type Couette flow apparatus, Fig. 1. The moving belt is made of polyurethane and the stationary wall of acrylic resin. At the inlet of the channel, a shear generating grid is installed which promotes fully developed Couette flow in a short inlet length. The channel heights are set to 47mm and 27mm resulting in an aspect ratio of 18.7 and 32.6, respectively. The measurements are carried out at 184h ( $2h = 47mm$ ) or 320h ( $2h = 27mm$ ) downstream of the flow entrance. It has been ensured that the mean velocity profile and turbulence intensity profile do not change downstream of this station. The coordinate system is shown in Fig. 1. The mean velocity and the fluctuating velocities are measured using I-wire of 5 $\mu$ m tungsten (0.8mm sensing length), and X-wire of 3 $\mu$ m tungsten (0.5mm sensing length with 0.5mm separation). The signals are digitized on a personal computer using a 12-bit A/D data acquisition system at a sampling frequency of 10 kHz/channel for



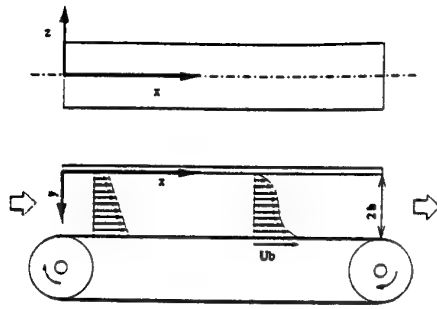


Figure 1: Experimental apparatus.

120 seconds. The sampled data are processed on a work station to obtain the mean and fluctuating velocities. Wall shear stresses are estimated by fitting the measured profiles to the universal profile in the range of  $2 \leq y^+ \leq 8$ . The present experimental conditions are shown in Tab. 1. In the table, the Reynolds number ( $Re_b = \frac{2hU_b}{\nu}$ ) is based on belt velocity  $U_b$  and channel height  $2h$ .

$Re_b$	20000	15000	10000	7000	5000	3000
$Re^*$	253.3	192.3	138.2	100.5	73.4	50.1

Table 1: Experimental conditions.

## RESULTS AND DISCUSSION

### Mean velocity profiles

Figure 2 shows a friction coefficient defined as

$$Cf = \frac{\tau_w}{\frac{1}{2}\rho U_b^2} \quad (3)$$

The lines in the figure represent a laminar flow relation,

$$Cf = \frac{2}{Re_b} \quad (4)$$

and an empirical relation of Robertson & Johnson for turbulent flow,

$$Cf = 20.095 / \log(Re_b/4)^2 \quad (5)$$

The present results agree with Eq. (5).

Figure 3 shows the velocity profiles plotted in wall variables. Some Reynolds number dependency can be seen among the profiles. The value of  $\kappa$  is found to be 0.40 for all Reynolds numbers. Additive constant  $B$  of logarithmic law is plotted in Fig. 4. Patel & Head reported that  $B$  increases as the Reynolds number decreases in Poiseuille flow. In Couette flow, however,  $B$  decreases with Reynolds number. As mentioned before, the Poiseuille flow results is explained by the effect of the shear stress gradient. At high Reynolds number, Couette and Poiseuille flows have constant value of  $B$ . Figure 5 shows Van Driest dumping factors  $A^+$  against  $Re^*$ . Huffman & Bradshaw reported that Van Driest dumping factor increases as  $Re^*$  decreases. In Couette flow, Van Driest dumping factor decreases with  $Re^*$  in low Reynolds number region.  $A^+$  and  $B$  have a similar trend against  $Re^*$  for both flows, because  $A^+$  is intimately related to  $B$ .

Figure 6 shows the distribution of  $y^+ \frac{dU^+}{dy^+}$  as a function of  $y^+$ . The distribution is the same irrespective of  $Re_b$  in

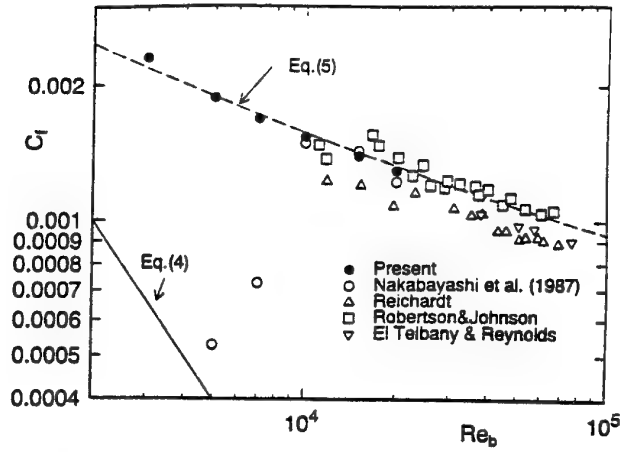


Figure 2: Wall friction coefficient.

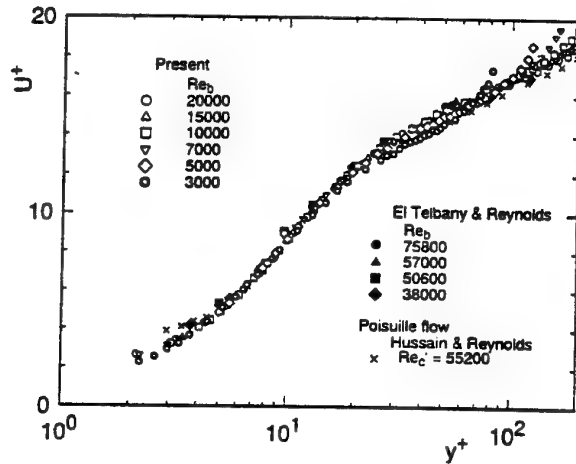


Figure 3: Law of the wall.

the range of  $Re_b \geq 7000$ . In the range of  $Re_b \leq 5000$ , the Reynolds number effects on the distribution appear. The value of  $y^+ \frac{dU^+}{dy^+}$  becomes smaller in the range of  $y^+ \geq 25$  for  $Re_b = 5000$  and  $y^+ \geq 10$  for  $Re_b = 3000$ . The Reynolds number effects invade smaller  $y^+$  as  $Re_b$  decreases.

In the core region, velocity profile follows the defect law;

$$\frac{U_c - U}{u_*} = Rs \left(1 - \frac{y}{h}\right) \quad (6)$$

Unlike the case of the ordinary defect law, Couette flow has an  $Re$ -dependent velocity profile even in the core region, because the shear exists there. Figure 7 shows the coefficient  $Rs$  of the defect law against  $U_b/u_*$ . The abscissa  $U_b/u_*$  increases with  $Re^*$ . Compared to the present data, others scatter rather widely. The overall trend of  $Rs$  is that  $Rs$  increases with  $U_b/u_*$ .

Eddy viscosity is shown in Fig. 8. Using Van Driest damping factor  $A^+$ , eddy viscosity  $\nu_t$  near wall region can be expressed as,

$$\frac{\nu_t}{2hu_*} = \frac{1}{4Re^*} \left( -1 + \sqrt{1 + 4\kappa^2 Re^{*2} \left(\frac{y}{h}\right)^2 \left[ 1 - \exp\left(\frac{-Re^* \left(\frac{y}{h}\right)}{A^+} \right) \right]^2} \right) \quad (7)$$



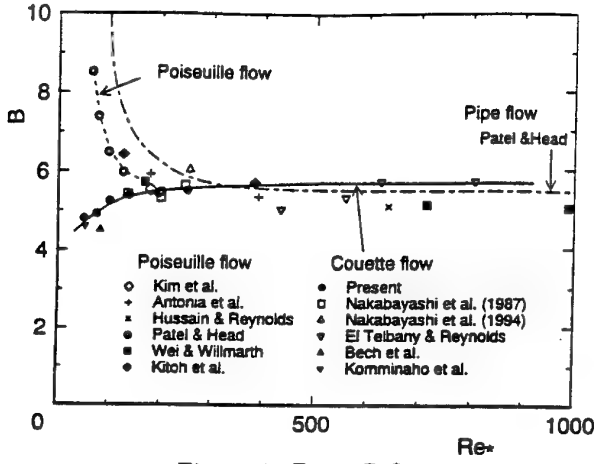


Figure 4:  $B$  vs.  $Re^*$ .

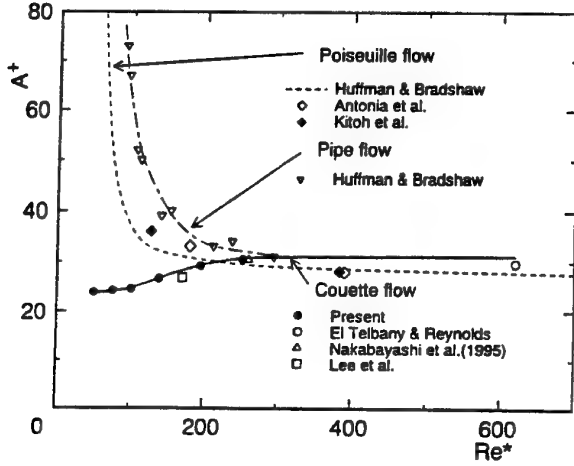


Figure 5:  $A^+$  vs.  $Re^*$ .

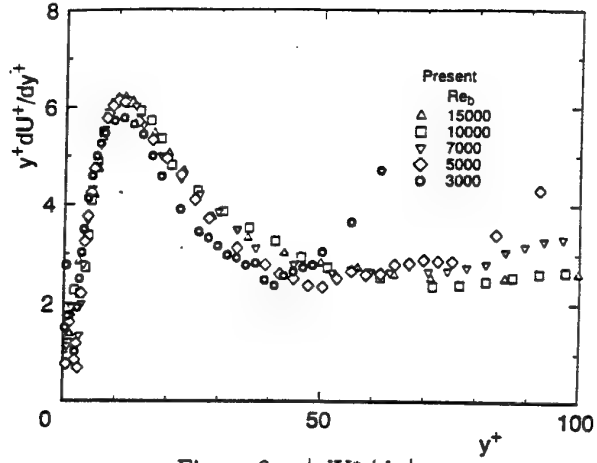


Figure 6:  $y^+ dU^+/dy^+$ .

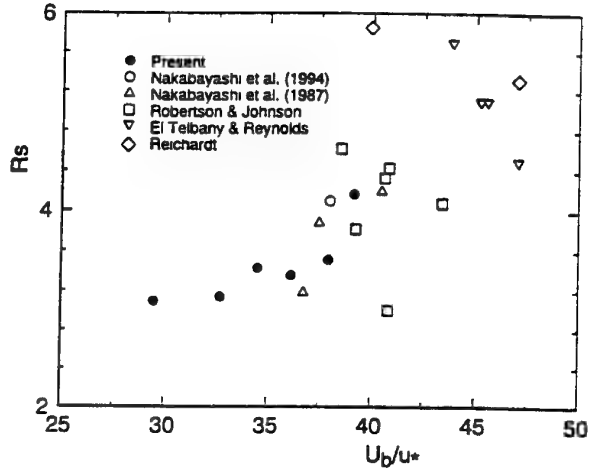


Figure 7:  $Rs$  vs.  $Re^*$ .

For the logarithmic region,  $\nu_t/2hu_*$  is expressed as,

$$\frac{\nu_t}{2hu_*} = \kappa \left( \frac{y}{2h} \right). \quad (8)$$

For the core region, assuming that  $\nu_t$  is constant against  $y$ , the following relation holds,

$$\frac{\nu_t}{2hu_*} = \frac{1}{2Rs} - \frac{1}{2Re^*}. \quad (9)$$

In each region, the present data follow the above equations, Eq. (7) ~ (9). The constant value of  $\nu_t/2hu_*$  increases as Reynolds number decreases. The first term in the right hand side of Eq. (9) is much larger than the second term (direct molecular viscosity). Because  $Rs$  increases with  $Re_b$  as shown in Fig. 7, the first term decreases with  $Re_b$  and it makes  $\nu_t/2hu_*$  smaller for high  $Re_b$ .

### Turbulence intensity and higher order moment

Figure 9 shows the turbulent kinetic energy production  $-\overline{u^+v^+}dU^+/dy^+$ . Here, Reynolds stress  $-\overline{u^+v^+}$  is calculated of  $-\overline{u^+v^+} = 1 - dU^+/dy^+$ . For high Reynolds number Couette flow ( $Re_b \geq 7000$ ), the value of  $-\overline{u^+v^+}dU^+/dy^+$  becomes independent of  $Re_b$ . From the results obtained by Antonia et al. and Wei & Willmarth, the curve of  $-\overline{u^+v^+}dU^+/dy^+$  for Poiseuille flow approaches to that for the Couette flow with increasing

$Re^*$ . This result can be shown as follows. The kinetic energy production for Poiseuille flow is written by

$$-\overline{u^+v^+} \frac{dU^+}{dy^+} = \left( 1 - \frac{y^+}{Re^*} \right) \frac{dU^+}{dy^+} - \left( \frac{dU^+}{dy^+} \right)^2. \quad (10)$$

In the above equation,  $Re^* \rightarrow \infty$  gives

$$-\overline{u^+v^+} \frac{dU^+}{dy^+} = -\left( \frac{dU^+}{dy^+} - \frac{1}{2} \right)^2 + \frac{1}{4}, \quad (11)$$

which is the same as the kinetic energy production for Couette flow. From Eq. (11), we obtain 0.25 as the maximum value of  $-\overline{u^+v^+}dU^+/dy^+$ . This value agrees with the present experimental result as shown in Fig. 9. For Couette flow, when  $Re_b$  decreases from high Reynolds number to 3000, the profile moves downward from the curve of higher Reynolds number production for  $y^+ > 18$ . Consequently, it can be known that low Reynolds number effects influence the buffer layer through the production term.

The streamwise turbulence intensities scaled by inner variable are shown in Fig. 10. The peak value of  $u'/u_*$ , whose location is unchanged ( $y^+ \approx 14$ ), increases with Reynolds number. For  $y^+ > 80$ ,  $u'/u_*$  has a constant value ( $u'/u_* \approx 2.0$ ). The dependence of the peak value of ( $u'/u_*$ ) on  $Re^*$  is plotted in Fig. 11. In Couette flow, the peak value which is greater than that of Poiseuille flow increases with  $Re^*$  for low Reynolds number range, but seems

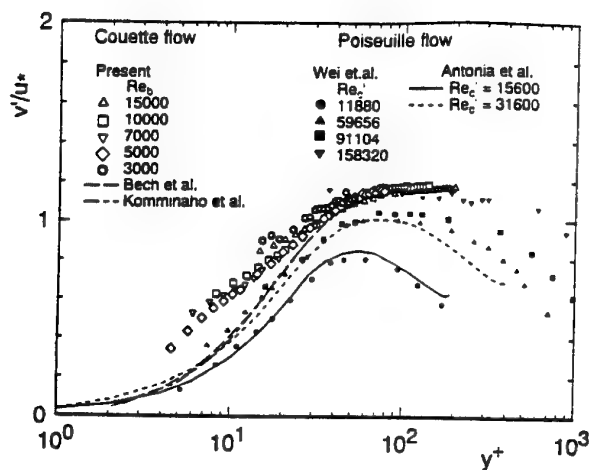


Figure 12: Turbulence intensity( $v'$ ).

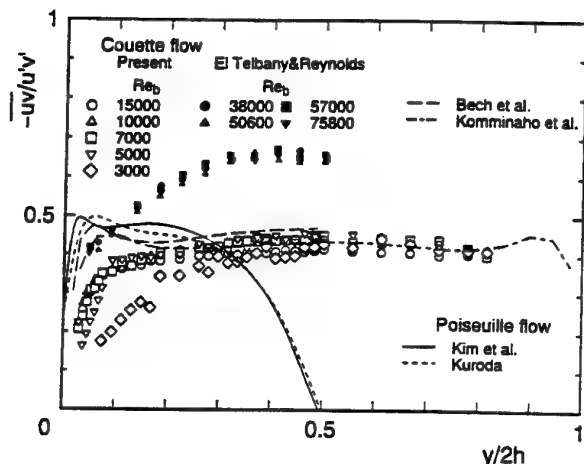


Figure 13: Correlation coefficient of  $\overline{uv}/u'v'$ .

Power spectra of  $u$  and  $v$  at  $y^+ = 40$  appear in Figs. 18 and 19. The power spectral density  $\phi$  of the velocity components  $u$  and  $v$  is given by

$$u^{+2} \text{ or } v^{+2} = \int_0^\infty \phi(\omega^+) d\omega^+. \quad (12)$$

The relation between  $\Psi^+(\omega^+)$  and  $\phi(\omega^+)$  is:

$$\Psi^+ = \omega^+ \phi(\omega^+) / \nu. \quad (13)$$

where  $\omega^+ = \omega \nu / u_\tau^2$  is the radian frequency scaled by inner variables. Large energy at the low frequency was observed in Couette flow, but not in Poiseuille flow, as shown in Fig. 18. The large energy at the low frequency is caused by the large longitudinal fluctuating eddies found by Lee et al. Following Wei & Willmarth, there was greater energy at the high frequencies with increasing Reynolds number. As seen in Couette flow, however, the power spectra is independent of the Reynolds number. In Fig. 19, the spectrum  $v$  is independent of Reynolds number, although it decreases as Reynolds number decreases in Poiseuille flow. Because the turbulence intensity  $v'$  decreases as Reynolds number decreases in Poiseuille flow. No effects of the large longitudinal fluctuating large eddies described above can be seen.

## CONCLUSION

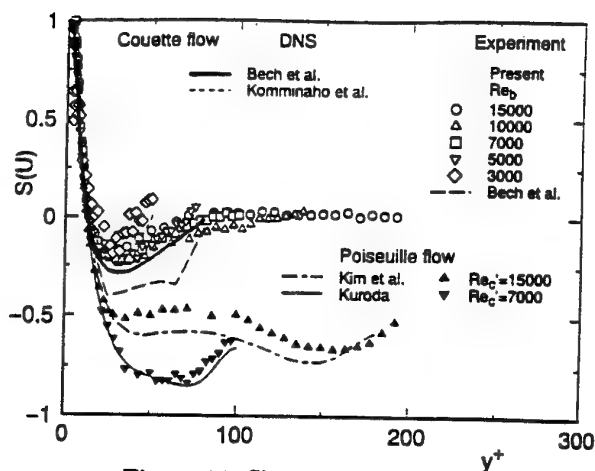


Figure 14: Skewness factor of  $u$ .

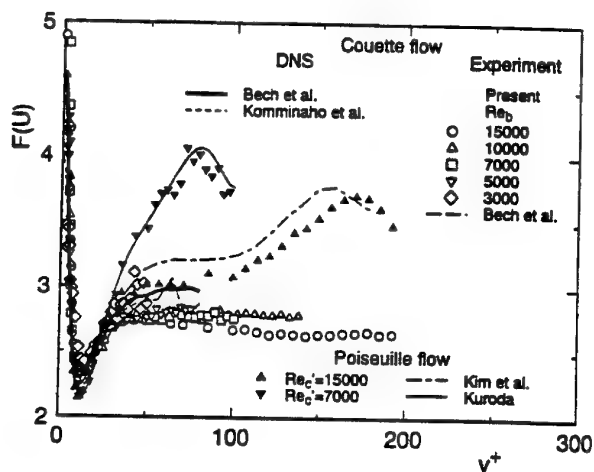


Figure 15: Flatness factor of  $u$ .

- (i) The Reynolds number effect on the wall law is that  $U^+$  in logarithmic region moves downward as  $Re^+$  decreases. Its effect on mean velocity appears in the buffer region.
- (ii) The  $R_s$  of the defect law increases with Reynolds number.
- (iii) The maximum value of  $u'/u_\tau$  decreases with decreasing Reynolds number in Couette and Poiseuille flows. The maximum value of  $u'/u_\tau$  in Couette flow is greater than that in Poiseuille flow. For  $y^+ > 80$  in Couette flow,  $u'/u_\tau$  and  $v'/u_\tau$  have respective constants values, which are independent of the Reynolds number.
- (iv) Profiles of skewness and flatness are independent of the Reynolds number in Couette flow, although these depend on Reynolds number in Poiseuille.
- (v) The distribution of power spectra of  $u$  and  $v$  are independent of Reynolds number. In power spectrum  $u$ , there is large energy at the low frequency, because the fluctuating longitudinal large eddies occur.

## REFERENCES

- Antonia, R.A., Teitel, M., Kim, J., Browne, L.W.B., 1992, "Low-Reynolds-number effects in a fully developed turbulent channel flow" *J. Fluid Mech.*, Vol.236, pp. 579-605

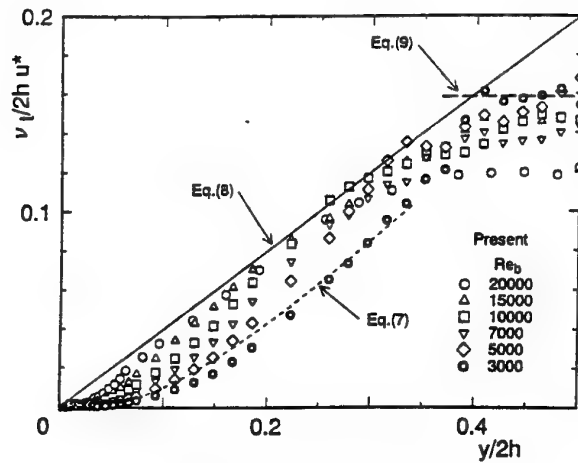


Figure 8: Eddy viscosity.

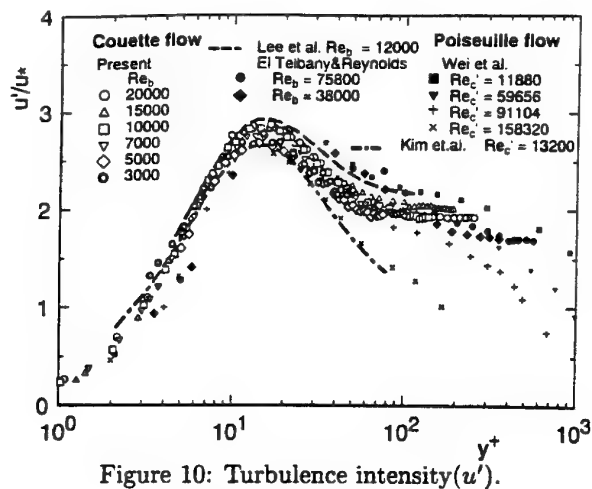


Figure 10: Turbulence intensity (\$u'\$).

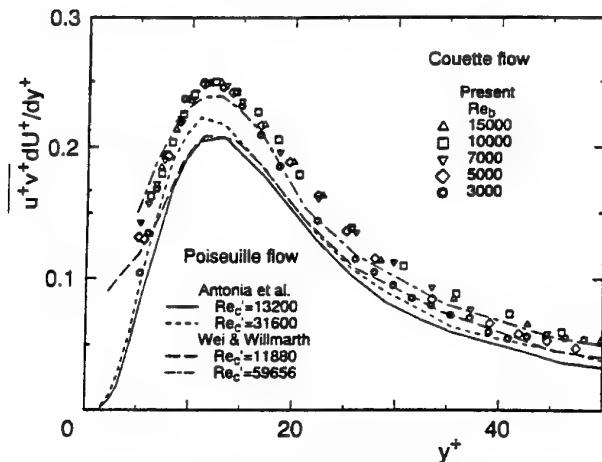


Figure 9: \$\overline{u^+v^+}dU^+/dy^+\$.

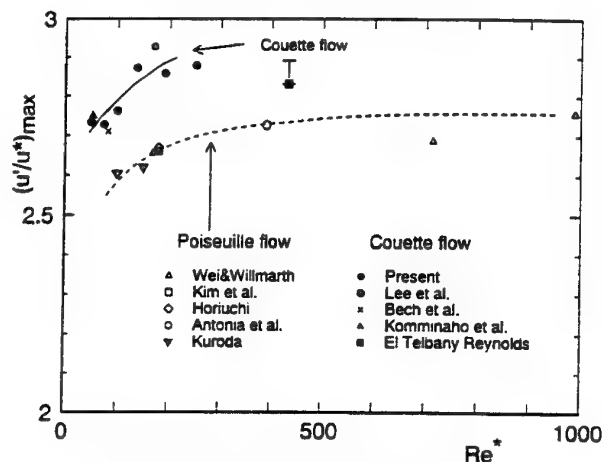


Figure 11: Maximum values of \$u'/u\_\*\$.

to remain constant for  $Re^+ > 200$ . In Poiseuille flow, however, the peak value of  $(u'/u_*)$  gradually increases with  $Re^+$  and approaches that of Couette flow.

The turbulence intensity normal to the wall scaled by inner variable is shown in Fig. 12. We also measured  $v'$  in Poiseuille flows by X-type probe. From the comparison between DNS data (Kim et al. and Kuroda) and the present result of  $v'$  in Poiseuille flow, we confirmed that the data were reliable for  $y^+ > 40$ . In Couette flow, present measurements for  $y^+ < 40$  are higher than those of Komminaho et al. or Bech et al., but the present result for  $y^+ > 40$  agrees with the latter's results. So that measured results for  $y^+ > 40$  are reliable. The profiles of  $v'/u_*$  approach a constant value which are independent of the Reynolds number ( $v'/u_* \approx 1.1$ ), as  $y^+$  goes to  $\infty$ . In Poiseuille flow, however, the  $v'/u_*$  curve approaches that of Couette flow as  $Re$  increases, as shown in this figure. Poiseuille flow at  $Re^+ = \infty$  is equivalent to that in Couette flow ( $\mu = \infty$ ) except for the turbulent core region, as described on the production.

Figure 13 shows the correlation coefficient. In Poiseuille flow,  $-\overline{uv}/u'v'$  is virtually constant and equal to 0.4 over a considerable region of the flow near the wall. In Couette flow,  $-\overline{uv}/u'v'$  remains constant over the channel height. The present measurement of  $-\overline{uv}/u'v'$  gives approximately 0.4, which agrees with the values obtained by Bech et al., Komminaho et al. and the value of the Poiseuille flow. El Tebany & Reynolds, however, reported  $-\overline{uv}/u'v' = 0.65$  which is too high.

The skewness factor and flatness factor of  $u$  are presented in Figs. 14 and 15, respectively. These graphs show good agreement between the simulation and the present measurements of  $S(u)$  and  $F(u)$  over the wide range of  $y^+$  for both Poiseuille and Couette flows. The distributions of  $S(u)$  and  $F(u)$  show Reynolds number independence near the wall for  $y^+ < 20$ , and Reynolds number dependence for  $y^+ > 20$  in Poiseuille flow; but Reynolds number independence is evident in Couette flow. In comparison with Poiseuille and Couette flows, distributions of  $S(u)$  and  $F(u)$  near the wall are similar, but quite different for  $y^+ > 20$ . The location for the maximum  $u'/u_*$  coincides with the position where the skewness is zero and the flatness has its minimum in the present measurement, as mentioned in Bech et al.

The skewness and flatness of  $v$  are presented in Figs. 16 and 17, respectively. The experimental data of  $S(v)$  and  $F(v)$  are different from the simulation near the wall, because of measurement errors. But the experimental data of  $S(v)$  and  $F(v)$  are reliable for  $y^+ > 60$ , because the present measurements of  $S(v)$  and  $F(v)$  agree with simulation (Kim et al. and Kuroda) for  $y^+ > 60$  in Poiseuille flow. The profiles of  $S(v)$  and  $F(v)$  show Reynolds number dependence for  $y^+ > 60$  in Poiseuille flow. Profiles of  $S(v)$  and  $F(v)$  do not show Reynolds number dependence more clearly in Couette flow than in Poiseuille flow. As the profile of  $S(v)$  and  $F(v)$  of Couette flow are in good agreement with those of Poiseuille flow for  $y^+ < 20$ , the mechanism of burst can be conjectured to be similar in both flows.

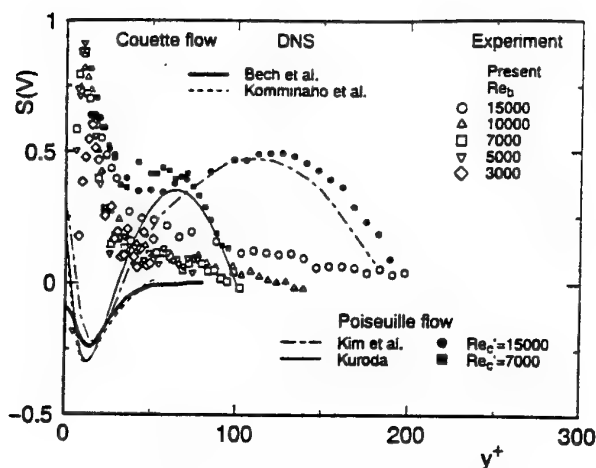


Figure 16: Skewness factor of  $v$ .

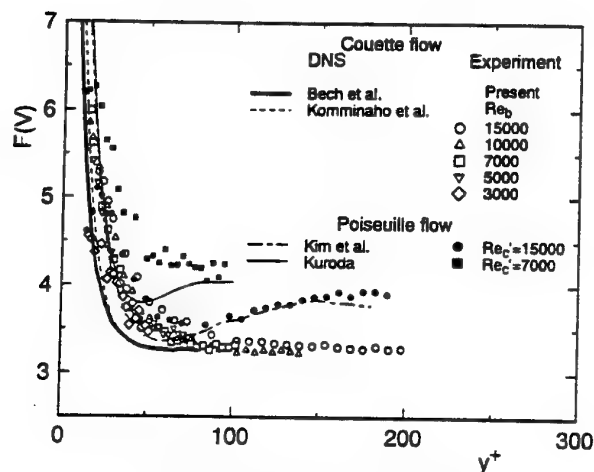


Figure 17: flatness factor of  $v$ .

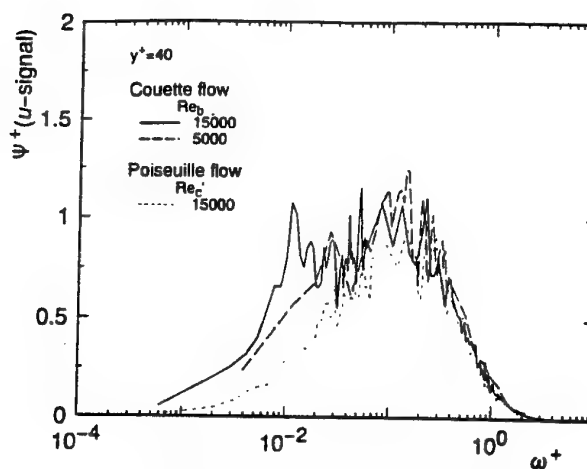


Figure 18: Power spectrum of  $u$ .

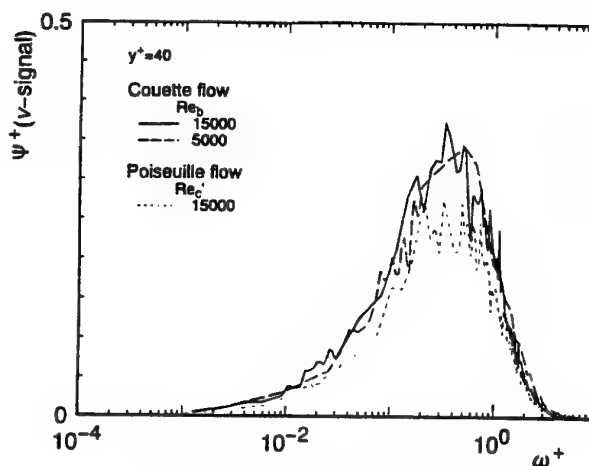


Figure 19: Power spectrum of  $v$ .

Bech, K. H., Tillmark, N., Alfredsson, P.H., Andersson H. I., 1995, "An investigation of turbulent plane Couette flow at low Reynolds numbers", *J. Fluid Mech.*, Vol.286, pp. 291-325

El Telbany, M.M.M., Reynolds, A.J., 1982 "The Structure of Turbulent Plane Couette Flow", ASME, *Journal of Fluids Engineering*, Vol. 104, pp. 367-372

Horiuchi, K., "Establishment of the Direct Numerical Simulation Data Bases of Turbulent Transport Phenomena", Co-operative Research No. 02302043 Supported by the Ministry of Education, Science and Culture 1990 - 1992 <Research Collaborators>, Kasagi, N. (Organizer), Horiuchi, K., Miyake, Y., Miyauchi, T., Nagano, Y.

Huffman, G.D., Bradshaw, P., 1972, "A note on von Kármán's constant in low Reynolds number turbulent flows" *J. Fluid Mech.*, Vol.53, pp.45-60

Hussain, A.K.M.F., Reynolds, W.C., 1975, "Measurements in Fully Developed Turbulent Channel Flow", ASME *Journal of Fluids Engineering*, DECEMBER, pp. 568-580

Kim, J., Moin, P., Moser, R., 1987, "Turbulence statistics in fully developed channel flow at low Reynolds number", *J. Fluid Mech.*, Vol.177, pp. 133-166

Kitoh, O., Nakabayashi, K., Katoh, Y., 1995, "Law of the Wall under Effect of Shear Stress Gradient" *Proceedings, THE SIXTH ASIAN CONGRESS OF FLUID MECHANICS*, Chew, Y.T., Tso, C.R., ed., Vol.2, pp. 1412-1415

Komminaho, J., Lundbladh, A., Johansson, A. V., 1996, "Very large structures in plane turbulent Couette flow" *J. Fluid Mech.*, Vol.320, pp.259-285

Kuroda, A., 1990, "Direct Numerical Simulation of Couette-Poiseuille Flows", Dr. Eng. Thesis, the University of Tokyo, Tokyo, Japan

Lee, M. J., Kim, J., 1991, "THE STRUCTURE OF TURBULENCE IN A SIMULATED PLANE COUETTE FLOW", *Proceedings 8th Symposium Turbulent Shear flow*, pp.5-3-1-5-3-6

Nakabayashi, K., Kitoh, O., Iwata, Y., Katoh, E., Uehara, T., 1987, "Basic Study on Turbulent Lubrication", *Trans. Jpn. Soc. Mech. Eng. B*, Vol. 54, No. 499, pp. 547-552

Nakabayashi, K., Kitoh, O., Adachi, M., Ikeya, T., 1994, "Turbulence Structure in Plane Turbulent Couette flow", *Trans. Jpn. Soc. Mech. Eng. B*, Vol. 60, No. 578, pp. 3249-3255

Patel, V.C., Head, M.R., 1969, "Some observations on skin friction and velocity profiles in fully developed pipe and channel flows", *J. Fluid Mech.*, Vol.38, pp. 181-201

Reichardt, H., 1959, "Gesetzmäßigkeiten der geradlinigen turbulenten Couetteströmung", *Max Plank Institute für Stromungs forschung, Mitteilunb Nr.22*

Robertson, J. M., Johnson, H. F., 1970 "TURBULENCE STRUCTURE IN PLANE COUETTE FLOW", ASCE *J.Eng. Mech. Div*, 96, pp.1171-1182

Wei, T., Willmarth, W.W., 1989, "Reynolds-number effects on the structure of a turbulent channel flow", *J. Fluid Mech.*, Vol. 204, pp.57-95

# APPLICATION OF OIL-SURFACE VISUALISATION AND TOPOLOGY PRINCIPLES TO IDENTIFY THE FLOW PATTERNS AROUND WALL-MOUNTED CUBES

E.R. Meinders<sup>(1)</sup>, R.J. Martinuzzi<sup>(2)</sup>, K. Hanjalić<sup>(1)</sup>

<sup>(1)</sup> Delft University of Technology  
Fac. of Applied Physics  
P.O. Box 5046, 2600 GA Delft  
The Netherlands

<sup>(2)</sup> University of Western Ontario  
Fac. of Engineering Science  
London, N6A 5B9  
Canada

## ABSTRACT

Topological principles were applied to flow patterns on the symmetry plane and solid surfaces to infer the three-dimensional flow field around configurations of multiple, surface-mounted cubes. Laser Doppler Anemometry measurements, oil-film and smoke visualisation observations provided complementary information for analysis. The configurations studied included a single *in-line* streamwise row and an *in line* matrix placed in a developing turbulent channel flow. The flow field inferred for the *in line* array showed a classical horseshoe vortex structure developing directly upwind of the leading obstacle base. The analysis for the cube matrix focused on the flow features in the deep matrix for which the flow was observed to be spatially periodic. For the tightly packed matrix ( $S/H=1$ ), the flow reattaches at the windward face of the subsequent cubes whilst for the case with  $S/H=3$ , the shear layer reattaches on the channel floor in the inter-cube gap and results in a two-cell vortex system.

## INTRODUCTION

Mean surface-flow patterns obtained with an oil-film visualisation technique are particularly well suited to topological analysis for deriving details on the local flow pattern in configurations of wall-mounted protrusions. Hunt *et al.* (1978) described applications of topology to oil-film visualisations to deduce the flow field around single wall-mounted prismatic obstacles. They provided details of the kinematic and topological principles necessary to infer the flow field from the identification of critical points (nodes and saddles) on the surfaces which bound the flow. Martinuzzi and Tropea (1993) applied these concepts to document the mean flow structure around surface-mounted, square cross-section blocks placed in a fully developed, turbulent channel flow. These results show the existence of two distinct flow regimes based on the obstacle height-to-span ratio. Devenport and Simpson (1991) studied the horseshoe vortex structure upstream of a wing-body junction. They observed that the flow patterns obtained using an oil-film technique differed from that observed from velocity measurements and attributed these inconsistencies to the dynamic, bimodal behavior of the flow. However, Larousse *et al.* (1991) showed that a detailed topological analysis of the flow patterns obtained with an oil-film technique, complemented by observations made from laser-light sheet experiments, allowed a more segregated reconstruction of the horseshoe vortex structure

upstream of a surface-mounted cube which agreed well with acquired velocity-data, (see Martinuzzi and Tropea, 1993). Hence, an accurate representation of the flow field must be consistent with information obtained with complementary techniques. Although the oil-film visualisation technique provides information only of the near wall flow features, careful topology analysis allows to extend these results to obtain a qualitative description of the macroscopic flow features away from the wall. Due to the fine detail possible with the technique, it is possible to easily identify small structures which could be difficult to detect with other methods. In addition to providing quantifiable information on the location of separation and reattachment lines, this method should also serve to guide anemometric studies.

This paper focuses on the flow features in configurations of surface-mounted cubes placed in a developing turbulent channel flow. The research was motivated by the need to identify the flow structure, which is important in understanding the local convective heat transfer. For example the improvement of the design and the reliability of high power electronic circuitry is closely linked with detailed knowledge of and the ability to predict the flow structure around individual components. The surface flow pattern for an *in-line* array and *in line* matrices of cubes are analysed topologically to reveal additional flow details not directly observed from Laser Doppler Anemometry (LDA) measurements. Smoke visualisation observations complement these results. Special attention is focused on the effect of the inter-obstacle separation between the cubes located deep within a matrix flow.

## EXPERIMENTAL TECHNIQUE

### Test-configuration

The configurations considered consisted of surface-mounted cubes placed in a channel flow at Reynolds numbers between 3000-6000, based on the cube dimension,  $H=15$  mm, and the bulk velocity. The channel height was  $h=50$  mm. The elements were placed with one face normal to the on-coming flow. The investigations were performed in a developing turbulent channel flow. The leading face of the first obstacle was located approximately 15 h downstream of the inlet, where the flow was tripped to enhance the transition to a turbulent boundary layer. The *in line* array consisted of six cubes located along the channel center-line with

inter-cube spacing  $S/H=1$ . *In line* matrix bundles spanning the entire channel width and at least 10 obstacles deep, were tested for separations of  $S/H=1, 2$  and 3.

### Oil-film mixture

A mixture of kerosene, oil and graphite was used to obtain mean surface flow patterns on the obstacle and channel floor. The mixture composition was chosen to prevent surface pattern diffusion due to turbulent fluctuations while still allowing the particles to follow the mean flow. The transport of the oil-film particles and the resulting streak lines on the surface are directly proportional to the surface stress vector, which must be parallel to the near-wall velocity vector. This condition is needed for the successful application of this technique (see Hunt *et al.*, 1978).

### Topology principles

The pattern of pigment accumulation or removal can serve to identify critical points, where the surface stress and velocity vectors identically vanish, or critical lines along which the surface shear stress component normal to the line is zero. There are two classes of critical points (see for example Hunt *et al.* (1978) and Perry and Fairlie, 1974). Nodes, or nodal points, are isolated singularities through which an infinite number of surface-stress trajectories pass either radially (simple nodes) or as high vorticity confocal spirals (foci). Reattachment (stagnation) and separation points correspond to divergent and convergent flow patterns, respectively. Typical examples are shown in Fig. 1a and b. Saddle points are singularities through which only two critical lines cross. The flow converges along one line and diverges along the other, see Fig. 1c, (the diverging critical line is often rich in pigment). Establishing the physical significance of saddle points depends on a proper interpretation of the local flow.

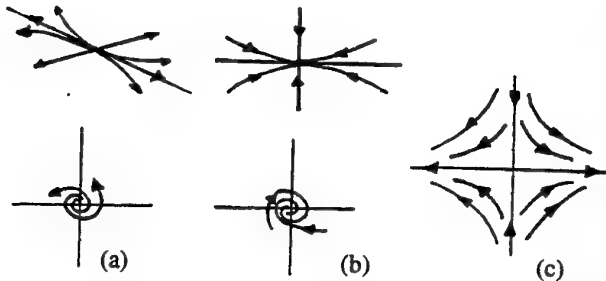


Figure 1: Types of topological critical points: Nodal points (N): (a) attachment, (b) separation and (c) Saddle points (S).

For a general flow-field, the difference between the total sum of nodes,  $\sum N$ , and saddles,  $\sum S$ , satisfies:

$$\sum N - \sum S = 2 - 2g \quad (1)$$

where  $g$  is the genus or connectivity of the surface. The flow on the channel walls and on the surface of wall-mounted cubes is topologically equivalent to a sphere ( $g=0$ ) with two additional nodal points (channel inlet and outlet) so that  $2 - 2g=0$ . Hunt *et al.* (1978) extended the topological principle to the analysis for the velocity field in planes normal to walls. It is shown that, for the symmetry plane  $y/H=0$ :

$$\left(\sum N + \frac{1}{2} \sum N'\right) - \left(\sum S + \frac{1}{2} \sum S'\right) = 0 \quad (2)$$

where  $N'$  and  $S'$  are half nodes and saddles, respectively, occurring at the solid boundaries.

The three-dimensional mean flow structure was inferred from these critical points and lines at the surface of both the obstacle and channel wall, together with Laser Doppler Anemometry

(LDA) measurements and smoke visualisations of the flow structure. Details of the used LDA-system can be found in Meinders *et al.* (1997).

### ARRAY OF CUBES

The structure of the flow field around an *in line* array of six cubes placed in a developing turbulent channel flow (spacing one cube height,  $S/H=1$ ) was deduced from the surface flow pattern shown in Fig. 2a. A cursory overview of that figure reveals that the pigment patterns on and around all but the first obstacle are qualitatively similar. However, the flow patterns are not fully developed (i.e. no spatial periodicity in the streamwise direction) even after six obstacles as can be seen from the nearly linear growth of the region bound by the pigment line A.



Figure 3: Smoke visualization of the front face of the leading cube in the array of cubes (flow from right to left).  $S_a$  and  $S_b$  correspond to the notation in the oil-film results.



Figure 4: Smoke visualization of the flow pattern around the single array of cubical protrusions at  $z/H = 0.5$ .

The rather complex surface patterns directly upstream of the leading cube is due to the horseshoe vortex system also observed along the symmetry plane,  $y/H = 0$ , with a laser light sheet technique (see Fig. 3). The primary vortex causes a flow separation resulting in the separation saddle, denoted as  $S_a$  in Fig. 2a. A tertiary system of induced vortices is located upstream of the primary vortex. It extends up to the primary separation saddle point  $S_b$ , seen as the accumulation of pigment in Fig. 2a about which a clear separation critical line originates. The critical lines through  $S_a$  and  $S_b$  mark the location of the horseshoe vortex system as it is deflected downstream along the lateral sides of the array. These join approximately  $1.5 H$  downstream of the leading obstacle trailing edge indicating that the horseshoe structure is consolidated in the primary vortex. In the wake of the leading and subsequent obstacles, two vorticity concentrations are denoted by the counter-rotating foci (N in Fig. 2a). These are the imprints of an arch-shaped vortex, confined in the inter-cube spacing. An instantaneous smoke visualization along the plane  $z/H = 0.5$ , given in Fig. 4, shows the main vortex structure in front of the leading cube and the symmetric recirculations in the gap between the leading and second cube.

Two saddles exist in the inter-cube area (S in Fig. 2a) suggesting that fluid is exhausted from the wake region between these points and the downstream windward face. Hence, the gap area does not form a closed recirculation bubble. The existence of a vortex tube extending up the cube lateral faces can be inferred from its

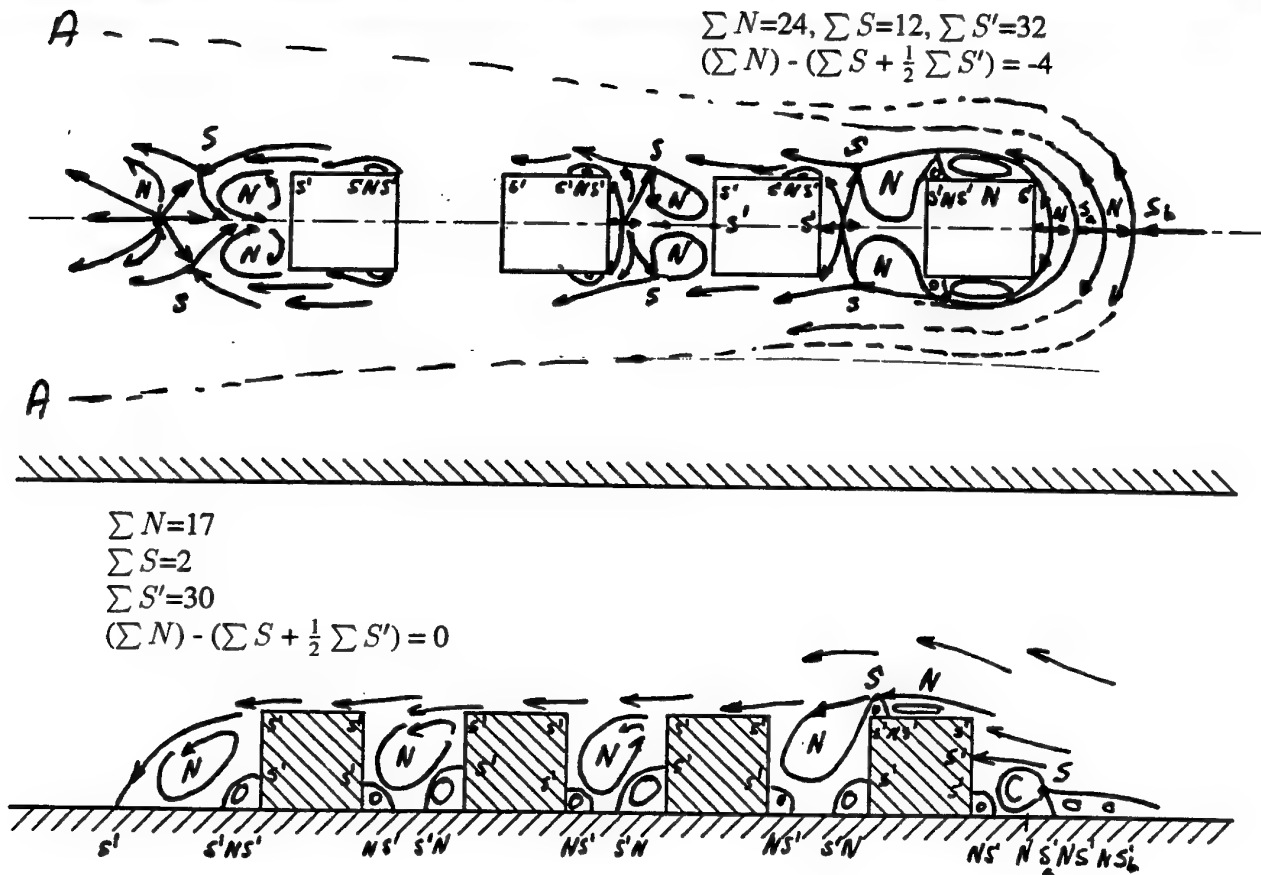
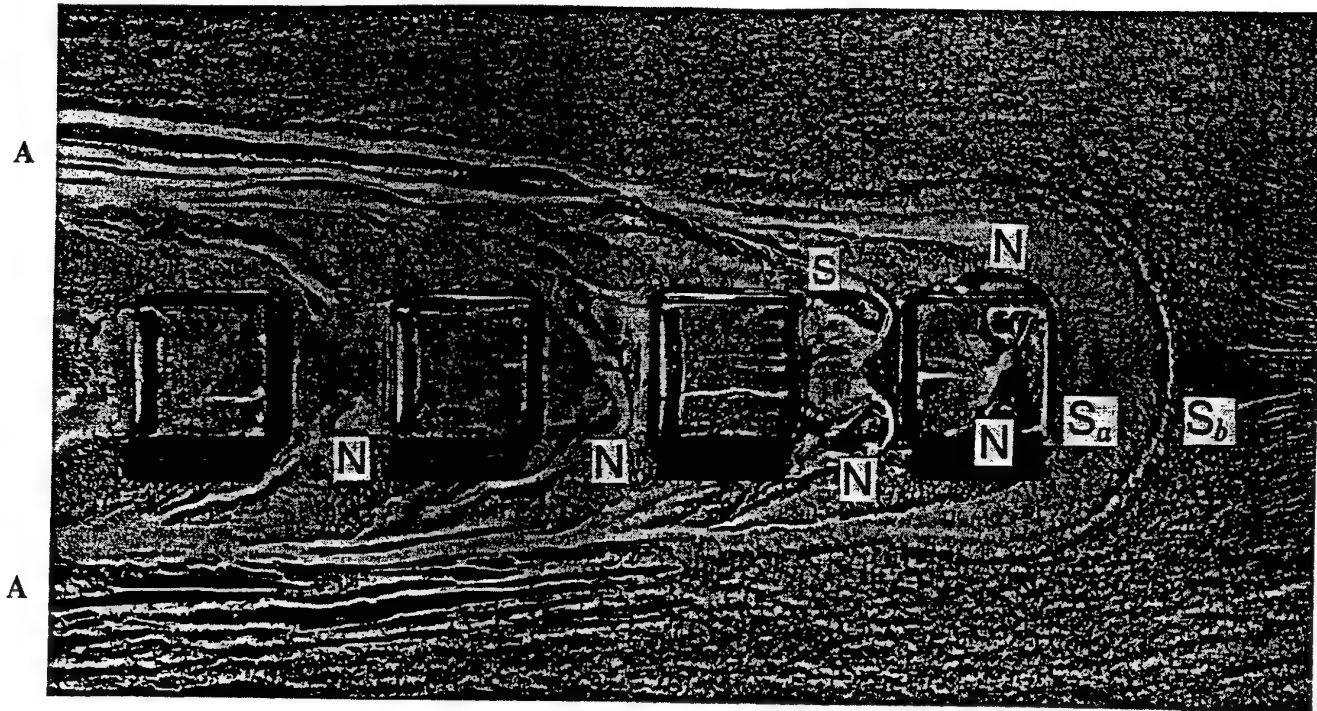


Figure 2: (a) Oil-film visualisation of an in-line single array of 6 cubes in a developing turbulent channel flow and the corresponding sketches of the critical points and stream lines for the planes (b)  $z/H=0$  and (c)  $y/H=0$ .



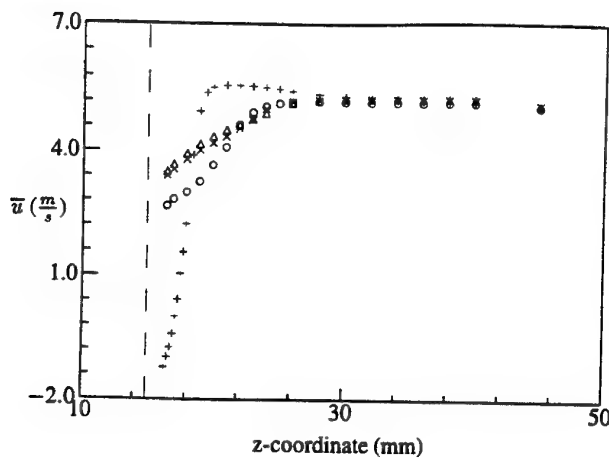


Figure 5: Profiles of the streamwise velocity  $\bar{u}$  in direction normal to the channel wall at  $y/H=0$  and the center of the top face: (+) E1, (o) E2, (x) E3 and ( $\Delta$ ) E4. The location of the top face, at  $z=15$  mm, is indicated with the dashed line.

footprint on the channel floor (marked N directly downstream of the leading side edge. Note that the side-wall vortices are much larger for the leading obstacle than on the subsequent cubes.

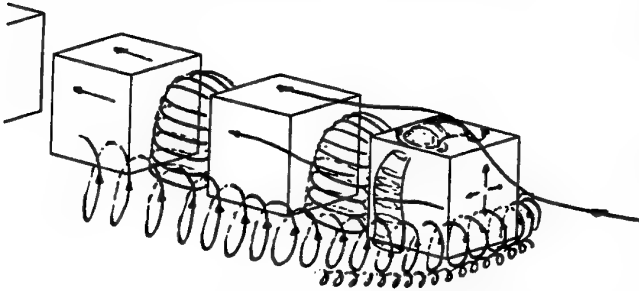


Figure 6: Three-dimensional sketch of the flow field around the first three cubes in the packed array.

The appearance of two foci on top of the leading cube, the imprint of the bound vortex at the top face, suggests flow reversal as is confirmed by LDA-measurements of the streamwise velocity component at the centerline of the cube, shown in Fig. 5. This flow pattern differs markedly from those on the top faces of the downstream obstacles, where the lack of pigment at and behind the leading edge suggests attached flow. The velocity profiles shown in Fig. 5 indicate a simple shear layer with no inflection further supporting this interpretation. Hence, the shear layer separating from the upstream obstacle must reattach on the front face of the subsequent obstacle. The significance of the pigment accumulation at the trailing edge of the obstacle top face is not clear. It may be a result of either surface adhesion (evacuation of the pigment being blocked by the return flow up the leeward face) or due to a local flow reversal. Fortunately, since both structures are topologically closed (i.e. removable mathematical singularities), their interpretation will not affect the deduced flow pattern for the remaining field.

The location of the aforementioned critical points on the channel surface  $z/H=0$  are schematically summarised in Fig. 2b. Since the flow pattern is topologically similar around each obstacle, except for the leading and trailing obstacle, an abridged array representation is shown. Note that the flow, however, is not fully developed (spatially periodic) since the pigment line A is still diverging. The summation of critical points is given in this figure. Also note that the removal of the obstacle surfaces is equivalent to increasing the surface connectivity. Hence, with four obstacles removed, the topological constraint of Hunt *et al.* (1978) becomes:

$(\sum N + \frac{1}{2} \sum N') - (\sum S + \frac{1}{2} \sum S') = -4$ . The critical points on  $z/H=0$  are transposed on the plane of symmetry  $y/H=0$  in Fig. 2c. For example, while a reattachment point appears as a simple node on  $z/H=0$ , it appears as a half saddle in the plane  $y/H=0$ . The existence and location of free saddle and nodal points in the plane of symmetry are then deduced to satisfy the topological constraints. The sums of the critical points are given in Fig. 2c and satisfy constraint (2). A sketch of the major features of the three-dimensional mean flow features is given in Fig. 6.

## MATRICES OF CUBES

The flow in a matrix of surface-mounted cubes was investigated for separations of  $S/H=1, 2$  and  $3$ . The surface patterns become spatially periodic in both the spanwise and the streamwise direction (developed condition) after the fourth row which is much earlier than for the array configuration. In the matrix, the presence of the obstacles to the sides serve to constrain the lateral expansion of the wake flow. Since the near-wall region develops first, the establishment of a fully developed condition for the entire flow is expected to be delayed by several rows.

The surface flow patterns around an obstacle deep in the matrix and the schematics for separation  $S/H=1$  are shown in Fig. 7. The oil-film pattern at the base reveals two counter-rotating foci in the wake, indicated with N, which is the imprint of the arch-vortex. Further, a line of pigment concentration is prevalent at the trailing edge of the top face. This spatially periodic pattern is topological analogous to that for the obstacles within the *in-line* array with  $S/H=1$ . The sums of the critical points, denoted in Fig. 7b, reveal that the topological constraint (2) is satisfied for the symmetry-plane  $y/H=0$ . Further, the sums in Fig. 7c indicate that:  $(\sum N + \frac{1}{2} \sum N') - (\sum S + \frac{1}{2} \sum S') = -1$ , which is the topological constraint with one cube removed.

An oil-film visualisation of the surface flow pattern for an *in-line* matrix with spacing  $S/H=3$  is given in Fig. 8 for a spatially periodic region in the matrix. The topologically consistent schematic for the channel floor is given in Fig. 8b. Two significant differences distinguish this situation from the previous flow patterns. First, the shear layer, separated from the leading edge, penetrates the inter-obstacle spacing and reattaches along the line of smooth pigment accumulation with a node N at the symmetry-line and the two saddles, S, symmetrically located upstream of the node (Fig. 8a). The reattachment flow also permits the formation of a horseshoe-type vortex at the upwind base of the subsequent obstacle. The presence of these multiple separations results in the appearance of a saddle along  $y/H=0$  directly downstream of the reattachment node. These structures are visible from the corresponding LDA-measurements of Fig. 9 at the symmetry-plane for one full period ( $4H$ ). Following a transposition of the critical points for the plane of symmetry, Fig. 8c, it is noted that the flow must reattach between the cubes to be topologically consistent. The reattachment point is found at  $x/H=1.4$  which is in good agreement with the oil-film result. The smaller vortices at the base of the obstacle, as indicated in Fig. 8b, could not be resolved with LDA. The second major difference is the separation along the leading edge denoted in Fig. 8a by the pigment accumulation present there. The arch-vortex in the wake, identified by the two counter-rotating foci N, behind the trailing edge, could also be observed from the vector representation of the velocity field in a plane parallel to the channel floor at  $z/H=0.25$ , given in Fig. 10.

An oil-film visualisation of the fully developed matrix flow with spacing  $S/H=2$  is given in Fig. 11. The topological features for this spacing are equivalent to the matrix flow with spacing  $S/H=3$  and therefore, the schematics from Fig. 8b and c apply also for this case.

## CONCLUSIONS

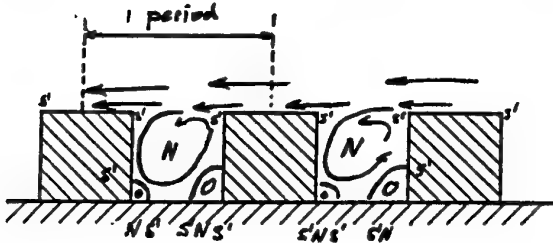
Topology principles were applied to flow field data obtained from Laser Doppler Anemometry measurements, oil-film and smoke visualisations to infer the three-dimensional macroscopic flow structure for multiple-obstacle configurations of wall-mounted cubes placed in a developing channel flow. This approach





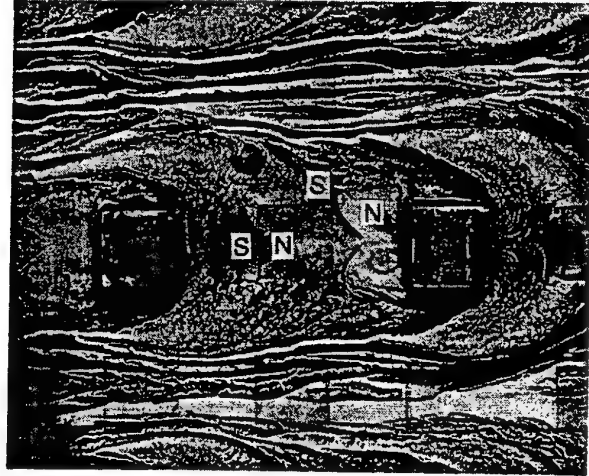
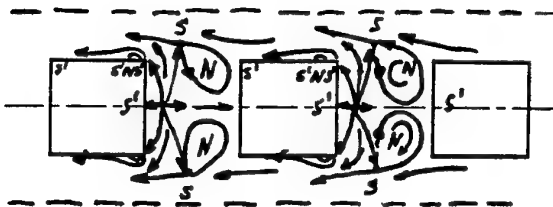
$$\sum N=3, \sum S'=6$$

$$(\sum N) - (\sum S + \frac{1}{2} \sum S') = 0$$



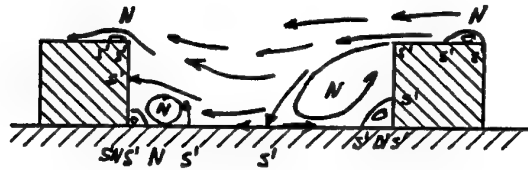
$$\sum N=5, \sum S=2, \sum S'=8$$

$$(\sum N) - (\sum S + \frac{1}{2} \sum S') = -1$$



$$\sum N=5, \sum S'=10$$

$$(\sum N) - (\sum S + \frac{1}{2} \sum S') = 0$$



$$\sum N=8, \sum S=5, \sum S'=8$$

$$(\sum N) - (\sum S + \frac{1}{2} \sum S') = -1$$

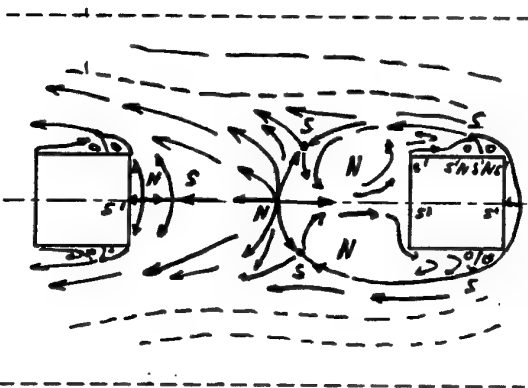


Figure 7: (a) Oil-surface visualisation of an in-line matrix of cubes with spacing  $S/H=1$  and the corresponding sketches for (b) the symmetry plane  $y/H=0$  and (c) the channel floor  $z/H=0$ .

Figure 8: (a) Oil-surface visualisation of an in-line matrix of cubes with spacing  $S/H=3$  and the sketches of the critical points and stream lines for the planes (b)  $y/H=0$  and (c)  $z/H=0$ .

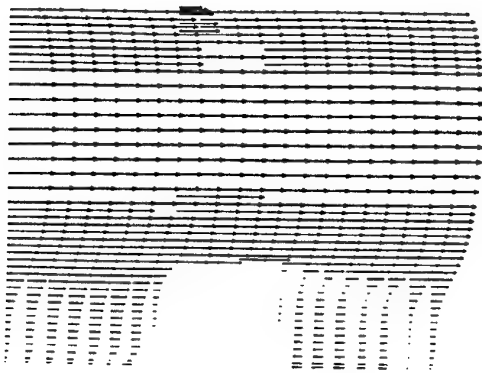


Figure 9: Vector-plot of the streamwise velocity  $u$  at the symmetry-plane  $y/H=0$ .

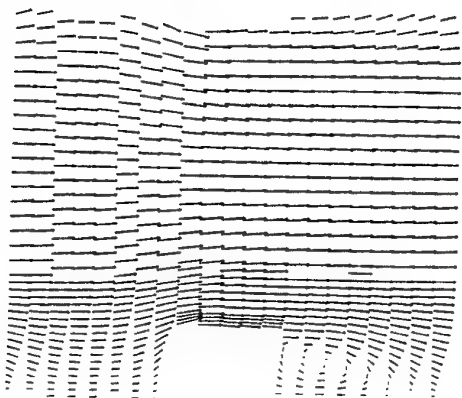


Figure 10: Vector plot of the velocity field at a plane parallel to the channel wall at half cube height  $z/H=0.25$ .

allowed a qualitative reconstruction of the flow with relatively little information. For the *in line* array of cubes with separation  $S/H=1$ , a horseshoe vortex structure originated directly upstream of the leading obstacle base. The flow field around each cube, except for the leading and closing one, was topologically equivalent to the fully developed matrix flow with tight spacing  $S/H=1$ . For both configurations, it was shown that the flow reattached at the windward face of the subsequent cubes. In contrast, the flow for the matrix with spacing  $S/H=3$  showed shear layer reattachment at the channel floor at roughly  $1.4 H$  from the trailing edge. Further, the fluid exchange between the wake region and the surrounding air was increased compared to the denser populated matrix with spacing  $S/H=1$ .

## REFERENCES

- Hunt, J. C. R., Abell, C. J., Peterka, J. A. & Woo, H., 1978, "Kinematical studies of the flows around free or surface-mounted obstacles; applying topology to flow visualisations", *J. Fluid Mech.*, Vol. 86, part 1, pp. 179-200
- Martinuzzi, R.J. & Tropea, C., 1993, "The flow around surface mounted, prismatic obstacles placed in a fully developed channel flow", *J. Fluids Engineering*, Vol. 115, pp. 85-92
- Larousse, A., Martinuzzi, R. & Tropea, C., 1991, "Flow around surface-mounted, three-dimensional obstacles", *8th Symp. on Turbulent Shear Flows*, TU-Munich/Germany, 1, pp. 14-4-1/14-4-6
- Devenport, W.J. & Simpson, R.J., 1990, "Time-dependent and time-averaged turbulence structure near the nose of a wing-body junction", *J. Fluid Mechanics*, Vol. 210, pp. 23-55
- Perry, A. E. & Fairlie, B. D., 1974, "Critical points in flow pattern", *Adv. Geophysics*, B 18, 299

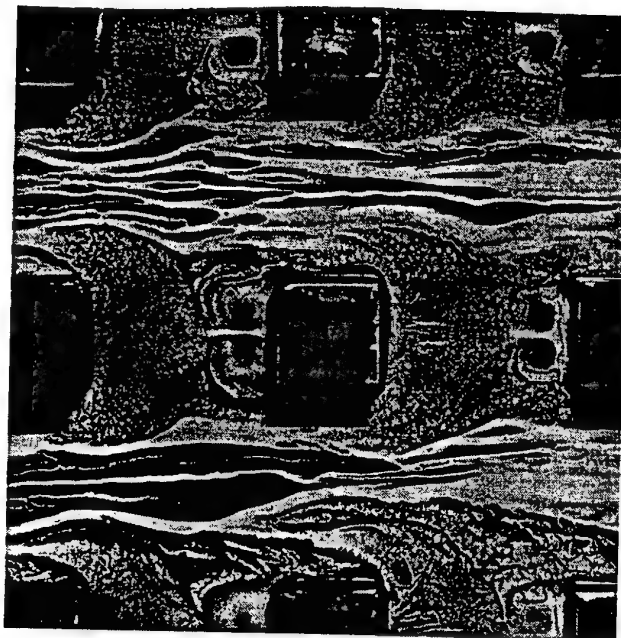


Figure 11: Oil-surface visualisation of an in-line matrix of cubes with separation  $S/H=2$ .

Meinders, E.R., Campen, J.B., Hanjalić, K. & Meer, T.H. van der, 1997, "LDA-analysis of the flow pattern around an array of cubical protrusions in low Reynolds number turbulent channel flow", *4th World conference on experimental heat transfer, fluid mechanics and thermodynamics*, June 2-6, Brussels, Belgium

Castro, I.P. & Robins, A.G., 1977, "The flow around a surface-mounted cube in uniform and turbulent streams", *J. Fluid Mech.*, Vol. 79, part 2, pp. 307-335

# LARGE EDDY SIMULATION OF ANNULAR DUCT FLOW

H.Y. Xu and A. Pollard  
 Department of Mechanical Engineering  
 Queen's University  
 Kingston, ON K7L 3N6  
 CANADA

## ABSTRACT

The numerical simulation of flow in the annular duct is performed using Large Eddy Simulation (LES). The initial conditions are prescribed as the laminar flows upon which are superimposed some disturbances that are derived from the solution to the Orr-Sommerfeld (O-S) equation. The entire flow history is simulated, i.e. from laminar to transitional and to fully developed turbulent flow. The number of control volumes are set at 393,216. The Reynolds number is 7325 based on the bulk velocities and hydraulic diameters. A variety of the statistical and structural information are extracted, particularly the turbulent kinetic energy and various correlations. The time averaged secondary flow for the annular duct shows strong, counter rotating vortex pair structures, symmetrically placed around the four outer corners of the inner square duct and weak, counter rotating vortex pair structures, symmetrically placed around the four inner corners of the outer square duct.

## 1. INTRODUCTION

The turbulent flow field in the vicinity of sharp corners is a subject of interest because there are significant alterations to the turbulence structures; also, this type of flow configuration is industrially relevant. In the paper the flow inside an annular duct, see Fig. 1, are considered, which, to our knowledge, there are no prior investigations.

The production of secondary flow inside straight duct can be attributed to two mechanisms, see Bradshaw (1987). These are skew-induced vortex generation by quasi-inviscid deflection of existing mean vorticity and stress-induced vortex generation by anisotropy and inhomogeneity of turbulent (Reynolds) stresses. Obviously, the stress induced mechanism is responsible for the generation of the secondary flow in an annular duct. However, there remains uncertainty about the individual contributions of the normal and shear stresses to

the production of and the transitional effects on the secondary flow.

In the paper, the turbulent flow inside annular duct is investigated by Large Eddy Simulation using temporal approach. The turbulent driven secondary flow structures are revealed. The mechanisms for the formation of the secondary flow are explored by interrogating the anisotropic distributions of streamwise vorticity generation.

## 2. GOVERNING EQUATIONS

The computational domain is shown in Fig. 1. By streamwise force balance relation, it can be obtained that:

$$(p_1 - p_2)(d_o^2 - d_i^2) = 4(\overline{\tau_{w_o}}d_o + \overline{\tau_{w_i}}d_i)l \quad (1)$$

where:  $p_1$  and  $p_2$  are pressures at inlet and outlet;  $l$  is the length of the annular duct;  $d_o$  and  $d_i$  are the hydraulic diameters and  $\overline{\tau_{w_o}}$  and  $\overline{\tau_{w_i}}$  are the mean wall shear stresses of the inner and outer ducts, respectively.

By defining an overall mean wall shear stress as:

$$\overline{\tau_w} = \frac{d_i(\overline{\tau_{w_o}}d_o + \overline{\tau_{w_i}}d_i)}{d_o^2 - d_i^2} \quad (2)$$

Eq. 1 can be rewritten as:

$$(p_1 - p_2)d_i = 4\overline{\tau_w}l \quad (3)$$

By choosing the characteristic length as  $d_i/2$  and the characteristic velocity as the mean frictional velocity,  $\overline{u_\tau} = (\overline{\tau_w}/\rho)^{1/2}$ , the non-dimensional mean pressure gradient can be obtained from Eq. 3:

$$-\frac{\partial \overline{P}}{\partial x} = \frac{p_1 - p_2}{l} = 2 \quad (4)$$

The governing equations are the filtered, see Madabhushi and Vanka (1991), three dimensional, time dependent N-S equations closed by the Smagorinsky eddy viscosity model:

$$\frac{\partial \bar{u}_i}{\partial x_i} = 0 \quad (5)$$

$$\frac{\partial \bar{u}_i}{\partial t} + \frac{\partial \bar{u}_j \bar{u}_i}{\partial x_j} = -\frac{\partial \bar{p}}{\partial x_i} + 2\delta_{i1} + \frac{1}{Re_\tau} \left\{ \frac{\partial}{\partial x_j} \left[ (1 + \bar{\nu}_t) \left( \frac{\partial \bar{u}_i}{\partial x_j} + \frac{\partial \bar{u}_j}{\partial x_i} \right) \right] \right\} \quad (6)$$

Index  $i = 1, 2, 3$  refers to the  $x, y$  and  $z$  directions, respectively, and  $x$  is the streamwise direction and  $y$  and  $z$  are the transverse directions.  $\delta_{ij}$  is the unit tensor and repeated indices imply summation.

The Reynolds number is defined by  $Re_\tau = \bar{u}_\tau d / \nu$ , where  $\nu$  is the molecular viscosity and  $d$  is half of the hydraulic diameter of annular duct. The term,  $2\delta_{i1}$  in Eq. 2, represents the mean pressure gradient and  $\bar{p}$  is the turbulent pressure fluctuation.

The use of the Smagorinsky SGS model is justified for low Reynolds number, since Madabhushi and Vanka (1991) and Breuer and Rodi (1994) demonstrate reasonably good agreement with experimental data at low Reynolds numbers using different types of SGS models, implying that the turbulence driven secondary flows are insensitive to the crudeness of the SGS model.

### 3. DISCRETIZATION

A second-order finite volume method is used to effect spatial discretization of the governing equations. The Adams-Bashforth second-order scheme is used for the convection terms and the Adams-Moulton second-order scheme is used for the diffusion terms. The implicit treatment of the diffusion terms eases significantly the stability requirement of the time marching step. The fractional step method on a staggered grid system is used for pressure-velocity coupling. All these discretization techniques lead to the following system of discretised equations:

$$\frac{\hat{u}_i - u_i^n}{\Delta t} = \frac{1}{2} (3C_i^n - C_i^{n-1}) + \frac{1}{2} (\hat{D}_i + D_i^n) \quad (7)$$

$$\frac{u_i^{n+1} - \hat{u}_i}{\Delta t} = -\frac{\delta \phi^{n+1}}{\delta x_i} \quad (8)$$

$$\frac{\delta u_j^{n+1}}{\delta x_j} = 0 \quad (9)$$

where:

$$C_i = -\frac{\delta u_i u_j}{\delta x_j} + 2\delta_{i1} + \frac{1}{Re_\tau} \frac{\delta}{\delta x_j} \left[ \bar{\nu}_t \frac{\delta u_j}{\delta x_i} \right] \\ D_i = \frac{1}{Re_\tau} \frac{\delta}{\delta x_j} \left[ (1 + \bar{\nu}_t) \frac{\delta u_i}{\delta x_j} \right] \quad (10)$$

where  $\delta$  is the finite difference operator, with the superscript  $n$  denoting the discrete time level;  $\hat{u}_i$  is used to denote the intermediate values of velocity.

### 4. INITIAL AND BOUNDARY CONDITIONS

Since it is believed that turbulence starts from some long wave lengths (at the order of characteristic length of relevant flows), the initial condition is constructed from a fully developed laminar velocity profile:

$$\frac{1}{Re_\tau} \left( \frac{\partial^2 u}{\partial y^2} + \frac{\partial^2 u}{\partial z^2} \right) = -\frac{\partial \bar{P}}{\partial x} = 2 \quad (11)$$

upon which are superimposed disturbances that are solutions to the O-S equation:

$$\left( \frac{d^2}{dy^2} - \alpha^2 \right)^2 \phi - i\alpha Re_\tau [(u - c) \left( \frac{d^2}{dy^2} - \alpha^2 \right) \phi - \frac{d^2 u}{dy^2} \phi] = 0 \quad (12)$$

where: the streamfunction  $\psi(y) = A\phi(y)e^{i\alpha(x-ct)}$  with  $\phi(y)$  being the eigenfunction;  $u$  is the basic laminar velocity;  $Re_\tau$  is the Reynolds number;  $\alpha$  is the spatial wave number;  $\alpha c = \alpha c_r + i\alpha c_i$  with  $\alpha c_r$  being the temporal frequency and  $\alpha c_i$  being the temporal amplification factor.

The periodic boundary conditions are imposed at the inlet and outlet surfaces of the annular duct. No slip boundary conditions are prescribed on the walls. The van Driest damping function is used to damping the length scales near the walls, which gives the following SGS eddy viscosity formulation:

$$\bar{\nu}_t = Re_\tau (C_s \bar{\Delta}) \sqrt{\frac{1}{2} \left( \frac{\partial \bar{u}_i}{\partial x_j} + \frac{\partial \bar{u}_j}{\partial x_i} \right)^2} \quad (13)$$

where  $C_s = 0.1$  and  $\bar{\Delta} = (h_x h_y h_z)^{\frac{1}{3}}$ .

The wall damping function is:

$$D = \left[ 1 - \exp \left( -\frac{y^+}{25} \right) \right] \left[ 1 - \exp \left( -\frac{z^+}{25} \right) \right] \quad (14)$$

where  $y^+$  and  $z^+$  is the coordinate scaled by the frictional velocity,  $u_\tau$ .

## 5. PRESENTATION OF RESULTS

The size of the nondimensional computation domain is  $16\pi \times 4 \times 4$  for the outer duct and  $16\pi \times 2 \times 2$  for the inner duct, in the  $x$ ,  $y$  and  $z$  directions, respectively. The grid size is set at  $130 \times 66 \times 66$  and the time step nondimensionalised by the large eddy turnover time (LETOT)  $d/u_r$ , is taken to be  $\Delta t = 5.0 \times 10^{-4}$ , which maintains a CFL number below 0.5.

The evolution of the flow from the initial perturbed laminar to a turbulent state is described in Fig. 2 to 5. This is observed by monitoring the secondary flow as it alters with time. The mass flux decreases as the streamwise velocity profile becomes non-parabolic. The prescribed average pressure gradient can not maintain the corresponding laminar flow rate since part of the pressure gradient is used to overcome the turbulent shear stresses.

The secondary flow first appears around the four outer corners of the inner square duct. The secondary flow builds there for about 500 time steps and then begins to diffuse throughout the entire flow field. Although there are significant changes occurring in the first 5000 time steps, the spatially-averaged secondary flow in this period has a clear and ordered structure. After 5000 time steps, these ordered structures become vaguer and finally disappear after about 10000 time steps.

The temporally and spatially averaged secondary flow, Fig. 6 and 7, indicate the existence of strong, counter rotating, vortex-pair structures, symmetrically placed around the four outer corners of the inner square duct and weak, counter rotating, vortex-pair structures, symmetrically placed around the four inner corners of the outer square duct.

The contour plots of turbulent kinetic energy indicate that most of the energy is concentrated near the wall and outer-corners of inner square duct regions. The lobes and indents of the contour plots of turbulent shear stresses demonstrate an alternating positive-negative sign structures coherently occurring in space, which are responsible for generating the turbulent secondary flow, as explained in the next section.

## 6. DISCUSSION

The mechanisms for the formation of the turbulent secondary flow are seen in the streamwise mean vorticity transport equation for statistically stationary flows, Bradshaw(1987),

$$U \frac{\partial \bar{\Omega}_x}{\partial x} + V \frac{\partial \bar{\Omega}_x}{\partial y} + W \frac{\partial \bar{\Omega}_x}{\partial z} =$$

$$\nu \left( \frac{\partial^2 \bar{\Omega}_x}{\partial x^2} + \frac{\partial^2 \bar{\Omega}_x}{\partial y^2} + \frac{\partial^2 \bar{\Omega}_x}{\partial z^2} \right) + \underbrace{\bar{\Omega}_x \frac{\partial U}{\partial x} + \bar{\Omega}_y \frac{\partial V}{\partial y} + \bar{\Omega}_z \frac{\partial W}{\partial z}}_{\text{shear stress contribution}} + \underbrace{\left( \frac{\partial^2}{\partial y^2} - \frac{\partial^2}{\partial z^2} \right) (-\bar{v}w) + \frac{\partial^2}{\partial y \partial z} (\bar{v}^2 - \bar{w}^2)}_{\text{normal stress contribution}} \quad (15)$$

As indicated in Eq. (15), the streamwise axial mean vorticity is generated by anisotropy in the Reynolds stresses. In Fig. 8 and 9, the vorticity production alternate regionally positive and negative in sign. The contributions of the normal stresses to the production of vorticity are not equal to that of shear stress; however, the production around the outer corners of inner duct is about one order of magnitude greater than that around the inner corners of outer duct. This provides some rationale for the existence of the very strong counter rotating vortex pair around the outer corners of inner duct.

The contour plots of vorticity productions around the inner corners of outer duct show structures similar to that given by Kajishima (1992) for LES of square duct flow. This suggests that the mechanism for the formation of weak counter rotating vortex pair is basically similar to that in a square duct. However, by magnifying the region around the outer corners of inner duct and ignoring the isovalues below 100 for shear stress and the isovalues below 50 for normal stress, Fig. 10 and 11 display a butterfly-shaped structure for both normal stress and shear stress contributions. This suggests that those distribution of normal and shear stress are responsible for the formation of the strong counter rotating vortex pairs.

It is interesting to note that there is a significant alteration in the structure of the streamwise kinetic energy taken between the time from 0 to 25 and the time from 5 to 25, where the time is measured by LETOT. The energy first accumulates in the middle region of the annular duct and then spreads to the near-wall region. Further investigation of this phenomenon is left for future work.

The current LES investigations of annular duct provide a database to interrogate the coherent structures, As demonstrated by Sullivan and Pollard (1996), four types of coherent structure identification techniques can be used, these are (1) Proper Orthogonal Decomposition (POD); (2) Linear Stochastic Estimation (LSE); (3) Gram-Charlier Estimation (GCE); (4) Wavelet Decomposition (WD). The POD technique is used by Gavrilakis (1997) to investigate the fluctuating velocity fields from the direct numerical simulation database of

square duct. It is expected that by using similar structure identification technique on the annular flow LES database, more interesting characteristic features for the outer corner flows can be obtained.

## 7. CONCLUSION

Large Eddy Simulation is performed for annular duct flow. The entire flow history is simulated using a temporal approach, i.e. from laminar to transitional and to fully developed turbulent flow. Significant streamwise turbulent energy redistribution is observed in the transitional stage. The time averaged secondary flow exhibits strong, counter rotating vortex pair structures, symmetrically placed around the four outer corners of the inner square duct and weak, counter rotating vortex pair structures, symmetrically placed around the four inner corners of the outer square duct. Contributions of the normal and shear stress gradients to the generation of streamwise vorticity was highlighted.

## 8. ACKNOWLEDGEMENTS

This research was supported by grants from the Natural Science and Engineering Research Council of Canada

## 9. REFERENCE

- 1 P. Bradshaw, Turbulent Secondary Flows, Ann. Rev. Fluid Mech. 1987, 19:53-74
- 2 M. Breuer and W. Rodi, Large Eddy Simulation of Turbulent Flow through Straight and Curved Ducts, ERCOFTAC Bulletin, pp 26-29, 1994
- 3 S. Gavrilakis, Numerical Simulation of low Reynolds number Turbulent Flow through a Straight Square Duct J. Fluid Mech. vol. 244, pp. 101-129, 1992
- 4 S. Gavrilakis, Turbulent-field Modes in the Vicinity of the Walls of a Square Duct, European Journal of Mechanics, B/Fluids, Vol. 16, N° 1, 1997
- 5 T. Kajishima and Y. Miyake, A Discussion on Eddy Viscosity Models on the Basis of the Large Eddy Simulation of Turbulent Flow in a Square Duct, Computer Fluids Vol.21, No. 2, pp. 151-161, 1992
- 6 J. Kim and P. Moin, Application of a Fractional Step Method to Incompressible Navier-Stokes Equations, J. Comput. Phys. 59, 308-323(1985)
- 7 R.K. Madabhushi and S.P. Vanka, Large Eddy Simulation of Turbulence driven Secondary Flow in a Square Duct, J. Phys. Fluids A, vol. 3, No. 11, 1991
- 8 P. Sullivan and A. Pollard, Coherent Structure identification from the Analysis of Hot-wire Data, Meas. Sci. Technol. 7 (1996) 1498-1516

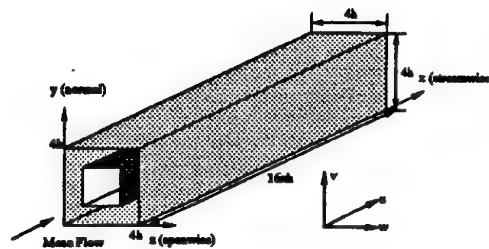


Figure 1: Annular duct flow geometry

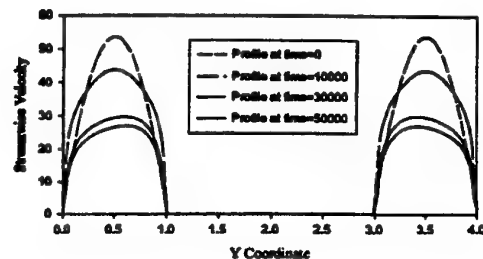


Figure 2: Annular duct velocity profile

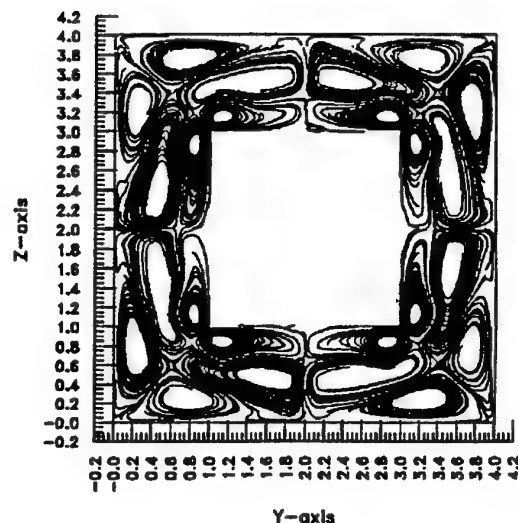


Figure 3: Secondary flow at 500 time steps

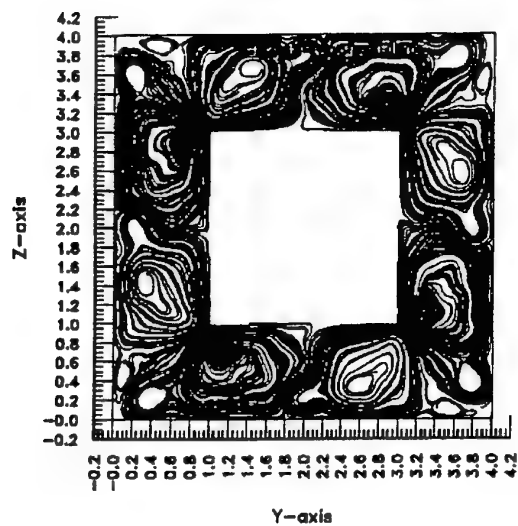


Figure 4: Secondary flow at 5000 time steps

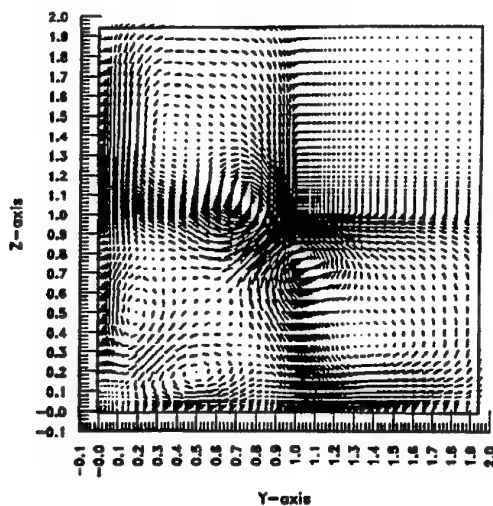


Figure 6: Time-averaged secondary flow inside annular duct at  $Re_d = 7325$

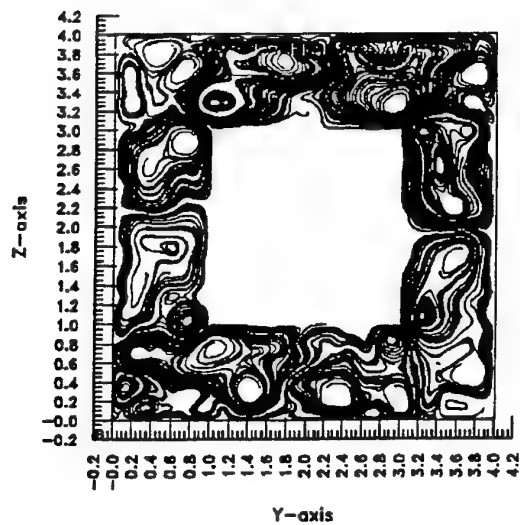


Figure 5: Secondary flow at 10000 time steps

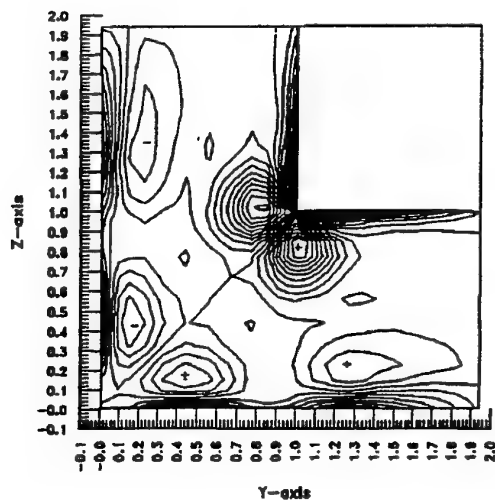


Figure 7: Time-averaged streamwise vorticity contours, +/- indicate sign of vorticity



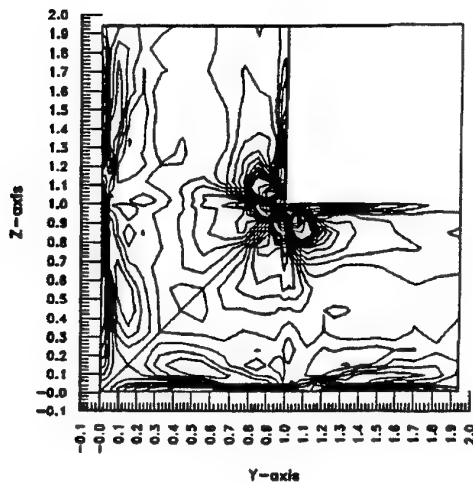


Figure 8: Time-averaged streamwise vorticity generation by shear stress contribution to mean vorticity in Eq. (15)

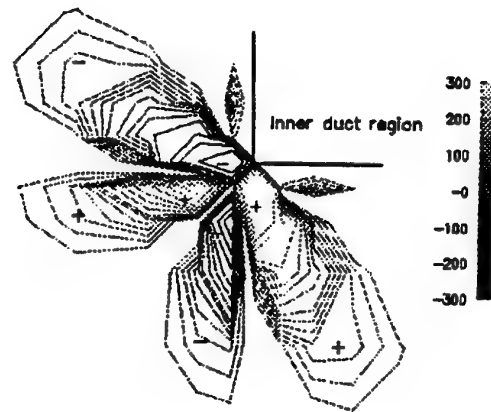


Figure 10: Time-averaged streamwise vorticity generation by shear stress contribution near inner duct region, +/- indicate sign of vorticity production

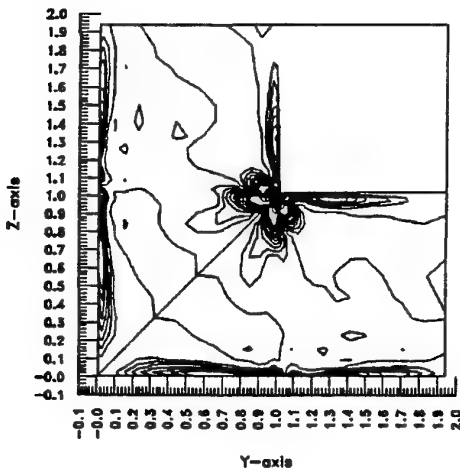


Figure 9: Time-averaged streamwise vorticity generation by normal stress contribution to mean vorticity in Eq. (15)

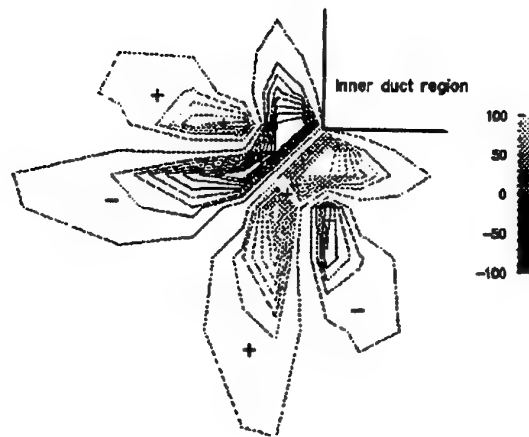


Figure 11: Time-averaged streamwise vorticity generation by normal stress contribution near inner duct region, +/- indicate sign of vorticity production



## **SESSION 12 - VARIABLE DENSITY FLOWS**

## REACTION OF NEAR WALL TURBULENCE TO STRONG DENSITY GRADIENTS

Sedat Tardu, Michel Favre-Marinet, Jean-Luc Harion  
Laboratoire des Ecoulements Géophysiques et Industriels  
Institut de Mécanique de Grenoble  
INPG, UJF, CNRS  
Grenoble - France

### ABSTRACT

Turbulent boundary layers with density variations have been generated by tangential injection of air or helium into a boundary layer of air-helium mixtures. Measurements at  $5\delta$  ( $\delta$ : Boundary layer thickness) show that the fine structure of the wall turbulence is significantly affected by large density variations. In particular, it has been found that ejection type events are considerably enhanced when helium is injected at the wall. In this case, the boundary layer is out of equilibrium near the injection slot due to the large density differences. Relaxation to an asymptotic state is much slower for the high-order moments than for the mean values of turbulent density and velocity. This result is surprisingly observed in the near-wall region.

### INTRODUCTION

Turbulent flows with strong density differences occur in a number of practical situations including premixed combustion over a strongly heated wall, the re-entry phase of a space shuttle into the atmosphere or the cooling of turbine blades by tangential injection. Although a number of well conducted studies exist on this topic (LaRue and Libby 1980, Cheng and Ng 1985, Wardana et al 1992, 1995) several questions concerning the detailed structure of the near wall turbulence remain unanswered. That is the case for instance when the mechanism generating the overall turbulent heat transfer is considered. Several investigations have converged to the observation that the heat transfer coefficient is independent of wall flux, even when the former is quite strong and enhances the ejection of low momentum fluid near the wall into the inner layer (Wardana et al 1995). The mechanism that compensates this phenomena and maintains unaffected the overall heat transfer mechanism is still not clear. The aim of the present investigation is to provide further experimental data obtained in a turbulent boundary layer subject to strong density

differences  $\Delta\rho$  in order to contribute to the understanding of these complex non equilibrium flows.

### DEFINITIONS, EXPERIMENTAL SET-UP and DATA REDUCTION

Density differences are generated by injecting different gas mixtures (air-helium) to the wall in a pressurized wind tunnel described in detail in Harion (1994). The present results were obtained at atmospheric pressure. Simultaneous measurements of the density  $\rho(t)$  and the velocity  $u(t)$  are performed by means of an interfering probe. The calibration procedure as well as the details concerning the frequency response of the probe together with first order statistics of fluctuating streamwise velocity and density may be found in Harion et al (1997). The measurements were performed at several distances  $x$  from the injection slot in the entire boundary layer. The closest point to the wall was  $y^+=20$  ( $+$  indicates variables non dimensionalized with local shear velocity  $u_\tau$  and viscosity  $\nu$ ). The accent here is mainly put on the characteristics obtained in the inner layer. The experimental conditions are:

External flow:  $\rho_\infty = 1 \text{ kg/m}^3$ ,  $U_\infty = 6 \text{ m/s}$ ;

Injection of pure air ( $\rho_{inj} = 1.2 \text{ kg/m}^3$ ) or pure helium ( $\rho_{inj} = 0.16 \text{ kg/m}^3$ ) through a slot of height 3mm with a bulk velocity  $U_{inj} = 2 \text{ m/s}$ .

At  $x = 100 \text{ mm}$  from the injection slot: Boundary layer thickness  $\delta = 20.5 \text{ mm}$ ,  $Re_\delta = 6000$ ,  $u_{\tau \text{ air}} = 0.24 \text{ m/s}$ ,  $u_{\tau \text{ He}} = 0.29 \text{ m/s}$ . Record length  $T_r = 3500 \delta/U_\infty$ .

### RESULTS

#### High order statistics

Previous results have shown that the rms of the streamwise velocity is not significantly affected by the presence of  $\Delta\rho = \rho_{inj} - \rho_\infty$ . This is no more the case when

the higher order statistics are considered. Figure 1a compares the distribution of the skewness of  $u'$  obtained with injection of helium and air at  $x/\delta = 5$  downstream of the injection slot, with the DNS data of Kim et al (1987) in the canonical ( $\Delta\rho = 0$ ) turbulent boundary layer. It is seen that  $\overline{u'^3}/\overline{u'^2}^{3/2}$  is significantly lower and negative in the low log layer ( $y^+ < 100$ ) when  $\Delta\rho < 0$  (injection of helium) while the skewness factor is quite similar to the results given by DNS in the case of small  $\Delta\rho > 0$ . This shows that the ejection like motions with  $u' < 0$  are intensified when  $\Delta\rho < 0$ . The skewness of the density fluctuations is even more interesting (Fig. 1b). The structural parameter  $\overline{\rho'^3}/\overline{\rho'^2}^{3/2}$  is strongly negative once  $y^+ > 50$ , i.e. in the constant shear region when helium is injected at the wall. The density gradient  $\partial\bar{\rho}/\partial y$  is positive in this case. According to a reasoning similar to Prandtl, a fluid particle coming at  $y_f$  from  $y_i < y_f$  and keeping its initial density will cause a density fluctuation  $\rho' \sim \rho(y_i) - \bar{\rho}(y_i) \sim -\partial\bar{\rho}/\partial y (y_f - y_i) < 0$  and by the same reasoning a fluctuating streamwise velocity  $u' < 0$  too. Now since the inner layer is in majority under the influence of ejection  $u' < 0$  type events (which correlate with  $\rho' < 0$ ), it is not surprising to find  $S_{\rho'} < 0$  at  $y^+ > 30$ . What is striking, in return, is the high absolute values of  $\overline{\rho'^3}/\overline{\rho'^2}^{3/2}$  observed in the low logarithmic zone and showing a strong coupling of flow structures with imposed density differences.

The Prandtl's model let us to suppose a similarity between the dynamic behaviour of the density and wall normal  $v'$  fluctuations. We compared  $S_{\rho'}$  with  $S_{v'}$  of the canonical layer (not shown here) in order to test this hypothesis. We noted a good correspondance between these quantities in the case of air injection. It may be argued therefore that, since the density gradient in this situation is quite low,  $\rho'$  behaves like a passive scalar. In the presence of relatively strong density gradient with helium, in return, the skewness of  $\rho'$  differ considerably from  $S_{v'}$ . Therefore, the density is no more passive and interacts strongly with the fine structure of the wall turbulence.

We compare in Fig. 2a the skewness of  $u'$  when  $\partial\bar{\rho}/\partial y > 0$  with the results of Wardana et al. (1992) obtained over a strongly heated wall. Both profiles coincide qualitatively well showing the qualitative similarity between these flows. The agreement can not be more than qualitative, since the density gradients are significantly different in the two investigations. The streamwise gradient  $\partial\bar{\rho}/\partial x \approx 0$  over the heated wall in a fully developed turbulent layer. Furthermore, the wall normal gradient is related to  $\partial\bar{T}/\partial y$  (where  $T$  stands for temperature) and  $\partial\bar{T}^+/ \partial y^+ = 1$  in the conduction sublayer while  $\partial\bar{T}^+/ \partial y^+ \approx A/y^+$  in the constant flux zone. The phenomena investigated in the present study deal with near wall relaxation and the streamwise gradient  $\partial\bar{\rho}/\partial x$  is not negligible near the injection slot. Furthermore, the gradient  $\partial\bar{\rho}/\partial y$  is almost constant in the entire inner layer and  $\partial\bar{\rho}/\partial y = 0$  at  $y=0$  because of impermeability. Fig. 2b shows  $\partial(\bar{\rho}/\rho_\infty)/\partial y^+$  in the developed zone at  $x/\delta = 5$  and the density gradient over the heated wall. The strong differences of  $\partial(\bar{\rho}/\rho_\infty)/\partial y^+$  between the two cases at  $y^+ < 50$  strengthen the discussion above.

The fine structure of the near wall turbulence is indeed closely linked with the density gradient. The energy equation in the presence of density differences contains

the term  $A = \frac{1}{\rho} \frac{\partial\bar{\rho}}{\partial y} \overline{v' \frac{u'_i u'_i}{2}}$  which may be interpreted as the

contribution of the density gradient to turbulent convection. It is seen that  $A \sim \frac{1}{\rho} S_{v'} \overline{v'^2}^{3/2} \frac{d\bar{\rho}}{dy}$  where  $S_{v'}$  is

the skewness of the wall normal velocity. In a canonical wall layer,  $S_{v'} \sim 0.3$  and  $v^{+*} \sim 1$ . Therefore  $A \sim \frac{0.3}{\rho} \frac{d\bar{\rho}}{dy} \overline{u'^2}$ .

One may compare  $A$  with the major production term  $B = -\overline{u'v'} \frac{\partial\bar{u}}{\partial y}$ . In the constant shear region,  $B^+ \sim \frac{2.5}{y^+}$ .

Consequently,  $\frac{A}{B} \sim 10 \frac{1}{\rho} \frac{d\bar{\rho}}{dy^+}$ . Near the injection slot,

$A/B \sim 0.3$  in the present investigation and this particular effect of density gradient may not be neglected. At  $x/\delta = 5$ , however,  $A/B \sim 0.02$ . Thus, the large negative values of  $\overline{u'^3}/\overline{u'^2}^{3/2}$  may not be explained by this kind of local effect. The persistance of negative skewness downstream of the injection slot is presumably due to a particularly slow relaxation of the near wall turbulence or through other mechanisms which could not be elucidated yet.

The skewness of the temperature fluctuations  $S_{\theta'}$  reported by Wardana et al. (1992) have to be compared with the skewness of the concentration  $S_{c'}$  rather than  $S_{\rho'} = -\overline{\rho'^3}/\sqrt{\overline{\rho'^2}^3} \text{sgn}(\partial\bar{\rho}/\partial y)$ . Indeed, the equation governing the instantaneous scalar  $c(t) = \bar{C} + c'(t)$  is

$\rho \frac{Dc}{Dt} = \frac{\partial}{\partial x_k} (\alpha \frac{\partial c}{\partial x_k})$ . This relationship is approximately

similar (although not identical) to the energy equation governing  $\theta = \bar{\theta} + \theta'(t)$ . Figure 3a shows that the profiles of  $S_{c'}$  obtained here are in global agreement with  $S_{\theta'}$  over the heated wall in the buffer layer. Large departures between these quantities are however noticeable in the constant shear region. It is asked here if the differences in density gradients (Fig. 2b) are sufficient to explain this discordance.

The distributions of the flatness of both  $u'$  and  $\rho'$  in the inner layer (not shown here) are found similar suggesting that the intermittency mechanism is not significantly affected by  $\Delta\rho$ . We further compared the distribution of the flatness  $F_{\rho'}$  with  $F_{v'}$ , in order to test once again the supposed similarity between the fine structure of wall normal velocity and density fluctuations. These profiles are shown in Fig. 3b. It is seen that  $\rho'$  is slightly less intermittent than  $v'$  at  $y^+ > 15$  and that the correspondance is acceptable. Note however that, the measurements in the viscous sublayer wherein  $v'$  is strongly intermittent are needed before drawing a final conclusion on this aspect.

### Conditional analysis

Fig. 4a shows the quadrant distributions of  $\rho'$  and  $u'$  obtained at  $y/\delta = 0.25$  and  $x/\delta = 0.5$ . It is seen that  $\rho' \cdot u'$  is oriented from quadrants 2-4 when  $\Delta\rho > 0$  (air injection) and from quadrants 1-3 when  $\Delta\rho < 0$ . This is in agreement with the distribution of the correlation coefficient

$\overline{\rho'u'}/\sqrt{\rho'^2}\sqrt{u'^2}$  which is positive or negative depending upon the injection of lighter or heavier fluid at the wall (Harion 1994). The data is further analyzed by means of a conditional analysis similar to that given by Wardana et al (1995). The large excursions of a quantity  $q'$  are determined by :

$$q'_{+, -} = \frac{\sqrt{\sum_i (S_{+, -})_i [q'_i - \langle q'_{i+, -} \rangle]^2}}{\sum_i (S_{+, -})_i}$$

where the subindices + or - correspond respectively to the ejections and sweeps,  $\langle \rangle$  denotes the conditional average and  $S$  is a detector function based both on  $u'$  and  $p'$ . The ejection phase is defined for injection of helium as:

$$(S_+)_i = 1 \text{ if } u'_i < -\sqrt{u'u'} \text{ and } p'_i < -\sqrt{p'p'} \text{ and } (S_+)_i = 0 \text{ otherwise.}$$

The data obtained this way (Fig. 4b) compares fairly well with the measurements of Wardana et al (1995) over a strongly heated wall. Close inspection of the results shows that the ejection type flow is intensified when lighter fluid (helium) is injected into the boundary layer and that, in return, the sweeps are weakened. This, too, is in agreement with the results of Wardana et al. Although the correlation coefficient between velocity and density fluctuations is significantly larger than the  $-u'v'$  correlation in the inner layer, it was thought first, that  $u'p'$  could be dynamically similar to  $-u'v'$  through the distributions of the quadrant contributions. A detailed analysis conducted for the reference case (injection of air with small  $\Delta\rho > 0$ ) has revealed that this is not exactly the case. Qualitative agreement has been found between the contributions of the ejection and sweep type events ( $\overline{C}_{ej}$ ,  $\overline{C}_{sw}$ ) when compared with the canonical boundary layer. However, some quantitative differences have been observed at  $y^+ > 30$ , in the ratio  $\overline{C}_{ej}/\overline{C}_{sw}$  (see Tardu et al 1997 for further details). The hole analysis as described in Willmarth and Lu (1972), and performed by Cheng and Ng (1985) has also been applied to the  $u'p'$  quadrants. The main result is that the ejections occupy a larger area in the quadrant 3 in the case of strong  $\Delta\rho < 0$  in particular in the constant shear region. Fig. 5 recapitulates the distributions of  $\overline{C}_{ej}$  vs. the hole size for the reference case and the injection of helium at  $y^+ = 80$ .

## CONCLUSION

The energetic events in the inner layer are intimately related to the presence of the quasi-streamwise vortices. The rate of change of  $\omega_x$  vorticity reads :

$$\frac{D\omega_x}{Dt} = \vec{\omega} \cdot \nabla u - \frac{\omega_x}{\rho} \frac{D\rho}{Dt} + \dots$$

The term  $-u \frac{\omega_x}{\rho} \frac{\partial \rho'}{\partial x}$  of this equation plays a role which is

similar to the stretching of vorticity via  $\omega_x \frac{\partial u}{\partial x}$ . When

helium is injected, and during the ejections it is likely that the stretching of the streamwise vorticity is intermittently enhanced by this term and that the quasi-streamwise vortices are consequently reinforced. Results

concerning the quantity  $S = \frac{(\frac{\partial u'}{\partial t})^2 \frac{\partial \rho'}{\partial t}}{(\frac{\partial u'}{\partial t})^2 (\frac{\partial \rho'}{\partial t})^2}^{1/2}$

(which is equivalent to the skewness of the velocity time derivatives related to the vorticity stretching strength) are further analyzed in Tardu et al (1997) and seem to strengthen this assumption. Further results concerning the conditional averages related to the shear layer events determined by an adapted version of VITA may also be found in Tardu et al (1997).

## REFERENCES

- Cheng, R.K., T.T., Ng, 1985, "Conditional Reynolds Stress in a Strongly Heated Turbulent Boundary Layer with Premixed Combustion", *Phys. Fluids*, 28, 2, pp. 473-488
- Harion, J.L., 1994, "Influence de différences de densité importantes sur les propriétés de transfert d'une couche limite turbulente", PhD Thesis INP Grenoble
- Harion, J.L., Favre-Marinet, M., Binder, G., 1997, "Density and Velocity Measurements in Turbulent He-Air Boundary Layers", *Exp. Thermal and Fluid Science*, 14, pp 92-100
- Kim, J., Moin, P., Moser, R., 1987, "Turbulence Statistics in Fully Developed Channel Flow at Low Reynolds Number", *J. Fluid Mech.*, 177, pp 133-166
- LaRue, J.C., Libby, P.A., 1980, "Further Results Related to the Turbulent Boundary layer with Slot Injection of Helium", *Phys. Fluids*, 23, 6, pp. 1111-1118
- Tardu, S., Soudani, A., Favre-Marinet, M., Harion, J.L., 1997, "Response of near wall turbulence to strong density differences", in preparation.
- Wardana, I.N.G., Ueda, T., Mizomoto, M., 1992, "Structure of Turbulent Two-Dimensional Channel Flow with Strongly Heated Walls", *Exp. Fluids*, 13, pp. 17-25
- Wardana, I.N.G., Ueda, T., Mizomoto, M., 1995, "Velocity-Temperature Correlation in Strongly Heated Channel Flow", *Exp. Fluids*, 18, pp. 454-461
- Willmarth, W.W., Lu, S.S., 1972, "Structure of the Reynolds Stress near the Wall", *J. Fluid Mech.*, 55, pp 65-92

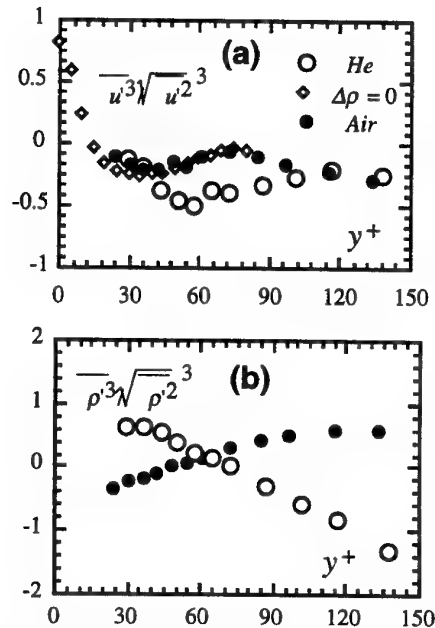


FIGURE 1: SKEWNESS OF THE VELOCITY (a) AND DENSITY FLUCTUATIONS (b) at  $x/\delta=5$ .

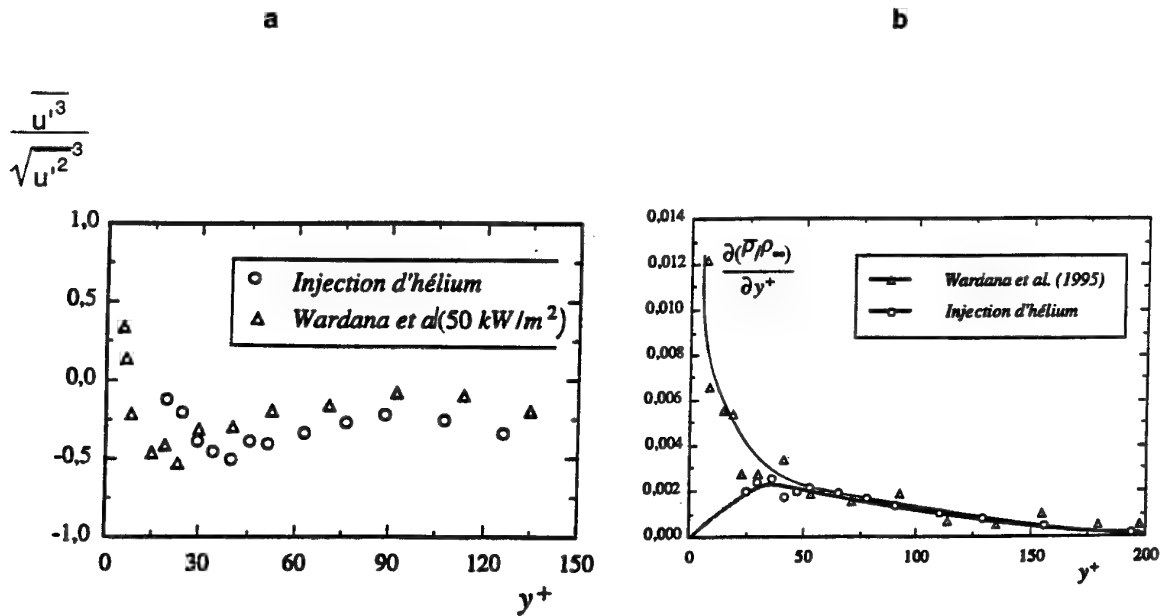


FIGURE 2 : COMPARISON OF (a) THE SKEWNESS FACTOR OF  $U'$  AND (b) THE DENSITY GRADIENT WITH THE EXPERIMENTS OF WARDANA et al.(1992)

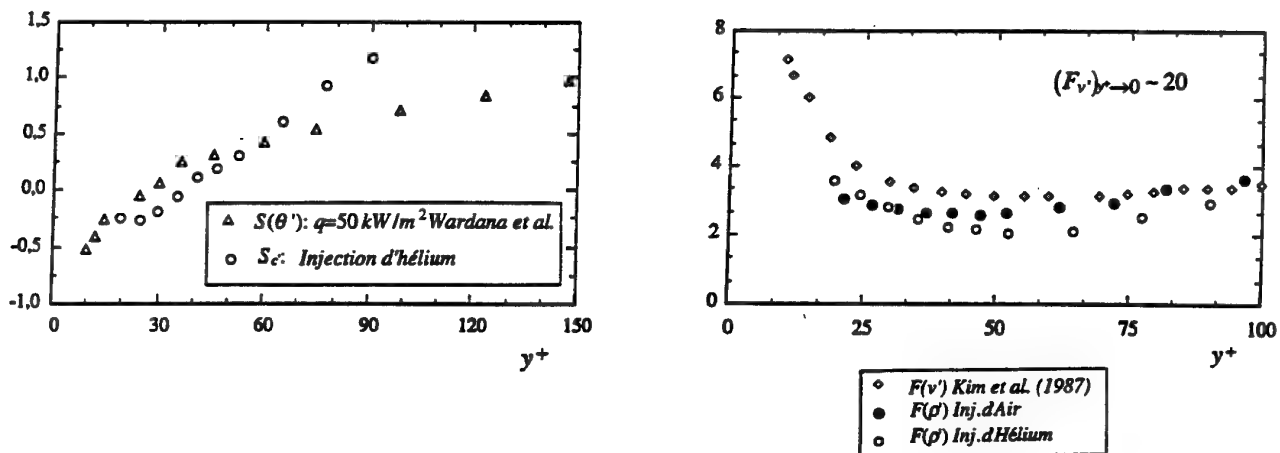


FIGURE 3 a : SKEWNESS OF THE FLUCTUATING CONCENTRATION WITH THE SKEWNESS OF TEMPERATURE REPORTED BY WARDANA et al. (1992);

b: FLATNESS OF  $p'$  COMPARED WITH THE FLATNESS OF WALL NORMAL VELOCITY FLUCTUATIONS IN THE CANONICAL LAYER;  $x/\delta= 5$  IN BOTH CASES.

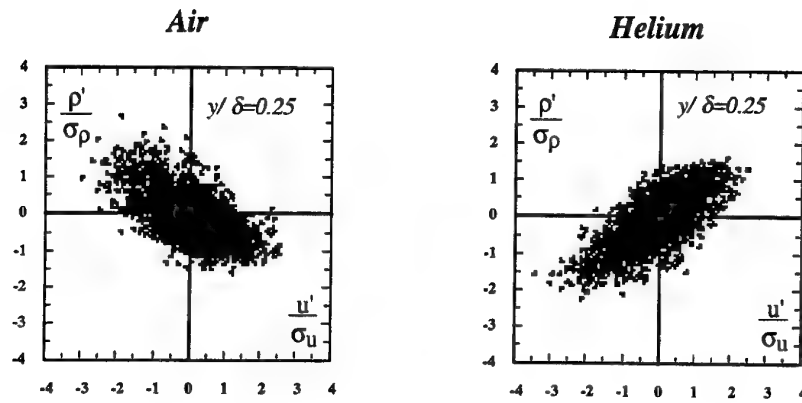


FIGURE 4a : QUADRANT DISTRIBUTION OF THE DENSITY AND VELOCITY DISTRIBUTIONS at  $y/\delta=0.25$ .

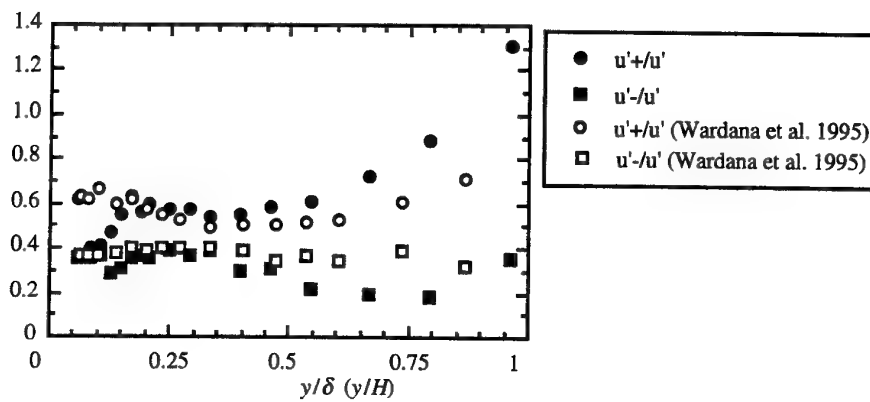


FIGURE 4b : CONDITIONAL VELOCITY CONTRIBUTIONS WITH HELIUM INJECTION.

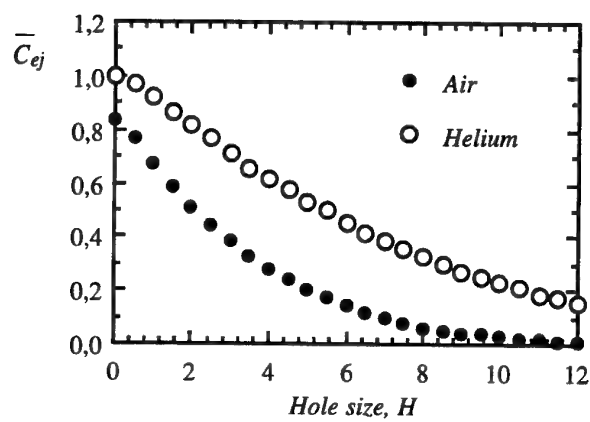


FIGURE 5 : HOLE ANALYSIS at  $x/\delta=2.75$  and  $y^+=80$ .

# MONTE CARLO COMPUTATIONS OF TURBULENT VARIABLE DENSITY JETS

J.P.H. Sanders and I. Gökalp

Laboratoire de Combustion et Systèmes Réactifs  
Centre National de la Recherche Scientifique  
1C Avenue de la Recherche Scientifique  
45071 Orléans Cedex 2, France

## ABSTRACT

A relatively simple solution algorithm for the PDF transport equation in turbulent variable density jets is used to calculate the statistics of the mixture fraction field. The classical transport equations for the mean and the variance of the mixture fraction are solved as well to compare the two solution methods. Also the computed mixture fraction PDF with the Monte Carlo method is compared with the presumed PDF based on the first two moments (mean and variance) using a  $\beta$ -function. The two methods compare favourably, as was to be expected and it is found that the  $\beta$ -function PDF is a good approximation.

## INTRODUCTION

Turbulent combustion models all make use of statistical properties of the scalar field. In particular the statistics of the mixture fraction, which is the mass fraction of the jet gas, is of great importance. For instance in the laminar flamelet model for turbulent combustion the thermochemical state is determined by the mixture fraction and a second parameter that accounts for non-equilibrium chemistry (Peters, 1984, 1986). The mixture fraction statistics are mostly approximated by calculating the mean mixture fraction and its variance by modelled transport equations. The probability density function (PDF) of the mixture fraction is then constructed by assuming a certain shape, for instance a  $\beta$ -function with the mean and variance as parameters. The mean thermo-chemical variables are calculated using this PDF and the (non linear) relationships that exist between the mixture fraction and the instantaneous thermo-chemical variables. For applications see for instance Liew et al. (1984), Fairweather et al. (1991), Sanders and Lamers (1994) or Sanders et al. (1997b). In this way the laminar flamelet method circumvents the evaluation of mean reaction rates, which is the central problem in turbulent combustion modelling.

Another type of turbulent combustion model is the one in which a transport equation for either the joint composition PDF (all considered species mass fractions and the temperature) is solved, or the joint velocity-composition PDF is solved (Pope, 1985; Hulek and Lindstedt 1996). Using this PDF, the mean reaction rates need no mod-

elling. However, in the joint composition PDF model the molecular diffusion term has to be modelled and in the joint composition-velocity PDF both the molecular diffusion and viscous dissipation terms have to be modelled. These are considered the weakest points in the model. Also, in general reduced chemistry has to be used since the computational expenses are proportional to the number of species mass fractions in the PDF. For hydrogen flames, the complete reaction mechanism is sufficiently small to allow full chemistry calculations (Chen et al., 1996). The PDF transport equation can only be solved in a computationally efficient manner by using Monte Carlo methods.

Because of the imperfections in the molecular diffusion models, the PDF method may be regarded most applicable when molecular diffusion is not very important, such as in flames with slow chemistry or low Damköhler numbers. On the other hand, the laminar flamelet model, valid for flames in which fast chemistry is predominant, treats molecular diffusion exactly, including differential diffusion effects. But these differential diffusion effects are up to now not considered a function of the Reynolds number of the flame, which can lead to problems when calculating turbulent hydrogen flames (Sanders and Gökalp, 1997a).

Pope (1982) solved the joint velocity-scalar PDF transport equation for the self similar region of a plane turbulent jet, the normalised cross stream distance being the only independent spatial variable. Jones and Kollmann (1985) computed a turbulent propane-air jet diffusion flame using a three-variable scalar Monte Carlo approach and a  $k - \epsilon$  turbulence model. Chen et al. (1989) predicted a turbulent methane-air jet diffusion flame using the five-variable PDF method and a second-order turbulence model. Biagioli (1997) compared the PDF's computed with a Monte Carlo method to the presumed PDF's based on the mean and variance of the mixture fraction. A  $k - \epsilon$  turbulence model was used in combination with a one step chemical reaction described by a reaction progress variable.

In the present work, the scalar PDF transport equation is solved for turbulent variable density (hydrogen) jets. The mean and the variance of the mixture fraction calculated with the PDF method are compared to their counterparts calculated in the classical manner, i.e., using the transport

equations for these variables. This comparison is meant to quantify the differences that can be expected when utilising two different computational methods for the same type of problem. The PDF computed with the Monte Carlo method will be compared to the  $\beta$ -function PDF based on the classical mean and variance of the mixture fraction. Also, two different models for molecular diffusion, i.e. the 'Interaction by Exchange with the Mean' (IEM) model and Curl's modified mixing model, will be compared. The IEM model is also called the Linear Mean Squared Estimation (LMSE) model (Dopazo, 1975).

## EQUATIONS AND NUMERICAL METHOD

A second order turbulence model is used to compute the turbulent flowfield which is based on the model of Launder et al. (1975) and it is described and used in Sanders et al. (1997a, 1997b). The numerical method used to compute the scalar PDF transport equation is based on the Monte Carlo method and the concept of fractional steps: the spatial integration of convection and turbulent diffusion is followed by a time integration of the molecular diffusion term. The latter process is computed by using the method of Chen (1996). The numerical integration of the convection and turbulent diffusion terms is performed following Pope (1981) and Jones and Kollmann (1985), although the present parabolic algorithm does not use a transformed radial coordinate. The Monte Carlo algorithm is of a Eulerian type. It uses particles that do not move with the velocity field.

### Equation for the Scalar PDF

The probability density function  $P$  of the scalar  $f$  (the mixture fraction) is governed by

$$\begin{aligned} \frac{\partial \bar{P}}{\partial t} + \frac{\partial \bar{P}U}{\partial x} + \frac{1}{r} \frac{\partial \bar{P}V}{\partial r} = & \quad (1) \\ - \frac{\partial \bar{P} < u'' | f = \phi > P}{\partial x} - \frac{1}{r} \frac{\partial \bar{P} < v'' | f = \phi > P}{\partial r} \\ - \bar{P} \frac{\partial^2}{\partial \phi^2} (< \chi_f | f = \phi > P) \end{aligned}$$

with the scalar dissipation rate

$$\chi_f = \mathcal{D} \frac{\partial f}{\partial x_k} \frac{\partial f}{\partial x_k} \quad (2)$$

in which  $\mathcal{D}$  is the molecular diffusion coefficient. Here,  $U$  and  $V$  designate the mean Favre (density weighted) averaged axial and radial velocity, respectively, and  $''$  denotes the Favre fluctuation. The turbulent diffusion terms are modelled as

$$- \bar{P} < u''_k | f = \phi > P = C_d \bar{P} \frac{k u''_k}{\varepsilon} \frac{\partial P}{\partial x_k} \quad (3)$$

with  $k$  the turbulent kinetic energy and  $\varepsilon$  its dissipation rate. In parabolic flow, axial diffusion is negligible. The modelled equation thus becomes

$$\begin{aligned} \frac{\partial \bar{P}}{\partial t} + \frac{\partial \bar{P}U}{\partial x} + \frac{1}{r} \frac{\partial \bar{P}V}{\partial r} = & \quad (4) \\ C_d \frac{1}{r} \frac{\partial}{\partial r} \left( r \bar{P} \frac{k v''^2}{\varepsilon} \frac{\partial P}{\partial r} \right) \\ - \bar{P} \frac{\partial^2}{\partial \phi^2} (< \chi_f | f = \phi > P) \end{aligned}$$

The constant  $C_d$  is given the value 0.18 by comparing the present model to the classical transport equation model for the mixture fraction.

### Numerical Solution of the PDF Equation

Equation (4) is solved numerically by a fractional step method: first the spatial terms are integrated (convection and turbulent diffusion) and subsequently the molecular diffusion is integrated in time. In terms of the parabolic solution algorithm, the procedure is as follows. Given the solution on gridline  $i$ ,  $P_{i,j}$ , the solution on the next gridline,  $P_{i+1,j}$ , is determined using an explicit finite difference scheme for the spatial terms.

$$P_{i+1,j} = a P_j + b P_{j+1} + c P_{j-1} \quad (5)$$

The subscript  $i$  for  $P$  on the right hand side has been suppressed. The index  $j$  indicates the radial direction. Subsequently, the molecular diffusion term is time integrated with a time step equal to the local convective residence time  $\delta t = \delta x / U$  in which  $\delta x$  is the axial stepsize and  $U$  is the local mean centreline velocity.

**Convection and Turbulent Diffusion.** To evaluate the coefficients  $a$ ,  $b$  and  $c$ , the (spatial) conservation equation is written in the non-conservation form:

$$\begin{aligned} \bar{P} \frac{\partial P}{\partial t} + \bar{P} U \frac{\partial P}{\partial x} + \bar{P} V \frac{\partial P}{\partial r} = C_d \frac{1}{r} \frac{\partial}{\partial r} \left( r \bar{P} \frac{k v''^2}{\varepsilon} \frac{\partial P}{\partial r} \right) & \quad (6) \\ - \bar{P} \frac{\partial^2}{\partial \phi^2} (< \chi_f | f = \phi > P) \end{aligned}$$

Applying an explicit difference scheme to the spatial part of this equation, one gets

$$\begin{aligned} \frac{\rho_j U_j}{\delta x} (P_{i+1,j} - P_j) + \frac{\rho_j V_j}{2 \delta r} (P_{j+1} - P_{j-1}) & \quad (7) \\ - \frac{1}{r_j} \frac{C_d r_{j+1/2} (\rho \frac{k}{\varepsilon} v''^2)_{j+1/2}}{\delta r^2} (P_{j+1} - P_j) \\ + \frac{1}{r_j} \frac{C_d r_{j-1/2} (\rho \frac{k}{\varepsilon} v''^2)_{j-1/2}}{\delta r^2} (P_j - P_{j-1}) = 0 \end{aligned}$$

Diffusion related coefficients are defined as

$$F_+ = \frac{1}{r_j} \frac{C_d r_{j+1/2} (\rho \frac{k}{\varepsilon} v''^2)_{j+1/2}}{\delta r^2} \frac{\delta x}{\rho_j U_j} \quad (8)$$

$$F_- = \frac{1}{r_j} \frac{C_d r_{j-1/2} (\rho \frac{k}{\varepsilon} v''^2)_{j-1/2}}{\delta r^2} \frac{\delta x}{\rho_j U_j} \quad (9)$$

and a radial convection coefficient as

$$C' = \frac{\rho_j V_j}{2 \delta r} \frac{\delta x}{\rho_j U_j} = \frac{\delta x V_j}{2 \delta r U_j} \quad (10)$$

so that the discretised equation becomes

$$\begin{aligned} P_{i+1} &= (1 - F_+ - F_-) P_j + & (11) \\ (F_+ + C') P_{j+1} &+ (F_- + C') P_{j-1} \end{aligned}$$

such that  $a$ ,  $b$  and  $c$  in Eq. (5) become

$$\begin{aligned} a &= 1 - F_+ - F_- & (12) \\ b &= F_+ + C' \\ c &= F_- + C' \end{aligned}$$

Thus,  $a + b + c = 1$  and for stability one should have all coefficients  $a, b, c > 0$ . This restricts the allowable axial stepsize  $\delta x$ . The number of particles to be randomly chosen from the upstream gridcells will be  $N_a = a \times N_p$ ,  $N_b = b \times N_p$  and  $N_c = c \times N_p$  with  $N_p$  the total number of particles in each gridcell. The numbers  $N_a$ ,  $N_b$  and  $N_c$  are not necessarily integers and they are rounded to the nearest integer. The rounded fractions of several steps in the axial direction are accumulated and when their values reach 1 or



-1, this is accounted for by adding or subtracting a particle from the corresponding variable  $N_a$ ,  $N_b$  or  $N_c$ .

**Molecular Diffusion.** As mentioned previously, the molecular diffusion term is integrated in time using either the IEM or the modified Curl's model. The IEM model, which is deterministic, can be written as

$$\phi^n(t + \Delta t) = \phi^n(t) - \frac{1}{2} C_\phi \frac{\Delta t}{\tau} (\phi^n(t) - \langle f \rangle) \quad (13)$$

where  $n$  indicates the particle index,  $C_\phi = 2$  and  $1/\tau = \omega = k/\varepsilon$  is the mixing frequency. All particles are submitted to this process, which is why it is called deterministic.

In Curl's mixing model, which is stochastic, a frequency  $\tau_{N_p} = \tau/(C_\phi N_p)$ , with  $C_\phi = 6$ , is defined. A probability  $P_{\text{curlmix}} = \Delta t/\tau_{N_p}$  gives the probability of mixing between two randomly chosen particles  $p$  and  $q$ . This mixing process is defined by

$$\begin{aligned} \phi^p(t + \Delta t) &= \phi^q(t + \Delta t) \\ &= \frac{1}{2} (\phi^p(t) + \phi^q(t)) \quad (p \neq q) \\ \phi^n(t + \Delta t) &= \phi^n(t), \\ n &= 1, \dots, N_p, n \neq p, n \neq q \end{aligned} \quad (14)$$

and with a probability  $P = 1 - P_{\text{curlmix}}$  the particles are not mixed:

$$\begin{aligned} \phi^n(t + \Delta t) &= \phi^n(t) \\ n &= 1, \dots, N_p \end{aligned} \quad (15)$$

The mean scalar dissipation rate  $\varepsilon_f = \tilde{\chi}_f$ , which is the rate at which mixture fraction fluctuations on the smallest scales are smoothed by molecular diffusion, is modelled by an algebraic expression based on equality of scalar and mechanical time scales

$$\varepsilon_f = \widetilde{f'^2} \frac{\varepsilon}{k} \quad (16)$$

The mechanical to scalar time scale ratio  $R = (k/\varepsilon)/(\widetilde{f'^2}/\varepsilon_f)$  has been set to 1 in this model. Sanders and Gökalp (1997b) discuss more elaborate existing transport equation models and another algebraic model that not relies on a constant  $R$  across the flow field. They conclude that for turbulent jet type of flows, the algebraic model of Eq. (16) is sufficiently accurate.

Since the computational grid is expanding in the radial direction, the newly calculated PDF  $P$  has to be interpolated on the new grid line. Also here, the fractions of particles are accumulated in the same way as mentioned before.

## RESULTS

Computations have been performed with 400 Monte Carlo particles per cell, 50 cells per grid line and using Curl's modified mixing model, unless otherwise specified. The axial stepsize was approximately  $0.005 \times$  the local jet halfwidth. Computations are performed for hydrogen into still air jets issuing from a nozzle with  $D = 3.75\text{mm}$  and with a mean jet exit velocity of 100 m/s. In the following no explicit comparisons with experimental data are shown because the main objective is to compare the Monte Carlo computations to the classical transport equation method. The latter has been extensively tested against experimental data (Sanders et al., 1997a).

### Comparison of Scalar Profiles

In Fig. 1 the centreline decay of the mean mixture fraction and of its variance are shown, computed by the two methods. It should be noted that the mean density in both

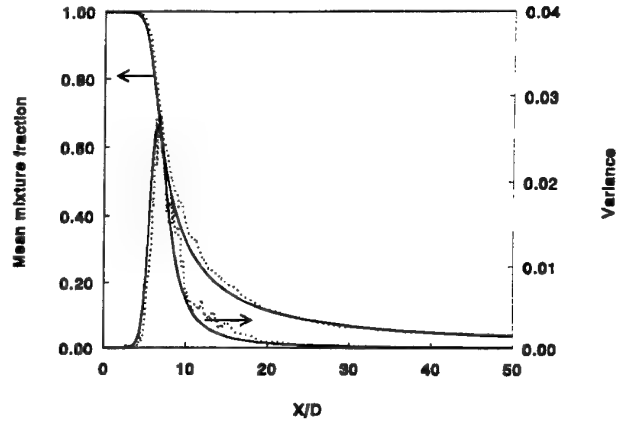


Figure 1: Centreline variation of the mean mixture fraction and its variance for a free turbulent hydrogen jet into stagnant air. Predictions with the classical transport equations (solid lines) and with the PDF transport equation (dotted lines).

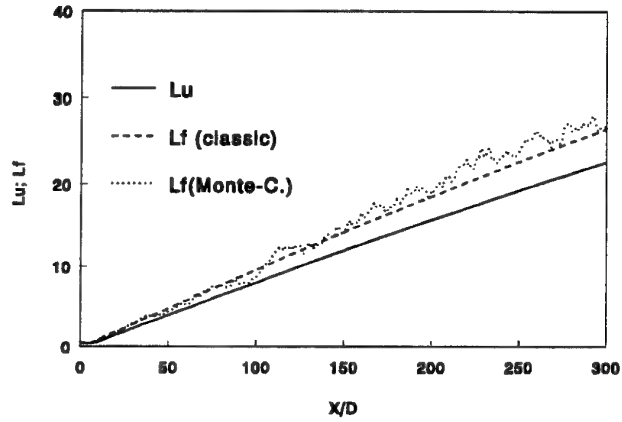


Figure 2: Halfwidth of the mean velocity (solid line) and the mixture fraction in a free turbulent hydrogen jet into stagnant air. Predictions of the scalar halfwidth with the classical transport equations (dashed line) and with the PDF transport equation (dotted line).

methods was obtained from the mixture fraction computed with the PDF method. Both methods agree relatively well with each other. The (non-smoothed) PDF method results show the inevitable statistical fluctuations. These diminish with increasing number of Monte Carlo particles per gridcell, as will be shown below. Fig. 2 shows the scalar spreading rates predicted with the two methods. Again the agreement is good. The scalar spreading rate is larger than the velocity spreading rate which agrees with previous work and experimental data (Sanders et al., 1997a). Fig. 3 shows the radial profiles of the mean mixture fraction and its variance at the axial station  $x/D = 50$ . Again, the agreement between the two models is quite good, but the variance shows larger statistical fluctuations. The same remarks can be made regarding the profiles at  $x/D = 150$ , see Fig. 4.

The computation of the mean mixture fraction with the PDF method does not depend on the molecular diffusion model used. Therefore, the mixture fraction profiles only present a test for the convection and turbulent diffusion

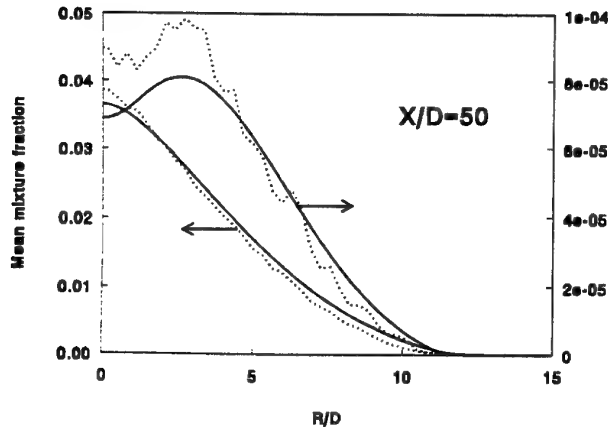


Figure 3: Radial profiles at  $x/D = 50$  of the mean mixture fraction and its variance for a free turbulent hydrogen jet into stagnant air. Predictions with the classical transport equations (solid lines) and with the PDF transport equation (dotted lines).

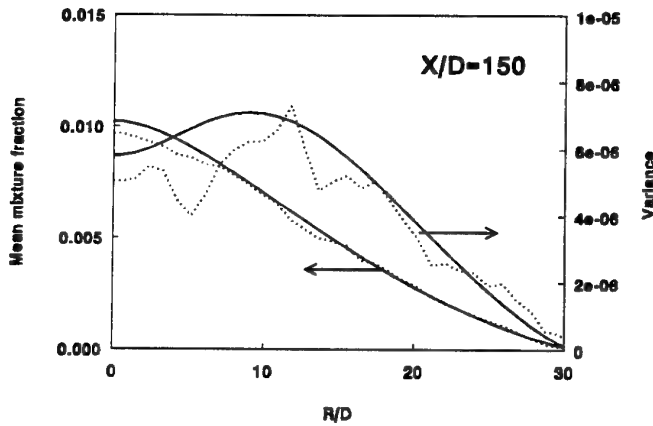


Figure 4: Same as Fig. 3 for  $x/D = 150$ .

models in the PDF method. They appear to be quite satisfactory.

The scalar variance, which does depend on the molecular diffusion model, is predicted relatively well using Curl's mixing model. In Fig. 5 the mean mixture fraction profiles at  $x/D = 100$  predicted with the classical transport equation method and the PDF method using Curl's mixing model and the IEM model are compared. The difference between Curl's and the IEM model is due to statistical errors since the molecular diffusion model will not influence the mean mixture fraction profiles except by its influence through the mean density. This density influence is small at the axial distance considered. Fig. 6 presents the scalar variance profiles at the same axial station, and here the difference will more likely be due to the different mixing models, although statistical errors will evidently still be present. Curl's mixing model agrees very well with the classical transport equation method. In Fig. 7 the centre-line evolution of the mean mixture fraction and its variance are shown calculated with the classical transport equation model and the PDF method using the IEM mixing model. The differences with Curl's modified mixing model are very small.

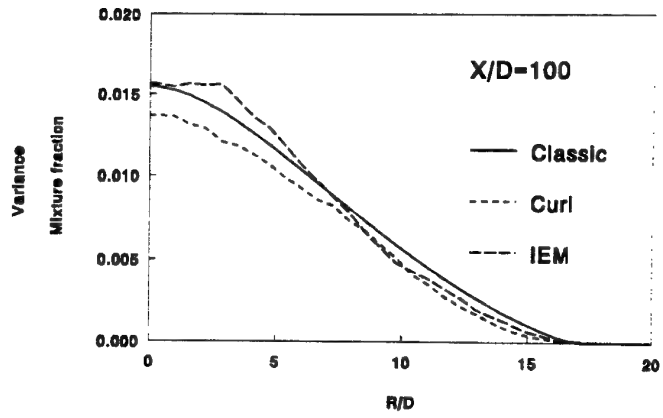


Figure 5: Radial profiles of the mean mixture fraction at  $x/D = 100$ . Predictions are made with the classical transport equation method (solid line), the PDF method using Curl's modified mixing model (dashed line) and the IEM mixing model (long dashed line).

### Probability Density Functions

Probability density functions predicted with the Monte Carlo method and calculated with the presumed PDF method using the  $\beta$  function based on the mean and variance of the mixture fraction are now compared for the axial station  $x/D = 50$  at  $r/D = 0$  (Fig. 8) and  $r/D = 6.3$  (Fig. 9). In both figures, the Monte Carlo based PDF is compared with the  $\beta$ -function that corresponds to the mean and variance associated with the Monte Carlo PDF at the given location. The Monte Carlo PDF values have been normalised to be comparable to the  $\beta$  function values. The PDF's in both figures correspond well to one another which implies that indeed for one dimensional PDF's in jet like flows, the  $\beta$ -function is a good approximation.

### Conservation of Mixture Fraction Flux

The flux of matter issued from the nozzle must remain constant all along the jet, i.e.

$$\dot{m}_f(x) = \int_0^\infty \bar{\rho}(x, r) U(r, x) F(r, x) r dr = \dot{m}_{f,0} \quad (17)$$

This flux based on the mean mixture fraction calculated by the Monte Carlo method and by the classical transport equation method is computed at each axial station. The flux based on the classical method is indeed constant while the Monte Carlo flux shows statistical fluctuations (Fig. 10).

The difference between the Monte Carlo based flux and the classical flux increases with increasing axial stepsize and with decreasing number of Monte Carlo particles. An increasing axial stepsize leads to occurrences of negative coefficients  $a$ ,  $b$  or  $c$  in Eq. (13), which has to be corrected for.

### Number of Monte Carlo Particles

The accuracy of the numerical solution depends on the number of Monte Carlo particles ( $N_p$ ). The numerical error  $\epsilon$  decreases as  $\epsilon \sim 1/\sqrt{N_p}$ . In Fig. 11 the mixture fraction profiles at  $x/D = 50$  with 2000 and 400 particles in each cell are compared. In Fig. 12 the same comparison is made for the mixture fraction variance. In theory a fivefold increase of the number of particles would represent an increase in accuracy of about a factor 2. Indeed, the statistical fluctuations with 2000 particles are less visible.

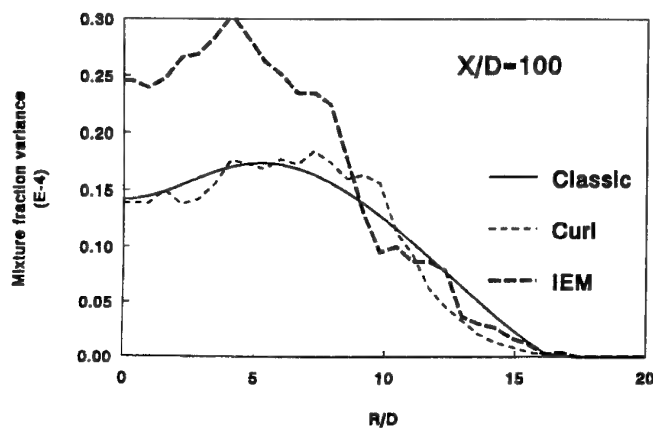


Figure 6: Radial profiles of the mean mixture fraction variance at  $x/D = 100$ . Predictions are made with the classical transport equation method (solid line), the PDF method using Curl's modified mixing model (dashed line) and the IEM mixing model (long dashed line).

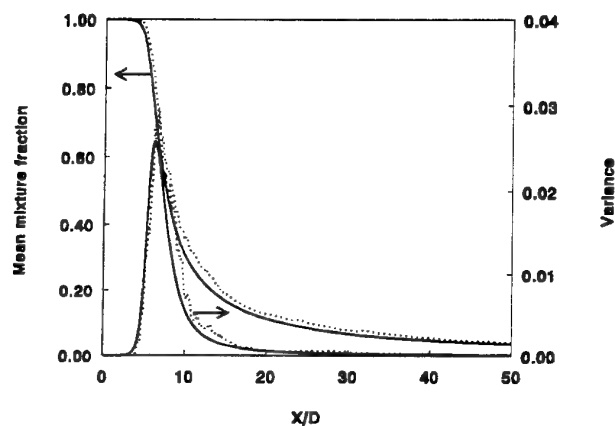


Figure 7: Centreline evolution of the mean mixture fraction and variance. Predictions are made with the classical transport equation method (solid lines), and the PDF method using the IEM mixing model (dotted lines).

## CONCLUSIONS

A relatively simple solution algorithm for the PDF transport equation in turbulent variable density jets has been used to calculate the statistics of the mixture fraction. For the mean and the variance of the mixture fraction, the corresponding classical transport equations were solved as well to compare the two solution methods. Also the computed mixture fraction PDF with the Monte Carlo method was compared with the presumed PDF based on the first two moments (mean and variance) using a  $\beta$ -function PDF. The two methods compare favourably, as was to be expected and it appears that the  $\beta$ -function is a good approximation. The Monte Carlo computations however, show the inevitable statistical scatter and is more demanding regarding computational resources. This is a clear disadvantage when non-reacting flows are computed. It is very beneficial, however, to use the PDF method in turbulent reacting flows, where the reaction terms are treated without modelling.

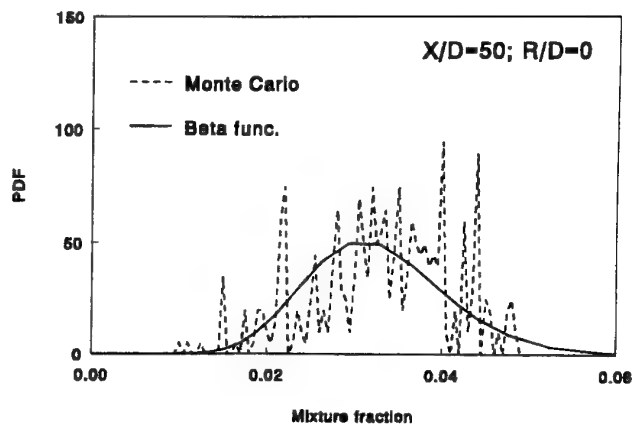


Figure 8: Probability density functions predicted with the Monte Carlo method and approximated with a  $\beta$  function based on the mean and variance of the classical method  $x/D = 50$  and  $r/D = 0$ .

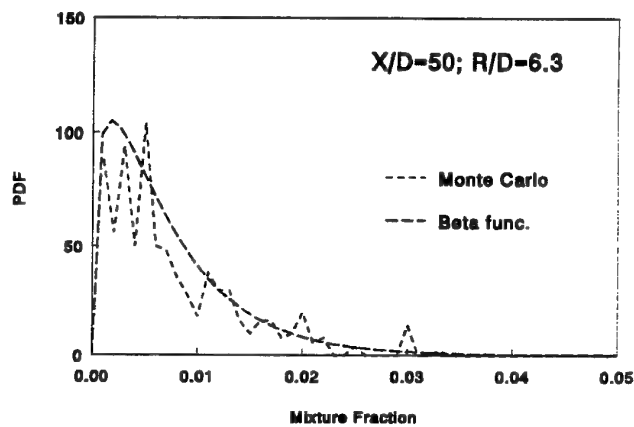


Figure 9: Probability density functions predicted with the Monte Carlo method and approximated with a  $\beta$  function based on the mean and variance of the classical method  $x/D = 50$  and  $r/D = 6.3$ .

**Acknowledgements :** Prof. J.-Y. Chen (U.C. at Berkeley) is thanked for providing the code for the molecular mixing model and for beneficial discussions.

## REFERENCES

- Biagioli, F., 1997, "Comparison between presumed and Monte Carlo probability density function combustion models", *J. Propulsion and Power* Vol. 13, pp. 109-116.
- Chen, J.-Y., Kollmann, W. and Dibble, R.W., 1989, "PDF modeling of turbulent nonpremixed methane jet flames", *Combust. Sci. Technology* Vol. 64, pp. 315-346.
- Chen, J.-Y., 1996, "Stochastic modeling of partially stirred reactors", *Combust. Sci. Technology*, in press.
- Chen, J.-Y., Chang, W.-C., and Koszykowski, M., 1996, "Numerical simulation and scaling of  $NO_x$  emissions from turbulent hydrogen jet flames with various amounts of He dilution", *Combust. Sci. Techn.* Vol. 110, pp. 505-529.
- Dopazo, C., 1975, "PDF approach for a turbulent axisymmetric heated jet: centerline evolution", *Physics of Fluids* Vol. 18, pp. 397-404.
- Fairweather, M., Jones, W.P., Lindstedt, R.P. and Mar-

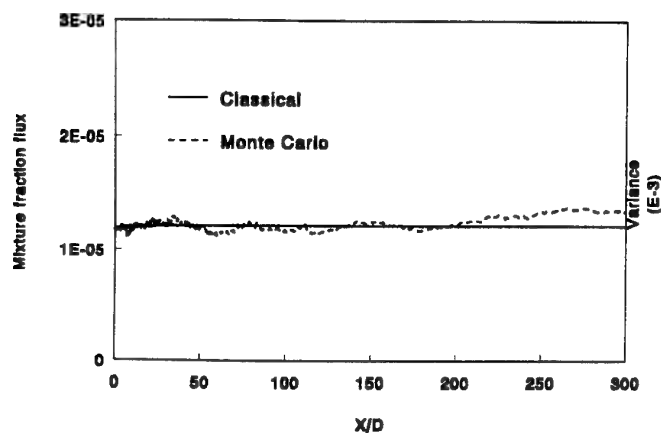


Figure 10: Mixture fraction flux of Eq. (17) as a function of  $x/D$  based on the mean mixture fraction obtained from the classical transport equation (solid line) and obtained from the Monte Carlo method (dashed line).

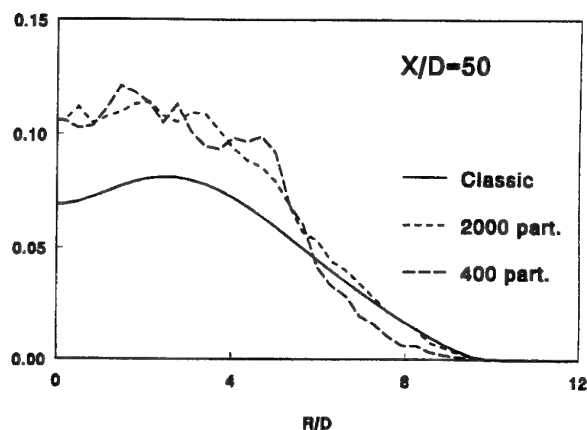


Figure 12: Mixture fraction variance profile at  $x/D = 50$  predicted with 2000 and 400 Monte Carlo particles in each cell. Curl's mixing model is used.

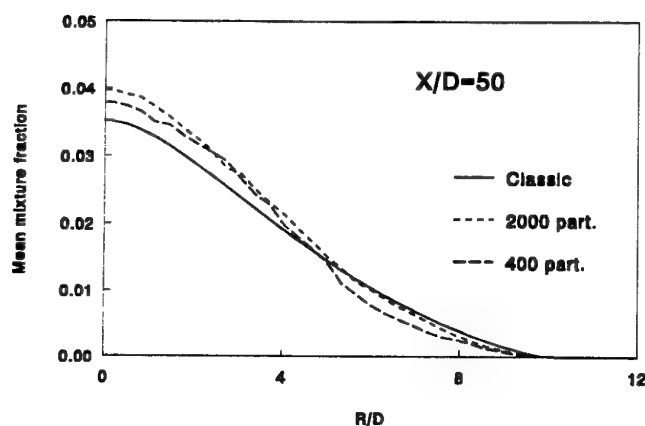


Figure 11: Mixture fraction profile at  $x/D = 50$  predicted with 2000 and 400 Monte Carlo particles in each cell. Curl's mixing model is used.

nology Vol. 25, pp. 159-174.

Pope, S.B., 1982, "Calculations of velocity-scalar joint pdf's", *Turbulent Shear Flows* Vol. 3, pp. 113-123.

Pope, S.B., 1985, "Pdf methods for turbulent reactive flows", *Progress Energy Combust. Sci.* Vol. 11, pp. 119-192.

Sanders, J.P.H. and Lamers, A.P.G.G., 1994, "Modeling and calculation of turbulent lifted diffusion flames", *Combust. Flame* Vol. 96, pp. 22-33.

Sanders, J.P.H. and Gökalp, I., 1997a, "Non-equilibrium and differential diffusion effects in turbulent hydrogen diffusion flames", *J. Thermophysics and Heat Transfer* Vol. 11, to appear.

Sanders, J.P.H. and Gökalp, I., 1997b, "Scalar dissipation rate modelling in turbulent jets and diffusion flames", *Physics of Fluids*, submitted.

Sanders, J.P.H., Sarh, B. and Gökalp, I., 1997a, "Variable density effects in axisymmetric isothermal turbulent jets: a comparison between a first- and a second-order turbulence model", *Int. J. Heat Mass Transfer* Vol. 40, pp. 823-842.

Sanders, J.P.H., Chen, J.-Y. and Gökalp, I., 1997b, "Flamelet based modeling of NO formation in turbulent hydrogen jet diffusion flames", *Comb. Flame* to appear.

quis, A.J., 1991, "Predictions of a turbulent reacting jet in a cross-flow", *Combust. Flame* Vol. 84, pp. 361-375.

Hulek, T. and Lindstedt, R.P., 1996, "Modelling of unclosed nonlinear terms in a PDF closure for turbulent flames", *Mathl. Comput. Modelling*, Vol. 24, pp. 137-147.

Jones, W.P. and Kollmann, W., 1985, "Multi-scalar PDF transport equations for turbulent diffusion flames", *Turbulent Shear Flows* Vol. 5, pp. 297-309.

Launder, B.E., Reece, G.J. and Rodi, W., 1975, "Progress in the development of a Reynolds-stress turbulence closure", *J. Fluid Mech.* Vol. 68, pp. 537-566.

Liew, S.K., Bray, K.N.C. and Moss, J.B., "A stretched laminar flamelet model of nonpremixed turbulent combustion", *Combust. Flame* Vol. 56, pp. 199-213.

Peters, N., 1984, "Laminar diffusion flamelet models in non-premixed turbulent combustion", *Progress Energy Combust. Sci.* Vol. 10, pp. 319-339.

Peters, N., 1986, "Laminar flamelet concepts in turbulent combustion", *21st Symposium on Combustion* The Combustion Institute, pp. 1231-1250.

Pope, S.B., 1981, "A Monte Carlo method for the PDF equations of turbulent reactive flow", *Combust. Sci. Tech-*

# EXPERIMENTAL DETERMINATION OF SOME CHARACTERISTIC SCALES IN VARIABLE DENSITY TURBULENT JETS

J. Pagé, Y. Haidous, B. Sarh and I. Gökalp

Laboratoire de Combustion et Systèmes Réactifs  
Centre National de la Recherche Scientifique  
1C, Avenue de la Recherche Scientifique  
45071 Orléans Cedex 2, France

## ABSTRACT

An experimental investigation of variable density turbulent axisymmetric jets is presented. Helium, methane, air and CO<sub>2</sub> jets exhausting into a coflowing air are investigated. Density ratio  $R_\rho$  varies between 7.2 (helium into air) to 0.66 (CO<sub>2</sub> in air). The experiments are conducted with a coflow velocity ratio  $m=0.075$ . Velocity field measurements are performed using two-component laser Doppler anemometry. A Fast Fourier Transform algorithm based on the discrete intervals method is applied to obtain the spectral density function; the integral time-scale  $\Lambda_u$ , the integral length-scale,  $L_u$ , the dissipation rates of the turbulent kinetic energy,  $(\epsilon_u, \epsilon_v)$ , and also Kolmogorov length-scales  $(\eta_u, \eta_v)$  are deduced. It is clearly shown that the axial evolution of these scales are influenced by large density variations, in the near-field and in the far-field as well.

## INTRODUCTION

The objective of this study is to gain a better understanding of the influence of density variations on the structure of turbulence in jets, and therefore on turbulent mixing of variable density jets. An experimental investigation of variable density turbulent axisymmetric jets is presented, where the velocity field measurements are performed using two-component laser Doppler anemometry. Helium, methane, air and CO<sub>2</sub> jets exhausting into a coflowing air are investigated. Hence, the density ratio  $R_\rho = \rho_j / \rho_i$  varies between 7.2 (helium into air) to 0.66 (CO<sub>2</sub> into air). The experiments are conducted with a coflow velocity ratio  $m = U_i / U_j = 0.075$ . The jets discharge into a large enclosure where the confinement effects are negligible for the total jet length. In the present paper, the macroscopic characteristics of the jets are first presented to confirm the global variable density effects (Sarh (1990); Sarh and Gökalp (1991); Richards and Pitts (1993); Panchapakesan and Lumley (1993); Ruffin et al. (1994); Sanders et al. (1996)). Second, the integral and dissipation

time and length-scales are presented with the corresponding energy spectral density. We also present the axial variation of the dissipation rate of the turbulent kinetic energy and the Kolmogorov length-scale. The variable density effects on these structural characteristics are discussed. The experimental conditions explored in this study are summarised on Table 1.

## EXPERIMENTAL SET-UP

### The jet

Experiments are performed in a 2 m high vertical wind tunnel. This enclosure has a square cross-section, with a width of 300 mm and a length of 1300 mm. This rectangular chamber houses the experimental configuration as shown in Fig. 1. Optical access is allowed by large optical quality glass windows (for laser beam transmission and light collection). A fully turbulent vertical pipe flow (with mean velocity  $U_j$  at the exit section) of helium, methane, air or CO<sub>2</sub>, discharges into the chamber. The diameter  $D_j$  of this pipe is 7 mm (giving a  $L/D_j$  ratio of 80) and is positioned in the centre of the chamber. The chamber is high enough to allow measurements up to 100 diameters. The coflowing stream of air (with mean velocity  $U_i$ ) is generated by a fan. To homogenise the coflow, air coming from the fan passes through a settling section and honeycomb structures (Fig. 2). Pressurised gas bottles are used to supply helium and methane (200 atm) and CO<sub>2</sub> (50 atm).

### Laser velocimetry

The flow field velocity characteristics are measured by a two-colour laser Doppler anemometer, consisting of a 7 W Argon-ion laser source, ColorBurst Multicolour Beam Separator and the transmitting optical fibre probe. The laser Doppler system uses 488 and 514.5 nm wavelengths. The light is transmitted from the source to the emission-reception head by an optical fibre.

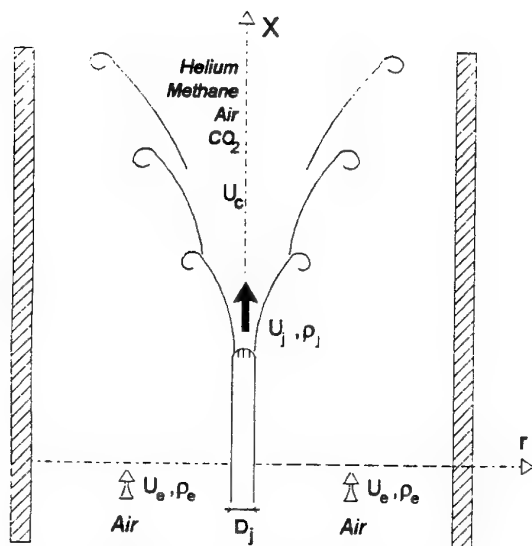


FIG. 1 SCHEMATIC REPRESENTATION OF THE FLOW CONFIGURATION

On the reception side, the scattered light is collected by a receiver, the signals of which are treated by ColorLinkPlus and the automatic burst correlator IFA 755 (Fig. 3). A coincidence time of 10  $\mu$ s is used for two component measurements. The measuring volume is located 310 mm from the transmitting probe head. The displacement of the measurement volume is performed by moving both the transmitting probe and receiver with the same 2D traversing mechanism driven by step motors.

Seeding of the jet is achieved by injecting olive oil particles upstream of the jet flow, with mean diameter between 1 to 2  $\mu$ m. The particles, generated by a spray, pass through a homogenisation box ("cyclone") and finally enter the chamber. The coflow is also seeded. A collection hood is placed at the upper end of the chamber, which serves as an exhaust for the flow and the seed particles.

For the measurements of both velocity components, we collect the data with 100 000 samples per measurement. The time between data points is stored for spectral analysis; thus, each data point is tagged with a reference clock count. During measurements, we try to keep a constant coincidence data rate about 15 000 Hz in order to obtain representative information for spectral analysis (after 70 diameter, this data rate fall under 10 000 Hz). Then, each data-file is re-sampled at 14 000 Hz. An FFT algorithm based on the discrete intervals method is applied to obtain the spectral density functions.

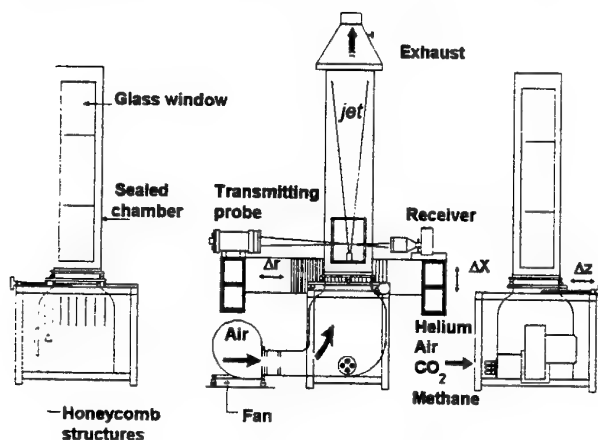


FIG. 2 DETAILS OF THE SET-UP

TABLE 1 : EXPERIMENTAL CONDITIONS

Gas	Helium	Methane	Air	CO <sub>2</sub>
$U_j$ (m.s <sup>-1</sup> )	40	40	40	40
$U_e$ (m.s <sup>-1</sup> )	3	3	3	3
$R_p$	7.2	1.8	1	0.66
$m$	0.075	0.075	0.075	0.075
$Re$	2420	18421	19231	34525
$\rho$ (kg.m <sup>-3</sup> )	0.167	0.667	1.202	1.815
$\nu \cdot 10^6$ (m <sup>2</sup> .s <sup>-1</sup> )	115.7	15.2	14.56	8.11

## RESULTS

### Mean longitudinal velocity

Figure 4 shows the centreline evolution of the mean longitudinal velocity  $U_c$  for the four gases using the non-dimensional presentation  $(U_j - U_e)/(U_c - U_e)$ . The influence of density is obvious, showing that light gases tend to mix more quickly with the coflowing stream than heavy gases. The normalised velocity follows the hyperbolic law,

$$\frac{(U_j - U_e)}{(U_c - U_e)} = \frac{1}{Ku} \frac{D_j}{(X - X_0)} \quad (1)$$

where  $X_0$  is the virtual origin and  $Ku$  the centreline velocity decay rate, whose value is in good agreement with the results of the literature as shown on figure 5.

### Turbulent intensity

The centreline evolution of the longitudinal and radial turbulence intensities are presented in figures 6a and 6b. The increase of  $u'/(U_c - U_e)$  is faster in light gases than in heavy gases. An asymptotic value of about 0.3 is reached for each gas at  $X/D_j = 30$ . This value agrees well with the results obtained by Way and Libby (1971) for helium jets and with those of Wygnansky and Fiedler (1969) for air jets. For the radial fluctuating component,  $v'/(U_c - U_e)$ , we found a plateau value of 0.22 at  $X/D_j = 30$  (see Figure 6b), lower than the results of Wygnansky and Fiedler, and Chua (1989).

### Turbulent kinetic energy

For symmetry reasons in axisymmetric jets ( $w'^2 \approx v'^2$ ), turbulent kinetic energy can be defined by  $k = 0.5 (u'^2 + 2 v'^2)$ . The centreline variation of  $k$  is presented in figure 7. Note that  $k$  is normalised by the excess exit velocity. We see that the position of maximum  $k$  depends on the density ratio.

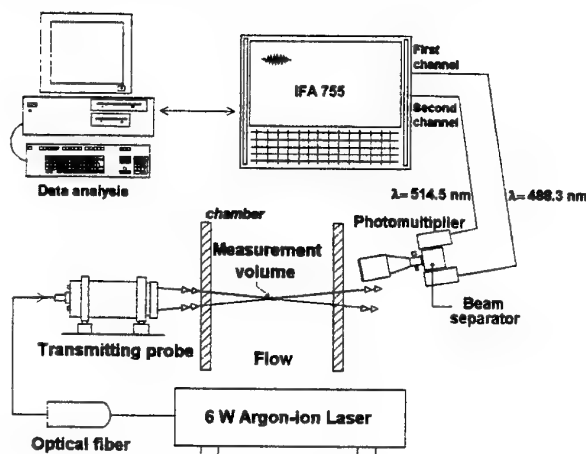


FIG. 3 OPTICAL SET-UP

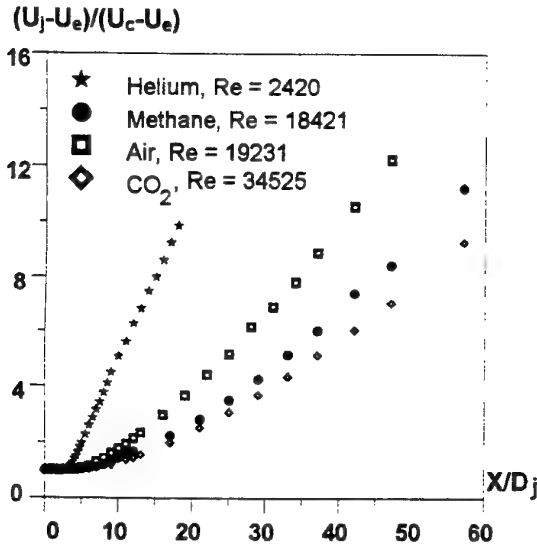


FIG. 4 CENTERLINE VARIATION OF THE NORMALISED LONGITUDINAL MEAN VELOCITY

For light gases, this position is near the exit section of the jet ( $X/D_j = 5$  and  $X/D_j = 8$  for helium and methane, respectively). For air and  $\text{CO}_2$ , this maximum is located further downstream (respectively,  $X/D_j = 10$  and  $X/D_j = 12$ ).

#### Characteristic scales

**Spectral density function** Spectral density functions of the u-component on the centreline for the air jet are shown for different downstream positions in figures 8a and 8b. The excellent frequency range obtained by these experimental spectra is noteworthy. With increasing  $X/D_j$ , the quasi-normal Markovian slopes of  $n^{-2}$  and  $n^{-1}$  disappear and the Kolmogorov slope of  $n^{-5/3}$  is established. The same behaviour is also observed for the jets of other gases (see figures 9a and 9b).

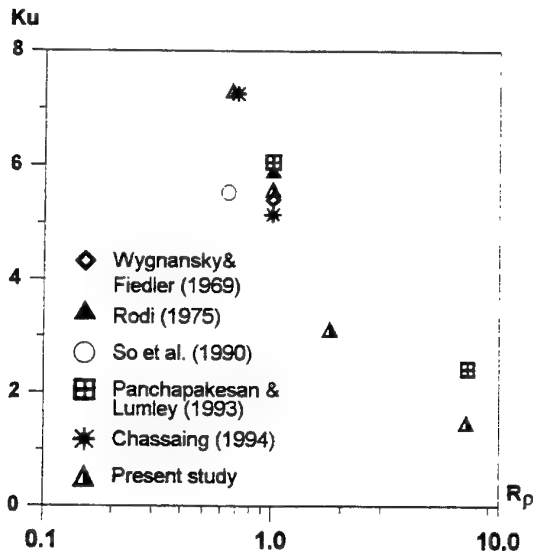


FIG. 5 CENTERLINE DECAY RATES

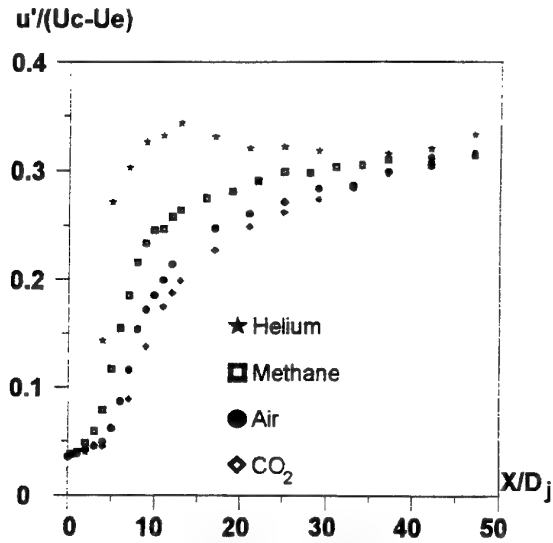


FIG. 6a CENTERLINE VARIATION OF u-COMPONENT TURBULENT INTENSITY

**Integral length-scale** The clearly observed plateau value of the velocity spectra are used to determine the integral time-scales by using the following relation (Hinze (1975))

$$\Lambda_u = \lim_{n \rightarrow 0} \frac{E_u(n)}{4u'^2} \approx \frac{E_u(0)}{4u'^2} \quad (3)$$

Figure 10 shows the centreline behaviour of  $\Lambda_u$  for each gas. In the near-field,  $\Lambda_u$  decreases with  $X/D_j$ , and we obtain a minimum at  $X/D_j$  value where  $k$  peaks (see fig. 7). Downstream,  $\Lambda_u$  increases almost linearly. For both regions,  $\Lambda_u$  ranks following the density ratio, with larger scales for the lightest gas. The integral length scale is deduced by using the Taylor hypothesis:  $L_u = \Lambda_u \cdot U_c$  (see fig. 11).

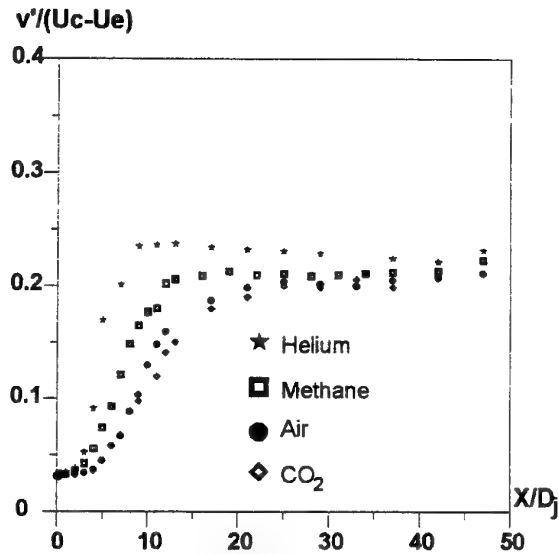


FIG. 6b CENTERLINE VARIATION OF v-COMPONENT TURBULENT INTENSITY

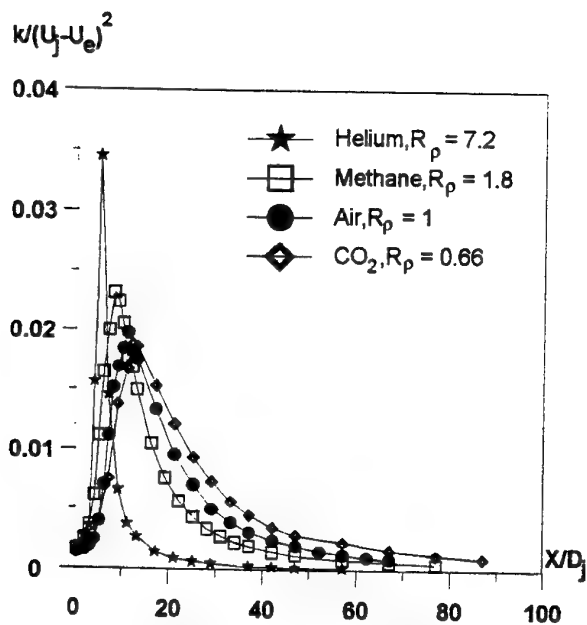


FIG. 7 CENTERLINE EVOLUTION OF THE TURBULENT KINETIC ENERGY

$L_u$  decreases with  $X/D_j$ , for all gases. In the near-field, the same ranking as before is observed. Downstream,  $X/D_j > 20$ , the variation of  $L_u$  is almost stopped and a plateau value of  $L_u/D_j = 0.25$  is obtained. The effect of the density ratio is cancelled out by mixing at large downstream distances. In the near field, the increased mixing efficiency of the light gas is therefore correlated by the presence of larger structures (Green and Whitelaw, 1988).

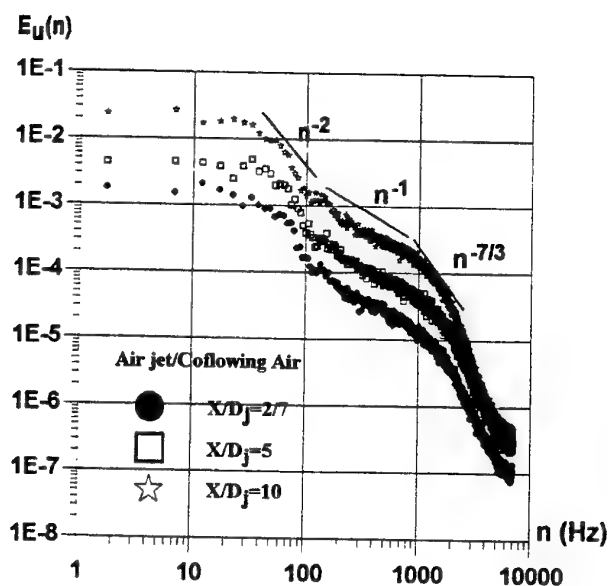


FIG. 8a U-COMPONENT SPECTRUM DENSITY FUNCTION AT THE CENTERLINE FOR THE AIR JET

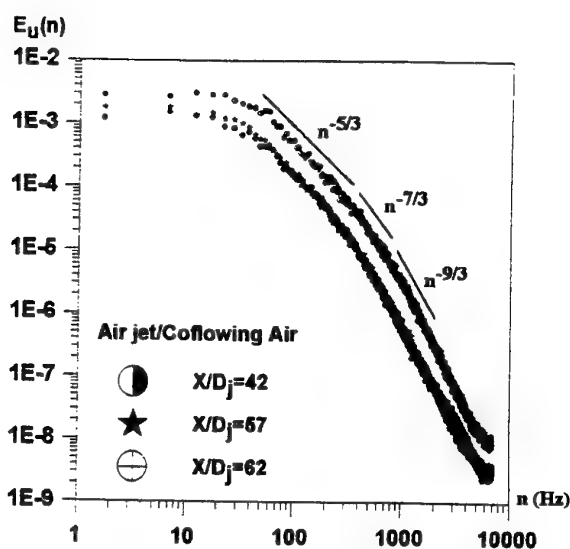


FIG. 8b U-COMPONENT SPECTRUM DENSITY FUNCTION AT THE CENTERLINE FOR THE AIR

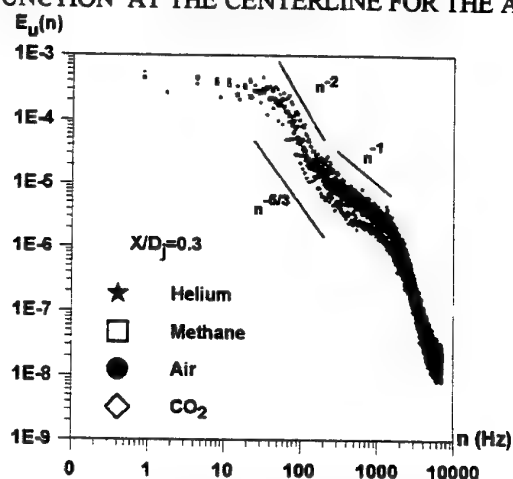


FIG. 9a U-COMPONENT SPECTRUM DENSITY FUNCTION AT THE CENTERLINE FOR EACH GAS IN THE NEAR-FIELD

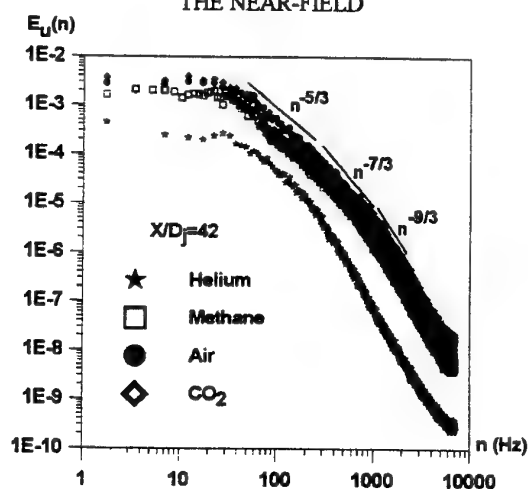


FIG. 9b U-COMPONENT SPECTRUM DENSITY FUNCTION AT THE CENTERLINE FOR EACH GAS IN THE FAR-FIELD



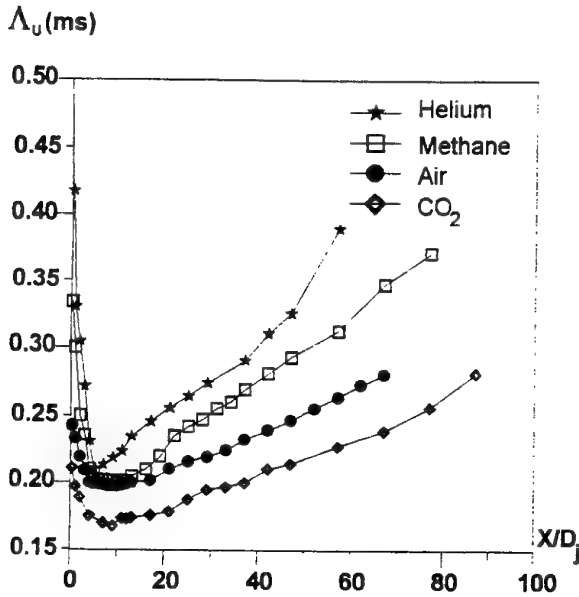


FIG. 10 CENTERLINE EVOLUTION OF THE INTEGRAL TIME SCALE  $\Lambda_U$

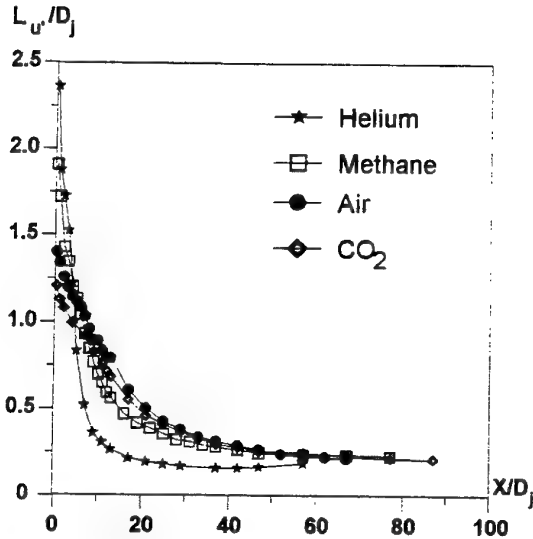
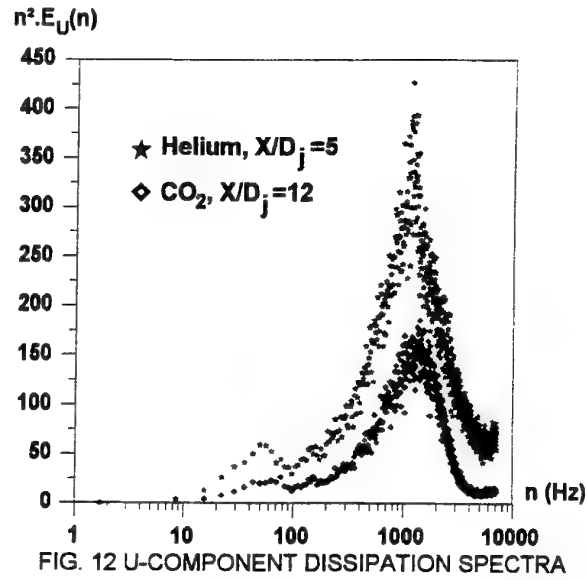


FIG. 11 CENTERLINE EVOLUTION OF THE INTEGRAL LENGTH-SCALE IN U-DIRECTION

**Dissipation rates of the turbulent kinetic energy and the Kolmogorov length scales** To estimate Kolomogorov length-scales  $\eta_u$  and  $\eta_v$ , we need the dissipation rates of the turbulent kinetic energy  $\epsilon_u$  and  $\epsilon_v$ . We calculate these by using the classical expression for locally isotropic turbulence

$$\epsilon_i = 30\nu \left( \frac{2\pi}{U_j} \right)^2 \int_0^\infty n^2 E_i(n) dn \quad (4)$$

where  $i=(u,v)$ . Figure 12 presents the dissipation spectra for the lightest and the heaviest gases (He and  $\text{CO}_2$ ) at centreline positions where the kinetic energy  $k$  peaks, respectively. Due to the correct spectral representation of the total frequency range by the LDA measurements, they show the expected behaviour, so that their integration provides the correct dissipation rates.



Figures 13a and 13b present the evolution of  $\epsilon_u D_j / U_j^3$  and  $\epsilon_v D_j / U_j^3$ , using logarithmic scales. For the near-field region ( $X/D_j < 10$ ), a rapid increase from the exit level is obtained. The dissipation rates present a maximum located at the same  $X/D_j$  values as noticed for  $k$ . We note that the dissipation rate for the  $u$ -component is higher than for the  $v$ -component. Throughout the jet, the dissipation rate of  $k$  is higher for lighter gases.  $\eta_u$  and  $\eta_v$  are directly obtained from  $\epsilon$  by the following relations :

$$\eta_u = (\nu / \epsilon_u)^{1/4} \quad (5a)$$

$$\eta_v = (\nu / \epsilon_v)^{1/4} \quad (5b)$$

The centreline variations of  $\eta_u$  is shown on Figure 14 for the four gases. They rank following the density ratio, with larger scales for lightest gas, and decrease strongly in the near-field. The curve for the helium jet is characterised by much larger  $\eta_u$  values and increases significantly in the far-field.

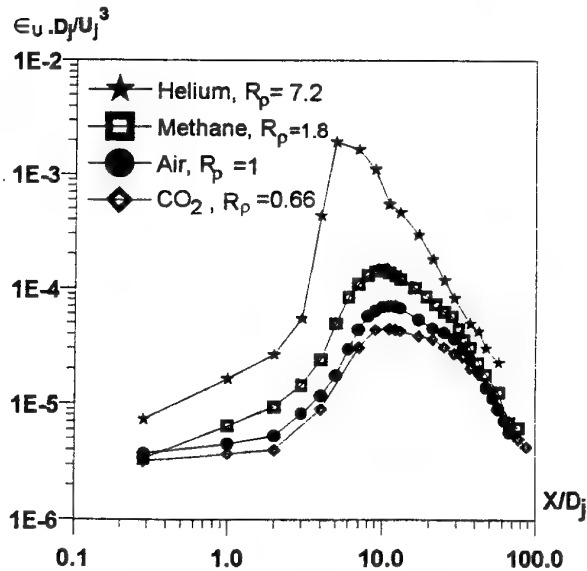


FIG. 13a CENTERLINE EVOLUTION OF THE U-COMPONENT DISSIPATION RATE

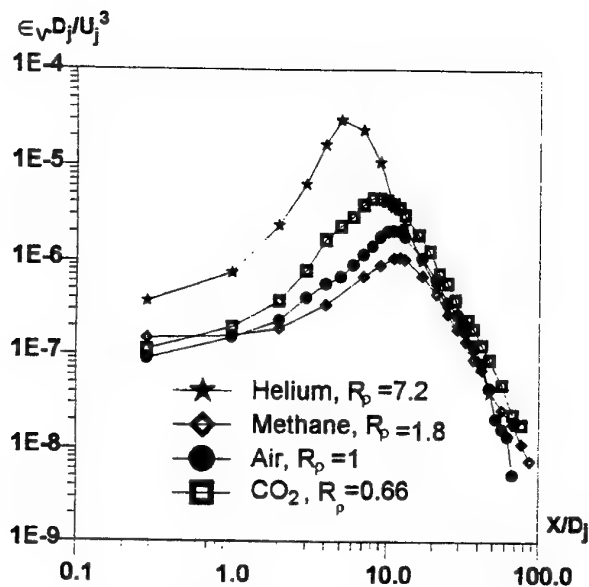


FIG. 13b CENTERLINE EVOLUTION OF THE V-COMPONENT DISSIPATION RATE

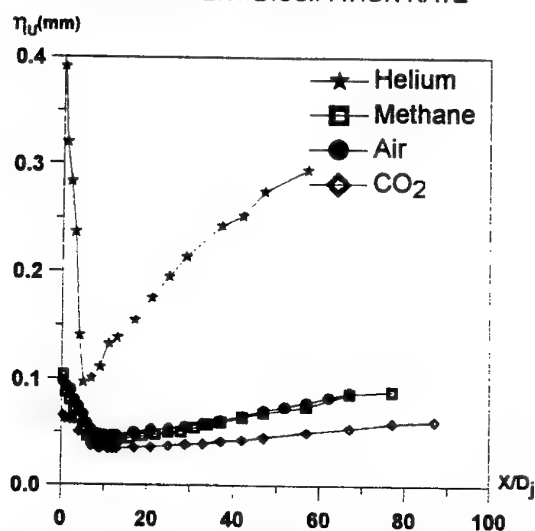


FIG. 14a CENTERLINE EVOLUTION OF THE KOLMOGOROV LENGTH-SCALE IN U-DIRECTION

The values of the Kolmogorov length scales determined here compare favourably with those determined by Gutmark and Wygnansky (1976) in an air jet with hot wire anemometry.

## CONCLUSIONS

We have presented experimental results on variable turbulent axisymmetric jets, with a density ratio  $R_p$  varying between 7.2 (helium jet in air coflow), to 0.66 ( $\text{CO}_2$  jet in air coflow). We have determined the velocity field using two-component laser Doppler anemometry. To obtain the spectral density functions, an FFT algorithm based on the discrete intervals method is applied. Results reported herein show that characteristic scales in variable density turbulent jets (integral length-scale and Kolmogorov length-scale) are strongly influenced by the large density ratios. However, the results for the helium jet may be influenced by the low value of the Reynolds number for this gas. Experiments are ongoing for helium jets with comparable Reynolds numbers as the other gases.

## ACKNOWLEDGMENTS

This work is supported by the CNRS and the *Conseil Régional du Centre*. JP is supported by a grant from the *Conseil Régional du Centre*.

## REFERENCES

- Chassaing, P., Harran, G., and Joly, L., 1994, "Density fluctuation correlations in free turbulent binary mixing," *J. Fluid Mech.*, Vol. 279, pp 239-278.
- Chua, L. P., 1989, "Measurements in a turbulent circular jet," Ph.D. Thesis, University Newcastle (Australia).
- Green, H. G., and Whitelaw, J. H., (1988) "Velocity and concentration Characteristics of the near-field of round jets," Coll. Eurocmec 234, Marseille, France.
- Gutmark, E., and Wygnansky, I., (1976) "The planar turbulent jet," *J. Fluid Mech.*, Vol 73, 465-495.
- Hinze, J. O., 1975, *Turbulence*, 2<sup>nd</sup> Edition, Mc Graw-Hill.
- Panchapakezan, N. R., and Lumley, J. L., 1993, "Turbulence measurements in axisymmetric jets of air and helium," Part 1. Air Jet. Part 2. Helium Jet. *J. Fluid Mech.*, Vol. 246, pp 197-223, pp 225-247.
- Richard, C. D., and Pitts, W. M., 1993, "Global density effects on the self-preservation behavior of turbulent free jets," *J. Fluid Mech.*, Vol. 254, pp 417-436.
- Rodi, W., 1975, "A new method of analysing hot-wire signals in highly turbulent flow and its evaluation in a round jet," DISA Information 17, Feb.
- Ruffin, E., and al., 1994, "Investigation of characteristic scales in variable density turbulent jet using a second-order model," *Phys. Fluids*, Vol. 6, (8), August.
- Sanders, H., Sarh, B., and Gökalp, I., 1996, "Variable density effects in axisymmetric isothermal turbulent jets: A Comparison between a first and a second-order turbulence model," *Int. J. of Heat Mass Transfer*, Vol. 40, 823-842.
- Sarh, B., 1990, "Contribution à l'étude des jets turbulents à masse volumique variable et de flammes de diffusion turbulentes," Thèse de Doctorat d'État, Université P. M. Curie, Paris VI.
- Sarh, B., and Gökalp, I., 1991, "Variable density effects on the mixing of turbulent rectangular jets," *Eight Symposium on Turbulent Shear Flow*, Technical University of Munich, pp 6-4-1 to 6-4-6.
- Sautet, J. C., 1995, "Effet de densité sur le développement scalaire et dynamique des jets turbulents," Thèse de l'Université de Rouen.
- So, R. M. C., Zhu, J. Y., Otügen, M. V., and Hwang, B. C., 1990, "Some measurements in a binary gas jet," *Exp. Fluids*, Vol. 9, pp 237-284.
- Way, J., and Libby, P. A., 1971, "Application of hot-wire anemometry and digital techniques to measurements in turbulent helium jet," *ALAA J.* Vol. 9, pp 1567-1573.
- Wygnanski, I., and Fiedler, H., 1969, "Some measurement in the self preserving gas jet," *J. Fluid Mech.* Vol. 38, pp 577-612.

# VELOCITY STATISTICS ASSOCIATED WITH SCALE DISTRIBUTIONS IN VARIABLE DENSITY TURBULENT JETS

**L. Pietri, J.F. Lucas, M. Amielh, F. Anselmet**  
Institut de Recherche sur les Phénomènes Hors Equilibre  
12, Avenue Général Leclerc  
13003 Marseille  
France

## INTRODUCTION

For variable density turbulent flows, the equations of mass, momentum and thermodynamic budgets are interlinked. In the jet configuration, specific features such as the ability to develop self-sustained instabilities (Monkewitz et al., 1990) or a strongly enhanced entrainment rate (Thring and Newby, 1952 ; Ricou and Spalding, 1961) when the jet fluid is lighter than the ambient one may appear. In flows considered herein, density variations may result from heat and/or mass exchanges, but such a configuration is also important for flows with combustion. In addition, there are numerous applications in pollution and environmental problems, plasma torches, jet engines, etc.

Over the last years, most of the experimental studies have been concerned with quantifying the influence of density variations on the axial evolutions of mean and rms values of the velocity and concentration fields, or on the flow spreading rate (e.g. Birch et al., 1978 ; Richards and Pitts, 1993). More recently (Panchakapesan and Lumley, 1993 ; Djeridane et al., 1996), detailed budgets of Reynolds stresses have been obtained, showing that the influence of density is rather small once the jets have reached their self-similar behaviour. However, this behaviour is attained for a station much closer to the nozzle when the gas is lighter than the ambient fluid. As far as turbulence characteristic scales are concerned, the most detailed results are those reported by Ruffin et al. (1994), showing that the exit momentum flux  $M_j$  is the main parameter governing the centerline scale behaviour in the far-field region. Obviously, detailed statistics associated with scale distributions, such as velocity spectra or velocity structure functions, are required. Indeed, for instance, they would be of great help for developing well-suited subgrid-scale models for large eddy simulations of variable density flows.

The objective of the present work is to investigate the influence of parameters such as the initial density ratio  $R$  ( $= \rho_j / \rho_a$ , where  $\rho_j$  and  $\rho_a$  denote the jet and ambient densities respectively) or the Reynolds number  $Re_j$  ( $= U_j D_j / \nu_j$ , where  $U_j$ ,  $D_j$  and  $\nu_j$  denote the jet exit velocity, diameter and viscosity respectively). Results reported herein concern velocity spectra and third- and fourth-order velocity structure functions obtained in air and helium ( $R=0.14$ ) jets using laser-Doppler anemometry as well as hot-wire anemometry when this technique is tractable.

## EXPERIMENTAL SETUP AND SPECTRAL ESTIMATION METHODS

The facility (e.g. Djeridane et al., 1996) consists in a fully developed turbulent vertical pipe flow of pure air or pure helium discharging into ambient air in a slightly confined configuration (mean velocity  $U_a = 0.9$  m/s, square section  $285 \times 285$  mm<sup>2</sup>).

Gas	$U_j$ (m/s)	$Re_j$	$R=\rho_j/\rho_a$	$Fr_j$
He	32	7000	0,14	643
Air	12	21000	1	---
He	55	12000	0.14	1900
Air	4	7000	1	---
Air	7	12000	1	---

**TABLE 1. EXPERIMENTAL CONDITIONS FOR THE SAME  $M_j$  (2 FIRST LINES) AND THE SAME  $Re_j$ .**

$$\text{with } Fr_j = \frac{\rho_j U_j^2}{D_j |\rho_j - \rho_a| g}, \text{ the Froude number.}$$

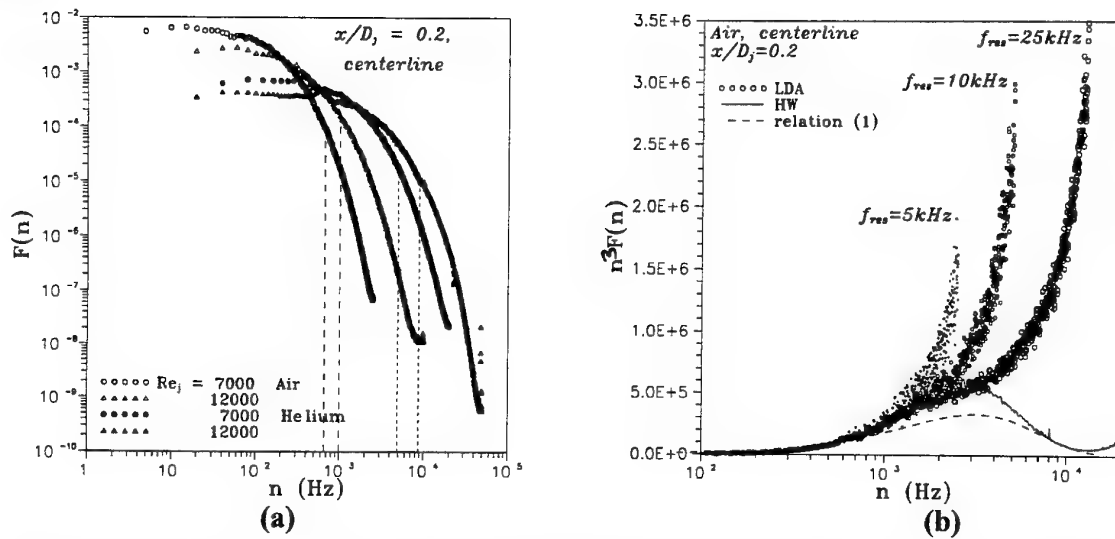


FIGURE 1. SPECTRA FOR THE LONGITUDINAL VELOCITY (a) AND ITS STREAMWISE DERIVATIVE (b).

In the basic nominal configuration, jets are compared at the same  $M_j$  (resulting in the same ratio  $M_j/M_a$  since  $M_a$  is the same for all configurations) so that, for air and helium respectively,  $U_j$  is then 12 m/s and 32 m/s while  $Re_j$  is 21000 and 7000.

However, as the Reynolds number is usually known to influence spectral distributions, measurements for comparisons at the same  $Re_j$  ( $= 7000$  and  $12000$ ) are also reported. Comparisons at the same  $Re_j$  are also important for testing, at the pipe exit, the spectral resampling procedures since, for such measurements, pure helium can then be probed without any particular difficulty using a single hot-wire.  $Re_j$  is then the only parameter influencing turbulence properties but the air and helium exit velocities are very different (cf. Table 1).

Most of velocity measurements are performed with a laser Doppler system (Argon 4W) fitted with fiber optics and a Burst Spectrum Analyser operated by a Dantec acquisition software. A very large sampling rate is required for obtaining reliable spectra so that forward scatter was used for the present experiments. The primary and secondary flows are simultaneously seeded using silicon oil particle diffusers (about  $1 \mu\text{m}$  in diameter). Measurements with  $5 \mu\text{m}$  hot wires are separately performed using a CTA system (overheat ratio of 0.8) connected to an A/D converter.

A detailed analysis of resampling techniques has been previously performed (Pietri et al., 1996), showing that a mixed method which is a compromise between a zero order (sample and hold) and a one order interpolation gives the most reliable results. The randomly sampled data were also found to be such that the seeding particle arrival times are approximately distributed following a Poisson distribution. In addition, this study confirmed that sufficiently large mean data rates  $DR$  are required since the equivalent cut-off frequency is then  $DR/2\pi$ . Indeed, figure 1 shows estimated spectra  $F(n)$  for the longitudinal velocity (normalized such that  $\int_0^\infty F(n)dn = 1$ ) and its streamwise derivative (this latter is inferred from  $n^2 F(n)$ , with  $n$ , frequency). All spectra on figure 1.a are obtained from hot-wire

measurements. They clearly illustrate the strong influence of the exit velocity  $U_j$  when they are plotted as a function of the frequency  $n$ . This feature is very important for optimizing the flow seeding and the mean data rates when performing laser-Doppler measurements. Figure 1.b shows in more detail the influence of the resampling frequency. Comparison with data inferred from hot-wire measurements (HW) and from the relation

$F(k) = 0.6 (k\eta)^{-5/3} \exp(-6.5k\eta)$  (1) (with  $k$ , the wavenumber and  $\eta$ , the Kolmogorov length-scale) indicates that quantitative agreement can be obtained only within the inertial range even though the data rate (about 10 KHz) and the resampling frequency are rather high. Therefore, it is not possible for us to infer quantities such as the Taylor micro-scale  $\lambda$ ,  $\eta$  or the isotropic value  $\bar{\epsilon} = 15\nu(\partial u/\partial x)^2$  of the dissipation rate of kinetic energy from LDA measurements. The values of 0.6 and 6.5 for the constants appearing in relation (1) are within the range of those usually found for flows with similar low Reynolds numbers  $R_\lambda$  (based on  $\lambda$  and the rms value of velocity fluctuations,  $u'$ ),  $R_\lambda \approx 20-30$ , as shown on figure 2.

## RESULTS AND DISCUSSION

### Velocity Spectra

Spectra for the exit section are plotted on figure 2 using Kolmogorov dimensionless scaling. Centerline values of quantities such as  $\eta$  and  $R_\lambda$  were inferred (Pietri, 1997) from the relations

$$\frac{\eta}{D_j} = \left[ 4 \left( \frac{u^*}{U_j} Re_j \right)^3 \right]^{-1/4}, \quad R_\lambda^2 = 15 \left[ \frac{\eta}{D_j} \frac{u'}{U_j} Re_j \right]^4 \quad (2)$$

using the property that, in a fully developed turbulent pipe flow (e.g. Townsend, 1976),  $u^*/U_j$  and  $u'/U_j$  only depend on  $Re_j$  while  $\epsilon D_j/2u^{*3} = 2$ . Using that scaling, spectra for air and helium which were reported on figure 1 as a function of frequency  $n$  are now remarkably similar, depending only on the value of  $R_\lambda$ . When these

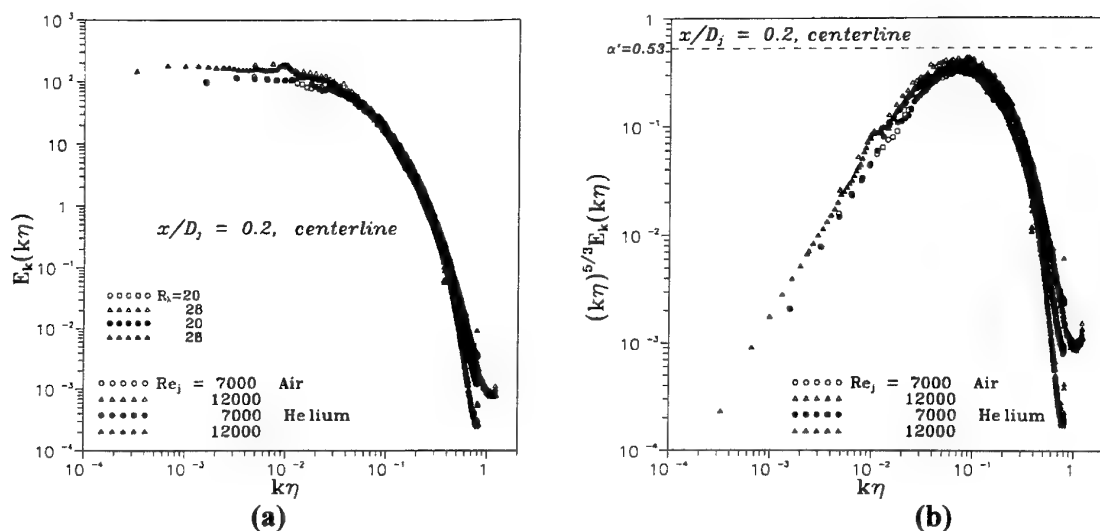
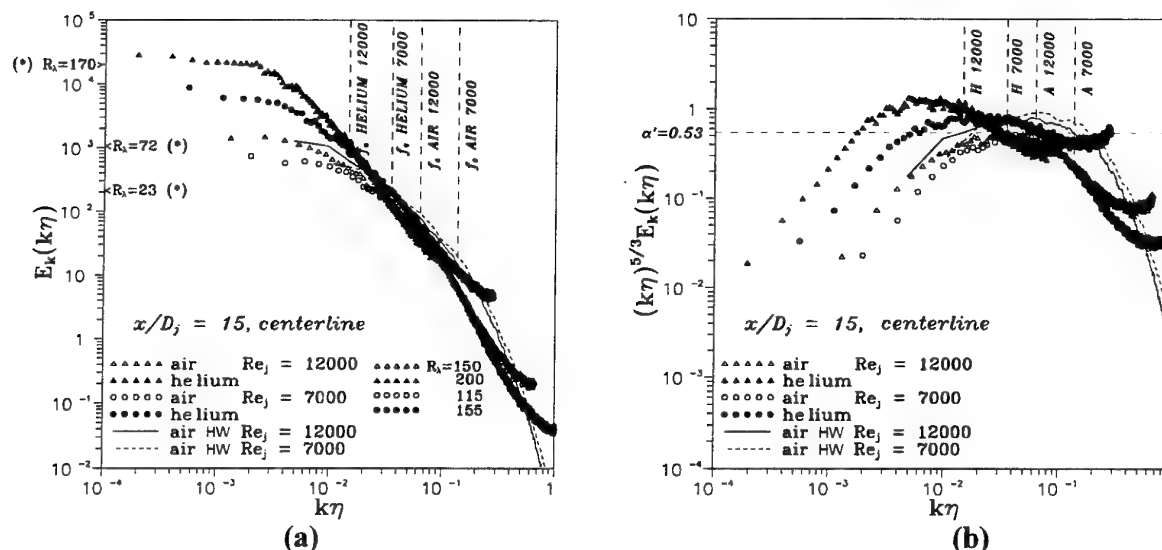


**FIGURE 2. VELOCITY SPECTRA (a) AND COMPENSATED SPECTRA (b) USING KOLMOGOROV SCALES AT THE STATION  $X/D_j=0.2$  FOR VARIOUS REYNOLDS NUMBERS.**

spectra are plotted with compensation by the factor  $(k\eta)^{5/3}$  (Fig. 2.b), it appears that there is no real plateau that would be characteristic of an inertial range, but this is not a surprise considering these low values of  $R_\lambda$  associated with the fact that the flow is then that exiting from the pipe. However, the value of the maximum of the curves is very close to the usual value of the Kolmogorov constant ( $\alpha'=0.53$ ), which is a quantitative check of the validity of relations (2) for evaluating the turbulence characteristic scales. Therefore, as expected, very close to the nozzle, the flow properties only depend on the Reynolds number  $Re_j$ .

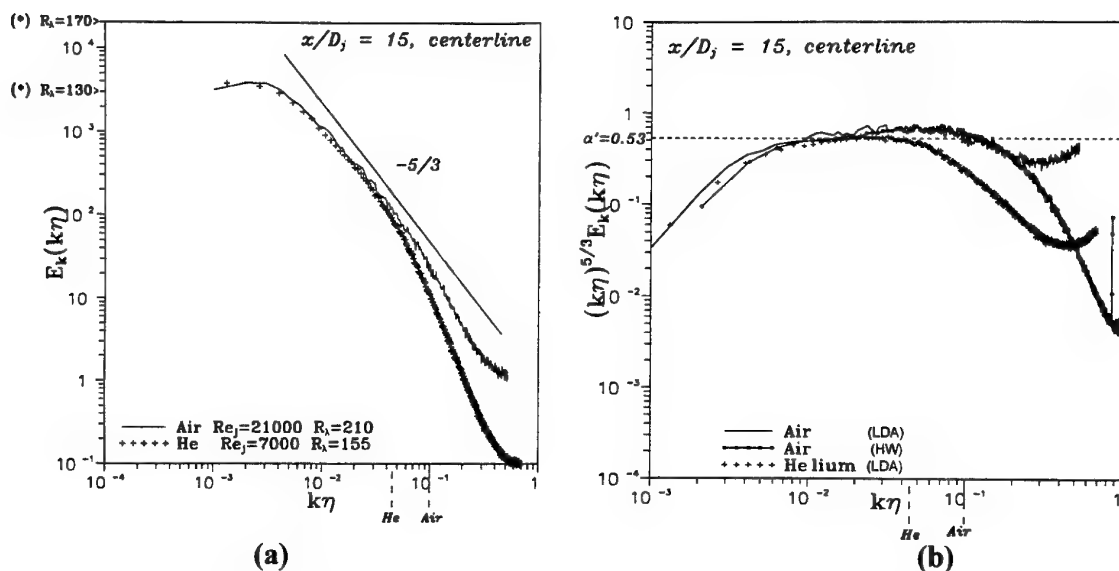
At stations further downstream ( $X/D_j=15$ , Figure 3), when the helium and air jets are compared for two values of the Reynolds number  $Re_j$ , the combined influence of the density ratio and the Reynolds number is then well illustrated, resulting on values of  $R_\lambda$  as displayed on

figure 3.a. These spectra are obtained from LDA measurements, but hot-wire data obtained in the air flows are also included for comparison. Characteristic scales are then deduced from results reported in Ruffin et al. (1994). The well-known evolution of spectra with  $R_\lambda$  is clearly visible, with a continuous widening towards low wavenumbers when  $R_\lambda$  increases, from the value of 115 for air at  $Re_j=7000$  to that of 200 for helium at  $Re_j=12000$ . The influence of the cut-off frequencies resulting from the LDA mean data rates is also shown to influence these spectra, the attenuation for the helium jet at  $Re_j=12000$  being obviously the strongest since the exit velocity  $U_j$  is then 55 m/s. This feature is quantitatively observed on the compensated spectra (Fig. 3.b) where the level of the maximum of the curve is almost equal to 1 since the cut-off then corresponds to  $k\eta$  about 0.02, which is right within the expected inertial range. For the



**FIGURE 3. VELOCITY SPECTRA (a) AND COMPENSATED SPECTRA (b) USING KOLMOGOROV SCALES AT THE STATION  $X/D_j=15$  FOR VARIOUS REYNOLDS NUMBERS.**

(\*) Chapman's data reported in Saddoughi and Veeravalli's (1994) paper



**FIGURE 4. VELOCITY SPECTRA (a) AND COMPENSATED SPECTRA (b) USING KOLMOGOROV SCALES AT THE STATION  $X/D_j=15$  FOR THE SAME EXIT MOMENTUM FLUX  $M_j$ .**

air flows, where the LDA cut-off is close to  $k\eta$  about 0.1, the agreement between LDA and HW spectra is rather good, in spite of the LDA spectra strong attenuation for  $k\eta$  larger than 0.1. The level of the maxima is then rather close to the value  $\alpha'=0.53$ .

When the flows at a downstream station such as  $X/D_j=15$  are compared for the same exit momentum flux  $M_j$ , the Reynolds numbers  $R_\lambda$  for the helium and air jets are then closer one to the other than when the jets are compared for the same  $Re_j$ . In particular,  $R_\lambda$  for the air jet is significantly enhanced. This induces an air spectrum which is much more developed towards low wavenumbers than those reported on figure 3, resulting in an almost perfect collapse (Fig. 4) of the helium and air spectra for the low and inertial wavenumber ranges. For larger wavenumbers ( $k\eta > 0.04$ ), the cut-off associated with the mean data rate results in a strong attenuation of the helium jet spectrum. Figure 4.b shows these trends in a more quantitative way. In particular, the level of the small plateau characteristic of the inertial range has a value very close to  $\alpha'=0.53$ . Here again, good agreement is obtained between the LDA and HW spectra for the air jet, at least for  $k\eta$  smaller than the cut-off wavenumber associated with the mean data rate. These experimental results confirm the trends obtained analytically and numerically by Ruffin et al. (1994), which showed that, in the asymptotic far-field region, the Reynolds number  $R_\lambda$  and scales such as  $\lambda$  or  $\eta$  only depend on the exit momentum flux  $M_j$ . When the turbulent jet is sufficiently developed, and this is obtained for stations closer to the nozzle the lighter the jet fluid with respect to the ambient fluid, all velocity spectra collapse and only depend on the particular value of  $R_\lambda$ .

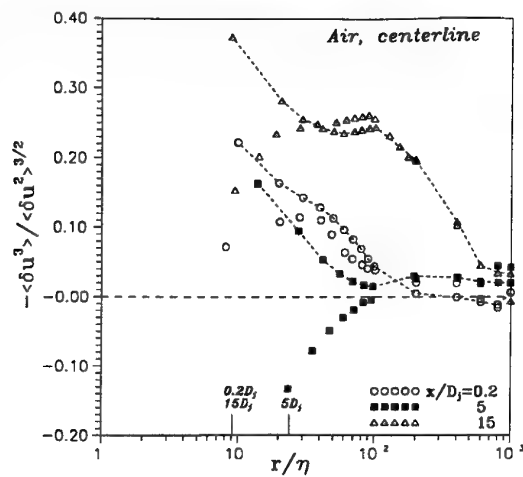
### Velocity Structure Functions

In order to investigate in more detail the statistics associated with the different scales of the flow, figures 5

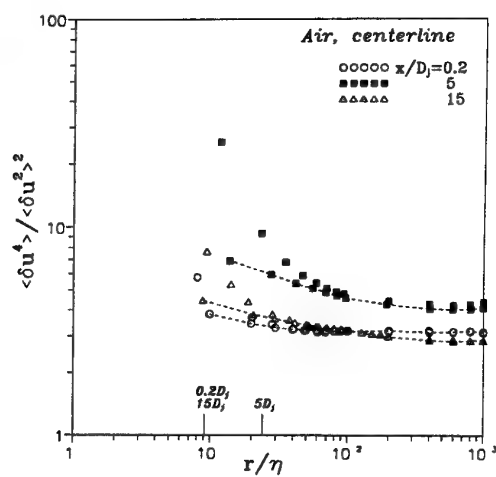
and 6 report the skewness  $S$  and flatness  $F$  factors for the velocity structure function  $\delta u(r) = u(x+r) - u(x)$ , as obtained at three different stations in the air and helium jets respectively, and for the same  $M_j$ . Separations  $r$  are obtained from time separations using Taylor's hypothesis. For fully developed homogeneous and isotropic turbulence, and for the present range of rather small  $R_\lambda$ , the distributions of  $S$  and  $F$  should display a plateau at  $-0.25$  and a rather slow evolution about 4 respectively in the inertial range, with limit values of  $-0.45$  and 5 respectively at very small separations (e.g. Monin and Yaglom, 1975 ; Mydlarski and Warhaft, 1996).

General good agreement can be observed between the LDA and the hot-wire data for separations  $r/\eta$  larger than about 2-3 times the equivalent separation inferred from the mean data rate. For values of  $r/\eta$  smaller than this limit,  $F$  values tend to be overestimated by LDA measurements : this is resulting from the resampling procedure which induces rather large errors as can be observed on figure 1.b for instance. Here as well, the equivalent cut-off separations are pointed on all graphs ( $0.2D_j$ ,  $5D_j$  and  $15D_j$ ). For both helium and air, these cut-off separations are largest for the station  $5D_j$  since the Kolmogorov frequencies are significantly larger (e.g. Ruffin et al., 1994) in this region where the initial mixing layers reach the jet centerlines, whereas the mean data rates slightly decrease when going downstream.

The very low  $R_\lambda$  values associated with the pipe exit result in the absence of any flat region for the  $S$  evolutions in both air and helium at  $0.2D_j$ . However, as, in this situation,  $Re_j$  is equal to 21000 ( $R_\lambda=40$ ) for air and only 7000 ( $R_\lambda=20$ ) for helium, data for the air inertial range significantly depart from zero, whereas data for helium are almost equal to zero even for  $r/\eta$  as small as about 30. On the contrary, at  $15D_j$  in air and  $5D_j$  and  $15D_j$  in helium, almost flat  $S$  distributions around the value  $-0.25$  can be observed for  $r/\eta$  between 30 and about 100.

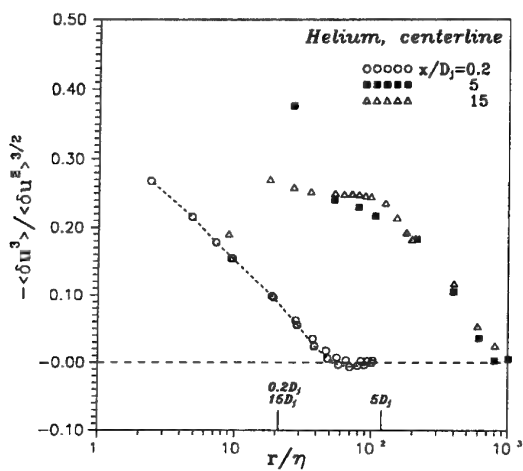


(a)

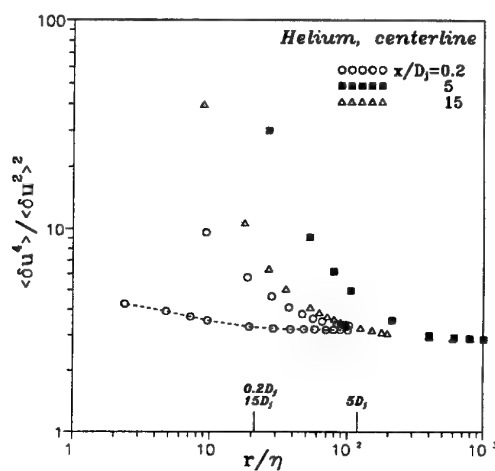


(b)

**FIGURE 5. SKEWNESS (a) AND FLATNESS (b) FACTORS FOR THE VELOCITY STRUCTURE FUNCTIONS IN THE AIR JET. SYMBOLS CORRESPOND TO LDA DATA AND CONNECTED SYMBOLS TO HW DATA.**



(a)



(b)

**FIGURE 6. SKEWNESS (a) AND FLATNESS (b) FACTORS FOR THE VELOCITY STRUCTURE FUNCTIONS IN THE HELIUM JET. SYMBOLS CORRESPOND TO LDA DATA AND CONNECTED SYMBOLS TO HW DATA.**

The more rapid development of the helium turbulent jet is clearly visible for the station  $X/D_j=5$  where the helium data almost present a plateau at the level of -0.25 whereas the air data values are much smaller. It is worth noticing that the skewness factor  $S$  of velocity increments is very sensitive to the local properties of turbulence for inertial range scales. Indeed, for very large scales, one can easily demonstrate that  $S$  is always equal to zero, regardless of the value of the velocity skewness factor  $S_u$ , whereas, for very small scales, the limit value only very slightly depends on the Reynolds number. In particular, for the pipe exit section,  $S_u$  is about -0.5 for both the air ( $Re_j=21000$ ) and helium ( $Re_j=7000$ ) flows. The flatness factor  $F$  of velocity increments is a parameter which is less sensitive to the local turbulence properties even though its large scale value (e.g. Pietri, 1997),  $F = \frac{1}{2}F_u + \frac{3}{2}$ , is directly related to the velocity flatness

factor  $F_u$ . A quantitative study of  $F$  data is not reported herein, but this quantity can be used for testing small-scale intermittency models (e.g. Antonia et al., 1997). For scales within the inertial range,  $F$  undergoes a power-law dependence with an exponent very close to -0.13.

## CONCLUSION

Results reported in this paper confirm that quantitative information about the scale distributions can be obtained from LDA measurements and resampling techniques, at least over the inertial range. It was shown that once the helium jet has reached its asymptotic regime, its properties associated with the fine scales of turbulence are the same as those for the air flow at the same  $M_j$ . The present study extends results reported by Ruffin et al. (1994) and more general studies where it was found that, in the far-field region where the turbulent

jets are fully developed, quantities such as second and third-order moments of velocity practically do not depend on the initial density ratio  $R$ .

In particular, results reported herein show that the skewness factor  $S$  of velocity increments is a quantity which is much more sensitive to the considered stage of turbulence development than velocity spectra. Such data can be obtained with great accuracy from LDA measurements and usual resampling methods.

The analysis of data for flows at the same  $Re_j$  confirmed that, very close to the nozzle, turbulence characteristic properties only depend on  $Re_j$  and not on the properties of the jet fluid. In fact, the main parameter is  $R_\lambda$ , which will depend, at any particular position - except very close to the nozzle -, on  $Re_j$  and on the density ratio  $R$ . In the far-field region, the influence of these two parameters is expressed in terms of the momentum flux  $M_j$ . In the flow development region, further investigations are required to better quantify the combined influence of these two terms.

## ACKNOWLEDGEMENTS

Financial support from EDF, GDF and INERIS is gratefully acknowledged. Considerable help was also provided by L. Fulachier for initiating this research program.

## REFERENCES

Antonia, R.A., Ould-Rouis, M., Zhu, Y. and Anselmet, F., 1997, "Fourth-order moments of longitudinal and transverse velocity structure functions", *Europhysics Letters*, Vol. 37, pp. 85-91.

Birch, A.D., Brown, D.R., Dodson, M.G. and Thomas, J.R., 1978, "The turbulent concentration field of a methane jet", *J. Fluid Mech.*, Vol. 88, pp. 431-449.

Djeridane, T., Amielh, M., Anselmet, F. and Fulachier, L., 1996, "Velocity turbulence properties in the near-field region of axisymmetric variable density turbulent jets", *Phys. Fluids*, Vol. 8, pp. 1614-1630.

Monin, A.S. and Yaglom, A.M., 1975, "Statistical fluid mechanics", MIT Press.

Monkewitz, P.A., Bechert, D.W., Barsikow, B. and Lehmann, B., 1990, "Self-excited oscillations and mixing in a heated round jet", *J. Fluid Mech.*, Vol. 213, pp. 611-639.

Mydlarski, L. and Warhaft, Z., 1996, "On the onset of high-Reynolds number grid-generated wind tunnel turbulence", *J. Fluid Mech.*, Vol. 320, pp. 331-368.

Panchakapesan, N.R. and Lumley, J.L., 1993, "Turbulence measurements in axisymmetric jets of air and helium", Part 2, Helium jet, *J. Fluid Mech.*, Vol. 246, pp. 225-247.

Pietri, L., 1997, "Etude expérimentale de jets turbulents à densité variable. Analyse des propriétés statistiques des échelles du champ dynamique", Ph. D. Thesis, IRPHE-Université d'Aix-Marseille II.

Pietri, L., Gharbi, A., Amielh, M. and Anselmet, F., 1996, "Estimation of velocity spectra in variable density jets using laser-Doppler anemometry", In *Engineering turbulence, modelling and experiments 3*, Ed. Rodi, W. and Bergeles, G., Elsevier, pp. 421-430.

Richards, C.D. and Pitts, W.M., 1993, "Global density effects on the self-preservation behaviour of turbulent free jets", *J. Fluid Mech.*, Vol. 254, pp. 417-435.

Ricou, F.P. and Spalding, D.B., 1961, "Measurements of entrainment by axisymmetrical turbulent jets", *J. Fluid Mech.*, Vol. 11, pp. 21-32.

Ruffin, E., Schiestel, R., Anselmet, F., Amielh, M. and Fulachier, L., 1994, "Investigation of characteristic scales in variable density turbulent jets using a second-order model", *Phys. Fluids*, Vol. 6, pp. 2785-2799.

Saddoughi, S.G. and Veeravalli, S.V., 1994, "Local isotropy in turbulent boundary layers at high Reynolds number", *J. Fluid Mech.*, Vol. 268, pp. 333-372.

Thring, M.W. and Newby, N.P., 1952, "Combustion length of enclosed turbulent jet flames", *4th International Symposium on Combustion*, Pittsburgh.

Townsend, A.A., 1976, "The structure of turbulent shear flow", Cambridge University Press.



# VARIABLE DENSITY MIXING IN KINEMATICALLY HOMOGENEOUS TURBULENCE

P. Chassaing<sup>(1)(2)</sup>, S. Castaldi<sup>(1)</sup>, G. Harran<sup>(1)</sup>, L. Joly<sup>(2)</sup>

<sup>(1)</sup> IMFT/ENSEEIH - UMR 5502 CNRS  
Avenue du Professeur Camille Soula, 31400 Toulouse  
France

<sup>(2)</sup> ENSICA - Fluid Mechanics Department  
1, Place Emile Blouin, 31056 Toulouse Cédex  
France

## ABSTRACT

Direct numerical simulations were performed of the turbulent mixing of an inhomogeneous density field by an homogeneous velocity field. The density ratio between patches of different density is 5, thus well beyond the passive scalar situation. This low Mach number variable density turbulence is then relevant to low speed turbulent mixing processes. In this paper the flow configuration is described along with its statistical proprieties. Depending on the ratio of the velocity and density characteristic length scales, two asymptotic situations are identified that correspond to a diffusion and a transport mixing mode. A pseudo-spectral method is presented that is tuned to get close to the diffusion case. The Poisson equation includes the divergence of the velocity field resulting from molecular diffusion of mass. The variable density case is compared to the constant density one from the kinetic energy decay and the statistical moments.

## INTRODUCTION

In any statistical approach, variations of fluid density in a turbulent motion introduce correlations with density fluctuations (d.f.c.). Such correlations can be included into macroscopic, mass weighted averages, as proposed and developed by Favre (1958,1992), or linked with higher order moments based on centered fluctuations, as suggested by Chassaing (1985). As shown in Chassaing *et al.* (1994) and Chassaing (1996), this last proposal leads to physical analysis and qualitative understanding of specific density effects in low speed, free turbulent shear flows. Thus, to improve numerical predictions of such types of flows, an adequate modelling of d.f.c. terms is required.

To study this question, a specific flow configuration has been imagined and analyzed from direct numerical simulations. The physical situation is described in section 2 and some major theoretical results are given in section 3. The numerical simulation is introduced in section 4 and some preliminary results presented in section 5.

## THE FLOW CONFIGURATION

In simple turbulent shear flows, mean density-velocity

products  $\bar{\rho}\tilde{U}_i$  compete with the corresponding density-velocity fluctuations correlations  $\overline{\rho'u'_i}$ . The first aim of the present study is to introduce a physical situation, although mainly conceptual, where a variable density mixing is driven by a pure turbulent agitation, so that the mean (conventional) velocity field is zero. In this case, the mean mass weighted velocity  $\tilde{U}_i(x_j, t)$  is :

$$\tilde{U}_i = \overline{\rho'u'_i} / \bar{\rho} \quad (1)$$

so that, as far as turbulent mass fluxes are concerned, the first previously quoted Favre averaging method becomes basically identical to the second one proposed in Chassaing (1985).

The corresponding flow configuration can be referred to as (variable) "Density Mixing In (kinematically) Homogeneous Turbulence" (De.M.I.H.T.). It can be conceptually depicted by considering an unbounded space including, at  $t < 0$ , several patches of different densities fluids, in thermodynamic and mechanical equilibrium over macroscopic domains of characteristic length scale, say  $\ell_p$ . This can be achieved for instance, with two non reactive gases, with the same pressure and temperature, or a unique, constant pressure, gas located in macroscopically distinct regions of different temperatures.

At  $t = 0$ , a pure turbulent velocity is applied to the whole space, which is statistically homogeneous and isotropic, independently of the density inhomogeneity. It can be characterized by the kinetic energy spectrum and at least a velocity scale  $v$  and a length scale  $\ell$ . For  $t \geq 0$ , this agitation induces a turbulent mixing throughout the whole space, forcing the homogenization of the density.

## THEORETICAL ANALYSIS

### The asymptotic situations

Dividing the mean continuity equation by  $\bar{\rho} (\neq 0)$  gives :

$$\frac{1}{\bar{\rho}} \frac{\partial \bar{\rho}}{\partial t} = - \frac{1}{\bar{\rho}} \frac{\partial}{\partial x_k} (\overline{\rho u'_k}) \quad (2)$$

which basically refers to a time scales equilibrium associated with the time evolution of the mixing process (L.H.S.)

and the spatial inhomogeneity (R.H.S.). This last one can be obtained from a velocity ( $v$ ) and length scale ( $\ell_p$ ) associated with the dominant spatial inhomogeneity during the mixing process.

Discarding molecular effects in the present discussion, two asymptotic situations can be introduced, depending on which one of  $\ell_p$  or  $\ell$  is the significant length scale.

- $\ell \ll \ell_p$

The turbulent agitation acts as a macroscopic diffusion of "large blobs" of different densities fluid. This is the situation which will be studied in the present paper;

- $\ell_p \ll \ell$

The turbulent agitation acts as a convective transport of "small bubbles" of fluid into an other density medium, and the topology of the initial distribution of the density could not be ignored.

### Density fluctuation correlations

Exact expressions of d.f.c. can be obtained, see Chassaing (1996), using the equation of state, for both variable concentration or variable temperature binary mixing. Restricting to second order moments, these expressions are respectively :

$$\frac{\overline{\rho\gamma'}}{\overline{\rho\gamma'^2}} = \frac{\overline{\rho u'_i}}{\overline{\rho\gamma' u'_i}} = \frac{a}{1 - aC} \quad (3)$$

$$\frac{\overline{\rho\theta'}}{\overline{\rho\theta'^2}} = \frac{\overline{\rho u'_i}}{\overline{\rho\theta' u'_i}} = -\frac{1}{T} \quad (4)$$

where  $C = \bar{C} + \gamma'$  is the mass fraction,  $T = \bar{T} + \theta'$ , the temperature and  $a$  a constant parameter depending upon the densities of the pure species. For sake of brevity, we shall only consider now the isothermal mixing of a two components gas.

### Statistical properties of the De.M.I.H.T.

When the gravity field is zero, and assuming a constant mean pressure field, the instantaneous balance equations of the De.M.I.H.T. of a binary mixture are :

$$\begin{aligned} \frac{\partial \rho}{\partial t} + \frac{\partial}{\partial x_i}(\rho u'_i) &= 0 \\ \frac{\partial \rho u'_i}{\partial t} + \frac{\partial}{\partial x_j}(\rho u'_i u'_j) &= -\frac{\partial p'}{\partial x_i} + \frac{\partial \tau'_{ij}}{\partial x_j} \\ \frac{\partial \rho C}{\partial t} + \frac{\partial}{\partial x_j}(\rho C u'_j) &= \frac{\partial}{\partial x_j} \left( \rho \mathcal{D} \frac{\partial C}{\partial x_j} \right) \end{aligned} \quad (5)$$

where  $\tau'_{ij} = \nu(2s'_{ij} - \frac{2}{3}s'\delta_{ij})$  is the specific stress tensor,  $s'_{ij}$  the symmetric fluctuating strain tensor and  $s'$  its trace.

Due to the peculiarities of the De.M.I.H.T. situation, the main following results can be obtained, cf. Chassaing (1992) when molecular effects are neglected :

a) The spatial inhomogeneity of the "Reynolds stresses"  $\rho u'_i u'_k$  acts as the source term of the momentum evolution equation, similarly to the mass flux for the mean density in the continuity equation, since :

$$\frac{\partial \overline{\rho u'_i}}{\partial t} = -\frac{\partial \overline{\rho u'_i u'_k}}{\partial x_k} \quad (6)$$

b) Taking the divergence of (6), and due to the mean continuity equation, it can be obtained that :

$$\frac{\partial^2 \bar{\rho}}{\partial t^2} = \frac{\partial^2 \overline{\rho u'_i u'_k}}{\partial x_i \partial x_k} \quad (7)$$

so that, to third order terms, the mean density can be developed as :

$$\begin{aligned} \bar{\rho}(\vec{x}, t) &= \bar{\rho}(\vec{x}, t_0) - \frac{t - t_0}{1!} \left( \frac{\partial \overline{\rho u'_k}}{\partial x_k} \right)_{t=t_0} \\ &+ \frac{(t - t_0)^2}{2!} \left( \frac{\partial^2 \overline{\rho u'_i u'_k}}{\partial x_i \partial x_k} \right)_{t=t_0} + \mathcal{O}(t - t_0)^3 \end{aligned} \quad (8)$$

c) Assuming kinematic homogeneity of velocity fluctuations correlations and combining with the equation of state  $\rho = a\rho C + b$ , where  $a$  and  $b$  are constant, it follows from the momentum and mass fraction equations that the following pressure correlation is identically zero :

$$\overline{\gamma' \frac{\partial p'}{\partial x_i}} \equiv 0 \quad (9)$$

## THE NUMERICAL SIMULATION

### The Relevant equations

Combining the continuity and mass-fraction equations in (5) gives that the fluctuation velocity field divergence  $s' = \nabla \cdot u'$  is a consequence of mass molecular diffusion :

$$s' = -\mathcal{D} \Delta(\ln \rho) \quad (10)$$

The nondimensional form of this statement is :

$$s'^* = -\frac{1}{\mathcal{R}_e \mathcal{S}_c} \Delta(\ln \rho)^* \quad (11)$$

which means that a high Reynolds/Schmidt evolution is asymptotically solenoidal. This situation falls under the scope of another paper, Joly *et al.* (1997), and is not considered here since the small scales resolution constraint does not allow high Reynolds simulations. With  $d_t = \partial_t + u' \cdot \nabla$  the material derivative and  $q$  standing for  $(\ln \rho)$ , the solved continuity equation turns, in the general case, into the following advection-diffusion equation :

$$d_t q = \mathcal{D} \Delta q \quad (12)$$

The momentum equation can be recasted in a transport form including previous conventions plus the gathering of the viscous stress  $\tau$  and the specific pressure  $p'/\rho$  in a global specific stress tensor  $\sigma = \tau - p'/\rho \mathcal{I}$  :

$$d_t u' = \nabla \cdot \sigma + \nabla q \cdot \sigma \quad (13)$$

The density gradient is seen to act through the second term in the right hand side of this compact momentum equation. With  $\omega' = \nabla \times u'$  the fluctuating vorticity field and taking the curl of (13) yields the vorticity transport equation :

$$d_t \omega = (\omega \cdot \nabla) u - \frac{1}{\rho} \nabla p' \times \nabla q - s' \omega' + \nu \Delta \omega \quad (14)$$

where the following vectorial algebra has been used :

$$\nabla \times (u' \times \omega') = (\omega' \cdot \nabla) u' - (u' \cdot \nabla) \omega' - s' \omega' \quad (15)$$

In the right hand side of (14) and from left to right are the vortex stretching term, the baroclinic torque, the generation-destruction of vorticity by fluctuating dilatation  $s'$  and the molecular diffusion. The baroclinic term is the additionnal torque that is felt when an inhomogeneous mass field is submitted to an acceleration orthogonal to the local density gradient. As such it is expected to be the main responsible of the differences between a constant-density turbulence decay and the proposed variable-density mixing turbulence.

## The Numerical Procedure

The hybrid explicit/implicit scheme of Spalart *et al.* (1991) has been used for the time integration. Let us form the temporal derivative of the density and velocity field as given by (12) and (13) :

$$\partial_t \varrho = \mathcal{N}_\varrho + \mathcal{L}_\varrho \quad (16)$$

$$\partial_t \mathbf{u}' = \mathcal{N}_u + \mathcal{L}_u \quad (17)$$

with the following non-linear terms and linear terms :

$$\mathcal{N}_\varrho = -\mathbf{u}' \cdot \nabla \varrho \quad (18)$$

$$\mathcal{N}_u = \mathbf{u}' \times \boldsymbol{\omega}' - p'/\rho \nabla \varrho \quad (19)$$

$$\mathcal{L}_\varrho = \mathcal{D} \Delta \varrho \quad (20)$$

$$\mathcal{L}_u = -\nabla \pi' + \nu \Delta \mathbf{u}' \quad (21)$$

where  $\pi'$  is the specific total pressure  $p'/\rho + u'^2/2$ . The density and velocity field are advanced together at each substep. The reader is referred to the original paper for more details on the time integration which is nearly third-order accurate. This choice was dictated by storage constraints and a need for a stable behaviour allowing high CFL numbers and an associated fast time marching.

The pressure contribution  $\nabla \pi'$  between substeps  $s-1$  and  $s$  is treated by the fractional step method of Choi and Moin (1994) ensuring a global second order accuracy. The Poisson equation needs the divergence of the new velocity field to be estimated. This is done by using (10) and the updated local mass diffusion :

$$\Delta t \mathcal{D}_s \Delta \pi'_s = -(\mathcal{D} \Delta \varrho_s + \nabla \cdot \mathbf{u}'_s) \quad (22)$$

The calculations were performed using a pseudospectral method on a  $2\pi^3$  periodic domain. Efficient IBM-tuned FFT libraries allowed reasonable run durations. Though not fully satisfactory, no anti-aliasing was performed in order to preserve the Reynolds number on the  $96^3$  mesh.

## Initial Velocity Fields

The initial conditions are set by a three step procedure, illustrated on figure 1, and developed by Mell (1994) which intends to get the maximum Taylor Reynolds number at full spectrum decay for a given resolution.

1. the velocity field of a constant-density homogeneous turbulence is evolved from a random field calibrated to a Batchelor-type analytical energy spectrum :

$$E(k) = C k^{*4} \exp(-2k^{*2}) \quad , k^* = k/k_0 \quad (23)$$

where  $k_0 \sim 5$  sets the wave number of the energy maximum and the initial integral length scale  $\ell \sim 2\pi/k_0$ . The coefficient  $C$  normalize the initial kinetic energy to  $3\nu_0^2/2$ . The resolution constraint on the smallest scales reads  $\eta_k \geq 2\pi/n$ . It is not strictly applied in order to get a full resolution at full spectrum decay despite the growth of all length scales. Till this point this is the classical Orszag and Paterson (1972) method. A compromise is to set the viscosity at  $\nu = 0.028$  for a  $96^3$  mesh. That is  $\mathcal{R}_\lambda = 10$  when turbulence has reached full spectrum decay which marks the end of this first stage.

2. The second step rescales the modulus of the Fourier coefficients to obtain smaller length scales and a higher  $\mathcal{R}_\lambda$ . This operation respects the self-preserving shape of the energy spectrum :

$$E(k) = \nu^2 \ell F(k\ell) \quad (24)$$

which gives that the new spectrum  $E'$  will behave as :

$$E'(k) = \nu'^2 \ell' F(k\ell') = \frac{\nu'^2 \ell'}{\nu^2 \ell} E(k[\ell'/\ell]) \quad (25)$$

3. Then this new field is evolved with a lower initial viscosity of  $\nu = 0.02$  which gives  $\mathcal{R}_\lambda = 15$  at the beginning of full spectrum decay. This time is considered hereinafter as the initial time. The initial turnover time is defined at that point as  $t = \ell/\nu$ .

Those values of the Taylor Reynolds number are lower than usually found in such simulations because of the relatively low resolution and a rigorous estimation of  $\lambda$  at the beginning of the self-preserving decay.

## Initial Density Fields

The density field, represented on figure 2, is a bicolor three dimensionnal chess-like distribution, with sinusoidal density profiles. The density ratio between the density extrema is  $S_\rho = \rho_{\max}/\rho_{\min}$ . It measures the density field contrast and is set to 5 for the presented results. The length scale of the initial density inhomogeneity  $\ell_\rho$  is half the cube width while the velocity field integral length scale is near its fifth.

This initial density field corresponds to the situation where the characteristic length scale of density inhomogeneity is slightly larger than the integral length scale. This initialisation gives an intermediate situation between the two asymptotic situations described previously. The full achievement of condition  $\ell \ll \ell_\rho$  is beyond our present computational power.

## FIRST RESULTS

### Length scales and energy decay

The figure 3 gives the kinetic energy decay due to dissipation by the small scales and the density variance decrease due to mixing process by the turbulence plus molecular diffusion. The energy decay is exactly the same as for the constant-density case (not-plotted). During this first stage the mixing of the bicolor density field does not result in a rapid decrease of the density variance. The time series of density 2D slices, figure 6, seem to illustrate that this stage is dominated by the straining of density patches with a rather slowly decreasing density variance.

The mixing process can be described by the ratio of the two characteristic length scales. The time evolution of this ratio is presented on figure 4 versus the non-dimensionnal time  $t^* = t\ell/\nu$ . Let us recall that the eddy turnover time is calculated from the turbulence field when the density field is activated, i.e at the end of the initialization procedure described before. The integral length scale still increases while the density inhomogeneity length scale slightly decreases with the mixing advancement. Hence, starting from an unmixed situation where  $\ell_\rho/\ell \sim 3$ , it can be seen that the density field inhomogeneity length scale falls to  $\ell_\rho/\ell \sim 1$  within an eddy turnover time.

### Statistical point of view

On figure 5 are presented the successive probability density functions of the density. The initial distribution of density gives a sharp peak on the mean level ( $\rho = 3$ ) with side-branches of extreme values and low probabilities. The mixing process induces a narrower probability density function but this first stage is far from the expected gaussian trend. Longer simulations will be necessary to get the description of that final stage. The statistics of the velocity field not presented here will be detailed during the conference.

## CONCLUSION

The frame for direct numerical simulation of variable density mixing has been described and an original flow configuration proposed. A theoretical approach has outlined

statistical characteristics of the variable density mixing in kinematically homogeneous turbulence. A pseudo-spectral method was used to look at the turbulence decay of a two-species case with a density ratio of 5. The variation of density did not alter significantly the kinetic energy decay. The statistics and spectral aspects will be investigated from longer simulations in order to analyse the relaxation of the variable density turbulence toward an homogeneous field.

## REFERENCES

- Chassaing P., 1985, "Une alternative à la formulation des équations du mouvement turbulent d'un fluide à masse volumique variable" *J. Méc. Th. et App.*, Vol. 4(3), pp. 375-389.
- Chassaing P., 1992, "La turbulence cinématiquement homogène et massivement inhomogène. Tentative de définition du concept", Rap. IMFT/TELET-ENSICA/DEF.
- Chassaing P., Haran G., Joly L., 1994, "Density fluctuation correlations in free turbulent binary mixing" *J. Fluid Mech.*, Vol. 279, pp. 239-278.
- Chassaing P., 1996, "Some problems on single point modeling of turbulent, low-speed, variable density fluid motions." *IUTAM Symp. Écoulements Turbulents à Faible Vitesse à Masse Volumique Variable*, Marseille.
- Choi, H., Moin, P., 1994, "Effects of the computational time step on numerical solutions of turbulent flow", *J. Comp. Physics*, Vol. 113, pp. 1-4.
- Favre A., 1958 "Equations statistiques des gaz turbulents", *C.R.A.S.*, Vol. 246, pp. 2573-3216.
- Favre A., 1992, "Equations statistiques des fluides à masse volumique variable en écoulements turbulents", *11ème J.E.E.T.M.V.V.*, Orléans.
- Joly L., Chassaing P., Castaldi S., 1997, "Direct simulation of a variable density incompressible homogeneous turbulence", *First AFOSR Int. Conf. on DNS-LES*, August 4-8, Ruston, LA.
- Orszag S.A., Paterson Jr. G.S., 1972, "Numerical simulation of the tridimensional homogeneous isotropic turbulence", *Phys. Fl. Rev. Let.*, Vol. 28, pp. 76-79.
- Sandoval D.L., 1994, "The dynamics of variable density turbulence", Los Alamos Thesis.
- Spalart, P.R., Moser, R.D., Rogers, M.M., 1991, "Spectral methods for the Navier-Stokes equations with one infinite and two periodic directions", *J. Comp. Physics*, Vol. 96, pp. 297-324.

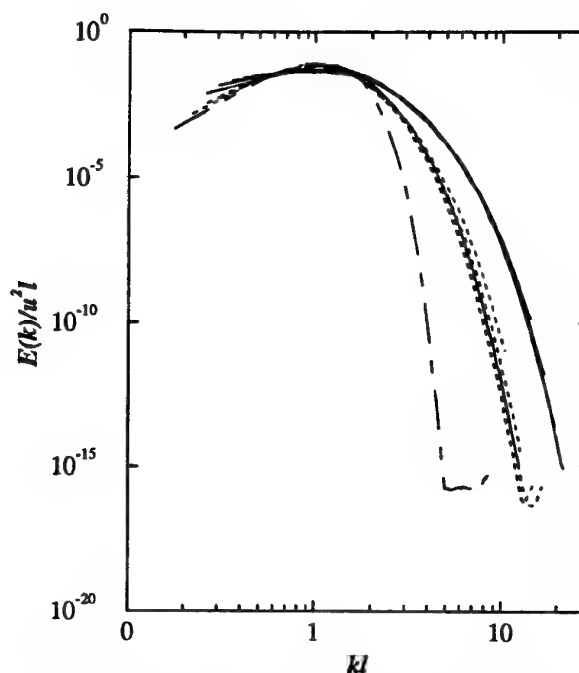


Figure 1: Spectral behaviour during the constant density initialization procedure within large-scale normalization : initial spectrum from (23) (dot-dashed), first evolution (dotted) and second run after the reconditioning step (solid).

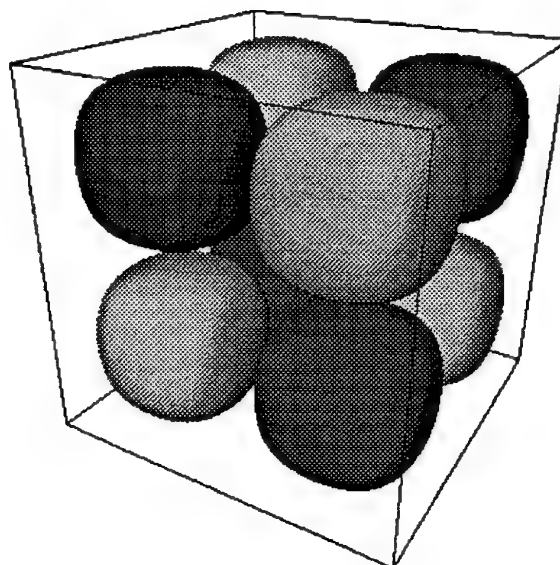


Figure 2: Initial iso-density surfaces at intermediate heavy (dark) and light (clear) levels.

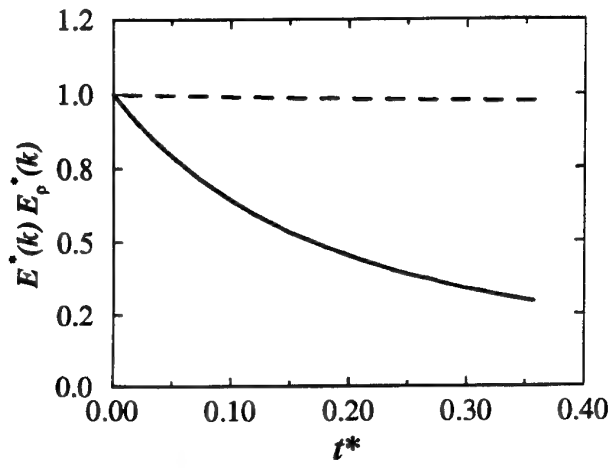


Figure 3: Evolution of the kinetic energy (solid) and density variance (dotted) normalized by their initial levels versus the non-dimensional time.

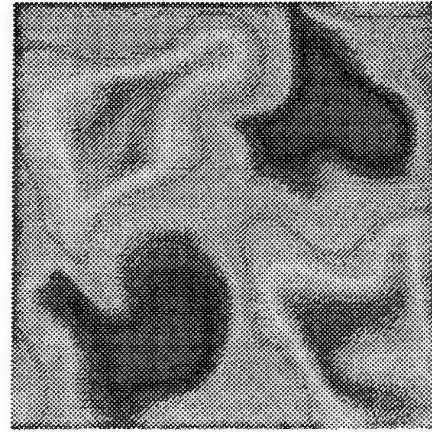
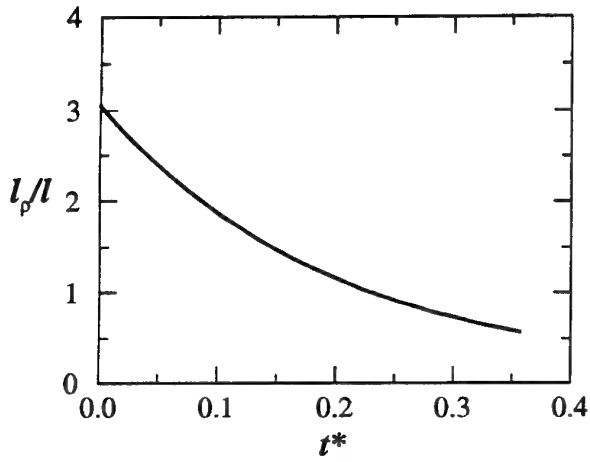
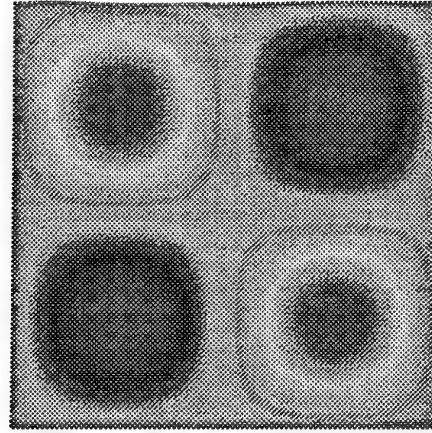


Figure 4: Evolution of the density to velocity integral length scales ratio  $l_\rho/l$  versus the non-dimensional time.

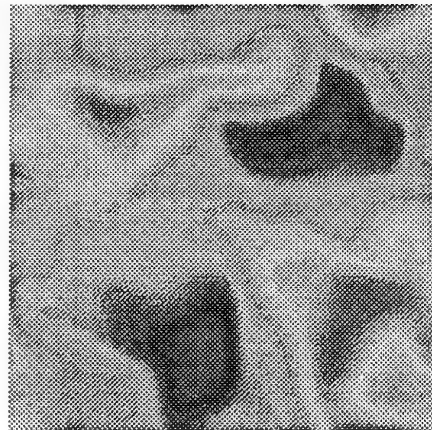
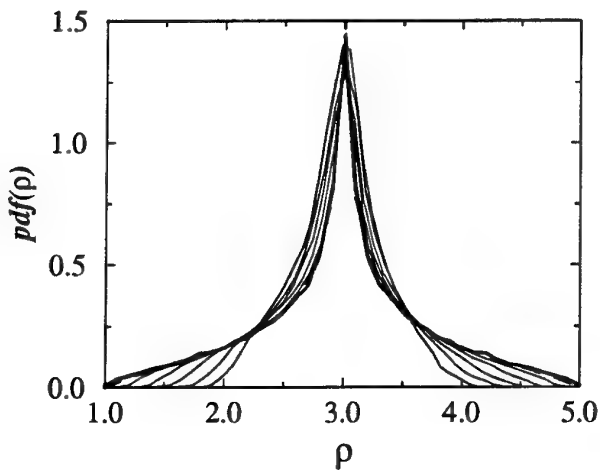


Figure 5: Evolution of the density probability density function.

Figure 6: Slices of the density field at  $t^* = 0, 1.5$  and 3 on constant  $y$  planes for  $j = N/4$ .

## **SESSION 13 - CLOSURES II**

# REALIZABILITY OF NON-LINEAR STRESS-STRAIN RELATIONSHIPS FOR REYNOLDS-STRESS CLOSURES

S. Fu<sup>(1)</sup>, T. Rung<sup>(2)</sup>, F. Thiele<sup>(2)</sup>

<sup>(1)</sup>Department of Engineering Mechanics  
Tsinghua University  
Beijing 100084  
PRC

<sup>(2)</sup>Hermann-Föttinger Institut für Strömungsmechanik  
Technische Universität Berlin  
Müller-Breslau-Strasse 8  
D-10623 Berlin  
Germany

## ABSTRACT

A class of recently developed explicit algebraic stress models for three-dimensional turbulent flows based on tensorially quadratic stress-strain relations (Gatski & Speziale 1993) is subjected to a systematical realizability analysis. It is found that these models, which are of particular interest for their rigorous derivation from linear second-moment closure models, tend to produce inappropriate unrealizable results even in simple shear flows. The cause of the defect is identified in conjunction with a set of realizability-furnishing constraints on the model coefficients. The emerging realizable quadratic eddy-viscosity model (RQEVm) shows encouraging predictive capabilities for some flows of practical interest. Examples included refer to the turbulent flow over a 2-D hill, homogeneous shear flow in non-inertial reference frames and rotating channel flow. The principal aim of the paper is to convey the relevance of the realizability principle to engineering turbulence modelling.

## INTRODUCTION

In the past few years, intensified research has taken place to remedy the shortcomings of the linear eddy-viscosity model, while retaining important numerical advantages of the concept. A typical feature of these attempts is that they lean on constitutive relations linking the Reynolds stresses to non-linear expressions of strain-rate and vorticity components. Following a wide range of different routes such as direct interaction approximation (Yoshizawa 1984), rational mechanics (Speziale 1987; Gatski *et al.* 1993), renormalization group analysis (Yakhot *et al.* 1992) or the realizability principle (Shih, Zhu & Lumley 1993), recently reported investigations of complex turbulent flows based on non-linear eddy-viscosity modelling often displayed encouraging results (Abid, Rumsey & Gatski 1995; Craft, Launder & Suga 1995). In the authors' view, however, Gatski and Speziale's (1993) tensorially quadratic generalization of an earlier suggestion by Pope (1975) which will hereinafter be referred to as the GS model, is of further significance. Based on the principles of rational mechanics, Gatski and Speziale proposed a non-linear model which constitutes an explicit solution to the algebraic stress

model (ASM) of Rodi (1976) in the limit of equilibrium turbulence, viz.

$$\overline{u_i u_j} = \frac{2}{3} \delta_{ij} k - 2\nu_t \left[ S_{ij} + \beta_2 \frac{k}{\epsilon} (S_{ik} W_{kj} + S_{jk} W_{ki}) - \beta_3 \frac{k}{\epsilon} \left( S_{ij}^2 - \frac{1}{3} \delta_{ij} S_{kk}^2 \right) \right] \quad (1)$$

where,  $S_{ij}^2 = S_{ik} S_{kj}$ ,  $S_{kk}^2 = S_{ik} S_{ki}$  etc. and

$$\nu_t = c_\mu^* \frac{k^2}{\epsilon}, \quad c_\mu^* = \frac{3\beta_1(1+\eta^2)}{3+\eta^2+6\xi^2(1+\eta^2)}, \quad (2)$$

and

$$\left. \begin{aligned} \beta_1 &= (2/3 - C_2/2)/g, & \beta_2 &= (1 - C_4/2)/g, \\ \beta_3 &= (2 - C_3)/g, & \eta^2 &= (\beta_3 S)^2/8, \\ \xi^2 &= (\beta_2 \Omega)^2/2, & g &= C_1 + C_5 - 1, \\ S &= (k/\epsilon)(2S_{kk}^2)^{1/2}, & \Omega &= (k/\epsilon)(-2W_{kk}^2)^{1/2}. \end{aligned} \right\} \quad (3)$$

The coefficients  $C_1, C_2, C_3$  and  $C_4$  conform with the linear pressure-strain model rooted in the GS model, viz.

$$\begin{aligned} \Pi_{ij} &= -2C_1 \epsilon b_{ij} + C_2 k S_{ij} \\ &+ C_3 k (b_{ik} S_{kj} + b_{jk} S_{ki} - \frac{2}{3} \delta_{ij} b_{lk} S_{kl}) \\ &- C_4 (b_{ik} W_{kj} + b_{jk} W_{ki}), \end{aligned} \quad (4)$$

with,

$$\begin{aligned} b_{ij} &= \frac{\overline{u_i u_j}}{2k} - \frac{1}{3} \delta_{ij}, \quad S_{ij} = \frac{1}{2} \left( \frac{\partial U_i}{\partial x_j} + \frac{\partial U_j}{\partial x_i} \right), \\ W_{ij} &= \frac{1}{2} \left( \frac{\partial U_i}{\partial x_j} - \frac{\partial U_j}{\partial x_i} \right) + e_{mji} \Omega_m \end{aligned}$$

whereas  $C_5$  actually marks the production of turbulence energy over dissipation-rate ratio  $P/\epsilon$ . Assuming the second-moment closure methodology to provide much more predictive realism than the eddy-viscosity concept, the GS model seems to represent the optimal non-linear eddy-viscosity model achievable, for it approximates the result of the ASM. A major drawback of the GS model is,

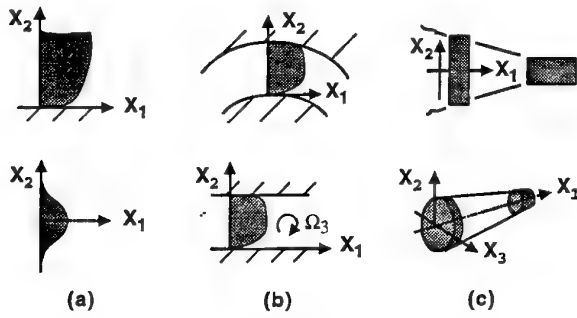


Figure 1: Illustration of the building-block flows for the realizability analysis: (a) plane shear flow, (b) curved- and rotating shear flow, (c) 2-D & 3-D irrotational flow straining.

Model	$C_1$	$C_2$	$C_3$	$C_4$	$C_5$	$g$
LRR	1.5	0.8	1.75	1.31	2.09	2.5
GL	1.8	0.8	1.2	1.2	2.09	2.8
SSG	3.4	0.36	1.25	0.4	1.89	4.29

Model	$\beta_1$	$\beta_2$	$\beta_3$	$\beta_2/\beta_3 \leq B$	$\beta_1/\beta_3$
LRR	0.107	0.14	0.1	$1.38 > 1.36$	1.07
GL	$2/21$	$1/7$	$2/7$	$1/2 < 2/3$	$1/3$
SSG	0.11	0.19	0.18	$1.07 < 1.34$	0.65

Table 1: Summary of model coefficients and important related constants of the three considered pressure-strain models rooted in the explicit Gatski and Speziale ASM (LRR: Launder, Reece & Rodi (1975); GL: Gibson & Launder (1978); SSG: Speziale, Sarkar & Gatski (1991)).

however, the inherent possibility of producing unrealizable physical quantities like negative turbulence-energy components. Superficially, the unrealizability can be traced back to the pressure-strain model, which is rooted in the non-linear stress-strain relation, as none of the linear pressure-strain models satisfies the realizability principle. However, it is unclear to what extent the source of the unrealizability is translated in the non-linear eddy-viscosity framework and whether it is possible to remedy the defect within this approach.

## REALIZABILITY ANALYSIS

The realizability principle requires a turbulence model to provide turbulence quantities which always satisfy the fundamental physics of turbulence. Particularly, the turbulence-energy components should always remain non-negative and the Schwartz' inequality must be satisfied (Schumann 1977; Lumley 1978). In the following, a set of fundamental flows, considered to be relevant for flow physics modelling such as plane and curved shear flows, shear flows in non-inertial frames and flows exposed to strong irrotational straining, will play the pivotal role for the realizability analysis of the GS explicit algebraic stress model (see figure 1).

### Realizability of plane shear flow

The plane shear flow is certainly an important example where a turbulence model should exhibit realizability. With attention directed to a boundary-layer flow, it is well understood the presence of rigid walls attenuates the turbulent fluctuations perpendicular to the wall (cf. figure 1a). The corresponding Reynolds stress, however, must not be driven to negative values, viz.

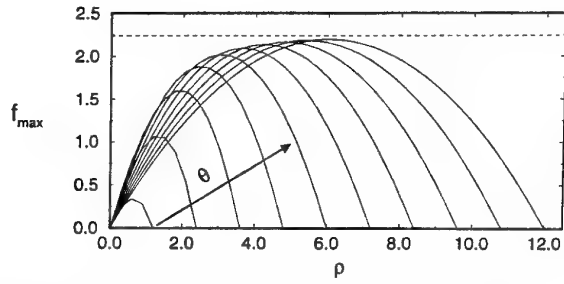


Figure 2: Variation of the amplification function (9) with the non-dimensional mean strain-rate and vorticity parameters  $\rho$  and  $\theta$ .

$$\begin{aligned} \overline{u_2^2} &= \frac{2}{3}k - 2\nu_t \left[ \beta_2 \frac{k}{\epsilon} (2S_{21}W_{12}) \right. \\ &\quad \left. - \beta_3 \frac{k}{\epsilon} \left( S_{21}S_{12} - \frac{1}{3}S_{kk}^2 \right) \right] \geq 0. \end{aligned} \quad (5)$$

Substituting the eddy-viscosity  $\nu_t$  by (2), and rearranging the resulting expression one arrives at

$$\frac{\beta_2}{\beta_3} \leq \frac{\beta_3}{\beta_1} \frac{3 + \theta + 24(\beta_2/\beta_3)^2\theta(1 + \theta)}{36\theta(1 + \theta)} + \frac{1}{6}, \quad (6)$$

$$\text{with } \theta = (\beta_3 S)^2/8.$$

The realizability constraint is associated with the minimum value of the r.h.s. of eq. (6) which occurs in conjunction with  $\theta$  approaching infinity, thus

$$\frac{\beta_2}{\beta_3} \leq \frac{2\beta_3}{3\beta_1} \left( \frac{\beta_2}{\beta_3} \right)^2 - \frac{1}{6} = B. \quad (7)$$

By reference to table 1, we can conclude that the GS model incorporating either the GL or SSG pressure-strain model satisfies the realizability principle for plane shear flow. When attention is drawn to the LRR pressure-strain model, a different picture emerges. Here, the realizability constraint is violated, even though only at very large shear rates.

### Realizability of curved- & rotating shear flow

The limitations of a turbulence model show up as soon as the flow conditions depart from simple unidirectional shear. For this reason, we focus on the convex surface of the curved shear layer and the suction side of the rotating channel flow, with attention confined to the energy component  $\overline{u_2^2}$  perpendicular to the wall (see figure 1b). The realizability principle requires that  $\overline{u_2^2}$  must not be driven to negative values, which yields

$$\begin{aligned} \frac{\beta_1}{\beta_3} &\leq \frac{3\bar{\rho}(3\bar{\theta} - \bar{\rho})}{1 + 3\bar{\theta}^2 + 4/(2 + \bar{\rho}^2)} \\ \text{with } \bar{\rho} &= \pm\beta_3(k/\epsilon)|S_{12}|, \\ \bar{\theta} &= \pm 2\beta_2(k/\epsilon)|W_{12}|. \end{aligned} \quad (8)$$

Further analysis on the global minimum of the r.h.s. of (8), yields

$$\frac{\beta_1}{\beta_3} \leq f_{\max}^{-1} \quad \text{with} \quad f(\theta, \rho) = \frac{3\rho(3\theta - \rho)}{1 + 3\theta^2 + 4/(2 + \rho^2)} \quad (9)$$

The evaluation of  $f_{\max}$ , however, is non-trivial. Fortunately, the local maxima of the amplification function approach an asymptotic limit for large values of  $\theta$  and  $\rho$ , as indicated by figure 2. In this case, we can infer

$$f = \frac{\rho}{\theta} \left( 3 - \frac{\rho}{\theta} \right), \quad (10)$$



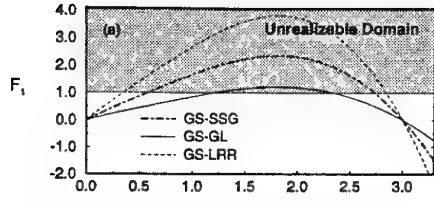


Figure 3: Variation of the realizability performance function (16) with the non-dimensional strain rate parameter  $\rho$ .

which implies

$$f_{\max} = 2.25 \quad \text{at} \quad \frac{\rho}{\theta} = 1.5. \quad (11)$$

Thus, the realizability constraint for the curved shear layer and rotating channel flow requires

$$\frac{\beta_1}{\beta_3} \leq \frac{4}{9}. \quad (12)$$

With respect to table 1 it is clear that only the coefficients of the GL model satisfy the realizability constraint (12), whereas those of the LRR and SSG variants result in a violation. Moreover, by analysing the situation which is most likely to stabilize turbulence one obtains:

$$C_3 < 2 \quad \text{and} \quad C_4 < 2, \quad (13)$$

$$\text{or} \quad C_3 > 2 \quad \text{and} \quad C_4 > 2. \quad (14)$$

As seen from table 1, all the GS model variants considered satisfy the relation (13).

#### Realizability of accelerated flow

Flow acceleration is another case where turbulence can be strongly attenuated. Here, the mechanism responsible for an attenuation of turbulence is characterized by irrotational straining rather than shear. The two cases in point are irrotational plane strain and axisymmetric contraction of the flow (see figure 1c). In both cases the realizability principle applied to the GS model implies that

$$\begin{aligned} \overline{u_1^2} &= \frac{2}{3}k \\ -2\nu_t \left[ S_{11} - \beta_3 \frac{k}{\epsilon} \left( S_{11}S_{11} - \frac{1}{3}S_{kk}^2 \right) \right] &\geq 0. \end{aligned} \quad (15)$$

With attention confined to the more restrictive 2-D plane-strain situation, the realizability condition is finally obtained from

$$F_1 = \frac{\beta_1}{\beta_3} \frac{3\rho(3-\rho)}{1+4/(2+\rho^2)} \leq 1 \quad \text{with} \quad \rho = \beta_3 S/2. \quad (16)$$

The realizability performance function  $F_1$  for the three considered GS model variants is given in figure 3. As seen from the graph, all considered pressure-strain models exhibit unrealizable features even at very moderate strain rates.

Similar conclusions emanate from the analysis of the 3D axisymmetric contraction. However, the models failure is less pronounced than in the plane-strain situation.

#### A realizable eddy-viscosity model (RQEVN)

A comprising realizability constraint for irrotational distortion can be derived from the inequality (16), viz.

$$\begin{aligned} \frac{\beta_1}{\beta_3} &\leq 0.272, \\ \text{as} \quad \left( \frac{3\rho(3-\rho)}{1+4/(2+\rho^2)} \right)_{\max} &\approx 3.675 \quad \text{at} \quad \rho \approx 3.63. \end{aligned} \quad (17)$$

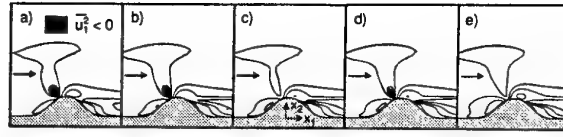


Figure 4: Contour plots of the predicted Reynolds-stress component  $\overline{u_1^2}$  for the turbulent flow over a 2-D hill measured by Almeida *et al.* (1993): (a) linear  $k-\epsilon$  model, (b) GS-LRR model, (c) GS-GL model, (d) GS-SSG model, (e) present RQEVN proposal.

Clearly, (17) is a stronger restriction on  $\beta_1$  and  $\beta_3$  than the previous constraint (12) obtained from the rotating shear flow, which leads to the first central result of this paper: *The satisfaction of the realizability constraint for the 2-D plane-strain case will also ensure the realizability of the curved- and rotating shear flow.* Returning to the plane shear flow, we can draw a second important conclusion (assuming  $\beta_i$  to be positive): *A generalized relation which satisfies the realizability principle for all the basic flows considered reads*

$$0 \leq \frac{\beta_1}{\beta_3} \leq 0.272. \quad (18)$$

In terms of the coefficients of the pressure-strain model (4), the general realizability constraint requires

$$0 \leq \frac{4-3C_2}{6(2-C_3)} \leq 0.272. \quad (19)$$

Assuming  $C_3 < 2$ , as confirmed by all the considered linear pressure-strain models, we can finally conclude

$$C_2 \leq \frac{4}{3} \quad \text{and} \quad C_3 \leq 1.84C_2 - 0.45 \quad \text{and} \quad C_4 < 2. \quad (20)$$

In conclusion, the pressure-strain correlation models of GL, LRR and SSG all satisfy the realizability requirements for  $C_2$  and  $C_4$ , but fail in the constraint on  $C_3$ . It is interesting to note that the Rotta coefficient  $C_1$  has obviously no impact on the realizability constraints in the present explicit ASM methodology, which is a major advantage of the approach. Since the Rotta coefficient exclusively represents the rate of return-to-isotropy of the Reynolds stresses it has no direct influence on the rapid term in which the Reynolds stresses interact with the mean strain rate and vorticity. In contrast to this, the linear return-to-isotropy model employed in most of the baseline Reynolds-stress transport models fails to ensure realizability (Sarkar & Speziale 1990). Finally, without further elaboration, we would like to emphasize that although the applied regularization of the coefficient  $C_\mu^*$  in (2) inherent in the GS model is punctiliously not appropriate for large strain rates, it considerably improves the GS model's realizability.

Assuming the non-linear eddy-viscosity model to be of  $k-\epsilon$  type, the realizable quadratic eddy-viscosity model is solved in conjunction with modeled transport equations for  $k$  and  $\epsilon$ , viz.

$$\frac{Dk}{Dt} = P - \epsilon + \frac{\partial}{\partial x_i} \left( \nu_t \frac{\partial k}{\partial x_i} \right) \quad (21)$$

$$\frac{D\epsilon}{Dt} = \frac{\epsilon}{k} (c_{\epsilon 1}P - c_{\epsilon 2}\epsilon) + \frac{\partial}{\partial x_i} \left( \frac{\nu_t}{1.3} \frac{\partial \epsilon}{\partial x_i} \right), \quad (22)$$

In view of the final formulation of a realizable quadratic eddy-viscosity model attention is confined to the log layer of a channel flow and the (rotating) homogeneous shear flow in equilibrium state. Further analysis and numerical optimization (Rung *et al.* 1996) with respect to these two

building-block flows yield the following set of coefficients entering the present formulation:

$$\begin{aligned} C_1=2.6 \quad C_2=0.45 \quad C_3=0.37 \quad C_4=0.5 \\ C_5=1.98 \quad C_{\epsilon 1}=1.42 \quad C_{\epsilon 2}=1.83 \quad g=3.58 \end{aligned}$$

## ILLUSTRATIVE EXAMPLES

The first example is concerned with the computation of a turbulent flow over a 2-D hill mounted on the bottom wall of a channel, where experiments are reported by Almeida, Durão & Heitor (1993). The flow approaches the obstacle in a fully-developed state, the Reynolds number based on the bulk velocity  $U_0$  and height  $h$  of the hill is  $Re = 60000$ , and the channel width is  $H = 6.07h$ . The numerical method is based on the finite-volume Navier-Stokes procedure within general body-fitted coordinates. Contours of the cartesian Reynolds-stress component  $u_1^2$  in the surrounding of the hill predicted by the standard linear  $k-\epsilon$  model, and the four GS model variants considered are given in figure 4(a-e). It is interesting to note that the results obtained from the GS model variants entirely confirm the foregoing theoretical derivations. In conjunction with the LRR and SSG pressure-strain variants, the GS model's predictive response to the simultaneous presence of curved shear and acceleration upstream of the summit does not satisfy the realizability principle. As distinct from this, the GS-GL model and the present RQEVm proposal return realizable solutions. Furthermore, a closer observation of figure 4(c) gives grounds for suspicion that the GL variant would also tend to drive the solution towards unrealistic results for more sustained accelerations.

In order to convey the predictive quality of the flow's gross characteristics obtained from the non-linear models, stream-function contours, are given in comparison with the linear  $k-\epsilon$  model and experimental data. As regards the size of the separation bubble illustrated in figure 5(a-f), the RQEVm and LRR variants seem to outperform the GL and SSG variants.

In the following, attention is drawn to the assessment of the model performance in the log layer of a channel flow and the homogeneous shear flow in equilibrium state. In table 2, the equilibrium values, predicted by five algebraic stress models for a prescribed non-dimensional mean strain-rate parameter  $S = (\partial U_1 / \partial X_2 \quad k / \epsilon) = 3.1$  are compared with experimental data of Laufer (1951) for the log layer of a turbulent channel flow. Examples included refer to the realizable non-linear model of Shih *et al.* (1993), the three standard pressure-strain models rooted in the GS model and the present RQEVm proposal of the GS model. In general, all models reflect a compromise between the two pivotal testcases, thus the rating for the log layer should be restricted to the predictive accuracy of the models with respect to turbulent shear. Here, the present RQEVm proposal and the SZL ASM return slightly higher values of  $b_{12}$ , which are in closer proximity to the experimental results than the other modelling practices.

Further scrutinizing of the models' capabilities results from the computed equilibrium values for an initially isotropic turbulence subjected to homogeneous, uniform, plane shear (see figure 6). In table 3, the equilibrium values returned by the five ASM models are compared with experimental data reported by Tavoularis & Corrsin (1981). From these results it is clear that the GS-SSG model performs best, for it predicts the correct dimensionless equilibrium strain-rate parameter  $S_\infty$  and also constitutes an excellent representation of the Reynolds-stress anisotropy tensor  $b_{ij\infty}$ . Despite the somewhat excessive level of the normal-stress anisotropy component  $b_{11\infty}$ , the present RQEVm proposal does a reasonably good job, particularly with respect to  $S_\infty$  and  $b_{12\infty}$ .

Amongst the many issues of turbulence modelling, the accurate predictive response to streamwise curvature and

	SZL	SSG	LRR	GL	RQEVm	Exp.
$b_{11}$	0.15	0.09	0.06	0.07	0.13	0.22
$b_{22}$	-0.09	-0.07	-0.05	-0.04	-0.06	-0.15
$b_{33}$	-0.06	-0.02	-0.01	-0.04	-0.07	-0.07
$b_{12}$	-0.15	-0.13	-0.14	-0.13	-0.15	-0.16
$S$	3.1	3.1	3.1	3.1	3.1	3.1

Table 2: Comparison of the model predictions for a prescribed  $S$  with the experimental data of Laufer (1951) for the log layer of turbulent channel flow (SZL-ASM: Shih, Zhu and Lumley (1993); GS-LRR: GS + Launder, Reece and Rodi (1975); GS-GL: GS + Gibson and Launder (1978); GS-SSG: GS + Speziale, Sarkar and Gatski (1991); RQEVm: GS + present proposal).

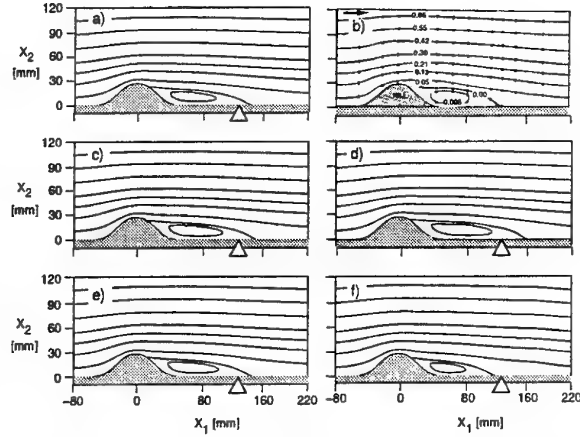


Figure 5: Comparison of predicted and measured stream-function contour lines for the turbulent flow over a 2-D hill: (a) present RQEVm proposal, (b) Measurements Almeida *et al.* (1993), (c) GS-GL model, (d) GS-SSG model, (e) GS-LRR, (f) linear  $k-\epsilon$  model.

non-inertial effects pose perhaps the biggest challenge. The curvature strain imposed on a shear layer has a disproportionately large influence on the evolution of the shear stress and the turbulence energy. Therefore the extension of the aforementioned homogeneous plane shear flow to non-inertial reference frames is of significance. In figure 6(a-d), the model predictions of the five considered explicit ASM for the time evolution of the turbulent kinetic energy are compared with large-eddy simulations reported by Bardina *et al.* (1983). The calculations were conducted using a Runge-Kutta integration scheme. Results refer to four different rotation rates, i.e.  $\Omega_3/S^* = -0.5$ ,  $\Omega_3/S^* = 0$ ,  $\Omega_3/S^* = 0.25$  and  $\Omega_3/S^* = 0.5$ , exposed to a common initial condition  $\epsilon_0/(S^* k_0) = 0.296$ . Results obtained from the GS-SSG and the RQEVm are in fairly good agreement with the LES for all four rotation rates. Here, the primary difference between the predictions and the LES is restricted to the early transient, where the models' response to the imposed shear is too excessive due to the absence of relaxational effects. With respect to the three other non-linear formulations, we recognize a disparity in the predictive accuracy. As opposed to their accurate predictions for  $\Omega_3/S^* = -0.5$  and  $\Omega_3/S^* = 0$ , the SZL ASM, GS-LRR and GS-GL models fail to capture the proper exponential growth of turbulence energy for the most unstable case  $\Omega_3/S^* = 0.25$  and give rise to noticeable deviations when the flow approaches the re-stabilizing regime at  $\Omega_3/S^* = 0.5$ . In conjunction with the GS-LRR and GS-GL model variants, the deteri-

	SZL	SSG	LRR	GL	RQEVM	Exp.
$b_{11}$	0.49	0.20	0.16	0.19	0.28	0.20
$b_{22}$	-0.29	-0.15	-0.12	-0.10	-0.13	-0.15
$b_{33}$	-0.19	-0.06	-0.03	-0.10	-0.15	-0.06
$b_{12}$	-0.16	-0.16	-0.19	-0.18	-0.16	-0.15
$S$	6.55	6.02	5.57	5.79	6.04	6.08

Table 3: Comparison of the model predictions with the experimental equilibrium values in homogeneous shear flow measured by Tavoularis *et al.* (1981).

Rotation	SSG	LRR	GL	RQEVM	Theory
$(\Omega_3/S^*)_1$	-0.07	-0.08	-0.07	-0.04	0.0
$(\Omega_3/S^*)_2$	0.51	0.34	0.36	0.47	0.5
$(\Omega_3/S^*)_m$	0.22	0.13	0.14	0.21	0.25

Table 4: Comparison of the model predictions with results from linear hydrodynamic stability analysis in the unstable regime of a rotating homogeneous shear flow.

oration of the predictive accuracy in the unstable regime is attributed to different degrees of Richardson number similarity inherent to the underlying pressure-strain model rooted in the ASM approach. To elucidate further, we compare the result of a fixed point analysis of the GS algebraic stress model variants. A straightforward analysis of the growth rate of turbulence energy ( $\sim S_\infty^{-1}$ ) indicates that the GS model returns unstable flow inside the interval  $(\Omega_3/S^*)_1 < (\Omega_3/S^*) < (\Omega_3/S^*)_2$ , with a maximum growth of turbulence kinetic energy at  $(\Omega_3/S^*)_m$ . These results are summarized in table 4. Linear stability analysis (Lezius & Johnston 1976; Speziale *et al.* 1995), among others, suggests that the uniform shear flow is unstable for approximately the range  $0 \leq \Omega_3/S^* \leq 0.5$ , where the Richardson number is positive, with the location of the most energetic state at  $(\Omega_3/S^*)_m \approx 0.25$ . Expecting the non-linear stability boundaries to be even somewhat broader, it is clear that a major drawback of the GL and LRR pressure-strain models results from a premature onset of re-stabilization caused by a too strong deviation from Richardson-number similarity. The latter is illustrated by the corresponding bifurcation diagram, figure 7, where the upper branch equilibrium values of  $S_\infty^{-1}$  are plotted as a function of  $\Omega_3/S^*$  for the GS algebraic stress models. In conclusion, both the SSG and RQEVM variants of the GS model offer a satisfactory amount of consistency with hydrodynamic stability theory for homogeneous shear flow in a rotating frame, with the SSG variant performing best. As opposed to this, the inconsistent behaviour inherent to the GS-GL and GS-LRR models erroneously yields predictions of decaying turbulence at  $\Omega_3/S^* = 0.5$  where the flow is still linearly unstable (cf. figure 6d). It should be noted, that, due to the lack of an underlying second-moment closure, the SZL algebraic stress model stands aloof from the fixed point analysis, hence it is not investigated further.

The final example to be presented herein is a fully-developed channel flow subjected to a constant spanwise rotation  $\Omega_3$  relative to the inertial frame at  $Re = 11500$  and  $Ro = 0.21$  (Johnston & Lezius 1972, see figure 1b). The test case represents a flow which is not in accord with the equilibrium turbulence assumption rooted in the ASM approximation, hence a careful examination of the applied GS model variants is recommended. It was established in the study of Gatski *et al.* (1993) that the response of the GS-SSG model and the SSG second-moment closure model to this testcase are almost identical. By reference to figure

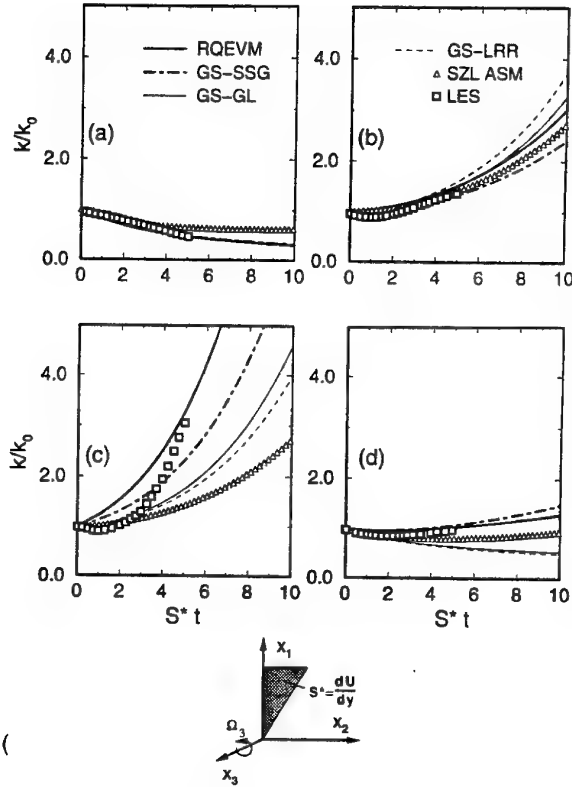


Figure 6: Comparison of the GS model predictions with large-eddy simulations of Bardina *et al.* (1983) for the rotating homogeneous shear flow ( $\epsilon_0/S^*k_0=0.296$ ): (a)  $\Omega_3/S^* = -0.5$ , (b)  $\Omega_3/S^* = 0$ , (c)  $\Omega_3/S^* = 0.25$ , (d)  $\Omega_3/S^* = 0.5$ .

8 it is argued that all the GS model variants return almost the same asymmetric mean-velocity profile, which is thus in close proximity to the results obtained from the SSG second-moment closure.

## CONCLUSIONS

To conclude this paper, we acknowledge that the GL pressure-strain model rooted in the explicit GS ASM has shown to outperform the LRR and SSG alternatives in a variety of realizability investigations. The GS-GL variant satisfies the realizability principle for plane and curved shear flows as well as for the irrotational distortion of the flow by an axisymmetric contraction. The only subtle failure of the GS-GL model emerges from the 2-D plane strain situation. Contrary to the GS-GL model, the GS-LRR variant is afflicted by a variety of failures and displays a poor performance with respect to the realizability principle. Both, the GS-GL and GS-LRR model, exhibit poor predictive performance in unstable flow situations. The GS-SSG model, which is quite successful in predicting homogeneous flows, tends to produce unrealizable results as soon as the mean flow departs from unidirectional shear. The satisfactory overall performance of the present RQEVM shows that, in spite of the popular view, adherence to the realizability principle does not, at least in the framework of the explicit ASM methodology, lead to an overly biased model performing poorly in more commonly encountered turbulent flows.

## ACKNOWLEDGEMENT

This research was partly funded by the German Ministry of Education and Research (BMBF) under the umbrella of the MEGAFLOW project (Grant No. 20A9501F) and

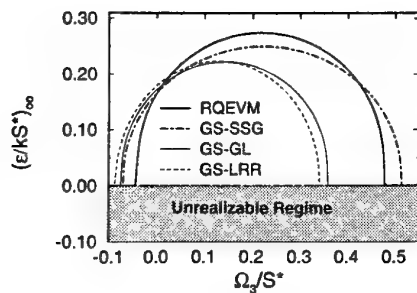


Figure 7: Bifurcation diagram for the GS explicit algebraic stress model corresponding to homogeneous shear flow in a rotating frame.

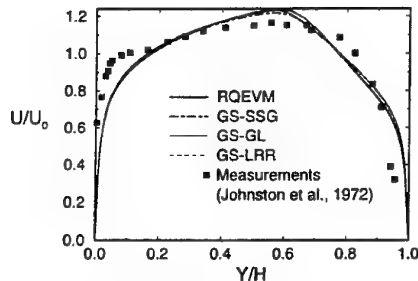


Figure 8: Performance of the GS explicit algebraic stress model variants for the fully-developed rotating channel flow ( $Re = 11500$ ,  $Ro = 0.21$ ).

Deutsche Forschungsgemeinschaft (Grant No. Fe 43/38). The authors greatly acknowledge the financial and administrative support by TU Berlin's foreign exchange program while the first author (SF) was in residence at TU Berlin.

## REFERENCES

- Abid, R., Rumsey, C. and Gatski, T., 1995, "Prediction of nonequilibrium turbulent flows with explicit algebraic stress models." *AIAA Journal*, Vol. 33, pp. 2026-2031.
- Almeida, G.P., Durão, D.F.G. and Heitor, M.V., 1993, "Wake flows behind two-dimensional model hills." *Experimental Thermal and Fluid Science*, Vol. 7, pp. 87-101.
- Bardina, J., Ferziger, J. H. and Reynolds, W.C., 1983, "Improved turbulence models based on large-eddy simulation of homogeneous, incompressible turbulent flows." *Stanford University Tech. Rep. TF-19*.
- Craft, T., Launder, B.E. and Suga, K., 1995, "A non-linear eddy-viscosity model including sensitivity to stress anisotropy." *Proc. of the 10th Symp. on Turbulent Shear Flows*, Pennsylvania State University, pp. 23-19.
- Gatski, T. and Speziale, C., 1993, "On explicit algebraic stress models for complex turbulent flows." *J. Fluid Mech.*, Vol. 254, pp. 59-75.
- Gibson, M.M. and Launder, B.E., 1978, "Ground effects on the pressure fluctuations in the atmospheric boundary layer." *J. Fluid Mech.*, Vol. 86, pp. 491-511.
- Johnston, J.P., Halleen, R.M. and Lezius, D.K., 1972, "Effects of a spanwise rotation on the structure of two-dimensional fully-developed channel flow." *J. Fluid Mech.*, Vol. 56, pp. 533-558.
- Laufer, J., 1951, "Investigation of turbulent flow in a two dimensional channel." *NACA Tech. Rep. 1053*.
- Launder, B.E. Reece, G. and Rodi, W., 1975, "Progress in the development of a Reynolds stress turbulence closure." *J. Fluid Mech.*, Vol. 68, pp. 537-566.
- Lezius, D.K. and Johnston, J.P., 1976, "Roll-cell insta-

bilities in rotating laminar and turbulent channel flow." *J. Fluid Mech.*, Vol. 77, pp. 153-175.

Lumley, J.L., 1978, "Computational modelling of turbulent flows." *Adv. Appl. Mech.*, Vol. 18, pp. 123-176.

Pope, S.B., 1975, "A more general effective viscosity hypothesis." *J. Fluid Mech.*, Vol. 72, pp. 331-340.

Rung, T., Fu, S. and Thiele, F., 1996, "Derivation of a Realizable Quadratic Explicit Reynolds Stress Model." Internal Report, Herman-Föttinger Institut, TU Berlin.

Sarkar, S. and Speziale, C.G., 1990, "A simple nonlinear model for the return to isotropy in turbulence." *Phys. Fluids A*, Vol. 2, pp. 84-93.

Schumann, U., 1977, "Realizability of Reynolds stress turbulence models." *Phys. Fluids*, Vol. 20, pp. 721-725.

Shih, T.H., Zhu, J. and Lumley, J.L., 1993, "A realizable Reynolds stress algebraic equation model." *NASA TM-105993 (ICOMP Report 92-27)*, NASA Lewis Research Center.

Speziale, C., Abid, R. and Blaisdell, G., 1995, "On the consistency of reynolds stress turbulence closure with hydrodynamic stability theorie." *ICASE Report 95-46*, NASA Langley Research Center.

Speziale, C.G., Sarkar, S. and Gatski, T.B., 1991, "Modelling the pressure-strain correlation of turbulence: an invariant dynamical systems approach." *J. Fluid Mech.*, Vol. 227, pp. 545-272.

Tavoularis, S. and Corrsin, S., 1981, "Experiments in nearly homogeneous turbulent shear flows with a uniform mean temperature gradient." *J. Fluid Mech.*, Vol. 227, pp. 245-272.

Yakhot, V., Orzag, S.A., Thangham, S., Gatski, T.B. and Speziale, C.G., 1992, "Development of turbulence models for shear flows by a double expansion technique." *Phys. Fluids A*, Vol. 4, pp. 1510-1520.

Yoshizawa, A., 1984, "Statistical analysis of the deviation of the Reynolds stress from its eddy viscosity representation." *Phys. Fluids*, Vol. 27, pp. 1377-1387.

# PREDICTING NON-INERTIAL EFFECTS WITH ALGEBRAIC STRESS MODELS WHICH ACCOUNT FOR DISSIPATION RATE ANISOTROPIES

T. Jongen<sup>(1)</sup>, L. Machiels<sup>(1)</sup>, T. B. Gatski<sup>(2)</sup>

<sup>(1)</sup> Fluid Mechanics Laboratory  
Swiss Federal Institute of Technology  
1015 Lausanne  
Switzerland

<sup>(2)</sup> Aerodynamic and Acoustic Methods Branch  
NASA Langley Research Center  
Hampton, VA 23681  
USA

## INTRODUCTION

Turbulent flows in non-inertial reference frames are of considerable interest in a variety of industrial applications. However, the success of a computational analysis of such flow phenomena relies heavily on the choice of turbulence model. It is well-known that, without some modifications, conventional isotropic eddy-viscosity models fail to predict the effect of non-inertial forces on turbulence, whereas second-moment closures, for example, can account for non-inertial effects in a systematic way.

An explicit algebraic stress model (EASM) has been developed by Gatski and Speziale (1993) which is a nonlinear extension to an isotropic eddy-viscosity two-equation model. An extension to this EASM which accounts for dissipation rate anisotropies in a systematic way and is applicable to wall-bounded flows, has been recently evaluated (Jongen *et al.* 1997, see also Xu and Speziale 1996), and is based on an analysis of the exact transport equation for the dissipation rate tensor (Speziale and Gatski 1997). This composite algebraic stress model (CASM) is extended here to include non-inertial effects in the determination of both the stress and dissipation rate anisotropies. The composite model differs from previously proposed algebraic stress models in two ways: dissipation rate anisotropies are accounted for in the constitutive relation and the coefficient of the production term in the transport equation for the scalar dissipation rate is now sensitized to the mean strain and rotation rate tensors.

The objective of this study is to systematically explore the predictive capabilities of explicit algebraic stress models in general and, in particular, the composite model for the case of a fully developed turbulent channel flow with strong spanwise rotation. This effort is an extension of previous work in that (1) the recent DNS obtained by Lamballais *et al.* (1996) has yielded new data for rotation numbers that are higher than those for the previous DNS study of Kristoffersen and Andersson (1993) and (2) the equations are integrated up to the wall, whereas most of the previous computations were limited to wall-function boundary conditions that are not suitable for (strongly) rotating flows where regions of relaminarization can occur.

## TURBULENCE MODELS

The incompressible, fully developed rotating channel flow is a unidirectional flow that results in simplified expressions for the mean flow in the non-inertial frame. In this frame, the mean strain rate and rotation rate tensors

$$S_{ij} = \frac{1}{2} \left( \frac{\partial \bar{u}_i}{\partial x_j} + \frac{\partial \bar{u}_j}{\partial x_i} \right), \quad \omega_{ij} = \frac{1}{2} \left( \frac{\partial \bar{u}_i}{\partial x_j} - \frac{\partial \bar{u}_j}{\partial x_i} \right) \quad (1)$$

reduce to

$$S_{ij} = \begin{pmatrix} 0 & S & 0 \\ S & 0 & 0 \\ 0 & 0 & 0 \end{pmatrix}, \quad \omega_{ij} = \begin{pmatrix} 0 & S & 0 \\ -S & 0 & 0 \\ 0 & 0 & 0 \end{pmatrix} \quad (2)$$

where  $S = S(y)$  and  $y$  is the distance measured from the (bottom) wall of the channel, as shown in Figure 1.

The common feature between linear and nonlinear eddy viscosity models is both require the solution of only two transport equations; an equation for the turbulent kinetic energy  $K$

$$\frac{\partial K}{\partial t} = \mathcal{P} - \varepsilon + D + \frac{\partial}{\partial y} \left[ \left( \nu + \frac{\nu_t}{\sigma_K} \right) \frac{\partial K}{\partial y} \right] \quad (3)$$

and an equation for the turbulent dissipation rate  $\varepsilon$

$$\frac{\partial \varepsilon}{\partial t} = C_{\varepsilon 1} \mathcal{P} \frac{\varepsilon}{K} - f_2 C_{\varepsilon 2} \frac{\varepsilon^2}{K} + E + \frac{\partial}{\partial y} \left[ \left( \nu + \frac{\nu_t}{\sigma_\varepsilon} \right) \frac{\partial \varepsilon}{\partial y} \right] \quad (4)$$

where

$$\nu_t = f_\mu C_\mu K \tau, \quad \tau = K/\varepsilon, \quad (5)$$

$\mathcal{P} = -2\tau_{12}S$  is the turbulent production,  $\tau_{12}$  is the Reynolds shear stress,  $f_2$  and  $f_\mu$  are wall damping functions,  $C_\mu$  is a closure constant, and  $\nu$  is the kinematic viscosity.

Three turbulence models will be evaluated by using (3) through (5): a Coriolis-modified eddy-viscosity model (EVM) proposed by Howard *et al.* (1980); a realizable algebraic stress model (ASM) (Shih *et al.* 1995); and a CASM that accounts for dissipation rate anisotropies (Xu and Speziale 1996; Jongen *et al.* 1997). These three models are distinct in the way rotational effects are incorporated into their formulations.

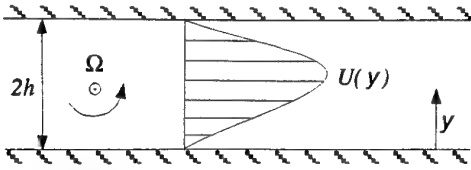


Figure 1. Schematic of fully developed turbulent channel flow in a rotating frame

In the EVM, the non-inertial modification is phenomenological and based on an analogy with curved boundary layers. The realizable ASM model of Shih *et al.* (1995) includes the effect of mean rotation and has been tested on rotating homogeneous shear flow. The CASM is an algebraic stress model which is directly extracted from a full Reynolds stress closure as well as a transport equation for the tensor dissipation rate  $\epsilon_{ij}$ . Thus, the model includes the effects of an anisotropic dissipation rate in a algebraic stress framework.

The Coriolis-modified eddy-viscosity model uses the Boussinesq-type relation for the Reynolds stresses:

$$b_{ij} = -f_\mu C_\mu^* \tau S_{ij}, \quad b_{ij} = \frac{(\tau_{ij} - \frac{2}{3} K \delta_{ij})}{2K} \quad (6)$$

coupled with the relations to close (3) through (5):

$$D = -2\nu \left( \frac{\partial \sqrt{K}}{\partial y} \right)^2, \quad E = 2\nu \nu_t \left( \frac{\partial S}{\partial y} \right)^2 \quad (7)$$

$$f_\mu = \exp \left[ -3.4 \left( 1 + \frac{Re_t}{50} \right)^{-2} \right], \quad Re_t = \frac{K^2}{\nu \epsilon} \quad (8)$$

$$C_{\epsilon 2}^* = \left[ C_{\epsilon 2} + 1.536 S^2 \tau^2 \left( \frac{\Omega}{S} \right) \left( 1 - \frac{\Omega}{S} \right) \right] \quad (9)$$

$$f_2 = 1 - 0.3 \exp(-Re_t^2) \quad (10)$$

where  $C_\mu^* = C_\mu = 0.09$ ,  $C_{\epsilon 1}^* = 1.44$ ,  $C_{\epsilon 2} = 1.92$ ,  $\sigma_K = 1$ ,  $\sigma_\epsilon = 1.3$ , and  $\Omega$  is the rotation rate of the reference frame.

The Reynolds stress algebraic equation model (Shih *et al.* 1995) is given by

$$b_{ij} = -C_\mu^* \tau S_{ij} + c_2 \tau^2 (S_{ik} W_{kj} - W_{ik} S_{kj}) \quad (11)$$

and

$$W_{ij} \equiv \omega_{ij} + \epsilon_{mji} \Omega_m, \quad \Omega_m = (0, 0, \Omega) \quad (12)$$

where for this unidirectional shear case

$$c_2 = -\frac{\sqrt{1 - 18 C_\mu^* (S\tau)^2}}{1 + 12 (S\tau)^2 \left| 1 - \frac{\Omega}{S} \right|}, \quad D = E = 0 \quad (13)$$

$$f_2 = \left[ 1 - \exp \left( -\frac{y^+}{5.5} \right) \right]^2, \quad y^+ = \frac{y u_\tau}{\nu} \quad (14)$$

$$C_\mu^* = \left[ 6.5 + 3\sqrt{2} |S\tau| \sqrt{1 - 3 \frac{\Omega}{S} + \frac{9}{2} \left( \frac{\Omega}{S} \right)^2} \right]^{-1} \quad (15)$$

$u_\tau$  is the friction velocity,  $f_\mu = 1.0$ ,  $C_\mu = 0.09$ ,  $C_{\epsilon 1}^* = 1.44$ ,  $C_{\epsilon 2} = 1.92$ ,  $\sigma_K = 1$ , and  $\sigma_\epsilon = 1.3$ .

The composite algebraic stress model that accounts for dissipation rate anisotropies (Xu and Speziale 1996; Jongen *et al.* 1997) is an extension of the EASM of Gatski and Speziale (1993) in inertial frames. In the non-inertial case, the process is complicated by the fact that the system rotation enters differently into the anisotropic dissipation rate and the algebraic stress relations.

First, non-inertial effects are introduced into the explicit algebraic anisotropic dissipation rate equation developed by Speziale and Gatski (1997) as

$$d_{ij} = -\frac{2g_\epsilon}{15} C_\mu^* \left[ \tau S_{ij} + \beta_1 \tau^2 (S_{ik} W_{kj}^* - W_{ik}^* S_{kj}) + 2\beta_2 \tau^2 \left( S_{ik} S_{kj} - \frac{1}{3} S_{kl} S_{kl} \delta_{ij} \right) \right], \quad (16)$$

and

$$W_{ij}^* \equiv \omega_{ij} + c_\omega^* \epsilon_{mji} \Omega_m, \quad c_\omega^* = \frac{7\beta_3 + 12}{7\beta_3 + 1} \quad (17)$$

$$d_{ij} = \frac{(\epsilon_{ij} - \frac{2}{3} \epsilon \delta_{ij})}{2\epsilon} \quad (18)$$

$$C_\mu^* = \left\{ 1 - \frac{4}{3} (S\tau)^2 \left[ \beta_2^2 - 3\beta_1^2 \left( 1 - c_\omega^* \frac{\Omega}{S} \right)^2 \right] \right\}^{-1} \quad (19)$$

$$\beta_1 = \left( \frac{7}{11} \beta_3 + \frac{1}{11} \right) g_\epsilon, \quad \beta_2 = \left( \frac{15}{11} \beta_3 - \frac{1}{11} \right) g_\epsilon \quad (20)$$

$$g_\epsilon = \left[ C_{\epsilon 5} + \frac{\mathcal{P}}{\epsilon} - 1 \right]^{-1}$$

$C_{\epsilon 5} = 5.8$ , and  $\beta_3 = 0.6$ .

In the absence of rotation, this explicit algebraic anisotropic dissipation rate model could be directly inserted into the explicit algebraic stress model and the resulting composite explicit algebraic equation could be solved in conjunction with the turbulent kinetic energy and the dissipation rate equations. In the non-inertial frame this direct substitution is not possible, and the problem can be quickly identified by examining the implicit relation for the algebraic stress model that is used as the starting point for the tensor polynomial expansions associated with the explicit representations. The implicit relation that accounts for dissipation rate anisotropies can be written as (Jongen *et al.* 1997)

$$b_{ij} + \alpha_3 \tau \left( b_{ik} S_{kj} + S_{ik} b_{kj} - \frac{2}{3} b_{mn} S_{mn} \delta_{ij} \right) - \alpha_2 \tau (b_{ik} \bar{W}_{kj} - \bar{W}_{ik} b_{kj}) = -\alpha_1 \tau S_{ij} - g d_{ij} \quad (21)$$

and

$$\bar{W}_{ij} \equiv \omega_{ij} + \bar{c}_\omega \epsilon_{mji} \Omega_m, \quad \bar{c}_\omega = \frac{C_4 - 4}{C_4 - 2} \quad (22)$$

$$\alpha_1 = \left( \frac{4}{3} - C_2 \right) \frac{g}{2}, \quad \alpha_2 = (2 - C_4) \frac{g}{2} \quad (23)$$

$$\alpha_3 = (2 - C_3) \frac{g}{2}, \quad g = \left[ \frac{C_1}{2} + \frac{\mathcal{P}}{\epsilon} - 1 \right]^{-1}$$

$C_1 = 3.4 + 1.8\mathcal{P}/\epsilon$ ,  $C_2 = 0.36$ ,  $C_3 = 1.25$ , and  $C_4 = 0.40$ . These constant closure coefficients are obtained from the SSG pressure-strain correlation model (Speziale *et al.* 1991). A comparison of (17) and (22) clearly shows that in general the rotation rate tensors in the non-inertial frame that are extracted from the algebraic dissipation rate model and the algebraic stress model are not the same. This difference precludes a simple combination of terms as suggested by (21) and shown to be possible in inertial frames (Xu and Speziale 1996; Jongen *et al.* 1997), where integrity bases were used to get a composite explicit representation for the Reynolds stresses.

As an alternative to this approach, consider (21) rewritten as the matrix system



$$\mathbf{Ab} = -(\alpha_1 \tau s + g d) \quad (24)$$

where

$$\mathbf{b} = [b_{11}, b_{12}, b_{22}]^T, \quad \mathbf{s} = [0, S, 0]^T, \quad \mathbf{d} = [d_{11}, d_{12}, d_{22}]^T \quad (25)$$

$$\mathbf{A} = \begin{bmatrix} 1 & \frac{2}{3} S \tau (\alpha_3 + 3\alpha_2 \mathcal{R}) & 0 \\ S \tau (\alpha_3 - \alpha_2 \mathcal{R}) & 1 & S \tau (\alpha_3 + \alpha_2 \mathcal{R}) \\ 0 & \frac{2}{3} S \tau (\alpha_3 - 3\alpha_2 \mathcal{R}) & 1 \end{bmatrix} \quad (26)$$

$$\mathcal{R} = 1 - \bar{c}_\omega \frac{\Omega}{S} \quad (27)$$

The system in (24) can be inverted analytically to obtain explicit expressions for the Reynolds stress anisotropies  $b_{ij}$  (and  $\tau_{ij}$ ). Once again, these stress relations are coupled with (3) and (4) for the turbulent kinetic energy and the turbulent dissipation rate, with

$$D = E = 0, \quad f_2 = \left[ 1 - \exp\left(-\frac{y^+}{6.5}\right) \right]^2 \quad (28)$$

$$C_{\epsilon 1}^* = 1 + (1 + \beta) \frac{d_{12}}{b_{12}}, \quad \beta = \frac{3}{4} \left( \frac{14}{11} \beta_3 - \frac{16}{33} \right) \quad (29)$$

$f_\mu = 1.0$ ,  $C_\mu = 0.094$ ,  $C_{\epsilon 2}^* = 1.83$ ,  $\sigma_K = 1$ , and  $\sigma_\epsilon = 1.3$ . The additional (nonconstant) term in the expression for  $C_{\epsilon 1}^*$  represents a production ratio of the turbulent dissipation rate ( $d_{12}S$ ) and turbulent kinetic energy ( $b_{12}S$ ).

## RESULTS

The turbulence models presented in the last section are coupled with the streamwise momentum equation

$$\frac{\partial U}{\partial t} = -G + \frac{2}{Re_b} \frac{\partial S}{\partial y} - \frac{\partial \tau_{12}}{\partial y} \quad (30)$$

where  $\bar{u}_i = (U, 0, 0)$ ;  $G$  is the (constant) effective pressure gradient, which includes the centrifugal force term; and the bulk Reynolds number  $Re_b = hU_b/\nu$ , with  $U_b$  as the bulk velocity. Equation (30), coupled with the transport equations for the turbulent kinetic energy (3) and the turbulent dissipation rate (4), is integrated to steady state by a one-dimensional second-order finite-difference scheme. This simple one-dimensional spatial problem allows for solutions with arbitrarily high numerical accuracy by using a sufficient number of points. Here, 200 points were typically used, with highly stretched meshes near the solid walls.

Because the different rotation regimes considered by the DNS (Lamballais *et al.* 1996) were obtained at the same bulk Reynolds number, the pressure gradient in the numerical code was adjusted in order to have  $Re_b = 2500$  at convergence. In the following, results for three different rotation numbers, defined by

$$Ro = 2|\Omega|h/U_b \quad (31)$$

are shown ( $Ro = 0$ ,  $Ro = 0.5$ , and  $Ro = 1.5$ ). In the earlier DNS study of Kristoffersen and Andersson (1993), the maximum rotation number studied was 0.5. Thus, the DNS data used in this study significantly increases the validation range for the turbulence closure models.

The profiles of the mean velocity and turbulent kinetic energy are shown in Figures 2 and 3, respectively. The turbulent kinetic energy, as well as the turbulent stresses to be presented, are scaled by an average friction velocity  $u_\tau$ , which is the half-sum of the friction velocities on both walls. The DNS results show the characteristic linear region of slope  $2\Omega$  in the mean velocity, which leads to a mean

absolute vorticity  $2(S - \Omega)$  that is close to zero. These results also show that the turbulent kinetic energy is higher on the anticyclonic or pressure side ( $y = 0$ ) than on the cyclonic or suction side ( $y = 2$ ), where relaminarization occurs. In Figure 2, for the mean velocity the composite model is able to reproduce all features of the flow for the three rotation numbers considered, including the linear portion of the profile and the relaminarization on the cyclonic side, characterized by a parabolic velocity profile. For the turbulent kinetic energy shown in Figure 3, the asymmetry of the profile and the higher turbulence intensity on the anticyclonic side of the channel are clearly visible and are consistent with the DNS results. In the case for which  $Ro = 0$ , the peaks in turbulent kinetic energy near the wall are not well predicted because in the CASM no  $f_\mu$  damping function has been introduced.

The Coriolis-modified model of Howard *et al.* (1980) gives reasonable predictions for the mean velocity at the different rotation numbers although not with the same degree of accuracy as the CASM. The algebraic model of Shih *et al.* (1995) does not correctly predict the mean velocity at these higher rotation numbers since it fails to predict the linear profile on the anticyclonic side and the relaminarization on the cyclonic side. For the turbulent kinetic energy, both the Howard and Shih models misrepresent the behavior of the kinetic energy in the higher rotation rate cases. At  $Ro = 0.5$  and  $Ro = 1.5$ , the Coriolis-modified EVM yields results that effectively damp out the turbulent kinetic energy in the relaminarizing portion of the flow, whereas the Shih algebraic stress model is somewhat insensitive to the effects of rotation.

With the success of the CASM, further investigation of the flow dynamics is worthwhile by examining the total shear stress. At steady state, (30) can be integrated with respect to  $y$  and expressed in wall units as

$$-\tau_{12}^+ + \frac{2}{Re_\tau} S^+ = u_{\tau 0}^2 \left[ 1 - \frac{y}{2} \left( 1 + \frac{u_{\tau 2}^2}{u_{\tau 0}^2} \right) \right] \quad (32)$$

where  $u_{\tau 0} = u_\tau|_{y=0}$ ,  $u_{\tau 2} = u_\tau|_{y=2}$ , and  $Re_\tau = hu_\tau/\nu$ . As this equation shows, the total shear must vary linearly across the channel for all rotation rates. The partition of the total shear stress between the turbulent  $\tau_{12}^+$  and viscous  $2S^+/Re_\tau$  stresses is illustrated in Figure 4 for the composite model. The region of neutral stability, where the velocity profile is linear, is characterized by a turbulent shear stress that varies linearly, and a viscous shear stress that remains constant.

In addition to the turbulent shear stress, the normal Reynolds stresses are significantly affected by the rotation. Figure 5 shows the attenuation of the normal stress components on the relaminarized side of the channel at both nonzero rotation numbers. On the turbulent side, the streamwise component  $\tau_{11}$  is attenuated relative to the  $Ro = 0$  case, and both the  $\tau_{22}$  and  $\tau_{33}$  components are enhanced relative to the  $Ro = 0$  case. The most significant effect is on the  $\tau_{22}$  component, but even at the high rotation case the  $\tau_{33}$  component also exceeds the  $\tau_{11}$  component on the anticyclonic side. This result is consistent with the DNS results and can be explained by the fact that the CASM is derived from a Reynolds stress model and will, therefore, inherit the right sensitivity of the production terms for the individual normal stresses to the rotation. On the other hand, the stress anisotropies predicted by the model of Shih *et al.* (1995) in (11) for unidirectional shear, where  $b_{11} = -b_{22} = 2c_2(S\tau)^2(1 - \frac{\Omega}{S})$  and  $b_{33} = 0$ , show that this coupling of the  $b_{11}$  and  $b_{22}$  forces the incorrect prediction of isotropic turbulence when  $\Omega = S$ , and which would preclude the correct prediction of the normal stresses as displayed in Figure 5.

Both the presence of the linear velocity profile and the relaminarization process can be explained. The CASM is

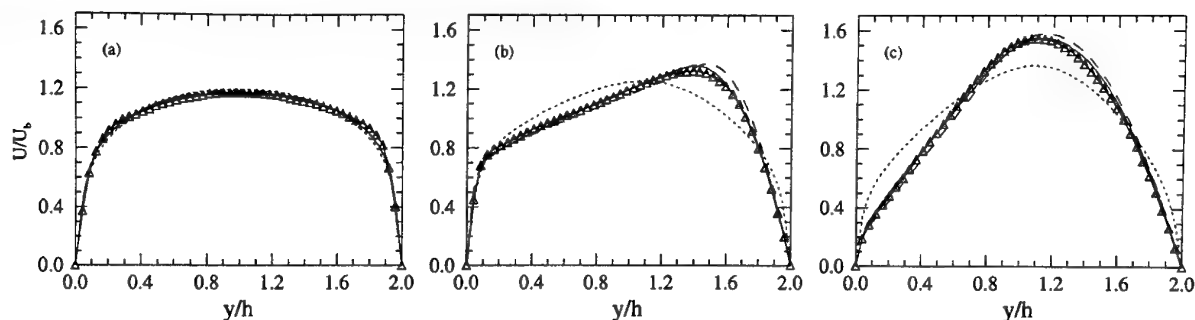


Figure 2. Mean velocity profiles for (a)  $Ro = 0$ , (b)  $Ro = 0.5$ , and (c)  $Ro = 1.5$ .  $\triangle$ — $\triangle$  DNS (Lamballais *et al.* 1996); —, CASM; ---, ASM (Shih *et al.* 1995); -.-, Coriolis-modified EVM.

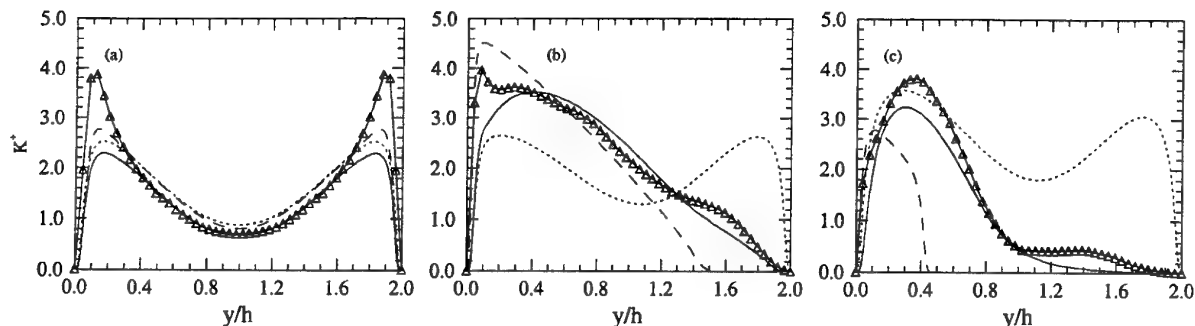


Figure 3. Turbulent kinetic energy profiles for (a)  $Ro = 0$ , (b)  $Ro = 0.5$ , and (c)  $Ro = 1.5$ .  $\triangle$ — $\triangle$  DNS (Lamballais *et al.* 1996); —, CASM; ---, ASM (Shih *et al.* 1995); -.-, Coriolis-modified EVM.

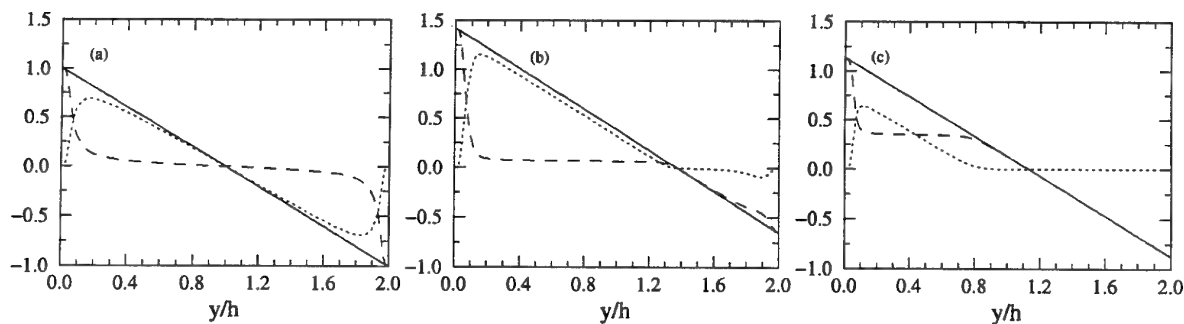


Figure 4. Partition of the total shear between turbulent and viscous shear stresses: computations by CASM for (a)  $Ro = 0$ , (b)  $Ro = 0.5$ , and (c)  $Ro = 1.5$ . —,  $-\tau_{12}^+ + 2S^+/Re_\tau$ ; ---,  $-\tau_{12}^+$ ; -.-,  $2S^+/Re_\tau$ .

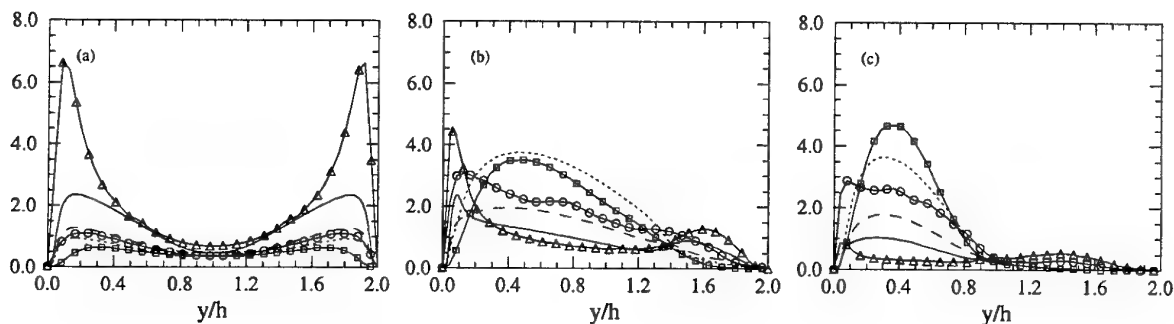


Figure 5. Turbulent normal stress profiles for (a)  $Ro = 0$ , (b)  $Ro = 0.5$ , and (c)  $Ro = 1.5$ . DNS (Lamballais *et al.* 1996) data:  $\triangle$ — $\triangle$ ,  $\tau_{11}$ ;  $\square$ — $\square$ ,  $\tau_{22}$ ;  $\circ$ — $\circ$ ,  $\tau_{33}$ . CASM: —,  $\tau_{11}$ ; ---,  $\tau_{22}$ ; -.-,  $\tau_{33}$ .



derivable from the Reynolds stress model

$$\begin{aligned} \dot{\tau}_{ij} - \frac{\tau_{ij}}{K} \dot{K} - \left( \bar{D}_{ij} - \frac{\tau_{ij}}{K} \bar{D}_K \right) \\ = -\frac{2\varepsilon}{g} \left[ b_{ij} + \alpha_3 \tau (b_{ik} S_{kj} + S_{ik} b_{kj} - \frac{2}{3} b_{mn} S_{mn} \delta_{ij}) \right. \\ \left. - \alpha_2 \tau (b_{ik} \bar{W}_{kj} - \bar{W}_{ik} b_{kj}) + \alpha_1 \tau S_{ij} + g d_{ij} \right] \quad (33) \end{aligned}$$

where  $\bar{D}_{ij}$  (and  $\bar{D}_K = \bar{D}_{jj}/2$ ) represent the effects of turbulent and viscous diffusion;  $\alpha_1$ ,  $\alpha_2$ ,  $\alpha_3$ , and  $g$  are given in (23). The implicit form of the algebraic stress model is obtained by setting the left side of (33) to zero and using the appropriate closure model for the dissipation rate anisotropies (such as the one shown in (16), which is used here). Note that the equilibrium hypothesis that underlies the algebraic stress models is exactly satisfied here ( $\dot{\tau}_{ij} = \dot{K} = 0$ ), and the only approximation that is made is  $\bar{D}_{ij} = \frac{\tau_{ij}}{K} \bar{D}_K$ .

An examination of (33) shows that the anisotropy component  $b_{12}$  must satisfy the following equation:

$$0 = b_{12} \left[ 1 - \frac{4}{3} \alpha_3^2 (S\tau)^2 + 4\alpha_2^2 (S\tau)^2 \mathcal{R}^2 \right] + \bar{\alpha}_1 S\tau \quad (34)$$

where  $\mathcal{R}$  is given in (27), and

$$\bar{\alpha}_1 = \alpha_1 + g \left[ \frac{d_{12}}{S\tau} + \alpha_3 (d_{11} + d_{22}) - \alpha_2 \mathcal{R} (d_{11} - d_{22}) \right] \quad (35)$$

As could be expected, this expression for  $b_{12}$  has the same functional form as the EASM:

$$b_{12} = -\bar{\alpha}_1 C_\mu^* S\tau, \quad C_\mu^* = \left[ 1 - \frac{4}{3} (S\tau)^2 (\alpha_3^2 - 3\alpha_2^2 \mathcal{R}^2) \right]^{-1} \quad (36)$$

Thus, in both the composite model and the EASM the production-to-dissipation rate ratio is *always* given by

$$\frac{P}{\varepsilon} \equiv -4b_{12} S\tau = 4\bar{\alpha}_1 C_\mu^* (S\tau)^2 \quad (37)$$

showing that  $\frac{P}{\varepsilon}$  is a function of both  $\Omega/S$  and  $S\tau$ . By interchanging this dependency, the behavior of  $\Omega/S$  as a function of  $\frac{P}{\varepsilon}$  and  $S\tau$ ,

$$\frac{\Omega}{S} = \frac{1}{\bar{c}_w} \left[ 1 \pm \frac{1}{\alpha_2} \sqrt{\bar{\alpha}_1 \left( \frac{P}{\varepsilon} \right)^{-1} + \frac{1}{3} \alpha_3^2 - \frac{1}{4(S\tau)^2}} \right] \quad (38)$$

can be studied. For comparative purposes, a corresponding  $\Omega/S$  relationship can also be obtained from an expression equivalent to (37) for the Shih *et al.* (1995) model;

$$\frac{\Omega}{S} = \frac{1}{3} \left\{ 1 \pm \sqrt{\left[ \frac{4}{3} S\tau \left( \frac{P}{\varepsilon} \right)^{-1} - \frac{6.5}{3S\tau} \right]^2 - 1} \right\} \quad (39)$$

Figure 6 shows the evolution of  $\Omega/S$  across the channel for the different rotation regimes and the three models considered. For the two rotating cases, several features are apparent. Starting from values near zero on the anticyclonic side (because  $S$  is high near the wall), the DNS results clearly show a plateau at  $\Omega/S = 1$ , then quickly grow and change sign at the location of the maximum velocity ( $S = 0$ ). On the cyclonic side,  $\Omega/S (< 0)$  then approaches zero with a  $y^{-1}$  behavior ( $S \sim -y$  in the relaminarized region). The figure shows that the CASM closely follows the DNS results and accurately predicts the location of maximum velocity. With (38), we can explain why the CASM model is able to predict such features, and we shall see that the reason is closely related to the expression for  $C_\mu^*$ , which must show the correct dependency on  $\Omega/S$  and  $S\tau$ .

By their nature, the CASM, and more generally, all of the algebraic stress models that are consistently derived from Reynolds stress models inherit the correct behavior for  $C_\mu^*$ , while algebraic stress models that provide a  $C_\mu^*$  expression based solely on constraints such as realizability, calibrations, and phenomenological arguments *may not* have the correct behavior and will fail to predict the neutral stability region and the relaminarized zone that is observed in the rotating channel.

For larger values of  $S\tau$  (i.e.,  $\gtrsim 3$ ), the last term under the root in (38) is negligible compared with the other terms, and  $\Omega/S$  becomes a function of  $\frac{P}{\varepsilon}$  only, and takes values on the two limit branches that correspond to the sign of  $S (= \pm |S|)$ . Now, it is also easy to verify that these two values of  $\Omega/S$  rapidly become independent of an increasing  $\frac{P}{\varepsilon}$ , and asymptote to either  $(\Omega/S)^+$  ( $S > 0$ ) or  $(\Omega/S)^-$  ( $S < 0$ ). Equation (38), therefore, shows that for a wide range of values of  $S\tau$  and  $\frac{P}{\varepsilon}$  the value of  $\Omega/S$  becomes effectively independent of these parameters, and takes values close to  $(\Omega/S)^\pm$ . These two limiting values only depend on the values of the model coefficients  $\alpha_i$ 's, and have the following values for the SSG pressure-strain model:  $(\Omega/S)^+ = 0.992$  and  $(\Omega/S)^- = -0.103$ . In the channel away from the walls, the diffusion of  $K$  may be expected to be small, and we should have  $\frac{P}{\varepsilon} \approx 1$  and  $S\tau \gtrsim 3$ . In this case, the scaled rotation rate will have values on the limit branches that will be close to the limit values  $(\Omega/S)^\pm$ .

Figure 7 illustrates this phenomenon by showing the evolution of the scaled rotation rate correlated with the variation of  $\frac{P}{\varepsilon}$  across the channel. In Figure 7(a), the two limit branches given by (38) with values of  $S\tau \geq 3$  are represented by dashed lines. At  $\frac{P}{\varepsilon} = 0$  and  $y = 0$ , the curves that correspond to the CASM simulation at the two rotation regimes first move in a region where  $(\Omega/S)^- < \Omega/S < (\Omega/S)^+$  because the values of  $S\tau$  that are given by the model are also very small. However, as  $\frac{P}{\varepsilon}$  rapidly increases with movement away from the near-wall region,  $S\tau$  increases also, and the points collapse on the (positive) limit branch. Until very near the wall at  $y = 2$ , the value of  $S\tau$  stays at values sufficiently high to force the points to stay on the limit branches. After having attained values close to  $(\Omega/S)^+ = 0.992$  for the major portion of the channel on the anticyclonic side, the maximum velocity point is reached,  $\frac{P}{\varepsilon}$  becomes very small (as  $S \rightarrow 0$ ) and the negative limit branch is followed after the maximum velocity. For most of the values  $\Omega/S < (\Omega/S)^-$ , the corresponding value of  $\frac{P}{\varepsilon}$  on the negative branch is very small, and according to (3), we can expect  $\partial K / \partial t < 0$ , which leads to relaminarization in this region.

This explanation for the occurrence of the linear profile and the relaminarization process is also valid for other Reynolds stress models (i.e. other pressure-strain correlation models). For example, the LRR model (Launder *et al.* 1975) yields limiting values for  $\Omega/S$  of  $(\Omega/S)^+ = 0.644$  and  $(\Omega/S)^- = -0.131$  for the anticyclonic and cyclonic sides, respectively. However, one would expect that the slope of the linear velocity profile, when compared to DNS, would not be correct. Note also that these results are independent of the particular model for  $\varepsilon$  that is used, because the effect enters only through  $S\tau$  and  $\frac{P}{\varepsilon}$ .

The same analysis can be carried out on the Shih *et al.* (1995) model by using (39). With this model, the evolution of  $S\tau$  always has an effect on  $\Omega/S$ , and no limiting behavior occurs. Therefore, the system is not forced to reach the asymptote  $\Omega/S \approx 1$ , which precludes attainment of a linear velocity profile on the anticyclonic side (Figure 7(b)). From  $\frac{P}{\varepsilon} = 0$  at  $y = 0$ ,  $\frac{P}{\varepsilon}$  quickly increases and the resulting curve is obtained from the balance of the model equations and (39). The fact that this model cannot reproduce the correct features for the rotating channel at high rotation numbers can be attributed to the lack of a mechanism in

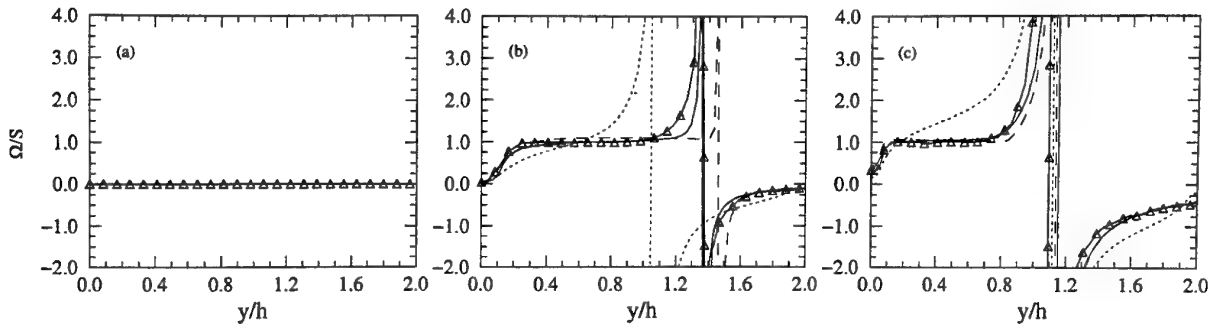


Figure 6. Scaled rotation rate variation across channel for (a)  $Ro = 0$ , (b)  $Ro = 0.5$ , and (c)  $Ro = 1.5$ .  $\triangle$ — $\triangle$  DNS (Lamballais et al. 1996); —, CASM; ---, ASM (Shih et al. 1995); -.-, Coriolis-modified EVM.

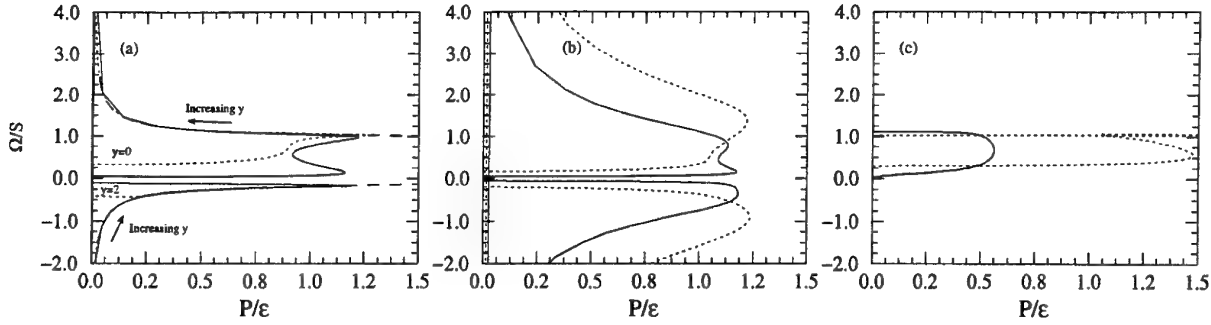


Figure 7. Scaled rotation rate variation versus  $\frac{P}{\epsilon}$  in the channel for (a) CASM, (b) ASM (Shih et al. 1995), and (c) Coriolis-modified EVM. —,  $Ro = .5$ ; ---,  $Ro = 1.5$ ; -.-, limit branches (shown for (a) only).

$C_\mu^*$  to render  $\Omega/S$  independent of  $S\tau$  and  $\frac{P}{\epsilon}$ .

Finally, for the Coriolis-modified EVM, relation (37) cannot be used to find a relation between  $\Omega/S$ ,  $\frac{P}{\epsilon}$ , and  $S\tau$ . Instead, (4) can be examined at steady state in regions away from the walls where the damping functions and diffusive terms can be neglected. The dissipation rate equation then yields the simple relation that the production-to-dissipation rate ratio is  $C_{e2}^*/C_{e1}^*$  and

$$\frac{\Omega}{S} = \frac{1}{2} \left[ 1 \pm \sqrt{1 - \frac{4}{1.536(S\tau)^2} \left( C_{e1}^* \frac{P}{\epsilon} - C_{e2}^* \right)} \right] \quad (40)$$

For sufficiently high values of  $S\tau$ , the dependency on  $\frac{P}{\epsilon}$  is totally removed, and  $\Omega/S$  takes a value of 0 or 1. Other values of  $\Omega/S$  can only be reached when  $\frac{P}{\epsilon}$  vanishes, as shown in Figure 7(c). Thus, the model then yields an abrupt and total damping of the turbulence. (See Figure 3.)

## CONCLUSIONS

This study has shown that algebraic stress models consistently derived from Reynolds stress models inherit the correct dependency to rotation, and non-inertial effects are automatically accounted for in a rigorous way. On the other hand, algebraic stress models that try to generalize the eddy-viscosity hypothesis in a phenomenological way are not necessarily directly extendible to non-inertial frames. As these results have shown, the nonlinear eddy-viscosity function  $C_\mu^*$  must be constructed with the correct dependency on  $S\tau$  and  $\Omega/S$ . This study also demonstrated that the key features of the rotating channel flow were controlled by mechanisms only remotely linked to the dissipation rate equation, which would mean that phenomenological models that attempt to account for non-inertial effects solely through modification of the source terms in the dissipation rate equation may not be properly accounting for essential flow physics.

**Acknowledgements:** The first author received support from the Commission Suisse pour l'Encouragement de la

Recherche Scientifique and Sulzer Brothers S.A. under contract number 3062.1. The second author is supported by the Swiss National Foundation for Scientific Research.

## REFERENCES

- Gatski, T. B., and Speziale, C. G., 1993, "On explicit algebraic stress models for complex turbulent flows," *J. Fluid Mech.*, Vol. 254, pp. 59–78.
- Howard, J. H. G., Patankar, S. V., and Bordnyuk, R. M., 1980, "Flow prediction in rotating ducts using Coriolis-modified turbulence models," *J. Fluid Engrg.*, Vol. 102, pp. 456–461.
- Jongen, T., Mompean, G., and Gatski, T. B., 1997, "Effect of dissipation rate anisotropies on the prediction of wall-bounded turbulent flows," *submitted for publication*.
- Kristoffersen, R., and Andersson, H. I., 1993, "Direct simulations of low-Reynolds-number turbulent flow in a rotating channel," *J. Fluid Mech.*, Vol. 256, pp. 163–197.
- Lamballais, E., Lesieur, M., and Métais, O., 1996, "Effects of spanwise rotation on the stretching in transitional and turbulent channel flow," *Int. J. Heat and Fluid Flow*, Vol. 17, pp. 324–332.
- Launder, B. E., Reece, G. J., and Rodi, W., 1975, "Progress in the development of a Reynolds-stress turbulence closure," *J. Fluid Mech.*, Vol. 68, pp. 537–566.
- Shih, T.-S., Zhu, J., and Lumley, J. L., 1995, "A new Reynolds stress algebraic equation model," *Comput. Methods Appl. Mech. Engrg.*, Vol. 125, pp. 287–302.
- Speziale, C. G., and Gatski, T. B., 1997, "Analysis and modeling of anisotropies in the dissipation rate of turbulence," *J. Fluid Mech.*, to appear.
- Speziale, C. G., Sarkar, S., and Gatski, T. B., 1991, "Modelling the pressure-strain correlation of turbulence: an invariant dynamical systems approach," *J. Fluid Mech.*, Vol. 227, pp. 245–272.
- Xu, X.-H., and Speziale, C. G., 1996, "Explicit algebraic stress model of turbulence with anisotropic dissipation," *AIAA J.*, Vol. 34(10), pp. 2186–2189.

# A NEW EXPLICIT ALGEBRAIC REYNOLDS STRESS TURBULENCE MODEL FOR 3D FLOW

**Stefan Wallin**

The Aeronautical Research Institute of Sweden (FFA),  
Box 11021, S-161 11 Bromma, Sweden

**Arne V. Johansson**

Royal Institute of Technology, Department of Mechanics,  
S-100 44 Stockholm, Sweden

## ABSTRACT

The capability of a newly proposed fully three-dimensional explicit algebraic Reynolds stress model (EARSIM) to predict the turbulent flow in an axially rotating circular pipe was assessed. The azimuthal velocity has a variation that is close to parabolic and the rotation causes the axial velocity profile to be less full, *i.e.*, more parabolic like. To capture these features the model description of the intercomponent transfer is crucial. This is included in most differential Reynolds stress models but not in standard eddy viscosity models and EARSIM formulations including only terms up to second order in the mean flow strain and rotation rate tensors. It was found that the newly proposed EARSIM was able to capture the main features of this kind of flows due to the necessary inclusion of tensorially cubic terms.

## INTRODUCTION

Standard two-equation models are still dominating in the context of industrial flow computations. Replacing the eddy viscosity hypothesis with an explicit algebraic Reynolds stress model may improve the prediction capability in flows with strong effects of streamline curvature, adverse pressure gradients, flow separation or system rotation.

It is convenient to express an EARSIM as an explicit relation for the Reynolds stress anisotropy,  $a_{ij}$ , defined as

$$a_{ij} = \frac{\overline{u_i u_j}}{K} - \frac{2}{3} \delta_{ij} \quad (1)$$

in terms of the mean strain and a mean rotation tensors normalized with the turbulent time-scale,  $\tau \equiv K/\epsilon$

$$\begin{aligned} S_{ij} &= \frac{\tau}{2} (U_{i,j} + U_{j,i}) \\ \Omega_{ij} &= \frac{\tau}{2} (U_{i,j} - U_{j,i}) \end{aligned} \quad (2)$$

$U_{i,j}$  denotes the mean velocity gradient tensor and  $K$  the turbulent kinetic energy.

Following Pope (1975), the most general form for  $a_{ij}$  in terms of  $S_{ij}$  and  $\Omega_{ij}$  consists of ten tensorially independent groups to

which all higher order tensor combinations can be reduced with the aid of the Cayley-Hamilton theorem.

$$a = \beta_1 S$$

$$\begin{aligned} &+ \beta_2 \left( S^2 - \frac{1}{3} I_S I \right) + \beta_3 \left( \Omega^2 - \frac{1}{3} I_\Omega I \right) + \beta_4 (S\Omega - \Omega S) \\ &+ \beta_5 (S^2\Omega - \Omega S^2) + \beta_6 \left( S\Omega^2 + \Omega^2 S - \frac{2}{3} N I \right) \\ &+ \beta_7 \left( S^2\Omega^2 + \Omega^2 S^2 - \frac{2}{3} V I \right) + \beta_8 (S\Omega S^2 - S^2\Omega S) \\ &+ \beta_9 (\Omega S\Omega^2 - \Omega^2 S\Omega) + \beta_{10} (\Omega S^2\Omega^2 - \Omega^2 S^2\Omega) \end{aligned} \quad (3)$$

The  $\beta$  coefficients may be functions of the five independent invariants of  $S$  and  $\Omega$ , which can be written as

$$\begin{aligned} I_S &= \{S^2\}, \quad I_\Omega = \{\Omega^2\}, \quad I_S = \{S^3\} \\ N &= \{S\Omega^2\}, \quad V = \{S^2\Omega^2\} \end{aligned} \quad (4)$$

Also other scalar parameters may be involved. In equation (3)  $a$ ,  $S$  and  $\Omega$  denote second rank tensors, and  $I$  is the identity matrix. The inner product of two matrices is defined as  $(SS)_{ij} \equiv (S^2)_{ij} \equiv S_{ik} S_{kj}$  and  $\{ \}$  denotes the trace. This notation will be kept through this paper.

The  $\beta$  coefficients in (3) may be determined from the algebraic Reynolds stress model. Girimaji (1995) and Johansson & Wallin (1996) have shown that an exact solution of the ARSM exists in two-dimensional mean flow. Moreover, Wallin & Johansson (1997) showed that the new model they proposed closely approximates also three-dimensional mean flow due to the necessary inclusion of tensor products of higher order than quadratic.

## DESCRIPTION OF THE MODEL

The explicit algebraic Reynolds stress model proposed by Wallin & Johansson (1997) is formulated using the traditional ARSM assumption, Rodi (1976), which results in the following implicit algebraic equation for  $a_{ij}$ ,

$$\frac{u_i u_j}{K}(\mathcal{P} - \varepsilon) = \mathcal{P}_{ij} - \varepsilon_{ij} + \Pi_{ij} \quad (5)$$

The dissipation rate tensor,  $\varepsilon_{ij}$ , and the pressure strain,  $\Pi_{ij}$ , need to be modeled whereas the production terms,  $\mathcal{P}_{ij}$  and  $\mathcal{P} = \mathcal{P}_{ii}/2$ , do not need any modelling since they are explicit in the Reynolds stress tensor. Wallin & Johansson chose an isotropic assumption for the dissipation rate tensor,  $\varepsilon_{ij} = 2\delta_{ij}/3$  and the Rotta model, Rotta (1951), for the slow pressure strain  $\Pi_{ij}^{(s)} = -c_1 \varepsilon a_{ij}$  where the Rotta constant  $c_1 = 1.8$ .

For the rapid pressure strain rate the general linear model of Launder, Reece & Rodi (1975) was used. The value of  $c_2$  in the rapid pressure strain model was originally suggested to be 0.4 by Launder *et al.* (1975), but more recent studies have suggested a higher value close to 5/9, see *e.g.* Lumley (1978) and Shabbir & Shih (1992). From (5) and with  $c_2 = 5/9$  the implicit algebraic equation for the Reynolds stress anisotropy tensor is then obtained to

$$\left(c_1 - 1 + \frac{\mathcal{P}}{\varepsilon}\right)\mathbf{a} = -\frac{8}{15}\mathbf{S} + \frac{4}{9}(\mathbf{a}\Omega - \Omega\mathbf{a}). \quad (6)$$

One should note that (6) represents a non-linear relation since  $\mathcal{P}/\varepsilon \equiv -\text{tr}\{\mathbf{a}\mathbf{S}\}$ .

### Formulation of an explicit algebraic model

The procedure to solve (6) is the following: First, the general form for the anisotropy, equation (3), is inserted into the ARSM equation (6) where  $\mathcal{P}/\varepsilon$  is not yet determined. The resulting linear equation system for the  $\beta$  coefficients is then solved by using the fact that higher order tensor groups can be reduced with the aid of Cayley-Hamilton theorem where the ten groups in the general form (3) forms a complete basis. The  $\beta$  coefficients are now functions of the production to dissipation ratio,  $\mathcal{P}/\varepsilon$ . The final step is to formulate the non-linear scalar equation for  $\mathcal{P}/\varepsilon$ .

For general three-dimensional mean flows the solution for the  $\beta$  coefficients is

$$\begin{aligned} \beta_1 &= -\frac{N(2N^2 - 7\mathcal{I}_\Omega)}{Q} & \beta_3 &= -\frac{12N^{-1}N}{Q} \\ \beta_4 &= -\frac{2(N^2 - 2\mathcal{I}_\Omega)}{Q} & \beta_6 &= -\frac{6N}{Q} & \beta_9 &= \frac{6}{Q} \end{aligned} \quad (7)$$

where all the other coefficients are identically zero. The denominator

$$Q = \frac{5}{6}(N^2 - 2\mathcal{I}_\Omega)(2N^2 - \mathcal{I}_\Omega) \quad (8)$$

cannot become singular since  $\mathcal{I}_\Omega$  always is negative and  $N$  is positive.  $N$  is related to the production to dissipation ratio as

$$N = c'_1 + \frac{9\mathcal{P}}{4\varepsilon} \quad (9)$$

where

$$c'_1 = \frac{9}{4}(c_1 - 1). \quad (10)$$

The non-linear equation for  $N$  or the corresponding equation for  $\{\mathbf{a}\mathbf{S}\}$  is then formulated. This equation is of sixth order and can, *e.g.*, be obtained by introducing the above solution (7) for  $\mathbf{a}$  into the definition of  $N$ . The equation for  $N$  cannot be solved in a closed form in three-dimensional mean flows but an approximation was obtained by making a perturbation solution of the sixth order equation for  $N$  around the solution in two-dimen-

sional mean flow which may be obtained exactly. The approximation for  $N$  reads

$$N = N_c + \frac{162(\phi_1 + \phi_2 N_c^2)}{D} + O(\phi_1^2, \phi_2^2, \phi_1 \phi_2) \quad (11)$$

where the parameters  $\phi_1$  and  $\phi_2$  are zero in two-dimensional mean flow and are connected to the mean flow invariants through  $\phi_1 = N^2$  and  $\phi_2 = V - \mathcal{I}_\Omega/2$ .  $N_c$  is the exact solution for  $N$  in two-dimensional mean flows and reads

$$N_c = \begin{cases} \frac{c'_1}{3} + (P_1 + \sqrt{P_2})^{1/3} + \text{sgn}(P_1 - \sqrt{P_2})|P_1 - \sqrt{P_2}|^{1/3}, & P_2 \geq 0 \\ \frac{c'_1}{3} + 2(P_1^2 - P_2)^{1/6} \cos\left(\frac{1}{3}\arccos\left(\frac{P_1}{\sqrt{P_1^2 - P_2}}\right)\right), & P_2 < 0 \end{cases} \quad (12)$$

with

$$\begin{aligned} P_1 &= \left(\frac{c'^2_1}{27} + \frac{9}{20}\mathcal{I}_\Omega - \frac{2}{3}\mathcal{I}_\Omega\right)c'_1 \\ P_2 &= P_1^2 - \left(\frac{c'^2_1}{9} + \frac{9}{10}\mathcal{I}_\Omega + \frac{2}{3}\mathcal{I}_\Omega\right)^3 \end{aligned} \quad (13)$$

The denominator,  $D$ , is given by

$$D = 20N_c^4\left(N_c - \frac{c'_1}{2}\right) - \mathcal{I}_\Omega(10N_c^3 + 15c'_1 N_c^2) + 10c'_1 \mathcal{I}_\Omega^2 \quad (14)$$

$N$  and  $D$  can be shown to always remain positive

### Near wall treatments

To obtain a proper behaviour in this region the model needs to be modified in a similar way as low Reynolds number two-equation turbulence models. An important difference compared to eddy viscosity models is that the effective  $C_\mu$  or  $\beta_1$  in the proposed model is not a constant and, which has been shown by Wallin & Johansson (1996, 1997), will adjust to the near wall flow in a more natural way than is possible with eddy viscosity models. A fully developed channel flow, DNS data by Kim (1989), was used by Wallin & Johansson to formulate and calibrate the very near wall correction.

The turbulence time-scale  $\tau = K/\varepsilon$ , which is used to scale the strain- and rotation rate tensors in (2) goes to zero as the wall is approached. A more appropriate expression for the time-scale is

$$\tau = \max\left(\frac{k}{\varepsilon}, C_\tau \sqrt{\frac{v}{\varepsilon}}\right) \quad (15)$$

which is just the usual time scale with a lower bound by the Kolmogoroff scale. The constant  $C_\tau = 6.0$ .

The correct near wall behaviour for the Reynolds stresses is then ensured by preserving the near wall asymptotic behaviour of the stress anisotropy. The asymptotic near wall components of the anisotropy is blended with the modelled anisotropy using the van Driest wall damping function

$$f_1 = 1 - \exp\left(-\frac{y^+}{A^+}\right) \quad (16)$$

where  $A^+ = 26$ .

A coordinate system invariant form of the near wall correction was obtained and the straight forward extension to three-dimensional flow reads

$$\begin{aligned}
a = & f_1 \beta_1 S + (1 - f_1^2) \frac{3B_2 - 4}{\max(\mathcal{H}_S, \mathcal{H}_S^{eq})} \left( S^2 - \frac{1}{3} \mathcal{H}_S \mathbf{I} \right) \\
& + \left( f_1^2 \beta_4 - (1 - f_1^2) \frac{B_2}{2\max(\mathcal{H}_S, \mathcal{H}_S^{eq})} \right) (S\Omega - \Omega S) \\
& + f_1^2 \beta_3 \left( \Omega^2 - \frac{1}{3} \mathcal{H}_S \mathbf{I} \right) + f_1 \beta_6 \left( S\Omega^2 + \Omega^2 S - \frac{2}{3} N \mathbf{I} \right) \\
& + f_1^2 \beta_9 (\Omega S \Omega^2 - \Omega^2 S \Omega)
\end{aligned} \quad (17)$$

The max function in the denominator is included to avoid problems in separated flows where the shear rate and thus  $\mathcal{H}_S$  may become small. To avoid this problem, the shear rate in the denominator of the near wall correction is limited to the equilibrium shear rate,  $\mathcal{H}_S^{eq}$  where the turbulence production balances the dissipation rate,

$$\mathcal{H}_S^{eq} = \frac{405c_f^2}{216c_1 - 160} \approx 5.74 \text{ for } c_1 = 1.8. \quad (18)$$

The near wall treatment ensures that all individual Reynolds stresses are fairly well predicted (see figure 1).

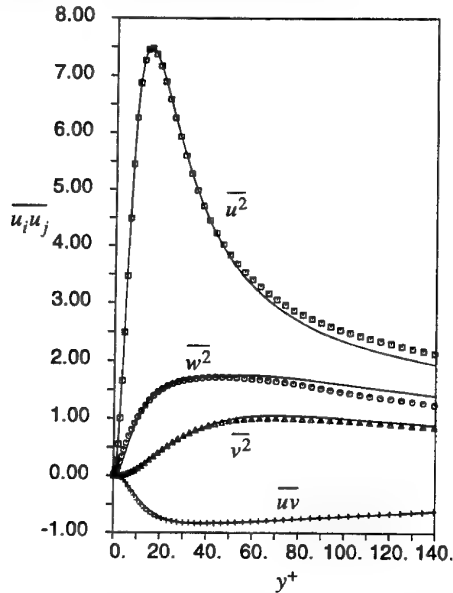


FIGURE 1. TURBULENT CHANNEL. THE MODELLED REYNOLDS STRESSES COMPARED TO DNS DATA (KIM 1989)

### ROTATING PIPE FLOW

Fully developed turbulent flow in a circular pipe rotating around its length axis is an interesting case, since it represents a three-dimensional flow that can be described with only one spatial coordinate,  $r$  in a cylindrical coordinate system  $(\hat{r}, \hat{\theta}, \hat{z})$ . If the flow is laminar, the tangential velocity,  $U_\theta$ , varies linearly with the radius,  $r$ , like a rigid body rotation. In turbulent flow, on the other hand, the tangential velocity is nearly parabolic, which cannot be described with an eddy viscosity turbulence model. The fully three-dimensional form of the proposed EARSIM is needed to capture this behaviour. Limited forms with only second order terms is not sufficient, as will be shown below.

The Navier-Stokes equation in the tangential direction can be written as

$$v \left( \frac{d^2 U_\theta}{dr^2} + \frac{1}{r} \frac{dU_\theta}{dr} - \frac{U_\theta}{r^2} \right) = \frac{d}{dr} (K a_{r\theta}) + 2 \frac{K a_{r\theta}}{r}. \quad (19)$$

After two integrations, the tangential velocity can be expressed as

$$U_\theta(r) = U_\theta(R) \frac{r}{R} - \frac{r}{v} \int \frac{K a_{r\theta}}{u} du \quad (20)$$

where  $R$  is the radius of the pipe. The first term corresponds to the linear  $U_\theta$  profile while the second term is the correction that may give a parabolic-like profile if the  $a_{r\theta}$  anisotropy is positive.

The strain- and rotation rate tensors are evaluated in an inertial frame. The non-zero components are

$$S_{r\theta} = \frac{dU_\theta}{dr} - \frac{U_\theta}{r} \quad S_{rz} = \frac{dU_z}{dr} \quad (21)$$

and

$$\Omega_{\theta r} = -\Omega_{r\theta} = \frac{dU_\theta}{dr} + \frac{U_\theta}{r} \quad \Omega_{zr} = -\Omega_{rz} = \frac{dU_z}{dr}. \quad (22)$$

The terms that contribute to the  $a_{r\theta}$  component in the general expression (3) are the terms associated with the  $\beta_1$ ,  $\beta_5$ ,  $\beta_6$  and  $\beta_{10}$  coefficients. In the case of a linear  $U_\theta$  profile,  $S_{r\theta}$  is zero and the contribution from the  $\beta_1$  term vanishes. This is consistent with the behaviour for an eddy viscosity model. In the proposed model for three-dimensional mean flows, the  $\beta_5$  and  $\beta_{10}$  coefficients vanishes so the only term that can give the desired behaviour is the term that corresponds to the  $\beta_6$  coefficient,  $S\Omega^2 + \Omega^2 S - 2N\mathbf{I}/3$ . For a linear  $U_\theta$  profile the  $a_{r\theta}$  anisotropy can then be written as

$$a_{r\theta} = -\frac{1}{4} \tau^3 \frac{dU_\theta}{dr} \left( \frac{dU_z}{dr} \right)^2 \beta_6 \quad (23)$$

and with the solution to  $\beta_6 = -6N/Q$  according to (7) we can see that  $a_{r\theta}$  is positive and thus gives the correct trend for the  $U_\theta$  velocity. The inclusion of the cubic term is necessary for describing this kind of turbulent rotating flow, which is not possible with models without higher order terms than quadratic.

Moreover, the simplified linear rapid pressure strain model of Launder *et al.* (1975), usually referred to as the isotropization of production model, does not have the necessary ingredients. Algebraic as well as differential Reynolds stress models using this pressure strain model predict a linear  $U_\theta$  velocity profile.

This can be understood by looking at the corresponding ARSM with  $c_2 = 1/4$  which reads

$$\begin{aligned}
\left( c_1 - 1 + \frac{P}{\epsilon} \right) a = & -\frac{8}{15} S + \frac{1}{4} (a\Omega - \Omega a) \\
& - \frac{1}{4} \left( aS + Sa - \frac{2}{3} \{aS\} \mathbf{I} \right)
\end{aligned} \quad (24)$$

The  $a_{r\theta}$  component must be coupled to  $dU_z/dr$  for a non-linear  $U_\theta$  profile. If the  $U_\theta$  profile is linear then  $S_{r\theta} = \Omega_{r\theta} = 0$  and

$$\begin{aligned}
(a\Omega - \Omega a)_{r\theta} = & -a_{\theta z} \Omega_{rz} = a_{\theta z} \frac{dU_z}{dr} \\
\left( aS + Sa - \frac{2}{3} \{aS\} \mathbf{I} \right)_{r\theta} = & a_{\theta z} S_{rz} = a_{\theta z} \frac{dU_z}{dr}
\end{aligned} \quad (25)$$

These two terms cancel each other when  $c_2 = 1/4$  and the  $U_\theta$  profile becomes linear. The full linear model, on the other hand,

together with linear models for the other terms is sufficient to capture the main features of the flow in the axially rotating pipe.

### Computational results

A fully developed turbulent rotating pipe flow has been computed using the proposed model. The Reynolds number is 20000 based on the bulk velocity and pipe diameter. Three different rotation ratios  $Z = 0, 0.5$  and  $1$  were computed where  $Z = U_\theta(R)/U_m$  i.e. the wall angular velocity divided by the axial bulk velocity. The results are compared to the experiment by Imao *et al.* (1996). The turbulence models used are the Chien (1982)  $K-\epsilon$  model and the EARSM proposed by Wallin & Johansson (1997) based on both the Chien  $K-\epsilon$  and Wilcox (1994)  $K-\omega$  models.

The three-dimensional form of the model has been used and the influence of the approximation of  $N$  was assessed by computing the case by using both the zeroth ( $N_c$ ) and first order perturbation solution of  $N$ . The former is given by (12) and labeled 'EARSM\_0' in the figures while the later 'EARSM\_1' is given by (11).

Figure 2 shows the predicted axial velocity for  $Z = 1$  using the Chien  $K-\epsilon$  model alone and as the platform for EARSM calculations. The original Chien  $K-\epsilon$  model is seen to be completely insensitive to rotation, while the EARSM predictions agree well with the experimental results. It is also seen that the different approximations of  $N$  only have a slight influence on the predicted velocity profile. In figure 3 predictions for different values of  $Z$  are shown for the  $K-\omega$  model as the platform of the EARSM. The calculated results are seen to well capture the trend with increasing rate of rotation. The EARSM predictions with the  $K-\epsilon$  and  $K-\omega$  platforms are quite similar except in a region close to the wall. The angular velocity (figure 4) is also seen to be reasonably well predicted with the different EARSM formulations, among which the differences are small.

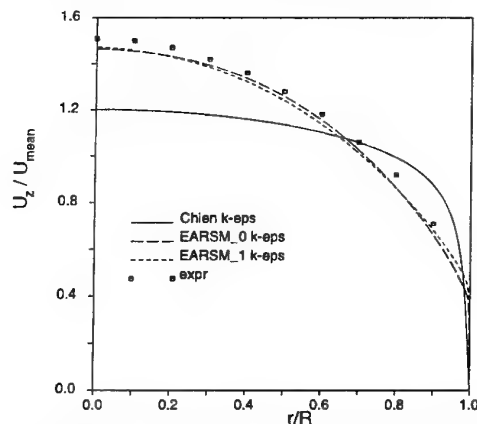


FIGURE 2. COMPUTED AXIAL VELOCITY IN ROTATING PIPE FLOW FOR ROTATION RATIO  $Z = 1$  COMPARED TO EXPERIMENT BY IMAO ET AL. (1996).

The zeroth and first order solutions of  $N$  are only different approximations of the exact solution for  $N$  or  $\mathcal{P}/\epsilon$ . The error can be investigated by computing the  $\mathcal{P}/\epsilon$  ratio using the different approximations of  $N$  from a given flow field. Figure 5 shows  $\mathcal{P}/\epsilon$  with  $N$  evaluated from the first (EARSM\_0) and second (EARSM\_1) order solutions of  $N$  given by (12) and (11) respectively, compared to the exact solution. The mean flow invariants of these expressions were taken from a fixed mean flow field,

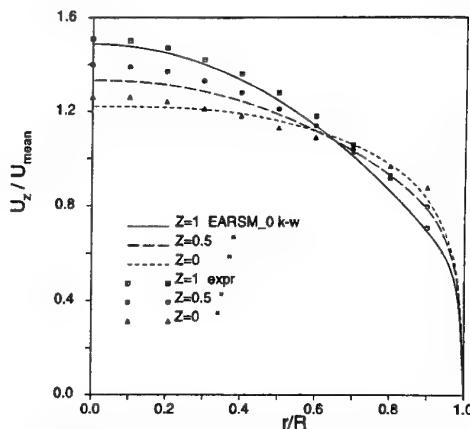


FIGURE 3. COMPUTED AXIAL VELOCITY IN ROTATING PIPE FLOW FOR DIFFERENT ROTATION RATIOS  $Z$  COMPARED TO EXPERIMENT BY IMAO ET AL. (1996).

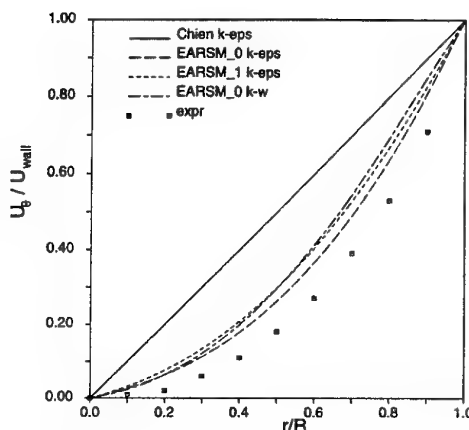


FIGURE 4. COMPUTED ANGULAR VELOCITY IN ROTATING PIPE FLOW FOR ROTATION RATIO  $Z = 1$  COMPARED TO EXPERIMENT BY IMAO ET AL. (1996).

which was the solution with EARSM\_0 based on  $K-\epsilon$  for  $Z = 1$ . We can see a substantial difference between the zeroth and first order solutions and also that the first order solution is quite close to the exact one. As seen from the previous figures this difference is still of rather small influence for the computed velocity profiles.

### REFERENCES

- Chien, K. Y. 1982. Predictions of Channel and Boundary-Layer Flows with a Low-Reynolds-Number Turbulence Model. *AIAA J.*, **20**, 33-38.
- Girimaji, S. S. 1995. Fully-explicit and self-consistent algebraic Reynolds stress model. *ICASE Report No. 95-82*.
- Imao, S., Itoh, M. & Harada, T. 1996. Turbulent characteristics of the flow in an axially rotating pipe. *J. Heat and Fluid Flow* **17**, 444-451.
- Johansson, A. V. & Wallin, S. 1996. A new explicit algebraic Reynolds stress model. *Proc. Sixth European Turbulence Conference, Lausanne*, July 1996, Ed. P. Monkewitz, 31-34.
- Kim, J. 1989. On the structure of pressure fluctuations in simulated turbulent channel flow. *J. Fluid Mech.* **205**, 421-451.

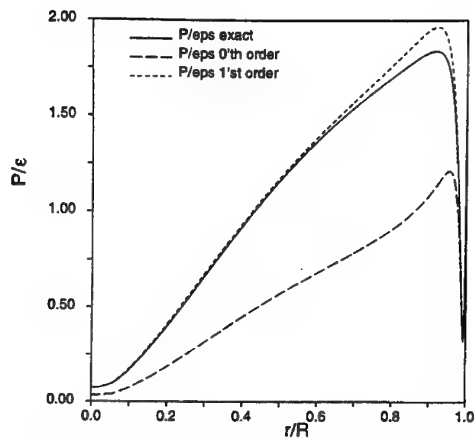


FIGURE 5. PRODUCTION TO DISSIPATION RATIO IN ROTATING PIPE FLOW FOR DIFFERENT APPROXIMATION LEVEL FOR  $N$ . THE MEAN FLOW FROM THE EARSM\_0  $K-\epsilon$  SOLUTION FOR  $Z = 1$  WAS USED.

Launder, B. E., Reece, G. J. & Rodi, W. 1975. Progress in the development of a Reynolds-stress turbulence closure. *J. Fluid Mech.* **41**, 537-566.

Lumley, J. L. 1978. Computational modeling of turbulent flows. *Adv. Appl. Mech.* **18**, 123-176.

Pope, S. B. 1975. A more general effective-viscosity hypothesis. *J. Fluid Mech.* **72**, 331-340.

Rodi, W. 1976. A new algebraic relation for calculating the Reynolds stresses. *Z. angew. Math. Mech.* **56**, T219-221.

Rotta, J. C. 1951. Statistische Theorie nichthomogener Turbulenz. *Z. Phys.* **129**, 547-572.

Shabbir, A. & Shih, T. H. 1992. Critical Assessment of Reynolds Stress Turbulence Models Using Homogeneous Flows. NASA TM 105954, ICOMP-92-24, CMOTT-92-12.

Wallin, S. & Johansson, A. V. 1996. A new explicit algebraic Reynolds stress turbulence model including an improved near-wall treatment. Proc. Flow Modeling and Turbulence Measurements VI, Tallahassee FL, Chen, Shih, Lienau & Kung (eds), 399-406.

Wallin, S. & Johansson, A. V. 1997. A new explicit algebraic Reynolds stress turbulence model for incompressible and compressible turbulent flows. Submitted for *J. Fluid Mech.*

Wilcox, D. C. 1994. Simulation of Transition with a Two-Equation Turbulence Model. *AIAA J.* **32**, 247-255.

# NONLINEAR EDDY VISCOSITY MODELLING WITH A TRANSPORT EQUATION FOR LUMLEY'S STRESS FLATNESS PARAMETER

K. Suga

Heat Transfer Lab., Toyota Central R & D Labs., Inc.  
Nagakute, Aichi, 480-11  
Japan

## ABSTRACT

A new nonlinear three equation eddy viscosity model (EVM) is proposed for capturing two-component turbulence that appears in flows near walls and free surfaces. This model employs dependence of Lumley's stress flatness parameter:  $A$ , by solving its transport equation. The proposed nonlinear  $k$ - $\varepsilon$ - $A$  three equation EVM has been tested in fully developed plane channel, open channel and plane Couette flows as well as several homogeneous strain fields. The results have shown its very encouraging performance in capturing anisotropic turbulence near both wall and shear-free boundaries without any recourse to topographical parameters.

## INTRODUCTION

Nonlinear terms are essential in the constitutive equation of an EVM for capturing anisotropic stress fields. Most of the nonlinear EVM's thus have employed up to quadratic products of mean velocity gradient tensors. Craft, Launder & Suga (1996), however, pointed out that at least cubic terms were necessary to capture stream-line curvature (including swirling flows) effects in turbulent flows. In order to widen the capability of their cubic nonlinear  $k$ - $\varepsilon$  model, they afterwards extended the model to a three equation nonlinear EVM by coupling an additional transport equation for the second anisotropic stress invariant,  $A_2 \equiv a_{ij}a_{ji}$  (Suga, 1995, Craft, Launder & Suga, 1997). Their three equation nonlinear eddy viscosity model, the CLS model hereafter, showed very encouraging results for predicting a wide range of wall-bounded flows.

However, on a shear-free boundary, such as a free surface and a moving wall of Couette flow, the usual linear or nonlinear stress-strain relations always return an isotropic stress field corresponding to the vanishment of the velocity gradients. Since the stress field is significantly anisotropic and reaches two-component turbulence at a shear-free boundary, capturing this anisotropic turbulence is crucial if the model is used to predict scalar diffusion processes near the boundary.

Moreover, as Fig 1 (a) illustrates, when the eddy viscosity,  $\nu_t$ , is estimated as  $-\overline{uv}/U_{y,y}$ , the blocking effect on the normal fluctuating velocity results in significant damping on  $\nu_t$  near a free surface ( $y = \delta$ ) as well. Here,  $\delta$  represents the channel half-width of a plane channel, the channel width of a plane Couette flow, or the channel depth of an open channel. Modelling this damping effect is generally difficult since local parameters used in the usual EVM's such as the local turbulent Reynolds number,  $R_t \equiv k^2/(\nu\varepsilon)$ , does not vanish on free surfaces.

Although the value of  $A_2$  reaches 2/3 on a shear-free boundary, it is still hard to characterize shear-free turbulence with the behaviour of  $A_2$ . Thus, the CLS model also keeps these inherent weaknesses of the eddy viscosity mod-

elling.

Now, the presently focused parameter is Lumley's stress flatness parameter (Lumley, 1978),  $A \equiv 1 - 9/8(A_2 - A_3)$ , ( $A_3 \equiv a_{ij}a_{jk}a_{ki}$ ). Since it always vanishes in two-component turbulence as shown in Fig 1 (b), this feature is believed to be very useful to model shear-free turbulence. Therefore, in the present study, it was decided to solve a transport equation for  $A$  instead of  $A_2$  while the proposed model took over basic modelling strategies of the CLS version.

## NONLINEAR $k$ - $\varepsilon$ - $A$ MODELLING

The present modelling strategy also complies with the basic modelling requirements of UMIST that are to avoid the use of topographical parameters and to restrict the effect of  $R_t$  to the viscous sublayer.

### The constitutive relation

The nonlinear constitutive relation used in this study is the cubic model of the CLS version.

$$\begin{aligned} a_{ij} \equiv & \overline{u_i u_j} / k - 2/3 \delta_{ij} = -c_\mu \tau S_{ij} \\ & + c_1 \tau^2 (S_{ik} S_{kj} - 1/3 S_{kl} S_{kl} \delta_{ij}) \\ & + c_2 \tau^2 (\Omega_{ik} S_{kj} + \Omega_{jk} S_{ki}) \\ & + c_3 \tau^2 (\Omega_{ik} \Omega_{jk} - 1/3 \Omega_{lk} \Omega_{lk} \delta_{ij}) \\ & + c_4 \tau^3 (S_{ki} \Omega_{lj} + S_{kj} \Omega_{li}) S_{kl} \\ & + c_5 \tau^3 (\Omega_{il} \Omega_{lm} S_{mj} + S_{il} \Omega_{lm} \Omega_{mj} \\ & - 2/3 S_{lm} \Omega_{mn} \Omega_{nl} \delta_{ij}) + c_6 \tau^3 S_{ij} S_{kl} S_{kl} \\ & + c_7 \tau^3 S_{ij} \Omega_{kl} \Omega_{kl} + c_a A_{ij} \end{aligned} \quad (1)$$

where  $\tau \equiv k/\varepsilon$ ,  $S_{ij} \equiv U_{i,j} + U_{j,i}$ ,  $\Omega_{ij} \equiv U_{i,j} - U_{j,i}$ ,  $\tilde{\varepsilon} \equiv \varepsilon - 2\nu(\sqrt{k},i)^2$ , and  $c_a A_{ij}$  is an additional term introduced to mimic shear-free turbulence described later.

The presently proposed form for  $c_\mu$  is

$$c_\mu = 0.09 c_{\mu A} c_{\mu R_t} c_{\mu S}, \quad (2)$$

and each contribution is modelled as:

$$c_{\mu A} = \min[1.05, 1.2 \{1 - \exp(-A - (A/0.6)^\alpha)\} + 0.18 \{1 - \exp(-10A)\}^{1/2}] \quad (3)$$

$$c_{\mu R_t} = 1 + 2A \exp(-R_t^2/8100) \quad (4)$$

$$c_{\mu S} = \min[1, 1.2/(1 + 0.06\eta)] \quad (5)$$

where

$$\eta = \max(\tilde{S}, \tilde{\Omega}) r_\eta$$

$$r_\eta = 1 + 0.9 \left\{ 1 + 0.4 \beta \exp\left(-\frac{R_t}{5}\right)^{\frac{1}{4}} \right\} \exp\left\{-\left(\frac{A}{0.7}\right)^2\right\}$$

$$\alpha = 1 + 2.6 \min[1, R_t/200]$$

$$\beta = \min[10, \max(0, \tilde{S} - 5)]$$



Table 1 THE EMPIRICAL COEFFICIENTS

$c_1$	$c_2$	$c_3$	$c_4$	$c_5$	$c_6$
$-0.05f_q$	$0.11f_q$	$0.42f_q \frac{\bar{S}}{\bar{S}+\bar{\Omega}}$	$-0.8f_c$	0	$-0.5f_c$
$c_7$	$f_q$		$f_c$		
$0.5f_c$	$\frac{2/3r_\eta^2(1-f_a)}{(1+1.8\eta)(1+0.0086\eta^2)^{1/2}}$		$\frac{2/3r_\eta^3}{(1+1.8\eta)(1+0.45\eta^{2.5})}$		

and  $\bar{S} \equiv \tau \sqrt{S_{ij}S_{ij}/2}$ ,  $\bar{\Omega} \equiv \tau \sqrt{\Omega_{ij}\Omega_{ij}/2}$ . Since  $\nu_t (= c_\mu k \tau)$  should be damped near the two-component limit, the primary damping effect for  $c_\mu$  has been designed to be obtained from  $c_{\mu A}$  which decreases as  $A$  does. The notable feature of the form of  $c_\mu$  is that the damping effect from  $R_t$  is not used, in fact,  $c_{\mu R_t}$  of Equation (4) is not a damping function.

The additional term  $c_a A_{ij}$  is

$$\begin{aligned} A_{ij} &= c'_a \tau^2 \left( \sqrt{A k_i} \sqrt{A k_j} - \frac{1}{3} \delta_{ij} \sqrt{A k_k} \sqrt{A k_k} \right) \quad (6) \\ c_a &= -(8/3)^{1/2} f_a / \{1 + 2(A_{ij} A_{ij})^{1/2}\} \\ c'_a &= 1 / \{1 - \exp(-\bar{R}_t/30)\} \\ f_a &= \exp\{- (\bar{S}/2.2)^2\} \end{aligned}$$

where  $\bar{R}_t \equiv k^2/(\nu \bar{\epsilon})$ . This additional term has been designed to produce the limiting values:

$$a_{11} (= c_a A_{11}) = 1/3, \quad a_{22} (= c_a A_{22}) = -2/3$$

at a shear-free boundary. (Here, the index "2" denotes the direction normal to the boundary.) Thus, the inclusion of this term enables an EVM to capture shear-free turbulence.

Corresponding to these modifications, the coefficients/functions given in Table 1 are slightly modified ones from the CLS model.

#### The $A$ transport equation

Deriving the exact transport equation for  $A$  is straightforward from its definition.

$$\begin{aligned} \frac{DA}{Dt} &= \underbrace{-\frac{9}{8k} (3/2 A_3 \mathcal{D}_{kk} + 2a_{ij} \mathcal{D}_{ij} - 3a_{jk} a_{ki} \mathcal{D}_{ij})}_{\mathcal{D}_A} \\ &\quad - \underbrace{\frac{9}{8k} (3/2 A_3 P_{kk} + 2a_{ij} P_{ij} - 3a_{jk} a_{ki} P_{ij})}_{P_A} \\ &\quad - \underbrace{\frac{9}{8k} (3/2 A_3 \Pi_{kk} + 2a_{ij} \Pi_{ij} - 3a_{jk} a_{ki} \Pi_{ij})}_{\Pi_A} \\ &\quad + \underbrace{\frac{9}{8k} (3/2 A_3 \epsilon_{kk} + 2a_{ij} \epsilon_{ij} - 3a_{jk} a_{ki} \epsilon_{ij})}_{\epsilon_A} \quad (7) \end{aligned}$$

where  $\mathcal{D}_{ij}$ ,  $P_{ij}$ ,  $\Pi_{ij}$  and  $\epsilon_{ij}$  are, respectively, the diffusive transport, shear generation, pressure correlation, and dissipation rate of  $\bar{u}_i \bar{u}_j$ . Amongst them, the shear generation:

$$P_{ij} \equiv -(\bar{u}_i \bar{u}_k U_{j,k} + \bar{u}_j \bar{u}_k U_{i,k})$$

needs no further approximation while the recent work at UMIST has been applied to the other terms.

**Pressure correlation.** Following Craft & Launder (1996),  $\Pi_{ij}$  is divided into two processes as:

$$\Pi_{ij} = \phi_{ij}^* + \Pi_k \frac{\bar{u}_i \bar{u}_j}{k}, \quad (8)$$

where  $\Pi_k$  is the pressure correlation of  $k$  and

$$\phi_{ij}^* = \phi_{ij1}^* + \phi_{ij2}^* + \phi_{ij}^{inh}.$$

Then, the pressure strain model developed and widely tested at UMIST (see Craft & Launder, 1996) has been adopted for  $\phi_{ij1}^*$  and  $\phi_{ij2}^*$ . After moderate algebra, the expression for the joint process of  $P_A + \Pi_A$  reduces to:

$$\begin{aligned} P_A + \Pi_A &= \frac{9\bar{\epsilon}}{8k} \left\{ (\bar{c}_1 + f_{A2})(2A_2 - 3A_3) \right. \\ &\quad \left. + \bar{c}_1 c'_1 (2A_3 - 0.5A_2^2) \right\} \\ &\quad + \frac{A}{k} \left\{ 0.45c'_2 a_{ij} P_{ij} - (0.6 + 0.3c'_2) P_{kk} \right\} \\ &\quad - \frac{9}{8k} (3/2 A_3 \phi_{kk}^{inh} + 2a_{ij} \phi_{ij}^{inh} - 3a_{jk} a_{ki} \phi_{ij}^{inh}). \end{aligned} \quad (9)$$

(Interestingly, the resultant form is considerably simple even though the nonlinear pressure strain model has been adopted.) Although Craft & Launder (1996) proposed inhomogeneity correction terms of  $\phi_{ij}^{inh}$ , their contribution combined with those of the terms with  $c'_2$  has been found to be fairly small in the present work. Therefore, currently  $\phi_{ij}^{inh} = 0$  and the coefficients/functions used are

$$\begin{aligned} \bar{c}_1 &= 3.1 \min(A_2, 0.5) f_A f_{Rt}, \quad c'_1 = 1.1, \quad c'_2 = 0 \\ f_{Rt} &= \min(R_t/160, 1) \end{aligned}$$

$$f_A = \begin{cases} (A_s/14)^{1/2} & A_s \leq 0.05 \\ A_s/0.7^{1/2} & 0.05 < A_s < 0.7 \\ A_s^{1/2} & A_s \geq 0.7 \end{cases}, \quad f_{A2} = A_s^3$$

where  $A_s$  is the stress flatness parameter simply processed from the calculated stress field and  $A_2$  is redefined as:

$$A_2 = A_3 + 8/9(1 - A) \quad (10)$$

using  $A_3$  and  $A$  obtainable from the stress field and the transport equation, respectively.

**Dissipation rate tensor.** Craft & Launder (1996) proposed a new  $\epsilon_{ij}$  form complying with the shear-free limit as well as the wall limit (Launder & Reynolds, 1983). After full consideration of their form, it has been found that the truncated form:

$$\epsilon_{ij} = (1 - f_\epsilon) (\epsilon'_{ij} + \epsilon''_{ij}) / D + 2/3 f_\epsilon \epsilon \delta_{ij} \quad (11)$$

might be enough in the present practice, where

$$\begin{aligned} \epsilon'_{ij} &= \left[ 2\nu f'_\epsilon k^{1/2} \left( k^{1/2} \frac{\bar{u}_j \bar{u}_m}{k} + k^{1/2} \frac{\bar{u}_i \bar{u}_m}{k} \right) \right. \\ &\quad \left. + 2\nu f'_\epsilon k^{1/2} \frac{\bar{u}_k \bar{u}_m}{k} \delta_{ij} + \frac{\bar{u}_i \bar{u}_j}{k} \epsilon \right] \\ \epsilon''_{ij} &= \epsilon \left( 2 \frac{\bar{u}_k \bar{u}_l}{k} d_k^A d_l^A \delta_{ij} - \frac{\bar{u}_i \bar{u}_l}{k} d_j^A d_l^A - \frac{\bar{u}_j \bar{u}_l}{k} d_i^A d_l^A \right) f_R \\ D &= (\epsilon'_{kk} + \epsilon''_{kk}) / 2\epsilon. \end{aligned}$$

Note that this form satisfies at least the wall limit. The  $\epsilon'_{ij}$  term follows the CLS model while the  $\epsilon''_{ij}$  term has been introduced after Craft & Launder (1996) with their inhomogeneity indicators:

$$d_i = N_i / [0.5 + (N_k N_k)^{1/2}], \quad N_i = l_{,i} \quad (12)$$

$$d_i^A = N_i^A / [0.5 + (N_k^A N_k^A)^{1/2}], \quad N_i^A = (l A^{1/2})_{,i} \quad (13)$$

where  $l = k^{1.5}/\epsilon$ . Thus,  $\epsilon_A$  reduces to:

$$\begin{aligned} \epsilon_A &= \frac{9}{8k} \left[ (3A_3 - 2A_2) f_\epsilon \epsilon + (1 - f_\epsilon) \nu f'_\epsilon / D \left\{ \right. \right. \\ &\quad (16/3 - 12A_2) a_{ij} k^{1/2} \frac{\bar{u}_j \bar{u}_k}{k} - 4(A_2 + A_3) k^{1/2} \frac{\bar{u}_k \bar{u}_k}{k} \\ &\quad \left. \left. - 2(1 - f_\epsilon) f_R \epsilon / D \left\{ (1.5A_2 + 4/3) a_{ij} d_i^A d_j^A \right. \right. \right. \\ &\quad \left. \left. \left. + (2A_2 - A_3) d_k^A d_k^A \right\} \right] \right] \quad (14) \end{aligned}$$

$$\begin{aligned} D &= 1 + 5f'_\epsilon \nu / \epsilon \left( a_{ij} k^{1/2} \frac{\bar{u}_j \bar{u}_k}{k} + 2/3 k^{1/2} \frac{\bar{u}_k \bar{u}_k}{k} \right) \\ &\quad + 2f_R (a_{ij} d_i^A d_j^A + 2/3 d_k^A d_k^A). \end{aligned}$$

The empirical functions used are

$$f_R = (1 - A) \min \left[ (R_t/80)^2, 1.0 \right]$$

$$f_\varepsilon = \begin{cases} A/0.15^{1/2} & A \leq 0.15 \\ A^{1/2} & 0.15 < A \end{cases}, \quad f'_\varepsilon = \{1 - \exp(-R_t/5)\}^{1/2}.$$

**Diffusive transport.** When the GGDH diffusion model of Daly & Harlow (1970):

$$\mathcal{D}_{ij} = \left\{ \left( \nu \delta_{kl} + c_s \overline{u_k u_l} \frac{k}{\varepsilon} \right) \overline{u_i u_j}, l \right\}_{,k} \quad (15)$$

is applied, the  $\mathcal{D}_A$  term reduces to:

$$\begin{aligned} \mathcal{D}_A = & \left\{ \left( \nu \delta_{kl} + c_s \overline{u_k u_l} \frac{k}{\varepsilon} \right) A, l \right\}_{,k} \\ & + \frac{1}{k} \left( \nu \delta_{kl} + c_s \overline{u_k u_l} \frac{k}{\varepsilon} \right) (k_{,k} A, l + k, l A, k) \\ & - \frac{9}{8} \left( \nu \delta_{kl} + c_s \overline{u_k u_l} \frac{k}{\varepsilon} \right) (6a_{ij} a_{jm, k} a_{mi, l} - 2a_{ij, k} a_{ij, l}). \end{aligned} \quad (16)$$

Although no further approximation may be needed for this expression, it was found that the turbulent part of the non diffusive elements sometimes led to an unstable solution. The following truncated form thus has been used with  $c_s = 0.22$ .

$$\begin{aligned} \mathcal{D}_A = & \left\{ \left( \nu \delta_{kl} + c_s \overline{u_k u_l} \frac{k}{\varepsilon} \right) A, l \right\}_{,k} \\ & + \frac{\nu \delta_{kl}}{k} (k_{,k} A, l + k, l A, k) \\ & - \frac{9}{8} \nu \delta_{kl} (6a_{ij} a_{jm, k} a_{mi, l} - 2a_{ij, k} a_{ij, l}) \end{aligned} \quad (17)$$

#### Modelling the $k$ equation

The transport equation for  $k$  may be written:

$$\frac{Dk}{Dt} = \mathcal{D}_k + \Pi_k + P_k - \varepsilon. \quad (18)$$

The terms which need modelling in the  $k$  equation are the diffusion process,  $\mathcal{D}_k$ , pressure correlation (pressure diffusion),  $\Pi_k$ , while the shear generation,  $P_k = P_k/2$ , needs no further approximation. The form used for  $\mathcal{D}_k$  is also the GGDH model:

$$\mathcal{D}_k = \left\{ \left( \nu \delta_{kl} + c_s \overline{u_k u_l} \frac{k}{\varepsilon} \right) k, l \right\}_{,k}. \quad (19)$$

The pressure diffusion  $\Pi_k$  has been modelled following Craft & Launder (1996) with slightly modified coefficients as:

$$\begin{aligned} \Pi_k = & \frac{1}{2} \left[ (0.35d_k + 0.77d_k^A) (\nu \varepsilon A A_2 k)^{1/2} \left\{ c_{pd1} A_2 \right. \right. \\ & \left. \left. + c_{pd2} R_t^{-1/4} \exp(-R_t/40) \right\} \right]_{,k} \end{aligned} \quad (20)$$

$$c_{pd1} = 1 + 2 \exp(-R_t/40), \quad c_{pd2} = 0.4.$$

#### Modelling the $\varepsilon$ equation

As in the CLS model, the present approach also takes the quantity  $\tilde{\varepsilon}$  as the subject of the transport equation due to its convenient wall condition:  $\tilde{\varepsilon}|_w = 0$ . The modelled equation for  $\tilde{\varepsilon}$  may be written:

$$\frac{D\tilde{\varepsilon}}{Dt} = \mathcal{D}_\varepsilon + c_{e1} P_k \frac{\tilde{\varepsilon}}{k} - c_{e2} \frac{\tilde{\varepsilon}^2}{k} + P_{e3} + S_{e1} + S_{e2}, \quad (21)$$

where  $P_{e3}$  is the gradient production and  $S_{e1}$ ,  $S_{e2}$  are additional source/sink terms. For the diffusive transport,  $\mathcal{D}_\varepsilon$ , the GGDH model has been also applied with a coefficient  $c_\varepsilon = 0.18$ .

$$\mathcal{D}_\varepsilon = \left\{ \left( \nu \delta_{kl} + c_\varepsilon \overline{u_k u_l} \frac{k}{\varepsilon} \right) \tilde{\varepsilon}, l \right\}_{,k} \quad (22)$$

The coefficients  $c_{e1}$  and  $c_{e2}$  are taken following the CLS practice:

$$c_{e1} = 1.0 + 0.15(1 - A), \quad c_{e2} = 1.92/(1 + 0.7A_d A_2^{1/2})$$

$$A_d = \max[0.2, A](R_t/20)^2 / \{1 + (R_t/20)^2\}$$

The gradient production term also takes over the CLS model with slightly retuned coefficients of  $c_{e3} = 1.3$  and  $c_{e4} = 1.0$ .

$$P_{e3} = c_{e3} \nu u_i U_{i,kj} U_{i,kj} + c_{e4} \nu \frac{u_i}{k} k, k U_{i,l} U_{i,kl} \quad (23)$$

The currently used additional term  $S_{e1}$  to balance the viscous diffusion is

$$S_{e1} = -(\varepsilon - \tilde{\varepsilon})(\tilde{\varepsilon} - P_k)/k. \quad (24)$$

The second additional term  $S_{e2}$  is a modified form of the additional term in the  $\varepsilon$  equation of Craft & Launder (1996) which is needed at a shear-free boundary.

$$S_{e2} = (1 - A) \tilde{\varepsilon} (c_\mu A k)^{1/2} A, k (l A^{1/2})_{,k} \quad (25)$$

Note that a further term composed of some length-scale gradients as in the CLS model should be involved when applications for impinging flows are considered.

## APPLICATIONS

### Homogeneous strain fields

Firstly, the proposed model has been tested in homogeneous strain fields such as plane strain, axisymmetric contraction, axisymmetric expansion and homogeneous shear flows.

Fig 2 illustrates the time evolution of turbulent quantities of the present model in a plane strain compared with the results of the DNS (Lee & Reynolds, 1985), the CLS model and a linear EVM (Launder & Sharma, 1974): LS. The compared DNS imposed a moderate (*slow*) initial strain:  $S_0^* = 1.0$ , at the normalized time:  $t^* = 0$ , where

$$S^* \equiv \frac{\overline{u_k u_k}}{\varepsilon} \sqrt{S_{ij} S_{ij}/2}, \quad t^* \equiv t \sqrt{S_{ij} S_{ij}/2}.$$

The time evolutionary profiles of  $k$  and  $\varepsilon$  of the present model accord with the DNS data closer than those of the CLS or the LS model as shown in Fig 2(a), (b). Fig 2(c) shows reasonable agreement between the present and the DNS results in the Reynolds stresses (results by the LS model are not included because comparison with a linear EVM in the Reynolds stresses would not be helpful). Since the turbulent Reynolds number,  $R_t$  of this case ranges between 9.8 and 17.3, even the very weak  $R_t$  damping function in the constitutive equation of the CLS model reduces anisotropy of turbulence. (The removal of the  $R_t$  damping function from the CLS model resulted in a better prediction.) The present model, however, shows encouraging results due to its exclusion of explicit  $R_t$  damping on Reynolds stresses. The obtained initial stress fields by the present and the CLS models are not isotropic because any algebraic expression for Reynolds stresses does not comply with the initial condition of isotropic turbulence with straining. This affects the evolutionary profile of  $A$ , consequently as shown in Fig 2(d), the presently predicted  $A$  evolves faster than the DNS result.

Fig 3 shows the time evolutionary profiles of Reynolds stresses in the other homogeneous strainings. The shown predicted tendency in the axisymmetric contraction and expansion is similar to that of the plane strain case. In Fig 3(c), the computation has started at  $t^* = 4$  for the homogeneous shear of Lee *et al.* (1990) with  $S_0^* = 33.5$ . When the initial strain is increased significantly to such a value, the present algebraic Reynolds stress expression: Equation (1) produces a highly anisotropic initial stress

field which is unacceptably inconsistent with the initially isotropic condition of the DNS. (This also implies that an algebraic model is not adequate for rapid deformations as pointed out by Reynolds & Kassinos (1995) while it might be possible to remedy this anomaly by introducing further dependence of  $A$ .) Then, the computation has started from some developed condition. Fig 3(c) shows that both the CLS and the present models produce fairly reasonable stress profiles. Note that the viscous effect has no effect on the results in this case since the range of  $Re$  is high enough.

### Wall and shear-free flows

Focusing on capturing shear-free turbulence, the model has been tested in a fully developed open channel flow and a plane Couette flow without shear on the moving wall, as well as plane channel flows for comparison. The computations have been performed using the PASSABLE code (Leschziner, 1982) with the boundary conditions for shear free regions ( $y = \delta$ ):

Plane Channel :  $U_y = 0, k_y = 0, \bar{\epsilon}_y = 0, A_y = 0$

Open Channel :  $U_y = 0, k_y = 0, \bar{\epsilon}_y = 0, A = 0$

Plane Couette :  $U_y = 0, k = 0, \bar{\epsilon} = 0, A = 0$ .

Fig 4 shows satisfactory agreement between the predicted mean velocity profiles and the DNS data (channel: Kim *et al.*, 1987, Kim, 1989; Couette: Kuroda *et al.*, 1995; open channel: Lombardi *et al.*, 1996). (Note that the plane Couette flow of Kuroda *et al.* (1995) is not purely shear-free at the moving wall while the shear is very low.) Then the predicted turbulent shear stress distributions agree quite well with the DNS results as shown in Fig 5. Although each strain field is nearly the same as the others, the stress field in the shear-free region is very different from one another. Fig 6 compares the predicted root mean square values of the Reynolds normal stresses with the DNS results. The agreement between the prediction and the DNS data is fairly satisfactory in each quantity of each flow field. Particularly, the present model successfully demonstrates its ability to capture the characteristic behaviours of the Reynolds normal stresses near the free surface where only the component normal to the surface vanishes.

Fig 7 compares the predicted stress flatness parameters with the DNS results. Although the agreement is generally satisfactory, values in high turbulent regions are underpredicted. This is partly because of the truncation made in Equation (17). (Adopting Equation (16) made the agreement closer.) According to the predicted behaviour of  $A$  which produces the primary damping effect on  $\nu_t$  in the present model, the predicted eddy viscosity behaves reasonably near both wall and shear-free boundaries as shown in Fig 8. (Obviously, further refinements are necessary.) Finally, Fig 9 shows good accord between the predicted dissipation rate and the DNS data.

### CONCLUDING REMARKS

- This paper has presented the development of a new non-linear  $k$ - $\epsilon$ - $A$  three equation EVM in which no topographical parameters are used and the effect of the local turbulent Reynolds number is limited to the viscous sublayer.
- The dependence of stress flatness parameter,  $A$ , has been used to capture shear-free turbulence as well as to damp the eddy viscosity near two-component turbulence boundaries.
- The latest second moment closure of Craft & Launder (1996) has been employed to close the  $A$  equation.
- The proposed model has demonstrated its encouraging performance to capture anisotropic turbulence near both wall and shear-free boundaries as well as in homogeneous strainings.

The tests of the model in more complex flow fields are currently underway.

**Acknowledgements :** The author thanks Professor B.E. Launder and Dr. T.J. Craft of UMIST for their fruitful suggestions. To develop a model with a transport equation for  $A$  was originally suggested by Professor Launder.

### REFERENCES

- Craft, T.J., and Launder, B.E., 1996, *Int. J. Heat Fluid Flow*, **17**, 245-254.
- Craft, T.J., Launder, B.E., and Suga, K., 1996, *Int. J. Heat Fluid Flow*, **17**, 108-115.
- Craft, T.J., Launder, B.E., and Suga, K., 1997, *Int. J. Heat Fluid Flow*, **18**, 15-28.
- Daly, B.J., and Harlow, F.H., 1970, *Phys. Fluids*, **13**, 2634.
- Kim, J., 1989, personal communication.
- Kim, J., Moin, P., and Moser, R., 1987, *J. Fluid Mech.*, **177**, 133-166.
- Kuroda, A., Kasagi, N., and Hirata, M., 1995, *Turbulent Shear Flows 9*, (ed. F. Durst *et al.*), 241-257, Springer, Berlin.
- Launder, B.E., and Reynolds, W.C., 1983, *Phys. Fluids*, **26**, 1157-1158.
- Launder, B.E., and Sharma, B.I., 1974, *Letters in Heat Mass Transfer*, **1**, 131-138.
- Lee, M.J., Kim, J., and Moin, P., 1990, *J. Fluid Mech.*, **216**, 561-583.
- Lee, M.J., and Reynolds, W.C., 1985, Stanford Univ. Tech. Rep., TF-24.
- Leschziner, M.A., 1982, UMIST Mech. Eng. Rep., TF/82/11.
- Lombardi, P., De Angelis, V., and Banerjee, S., 1996, *Phys. Fluids*, **8-6**, 1643-1665.
- Lumley, J.L., 1978, *Adv. in Applied Mech.*, **18**, 123.
- Nezu, I., and Rodi, W., 1986, *J. Hydraulic Engng.*, **112**, 335-355.
- Reynolds, W.C., and Kassinos, S.C., 1995, *Proc. Roy. Soc. London A*, **451**-1941, 87-104.
- Suga, K., 1995, PhD thesis, UMIST, Manchester, U.K.

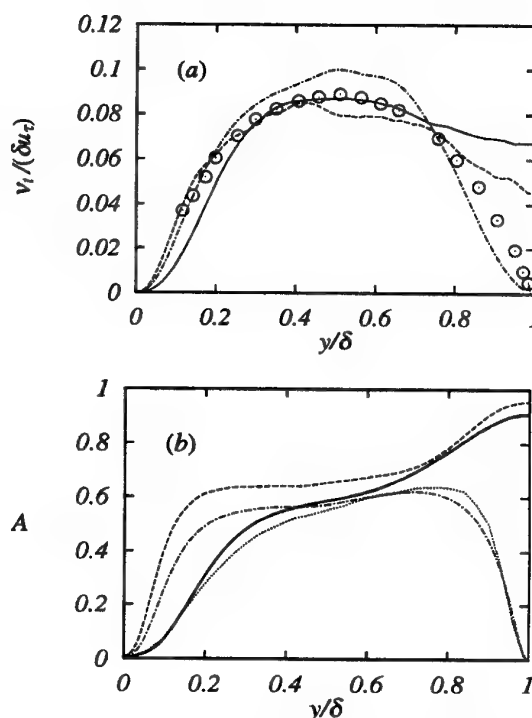


Fig 1 (a) EDDY VISCOSITY; (b) STRESS FLATNESS PARAMETER:  $\circ \circ$ , Open-channel (Nezu & Rodi, 1986);  $\cdots$ , Open-channel (Lombardi *et al.*, 1996);  $- \cdot -$ , Couette (Kuroda *et al.*, 1995);  $—$ , Channel at  $Re = 2800$  (Kim *et al.*, 1987);  $- - -$ , Channel at  $Re = 6875$  (Kim, 1989).

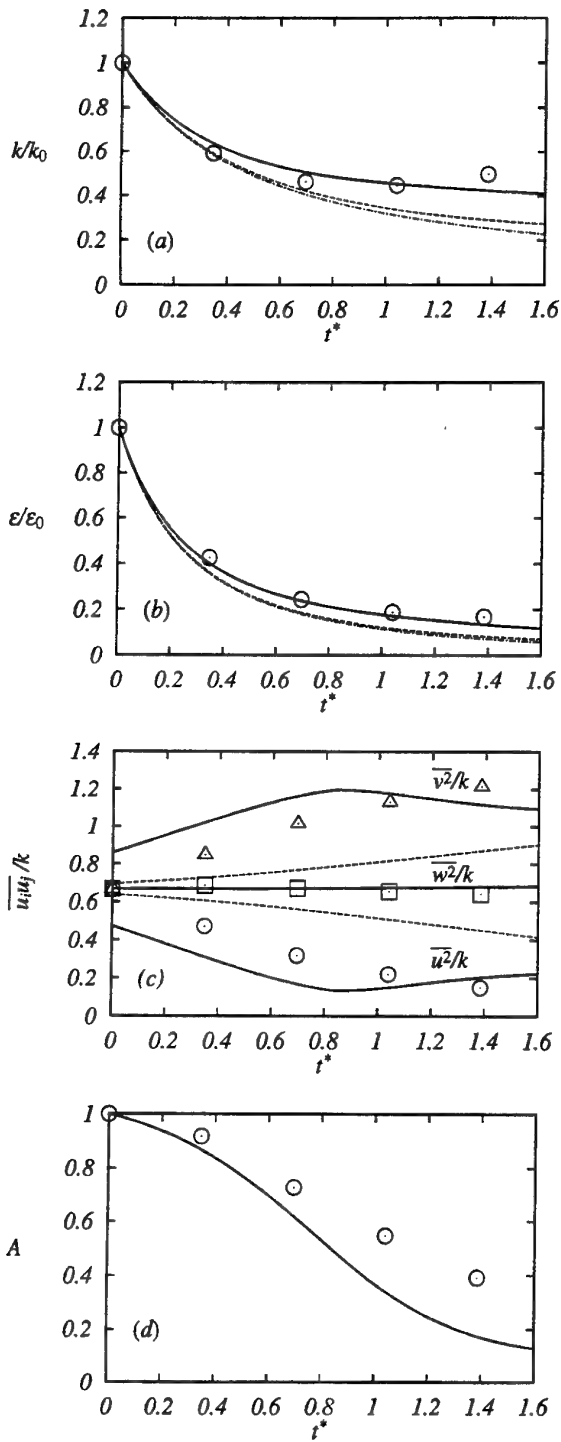


Fig 2 TIME EVOLUTION OF TURBULENT QUANTITIES DURING PLANE STRAIN,  $S_0 = 1.0$ : symbols, DNS; —, present; ---, CLS; -.-, LS.

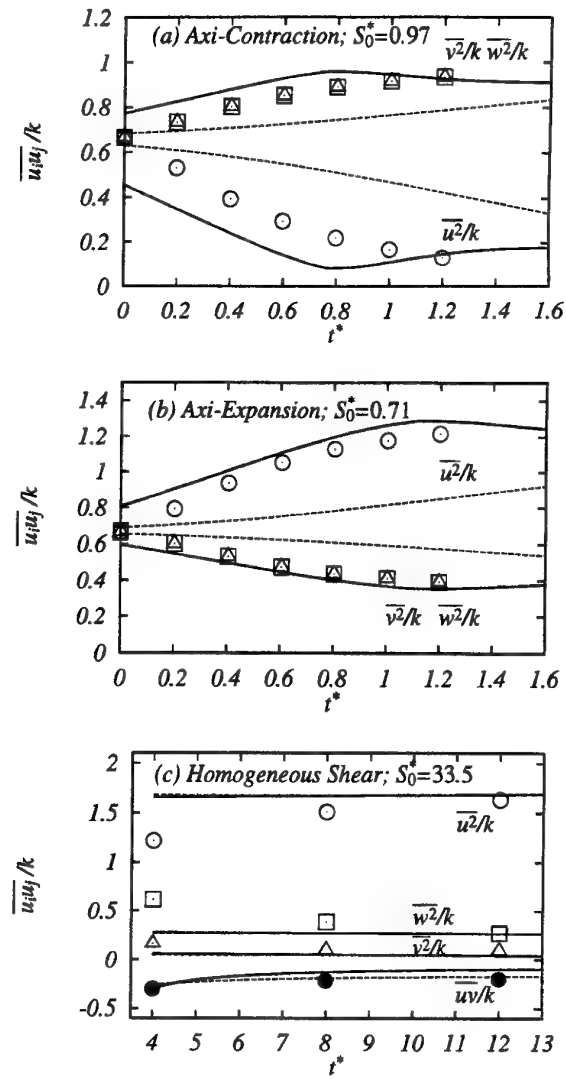


Fig 3 TIME EVOLUTION OF REYNOLDS STRESSES IN HOMOGENEOUS STRAIN FIELDS: symbols, DNS; —, present; ---, CLS.

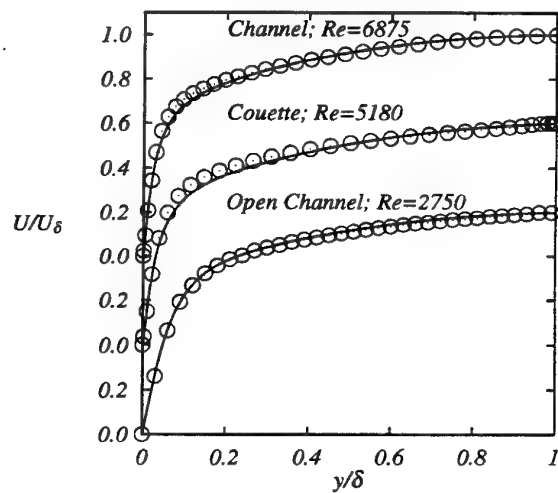


Fig 4 MEAN VELOCITY: symbols, DNS; lines, present.

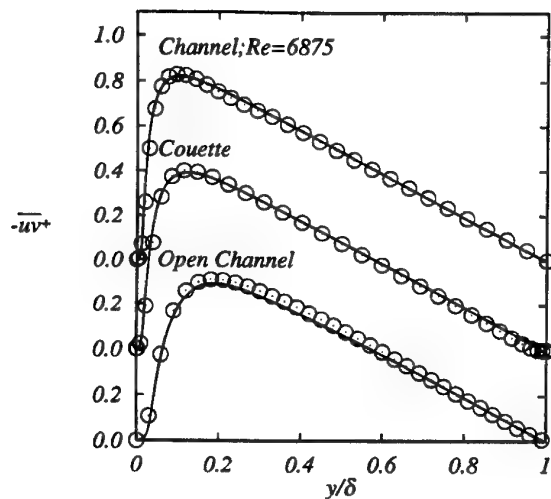


Fig 5 TURBULENT SHEAR STRESS DISTRIBUTIONS: key as Fig 4.

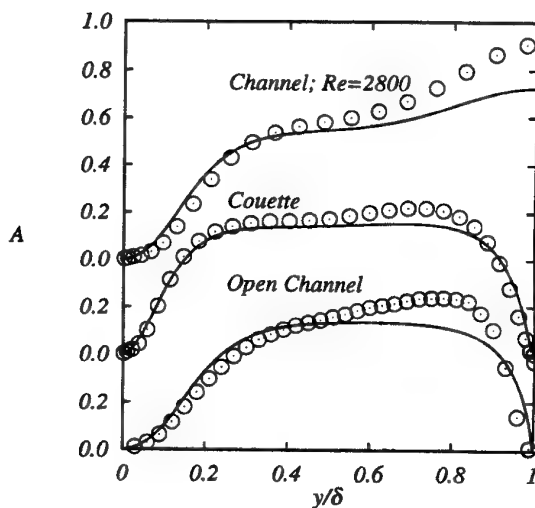


Fig 7 STRESS FLATNESS PARAMETER: key as Fig 4.

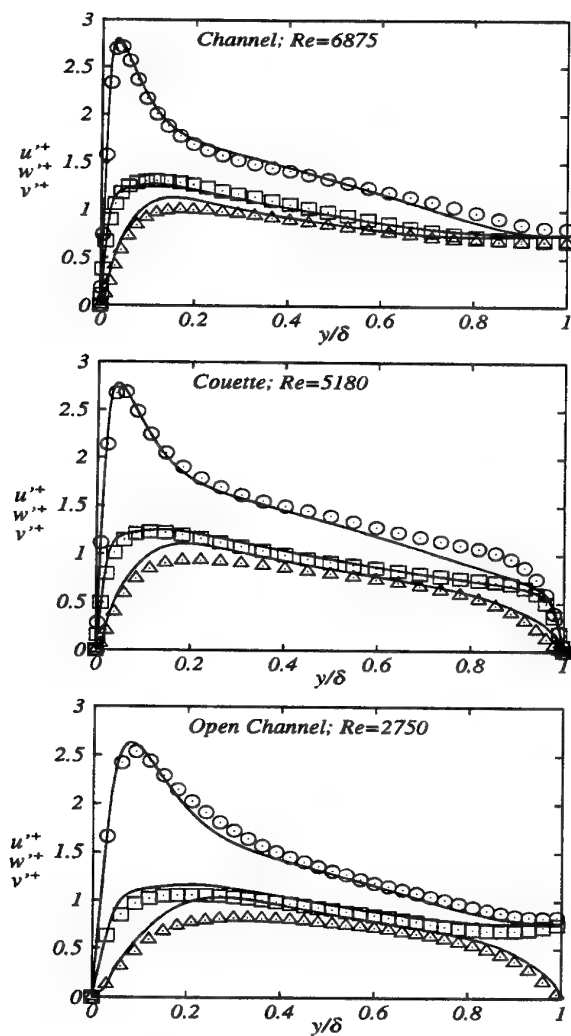


Fig 6 TURBULENT INTENSITIES: key as Fig 4.

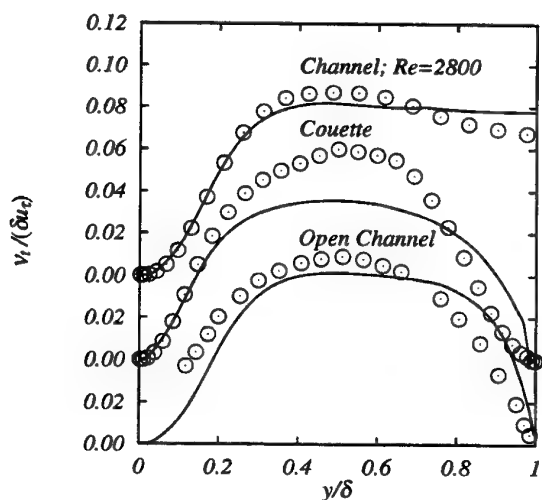


Fig 8 EDDY VISCOSITY: symbols: data as in Fig 1(a); lines: present.

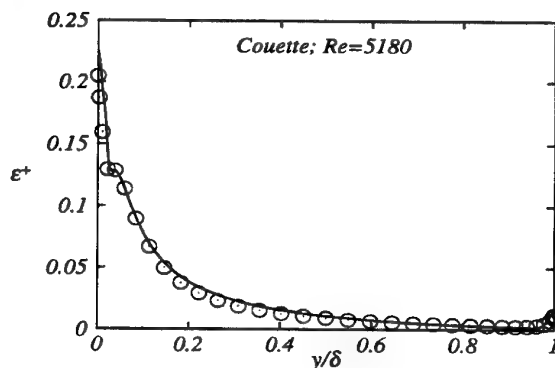


Fig 9 TURBULENT DISSIPATION IN THE COUETTE FLOW: key as Fig 4.

# DEVELOPMENT OF THE $k - \varphi$ TURBULENCE MODEL

J. Cousteix<sup>(1)</sup>, V. Saint-Martin<sup>(1)</sup>, R. Messing<sup>(1,2)</sup>, H. Bézard<sup>(1)</sup>, B. Aupoix<sup>(1)</sup>

<sup>(1)</sup> ONERA/CERT, Aerothermodynamics Department

B.P. 4025

31055 Toulouse-Cedex

France

<sup>(2)</sup> Present address: Institut für Aero-und Gasdynamik der Universität Stuttgart

Pfaffenwaldring 21

70569 Stuttgart

Germany

## ABSTRACT

The purpose of the work is to develop a two-equation model of turbulence for aeronautical applications. Among others, the main required qualities of the model are its robustness, its ability to predict the skin-friction and boundary layer separation. To achieve these goals, certain constraints have been imposed, for example the logarithmic law of the wall or a good behaviour near the edge of a shear layer. A  $k - \varphi$  model has been developed in which the second variable is  $\varphi = \varepsilon/\sqrt{k}$ . Comparisons with different experimental data are promising.

## INTRODUCTION

The goal is to derive a new two-equation model which improves predictions, compared to the standard  $k - \varepsilon$  and  $k - \omega$  models, with special attention to aeronautical applications such as the flow over wings and fuselages.

$k - \varepsilon$  models are well known to poorly predict flows in adverse pressure gradient. Moreover, near-wall corrections often lead to numerical stiffness. The  $k - \omega$  model proposed by Wilcox (1988) seems a good alternative as it better predicts adverse pressure gradient flows, is easy to implement and numerically robust. However, Menter (1992) has shown that the predictions are very sensitive to the value of the specific dissipation  $\omega$  in the external flow. This paper presents an attempt to develop a new model which has the same numerical stability and good predictions ability as the  $k - \omega$  model but is not sensitive to the free-stream values.

## BASIS OF THE $k - \varphi$ MODEL

### Model form

A two-equation model, together with the Boussinesq hypothesis for the eddy viscosity

$$-\langle u'_i u'_j \rangle = \nu_t \left( \frac{\partial U_i}{\partial x_j} + \frac{\partial U_j}{\partial x_i} \right) - \frac{2}{3} k \delta_{ij} \quad (1)$$

is sought for. The transport equation for the turbulent kinetic energy  $k$ , which is exact except for the diffusion

term, is modelled as:

$$\frac{Dk}{Dt} = P_k - \varepsilon + \frac{\partial}{\partial x_k} \left[ \left( \nu + \frac{\nu_t}{\sigma_k} \right) \frac{\partial k}{\partial x_k} \right] \quad (2)$$

where  $P_k = -\langle u'_i u'_j \rangle \partial U_i / \partial x_j$  stands for the production of turbulent kinetic energy. The length-scale determining equation is sought for a quantity

$$\varphi = k^n \varepsilon^m \quad (3)$$

so that the eddy viscosity reads

$$\nu_t = C_\mu k^{2+n/m} \varphi^{-1/m} \quad (4)$$

In order to achieve numerical robustness, the length-scale determining equation is assumed to have the following form

$$\frac{D\varphi}{Dt} = C_{1\varphi} P_k \frac{\varphi}{k} - C_{2\varphi} \frac{\varepsilon}{k} \varphi + \frac{\partial}{\partial x_k} \left[ \left( \nu + \frac{\nu_t}{\sigma_\varphi} \right) \frac{\partial \varphi}{\partial x_k} \right] \quad (5)$$

i.e. a simple production/destruction balance together with a first gradient diffusion law.

### Constraints

The model is required to satisfy the following four constraints :

- The model must be consistent with the decay law of turbulence in homogeneous, isotropic turbulence, in order to reproduce the turbulence evolution in the free-stream;
- The model must predict a  $y^2$  behaviour of the turbulent kinetic energy near the wall;
- The model must be consistent with the standard equilibrium in the logarithmic layer;
- The model must give the correct behaviour of the turbulent quantities near a laminar/turbulent interface.

### Near-wall behaviour of the model

In the near-wall region, advection, production and turbulent diffusion are negligible so that the transport equations reduce to

$$0 = -k^{-n/m} \varphi^{1/m} + \frac{\partial}{\partial y} \left[ \nu \frac{\partial k}{\partial y} \right] \quad (6)$$

$$0 = -C_{2\varphi} k^{-(1+n/m)} \varphi^{1+1/m} + \frac{\partial}{\partial y} \left[ \nu \frac{\partial \varphi}{\partial y} \right] \quad (7)$$

As  $k \sim A_k y^2$  and  $\varepsilon \sim y^0$ , we have  $\varphi \sim A_\varphi y^{2n}$ . Replacing the above expansions in the equations yields the following relation

$$n(2n-1) = C_{2\varphi} \quad (8)$$

The decay of isotropic turbulence imposes  $C_{2\varphi} = n + mC_{\varepsilon_2}$  where  $C_{\varepsilon_2}$  is the constant used in the  $k-\varepsilon$  model. A value of 1.92 has been kept for this constant. No simple values can be obtained for  $n$  and  $m$ . An approximate solution ( $n = -0.5, m = 1$ ) has thus been selected so that

$$\varphi = \frac{\varepsilon}{\sqrt{k}} \sim \frac{k}{l} \quad (9)$$

This choice of variable yields  $k \sim y^{1.85}$  and  $\nu_t \sim y^{3.85}$ .

### Logarithmic region behaviour

The balance in the logarithmic region of a zero pressure gradient boundary layer, assuming a constant shear stress proportional to the turbulent kinetic energy, gives the relation

$$\sigma_\varphi = \frac{\kappa^2}{(C_{2\varphi} - C_{1\varphi})\sqrt{C_\mu}} \quad (10)$$

where  $\kappa$  and  $\sqrt{C_\mu}$  are respectively the von Kármán and Bradshaw constants.

### Behaviour at a laminar/turbulent interface

At the outer edge of the boundary layer, production and destruction terms as well as longitudinal advection and viscous diffusion are neglected. In the boundary layer, near the edge, it can be shown that a possible solution is

$$U = U_e - A \left(1 - \frac{y}{\delta}\right)^{1/\gamma} \quad (11)$$

$$k = B \left(1 - \frac{y}{\delta}\right)^{\sigma_k/\gamma} \quad (12)$$

$$\varphi = C \left(1 - \frac{y}{\delta}\right)^{\sigma_\varphi/\gamma} \quad (13)$$

where  $\gamma = (2 + n/m)\sigma_k - \sigma_\varphi/m$  and  $A, B$  and  $C$  are constants. Following Cazalbou et al. (1994), a correct edge behaviour of the mean velocity profile and turbulent quantities imposes

$$\frac{1}{2m+n} \sigma_\varphi < \sigma_k < \frac{m}{2m+n} \left(1 + \frac{\sigma_\varphi}{m}\right) \quad (14)$$

### Discussion

It turns out that the near-wall  $y^2$  behaviour is a strong constraint which leads to the form of the variable  $\varphi$  but cannot achieve the correct near-wall behaviour for the eddy viscosity. Moreover, it will be shown later that the model requires near-wall corrections. However, the choice of  $\varphi$  can be justified in different ways. This paper will focus on the improvement that this choice of variable brings for the prediction of the outer region of the boundary layer with adverse pressure gradient. The choice of  $\varphi$  also greatly improves compressible flows but this is out of the scope of the present paper.

### MODEL CALIBRATION: SELF-SIMILAR BOUNDARY LAYER SOLUTIONS

The  $k-\varphi$  model has first been tested in the outer part of self-similar boundary layers. These tests were used to set the values of the constants namely :

$$C_{1\varphi} = 1.14, C_{2\varphi} = 1.42, \sigma_k = 1.5, \sigma_\varphi = 2$$

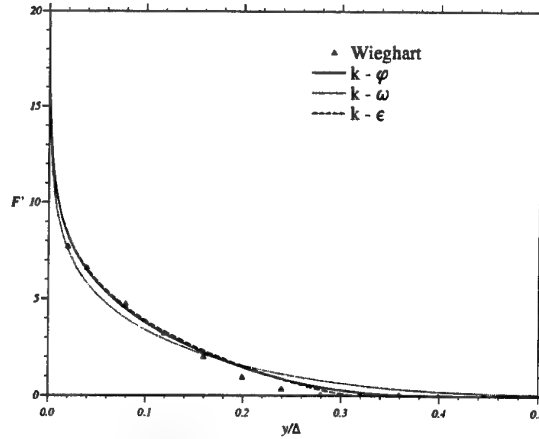


Figure 1: Self-similar solution for the outer part of the boundary layer - Zero pressure gradient flow.

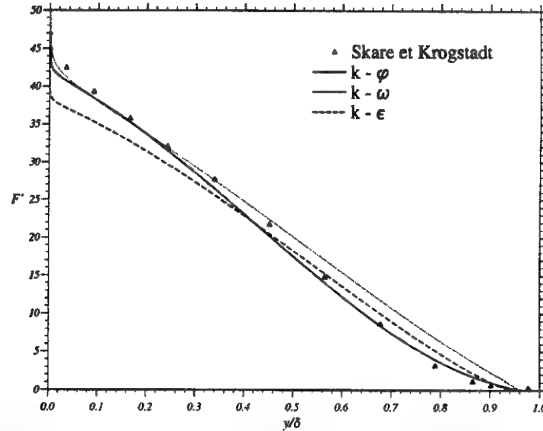


Figure 2: Self-similar solution for the outer part of the boundary layer - Strong adverse pressure gradient flow.

For the outer part of the boundary layer, self-similarity is achieved provided that the Reynolds number is large enough and the pressure gradient parameter  $\beta^* = (\delta_1/\tau_w) dP/dx$  is constant, where  $\delta_1$  is the displacement thickness and  $\tau_w$  the wall shear stress.

The defect velocity  $F'$  is assumed independent of the streamwise distance  $x$  :

$$\frac{U_e - U}{U_\tau} = F'(\eta) \quad \eta = \frac{y}{\delta} \quad (15)$$

where  $U_\tau$  is the friction velocity and  $\delta$  the boundary layer thickness. Self-similarity is also assumed for the reduced turbulent shear stress profile  $-\langle u'v' \rangle / U_\tau^2$ . Then, the equation for similarity solutions is deduced from the streamwise momentum equation and is solved by a Newton procedure.  $F'$  is depicted for the zero pressure gradient case and a strong adverse pressure gradient case. For the zero pressure gradient case, the profile is plotted versus the Clauser thickness  $\Delta = \int F' d\eta$  in figure 1. The present model gives good results, as the  $k-\varepsilon$  model does, whereas the  $k-\omega$  is less accurate.

For the strong adverse pressure gradient case, the predictions are compared to Skåre and Krogstad (1994) results

in figure 2. As in the experiments, the profiles are plotted with respect to the boundary layer thickness  $\delta$ . The present model is far better than the  $k - \varepsilon$  model and even the  $k - \omega$  model in the second case close to separation, and manages to predict the bending point of the velocity profile.

It has also been tried to optimize the constants of the  $k - \varepsilon$  and  $k - \omega$  models to improve their predictions but no significant improvement has been achieved.

### APPLICATION TO FREE SHEAR FLOWS

Fully turbulent, high Reynolds number free shear flows developing over a long distance tend towards a self-similar state, both for the mean and the turbulent motion. These self-similarity solutions provide good challenges to test turbulence models without the difficulties linked to the vicinity of the wall. Four two-dimensional, incompressible self-similar flows have been investigated.

For the plane wake (figure 3), the self-similar solution is sought as

$$\frac{U_\infty - U}{U_\infty - U_{CL}} = F'(\eta) \quad \eta = \frac{y}{\delta} \quad (16)$$

where  $U_\infty$ ,  $U_{CL}$  and  $\delta$  are respectively the external velocity, the centerline velocity and the wake thickness. Both the reduced mean velocity and Reynolds stress profiles compare favorably with the Wygnanski et al. (1986) experiment, as shown in figure 3. Both profiles smoothly reach a zero value at the wake edge. However, the turbulent kinetic energy is overestimated near the wake axis and underestimated in the outer region. The good comparison is not surprising as the constants of the  $k - \varphi$  model have been optimized according to the outer region of a boundary layer which behaves like a wake. The wake spreading rate is the longitudinal variation of the wake thickness defined as the distance between the centerline and the point where  $F' = 0.5$ . The model predictions are in fair agreement with the experiment, both giving a value close to 0.27.

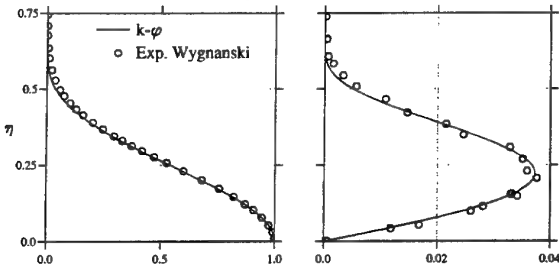


Figure 3: Non-dimensional velocity (left) and Reynolds stress (right) profiles for the self-similar plane wake.

For the plane mixing layer (figure 4), the self-similar solution is sought as

$$\frac{U - U_2}{U_1 - U_2} = F'(\eta) \quad \eta = \frac{y}{\delta} \quad (17)$$

where  $U_1$ ,  $U_2$  and  $\delta$  are respectively the velocities of the fast and slow streams and the mixing layer thickness. Various velocity ratios  $U_2/U_1$  have been investigated and results for a ratio of 0.6 are presented in figure 4 and compared with Bell and Mehta (1990) experiment. The velocity profile is fairly reproduced but both the turbulent kinetic energy and the Reynolds stress are slightly underestimated. Therefore, the mixing layer spreading rate is underestimated. When the mixing layer thickness is defined as the distance between the points where  $F' = 0.1$  and  $F' = 0.9$ ,

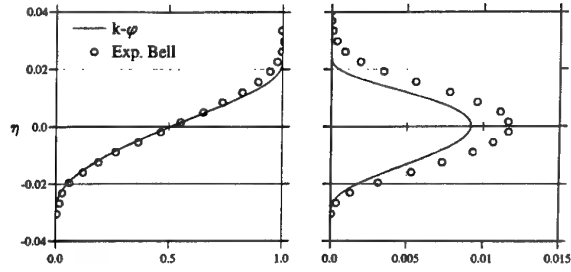


Figure 4: Non-dimensional velocity (left) and Reynolds stress (right) profiles for the self-similar plane mixing layer.

the experiment gives a spreading rate value of 0.032 while the model yields 0.030.

For the plane or round jet, the self-similar solution is sought as

$$\frac{U}{U_{CL}} = F'(\eta) \quad \eta = \frac{y}{\delta} \quad (18)$$

where  $U_{CL}$  and  $\delta$  are respectively the centerline velocity and the jet thickness. Model predictions for the plane jet are compared to the Gutmark and Wygnanski (1976) experiment in figure 5. As previously, the maximum turbulent kinetic energy and Reynolds stress are underestimated. However, both the turbulent kinetic energy and Reynolds stress are now overestimated in the outer part of the jet. Therefore, the predicted mean velocity profile exhibits less curvature than the experimental one. The model reproduces fairly well the jet spreading rate, defined in the same way as for the wake; model and experiment both give values of 0.10.

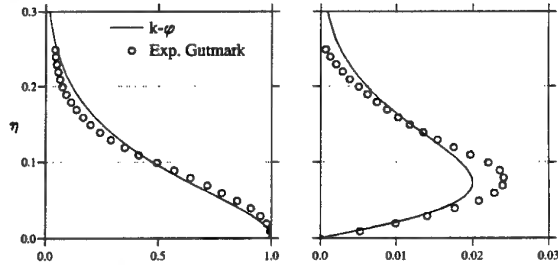


Figure 5: Non-dimensional velocity (left) and Reynolds stress (right) profiles for the self-similar plane jet.

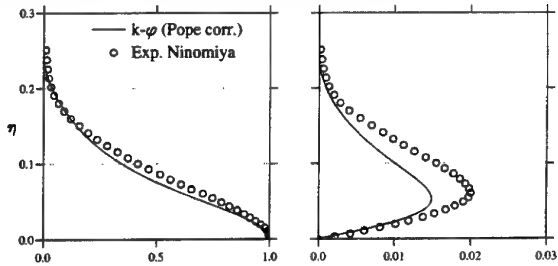


Figure 6: Non-dimensional velocity (left) and Reynolds stress (right) profiles for the self-similar round jet.

As expected, the model is unable to solve the round jet/plane jet anomaly. Compared to Ninomiya and Kasagi experiment (1993), the model overestimates the turbulence levels and hence the spreading rate. The experimen-



tal spreading rate is 0.09 while the predicted one is 0.14! Pope's correction (1978), which adds a source term based on the vortex stretching invariant in the dissipation rate equation, improves the prediction. Without any tuning of the constant in Pope's correction, the agreement is good, as shown in figure 6 but the Reynolds stress and the spreading rate are underpredicted, the spreading rate is now 0.076.

## EXTENSION TO BOUNDARY LAYERS

### Wall damping functions

Tests of the model in a boundary layer program have shown that it reproduces the near-wall region and the slope of the logarithmic region but not the buffer region, in agreement with Huang and Bradshaw (1995) analysis. Therefore, wall corrections are required.

A first strategy is to derive wall damping functions. The technique developed by Aupoix et al. (1993) has been extended to two-equation models. The wall region is treated as a one-dimensional flow. In the wall unit system, the equations reduce to

$$\begin{aligned} P_k^+ - \varphi^+ \sqrt{k^+} + \frac{\partial}{\partial y^+} \left[ \left( 1 + \frac{\nu_t^+}{\sigma_k} \right) \frac{\partial k^+}{\partial y^+} \right] &= 0 \\ C_{1\varphi} \frac{P_k^+ \varphi^+}{k^+} - C_{2\varphi} \frac{\varphi^{+2}}{\sqrt{k^+}} + \frac{\partial}{\partial y^+} \left[ \left( 1 + \frac{\nu_t^+}{\sigma_\varphi} \right) \frac{\partial \varphi^+}{\partial y^+} \right] &= 0 \end{aligned}$$

where  $P_k^+ = \nu_t^+ (\partial U^+ / \partial y^+)^2$  is the turbulent production. The mean flow profile is imposed from a corrected mixing length model solution. The assumption of a constant total shear in the near-wall region yields the eddy viscosity profile. The above two equations can be solved to determine the  $k^+$  and  $\varphi^+$  profiles from which a damping form for the eddy viscosity can be deduced to retrieve the imposed eddy viscosity profile. However, no correct solution can be achieved this way as the near wall balance of  $\varphi$  is poor. A damping term is also needed for  $C_{2\varphi}$ .

To determine it, the dissipation length scale is imposed using Chen's model. The dissipation thus reads

$$\varphi^+ \sqrt{k^+} = k^{+3/2} / l^+ \quad (19)$$

With an imposed distribution for  $l^+$ , the  $k^+$  equation can first be solved and yields the kinetic energy profile. The  $\varphi^+$  profile is thus given by equation (19). As  $\varphi^+$  must still satisfy its transport equation, a damping of the  $C_{2\varphi}$  coefficient is determined to balance the  $\varphi^+$  transport equation. The damping of the eddy viscosity is obtained as previously to retrieve the prescribed eddy viscosity profile.

The so-derived model allows to finely reproduce the near-wall region but the original simplicity and robustness of the model in the near-wall region is lost.

### Two-layer approach

An alternative is to use the  $k - \varphi$  model only in the outer part of the boundary layer where it has an excellent behaviour and to use another model to treat the near-wall region. First tests were performed with the modified version of the Norris and Reynolds one-equation model proposed by Aupoix et al. (1993).

As the  $k - \omega$  model has a good numerical behaviour in the wall region, it is now currently used as the near-wall model. The  $k - \omega / k - \varphi$  composite model has a good numerical robustness but is unable to finely predict the turbulent kinetic energy profile, as the  $k - \omega$  model. Moreover, both  $\omega$  and  $\varphi$  are infinite at the wall as, in the near-wall region

$$\omega = \frac{6\nu}{C_{2\omega} y^2} \quad \varphi = \frac{6\nu C_\mu \sqrt{k}}{C_{2\omega} y^2} \sim y^{-1} \quad (20)$$

The second equation shows that the behaviour of  $\varphi$  near the wall is coupled to the behaviour of  $k$ . The use of  $\omega$  near the wall leads to a simpler boundary condition.

As it is difficult to implement a two-layer model in a Navier-Stokes solver, the  $\varphi$  equation is rewritten in terms of  $\omega$ . In equation (5), the variable change  $\varphi = C_\mu \omega \sqrt{k}$  leads to :

$$\begin{aligned} \frac{D\omega}{Dt} &= C_{1\omega} P_k \frac{\omega}{k} - C_{2\omega} \frac{\varepsilon}{k} \omega + \frac{\partial}{\partial x_i} \left[ \left( \nu + \frac{\nu_t}{\sigma_\varphi} \right) \frac{\partial \omega}{\partial x_i} \right] \\ &+ f_1 \frac{1}{k} \left( \nu + \frac{\nu_t}{\sigma_\varphi} \right) \frac{\partial k}{\partial x_i} \left( \frac{\partial \omega}{\partial x_i} - \frac{\omega}{4k} \frac{\partial k}{\partial x_i} \right) \\ &+ f_1 \frac{\omega}{2k} \left( \frac{1}{\sigma_\varphi} - \frac{1}{\sigma_k} \right) \frac{\partial}{\partial x_i} \left( \nu_t \frac{\partial k}{\partial x_i} \right) \end{aligned}$$

with  $\nu_t = k/\omega$ , and the constants :

$$C_{1\omega} = (C_{1\varphi} - 1/2) = 0.64, \quad C_{2\omega} = C_\mu (C_{2\varphi} - 1/2) = 0.0828$$

$$\sigma_k = 1.5, \quad \sigma_\varphi = 2$$

In the inner and logarithmic layer, the blending function  $f_1$  is set to 0 since additional diffusion terms must be removed in order to obtain a  $k - \omega$  model. The model thus reduces to a  $k - \omega$  model with modified coefficients  $C_{1\omega}$  and  $C_{2\omega}$  to be consistent with the  $k - \varphi$  model.

In the outer layer, the additional diffusion terms are active and  $f_1$  is gradually set to 1. Tests on self-similar flows showed that the blend between both models must be performed below  $y/\delta = 0.3$  so as to keep the  $k - \varphi$  model characteristics in the outer region. Presently, only a tentative form for  $f_1$  has been used. It reads

$$\begin{aligned} \frac{y}{\delta} &\leq 0.15 & f_1 &= 0 \\ 0.15 &\leq \frac{y}{\delta} \leq 0.3 & f_1 &= \frac{\frac{y}{\delta} - 0.15}{0.3 - 0.15} \\ 0.3 &\leq \frac{y}{\delta} & f_1 &= 1. \end{aligned}$$

Moreover, for Navier-Stokes computations, the additional terms have to be set to zero ( $f_1 = 0$ ) outside of the boundary layer in order to avoid numerical problems.

### Examples of test cases

This  $k - \omega / k - \varphi$  composite model has been implemented in a boundary layer code.

The skin friction prediction versus Reynolds number for a zero pressure gradient boundary layer flow has first been investigated. Figure 7 shows that skin friction remains 3% to 5% higher than the Kármán-Schoenherr correlation (noted K-S) over all the studied Reynolds number range, i.e. up to  $Re_\theta = 10^5$ . This is consistent with a slight underestimation of the intercept of the logarithmic law of the wall due to the change of coefficients in the model near the wall, compared to the original  $k - \omega$  model.

The Samuel and Joubert flow (1974) has been selected to investigate the response of the model to an adverse pressure gradient. While  $k - \varepsilon$  models are unable to reproduce the fall of the skin-friction coefficient, the present model performs well, as shown in figure 8. Quite similar results can be achieved with the  $k - \omega$  model but the prediction is thus very sensitive to the edge value of the specific dissipation  $\omega$ .

## APPLICATIONS TO NAVIER-STOKES SOLUTIONS

A transonic two-dimensional computation around the CAST7 airfoil is reported here. The flow has been investigated by Séraudie et al. (1984). Free-stream conditions

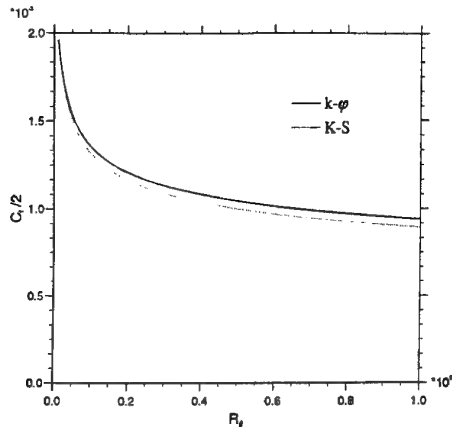


Figure 7: Skin-friction coefficient prediction for zero-pressure gradient boundary layer.

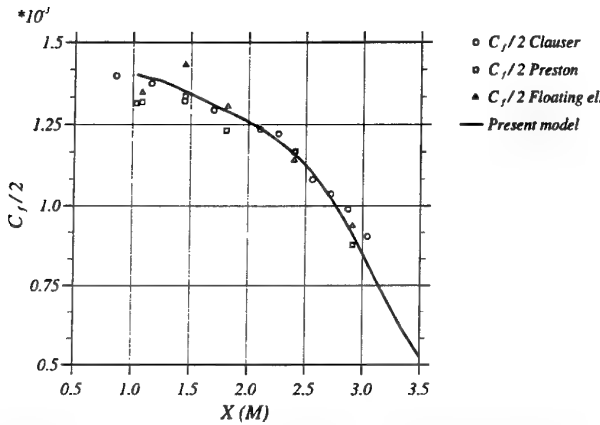


Figure 8: Skin-friction coefficient prediction for the Samuel and Joubert adverse pressure gradient experiment.

are  $M_\infty = 0.7$ ,  $\alpha = 1^\circ, 2^\circ, 3^\circ$  and  $Re_c = 4 \cdot 10^6$ . Transition is tripped by a roughness band at 7% of chord length. Figures 9 to 11 show the local isentropic Mach number  $M_t$  calculated from the pressure coefficient for the different an-

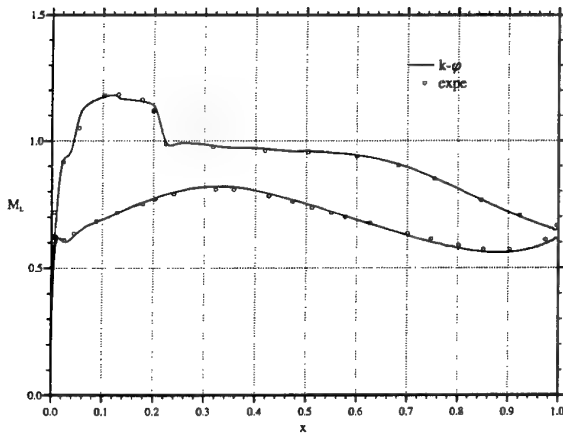


Figure 9: CAST7 airfoil - Local Mach number -  $\alpha = 1^\circ$ .

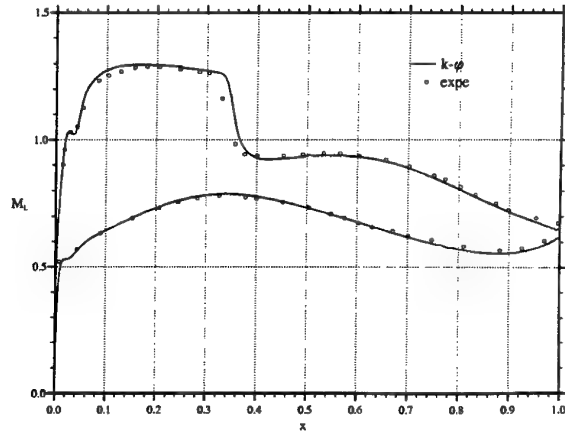


Figure 10: CAST7 airfoil - Local Mach number -  $\alpha = 2^\circ$ .

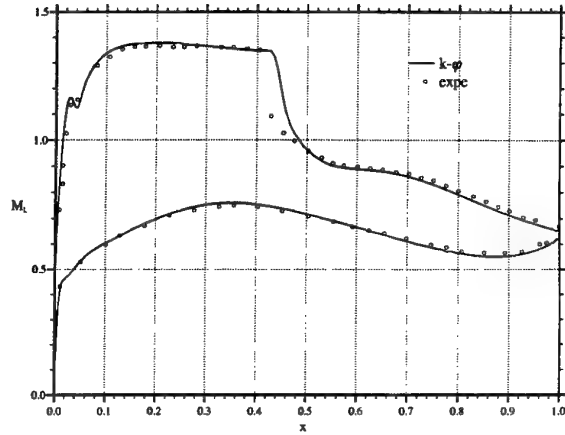


Figure 11: CAST7 airfoil - Local Mach number -  $\alpha = 3^\circ$ .

gles of attack. Surface pressure is well predicted. In particular, the evolution of the shock wave location with the angle of attack is close to experiment: between  $1^\circ$  and  $3^\circ$  angle of attack, the shock wave moves from the reduced abscissa  $x/c = 0.215$  to  $x/c = 0.45$ . At  $3^\circ$  angle of attack, the slope of the pressure increase corresponding to the shock is accurately predicted, but the computed shock location is 3% downstream the experimental one. It must be noticed that shock location is very sensitive in the case of CAST7 airfoil. The presence of boundary layers along the side-walls of the wind tunnel generates three-dimensional effects which may explain this discrepancy with the experiment. These effects are negligible at low angle of attack, which explains good results for  $\alpha = 1^\circ$ . For  $\alpha = 3^\circ$ , a perfect agreement with experiment is obtained with a 0.005 decrease on  $M_\infty$ . This value is consistent with correction bracket of side-wall effects deduced from numerical studies of the viscous/inviscid coupling (Archambaud et al. (1993), Bézard (1996)).

Figure 12 shows the shape factor  $H$  on the upper surface of the airfoil for  $\alpha = 3^\circ$ . Shock/Boundary-Layer interaction is characterized by a sharp increase of  $H$ . This rise of integral quantities increases with shock intensity. The  $k-\varphi$  model predicts the higher maximum which confirms that this model gives good results in pressure gradient flows. As a consequence, the distortion of the velocity profiles caused by the destabilization of the boundary layer is more significant with the  $k-\varphi$  model. Moreover, this model gives thicker boundary layers downstream the shock wave. Though the  $k-\varepsilon$  model gives correct shapes of ve-

locity profiles, it does not predict separation at Mach stem unlike the other three models.

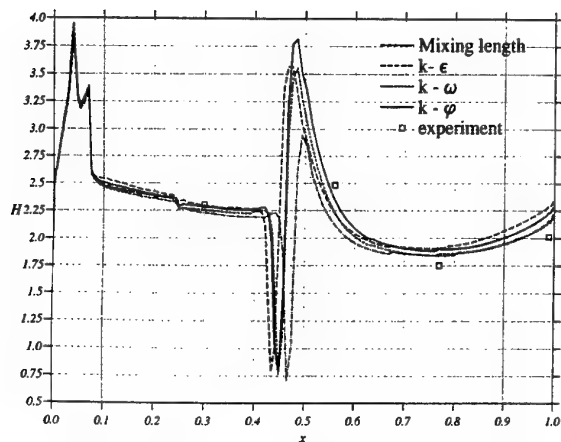


Figure 12: Shape factor on the upper surface of CAST7 airfoil.

Velocity profile upstream the shock wave is depicted in figure 13 for two free-stream values of  $\omega$ ,  $\omega_{e2}$  and  $\omega_{e1}$  with  $\omega_{e2} = 20\omega_{e1}$ . The solution obtained with the  $k-\varphi$  model is not sensitive to free-stream values, while the one obtained with the  $k-\omega$  model is.

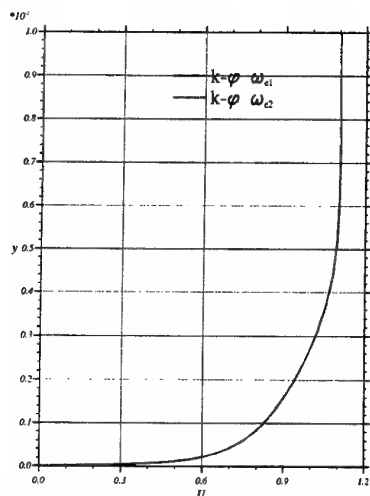


Figure 13: CAST7 airfoil - Velocity profile at  $x/c = 0.3$

## CONCLUSION

In order to construct a two-equation model, the choice of the  $k$ -equation seems to be very natural but there are many possibilities for the second variable. Following the same lines as in this paper, a systematic study of different choices could be interesting.

The new  $k-\varphi$  model which has been described has good qualities of robustness. In particular, its behaviour at the edge of a shear layer is much better than for a  $k-\omega$  model. The tests have shown that the model produces good results for boundary layers, especially with positive pressure gradients, for wakes, mixing layers and two-dimensional jets. These characteristics are important for aeronautical applications. Corrections were necessary for the round jet. At the present stage of development, the model needs to be refined in the vicinity of the wall.

**Acknowledgments :** The authors wish to acknowledge S. Catris and S. Viala for their contributions to the model development and testing.

## REFERENCES

- Archambaud, J.P., Michonneau, J.F., and Mignosi, A., 1993, "Effets latéraux dans une veine d'essais autour d'un profil d'aile bidimensionnel : Études expérimentale et numérique", *AGARD Meeting on Wall Interference, Support Interference and Flow Field Measurements*, CP-535, Paper 26.
- Aupoix, B., Desmet, E., and Viala, S., 1993, "Hypersonic turbulent boundary layer modelling", *Symposium on Transitional and Compressible Turbulent Flows*, 1993 ASME Fluids Engineering Conference, Washington D.C.
- Bell, J.H., and Mehta, R.D., 1990, "Development of a two-stream mixing layer from tripped and untripped boundary layers", *AIAA Journal*, Vol. 28, number 12, pp 2034-2042.
- Bézar, H., 1996, "Correction des effets dus aux couches limites latérales dans une veine de soufflerie". Technical Report 74/5006.70, ONERA.
- Cazalbou, J.B., Spalart, P.R., and Bradshaw, P., 1994, "On the behaviour of two-equation models at the edge of a turbulent region" *Physics of Fluids*, Vol. 5, number 6, pp 1797-1804.
- Gutmark, E., and Wygnanski, I., 1976, "The planar turbulent jet", *Journal of Fluid Mechanics*, Vol. 73, pp. 465-495.
- Huang, P.G., and Bradshaw, P., 1995, "The law of the wall for turbulent flows in pressure gradients", *AIAA Journal*, Vol. 33, number 4, pp 624-632.
- Menter, F.R., 1992, "Influence of free-stream values on  $k-\omega$  model predictions", *AIAA Journal*, Vol. 30, number 6, pp 1657-1659.
- Norris, L.H., and Reynolds, W.C., 1975, "Turbulent channel flow with a moving wavy boundary" Report FM-10, Department of Mechanical Engineering, Stanford University, California.
- Ninomiya, N., and Kasagi, N., 1993, "Measurements of the Reynolds stress budgets in an axisymmetric free jet with the aid of three-dimensional particle tracking velocimetry", *Ninth Symposium on Turbulent Shear Flows*, Kyoto, Japan.
- Pope, S.B., 1978, "An explanation of the turbulent round-jet/plane-jet anomaly", *AIAA Journal*, Vol. 16, number 3, pp 279-281.
- Samuel, A.E., and Joubert, P.M., 1974, "A boundary layer developing in an increasingly adverse pressure gradient", *Journal of Fluid Mechanics*, Vol. 66, Part 3, pp. 481-505.
- Séraudie, A., Archambaud, J.P., and Plazenet, M., 1984, "Qualification des couches limites et du proche sillage d'un profil CAST7", Technical Report 1/5019DN, ONERA.
- Skåre, P.E., and Krogstad, P.Å., 1994, "A turbulent equilibrium boundary layer near separation" *Journal of Fluid Mechanics*, Vol. 272, pp 31-348.
- Wilcox, D.C., 1988, "Reassessment of the scale-determining equation for advanced turbulence models", *AIAA Journal*, Vol. 26, number 11, pp 1299-1310.
- Wygnanski, I., Champagne, F., and Marasli, B., 1986, "On the large-scale structures in two-dimensional, small-deficit, turbulent wakes", *Journal of Fluid Mechanics*, Vol. 168, pp. 31-71.

## **SESSION 14 - WALL FLOWS II**

# COMPARISON BETWEEN DIRECTLY SIMULATED NUMERICAL AND EXPERIMENTAL DATA OF THE UNSTEADY TURBULENT CHANNEL FLOW

M. Hartmann, C. Völtz, D. Ronneberger

Drittes Physikalisches Institut

- Universität Göttingen -

Bürgerstraße 42-44

D-37073 Göttingen Germany

## INTRODUCTION

While the turbulent 2D channel flow at time invariant boundary conditions is one of the most studied shear flows in turbulence research, far less is known about the same flow when subjected to unsteady boundary conditions. On the other hand, the effects of unsteadiness imposed on turbulent shear flows are encountered in quite a few cases of practical importance (e.g., sound propagation through flow ducts, heat transfer in pulsating flow, sediment transport by unsteady flow, etc). Several experimental investigations of the unsteady channel flow have been performed during the past decade, however, these have been constricted to local measurements of the fluctuating velocity or wall shear stress in most cases. So our knowledge on the spatial and temporal structure of the flow is mainly based on the temporal structure of the measured signals. The temporal modulation of the spatial structure of the flow that is caused by the imposed unsteadiness is far from being fully accessible so far.

The unsteadiness is imposed on the mean flow either by harmonic oscillation of the longitudinal pressure gradient or, alternatively, longitudinal oscillation of one or both the walls of the 2D channel:  $u_{\text{wall}}(t) = u_w \cos(2\pi f_w t)$ ,  $u$  = velocity component in the streamwise direction (for further notations see the appendix). From a physical point of view both these methods to impose unsteadiness on the flow are equivalent: in both cases the unsteady deformation of the phase averaged flow field consists of a shear wave going out from the wall.

The decay of the shear wave as a function of the distance from the wall becomes steeper when the frequency is increased, so above a certain frequency, the unsteady deformation of the flow is restricted to the passive viscous sublayer. Therefore, the reaction of the turbulence to the imposed unsteadiness is expected to disappear at these high frequencies; this is even more so since the structure of the turbulence needs some time to adjust to a change of the mean flow field, i.e. the turbulence is expected to be unable to follow rapid oscillations of the mean flow. In fact, this anticipated dependency on the frequency is found, e.g., with the response of the intensity of the streamwise velocity fluctuations.

On the other hand the power spectral density of the streamwise velocity is strongly modulated even at high imposed frequencies, particularly when the flow is forced by an unsteady pressure gradient. It could be shown that this periodic redistribution of the intensity within the spectrum is caused by the periodic change of the speed by which the turbulence is convected past the probe (Ickler et al., 1997). While the change of the convection speed cannot change the intensity of the measured velocity fluctuations, the intensity of the turbulent wall shear stress fluctuation has been found to sensibly respond to oscillations of the mean pressure gradient even at the highest imposed frequency (Mao & Hanratty, 1986, Finnicum & Hanratty, 1988, Tardu & Binder, 1993). In fact it is conceivable that convected pressure fluctuations generate a convected viscous shear stress pattern at the wall the intensity of which depends on the convection speed, however, the amplitude and even the sign of this effect depends on details. So the physical mechanisms behind the observed response of the shear stress fluctuation remains an open question.

The direct numerical simulation of the flow under consideration is performed in order to support the experimental findings and, above all, to get access to quantities that cannot be measured but by unreasonable efforts. At the time of writing only the first results of the simulation are available. Regarding the question outlined in the previous paragraph these first simulations have been focussed on high forcing frequencies. The result will be presented and will be compared to the available experimental data. However, in view of some minor not yet fully explained discrepancies between the experimental and the numerical results concerning the unforced part of the flow, we restrain ourselves from extensive interpretations of the results (nevertheless it is rather unlikely that these discrepancies have a large effect on the unsteady response of the flow). We expect that the problems will be fixed and the set of numerical data will be more complete at the time of the meeting.

## THE NUMERICAL SIMULATION

In the direct numerical simulation a finite difference scheme is used to solve the three-dimensional, time-dependent incompressible Navier Stokes equations. The

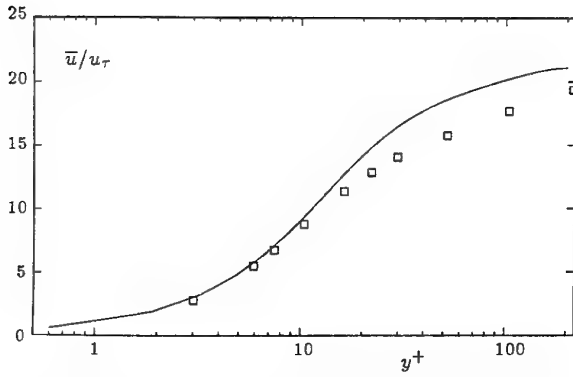


Figure 1: Mean velocity profile, numerical experiment: —, real experiment:  $\square \square \square$

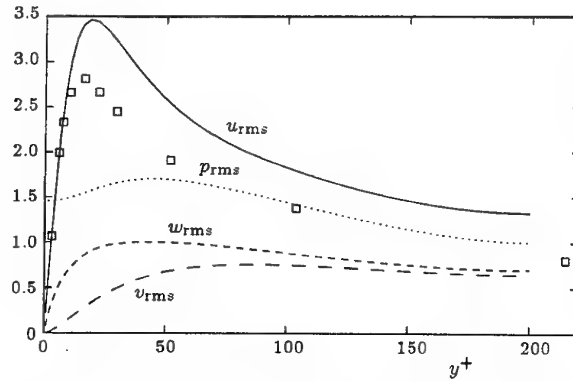


Figure 2: Root-mean-square velocity and pressure fluctuations normalized by wall parameters, the symbols denote the results of a real experiment

applied algorithm is based on a fractional-step scheme developed by Chorin (1969). The time-advancement is divided into two half steps. First an intermediate velocity field is computed from the diffusion-convection Navier Stokes equations, i.e. without consideration of any pressure gradients, while in the second step this intermediate field will be projected onto a divergence-free vector field. For this purpose a Poisson equation for the pressure has to be solved which is accomplished directly by means of a Fourier transform method. Upwind-biased differences are used for the spatial discretisations and an explicit Adams Bashforth scheme for the time discretisation. The fully developed turbulent flow is homogeneous in the streamwise and the spanwise directions, and we make use of periodic boundary conditions in these directions. The no-slip boundary condition for the velocity is used at the walls, while ad hoc boundary conditions for the pressure are unnecessary because of the employment of a staggered grid.

The numerical experiments are carried out at a Reynolds number of  $Re_\tau = 200$  based on the friction velocity and the channel half width, which compares well with the Reynolds number of the real experiments ( $Re_\tau = 214$ ). While the real experiments besides being performed with an oscillating wall have also been carried out with an oscillating pressure gradient, the numerical experiment was restricted to the case of oscillating walls; in fact both the walls were oscillated in antiphase.

Because of the limited core memory of the workstation (Sparc Ultra 1) that has been used for the simulation so far, the grid had to be confined to  $64 \times 65 \times 64$  ( $n_x, n_y, n_z$ ) grid points. In the direction of the mean flow  $x$ , the grid points are equally spaced over a length of 5 channel heights while only a width of 1.5 channel heights is covered in the spanwise direction  $z$ . There are indications that the compromise between the extension of the computational domain and the spatial resolution is particularly critical in the spanwise direction. In the normal direction  $y$  the spacing smoothly increases from the wall to the centerline of the channel. While the autocorrelation function of the velocity can be expected to decay within the computational domain the correlation length of the pressure probably exceeds the extension of the computational domain. So we have to be prepared for certain effects of the restricted computational domain on the results. However, the future simulations by means of a more powerful computer will be performed on a finer grid and a more extended computational domain. So the effects of these parameters should become obvious.

## FIRST RESULTS

The results obtained so far are based on two simulations that have been performed at two different frequencies

$f_M^+ = 0.01$  and  $f_M^+ = 0.025$  in the quasilinear regime (i.e. the effect of the Reynolds shear stress on the propagation of the shear wave can be disregarded). The phase averages of the streamwise velocity  $u$  and of the Reynolds stress tensor as well as of the variance of the pressure have been evaluated. The departure of the mean values of these quantities from experimental data or from simulated flows with time invariant boundary conditions (e.g. Kim et al., 1987, Rai & Moin, 1991) is not negligible and needs further investigation. Whether or not these differences significantly affect the response of the flow to the oscillation of the walls remains to be studied as well. However, we suppose that the results reflect the right order of the effects.

## Long Time Averages

The figures 1 and 2 show as functions of the normal coordinate  $y$  the mean flow velocity  $\bar{u}$  as well as the turbulent fluctuations of the three velocity components  $u_{rms}$ ,  $v_{rms}$ ,  $w_{rms}$  and of the pressure  $p_{rms}$ . While the experimental data of  $\bar{u}$  and  $u_{rms}$  are satisfactorily reproduced in the viscous sublayer the results of the simulation clearly exceed the experimental values in the buffer layer and in the outer layer. Yet the ratio  $u_{rms}/\bar{u}$  is fairly reproduced for all distances from the wall. It should be mentioned in this context, that the average of the wall shear stress averaged over both the walls has been kept constant at each time step. This implies that the pressure gradient as well as the volume flux vary. While these variations are very slow the amplitudes are high (rms-value of the centerline velocity: ca. 5%). This possibly explains the high values of  $u_{rms}$ . The fluctuations of the normal and the spanwise velocity as well as of the pressure have been compared to simulations that have been performed at time invariant boundary conditions (Kim et al., 1987), and have been found in much better agreement than  $u_{rms}$ . The high value of the mean shear rate  $d\bar{u}/dy$  in the buffer layer coincides with an overshoot of the Reynolds shear stress. So it seems that the divergence of the momentum transport is underestimated maybe due to the large spacing of the grid points in the core region of the flow.

## Shear wave

The most prominent feature of the response of the flow to the oscillation of the walls is the shear wave that is excited at the wall and is propagated towards the central region of the flow. Figure 3 shows the logarithm of the normalized amplitude and the phase of  $\tilde{u}(t) = \langle u(t) \rangle - \bar{u}$  compared to the Stokes solution  $\tilde{u}(t) = u_w \mathcal{R}\{\exp[i2\pi f_M t - (1+i)y/l_s]\}$  that describes the laminar flow field in front of an oscil-

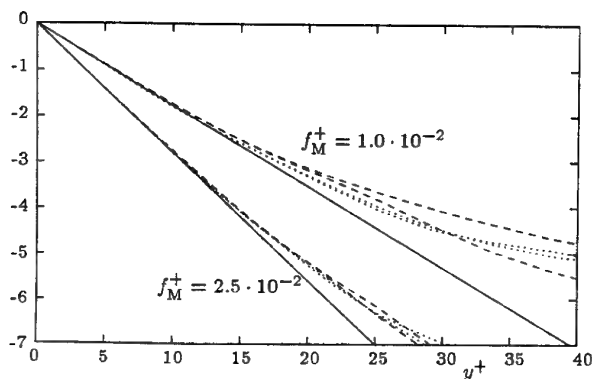


Figure 3: The natural logarithm of the magnitude (···) and the phase (---) of  $\tilde{u}/u_w$  compared to the Stokes solution (—). Equivalent curves pertain to the shear waves at the two oscillating walls in the numerical simulation, indicating the uncertainty of the phase averages.

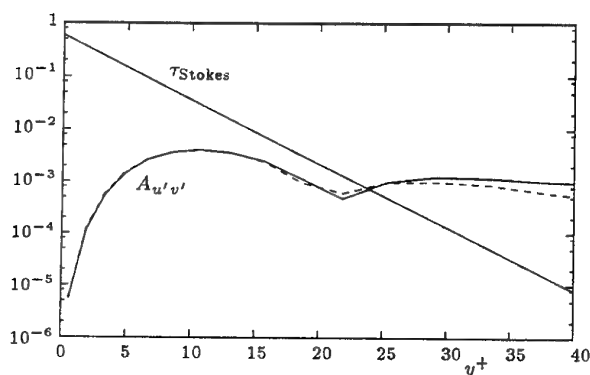


Figure 4: Comparison between the turbulent part of oscillating shear stress and the viscous shear stress of the Stokes wave,  $f_M^+ = 0.025$ . The solid and the dashed curve are obtained at the two walls.

lating wall. Within the first two or three Stokes lengths ( $l_s = \sqrt{\nu/\pi f_M}$ ) excellent agreement between the numerical simulation and the Stokes solution is found. This indicates that according to the expectation the interaction between the turbulent flow and the shear wave is too weak to cause any sensible effect on the propagation of the shear wave in the near wall region. This is so at both the frequencies of the two numerical experiments reported here. A comparison between the turbulent part of oscillating shear stress and the viscous shear stress of the Stokes wave is shown in figure 4 for the higher modulation frequency. The penetration depth of the shear wave, i.e., the Stokes length increases when the frequency decreases; so only at low frequencies the wave enters the buffer layer at an appreciable amplitude which is one of the requirements for a substantial reaction of the turbulence.

### Modulation of Turbulent Intensities

As mentioned earlier the first numerical experiments have been focussed on the high frequency (quasilaminar) regime of the interaction between oscillating shear and wall turbulence. Besides the unexpected modulation of the turbulent intensity of the wall shear stress that has been observed in real experiments, it is the fast convergence of the modulation amplitudes which makes it advisable to start the numerical experiments at the high frequency end. The

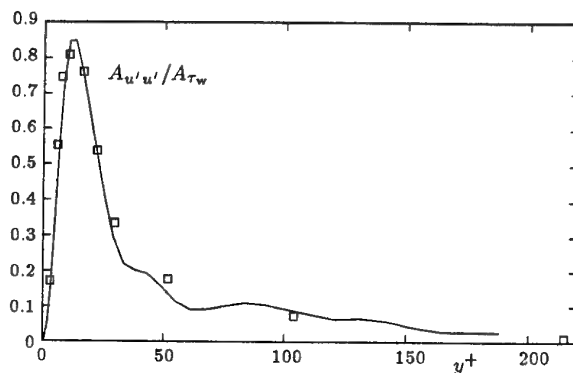


Figure 5: Amplitude of the intensity of the streamwise velocity component ( $\tilde{u}'u'$ ), numerical experiments: —, real experiment: □ □ □,  $f_M^+ = 0.01$

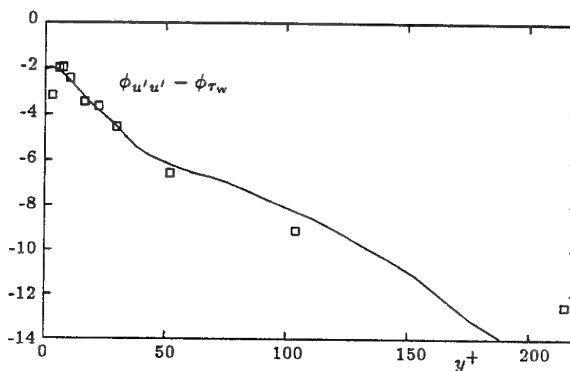


Figure 6: Phase of the intensity of the streamwise velocity component ( $\tilde{u}'u'$ ), same notation as in figure 5

rate of convergence depends on the power spectral density of the quantity to be phase averaged at the modulation frequency, so the steep roll off of the spectra favours the high modulation frequencies. In fact, the amplitudes at the higher frequency became stable faster than at the lower frequency although the amplitudes are much higher at the low frequency.

On the other hand, experimental results in the high frequency regime are rare. Recent experiments that have been performed by one of the authors (C.V.) reach only the lower of the two frequencies of the simulated experiments. A comparison of the modulation amplitude (magnitude and phase) of the intensity of the streamwise velocity component ( $\tilde{u}'u'$ ) is shown in the figures 5 and 6. Actually, the ratio between the complex amplitudes of  $\tilde{u}'u'$  and of the wall shear stress is plotted, and all quantities are nondimensionalized by the friction velocity  $u_\tau$  and the kinematic viscosity. The velocity of the walls had an amplitude of  $1.5u_\tau$  in the numerical experiment and the simulation was extended over 250 periods of the wall oscillation. The agreement is better than could be expected with regard to the uncertainties of both the experiments. The maximum of the response is found close to the wall as expected because of rapid decay of the shear wave. Nevertheless, the amplitude of  $\tilde{u}'u'$  that is detectable even on the centerline of the channel decays much less than the amplitude of  $\tilde{u}$ . The propagation of  $\tilde{u}'u'$  at a speed in the order of  $u_\tau$  has been detected earlier at lower frequencies (Schildknecht et al., 1979, Tardu & Binder, 1994), however, the nature of this type of propagation that can be observed over a distance of

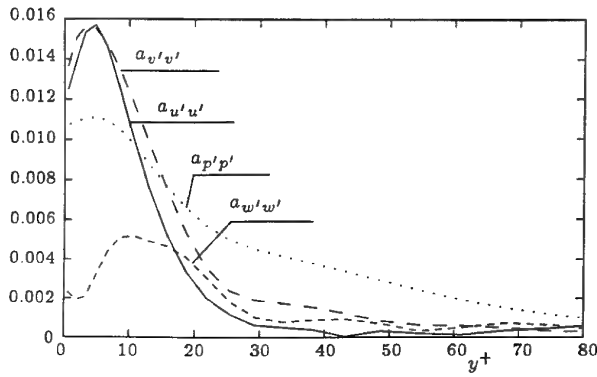


Figure 7: Relative modulation of the three Reynolds normal stress components and the intensity of the pressure fluctuation,  $f_M^+ = 0.025$

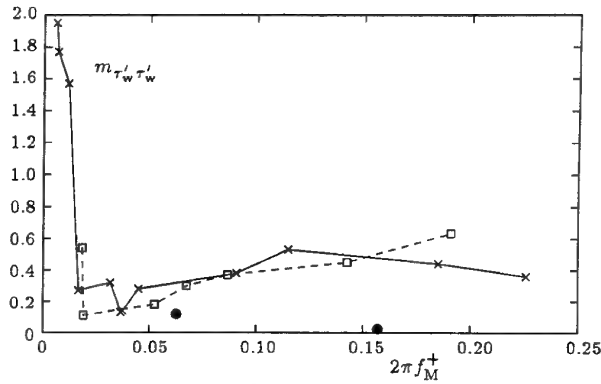


Figure 9: Modulation factor of the intensity of the wall shear stress fluctuation. Experiments: Mao & Hanratty (1986)  $\square$ , Tardu & Binder (1993)  $\times$ , Simulation:  $\bullet$

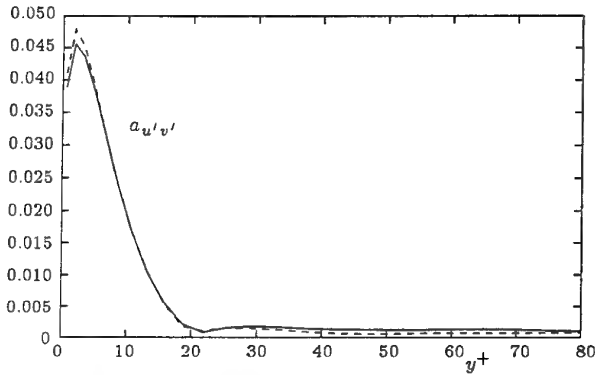


Figure 8: Relative modulation of the Reynolds shear stress component. Results are obtained at both walls, shown as solid and dashed lines.  $f_M^+ = 0.025$

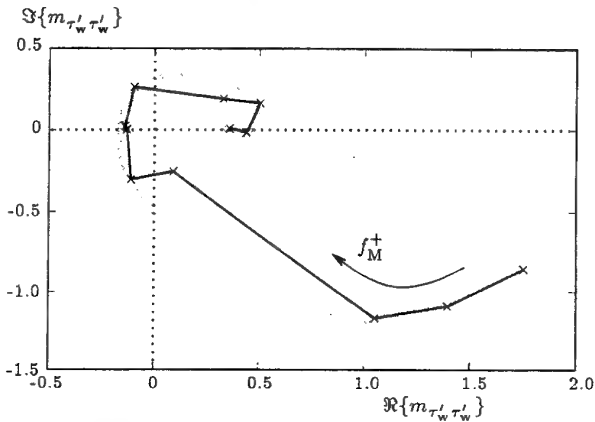


Figure 10: Modulation factor of the intensity of the wall shear stress fluctuation in the complex plane, experiment by Tardu & Binder (1993)

nearly two wavelengths in the present experiments is still unclear.

This kind of propagation could be detected also in the high frequency numerical simulation although the amplitudes of  $\overline{u'u'}$  and the turbulent intensities of the other quantities evaluated so far are even smaller than at the low frequency shown on figures 5 and 6. The amplitudes are depicted on the figures 7 and 8. As expected the maximum of the response has been shifted towards the wall by the increase of the frequency. While the modulation of  $\overline{u'u'}$ ,  $\overline{v'v'}$ , and  $\overline{p'p'}$  is in same order of magnitude,  $\overline{w'w'}$  is remarkably small, and  $\overline{u'v'}$  has a much greater amplitude than  $\overline{u'u'}$  and  $\overline{v'v'}$ . This latter finding indicates that the correlation between the normal and the streamwise velocity and consequently the structure of the flow is considerably affected by the unsteady deformation of the flow.

Finally the modulation of the intensity of the wall shear stress fluctuation is shown in figure 9 for the two simulations. They are compared to results of real experiments that have been performed in two different laboratories (Mao & Hanratty, 1986, Tardu & Binder, 1993). The simulation and the real experiment differ by a factor of about 20, at the high frequency. In order to discuss this discrepancy the complex amplitude of  $\overline{\tau'\tau'}$  for one of the real experiments (Tardu & Binder, 1993) is shown on figure 10. The measured amplitudes can be regarded to more or less follow a spiral that is depicted on the graph. This spiral is typical of the response of a system that is characterized by a delay and a low pass transfer function. However, in

contrast to such a system the spiral converges to a nonzero amplitude. This indicates that the measured response of  $\overline{\tau'\tau'}$  is the sum of the response of a low pass system with a certain group delay and an immediate broadband response characterized by the high frequency amplitude (center of the spiral). So it seems that the numerical experiment reproduces the first part of the response (even though not quantitatively) but gives no indication of the existence of the spectacular latter part.

## CONCLUSIONS

The first results of the direct numerical simulation of a turbulent channel flow that is forced by longitudinal oscillations of the walls show some encouraging agreement with real experiments when the unsteady response is regarded even though some discrepancies with respect to the mean flow are encountered. Particularly striking is the reproduction of the wavelike propagation of the distortion that is introduced at the walls. It is the first time that this phenomenon has been observed in the high frequency regime when the wave can be tracked over three wavelengths at the highest frequency.

Since the interaction between the high frequency deformation of the flow and the turbulence is rather weak the further inspection of the data is promising in so far as practically no feed back on the propagation of the shear wave is to be expected in the near wall region. So the physical



interpretation of the results can be expected to be within the reach of simple models.

In this respect it is interesting to note that the spectacular high frequency modulation of the turbulent shear stress intensity that has been interpreted as the result of a strong nonlinear interaction between the turbulence and the imposed shear deformation could not (yet) be reproduced in the simulated experiment.

## APPENDIX: NOTATIONS

The evaluation of the unsteady response to some forcing of the flow is always based on the phase average  $\langle q(t) \rangle$  of the quantity  $q(t)$  under consideration

$$q(t) = \langle q(t) \rangle + q'(t) \quad (1)$$

where  $q'(t)$  is the "turbulent" part of  $q(t)$ . In many cases the imposed forcing is sinusoidal and the amplitude is small enough to guarantee a linear response of  $\langle q(t) \rangle$ . So in the Fourier series of  $\langle q(t) \rangle$  only the zero and first order terms are important.

$$\langle q(t) \rangle = A_q^{(0)} + 2 \Re \{ A_q^{(1)} e^{i2\pi f_M t} \} \quad (2)$$

$$= \bar{q} + A_q \cdot \cos(2\pi f_M t + \phi_q) \quad (3)$$

$$= \bar{q} + \tilde{q}(t) \quad (4)$$

Then the amplitude  $A_q = |2 A_q^{(1)}|$  is a measure of the sensitivity of  $q$  with respect to the forcing, and the phase  $\phi_q = \arg(A_q^{(1)})$  is a measure of the delay of the response. In order to make different quantities comparable an appropriate normalisation and a physically meaningful phase reference must be chosen. For this purpose the amplitude of the quantity is referred to its mean value:  $a_q = 2 A_q^{(1)} / A_q^{(0)}$ . A more general measure of the strength of the response is the ratio between this relative amplitude  $a_q$  and some relative amplitude of the forcing. Actually the wall shear stress is regarded as the physical quantity that forces the flow. So  $m_q = a_q / a_{\tau_w}$  is used in many cases to quantify the response of the quantity  $q$ , and the phases are measured with respect to  $\phi_{\tau_w}$ .

## REFERENCES

- Chorin, A. J., 1969, "On the convergence of discrete approximations to the Navier Stokes equations", *Math. Comput.*, **23**, pp. 341-353
- Finnicum, D. S., Hanratty, T. J., 1988, "Influence of imposed flow oscillations on turbulence", *PCH PhysicoChemical Hydrodynamics*, Vol. 10, No. 5/6, pp. 585-598
- Ickler, A., Völtz, C., Ronneberger, D., 1997, "Reaktion der turbulenten Kanalströmung auf longitudinale Wandschwingungen bei hohen Frequenzen", *to be published in ZAMM*
- Kim, J., Moin, P., Moser, R., 1987, "Turbulence statistics in fully developed channel flow at low Reynolds number", *J. Fluid Mech.*, Vol. 177, pp. 133-166
- Mao, Z.-X., Hanratty, T. J., 1986, "Studies of the wall shear stress in a turbulent pulsating pipe flow", *J. Fluid Mech.*, Vol. 170, pp. 545-564
- Rai, M. M., Moin, P., 1991, "Direct simulation of turbulent flow using finite-difference schemes", *J. Comput. Phys.*, **96**, pp. 15-53
- Schildknecht, M., Miller, J. A., Meier, G. E. A., 1979, "The influence of suction on the structure of turbulence in fully developed pipe flow", *J. Fluid Mech.*, Vol. 90, part 1, pp. 67-107
- Tardu, S. F., Binder, G., 1993, "Wall shear stress modulation in an unsteady turbulent channel flow with high

imposed frequencies", *Phys. Fluids*, Vol. 5(8), pp. 2028-2037

Tardu, S. F., Binder, G., Blackwelder, R. F., 1994, "Turbulent channel flow with large-amplitude velocity oscillations", *J. Fluid Mech.*, Vol. 267, pp. 109-151

# SECOND-MOMENT MODELLING OF PERIODIC AND TRANSIENT PIPE FLOW

M. A. Cotton<sup>(1)</sup>, A. W. Guy<sup>(1)(2)</sup>, B. E. Launder<sup>(2)</sup>

<sup>(1)</sup> School of Engineering  
University of Manchester  
Manchester M13 9PL  
United Kingdom

<sup>(2)</sup> Department of Mechanical Engineering  
UMIST  
Manchester M60 1QD  
United Kingdom

## ABSTRACT

Periodic and ramp-transient flows provide circumstances where non-equilibrium (stress transport) effects on turbulence may be large. Thus, in application to such flows, it might be expected that Reynolds stress transport models would be inherently superior to simpler linear eddy viscosity models. The computations reported here have explored this proposition. The basic flow considered is that of spatially fully-developed flow in a circular pipe onto which prescribed temporal variations of the mass flow rate or bulk velocity are imposed. It follows that the strain field is one of simple shear and the question of non-equilibrium effects may therefore be considered separately from other aspects of Reynolds stress transport modelling pertinent to more complex strain fields.

## INTRODUCTION

All turbulent flows are unsteady if examined in terms of a series of instantaneous realizations; in discussion of steady conditions reference is made to the statistically stationary property of some flows. The more general case, however, is clearly of a turbulent flow with statistical features (phase- or ensemble-averages) that vary in time. It is common practice to analyse unsteady flows using an assumption of pseudo-steadiness: thus, at a given phase position of a periodic flow, the flow is taken to be identical to a steady flow generated at the same prescribed conditions (e.g. Reynolds number) as those of the selected phase angle.

A number of experiments on pipe flow (as well as other geometries) have been conducted in order to better understand the dynamics of unsteady flows, and hence, by implication, more accurately delineate the applicable range of pseudo-steady assumptions. Imposed unsteadiness can have marked effects upon a range of flow features (however, provided that separation does not occur, it would appear that the long-time averages of a periodic flow are not greatly affected). The present contribution concentrates on the data of Finnium and Hanratty (1988) and Tu and Ramaprian (1983) for periodic flows, and the data of He (1992) for ramp-transient flows.

Perhaps surprisingly, relatively little work concerning the calculation of unsteady turbulent flows has appeared

in the literature. Amongst isolated examples, two-equation modelling studies were undertaken by Blondeaux and Colombini (1985) and Ismael and Cotton (1996); Kebede et al. (1985) reported Reynolds stress transport model results, although their conclusions were uncertain due to the incomplete convergence of the model solutions. The present study represents a renewed attempt to examine the unsteady flow performance of a Reynolds stress transport model and to make comparisons with a two-equation eddy viscosity model.

## TURBULENCE MODELLING

The appropriate average for the periodic flow cases examined here is the phase-average,  $\langle \chi \rangle$ , defined as:

$$\langle \chi(r, \theta) \rangle = \lim_{N \rightarrow \infty} \frac{1}{N} \sum_{n=0}^{N-1} \tilde{\chi}(r, \theta + 2\pi n) \quad (1)$$

where  $\tilde{\chi}$  represents an instantaneous quantity,  $\theta = \omega t$ , and  $r$  is the radial coordinate. In ramp-transients, the ensemble-average is formed in an analogous manner, but is now based upon repeated realizations of the unsteady flow. The phase- or ensemble-averaged spatially fully-developed momentum equation then parallels the familiar Reynolds-averaged form for application to steady flows:

$$\frac{\partial U_i}{\partial t} = -\frac{1}{\rho} \frac{\partial p}{\partial x_i} + \frac{\partial}{\partial x_j} \left[ \nu \frac{\partial U_i}{\partial x_j} - \langle u_i u_j \rangle \right] \quad (2)$$

Upon transformation to cylindrical polar coordinates the only Reynolds stress component appearing in the axial momentum equation is the shear stress  $\langle u_r u_z \rangle$  (where the  $z$ -coordinate is aligned with the pipe axis). Other elements of the Reynolds stress tensor arise in achieving closure at the second-moment level.

The results reported below are based upon low-Reynolds-number versions of a  $k$ - $\epsilon$  eddy viscosity model and a Reynolds stress transport model. The  $k$ - $\epsilon$  model selected is the widely-adopted scheme of Launder and Sharma (1974) (the model which formed the basis of the earlier study of Ismael and Cotton). The Reynolds stress transport model

employed is due to Shima (1989) and represents a minor re-optimization of the Launder and Shima (1989) model. The chosen model possesses some acknowledged disadvantages with regard to more recent stress transport models, but has nonetheless established a good track record in a range of steady two- and three-dimensional thin shear flows. In the following text the abbreviations 'EVM' and 'RSTM' are generally used to denote the two specific models adopted. The essential features of the two models are outlined below and the reader interested in complete descriptions is referred to the relevant original papers.

### Eddy Viscosity Model

The EVM consists of a constitutive equation and transport equations for the turbulent kinetic energy,  $k$ , and a modified dissipation variable,  $\hat{\epsilon}$ :

$$-\langle u_i u_j \rangle = \nu_t \left( \frac{\partial U_i}{\partial x_j} + \frac{\partial U_j}{\partial x_i} \right) - \frac{2}{3} \delta_{ij} k \quad (3)$$

where

$$\nu_t = c_\mu f_\mu \frac{k^2}{\hat{\epsilon}} \quad (4)$$

and

$$\frac{\partial k}{\partial t} = P + d - \epsilon \quad (5)$$

$$\frac{\partial \hat{\epsilon}}{\partial t} = c_{e1} \frac{\hat{\epsilon}}{k} P + d_\epsilon - c_{e2} f_2 \frac{\hat{\epsilon}^2}{k} + E \quad (6)$$

$P$  is the rate of production of  $k$  by mean strain. The turbulent contributions to diffusion (elements of  $d$  and  $d_\epsilon$ ) are modelled using the isotropic eddy viscosity concept and the additional source term,  $E$ , appearing in the  $\hat{\epsilon}$ -transport equation is a function of second derivatives of the mean velocity.  $c_\mu$ ,  $c_{e1}$ , and  $c_{e2}$  are constant coefficients. The damping function,  $f_\mu$ , and the destruction-of-dissipation function,  $f_2$ , are dependent on the turbulent Reynolds number,  $Re_t$ . It follows that, in contrast to a number of other two-equation models, the presently adopted model is entirely local, i.e. wholly independent of wall distance; note, however, that reliance is placed upon viscosity as the sole agent of damping via the use of  $Re_t$ .

### Reynolds Stress Transport Model

Individual Reynolds stresses now appear as the dependent variables of rate-of-change equations:

$$\frac{\partial \langle u_i u_j \rangle}{\partial t} = P_{ij} + \phi_{ij} + d_{ij} - \epsilon_{ij} \quad (7)$$

At this level of closure the mean strain production,  $P_{ij}$ , is an exact expression and the redistributive pressure-strain correlation,  $\phi_{ij}$ , must be modelled. In the Shima closure  $\phi_{ij}$  is modelled conventionally as the sum of linear return-to-isotropy and isotropization-of-production elements; associated with each of these two elements is a wall-reflection expression (corrections that are non-local, being based upon wall distance). The coefficients of the pressure-strain correlation, originally taken to be constant by Gibson and Launder (1978), are extended to incorporate functions of the Reynolds stress tensor invariants and  $Re_t$ . The turbulent contribution to  $d_{ij}$  is modelled using the generalized gradient diffusion hypothesis (GGDH), and local isotropy is assumed for the determination of  $\epsilon_{ij}$ .

The turbulent kinetic energy dissipation rate,  $\epsilon$ , is obtained from a further transport equation:

$$\frac{\partial \epsilon}{\partial t} = (c_{e1} + \psi_1 + \psi_2) \frac{\epsilon}{k} P + d_\epsilon - c_{e2} \frac{\epsilon^2}{k} \quad (8)$$

$\psi_1$  and  $\psi_2$  are functions of the Reynolds stress tensor invariants,  $Re_t$ , and  $(P/\epsilon)$ ; the Shima model differs from that of Launder and Shima in the tuning of these expressions. The GGDH is again employed in the determination of  $d_\epsilon$ .

The EVM and RSTM equations are transformed to cylindrical polar coordinates prior to numerical solution. In the spatially fully-developed pipe flows considered, RSTM transport equations must be solved for the Reynolds shear stress,  $\langle u_r u_z \rangle$ , the three normal stresses, and the dissipation rate. The well-established parabolic solver PASS-ABLE, see Leschziner (1982), has been adapted to march in time and hence compute successive radial distributions of flow quantities. An expanding radial grid of 101 nodes, with approximately half the nodes distributed across the near-wall region ( $y^+ < 50$ ), is used for all calculations. In the EVM all flow quantities are computed on a single set of radial nodes; this primary grid is used for the velocity in the RSTM scheme, but all turbulence quantities are stored on a second staggered grid. The maximum time step is obtained as a time-of-travel analogue of one hundred viscous length units (thus  $100(\nu/U_r)/U_b$ ), where both velocities correspond to peak  $Re_b$ . The value derived corresponds to approximately 1000 steps per cycle for the periodic flows considered. An under-relaxation factor of 0.2 is applied to all turbulence quantities in order to improve stability, and convergence is assessed by considering the residuals of the computed  $k$ -transport equations. Tests have been carried out to ensure that the reported numerical solutions are accurate to within 1% on wall shear stress.

## RESULTS

The EVM and RSTM closures are compared below with experimental data for unsteady spatially fully-developed pipe flows. Two forms of imposed unsteadiness are considered: periodic flows in which the bulk velocity varies as a sinusoid imposed upon a steady level, and ramp-transients in which the bulk velocity increases linearly between two steady levels.

### Periodic Flows

The bulk velocity is here referenced as a cosine variation:

$$U_b(t) = \bar{U}_b + |U_b| \cos \omega t \quad (9)$$

A single instantaneous flow variable may be decomposed into a phase-average and a turbulent fluctuation, equation (1). Correlations, such as elements of the Reynolds stress tensor, may be decomposed in a similar manner. The variation of such phase-averages is examined against phase angle (at prescribed radial positions) in Figures 3 to 6. Firstly, however, an overview of periodic flow behaviour is obtained using an approximate representation of the phase-averaged wall shear stress as characterized by its long-time mean level and fundamental harmonic:

$$\langle \tau_w \rangle \approx \bar{\tau}_w + |\tau_w| \cos(\omega t + \varphi_\tau) \quad (10)$$

Comparison is drawn with the experiments of Finnium and Hanratty (1988) which span a two-decade range of the frequency parameter,  $\omega^+ = \omega \nu / \bar{U}_\tau^2$ , where  $\bar{U}_\tau^2 = \bar{\tau}_w / \rho$ . Water was used as the working fluid in a pipe of 5.08 cm diameter. Sinusoidal oscillations were imposed on the flow rate and the amplitude of the centreline velocity was fixed at  $10.0 \pm 0.2\%$  of the long-time mean level. The mean bulk Reynolds number,  $Re_b (= \bar{U}_b D / \nu)$ , was different for each individual test case (in fact  $8,650 \leq Re_b \leq 44,900$ ). Values of the wall shear stress were obtained using an electrochemical technique. Figures 1 and 2 show the variation of the amplitude and phase of the first harmonic of wall shear stress plotted against the frequency parameter. At low frequencies (below  $\omega^+ \approx 0.001$ ) the wall shear stress response is approximately 'quasi-steady', while at sufficiently high

frequencies (above  $\omega^+ \approx 0.05$ ) 'quasi-laminar' behaviour is evident. Mao and Hanratty (1986) derived the following relations for quasi-laminar oscillations :

$$|\tau_w|/\rho|U_c|\overline{U}_\tau = \sqrt{\omega^+}, \quad \varphi_\tau - \varphi_{-dp/dz} = -45^\circ \quad (11)$$

which indicate a collapse of data at high frequencies. However, for oscillations where the wall shear stress responds in a quasi-steady manner, the asymptotic relations are dependent on Reynolds number. In equation (11) and Figure 1  $|\tau_w|$  is normalized using density, the amplitude of the centreline velocity, and the mean friction velocity. The experimental data for wall shear stress amplitude reveal a distinct minimum at frequencies centred upon  $\omega^+ \approx 0.01$ , a value intermediate between the quasi-steady and quasi-laminar asymptotes. This feature is resolved by the EVM, but not by the RSTM. The wall shear stress phase results shown in Figure 2 are stated relative to the phase of the (positive) pressure gradient. In this case the EVM results exhibit an overshoot with respect to data at  $\omega^+ \approx 0.02$ , whereas the RSTM results increase monotonically up to the asymptote. On close examination it is seen that the data might indicate the presence of a poorly-defined maximum at  $\omega^+ \approx 0.02$ , but alternatively experimental uncertainties might account for the distribution of the measured points.

Tu and Ramaprian (1983) employed water as the working fluid in a 5.08cm diameter pipe. The flow rate was varied sinusoidally on a long-time mean level and detailed flow data (including wall shear stress, axial velocity, and Reynolds normal and shear stress) were obtained. The wall shear stress was measured using a thermal technique and the axial velocity was measured using a single-component LDA system. The phase-averaged Reynolds shear stress,  $\langle u_r u_z \rangle$ , was not measured directly, but instead deduced from an integrated form of the momentum equation and evaluated using measurements of the wall shear stress and axial mean velocity. Present attention is focused upon a single test case for which  $Re_b = 49,000$ , Strouhal number  $\omega D/\overline{U}_b = 0.175$ , and relative amplitude  $|U_b|/\overline{U}_b = 0.64$ . (The actual bulk velocity modulation was reported by Tu and Ramaprian to be 'very nearly sinusoidal'. In a sensitivity test turbulence model solutions were obtained for this prescribed 'point-by-point' bulk velocity variation, however, it was found that the solutions obtained were essentially identical to those obtained using equation (9).) The conditions of Tu and Ramaprian's experiment correspond to  $\omega^+ \approx 0.0014$ , a dimensionless frequency which is sufficiently high to produce marked departures from the quasi-steady state in the appearance of flow profiles, but sufficiently low that the indirect measurements of  $\langle u_r u_z \rangle$  are believed to be reliable. (Note, however, that the wall shear stress would be deduced from Figures 1 and 2 to be approaching the quasi-steady condition.)

In Figure 3 the two models are compared against data for the phase-averaged Reynolds shear stress at a quarter radius from the pipe wall (corresponding to a long-time mean  $y^+$  of approximately 300) : it is seen that the RSTM is in closer agreement with the data than is the EVM and that, as expected, the RSTM which incorporates a rate equation for  $\langle u_r u_z \rangle$  lags the algebraic EVM. These findings are reinforced by results for a second location much closer to the pipe axis (corresponding to a long-time mean  $y^+$  of approximately 1100) where diffusion becomes more important, see Figure 4.

Experimental data for the phase-averaged axial normal stress together with RSTM results are shown in Figures 5 and 6. In addition, computed variations of the turbulent kinetic energy have been included in order to allow comparison between the EVM and RSTM. The RSTM results for  $\langle u_z^2 \rangle$  are in fairly close accord with the measurements at  $y/R=0.25$  (Figure 5), but exhibit a lag at  $y/R=0.9$  (Figure 6).

Comparing Figures 4 and 6 (i.e. the variations at  $y/R=0.9$ ), it is seen that the experimental data for  $\langle u_r u_z \rangle$  and  $\langle u_z^2 \rangle$  are approximately in phase. In contrast, the RSTM indicates a moderate lag (approximately  $20^\circ$ ) of the normal stress and turbulent kinetic energy with respect to the shear stress. It is interesting to note that the EVM yields the same lag in  $k$  with respect to  $\langle u_r u_z \rangle$ ; this shared feature of the EVM and RSTM results might be attributable to the temporal variation of the dissipation rate,  $\epsilon$ , which is calculated from similar transport equations in the two models (some similarities and differences between the EVM and RSTM are further highlighted below).

### Ramp-Transients

A second LDA dataset for unsteady flow in pipes has been compiled by He (1992). The data are for water flow in a pipe of diameter 5.04cm and the imposed transient takes the form of a linearly-increasing ramp between initial and final steady levels ( $Re_b=7,000$  and  $Re_b=45,400$ ; a 6.5 fold increase in flow rate). The test case selected is that with the shortest ramp period ( $T=5$  seconds) for which stress transport effects are the greatest. A two-component LDA system was employed by He and hence it was possible to measure all elements of the Reynolds stress tensor. In the present study the EVM and RSTM are compared with data for the ensemble-averaged Reynolds shear stress and turbulent kinetic energy. Results are normalized using the initial value of bulk velocity,  $(U_b)_0$ , and are plotted against  $T_r = t/T$ .

Figure 7 shows the ensemble-averaged Reynolds shear stress data as measured at near-wall ( $y/R=0.07$ ) and near-axis ( $y/R=0.84$ ) locations together with the corresponding EVM and RSTM results. (At the initial steady level these positions correspond to  $y^+$  values of approximately 20 and 200, respectively; at the higher steady level the corresponding  $y^+$  values are approximately 80 and 1000.) Near the wall both models respond in a similar manner and are in quite close agreement with the experimental data. In greater detail it may be observed that the RSTM responds more rapidly in the initial stage of the transient. The RSTM variation in the vicinity of  $T_r=0.4$  exhibits a brief plateau in an otherwise smoothly increasing level (although the scattered data do not wholly support the existence of such a plateau). The differences between the EVM and RSTM are quite possibly attributable to the model 'fundamentals', i.e. that the RSTM incorporates rate equations for the individual stresses and the production of each Reynolds stress is exact within the closure. Closer to the pipe axis the representation of diffusion again becomes more critical and the measured delay of  $\langle u_r u_z \rangle$  is evidently captured better by the RSTM. (The mechanisms governing the delay of the core flow response are considered in some detail by Jackson and He, 1993.)

Results for the ensemble-averaged turbulent kinetic energy are shown in Figure 8. Trends in the experimental data for  $k$  are generally similar to those for  $\langle u_r u_z \rangle$ , however, a plateau is now clearly evident in the near-wall variation. The two models show the same general behaviour in the development of  $k$  as in the development of  $\langle u_r u_z \rangle$ . Now, however, there is poorer agreement with data, at least at lower levels of turbulent kinetic energy. It has been suggested by He (personal communication) that signal noise might have given rise to spuriously high experimental levels of the single component correlations ( $\langle u_z^2 \rangle$ ,  $\langle u_r^2 \rangle$ , and  $\langle u_\theta^2 \rangle$ ) occurring in  $k$ . Such systematic experimental uncertainty does not occur for  $\langle u_r u_z \rangle$  because the noise from two distinct instantaneous velocity signals is uncorrelated. A related point is that the slow increase in the level of the near-axis experimental data for  $k$  may, in fact, reflect increasing noise and not the true response of turbu-

lence which experiences a delay associated with propagation from the wall region.

## SUMMARY

The EVM of Launder and Sharma (1974) and the RSTM of Shima (1989) have been compared against experimental data for spatially fully-developed turbulent pipe flow onto which controlled temporal flow variations have been imposed. Two types of unsteadiness have been examined, namely periodic flows (using the data of Finnium and Hanratty, 1988 and Tu and Ramaprian, 1983) and ramp-transient flows (using the data of He, 1992).

Within the framework of the RSTM the Reynolds stresses are determined from transport equations, whereas an algebraic expression is employed in the EVM. Other differences exist between the two formulations: for example, the EVM is entirely local (however 'damping' is achieved solely through the use of  $Re_t$ , a viscous parameter); the RSTM includes wall distance corrections, rendering the model non-local, although expressions involving the turbulence anisotropy largely replace  $Re_t$  in various model functions. The two diffusion models are also different, as are the detailed treatments of dissipation. Thus, although our principal interest lies in the treatment of non-equilibrium effects associated with unsteadiness, there exist other factors which influence model performance.

The above caveat is particularly relevant to the comparisons with the phase-averaged wall shear stress data of Finnium and Hanratty: here the EVM appears to perform better in relation to the amplitude data, whereas, in the approach to quasi-laminar behaviour, the RSTM captures the measured phase response more accurately. Work continues in an effort to improve our understanding of these findings. Clearer results emerge in examination of the periodic flow measurements of Tu and Ramaprian: comparison of the computed  $\langle u, u_z \rangle$  variations show that the RSTM lags the EVM and is in better agreement with the data. Such a result is to be expected because of the inclusion of transport equations in the former closure. The RSTM variation of  $\langle u_z^2 \rangle$  at  $y/R=0.25$  shows encouraging agreement with the data, but poorer agreement at  $y/R=0.9$ .

The comparisons reported with the ramp-transient flow data of He show that the RSTM resolves the near-axis delay in the response of  $\langle u, u_z \rangle$  more accurately than does the EVM. The findings are somewhat less clear-cut in relation to He's data for  $k$ . It appears, however, that LDA signal noise may have contributed to artificially high values of  $k$ .

The present investigation sought to establish whether a Reynolds stress transport model would prove superior to an eddy viscosity model in application to unsteady pipe flows. To summarize our findings to date, the Reynolds stress transport model is better suited to the task of capturing temporal response; nonetheless, apparent failings in the calculation of the wall shear stress and the core flow have been identified.

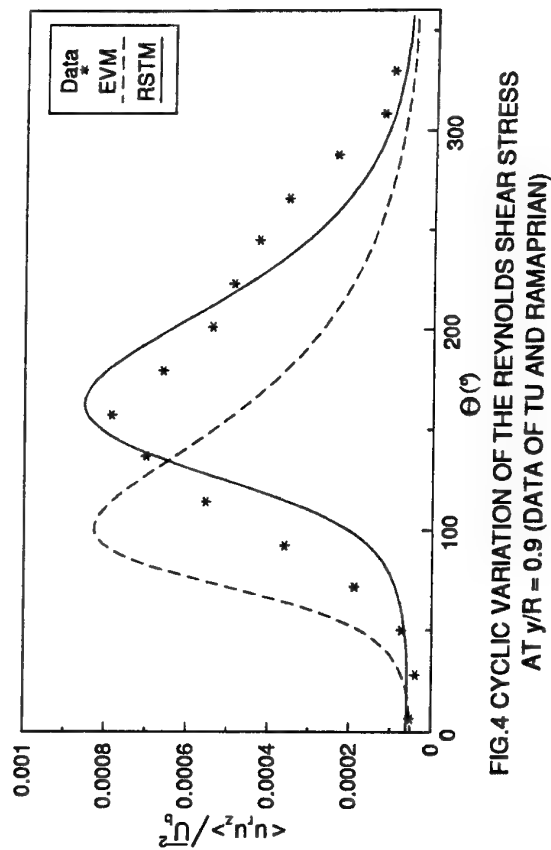
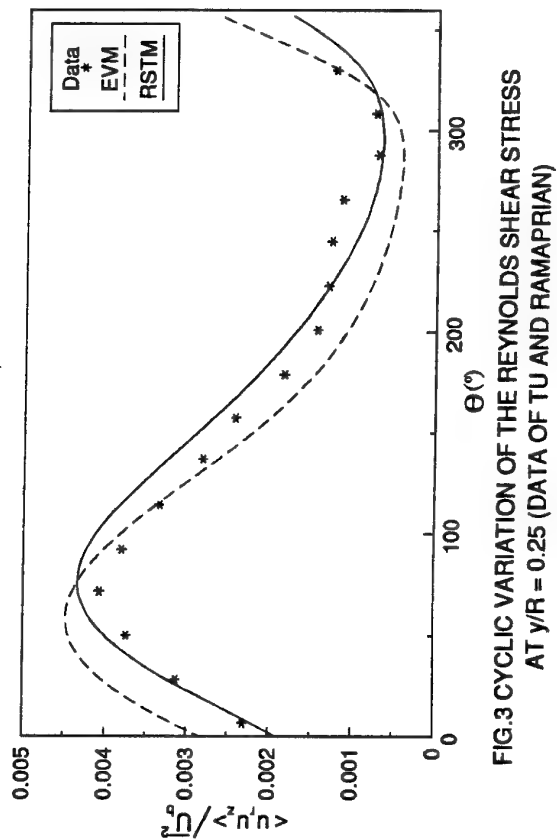
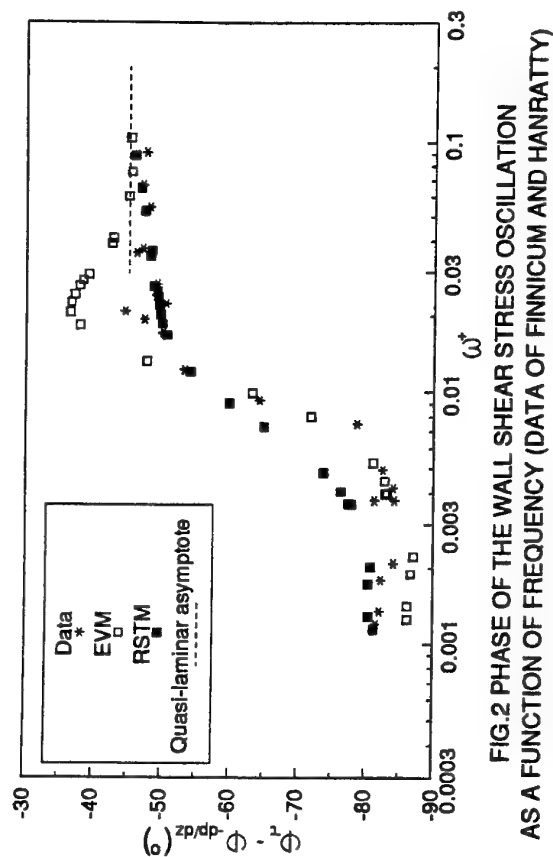
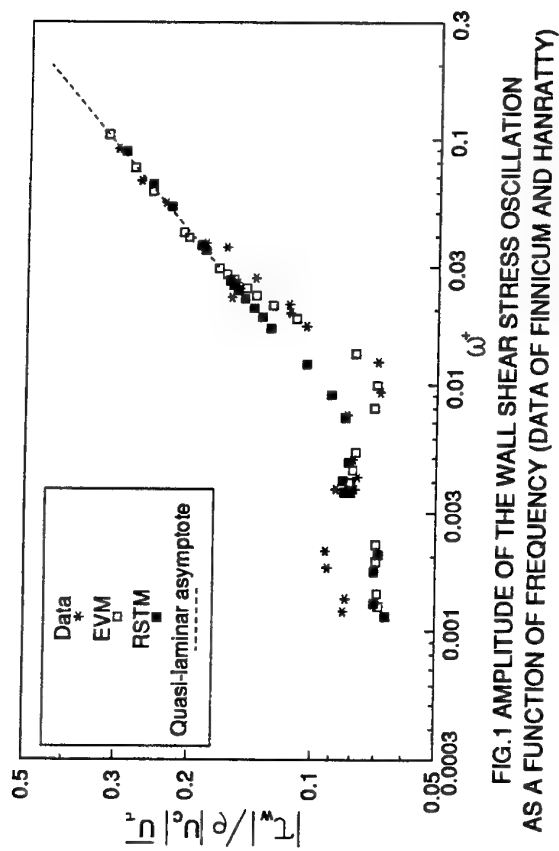
## ACKNOWLEDGEMENTS

We are grateful to our colleagues Dr.S.He and Dr.T.J.Craft for their input at several stages of the research.

A.W.Guy was supported by an EPSRC Research Studentship over the period of this study.

## REFERENCES

- Blondeaux, P., and Colombini, M., 1985, "Pulsatile Turbulent Pipe Flow", *Proc. 5th Symposium on Turbulent Shear Flows*, Cornell University, USA.
- Finnium, D.S., and Hanratty, T.J., 1988, "Influence of Imposed Flow Oscillations on Turbulence", *Physico-Chemical Hydrodynamics*, Vol.10, pp.585-598.
- Gibson, M.M., and Launder, B.E., 1978, "Ground Effects on Pressure Fluctuations in the Atmospheric Boundary Layer", *J. Fluid Mechanics*, Vol.86, pp.491-511.
- He, S., 1992, "On Transient Turbulent Pipe Flow", Ph.D. Thesis, University of Manchester, UK.
- Ismael, J.O., and Cotton, M.A., 1996, "Calculations of Wall Shear Stress in Harmonically Oscillated Turbulent Pipe Flow Using a Low-Reynolds-Number  $k-\epsilon$  Model", *ASME J. Fluids Engineering*, Vol.118, pp.189-194.
- Jackson, J.D., and He, S., 1993, "Turbulence Propagation in Transient Turbulent Shear Flows", in *Near-Wall Turbulent Flows*, (eds. So, R.M.C., Speziale, C.G., and Launder, B.E.), Elsevier, pp.939-948.
- Kebede, W., Launder, B.E., and Younis, B.A., 1985, "Large-Amplitude Periodic Pipe Flow: A Second-Moment Closure Study", *Proc. 5th Symposium on Turbulent Shear Flows*, Cornell University, USA.
- Launder, B.E., and Sharma, B.I., 1974, "Application of the Energy-Dissipation Model of Turbulence to the Calculation of Flow Near a Spinning Disc", *Letters in Heat and Mass Transfer*, Vol.1, pp.131-138.
- Launder, B.E., and Shima, N., 1989, "Second-Moment Closure for the Near-Wall Sublayer: Development and Application", *AIAA Journal*, Vol.27, pp.1319-1325.
- Leschziner, M.A., 1982, "An Introduction and Guide to the Computer Code PASSABLE", Report, UMIST, UK.
- Mao, Z.-X., and Hanratty, T.J., 1986, "Studies of the Wall Shear Stress in a Turbulent Pulsating Pipe Flow", *J. Fluid Mechanics*, Vol.170, pp.545-564.
- Shima, N., 1989, "Calculation of a Variety of Boundary Layers with a Second-Moment Closure Applicable up to a Wall", *Proc. 7th Symposium on Turbulent Shear Flows*, Stanford University, USA.
- Tu, S.W., and Ramaprian, B.R., 1983, "Fully Developed Periodic Turbulent Pipe Flow. Part 1. Main Experimental Results and Comparison with Predictions", *J. Fluid Mechanics*, Vol.137, pp.31-58.



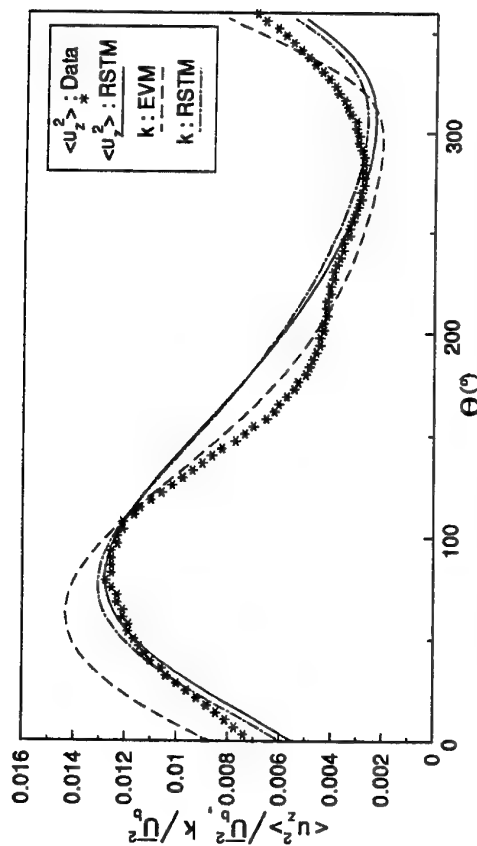


FIG.5 CYCLIC VARIATION OF THE AXIAL NORMAL STRESS AND k  
AT y/R = 0.25 (DATA OF TU AND RAMAPRIAN)

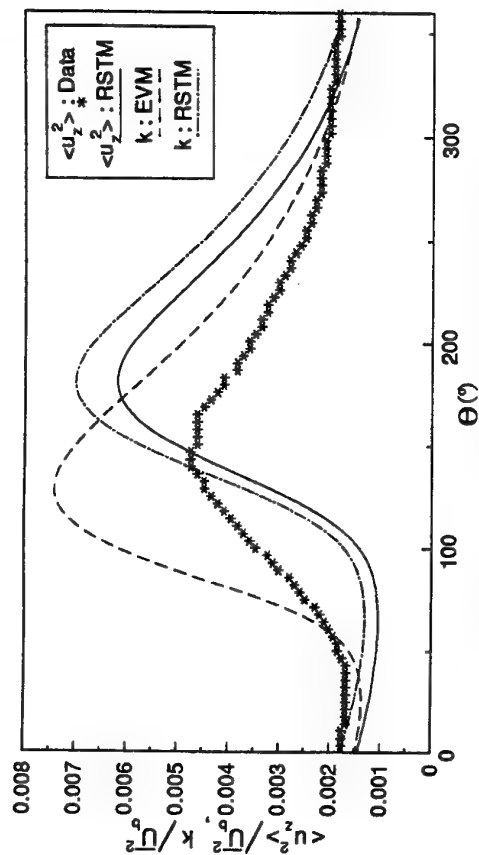


FIG.6 CYCLIC VARIATION OF THE AXIAL NORMAL STRESS AND k  
AT y/R = 0.9 (DATA OF TU AND RAMAPRIAN)

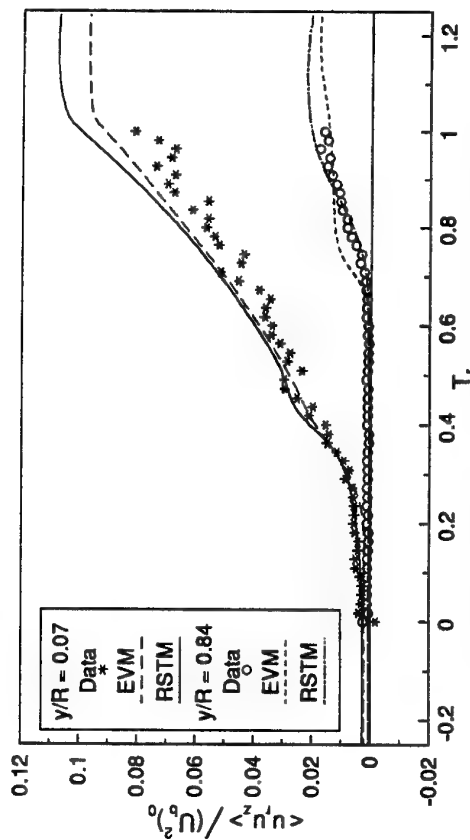


FIG.7 VARIATIONS OF THE REYNOLDS SHEAR STRESS  
AT TWO RADIAL POSITIONS IN A RAMP TRANSIENT (DATA OF HE)

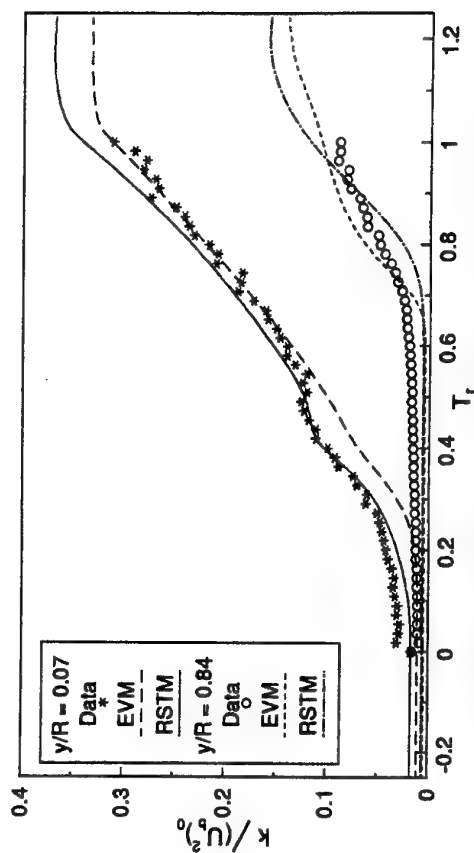


FIG.8 VARIATIONS OF THE TURBULENT KINETIC ENERGY  
AT TWO RADIAL POSITIONS IN A RAMP TRANSIENT (DATA OF HE)

# RELAXATION PROCESS OF 2D ASYMMETRIC TURBULENT CHANNEL FLOW SUBJECTED TO SUDDEN REPLACEMENT OF SMOOTH AND ROUGH WALLS

Masafumi Miyata  
Department of Mechanical System Engineering  
Yamanashi University  
Takeda 4-3-11  
Kofu 400  
Japan

## ABSTRACT

This paper describes the experimental results obtained in the relaxation process of a two-dimensional smooth-rough asymmetric turbulent channel flow into its anti-symmetric state with respect to the channel mid-point. Extensive measurements of the mean velocity, the Reynolds stresses and the wall shear stress conducted for the protruding and flush-mounted roughness elements revealed that no significant change in the relaxation process is found between them except for the region just upstream and downstream of the step. The streamwise variations of the mean and the fluctuating velocity profiles as well as the wall shear stress correspond well with that for the maximum mean velocity in a cross-section and it can sensitively represent how far the relaxation proceeds. The so-called universal Karman constant does vary in the region  $x < 20h$ , which may cause the log-law dependent methods for the wall shear stress to give a result showing an over- or under-shooting.

## NOMENCLATURE

$h$ ; channel half height  
 $U$ ;  $x$  component of mean velocity  
 $U_{max}$ ; maximum mean velocity in a cross-section  
 $U_e$ ; maximum mean velocity at the channel exit  
 $U^+ = U/u_\tau$   
 $u, v$ ;  $x, y$  components of fluctuating velocity  
 $p$ ; static pressure  
 $-\rho \bar{u}v$ ; Reynolds shear stress  
 $x, y$ ; streamwise and transverse coordinates, respectively  
(see Figs.1 and 2)

$y^+ = yu_\tau/\nu$   
 $\tau_w$ ; wall shear stress  
 $u_\tau$ ; friction velocity  $= \sqrt{\tau_w/\rho}$

## INTRODUCTION

The problem of a response of a fully developed or self-preserving flow to a sudden change in the boundary condition

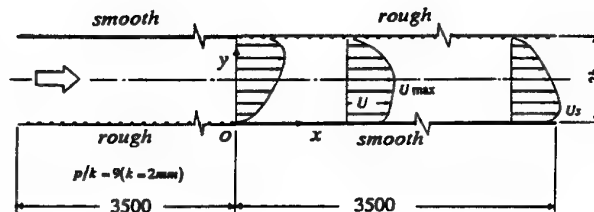


Fig.1 Schematic of flow configuration and coordinate system. The origin of  $x$  is the mid point between the last and the first roughness elements in the upstream and the downstream halves of the channel, respectively.

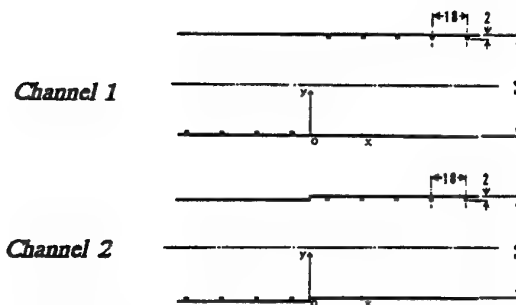


Fig.2 Details of wall geometry in channels 1 and 2.

has long attracted the interest of many researchers, because it provides a useful way of understanding the complex mechanism of the turbulent shear flow in analogy with the black box concept as proposed by Clauser(1956). Many investigations were made on the boundary layer flow subject to sudden change in wall roughness: Antonia & Luxton(1971) made measurements of the zero pressure gradient boundary layer subject to step change in wall roughness and the response



of a turbulent boundary layer to a short length of surface roughness was investigated by Andreopoulos & Wood(1982). Less is the case for the conduit flow. A general review on these materials was given by Smits & Wood(1985).

The fully developed asymmetric channel flow studied by Hanjalic & Launder(1972) is itself a complex flow in the sense that the flows on different surface roughness and hence with different turbulent structures interact with each other. Therefore, it will be very interesting and useful to investigate the relaxation process of a fully developed smooth-rough asymmetric flow in a two-dimensional channel into its anti-symmetric state, i.e. a fully developed rough-smooth asymmetric one.

The main purpose of this study is to document a comprehensive set of reliable data in the relaxation process of the perturbed asymmetric channel flow into its anti-symmetric one to improve physical understanding of the non-equilibrium turbulent shear flow.

## EXPERIMENTAL APPARATUS AND METHOD

The two-dimensional channel used has a length of 7m, where one of the walls in the upstream half and the opposite wall in the downstream half were roughened with 2 mm square ribs spaced to give a pitch to height ratio of 9 and all the remaining parts were left smooth. Fig.1 shows a schematic diagram of the flow geometry, the coordinate system and some symbols employed. The flow configuration provides a fully developed asymmetric flow similar to that studied by Hanjalic & Launder (1972) in the channel mid-section and its anti-symmetric one at the channel exit. Two types of the step change in wall roughness were employed to clarify a possible displacement effect of the roughness elements themselves: the roughness elements are protruding from the smooth wall in the channel 1 (Fig.2a,  $2h=50\text{mm}$ ) and they are flush with the smooth wall in the channel 2 (Fig.2b,  $2h=52\text{mm}$ ).

Measurements of the static pressure, the mean velocity, the Reynolds normal and shear stresses as well as the wall shear stress were made downstream of the step change in wall roughness, under a constant bulk Reynolds number  $U_b h/\nu$  of  $5 \times 10^4$  ( $U_b=30-34 \text{ m/s}$ ).

The main body of data was obtained by hot-wire anemometers with I- and X-probes having 0.5 mm and 1.0 mm unplated, heated lengths of  $5\mu\text{m}$  diameter tungsten wire, respectively. To obtain data as close to the wall as possible, at least two traverses were made at each streamwise section: one starting from the each wall, overlapping 10-20 mm in the central region including the position of the maximum mean velocity. The closest positions of the I- and X-probes were  $0.03 \pm 0.006 \text{ mm}$  and  $1.5 \pm 0.1 \text{ mm}$ , respectively. No wall proximity correction was made.

To calculate fluctuating velocity components and their statistics, two signals from the X-probe were processed with commercially available analogue devices for the channel 1 but they were processed digitally in a computer for the channel 2 and the latter can be considered more reliable.

On the other hand, the maximum mean velocity in a cross-section, which occurs at a different point in each streamwise section, was measured by a Pitot tube with a tip height of 0.2 mm to exclude any uncertainty arising from the drift of a hot wire anemometer. The wall shear stress was measured by a log-law independent sub-layer fence having a fence height of  $40\mu\text{m}$ , which was carefully calibrated in the channel with all smooth walls using a digital manometer capable of resolving

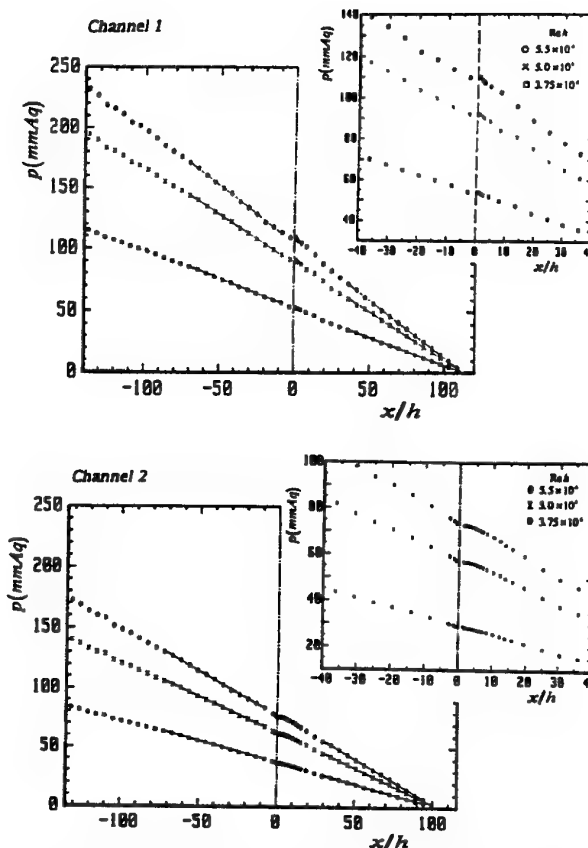


Fig.3 Streamwise distributions of wall static pressure.

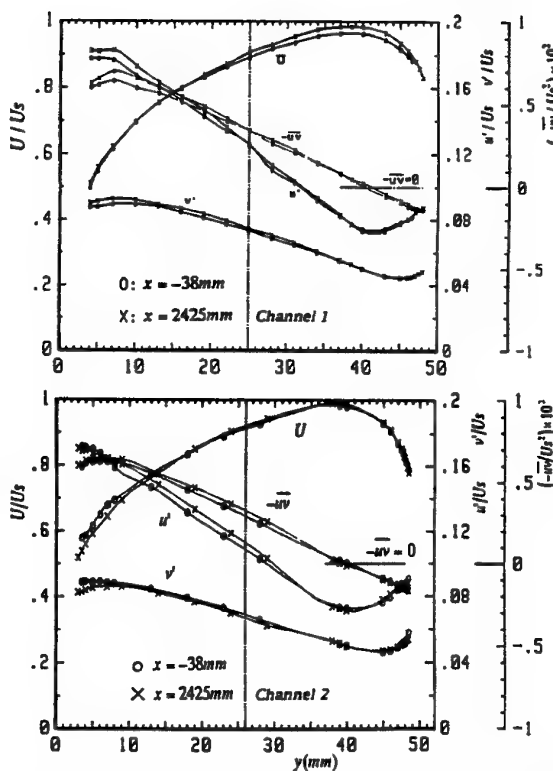


Fig.4 Comparison of fully developed asymmetric flows in upstream and downstream sections.

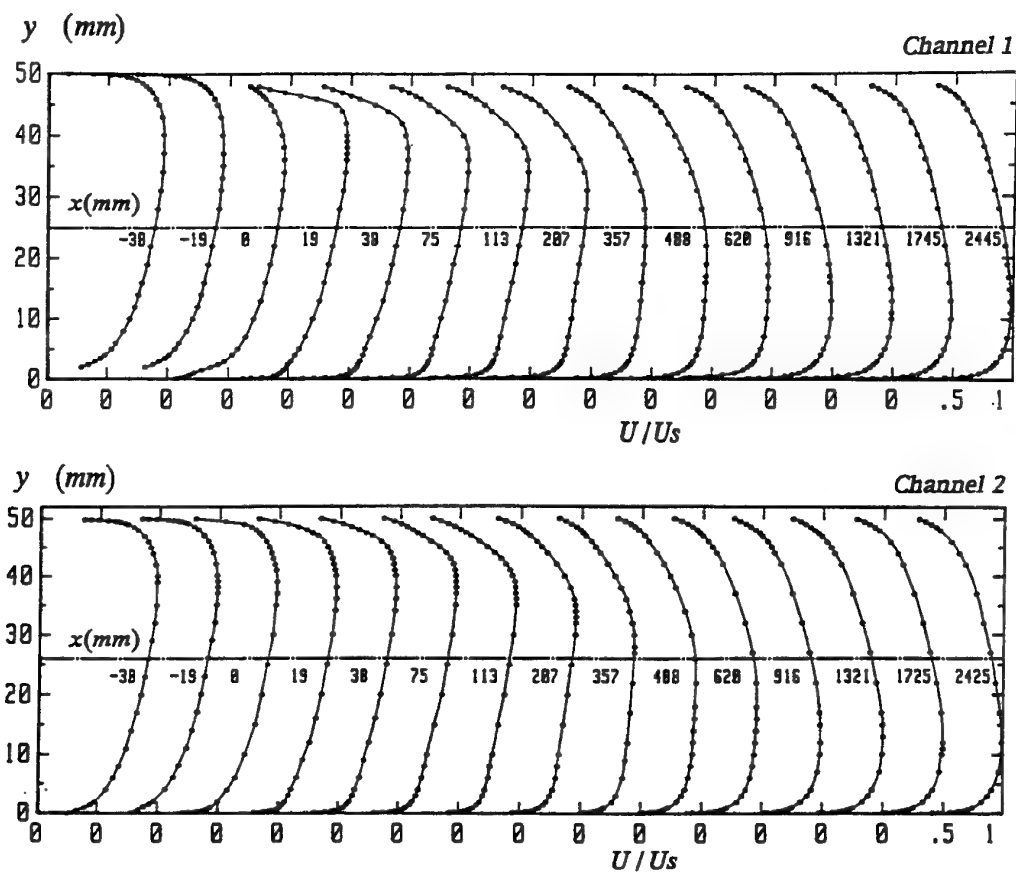


Fig.5 Streamwise variation of mean velocity profiles.

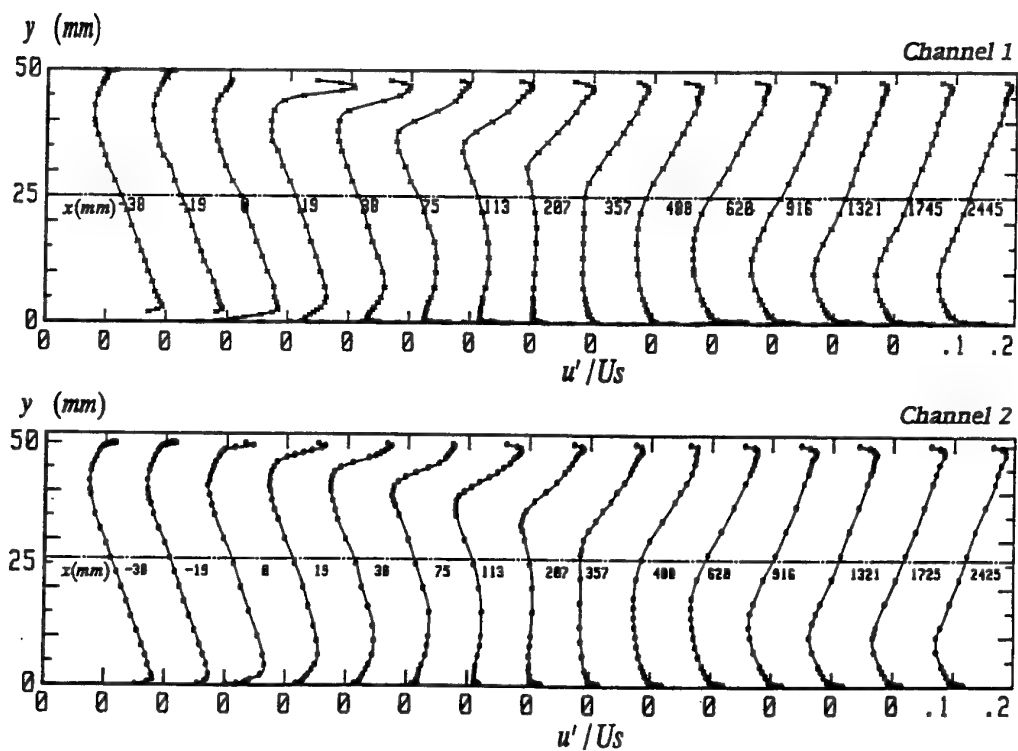


Fig.6 Streamwise variation of fluctuating intensity profiles.

## RESULTS AND DISCUSSION

Fig. 3 shows the streamwise variations of wall static pressure at three Reynolds numbers indicated in the figure. All static holes are mounted on the smooth wall side and the effect of the relative position of roughness elements of the opposite wall on the smooth wall static pressure was confirmed to be negligible. The static pressure shows a linear decrease over a wide region in the downstream part of the upstream and the downstream halves of the channel and their slopes coincide very well with each other, though immediately downstream the step the static pressure deviates upward from the linear distribution. The upward deviation is more pronounced for the channel 1 with increasing the Reynolds number, because the extra effect of displacement by the upstanding roughness elements forces an disturbance of streamwise curvature. Detailed measurements with a static tube revealed that the static pressure changes appreciably over the cross-section in the region of  $-2h < x < 2h$ .

Mean and fluctuating velocity profiles as well as those for the Reynolds shear stress obtained by an X-probe at  $x=38\text{mm}$  and  $2425\text{mm}$  are shown in Fig. 4, indicating how closely the flow assumes an equilibrium state in the mid and exit sections, where velocities are all referred to the maximum velocity in the channel exit (denoted by  $U_s$ ), where the profiles at  $x=2425\text{mm}$  are shown plotted conveniently on the inverted y-axis with the origin at the rough wall for the ease of comparing the corresponding profiles. A little bit loose coincidence of the mean velocity near the maximum point in the channel 1 can be considered as an upstream effect of the step change in the protruding roughness.

Streamwise variations of the mean velocity and the fluctuating intensity profiles are shown plotted in Fig. 5 and Fig. 6, respectively. The results show that the overall adjustment to the anti-symmetric flow proceeds very gradually and no significant difference can be found between the channels 1 and 2, but the recovery to a new equilibrium state takes place rather quicker than in the rough-smooth asymmetric to smooth-smooth symmetric channel flow (Miyata et al., 1987). Essentially, the flow in the rough to smooth side is accelerated and that in the smooth to rough side is decelerated after the step, although the flow near the step is directly affected by the roughness elements, especially in the smooth to rough side of the channel 1, as shown in Fig. 7 which shows the streamwise variation of the mean velocity at constant distance from the wall near the step for the channels 1 and 2. It is clear that the flow within the region a few roughness heights from the wall of smooth to rough side of the channel 1 is strongly affected by the first and the second roughness elements but it cannot be found in the channel 2.

Partly because of this displacement effect, but mostly because of the needs for adjusting to a new boundary condition and the continuity constraint, the maximum mean velocity in a cross-section varies in a complex and sensitive manner in the downstream direction, as shown in Fig. 8 where an abrupt change just up- and downstream the step in the channel 1 can be considered to originate from the displacement effect of the protruding roughness just mentioned. Except for this rather confined difference, characteristic, non-monotonous variations of the maximum mean velocity in the channels 1 and 2 are very similar. A decrease of the maximum velocity results inevitably a flattened velocity profile as can be seen in Fig. 5, which leads to a spreading region of a smaller production rate of the

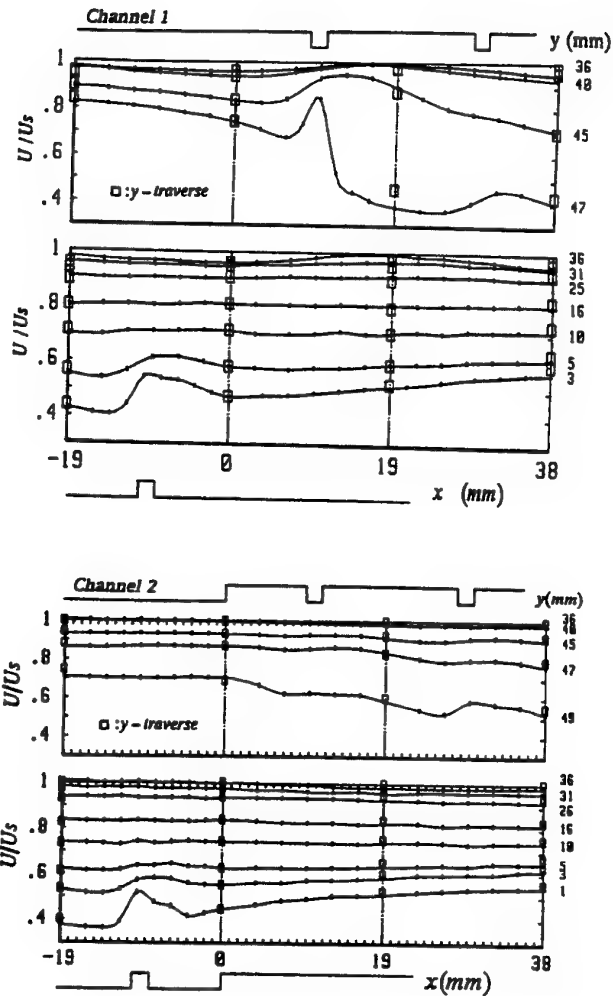


Fig. 7 Streamwise variation of mean velocity at constant distance from the wall near step change in wall roughness. These data were obtained by x-traversing of I-probe and the square symbols indicate the results obtained separately by y-traversing.

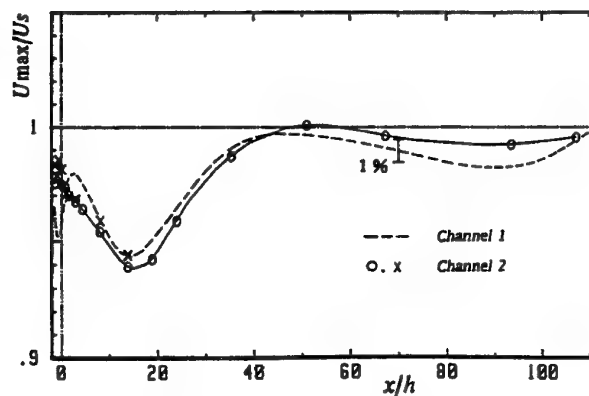


Fig. 8 Streamwise variation of maximum mean velocity in a cross-section.

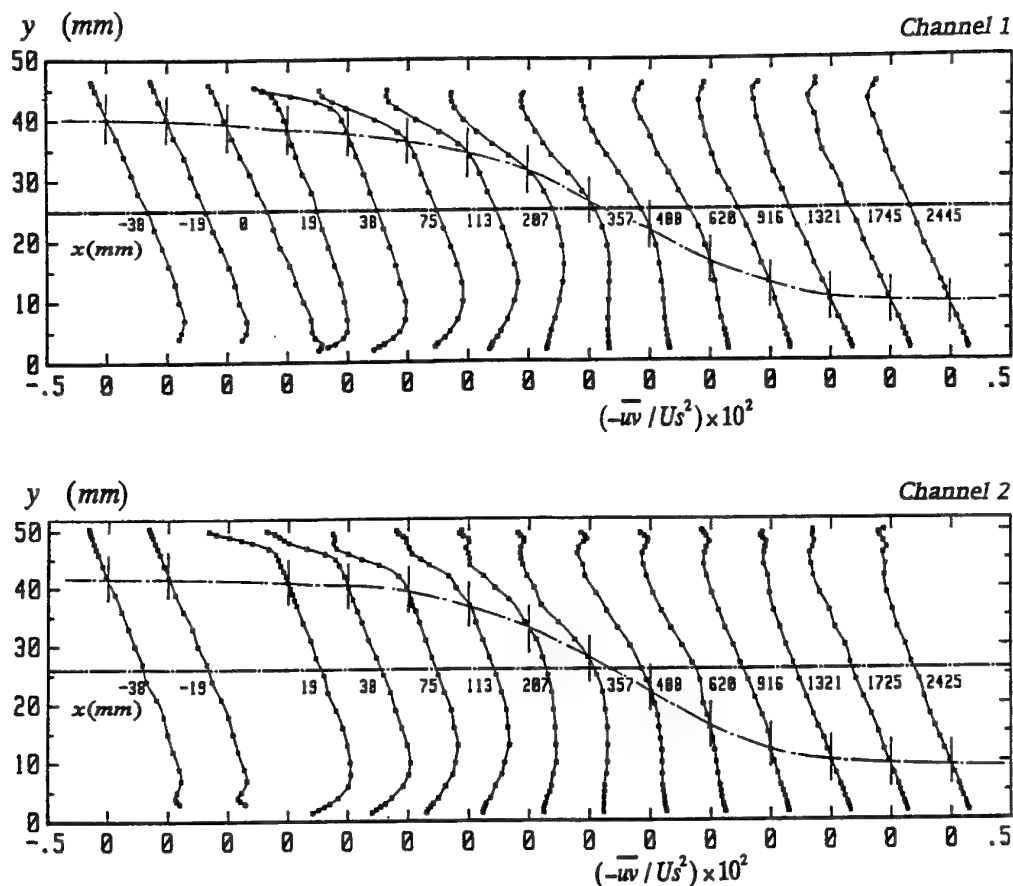


Fig.9 Streamwise variation of Reynolds shear stress profiles.

turbulent energy. Indeed, the turbulent kinetic energy integrated over the cross-section varies in a similar way as that for the maximum velocity and takes a minimum at nearly the same position, i.e. at nearly  $x=20h$ .

Up to  $x=20h$ , the position of zero Reynolds shear stress has moved across the channel center line, as shown by the chain lines in Fig. 9 which shows the streamwise variation of the Reynolds shear stress profiles. The relative positions of zero Reynolds shear stress and zero velocity gradient are also replaced with each other.

Fig.10 shows the streamwise variation of the wall shear stress in the rough to smooth side, where the wall shear stress was measured by a carefully calibrated sublayer fence and the nearly constant wall shear stresses obtained for the downstream part of the channel agree with those by the static pressure gradient assuming an equilibrium state within an error of 5%. The results show that the wall shear stress adjusts itself not so quickly as usually accepted and no overshooting was found for the both channels. A streamwise distance as large as 40 times the channel half height is required for the wall shear stress to take a new equilibrium value. The wall shear stress thus obtained by a log-law independent method makes it possible to test the validity of law of the wall, especially to examine the universality of the von Karman constant.

Fig.11 shows the law of the wall representation of mean velocity profiles downstream of the step change in the rough to smooth side. Straight curves in the figures show the best fit curve for the profiles near the exit of the present channel. A

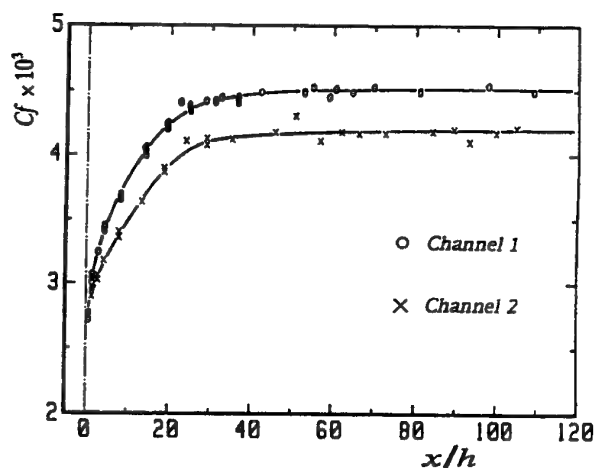


Fig.10 Streamwise variation of wall shear stress in rough to smooth side.

large deviation from this line is evident in the region several channel heights downstream the step and here again non-monotonous recovery to the fully developed profile can be observed: the inner profile of the smooth wall reaches the equilibrium state at nearly  $x=20h$ , where the wall shear stress has attained a value larger than 90% of the equilibrium value.

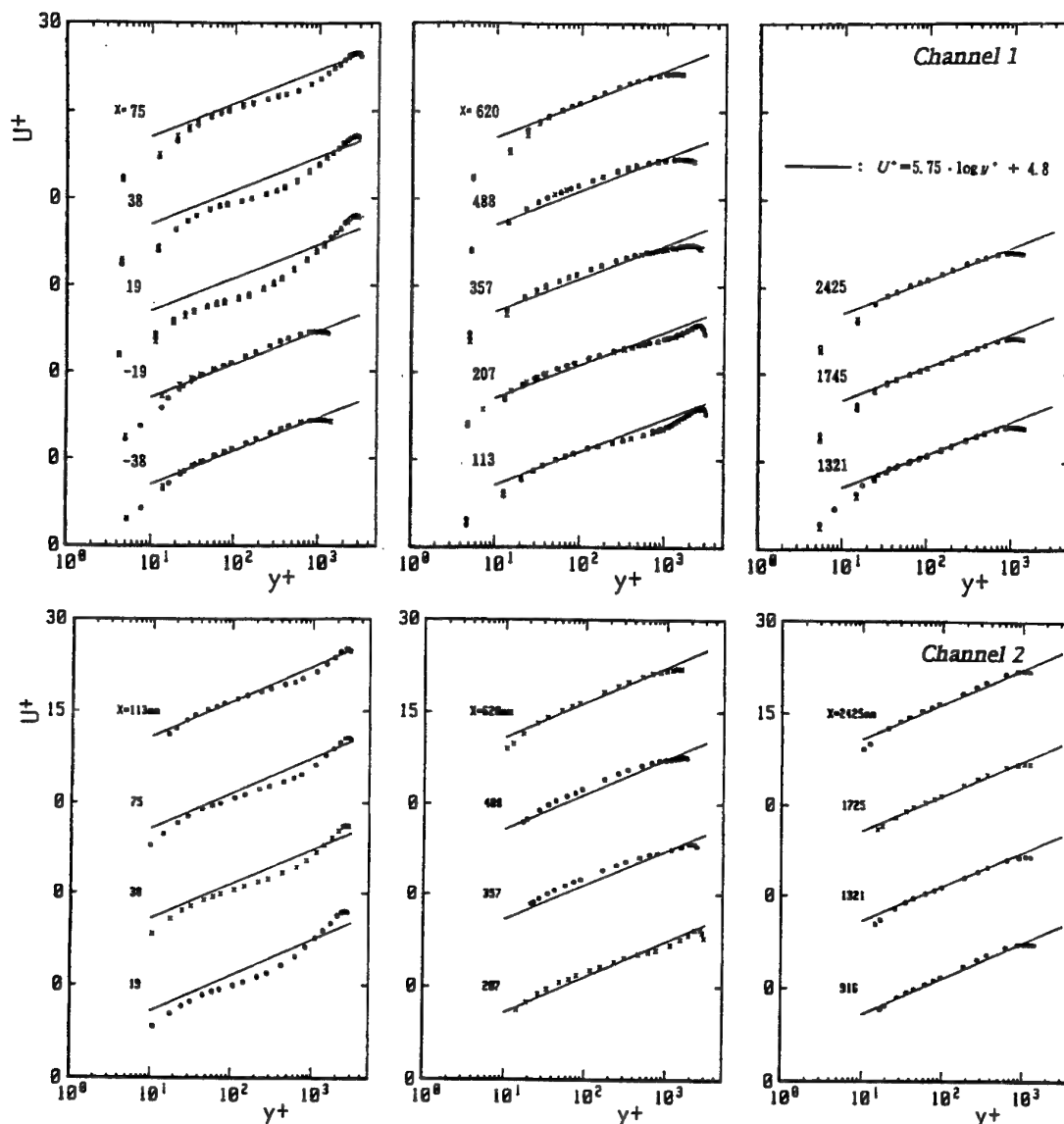


Fig.11 Law of the wall representation of mean velocity profiles in rough to smooth side.

## CONCLUSION

No significant difference in the relaxation process of a two-dimensional asymmetric turbulent channel flow subject to a sudden replacement of smooth and rough walls was found between the protruding and the flush mounted roughness elements except for the region just upstream and downstream the step. The streamwise variations of the mean and fluctuating velocity profiles as well as the wall shear stress correspond well that for the maximum mean velocity in a cross-section and it can sensitively represent how far the relaxation proceeds. The so-called universal Karman constant does vary in the region  $x/h < 20$ , which may cause the log-law dependent methods for the wall shear stress such as the Preston tube to give a results which shows an over- or under-shooting.

## ACKNOWLEDGMENTS

The author would like to thank Y. Komai, M. Itoh, T. Saitoh and H. Kadokura for their helps in performing the

measurements.

## REFERENCES

- Andreopoulos, J. and Wood, D.H., 1982, "The Response of Turbulent Boundary Layer to a Short Length of Surface Roughness", *J. Fluid. Mech.*, Vol.118, pp.143-164.
- Antonia, R.A. and Luxton, R.E., 1971, "The Response of a Turbulent Boundary Layer to a Step Change in Surface Roughness", *J. Fluid Mech.*, Vol.48-4, pp.721-761.
- Clauser, F.H., 1956, "The Turbulent Boundary Layer", Vol.4, Academic Press, pp.1-51.
- Miyata, M., Ishida, N. and Nakamura, I., 1987, "Relaxation of Asymmetric 2-D Channel into a Symmetric State Caused by a Step Change in Wall Roughness, Proceedings, 8th Symposium on Turbulent Shear Flows, pp.2.3.1-2.3.6.
- Smits, A.J. and Wood, D.H., 1985, "The Response of Turbulent Boundary Layers to sudden Perturbations", *Ann. Rev. Fluid Mech.*, Vol.17, pp.321-358.

# TURBULENCE MEASUREMENTS IN A ROUGH WALL BOUNDARY LAYER

Steven Young, Donald J. Bergstrom  
Department of Mechanical Engineering  
University of Saskatchewan  
57 Campus Drive  
Saskatoon, Saskatchewan S7N 5A9  
CANADA

## INTRODUCTION

The turbulent boundary layer is of fundamental importance to modelling transport in engineering flows. Over the past decade substantial progress has been made in developing more accurate computational models for turbulent near-wall flows. For example, with the use of data bases generated by Direct Numerical Simulations, low Reynolds number (LRN) formulations of two-equation and second-moment closures have been developed which reproduce many details of the turbulence structure in the near-wall region. The ability to accurately reproduce the flow structure then translates into more realistic predictions for transport in complex flows.

Unfortunately, whereas most of the computational models have considered boundary layer flows over surfaces which are smooth, in fact many practical applications involve surfaces which are rough. In both industrial and environmental applications, computational models are limited by their ability to incorporate the effects of a rough surface. This is not to say that a turbulent flow field is predominantly affected by surface roughness even far from the surface. The 'wall similarity' hypothesis, as identified by Raupach *et al* (1991), suggests that outside the roughness sublayer, the roughness length scales become irrelevant. On the other hand, recent experimental evidence suggests that the effect of surface roughness may actually extend beyond the proximity of the roughness surface layer. The recent study of Krogstad *et al* (1992) specifically compared measurements in zero-pressure gradient turbulent boundary layers over rough and smooth surfaces. They showed significant differences between both the mean and turbulent velocity components in rough and smooth wall boundary layers. These differences included: 1) a stronger wake component in the outer region of the rough wall boundary layer; and 2) a distinct increase in the level of the normal velocity fluctuation ( $v^2$ ) for the rough wall boundary layer. These findings are supported in part by the earlier experiment of Acharya and Escudier (1987), who also measured significantly higher values of the normal velocity fluctuation over a rough surface compared to

a smooth surface. The level measured for ( $v^2$ ) was also found to be sensitive to the included angle of the x-wire probe. Perry *et al* (1987) also observed the effect of sensor angle on near-wall measurements over a rough surface.

Given the discussion above, the present paper reports the results of velocity measurements in a rough wall turbulent boundary layer. We used 'off the shelf' x-wire anemometers with an angle of  $90^\circ$  to measure the mean and fluctuating components in the boundary layer produced by flow over a perforated metal sheet attached to the ground plane of our wind tunnel. Within the experimental uncertainty of the measurements, we observe evidence that roughness affects flow structure well outside the extent of the roughness sublayer.

## EXPERIMENT

The experiment was conducted in the low speed test section of our recirculating wind tunnel, at a nominal freestream velocity of  $20\text{ m/s}$  and 0.5 percent turbulence intensity. The freestream velocity and Reynolds number based on momentum thickness,  $R_\theta = 15900$ , were close to those used in the experiment of Krogstad *et al* (1992). Whereas they used a steel woven mesh screen to create the surface roughness, we used a perforated sheet  $1.6\text{ mm}$  thick with the perforations arrayed in a hexagonal pattern. The perforation diameter was  $4.8\text{ mm}$  with a spacing of  $6.3\text{ mm}$  on centers, yielding an openness ratio of 52.6 percent. The test surface was  $2\text{ m}$  long and  $1\text{ m}$  wide. A combination of three small spires and a thin rod were used to promote rapid development of the boundary layer given the relatively short test section. The measurement station was located  $1.5\text{ m}$  from the leading edge of the plate.

An x-wire anemometer probe (TSI model no. 1243-T1.5) was selected for measuring the streamwise and normal velocity components. The fact that the probes used an angle of approximately  $90^\circ$  limited the accuracy below  $y/\delta \sim 0.2$ . The x-wire sensors selected are platinum coated tungsten wires. The diameter of each sensor is  $4\text{ }\mu\text{m}$ , with a sensor length of  $1.25\text{ mm}$  giving a length-to-diameter ratio of 313, which value

is relatively high.

The x-wires were calibrated in situ against a pitot-static tube using a static calibration procedure. The calibration analysis procedure follows the technique of Bradshaw (1971). The probe was placed in a holder that was yawed through a series of angles over a range of mean flow velocities. At each velocity and angle, a voltage record was taken, as well as a record of the mean velocity using the pitot-static tube. From this record of voltage for each discrete angle and velocity, the calibration relationship was determined.

The first step in the calibration analysis was to develop a relationship between voltage and velocity in the unyawed position i.e. with both wires at approximately 45 degrees to the incident flow. The voltage record was compared to the pitot-static tube measurements over the calibration range of velocities, approximately 7–24 m/s. A separate relationship of the form

$$U = A + Bx + Cx^2 + Dx^3 \quad (1)$$

was assumed for each sensor. A least squares regression was used to determine the calibration constants for each sensor. The second step in the analysis was to assess the probe sensitivity to yaw. The calibration provided a record of voltage against known yaw angle at each test velocity. The velocity calibration was used to determine an 'indicated velocity' for each sensor at each yaw position. The relationship between the indicated voltage and yaw angle was determined by comparing the velocity calculated in the unyawed position to the indicated velocity in the yawed position. The effective velocity was assumed to be proportional to the actual velocity times a yaw function,  $f(\alpha)$ , i.e.

$$V_e = V f(\alpha)$$

Following the effective angle method proposed by Bradshaw (1971), we assumed  $f$  to have the following form;

$$f(\alpha) = \cos \alpha_e$$

where  $\alpha_e$  is the effective angle. The value of the effective angle for each sensor was determined using the following relationship:

$$\cos \theta - V_\theta / V_o = \tan \alpha_e \sin \theta \quad (2)$$

where  $\theta$  is the known yaw angle;  $V_\theta$  is the indicated velocity at yaw angle; and  $V_o$  is the velocity in the unyawed position. This relationship yields a straight line slope of  $\tan \alpha_e$ . Each test velocity infers its own effective angle. In our investigation, the effective angle was approximately constant over the range of test velocities considered.

The two velocity components,  $U$  and  $V$ , were determined using the sum and difference method. For two non-identical wires,

$$U = (V_1 g_1 + V_2 g_1) / (g_1 + g_2) \quad (3)$$

$$V = (V_2 - V_1) / (g_1 + g_2) \quad (4)$$

where  $V_i$  is the output of the speed calibration for sensor  $i = 1, 2$ ; and  $g_i = \tan \alpha_{ei}$  relates to the effective angle of that sensor. The calibration was checked throughout the test period to ensure that no drift in calibration was experienced.

The x-wire voltage records were filtered using an analog filter with a cut-off frequency of 8000 Hz. The sampling frequency was 16,000 Hz and ten seconds of data was acquired at each point.

## RESULTS

The mean velocity profile is shown in Fig.'s 1 and 2. Fig. 1 uses physical coordinates, i.e. normalising with the free-stream velocity,  $U_e$ , and boundary layer thickness,  $\delta$ . Fig. 2 uses the inner coordinates, i.e. normalising with the friction velocity,  $U_\tau$ , and viscous length scale,  $\nu / U_\tau$ . We observe in Fig. 1 the characteristically blunt profile of a turbulent boundary layer. In Fig. 2, the effect of roughness is to increase the wall friction, so that the logarithmic profile is displaced below that of a smooth surface.

One of the central questions in a boundary layer experiment is the determination of the wall shear stress,  $\tau_w$ , or its equivalent, the friction velocity,  $U_\tau = \sqrt{(\tau_w / \rho)}$ . The different methods which are used include direct measurement, e.g. with a floating element gauge (Archaya and Escudier, 1987), use of a momentum balance, or by fitting the mean velocity profile to a standard profile. We adopt the third approach following Krogstad *et al* (1992). We assume the mean velocity profile across the inner and outer regions to be of the following form:

$$U^+ = \frac{1}{\kappa} \ln y^+ + A - \Delta U^+ + \frac{2\Pi}{\kappa} \omega(\eta) \quad (5)$$

where  $U^+ = U / U_\tau$ ,  $y^+ = (y + \epsilon) U_\tau / \nu$  and  $\eta = (y + \epsilon) / \delta$ ;  $\kappa = 0.41$  and  $A = 5.3$  are assumed to be constants. In this case,  $y$  is measured from the top of the perforated sheet, and  $\epsilon$  is the shift in origin produced by the rough surface.  $\Delta U^+$  is the (dimensionless) roughness function, and  $\Pi$  determines the strength of the wake function  $\omega(\eta)$ . In order to specify the velocity profile, the values of four parameters must be determined:  $U_\tau$ ,  $\epsilon$ ,  $\Delta U^+$  and  $\Pi$ .

Again following Krogstad *et al* (1992), we fit our profile in terms of the velocity defect obtained by subtracting  $U^+$  from its own value at the edge of the boundary layer, i.e.

$$U_e^+ - U^+ = \frac{2\Pi}{\kappa} [\omega(1) - \omega(\eta)] - \frac{1}{\kappa} \ln \eta \quad (6)$$

They suggest that the formulation used for the wake function should not fix the value of the wake strength,  $\Pi$ , implicitly. Therefore, instead of adopting the commonly used function originally proposed by Hama (1954), they choose a formulation attributed to Finley, Koo Chong Phoe and Chin Jeck Poh (1966), namely:

$$\omega(\eta) = \frac{1}{2\Pi} [(1 + 6\Pi) - (1 + 4\Pi)\eta]\eta^2 \quad (7)$$

which is fitted to the data using a nonlinear least-squares optimisation which determines the three parameters:  $\Pi$ ,  $\epsilon$  and  $U_\tau$ . The optimisation procedure is described in greater detail in their paper.

Following this method, we fitted our mean velocity data to the defect law given in equation (6). The values obtained for the parameters were as follows:

$$U_\tau = 0.84 \text{ m/s}; \epsilon = 0.64 \text{ mm}; \Pi = 0.429$$

The mean velocity defect profile is presented in Fig. 3. The value obtained for the strength of the wake in our experiment,  $\Pi = 0.429$ , was somewhat low, although certainly well within the range of 0.4 to 0.7 quoted by Tani (1988) for  $k$ -surfaces. The value obtained by Krogstad *et al* (1992) of  $\Pi = 0.70$  was significantly higher. The difference in  $\Pi$  for the two experiments may be partly attributed to the fact that in our case



the roughness was produced by a perforated plate attached to the ground board, while they used a woven mesh. The value obtained for the friction velocity,  $U_\tau = 0.84$  corresponded to a skin friction coefficient of  $c_f = 3.6 \times 10^{-3}$ .

The profiles measured for the three Reynolds stress components ( $u^2$ ), ( $v^2$ ) and ( $uv$ ) are given in Fig.'s 4, 5 and 6, respectively. In each case we have shown for comparison the measurements of Krogstad *et al* (1992) extracted from the figures in their paper. Since our x-wire probes used an angle of  $90^\circ$ , they begin to lose accuracy below  $\eta \sim 0.3$ . In Fig. 5 for the normal Reynolds stress component, our measurements fall between those of Krogstad *et al* (1992) using  $95^\circ$  and  $120^\circ$  angle probes. We suspect that the sharp rise in the streamwise Reynolds component near the wall in Fig. 4 which is erroneous can also be attributed to this angle effect.

Overall the measured Reynolds stress profiles lend support to the notion that rough wall boundary layers are characterised by higher Reynolds stress levels. This is most pronounced for the case of the normal component, ( $v^2$ ), as would be expected. From Fig. 6, the Reynold shear stress profile, when plotted in terms of inner coordinates, extrapolates to a value close to unity at the wall. This suggests that the wall friction velocity inferred from the mean velocity profile was consistent with the Reynolds stress measurements.

## CONCLUSIONS

We present experimental measurements of the mean and fluctuating velocity components in a rough wall turbulent boundary layer produced by flow over a perforated plate. Our results are further evidence of distinct differences between the turbulence structure in a rough wall and smooth wall boundary layer.

## REFERENCES

- Archarya, M. and Escudier, M.P., 1987, "Turbulent Flow Over Mesh Roughness", *Turbulent Shear Flows 5: Selected Papers from the Fifth International Symposium on Turbulent Shear Flows*, Springer-Verlag, Berlin, pp. 176-185.
- Bradshaw, P., 1971, *An Introduction to Turbulence and Its Measurement*, Pergamon Press, New York.
- Finley, P.J., Khoo Chong Phoe and Chin Jeck Poh, 1966, "Velocity Measurements in a Thin Turbulent Wake Layer", *La Houille Blanche*, Vol. 21, pp. 713-721.
- Krogstad, P.-A., Antonia, R.A., and Browne, L.W.B., 1992, "Comparison Between Rough- and Smooth-Wall Turbulent Boundary Layers", *J. Fluid Mech.*, Vol. 245, 599-617.
- Perry, A.E., Lim, K.L., and Henbest, S.M., 1987, "An Experimental Study of the Turbulence Structure in Smooth- and Rough-Wall Boundary Layer", *J. Fluid Mech.*, Vol. 177, pp. 437-466.
- Raupach, M.R., Antonia, R.A., and S. Rajagopalan, 1991, "Rough-Wall Turbulent Boundary Layers", *Appl. Mech. Rev.*, Vol. 44 (1), pp. 1-25.
- Tani, I., 1988, "Turbulent Boundary Layer Development over Rough Surfaces", in *Perspectives in Turbulence Studies*, H.U. Meier & P. Bradshaw, eds., Springer, pp. 223-249.

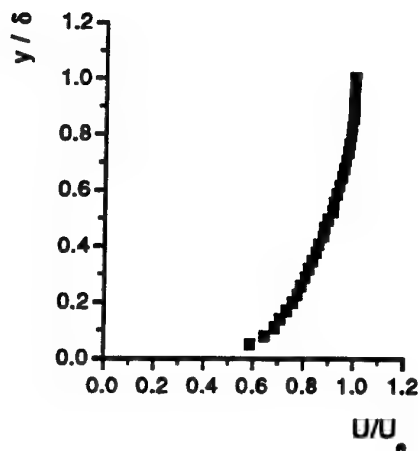


Figure 1: Mean velocity profile in physical coordinates.

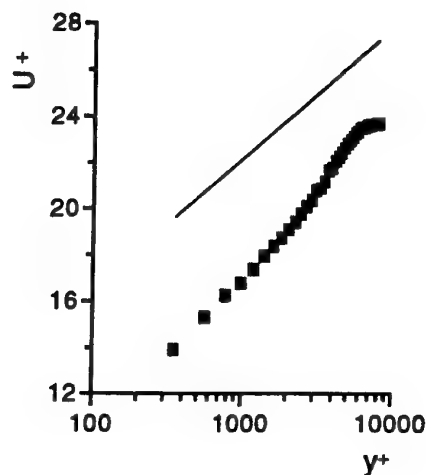


Figure 2: Mean velocity profile using inner coordinates.

■ x-wire; — log-law for smooth wall.



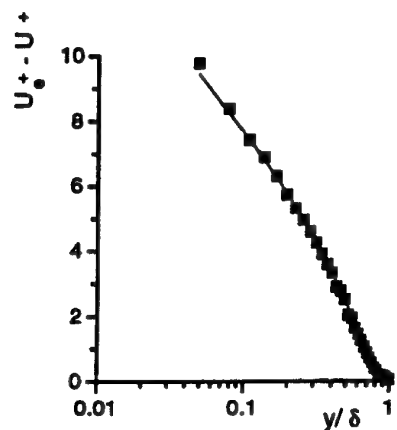


Figure 3: Mean velocity defect profile.

— curve fit to eqn (6).

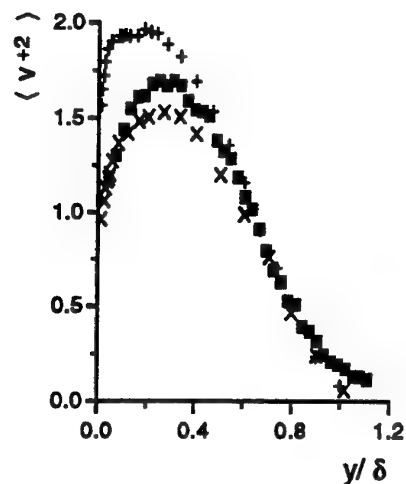


Figure 5: Normal Reynolds stress component.  
■ x-wire; + 120° probe, × 95° probe  
from Krogstad *et al* (1992).

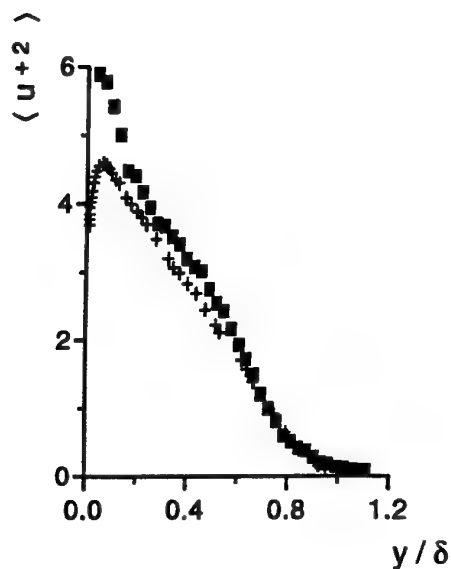


Figure 4: Streamwise Reynolds stress component.

■ x-wire; + Krogstad *et al* (1992)

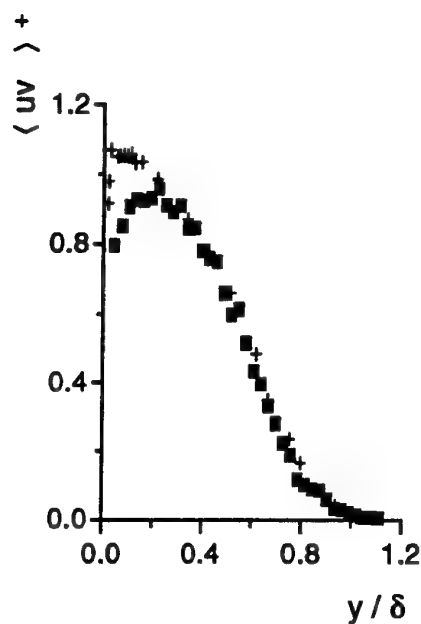


Figure 6: Reynolds shear stress component.

■ x-wire; + Krogstad *et al* (1992)

# DRAG REDUCTION IN TURBULENT MHD PIPE FLOWS

Paolo Orlandi

Università di Roma "La Sapienza"  
Dipartimento di Meccanica e Aeronautica  
via Eudossiana 18 00184 Roma  
Italy.

## ABSTRACT

This is a preliminary study devoted to verify whether the direct simulations of MHD flows reproduce the experimental observations of a drag reduction for liquid metals. Two different cases have been simulated by a finite difference scheme second order accurate in space and time with staggered velocities. In the first case an external azimuthal magnetic field is imposed. In this case the magnetic field acts on the mean axial velocity and the complete laminarization of the flow at  $Ha = 30$  has been achieved. In the second case an axial magnetic field is imposed which affects only the fluctuating velocities and thus the action is less efficient. This second case is more interesting and the comparison between the numerical and the experimental results is only qualitative.

## INTRODUCTION

The present study is devoted to show that some of the experimental observations in liquid metals can be qualitatively described by a coarse direct simulation of the Navier-Stokes and of the magnetic field equations without any low Reynolds magnetic number approximation. Dealing with liquid metals as sodium or mercury, in the real applications, the Reynolds numbers are in the range affordable by the direct simulations. The direct simulation can, then be used as a design tool in practical applications. Since in the experiments with liquid metals it is almost impossible to perform flow visualizations and the measurements of turbulent quantities are difficult, direct simulations give the desired turbulent and velocity profiles and by vorticity visualizations permit to understand better the physics of the flows.

The previous direct simulations of MHD flows for the major part were devoted to isotropic turbulence (Kida *et al.* (1991)) and, to my knowledge, there it was only one devoted to the LES of flows in presence of solid boundaries. Shimomura (1991) considered the case of a magnetic field perpendicular to the wall, and in this case the drag increases as observed in the experiment by Reed & Likoudis (1978). On the other hand, drag reduction occurs when the magnetic field is directed in the streamwise or in the spanwise direction. The realization in the laboratory of

the second case is easy for a plane channel with a reasonable aspect ratio, but the Hartmann boundary layers on the side walls play a role. In a circular pipe one way to assign the external azimuthal magnetic field is by an electrical wire as thinner as possible located at the center of the pipe and this set-up is difficult to realise and could influence the flow-field. This is the reason why for the case of spanwise external magnetic fields there are a large number of experiments for plane geometries, and some of these are listed in the review papers by Moffatt and Tsinober (1992) and by Tsinober (1990).

The realizations of an axial magnetic field inside a circular pipe is easier to setup and two well documented experiments by Fraim & Heiser (1968) and by Krasil'nikov *et al.* (1973) are available. The friction coefficient reduction was measured at different  $Re$  and intensities of the external magnetic field. The main difference between the two cases is that in the case of an azimuthal field the Lorentz force acts on the mean streamwise velocity profile reducing the mean shear and thus the production of turbulent energy. In presence of an axial field, instead the Lorentz force acts on the fluctuating components and thus it is less effective.

In both cases, without using any superconducting materials, the efficiency, that is the ratio between the input of energy and the benefit achieved by the skin friction reduction, is very low. Thus this mechanism leading to drag reduction could be used in applications where it is not important the efficiency but it is important to reach the goal of a drag reduction.

## PHYSICAL AND NUMERICAL MODEL

The dimensionless Navier-Stokes equations when a conducting fluid is subjected to a magnetic field are

$$\frac{DU}{Dt} = -\nabla p + \frac{1}{Re} \nabla^2 U + \frac{Ha^2}{Re^2 Pm} \nabla \times \mathbf{B} \times \mathbf{B} \quad (1)$$

where in the Lorentz force the relationship between  $\mathbf{J}$  and  $\mathbf{B}$ ,  $\mathbf{J} = \nabla \times \mathbf{B}$  was used.  $\mathbf{B}$  is calculated by

$$\frac{D\mathbf{B}}{Dt} = \frac{1}{Re Pm} \nabla^2 \mathbf{B} + (\mathbf{B} \cdot \nabla) \mathbf{U} \quad (2)$$

The dimensionless equations have been obtained by taking the pipe radius  $R$  as reference length, the laminar Poiseuille velocity  $U_P$  as velocity scale and the magnitude of the external magnetic field  $B_0$ . Together with the fluid properties,  $\nu$  the kinematic viscosity,  $\mu$  the magnetic permeability and  $\sigma$  the electrical conductivity the dimensionless number are.  $Re = U_P R / \nu$  is the Reynolds number  $P_m = \nu \mu \sigma$  is the magnetic Prandtl number and  $Ha = B_0 R \sqrt{\sigma / \rho \nu}$  is the Hartmann number.

These equations can be solved when boundary conditions are assigned. This paper deals with flows inside a circular pipe, hence the usual no-slip conditions are assumed on the wall. Being interested to the statistical steady state, periodicity is assumed along the streamwise direction. About the external magnetic field two different distributions can be assigned, and these should be solution of the  $\mathbf{U}$  and  $\mathbf{B}$  equations averaged in the  $\theta$  and  $x$  directions. The components of the mean velocity  $\mathbf{U}$  are  $U_r = U_\theta = 0$  and  $U_x(r) \neq 0$ , from these conditions if we assume that the external magnetic field is only azimuthal it must be  $B_\theta = B_0 r$ . On the other hand if there is only an axial field it must be  $B_x = B_0$ . By these boundary conditions, in the  $B_\theta$  case, it results that on the pipe wall there is a strong density current, on the  $B_x$  case, instead the density current is low.

From a physical point of view it is interesting to compare the action of the Lorenz force in the two cases and the low Reynolds number approximations can facilitate this analysis. Within this approximation the equations of the magnetic field are replaced by the equation of the potential of the electric field  $\Phi$  which is related to the current density by  $\mathbf{J} = -\nabla\Phi + \mathbf{U} \times \mathbf{B}$ .  $\Phi$  can be calculated by the equation

$$\nabla^2 \Phi = \nabla \cdot \mathbf{U} \times \mathbf{B} \quad (3)$$

obtained by imposing  $\nabla \cdot \mathbf{J} = 0$ . The component of the Lorenz force for  $B_\theta = B_0 r$  are

$$\frac{\partial q_r}{\partial t} \approx \frac{Ha^2}{Re} \left[ -\frac{r \partial \Phi}{\partial x} - q_r B_\theta \right] B_\theta \quad (4)$$

$$\frac{\partial q_x}{\partial t} \approx \frac{Ha^2}{Re} \left[ -\frac{\partial \Phi}{\partial r} - q_x B_\theta \right] B_\theta \quad (5)$$

and for  $B_x = B_0$

$$\frac{\partial q_r}{\partial t} \approx \frac{Ha^2}{Re} \left[ -\frac{r \partial \Phi}{\partial \theta} - q_r B_x \right] B_x \quad (6)$$

$$\frac{\partial q_\theta}{\partial t} \approx \frac{Ha^2}{Re} \left[ -\frac{r \partial \Phi}{\partial r} - q_\theta B_x \right] B_x \quad (7)$$

It results that in the first case the external magnetic field decreases  $U_x$  and thus the reduction of turbulence is more effective since the mean shear is reduced. On the second case the magnetic field acts only on the fluctuating components.

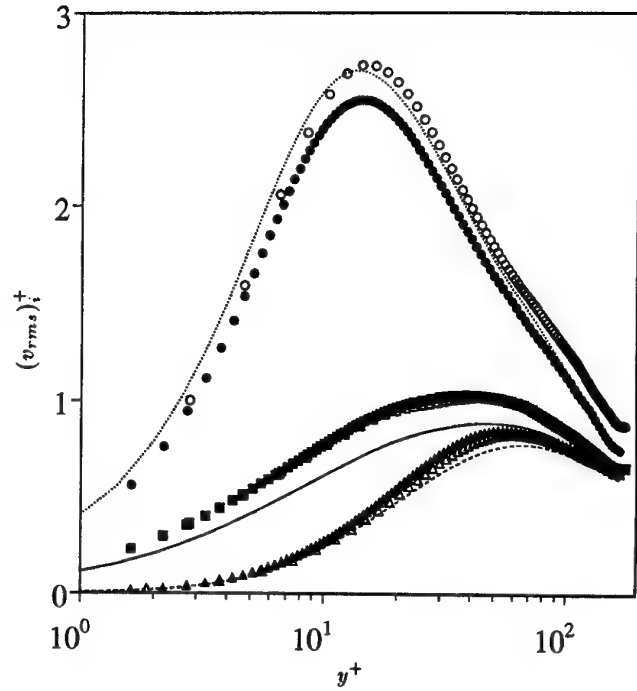


FIGURE 1. Profiles of rms vorticity fluctuations in wall units, a) lines, present  $65 \times 65 \times 65$ , b) closed symbols present  $129 \times 97 \times 129$  c) open symbols Eggels *et al.*  $257 \times 129 \times 129$  (—, ■, □,  $v'_\theta$ ), (---, △, △,  $v'_r$ ), (·····, ●, ○,  $v'_x$ ).

A first attempt has been done to solve this simplified set of equations but the results were not satisfactory. A first explanation is that to maintain a constant flow rate the pressure gradient has to account for the part of the Lorenz force proportional to  $B_\theta^2$  and since this term at high  $Ha$  is greater than the friction losses the evaluation of the skin friction was not accurate. Dealing with the full system of equations the contribution of Lorenz force to the mean pressure gradient is zero.

The second order finite difference scheme in space and time developed by Verzicco & Orlandi (1996) tested for several laminar flows and for rotating and non-rotating turbulent pipes (Orlandi & Fatica (1996)) was adapted to solve the magnetic equations. To deal with the axis the quantities  $h_r = r b_r$ ,  $h_\theta = r b_\theta$ ,  $h_x = b_x$  have been used, as it was done for the velocity components ( $q_r = r v_r$ ,  $q_\theta = r v_\theta$ ,  $q_x = v_x$ ). The  $\mathbf{B}$  and  $\mathbf{U}$  components are located at the center of the face of the cell. The fractional step method used for the velocity field was used for the magnetic field.

## RESULTS

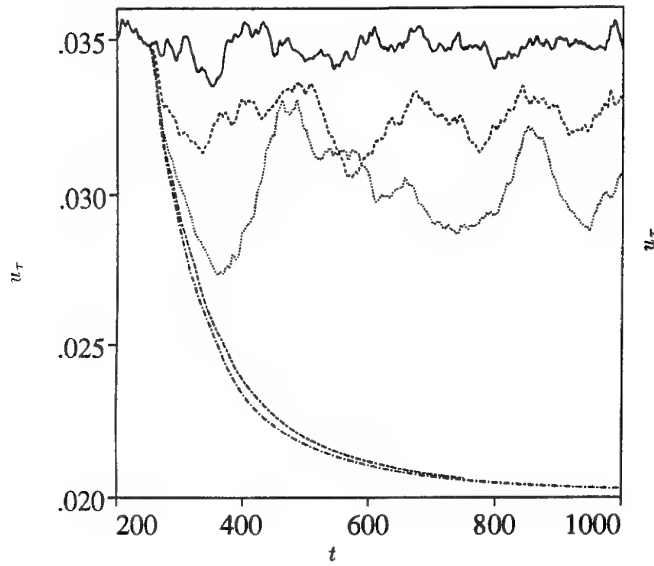


FIGURE 2. Time evolution of  $u_r$  for external  $B_\theta$  (—  $Ha = 0$ ), (.....  $Ha = 20$ ), (----  $Ha = 28$ ), (— · —  $Ha = 30$ ), (— — —  $Ha = 32$ ).

Without magnetic field there is higher turbulence level, therefore the validation of the grid adequacy has been performed for  $Ha = 0$ . The simulation with the magnetic field requires more memory and longer CPU time because of three more parabolic equations. Thus in this study limited to investigate whether the direct simulation reproduces the drag reduction observed in the experiments, the grid should be kept as small as possible but such as to give satisfactory results for the second order statistics. Fig.1 shows that a grid  $65 \times 65 \times 65$  gives normal stresses profiles in wall units in good agreement with those by a more refined simulations ( $129 \times 97 \times 129$ ) and with that by Eggels *et al.* (1994) with a more refined grid in  $x$ . A coarse simulation does not resolve the velocity gradients and this affects the *rms* profiles in a different manner. From previous simulations (Orlandi & Fatica (1996)) at  $Ha = 0$  has been observed that the insufficient resolution in  $\theta$  and  $x$  produces a reduction on  $v'_r$  and  $v'_\theta$  while that in  $r$  affects  $v'_x$ . This explains why the present coarse  $v_x$  *rms* profile near the wall agrees with that by Eggels *et al.* (1994) which was obtained by a uniform grid in  $r$ . 97 equidistant points in  $r$  located only 7 points within  $y^+ = 15$  while the present nonuniform grid located 18 points in the same distance. The differences are not so elevated thus this resolution is satisfactory for a preliminary understanding of MHD drag reduction.

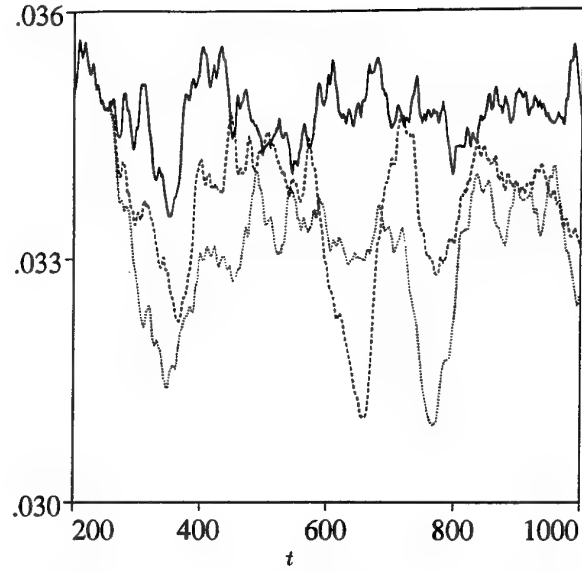


FIGURE 3. Time evolution of  $u_r$  for external  $B_x$  (—  $Ha = 0$ ), (.....  $Ha = 20$ ), (----  $Ha = 60$ ).

The simulations of an external azimuthal magnetic field have been performed for  $Ha = 20, 28, 30$  and  $32$  starting from the field at  $t = 250$  of  $Ha = 0$  and advancing for 750 dimensionless time units. The statistics were computed from 50 fields distant each other 10 time units. The evolution within the first 250 time units was discarded since in this period the flow adjusts to the abrupt effects of the magnetic field. The  $u_r$  time evolution in Fig.2 shows that this transitory period is as longer as higher is the  $Ha$  number. Fig.2 furthermore shows that the magnetic field reduces the high frequency oscillations, and that for high Hartmann numbers ( $Ha \geq 30$ ) the flow becomes laminar. In the experiment by Branover *et al.* (1966), in a plane channel with an aspect ratio  $b/a = 0.067$ , the Hartman layers on the vertical wall should not play a substantial role. Thus the results could be considered for a comparison with the present simulations. However also in absence of magnetic field the pipe and the two dimensional channel differ, as for example shown by Durst *et al.* (1995), thus differences should be expected in presence of the magnetic field. In the experiment  $\lambda = C_{fHa}/C_{f0}$ , that is the ratio between the  $C_f$  with and without magnetic field depends on the Reynolds number. At  $Re = U_b D/\nu = 7600$  for  $Ha = 20$  and  $28$   $\lambda$  is respectively equal to 0.82 and 0.62. In the pipe it was found 0.86 and 0.77 and approximately at  $Ha = 30$  the laminar state was achieved. I wish to recall that at  $Re = 180$  in the channel it corresponds  $Re = U_b 2\delta/\nu = 5600$  and at this Reynolds number the experiments of Branover *et al.* (1966) show a laminar state and the present simulations differs more from the experiments.

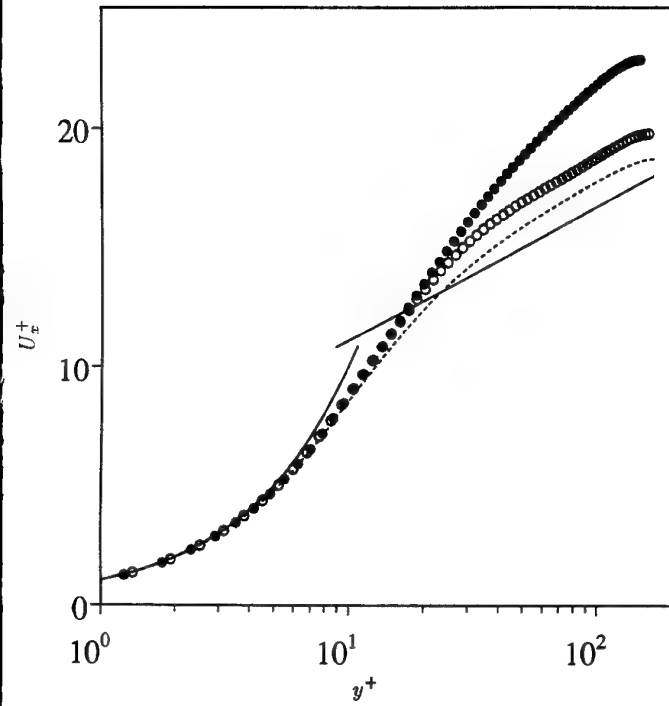
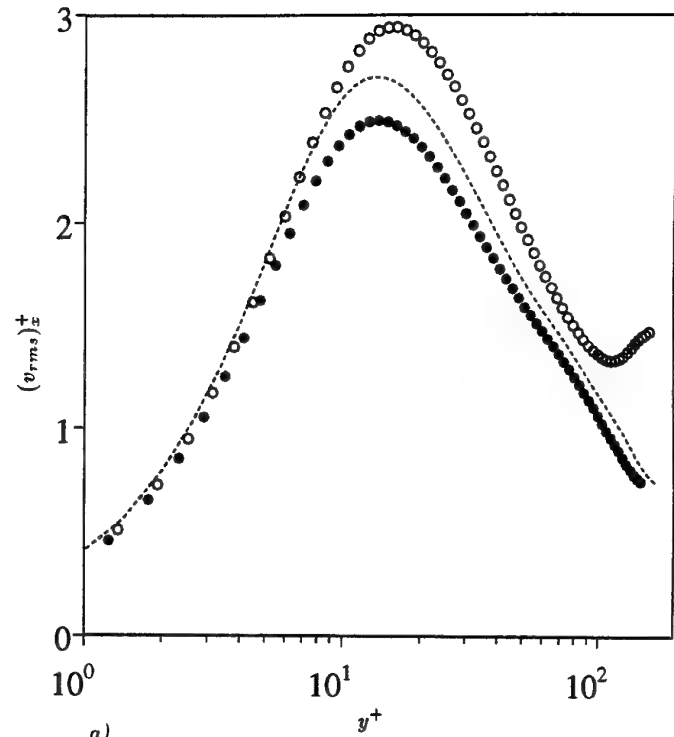


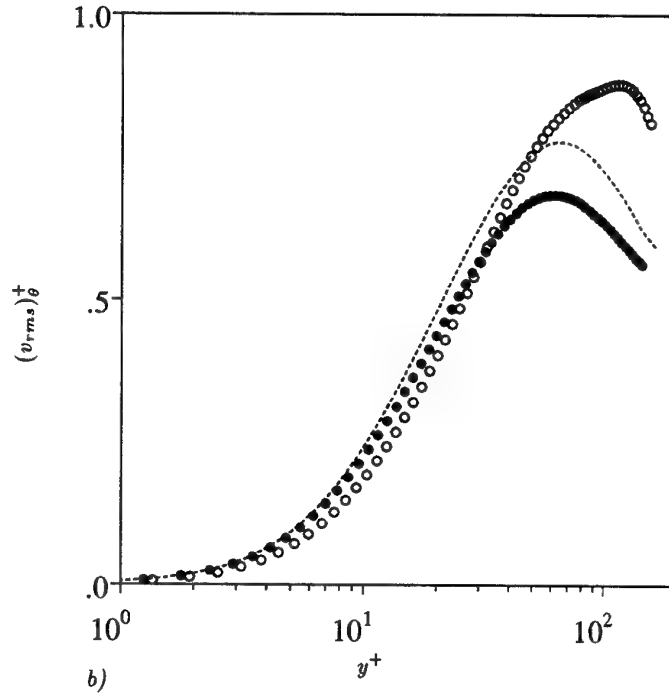
FIGURE 4. Radial streamwise velocity profile in wall units (— *log law*), (.....  $Ha = 0$ ), ( $\bullet$   $Ha = 28, B_\theta$ ), ( $\circ$   $Ha = 60, B_x$ ).

The same initial conditions were used to solve the case of an axial magnetic field. Fig.3 shows that  $u_r$  does not change considerably going from  $Ha = 20$  to  $60$ . The experiment by Fraim & Heiser for  $Re = 4900$  at  $Ha/Re = 0.122$  gives for the friction factor  $\lambda = 0.0305$ , a value smaller than  $0.035$  found in the present simulation. The experimental and the numerical simulations produce a value of  $0.385$  for  $Ha = 0$ . Attempts were done to perform simulations at higher Hartmann numbers to investigate whether the numerical simulation also in this case reproduces a laminar state. The numerical simulation after the initial  $u_r$  drop showed an increase of the drag, associated to larger turbulent intensities near the center, and the calculation was diverging. Different initial conditions such as the field for  $Ha = 60$  at  $t = 1000$  have been also assigned without any success.

Before discussing the velocity and *rms* velocity profiles it is interesting to understand why in these conditions the efficiency is very low. The efficiency is defined as the ratio between the energy saved by skin friction reduction and the input energy necessary to generate the magnetic field. It is  $\epsilon = (1 - \lambda)ReR_\tau^2Pm^2/Ha^2$ . Since for liquid metals the magnetic Prandtl number is  $O(10^{-7})$  it is clear why the efficiency is very low.



a)



b)

FIGURE 5. *rms* velocity profiles in wall units a)  $v'_x$ , b)  $v'_\theta$ , (.....  $Ha = 0$ ), ( $\bullet$   $Ha = 28, B_\theta$ ), ( $\circ$   $Ha = 60, B_x$ ).

It is interesting to make a comparison between the two cases respectively at  $Ha = 28$  and at  $Ha = 60$ . Recalling that, in presence of  $B_\theta$ , the Lorentz force effects the mean velocity, Fig.4 shows that the velocity profile does not have any more the *log law* and that the profile is getting close to a laminar profile. On the contrary the case with  $B_x$  has a well defined *log law* shifted upwards reminiscent of other flows with drag reduction.

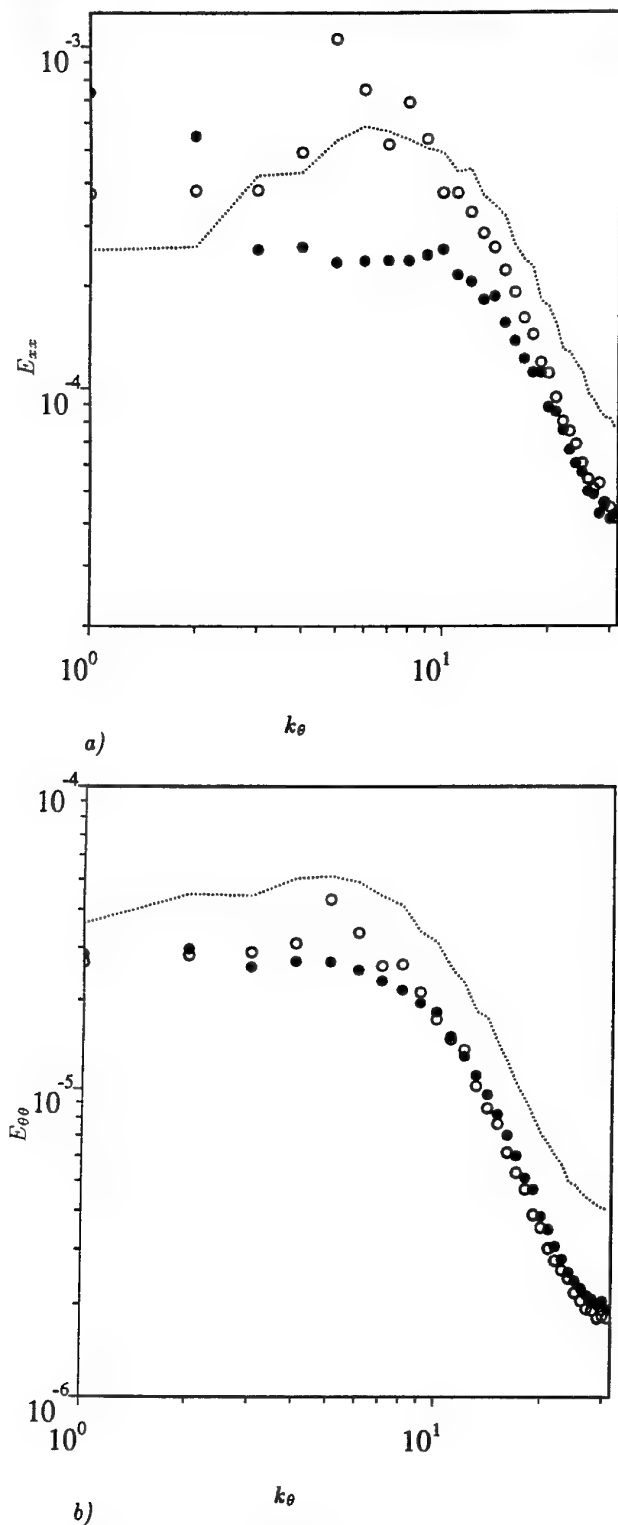


FIGURE 6. One-dimensional energy spectra a) azimuthal, b) axial directions, (.....  $Ha = 0$ ), ( $\bullet$   $Ha = 28$ ,  $B_{\theta}$ ), ( $\circ$   $Ha = 60$ ,  $B_x$ ).

The direct simulations explain through the profiles and the spectra of the normal turbulent stresses that the effects of the magnetic field are different in the two cases. The profiles of  $v'_x$  and  $v'_r$  in Fig.5a-b show that  $B_{\theta}$  reduces both everywhere and that  $B_x$  on the other hand has a more complex effect. In fact, while the axial stress increases ev-

erywhere,  $v'_{\theta}$  is reduced in the buffer region and increases at the center. For  $B_{\theta}$  the drag reduction is associated to a reduction of turbulent intensity on the other hand for  $B_x$  the reduction is associated to modifications of the vortical structures. The one dimensional azimuthal energy spectra detect the size of the energy containing eddies which near the wall are those responsible to the wall friction. These spectra are shown for the axial and azimuthal components at  $y^+ \approx 10$ , the location of high turbulence production. In discussing the spectra in Fig.6a-b I am having in mind contours plots of fluctuating velocity even if these plots are not presented. The spectra show that  $B_{\theta}$  reduces the energy level at small scales and that there is a transfer of energy to the large scales. The spectrum for the  $B_x$  case shows that the containing energy scale of the  $v'_x$  components are larger than those without magnetic field. These then are located at a greater distance from the wall and thus the friction decreases. For the azimuthal stresses  $B_x$  produces a similar transfer at the large scales but in this case also the energy level is reduced at each wave number.

## CONCLUSIONS

The present study has shown that the numerical simulation of MHD flows for liquid metal is feasible and that qualitatively reproduces the experiments. It has been shown that for these fluids the drag reduction is inefficient, that is that a large amount of electrical power must be furnished to achieve the desired goal. The reduction of the turbulent levels could be of large interest in several applications where the energy saving is not important. These direct simulations moreover have a large interest *per se* to study the turbulence physics when it is subjected to external forces. There are in fact similarities between MHD turbulence and turbulence subjected to background rotation as it was claimed by Tsinober (1990). In both cases a drag reduction is achieved but the mechanism is different. In a previous study (Orlandi (1995)) it was found that the background rotation breaks the symmetry of right- and left-handed vortical structures by increasing the helicity density near the wall. Thus the vortical structures have a greater degree of order leading to a reduction of production and dissipation near the wall. In the case of MHD flows the helicity density was null across the pipe as for  $Ha = 0$  and so the decrease of production and dissipation are due to the reduction of turbulence intensities, that is greater as smaller are the scales. Thus the small scale structures near the wall disappear and remain the large scales producing bursting events less intense. However the amount of disorder near the wall for MHD flows remain unchanged with respect to that of a non-rotating pipe.

These preliminary coarse direct simulations have the capability to reproduce the different behavior between the case with an azimuthal and an axial magnetic field. On the contrary the quantitative comparison between the experiments and the numerics was poor. This is something that should be explained and it requires a careful grid resolution checks. From the turbulence point of view the case of an axial magnetic field is more interesting because the external force acts only on the turbulence. A close comparison between this case and rotating pipes is useful to investigate whether or not there is a common physical mechanism on drag reduction.

**Acknowledgements :** The author is sincerely grateful to the CTR for hosting him on the summer 1996 and to the stimulating discussions with Prof. H.Choi. A private communication by Prof. A. Tsinober is appreciated. The research was partially supported by MURST grants.

## REFERENCES

- Branover, G., G., Gel'fat, Yu., M., & Tsinober A., 1966 "Turbulent magnetohydrodynamic flows in prismatic and cylindrical ducts" *Magnetohydrodynamics*, Vol.2, pp. 3-21.
- Durst, F., Jovanovic, J. & Sender, J., 1995 "LDA measurements in the near-wall region of a turbulent pipe flow" *J. Fluid Mech*, Vol. 295, pp. 305-335.
- Kida, S., Yanase, S., & Mizushima, J., 1991 "Statistical properties of MHD turbulence and turbulent dynamo" *Phys. Fluids A*, Vol.3, pp. 457-465.
- Eggels, J.G.M., Unger, F., Weiss, M.H., Westerweel, J., Adrian, R.J., Friedrich, R. & Nieuwstadt, F.T.M., 1994 "Fully developed turbulent pipe flow: a comparison between direct numerical simulation and experiment" *J. Fluid Mech*, Vol.268, pp. 175-209.
- Fraim, F. W., & Heiser, W., H., 1968 "The effect of a strong longitudinal magnetic field on the flow of mercury in a circular tube" *J. Fluid Mech*, Vol.33, pp. 397-413.
- Krasil'nikov, E., Yu, Lushchick, V., G., Nikolaenko, V., S. & Panevin, I., G., 1970 "Experimental study of the flow of an electrically conducting liquid in a circular tube in an axial magnetic field" *Fluid Dynamics*, Vol.6, pp. 317-320.
- Moffatt, H., K. & Tsinober, A., 1992 "Helicity in laminar and turbulent flow" *Annu. Rev. Fluid. Mech.*, Vol.24, pp. 281-312.
- Orlandi P., 1997 "Helicity fluctuations and turbulent energy production in rotating and non-rotating pipes" To appear *Phys. Fluids A* and *Annual Research Brief of CTR* 1995, pp. 198-208.
- Orlandi P. & Fatica, M., 1996 "Direct simulations of a turbulent pipe rotating along the axis" To be published on *J. Fluid Mech.*
- Reed, C. B. & Likoudis, P., S., 1978 "The effect of a transverse magnetic field on shear turbulence" *J. Fluid Mech*, Vol.89, pp. 147-171.
- Shimomura, Y., 1991 "Large eddy simulation of magnetohydrodynamic turbulent channel flows under a uniform magnetic field" *Phys. Fluids A*, Vol.3, pp. 3098-3106.
- Tsinober, A., 1990 "MHD flow drag reduction" *Viscous drag reduction in boundary layers* edited by D., M., Bushnell & J., N., Hefner *Progress in Astronautics and aeronautics*, Vol.123, pp. 327-349.
- Tsinober, A., 1990 "Turbulent Drag Reduction Versus Structure of Turbulence" *Structure of Turbulence and Drag Reduction* ed. A. Gyr. Berlin: Springer Verlag, 313-340.
- Verzicco, R. & Orlandi P., 1996 "A finite difference scheme for direct simulation in cylindrical coordinates" *J. of Comp. Phys*, Vol. 123, pp. 402-414.

## **SESSION 15 - APPLICATIONS I**



# COMBINED P.I.V. AND L.D.V. ANALYSIS OF THE EVOLUTION AND BREAKDOWN OF A COMPRESSED TUMBLING VORTEX

Daniel Marc, Jacques Borée, Rudy Bazile and Georges Charnay

Institut de Mécanique des Fluides  
UMR CNRS/INPT-UPS 5502  
Allée du Professeur Camille Soula  
31400 TOULOUSE  
FRANCE

**ABSTRACT:** A model experimental set-up dedicated to the study of a compressed tumbling motion is presented. Measurements are obtained by using LDV and PIV in a complementary way. We quantify effects of cycle to cycle variations on ensemble mean and fluctuating velocity fields at the end of the admission phase. The influence of initial charge rotation on turbulence is discussed. During the compression phase, the breaking down of the tumbling vortex is a gradual process and the vortex/wall interaction is proved to be an essential mechanism responsible for abrupt modifications of the flow field and for the generation of 3D turbulence. The problem of turbulence level estimation appears very complex owing to cyclic variations. This point is discussed by computing both ensemble and in-cycle rms velocities from PIV velocity fields. We show that the turbulent velocity field at TDC is quasi homogeneous and isotropic. The turbulent integral length scales are computed.

## 1 - INTRODUCTION

An important research is presently dedicated to the optimisation of in cylinder flow motion in spark ignition engines in order to meet emission and fuel economy requirements (Arcoumanis and Whitelaw 1987; Hill and Zhang 1994). To save time and money in engine development, computer codes are developed to deal with these complex unsteady flows. However, owing to the complexity – and often uncertainty – of measurements in real engines, validation of existing predictions and development of new turbulence models often require the use of model experiment set-up to isolate and analyse precisely typical physical mechanisms.

A square piston compression machine (Marc *et al* 1996) is presently used at IMFT to study the compression of a bidimensional tumbling motion (fig. 1). The tumbling motion sketched in figure 1 is a rotating flow generated during the admission phase which axis is perpendicular to the cylinder axis. A complex "vortex breakdown" occurs during the compression phase and results in the generation of a significant turbulence level. This feature is used to obtain a

shorter combustion period and to widen air-fuel ratio limits in engines and is highly linked with present environmental preoccupations. The compression chamber is equipped with large optical access in order to study the generation, evolution and further breakdown of the large tumbling motion with optical diagnostic techniques. Results and interpretations based on both Particle Image Velocimetry (PIV) and Laser Doppler Velocimetry (LDV) enable an accurate and complementary study of the compressed tumbling motion.

The experimental set-up and flow measurement techniques will be first described. The flow structure obtained at the end of the admission phase and the very well known problem associated with cycle to cycle variations will be presented. Data will show that a major effect of rotation on turbulence can be expected. In such a situation, the so called "vortex breakdown" process is highly complex and is not yet fully understood. Moreover, the nature of the turbulent velocity field obtained after the destabilisation of the initial basic organised flow is not known. Combined PIV and LDV measurements during the compression will provide a good picture of the compressed tumble and will particularly show the importance of the vortex interaction with walls as the gradual "breakdown" process is concerned. The nature of the turbulent field at the end of the compression phase will be further analysed from refined PIV velocity fields. Integral length scales will be computed and discussed.

## 2 - EXPERIMENTAL ARRANGEMENT

### a/ Compression chamber

The compression engine available at IMFT has a square cylinder ( $100 \times 100 \text{ mm}^2$ ) equipped with a flat head. The distance between the piston and cylinder head at Bottom Dead Centre (BDC) is  $H=100 \text{ mm}$ . The present data have been obtained with a volumetric ratio of  $\epsilon=5$  corresponding to a stroke of the piston of  $80 \text{ mm}$ . The optical access and PIV laser sheets orientations are sketched in figure 1. Laser sheet 1 (LS1) is perpendicular to the axis of the tumble and lights the upper 60% of the compression chamber. Laser sheet 2 (LS2) is parallel to the axis of the tumble. The piston

is driven at 200 rpm by an alternative machine tool and the maximum piston velocity reaches one meter per second. The location of the piston within the chamber is accurately measured by a magnetic ruler fixed on the machine tool. This device makes it possible to perform statistical PIV and LDV measurements at a given position of the piston in the 'intake-compression' phases.

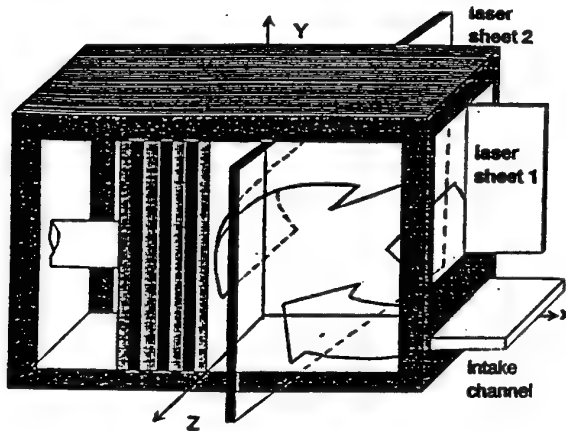


FIGURE 1: Sketch of the compression machine

The intake system is a portion of a flat canal (length :  $L_e = 150$  mm); the ratio width/height is equal to 9.6 ( $h_e \times l_e = 10 \times 96$  mm) which is sufficient to ensure the bidimensionality of the flow over a large part – 80% – of the intake canal. The intake port is closed by a "guillotine device" the motion of which is directly controlled by the machine tool. A particular development was necessary to obtain an airtight device. Insofar as the Reynolds number based on the hydraulic diameter reaches high values with a maximum  $Re_{max} = 12000$  the boundary layers are turbulent during the main part of the intake stroke. During the admission phase, the bidimensional intake jet flow, tangential to the cylinder floor, is deflected by the moving piston and generates the tumbling vortex. A four-stroke cycle has been defined. The channel is closed during the compression/expansion strokes. The turbulence generated before piston TDC therefore decays during the expansion stroke. The guillotine opens for the exhaust and admission phase.

#### b/ PIV and LDV configurations

Velocity measurements are performed using two complementary optical techniques : PIV and LDV. The intake air is seeded with silicone oil particles (diameter =  $5 \mu m$ ) which do not modify the fluid properties while being able to track accurately the fluid motion (low Stokes number). For PIV application a Yag laser beam ( $\lambda = 532$  nm,  $\Delta t = 10$  ns, double impulsion :  $\epsilon = 2 \times 100$  mJ,  $f = 10$  Hz) is focused into a vertical light sheet passing through the compression chamber. Mie scattering emissions from the oil droplets are imaged at  $90^\circ$  onto a gated 'Charge Coupled Device' camera (LHESA 510). Piston motion, laser firing and camera timing are synchronised so that both images formed at each laser shot are respectively restored in the odd and even frames of the video signal. This two frames are digitised by a frame grabber board (OFG,  $768 \times 512$  pixels, 8 bits) connected to a PC. The particle displacement is obtained by 2D intercorrelation (this solves directional ambiguity) with post processing V2IP software (CORIA). Each image frame is interrogated in  $32 \times 32$  pixels sub-images at intervals of 16 pixels (i.e. a 50% overlap). The corresponding width of the

interrogation cell in the flow varies from 1.5 mm to 3,8 mm depending on the optical magnification. Sub pixel accuracy is achieved by a 2D Gaussian curve fit of the cross-correlation peak (Lecordier *et al* 1994). Problems occur occasionally in bright regions very near black painted walls or when the data density is too low. Two different thresholds based on predetermined SN ratio and on velocity vector amplitude are applied. No interpolation is employed to make up for incomplete data.

LDV system comprises an Argon-ion laser (8 W,  $\lambda_1 = 488$  nm,  $\lambda_2 = 514,5$  nm), a conventional fibre optical unit and a bragg cell (40 Mhz). The receiving optic (backscattering configuration) is a Dantec unit equipped with two photomultipliers connected to Burst Spectrum Analysers (BSA). Velocities are measured during the intake/compression strokes. A correction by residence time of the seeding particles is systematically used to reduce the velocity bias present in velocity measurements (Petrie *et al* 1988). Ensemble mean and rms velocity fluctuations are computed from the instantaneous values collected over crank angle windows ( $\Delta\alpha = 3.6^\circ$ ).

### 3 - TUMBLING MOTION OBTAINED AT THE END OF THE ADMISSION PHASE

The mean tumble velocity at BDC displayed in figure 2 was obtained by averaging 50 instantaneous velocity fields. A laser sheet LS1 in the symmetry plane of the chamber was used. A very clear rotation is observed and the Reynolds number of the structure is  $Re = (H \cdot V_{max}) / \nu = 12500$ . As an order of magnitude estimation, we note that the angular rotation rate of a solid body vortex of radius  $R/H = 0.4$  having the same angular momentum is roughly  $\Omega_T = 100$  rad/s. The corresponding tumble vortex ratio  $c_T = \Omega_T / \Omega_{piston}$  is  $c_T = 4.8$ . PIV velocity fields in the LS2 plane have shown that the mean flow is bidimensional (Marc *et al.* 1996). Moreover, an estimation of the large vortex decay time imposed by the two lateral Eckman layers on the side wall (Schlichting 1979) shows that this time is significantly large compared with the compression time scale.

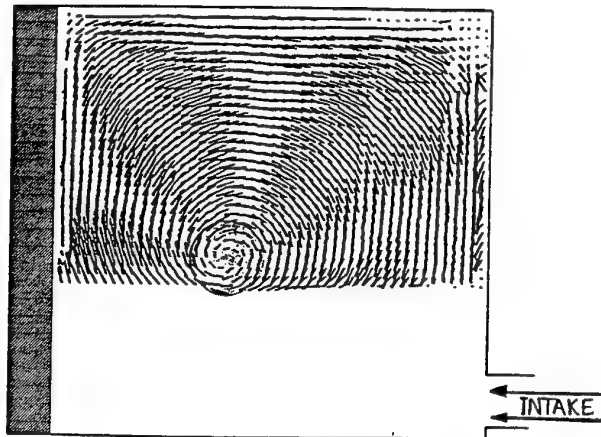


FIGURE 2: Mean tumble velocity at BDC  
(Hatched region corresponds to the region where instantaneous vortex centres were detected)

An automatic centre extraction procedure was developed in order to localise the position of the vortex centre on mean or instantaneous PIV velocity fields (Marc *et al.* 1997). The location of the mean vortex axis is  $x_c/H = 0.45$  and

$y_c/H=0.43$ . The hatched region in figure 2 corresponds to the region where instantaneous vortex centres were detected. The averaged distance between instantaneous and mean vortex axis is  $d_c/H=3.10^{-2}$ . These cycle to cycle variations are classical features due to either slight boundary condition variations or to the natural precession of the confined structure (Van Geffen *et al* 1996). Profiles of the velocity statistics on the horizontal line passing through the mean vortex centre are plotted in figure 3.  $U, V$  are respectively the velocity in the X and Y directions sketched in fig. 1. With 50 samples and a 95% confidence level, the absolute error on  $\bar{V}$  is 0.3 m/s and the relative error on second order moments is 20%. Moreover, for an estimated turbulent integral length scale  $\Lambda$  of the order of the channel height  $h_e$ , the PIV intercorrelation window is roughly of size  $(\Lambda/3) \times (\Lambda/3)$ . Only the energetic mode is therefore obtained with this low pass filtering mesh. Direct comparison with LDV data (Marc *et al* 1997) show however a good accuracy of these estimates.

A distinct peak of rms velocities appears on the mean vortex axis in fig. 3. This peak can only be a consequence of the cyclic variations of vortex position. For a solid body rotation of azimuthal velocity  $U_\theta = \omega r$ , exact relations can be derived between the statistics of the vortex axis position and the local velocity. For a given pdf of instantaneous axis position, one obtains  $u' = \omega \sigma_{y_c}$  and  $v' = \omega \sigma_{x_c}$  where  $\sigma_{x_c}$  and  $\sigma_{y_c}$  are respectively the standard deviation in vortex centre abscissa  $x_c$  and ordinate  $y_c$ . An equivalent rotation rate  $\omega_e$  can be therefore derived from the PIV measurements of the rms velocity at the mean vortex axis location and from the measured  $\sigma_{x_c} = 2.2$  mm and  $\sigma_{y_c} = 1.9$  mm. The corresponding local velocity profile is drawn in dashed line in figure 3 and is seen to correspond closely to the characteristics of the core of the mean vortex. This point validates several different aspects of our PIV results and shows that a moderate cyclic variation produces surprisingly high levels of velocity fluctuations.

Away from the mean axis, an order of magnitude of the rms velocity is  $u' \approx 0.7$  m/s. With  $\Omega_T = 100$  rad/s and  $\Lambda = h_e = 10$  mm, one obtains for the Rossby number :  $Ro = (u'/\Omega_T \Lambda) = 0.7$ . Rotation is expected to have a significant influence (Jacquin *et al* 1990; Le Roy and Le Penven 1997) on the turbulent velocity field.

#### 4 - EVOLUTION OF THE TUMBLING MOTION DURING THE COMPRESSION PHASE

During the compression phase, the tumbling motion is known to experience a transition from an organised 2D structure to a fully 3D flow at piston Top Dead Centre (TDC). However, the precise "vortex breakdown" process is not fully understood yet and is very hard to analyse from LDV local measurements in which cyclic variations can hide the true mechanisms. As an example, the time evolution of ensemble mean and rms velocities measured at the geometric centre of the clearance volume during the compression stroke are displayed in figure 4. The evolutions are very similar to those presented by (Floch *et al* 1995; Gosman *et al* 1985). Fluctuations generated by the intake jet first undergo a slight decrease. At the same time, the reduction of the cylinder volume by the moving piston gives rise to higher tumble velocity. Looking at this graph only, the breakdown process of the tumble would be said to occur after  $\epsilon=2$  corresponding

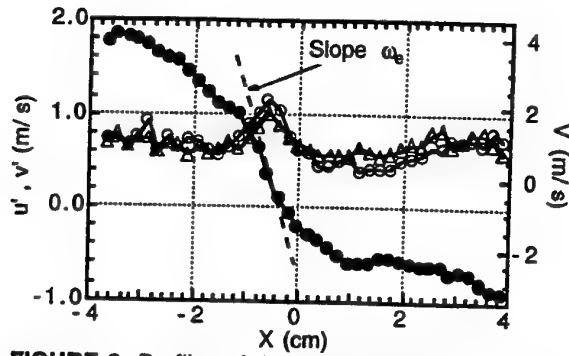


FIGURE 3: Profiles of the velocity statistics on the horizontal line passing through the mean vortex centre.

●, V; Δ, u'; ○, v'

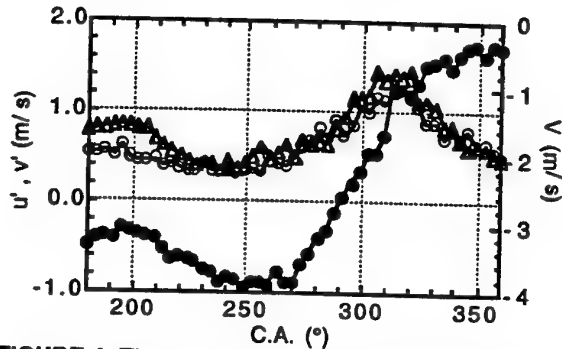


FIGURE 4: Time evolution of ensemble mean and rms velocities at the geometric centre of the clearance volume during the compression stroke.

●, V; Δ, u'; ○, v'

to 270 °CA. This explains the rapid decrease of the tangential velocity to reach a zero value and the correlated significant increase of the turbulence intensity up to 1.8 m/s. LDV measurements performed systematically in the chamber (Marc *et al* 1997) however show that the ensemble turbulence is significantly inhomogeneous.

PIV velocity fields were measured during compression in the same plane LS1 at four volumetric ratio  $\epsilon=2.5$ ; 3.3; 4 and 5 corresponding respectively to a chamber height of 40mm; 30mm; 25mm and 20mm. 30 realisations were stored in each case. Many graphs could be shown here. Mean velocity fields are shown in figure 5a and 6a,b,c. The shaded regions correspond to vortex regions according to the definition of Jeong and Hussain (1995). The symmetric (S) and antisymmetric ( $\Omega$ ) part of the velocity gradient tensor are computed from the mean PIV velocity field and the vortex core corresponds to negative second largest eigenvalue of  $(S^2 + \Omega^2)$ . Despite the convoluted contours due to the experimental resolution, we see that this definition effectively captures the main vortex and the recirculating region.

The large scale vortex is clearly seen in fig. 5a at  $\epsilon=2.5$ . The streamlines in the vortex core are of elliptical nature and the 2D structure is expected to experience a natural 3D instability (Lundgren and Mansour 1996; Waleffe 1990) if this instability has sufficient time to develop. This last point is under question in the present case as the vortex interaction with wall can induce flow separation and an abrupt modification of the flow field. Fig. 5a shows indeed a large separation zone along the piston wall in the adverse pressure gradient region induced by the vortex and a similar

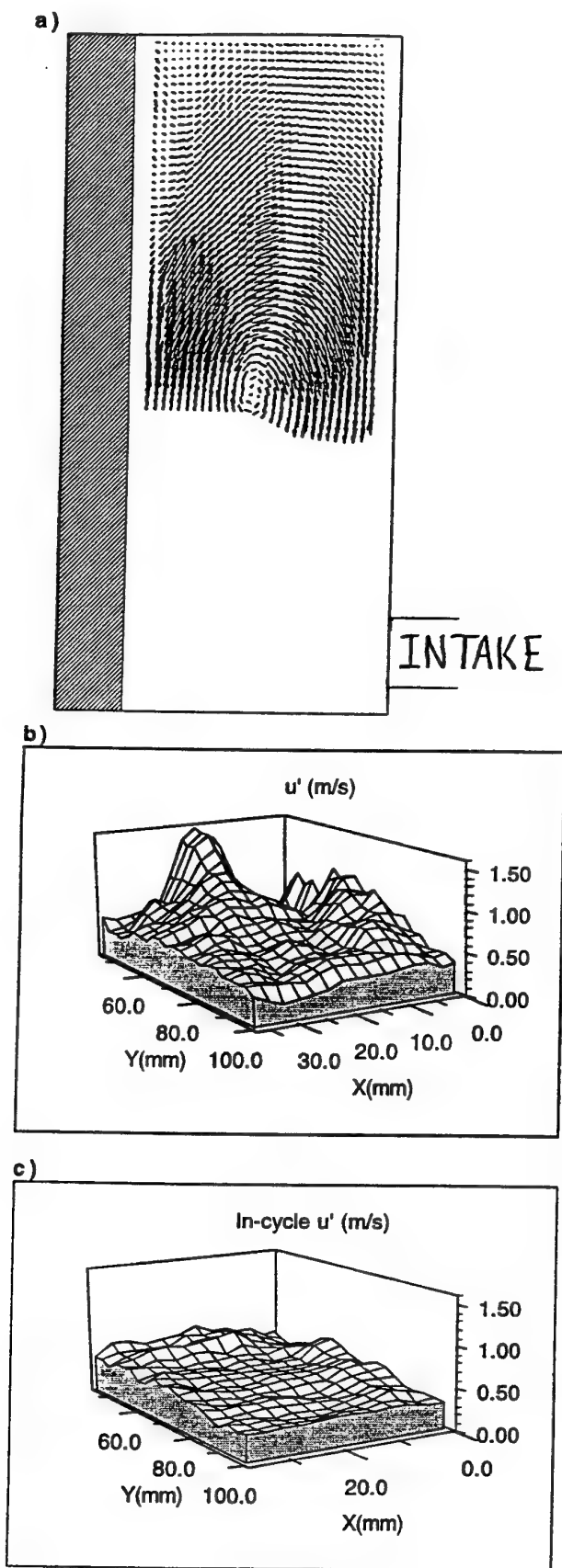


**FIGURE 5:** a- Mean PIV velocity field at  $\epsilon=2.5$   
b- 3D plot of the rms longitudinal velocity  
c- 3D plot of the in-cycle rms longitudinal velocity

phenomena is expected to appear along the cylinder head at the bottom of the figure where no measurement were made.

On the 3D plot of the ensemble longitudinal rms velocities (fig. 5b ;  $X=0$  plane corresponds to the piston head), a sharp peak is again associated with the mean vortex axis and should be the signature of a significant cyclic variation when confinement increases. A higher level of  $u'$  is also associated with the recirculation zone. The flow separation is of course cycle dependant and this region of higher  $u'$  can be the result of both intense turbulence production and cyclic variations of vortex/wall interactions.

The separation zone spreads over the entire upper part of the measurement region as the piston progresses (see fig 6a- $\epsilon=3.3$ ) and the remaining mean vortex is confined in the middle of the chamber at  $\epsilon=4$  (fig.6b). Confinement effects are expected to increase the strength of the vortex/wall interactions. This point is further analysed and emphasised using Direct Numerical Simulation in a companion paper (Borée *et al* 1997).

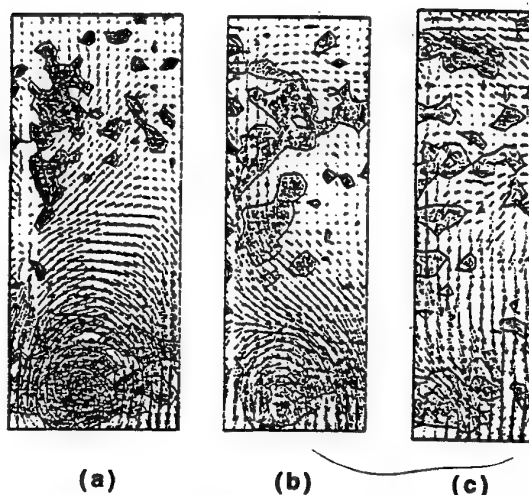


**FIGURE 6:** Mean PIV velocity field at  $\epsilon=3.3$  (a) ;  $\epsilon=4$  (b) and  $\epsilon=5$  (c). Shaded regions correspond to vortex regions

Assuming that a spatial separation distinguishes the instantaneous bulk flow structure and the largest turbulent eddies, in-cycle fluctuations can be defined as the difference between the instantaneous velocity and the spatial low pass filtered PIV velocity field. A 3D plot of the in-cycle longitudinal rms velocities is shown at  $\epsilon=2.5$  (fig. 5c). A top hat filter of width  $8.5 \times 8.8 \text{ mm}^2$  corresponding to  $7 \times 7$  PIV vectors was used to compute in cycle-turbulence. The width of the filter is chosen to be larger than the estimated integral length scale (see next section). With 30 realisations, only qualitative trends can of course be discussed. In figure 5c, in-cycle rms velocities are rather uniform all over the chamber. The same contrast between ensemble and in-cycle turbulence holds for larger  $\epsilon$  (Marc *et al.* 1997). Moreover, the level of in-cycle rms velocities is of the order of the rms velocities measured at piston TDC in next section. PIV offers the possibility of post-processing techniques closely related with the development of Large Eddy Simulation techniques in turbulence modelling. The usual large peak in ensemble rms velocity seems to be mainly associated with cycle to cycle variations.

The breaking down of the tumbling vortex shown here is a gradual process. No mean or instantaneous tumbling motion would be detected at  $\epsilon=5$  (fig. 6c). Moreover, the mean

secondary flows measured by PIV are weak and 3D effects are therefore expected to be responsible for a significant generation of 3D turbulence during the separation process (Borée *et al.* 1997).

## 5 - NATURE OF THE TURBULENT FIELD AT TDC

The laser sheet LS2 was used to study the transverse structure of the flow in the symmetry plane of the clearance volume at TDC. The PIV image (width x height = 35x24 mm<sup>2</sup>) is a zoom of the middle part of plane LS2 and the width of the interrogation cells is lower than 1/6 of the integral length scale computed below. A typical instantaneous velocity map is displayed in figure 7. It shows that the flow field is fully tridimensional and turbulent. No particular structured motion is detected after the tumble breakdown. 30 instantaneous velocity fields were stored and a computation of the rms velocities shows that the turbulent field is quasi homogeneous and isotropic with  $v' = w' = 0.6$  m/s. Note that this corresponds to the values measured for  $u'$  at TDC (Marc *et al.* 1997).

The turbulent integral length scales at TDC are particularly important to compute when simulating an engine operating characteristics in order to predict the propagation of the flame. The use of Taylor hypothesis in a zero mean velocity turbulent field is clearly not possible and PIV technique offers an alternative really suited for this computation if the cells are small enough with respect to the integral length scale. The correlation tensor  $R_{ij}(P_1, P_2, t)$  is defined by :

$$R_{ij}(P_1, P_2, t) = \frac{u_i(P_1, t)u_j(P_2, t)}{\sqrt{u_i^2(P_1, t)}\sqrt{u_j^2(P_2, t)}}$$

For an homogeneous turbulent flow field,  $R_{ij}(P_1, P_2, t)$  does not depend on the location of points  $P_1$  and  $P_2$  but only on the separation vector  $\vec{r} = \overrightarrow{P_1 P_2}$ . In plane LS2, the components of the separation vector is  $\vec{r} = (0, r_2, r_3)$ .

$R_{ij}(r_2, r_3, t)$  at TDC is thus deduced from PIV data by averaging first on the different flow realisations and then on the different spatial locations in a given realisation. The velocity components are  $v = u_2$  and  $w = u_3$  and a contour plot of  $R_{22}(r_2, r_3, t)$  is displayed in figure 8. All averages in figure 8 are deduced from more than 5000 samples. Longitudinal and lateral correlation functions corresponding respectively to  $f(r, t) = R_{22}(r, 0, t)$  and  $g(r, t) = R_{22}(0, r, t)$  are displayed in figure 9. In an incompressible, isotropic and homogeneous turbulent velocity field,  $g(r, t)$  can be deduced from  $f(r, t)$  (Howarth and Von Karman 1938). The computed  $g$  is compared with the measured  $g$  in figure 9 and the fair agreement shows that the flow behaviour is typical of isotropic and homogeneous turbulence. Turbulent length scales are then computed by integrating the longitudinal correlation curves. After integration, one finds :

$$L_{22,2}(TDC) = 8.0 \text{ mm} \text{ and } L_{33,3}(TDC) = 8.4 \text{ mm}$$

With  $L_{22,2}(TDC) = L_{33,3}(TDC)$ , we confirm the tendency to isotropy of the turbulent field at TDC. Moreover, these length scales are of the order of half the clearance height.

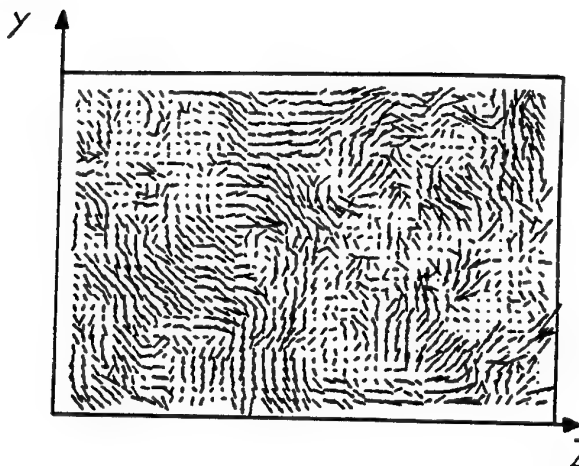


FIGURE 7: Typical instantaneous velocity map at TDC

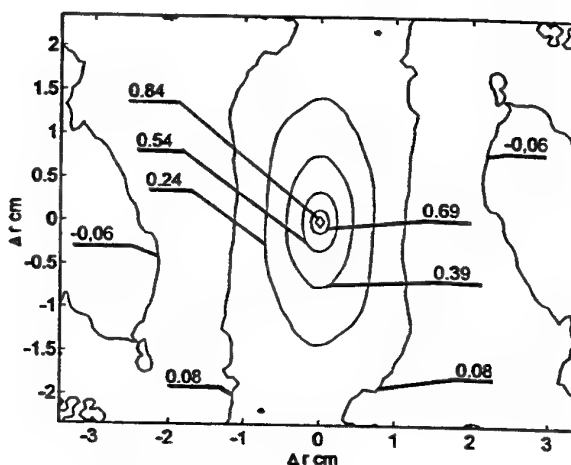


FIGURE 8: Contour plot of  $R_{22}(r_2, r_3, t)$  at TDC

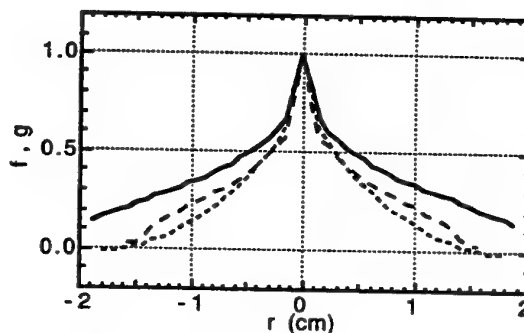


FIGURE 9: Longitudinal and lateral correlation functions at TDC ———,  $f(r, t)$  ; - - - - - ,  $g(r, t)$   
- - - - - ,  $g(r, t)$  computed from  $f(r, t)$  in TH1



## 6 - CONCLUSION

A model experimental set-up dedicated to the study of a compressed tumbling motion has been presented in this paper. Measurements were obtained by using Laser Doppler Velocimetry and Particle Image Velocimetry in a complementary way. At BDC, a strong bidimensional tumbling motion develops in the entire volume of the square chamber and the instantaneous rotation axis of the tumbling motion varies from cycle to cycle. The computed rms distance from the mean axis is only 3% of the chamber height and such a moderate cyclic variation is seen to produce surprisingly high levels of ensemble velocity fluctuations. Exact relations were derived between the statistics of the vortex axis position and the local velocity statistics. Using these relations, we verified quantitatively that the rms velocities at the mean vortex axis location are only the results of the cyclic variations in the position of the large vortex.

PIV gave an opportunity to educe instantaneous spatial flow fields during the compression phase. The breakdown of the tumbling vortex was proved to be a gradual process and the vortex/wall interaction is an essential mechanism. Indeed, very clear separation zones initiate in the adverse pressure gradient region induced by the vortex along the chamber walls. Tridimensional effects are expected to be responsible for a significant generation of 3D turbulence during the separation process and the mean secondary flows induced in the separation zones are very weak. The compression unsteadiness, the vortex motion, the separation process and the turbulence were shown to be linked in an intricate way. Assuming that a spatial separation distinguishes the instantaneous bulk flow structure and the largest turbulent eddies, in-cycle fluctuations were defined as the difference between the instantaneous velocity and the spatial low pass filtered PIV velocity field. Contrary to ensemble rms velocities, in-cycle rms velocities were shown to be rather uniform all over the chamber with no peaks associated with tumble vortex or separation. The usual large peak in ensemble rms velocity therefore seems to be mainly associated with cycle to cycle variations.

A PIV zoom at TDC in the symmetry plane of the clearance volume parallel to the cylinder head was analysed to show that the 3D turbulent field is quasi homogeneous and isotropic. The turbulent integral length scales were computed and are of the order of half the clearance height.

While providing a good understanding of the evolution of the tumbling motion during compression, these results also show the complexity of turbulence modelling in such situations. The models should be very accurate to predict vortex/wall interactions and tridimensional effects. Moreover, when comparing the predictions of the models with experiments, one might not focus on intermediate stages where cyclic variations are prominent but on the final turbulent field obtained after the tumble "breakdown".

## Acknowledgements

This research was supported by CNRS ECOTECH, Renault and PSA in a joint "ARC Moteur Propre" program. D. Marc's research is supported by a grant ADEME. We wish to thank Dr M. TRINITE for his helpful comments about this work. We have benefited greatly from discussions with Dr H.J. NUGLISCH and A. LECERF. The technical support of G. COUTEAU, J.F. ALQUIER and C. JARNOT is greatly acknowledged.

## REFERENCES

- Arcoumanis, C. & Whitelaw, J.H. 1987 Fluid mechanics of internal combustion engines-a review. *IMechE* 201, 57-74.
- Borée, J., Corjon, A. & Marc, D. 1997 Analytical and direct numerical study of the evolution and breakdown of a compressed tumbling vortex. In *11th Symp. on Turbulent Shear flows*, Grenoble, France, Sept. 8-11
- Floch, A., Van Frank, J. & Ahmed, A. 1995 Comparison of the effects of intake-generated Swirl and Tumble on Turbulence characteristics in a 4-Valve engine. *SAE Paper* 952457.
- Gosman, A.D., Tsui, Y.Y. & Vafidis, C. 1985 Flow in a model engine with a shrouded valve. A combined experimental and computational study. *SAE Paper*. 850498
- Hill, P.G. & Zhang, D. 1994 The effects of swirl and tumble on combustion in spark-ignition engines. *Prog. Energy Combust. Sci.* 20, 373-429.
- Howarth, L. & Von Karman, T. 1938 On the statistical theory of isotropic turbulence. *Proc. Roy. Soc. Gottingen Nachrichte A* 164 (917), 192-215.
- Jacquin, L., Leuchter, O., Cambon, C. & Mathieu, J. 1990 Homogeneous turbulence in the presence of rotation. *J. Fluid Mech.* vol. 220, 1-52.
- Jeong, J. & Hussain, F. 1995 On the identification of a vortex. *J. Fluid Mech.* vol. 285, 69-94.
- Le Roy, O. & Le Penven, L. 1997 Compression of a turbulent vortex flow. In *11th Symp. on Turbulent Shear flows*, Grenoble, France, Sept. 8-11
- Lecordier, B., Mouqallid, M., Vottier, S., Rouland, E., Allano, D. & Trinité, M. 1994 CCD Recording method for cross-correlation PIV development in unstationary high speed flow. *Experiments in fluids* 17, 205-208.
- Lundgren, T.S. & Mansour, N.N. 1996 Transition to turbulence in an elliptic vortex. *J. Fluid Mech.* vol. 307, 43-62.
- Marc, D., Borée, J., Bazile, R. & Charnay, G. 1997 PIV and LDV measurements of tumbling vortex flow in a model square section motored engine. In *Submitted to 1997 SAE Int. Fuel and Lubricants Meeting*.
- Marc, D., Borée, J., Bazile, R., Charnay, G., Trinité, M. & Lecerf, A. 1996 Etude expérimentale modèle de l'aérodynamique interne des moteurs: Cas de l'écoulement de rouleur. In *5 eme Congrès Francophone de Vélocimétrie Laser, Rouen*.
- Petrie, H.L., Samimy, M. & Addy, A.L. 1988 Laser doppler velocity bias in separated turbulent flows. *Exp. Fluids* 6, 80-88.
- Schlichting, H. 1979 *Boundary layer theory*. McGRAW Hill Company, New-York.
- Van Geffen, J.H.G.M., Meleshko, V.V. & Van Heijst, G.J.F. 1996 Motion of a two dimensional monopolar vortex in a bounded rectangular domain. *Phys. Fluids* 8 (9), 2393-2399.
- Waleffe, F. 1990 On the three- dimensional instability of strained vortices. *Phys. Fluids A* 2, 76-80.

# COMPRESSION OF A TURBULENT VORTEX FLOW

O. LE ROY, L. LE PENVEN

Laboratoire de Mécanique des Fluides et d'Acoustique  
UMR 5509, ECL-UCB-CNRS  
Ecole Centrale de Lyon  
36, avenue Guy de Collongue  
BP 163 - 69131 Ecully Cedex  
France

## INTRODUCTION

In recent years, much effort has been devoted by car manufacturers to control the turbulent flow in internal engines in order to improve mixing and combustion. One promising way is to generate during the intake process a large-scale vortical motion whose axis is perpendicular to piston velocity (tumbling flow). In this case, it is observed that the mean vortex breaks up at some stage of the compression and produces a high level of turbulence. This phenomenon improves the mixing and the burning rate significantly. There is not yet a clear explanation for the vortex breakdown. Moreover, we do not know much about the ability of standard turbulence models to predict the observed evolution.

The purpose of this communication is

- to present numerical simulations of a turbulent tumbling flow using the Reynolds-averaged flow equations and different classes of turbulence models ( $k-\epsilon$  models,  $\overline{u_i u_j}-\epsilon$  models).
- to interpret the evolution of the mean flow during compression by comparison to laminar computations of a simplified vortex (Taylor-Green vortex) with different boundary conditions (no-slip, no shear).

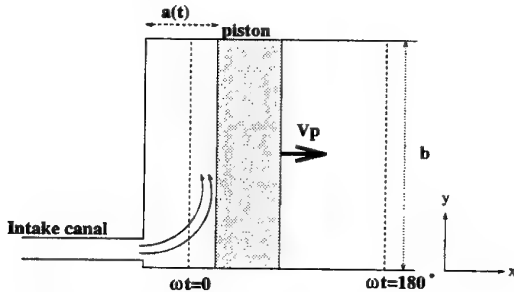


Figure 1: Geometry of the IMFT experiment

The geometry considered for numerical simulations corresponds to the experiment of Marc *et al.* (1997) (hereafter: IMFT experiment) also presented in this TSF

(Fig.1). The flow develops in a chamber equipped with a square piston moving alternatively with the velocity

$$Vp = Vp_{max} \sin(\omega t),$$

$$Vp_{max} = 0.9 \text{ m s}^{-1}, \omega = 220 \text{ rev/min}$$

At top dead center ( $\omega t = 0^\circ$ ), the intake canal flow is accelerated by the piston motion and creates a tumbling flow in the chamber. At bottom dead center ( $\omega t = 180^\circ$ ) the chamber is a cube of edge  $b = 1 \text{ cm}$ , the intake canal is closed and the compression starts. The compression ratio is  $a/b = 5$ .

## NUMERICAL SIMULATIONS WITH TURBULENCE MODELS

### Numerics

The Reynolds-averaged equations have been solved numerically assuming that the flow be two-dimensionnal in the plane  $x, y$ . We have used an elliptic solver of the Navier-Stokes equations employing a finite element discretisation on a moving grid, a semi-implicit time-stepping ensuring linearisation of the differential operators and a convection scheme based on the streamline upwind finite element technique (Mao, Buffat, Jeandel 1994). Walls are assumed athermal, and temperature and density uniform throughout the flow. Typically, the mesh has 25000 nodes. Turbulence models are standard ones:  $k-\epsilon$  model and  $\overline{u_i u_j}-\epsilon$  model (RSM). For near wall layers, these models are used in conjunction with wall functions and an algebraic model to evaluate the components of the Reynolds tensor (Debaty 1994).

### Turbulence modelling

The standard  $k-\epsilon$  adopted is written as :

$$\frac{Dk}{Dt} = \frac{\partial}{\partial x_j} \left[ \left( \nu + \frac{\nu_t}{\sigma_k} \right) \frac{\partial k}{\partial x_j} \right] - \overline{u_i u_j} \frac{\partial U_i}{\partial x_j} - \epsilon \quad (1)$$

$$\begin{aligned} \frac{D\epsilon}{Dt} = & \frac{\partial}{\partial x_j} \left[ \left( \nu + \frac{\nu_t}{\sigma_\epsilon} \right) \frac{\partial \epsilon}{\partial x_j} \right] - c_{\epsilon 1} \frac{\epsilon}{k} \overline{u_i u_j} \frac{\partial U_i}{\partial x_j} \\ & - c_{\epsilon 2} \frac{\epsilon^2}{k} + c_{\epsilon 3} S_{II} \epsilon \end{aligned} \quad (2)$$

The Reynolds tensor is related to the mean strain  $S_{ij}$  by the means of an eddy viscosity coefficient  $\nu_t = c_\mu k^2 / \epsilon$

$$-\overline{u_i u_j} + \frac{2k}{3} \delta_{ij} = \nu_t (S_{ij} - S_{ii} \frac{\delta_{ij}}{3}) \quad (3)$$

$D./Dt$  stands for the material derivative following the mean velocity field. We used standard values for the constants :

$$c_\mu = 0.09, c_{\epsilon 1} = 1.44, c_{\epsilon 2} = 1.92, \sigma_k = 1.0$$

$$\sigma_\epsilon = 1.3, c_{\epsilon 3} = -\frac{4}{3} + \frac{2}{3} c_{\epsilon 1}$$

In  $\overline{u_i u_j} - \epsilon$  model the Reynolds tensor equation is written as

$$\frac{D\overline{u_i u_j}}{Dt} = P_{ij} + \Phi_{ij} + d_{ij} - \frac{2}{3} \epsilon \delta_{ij} \quad (4)$$

The production term  $P_{ij}$  is treated exactly :

$$P_{ij} = -\overline{u_i u_k} \frac{\partial U_j}{\partial x_k} - \overline{u_j u_k} \frac{\partial U_i}{\partial x_k} \quad (5)$$

The turbulent transport  $d_{ij}$  is modelled using a turbulent diffusion hypothesis :

$$d_{ij} = \frac{\partial}{\partial x_k} \left( \frac{\nu_t}{\sigma_k} \frac{\partial \overline{u_i u_j}}{\partial x_k} \right) \quad (6)$$

The pressure strain correlation is split into three contributions:

$$\Phi_{ij} = \Phi_{ij}^1 + \Phi_{ij}^2 + \Phi_{ij}^w \quad (7)$$

The so-called slow and rapid parts  $\Phi_{ij}^1$  and  $\Phi_{ij}^2$  are modelled following Launder *et al.* (1975).  $\Phi_{ij}^w$  is a correction depending on the distance to the solid boundaries ("wall echo" term). The main effect of this term is to transfer some part of the normal fluctuation to the direction parallel to the wall. For the present purpose, this term is expected to be of some importance especially at top dead center. We used for  $\Phi_{ij}^w$  the proposal of Craft and Launder (1991) instead of the more popular Gibson-Launder model (1978), since it has been proved to give the correct sign of transfer in the case of mean strain normal to the wall (wall impinging jets, piston-induced compression). Finally, it must be noted that the additional term ( $c_{\epsilon 3} S_{ii} \epsilon$ ) has been included in  $\epsilon$  equation to account for compression effect (Reynolds 1980).

## Results

**Intake flow.** At the end of the intake, both models predict a well-defined vortex dominating the entire flow field (see the streamlines in Fig.2(a),(d)). A slight difference is observed on the mean angular momentum which is 30% higher for the  $k-\epsilon$  model. As shown in figure 2(b),(e) the mean vorticity distribution predicted by the  $\overline{u_i u_j} - \epsilon$  model results from the roll-up of the mixing layer produced in the upper edge of the intake jet. The spiral shape is not discernible in the  $k-\epsilon$  model predictions and the vortex core motion looks like a solid body rotation.

Fig.3 shows the evolutions of the averaged value of  $k$  calculated over the entire chamber. During the first half of the intake, both models predict an increase in  $k$  caused by the acceleration of the piston, afterwards  $k$  decreases. A striking feature is that kinetic energy is significantly higher in the case of  $k-\epsilon$  model. The most important difference is observed at the end of intake. At this time, the ratio of the two predicted levels is about 4. Kinetic energy levels at the end of the intake are shown in Fig.2(c),(f). Both models behave similarly. The maxima of  $k$  are associated to an increase in the fluctuation normal to the wall in the jet impact zones. A minimum is observed in the vortex

core. This minimum is more pronounced in the case of RSM model.

The differences observed in the middle of the chamber can be explained in part by the effects of the mean rotation. To a large extent, the kinetic energy in the core of the vortex results from production effect by the mean shear in the upper edge of the intake jet. In this mixing layer, the streamlines curvature has a stabilizing effect on turbulence and leads to a decrease in turbulent production. Indeed, these effects appear in the Reynolds stress equation through the production term and the pressure-strain correlations. In contrast, because of the use of eddy viscosity hypothesis, the  $k-\epsilon$  model gives a production term insensitive to the mean rotation (for example ; Speziale *et al.* 1990).

**Compression.** During compression, both models predict an acceleration of the vortex due to the reduction of the chamber volume associated to an increase of kinetic energy. Between 300° and 330°, the  $\overline{u_i u_j} - \epsilon$  model predicts a separation of the wall layers in the upper right corner and in the lower left corner which are adverse pressure gradient regions then the generation of two vortical structures above and below the initial vortex. These vortices are very intense and have an opposite rotation sign relative to the original vortex (fig.6(b)). They spread in the chamber until the end of compression and simultaneously the initial vortex becomes smaller and is confined in the middle of the chamber with a quasi circular shape. The generation of the two intense vortices involves important velocity gradients and leads to an increase of  $k$  level (Fig.3).

With the  $k-\epsilon$  model no separation occurs. We obtain at the same time a strong decrease in the tumble intensity involving the dissociation of the initial vortex in a pair of slow eddies with the same rotation sign (fig.6(a)) at the edges of the chamber. This collapse is associated to a strong decrease in the kinetic energy. The prediction of RSM without wall echo term is also plotted on Fig.3. The main effect of this term is observed in late compression. At this time, its role is to transfer in the  $y$  direction some part of the normal stress aligned with the direction of the compression and thereby to reduce the overall turbulent production.

## Comparison with the IMFT experiment.

The experimental data obtained by Marc *et al.* (1997) are now compared to the models predictions. The absence of appreciable mean velocity (Marc *et al.* 1997) in the spanwise direction during the intake gives support to the hypothesis of 2D calculations. The profiles of  $U$ ,  $V$ ,  $u^2$  and  $\overline{v^2}$  are taken at the middle of the chamber along the  $x$  and  $y$  axes at the end of intake (Figure 5). Concerning the mean velocity, the nearly linear profiles predicted by the  $k-\epsilon$  model overestimate the data especially near the walls and a better agreement is obtained from the RSM model. Clearly both models fail to predict the maximum of  $\overline{u^2}$  measured in the center of the chamber. Similar peaks have been detected in the IMFT experiment on  $x$  profiles (not shown here). Discarding this local anomaly that will be discussed at the end of the paper, the overall tendency is that the  $k-\epsilon$  model overestimates the turbulence levels especially near the walls and that the RSM predictions are closer to the experimental data.

Concerning the compression, only partial comparison has been obtained at this time. The development of secondary vortices is also evident from the PIV measurement. However the main flow structure disappears gradually as the compression proceeds in contrast with the reinforcement of the three-eddy pattern shown by the computations. Marc *et al.* (1997) suggest the occurrence of strong large-scale and cycle dependant motions. This question will be also



discussed in the next section.

## NUMERICAL SIMULATION IN LAMINAR REGIME

Both turbulence models lead to similar mean velocity fields at the end of intake. However, predictions for the compression differ markedly. The first objective of this section is to illustrate by some direct numerical simulations that the differences obtained in the averaged levels of eddy viscosity at the end of intake (4 times higher in the case of  $k-\epsilon$  model) are mainly responsible for these differences. Then, in the particular case of no-shear boundary conditions, we shall show that the compressed flow may exhibit strong three-dimensionality. Finally, we shall propose an explanation for the anomalous peaks of fluctuation detected at the end of intake.

As initial conditions when the compression starts, we take a 2D velocity field  $\mathbf{v} = \nabla \times \psi \mathbf{z}$  with the streamfunction

$$\psi = \frac{b^2 \Omega_0}{2\pi^2} \sin \frac{\pi x}{b} \sin \frac{\pi y}{b} \quad (8)$$

corresponding to one cell of the plane Taylor vortex flow. This particular field satisfies a zero-shear boundary condition rather than the no-slip one. However, as shown on Fig.(4), the deduced vorticity which is in the present case constant along streamlines is, except in the thin wall layers, a fairly good approximation of the vorticity fields deduced from the models. For these computations, the molecular viscosity is taken as a constant equal to the averaged value of the eddy viscosity. The Reynolds numbers  $Re = \frac{\Omega_0 b^2}{\nu}$  based on the maximum value of the initial vorticity  $\Omega_0$  is thus 1570 and 7340 corresponding respectively to  $k-\epsilon$  and RSM models.

### 2D simulations with no-slip conditions

A first set of evolutions has been obtained imposing zero velocity on boundaries at initial time. In that case, viscous layers develop rapidly during the first steps of the computation. For the higher value of  $Re$ , separation occurs during compression and a final state consisting of three counterrotating eddies similar to the pattern observed in the case of  $\overline{u_i u_j} - \epsilon$  model (fig.6(f)). For the lower value of  $Re$ , no clear separation is observed (fig.6(e)). The evolution is also similar to that obtained with the  $k-\epsilon$  model. The mean flow decay is however stronger in the present case. This may be explained by the fact that  $\nu_t$  decreases at the end of the compression whereas the molecular viscosity is assumed to be constant in the present case.

### 3D simulations with no shear conditions

When the fluid is allowed to slip along the solid boundaries, one can find a solution giving the evolution of initial Taylor vortex during the compression. This solution reads

$$\mathbf{v} = \nabla \times \psi \mathbf{z} - \frac{1}{a} \frac{da}{dt} \mathbf{x} \quad (9)$$

with

$$\psi = A(t) \sin \frac{\pi x}{a(t)} \sin \frac{\pi y}{b} \quad (10)$$

$$A(t) = \frac{b^2 \Omega_0}{\pi^2} \left( \frac{b}{a(t)} + \frac{a(t)}{b} \right) \quad (11)$$

$$\times \exp \left( -\nu \pi^2 \int_0^t ds (a(t)^{-2} + b^{-2}) \right)$$

When  $a \neq b$  is a constant, this solution reduces to the flow studied by Mansour and Lundgren (1986). In that case, the solution is linearly stable under 2D disturbances and

Mansour and Lundgren have proved the instability with respect to 3D perturbations when the Reynolds number is large enough. To some extent, this instability is similar to the three-dimensional instability of unbounded flow with elliptical streamlines (Bayly (1986), Waleffe (1990)).

For the compressed Taylor vortex, a similar evolution may be expected. We have tested numerically the stability of this solution by introducing a small perturbation (1% of the main flow) consisting in a Taylor vortex similar to (Equ.8) with vorticity directed toward negative values of  $x$ . A pseudo-spectral is used for this purpose and reflectional symmetries are assumed to ensure zero normal velocity conditions at the boundaries. Fig.7 shows surfaces of constant magnitude (one half of the maximum value) at four times during compression. At the initial time, the surface is aligned along  $z$  axis and the perturbation is not discernible. For the lower value of the Reynolds number, the perturbation is attenuated and the vorticity surface remains virtually identical to the case of unperturbed solution. For the higher value, the perturbation is strongly amplified. The initial sinusoidal shape of the perturbation steepens gradually. At the same time, the vorticity surface shrinks indicating some local amplification of the maximum vorticity. At the end of compression, this surface tilts suddenly towards negative  $z$ . Thus, one may conclude that the low value of the eddy viscosity given by RSM can give rise to substantial three-dimensional motion during the compression. Indeed, a more detailed is needed, in particular to prove the stability of the mean at the Reynolds number predicted by the  $k-\epsilon$  model.

### Precession of the vortex core

As noted above, turbulence models cannot capture the local maxima of fluctuation in the center of the chamber. Marc *et al.* suggest that these peaks result from cyclic variations of the vortex center. We can refer to the dynamics of the Taylor vortex to test this hypothesis. For a square geometry ( $a = b$ ), 2D linear eigenmodes of the non viscous Taylor vortex are oscillatory. The lowest frequency mode ( $0.16 \Omega_0^{-1}$ ) corresponds to a precession motion of the vortex center. Reasonably, this first eigenmode may be approximated by a combination in quadrature of the first two harmonics of the basic streamfunction (Equ.8). Averaging over the phase of this oscillating motion and assuming that the perturbation is small, the mean squared value of the fluctuation can be expressed as a function of the radius  $\Delta r$  of the trajectory of the vortex center. We have for the  $x$  component

$$\overline{u^2} = \frac{\Delta r^2 \Omega_0^2}{16} \left( 2 \sin^2 \left( \frac{\pi x}{b} \right) \cos^2 \left( \frac{2\pi y}{b} \right) + \frac{1}{2} \sin^2 \left( \frac{2\pi x}{b} \right) \cos^2 \left( \frac{\pi y}{b} \right) \right) \quad (12)$$

This identity, and the similar one for  $\overline{v^2}$ , are plotted in Fig.5(b) with the value  $\Delta r = 0.002 m$  obtained from PIV measurements. Since the length scale of the vortex center motion is large compared to the integral length scale of the background turbulence ( $(\overline{u^2})^{3/2} / \epsilon \sim 0.01 m$ ), one may consider that the corresponding contributions to the velocity are almost uncorrelated. Thus, it is tempting to filter the precession velocity by removing the mean-squared contribution from the total stress. Doing this, we cannot erase the central peak completely. One may consider however that the width and the maximum of the precession profile agree reasonably with the experimental data.

## CONCLUSION

A numerical study of a turbulent vortex flow corresponding to Marc *et al.* (1997) experiment is presented. First, 2D computations of the Reynolds-averaged equations with  $k-\epsilon$  and  $\overline{u_i u_j} - \epsilon$  models have been performed.

During the intake, both models predict a well organized vortex with comparable angular momentum. During the compression, the evolutions of the mean flow are however dissimilar. Strong secondary vortices are predicted by the  $\overline{u_i u_j} - \epsilon$  model, whereas, in the case of  $k - \epsilon$  model, we observe a rapid decay of the mean velocity in the late compression without significant secondary flow. This may be explained by the large difference between the eddy viscosity levels at the end of intake (5 times higher in the case of  $k - \epsilon$  model), which in turn results from the well-known inadequacy of  $k - \epsilon$  models in swirling flows. This fact has been checked by direct numerical simulations with a constant viscosity equivalent the eddy viscosity of the models.

The experiment of Marc *et al.* shows that the main flow remains essentially two-dimensional during the intake. At the beginning of compression, kinetic energy levels lie between  $k - \epsilon$  and  $\overline{u_i u_j} - \epsilon$  predictions, with a better agreement however for the latter. The anomalous peaks of rms velocity detected in the center of the chamber are interpreted here in terms of precession of the vortex core. Some difference is observed with the  $\overline{u_i u_j} - \epsilon$  predictions in the second part of compression. The existence of three-dimensional and large-scale flow is suspected. Such an evolution that could be sensitive to perturbations in the initial state and thus cycle-dependant would have a smoothing effect on the average. Thus, an important question is to know if RSM computations or direct simulations with an equivalent viscosity could generate substantial three-dimensional flow. This 3D evolution could be generated by elliptical-type instability as illustrated by our direct simulations of the compressed Taylor vortex. In these simulations, no-shear

boundary conditions are used. With no-slip conditions, the stability of the flow may be rather different and further investigation is needed to verify this hypothesis.

#### Acknowledgments

The authors would like to acknowledge the CNRS-Ecotech, PSA and Renault for their financial support. O.L.R. has received a grant from the Agence pour le Développement et la Maîtrise de l'Energie (ADEME).

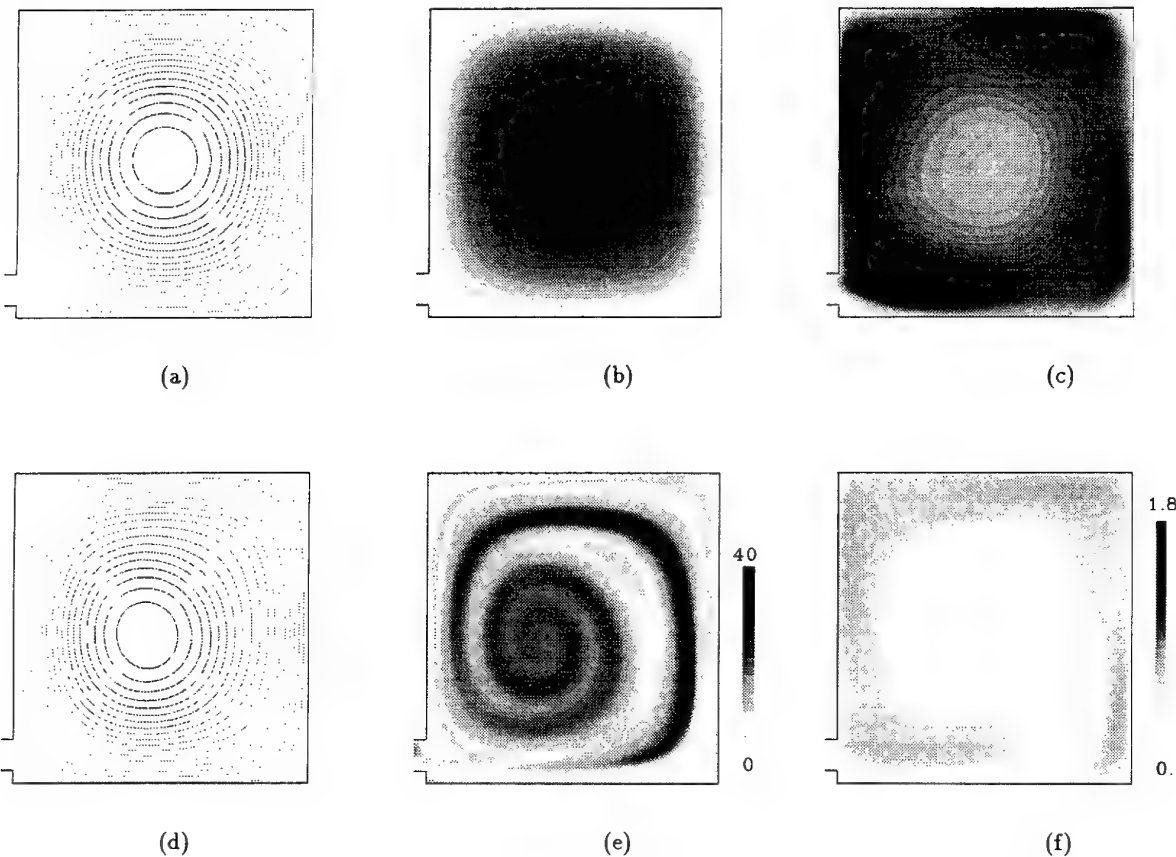


Figure 2: 180°. Streamlines :  $k - \epsilon$  (a) ; RSM (d). Normalized vorticity  $\Omega a / V p_{max}$  :  $k - \epsilon$  (b) ; RSM (e). Normalized kinetic energy  $k / V p_{max}^2$  :  $k - \epsilon$  (c) ; RSM (f)

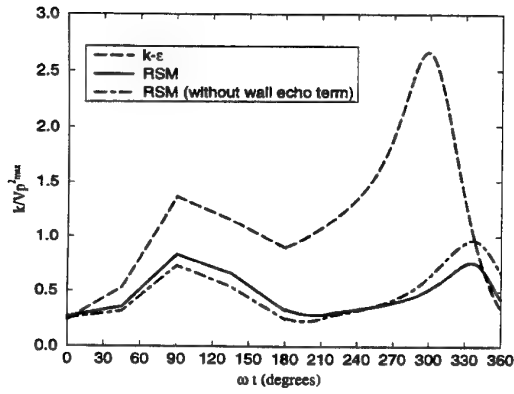


Figure 3: Evolution of the averaged value of kinetic energy

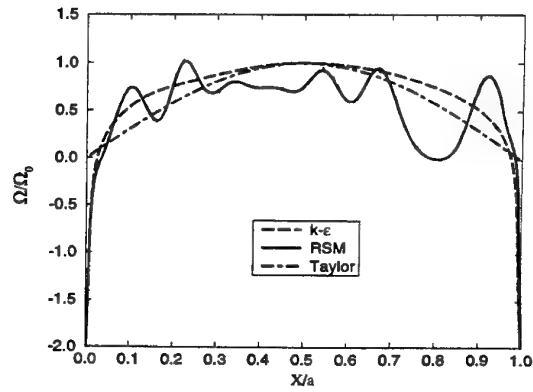
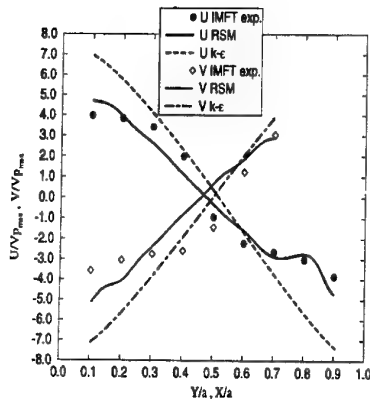
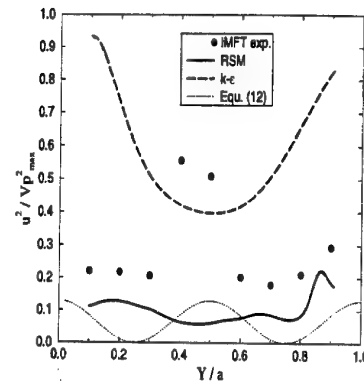


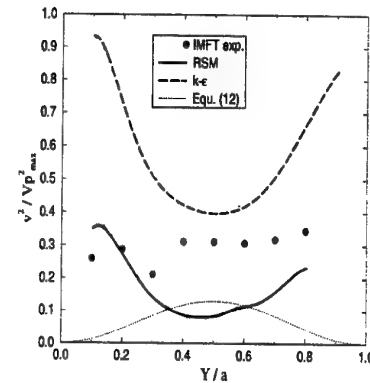
Figure 4: Comparison models/Taylor for  $\Omega/\Omega_0$  at  $180^\circ$



(a)



(b)



(c)

Figure 5: Comparison IMFT experiment/model at  $180^\circ$  : (a)  $U/Vp_{max}$ ,  $V/Vp_{max}$ . (b)  $\overline{u^2}/Vp_{max}^2$ . (c)  $\overline{v^2}/Vp_{max}^2$

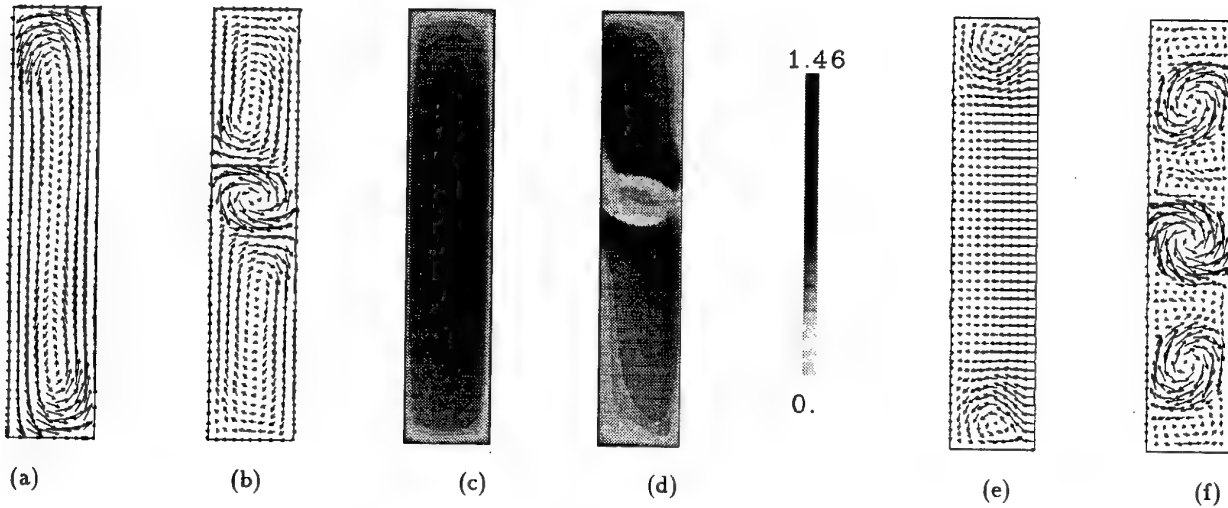


Figure 6: Velocity at  $\omega t = 360^\circ$  (a):  $k-\epsilon$  (maximum value: 1) ; (b): RSM (maximum value: 15) ; (c):  $k-\epsilon$  (maximum value: 0.05) ; (d): RSM (maximum value: 15) ; (e): no-slip laminar case  $Re=1570$  (maximum value: 0.05) ; (f): no-slip laminar case  $Re=7340$  (maximum value: 15). Normalized kinetic energy  $k/Vp_{max}^2$  (c)  $k-\epsilon$  ; (d) RSM.

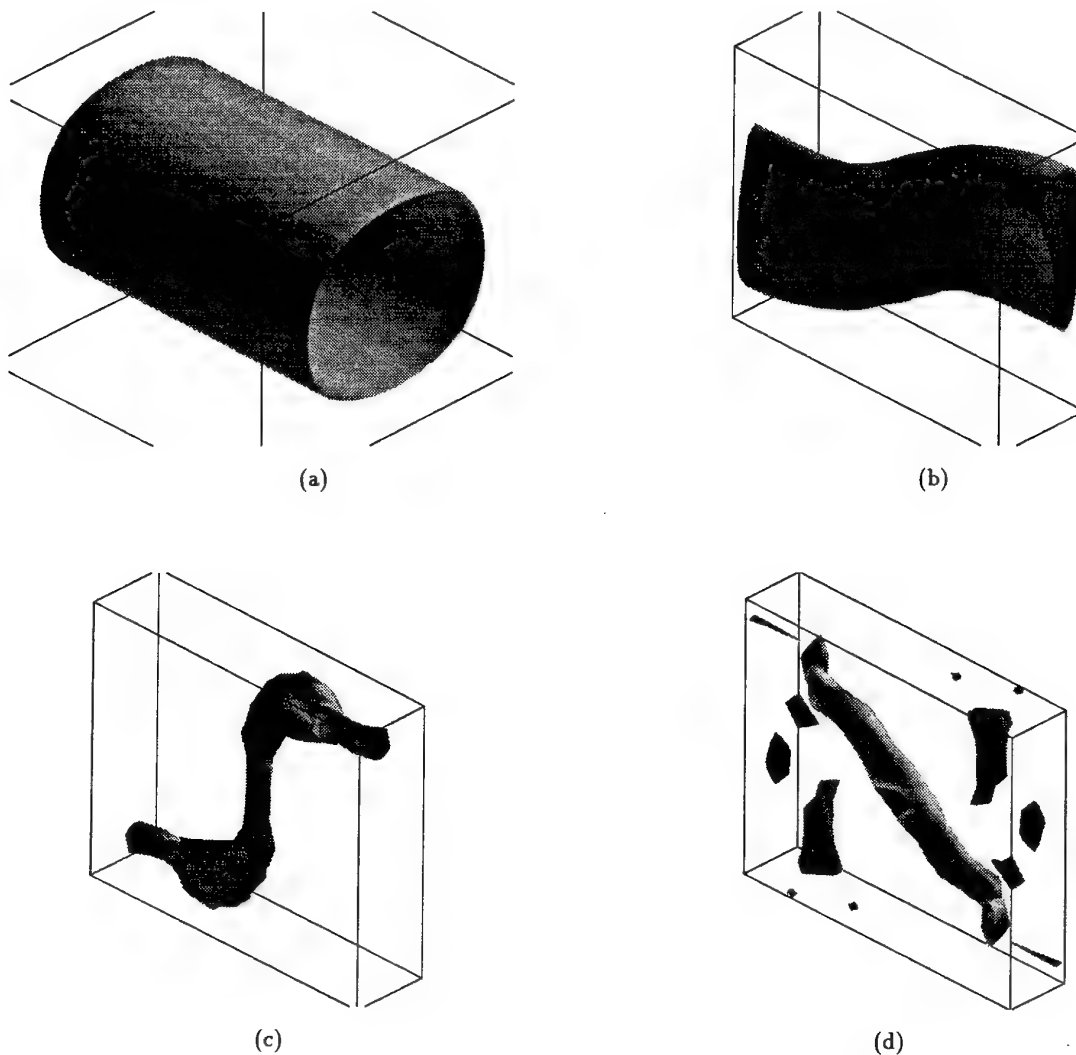


Figure 7: Surfaces of magnitude of vorticity (half of maximum value) (a)  $b/a=1$ , (b)  $b/a=3$ , (c)  $b/a=4$ , (d)  $b/a=5$ . Ratios between maximum vorticity and maximum vorticity without perturbation are respectively : 1, 1.38, 2.28, 1.39.

## REFERENCES

- Bayly, B. J., 1986, "Three-dimensional instability of elliptical flow", *Phys. Rev. Lett.*, 57, pp.2160-2163.
- Craft, T. J., and Launder, B. E., 1991, "Computation of Impinging Flows Using Second-Moment Closures", *Turbulent Shear Flows*, Technical University of Munich.
- Debaty, P., 1994, "Performances des modèles de turbulence au second ordre appliqués à des configurations axismétriques simulées par éléments finis", Thèse, Ecole Centrale de Lyon.
- Gibson, M. M., and Launder, B. E., 1978, "Ground Effects on Pressure Fluctuations in the Atmospheric Boundary Layer", *J. Fluid Mech.*, Vol.86, pp.491-511.
- Godeferd, F. S., Mansour, N. N., and Cambon, C., 1996, "Compressing an elliptic vortex: transition to turbulence by tumble breakdown", *CTR Annual Research Briefs*.
- Launder, B. E., Reece, G. J., and Rodi, W., 1975, "Progress in the Development of a Reynolds-Stress Turbulence Closure", *J. Fluid Mech.*, Vol. 68, pp.537-66.
- Lundgren, T. S., and Mansour, N. N., 1986, "Transition to turbulence in an elliptic vortex", *J. Fluid Mech.*, vol.307, pp.43-62.
- Mao, Y., Buffat, M., Jeandel, D., 1994, "Simulation of the Turbulent Flow inside the Combustion Chamber of a Reciprocity Engine with a Finite Element Method", *J. Fluid Eng.*, 116, pp. 363-9
- Marc, D., Borée, J., Bazile, R., and Charnay, G., 1997, "Combined P.I.V and L.D.V Analysis of the Evolution and Breakdown of a Compressed Tumbling Vortex", *11th Symp. on Turbulent Shear flows*, Grenoble, France.
- Reynolds, W. C., 1980, "Modeling of Fluid Motions in Engine—An Introductory Overview", *Combustion Modeling in Reciprocating Engine*. Plenum Press.
- Speziale, C. G., Gatski, T. B., and Mac Giolla Mhuiris, N., 1990, "A critical comparison of turbulence models for homogeneous shear flows in a rotating frame", *Phys. Fluids*, A 2, pp. 1678-1684
- Waleffe, F., 1990, "On three-dimensional instability of strained vortices", *Phys. Fluids*, A 2, pp. 76-80

# ANALYTICAL AND DIRECT NUMERICAL STUDY OF THE EVOLUTION AND BREAKDOWN OF A COMPRESSED TUMBLING VORTEX

Jacques Borée\*, Alexandre Corjon\*\* and Daniel Marc\*

\* Institut de Mécanique des Fluides de Toulouse  
UMR CNRS/INPT-UPS 5502  
Allée du Professeur Camille Soula  
31400 TOULOUSE, FRANCE

\*\*CERFACS  
42, Av. G. Coriolis  
31057 TOULOUSE, FRANCE

**ABSTRACT:** An analysis of vortex/wall interactions for a compressed tumbling vortex is proposed here. This situation is typical of in-cylinder flows developing in combustion chambers of premixed spark ignition engines. In an inviscid fluid, we discuss analytically the motion of a point vortex of constant intensity submitted to a compression in a time dependant rectangular domain. A relevant non dimensional number comparing the velocity induced respectively by the vortex and by the piston displacement is obtained. We show that the compression unsteadiness is expected to delay the viscous response of the near wall flow. This viscous response is studied by DNS for an initial Lamb-Oseen vortex of moderate Reynolds number placed in a rectangular box of given aspect ratio. Strong separation events initiate in small aspect ratio domains. Finally, the effect of a slight initial 3D deformation of the vortex axis is discussed. The complex interaction with walls of the initial structure is responsible for the further generation of 3D vorticity at the wall, leads to a severe distortion of the main vortex itself and is expected to be responsible for a complete destabilisation of the flow.

## 1 - INTRODUCTION

A production of small turbulent scales from a basic organised flow is a typical feature of compressed tumbling motion in combustion chambers of premixed spark ignition engines (Arcoumanis *et al* 1990; Hill and Zhang 1994). The tumbling motion is a rotating flow which axis is perpendicular to the cylinder axis and is generated during the admission phase. A complex "vortex breakdown" occurs during the compression phase and results in the generation of a significant turbulence level. This feature is used to obtain a shorter combustion period, to widen air/fuel ratio limits in engines and is highly linked with present environmental preoccupations.

In such a situation, the so called "vortex breakdown" process is highly complex and is not yet fully understood. During the compression phase, the sharp density increase is expected to intensify the vorticity of the structure.

Moreover, streamlines of the confined basic flow become clearly more and more elliptical as the piston progresses. Finally, we can expect vortex interaction with walls to induce abrupt changes in the flow. The work presented here is closely related to an experimental study on its way at IMFT where a square piston compression machine is used to study the behaviour of a 2D tumble. Velocity fields obtained by Particle Image Velocimetry (Marc *et al* 1997a; Marc *et al* 1997b) show a clear separation of the boundary layer in the adverse pressure gradient region induced by the vortex.

Many fundamental studies have addressed the problem of three dimensional instability of two dimensional large vortices in unbounded domains (Waleffe 1990) or in bounded geometries (Lundgren and Mansour 1996). This instability is due to the elliptical nature of the two dimensional vortex streamlines and a typical effect is the production of small scales directly from a smooth basic state which may be a typical feature of turbulent shear flows. However, bounded domains of Lundgren and Mansour (1996) have free slip boundaries. To describe the tumble evolution, one has to take into account a no slip condition at the wall and the generation of opposite vorticity. The works of Orlandi (1990) ; Van Geffen *et al* (1996) ; Corjon and Poinot (1996) provide a good illustration of the importance of vortex interactions with walls.

A first analysis of these complex vortex/wall interactions for a compressed tumbling vortex is proposed in the present paper. To focus on the vortex evolution, a two-dimensional or quasi two-dimensional vortex in a rectangular domain of varying aspect ratio will be considered. An analytical solution will be analysed in part 2 for the motion of a point vortex of constant intensity submitted to compression in an inviscid fluid in a time dependant rectangular domain. The influence of compression on pressure gradients due to the vortex along the walls will be discussed. Two-dimensional (2D) Direct Numerical Simulation (DNS) results in a viscous fluid will then be presented to illustrate the viscous response of the near wall flow induced by a vortex in rectangular domains of different fixed aspect ratio. Finally, three-dimensional (3D) DNS will show that unsteady wall/vortex

interactions can lead to a breakdown of the large structure for an initial slight 3D deformation of the vortex core.

## 2 - ANALYTICAL SOLUTION FOR THE COMPRESSED POINT VORTEX

The situation considered in this part is sketched in figure 1. The point vortex of intensity  $\Gamma$  moves in an inviscid fluid. The domain is rectangular and its aspect ratio  $b(t)/a$  varies during the compression. In the computations presented below, the movement of the "piston" is sinusoidal from  $b(t=0)/a=1$  to  $b(t_f)/a=0.2$ . In the low Mach number approximation, the flow divergence is uniform in the domain with, as the total mass of gas is constant :

$$\nabla \cdot \mathbf{V} = -\frac{1}{\rho} \frac{d\rho}{dt} = \frac{\dot{b}}{b} \quad \text{where} \quad \dot{b} = \frac{db}{dt}$$

Following (Batchelor 1967), the velocity field  $\mathbf{V}$  of the compressed flow is the sum of two contributions  $\mathbf{V} = \mathbf{V}_0 + \mathbf{V}_1$ .  $\mathbf{V}_0$  is the solenoidal and irrotational flow induced by the point vortex in the bounded domain at time  $t$  and  $\mathbf{V}_1$  is the velocity field induced by the dilatation rate at time  $t$  satisfying:  $\nabla \cdot \mathbf{V}_1 = \dot{b}/b$  and  $\nabla \times \mathbf{V}_1 = 0$ .

The stream function  $\psi_0$  of the velocity field  $\mathbf{V}_0$  is an infinite sum of elementary stream functions corresponding to the point vortex itself and its images. It can be conveniently expressed in term of elliptical functions (Choi and Humphrey 1984). The computation of  $\mathbf{V}_1$  is straightforward. In non dimensional form, we use respectively  $b$ ,  $\Gamma/b$  and  $b^2/\Gamma$  as length, velocity and time scales. The length scale  $b$  is chosen here as a measure of the distance between the vortex and the nearest wall which changes during the compression.  $\Gamma/b$  is an order of magnitude of the velocity induced by the vortex on the upper and lower near walls while  $b^2/\Gamma$  represents a typical turnover time scale.

The two non dimensional velocity components ( $U^*, V^*$ ) writes for  $(x, y) \neq (x_v, y_v)$ :

$$U^*(x^*, y^*, t^*) = U_0^*(x^*, y^*, x_v^*, y_v^*, b(t)/a)$$

$$V^*(x^*, y^*, t^*) = V_0^*(x^*, y^*, x_v^*, y_v^*, b(t)/a) + \left[ \frac{b \dot{b}}{\Gamma} \right] y^*$$

$(x_v, y_v)$  is the instantaneous location of the point vortex. The displacement of the point vortex is induced by all its images and by the dilatation component with :

$$U_v^*(t^*) = U_{v0}^*(x_v^*, y_v^*, b(t)/a)$$

$$V_v^*(t^*) = V_{v0}^*(x_v^*, y_v^*, b(t)/a) + \left[ \frac{b \dot{b}}{\Gamma} \right] y_v^*$$

The solution is particularly simple when the point vortex is initially at the centre of the domain. The dilatation component just maintain it at the centre of the time varying domain at all times with  $U_{v0}^* = V_{v0}^* = 0$  and  $(x_v, y_v) = (0.5a, 0.5b(t))$ . In other situations,  $N_c = |b \dot{b}/\Gamma|$

is a measure of the competition between the velocity  $\dot{b}$  induced by the piston displacement and the velocity  $\Gamma/b$  induced by the vortex at time  $t$ . Examples of point vortex displacement in the inviscid fluid for two different values of  $N_{cmax}$  are shown in figures 2.

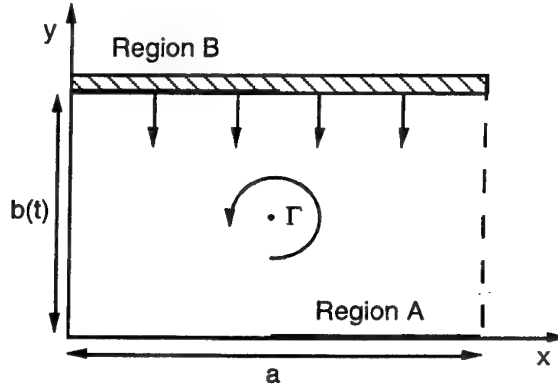
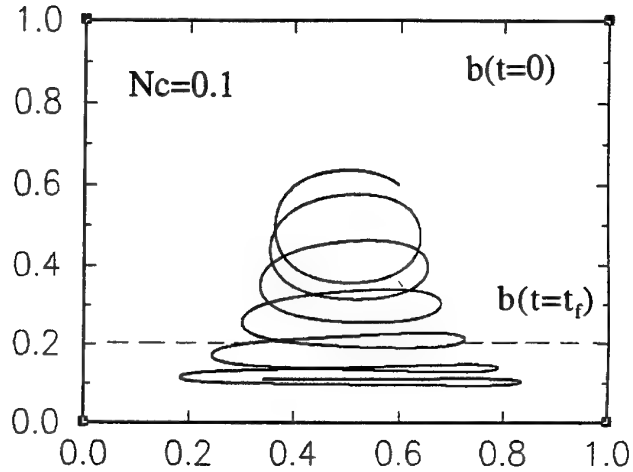
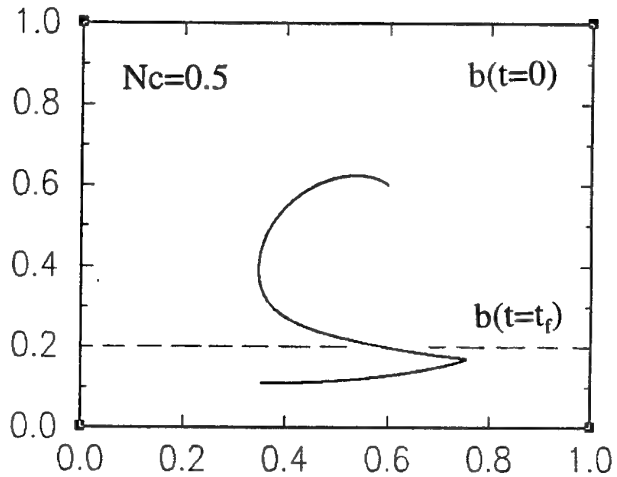


FIGURE 1: Compression of a point vortex in a rectangular domain



2 a



2 b

FIGURE 2: Point vortex displacement for two different values of  $N_{cmax}$  (2a : 0.1 ; 2b : 0.5.) Initial position  $(x_v^*, y_v^*) = (0.6, 0.6)$ . Only the initial and final position of the piston are represented

The pressure gradient induced along the piston wall or along the opposite stationary wall writes:

$$-\frac{1}{\rho} \frac{\partial p}{\partial x} = \frac{\partial U_0}{\partial t} + U_0 \frac{\partial U_0}{\partial x}$$

It can be simply estimated for a centred point vortex. For  $\Gamma > 0$ , in the region A of figure 1 :

$$U_0 = \left( \frac{\Gamma}{\pi b(t)} \right) > 0 \text{ and } \frac{\partial U_0}{\partial x} = -\frac{(\Gamma/\pi b(t))}{b/2} < 0$$

$$\Rightarrow \frac{1}{\rho} \frac{\partial p}{\partial x} = \left[ \frac{2}{\pi} - N_c \right] \frac{\Gamma^2}{\pi b^3}$$

In a steady situation,  $N_c = 0$  and we see that region A (or region B along the piston wall) is a region of adverse pressure gradient with  $U > 0$  and  $(\partial p / \partial x) > 0$  increasing sharply as  $b^{-3}$ . We therefore expect a significant viscous response of the boundary layer in a viscous fluid. This point will be addressed in fixed domains in the next part. However, this simple computation shows that a sufficiently high value of  $N_c$  ( $N_c > 2/\pi$ ) can induce a favourable pressure gradient with  $U > 0$  and  $(\partial p / \partial x) < 0$  during the compression and can therefore delay the boundary layer separation. In such cases, an abrupt viscous response of the near wall flow is expected when the piston slows down at the end of the compression phase with  $\dot{b}$  and thus  $N_c$  tending toward zero.

For a non centred initial point vortex, the location of the pressure gradient maximum at the wall is time dependant and the boundary layer response will depends on the initial point vortex position in a complex way.

### 3 - DNS OF THE VISCOUS RESPONSE OF THE BOUNDARY LAYER IN FIXED RECTANGULAR DOMAINS

#### a/ Presentation of the simulations

DNS is used here to compute the flow field induced by a vortex in rectangular boxes of given aspect ratio  $b/a = 1$  ;  $1/2$  and  $1/4$ . The code NTMIX3D (Stoessel 1995) solves 3D unsteady and compressible Navier Stokes equations. A Cartesian grid is used. Spatial derivatives are computed with a 6<sup>th</sup> order compact scheme (Pade scheme - (Lele 1992)) which provides low dispersive and dissipative errors. These schemes are allowing a quasi spectral accuracy. Time advancement is achieved with a 3<sup>rd</sup> order Runge-Kutta method. The code is supporting different types of boundary conditions (Poinso and Lele 1992). The code is written in parallel and the simulations presented here have been run on a Cray T3D 128 processors. The 2D numerical simulations have been performed on a  $128 \times 128$  regular grid though no significant differences are found when a coarser  $64 \times 64$  grid is tested. For the 3D case, we use a  $64 \times 64 \times 64$  regular grid in a periodic box in the z directions.

The initial vortex is a Lamb Oseen vortex. The azimuthal velocity of a single vortex in an infinite domain reads:

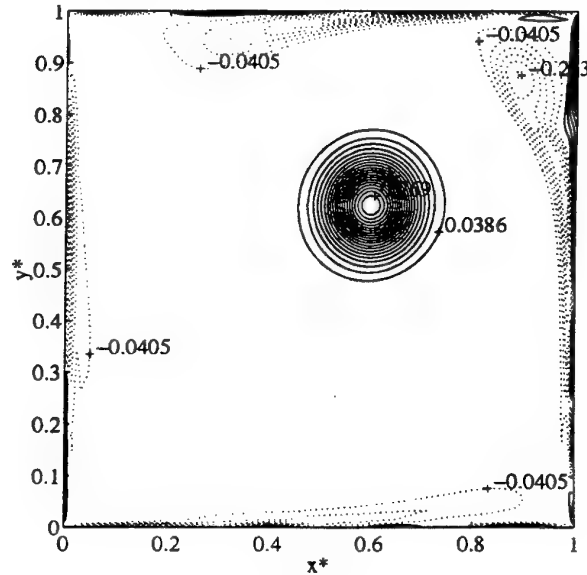
$$U_\theta = \alpha V_m \frac{r_c}{r} \left( 1 - e^{-\beta(r/r_c)^2} \right). \text{ A quasi solid body rotation}$$

occurs in the core and the circulation  $\Gamma$  is constant at infinity with  $\Gamma = 2\pi\alpha V_m r_c$ .  $V_m$  is the maximum azimuthal velocity at  $r = r_c$ . These two conditions imply the two relations

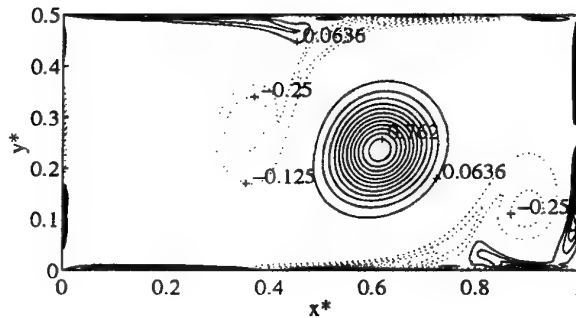
$$1 + 2\beta = e^\beta \text{ and } \alpha = \left( 1 - e^{-\beta} \right)^{-1} \text{ i.e. } \beta = 1,2544 \text{ and } \alpha = 1,40.$$

In an infinite viscous fluid, an exact solution of the unsteady Navier Stokes equations would give  $r_c \approx \sqrt{\nu t}$  and

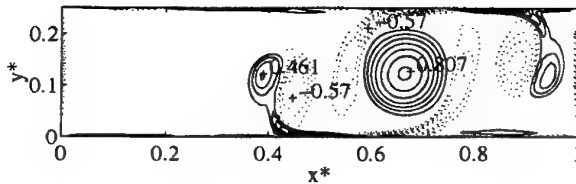
$V_m = \Gamma / \sqrt{\nu t}$ . The chosen vortex has a Reynolds number  $Re_\Gamma = \Gamma / \nu = 4000$  and a core radius  $r_c/a = 0.083$ . The initialisation of the vortex velocity and pressure field in the box involves nine vortices: The superposition of the vortex and of the velocity field of its eight first images ensures a (quasi) zero normal velocity at the wall. The no slip condition is imposed by setting a zero velocity at the wall. Three grid points are used initially to smooth out the induced velocity change.



3 a



3 b



3 c

FIGURE 3: spanwise vorticity contours at  $t_v = 22.8$   
(Dashed: negative values ; Solid: positive values)  
3a :  $b/a = 1$  ; 3b :  $b/a = 0.5$  ; 3c :  $b/a = 0.25$



## b) 2D Numerical simulations

For the three different aspect ratio boxes, the vortex is initially non centred with  $x_c/a=2/3$  and  $y_c/b=1/2$ . ( $x,y$ ) are the coordinates associated with the lower left corner of the box. Figure 3 a-b-c shows the computed spanwise vorticity at the non dimensional vortex time  $t_v = t\Gamma/r_c^2 = 22.8$ . Numerical values correspond to the ratio of the vorticity of the pointed contours divided by the core vorticity of the initial vortex at  $t=0$ . In the case of the square box, the vortex has significantly moved in the box. The study of a sequence would show that negative vorticity is generated at the wall and rolled up into the flow as the vortex moves and rotates. Such phenomena are explained in details in the study of Van Geffen *et al* (1996). Similar results are obtained here; the vortex tends to drift toward the centre of the box along a non smooth spiral and decays due to the viscous effects.

A sharper response of the viscous boundary layer is already observed in the  $1/2$  box. The negative vorticity sheets originate from the near wall flow and spill out into the domain. These sheets are seen to roll up into vortex structures which are still feeded by the wall flow in figure 3b. We can expect these vortices to grow until their diameter reach the width of the box. A even faster evolution is computed in the  $1/4$  box as predicted in part 2. The very high adverse pressure gradient induces strong separation events on both upper and lower walls and an immediate roll-up into two vigorous vortices of negative vorticity. The strong secondary vortices are disconnected from the wall flow in figure 3c. We see that they lead themselves to further separation of the boundary layer. Moreover, the flow remains quasi-symmetrical with respect to the main vortex centre for a long time until the nearer left side wall is reached by the perturbed field. The initial evolution is therefore only induced by the upper and lower wall and controls initially the movement of the main vortex. Significant precessions found with free slip walls (see part 2) are inhibited by this strong vortex interaction.

The 2D results confirm that the no slip condition at the wall is of major importance if one wants to predict the evolution of the compressed vortex. New effects associated with sharp separations and strong secondary structures appear particularly when the aspect ratio of the box decreases.

## c) 3D Numerical simulations: effect of a slight initial 3D deformation of the vortex axis

The effect of a slight initial 3D deformation of the vortex axis is discussed in this section. By slight deformation, one means a perturbation of the vortex axis of wave length  $\lambda$  and of initial amplitude  $d \ll a$ . The 3D vortex is therefore quasi-parallel to the wall of the box. The initial core deformation can be the result of the complex vortex generation during admission. It is expected to be amplified during the compression. Recent theoretical works have been published for captive vortices in domains with free slip walls. Lundgren and Mansour (1996) have shown that a transition to turbulence occurs for a smooth initial vorticity distribution in the rectangular box (Taylor vortex) and is due to the elliptical nature of the streamlines of the basic flow. For narrow cross section vortices ( $r_c \ll a$ ) of wave length  $\lambda \gg a$ , Klein *et al.* (1995) have shown that a finite time collapse occurs for any vortex pair with a negative circulation ratio. The situation is more complicated for the infinite number of images of the vortex in the box. However, as the vortex filament approaches the wall, it mainly interacts with its first image symmetric to that wall and the circulation ratio of this leading vortex pair is  $-1$ . With slip conditions at the wall, we can therefore expect a

finite time collapse of the perturbed vortex which duration is reduced for boxes of small aspect ratio.

A 3D numerical simulation was performed in a box of small aspect ratio  $b/a=1/4$ . The height of the box is  $h=a$ . The wave length of the sinusoidal initial perturbation of the vortex is  $\lambda=a$ . Periodic conditions are prescribed at the upper and lower boundaries. The initial deformation is  $d/a \approx 5\%$  for an initial core equation:  $x_c/a = 0.62 + 0.05\cos(2\pi z/a)$  and  $y_c/b = 0.5 + 0.05\cos(2\pi z/a)$ . The corresponding unperturbed vortex therefore lie in the middle plane  $y_c/b = 0.5$ . Other initial elevations not discussed here would lead to an initial dissymetry in the role of upper and lower walls and to different further evolution of the structure. Figures 4 and 5a, b and c show surfaces of constant  $z$ -component of vorticity for respectively the initial vortex and the 3D flow field at  $t_v=22.8$ ,  $t_v=34.2$  and  $t_v=45.6$ . In each figure, the surface is of the vorticity value that is 20% of the maximum vorticity value at that time. In figures 5, we see clearly that the distortion of the vortex core increases with time. In fact, the early strong secondary vortices induced by the separation of the near wall flow (not shown here for clarity) are significantly curved. Moreover, their intensity varies in the spanwise direction as the distance between the wall and the primary structure is  $z$ -dependant. Their curvature therefore continuously amplify as they roll around the primary structure and they are expected to induce the severe contortions of the main vortex seen in fig. 5a, b and c. Such situation can lead to vortex reconnection (Corjon *et al* 1996; Hussain 1986) and to a short life-time of the initial quasi 2D structure. This complex dynamics is obviously also responsible for the further generation of 3D vorticity at the wall.

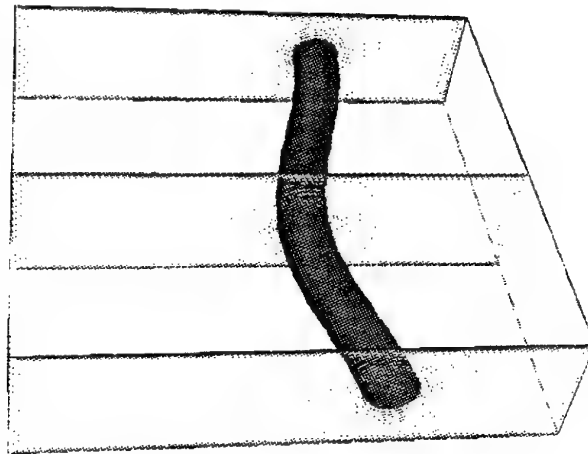


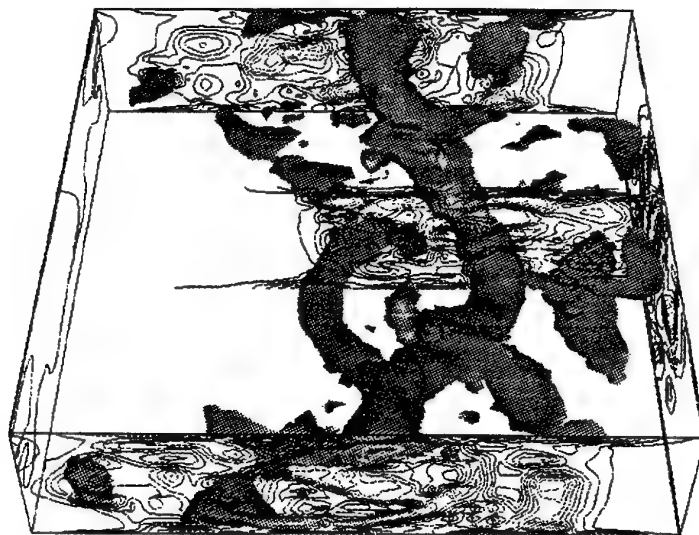
FIGURE 4: Surface of  $z$ -component of vorticity of the initial vortex

The iso-contours of the spanwise vorticity in the  $z/a=0.5$  slice at  $t_v=22.8$  (fig. 6a) differs from fig. 3c with less apparent secondary structures and a lower level of the core vorticity of the primary structure. Fig. 6b and 6c at  $t_v=34.2$  and  $t_v=45.6$  show a greatly distorted vortex core interacting with the induced near wall flow. Typical instability mechanisms (Lundgren and Mansour 1996) should appear in such a situation. The complex 3D interactions between the primary and secondary vortices are therefore expected to lead

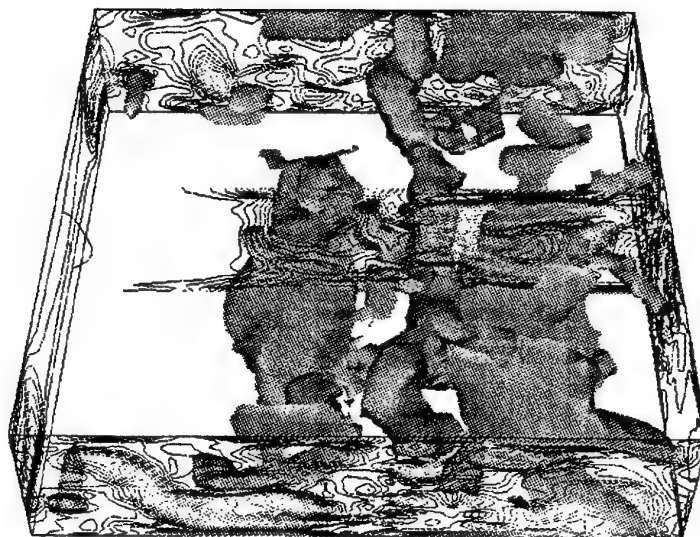




(5a)



(5b)



(5c)

FIGURE 5: Surface of z-component of vorticity at 5a:  $t_v = 22.8$  ; 5b:  $t_v = 34.2$  ; 5c:  $t_v = 45.6$

to a complete breakdown of the initial structure as time proceeds for boxes of small aspect ratio.

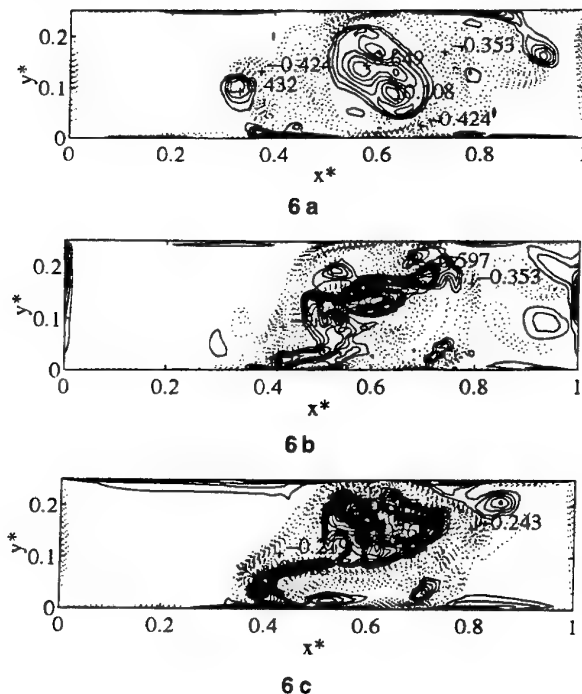


**FIGURE 6:** spanwise vorticity contours for  $z/a=0.5$   
(Dashed: negative values ; Solid: positive values)  
6a:  $t_v = 22.8$  ; 6b:  $t_v = 34.2$  ; 6c:  $t_v = 45.6$

#### 4 - CONCLUSION

A first analysis of vortex/wall interactions for a compressed tumbling vortex has been proposed in the present paper. This work is closely related to an experimental study on its way at IMFT where a square piston compression machine is used to study the behaviour of a 2D tumble. In an inviscid fluid, an analytical solution has been obtained to discuss the motion of a point vortex of constant intensity submitted to a compression in a time dependant rectangular domain. A relevant non dimensional number  $N_c$  comparing the velocity induced respectively by the vortex and by the piston displacement is obtained and the displacement of the point vortex is displayed for representative  $N_c$ . Moreover, if  $N_c$  exceeds a given limit, the compression unsteadiness leads to a favourable pressure gradient along the cylinder wall and is therefore expected to delay the viscous response of the near wall flow.

This viscous response is the result of a complex process and was studied by direct numerical simulation for an initial Lamb-Oseen vortex of moderate Reynolds number ( $Re=4000$ ) placed in a rectangular box of given aspect ratio. 2D simulations show that the viscous response is relatively muted in a square box and that the vortex moves significantly under the influence of the four side walls. On the contrary, for a box of small aspect ratio, the very high adverse pressure gradient induces strong separation events which lead themselves to further separation. Moreover, the initial evolution of the structure is only controlled by the two opposite nearer walls. The effect of a slight initial 3D deformation of the vortex axis was discussed in the last section. For an initial sinusoidal deformation in a box of aspect ratio  $b/a=1/4$ , the 3D flow field differs significantly from the 2D flow field also computed. In fact, the early

strong secondary vortices induced by the separation of the near wall flow are significantly curved. Moreover, their intensity varies in the spanwise direction as the distance between the wall and the primary structure is  $z$ -dependant. Their complex interaction with the initial structure is responsible for the further generation of 3D vorticity at the wall, leads to a severe distortion of the main vortex and is expected to be responsible for a complete destabilisation of the flow.

In analysing the "breakdown" of a compressed tumbling motion, one has to take into account the role of the no slip condition at the wall and the eventually abrupt generation of opposite vorticity. The present work shows that the compression unsteadiness interacts with this process.

#### Acknowledgements

I.M.F.T. is supported by CNRS ECOTECH, Renault and PSA in a joint "ARC Moteur Propre" program. D. Marc's research is supported by a grant ADEME. We wish to thank Dr T. POINSOT for his helpful comments about this work.

#### REFERENCES

- Arcoumanis, C., Hu, Z. & Whitelaw, J.H. 1990 Tumbling motion: a mechanism for turbulence enhancement in spark-ignition engines. *SAE paper 900060*.
- Batchelor, G.K. 1967 *An introduction to fluid dynamics*. Cambridge University Press.
- Choi, Y. & Humphrey, J.A.C. 1984 Analytical prediction of two-dimensional potential flow due to fixed vortices in a rectangular domain. *J. Computational physics* **56**, 15-27.
- Corjon, A. & Poinso, T. 1996 The behavior of Wake vortices near the ground. *AIAA J.* **35** n°5.
- Corjon, A., Risso, F., Stoessel, A. & Poinso, T. 1996 3D Direct Numerical Simulations of Wake Vortices: Atmospheric Turbulence Effects and Rebound with Crosswind. In vol. NATO-AGARD-CP-584, 28-1,28-21.
- Hill, P.G. & Zhang, D. 1994 The effects of swirl and tumble on combustion in spark-ignition engines. *Prog. Energy Combust. Sci.* **20**, 373-429.
- Hussain, A.K.M.F. 1986 Coherent structures and turbulence. *J. Fluid Mech.* vol. **173**, 303-356.
- Klein, R., Majda, A.J. & Damodaran, K. 1995 Simplified equations for the interaction of nearly parallel vortex filaments. *J. Fluid Mech.* vol. **288**, 201-248.
- Lele, S.K. 1992 Compact finite difference schemes with spectral like resolution. *J. Comp. Phys.* **103**, 16-42.
- Lundgren, T.S. & Mansour, N.N. 1996 Transition to turbulence in an elliptic vortex. *J. Fluid Mech.* vol. **307**, 43-62.
- Marc, D., Borée, J., Bazile, R. & Charnay, G. 1997a Combined PIV and LDV analysis of the evolution and breakdown of a compressed tumbling motion. In *11th Symp. on Turbulent Shear flows, Grenoble, France, Sept. 8-11*.
- Marc, D., Borée, J., Bazile, R. & Charnay, G. 1997b PIV and LDV measurements of tumbling vortex flow in a model square section motored engine. In *Submitted to 1997 SAE Int. Fuel and Lubricants Meeting*.
- Poinso, T. & Lele, S.K. 1992 Boundary conditions for direct simulations of compressible viscous flows. *J. Comp. Phys.* **101**, 104-129.
- Stoessel, A. 1995 An efficient tool for the study of 3D turbulent combustion phenomena on MPP computers. In *Proc. of the HPCN 95 conference*, Springer Verlag, Millan, 306-311.
- Van Geffen, J.H.G.M., Meleshko, V.V. & Van Heijst, G.J.F. 1996 Motion of a two dimensional monopolar vortex in a bounded rectangular domain. *Phys. Fluids* **8** (9), 2393-2399.
- Waleffe, F. 1990 On the three- dimensional instability of strained vortices. *Phys. Fluids A* **2**, 76-80.

# EVOLUTION OF CYLINDER SPIN-DOWN TURBULENCE SUBJECTED TO A SINGLE-STROKE COMPRESSION: EXPERIMENTS AND MODELLING

K. Hanjalić<sup>1</sup>, S. Jakirlić<sup>2</sup>, J. Keller<sup>2</sup>, C. Tropea<sup>2</sup> and J. Volkert<sup>2</sup>

<sup>1</sup>Faculty of Applied Physics  
Delft University of Technology, Delft, The Netherlands

<sup>2</sup>Lehrstuhl für Strömungsmechanik  
University of Erlangen, Germany

## ABSTRACT

This paper reports on experimental and numerical investigations of joint effects of compression and swirl on turbulence in a cylinder, idealizing essential flow features found in IC engines. Experiments were performed in a single-stroke, rapid compression machine (RCM), with a transparent rotatory cylinder end-section and a stationary part accommodating a piston. The numerical simulations were performed using a new low-Re version of the Reynolds-stress model, which has been previously tested on a wide variety of swirling flows. Comparisons are drawn to the data and to simulations using other standard turbulence models. In general, good agreement is achieved for the global flow patterns, however some details of the turbulence evolution must be examined further.

## 1. INTRODUCTION

The global aim of the present study is to improve the predictability of flow aerodynamics in cylinders of IC engines. These flows are exceedingly complex, involving high swirl numbers, high degrees of anisotropy, compression effects and in the case of fired engines, the interaction with the combustion process. Even restricting attention to the isothermal case, large differences can be found among the predictions of the same flow using different codes and turbulence models, a situation which is highly unsatisfactory from the viewpoint of the engine developer. The complexity of the flow makes it difficult however, to identify the weaker components of the models used and furthermore, comprehensive experimental data for systematic parameter variations are rare. In the past, this situation has led to the use of various rapid compression machines, in which the geometry of the problem has been simplified and the flow is experimentally more accessible over a wide range of parameters ([1]-[5]).

In the present study, a novel facility is introduced in which not only the compression is achieved, but also an initial swirl, without the use of valve-generated inlet flow, which tends to induce complicating secondary flows. The intention is to reduce the engine flow to some of its individual

flow components, i.e. swirl and compression, in a systematic manner, to allow the performance of the simulations to be evaluated with respect to certain flow features.

Both experiments and numerical simulations examine three flow cases:

- steady rotation of the cylinder
- spin-down (flow evolution after cylinder rotation is abruptly stopped)
- spin-down with compression

Besides providing validation data for the simulations, the experiments yield information about the effect of single-stroke compression upon swirl and on the evolution of turbulence. Also some interesting observations about the global flow pattern can be made. Nevertheless, it must be emphasized that this experimental investigation, although related closely to flows encountered in an IC engine, remains an idealization and finds its true value only together with the numerical simulations.

The following section briefly describes the experimental facilities and the numerical details. This is followed by a presentation of the results according to the three cases mentioned above.

## 2. DETAILS OF THE EXPERIMENT AND NUMERICAL SIMULATIONS

### 2.1 Experimental Apparatus

The rapid compression machine (RCM) allows observation of the time-dependent behavior of an in-cylinder flow with a specified swirl strength under the influence of a one dimensional compression. Fig. 1 shows the design and the dimensions of the RCM. With the current apparatus, the available range of operational parameters corresponds to those typically found in combustion engines, but also encompasses conditions corresponding to Rapid Distortion Theory. Note that Güntsch and Friedrich (1994, [6]) have used the same geometry for their DNS computations.

The experimental operation consists primarily of two phases. The first phase is that related to the generation of swirl inside the cylinder. The cylinder consists of a rotating

part (section  $z_h + z_c$ ) and a non-rotating part (section  $z_s$ ), where the rotating section is driven by an external motor. Both sections are separated by a small gap ( $\Delta z = 1\text{mm}$ ).

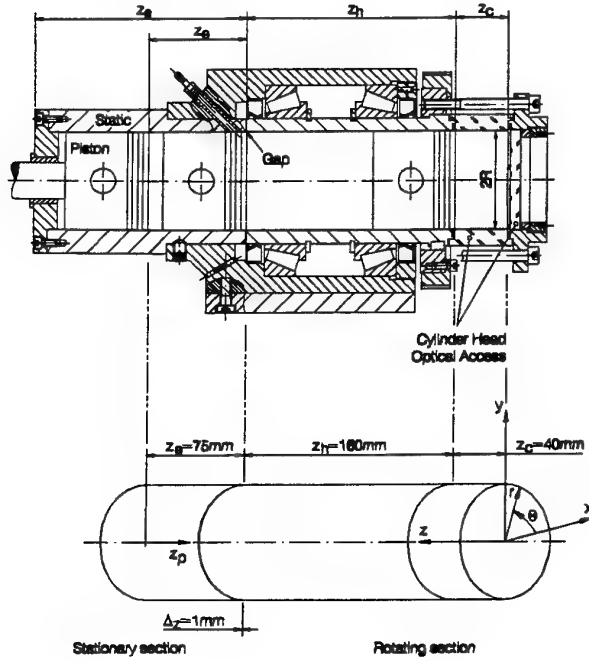


Figure 1: Design of the Rapid Compression Machine

After stopping the cylinder rotation, a compression stroke is performed by a hydraulically driven piston. For optical access, the cylinder head (module section  $z_c$ ) is made out of glass. Its length may easily be changed to enable experiments at different compression ratios  $\epsilon_c = (z_h + z_c)/z_c$ . Note that section  $z_c$  serves as acceleration length of the piston to its desired initial compression velocity when passing the gap. The swirl is characterized by the rotation rate of the cylinder. The motor used to drive the cylinder is capable of rotation rates up to 3000 rpm, with experiments being performed at 30, 300, 1200 and 1800 rpm. The compression mode is characterized by two parameters. The compression ratio, while experimentally-adjustable by changing the clearance height  $z_c$ , has been fixed to a value of  $\epsilon_c = 5.0$ . The second compression-related parameter is the compression (or strain) rate  $S$ , which is defined as the instantaneous piston speed  $v_p$  versus the length of the current volume to be compressed ( $z$ ):

$$S = \frac{1}{z} \frac{dz_p}{dt} = \frac{v_p}{z} \quad (1)$$

The piston velocity can be controlled during the entire stroke and in the present experiments an exponentially decaying velocity is used, corresponding to a constant strain rate, although recent work of Güntsch and Friedrich (1994, [6]) suggest that the flow is rather insensitive to the piston velocity function. Since the hydraulic system allows experiments being performed at constant  $S$  in the range of  $0.0 \leq S \leq 11.5 \text{ Hz}$ , measurements have been carried out at  $S = 0.5 \text{ Hz}$  and  $S = 11.5 \text{ Hz}$ .

A four-beam, two-component backscatter LDA with rather small measurement volumes of  $25.8 \mu\text{m}$  and  $27.2 \mu\text{m}$  was

used for velocity measurements. The essential specifications of the system are given in table 1.

2-COMPONENT-LDA PROBE		
BEAM SEPARATION:	$D = 22\text{mm}$	
NUMBER OF FRINGES :	$N_f = 9.96$	
FOCAL LENGTH $f$	$120\text{mm}$	
	$\lambda = 488\text{nm}$	$\lambda = 514\text{nm}$
INTERS. HALF ANGLE $\phi$	$5.237^\circ$	$5.237^\circ$
MCV DIAMETER $d_m$	$25.82 \mu\text{m}$	$27.22 \mu\text{m}$
LENGTH OF MCV $l_m$	$281.65 \mu\text{m}$	$296.9 \mu\text{m}$
FRINGE SPACING $\Delta x$	$2.67 \mu\text{m}$	$2.82 \mu\text{m}$
MCV : MEASUREMENT CONTROL VOLUME		

Table 1: Specifications of the LDA probe

Oil droplets (mixture 1:1) with diameters of  $d_p \leq 1 \mu\text{m}$  produced in a pressure atomizer were used for seeding, injected through the gap during the spin-up phase. The experiment is a one-shot experiment, thus all data acquisition was synchronized to the cylinder stop signal. Typically 50, and sometimes up to 200 repetitions were performed to build statistics about the flow field. Thus the mean velocity refers to the time mean velocity for steady rotation but to a phase mean velocity for all other measurements. Further details of the experimental facility can be found in the work of Volkert et al. (1996, [7]) and Hanzalić et al. (1996, [8]).

Symmetry of the flow statistics was checked by performing measurements across the entire cylinder diameter as shown in Figure 2. Together with repeatability checks, this leads to estimations of the measurement accuracy for the mean velocity of 2% for normalized radii  $r/R \geq 0.1$ . The statistical certainty of the turbulence measurements was of similar order of magnitude, however several factors may introduce a bias into measured fluctuating quantities. These include finite phase-window averaging, especially in the presence of strong time gradients of velocity. More severe are biases introduced by vortex precession, which was observed using PIV. A method for estimating and correcting for this bias is introduced in Volkert et al. (1996, [7]).

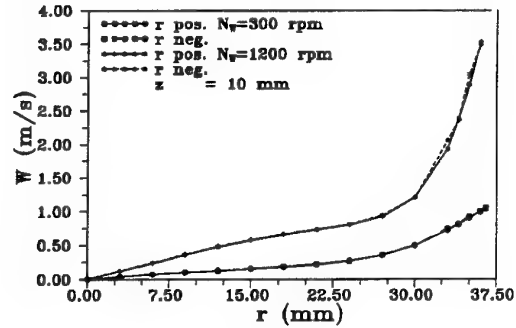


Figure 2: Tangential velocity profiles, showing a symmetrical swirl structure during steady cylinder rotation

## 2.2 Numerical Method and Turbulence Model

Three operational modes of the RCM are to be simulated: steady rotation ( $\partial/\partial t = 0$ ), spin-down and compression, for which all three velocity components and all six Reynolds stress components must be accounted for. The Reynolds averaged continuity and momentum equations

are solved under simplifying assumption of axisymmetry ( $\partial/\partial\theta = 0$ ), but allowing the density to change.

$$\frac{1}{\rho} \frac{\partial(\rho U_i)}{\partial t} + \frac{1}{r} \frac{\partial(r U_j)}{\partial x_j} = 0 \quad (2)$$

$$\frac{1}{\rho} \frac{\partial(\rho U_i)}{\partial t} + \frac{1}{r} \frac{\partial(r U_j U_i)}{\partial x_j} = \frac{1}{r} \frac{\partial}{\partial x_j} \left[ r \left( \nu \frac{\partial U_i}{\partial x_j} - \overline{u_i u_j} \right) \right] - \frac{1}{\rho} \frac{\partial P}{\partial x_i} + S_{U_i} \quad (3)$$

The source terms  $S_{U_i}$  arising from the coordinate transformation are given in table 2.

$S_{U_i}$	Convection	Visc. diffusion	Turb. diffusion
$S_U$	-	-	-
$S_V$	$+W^2/r$	$-\nu V/r^2$	$+w^2/r$
$S_W$	$-VW/r$	$-\nu W/r^2$	$-\overline{wv}/r$

Table 2: Sources of mean momentum equations

Assuming acoustic waves are not significant ([6], [9], [10]), the gas density is only a function of time and temperature, given for adiabatic compression by the compression ratio and related to the temperature through

$$\left[ \frac{\rho(t)}{\rho_o} \right]^{\kappa-1} = \frac{T(t)}{T_o} \quad (4)$$

The time variation of viscosity is accounted for through Sutherland's law:

$$\frac{\mu(t)}{\mu_o} = \left[ \frac{T(t)}{T_o} \right]^{0.75} \quad (5)$$

where in both Equations (4) and (5) the index "o" refers to the beginning of the compression process. The homogeneous density also implies a homogeneous divergence of the mean velocity so that the terms in Eq. (3) representing molecular conditioned momentum transport are free of dilatational effects.

In order to conserve the number of mesh cells during the compression stroke the so called *space conservation law* (SCL, Demirdžić und Perić [11]) is applied. The method, incorporated into a finite volume procedure, involves the solving of an additional equation describing conservation of space simultaneously with the continuity and momentum equations. This new equation reads for a spatial region of volume  $V$  bounded by a closed surface  $S$ :

$$\frac{d}{dt} \int_V dV - \int_S \mathbf{V}_b \cdot \mathbf{n} dS = 0 \quad (6)$$

where  $\mathbf{V}_b$  stands for the velocity of moving boundaries of the computational domain. In a case of an one-dimensional compression is  $\mathbf{V}_b = (U_P, 0, 0)$ , where  $U_P$  represents the piston velocity. The convective parts of Equations (2) and (3) take the following forms in the moving coordinate frame:

$$\frac{1}{r} \frac{\partial(r U_j)}{\partial x_j} \sim \frac{1}{r} \frac{\partial[r (U_j - U_{bj})]}{\partial x_j} \quad (7)$$

$$\frac{1}{r} \frac{\partial(r U_j U_i)}{\partial x_j} \sim \frac{1}{r} \frac{\partial[r U_i (U_j - U_{bj})]}{\partial x_j} \quad (8)$$

Without further elaboration it can be stated that simple eddy-viscosity models are not expected to capture essential features of this flow, in which strong swirl and compression

effects lead to strong anisotropy of turbulence. This extends also to the use of wall functions. As an illustration, Figure 3 presents measured and computed near-wall profiles of the tangential and axial velocity for the spin-down case.

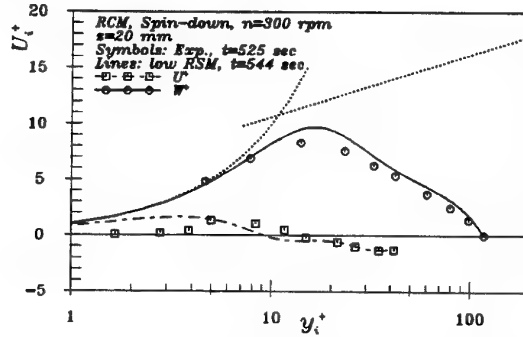


Figure 3: Departure of the mean axial and the mean tangential velocities from the logarithmic law

Clearly there is considerable deviation from a logarithmic behaviour at the wall. For these reasons the numerical simulations were performed using a low-Re Reynolds-stress model, based on the standard high-Re-number  $\overline{u_i u_j} - \epsilon$  closure (Gibson and Launder (1978)), which serves as high-Re-number asymptote, Hanjalić et al. (1997, [12]). The special features of the model are new modifications accounting for the low-Re-number and non-viscous wall blockage effects as well as pressure reflection. In addition to satisfying most of the basic physical constraints, the model was validated by the high quality of reproduction of flow and turbulence details, particularly, in the vicinity of solid wall, in a broad variety of non-equilibrium flows featuring different phenomena: a series of attached and separating flows with strong time- or space-variations or abrupt changes of boundary conditions in a wide range of Re-numbers. Particular validation efforts were given to the computations of flows relevant to the flow in the RCM: rotating and swirl flows in pipes and combustor chambers (Jakirlić, (1997, [13])).

### 3. RESULTS

#### 3.1 Steady Rotation

The flow field during steady rotation is the start condition for the spin-down and compression experiments and is characterized by a strong tangential fluid motion (desired initial swirl intensity) and a weak axial circulation of the flow from the piston to the cylinder head on the centerline and returning along the cylinder wall, which is induced by the stationary part of the cylinder and the piston surface (Figure 4).

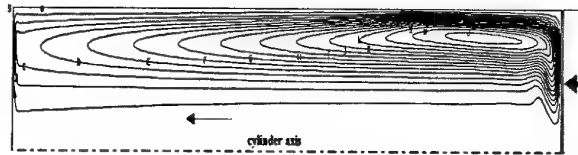


Figure 4: Stream line plot documenting the secondary fluid motion

Thus the flow does not achieve the state of solid body rotation, which can be seen directly from tangential velocity profiles across the cylinder radius, as presented in Figure 5.

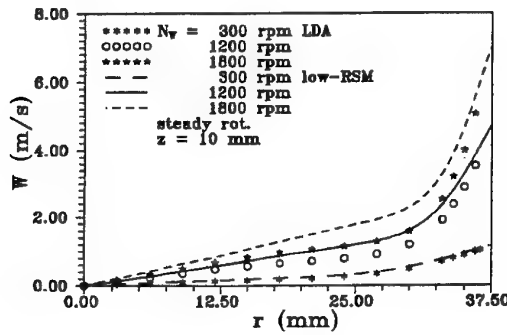


Figure 5: Radial profiles of the swirl velocity for different rotation rates  $N_W$  - comparison of experimental and numerical results

Agreement between experiments and computation is good for a rotational speed of  $N_W = 300 \text{ rpm}$  ( $Re_\theta = 5890$ , based on cylinder diameter and rpm velocity), however at higher rotations, the computations show complete laminarization, which leads to a weaker influence of the momentum loss effects by the stationary part of the cylinder, and thus to higher swirl velocities at the wall.

The experimentally determined velocity fluctuations were very low, but not typical of laminar flow, as shown in Figure 6 for three rotation rates and for two components,  $v'$  and  $w'$ . Not only are  $v'$  and  $w'$  close to one another, but also  $u'$  (not shown) is of similar magnitude, so that an isotropic assumption is plausible for this operation condition.

Radial profiles of the axial velocity are shown in Figure 7, showing the weak axial circulation amounting to about 1-2 % of the rotation speed for 1200 rpm.

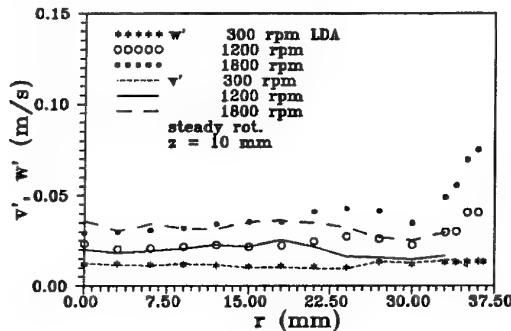


Figure 6: Measured radial profiles of the tangential ( $w'$ ) and the radial ( $v'$ ) rms components for different rotation rates  $N_W$

Again, good agreement between experiment and computations is achieved for low rotation speeds ( $N_W = 30/300 \text{ rpm}$ ), with considerable deviations for  $N_W = 1200 \text{ rpm}$ . The development of the flow in the axial direction is weak, as demonstrated by comparing several axial velocity profiles at the positions  $z = 10, 20$  and  $30 \text{ mm}$  (Figure 8). Both experiments and computations confirm this.

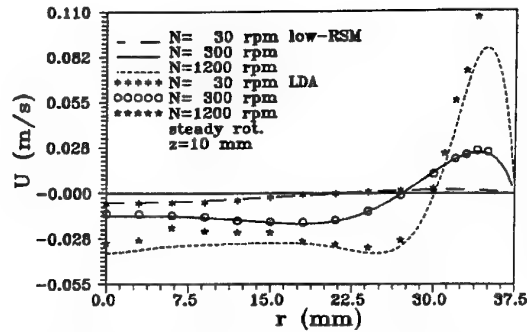


Figure 7: Radial profiles of the axial velocity for different rotation rates  $N_W$  - comparison of experimental and numerical results

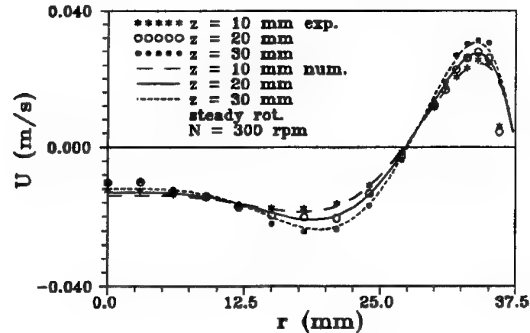


Figure 8: Radial profiles of the axial velocity at different axial positions for  $N_W = 300 \text{ rpm}$  - comparison of experimental and numerical results

### 3.2 Spin Down

Experimentally the spin-down condition was investigated by performing a series of one-shot experiments and the results presented below are averages over about 50 "shots". Figure 9 presents the evolution of the tangential component for a spin-down from  $300 \text{ rpm}$  at three radii ( $r/R = 0.48, 0.80, 0.96$ ), plotted all with the same velocity scale normalized with the initial wall rotation velocity.

The profile at  $r/R = 0.48$  has been replotted with an expanded vertical scale to allow better comparison between experiment and computations. Generally this comparison shows good agreement, even reproducing some of the finer, non-monotonic behaviour of the swirl decay, particularly immediately after the cylinder has been stopped ( $t = 0$ ). All profiles exhibit a systematic offset of about 3-4% between experiment and computations, which may be partially due to small uncertainties in the positioning of the LDA measurement volume but more likely due to the slightly different start distributions of the tangential velocity, as seen already in Figure 5.

Figure 10 compares the evolution of the axial velocity profiles at  $z = 20 \text{ mm}$  for a spin down from  $N_W = 300 \text{ rpm}$ . It is very interesting to note that at this axial position a reverse circulation arises at  $t = 0.5 \text{ s}$ , confirmed by both experiments and computations.

### 3.3 Spin-Down with Compression

Experimental results of the decaying swirl velocity are presented in Figure 11 for two compression rates ( $S = 0.5 \text{ Hz}$

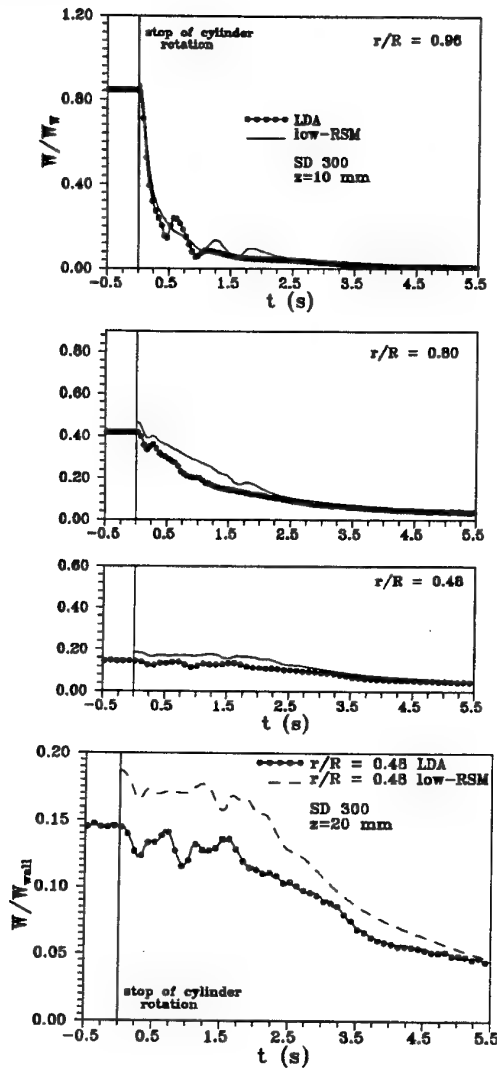


Figure 9: Evolution of the decaying swirl velocity during spin down - comparison of experiment and simulations

and  $S = 11.5 \text{ Hz}$ ), whereby the spin-down results are given as reference. The time at which the piston reaches top dead center (TDC) is shown as a dashed line. Clearly the compression effects the swirl behaviour, in general accelerating its decay. Negative swirl appears over some portions of the cross section at certain times, which indicates a more complex vortex structure upon compression. However the diagrams in Figure 11 only show the velocity at one radial position. In Figure 12, the entire radial profile of the tangential velocity is shown for the same conditions and at two time steps during compression. The first two diagrams, taken at 300 rpm, indicate, that, compared with spin-down results, the swirl structure changes dramatically during and after compression for both compression rates. The deviation from spin-down behaviour occurs sooner at the high compression rate, however, relative to the piston motion, the reverse is true. In any case, in accordance with DNS computations of Güntsch ([14], 1996), a reverse swirl over a large portion of the cylinder radius occurs already before top dead center.

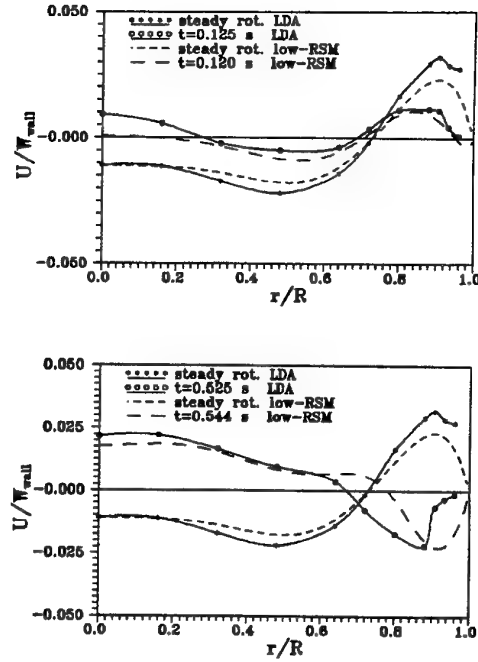


Figure 10: Evolution of the axial velocity profile during spin down - comparison of experiment and simulations (experimental points are connected using a spline interpolation)

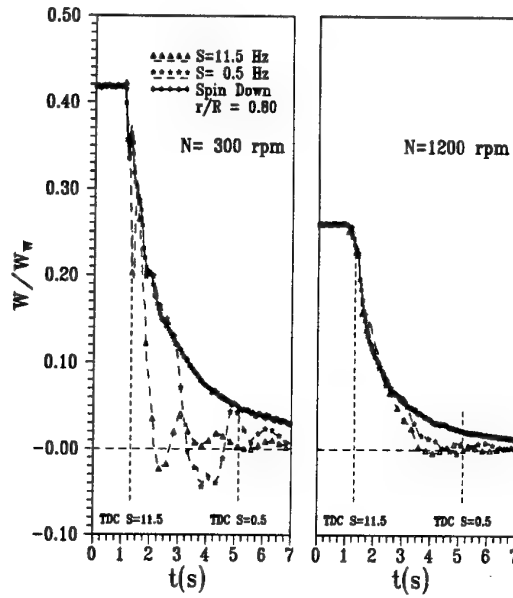


Figure 11: Evolution of the decaying swirl velocity as function of the initial swirl intensity  $N_W$  and the compression rate  $S$



Thus the induced secondary flow from the piston motion strongly influences the swirl structure. Current experiments and simulations are complementing the available data to define more precisely the induced secondary flow.

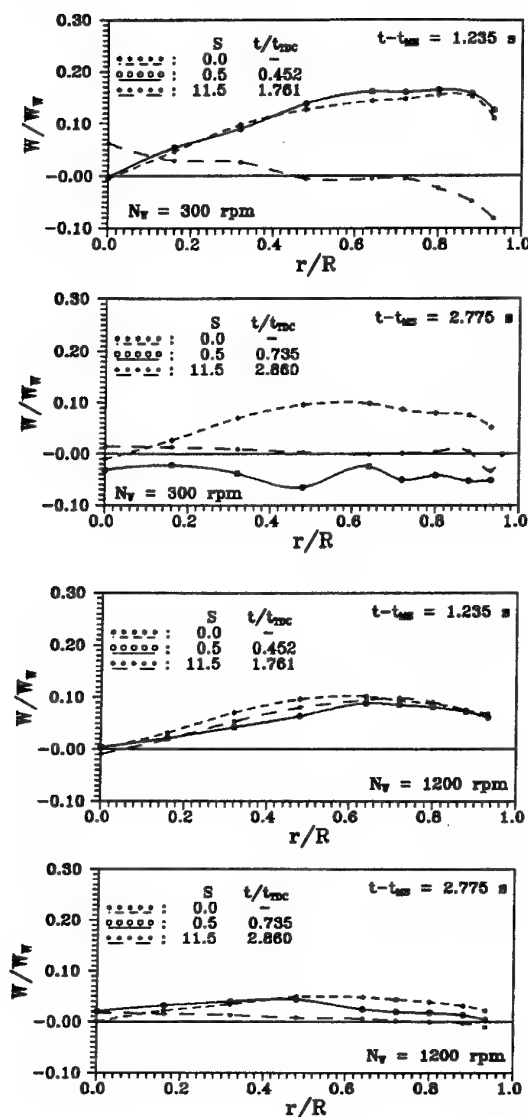


Figure 12: Evolution of the tangential velocity profiles as function of the compression rate  $S$  (upper plots  $N_W = 300 \text{ rpm}$ , lower plots  $N_W = 1200 \text{ rpm}$ )

At the higher initial rotation rate of  $1200 \text{ rpm}$ , the swirl development is much more uniform across the cylinder radius and also shows less departure from the spin-down case. Thus, the swirl appears to be more dominant over the induced secondary flows, at least up to the times shown in Figure 12, as might be expected.

The above results and discussions have concentrated primarily on the development of the transient flow during spin-down and compression, for which initial comparisons between experiment and simulations are encouraging. More detailed comparisons of the turbulence quantities are in progress.

## Acknowledgements

The authors would like to acknowledge support of different aspects of this research by the Deutsche Forschungsgemeinschaft through grant Tr 194/7, by the EEC Joule III program and through the PROCOPE program for scientific exchange between France and Germany.

## References

- [1] KAMIMOTO, T., KOBAYASHI H., NATSUOKA, S. (1981) *A Big Size Realization of a Rapid Compression Machine for Fundamental Studies of Diesel Combustion*, SAE 811004
- [2] KAGEYAMA, T. AND FISSON, F. (1989) *Une Chambre de Combustion a Conditions Hydrodynamiques variables* Colloque de l'ARC "Moteurs a Pistons", CNRS-PRISEM, Paris
- [3] NUGLISH, H.J., BOREE, J., CHARNAY, G. (1990) *LDV Measurements in a Compressed Air as Support for the Modelling of Compressed Turbulence* 5th Int. Symp. on Appl. of Laser techniques to Fluid Mechanics, Lisbon, Portugal
- [4] SERRE, G. AND LEPENVEN, L. (1992) *LDA Measurements of a Grid-generated Turbulence undergoing a Volume Reduction* 6th Int. Symp. on Appl. of Laser techniques to Fluid Mechanics, Lisbon, Portugal
- [5] GRUNDO, A., TRAUTWEIN, S.E., BIELERT, U., WASSENBERG, H., ADOMEIT, G. (1993) *Untersuchungen der turbulenten Flammenausbreitung unter ottomotorischen Bedingungen im Einhubtriebwerk*, SFB 224, RWTH Aachen
- [6] GÜNTSCH, E., FRIEDRICH, R. (1994) *On the Influence of Compression and Rotation on Initially Isotropic Turbulence in a Cylinder* Proc. 2nd European CFD Conf., Stuttgart, Eds. S. Wagner et al., pp 525-534,
- [7] VOLKERT J., TROPEA C., DOMANN R., HÜBNER W. (1996) *Combined Application of PIV and LDA to Swirling Flows under Compression*. 8th Int. Symp. on Appl. of Laser Techniques to Fluid Mechanics, Lisbon, Portugal
- [8] HANJALIĆ K., JAKIRLIĆ S., TROPEA, C., VOLKERT, J. (1996) *Exp. und Num. Untersuchung des Kompressionseinflusses auf Drallströmungen und Turbulenz* DFG-Zwischenbericht zu Tr194/7
- [9] WU C.T., FERZIGER J.H. & CHAPMAN D.R. (1985) *Simulation and modelling of homogeneous, compressed turbulence* 5th Symp. on Turbulent Shear Flows, Ithaca, New York, USA
- [10] LE PENVEN L. & SERRE G. (1993) *Homogeneous turbulence submitted to compression: experimental study & modelling* 9th Symp. on Turbulent Shear Flows, Kyoto, Japan
- [11] DEMIRDŽIĆ, I. & PERIĆ, M. (1990) *Finite volume method for prediction of fluid flow in arbitrarily shaped domains with moving boundaries* Int. J. for Numerical Methods in Fluids, Vol. 10, pp 771-790
- [12] HANJALIĆ K., JAKIRLIĆ S., HADŽIĆ I. (1997) *Expanding the limits of "equilibrium" second-moment turbulence closures*. Fluid Dynamics Research, Vol. 20, pp 25-41
- [13] JAKIRLIĆ, S. (1997) *Reynolds-Spannungs-Modellierung komplexer turbulenter Strömungen*, Ph.D. Thesis, University of Erlangen
- [14] GÜNTSCH, E. (1996) *Kompression isotroper Turbulenz im Zylinder - Eine numerische Studie -*, Ph.D. Thesis, Technical University of Munich



## A MODEL DEFROSTER FLOW

Klaus Willenborg, John F. Foss, Ramez AbdulNour, John J. McGrath  
Department of Mechanical Engineering  
Michigan State University  
East Lansing, Michigan 48824  
USA

Bashar S. AbdulNour  
Climate Control Operations  
Ford Motor Company  
Dearborn, Michigan 48120-1238  
USA

### ABSTRACT

Velocity and temperature field data are presented for a model defroster flow: a wall jet formed by a slit jet discharging next to a planar surface. The velocity field is characterized by the fluid acceleration from the plenum to the vena contracta ( $x/w \approx 1.7$ ) and the subsequent development of a region of apparent self-preservation:  $x/w \geq 7$ . Near wall temperature measurements successfully resolved the linear  $T(y)$  distribution which permitted the heat flux ( $q''$ ) and the Nusselt number to be inferred for the downstream locations.

### INTRODUCTION

A typical automotive vehicle defrost/defog system can be characterized as the oblique impingement of a three-dimensional rectangular (and — quite likely — non-uniform) jet on an inclined surface. Representative measurements and computational results for a defroster flow in a production vehicle, which show the complexities of such flows, have been reported by AbdulNour and Foss (1997).

The defroster flow, and its contribution to removing/preventing the build-up of frost on the windshield, is an important element in the safe operation of the vehicle in cold climates and strict regulations on its performance must be addressed by vehicle manufacturers.

The present communication reports on an investigation that is motivated by this technological application. It is, appropriately, a simplified representation of the prototype problem. The geometry for the present flow field is shown schematically in Fig. 1. The pressurized plenum delivers symmetric ( $y > 0$  and  $y < 0$ ) slit-jet flows past the centered test element; the coordinate system is shown in Fig. 2. This symmetric arrangement ensures a thermally symmetric condition in which the thermal energy is transferred from the circulating liquid to the two airstreams

through the walls of the test chamber. The large conductivity of the thin (aluminum) chamber walls and the relatively large flow rate of the circulating liquid ensure that the surface temperature ( $45^\circ\text{C}$ ) of the chamber walls is both uniform and time invariant.

The slit jet configuration, shown in Fig. 1, was selected to provide a universal initial condition for the wall jet. Specifically, the flow that is delivered from this orifice is

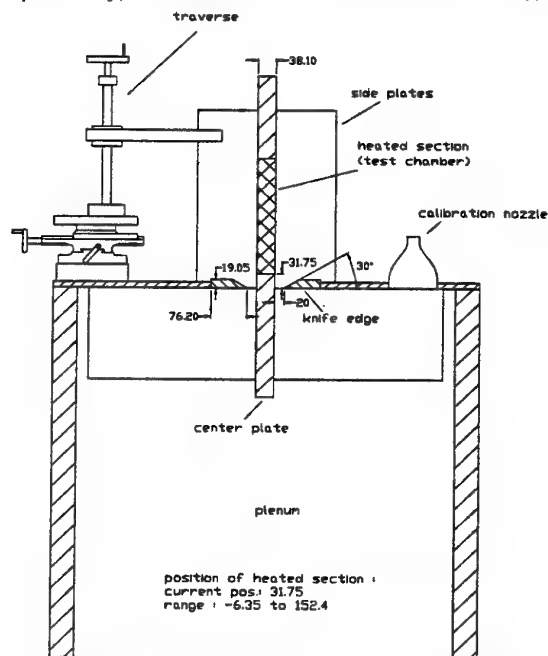


FIGURE 1a: Details of the subject flow field.  
Elevation - side view of the plenum and the centered divider plate.

Note dimensions in millimeters

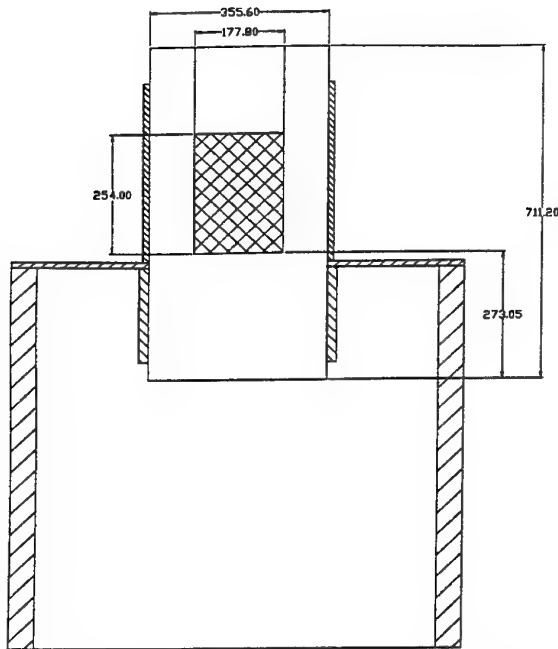


FIGURE 1b: Details of the subject flow field.  
Elevation - front view of the plenum and the centered divider plate.

Note the side plates that ensure a planar flow.

characterized by a thin boundary layer at the separation lip ( $\delta \ll w$ ). Hence, the trajectory of the separation streamline, the pressure gradient on the test surface and the location of the vena contracta are independent from the magnitude of the Reynolds number.

The selected orifice, and the relatively close ( $x_{\text{meas}} \lesssim 14w$ ) measurement region do not permit useful comparisons with other wall jet studies as discussed by, for example, Launder and Rodi (1979), Akfirat (1966), and Nizou (1981).

One aspect of the "idealization" that is reflected in the present study is the use of a heated surface with a cold air flow. Since body force effects are not important in this investigation, the direction of the heat transfer between the plate and the air flow is not of qualitative significance.

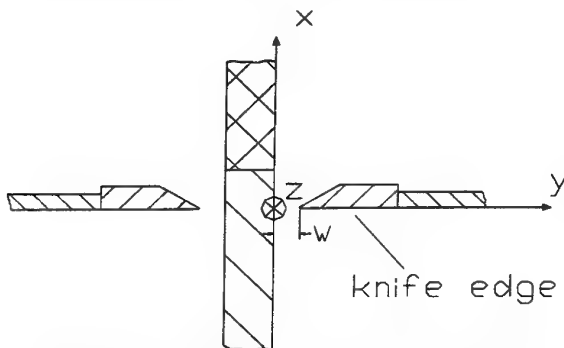


FIGURE 2: Coordinate system that is used to describe the subject flow field.

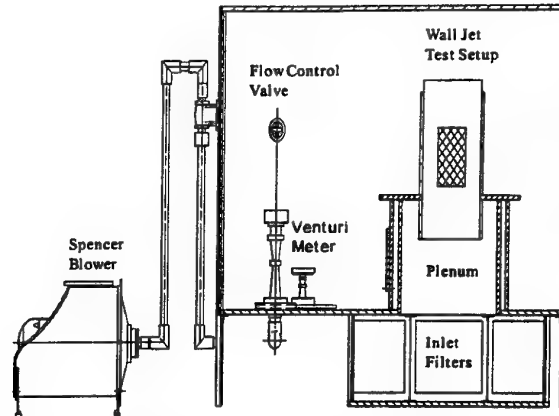


FIGURE 3: Elevation - side view

Notes: i) Inside working space: 2.41 m high, 1.82 m wide and 2.68 deep; ii) Flow system of Fig. 1 is located atop plenum; iii) A honeycomb (3x25 mm cell size) and 3-40 mesh screens are located below the 850 mm x 850 mm x 600 mm plenum

The indicated flow system of Fig. 1 is contained within the subatmospheric domain of the flow facility that is shown in Fig. 3. This facility delivers air from a low disturbance plenum into the subatmospheric receiver. The receiver is evacuated, through a metering Venturi tube, by a two-stage Spencer Blower. Hence, the wall jets are formed from a quite well defined initial condition.

The present results are taken from the second Studienarbeit thesis of the first author. An internal report, that is based upon this thesis effort, is available as Willenborg and Foss (1996). A complementary study of the constant heat flux ( $q''$ ) condition, the report on which is available from the second author and which uses the same flow facility, has been submitted to the ASME for publication.

#### EXPERIMENTAL EQUIPMENT AND PROCEDURE

Conventional hot-wire techniques are used to record the mean and rms velocity magnitudes in the isothermal slit jet at  $z=0$ . (Side wall barriers and the uniformity of the relatively narrow slit --  $w=2$  cm,  $L=35.6$  cm -- ensure that the central region exhibits a planar character.) The hot-wire calibrations cover the relevant range of velocity values  $1 \leq u \leq U_o (=10$  mps) where  $U_o$  is the velocity at the vena contracta as defined by:

$$U_o = [(2/\rho)(p_p - p_{\text{rec}})]^{1/2} \quad (1)$$

Representative calibrations using a 1 Torr Baratron transducer involve standard deviations between the analytical form

$$E^2 = A + BQ^n \quad (2)$$

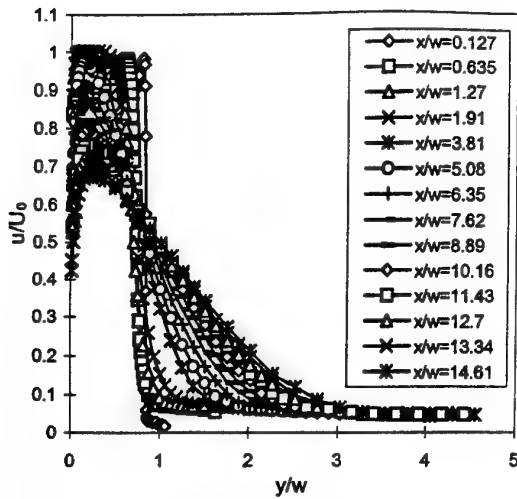


FIGURE 4: A composite representation of the mean velocity values in the slit-wall jet flow.

and the measured  $\bar{Q}$  values of 0.05 mps where the measured hot-wire voltage ( $E$ ) is accepted as having negligible uncertainty.

Thermal measurements were made with a small bead ( $d=7.6 \mu\text{m}$  diameter) thermocouple for the time-mean:  $\bar{T}(y)$ , data. This thermocouple was calibrated using the reference thermocouple that was used to determine the liquid temperature ( $\approx 45^\circ\text{C}$ ) in the circulating liquid of the chamber.

## RESULTS AND DISCUSSION

### The Velocity Field

A composite representation of the mean velocity distributions from a station near the nozzle exit plane ( $x/w=0.127$ ) to the upper region of the test plate ( $x/w=14.61$ ) is shown in Fig. 4. This figure, which is difficult to interpret given the density of points, is to convey the level of detailed information that is available regarding this flow field. Willenborg and Foss (1996) provide this detailed information. The rapid development of the velocity field is shown more explicitly in the mean and rms distributions for the locations  $x/w=0.127$  and  $0.635$ , Fig. 5a, and for locations  $x/w=1.27$  and  $1.91$ , Fig. 5b.

Figure 6 shows the same data plotted in a scaled manner:

$$u/U_{\max} = f(y/\delta_2) \quad (3)$$

where  $U_{\max}$  is the maximum velocity of the traverse and  $\delta_2$  is the location for which

$$u(x,y)/U_{\max} = 0.5 \text{ and } \partial \bar{u} / \partial y < 0. \quad (4)$$

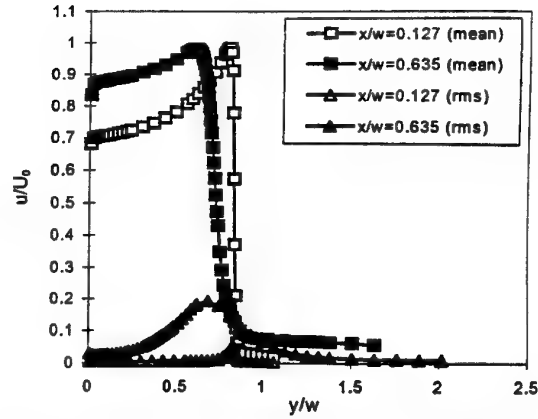


FIGURE 5a: Detailed mean velocity distributions near the jet exit; these data are from the accelerating flow region.

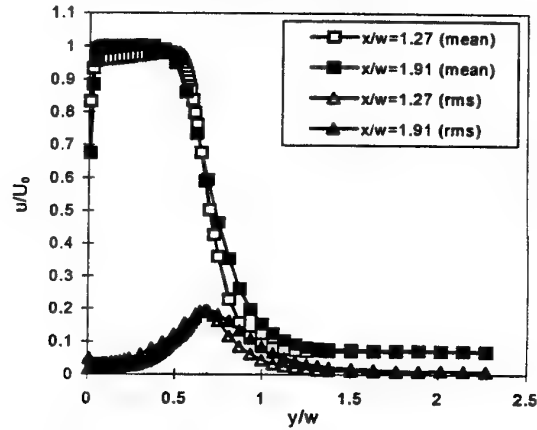


Figure 5b: Mean velocity distributions prior to ( $x/w = 1.27$ ) and following ( $x/w = 1.91$ ) the vena contracta ( $x/w \approx 1.7$ ).

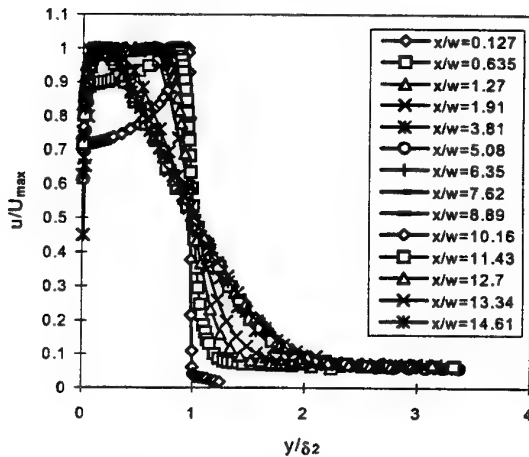


FIGURE 6: Mean velocity distributions scaled with the intrinsic parameters:  $U_{\max}$  and  $\delta_2$ .

Figure 7 presents the scaled data for the region:  $w/x \geq 7$ . It is evident that the mean velocity has reached a self-preserving state in this range of downstream distances. Similarly, the experimental results for the rms fluctuation levels exhibit a self-preserving character for  $x/w \geq 7$ ; see Fig. 8.

The  $x$ -dependencies of these scaling values:

$$(\delta_2(x))/w \text{ and } (U_{\max}(x))/U_o$$

are shown in Figs. 9a and 9b.

A distinctive attribute of these data is the apparent "laminar" (albeit "disturbed") character of the near wall region for the full length of the test plate. Namely, Fig. 10 shows the mean and rms velocity distributions at  $x/w=13.34$ . The peak rms values reflect the production of turbulence energy in the  $y \approx \delta_2$  region with only a minimal rise in  $\bar{u}$  in the strong  $\partial \bar{u} / \partial y$  gradient region ( $0 \leq y/w \leq 0.05$ ). This observation is rational given the relatively small  $R_x$  values:

$$R_x = \frac{U_o x}{\nu} \leq 2 \times 10^5, \quad (5)$$

that characterize the flow at the farthest downstream location. Figure 11 further clarifies the non-standard character of the boundary layer region. Namely, the mean velocity data of Fig. 10 are compared with the Blasius (laminar) and a  $1/7$  power law form (turbulent) in this figure.

#### The Thermal Field

Figure 12 shows the time averaged temperature distribution in the heated region of the plate as expressed by the non-dimensional quantity:  $\theta(x)$ .

$$\theta(x) = \left[ \frac{T(x, y) - T_{pl}}{T_s - T_{pl}} \right]. \quad (6)$$

The indicated distributions show that  $\theta(y)$  has reached its limiting (i.e., minimum) condition for  $y/w \leq 0.25$ . However, this minimum is also seen to be a function of the streamwise position. This seemingly anomalous situation is clarified by noting that the mass flow entering the receiver of Fig. 3 is the same as the exiting mass flow from the receiver. There is, however, entrainment at the free boundary with the consequence that the ambient fluid, which has previously been thermally contaminated, will be present for relatively large  $x/w$  values at the outer edge ( $\delta_2$ ) of the heated portion of the flow. Since unmixed (i.e., jet core) fluid is present at a given  $x/w$  location sufficiently near the nozzle, the elevated ambient temperature effects are not present near ( $x/w \leq 7$ ) the nozzle exit.

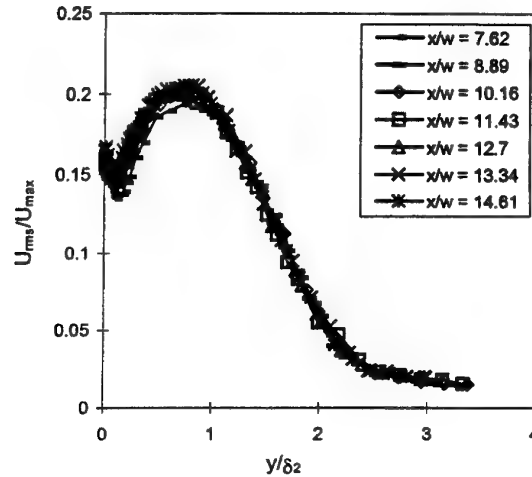


FIGURE 8: The rms intensity distribution in self-similar coordinates for  $x/w > 7$ .

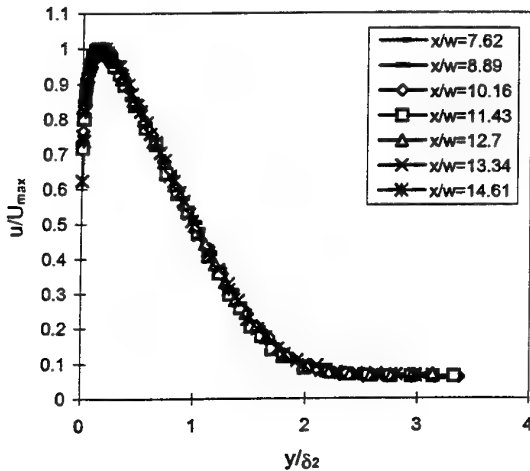


FIGURE 7: Mean velocity distributions in the self-preservation region:  $x/w \geq 7$ .

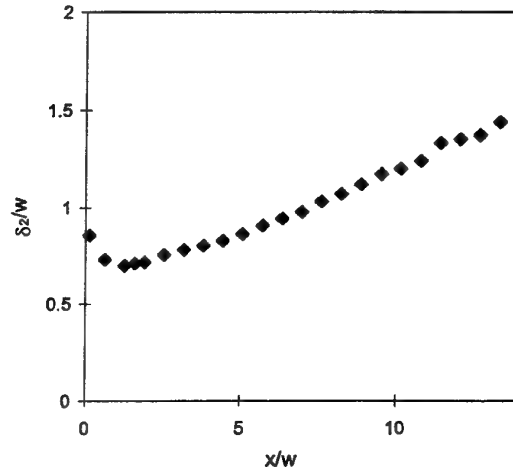


FIGURE 9a: Streamwise variations of the scaling quantities. Length scale distribution.

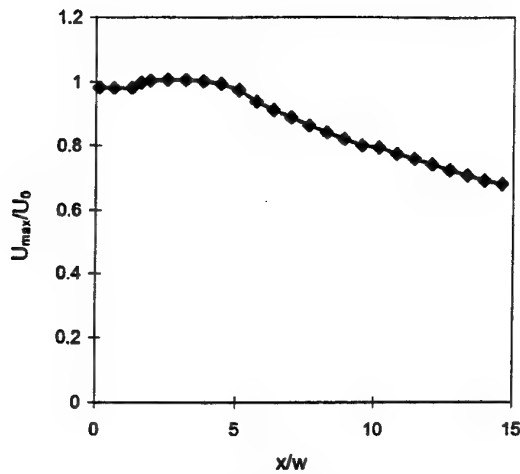


FIGURE 9b: Streamwise variations of the scaling quantities. Velocity scale distribution.

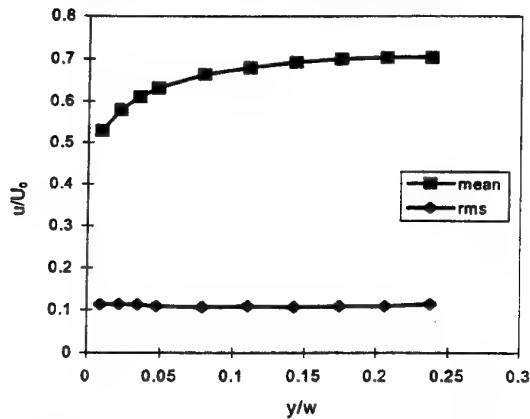


FIGURE 10: Mean and rms fluctuation intensity distributions at  $x/w = 13.34$

The extent of the thermal field is represented by  $\delta_T(x)$  in Fig. 13. As shown, this width measure is dependent upon the threshold level used for its definition. It is instructive to note that each of the  $\delta_T(x)$  distributions indicate an enhanced growth rate at the locations for which the flow exhibits self-preservation of the velocity field.

As shown in Fig. 12, the temperature profiles are dominated by the strong temperature rise near the wall. The wall heat flux per unit area,  $q''$ , was determined from the  $\bar{T}(y)$  measurements in the near wall region. Specifically, as shown in Fig. 14, a linear  $\bar{T}(y)$  distribution was observed for the measured values of  $\bar{T}$  in the range  $0.1 \lesssim y \lesssim 0.2$  mm.

The extremely small distances resulted in some uncertainty of the probe position and hence the establishment of  $\partial \bar{T} / \partial y|_{y=0}$  that was required to infer  $q''$ .

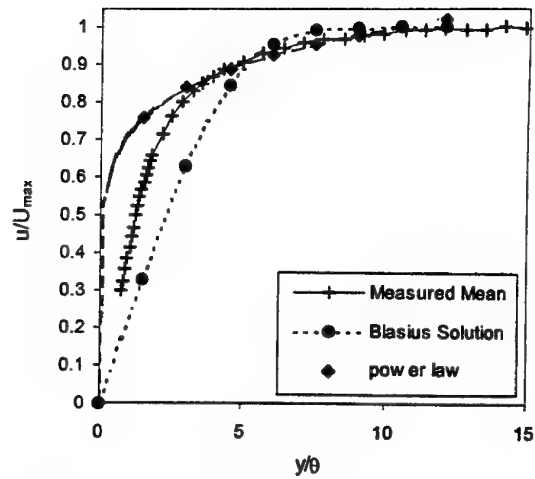


FIGURE 11: Comparison of the mean velocity distribution to "standard" boundary layer distributions at  $x/w = 13.34$ .

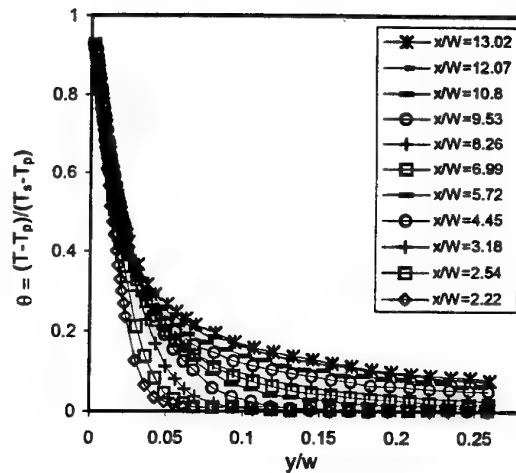


FIGURE 12: The time mean temperature distributions for  $2.2 < x/w \leq 13$

Confidence in the current estimates was, however, provided by using the measured data to extrapolate  $\bar{T}(y)$  to  $y=0$ . Specifically, using the inner portion of Fig. 14, the extrapolated curve is used to predict  $(T_s)$  the surface temperature as

$$T_s = \bar{T}(\delta y) - \frac{\partial \bar{T}}{\partial y} \delta y. \quad (7)$$

In this expression,  $\delta y$  is the closest point to the wall in the measured data set.

The required  $(\partial \bar{T} / \partial y)$  value was readily obtained from the direct measurements. A dial indicator (precision=2.5  $\mu$ m) was used to record the movements of the 7.6  $\mu$ m sensor.

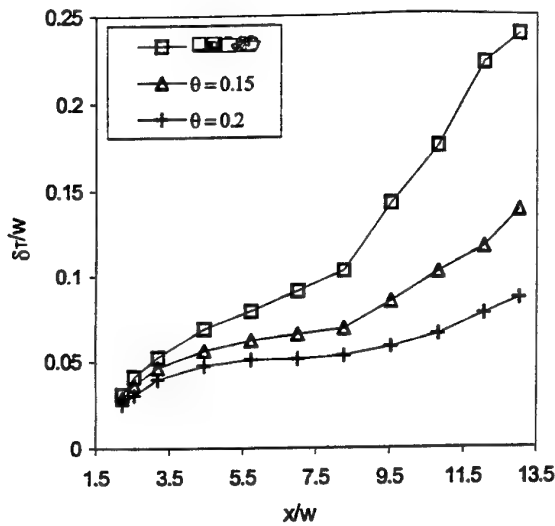


FIGURE 13: Near wall temperature distribution at  $x/w = 13.34$

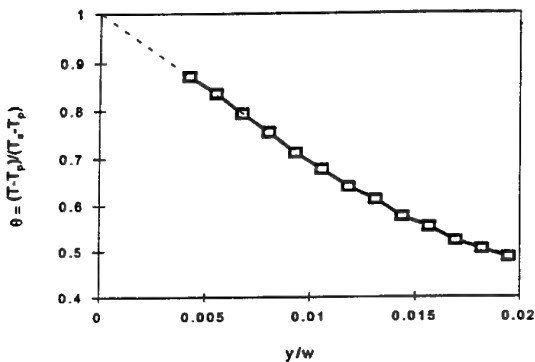


Figure 14: A representative  $\bar{T}(y)$  in the near wall region,  $x/w = 9.35$ .

The more difficult task was to assess the distance to the wall ( $\delta y$ ) of the closest measurement. For this, a 0.1 mm shim stock was pressed against the wall while the probe was brought into alignment with it. A binocular microscope was used to view the alignment.

This procedure was used at several  $x$  stations. The agreement between the measured (shim stock) and the estimated (see Fig. (14)) positions was typical of the agreement for all measurements. The maximum variation in these two estimates of  $\delta y$  was 50  $\mu\text{m}$ .

The local heat transfer coefficient ( $h$ ) and the corresponding Nusselt No. are

$$h = 38.5 \text{ (watts/m}^2\text{ }^\circ\text{C)}$$

and

$$N_{Nu} = 28.5$$

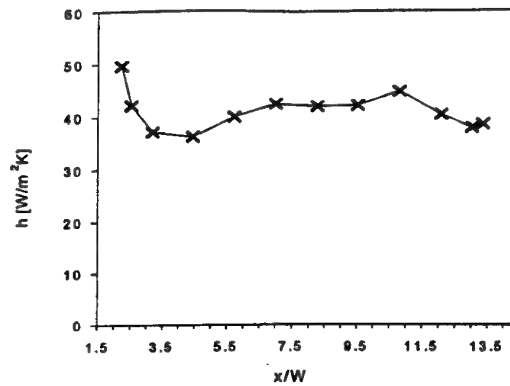


FIGURE 15: Heat transfer coefficient as a function of downstream distance.

for the  $x/w = 13.34$  location. The heat transfer coefficients for other  $x$  locations are shown in Fig. 15.

### CONCLUSIONS

The velocity field in this slit jet/wall jet configuration exhibits the expected behaviors of

- i) an acceleration to the vena contracta (at  $x/w \approx 1.7$ ), and
  - ii) the development of a self-preservation region ( $x/w \gtrsim 7$ ).
- The Nusselt number, for the present case of an isothermal surface, was nominally 25 for the downstream ( $x/w \gtrsim 7$ ) region. Higher values were observed in the region closer to the jet exit and the beginning of the heated region.

The present data can serve as a viable test case for CFD codes which seek to model defroster flows.

### ACKNOWLEDGMENTS

The MSU authors express their appreciation to the Ford Motor Company for the financial support which enabled this project. Appreciation is also expressed to Dr. M. Shabana who provided technical support in the early stages of the effort.

### REFERENCES

- AbdulNour, B.S. and Foss, J.F., "Computational and Experimental Predictions of Automotive Windshield Flow," FEDSM97-3022, June 1997.
- Akfirat, J.C., "Transfer of Heat from an Isothermal Flat Plate to a Two-Dimensional Wall Jet," Proc. 3rd International Heat Transfer Conference, ASME, Paper 41-80, Vol II, pp. 274-279 (1966).
- Launder, B.E. and Rodi, W., "The Turbulent Wall Jet," Prog. Aerospace Sci., Vol. 19, pp. 81-128 (1979).
- Nizou, P.Y., "Heat and Momentum Transfer in a Plane Turbulent Wall Jet," Jour. Heat Transfer, Vol. 103, pp. 138-140 (1981).
- Willenborg, K. and Foss, J.F., "Investigation of the Velocity and Temperature Fields of a Model Defroster Flow," MSU-ENGR-007-96, TSFL-R-046 (1996).

**SESSION 16 - DNS AND LARGE EDDY  
SIMULATIONS - I**

# Stimulated small scale SGS model and its application to channel flow

Kishan B. Shah and J. H. Ferziger

Department of Mechanical Engineering

Stanford University

Bldg. 500

Stanford, CA 94305-3030

U.S.A.

## ABSTRACT

In this paper, a new non-eddy viscosity subgrid scale model for large eddy simulations is introduced. The unfiltered velocity ( $u_i$ ) in the SGS stress tensor ( $\tau_{ij} = \overline{u_i u_j} - \bar{u}_i \bar{u}_j$ ) is replaced by the filtered velocity ( $\bar{u}_i$ ) whose small scales have been stimulated in a prescribed manner. Simulations with this model are computationally efficient; the cost is approximately the same as for the Smagorinsky's model. This model does not require an assumption of homogeneity, permits backscatter of energy from small to large scales, and is readily implemented in finite difference codes, even in complex geometries. We examine one version of this model in which the parameters are determined from one dimensional approximations of unfiltered quantities in terms of filtered ones for a box filter. Results of applying the proposed model to a second order finite volume simulation of plane channel flow at low and high Reynolds numbers ( $Re_b = 3000, 38000$ ) are given. This model provides mean dissipation while retaining the good qualities of Bardina's model. It predicts both mean and turbulence quantities more accurately than the conventional and dynamic Smagorinsky models.

## INTRODUCTION

Smagorinsky's eddy viscosity model is the most widely used subgrid scale (SGS) model. Its success is attributed to the ability of eddy viscosity models to drain energy from the large scales, thus simulating the dissipative nature of turbulence. However, it does not provide adequate representation of instantaneous energy transfer between the resolved and subgrid scales. Most eddy viscosity models remove energy from the large scales at every instant and cannot represent reverse transfer of energy from subgrid to resolved scales (backscatter). Dynamic eddy viscosity models allow negative eddy viscosity but it is questionable whether such a model can produce realistic backscatter. Another shortcoming of such models is that they may lack consistency. For example, Smagorinsky model does not give zero SGS stress in the limit of zero SGS velocity.

Primary concerns in LES of complex flows are the robustness of the SGS model and ease of implementation. The

popularity of the constant coefficient Smagorinsky model attests to its meeting these criteria. Dynamic versions of Smagorinsky's model are more difficult to implement and require special procedures to avoid instabilities arising from large negative eddy viscosities. In the following, we develop a SGS model that has many desirable features. We believe it is also more natural than Smagorinsky's model.

## PROPOSED MODEL

The basis for the scale similarity model of Bardina (1983) is a useful guide in developing this model. It provides a good representation of instantaneous energy transfer between the large and small scales but fails to provide enough mean dissipation. Bardina's model can be derived by substituting  $u_i \approx \bar{u}_i$  in the expression for the exact SGS stress  $\tau_{ij} = \overline{u_i u_j} - \bar{u}_i \bar{u}_j$ ; this yields a Galilean invariant version of this model:

$$\tau_{ij} = \overline{u_i u_j} - \bar{u}_i \bar{u}_j$$

The mean dissipation is small because forward and backward energy transfer are nearly balanced.

It is plausible that if higher order terms are included in the approximation for  $u_i$  (instead of  $u_i \approx \bar{u}_i$ ), this model might provide sufficient mean dissipation, yet retain the other favorable characteristics. Thus, the following form for the SGS stress is proposed:

$$\tau_{ij} = \widehat{u_i^* u_j^*} - \bar{u}_i \bar{u}_j \quad (1)$$

where  $u_i^*$  is defined as the solution of a partial differential operator using the filtered velocity  $\bar{u}_i$  as a source term:

$$\mathcal{L}(u_i^*) = \bar{u}_i \quad \mathcal{L} = \mathcal{L}_x \mathcal{L}_y \mathcal{L}_z \quad (2)$$

where  $\mathcal{L}_x$  is the differential operator:

$$\mathcal{L}_x = \left( 1 + C_1 \frac{\partial}{\partial x} + C_2 \frac{\partial^2}{\partial x^2} \right)$$



$\mathcal{L}_y$  and  $\mathcal{L}_z$  are of similar form. The filtering operation  $\hat{\cdot}$  is defined in a similar manner:

$$\hat{u}_i^* = \mathcal{V}(u_i^*) \quad \mathcal{V} = \mathcal{V}_x \mathcal{V}_y \mathcal{V}_z \quad (3)$$

where  $\mathcal{V}$  is similar to the  $\mathcal{L}$  operator:

$$\mathcal{V}_x = \left(1 + D_1 \frac{\partial}{\partial x} + D_2 \frac{\partial^2}{\partial x^2}\right)$$

The operators were chosen to have factored form rather than a simpler three dimensional form for computational convenience. Substituting  $u^*$  and  $\hat{u}^*$  into Eq. (1) gives the modeled SGS stress. Both  $\mathcal{L}$  and  $\mathcal{V}$  are smoothing operators (for  $C_2, D_2 > 0$ ). The coefficients  $C_1, C_2$  and  $D_1, D_2$ , which are the parameters of this model, determine the extent to which the small scales of the resolved field are used in the SGS model.  $u^*$  is obtained by sequential inversion of  $\mathcal{L}_x, \mathcal{L}_y$  and  $\mathcal{L}_z$  in Eq. (2). The filtering operation  $\hat{\cdot}$  in Eq. (3) requires an explicit application of  $\mathcal{V}_x, \mathcal{V}_y$  and  $\mathcal{V}_z$  to  $u^*$ . If the coefficients in  $\mathcal{L}$  and  $\mathcal{V}$  operators are identical then  $\mathcal{V}\mathcal{L}^{-1} = I$ , i.e.  $\mathcal{V}$  is the inverse of  $\mathcal{L}^{-1}$ . In such a case, Eq. (3) reduces to  $\hat{u}_i^* = \bar{u}_i$ .

The proposed model is "similar" to the exact SGS stress. As the inversion of  $\mathcal{L}$  is a "defiltering" operation,  $u^*$  mimics the unfiltered velocity. The relationship between  $\bar{u}$  and  $u$  depends on the filter used, here the filter is replaced by  $\mathcal{L}$ . How well it approximates the LES filter depends on the choice of parameters. These parameters may be determined by analogy to a filter, or on the basis of physical or numerical considerations. The essence of the model is the stimulation of small scales of filtered field to create the SGS stress. It is hoped that with a proper choice of coefficients, it will be possible to combine the best features of Bardina's model (good representation of energy transfer) and Smagorinsky's model (net dissipation).

## PARAMETER DETERMINATION

We will now present a procedure for determining the coefficients in the  $\mathcal{L}$  and  $\mathcal{V}$  operators. To understand this procedure, consider the expression for  $u^*$  in one dimension:

$$\bar{u} = u^* + C_1 \frac{du^*}{dx} + C_2 \frac{d^2 u^*}{dx^2} = \mathcal{L}_x(u^*) \quad (4)$$

This is a local Taylor series approximation for the filtered quantity in terms of the unfiltered quantity. For the non-symmetric box filter shown in Fig. (1) (here  $j$  refers to computational node):

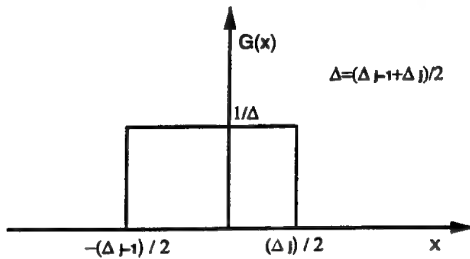


Figure 1: A non-symmetric box filter.

$$G_j = G(x - x_j) = \begin{cases} \frac{1}{\Delta} & \text{if } -\frac{\Delta_j - 1}{2} < x - x_j < \frac{\Delta_j}{2} \\ \frac{1}{2\Delta} & \text{if } x - x_j = -\frac{\Delta_j - 1}{2} \text{ or } x - x_j = \frac{\Delta_j}{2} \\ 0 & \text{if } x - x_j < -\frac{\Delta_j - 1}{2} \text{ or } x - x_j > \frac{\Delta_j}{2} \end{cases}$$

where  $\Delta = (\Delta_j + \Delta_{j-1})/2$  is the filter width, the filtering operation defined by:

$$\bar{u}(x) = \int_{-\infty}^{\infty} G(x - x') u(x') dx'$$

gives:

$$\bar{u}(x_j) = \frac{2}{(\Delta_j + \Delta_{j-1})} \int_{x_j - \frac{\Delta_j - 1}{2}}^{x_j + \frac{\Delta_j}{2}} u(x') dx' \quad (5)$$

Taylor series expansion of  $u(x')$  around  $x_j$  leads to

$$\bar{u}(x_j) = u(x_j) + \frac{(\Delta_j - \Delta_{j-1})}{4} \frac{du}{dx} \Big|_j + \frac{(\Delta_j^2 - \Delta_j \Delta_{j-1} + \Delta_{j-1}^2)}{24} \frac{d^2 u}{dx^2} \Big|_j + O(\Delta^3) \quad (6)$$

Thus,  $u^*$  will be a second order approximation to  $u$  if the coefficients in Eqs. (4) and (6) are matched. Extension to three dimensions consists of sequential application of  $\mathcal{L}$  operators in each direction, however,  $u^*$  will no longer be a second order approximation  $u$ . A finite difference approximation to the operator  $\mathcal{L}_x$  of Eq. (4) can be written as:

$$\bar{u}_j = a u_{j-1}^* + b u_j^* + c u_{j+1}^* \quad (7)$$

The coefficients  $C_1$  and  $C_2$  and the derivatives in Eq. (4) are functions of the filter width  $\Delta$  and the grid size  $h$ , as are  $a, b$  and  $c$ . Substituting the Taylor series expansion for  $u_{j-1}^*$  and  $u_{j+1}^*$  about the node  $j$  into Eq. (7), we obtain:

$$\bar{u}_j = (a + b + c) u_j^* + (ch_j - ah_{j-1}) \frac{du_j^*}{dx} \Big|_j + \left(c \frac{h_j^2}{2} + a \frac{h_{j-1}^2}{2}\right) \frac{d^2 u_j^*}{dx^2} \Big|_j + O(ch_j^3 - ah_{j-1}^3) \quad (8)$$

where  $h_j = x_{j+1} - x_j$ . Matching the coefficients in Eqs. (6) and (8), we obtain three simultaneous equations for  $a, b$  and  $c$ , solution of which yield:

$$\begin{aligned} a &= \frac{h_j^2(m^2 - 3m) + h_j h_{j-1}(3m - m^2) + h_{j-1}^2 m^2}{12h_{j-1}(h_j + h_{j-1})} \\ b &= 1 - (a + c) \\ c &= \frac{h_j^2 m^2 + h_j h_{j-1}(3m - m^2) + h_{j-1}^2(m^2 - 3m)}{12h_j(h_j + h_{j-1})} \end{aligned} \quad (9)$$

where  $m$  is the filter-grid ratio  $m = (\Delta_j + \Delta_{j-1})/(h_j + h_{j-1})$ . The coefficients are determined by choosing a particular  $m$  and  $u^*$  is obtained by inverting Eq (7). This requires boundary conditions for  $u^*$ , which are chosen to be same as those for  $\bar{u}$  on the boundary. Extension to three dimensions involves sequential application of Eq. (7) in each direction and inversion of a sequence of tridiagonal systems.

Table 1 shows the coefficients  $(a, b, c)$  for the finite difference stencil (Eq. (7)) for various  $m$  for a uniform grid. Since only three neighboring grid points are used, the maximum filter width should be  $2h$ . But if this process is seen from a perspective of determining coefficients  $C_1$  and  $C_2$  in Eq. (4), it may be possible to use larger filter width.

Even though the forms of  $\mathcal{L}$  and  $\mathcal{V}$  are identical, the coefficients in the  $\mathcal{L}$  and  $\mathcal{V}$  operators can be different. Bardina's scale similarity model is a special case of this model; for  $\mathcal{L} = I$  and the  $\hat{\cdot}$  filter corresponding to the grid filter.

(a,b,c)	Filter-grid ratio $m = \sqrt{12(1-b)}$
(1,22,1)/24	1
(1,6,1)/8	$\sqrt{3}$
(1,4,1)/6	2

Table 1: Coefficients (a, b, c) corresponding to various filter-grid ratio (m) for uniform grid

Bardina's model may be viewed as a zeroth order approximation ( $u_i \approx \bar{u}_i$ ) of the above model.

Even though the Taylor series expansion cannot be used for Fourier cutoff filters, the model equations (for  $\mathcal{L}$  and  $\mathcal{V}$ ) are still valid. The fundamental idea is the construction of the SGS stress from the filtered velocity by stimulating the small scales. These small scales i.e. the high wavenumber region of LES are assumed to be representative of the SGS. Finally, it must be pointed out that the optimal values of coefficients  $C_1$  and  $C_2$  need not be same as the coefficients in the one dimensional expansion Eq (5). Two major approximations have been made to the filtering operation; the cross derivative terms that arise in three dimensions and the higher order terms were ignored. In the present work, we have taken the value of  $C_1$  and  $C_2$  to be what one gets by truncating the expansion for a box filter in one dimension (Eq. (5)).

## NUMERICAL IMPLEMENTATION

The procedure for computing the SGS stress consists of the following three steps:

1. Chose a filter-grid ratio (m) for each direction. This determines the coefficients a, b and c in Eq. (9).
2. Compute  $u^*$  by inverting a set of tridiagonal systems (Eq. (7)) in each direction x, y and z. Note that a staggered formulation is used in the computation so  $\bar{u}$  needs to be interpolated to the center of the control volume before computing  $u^*$  which is defined there. The boundary conditions for  $u^*$  are same as for  $\bar{u}$ .
3. Substitute  $u^*$  into Eq. (1) and apply the filtering ( $\mathcal{V}$ ) operator. The coefficients a, b and c can be different from those of  $\mathcal{L}$ ; for our test cases, we used the same coefficients.

In the present calculations, the SGS and convective terms were treated explicitly. Since the SGS contribution can be significant, the time step has to be reduced to respect the numerical stability limit.

## NUMERICAL METHOD

A second order staggered finite volume formulation is used to discretize the Navier-Stokes equations. Uniform meshes are used in the streamwise and the spanwise directions, and hyperbolic tangent stretching (Thompson & Warsi 1985) is used in the wall-normal direction. A fractional step method is used to decouple the pressure from the momentum equation. The momentum equations are first advanced without satisfying continuity, then the velocity field is adjusted to satisfy continuity. The time advancement of the momentum equation is semi-implicit using third order Runge-Kutta for the non-linear (convective) terms and second order Crank-Nicolson for the diffusive (viscous) terms. Continuity is enforced by solving a Poisson equation for a pressure-like variable; a fast Fourier

$Re_b$	$N_x, N_y, N_z$	$\Delta x^+, \Delta z^+$	$\Delta y_{min}^+, \Delta y_{max}^+$
3000	48,64,48	25,28	1,10
38000	64,80,80	221,35	1.5,150

Table 2: Simulation parameters

transform (FFT) procedure solves this problem efficiently. A full description of this numerical method can be found in Shah and Ferziger (1997)

## COMPUTATIONAL DOMAIN

The computational domain parameters are listed in table 2. The x, y, and z axes are in the streamwise, wall-normal, and spanwise directions, respectively. The physical domain sizes in these directions are  $(2.0\pi, 2.0, 7.0)$  for the low  $Re$  case and  $(2.5\pi, 2.0, 0.5\pi)$  for the high  $Re$  case. Simulations were carried out by fixing the mass flow (or  $Re_b$ ).  $Re_b = 3000$  corresponds to  $Re_\tau \approx 190$  and high  $Re_b = 38000$  corresponds to  $Re_\tau \approx 1800$ . For the high  $Re$  case, the physical domain and grid sizes are similar to those of Piomelli (1993); however, since our  $Re_\tau \approx 1800$  is slightly lower than Piomelli's value ( $Re_\tau = 1995$ ), the domain and grid sizes in wall units are slightly different. Reynolds numbers are based on the half channel height  $\delta$ , bulk velocity  $U_b$  for  $Re_b$ , and the friction velocity  $u_\tau$  for  $Re_\tau$ .

## RESULTS

For the low  $Re$  case, we have computed channel flow with the proposed model, the Smagorinsky model with  $C_s = 0.065$  and Van Driest wall damping, a dynamic model with filtering in all three directions and coefficient averaging on horizontal planes ( $x-z$ ), and no model, all on the same mesh. For the proposed model, the coefficients are based on  $m = 1.0$ .

Figure 2 shows the mean velocity profiles in wall units. All models except the proposed model over-predict  $U^+$  in the logarithmic region. The results of the proposed model agree well with the DNS results of Kim *et al.* (1987). The dynamic model gives the worst result, an over-prediction of  $U^+$  due to under-prediction of the skin friction velocity  $u_\tau = \sqrt{\tau/\rho}$ . The turbulence statistics are also improved using the new model. For details see Shah and Ferziger (1997).

For the high  $Re$  case, we present mean and turbulent quantities for four cases: no model (CDNS1), Smagorinsky's model with Van Driest wall damping (SMAG1), the dynamic Smagorinsky model with filtering in the homogeneous directions (DSMAG1) and the proposed model with  $m = 2.0$  (NEWM3).

The profiles of the mean velocity normalized by skin friction velocity ( $u_\tau$ ) is shown in Figs. 3 and 4 along with Piomelli's spectral LES data and the log law  $u^+ = (1/\kappa) \log y^+ + B$  with  $\kappa = 0.4$  and  $B = 5.5$ . The profiles obtained from all cases have bulges in the region  $10 < y^+ < 200$  and the slope in the log region is smaller than  $1/\kappa = 2.5$ . The coarse grid DNS gives a smaller bulge but there is no improvement in the log-slope. The mean velocity profile produced by the new model is in better agreement with Piomelli's LES and the log law, but a bulge is still present. Interestingly, the new model profile falls below the log law for  $300 < y^+ < 800$ , in contrast to other

	$Re_b$	$\frac{c_f - c_f^{Dean}}{c_f^{Dean}} \times 100$	$U_c/U_b$
Dean	38000		1.124
SMAG1	38000	-5.77	1.086
DSMAG1	38000	-8.31	1.090
NEWM3	38000	+2.30	1.110
CDNS1	38000	+0.25	1.094
Piomelli	42598	+1.75	1.105

Table 3: Comparison of the skin friction and centerline velocity with experimental correlations of Dean (1978)

models which over-predict the mean velocity throughout the channel. Both coarse DNS and the new model fall on the log law and Piomelli's LES for  $y^+ > 1000$ . Table 3 compares the skin friction coefficient  $c_f = \tau_w / \frac{1}{2} \rho U_b^2$  and the ratio of centerline velocity ( $U_c$ ) to bulk velocity ( $U_b$ ) to the experimental correlations proposed by Dean (1978). The skin friction and centerline velocity predicted by the new model and the coarse DNS are within 2.5% of Dean's correlation. The conventional Smagorinsky and dynamic models under-predict the skin friction which causes the mean velocity to be too large.

Figure 5 shows the SGS shear stress  $\tau_{12}^{SGS}$  for various models; the new model produces the largest SGS stress by far. The SGS stress accounts for 28% of the total stress  $\langle \bar{u} \bar{v} + \tau_{12}^{SGS} \rangle$  in the new model as opposed to 2% for the Smagorinsky and dynamic models. Far from the walls, the new model produces a significant SGS contribution. It is desirable to compare the total fluctuations but for the Smagorinsky models, it is difficult to compute the SGS contribution. Bardina (1983) proposed the following expression for computing the total turbulent intensity  $Q^2$  from the turbulent intensity of the filtered field  $Q_f^2$  and the SGS dissipation rate  $\epsilon_f$ :

$$Q^2 = \frac{Q_f^2}{Q_f^2 - c(2\Delta_f \epsilon_f)^{2/3}} \quad (10)$$

where  $\Delta_f$  is the filter width and  $c = 1.04$ . Figure 6 shows the total turbulence kinetic energy  $Q^2/2$  for the various models in wall units; Eq. (10) was applied to all models except the new model. From Fig. (6) it is evident that SGS models do poorly near the walls. Figure 6 shows Piomelli's filtered fluctuation since it is in good agreement with the experiments, but it too will deteriorate near the wall if the SGS contribution is included. All models except the new model over-predict the peak by almost 70%; the new model does better but still over-predicts it by 20%.

Figure 7 shows the mean SGS dissipation rate  $\langle \epsilon_{SGS} \rangle = \langle \tau_{ij} \bar{S}_{ij} \rangle$  near the wall normalized by  $U_b$  instead of  $u_\tau$  which is different for each model. The dynamic model has the smallest peak and the smallest overall SGS dissipation rate. For fully developed channel flow the total dissipation rate (viscous+SGS) is proportional to the pressure drop. Since the dynamic model has the lowest skin friction, the total dissipation is also the smallest. In the Smagorinsky and dynamic models, energy piles up in the large scales because the SGS stress is unable to drain enough energy from the large scales. As a result, the skin friction is under-predicted.

Figures 8 and 9 show time series of SGS dissipation rate at  $x = 1.25\pi$ ,  $z = 0.25\pi$  and  $y^+ = 2$  and 12. Significant backscatter of energy is seen in the buffer region

and beyond. In the region close to the wall,  $y^+ = 2$ , the dissipation rate is mostly negative. Away from the walls, large backscatter usually follows large forward scatter. The backscatter in the new model is an integral part of the model and is not modeled separately as in stochastic backscatter models. Backscatter is approximately 50% of the net SGS dissipation and 40% of the volume exhibits backscatter.

## CONCLUSION

A new non-eddy viscosity model, the stimulated small scale ( $S^3$ ) SGS model, has been presented. The SGS stress is constructed by exciting the high wavenumbers of the filtered field. Its utility was demonstrated for plane channel flow for both low and high Reynolds number. The model provides a good representation of the SGS dissipation and predicts total stresses more accurately, especially at high Reynolds numbers. The skin friction and centerline velocity are predicted accurately. At both low and high Reynolds numbers, the Smagorinsky and dynamic models produce lower net dissipation than the new model leading to under-prediction of skin friction. Overall, the dynamic model gives the worst results.

The only parameter in the proposed model is the filter-grid ratio  $m$ . With  $m = 0$ , we have coarse DNS. If three neighboring points in each direction are employed to construct the filter, the maximum filter width is  $2h$ . On the other hand, the grid cannot resolve wavelength smaller than  $2h$ , so the filter width cannot be smaller than  $2h$ . So  $m = 2.0$  seems to be ideal. These arguments are based on an analogy to filtering, but as mentioned earlier, it is possible to use other values of  $m$ . In fact,  $m = 2$  may provide excess dissipation. As with any SGS model that uses small scale information to model the subgrid scales, this model is sensitive to the spectrum at high wavenumbers. When the resolution is marginal, the high wavenumbers are poorly predicted. For the high  $Re$  case,  $m = 2.0$  gives excess dissipation. When a pre-filter is applied to filtered velocity just before SGS stress is computed, the SGS dissipation is reduced. Thus it may be better to use pre-filtering or a smaller  $m$ .

In the current simulations same  $m$  was used in all three directions and in defining the  $\mathcal{L}$  and  $\mathcal{V}$  operations. Increasing  $m$  corresponds to a larger filter width so the subgrid scales are more energetic. The SGS dissipation is reduced considerably if the filter-grid ratio in the definitions of the  $\mathcal{L}$  and  $\mathcal{V}$  operations do not match. This is the case for Bardina's scale similarity model, for which  $\mathcal{L}$  corresponds to  $m = 0$  and  $\mathcal{V}$  corresponds to the grid filter.

The new model is efficient and easy to implement. In the present implementation, the new model takes 7% (same as Smagorinsky) more CPU time than coarse DNS, whereas the dynamic model takes 30% more CPU time than coarse grid DNS, on a CRAY C90.

More details on the model and further test cases are given in Shah and Ferziger (1997).

## ACKNOWLEDGMENTS

We are grateful to Dr. Thomas Lund for stimulating discussions and thoughtful advice. Computing resources were provided by the San Diego Supercomputer Center (SDSC).

## REFERENCES

Bardina J., Ferziger J. H., Reynolds W. C. (1983) Improved turbulence models based on large eddy simulation of homogeneous, incompressible, turbulent flows, *Report TF-19, Thermosciences Division, Dept. of Mech. Engr., Stanford University, Stanford, California, USA.*

Dean, R.B. (1978) Reynolds number dependence of skin friction and other bulk flow variables in two-dimensional rectangular duct flow, *J. Fluids Eng.*, 100, 215-223, 1978.

Germano M. (1986) A proposal for a redefinition of the turbulent stresses in the filtered Navier-Stokes equations, *Phys. Fluids* 29 (7), 2323-2324, July 1986.

Kim J., Moin P., Moser R. (1987) Turbulence statistics in fully developed channel flow at low Reynolds number, *Journal of Fluid Mechanics*, Volume 177, 133-166, 1987.

Piomelli U. (1993) High Reynolds number calculations using the dynamic subgrid-scale stress model, *Phys. Fluids A* 5 (6), 1484-1490, June 1993.

Shah K. B., Ferziger J. H. (1995) A new non-eddy viscosity subgrid-scale model and its application to channel flow, *Annual Research Briefs - 1995, Center for Turbulence Research, NASA Ames/Stanford University.*

Shah K. B., Ferziger J. H. (1997) Large eddy simulations of flow past a cubic obstacle, *Report TF-70, Thermosciences Division, Dept. of Mech. Engr., Stanford University, Stanford, California, USA.*

Thompson J.F., Warsi Z.U.A., Martin C.W. (1985) Numerical Grid generation: Foundations and Application, North Holland, Elsevier Science Publishing Co., Inc., 1985.

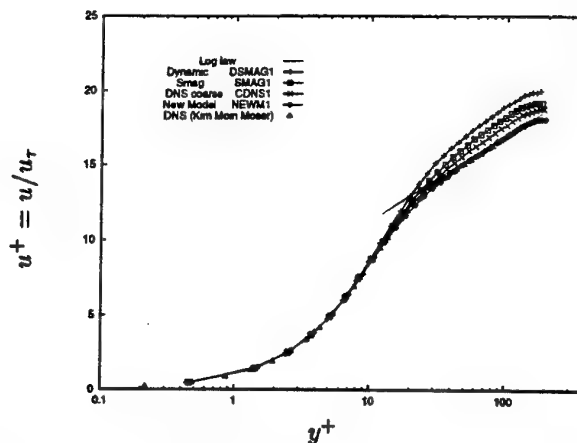


Figure 2: Mean velocity profiles at  $Re_b = 3000$ . ..... log law; —■— Smagorinsky (SMAG1); - - - dynamic (DSMAG1); —×— no model (CDNS1); —◆— proposed model (NEWM1); Δ DNS of Kim et al. (1987).

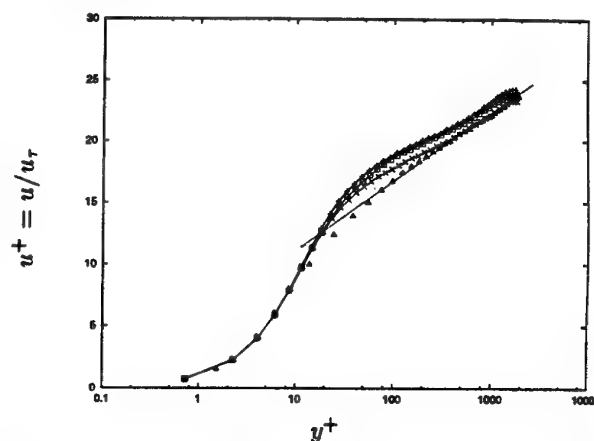


Figure 3: Mean velocity profiles at  $Re_b = 38000$ . ..... log law; —■— Smagorinsky (SMAG1); - - - dynamic (DSMAG1); —×— no model (CDNS1); Δ spectral LES of Piomelli (1993).

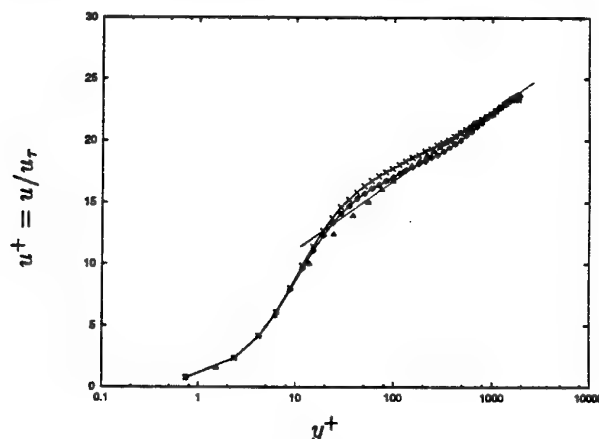


Figure 4: Mean velocity profiles at  $Re_b = 38000$ . ..... log law; —×— no model (CDNS1); —◆— proposed model; Δ spectral LES of Piomelli (1993).

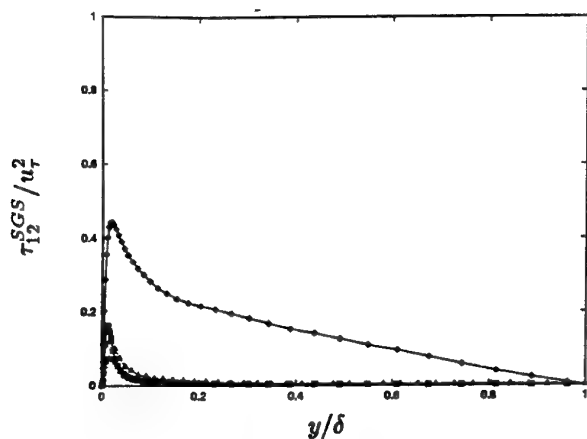


Figure 5: SGS shear stress at  $Re_b = 38000$ . —■— Smagorinsky (SMAG1); -+- dynamic (DSMAG1); —◆— proposed model (NEWM3);  $\Delta$  spectral LES of Piomelli (1993).

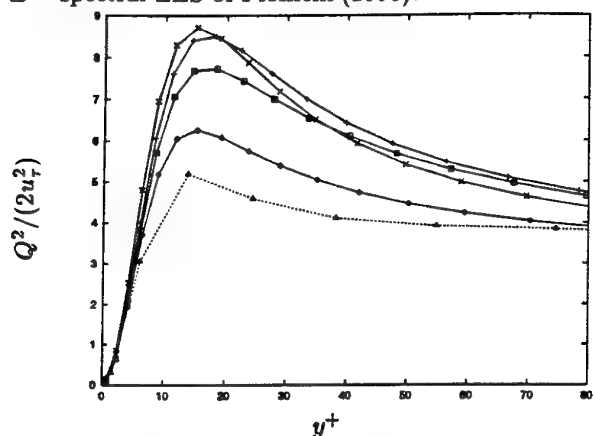


Figure 6: Total (resolved+SGS) turbulent kinetic energy (TKE) at  $Re_b = 38000$ . —■— Smagorinsky (SMAG1); -+- dynamic (DSMAG1); —×— no model (CDNS1); —◆— proposed model (NEWM3);  $\Delta$  resolved TKE of Piomelli (1993).

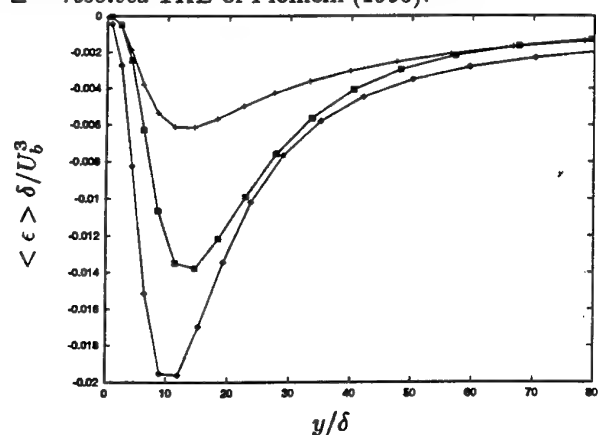


Figure 7: SGS dissipation rate at  $Re_b = 38000$  in global units. —■— Smagorinsky (SMAG1); -+- dynamic (DSMAG1); —◆— proposed model (NEWM3).

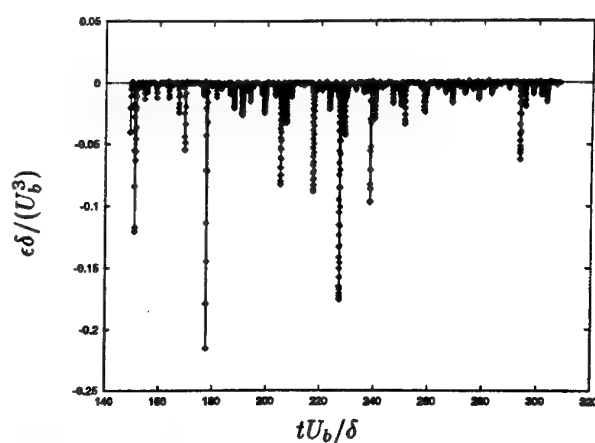


Figure 8: Time series of SGS dissipation rate at  $Re_b = 38000$  for the proposed model (NEWM3) at  $x = 1.25\pi, z = 0.25\pi$  and  $y^+ = 2.3$ . Positive values signify backscatter.

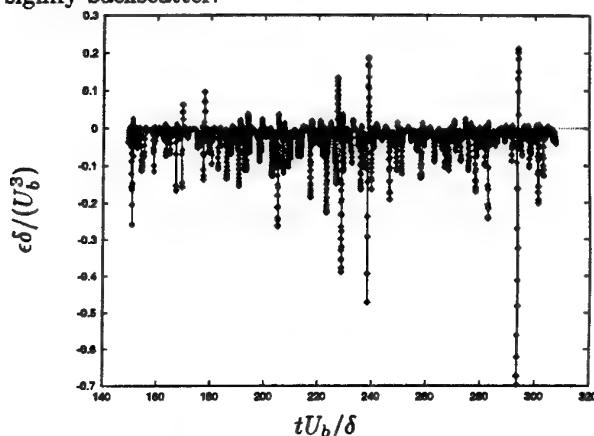


Figure 9: Time series of SGS dissipation rate at  $Re_b = 38000$  for the proposed model (NEWM3) at  $x = 1.25\pi, z = 0.25\pi$  and  $y^+ = 12.0$ . Positive values signify backscatter.

# SUBGRID-SCALE MODELING BASED ON THE GENERALIZED SCALE-SIMILARITY MODELS

Kiyosi Horiuti

Department of Mechano-Aerospace Engineering  
Tokyo Institute of Technology  
2-12-1 O-okayama, Meguro-ku  
Tokyo 152  
Japan

## Abstract

A general procedure for modeling the SGS stress tensor in large-eddy simulation of turbulent flows is presented. This procedure is based on the decomposition of the SGS stress tensor into the modified Leonard, modified cross and modified SGS Reynolds stress terms. Each term in the decomposition is assumed to be proportional to a new model term, the form of which is comparable to the generalized central moments reported by M. Germano [J. Fluid Mech. 238, 325 (1992)]. Using a linear combination of this new model with the Smagorinsky model, the derived model contains multi model parameters, which are computed dynamically. Previous dynamic models are derived as a subset of the proposed model. Two formulations for the test-filtered SGS stress reported by Zang *et al.* [Phys. Fluids A 5, 3186 (1993)] and Vreman *et al.* [Phys. Fluids 6, 4057 (1994)] are compared, and the compatibility of the SGS models with the standard dynamic SGS model procedure is discussed. It can be inferred that the SGS models represented in a form comparable to the generalized scale-similarity model with the test-filtered stresses approximated using the formulation by Zang *et al.* generally yield accurate estimates of the model parameter. The proposed model is assessed for incompressible channel and mixing layer flows, in comparison with the dynamic Smagorinsky model of Germano *et al.* [Phys. Fluids A 3, 1760 (1991)], the dynamic mixed model of Zang *et al.* and the dynamic two-parameter mixed model of Salvetti and Banerjee [Phys. Fluids 7, 2831 (1995)]. In the 'a priori' test, the proposed model gave the closest agreement with the modified cross term as well as the modified SGS Reynolds stress term. The results in the 'a posteriori' tests were consistent with those of the 'a priori' tests.

The proposed procedure is applied to the modeling of the SGS passive scalar flux. Assessment of the derived model is carried out in the scalar transport inside the channel.

## INTRODUCTION

Large-eddy simulation (LES) is a turbulence simulation method in which the large-scale (grid-scale) field is directly calculated, while the small-scale (subgrid-scale or SGS) field is modeled. The velocity and pressure fields are

decomposed into grid scale and SGS components using a filtering procedure.

A decomposition of the SGS stress tensor,  $\tau_{ij}$ , which results from filtering the Navier-Stokes equations, consists of three terms: [1, 2]

$$\tau_{ij} = L_{ij}^m + C_{ij}^m + R_{ij}^m, \quad (1)$$

where

$$\begin{aligned} L_{ij}^m &= \overline{u_i u_j} - \overline{u_i} \overline{u_j}, \\ C_{ij}^m &= \overline{u_i u_j'} + \overline{u_j' u_i} - (\overline{u_i} \overline{u_j'} + \overline{u_j'} \overline{u_i}), \\ R_{ij}^m &= \overline{u_i' u_j'} - \overline{u_i'} \overline{u_j'}, \end{aligned}$$

where  $\overline{u_i}$  denotes the grid-scale velocity component of  $u_i$  and  $u_i' = u_i - \overline{u_i}$  denotes the SGS component of  $u_i$ .  $L_{ij}^m$  is the modified Leonard term,  $C_{ij}^m$  is the modified cross term, and  $R_{ij}^m$  is the modified SGS Reynolds stress. The indices  $i = 1, 2, 3$  correspond to the directions  $x$ ,  $y$ , and  $z$ , respectively, where  $x$  is the streamwise direction,  $y$  is the wall-normal or cross-stream direction, and  $z$  is the spanwise direction. In the present study we consider fields which are homogeneous in two directions ( $x$  and  $z$ ). In the following,  $\langle \rangle$  denotes the average in the  $x - z$  plane. In the present study, we adopted the Gaussian filter because scale-similarity models are used to approximate the SGS stress tensors.

In the present work, we have primarily focused on assessing the model in homogeneous flow fields. No filter was applied in the inhomogeneous direction, but the same numerical discretization method was used in the  $y$  direction both in the direct numerical simulation (DNS) data generation and in assessing the LES models.

## GENERALIZED SIMILARITY MODEL

The basic principle which we adopted in the present study is to represent and model the SGS central moments in a form comparable to the generalized central moment, [3] because it was shown that the structure of the constitutive equations for the SGS central moments is invariant to the particular averaging operation (averaging invariance) when the moments are represented in this form. This property

is particularly important when the multilevel filtering operation is applied to the SGS central moments, as is done in the dynamic SGS model. We model various SGS central moments as follows (the generalized scale-similarity model):

$$\overline{fg} - \overline{f}\overline{g} \simeq C\{\overline{f\overline{g}} - \overline{\overline{f}\overline{g}}\}, \quad (2)$$

where  $C$  denotes the model parameter. The term in the right-hand side of Eq. (2) is comparable to the generalized central moment, and retains the Galilean invariance.

When the modified cross term is approximated in the form of the generalized scale-similarity model, it becomes

$$C_{ij}^m \simeq C_C\{\overline{\overline{u_i} \overline{u_j}} + \overline{\overline{u_i'} \overline{u_j'}} - (\overline{\overline{u_i} \overline{u_j'}} + \overline{\overline{u_i'} \overline{u_j}})\} = \quad (3)$$

$$C_C\{(\overline{\overline{u_i} \overline{u_j}} + \overline{\overline{u_i} \overline{u_j'}} - (\overline{\overline{u_i} \overline{u_j}} + \overline{\overline{u_i} \overline{u_j'}})) - 2(\overline{\overline{u_i} \overline{u_j}} - \overline{\overline{u_i} \overline{u_j'}})\},$$

where  $C_C$  denotes a model parameter.

Similarly, the  $R_{ij}^m$  term is approximated as

$$R_{ij}^m \simeq C_R(\overline{\overline{u_i' u_j'}} - \overline{\overline{u_i'} \overline{u_j'}}) \equiv C_R L_{ij}^R, \quad (4)$$

$$L_{ij}^R = (\overline{\overline{u_i} - \overline{u_i}})(\overline{\overline{u_j} - \overline{u_j}}) - (\overline{\overline{u_i} - \overline{u_i}})(\overline{\overline{u_j} - \overline{u_j}}). \quad (5)$$

where  $C_R$  is a parameter. The first term in the right-hand side of Eq. (5) is equivalent to the filtered-Bardina model for the SGS Reynolds stress in the classical decomposition of  $\tau_{ij}$ . [5] Eq. (5) can be rewritten as

$$L_{ij}^R = L_{ij}^m - \quad (6)$$

$$\{\overline{\overline{u_i} \overline{u_j}} + \overline{\overline{u_i} \overline{u_j'}} - (\overline{\overline{u_i} \overline{u_j}} + \overline{\overline{u_i} \overline{u_j'}})\} + (\overline{\overline{u_i} \overline{u_j}} - \overline{\overline{u_i} \overline{u_j'}}).$$

Using Eq. (6), Eq. (3) is rewritten as

$$C_{ij}^m \simeq C_C[L_{ij}^C - L_{ij}^R], \quad (7)$$

$$L_{ij}^C = L_{ij}^m - (\overline{\overline{u_i} \overline{u_j}} - \overline{\overline{u_i} \overline{u_j}})$$

It is found in Eqs. (4), (6) and (7) that the models represented in the form of the generalized scale-similarity model for the  $C_{ij}^m$  term and the  $R_{ij}^m$  term are not mutually independent, thus, a general model for the SGS stress tensor is obtained as

$$\tau_{ij}^* \simeq L_{ij}^{m*} + C_C L_{ij}^{C*} + C_B L_{ij}^{R*}, \quad (8)$$

Here  $f_{ij}^*$  indicates  $f_{ij} - \frac{1}{3}\delta_{ij}f_{kk}$ , and  $C_B = C_R - C_C$ .

## 'A PRIORI' TEST OF SGS MODELS

In this section, we directly assess the SGS models using the DNS databases for channel and mixing layer flows. The SGS stresses computed by filtering the DNS data are compared with those calculated using the SGS models.

The wall-bounded turbulence DNS data that we used were for fully developed incompressible channel flow with  $Re_\tau$  (Reynolds number based on the wall-friction velocity,  $u_\tau$ , and the half-channel height,  $\delta$ ) = 180 with 128, 129 and 128 grid points, respectively, in the  $x$ ,  $y$  and  $z$  directions. [4, 5]

For free shear turbulence, we have chosen incompressible mixing layer flow that develops in time, and generated DNS data with 192, 128 and 128 grid points, respectively, in the  $x$ ,  $y$  and  $z$  directions. [5] The Reynolds number,  $Re_\theta$ , based on the mean velocity difference between the two edges of the mixing layer,  $\Delta U$ , and the initial momentum thickness was set equal to 200.

The channel flow field was filtered to  $32 \times 129 \times 32$  in the  $x$ ,  $y$  and  $z$  directions, respectively. The mixing layer flow field was filtered to  $48 \times 128 \times 32$  grid points, respectively, in the  $x$ ,  $y$  and  $z$  directions.

$(i, j)$	Channel			Mixing layer		
	$L_{ij}^C$	$L_{ij}^m$	$L_{ij}^R$	$L_{ij}^C$	$L_{ij}^m$	$L_{ij}^R$
(1,1)	0.88	0.82	0.94	0.90	0.79	0.92
(1,2)	0.88	0.80	0.94	0.91	0.75	0.90
(2,2)	0.89	0.85	0.95	0.90	0.82	0.93
(3,3)	0.87	0.82	0.94	0.89	0.79	0.93

Table 1: Correlation coefficients between the exact  $C_{ij}^m$  term and the  $L_{ij}^C$ ,  $L_{ij}^m$  and  $L_{ij}^R$  terms.

$(i, j)$	Channel			Mixing layer		
	$L_{ij}^C$	$L_{ij}^m$	$L_{ij}^R$	$L_{ij}^C$	$L_{ij}^m$	$L_{ij}^R$
(1,1)	0.67	0.59	0.84	0.71	0.60	0.88
(1,2)	0.58	0.41	0.71	0.59	0.42	0.83
(2,2)	0.68	0.62	0.82	0.75	0.63	0.91
(3,3)	0.62	0.54	0.82	0.66	0.52	0.88

Table 2: Correlation coefficients between the exact  $R_{ij}^m$  term and the  $L_{ij}^C$ ,  $L_{ij}^m$  and  $L_{ij}^R$  terms.

In order to examine the accuracy of the  $L_{ij}^C$ ,  $L_{ij}^m$  and  $L_{ij}^R$  terms for approximating the  $C_{ij}^m$  term, the exact values of the  $C_{ij}^m$  term obtained from the DNS data are compared with the model term values estimated using the exact filtered velocity field obtained from the DNS data. The (volume-averaged) correlation coefficients between components of the  $C_{ij}^m$  term and the corresponding components of the model terms are shown in Table I. The correlation coefficients of the  $L_{ij}^C$  term are higher than those of the  $L_{ij}^m$  term, but those of the  $L_{ij}^R$  term are still higher than those of the  $L_{ij}^C$  term.

We examined the correlation coefficients between the  $R_{ij}^m$  term and the  $L_{ij}^R$  term in Table II. For comparison, the correlation coefficients between the  $R_{ij}^m$  term with the  $L_{ij}^C$  and  $L_{ij}^m$  terms are shown.

It can be seen in Table II that the correlation coefficients between the  $R_{ij}^m$  term and the  $L_{ij}^R$  term are high for both channel and mixing layer flows, [5] whereas the correlation coefficients between the  $R_{ij}^m$  term and the  $L_{ij}^m$  term are low, although the correlation of the  $L_{ij}^C$  term shows improvement compared with that of the  $L_{ij}^m$  term. We consider that this result is obtained because the  $L_{ij}^m$  term contains no information regarding the transfer field  $\overline{u_i'}$ . [1] The present results indicate that the  $L_{ij}^R$  term is an accurate model for both the modified cross term and the modified SGS Reynolds stress. Therefore, the  $L_{ij}^R$  term is a more general approximation for the SGS stress tensor.

In fact, a Taylor expansion of the SGS stress terms [6] shows that the modified cross term and the modified SGS Reynolds stress include terms with higher-order derivatives of grid-scale velocity components. It was shown that these higher-order terms are better represented by the  $L_{ij}^R$  term than by the  $L_{ij}^m$  term. [7]

Although some improvements were found in the correlation coefficients, the performance of the  $L_{ij}^C$  term was not so impressive as that of the  $L_{ij}^R$  term. In addition, a significant increase of CPU time is required to compute the second term in the  $L_{ij}^C$  term. In the present study, we ignore this second term for practicability.

Using a linear combination with the Smagorinsky model, [8] we propose the dynamic three-parameter mixed model as

$$\tau_{ij}^* \simeq C_L L_{ij}^{m*} + C_B L_{ij}^{R*} - 2C_S \overline{\Delta^2} |\overline{S}| \overline{S}_{ij}. \quad (9)$$



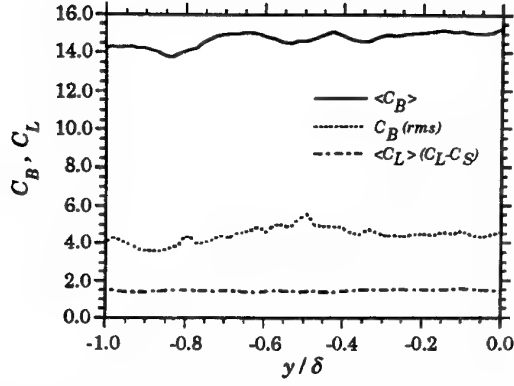


Figure 1:  $y$ -distributions of the plane-averaged and rms values of  $C_B$  and the plane-averaged value of  $C_L$  obtained using the formulation by Zang *et al.*

where  $C_L = 1 + C_C$ , and  $\bar{S}_{ij} = \frac{1}{2} \left( \frac{\partial \bar{u}_i}{\partial x_j} + \frac{\partial \bar{u}_j}{\partial x_i} \right)$ .

The drawback of this model is that when the three parameters in the model are determined using the dynamic procedure, a considerable increase of CPU time as well as memory size is still required. In the present study, we have confined our analysis to one- or two-parameter mixed models, which are obtained as a subset of this three-parameter model: the dynamic Smagorinsky model [9] (DSM,  $C_L = C_B = 0$ ), the dynamic mixed model [10] (DMM,  $C_L = 1, C_B = 0$ ), the dynamic two-parameter  $C_L - C_S$  mixed model [11] (DTM ( $C_L - C_S$ ),  $C_B = 0$ ), and the following dynamic two-parameter  $C_B - C_S$  mixed model (DTM ( $C_B - C_S$ ),  $C_L = 1$ ):

$$\tau_{ij}^* \approx L_{ij}^{m*} + C_B L_{ij}^{R*} - 2C_S \bar{\Delta}^2 |\bar{S}| \bar{S}_{ij}. \quad (10)$$

### Dynamic model procedure

In the present study, two parameters included in the models are determined using the same dynamic procedure [9] combined with the least squares method. [12]

In the dynamic procedure, the test-filtered field  $T_{ij}$  ( $= \bar{u}_i \bar{u}_j - \tilde{u}_i \tilde{u}_j$ ) should be properly determined, where the tildes ( $\tilde{\cdot}$ ) denote the 'test' filter, the width  $\tilde{\Delta}$  of which was chosen as  $\tilde{\Delta} = 2\bar{\Delta}$ . [9] In SB, the formulation proposed by Zang *et al.* [10] was adopted. This formulation may violate similarity in the stresses at the grid-filtered and test-filtered levels. An alternative formulation which is mathematically more consistent with the essence of the dynamic models is that proposed by Vreman *et al.* [13] In this section, we compare these two formulations using the DNS data.

The  $y$ -distribution of the plane-averaged values of  $C_B$  and  $C_L$ , and the rms values of  $C_B$  obtained in the channel flow using the formulation of Zang *et al.* are shown in Fig. 1. The  $C_B$  value was obtained using the  $C_B - C_S$  model, whereas the  $C_L$  value was obtained using the  $C_L - C_S$  model. The average  $C_B$  value is positive throughout the channel, while the rms value is much smaller than the average value, indicating that the  $C_B$  values obtained using the dynamic procedure are mostly positive, which is in good agreement with the estimate of the exact values. An average value of  $C_B \approx 14.5$  is close to the optimized values obtained for the exact DNS data.  $\langle C_L \rangle$  is approximately 1.4 throughout the channel, which is in good agreement with the results reported by SB. The same positive  $C_B$  was found in the mixing layer.

Figure 2 shows the profiles of  $C_B$  obtained using Vreman *et al.*'s formulation in the channel flow. As shown in Fig.

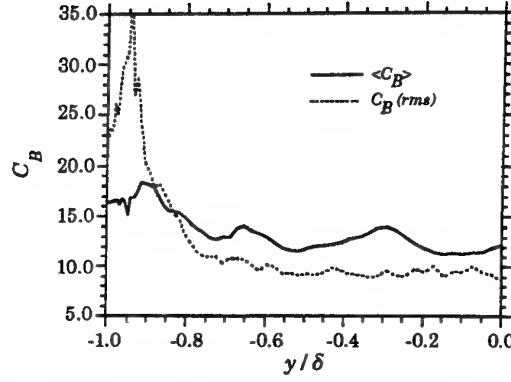


Figure 2:  $y$ -distributions of the plane-averaged and rms values of  $C_B$  obtained in channel flow using the formulation of Vreman *et al.*

1, the average  $C_B$  value is positive, but its rms value is more than twice as large as the average value near the wall, indicating a considerable occurrence of negative  $C_B$  values. The rms values obtained from the DNS exact data were in the range between 30 % to 70 % of the average values. In Vreman *et al.*'s formulation, it was found that the sign of  $C_B$  was very sensitive to the Reynolds numbers and grid resolutions. In fact, in the 'a posteriori' test in a channel flow LES at a higher Reynolds number with a coarse grid resolution, the predicted sign of  $C_B$  was negative even on average with a very large variance, when Vreman *et al.*'s formulation was used.

In the dynamic procedure, the coefficients are determined by extrapolating the information in the smallest grid scale into SGS. In Vreman *et al.*'s formulation, the data contained in the range between grid-filtered and test-filtered fields are not rigorously used because the decomposition of the velocity,  $u_i = \bar{u}_i + u_i''$ , is inserted into the SGS stress tensor. This formulation is mathematically more consistent with the dynamic procedure, particularly when the test-filtered field is calculated by reducing the number of grid points to that corresponding to the characteristic grid interval associated with the test-filter. This reduction of grid points is not carried out in the conventional computations using the dynamic procedure, except for the case in which the Fourier cutoff filter is used. When the Gaussian or top-hat filter is used, we consider it more advantageous to utilize the information contained between the grid-filtered and test-filtered fields, which are actually resolved, to make the extrapolation into SGS more accurate. This is achieved in Zang *et al.*'s formulation by decomposing  $u_i$  into  $u_i = \bar{u}_i + u_i'$ .

When Zang *et al.*'s formulation was used, the results consistently yielded a correct prediction of positive  $C_B$  in all tested cases. It can be inferred that the SGS models represented in a form comparable to the generalized scale-similarity model with the test-filtered stresses approximated using the formulation by Zang *et al.* generally yield accurate estimates of the model parameter inasmuch as the desired sign of the estimated parameter is positive.

Based on these observations, we adopted the formulation by Zang *et al.* [10] to define the test-filtered SGS stress tensor.

### Assessment of dynamic mixed models

In this section, we compare the SGS stresses computed by filtering the DNS data with those calculated using the DSM, the DMM, the DTM( $C_L - C_S$ ), and the DTM( $C_B - C_S$ ).

In the 'a posteriori' assessment of the models, which is



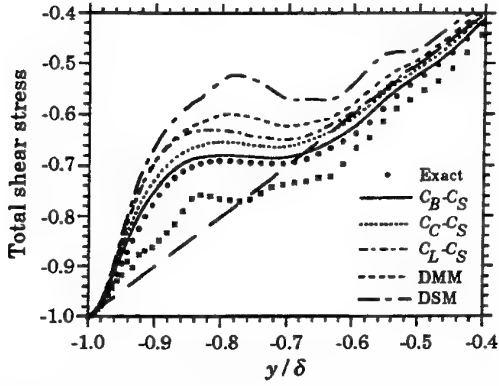


Figure 3:  $y$ -profiles of the plane-averaged total shear stress for channel flow, obtained from exact DNS data and using the DSM, the DMM, the  $C_L - C_S$ ,  $C_C - C_S$  and  $C_B - C_S$  models.  $\times$  denotes the result obtained using the  $C_B - C_S$  model with Vreman *et al.*'s formulation.

described in the following section, it was found that care should be taken for the treatment of negative  $C_S$  value. To observe, a priori, the effect of the parameter treatment in the models, an identical treatment to that used in the 'a posteriori' test was adopted in the present section.

For the DSM and the DMM,  $C_S$  was averaged over the  $x - z$  plane for channel and mixing layer flows.

For the  $C_L - C_S$  model, for the channel flow, both  $C_L$  and  $C_S$  were averaged over the  $x - z$  plane. For the mixing layer, both  $C_L$  and  $C_S$  were computed locally, and clipping was carried out locally for  $C_S$ .

For the  $C_B - C_S$  model, for both channel and mixing layer flows, the parameters  $C_B$  and  $C_S$  were computed locally, and clipping was carried out locally for  $C_S$ .

In Fig. 3, the exact DNS total shear stress, i.e., a summation of the grid-scale shear stress ( $\overline{u_1' u_2'}$ ), the SGS terms ( $\tau_{12}$ ) and the viscous stress,

$$\langle \overline{u_1' u_2'} \rangle + \langle \tau_{12} \rangle = -\frac{1}{Re} \frac{\partial \langle \overline{u_1} \rangle}{\partial x_2}, \quad (11)$$

is shown with the values obtained using the different models for channel flow ( $f''$  denotes  $f - \langle f \rangle$ ). Note that because the number of grid points is reduced in order to obtain the LES data from the DNS data, the exact value deviates from the mean pressure gradient which is imposed in the flow and is indicated by a heavy dashed line in the figure. The best agreement with the exact value is obtained using the  $C_B - C_S$  model. As reported by SB, in spite of its many desirable features, the value obtained using the DSM has poor agreement with the exact DNS value compared to the values obtained using other models. The DMM, which accounts for the modified Leonard term, gave better results than the DSM, and the  $C_L - C_S$  model, which more closely accounts for the modified cross term than the DMM, shows much better correspondence to the exact value. Because the  $L_{ij}^R$  term more closely accounts for both the modified cross term and the modified SGS Reynolds stress tensor than the  $L_{ij}^m$  term, the results obtained using the  $C_B - C_S$  model gave the best agreement with the exact values.

For the actual LES values computed using these models to reach equilibrium, the grid-scale component had to increase to compensate for the deviation from the exact DNS data. The subsequent effect resulting from this imbalance is observed below.

In Fig. 3, we include the result obtained using the  $C_C - C_S$  model in which the  $L_{ij}^C$  term was used in place of the  $L_{ij}^m$  term in the  $C_L - C_S$  model. In good accordance with the observation that the  $L_{ij}^C$  term has higher correlation

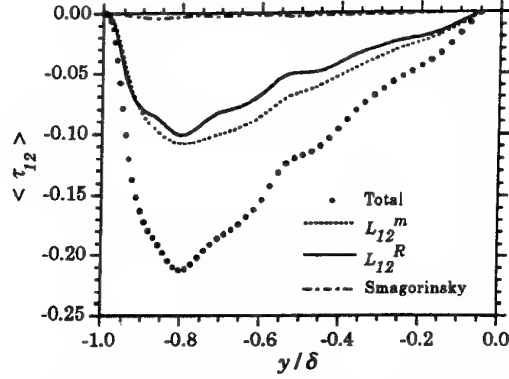


Figure 4:  $y$ -profiles of the decomposition of the plane-averaged  $\tau_{12}$  component of the SGS tensor obtained using the  $C_B - C_S$  model.

with the  $C_{ij}^m$  and  $R_{ij}^m$  terms, the  $C_C - C_S$  model yields better results than those obtained using the  $C_L - C_S$  model, but the  $C_B - C_S$  model still yields better results.

For comparison, we include the result obtained using the  $C_B - C_S$  model with Vreman *et al.*'s formulation, which overestimates the exact DNS data.

Figure 4 shows the components of the plane-averaged  $\tau_{12}$  term obtained using the  $C_B - C_S$  model from the channel flow. The contribution of the Smagorinsky model term was largest in the DSM. It was smaller in the DMM, and much smaller in the  $C_L - C_S$  model, as shown by SB (Figure not shown). In the  $C_B - C_S$  model, the Smagorinsky model contribution is negligible, but the contribution of the  $L_{ij}^R$  term is comparable to that of the  $L_{ij}^m$  term. Similar results were obtained for the mixing layer flow (Figure not shown).

## 'A POSTERIORI' TEST OF SGS MODELS

In this section, we show the 'a posteriori' test results for the channel flow. We have compared four models, namely the DSM, the DMM, the  $C_L - C_S$  model and the  $C_B - C_S$  model.

As stated in the 'a priori' test, the model parameters were averaged or clipped in order to avoid negative values of  $C_S$ .

$Re_\tau$  was set at a Reynolds number of 640 which is larger than that in the 'a priori' test to establish the validity of the models. The grid resolution was  $32 \times 62 \times 32$ , respectively, in the  $x$ ,  $y$  and  $z$  directions. The computed results are compared with the DNS data for fully developed incompressible channel flow with  $Re_\tau = 590$  generated with 384, 257 and 384 grid points, respectively, in the  $x$ ,  $y$  and  $z$  directions. [14] This flow field was filtered to  $64 \times 257 \times 64$  in the  $x$ ,  $y$  and  $z$  directions.

Figure 5 shows a comparison of the mean velocity profiles obtained using the different models. The intercepts of the logarithmic law profile (constant  $B$ ) for the DSM ( $\approx 11.5$ ) and the DMM ( $\approx 8.0$ ) are much larger than that determined from DNS data and the experimentally determined value of 5.0. [15] This overestimate of  $B$  is much lower for the  $C_L - C_S$  and  $C_B - C_S$  models, although the result obtained using the  $C_L - C_S$  model is slightly larger in the region of  $50 < y_+ < 200$ . The result obtained using the  $C_B - C_S$  model shows the best agreement with the DNS data.

Deviation of the results obtained using the  $C_L - C_S$  and  $C_B - C_S$  models from the logarithmic law profile in the central region of the channel is observed. We note, however, that the experimental results obtained for the same Reynolds number [15] and the DNS data for a sim-

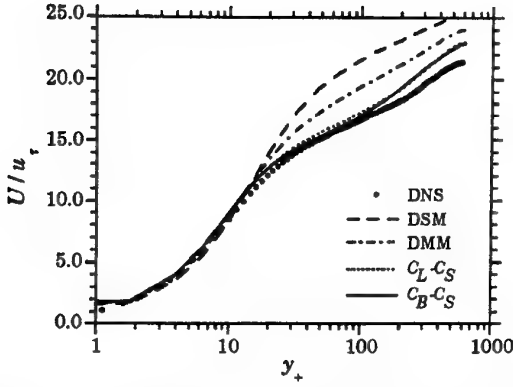


Figure 5: Mean streamwise velocity profiles obtained from the DNS and LES results for channel flow.

ilar Reynolds number show a similar deviation, although it is more pronounced in the present results. Taking into account the small number of grid points used in the  $x$  and  $z$  directions (32), the agreement with the DNS data is reasonably good.

The intensity of each component in the SGS shear stress  $\langle \tau_{12} \rangle$  was qualitatively in good agreement with the results of the 'a priori' test. The contribution of the modified Leonard term was significant except for the DSM. The contribution of the Smagorinsky model was the largest in the DSM, slightly lower in the DMM, much lower in the  $C_L - C_S$  model and still lower in the  $C_B - C_S$  model. The contribution of the grid-scale Reynolds shear stress  $\langle \bar{u}_1' \bar{u}_2' \rangle$  to the total shear stress was the largest in the DSM, and became smaller in the order of the DMM, the  $C_L - C_S$  model and the  $C_B - C_S$  model (Figure not shown). In the 'a priori' test, an imbalance of the modeled total stress with the mean pressure gradient was observed (Fig. 3). A subsequent effect is observed here.

The profiles of the grid-scale components of the turbulence intensities in the vicinity of the lower wall are shown in Fig. 6. The streamwise component is substantially overestimated in the DSM. It is overestimated to a lesser extent in the DMM, and much lesser extent in the  $C_L - C_S$  model, but the amplitude is still larger than that obtained using the DNS data. The excessively large grid-scale component  $\langle \bar{u}_1' \bar{u}_2' \rangle$  in the DSM, the DMM and the  $C_L - C_S$  model, in turn, resulted in the generation of excessive grid-scale energy via the  $i = 1, j = 2$  component of the grid-scale production term,  $-\langle \bar{u}_1' \bar{u}_2' \rangle \partial \langle \bar{u}_1 \rangle / \partial x_2$ . The correlation of the results obtained using the  $C_B - C_S$  model with the DNS data is significantly better than that for the other three models.

The peak position is better predicted using the  $C_L - C_S$  and  $C_B - C_S$  models, i.e., the peak is located closer to the wall, than using the DSM and the DMM. Using the DSM, the wall layer thickness is overestimated.

The normal component of the grid-scale turbulence intensity is better predicted using the DMM and the  $C_L - C_S$  model, but the amplitude of the DNS data filtered to  $32 \times 257 \times 32$  will be much smaller than the data presented in Fig. 6. In the results obtained using the DMM and the  $C_L - C_S$  model, the spanwise component of the grid-scale turbulence intensity is overestimated throughout the channel, whereas using the  $C_B - C_S$  model, it is overestimated at  $y_+ \approx 20$  and underestimated at a distance from the wall. In the results obtained using the DSM, both the normal and spanwise components of the grid-scale turbulence intensities are underestimated.

The profiles of  $C_B$  and  $C_L$  values obtained using Zang *et al.*'s formulation were generally in good agreement with those of the 'a priori' test (Figure not shown). When the

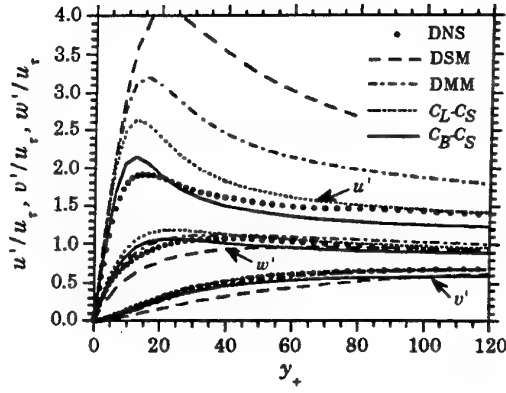


Figure 6:  $y$ -distributions of grid-scale turbulence intensities in the vicinity of the lower wall obtained from the DNS and LES results for channel flow.

$C_B$  value was determined using Vreman *et al.*'s formulation, in contrast to the results obtained in the 'a priori' test (Fig. 2), the predicted sign of the average  $C_B$  value was negative, although its variance was very large (Figure not shown). Therefore, the mean direction of the predicted grid-scale-SGS energy flow was backward, which led to a growing unstable numerical solution. The correct prediction of the positive  $C_B$  value found in the 'a priori' test may be due to the low Reynolds number characteristics of the DNS data.

We comment on the computational cost. A drawback of the proposed  $C_B - C_S$  model is in the increase of CPU time. The increase of the CPU time in the  $C_B - C_S$  model against the DSM (60 %) was large. We consider that the significant improvement in the predictions of mean velocity and the (streamwise) turbulence intensities obtained using the  $C_B - C_S$  model is worth the increased cost. We note that this increase was mostly attributable to the aliasing error elimination in the bi- and triple products. We note that aliasing error removal may not be necessary in the  $C_B - C_S$  model because the filter is applied two more times to the grid-scale velocity field, thus eliminating the higher wave number range of the energy spectrum.

Another drawback of the  $C_B - C_S$  model is that the number of successive filtering operations contained in the model is three, whereas it is two for the DMM and the  $C_L - C_S$  model. A higher number of operations requires additional conditions near the boundaries in the inhomogeneous directions. This issue will be left to future studies.

## MODELS FOR SGS SCALAR FLUX

Advantage of the proposed generalized scale-similarity model (Eq. (2)) is that it can be directly used to model other SGS correlation, e.g., the SGS scalar flux which appears in the filtered transport equation for the passive scalar. We derive the following model for the scalar flux,

$$\tau_i = \bar{u}_i \bar{\theta} - \bar{u}_i' \bar{\theta}' \simeq C_L^\theta \left( \bar{u}_i' \bar{\theta}' - \bar{u}_i' \bar{\theta}' \right), \quad (12)$$

where  $C_L^\theta$  is a model parameter.

This model was tested on the passive scalar field which was driven by the velocity field inside the channel obtained by LES using the  $C_B - C_S$  model shown in the previous section. The scalar was uniformly input within the fluid and then removed at both walls. The Prandtl number  $Pr$  was set equal to 0.025, and the results were compared with the DNS result. [16] The model parameter  $C_L^\theta$  was determined using the dynamic procedure.

This low Prandtl number was chosen because in the conventional SGS eddy diffusivity model, the damping func-

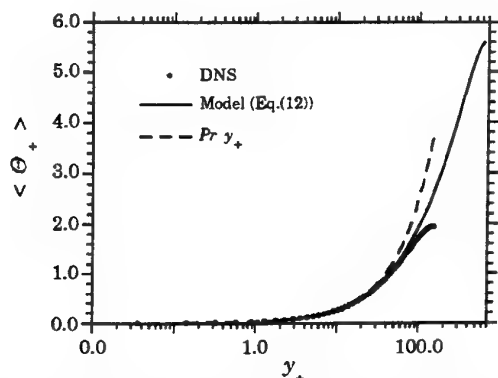


Figure 7: Mean scalar profiles obtained from the DNS and LES results.

tion should be properly determined. It seems that this determination is not easily manageable.

It should be noted that a model similar to that of Eq. (12) was proposed in [17] and [18], which were obtained by filtering products of resolved velocity and scalar on a scale equal to twice the grid scale. Similar approach was used to model the SGS stress tensor,  $\tau_{ij}$ , in [19]. These models correspond to the most primitive level in the present generalized scale-similarity model. We note that the terms in the SGS scalar flux which corresponds to the modified cross and Reynolds stress terms in the SGS stress tensor can be modeled in the same manner as is previously stated. More accurate models can be derived at this level. It was found in actual LES, however, that the model, Eq. (12), is sufficiently accurate at the present low  $Pr$ . A sufficient drain of the grid-scale scalar variance to sustain the turbulence was provided without turning to the SGS eddy diffusivity model.

Figure 7 shows the mean scalar profile obtained using this model. Agreement of the result with the DNS data is good, and a linear distribution of the scalar in the vicinity of the wall is obtained.

## CONCLUSIONS

We have proposed a new model for the SGS stresses in large-eddy simulation. A new dynamic two-parameter mixed model for the incompressible SGS stress tensor was derived based on this modeling procedure. The obtained mixed model was tested in both 'a priori' and 'a posteriori' tests. The flow fields for both tests were fully developed channel flow and time-developing mixing layer flow.

In this new model, all of the stress terms were modeled in a form compatible with that of the generalized central moment [3] (generalized scale-similarity model (Eq.(2))). The modified cross term and the modified SGS Reynolds stress tensor were assumed to be proportional to the  $L_{ij}^R$  term (Eq.(5)). The Smagorinsky model was linearly combined with the  $L_{ij}^R$  term in order to provide a sufficient drain of the grid-scale energy into the SGS. The two parameters used in the model were determined using the standard dynamic SGS model procedure [9] and the least squares method [12] (the  $C_B - C_S$  model).

The compatibility of the SGS models with the standard dynamic procedure is discussed, and it is suggested that models expressed in the form of the generalized scale-similarity model yield accurate predictions of the behavior of the model parameters when the test-filtered SGS tensor is defined using the formulation of Zang *et al.* [10]

The proposed model was compared with the previous dynamic models which can be derived as a subset of the proposed model. [9] [10] [11]

In the 'a priori' test, it was shown that the  $L_{ij}^R$  term is highly correlated with both the modified cross term and the modified SGS Reynolds stress tensor, the correlation of which was even higher than that for the other model terms. The contribution of the Smagorinsky model was smallest for the  $C_B - C_S$  model.

These SGS models were further assessed via an 'a posteriori' test for fully developed turbulent channel and mixing layer flows. For both flows, the test results were consistent with those of the 'a priori' test. The DSM results had the lowest correlation with the filtered DNS data. This poor correlation was improved to some extent in the DMM. A significant improvement was achieved using the  $C_L - C_S$  model, but the best results were obtained using the proposed  $C_B - C_S$  model.

The validity of the proposed two-parameter mixed model was established for two different flows, with the advantage that the model parameters contained in the proposed model were determined locally on a point-by-point basis. The proposed generalized scale-similarity model was applied to the passive scalar transport at a low Prandtl number. The results showed a good agreement with the DNS data.

## Acknowledgements :

This work was partially supported by a Grant-in-Aid from the Ministry of Education, Science and Culture, Japan (No.05240108), and the Project for Parallel Processing and Supercomputing at the Computer Centre, University of Tokyo.

## References

- [1] J. Bardina, Ph.D. dissertation, Stanford University, Stanford, California (1983).
- [2] M. Germano, Phys. Fluids 29, 2323 (1986).
- [3] M. Germano, J. Fluid Mech. 238, 325 (1992).
- [4] K. Horiuti, Phys. Fluids A 5, 146 (1993).
- [5] K. Horiuti, J. Phys. Soc. Japan 66, 91 (1997).
- [6] R.A. Clark, J.H. Ferziger and W.C. Reynolds, J. Fluid Mech. 91, 1 (1979).
- [7] K. Horiuti, submitted to Phys. Fluids (1997).
- [8] J. Smagorinsky, Mon. Weath. Rev. 91, 99 (1963).
- [9] M. Germano, U. Piomelli, P. Moin and W.H. Cabot, Phys. Fluids A 3, 1760 (1991).
- [10] Y. Zang, R.L. Street and J. Koseff, Phys. Fluids A 5, 3186 (1993).
- [11] M.V. Salvetti and S. Banerjee (referred to as SB), Phys. Fluids 7, 2831 (1995).
- [12] D.K. Lilly, Phys. Fluids A 4, 633 (1992).
- [13] B. Vreman, B. Geurts and H. Kuerten, Phys. Fluids 6, 4057 (1994).
- [14] N.N. Mansour, unpublished data (1996).
- [15] A.K.M.F. Hussain and W.C. Reynolds, Trans. of ASME, J. Fluid Eng. Dec., 568 (1975).
- [16] N. Kasagi, Y. Ohtsubo and Y. Tomita, Proc. 8th Symp. Turbulent Shear Flows, Vol. 2, pp. 11.11.1-11.11.2 (1991).
- [17] A. W. Cook and J. J. Riley, Phys. Fluids 6, 2868 (1994).
- [18] M. Germano, A. Maffio, S. Sello, and G. Mariotti, Second Ercoftac Workshop on DNS and LES, Grenoble, France (1996).
- [19] S. Liu, C. Meneveau and J. Katz, J. Fluid Mech. 275, 83 (1994).

# A SUBGRID-SCALE MODEL FOR NONPREMIXED TURBULENT COMBUSTION

Andrew W. Cook<sup>(1)</sup>, James J. Riley<sup>(2)</sup>, Stephen M. deBruynKops<sup>(2)</sup>

(1) Los Alamos National Laboratory  
Los Alamos, New Mexico 87545  
USA

(2) Department of Mechanical Engineering  
University of Washington  
Seattle, Washington 98195  
USA

## ABSTRACT

A method is presented for predicting filtered chemical species concentrations and filtered reaction rates in Large Eddy Simulations of nonpremixed, turbulent reacting flows. The subgrid-scale model is based on laminar flamelet theory and uses presumed forms for the dissipation rate and subgrid-scale probability density function of a conserved scalar. Inputs to the chemistry model are the Favre-filtered scalar, its subgrid-scale variance and filtered dissipation rate. A model for the filtered dissipation rate is discussed. The chemistry model and the dissipation rate model are evaluated by filtering data from  $(256)^3$  point Direct Numerical Simulations of incompressible, nonisothermal decaying turbulence with a single-step reaction. Results show the chemistry model and the dissipation rate model to be quite accurate.

## INTRODUCTION

Accounting for chemical reactions in a Large Eddy Simulation (LES) requires knowledge of the distribution of reactants within each LES grid cell. One aspect of a strategy for accounting for subgrid-scale mixing is to employ an assumed form for the Probability Density Function (PDF) of a conserved scalar within a grid volume. Gao and O'Brien (1993) refer to this type of PDF as a Large Eddy Probability Density Function (LEPDF). Bilger (1980) and Lentini (1994) found that errors in assumed PDFs are greatly reduced upon integration, a common operation which is required in order to obtain, e.g., average concentrations. Frankel *et al.* (1993) and Cook and Riley (1994) demonstrated the assumed LEPDF approach to be both practical and accurate for LES with equilibrium chemistry. In treating non-equilibrium chemistry, Frankel *et al.* (1993) employed a joint Beta distribution for the fuel and oxidizer in a flow with a single-step reaction. Specification of the joint LEPDF requires modeling of the subgrid-scale species covariance, a quantity that is very difficult to obtain accurately. An alternative method of accounting for non-equilibrium chemistry is to invoke the laminar flamelet approximation of Peters (1984). This requires knowledge of the filtered scalar dissipation rate, a quantity more easily modeled in an LES because it is established by the large

scales.

Cook *et al.* (1997) used laminar flamelet theory, in conjunction with an assumed LEPDF, to derive a model for the filtered chemical species in an incompressible, isothermal flow with a single step reaction. The model was termed the Large Eddy Laminar Flamelet Model (LELFM). *A priori* tests of the model using data from Direct Numerical Simulations (DNS) indicated that the LELFM is accurate, and improves with increasing Damköhler number. The purpose of this paper is twofold: firstly, to extend the LELFM theory to the case of compressible flows with multi-step, Arrhenius-rate chemistry, and secondly, to investigate a proposed model for the filtered dissipation rate, a parameter required by LELFM. The models are tested using DNS data of incompressible, nonisothermal turbulence with a single-step reaction. Although the theory is more general, this simplified case is addressed in order to isolate the effects of activation temperature on the performance of LELFM, and to test the model for the filtered dissipation rate.

## SUBGRID-SCALE CHEMISTRY MODEL

### Reaction Zone Physics

In this paper, all variables are nondimensional. We consider a two-feed combustion problem with fuel carried by feed 1 and air carried by feed 2. As the fuel and air are mixed, chemical reactions occur, forming various combustion products. The mass fractions of the chemical species are denoted as  $Y_i$  and the reaction rates are denoted as  $\dot{\omega}_i$ . A mixture-fraction  $\xi(x, t)$  is defined, as in Bilger (1980), so that, with the assumption of equal diffusivities of all species,  $\xi$  is a conserved scalar in the flow, having a value of unity in feed 1 and a value of zero in feed 2.

In typical combustion problems the zones of reaction are too small to be resolved by the LES; therefore, the chemistry must be modeled in its entirety. In deriving a model for the subgrid-scale chemistry, it is useful to note that the universal nature of  $\xi$  mixing at the small scales of turbulence is well documented, supported by detailed experimental evidence, DNS data and local solutions of

the Navier-Stokes and scalar transport equations (see Buch and Dahm, 1996; Southerland and Dahm, 1994; Siggia, 1981 and Reutsch and Maxey, 1991). This motivates the use of laminar flamelet theory in formulating a subgrid-scale model for  $Y_i$  and  $w_i$ .

Peters (1984) proposed the following set of equation as a means of relating the species mass fractions  $Y_i$  to the mixture-fraction  $\xi$ ,

$$\chi \frac{d^2 Y_i}{d\xi^2} = \dot{w}_i, \quad i = 1, \dots, N \quad (1)$$

where  $N$  is the total number of chemical species in the flow and  $\chi$  is the scalar dissipation rate, defined as

$$\chi = \frac{\rho D}{Pe} \nabla \xi \cdot \nabla \xi.$$

Here  $\rho$  and  $D$  are the density and molecular diffusivity, respectively, and  $Pe$  is the Peclet number. The equation set is coupled through the reaction rates, i.e.,  $\dot{w}_i$  terms, which are functions of  $Y_i$ ,  $\rho$  and temperature  $T$ . Equation 1 satisfies the boundary conditions:

$$Y_i(\xi = 0) = Y_{i2} \quad (2)$$

$$Y_i(\xi = 1) = Y_{i1} \quad (3)$$

where  $Y_{i1}$  and  $Y_{i2}$  are the uniform values of  $Y_i$  in feeds 1 and 2, respectively.

#### Counterflow Model

Bish (1996) demonstrated that the dynamics of the local strain-diffusion competition involved in scalar mixing dictate that  $\chi$  must be concentrated in locally one-dimensional layer-like structures. The  $\xi$  dependence of  $\chi$  is therefore prescribed as the solution to a one-dimensional, laminar counterflow problem. The result is

$$\chi = \chi_o F(\xi) \quad (4)$$

where

$$F(\xi) = \exp(-2[\text{erf}^{-1}(2(\xi - \xi^-)/(\xi^+ - \xi^-) - 1)]^2).$$

Here  $\chi_o$  is the local peak value of  $\chi$  within the reaction layer,  $\text{erf}^{-1}$  is the inverse error function (not the reciprocal), and  $\xi^-$  and  $\xi^+$  are the minimum and maximum values of  $\xi$  on either side of the layer, i.e., locations in the flow where  $\nabla \xi = 0$ . Cook *et al.* (1997) argued that  $\xi^- = 0$  and  $\xi^+ = 1$  are acceptable modeling assumptions, even though the layer-like mixing structures are rarely bounded by pure fuel and oxidizer. This assumption will also be made here.

#### Simplifying Assumptions

In many devices, such as industrial gas furnaces, the combustion occurs at flow speeds much slower than the local speed of sound. The Mach number of these flows is low, yet the density varies due to heat release. In simulating these flows, the acoustic modes can be removed from the governing equations, resulting in significant computational savings. If a low Mach number approximation is applied to the governing equations, then the ideal gas equation becomes (see McMurtry *et al.*, 1989)

$$p^{(0)} = \rho T \quad (5)$$

where  $p^{(0)}$  is the first-order or thermodynamic pressure, which is constant in space. If combustion takes place in an open domain, then  $p^{(0)}$  is also constant in time, in which case  $\rho$  is known in terms of  $T$  alone. In such a regime, the number of parameters in Eq. 1 can be reduced by relating

$T$ , and thereby  $\rho$ , to  $\xi$  and  $Y_i$  (see Libby and Williams, 1980). This is accomplished by using the total enthalpy, defined as

$$H = \frac{\gamma}{(\gamma - 1)} T + \sum_{i=1}^N h_i Y_i \quad (6)$$

where  $\gamma$  is the ratio of specific heats and  $h_i$  are the enthalpies of formation of the various species. If the Prandtl number of the flow is equal to the Schmidt number, then the transport equations for  $H$  and  $\xi$  are identical. In such case,  $H$  is linearly related to  $\xi$  as long as the initial and boundary conditions are consistent. The relationship is given by

$$H = \left[ \frac{\gamma}{(\gamma - 1)} (T_1 - T_2) + \sum_{i=1}^N h_i (Y_{i1} - Y_{i2}) \right] \xi + \frac{\gamma}{(\gamma - 1)} T_2 + \sum_{i=1}^N h_i Y_{i2} \quad (7)$$

where  $T_1$  and  $T_2$  are the temperatures in feeds 1 and 2 respectively. Using Eqns. 6 and 7,  $T$  can be expressed as a function of  $Y_i$  and  $\xi$ , i.e.,

$$T = \left[ T_1 - T_2 + \frac{(\gamma - 1)}{\gamma} \sum_{i=1}^N h_i (Y_{i1} - Y_{i2}) \right] \xi + T_2 + \frac{(\gamma - 1)}{\gamma} \sum_{i=1}^N h_i (Y_{i2} - Y_i). \quad (8)$$

With  $\rho$  and  $T$  known in terms of  $\xi$  and  $Y_i$ , Eq. 4 is inserted into Eq. 1 and the system, Eqs. 1, 2 and 3, is solved to obtain  $Y_i(\xi, \chi_o)$ . With the species mass fractions known in terms of  $\xi$  and  $\chi_o$ , the reaction rates, i.e.,  $\dot{w}_i(\xi, \chi_o)$ , can also be computed.

#### Subgrid-Scale PDF

By assuming that reactions occur in thin regions of one-dimensional counterflow, the  $\xi$  dependence of  $\chi$  is known through Eq. 4. Furthermore, by assuming that  $\xi^- = 0$  and  $\xi^+ = 1$ ,  $\chi_o$  then represents the value of  $\chi$  where  $\xi = 0.5$ . The modeling thus implies that  $\chi_o$  is independent of  $\xi$ ; therefore, the average value of  $Y_i$  within an LES grid cell can be expressed as

$$\bar{Y}_i = \int_0^1 \int_{\chi_o^{\min}}^{\chi_o^{\max}} Y_i(\xi, \chi_o) P(\chi_o) P(\xi) d\chi_o d\xi \quad (9)$$

where  $\chi_o^{\min}$  and  $\chi_o^{\max}$  are the minimum and maximum values of  $\chi_o$  within the grid cell. In Eq. 9,  $P(\xi)$  is the LEPDF, giving the subgrid-scale frequency distribution of  $\xi$  within the cell. Likewise,  $P(\chi_o)$  gives the subgrid-scale probability density of  $\chi_o$ . To simplify notation, no distinction is made between the random variables and their probability space counterparts.

Kuznetsov and Sabel'nikov (1990) and Mell *et al.* (1994) showed that  $Y_i(\xi, \chi_o)$  is a slow function of  $\chi_o$ , and hence of  $\chi_o$ . Therefore, if the interval  $\chi_o^{\max} - \chi_o^{\min}$  is not too large, then  $Y_i(\xi, \chi_o)$  and  $\dot{w}_i(\xi, \chi_o)$  can be approximated by the first two terms in the Taylor series expansion about the average of  $\chi_o$ , i.e.,

$$Y_i(\xi, \chi_o) \approx Y_i(\xi, \bar{\chi}_o) + \frac{\partial Y_i}{\partial \chi_o} \bigg|_{\bar{\chi}_o} (\chi_o - \bar{\chi}_o). \quad (10)$$

Inserting Eq. 10 into Eq. 9 and integrating over  $\chi_o$  gives

$$\bar{Y}_i = \int_0^1 Y_i(\xi, \bar{\chi}_o) P(\xi) d\xi. \quad (11)$$

The integral in Eq. 11 is carried out by assuming a Beta distribution for  $P(\xi)$ . Williams (1985) gives this as

$$P(\xi) = \frac{\xi^{a-1}(1-\xi)^{b-1}}{B(a,b)} \quad (12)$$

where

$$a = \bar{\xi} \left[ \frac{\bar{\xi}(1-\bar{\xi})}{\xi^2} - 1 \right], \quad b = a/\bar{\xi} - a, \quad \xi_v^2 = \bar{\xi}^2 - \bar{\xi}^2.$$

In Eq. 12  $B(a,b)$  is the Beta function and  $\xi_v^2$  is the subgrid-scale variance of  $\xi$ .

Filtered reaction rates are computed in the same manner as the filtered species mass fractions, i.e., by expanding  $\bar{w}_i(\xi, \chi_o)$  in a Taylor series about  $\bar{\chi}_o$  and then integrating  $\bar{w}_i(\xi, \bar{\chi}_o)$  with  $P(\xi)$ . Finally,  $\bar{\chi}_o$  is related to  $\bar{\chi}$  by integrating Eq. 4 with  $P(\xi)$ , i.e.,

$$\bar{\chi} = \bar{\chi}_o \int_0^1 F(\xi) P(\xi) d\xi. \quad (13)$$

#### Constructing Tables

In simulating compressible flows, it is common to work with Favre-filtered variables. The chemistry model may be employed in an LES by constructing tables for  $\bar{Y}_i(\bar{\xi}, \bar{\xi}^2, \bar{\chi})$  and  $\bar{w}_i(\bar{\xi}, \bar{\xi}^2, \bar{\chi})$ , where a tilde denotes a Favre-filtered quantity. The tables will depend on the flow parameters:  $p^{(0)}$ ,  $T_1$ ,  $T_2$ ,  $h_i$ ,  $Y_{i1}$ ,  $Y_{i2}$ ,  $Re$ ,  $Sc$ , the various activation temperatures  $T_{ai}$  and the various Damköhler numbers  $Da_i$ . The tables are constructed in the following way. Firstly,  $\bar{\xi}$  and  $\bar{\xi}^2$  are chosen and  $P(\xi)$  is computed from Eq. 12. Then  $\bar{\chi}_o$  is chosen and  $\bar{\chi}$  is computed using Eq. 13. The LFM solutions can then be specified in terms of  $Y_i(\xi, \bar{\chi})$ . Next, Eq. 8 is used, along with Eq. 5 and the LFM solutions  $Y_i(\xi, \bar{\chi})$ , to compute  $\rho(\xi, \bar{\chi})$ . With  $P(\xi)$  and  $\rho(\xi, \bar{\chi})$  known,  $\bar{\xi}$  and  $\bar{\xi}^2$  can then be computed. Finally,  $\bar{Y}_i$  is computed from Eq. 11 and  $\bar{w}_i$  is obtained similarly. Note that  $\bar{Y}_i$  and  $\bar{w}_i$  are initially obtained in terms of  $\bar{\xi}$ ,  $\bar{\xi}^2$  and  $\bar{\chi}_o$ , but may be tabulated as functions of  $\bar{\xi}$ ,  $\bar{\xi}^2$  and  $\bar{\chi}$ . Also, since  $\rho$  is a known function of  $\xi$  and  $\bar{\chi}$ , the Favre-filtered variables  $\bar{Y}_i$  and  $\bar{w}_i$  can also be computed and tabulated.

#### Obtaining $\bar{\xi}$ and $\bar{\xi}^2$

The tables for  $\bar{Y}_i$  and  $\bar{w}_i$  require  $\bar{\xi}$ ,  $\bar{\xi}^2$  and  $\bar{\chi}$  as inputs. Therefore, these quantities must be obtained in addition to the velocity field and other LES variables. In an LES,  $\bar{\xi}$  is computed by integrating its governing equation. The transport equation for  $\xi$  is

$$\frac{\partial \rho \xi}{\partial t} + \frac{\partial \rho \xi u_j}{\partial x_j} = \frac{1}{Pe Sc} \frac{\partial}{\partial x_j} \left( \mu \frac{\partial \xi}{\partial x_j} \right). \quad (14)$$

An equation for  $\bar{\xi}$  is derived by Favre-filtering Eq. 14 and neglecting the term due to subgrid fluctuations in  $D$ ; this gives

$$\frac{\partial \bar{\rho} \bar{\xi}}{\partial t} + \frac{\partial \bar{\rho} \bar{\xi} \bar{u}_j}{\partial x_j} = \frac{1}{Pe} \frac{\partial}{\partial x_j} \left( \bar{\rho} \bar{D} \frac{\partial \bar{\xi}}{\partial x_j} \right) - \frac{\partial \zeta_j}{\partial x_j}, \quad (15)$$

where  $\zeta_j \equiv \bar{\rho} (\bar{u}_j \bar{\xi} - \bar{u}_j \xi)$  must be modeled.

There are several ways of obtaining  $\bar{\xi}^2$ , one of which is to integrate its governing equation. This is obtained by multiplying Eq. 14 by  $\xi$  and Favre-filtering (again ignoring subgrid fluctuations in diffusivity). The result is

$$\frac{\partial \bar{\rho} \bar{\xi}^2}{\partial t} + \frac{\partial \bar{\rho} \bar{\xi}^2 \bar{u}_j}{\partial x_j} = \frac{1}{Pe} \frac{\partial}{\partial x_j} \left( \bar{\mu} \frac{\partial \bar{\xi}^2}{\partial x_j} \right) - 2\bar{\chi} - \frac{\partial \eta_j}{\partial x_j}, \quad (16)$$

where  $\eta_j \equiv \bar{\rho} (\bar{u}_j \bar{\xi}^2 - \bar{u}_j \xi^2)$  must also be modeled. Another approach is to use a scale similarity model, as proposed by Cook and Riley (1994). Such a model was successfully used by Réveillon and Vervisch (1996) in an LES of reacting turbulence.

#### A Model for $\bar{\chi}$

In order to develop a model for  $\bar{\chi}$ , consider the equation for  $\bar{\xi}$ -energy, obtained by multiplying Eq. 15 by  $2\bar{\xi}$ , which, after some algebra, gives

$$\begin{aligned} \frac{\partial \bar{\rho} \bar{\xi}^2}{\partial t} + \frac{\partial \bar{\rho} \bar{\xi}^2 \bar{u}_j}{\partial x_j} \\ = \frac{1}{Pe} \frac{\partial}{\partial x_j} \left( \bar{\rho} \bar{D} \frac{\partial \bar{\xi}^2}{\partial x_j} \right) - 2 \frac{\bar{\rho} \bar{D}}{Pe} \left( \frac{\partial \bar{\xi}}{\partial x_j} \right)^2 - 2 \bar{\xi} \frac{\partial \zeta_j}{\partial x_j}. \end{aligned} \quad (17)$$

We model  $\zeta_j$  in a manner similar to Smagorinsky (1966), i.e.,

$$\zeta_j = - \frac{\mu_{sgs}}{Sc_{sgs}} \frac{\partial \bar{\xi}}{\partial x_j}, \quad (18)$$

where  $Sc_{sgs}$  is a subgrid-scale Schmidt number, assumed constant, and the subgrid-scale viscosity is defined as

$$\mu_{sgs} = C_{\epsilon,t} \bar{\rho} \Delta^2 |\bar{S}|. \quad (19)$$

Here,  $C_{\epsilon,t}$  is a dynamically determined coefficient and  $|\bar{S}|$  is the magnitude of the resolved strain-rate tensor.

An equation for the  $\bar{\xi}$ -energy can be obtained by multiplying Eq. 15 by  $2\bar{\xi}$ , using Eq. 18:

$$\begin{aligned} \frac{\partial \bar{\rho} \bar{\xi}^2}{\partial t} + \frac{\partial \bar{\rho} \bar{\xi}^2 \bar{u}_j}{\partial x_j} = \frac{2}{Pe} \frac{\partial}{\partial x_j} \left( \bar{\xi} \bar{\rho} \bar{D} \frac{\partial \bar{\xi}}{\partial x_j} \right) \\ + \frac{1}{Sc_{sgs}} \frac{\partial}{\partial x_j} \left( \mu_{sgs} \frac{\partial \bar{\xi}^2}{\partial x_j} \right) \\ - \frac{2 \bar{\rho} \bar{D}}{Pe} \left( \frac{\partial \bar{\xi}}{\partial x_j} \right)^2 - \frac{2 \mu_{sgs}}{Sc_{sgs}} \left( \frac{\partial \bar{\xi}}{\partial x_j} \right)^2. \end{aligned} \quad (20)$$

The last two terms represent the dissipation rate of  $\bar{\xi}$  due to molecular effects and to transfer of  $\bar{\xi}$  energy to the subgrid-scales, respectively.

We note that, at the larger scales,  $\bar{\xi}^2$  is approximately equal to  $\xi^2$ , the difference between the two being due to the filtering of  $\xi$  at the smaller scales. This implies, in particular, that the transfer rate of both quantities to the subgrid scales is nearly identical. Assuming in addition that the transfer rate of  $\bar{\xi}$  to the subgrid scales is equal to its dissipation rate at those scales, a comparison of Eqs. 16 and 20 suggests the model for  $\bar{\chi}$ :

$$\bar{\chi}_m \equiv \left( \frac{\bar{\rho} \bar{D}}{Pe} + \frac{\mu_{sgs}}{Sc_{sgs}} \right) \left( \frac{\partial \bar{\xi}}{\partial x_j} \right)^2. \quad (21)$$

This is the first term in a model for  $\bar{\chi}$  proposed by Girimaji and Zhou (1996). We will take Eq. 21 as our model for  $\bar{\chi}$ .



## RESULTS

### DNS Data

Data sets from  $(256)^3$  point Direct Numerical Simulations of incompressible, isotropic, temporally-decaying, reacting turbulence were used to investigate the accuracy of the chemistry model. A key issue is the behavior of the model for a range of the activation temperature  $T_a$ . Therefore, in the DNS,  $\mu$  and  $\rho$  were kept constant in order to isolate the effects of  $T_a$  on the model performance. The chemical mechanism followed the single-step reaction:  $Fuel + (r)Oxidizer \rightarrow (1+r)Product + Heat$ , where  $r$  is the mass of oxidizer required to react with a unit mass of fuel. The  $\xi$  field was initialized in a statistically homogeneous manner with regions of ones (fuel) and zeros (oxidizer) separated by thin mixing zones. The mean value of  $\xi$  was  $\langle \xi \rangle = 0.25$ , where the angle brackets denote an average over the entire  $(256)^3$  domain. An equation for fuel was solved with the oxidizer and product obtained from the relations:

$$Y_o = Y_{o2} (1 - \xi) + r(Y_f - \xi Y_{f1}), \quad (22)$$

$$Y_p = (r+1)(\xi Y_{f1} - Y_f). \quad (23)$$

Here  $Y_f$ ,  $Y_o$  and  $Y_p$  are the fuel, oxidizer and product mass fractions, respectively. For this case, the stoichiometric value of the mixture-fraction is given by

$$\xi_{st} \equiv \frac{Y_{o2}}{(rY_{f1} + Y_{o2})}. \quad (24)$$

In the DNS, the feed concentrations were set to  $Y_{f1} = Y_{o2} = 1$  and  $r$  was assigned a value of 3, resulting in  $\xi_{st} = 0.25$ . The  $Y_f$  field was initialized according to the fast chemistry limit, i.e.,

$$Y_f = Y_{f1} \begin{cases} 0 & \text{where } \xi \leq \xi_{st} \\ (\xi - \xi_{st}) / (1 - \xi_{st}) & \text{where } \xi > \xi_{st} \end{cases} \quad (25)$$

This provided initially high temperatures in the thin mixing regions, thus giving a 'spark' to initiate the reaction. The Schmidt number of the simulation was set to correspond to combustion in air, i.e.,  $Sc = 0.72$ .

For single-step chemistry, it is only necessary to solve one laminar flamelet equation, which can be formulated in terms of  $Y_f$ ,  $Y_o$  or  $Y_p$ . In terms of fuel, Eq. 1 is

$$\chi \frac{d^2 Y_f}{d\xi^2} = \dot{w}_f, \quad (26)$$

where

$$\dot{w}_f = Da \rho Y_f \rho Y_o \exp(-T_a/T). \quad (27)$$

Note that Eqs. 4, 22 and 27 are needed, in addition to the boundary conditions  $Y_f(\xi = 0) = 0$  and  $Y_f(\xi = 1) = Y_{f1}$ , in order to solve Eq. 26.

Several simulations were performed, in which  $T_a$  took on different values. The adiabatic flame temperature, defined as

$$T_f = \frac{Y_{o2} + rY_{f1} + Y_{f1}Y_{o2}q(\gamma-1)/\gamma}{Y_{o2} + rY_{f1}}, \quad (28)$$

was assigned a value of 8.14. Here  $q$  is the heat of combustion, defined as

$$q = h_f + rh_o - (r+1)h_p, \quad (29)$$

where  $h_f$ ,  $h_o$  and  $h_p$  are the enthalpies of formation of the fuel, oxidizer and product respectively.

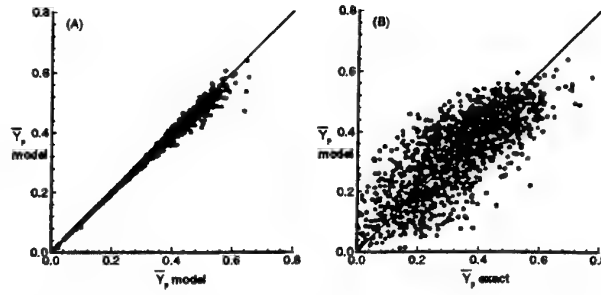


Figure 1: (A) CORRELATION OF LELFM PREDICTIONS FOR  $\bar{Y}_p$  USING THE EXACT  $\bar{\chi}$  ON THE HORIZONTAL AND THE MODELED  $\bar{\chi}$  ON THE VERTICAL. (B) CORRELATION OF LELFM PREDICTIONS FOR  $\bar{Y}_p$  WITH EXACT RESULTS.

In order to test the model, the DNS data fields were filtered onto a  $16 \times 16 \times 16$  point LES mesh. Then exact values for  $\bar{Y}_p$ ,  $\bar{w}_f$ ,  $\bar{\xi}$ ,  $\bar{\xi}^2$ , and  $\bar{\chi}$  were computed by averaging over the  $(16)^3$  DNS grid points in each LES grid cell. The latter three quantities were then used to obtain model values for  $\bar{Y}_p$  and  $\bar{w}_f$ . The data were taken at one large-eddy turnover time after initialization of the  $\xi$  and  $Y_f$  fields. The eddy turnover time is defined as  $u_{rms}^o t / l^o$ , where  $u_{rms} \equiv ((\bar{u} \cdot \bar{u})/3)^{1/2}$  and  $l$  is the integral scale. The superscript  $()^o$  indicates a value at  $t = 0$ .

Since the intent of LES is to resolve the large eddies, the filtered DNS fields represent an LES only if the filter width  $\Delta$  is significantly smaller than the integral scale  $l$ . Furthermore, since the subgrid models appear to rely on inertial range behavior of the eddies near the grid-scale,  $\Delta$  should be much greater than the Kolmogorov scale. At the time of filtering, the ratio of filter width to the integral, Taylor and Kolmogorov scales of the DNS turbulence was  $\Delta/l = 0.347$ ,  $\Delta/\lambda = 1.59$  and  $\Delta/\eta = 29.8$ , respectively. The turbulent Damköhler number was  $Da_t \equiv K^* l^* / u_{rms}^* = 11.2$ , where a  $*$  indicates a dimensional quantity and  $K^*$  is the pre-exponential factor in the reaction rate. The large-eddy Reynolds number was  $Re_l \equiv \rho^* u_{rms}^* l^* / \mu^* = 417$  and the Taylor Reynolds number was  $Re_\lambda \equiv \rho^* u_{rms}^* \lambda^* / \mu^* = 91$ . The segregation of fuel and oxidizer was measured as  $[(\xi^2) - \langle \xi \rangle^2] / [\langle \xi \rangle - \langle \xi \rangle^2] = 0.533$ ; initially this parameter had a value of 0.814.

### Effect of $\bar{\chi}$ Model on LELFM

The model for  $\bar{\chi}$  is first tested by comparing results of the LELFM using exact (i.e., filtered DNS data) and modeled values for  $\bar{\chi}$ . In modeling  $\bar{\chi}$ ,  $Sc_{sgs}$  is determined by finding the least squares solution of  $\bar{\chi}_m = \bar{\chi}$ , giving  $Sc_{sgs} \approx 0.3$ . The Pearson correlation coefficient for  $\bar{\chi}$  versus  $\bar{\chi}_m$  is about 0.47, indicating significant scatter. With  $Sc_{sgs}$  empirically determined, Figure 1a shows such a comparison for the filtered product mass fraction for a case with  $T_a = 0$  and  $Da_t = 11.2$ . In making the comparisons, the local exact (i.e., filtered DNS data) for  $\bar{\xi}$  and  $\bar{\xi}^2$  are employed. The agreement is very good (the correlation coefficient is 0.99), especially given the somewhat low correlation between the exact and modeled values for  $\bar{\chi}$ . There appear to be two reasons for this good agreement. First, the greatest errors in  $\bar{\chi}_m$  occur at high values of  $\bar{\chi}$ , which are least likely to occur. Second, the species mass fraction is proportional to  $\bar{\chi}^{1/3}$  (see Mell et al. 1994), so that chemical concentrations will not be very sensitive to errors in  $\bar{\chi}_m$ .

Figure 1b gives a comparison of results of the LELFM for the filtered product mass fraction, using the model for  $\bar{\chi}$ , with the exact values obtained by filtering the DNS data. Again the agreement is very good; however the model for  $\bar{\chi}$

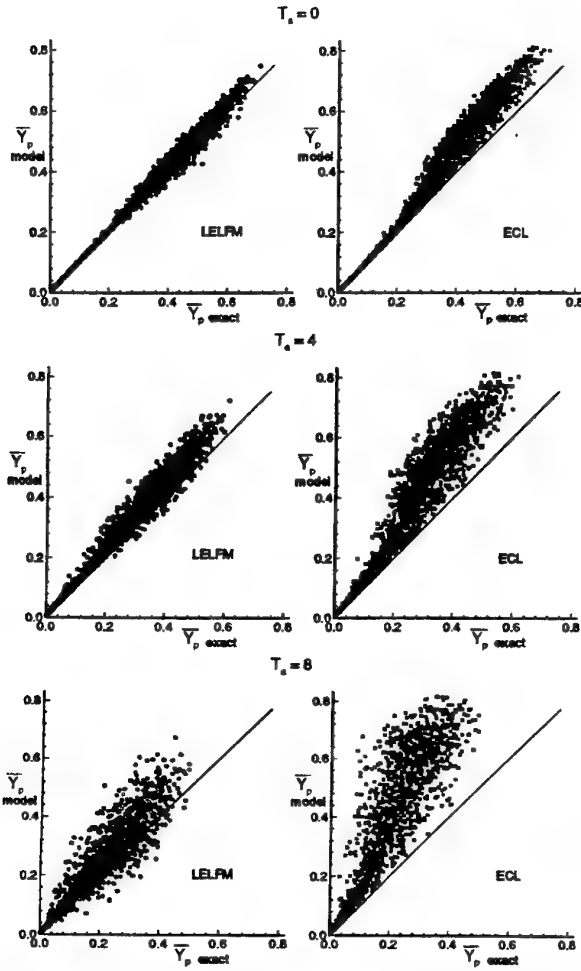


Figure 2: CORRELATION OF EXACT AND MODELED PRODUCT MASS FRACTION FOR DIFFERENT ACTIVATION TEMPERATURES.

has increased the scatter in the predictions for  $\bar{Y}_p$  compared to LELFM results computed from the exact  $\bar{x}$ . This is apparent when comparing Figure 1b to Figure 2, which is discussed next.

#### Effect of Arrhenius Kinetics on LELFM

Figure 2 shows the correlation of exact and model values for  $\bar{Y}_p$  for the cases with  $T_a = 0, 4$ , and  $8$ . In these comparisons, locally exact values for  $\bar{\xi}$ ,  $\bar{\xi}^2$ , and  $\bar{x}$  are utilized. Each point in the plots represents  $\bar{Y}_p$  at a particular LES grid point. The plots on the left demonstrate the performance of LELFM, whereas the plots on the right display the results of assuming equilibrium, i.e., infinite Damköhler number, chemistry. In the plots on the right hand side ECL stands for Equilibrium Chemistry Limit. This limit provides a reference for judging the performance of LELFM. In the equilibrium chemistry limit

$$\bar{Y}_p = (r+1)Y_{f1}\xi_{st} \begin{cases} \xi/\xi_{st} & \text{if } \xi \leq \xi_{st} \\ (1-\xi)/(1-\xi_{st}) & \text{if } \xi > \xi_{st} \end{cases} \quad (30)$$

so that, with the beta-pdf for  $\xi$ , the model prediction for  $\bar{Y}_p$  becomes

$$\frac{\bar{Y}_p}{(r+1)Y_{f1}\xi_{st}} = \frac{I_{\xi_{st}}(a+1, b)}{\xi_{st}} \left[ \frac{a}{a+b} \right] + \frac{I_{1-\xi_{st}}(b+1, a)}{1-\xi_{st}} \left[ \frac{b}{a+b} \right] \quad (31)$$

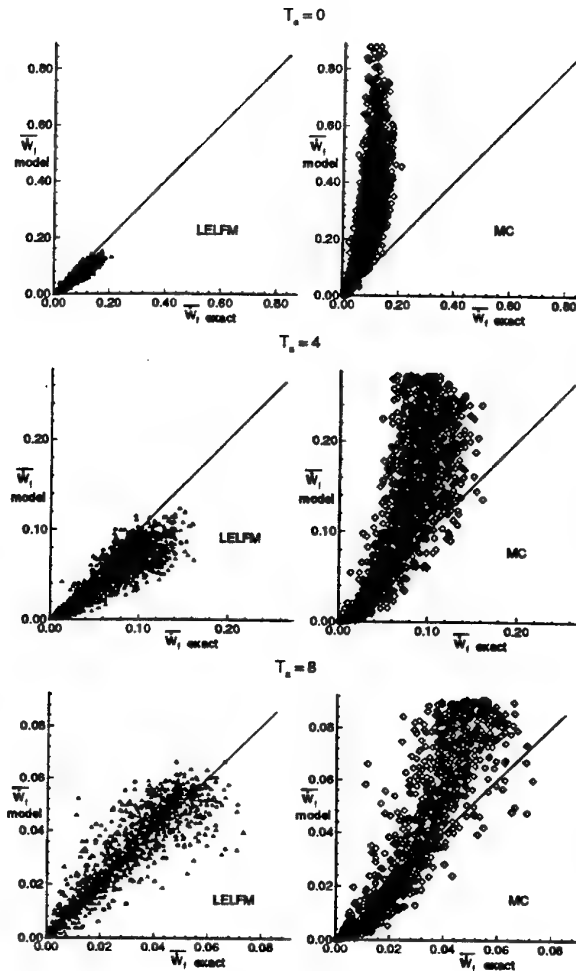


Figure 3: CORRELATION OF EXACT AND MODELED REACTION RATE FOR DIFFERENT ACTIVATION TEMPERATURES.

where  $a$  and  $b$  are given after Eq. 12 and  $I_\lambda(\alpha, \beta)$  is the Incomplete beta function (see Madnia and Givi, 1993, and Cook and Riley, 1994). The LELFM results for  $\bar{Y}_p$  degrade somewhat with increasing  $T_a$ . This is due to the increase of chemical time scales relative to local flow time scales. However, as  $T_a$  is increased, the ECL data move away from the 45° line much more than the LELFM data. As the chemical equilibrium departures increase, the accuracy of LELFM relative to ECL improves due to the fact that there are no mechanisms in ECL to account for these departures. At higher  $T_a$  the reaction zones are narrower, thus several of the assumptions of laminar flamelets should be more valid.

The results for the reaction rate  $\bar{w}_f$  are displayed in Figure 3 for the three cases mentioned. The LELFM prediction is shown in the plots on the left hand side and the Means Closure (MC) prediction is shown on the right hand side for comparison. The Means Closure is given by

$$\bar{w}_f \approx Da\rho\bar{Y}_f\rho_o \exp(-T_a/\bar{T})$$

The results for  $\bar{w}_f$  show that the LELFM and MC predictions both improve with increasing  $T_a$ . However, LELFM is much better than MC at predicting  $\bar{w}_f$ . The chemistry model was also applied to  $(128)^3$  DNS fields at a Reynolds number of  $Re_t = 135$  with virtually identical results.

#### CONCLUSIONS

This paper has presented a method for predicting fil-



tered chemical species  $\bar{Y}_i$  and filtered reaction rates  $\bar{w}_i$  in LES of turbulent reacting flows. Inputs to the chemistry model are a Favre-filtered mixture-fraction, its subgrid-scale variance and filtered dissipation rate. The model for  $\bar{Y}_i$  and  $\bar{w}_i$ , termed the Large Eddy Laminar Flamelet Model (LELFM), is employed by constructing tables for  $\bar{Y}_i$  and  $\bar{w}_i$  prior to running an LES. Since these quantities are obtained in an LES via table lookup, the model is very inexpensive.

A model for the filtered scalar dissipation rate  $\bar{\chi}$  was evaluated using DNS data. Although there was some scatter in the prediction of  $\bar{\chi}$ , the LELFM predictions for  $\bar{Y}_p$  were good. This result appears due to the fact that  $Y_p$  is a weak function of  $\chi$ . It remains to be seen whether this will be the case for higher Reynolds number flows with slower reaction rates.

The accuracy of LELFM was found to degrade with increasing activation temperature. This is due to the fact that as  $T_a$  is increased, the rate of reaction decreases. However, at higher activation temperatures, LELFM is much better than an assumption of equilibrium chemistry. Finally, LELFM was demonstrated to be much better than the Means Closure at predicting filtered reaction rates.

**Acknowledgments :** This work was supported by NSF under grant number CTS-9415280. The simulations were performed on the Connection Machine Model-5 at the National Center for Supercomputing Applications. The DNS data were generated using a spectral code written by Vebjorn Nilsen. We are also grateful to Professor George Kosály for much useful input and suggestions.

## REFERENCES

- Bilger, R. W., 1980, "Turbulent Flows with Non-premixed Reactants," in *Topics in Applied Physics*, Springer-Verlag, Berlin, Vol. 44, Ch. 3, pp. 2-36.
- Bish, E. S., 1996, "A New Model for Nonequilibrium Mixing-Chemistry Coupling in Nonpremixed and Partially Premixed Turbulent Combustion," PhD thesis, The University of Michigan, Ann Arbor, MI.
- Bish, E. S., and Dahm, W. J. A., 1995, "Strained Dissipation and Reaction Layer Analyses of Nonequilibrium Chemistry in Turbulent Reacting Flows," *Combust. Flame*, Vol. 100, p. 457.
- Buch, K. A., and Dahm, W. J. A., 1996, "Experimental Study of the Fine-Scale Structure of Conserved Scalar Mixing in Turbulent Shear Flows. Part I:  $Sc \gg 1$ ," *J. Fluid Mech.*, Vol. 317, pp. 21-71.
- Cook, A. W., and Riley, J. J., 1994, "A Subgrid Model for Equilibrium Chemistry in Turbulent Flows," *Phys. Fluids*, Vol. 6, pp. 2868-2870.
- Cook, A. W., Riley, J. J., and Kosály, G., 1997, "A Laminar Flamelet Approach to Subgrid-Scale Chemistry in Turbulent Flows," *Combust. Flame*, Vol. 109, pp. 332-341.
- Frankel, S. H., Adumitroaie, V., Madnia, C. K., and Givi, P., 1993, "Large-Eddy Simulation of Turbulent Reacting Flows by Assumed PDF Methods," in *Engineering Applications of Large Eddy Simulations*, Fluids Engineering Division, ASME, Vol. 162, pp. 81-101.
- Gao, F., and O'Brien, E. E., 1993, "A Large-Eddy Simulation Scheme for Turbulent Reacting Flows," *Phys. Fluids*, Vol. 5, pp. 1282-1284.
- Girimaji, S. S., and Zhou, Y., 1996, "Analysis and modeling of Subgrid Scalar Mixing Using Numerical Data," *Phys. Fluids*, Vol. 8, pp. 1224-1236.
- Kuznetsov, V. R., and Sabel'nikov, V. A., 1990, "Turbulence and Combustion," in *Combustion: An International Series*, N. Chigier, ed., Hemisphere Publishing Corp.
- Lentini, D., 1994, "Assessment of the Stretched Laminar Flamelet Approach for Non-Premixed Turbulent Combustion," *Combust. Sci. Technol.*, Vol. 100, pp. 95-122.
- Libby, P. A., and Williams, F. A., 1980, "Turbulent Reacting Flows," in *Topics in Applied Physics*, Springer-Verlag, Berlin, Vol. 44, Ch. 1.
- Madnia, C. K., and Givi, P., 1993, "Direct Numerical Simulation and Large Eddy Simulation of Reacting Homogeneous Turbulence," in *Large Eddy Simulation of Complex Engineering and Geophysical Flows*, Cambridge University Press, pp. 315-346.
- Mell, W. E., Nilsen, V., Kosály, G., and Riley, J. J., 1994, "Investigation of Closure Models for Nonpremixed Turbulent Reacting Flows," *Phys. Fluids*, Vol. 6, pp. 1331-1356.
- McMurtry, P. A., Riley, J. J., and Metcalfe, R. W., 1989, "Effects Of Heat Release On The Large-Scale Structure In Turbulent Mixing Layers," *J. Fluid Mech.*, Vol. 199, p. 297.
- Peters, N., 1984, "Laminar Diffusion Flamelet Models in Non-Premixed Turbulent Combustion," *Prog. Energy Combust. Sci.*, Vol. 10, pp. 319-339.
- Reutsch, G. R., and Maxey, M. R., 1991, "Small-Scale Features of Vorticity and Passive Scalar Fields in Homogeneous, Isotropic Turbulence," *Phys. Fluids*, Vol. 3, p. 1587.
- Révillon, J., and Vervisch, L., 1996, "Response of the Dynamic LES Model to Heat Release Induced Effects," *Phys. Fluids*, Vol. 8, pp. 2248-2250.
- Siggia, E. D., 1981, "Numerical Study of Small-Scale Intermittency in Three-Dimensional Turbulence," *J. Fluid Mech.*, Vol. 107, p. 375.
- Smagorinsky, J., 1963, "General Circulation Experiments With the Primitive Equations. I. The Basic Experiment," *Mon. Weather Rev.*, Vol. 91, pp. 99-164.
- Southerland, K. B., and Dahm, W. J. A., 1994, "A Four-Dimensional Experimental Study of Conserved Scalar Mixing in Turbulent Flows," Report No. 026779-12, The University of Michigan, Ann Arbor, MI.
- Williams, F. A., 1985, *Combustion Theory 2nd ed.*, Addison-Wesley.

# Large-Eddy Simulation of turbulent reactive flows

F. Mathey, J.P. Chollet  
LEGI/IMG  
BP53  
38041 Grenoble-Cedex 09  
France

## INTRODUCTION

The understanding of turbulent mixing is crucial for the improvement of many systems, as combustion and propulsion devices, chemical processing and environmental applications. Because the plane turbulent shear layer is a generic model arising in these systems, it has been studied for several decades. It is now generally recognized that in this flow, entrainment and mixing are dominated by the dynamics of large-scale vortical structures, even at high-Reynolds number (Brown and Roshko, 1974). These structures are linked to the Kelvin-Helmholtz instability mode, and experiments (Winant and Brownand, 1974) showed that pairings and tearing among them contribute significantly to the layer's development. A secondary instability mode associated with streamwise vortical structures, was also observed in the mixing layer (Breidenthal, 1981). These streamwise vortices play a role in the development of three dimensionality, since they become part of the spanwise vortex core after pairing. As the mixing layer becomes more three-dimensional, it undergoes a transition to turbulence (Breidenthal 1981). This transition is accompanied by a marked increase in the degree of scalar mixing, which corresponds to the mixing transition. Taking into account these results and the large-scale visualizations, Broadwell and Breidenthal (1982) developed a model for turbulent mixing, past this mixing transition. The basic idea is that the fluid in the layer is in either a homogeneous mixture or in strained laminar diffusion layers. Earlier comparisons with fast chemical reaction experiments in both gases and liquids (Mungal and Dimotakis, 1984; Koochesfahani and Dimotakis, 1986; Karasso and Mungal, 1996) gave good results. However, there are several unanswered questions regarding the contribution of the different parts of the model. Past the mixing transition, the Reynolds and Schmidt number dependence of the flame sheet is only qualitatively verified by the experiments. And it is still unknown in which way the streamwise vortices play a role during the mixing transition, and what is their contribution to the overall level of mixing past the mixing transition.

The purpose of the present investigation is to provide insight on these issues using Large Eddy Simulation at large Reynolds numbers. Because of the limited capac-

ity of the computers, an explicit calculation of the large scales cannot be simultaneously ran with the calculation at smaller scales. As the velocity field is concerned, the Large Eddy Simulation (LES) consists in computing explicitly the largest scales, and modeling the smallest scales by an eddy viscosity. But flows with chemical reactions are typical of problems where scalar mixing must also be described at all scales. In this work, the presumed probability density function approach (Gao and O'Brian 1993, Cook and Riley 1994) is considered with a model for the sub-grid scalar variance developed by the authors (Mathey and Chollet, 1996).

## LARGE EDDY SIMULATION

The large eddy field  $\bar{f}$ , explicitly simulated in the LES, can be obtained from its full field by using a filter  $G$  of specified width  $\Delta$  (typically the grid mesh size):

$$\bar{f}(x, t) = \int_{-\infty}^{\infty} f(x', t) G(x' - x) dx' \quad (1)$$

By applying this filter to the compressible Navier-Stokes equations, we obtain a set of equations describing the evolution of the resolved part of the flow. The unresolved quantities which appear in these equations are the sub-grid stress tensor and the unresolved enthalpy flux term. These terms can be modeled by an eddy-viscosity model. In the present simulations, we used the dynamical model of Germano et al. (1991), extended to compressible flows by Moin et al. (1991). In this model, the coefficients are dynamically estimated by introducing a test filter, with a size wider than the size of the filter  $G$ . If the grid filter is now applied to the scalar ( $\xi$ ) evolution equation, we get:

$$\frac{\partial \bar{\xi}}{\partial t} + \bar{u}_k \frac{\partial \bar{\xi}}{\partial x_k} = \frac{\partial}{\partial x_k} \left( D \frac{\partial \bar{\xi}}{\partial x_k} \right) - \frac{\partial}{\partial x_k} (q_k) + \bar{\omega}(\xi) \quad (2)$$

where  $D$  is the molecular diffusivity. The last two terms of the right-hand side of the equation (2), the unresolved scalar fluxes  $q_k$  and the filtered reaction rate  $\bar{\omega}(\xi)$  need closure hypotheses. First, eddy-diffusivity models similar to

eddy viscosity models can be developed for the unresolved flux term:

$$q_k = (\overline{u_k \xi} - \overline{u_k} \overline{\xi}) = -D_t \frac{\partial \overline{\xi}}{\partial x_k} \quad (3)$$

where  $D_t$  can be obtained with the dynamical procedure. The second term, the filtered reaction rate, involves strong correlations between concentrations of different species, and concentrations and temperature in case of heat release. An accurate modeling of that term requires the knowledge of the sub-grid field structure. Inspired from the Reynolds averaged approach for combustion, one can model  $\overline{\omega}(\xi)$  according to Gao and O'Brien (1993) :

$$\overline{\omega}(\xi; \vec{x}, t) = \int_{\psi=-\infty}^{\psi=+\infty} \omega(\psi) p(\psi; \vec{x}, t) d\psi \quad (4)$$

where  $\psi$  represents the probability space variable corresponding to the scalar  $\xi$  and  $p()$  the sub-grid p.d.f..  $p()$  can be determined by solving a transport equation, but this equation needs other closure hypotheses and can significantly increase the computational cost. A less expensive solution is to presume this p.d.f according to its two first moments ( $\overline{\xi}$  and  $\overline{\xi^2}$ ) and the beta function. Cook and Riley (1994) have suggested to evaluate  $\overline{\xi^2}$  according to a scale similarity model:

$$\overline{\xi^2} - \overline{\xi}^2 = c_f (\widehat{\xi^2} - \widehat{\xi}^2)$$

Where the symbol  $\widehat{\phantom{x}}$  corresponds to the same kind of test filter used in the dynamical model of Germano with a size wider than the size of the mesh. But different values for  $c_f$  were suggested according to several investigations (Cook and Riley, 1994; Reveillon and Vervish, 1996; Jiménez et al., 1996). Mathéy and Chollet (1996) suggest a model for the sub-grid variance without any adjustable parameters, given by:

$$\overline{\xi^2} = \alpha \overline{\Delta^2} \left( \frac{\partial L \overline{\xi}}{\partial x_i} \frac{\partial L \overline{\xi}}{\partial x_i} \right) \quad (5)$$

where  $L$  is a high pass filter (Laplacian) applied on the scalar field,  $\overline{\Delta}$  the typical size of the mesh, and the coefficient  $\alpha$  is estimated according to:

$$\alpha = \frac{\widehat{\xi^2} - \widehat{\xi}^2}{M^* - \widehat{M}} \quad (6)$$

where  $\widehat{\xi^2} - \widehat{\xi}^2$  is the equivalent Leonard term for the scalar, which is expressing thanks to an equivalent Germano identity.  $M$  is the model formulation given in equation (5) at the level of the grid filter, and  $M^*$  its counterpart at the level of the test filter.

## MIXING AND REACTION IN A TURBULENT SHEAR LAYER

In the study of the mixing layer, the time-developing formulation is used, because it makes possible the Large Eddy Simulation of the reactive mixing layer with a reasonable computational cost. Except for some differences which will be afterwards detailed, the evolution of a spatially developing mixing layer is expected to be similar. The compressible Navier-Stokes solver (Gathmann, 1994) uses the Piecewise Parabolic Method (Colella and Woodward, 1986), and the filtered equations are closed by the compressible dynamical model (Moin et al., 1993). The monotonic constraints of the PPM scheme are set only when the flow is two dimensional, in order to avoid too much numerical dissipation. The chemical reaction in the layer is the irreversible reaction  $A + B \rightarrow P$ , with the

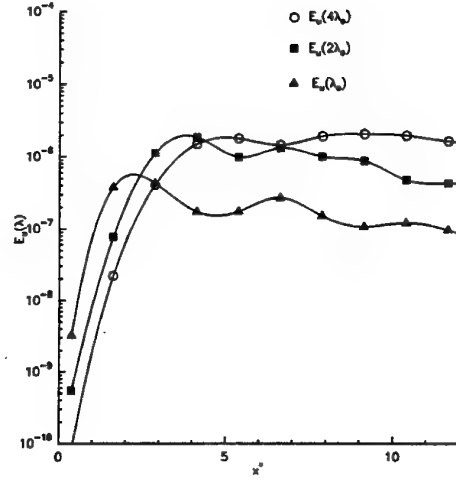


Figure 1: Spectral amplitude associated with  $u(\lambda_0)$ ,  $u(2\lambda_0)$  and  $u(4\lambda_0)$

assumption of infinite rate chemistry. Equal diffusivities are assumed for the species, and the passive scalar transported with this hypothesis is the Shvab-Zeldovich mixture fraction  $\xi$ . The product concentration  $C_p$  can be evaluated from the mixture fraction by:

$$C_p(\xi) = f \quad \text{if } \xi < \xi_{st} \quad (7)$$

$$C_p = (1 - \xi) \quad \text{if } \xi > \xi_{st}$$

$\xi_{st}$  where  $\xi_{st} = \frac{C_{B\infty}}{C_{A\infty} + C_{B\infty}}$  is the stoichiometric mixture fraction, and  $C_{A\infty}$  and  $C_{B\infty}$  are the free stream concentrations. The presumed p.d.f approach is used with the model for the sub-grid scalar variance described in the previous section. The filtered product concentration is then computed according to:

$$\overline{C_p}(\xi; \vec{x}, t) = \int_{\psi=-\infty}^{\psi=+\infty} C_p(\psi) p(\psi; \vec{x}, t) d\psi \quad (8)$$

The Reynolds number of the shear layer, based on the initial vorticity thickness  $\delta_i$  and the velocity difference across the layer  $\Delta U$  is equal to 4000. The Schmidt number  $Sc = \frac{\nu}{D}$  is equal to unity. A random white noise is superposed isotropically on the initial velocity field (hyperbolic-tangent), with an amplitude of  $0.01 \Delta U$ . The physical length of the domain is  $168\delta_i \times 88\delta_i \times 48\delta_i$  in the streamwise ( $x$ ), vertical ( $y$ ) and spanwise ( $z$ ) directions of the layer. The size of the corresponding computational domain is  $328 \times 50 \times 48$ . The unit of time  $t^*$  is defined by  $\frac{2\delta_i}{\Delta U}$ .

## Transition

The most amplified spanwise wavelength of the shear layer  $\lambda_0 \approx 8\delta_i$  corresponding to the Kelvin-Helmholtz instability is found to be in sufficiently good agreement with the linear stability analysis of Michalke (1964). Velocity spectral amplitudes for the fundamental and sub-harmonic modes are given in figure (1). As shown by Huang and Ho (1990), the merging parameter, given by the relation:

$$x^* = R \frac{\Delta U}{\lambda_0} = \frac{\delta_i}{\lambda_0} t^* \quad (9)$$

is found to be approximately equal to 2, 4 and 6 when the fundamental and sub-harmonic modes are saturated (i.e. at the time of roll-up and successive pairing). Huang and Ho (1990) found that the transition to the fully developed

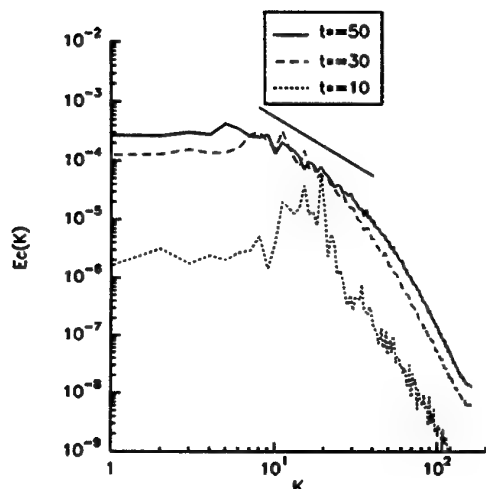


Figure 2: Kinetic-energy spectrum at time  $t^* = 10, 30, 50$  ( $x^* \approx 1, 4, 6$ )

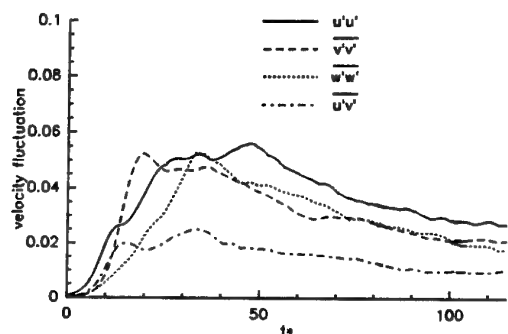


Figure 3: Maximum Reynolds stress  $\overline{u'v'}$  and mean velocity fluctuations  $u'^2, v'^2, w'^2$  (normalized by  $\Delta u^2$ ) versus  $t^*$

regime correlates with the number of pairings of the large scale vortices. In the simulation, the small-scale transition is found to occur between the first and the second pairing, as it is shown by the evolution of the spectral distribution of the kinetic energy in figure (2), where the slope of the distribution reaches  $-5/3$  for  $t^* = 50$  ( $x^* \approx 6$ ). The evolution of the maximum velocity fluctuations and the maximum Reynolds stress, from the beginning to the end of the simulation, are given in figure (3). Velocity fluctuations and Reynolds stress tend towards an asymptotic value for  $t^* > 80$ , which characterizes the end of the transition. The amount of product formed in the layer can be characterized by the normalized product thickness, which is defined by:

$$\delta_p = \frac{1}{\delta} \int_{-\infty}^{\infty} \frac{C_p(y)}{C_{\infty}} dy \quad (10)$$

where  $C_p$  is the molar product concentration,  $C_{\infty}$  the concentration in the free stream, and  $\delta$  the visual thickness of the layer, defined as the distance between the point at which the mean product concentration rise is equal to 1% of the maximum mean concentration. As shown by Breidenthal (1981),  $\delta_p$  undergoes a transition when the flow becomes turbulent. This transition shown in figure (8) is completed for  $t^* = 80$ . As pointed out by Breidenthal (1981), the time at which this mixing transition is completed correlates well with the time at which the velocity fluctuations approach their asymptotic values. These val-

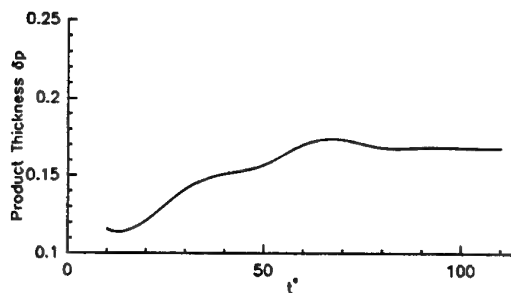


Figure 4: Normalized product thickness versus  $t^*$

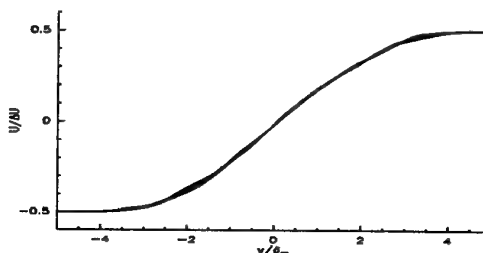


Figure 5: Mean streamwise velocity profiles for  $t^* = 70$  to 120

ues, both for the velocity fluctuations and product thickness are in agreement with the results of Bell and Metha (1990) and Mungal and Dimotakis (1984) (for a stoichiometric ratio  $\phi = \frac{C_{A\infty}}{C_{B\infty}} = 1$ ).

#### Self-similar profiles

Past the mixing transition, the mean velocity profiles plotted in function of  $y/\delta_m$  ( $\delta_m$  the momentum thickness) are self-similar (figure 5). At the end of the simulation the mean velocity fluctuation profiles (figure 6) are also self similar, and in good agreement with the experimental results of Bell and Metha (1990).

The mean product concentration profiles versus  $y^* = \frac{y}{\delta}$ , are given in figure (7). These profiles are in good agreement with the results of Mungal and Dimotakis (1984).

Up to now, the good agreement between the simulation and experiments, demonstrates the ability of the Large Eddy Simulation to reproduce correctly the large scale velocity field, and the mixing at the sub-grid scales, which are responsible for the large scale product concentration. In the next section, the physical mechanisms, responsible for mixing in the shear layer, are studied in more details.

#### Mixing and the Broadwell and Breidenthal model

The evolution of the volume fraction of molecularly mixed fluid across the layer can be studied by varying the stoichiometric ratio  $\phi = \frac{C_{A\infty}}{C_{B\infty}}$  (Mungal and Dimotakis, 1984; Koochesfahani and Dimotakis, 1986; hereafter respectively referred to as MD and KD). The figure (8) gives the evolution of  $\delta_p(\phi)$  computed in the simulation, for  $t^* = 110$ .

In a spatial evolving mixing layer, the layer entrains more fluid from the high-speed side than from the low-speed side. As a result, the normalized product thickness depends on the choice of the concentration  $C_{\infty}$  (equation 10). Thus  $\delta_p$  can evolve in two different ways according to a flip experiment (where  $C_{\infty}$  is chosen to be the high speed-side concentration or the low speed-side concentration). As it is expected for a temporal (symetric) evolving shear layer, the results of the simulation are located between the two

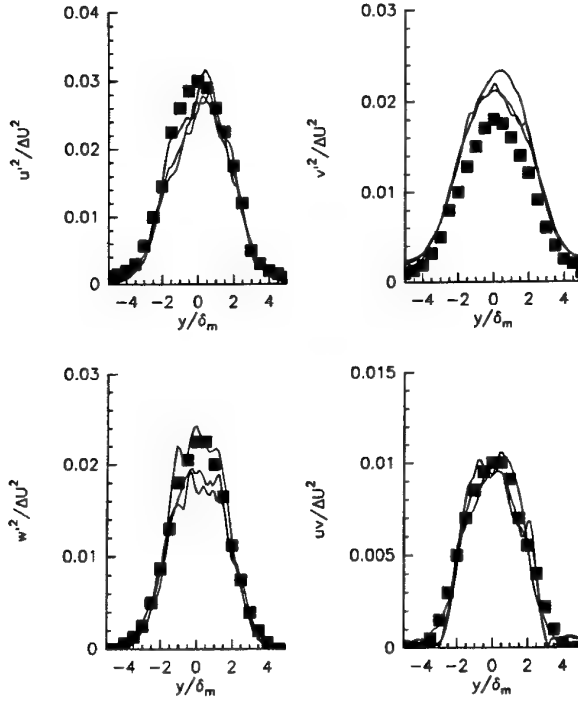


Figure 6: Mean velocity fluctuation profiles: comparison with Bell and Metha (1990)(symbols) and the simulation for  $t^* = 90, 100, 110$

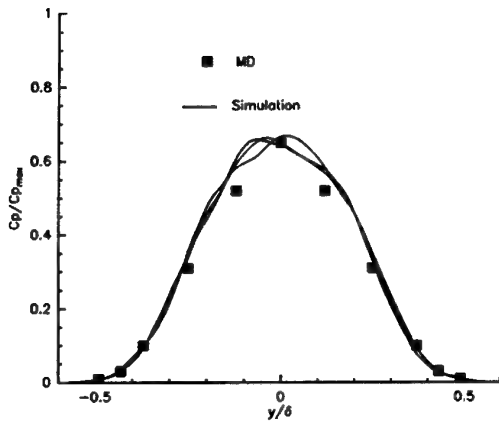


Figure 7: Mean product concentration profile for  $t^* = 80, 90, 100, 110$

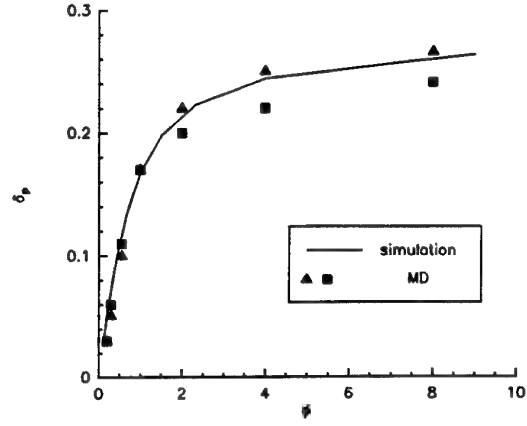


Figure 8: Normalized product thickness versus the Stoichiometric ratio  $\phi$ . Comparison between experiments Mungal and Dimotakis (1984) and the Large Eddy Simulation

results of MD.

In order to compute this quantity, the Broadwell and Breidenthal model of mixing (Broadwell and Breidenthal, 1982, referred to as B-B) considers that the fluid in the layer is in two states, in strained laminar diffusion layers near the stagnation point in the braids, and in a homogeneous mixture in the core of the rolls. In the latter, the basic idea is that the molecular mixing takes place at the end of a Kolmogorov-like cascade from the largest to the smallest scales of the flow. When the scale of the reactant concentration fluctuations in the streams reaches the Batchelor's scale  $\lambda_B$ , the time required for diffusion to homogenize the mixture is then negligible compared to the time necessary to reach  $\lambda_B$ . According to this mechanism, the volume fraction of molecularly mixed fluid formed in the core of the rolls is independent of the Reynolds and Schmidt numbers. If the reaction is fast and consists of a single step forward process, the product thickness is then directly proportional to this volume fraction of molecularly mixed fluid. With the same assumptions, chemical reactions in the second region, the laminar diffusion layers, or flame sheet, can be treated exactly (Carrier et al., 1975). Finally, the normalized product thickness corresponding to the two parts of the flow is given by (Broadwell and Mungal, 1988):

$$\delta_p = \frac{A}{E+1} + B(\phi+1)e^{-\lambda^2}(ScRe)^{-1/2} \quad (11)$$

where  $E$  is the entrainment ratio, and  $\lambda = erf^{-1} \left( \frac{\phi-1}{\phi+1} \right)$ . The first term in the right-hand side of the relation gives the constant contribution of the homogeneous mixture. The second term corresponds to the flame sheet and is Reynolds and Schmidt dependent. The soundness of this model decomposition was verified by experiments in gases (MD), and in liquids (KD, where the flame sheet contribution is negligible).

Similar experiments can be done with the Large Eddy Simulation by using a filter, which decomposes the flow into two regions, regions of concentrated vorticity, and regions of strain dominance. It is expected that these two regions correspond respectively to the homogeneous and flame sheet parts of the B-B model. This filter is based on a local comparison between vorticity and rate of strain. The results are given in figure (9), where the contribution of the homogeneous and flame sheet parts to  $\delta_p$  are referred to as  $\delta_{ph}$  and  $\delta_{pf}$  (and then  $\delta_p = \delta_{ph} + \delta_{pf}$ ). With  $A$  and  $B$  fixed, the B-B model prediction given in equation (11) can be compared with the Large Eddy Simulation results.

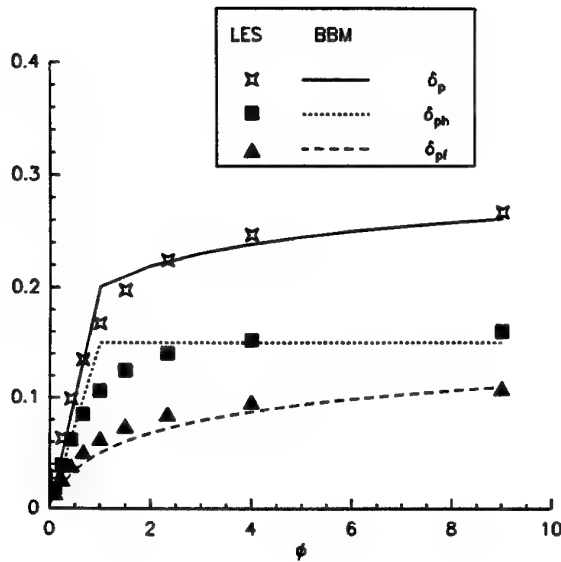


Figure 9: Contribution of the flame sheet  $\delta_{pf}$  and the homogeneous region  $\delta_{ph}$  to the product thickness  $\delta_p$ . Comparison with the Large Eddy Simulation and the B-B Model at  $t^* = 110$

For the two parts of the flow, the symbols of the simulation are in good agreement with the curve of the model. In the region dominated by rotation,  $\delta_{ph}$  first increases until  $\phi \approx 2$ , and then reaches approximately a constant level. The asymptotic value of  $\delta_{ph}$  (0.16) is in the range of the results of KD in water. Thus, the B-B model decomposition of the flow is directly linked to the large scale vortical structures.

### Mixing transition

In this last section, two questions are addressed. First, despite the fact that the model ignores vortex pairing and streamwise vortices, it gives very good results past the mixing transition. This suggests that the homogeneous part of the model takes into account both the contribution of the streamwise vortices and the primary Kelvin-Helmholtz structures. Second, if during the transition, one can expect that the flame sheet contribution remains the same, as it is a laminar contribution, on the contrary, the contribution of the Kelvin-Helmholtz structures which undergo successive pairing, and the streamwise vortices which become more and more dynamically active, is badly known.

In order to separate the contribution of the spanwise and streamwise vortices, during and past the transition, a second filter is used which locates the roller and braid regions. This filter is the  $R$ -diagnostic proposed by Rogers and Moser (1994). Thanks to this filter, and the filter presented in the previous section, the contribution of the streamwise vortices in the braids ( $\delta_{pVB}$ ), and the contribution of the rollers ( $\delta_{phR}$ ) are studied separately (with  $\delta_{ph} = \delta_{phR} + \delta_{phB}$ ). These quantities are given in figure (10) during and past the transition (for  $\phi = 1$ ). The more important result is that for the flow considered, the mixing transition is mainly due to the increasing contribution of the streamwise vortices. Indeed  $\delta_{phB}$  increases until  $t^* > 60$ , where it reaches a constant value when the mixing transition is completed. On the other hand,  $\delta_{phR}$ , the contribution of the Kelvin-Helmholtz structures, is almost constant during the transition, except for a small jump near  $t^* = 60$ . At the beginning of the simulation, the layer is two-dimensional, and the product is distributed along the material interface that originally separates the

two streams. It is distorted during roll-up in a series of spiraling sheets. In this situation, the evolution of the volume fraction of mixed fluid is given by Corcos and Sherman (1984), and indeed the results of their 2D simulation, are similar to the earlier development of  $\delta_{phR}$ . The earlier development of  $\delta_{phB}$  can be, described by the model of Lin and Corcos (1984). The streamwise vortices, submitted to a constant strain, collapse to form the counter-rotative vortex pair only if their circulation are strong enough (the collapse criterion). Only collapsed vortices are able to wind material surfaces around their centers. As a result, the volume fraction of mixed fluid, or  $\delta_{phB}$ , starts to increase when this collapse criterion is verified, after the roll-up ( $t^* \approx 15$ ) in the simulation. When the vortices have collapsed, the volume fraction of mixed fluid is directly linked to their circulation. As shown by (Moser and Rogers, 1993), this circulation increases as the layer evolves, which explains the evolution of  $\delta_{phB}$ .

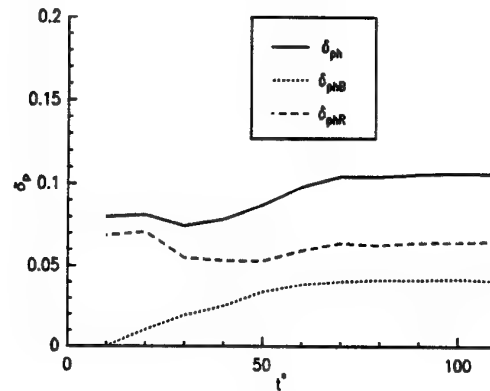


Figure 10: Contribution of the spanwise  $\delta_{phB}$  and streamwise  $\delta_{phR}$  vortex structures to the total normalized product thickness associated with the homogeneous region  $\delta_{ph}$

For  $t^* \approx 60$ ,  $\delta_{phR}$  undergoes a small transition. This transition correlates with the small scales transition for the velocity field shown figure (2). Past this small scales transition, both  $\delta_{phR}$  and  $\delta_{phB}$  become constant, as it is expected when the homogeneous part of the flow corresponds to the streamwise and spanwise vortex structures.

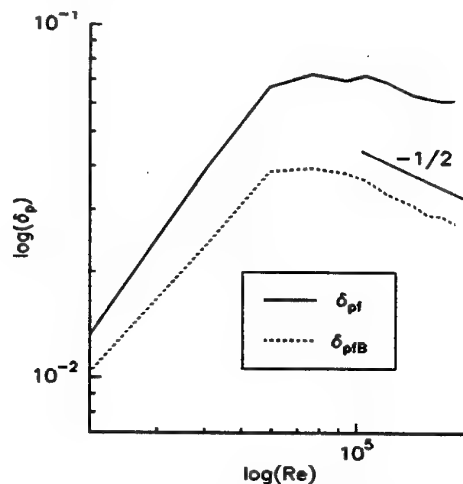


Figure 11: Evolution of the total flame sheet contribution  $\delta_{pf}$  and the flame sheet contribution in the braids  $\delta_{pfb}$  with the Reynolds number

Concerning the flame sheet contribution  $\delta_{pf}$ , the B-B

model predict a Reynolds and Schmidt dependence through the relation given in equation (11). The evolution of  $\delta_{pf}$  and  $\delta_{pfB}$  (contribution of the braids to  $\delta_{pf}$ ) with  $Re$  are given in figure (11). The correct behaviour ( $\approx Re^{-1/2}$ ) is obtained only for  $\delta_{pfB}$ . Indeed, the B-B model hypothesis for the flame sheet is verified at the stagnation point of the layer, where the flame sheet separates the two free streams. This stagnation point corresponds to the braids contribution  $\delta_{pf}$ , whereas  $\delta_{pf} = \delta_{pfB} + \delta_{pfR}$  involves the contribution of both  $\delta_{pfB}$  and the strained diffusion layers  $\delta_{pfR}$  in the periphery of the Kelvin-Helmholtz vortex core, which are not taken into account by the model. The slope  $-1/2$  is reached by  $\delta_{pfB}$  before that the second pairing has occurred. These results provide insight on experimental results (Hermanson and Mungal, 1985) showing a  $\log(Re)$  dependence for the total normalized product thickness  $\delta_p$  past the mixing transition. In these experiments, the contribution of the flame sheet cannot be separately taken into account. This contribution together with the contribution of the other parts of the flow which evolve in a different way, could be responsible for the observed  $\log(Re)$  dependence.

## Conclusion

In this study, it has been shown that, a large eddy simulation of a reactive turbulent shear layer can be conducted without any adjustable parameter. The shear layer was simulated from the beginning of the transition to a self-similar state. Past the mixing transition, the product concentration field computed by the simulation was compared with the model decomposition of the flow, suggested by Broadwell and Breidenthal (1982). It is found that regions of concentrated vorticity correlate with the homogeneous part of the model, whereas the strain dominance regions correlates with the strained diffusion layers. As expected, the amount of product formed in the homogeneous region is found to be independent on the local Reynolds number (for the small range considered), whereas the flame sheet contribution in the stagnation point between the rolls decreases as  $Re^{-1/2}$ .

For the Schmidt number considered ( $Sc = 1$ ), it is found that the mixing transition starts with the growing contribution of the streamwise vortices, before the small scales transition occurs. On the contrary, the amount of product formed in the spanwise vortex cores undergoes a transition with the small scales transition of the velocity field. However, the resulting increase in the total amount of product is small compared to the streamwise vortices contribution.

## Acknowledgments

The numerical calculations were carried out on the CRAY C98 of the IDRIS (CNRS) and on the CRAY C94 of the CENG computing centers.

## REFERENCES

- Bell, J., Metha, R., 1990, "Development of a two-stream mixing layer from tripped and untripped boundary layers", *AIAA Journal* Vol. 28, 2034-2042.
- Breidenthal, R., 1981, "Structure in turbulent mixing layers and wakes using chemical reaction", *J. Fluid Mech.* Vol. 109, 1-24.
- Broadwell, J.E., Breidenthal, R.E., 1982, "A simple model of mixing and chemical reaction in a turbulent shear layer", *J. Fluid Mech.* Vol. 125, 397-410.
- Broadwell, J.E., Mungal, M.G., 1988, "Molecular mixing and chemical reactions in turbulent shear layers", Twenty-Second Symposium (International.) on Combustion, The Combustion Institute, 579-587.
- Brown, G.L., Roshko, A., 1974, "On density effects and large structure in turbulent mixing layers", *J. Fluid Mech.* Vol. 64, No. 4, 775-816.
- Carrier, G.F., Fendell, F.E., Marble, F.E., 1975, "The effect of strain rate on diffusion flames", *SIAM J. Appl. Math.* Vol. 28, No. 2, 463-500.
- Colella, P., Woodward, P.R., 1984, "The piecewise parabolic method for gas-dynamical simulations", *J. Comp. Phys.* Vol. 54, 174-201.
- Corcos, G.M., Sherman, F.S., 1984, "The mixing layer: deterministic models of a turbulent flow. Part 1. Introduction and the two-dimensional flow", *J. Fluid Mech.* Vol. 139, 29-65.
- Cook, A.W., Riley, J.J., 1994, "A subgrid model for equilibrium chemistry in turbulent flows", *Phys. Fluids* Vol. 6 (No. 8), 2868-2870.
- Gao, F., O'Brien, E.E., 1993, "A large-eddy simulation scheme for turbulent reacting flows", *Phys. Fluids A* Vol. 5, 1282-1284.
- Gathmann, R.J., 1993, "Analyse d'écoulements supersoniques et réactifs par simulation numérique instationnaire tridimensionnelle", Thèse de l'Université Joseph-Fourier - Laboratoire des Écoulements Géophysiques et Industriels.
- Germano, M., Piomelli, U., Moin, P., Cabot, W.H., 1991, "A dynamic sub-grid-scale eddy viscosity model", *Phys. Fluids A* Vol. 3, 1760-1765.
- Huang, L.S., Ho, C.M., 1990, "Small-scale transition in a plane mixing layer", *J. Fluid Mech.* Vol. 210, 475-500.
- Jiménez, J., Liñán, A., Rogers, M.M., Higuera, F.J., 1996, "A-priori testing of sub-grid models for chemically reacting non-premixed turbulent shear flows", Center of Turbulent Research, Proceedings of the Summer Program.
- Karasso, P.S., Mungal, M.G., 1996, "Scalar mixing and reaction in plane liquid shear layers" *J. Fluid. Mech.* Vol. 323, 23-63.
- Koochesfahani, M.M., Dimotakis, P.E., 1986, "Mixing and chemical reactions in a turbulent liquid mixing layer", *J. Fluid. Mech.* Vol. 170, 83-112.
- Lin, S.J., Corcos, G.M., 1984, "The mixing layer: deterministic models of a turbulent flow. Part 3. The effect of plane strain on the dynamics of streamwise vortices", *J. Fluid. Mech.* Vol. 141, 139-178.
- Mathey, F., Chollet, J.P., 1996, "Sub-grid Model of Scalar Mixing for Large Eddy Simulations of Turbulent Flows", The Second ERCOFTAC Workshop on Direct and Large Eddy Simulation, Grenoble.
- Michalke, A., 1964, "On the inviscid instability of the hyperbolic tangent velocity profile", *J. Fluid Mech.* Vol. 19, 543-556.
- Moin, P., Squires, K., Cabot, W., Lee, S., 1991, "A dynamic subgrid-scale model for compressible turbulence and scalar transport", *Phys. Fluids A* vol. 3, 2746-2757.
- Moser, R.D., Rogers, M.M., 1993, "The three-dimensional evolution of a plane mixing layer: pairing and transition to turbulence", *J. Fluid Mech.* Vol. 247, 275-320.
- Mungal, M.G., Dimotakis, P.E., 1984, "Mixing and combustion with low heat release in a turbulent shear layer", *J. Fluid Mech.* Vol. 148, 349-382.
- Mungal, M.G., Hermanson, J.C., Dimotakis, P.E., 1985, "Reynolds Number effects on Mixing and Combustion in a Reacting Shear Layer", *AIAA Journal* Vol. 23 (9), 1418-1423.
- Reveillon, J., Vervish, L., 1994, "Modèle probabiliste de sous-maille pour la combustion turbulente non-premelagée", Actes du XIIème congrès de mécanique, Vol. 2, 413-416.
- Rogers, M.M., Moser, R.D., 1994, "Direct simulation of self-similar turbulent mixing layer", *Phys. Fluids* Vol. 6 (No. 2), 903-923.
- Winant, C.D., Browand, F.K., 1974, "Vortex pairing: The mechanism of turbulent mixing-layer growth at moderate Reynolds number", *J. Fluid Mech.* Vol. 63, No. 2, 237-255.



# A PRIORI TESTING OF SUBGRID-SCALE MODELS IN ANISOTROPIC HOMOGENEOUS TURBULENCE

Anurag Juneja and James G. Brasseur

Department of Mechanical Engineering  
The Pennsylvania State University  
University Park, Pennsylvania 16802  
USA

## ABSTRACT

One of the major challenges in modeling the resolved-scale-subgrid-scale (RS-SGS) dynamics in large-eddy simulation (LES) of the atmospheric boundary layer (ABL) occurs near the ground, a region characterized by strong shear- and buoyancy-induced anisotropies, where pressure transport is important, and where integral scale motions are significantly under-resolved. By contrast, all existing subgrid-scale (SGS) closures have been formulated assuming well-resolved integral scale motions and locally isotropic turbulence at the filter cutoff. Moreover, deficiencies in the model for SGS stress are amplified in the prediction of SGS pressure through a Poisson equation. To examine the reasons for the failure of existing SGS models in under-resolved anisotropic turbulence and the role of SGS pressure in the evolution of resolved fields, we use direct numerical simulation (DNS) datasets of shear- and buoyancy-generated homogeneous turbulence and compare the actual and modeled RS-SGS dynamics at several locations of the filter cutoff for the classical Smagorinsky closure and its "dynamic" variants. We find that the underlying assumption of eddy-viscosity models, that the deviatoric part of the subgrid stress tensor is well aligned with the resolved strain rate tensor, is a poor approximation. More importantly, the structure of the SGS stress divergence, which directly evolves the resolved velocity field, is poorly predicted by the Smagorinsky and dynamic models, although there is some improvement with the dynamic model. These models predict a strong preference in direction for SGS stress divergence which does not exist in reality. Pressure effects are under-predicted by the Smagorinsky closure, while the dynamic model leads to errors in the anisotropic structure of SGS pressure gradient. Because both SGS stress divergence and SGS pressure gradient directly affect the evolution of the resolved velocity, these shortcomings contribute to the deficiencies of LES in under-resolved anisotropic turbulence.

## INTRODUCTION

Beginning with the pioneering work of Lilly (1967) and

Deardorff (1970), large-eddy simulation has become well established as an important tool for turbulence research atmospheric (Wyngaard and Moeng, 1993) and engineering (Reynolds, 1990) applications. The objective of LES is to compute the three-dimensional time-dependent details of only the largest scales of motion and use a simple model to parameterize the effects of smaller scales. To do so, the velocity field  $u_i$  is decomposed into a resolvable ( $u_i^r$ ) and a subgrid ( $u_i^s$ ) part by means of a filtering operation:

$$u_i^r(\mathbf{x}) = \int u_i(\mathbf{x}') G(\mathbf{x} - \mathbf{x}') d\mathbf{x}', \quad (1)$$

$$u_i^s(\mathbf{x}) = u_i(\mathbf{x}) - u_i^r(\mathbf{x}), \quad (2)$$

where  $G(\mathbf{x})$  is the filter function defining the grid filter. The evolution equations for the resolved-scale velocity, obtained by filtering the Navier-Stokes equations, are

$$\frac{\partial u_i^r}{\partial t} = 0, \quad (3)$$

$$\frac{\partial u_i^r}{\partial t} + \frac{\partial(u_i^r u_j^r)}{\partial x_j} = -\frac{1}{\rho} \frac{\partial p^r}{\partial x_i} + \nu \frac{\partial^2 u_i^r}{\partial x_j \partial x_j} - \frac{\partial \tau_{ij}}{\partial x_j}, \quad (4)$$

where the subgrid-scale stress  $\tau_{ij} = (u_i u_j)^r - (u_i^r u_j^r)^r$  represents the contribution of the SGS motions to the evolution of the resolved-scale velocity.

Traditionally the SGS stress has been modeled by relating it to the resolved strain rate  $S_{ij}^r$  through an eddy viscosity:  $\tau_{ij}^a = -2\nu_t S_{ij}^r$ , where  $\tau_{ij}^a$  is the deviatoric part of the SGS stress tensor ( $\tau_{ij}^a = \tau_{ij} - (1/3)\tau_{kk}\delta_{ij}$ ). Smagorinsky's (1963) formulation that the eddy viscosity  $\nu_t = C l_s v_s$ , where  $l_s$  is the characteristic length of the subgrid-scale motions and  $v_s$  the corresponding characteristic velocity, is the basis of the most commonly used SGS models. Whereas the SGS constant of proportionality,  $C$ , was determined theoretically by Lilly (1967) for locally isotropic turbulence with the filter cutoff in the inertial range, it has been found necessary to make modifications by reducing  $C$  significantly in shear flows (Deardorff, 1970), including ad-hoc damping functions in the near-wall regions of plane channel flows (Moin and Kim, 1972), or using intermittency functions that effectively set the constant to zero in the early



stages for transitional flows (Piomelli and Zang, 1991). On the other hand, Germano *et al.* (1991) used resolved-scale information to devise a dynamic procedure for obtaining the constant of proportionality, which led to better agreement of LES with experiments in transitional and fully turbulent channel flows. Mason and Thomson (1992) showed that the addition of a stochastic backscatter term to the Smagorinsky closure improved the mean shear profiles near the surface in planetary boundary layers, while Sullivan *et al.* (1994) achieved similar improvement by incorporating a two-part eddy viscosity formulation.

The popularity of the Smagorinsky model stems from its simplicity and, more importantly, the insensitivity of resolved-scale statistics to the details of subgrid-scale closure when the integral scales are well resolved. In particular when the closure is calibrated to yield the correct net-energy flux from the resolved to the subgrid scales for the filter cutoff in the locally isotropic inertial range, the low-order statistics of resolved scale motions are not strongly influenced by the model, and the Smagorinsky closure yields reasonable predictions of integral scale motions. In applications such as the atmospheric boundary layer, the integral scales in the near-ground and capping-inversion regions are under-resolved while dominated by strong shear and buoyancy-induced anisotropies and pressure transport dynamics. Here the RS-SGS dynamics affects the integral scale motions directly and eventually dominates the evolution of the resolved velocity (Brasseur *et al.*, 1996). When this happens, the demands on a good SGS model not only requires that the net energy flux be right but also, at some reasonable level, the local flux and acceleration vector.

Our long-term goal is to develop improved subgrid-scale closures for the near-ground surface layer in large-eddy simulation of the atmospheric boundary layer. Because the integral scales are under resolved and strongly anisotropic in these regions, we must first explore the reasons for the failure of existing SGS models by examining actual and modeled SGS-RS dynamics from simulations which incorporate these features. To do so, we use direct numerical simulation (DNS) datasets of homogeneous buoyancy-driven turbulence and homogeneous shear-flow turbulence, and compute the actual and modeled subgrid terms at several locations of the filter cutoff.

This “*a priori*” testing, pioneered by Clark *et al.* (1979), offers the ability to probe the physical content of a model by comparing exact SGS terms with model prediction locally and instantaneously. To date, *a priori* testing has mostly been employed to examine the correlations between actual and modeled stresses in homogeneous isotropic turbulence by Clark *et al.* (1979), McMillan and Ferziger (1980), and Meneveau (1994), among others. Because the SGS stress tensor is modeled from resolved fields deterministically thereby missing the stochastic nature of small-scale turbulence, any such model must necessarily yield low correlations in *a priori* testing. Hence it is our opinion that correlations do not provide an accurate barometer of model performance.

We focus instead on whether the model can replicate some of the important local and statistical features of the actual SGS stress tensor. In anisotropic turbulence, this implies that we ask whether the modeled SGS stress tensor exhibits anisotropies similar to the actual SGS stress tensor. Noting that the SGS stress divergence, rather than SGS stress, directly influences the evolution of resolved velocity, we compare the actual and modeled SGS stress divergence as well.

The errors in the model for SGS stress can be amplified by the SGS pressure gradient, given that SGS pressure is from  $\tau_{ij}$  through a Poisson equation. SGS pressure gradient is particularly important near boundaries. Conse-

quently, we examine the role of SGS pressure gradient and analyze the relative contributions of pressure gradient and stress divergence to the evolution of resolved velocity.

## BACKGROUND AND OBJECTIVES

We examine the performance of the Smagorinsky and dynamic models in shear- and buoyancy-generated homogeneous turbulence by evaluating the extent to which the models are successful in predicting the desirable features of SGS stress tensor, SGS stress divergence, and SGS pressure gradient. In this section, we present an overview of the SGS models, LES equations, and the specific protocols of analyses used in this study.

The Smagorinsky model closes the deviatoric part of the SGS stress tensor:

$$\tau_{ij}^a = -2\nu_t S_{ij}^r, \quad (5)$$

where  $S_{ij}^r$  is the resolved rate of strain tensor:

$$S_{ij}^r = \frac{1}{2} \left( \frac{\partial u_i^r}{\partial x_j} + \frac{\partial u_j^r}{\partial x_i} \right), \quad (6)$$

and the eddy viscosity  $\nu_t$  is given by

$$\nu_t = C\Delta^2 |S_{ij}^r|. \quad (7)$$

The characteristic length scale of SGS motions,  $\Delta$ , is usually set equal to the grid filter width  $\Delta = (\Delta_x \Delta_y \Delta_z)^{1/3}$ , where  $\Delta_x$ ,  $\Delta_y$  and  $\Delta_z$  are the grid filter scales in the  $x$ ,  $y$  and  $z$  direction respectively. The constant of proportionality in Eq. (7) was theoretically determined by Lilly (1967), to be  $C \approx 0.04$ , and we use this value in our analyses.

In the dynamic model by Germano *et al.* (1991), resolved-scale information from the LES fields is used to determine  $C$  locally in space and time. This is achieved by test-filtering the resolved scale velocity at a scale,  $\Delta^t$ , larger than the grid filter scale. Denoting the test-filtered velocity as  $u^{rt}$ , the subtest-scale stress is  $T_{ij} = (u_i u_j)^{rt} - (u_i^{rt} u_j^{rt})^{rt}$ . The assumption that the Smagorinsky model can be used to parameterize both the subtest-scale stress and the subgrid-scale stress with the same  $C$  locally, leads to

$$C(x, t) = \frac{\langle L_{ij} R_{ij} \rangle}{\langle R_{kl} R_{kl} \rangle}, \quad (8)$$

where  $L_{ij} = (u_i^r u_j^r)^{rt} - (u_i^{rt} u_j^{rt})^{rt}$  and  $R_{ij} = -2(\Delta^t)^2 |S_{ij}^r| S_{ij}^r + (2\Delta^2 |S_{ij}^r| S_{ij}^r)^t$  can be determined completely from the resolved fields. It has been customary to perform the averaging in Eq. (8) in the homogeneous directions during LES. In our implementation,  $C$  was calculated using: (i) no averaging, (ii) averaging along a line, (iii) averaging on a plane; the averaging in (ii) and (iii) was performed along lines or planes perpendicular to the direction of gravity in buoyant flow or the direction of mean gradient in shear turbulence. We obtained qualitatively similar model performance in all three cases.

Only the deviatoric part of the SGS stress is modeled, and its trace is included in a redefinition of the resolved pressure,  $\hat{p}^r = p^r + \frac{1}{3} \tau_{kk}$ , so that the momentum equation (4) becomes

$$\frac{\partial u_i^r}{\partial t} + \frac{\partial (u_i^r u_j^r)^r}{\partial x_j} = -\frac{1}{\rho} \frac{\partial \hat{p}^r}{\partial x_i} + \nu \frac{\partial^2 u_i^r}{\partial x_j \partial x_j} - \frac{\partial \tau_{ij}^a}{\partial x_j}. \quad (9)$$

The modified pressure is determined from the following Poisson equation:

$$\frac{\partial^2 \hat{p}^r}{\partial x_j \partial x_j} = -\rho \frac{\partial}{\partial x_i} \left( \frac{\partial (u_i^r u_j^r)^r}{\partial x_j} - \nu \frac{\partial^2 u_i^r}{\partial x_j \partial x_j} + \frac{\partial \tau_{ij}^a}{\partial x_j} \right). \quad (10)$$

The resolved pressure  $p^r$  can be decomposed into contributions involving only resolved velocity ( $p_R$ ) and contributions involving the SGS stress ( $p_S$ ):

$$p^r = p_R + p_S. \quad (11)$$

Absorbing the trace of the SGS stress tensor into a redefinition of the subgrid component yields  $\hat{p}^r = p_R + \hat{p}_S$  where  $\hat{p}_S = p_S + \frac{1}{3}\tau_{kk}$ , and

$$\frac{\partial^2 p_R}{\partial x_j \partial x_j} = -\rho \frac{\partial}{\partial x_i} \left( \frac{\partial(u_i^r u_j^r)}{\partial x_j} - \nu \frac{\partial^2 u_i^r}{\partial x_j \partial x_j} \right), \quad (12)$$

$$\frac{\partial^2 \hat{p}_S}{\partial x_j \partial x_j} = -\rho \frac{\partial}{\partial x_i} \left( \frac{\partial \tau_{ij}^s}{\partial x_j} \right). \quad (13)$$

Finally, we rewrite Eq. (9) such that all subgrid (i.e., modeled) terms appear on the right hand side:

$$\frac{\partial u_i^r}{\partial t} + \frac{\partial(u_i^r u_j^r)}{\partial x_j} + \frac{1}{\rho} \frac{\partial p_R}{\partial x_i} - \nu \frac{\partial^2 u_i^r}{\partial x_j \partial x_j} = -\frac{1}{\rho} \frac{\partial \hat{p}_S}{\partial x_i} - \frac{\partial \tau_{ij}^s}{\partial x_j}. \quad (14)$$

With this background, we summarize the specific issues investigated in this study:

1. *Actual vs. modeled  $\tau_{ij}^s$* : The ability of the SGS model to accurately predict the actual SGS stress is evaluated in terms of: (a) local alignment between the tensors on a point-by-point basis, and (b) global agreement in the statistical structure of the tensors.

To investigate whether the modeled SGS stress is locally well aligned with the actual quantity, we compute the angles,  $\phi$  and  $\theta$ , through which the principal axes of modeled SGS stress tensor must be rotated to make them coincident with the principal axes of actual SGS stress tensor.

A good SGS closure should replicate primary statistical features of the actual SGS stress. We compare the root mean square (*rms*) values of actual SGS stress tensor components (denoted by a prime) with those predicted by the model. In anisotropic turbulence, it can be expected that  $\tau_{11}' \neq \tau_{22}' \neq \tau_{33}'$ , and we examine whether the modeled stress exhibits anisotropies similar to the actual stress.

2. *Actual vs. modeled  $A_i \equiv \partial \tau_{ij}^s / \partial x_j$* : The local alignment between the divergence of actual and modeled tensors can be expected to be different from the alignment between the tensors. We quantify this alignment by computing the angle  $\phi$  through which the modeled acceleration vector  $A_i$  must be rotated to make it coincident with the actual  $A_i$ .

To investigate whether the closure accurately predicts some of the statistical features of the actual SGS stress divergence, we compare the *rms* values of actual and modeled  $A_i$  and examine whether they exhibit similar anisotropies.

3. *Role of SGS pressure gradient  $G_i \equiv (1/\rho) \partial \hat{p}_S / \partial x_i$* : Both SGS pressure gradient and SGS stress divergence influence the evolution of resolved velocity (Eq. 14). We compute the component *rms* of the actual and modeled SGS pressure gradient, and compare it with the component *rms* of SGS stress divergence. To quantify their relative importance locally, we compute the ensemble mean of the ratio of the two terms:

$$r = \left\langle \frac{|A_i|}{|G_i|} \right\rangle. \quad (15)$$

In accordance with the type of filter commonly used in actual large eddy simulations, we also use a cubic filter in spectral space, which contains  $k_c$  wavenumber modes in each direction, to define the resolved and subgrid fields from our numerical datasets.

## NUMERICAL DATASETS

### Homogeneous Buoyancy-generated Turbulence

To generate buoyancy-driven turbulence, we followed the technique of Batchelor *et al.* (1992), whereby the flow is created by specifying homogeneous random fluctuations in the density of a stationary infinite fluid at the initial instant, using the Boussinesq approximation for the gravity force. We use a parallel implementation of a DNS code (Juneja and Pope, 1996) extended from that developed by Rogallo (1981) to solve the Navier-Stokes equations pseudo-spectrally on a cubic three-dimensional grid. Whereas the equations are solved in spectral space to retain high accuracy in spatial derivatives, the bilinear products required for the convective terms are computed in physical space. De-aliasing is carried out by a combination of phase shifts and truncation, and the viscous terms are treated exactly. Explicit second-order Runge-Kutta is used to advance in time and periodic boundary conditions are applied in all directions on a cubic  $128^3$  grid. The calculations were carried out on the Cray-T3D at the Pittsburgh Supercomputing Center.

Buoyancy generated flow of this kind has a well defined birth, a quasi-stationary intermediate state, and eventual death as the initial density fluctuations are smoothed out by the action of molecular diffusion. We employed the middle stages of the evolution for the analysis of SGS model performance. Figure 1 shows the one-dimensional spectra of the three velocity components at the time of analysis (the buoyancy force is in the  $x_3$  direction). At this instant, the anisotropy in the intensity of the three velocity components is such that *rms* of  $w$ , denoted by  $w'$ , is twice as large as  $u'$  and  $v'$ . Further, the integral length-scale of  $w$  in the  $x_3$  direction, denoted by  $l_{w3}$ , is also twice as large as  $l_{u1}$  and  $l_{v2}$ . The dashed lines in the figure show the filter cutoffs used in this study.

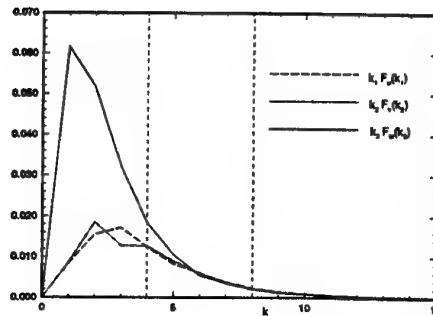


Figure 1: 1-D energy spectrum of velocity components in buoyancy-generated turbulence.

### Homogeneous Shear Flow Turbulence

The datasets of homogeneous shear flows were generated by Lin (1993), who also used a pseudospectral algorithm on a periodic  $128^3$  rectangular grid corresponding to physical dimensions of  $2L \times L \times L$  in the  $x$ ,  $y$ , and  $z$  directions respectively. The mean velocity is in the  $x$  direction and the mean gradient in the  $y$  direction.

The cubic filter cutoff for this flow is specified in terms of the number of wavenumber modes in the shorter ( $y$  or  $z$ ) directions. At the time of analysis, the anisotropy in the intensity and length-scale of the three velocity components is such that  $v'/u' = 0.61$ ,  $w'/u' = 0.75$  and  $l_{v2}/l_{u1} = 1.32$ ,  $l_{w3}/l_{u1} = 0.62$ . While the anisotropies in this flow are not as pronounced as in buoyancy-generated turbulence, it provides an opportunity to examine potential differences in the performance of an SGS model between anisotropic buoyancy and shear dominated turbulence.

## RESULTS AND DISCUSSION

We describe our results on the performance of SGS models in buoyancy-generated turbulence as a function of filter cutoff location, and compare with results obtained in shear flow turbulence.

### Actual vs. Modeled SGS Stress

Let  $\phi$  be the angle required to align the principle longitudinal strain axes of the modeled and actual  $\tau_{ij}^a$ , and  $\theta$  the angle of the second rotation required to fully align the tensors. The values  $\phi = 0$  and  $\theta = 0$  would imply a perfect alignment between the two tensors locally. Figure 2 shows that the probability density functions (pdf) of  $\phi$  and  $\theta$  have broad distributions over a range of angles using the Smagorinsky closure. This lack of alignment is consistent with the existence of significant backscatter of energy from subgrid to resolved scales, since the local flux of energy from the resolved to subgrid scales is given by  $\tau_{ij} S_{ij}^r$  (perfect alignment would imply that  $\tau_{ij} S_{ij}^r$  is positive definite). We also found that the location of the filter cutoff or the type of flow has only minor effects on the alignment.

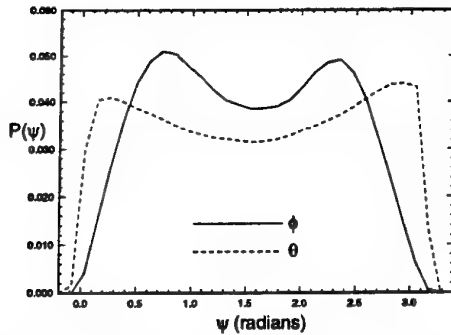


Figure 2: Probability density function of the angles  $\phi$  and  $\theta$  which quantify the alignment of actual and modeled SGS stress tensor, for Smagorinsky model at  $k_c = 4$ .

The *rms* values of the actual and modeled SGS stress tensor components in buoyancy-generated turbulence are listed in Table 1. (We did not compute the SGS stress using the dynamic model at  $k_c = 4$ ). We find that the anisotropy of the modeled SGS stress tensor is similar to that of the actual SGS stress tensor, since  $\tau_{33}^a/\tau_{11}^a \sim \tau_{33}^m/\tau_{11}^m$  and  $\tau_{12}^a/\tau_{13}^a \sim \tau_{12}^m/\tau_{13}^m$  in all cases. As expected,  $\tau_{ij}^a$  is largest if  $i$  or  $j$  is in the direction of  $w$  (the velocity component with the largest intensity and lengthscale). This was also true at other locations of the filter cutoff ( $k_c = 16$  and  $k_c = 32$ ) in buoyancy-generated turbulence.

In shear flow turbulence, the anisotropy in the SGS stress tensor components is not as pronounced (just as the anisotropy in intensity and length-scale of the velocity is not very pronounced). Nevertheless, both SGS models predict the same ratios of component *rms* as the actual

$k_c$	component	actual	Smag.	dynamic
4	$\tau_{11}^a$	0.045	0.061	-
	$\tau_{22}^a$	0.045	0.061	-
	$\tau_{33}^a$	0.080	0.095	-
	$\tau_{12}^a$	0.021	0.037	-
	$\tau_{13}^a$	0.038	0.071	-
	$\tau_{23}^a$	0.037	0.072	-
8	$\tau_{11}^a$	0.018	0.018	0.013
	$\tau_{22}^a$	0.018	0.018	0.013
	$\tau_{33}^a$	0.031	0.027	0.020
	$\tau_{12}^a$	0.010	0.012	0.008
	$\tau_{13}^a$	0.017	0.021	0.015
	$\tau_{23}^a$	0.017	0.021	0.015

Table 1: Component *rms* of actual and modeled SGS stress in homogeneous buoyancy-driven turbulence.

SGS stress tensor. Hence we can conclude that both the Smagorinsky and dynamic models will likely predict the global anisotropy of the SGS stress tensor reasonably well in LES of anisotropic turbulence.

### Actual vs. Modeled SGS Stress Divergence

We computed the angle  $\phi$  between the actual and modeled SGS stress divergence to quantify the local alignment between the vectors. The pdf of  $\phi$ , for Smagorinsky model at  $k_c = 4$ , is shown in Figure 3. Similar pdfs were obtained at other filter cutoff locations, suggesting that the Smagorinsky model does not correctly predict the direction of the SGS contribution to acceleration locally.

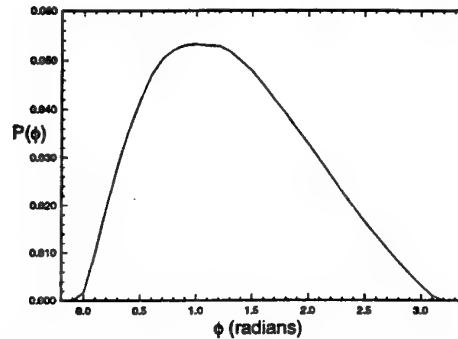


Figure 3: Pdf of the angle  $\phi$  between actual and Smagorinsky modeled SGS divergence vector at  $k_c = 4$ .

Interestingly, whereas the average SGS stress tensor is strongly anisotropic in buoyancy-driven turbulence, SGS stress divergence is found to be only mildly anisotropic. The ratios of component *rms*,  $A_2/A_1$  and  $A_3/A_1$ , at different filter cutoff locations in buoyancy-generated turbulence are listed in Table 2. At  $k_c = 4$ , we find that  $A_1 \sim A_2 \sim A_3$  for the actual SGS stress divergence, whereas the Smagorinsky model predicts a strong pref-

$k_c$	ratio	actual	Smag.	dynamic
4	$A'_2/A'_1$	1.01	1.00	-
	$A'_3/A'_1$	1.03	4.34	-
8	$A'_2/A'_1$	0.98	0.98	1.21
	$A'_3/A'_1$	0.79	3.52	2.25
16	$A_2/A_1$	0.94	0.95	1.09
	$A'_3/A'_1$	0.67	3.44	2.52

Table 2: Ratio of component *rms* for actual and modeled SGS stress divergence at different filter cutoff locations in buoyancy-generated turbulence.

$k_c$	ratio	actual	Smag.	dynamic
8	$A'_2/A'_1$	0.84	0.44	0.68
	$A'_3/A'_1$	1.08	0.87	1.40
12	$A'_2/A'_1$	1.01	0.51	0.62
	$A'_3/A'_1$	1.21	0.96	1.06
16	$A_2/A_1$	1.07	0.56	0.80
	$A'_3/A'_1$	1.14	1.01	1.07

Table 3: Ratio of component *rms* for actual and modeled SGS stress divergence at different filter cutoff locations in shear flow turbulence.

erence of  $A_i$  in the direction of  $w$ , as  $A'_3/A'_1 \sim 4.3$  and  $A'_3/A'_2 \sim 4.3$ . When the filter cutoff is moved to smaller scales, the actual  $A'_3$  decreases slightly relative to  $A'_1$  and  $A'_2$ . By contrast, both the Smagorinsky and dynamic models predict that  $A'_3$  is much larger than the other two components (although the dynamic model is better than the Smagorinsky model).

A similar result is found in our analysis of shear flow turbulence (Table 3). Recalling that  $v'/u' \sim 0.6$  for this case, the Smagorinsky and dynamic models predict that at  $k_c = 8$ , the ratio  $A'_2/A'_1$  is 0.44 and 0.68 respectively, whereas in reality  $A_i$  is not strongly anisotropic ( $A'_2/A'_1 = 0.84$ ). As before, the dynamic model offers some improvement over the standard Smagorinsky model. This result is also confirmed at other filter cutoff locations analyzed.

These results are interesting in that they suggest that when anisotropic integral scales are poorly resolved, the influence of SGS motions on RS dynamics may be roughly isotropic, on average. Consequently, a model such as Smagorinsky, which directly couples SGS-RS dynamics to large-scale anisotropy, may lead to spurious over-prediction of resolved scale anisotropy.

### Role of SGS Pressure Gradient

The evolution of resolved velocity is directly influenced by the SGS stress divergence  $A_i$  and SGS pressure gradient  $G_i$  (Eq. 14). The model for SGS stress determines

quantity	i	actual	Smag.	dynamic
$G'_i$	1	0.099	0.094	0.062
	2	0.096	0.091	0.208
	3	0.076	0.099	0.287
$A'_i$	1	0.162	0.062	0.072
	2	0.163	0.062	0.086
	3	0.131	0.224	0.161

Table 4: Comparison of component *rms* of SGS pressure gradient  $G_i$  and SGS stress divergence  $A_i$  in homogeneous buoyancy-generated turbulence at  $k_c = 8$ .

both (Eq. 13). Thus errors in SGS stress appear both in  $A_i$  and  $G_i$ . We compare the anisotropic structure of actual and modeled  $G_i$ , and examine whether the Smagorinsky and dynamic models correctly predict the relative magnitudes of the two SGS contributions to the evolution of resolved velocity.

In table 4, we list the component *rms* of  $G_i$  and  $A_i$  in buoyancy-generated turbulence at  $k_c = 8$ . The anisotropic structure of  $G_i$  is such that  $G'_2/G'_1 \sim 1.0$  and  $G'_3/G'_1 \sim 0.76$ . We find that the Smagorinsky model yields reasonable prediction of  $G'_i$ , and its anisotropic structure ( $G'_2/G'_1 \sim 1.0$  and  $G'_3/G'_1 \sim 1.0$ ). However, the dynamic model leads to significantly higher values of  $G'_2$  and  $G'_3$ , as well as incorrect anisotropic structure of  $G_i$  because we find that  $G'_2/G'_1 \sim 3.3$  and  $G'_3/G'_1 \sim 4.6$ . A comparison of  $G'_i$  and  $A'_i$  shows that whereas pressure gradients are less than stress divergence in reality, both Smagorinsky and dynamic models overpredict  $G'_i$  relative to  $A'_i$  in two of the three components. More importantly, the relative values of  $G'_i$  and  $A'_i$  are poorly predicted by both closures.

The local ratio of the magnitudes of  $A_i$  and  $G_i$  can be quantified by the parameter  $r$  (Eq. 15). We find that, in both buoyancy-generated turbulence and shear flow turbulence,  $r \approx 2.0$ , whereas the Smagorinsky model predicts that  $r \approx 5.0$  at all filter cutoff locations. The over-prediction of  $A'_i$  in the direction of velocity with largest intensity by the Smagorinsky model may be responsible for the mismatch in  $r$ . On the other hand, the dynamic model yields  $r \approx 2.0$  in agreement with the correct ratio. The cause for this agreement may, however, be due to the over-prediction of  $G'_i$  locally by the dynamic model, as just discussed.

Given the importance of pressure transport near boundaries where integral-scales are often under-resolved, the above analysis suggests that both the Smagorinsky and dynamic models may cause errors in the evolution of resolved fields in wall-bounded flows, as found by Khanna and Brasseur (1997) in LES of the atmospheric boundary layer.

### CONCLUSIONS

We have examined the performance of the Smagorinsky and dynamic models in anisotropic turbulence through a detailed comparison of modeled and actual SGS quantities using DNS datasets of homogeneous buoyancy-generated turbulence and homogeneous shear flow turbulence.

We find that the local alignment between the actual and modeled SGS stress tensor is poor. However, the anisotropy in the *rms* values of the SGS stress tensor com-

ponents is correctly predicted by both the Smagorinsky and dynamic models regardless of the filter cutoff location.

We also find poor alignment locally between the actual and modeled SGS stress divergence vectors. Furthermore, the anisotropic structure of the SGS stress divergence predicted by the models is incorrect. Both Smagorinsky and dynamic models predict a strong preference of the SGS stress divergence vector to point in the direction of the resolved velocity component with the largest intensity, whereas in reality, when a preferred direction exists (higher wavenumber filter cutoffs), it is in the other two directions.

The relative local importance of the SGS pressure gradient when compared to the SGS stress divergence, is under-predicted by the Smagorinsky closure, while the dynamic model leads to the incorrect anisotropic structure of the SGS pressure gradient term.

Because the contributions from the SGS terms to the evolution of resolved velocity dominate when the filter cutoff lies near the energy-containing range, these models can lead to errors in LES of anisotropic turbulence.

**Acknowledgments:** This work was supported by the Army Research Office under grant DAAL03-92-G-0117 and the Pittsburgh Supercomputing Center under grant ACS920029P. We thank Prof. John C. Wyngaard, Dr. Chenning Tong and Dr. Samir Khanna for useful discussions.

## REFERENCES

- Batchelor G. K., Canuto V. M. and Chasnov J. R., 1992, "Homogeneous buoyancy-generated turbulence," *J. Fluid Mech.*, Vol. 235, pp. 349-378.
- Brasseur J. G., Gong H. and Chen S., 1996, "Subgrid-resolved scale dynamics in isotropic turbulence," *Advances in Turbulence VI*, S. Gavrilakas et al. ed., Kluwer Academic Publishers, Boston, pp 201-204.
- Clark R. A., Ferziger J. H. and Reynolds W. C., 1979, "Evaluation of subgrid-scale models using an accurately simulated turbulent flow," *J. Fluid Mech.*, Vol. 91, pp. 1-16.
- Deardorff, J. W., 1970, "A numerical study of three-dimensional turbulent channel flow at large Reynolds number," *J. Fluid Mech.*, Vol. 41, pp. 453-480.
- Germano M., Piomelli U., Moin P. and Cabot W. H., 1991, "A dynamic subgrid-scale eddy viscosity model," *Phys. Fluids A*, Vol. 3, pp. 1760-1765.
- Juneja A. and Pope S. B., 1996, "A DNS study of turbulent mixing of two passive scalars," *Phys. Fluids*, Vol. 8, pp. 2161-2184.
- Khanna, S. and Brasseur, J. G., 1997, "Three dimensional buoyancy- and shear-induced local structure of the atmospheric boundary layer," to appear, *J. Atmos. Science*.
- Lilly, D. K., 1967, "The representation of small-scale turbulence in numerical simulation experiments," *Proc. IBM Sci. Comput. Symp. on Environmental Sci.*, H. H. Goldstine ed., pp. 195-210.
- Lin, W. Q., 1993, "Structural and dynamical characteristics of intermittent structures in homogeneous turbulent shear flow," Ph.D. Thesis, The Pennsylvania State University, University Park, PA.
- Mason, P. J., and Thomson, D. J., 1992, "Stochastic backscatter in large-eddy simulations of boundary layers," *J. Fluid Mech.*, Vol. 242, pp. 51-78.
- McMillan O. J. and Ferziger J. H., 1980, "Tests of new subgrid scale models in strained turbulence," AIAA Pap. 80-1339.
- Meneveau, C., 1994, "Statistics of turbulence subgrid-scale stresses: necessary conditions and experimental tests," *Phys. Fluids*, Vol. 6, pp. 815-822.
- Moin P. and Kim, J. 1982, "Numerical investigation of turbulent channel flow," *J. Fluid Mech.*, Vol. 118, pp. 341-377.
- Piomelli, U. and Zang, T. A., 1991, "Large-eddy simulation of transitional channel flow," *Comput. Phys. Commun.*, Vol. 65, pp. 224-230.
- Reynolds, W. C., 1990, "The potential and limitations of direct and large-eddy simulations," *Whither Turbulence? or Turbulence at Crossroads*, J.L. Lumley, ed., Springer Verlag, pp 313-342.
- Rogallo R. S., 1981, "Numerical Experiments in homogeneous turbulence," NASA TM-81315.
- Smagorinsky J., 1963, "General circulation experiments with the primitive equations," *Mon. Weather Rev.*, Vol. 91, pp. 99-164.
- Sullivan, P. P., McWilliams, J. C. and Moeng, C.-H., 1994, "A subgrid-scale model for large-eddy simulation of planetary boundary layer flows," *Boundary-Layer Meteorology*, Vol. 71, pp. 247-276.
- Wyngaard, J. C. and Moeng C.-H., 1993, "Large eddy simulation in geophysical turbulence parameterization: an overview," *Large Eddy Simulation of Complex Engineering and Geophysical Flows*, B. Galperin and S.A. Orszag eds., Cambridge University Press, pp. 349-368.

## **SESSION 17 - INSTABILITY AND TRANSITION**



# LARGE-SCALE INSTABILITY AND SMALL-SCALE TRANSITION IN VORTEX PAIRS

T. Leweke\* and C. H. K. Williamson

Sibley School of Mechanical & Aerospace Engineering  
Cornell University  
252 Upson Hall  
Ithaca, New York 14853-7501, U. S. A.

\*presently at:

IRPHE  
CNRS / Universités Aix-Marseille I & II  
12, avenue Général Leclerc  
F-13003 Marseille, France

## ABSTRACT

We present new experimental results concerning the dynamics of a pair of counter-rotating vortices. The flow was studied in water using detailed visualization and quantitative measurements via digital particle image velocimetry. We focus on two features observed in our experiments: 1. a long-wavelength instability, including the associated phenomenon of vortex reconnection, for which precise comparisons with theoretical predictions and numerical simulations are carried out, and 2. a short-wavelength instability occurring above a certain critical Reynolds number, whose spatial structure and symmetry is analyzed here for the first time experimentally. The interaction between the two instabilities is found to result in an efficient destruction of the large-scale vortical structures.

## INTRODUCTION

The dynamics of a pair of parallel counter-rotating vortices has been the object of a large number of studies in the last three decades. The continued interest in this flow is, to a great extent, due to its relevance to the problem of aircraft trailing wakes, whose far field is primarily composed of such a pair. For large modern aircraft, these vortices can reach considerable strengths and represent a danger for following aircraft, especially smaller ones, due to the rolling moment they induce. Knowledge about the dynamics and decay characteristics of the large-scale organised vortex motion is therefore strongly needed. An account on recent developments in this field can be found in the proceedings of the latest NATO AGARD Wake Symposium (NATO 1996). In addition to this practical aspect, the counter-rotating vortex pair also represents one of the simplest flow configurations for the study of elementary vortex interactions, which can yield useful information for our understanding of the dynamics of more complex transitional or turbulent flows.

A prominent feature of this flow, leading to the decay of the pair, is a long-wavelength wavy instability, which can frequently be observed in the sky (see, e.g., the photographs shown in Van Dyke 1982). The first theoretical analysis of this phenomenon was made by Crow (1970). He showed that the mutual interaction of the two vor-

tices can lead to an amplification of sinusoidal displacement perturbations, whose axial wavelength is typically several times the initial vortex separation distance. The vortex displacements are symmetric with respect to the mid-plane between the two vortices, and they lie in planes inclined approximately  $45^\circ$  with respect to the line joining the vortices. The origin of this instability is linked to the balance between the stabilizing effect of self-induced rotation of the perturbations and the destabilizing influence of the strain field that each vortex induces at the location of its neighbour. A good description of this mechanism is given by Widnall, Bliss & Tsai (1974).

Observations of full-scale aircraft wakes indicate that, when the amplitude of the long-wavelength perturbation grows large enough so that the vortex cores touch, the pair breaks up into an array of vortex rings via a cross-linking, or reconnection, of vorticity. Precise analyses of this interesting phenomenon, which involves a change in the topology of the vortex lines, have mainly been achieved by numerical simulations, the experimental results available so far being rather qualitative (see the review by Kida & Takaoka 1994). In the present investigation, we obtain quantitative results concerning vortex reconnection, as well as the late stages of the long-wavelength instability.

Motivated by Crow's (1970) work, Widnall *et al.* (1974) and Tsai & Widnall (1976) proposed a second mechanism for instability in flows with strained concentrated vortices, of which the counter-rotating vortex pair is one example. It involves more complex perturbations leading to internal deformations of the vortex cores; their axial wavelength scales on the vortex core diameter and is typically less than the initial separation of the pair. As for the Crow instability, no detailed observations or measurements concerning this short-wave instability in controlled laboratory experiments can be found in the literature.

## EXPERIMENTAL SET-UP AND TECHNIQUES

In our experiments, vortex pairs were generated in a water tank at the sharpened parallel edges of two flat plates, hinged on one side to a common base and moved in a prescribed symmetric way by a computer-controlled step mo-



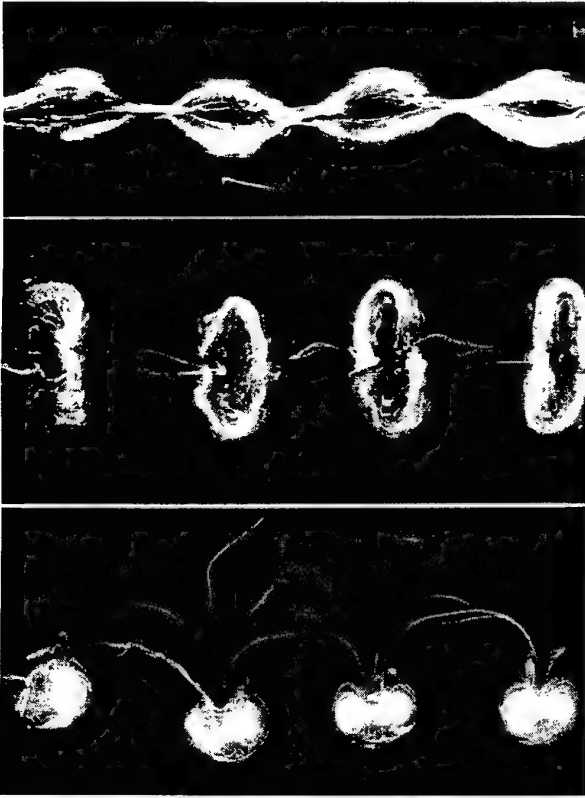


Figure 1: Visualization of the large-scale vortex pair instability for  $Re = 1450$ ,  $a/b = 0.23$ , and  $\lambda/b = 5.4$ . Top: front view at  $t^* = 5.3$ , the pair is moving towards the observer. Middle and bottom: simultaneous front and side views at  $t^* = 9.3$ . In the latter image the vortices move down.

tor. The vortices are typically separated by a distance of 2–3 cm, and their length is approximately 170 cm. This high aspect ratio of the pair is necessary to minimize the influence of end effects that spread rapidly into the central part of the flow. Visualization is achieved using fluorescent dye, illuminated by laser light. The vortex pair characteristics, i.e. the circulation  $\Gamma$ , the core radius  $a$ , and the vortex spacing  $b$ , are found from flow field measurements using Digital Particle Image Velocimetry (DPIV). The initial distribution of vorticity was found to be approximately Gaussian, and values of  $a/b$  are typically in the range 0.20–0.25. Other measurements concerning the spatial structure and the growth rates of the instability were obtained from image analysis of flow visualizations recorded on video. The Reynolds number is based on the initial vortex circulation ( $Re = \Gamma_0/\nu$ ,  $\nu$ : kinematic viscosity), and lies in the range 1000–3000 in this study. More details about the experimental conditions are given in Lewke & Williamson (1997a,b).

## LARGE-SCALE INSTABILITY AND RE-CONNECTION

The dye visualizations in Fig. 1 shows the general features of the large-scale instability observed for all Reynolds numbers in a counter-rotating vortex pair. It leads to a growing waviness of the initially straight and parallel vortices, which is symmetric with respect to the central plane of the pair and has an axial wavelength of several times the vortex separation (Fig. 1 top). Simultaneous views from two perpendicular directions show that the plane of the wavy perturbation is inclined by approximately  $45^\circ$  with respect to the plane of the initial vortex pair, confirming

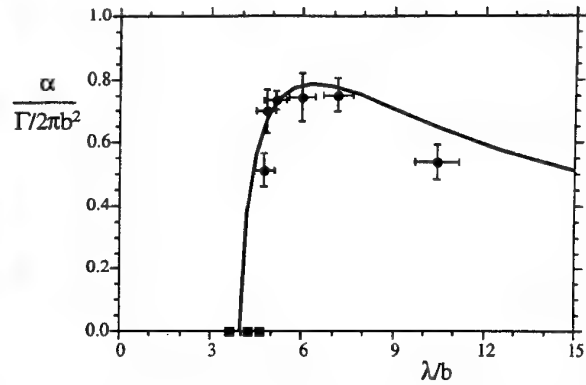


Figure 2: Growth rate of the Crow instability as function of axial wavelength. Round symbols represent experimental measurements made in the range  $1500 < Re < 2500$ . The instability could not be forced at wavelengths marked by a square symbol. The line shows the theoretical prediction for  $a/b = 0.25$ , which is representative for all experiments.

Crow's (1970) theoretical prediction. The amplitude of the waves continues to increase until the cores of the vortices touch and cross-link to form an array of three-dimensional vortex rings. Figure 1 (top) shows the flow shortly before the end of the reconnection process. At later times, the rings elongate into oval vortices, seen in Fig. 1 (middle and bottom) from two directions. The side view reveals that the rings are linked by thin strands of dyed fluid. The oval rings exhibit a well-known oscillatory behaviour (Lim & Nickels 1995), due to their varying curvature; they remain very energetic until they reach the bottom of the water tank. It is worth noting that, despite the significant change in the vortex geometry and topology, the average translation (or descent) speed of the vortices remains practically unchanged during and after the reconnection.

Here and in the following, time  $t$  is measured from the start of the plate motion, and non-dimensionalized by the time it takes the fully developed initial vortex pair to move one vortex spacing  $b$ :

$$t^* = t \frac{\Gamma_0}{2\pi b^2}. \quad (1)$$

The linear growth rate of the instability was measured for different axial wavelengths  $\lambda$ , which could be imposed on the flow using a slight modulation of the vortex-generating plate edges. This method had the additional advantage of controlling the phase of the wavy perturbation along the axial direction. Therefore, the vortex centers could be visualized simultaneously by two laser light sheets placed precisely in the planes of maximum and minimum separation, yielding the perturbation amplitude as a function of time. The measured growth rates are shown in Fig. 2. They are compared to the theoretical prediction that can be derived from the work of Crow (1970) and Widnall *et al.* (1971) for the present case. This prediction involves precise information about the initial velocity profiles of the vortices, which, in our case, were obtained by DPIV measurements. Fig. 2 shows good agreement between theory and experiment.

The reconnection process was also studied in detail using visualizations and velocity measurements in the reconnection plane, i.e. the plane perpendicular to the vortex axes where the vortices are closest to each other and where the “pinching-off” occurs. The minimum separation between the vortices decreases rapidly during the non-linear growth of the Crow instability (see Fig. 3), up to the time when the cores start to overlap and the cross-linking be-

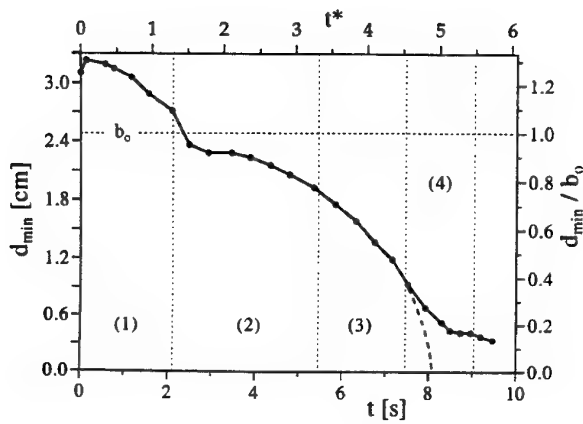


Figure 3: Evolution of the minimum vortex spacing at  $Re = 2560$ . The four stages leading to the formation of vortex rings are: (1) the vortex generation (moving plates), (2) the linear and (3) non-linear growth of the Crow instability, and (4) overlapping cores and reconnection.

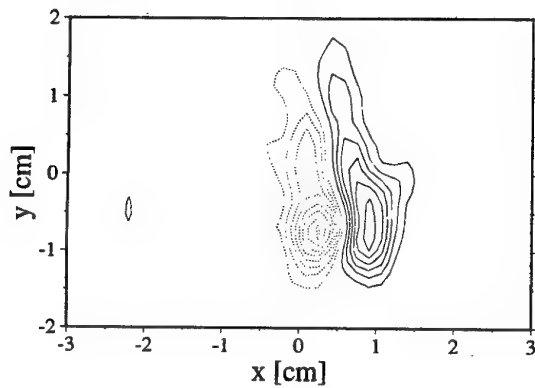


Figure 4: Contours of axial vorticity  $\omega_z$  in the reconnection plane at  $Re = 2340$  and  $t^* = 5.2$ . The pair is moving down. Contours are separated by  $\Delta\omega_z = 1.85 (\Gamma_0/2\pi b^2)$ .

gins. During this process, the distance between the vortex centers remains approximately constant at about 15% of the initial spacing, whereas the distribution of vorticity changes quite drastically. Fig. 4 shows the axial vorticity in the reconnection plane at the same (non-dimensional) time as in Fig. 1 (top). The measurements show that the initially more or less axisymmetric vortices flatten out during reconnection and develop a tail.

From vorticity distributions like in Fig. 4 one can determine the time-dependent circulation around each vortex in the reconnection plane. The result is given in Fig. 5. After the initial vortex formation (plate motion ends at  $t^* = 1.3$ ), the circulation remains approximately constant. During the cross-linking process, it decreases, first slowly, but then quite rapidly, until it reaches a level of about 10% of the initial vortex circulation. It then continues to decrease, but much slower, and the vorticity distribution recovers its approximately circular shape. These measurements confirm that the dye filaments in Fig. 1 that link the vortex rings at late times correspond indeed to threads of vorticity which still contain a noticeable fraction of the initial circulation.

Following Melander & Hussain (1989), one can use the circulation history to define a characteristic reconnection time (see Fig. 5), which, in our experiments is found to be approximately  $t_{rc} = 1$ .

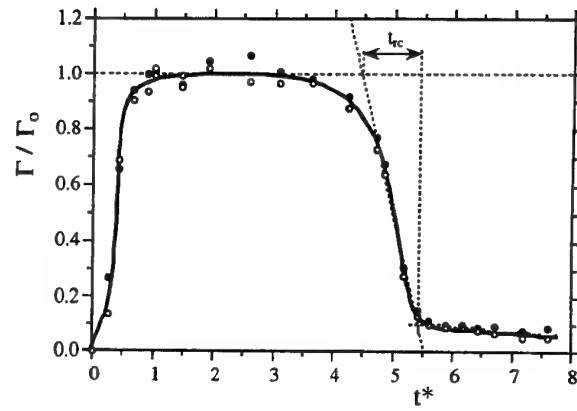


Figure 5: Evolution of the circulation in the reconnection plane at  $Re = 2340$ , and definition of the reconnection time. Results for left and right vortex are represented by different symbols.

In their numerical simulations, Melander & Hussain (1989), as well as Shelley *et al.* (1993), used as initial condition a perturbed vortex pair which is very close to the flow developing as a result of the Crow instability. Their results concerning vorticity distributions and circulation are qualitatively similar and are confirmed by our experimental measurements.

## SMALL-SCALE INSTABILITY AND TRANSITION

At higher Reynolds numbers, a second instability develops in the vortex pair at the same time as the Crow instability, but it has an axial wavelength of less than one vortex separation. The close-up visualization of the vortex pair in Fig. 6 shows the general features of this short-wavelength instability. The corresponding perturbation has a much more complicated spatial structure than the sinusoidal displacement of the long-wavelength instability. From Fig. 6 it is clear that it involves a modification of the internal structure of the vortex cores. Although the vortex centers, marked by bright dye filaments, are again perturbed into a wavy shape, one observes the existence, in each vortex, of a dye layer which remains unchanged. Inside and outside of this invariant stream tube, fluid is displaced in opposite radial directions. Simultaneous visualizations from two perpendicular directions reveal that the sinusoidal displacements of the vortex centers again lie in planes inclined by  $45^\circ$  with respect to the plane of the pair, i.e. they are oriented in the direction of the mutually induced strain in the vortex cores.

The above observations strongly suggest that this short-wavelength instability is linked to an instability occurring in flows with elliptical streamlines, which is a flow resulting from the interaction of a rotational flow and a plane strain. In the present case, it is found in the cores of the vortices. From theoretical studies treating this phenomenon (Landman & Saffmann 1987, Waleffe 1990), one can deduce the following expression for the growth rate  $\sigma$  of the short-wavelength instability for the vortex-pair flow (Lewke & Williamson 1997a):

$$\frac{\sigma}{\Gamma/2\pi b^2} = \frac{9}{8} - \frac{32\pi^3}{Re (\lambda/b)^2}. \quad (2)$$

This relation shows that, for a given wavelength  $\lambda$ , the instability only occurs above a critical Reynolds number

$$Re_c = \frac{2^8 \pi^3}{9 (\lambda/b)^2} = \frac{16\pi^3}{9 (a/b)^2}. \quad (3)$$

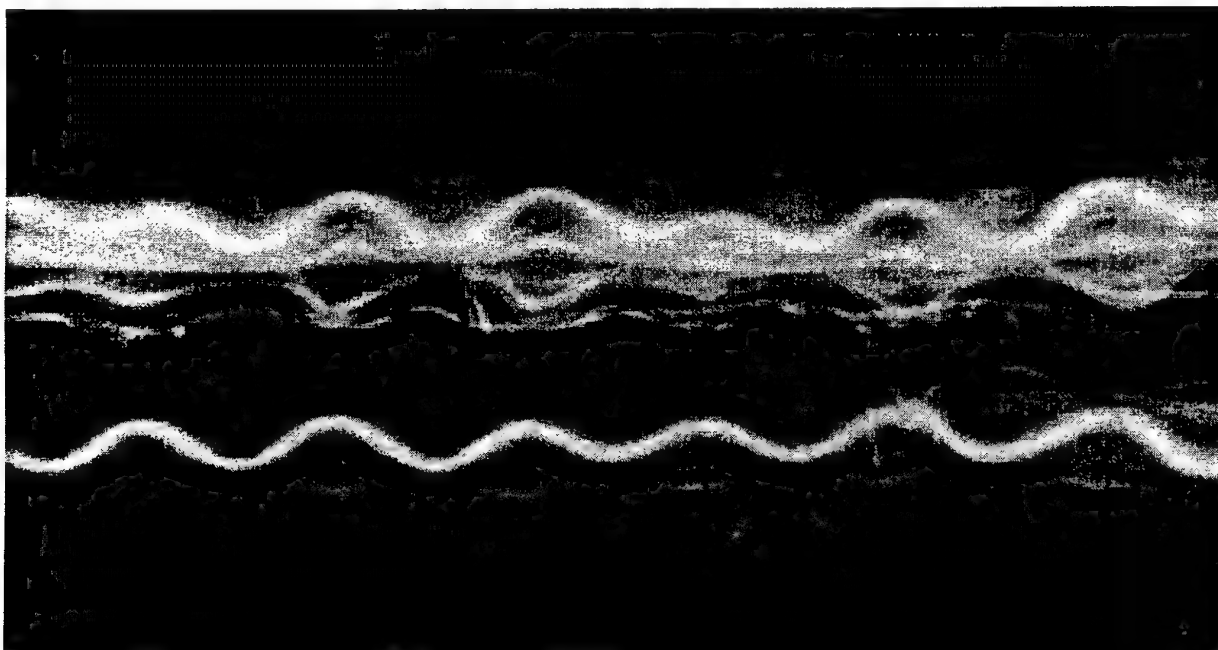


Figure 6: Close-up view of the short-wavelength perturbation, showing the characteristic internal deformations; as well as the distinct phase relationship between the two vortices.  $Re = 2750$ ,  $t^* = 6.2$ .

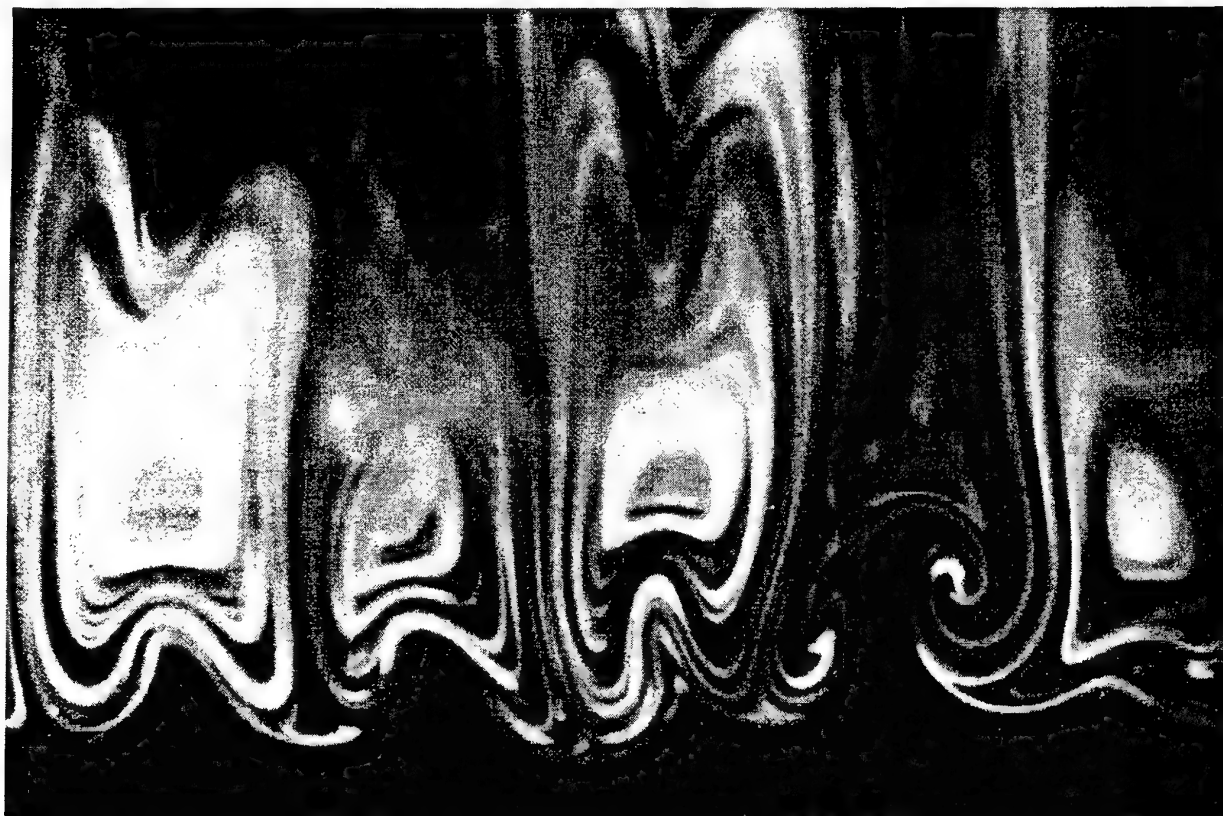


Figure 7: Side view of the "leading edge" secondary vortex pairs, visualized in the plane of symmetry of the primary pair. The field of view is about half as wide as in Fig. 6.

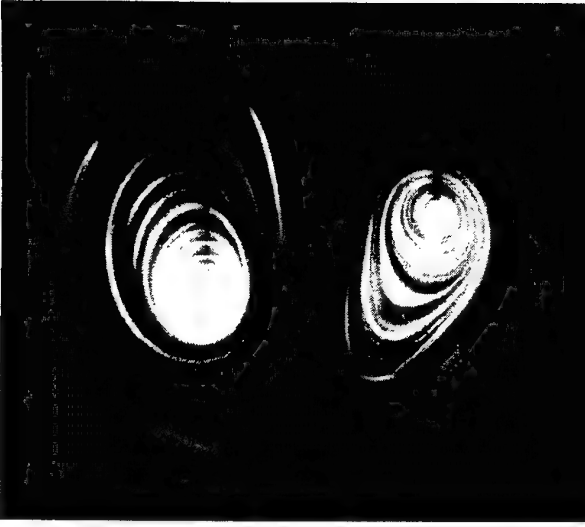


Figure 8: Visualization of the short-wave perturbation in a cross-cut plane.  $Re = 2400$ ,  $t^* = 7.5$ .

The second equality in Eq. 3 results from the fact that the most unstable wavelength scales on the size of the vortical region, i.e. on the vortex core size  $a$ . For the vortex pair, our measurements have shown that

$$\lambda/a \approx 4.0. \quad (4)$$

Quantitative measurements of the growth rate of the short-wavelength instability are difficult because of the simultaneous development of the long-wavelength Crow instability. However, some values were obtained in cases where the amplitude of the latter remained low for long times, and the agreement with Eq. 2 is satisfactory, considering the idealized nature of the theoretical flow.

In most cases, the effect of the Crow instability on the short-wave instability is a modulation of the growth of the latter. Equation 2 shows that the growth rate scales on the strain  $\Gamma/2\pi b^2$  induced by the vortices on each other. The Crow instability results in a periodic variation of the vortex separation distance, and therefore of the local strain. The short-wavelength instability therefore develops much faster at the locations where the large-scale instability brings the vortices closer together. This non-uniformity in the development of the small-scale instability has a strong effect on the late stages of the flow (see below).

An interesting and unexpected observation relates to the phase relationship between the short-wave perturbations on the two vortices. In the front view of Fig. 6, the vortex centers are, at each axial position, displaced in the same transverse direction. This means that the initial reflectional symmetry of the flow, with respect to the plane separating the vortices, is lost. It should be emphasized that no forcing of the phase was applied in the study of the short-wave instability; the initial vortex pair was completely uniform and the flow evolved freely. The symmetry breaking is further illustrated by the cross-sectional view in Fig. 8: the vortex center is displaced to the lower right in the left vortex, and to the upper right in the right one. DPIV measurements in the same plane (Fig. 9) confirm that this is not simply an effect caused by the dye visualization method. The maxima of vorticity are displaced in the same way as in Fig. 8, in close agreement with theoretical predictions for the elliptic instability of a strained vortex (Waleffe 1990). The observed phase relationship between the two vortices can be explained by a kinematic matching condition for the perturbations on each vortex (see Lewke & Williamson 1997a).

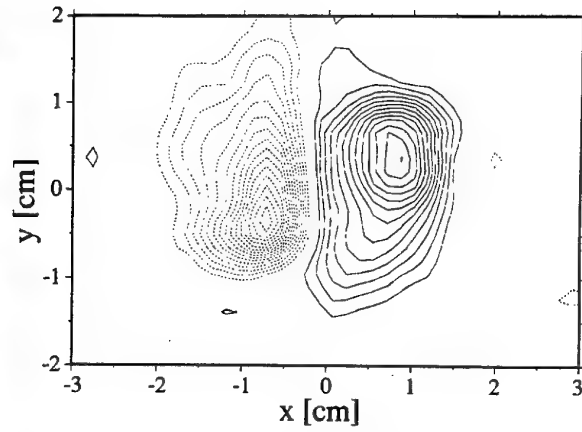


Figure 9: Contours of axial vorticity in a cross-cut plane.  $Re = 2660$ ,  $t^* = 7.1$ . Contours are separated by  $\Delta\omega_z = 0.86 (\Gamma_0/2\pi b^2)$ .

At later times, the complicated, but relatively well-organized regular short-wave perturbation breaks down. First signs of this can already be detected in Fig. 6: near the front edge of the pair, the parts of the fluid orbiting each vortex individually begin to mix. In a periodic interlocking way, tongues of fluid from one side are drawn around the respective other vortex.

This cross-over is a direct consequence of the internal vortex deformations. In Fig. 8, the center of rotation (maximum of vorticity) of the right vortex is displaced toward the front stagnation point, whereas the one on the left is pushed away. On the other hand, we know that the outer layers of each vortex are displaced in the opposite directions. This means that the outer parts of the right vortex are actually brought closer to the stagnation point and the approaching left vorticity maximum, which will eventually capture some of this fluid and pull it to the left. Once the tongues have crossed over, they are quickly pulled apart by the stagnation point flow and wrapped around the primary vortices. This results in the formation of an array of perpendicular counter-rotating secondary vortex pairs. Fig. 9 reveals that, with the fluid, axial vorticity is pulled to the left, which is subsequently tilted and stretched by the stagnation point strain. By this process the circulation of the primary vortices is reduced, which results in a decrease of the self-induced translation velocity of the pair by about 65%.

The development and intensity of the secondary vortices can be appreciated in the visualization in Fig. 7, where a light sheet illuminates the plane between the two primary vortices. This view shows that, for each wavelength of the short-wave instability, two secondary vortex pairs are generated at the lower edge.

The formation of the secondary vortex pairs has a strong effect on the further development of the overall flow. It was mentioned earlier that the elliptic instability develops faster where the Crow instability brings the vortices together. At these periodic locations along the axes, the organized structure of the primary vortices breaks down first, due to the presence of the perpendicular vortices in the outer layers. Flow visualization reveals that subsequently the primary vortices are stripped of these outer layers, which seem to move away from the locations of the initial break to leave only a skeleton of the initial vortex pair. This process may be seen as the result of an 'attempted' vortex reconnection (see preceding section). As a result of this axial motion, the dyed fluid concentrates in large clusters, whose internal motion is relatively unorganized, and whose spacing is dictated by the initial large-



Figure 10: Visualization of the late stages of the vortex pair under the combined influence of short- and long-wavelength instabilities. The flow is seen in side view, the pair moves down, and only one vortex is dyed.  $Re = 2700$ ,  $t^* = 11.2$ .

scale Crow instability (see Fig. 10). This late-time development of a vortex pair in the presence of both instabilities is quite different from the one of a pair with the Crow instability alone, where the vortices undergo a complete reconnection and most of the initial circulation is conserved in large-scale structures for very long times. For the case of combined long- and short-wavelength instabilities, Fig. 10 suggests that the interaction between the two phenomena enhances mixing and distributes the initial large-scale energy to the small scales much more effectively.

This qualitative observation from flow visualisation can be made more quantitative by measuring the actual vortex circulation. For this, sequences of DPIV measurements were made in a cross-plane of the vortices. In Fig. 11, the time-dependent vortex circulation is plotted for two cases: in a plane where the vortices approach each other, i.e. where the short-wavelength disturbance breaks down first and where the short-wave core displacement is maximal; and in a plane where the primary vortices move away from each other. Since the phase of the long-wavelength instability was not controlled in this series of experiments, several runs were necessary before the phase had the desired value in the measurement plane. At the location of approaching vortices, the primary circulation starts to decrease first. After a transition period it reaches a value of about 30% of the initial circulation. This circulation of the final skeleton pair is about three times the value of the corresponding threads in the case of a pure Crow instability. The drop of circulation in the other plane sets in a little delayed, but for large times it decreases to much lower values, confirming the absence of large coherent structures in the late stages of this flow.

## CONCLUSIONS

Our study provides the first clear demonstration of two distinct vortex pair instabilities in controlled experiments. Extensive flow visualization and quantitative velocity measurements using DPIV give detailed information about the development and long-term evolution of these instabilities. Concerning the long-wavelength instability, a complete comparison between experimental measurements and theoretical predictions of its initial growth rate was achieved for the first time, and the vortex reconnection phenomenon, occurring at later times, was characterized quantitatively. Regarding the short-wave instability, the spatial structure and symmetry of the associated perturbation was clearly demonstrated, suggesting that they are due to an elliptic instability of the vortex cores. The interaction between short- and long-wave instabilities lead to a more efficient destruction of the large-scale vortical structures than the action of the long-wavelength instability alone.

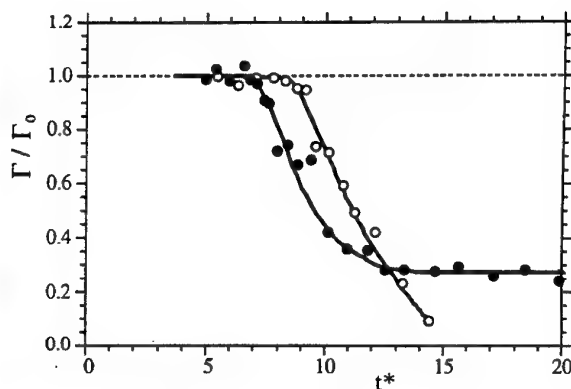


Figure 11: Evolution of the circulation in the presence of short-wavelength instability. Solid symbols represent data measured in a plane where the Crow instability brings the vortices closer together, open symbols show data in a plane where they are separated.  $Re = 2600$ .

This work is supported by the Office of Naval Research under Contract No. N00014-95-1-0332. TL acknowledges the financial support from the Deutsche Forschungsgemeinschaft, Grant No. Le 972/1-1.

## REFERENCES

- Crow, S.C., 1970, "Stability theory for a pair of trailing vortices", *AIAA J.*, Vol. 8, pp. 2172-2179.
- Kida, S., and Takaoka, M., 1994, "Vortex reconnection", *Annu. Rev. Fluid Mech.*, Vol. 26, pp. 168-189.
- Landman, M.J., and Saffman, P.G., 1987, "The three-dimensional instability of strained vortices in a viscous fluid", *Phys. Fluids*, Vol. 30, pp. 2339-2342.
- Leweke, T., and Williamson, C.H.K., 1997a, "Short-wavelength instability of a counter-rotating vortex pair", submitted to *J. Fluid Mech.*
- Leweke, T., and Williamson, C.H.K., 1997b, "Long-wavelength instability and reconnection of a vortex pair", submitted to *J. Fluid Mech.*
- Lim, T.T., and Nickels, T.B., 1995, "Vortex rings", in *Fluid Vortices*, S.I. Green, ed., Kluwer Academic Publishers, Dordrecht (NL), pp. 95-153.
- Melander, M. V., and Hussain, F., 1989, "Cross-linking of two antiparallel vortex tubes", *Phys. Fluids A*, Vol. 1, pp. 633-636.
- NATO, 1996, *The Characterization & Modification of Wakes from Lifting Vehicles in Fluids*, NATO-AGARD-CP-584.
- Shelley, M.J., Meiron, D.I., and Orszag, S.A., 1993, "Dynamical aspects of vortex reconnection of perturbed antiparallel vortex tubes", *J. Fluid Mech.*, Vol. 246, pp. 613-652.
- Tsai, C.-Y., and Widnall, S.E., 1976, "The stability of short waves on a straight vortex filament in a weak externally imposed strain field", *J. Fluid Mech.*, Vol. 73, pp. 721-733.
- Van Dyke, M., 1982, *An Album of Fluid Motion*, Parabolic Press, Stanford, p. 69.
- Waleffe, F., 1990, "On the three-dimensional instability of strained vortices", *Phys. Fluids A*, Vol. 2, pp. 76-80.
- Widnall, S.E., Bliss, D.B., and Tsai, C.-Y., 1974, "The instability of short waves on a vortex ring", *J. Fluid Mech.*, Vol. 66, pp. 35-47.
- Widnall, S.E., Bliss, D., and Zalay, A., 1971, "Theoretical and experimental study of the stability of a vortex pair", in *Aircraft Wake Turbulence and its Detection*, J.H. Olsen et al., ed., Plenum Press, New York, pp. 339-354.

# TRANSITION TO TURBULENCE IN THE WAKES OF AXISYMMETRICAL OBJECTS

Michel Provansal and Delphine Ormières

Institut de Recherche sur les Phénomènes Hors  
Equilibre U.M.R. 6594 du C.N.R.S. Centre de Saint-  
Jérôme - S 252 Marseille 13013 Cedex 20 FRANCE

## ABSTRACT

Experimental information concerning the first steps of transition to turbulence, i.e. change from steady to periodic regime, in the wake of a sphere is reported. First, visualizations precise the shape and the evolution of the downstream bubble and of shedding vortices behind the sphere. The Strouhal-Reynolds curve as well as variation of amplitude and phase of oscillations have been measured and compared to the prediction of Landau model. Similar results obtained for different axisymmetrical objects (cone and disk) have shown the general character of this bifurcation.

## INTRODUCTION

Despite its technological and practical importance, many fundamental aspects of the wake behind a sphere remain unknown. Among the difficulties are the full three-dimensional character of this flow and the way of holding the sphere. Recent studies of the Strouhal-Reynolds curve for a cylindrical configuration, which was thought two-dimensional and much simpler than the sphere case, exhibited scattered data larger than the inaccuracy of the measurements. This discrepancy (cf. Williamson 1996 for a review) has shown the need of a precise knowledge of the spatial structure. Moreover, its description by an oscillator model has lead to interpret and design new experiments. In the same spirit, on the sphere configuration, we have inquired the supercritical or subcritical nature of the bifurcation from steady to periodic regime. The lack of experimental information concerns mainly the convective or absolute character of this instability (cf. Huerre and Monkewitz 1990), the non-linear character of the unsteady fluctuations and the importance of spatial effects.

## EXPERIMENTAL SET-UP AND VISUALIZATIONS

Visualizations have been done in a vertical circular water (diameter 80 mm) channel (Fig. 1). The sphere of diameter 1 cm was kept by a thin upstream metallic pipe (diameter 2mm) which fed the one per cent diluted purple ink through three regularly disposed holes. In the Reynolds number range [150, 180],  $Re = Ud/\nu$ , determined here with a five per cent calibration, the bubble formed downstream of the sphere is no more axisymmetrical and one steady trail is visible. Between  $Re = 180$  and  $Re_c$ , two trails appear downstream of the bubble (Fig. 2a). These two trails oscillate above the critical Reynolds number and move downstream along helical lines. The periodic modulation is clearer and clearer when the Reynolds number is increased. Above  $Re = 310$ , vortex loops (Fig. 2b) are periodically shed from the location where the bubble has the smaller transverse size. This location has been changed in any orientation of the water channel by a very slight inclination of the upstream pipe. When the sphere is hold by four wires, dye visualizations have shown that the perturbation due to the wires is a stabilising effect which controls the wake in a precise orientation. This last result is in good agreement with the report of Sakamoto and Haniu (1995) concerning the shape of the wake of a sphere in a small upstream gradient of velocity.

Quantitative laser-Döppler and hot-wire anemometer measurements have been performed in an open-circuit low-speed wind-tunnel for the Reynolds number range [100, 400]. In the 1m long square test section (25x25cm), the free-stream turbulence level was close to 0.1% and flow uniformity better than 0.5% over 80 % of the tunnel width. The free stream velocity  $U$  was



measured by LDA in the centre of the tunnel cross-section, 50 mm upstream of the sphere. Corrections were made for blockage effects and the downstream evolution of  $U$  due to wind tunnel boundary layer growth. The kinematics viscosity  $\nu$  was deduced from the temperature measurement by a calibrated platinum resistance. The uncertainty upon the Reynolds number has been estimated as equal to 1%.

The sphere (diameter  $d = 10$  mm) was held by four thin metal wires (diameter 0.08 mm) which were fixed on a frame outside the test section tightened by weight, similarly to the experiments on the torus wake (Lewke and Provansal 1995). Although the body-to-wire diameter ratio was larger than 100, this configuration froze the spatial mode which gave the way to repetitive experiments. A laser-photo diode was used to monitor the vibration of the sphere. The amplitude of the measured oscillations remained well below the diameter of the sphere and were mainly longitudinal in the flow direction. If the frequency of vortex shedding was visible in the spectrum of vibrations, no influence of sphere oscillation on this frequency could be detected. In the following, cartesian co-ordinates ( $Ox, Oy, Oz$ ) will be used with the origin  $O$  at the centre of the sphere,  $Ox$  is the streamwise (horizontal) direction,  $Oz$  is the vertical one (up) and  $Oy$  the transverse horizontal one.

## RESULTS

Spectral analysis of the streamwise velocity fluctuations shows the appearance of a peak and its harmonics (Fig. 3a) when the Reynolds number is above the critical value  $Re_c = 273$ . Below the threshold (Fig. 3b), it was impossible to detect any precise peak in the spectrum. Above the periodic range, the velocity fluctuations are irregular and their spectrum exhibits a low frequency and its non-linear interaction with the Strouhal frequency (Fig. 3c). We have plotted (Fig. 4.) the energy of the velocity fluctuations  $u_x'^2$  as function of the Reynolds number for the same location of the measurement point. Near the threshold, this variation is linear. This behaviour is in agreement with the Landau model which has been often used to interpret the transition from steady to periodic flow as a supercritical bifurcation [Landau and Lifschitz 1971, Guyon et al 1987]. The extrapolation of zero energy provides a quantitative criterion for an accurate determination of the critical Reynolds number. This value  $Re_c$  is independent of the position of the probe. Moreover, it was impossible to detect any kind of hysteresis when increasing and decreasing the upstream velocity (at least at one per cent of accuracy). Our value is close to the previous determination, 300, by Sakamoto and Haniu (1995) deduced from visualization and in good agreement with experimental data, between 270 and 290, reported by Magarvey and Bishop (1961) and E. Levi (1980). The older values of Taneda (1956) are in a wider range [200, 300]. We believe that small inhomogeneities and perturbation in the upstream flow due to method of visualization can be responsible for a slight change in the value of the threshold. Furthermore, our critical Reynolds number is pretty close to the threshold 277 deduced by Natarajan and Acrivos (1993), from numerical simulations, and in the range [250-280] predicted from direct numerical simulation by Tomboulides et al (1993).

In both these studies, the authors have inquired the existence of a Landau -Hopf bifurcation for the transition from steady to periodic flow. Our measurements of the energy of velocity fluctuation  $u_x'^2$  confirm the validity of this scenario.

The vortex shedding frequency  $f$  was determined by spectral analysis, and used to calculate the Strouhal number  $St = fd/U$  and the Roshko number  $Ro = fd^2/\nu$  (Fig. 5&6). The periodic regime is limited to a narrow Reynolds number range, [275,320], where the Strouhal number satisfies the relation:

$$St = A.Re^{-1} + B + C.Re$$

$$\text{with } A = -48.2 \quad B = 0.391 \quad C = -3.6.10^{-4}$$

Our fit is in agreement (within 3%) with the renewed values of Sakamoto and Haniu (1995) and we confirm that their previous values (1990) were based on a wrong estimation of the Reynolds number. We do underline the fact that, in the periodic regime, the difference between measurements should be within the margin of uncertainty in the determination of the Strouhal and Reynolds numbers, i.e. around two per cent, except if different spatial modes are excited in different configurations. The large dispersion on data collected in the literature (cf. figure 3 of Sakamoto et al, 1990) is probably due to the lack of focused investigation of the periodic regime in wide number Reynolds range studies.

In the periodic regime, preliminary measurements in different points,  $5d$  downstream on the streamwise axis and along a circle of radius  $d$  in the transverse plane, have shown a strong spatial variation of this amplitude. We have determined the variation of the energy (Fig. 7) along the axis of the flow. Immediately behind the sphere, the energy increases linearly from the zero boundary value on the wall. This behaviour is coherent with the growth of a convective unstable perturbation in the near-wake where the transverse mean-velocity profile exhibits a strong deficit. Non-linear effects play the dominant rôle in the Landau model; thus, it is not surprising that the saturation occurs further downstream. The decrease of the amplitude of fluctuation along the downstream direction is due to the evolution of the velocity profile and to the diffusion of vorticity. This curve is quite similar to the report by Weisfreid et al (1993) about the variation of velocity fluctuation in the wake of a cylinder. We have also investigated the location of the maximum in amplitude (Fig. 8) along the streamwise direction and its variation with the Reynolds number. There is a small variation from six diameters near the threshold to four diameters at the upper Reynolds value of the periodic range. This behaviour is quite different from the measurement by Weisfreid et al (1993) of a downstream evolution of the maximum of amplitude in the wake of a cylinder, near the threshold leading to a scaling of  $x_{max}/d$  as function of  $(Re - Re_c)^{-\alpha}$ .

Different investigations have been done on the cone and disk configurations: results are similar to the case of the sphere. The axial symmetry of the wake is broken before the transition from steady to periodic flow occurs. Because the periodic regime range is wider for the cone case, it will be worthwhile to go further on this configuration.

## CONCLUSION

Measurements of the velocity amplitude and spectral analysis as well as visualizations give a more precise description of the different regimes occurring when one increases the Reynolds number from subcritical value. Though an extrinsic velocity gradient controls the spatial organisation of the wake, the shedding of horseshoe vortices appear as an intrinsic phenomenon common to different configurations.

This work has benefited from the Financial Support of "Action Incitative en Mécanique des Fluides" D.S.P.T.8 Ministère Français de l'Enseignement Supérieur et de la Recherche and Groupement de Recherche C.N.R.S. "Mécanique des Fluides Active".

## REFERENCES

- Guyon E., Hulin J.P., Petit L., 1987, *Hydrodynamique Physique*, Intersciences Edition.
- Huerre P., Monkewitz P.A., 1990, *Ann. Rev. Fluid Mech.* vol. 22 pp. 473.
- Landau L., Lifchitz E., 1976, *Mécanique des Fluides*. Moscow: Mir.
- Levi E., 1980, *J.Eng. Mech.* pp. 659-676.
- Leweke T. and Provansal M., 1995, *J. Fluid Mech.* vol 288, pp. 265-310.
- Magarvey R. and Bishop R.L., 1961, *Can. J. Phys.* vol 39 pp. 1418-1422.
- Natarajan and Acrivos, 1993, *J.F.M.* vol 254, pp. 323-344.
- Provansal M., 1996, 6th European Turbulence Conference, Lausanne.
- Rivet J.P., 1989, Thèse Université de Nice
- Sakamoto H. and Haniu H., 1990, *Transactions of the A.S.M.E.* vol 112, pp. 386-392.
- Sakamoto H. and Haniu H., 1995, *J.F.M.* vol 287, pp. 151.
- Taneda S., 1956, *J. of the Physical Society of Japan.* vol 11, N° 10, pp. 1104-08.
- Tomboulidès A.G., Orszag S., Karniadakis G.E., 1993, 31st Aerospace Sciences Meeting A.I.A.A. Reno.
- Wesfreid J.E., Goujon-Durand S., and Zielinska B.J.A., 1993, Global mode of the streamwise velocity in wake.
- Williamson C.H.K., 1996, *Ann. Rev. Fluid Mech.* vol. 28 pp. 477-539.

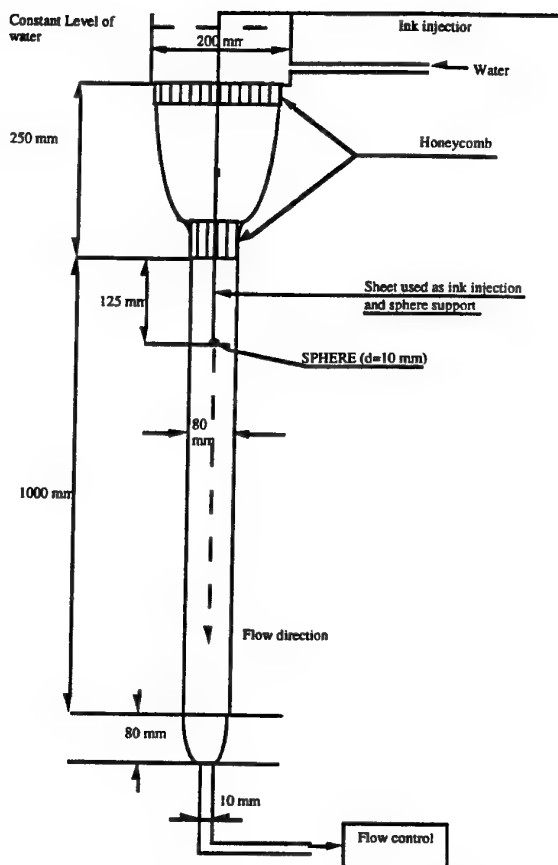


FIG.1 EXPERIMENTAL SET-UP:  
CHANNEL WATER

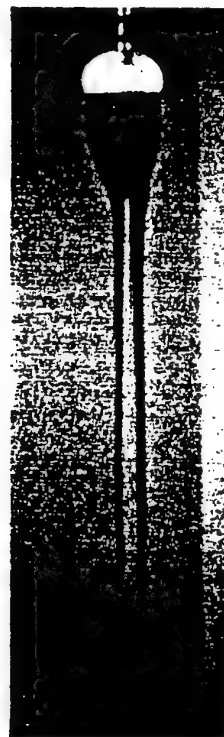


FIG.2A VISUALIZATION RE = 180





FIG.2B VISUALIZATION RE = 330

energy (arbitrary units)

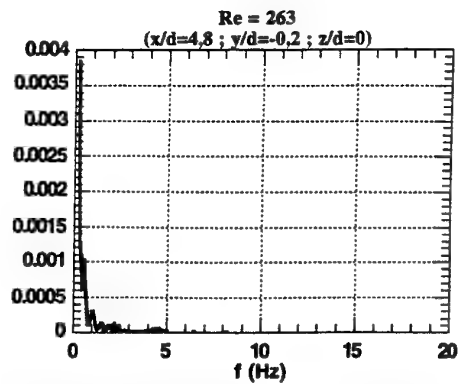


FIG.3B SPECTRUM OF VELOCITY FLUCTUATIONS (SUBCRITICAL REGIME)

energy (arbitrary units)

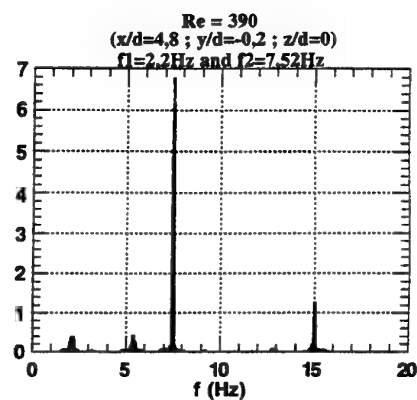


FIG.3C SPECTRUM OF VELOCITY FLUCTUATIONS (IRREGULAR REGIME)

energy (arbitrary units)

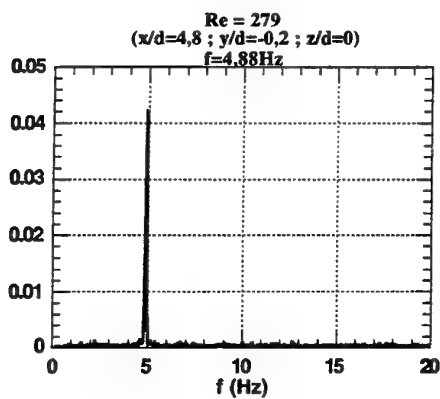


FIG.3A SPECTRUM OF VELOCITY FLUCTUATIONS (PERIODIC REGIME)

energy (arbitrary units)

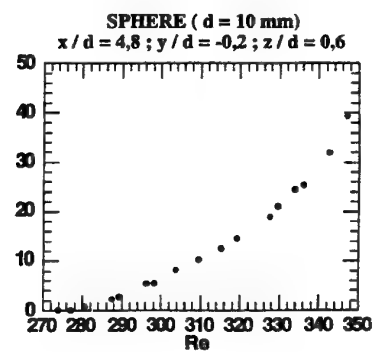
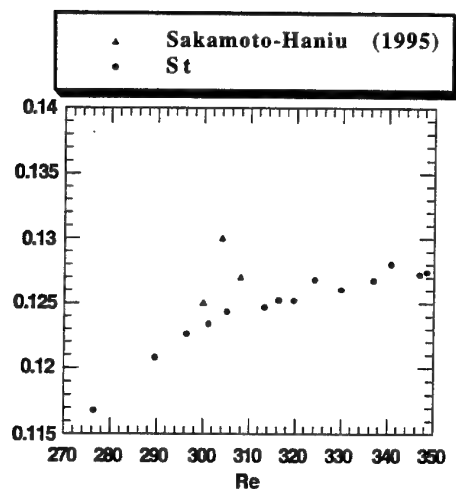
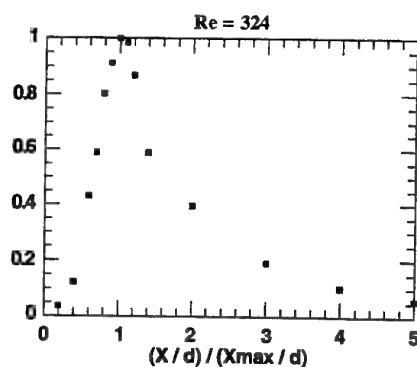


FIG.4 ENERGY VERSUS REYNOLDS NUMBER



**FIG.5 STROUHAL-REYNOLDS NUMBERS CURVE**  
(SPHERE  $d=10$  mm)

renormalized energy



**FIG.7 VARIATION OF THE ENERGY**  
( $E / E_{max}$ ) ALONG THE FLOW AXIS  
( $d=10$  mm,  $X_{max}=40$  mm)

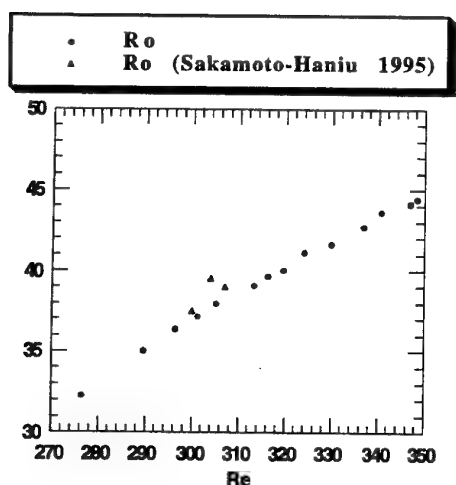


**FIG.6 ROSHKO-REYNOLDS NUMBERS CURVE** ( $Ro = f d^2 / \nu$ )  
(SPHERE  $d=10$  mm)

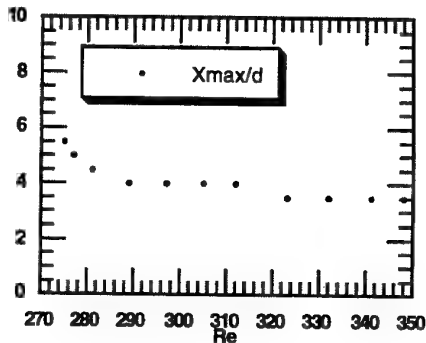


**FIG.8 VARIATION OF THE STREAMWISE LOCATION OF THE MAXIMUM OF ENERGY WITH THE REYNOLDS NUMBER**

# DISTINCT MODES OF SMALL-SCALE INSTABILITY IN WAKE TRANSITION

C.H.K. Williamson and T. Leweke\*

Mechanical and Aerospace Engineering  
Upson Hall, Cornell University  
Ithaca, NY 14853, USA.

\* presently at:

IRPHE CNRS / Universite Aix-Marseille  
12 Avenue general Leclerc  
F-13003 Marseille, France.

## ABSTRACT

It is now well-known that the wake transition regime for a circular cylinder involves two modes of small-scale three-dimensional instability (modes "A" and "B"), depending on the regime of Reynolds number ( $Re$ ), although we now seek to understand the physical origins of these instabilities. Each mode is quite distinct in lengthscale and in symmetry, and thus one might expect, and indeed we find, that the two different modes A and B scale on different physical features of the flow.

Mode A has a larger spanwise wavelength of around 3-4 diameters, and scales on the larger physical structure in the flow, namely the *primary vortex core*. We present evidence to suggest that the wavelength for Mode A is the result of an "elliptic instability" in the near-wake vortex cores. The subsequent nonlinear growth of streamwise vortex loops is due to a feedback from one vortex to the next. This mode gives an *out-of-phase* streamwise vortex pattern.

In contrast, mode B instability has a distinctly smaller wavelength (1 diameter) which scales on the smaller physical structure in the flow, namely the *braid shear layer*. It is quite distinct from studies of other shear flows, in that it depends on the reverse flow of the bluff-body wake; the presence of a fully-formed streamwise vortex system, brought upstream from a previous half cycle, in proximity to the newly-evolving braid shear layer, leads to an *in-phase* streamwise vortex array, in strong analogy with the "Mode 1" of Meiburg & Lasheras (1988) for a forced unseparated wake.

## INTRODUCTION

A number of investigations have recently been concerned with the general problem of the development of three-dimensional structure in turbulent shear flows, and with the corresponding implications for mixing in such flows. Over the past eight years, there has been a surge of activity in wake flows from analytical, computational and

experimental approaches. Many of these developments have been described comprehensively in a review in Williamson (1996a). It is perhaps not surprising that the bulk of the recent experimental developments have been studied at low Reynolds numbers, where one avoids the confusion between the length scales based on the transition of the wake, the separating shear layers, and the boundary layer, each of which successively becomes unstable as one increases Reynolds numbers. A number of new flow phenomena have been discovered at low Reynolds numbers in the wake transition regime. In particular, we are concerned with two distinct modes of small-scale secondary instability in the near wake, defined as modes A and B (Williamson, 1988). Their distinction, in terms of their symmetries, their wavelength, and their physical bases, are to be described in our presentation. There appears to be a vital interest in these wake modes at the present time, as evidenced by the collection of energetic talks presented at the recent *American Physical Society Meeting* in 1996. The physical origins of the two instabilities have implications to turbulence transition of concentrated vortices in other shear flows.

The first definition of wake flow regimes based on measurements of velocity fluctuation, spectra and frequency was given by Roshko (1954). He found a "stable" (periodic) laminar vortex shedding regime for  $Re=40-150$ , a transition regime in the range  $Re=150-300$ , with an "irregular" regime for  $Re=300-10,000+$ , where velocity fluctuations showed distinct irregularities. Similar regimes were confirmed by Bloor (1964). A surge of recent work has shed further light on phenomena occurring in these regimes and their precise Reynolds number ranges. However, only surprisingly few investigations have focused on the wake transition regime (in the approximate range,  $Re=190 - 260$ ). Of these studies, we presently have almost no understanding of the physical origin of the three-dimensional small-scale instabilities that are fundamental to wake transition.

## INSTABILITY MODES A AND B.

The existence of two different modes of 3-D shedding in wake transition (modes "A" and "B"), involving vortex loops and streamwise vortex pairs, was briefly presented by Williamson (1988) and more comprehensively studied in Williamson (1996b). In mode "A", which is clearly evident in the range  $Re=194$  to  $240$ , the primary vortices deform in a wavy fashion along their length. The spanwise length scale of these vortex loops is around 3 to 4 diameters, and is a function of  $Re$  (see Williamson (1996b)). Visualisation of such structure is shown in Figure 1, near the start of motion, and illustrates the incipience of the vortex core instability. As the flow progresses, the instability grows from one cycle to the next, resulting in the local spanwise formation of vortex loops, which become stretched into streamwise vortex pairs in the braid regions between the primary Karman vortices. At higher Reynolds numbers, around  $Re=240$  and above, finer-scale streamwise vortex pairs are formed, comprising a Mode B instability. In this case the primary vortex deformation is more spanwise-uniform than for mode A, and the streamwise vortex structure has a markedly smaller spanwise wavelength of around one diameter, or  $1/5$  of a primary wavelength.

The marked disparity in spanwise wavelength and visual appearance, between modes A and B secondary instability, corresponds with the fact that the modes are due to two distinct instabilities. The (long-wavelength) mode A scales on the larger physical feature in the wake flow, namely the *primary vortex cores*. Evidence will be presented below that suggests this mode A instability is due to an *elliptic instability* in the vortex cores. Predictions of spanwise instability wavelength, based on elliptic instability, yields a lengthscale close to what is measured for the mode A vortex core instability. Mode A has an *out-of-phase* symmetry of the streamwise vortices, as shown in Figure 2. In Figure 3, we show a schematic of the streamwise vortex symmetries corresponding to modes A and B, and which are now confirmed in several numerical simulations (see Thompson et al., 1994; Zhang et al., 1995; Noack, private communication; Barkley & Henderson, 1996).

The (short-wavelength) mode B, contrary to mode A, scales on the smaller physical length scale, namely the *"braid" shear layer*. If mode A represents an instability akin to that found for free shear layers (Bernal & Roshko, 1986), with comparable lengthscales, then mode B is altogether a different instability, which is strongly influenced by the existence of the reverse flow region in the bluff-body wake. The disturbances imposed on the forming braid (separating shear layer), by a pre-existing set of rolled-up streamwise vortices, sets the preferred locations of the new braid vortices, giving a specific symmetry quite distinct from mode A; mode B has an *in-phase* symmetry for the streamwise vortex pattern, which is analogous with Meiburg & Lasheras' mode 1 streamwise vortex pattern for a forced "unseparated" wake from a splitter plate. These symmetries are shown in Figures 2 and 3.

## ELLIPTIC INSTABILITY OF WAKE VORTICES: MODE A.

It is known from experimental observations that Mode A is caused by an instability in the vortex cores. We shall present in this paper further evidence to suggest that this mode is a manifestation of an "elliptic instability" of the vortex cores.

An elliptic instability represents the exponential growth of inertial waves in a flow with uniform vorticity and uniform strain, which occurs in the case when the perturbation vorticity remains aligned with the principal stretching axis (a result made clear by Waleffe, 1990; see also Pierrehumbert (1986), Bayly (1986), Landman & Saffman (1987)). A flow with elliptical streamlines is generated when there is uniform rotation  $\gamma$  (which is half the vorticity  $=\omega/2$ ), and uniform strain rate  $\epsilon$ , and corresponds interestingly to where the principal stretching axis is oriented at  $45^\circ$  relative to the major axes of the elliptic streamlines. The aspect ratio (or eccentricity) of these ellipses is given by  $\alpha = \sqrt{(\gamma + \epsilon) / (\gamma - \epsilon)}$ , and the ratio of strain to vorticity is defined by  $\beta = (\epsilon/\gamma) = (2\epsilon/\omega)$ . Elliptic flow ensues if  $0 < \beta < 1$ . The value  $\beta=0$  refers to circular rotating flow, while  $\beta=1$  refers to planar Couette flow. In the case of near-wake vortex II, to be discussed in Figure 4, we find

$$\omega D/U \approx 3 \quad \epsilon D/U \approx 0.9 \quad \alpha \approx 2 \quad (1)$$

and the lengthscale (minor diameter) of the vortex region is of order  $1D$ . The values of strain and vorticity yield a value of  $\beta \approx 0.6$ .

We now observe the two-dimensional base flow of the cylinder wake from direct numerical simulation (data kindly made available by Helene Persillon, while working with us at Cornell). Observations of streamlines using the standard reference frame whereby the observer is fixed with the cylinder, as in Figure 4(a), shows very little information regarding the near wake vortices. If, however, we subtract the velocity of the centre of vortex II (the lower (anticlockwise) vortex in Figure 4(b)) from the whole flow field, then the resulting streamlines indicate a striking elliptic vortex. It is distinctly relevant that the roughly elliptical streamlines region in Figure 4 (b) is associated with a principal stretching axis, shown in (c), which is aligned at  $45^\circ$  to the major axis of the elliptic near-wake vortex, consistent with the conditions to promote "elliptic" instability. Of course, one is concerned in the real flow with a finite vortical region, not unbounded as in the above theories. However, it is clear from Lewke and Williamson (1997) that the *internal* experimental instabilities in a finite vortex (in that case one vortex of a pair) are remarkably close to the form predicted from the unbounded elliptic theory. Indeed, one also finds that for small strain the theoretical form of the instability perturbation internal to a bounded vortex is precisely the same as found for the unbounded elliptic theories, in the vicinity of the vortex centre.

Waleffe has superposed the unstable inertial-wave Fourier modes to construct localized solutions, which for small strain, consist of Bessel function expressions for the

perturbation velocities and vorticities. We have plotted the streamlines of the flow resulting from the growth of such unstable localised solutions, in Figure 5. The structure of the perturbation results in a displacement of the central axis of rotation in the direction of the principal stretching axis, but whose displacement is modulated along the span in a wavy fashion. An "invariant surface" exists around the vortex axis which remains undeformed, and corresponds with the zero of the Bessel function type of disturbance. The inner and outer vortex layers (relative to this invariant surface) are displaced in opposite radial directions. The spanwise wavelength of instability depends on the eccentricity ( $\alpha$ ) of the elliptic flow. For small strain this modulation has a wavelength close to twice the diameter of the invariant streamline. The elliptic instability theory shows that the spanwise waviness of the core of an elliptical vortex region will be in the direction of principal stretching, which from the numerical simulation in Figure 4(c), will be in the upstream-downstream direction (horizontal).

It appears that the key to deducing a reasonable estimate for the spanwise wavelength and growth rate in the present problem is the inclusion of viscosity in the analysis, which has been mentioned by several authors, although it is the paper of Landman & Saffman (1987) which explicitly demonstrates the effects on the instability of including viscosity. Including viscosity in this problem has two essential effects. First, it yields a cut-off lengthscale below which the elliptic instability is not unstable. Secondly, and quite significantly, the effect of viscosity leads us to predict that the largest wavelength, in a given problem, is the most unstable. Landman & Saffman (1987) show usefully, in their Figure 1, the maximum inviscid growth rate  $\sigma_{\text{INVISID}}$  versus the strain parameter  $\beta$ , and demonstrate that there is a maximum instability for  $\beta = 0.8$ . This is relevant to the near wake vortices, where  $\beta \approx 0.6$  typically, suggesting a rapid growth of instability in our case. When viscosity is included in the analysis, as in Figure 2 of Landman & Saffman, in the form of Ekman number,  $E$ , versus  $\beta$  ( $E = 2\pi\nu k_0^2/\gamma$ , where  $\nu$ =viscosity,  $k_0$ =lengthscale of the instability), then it is immediately seen that for a given  $\beta$ , the growth rate increases as one decreases Ekman number, with a maximum growth rate for the inviscid case (horizontal axis in their Figure 2). This trend is seen clearly from the total growth rate expression below (noting that  $\theta$  is the minimum angle of the wave vector, which actually precesses around an elliptic path):

$$\sigma_{\text{TOTAL}} = \sigma_{\text{INVISID}} + \sigma_{\text{VISCOUS}} \quad (2)$$

$$\sigma_{\text{TOTAL}} = \sigma_{\text{INVISID}} - \nu k_0^2 [1 + 1/2(\alpha^2 - 1)\sin^2\theta] \quad (3)$$

or normalised with respect to wake quantities,

$$(\sigma_{\text{TOTAL}} D/U) = (\sigma_{\text{INV}} D/U) - 4\pi^2 \text{Re}^{-1} (\lambda/D)^{-1} [1 + 1/2(\alpha^2 - 1)\sin^2\theta] \quad (4)$$

The total growth rate increases, for a given value of viscosity (or  $\text{Re}$ ) and given ellipse aspect ratio ( $\alpha$ ), as the lengthscale of the instability increases. In a finite size

vortex, the most unstable wave will be the largest that can be fit into the vortex. Although this is not a surprising result, since one expects that the smallest waves will be the most damped by viscosity, it is nevertheless a significant point. In fact, we shall find below that one expects discrete relationships to match the perturbation dimensions with the vortex dimensions, so that the effect of viscosity is to select the largest of these possible perturbation dimensions within the vortical flow regions.

The second principal effect of viscosity is the imposition of a viscous cut-off length, below which the elliptic flow is stable. One can think in terms of a critical Ekman number,  $E^*$  for marginal stability, for which  $\sigma(E^*, \beta) = 0$ . The existence of a short wavelength viscous cut-off means that the region of elliptical flow must be larger than a minimum size for the instability to manifest itself. The instability lengthscale  $L$  ( $=2a$ , see Figure 5) in the x-y plane perpendicular to the rotation axis, is given:

$$L = 2\pi / [k_0 \sqrt{(1 + \alpha^2) \sin \theta_m}] \quad (5)$$

We can deduce the critical length  $L^*$  from the relation  $E^* = E(L^*)$ , and using equations (4,14):

$$L^* = 4\pi^{3/2} D [\sin^2\theta_m (\omega D/U) \text{Re} (1 + \alpha^2) E^*]^{-1/2} \approx 0.5D \quad (6)$$

The elliptical region II in Figure 4 therefore has a size which is  $L \approx D > L^*$ , which is large enough to support unstable disturbances. (The parameter  $\theta_m$  is the most unstable wave vector angle, which for  $\beta=0.6$  in Landman & Saffman, Figure 3, gives  $\theta_m \approx 53^\circ$ ). With the non-dimensional parameters for the vortex in the near wake varying only slowly with Reynolds number, the critical length varies roughly as  $\text{Re}^{-1/2}$ , in other words it decreases with  $\text{Re}$ . The fact that at  $\text{Re} \approx 200$ , the critical length is of the same order of magnitude as the sizes of the different elliptical regions in the two-dimensional wake is consistent with the fact that the critical  $\text{Re}$  for the three-dimensional transition is found in this range.

It is important to consider the growth rate for the near wake vortices, and its relation to the characteristic time of the periodic base flow. The vortices of Figure 4 retain their elliptic shape for at least one shedding period,  $T = D/US$ , where the Strouhal number  $S$  equals roughly 0.2. We can deduce that  $E \approx (1/4)E^*$ , using the fact that the elliptical region is about twice the critical length  $L^*$ , and that  $E \sim L^{-2}$ . From the Figure 2 of Landman & Saffman, for our case  $\beta=0.6$ , we find  $E^* \approx 1$ , so that  $E \approx 1/4$ , and the non-dimensional growth rate is thus  $2\sigma/\omega = 0.25$ . Normalising with respect to wake parameters gives,  $\sigma D/U \approx 0.375$ . Using the fact that  $S \approx 0.2$ , we find  $\sigma T \approx 2$ , which means that the instability will grow by a factor 10, while instability conditions are favourable. Considering the feedback mechanism found in Williamson (1996b), whereby the waviness grows from one primary vortex to the next until vortex loops are formed, the elliptic instability discussed above is suggested to be

sufficient to trigger ultimately the appearance of the nonlinear mode A instability.

One of the significant results to come from the theoretical analysis of elliptic instability in the near wake, is the prediction of spanwise wavelength. The spanwise wavelength is related to the magnitude  $k_0$  of the three-dimensional wave vector by  $\lambda = 2\pi / (k_0 \cos\theta_m)$ , see Landman & Saffman (1986), which when divided by  $L$  using equation (5), gives a value for the "aspect ratio of the instability", from which we find:

$$\lambda = L \sqrt{(1 + \alpha^2) \tan \theta_m} = 3D \quad (7)$$

This final result appears to be in reasonable agreement with the measured spanwise wavelengths for mode A instability (Williamson, 1996b), although (as pointed out by Maurice Rossi), it is perhaps too precise in the light of the fact that one does not know precisely how the length scale of the perturbation,  $L$ , will relate to the diameter of the finite-size vortex. In the case of the Rankine-type uniform vortex, Kelvin (1880) shows that the first zero of a neutrally-stable Bessel function disturbance has a diameter  $D_{INV}$  (defining the invariant surface) which is 0.6 of the vortex diameter, for his first mode of vortex inertial waves. It is nevertheless clear that the major problem for the present case, is that one does not know the precise relationship between  $D_{INV}$  and the cross-sectional dimensions of a *distributed* vortex. However, our very recent experimental results from elliptic instability in vortex pairs (Leweke & Williamson, 1997), clearly yields such a relationship, from which it appears one may reasonably predict instability lengthscales in the present wake problem.

We shall firstly use a more precise estimate for the cross-sectional length scale of the disturbance ( $D_{INV}$ ), rather than the order of magnitude value, taken from Landman & Saffman, in equation (5). The wave vector of the disturbance is given by:

$$\mathbf{k} = k_0 [\sin\theta, \alpha \sin\theta, \cos\theta] \quad (8)$$

Using the result from Waleffe (1990, page 80) for the first zero of the Bessel function disturbance, we have an estimate for the dimensions of the invariant streamline ( $D_{INV}$ ) in the minor axis (Y) direction:

$$(k_0 \alpha \sin\theta) D_{INV} = 5.47 \quad (9)$$

giving an aspect ratio of the disturbance given as:

$$(\lambda / D_{INV}) = (\pi / 2.735) \alpha \tan\theta = 3.05 \quad (10)$$

using previous values for the variables ( $\alpha, \theta$ ). In the study of elliptic instability of an interacting vortex pair of Leweke & Williamson (1997), it has been found possible to measure *directly* the value of  $D_{INV}$ , as well as to undertake velocity field measurements, which yield accurately the diameter at which the circumferential velocity is a maximum ( $D_{MAX}$ ). We find the ratio as:

$$(D_{INV} / D_{MAX}) = 0.92 \quad (11)$$

It is found that the vortex velocity distribution within the vortex pair problem and in the near wake are similar (in both cases, the vorticity in the minor axis direction is well represented by a Gaussian distribution), suggesting that one might expect a similar relationship will hold for the near wake vortex II (of figure 4). This vortex has an aspect ratio of close to 2, and with a minor axis diameter ( $D_{MAX}$ ):

$$(D_{MAX} / D) = 1.03 \quad (12)$$

We are now in a position to make a more precise prediction of spanwise wavelength of elliptic instability by combining equations (10, 11 and 12), as follows:

$$(\lambda / D) = (\lambda / D_{INV}) (D_{INV} / D_{MAX}) (D_{MAX} / D) = 2.9 \quad (13)$$

although in view of the obvious assumptions made, the best we can predict is that :

$$(\lambda / D) \approx 3 \quad (14)$$

again giving a predicted wavelength in good agreement with those values measured for the mode A instability. In this case, however, we have a firm footing upon which to base the relation between instability lengthscale and the vortex dimensions. In summary, we may suggest, from both experimental and analytical work, that the spanwise lengthscale of mode A is indeed caused by an elliptic instability of the primary vortex core in the strain field of neighbouring structures in the near wake.

## 10. Conclusions.

The marked disparity in spanwise wavelength, and visual appearance, between modes A and B instability corresponds with the fact that the modes are due to two distinct instabilities. The two instabilities scale on the two principal physical features of the wake flow. The (long-wavelength) mode A scales on the larger physical feature in the wake flow, namely the *primary vortex cores*, and is suggested to be due to an elliptic instability in these vortices. Predictions of spanwise instability wavelength, based on theory applied to the elliptic near wake vortices, yield values which are in reasonable agreement with measured wavelengths. We utilise, in this prediction, the discrete relationship between the instability dimensions and finite (Gaussian) vortex dimensions, that is found experimentally for the vortex-pair instability problem (Leweke & Williamson, 1997). It does seem probable that such elliptic instability, in the wake vortex and in the vortex pair problem, is generic to all shear flows, under conditions where the coherent vortex size exceeds the viscous cut-off scale.

## Acknowledgements:

The support from the Ocean Engineering Division of the O.N.R., monitored by Tom Swain, is gratefully acknowledged. (O.N.R. Contracts No. N00014-94-1-1197 and N00014-95-1-0332). Thomas Leweke acknowledges the financial support from the Deutsche Forschungsgemeinschaft, Grant No. Le 972/1-1.

## REFERENCES

- Barkley, D. & Henderson, R.D. 1996 Three-dimensional Floquet stability analysis of the wake of a circular cylinder. *J. Fluid Mech.* **322**, 215.
- Bayly, B.J. 1986 Three-dimensional instability of elliptical flow. *Phys. Rev. Lett.* **57**, 2160.
- Bernal, L.P. & Roshko, A. 1986 Streamwise vortex structure in plane mixing layers. *J. Fluid Mech.* **170**, 499.
- Bloor, M.S. 1964 The transition to turbulence in the wake of a circular cylinder. *J. Fluid Mech.* **19**, 290.
- Landman, M.J. & Saffman, P.G. 1987 The three-dimensional instability of strained vortices in a viscous fluid. *Phys. Fluids*, **30**, 2339.
- Leweke, T. & Williamson, C.H.K. 1997 Short wavelength instability of a counter-rotating vortex pair. Accepted for *J. Fluid Mech.*
- Meiburg, E. & Lasheras, J.C. 1988 Experimental and numerical investigation of the three-dimensional transition in plane wakes. *J. Fluid Mech.* **190**, 1.
- Pierrehumbert, R. 1986 A universal short wave instability of two-dimensional eddies in an inviscid fluid. *Phys. Rev. Lett.* **57**, 2157.
- Roshko, A. 1954 On the development of turbulent wakes from vortex streets. *NACA Report* 1191.
- Thompson, M., Hourigan, K. & Sheridan, J. 1994 Three-dimensional instabilities in the cylinder wake. *Int. Colloq. on Jets, Wakes and Shear Layers*, Melbourne, Australia, 18-20 April, 1994.
- Waleffe, F. 1990 On the three-dimensional instability of strained vortices. *Phys. Fluids*, **A2**, 76.
- Williamson, C.H.K. 1988 The existence of two stages in the transition to three-dimensionality of a cylinder wake. *Phys. Fluids*, **31**, 3165.
- Williamson, C.H.K. 1996a Vortex dynamics in the cylinder wake. *Ann. Rev. Fluid Mech.* **28**, 477.
- Williamson, C.H.K. 1996b Three-dimensional wake transition *J. Fluid Mech.* **328**, 345.
- Zhang, H., Fey, U., Noack, B.R., Koenig, M. & Eckelmann, H. 1995 On the transition of the cylinder wake. *Phys. Fluids*, **7**, 1.



Figure 1. Visualisation of the near wake structure behind a circular cylinder at  $Re=200$ , near the start of motion and the incipience of the long-wavelength instability of mode A. This mode corresponds with an instability of the vortex cores, and is quite distinct from the mode B.

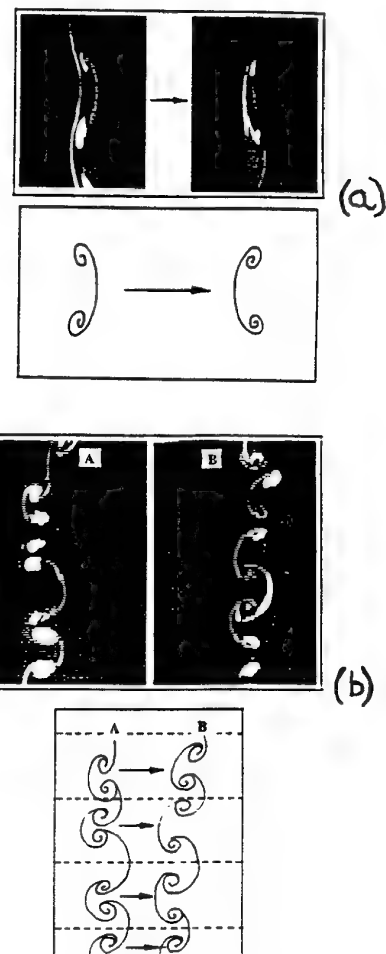


Figure 2. Video evidence of streamwise vortex symmetries for modes A and B.

(a) Mode A : Out-of-phase symmetry;

(b) Mode B: In-phase symmetry

Each pair of photographs, taken half a cycle apart, is extracted from video images looking upstream from behind the cylinder, and normal to a planar light sheet in the near wake. The passage of fluorescent dye (washed off the body) passing through the sheet shows the distinct symmetries of the streamwise vortices.



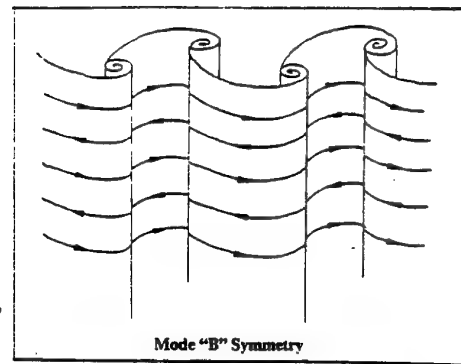
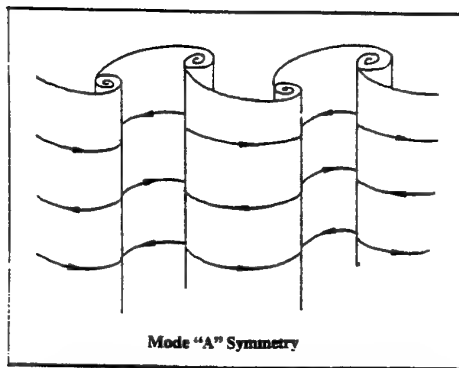
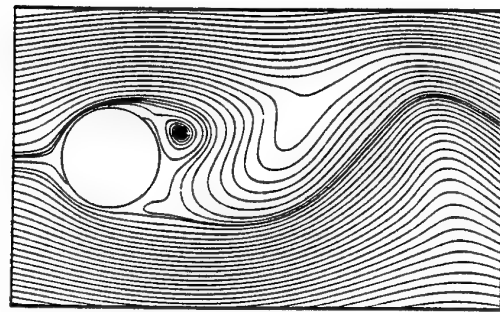
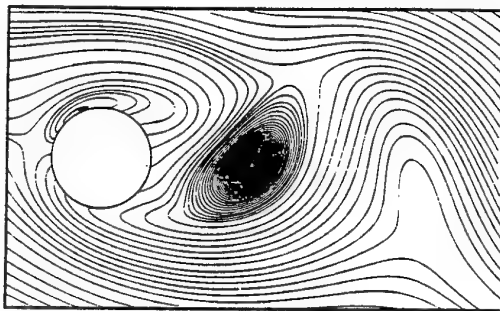


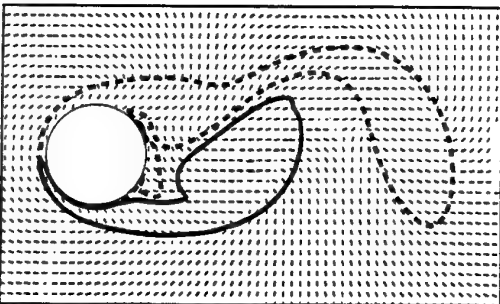
**Figure 3** Symmetry diagrams of modes A and B. Mode A, of large spanwise wavelength, comprises an out-of-phase sequence of streamwise vortices from one braid to the next one. Mode B, of small spanwise wavelength, comprises an in-phase arrangement.



(a)



(b)



(c)

**Figure 4.** Streamlines for Reynolds number of 200, found from DNS computations. In (a) we show the streamlines which suggest very little information regarding the near wake vortices. If, however, we subtract the velocity of the centre of vortex II from the whole flow field, the result in (b) shows a striking elliptic vortex from which we can make measurements. In (c) we show the directions of the principal stretching axes throughout the near-wake flow. This plot is made from data kindly supplied by H. Persillon (Cornell) and M. Braza

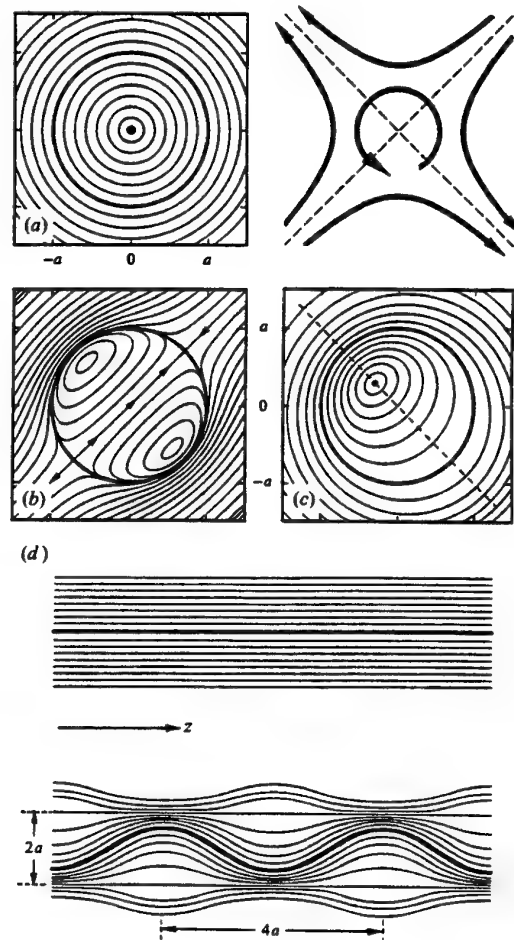


**FIGURE 5.** Effect of the elliptic instability on the streamlines of an elliptical flow, shown for the asymptotic limit of vanishing strain rate. (a) Base flow (solid rotation). (b) Perturbation due to the inertial waves (from Waleffe 1990). Its characteristic lengthscale (wavelength) in this plane is  $2a$ . (c) The resultant total flow, indicating clearly the displacement of the centre of rotation out along the principal stretching axis. The bold line shows the streamline that remains unchanged under the perturbation (described as the 'invariant streamline' in the text), and the dashed line indicates the plane that is shown in (d). (d) Schematic representation of the vortex deformation in the plane of maximum strain rate. The upper diagram shows the initial situation with concentric vortex layers. The lower diagram shows the vortex perturbed by the elliptic instability. The thick line shows the centre of rotation, which is periodically displaced along the stretching axes with wavelength  $\lambda$ .



# ABSOLUTE INSTABILITY OF ROUND HEATED AIR JET

**A. Bogusławski, S. Drobnik**  
Institute of Thermal Machinery  
Technical University of Częstochowa  
Al. Armii Krajowej 21  
Częstochowa, 42-200  
Poland

## 1. INTRODUCTION

During the last decade the problem of absolute/global instability in various flow types was investigated experimentally and numerically with the use of spatio-temporal stability theory by many authors. The phenomenon was first observed in variable density axi-symmetric jets by Sreenivasan et al. (1989), Monkewitz et al. (1990) and Riva (1991). Sreenivasan et al. (1989), Riva (1991) and Kyle & Sreenivasan (1993) studied helium-air mixtures jet stability while Monkewitz et al. (1990) and Russ & Strykowski (1993) considered heated air jet. The measurements carried out in these two flow types show significant discrepancy of the critical density ratio at which the global mode appears i.e. in helium-air round jet the critical density ratio determined by Kyle & Sreenivasan (1989) was equal 0.6 while Monkewitz et al. (1990) found the value 0.73 in the hot air jet. This discrepancy could be attributed to the different transition mechanism observed in these two flow types. In hot air jet Monkewitz et al. (1990) observed two unstable modes. The first one called Mode I, is supposed to be linked to the break-up of coherent vortices characterised by Strouhal number 0.3. This Mode I appears when the density ratio is lower than 0.73. Below the density ratio equal 0.6 the Mode II becomes visible which, according to Monkewitz et al. (1989), is supposed to be a result of Widnall instability of the axi-symmetric vortex rings characterized by Strouhal number 0.45. On the other hand Kyle & Sreenivasan observed in the air-helium jet only Mode II (called in their paper the oscillating mode) that appears at the density ratio 0.6. A discrepancy, even more significant, was also observed in the stability of plane density jets. Yu and Monkewitz (1993) determined the critical density ratio at which the oscillating mode appears in heated air plane jet as equal to 0.9, while Raynal et al. (1996) found the value 0.7 in the air-helium plane jet. An interesting question that could be posed now is why variable density jets behave differently depending on the medium applied. The possible explanation was proposed

by Raynal et al. (1996) in stability calculations carried out for the case of the plane variable density jet. His results show that amplification rate of the oscillations can be influenced significantly by a relative displacement of the velocity and density profiles. It turns out that the maximum of the amplification rate or the most unstable conditions are reached when the inflexion points of the density and velocity profiles coincide. It is supposed to be the case of the hot air jet while in helium-air jet the velocity and density profiles are mutually shifted that results in a jet stabilization. It seems that the problem of the parameters governing the transition conditions from convective to absolute instability remains still open question. The preliminary experimental study, reported in the paper, is aimed at the investigations of the parameters controlling the oscillating mode development in heated air round jet with a special reference to a relative shift of the velocity and density profiles. Furthermore, the present study has been performed for boundary layer thickness range which was not investigated so far with full particulars.

## 2. EXPERIMENTAL SET-UP AND APPARATUS

The experimental set-up prepared for the heated air jet stability study consists of the cubic equation nozzle with no straight tail and the surface contraction ratio equal to 144. The settling chamber was filled by the plate of the porous bronze and the layer of turbulence screens. The setup is equipped with air jet heaters of power about 3 kW and the nozzle heater of power about 1 kW. The set-up allows to obtain Reynolds number up to 30000 for the density ration in the range 0.5 - 1. Turbulence level at the centerline of the nozzle exit plane determined by a hot wire measurements was about 0.3%. Fig.1. shows velocity profile and turbulence level in the laminar boundary layer at the nozzle exit without any extension tube. It is believed that the set-up with the independent nozzle heater will allow to control thermal boundary layer characteristics and in this way to move

the density profile in reference to velocity one providing the explanation to what extent the jet stability can be controlled by this parameter. Another important factor controlling the oscillating mode is the boundary layer thickness. Fig.2 presents the momentum thickness normalized by the nozzle outlet diameter as a function of Reynolds number compared with the data obtained by Kyle & Sreenivasan (1993) and Riva (1991). As can be seen the present set-up is characterized by thinner boundary layer thickness than the ones applied by other authors. The boundary layer thickness may easily be increased by the extension tubes that can be fitted at the jet outlet. The possibility to obtain a wide range of the  $\theta/D$  parameter may be important because of the presence of so called broadband mode observed by Kyle & Sreenivasan (1993) that is persistent even for very thin boundary layer when oscillating mode vanishes.

Near field pressure oscillations were measured by a sound level meter and analysed by the use of HP Spectral Analyser HP 3566A/3567A. During next steps of the experiment it is intended to study velocity field in the near field as well as in the region of side jets using the LDA system.

### 3. PRELIMINARY EXPERIMENTAL RESULTS

Fig.3 presents a microphone spectra measured for Reynolds number  $Re=9400$  at relatively low density ratio  $s=0.48$ . The 1/2 in. microphone was situated at  $x/D=0.67$  and  $r/D=1.3$ . The measurements were performed in two cases. The first one corresponds to the measurements performed without any extensions attached to the nozzle (Fig.3a) and the second case to the measurements performed with the extension tube of the length  $L/D = 3$ . Acoustic pressure in the first case seems to be dominated by a disturbance with a broadband spectral content characterized by Strouhal number  $St=0.46$ . When the extension tube  $L/D=3$  was attached to the nozzle two new peaks appeared besides the broadband disturbance (Fig. 3b). The broadband fluctuation was then characterized by Strouhal number  $St = 0.401$ , which seems to be in agreement with the observation of Kyle & Sreenivasan (1993) stating that Strouhal number of the fluctuations decreases with increasing boundary layer thickness. Two other sensitive frequency ranges visible in the spectrum at Fig.3b are more peaky and are characterized by Strouhal numbers  $St = 0.222$  and  $St = 0.566$  respectively.

Fig.4 presents the evolution of the sound pressure spectrum for various density ratios. For the cold jet (Fig. 4a) evidently no global oscillation of the sound pressure level can be observed. When the density ratio is decreased to  $s = 0.76$  strong oscillation appears at  $St=0.413$  (Fig. 4b) and this mode becomes more broadband when density ratio is decreasing (Fig. 4c, d and Fig. 3b).

For the density ratio  $s = 0.67$  two more peaks of acoustic pressure fluctuations appear at  $St = 0.225$  and  $St = 0.584$ . The first peak can may be interpreted as a subharmonic of the main mode of oscillations that indicates the presence of vortex pairing first noticed by Monkewitz et al. (1990). The amplitudes of both peaks are growing when density ratio is decreasing and on the contrary to the main oscillation these two modes do not become more broadband.

Comparison of these preliminary results with the experiment performed by Monkewitz et al. (1990) shows some important

discrepancies. First of all an oscillating mode seems to appear in the present experiment at higher density ratio  $s \approx 0.76$  while Monkewitz et al. (1990) measured the critical density ratio  $s \approx 0.73$ . Moreover the mode characterized by  $St \approx 0.4$ , called by Monkewitz et al. (1990) Mode II, appears first, just below the critical density ratio, while in the experiment of Monkewitz et al. this mode dominates for the density ratio  $0.47 \leq s \leq 55$ . On the other hand the Mode I observed by Monkewitz et al. which appears below the critical density ratio and dominates for  $s \geq 0.62$  was not found during present study.

### 4. CONCLUDING REMARKS

Preliminary experimental results of the study of the heated jet stability were presented. Spectra of the sound pressure level measured at the nozzle outlet with and without extension tube were discussed briefly. Without any extension tube, for the thinnest boundary layer, one broadband mode at  $St \approx 0.46$  was observed. When the extension tube was applied, making boundary layer thicker, the spectrum became more peaky for the density ratio  $s = 0.76$ , with fundamental peak at  $St = 0.413$ . Evolution of this spectrum for various density ratios was also discussed pointing out some discrepancies between the present results and previous experimental work in this field.

### 5. ACKNOWLEDGMENTS

The work was supported by the Polish State Committee for Scientific Research, Grant No. 7T07C05008 and by the Common Project No. 6413 supported by Polish State Committee for Scientific Research and CNRS.

### REFERENCES

- Kyle, D.M., Sreenivasan, K.R., 1993, "Instability and breakdown of a round variable-density jet", *J.Fluid Mech.*, 249, 619
- Monkewitz, P.A., Bechert, W.B., Barsikow, B., Lehman, B., 1990, "Self-excited oscillation and mixing in a heated round jet", *J.Fluid Mech.*, 213, 611
- Monkewitz, P.A., Lehman, B., Barsikow, B., Bechert, W.B., 1989, "The spreading of self-excited hot jets by side jets", *Phys.Fluids A*, 1(3)
- Raynal, L., Harion, J-L, Favre-Marinet, M., Binder, G., 1996, "The oscillatory instability of plane variable-density jets", *Phys. Fluids*, 8 (4)
- Riva, R., 1991, "Ecoulement de fluides inhomogenes: Stabilité des jets, transfert turbulent dans les couches limites", Ph.D. Thesis, INPG, Grenoble
- Russ, S., Strykowski, P.J., 1993, "Turbulent structure and entrainment in heated jets: The effect of initial conditions", *Phys. Fluids A* 5(12)
- Sreenivasan, K.R., Raghu, S., Kyle, D.M., 1989, "Absolute instability in variable density round jets", *Exp.Fluids* 7, 309
- Yu, M-H., Monkewitz, P.A., 1993, "Oscillations in the near field of a heated two-dimensional jet", *J.Fluid Mech.*, 255, 323

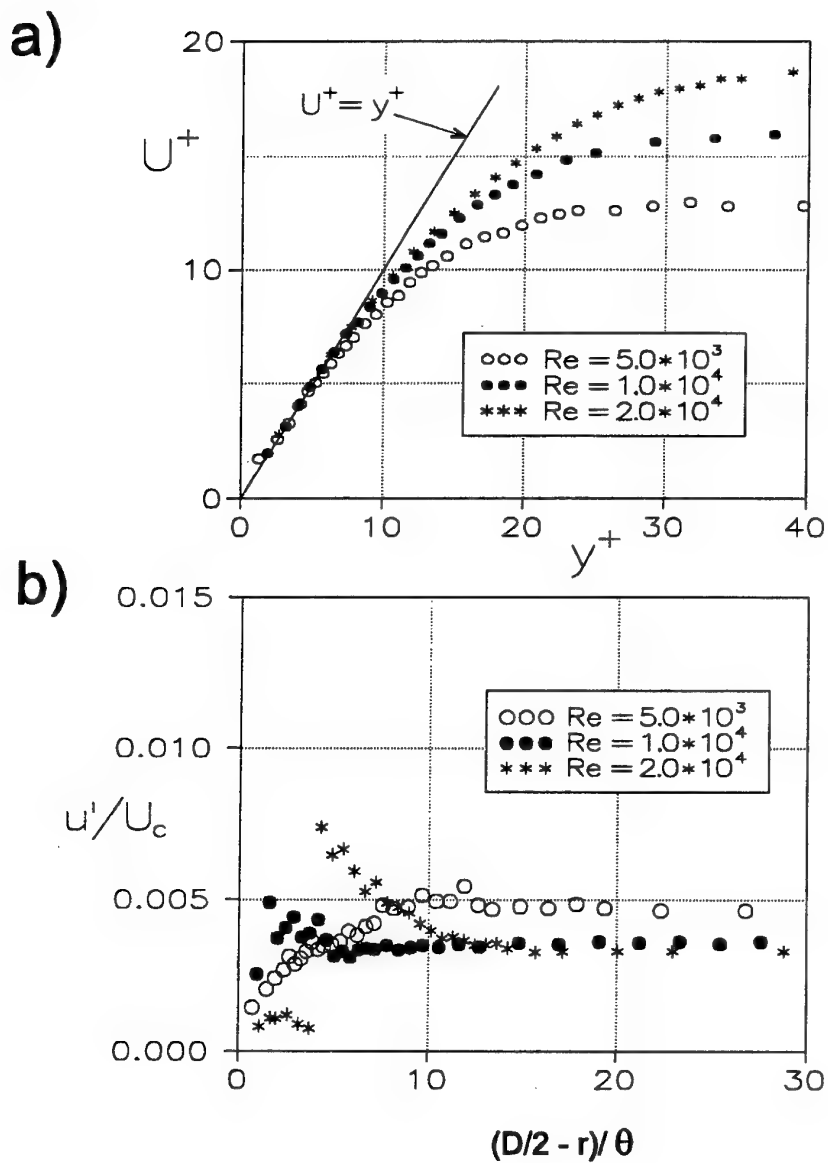


Fig.1. TIME-AVERAGED (a) AND FLUCTUATING (b) AXIAL VELOCITY PROFILE MEASURED AT THE NOZZLE EXIT WITHOUT ANY EXTENSION TUBE

- ■ ■ ■ Kyle & Sreenivasan -ASME nozzle
- ● ● ● Kyle & Sreenivasan - cubic equation nozzle
- △ △ △ △ Riva
- ▲ ▲ ▲ ▲ present results

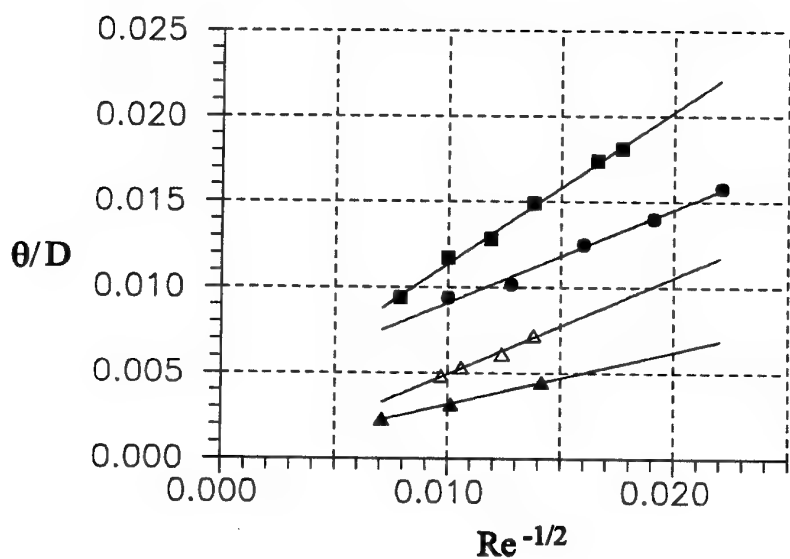


Fig.2. MOMENTUM THICKNESS AS A FUNCTION OF REYNOLDS NUMBER

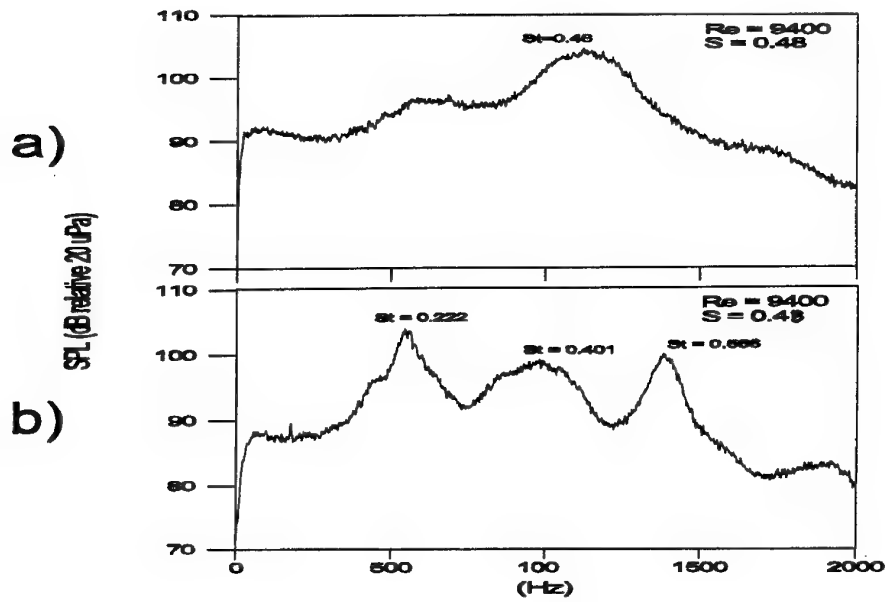


FIG.3. SOUND PRESSURE LEVEL SPECTRA MEASURED WITHOUT EXTENSION TUBE (a) AND WITH EXTENSION TUBE  $L/D=3$ , FOR THE DENSITY RATIO  $s=0.48$  AND  $Re = 9400$

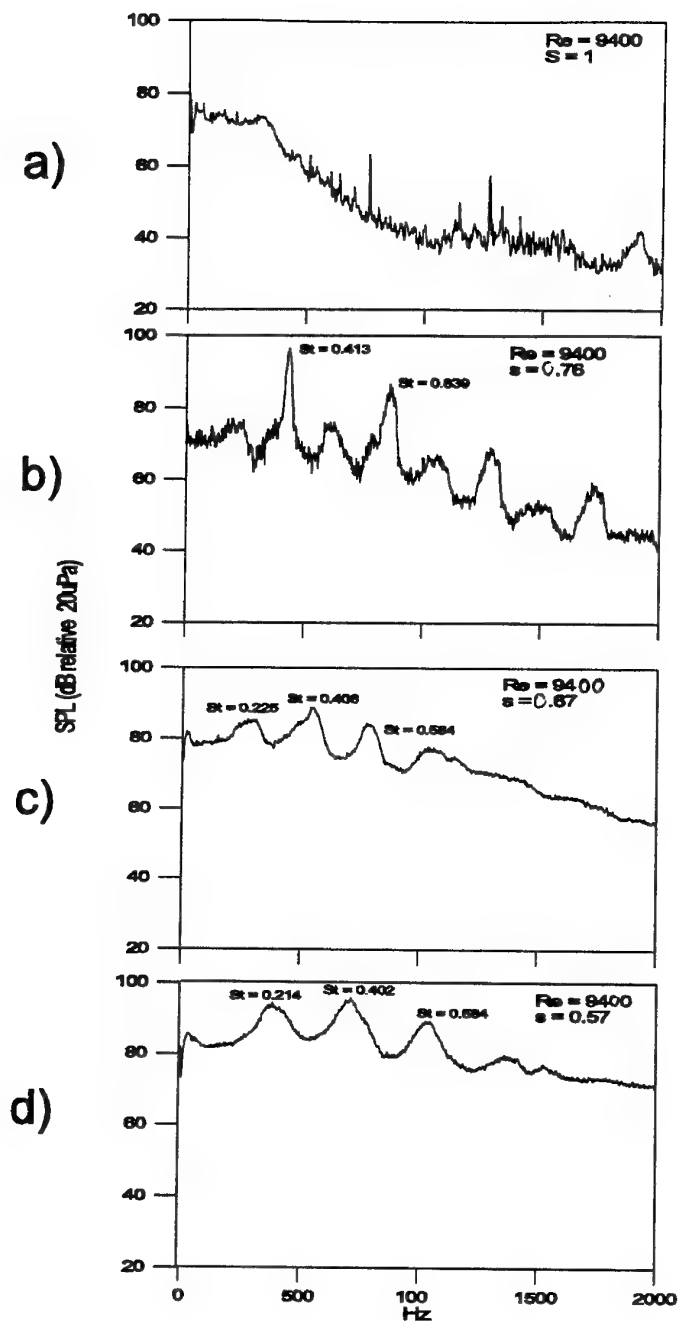


FIG.4. SOUND PRESSURE LEVEL SPECTRA MEASURED WITH THE EXTENSION TUBE  $L/D = 3$  FOR  $Re = 9400$  AND VARIOUS DENSITY RATIOS:  $s = 1$  (a),  $s = 0.76$  (b),  $s = 0.67$  (c) AND  $s = 0.57$  (d)

**Instability induced by a roughness**

**Kiyoaki Ono**

**Department of Mechanical Engineering**

**Nihon University**

**1-8 Kanda-Surugadai**

**Chiyoda, Tokyo 101**

**Japan**

**Tatsuo Motohashi**

**Department of Aerospace Engineering**

**Nihon University**

**7-24-1 Narashinodai**

**Funabashi, Chiba 274**

**Japan**

# Instability induced by a roughness

Kiyoaki Ono and Tatsuo Motohashi

## Abstract

Instability induced by an isolated roughness in a laminar boundary layer is investigated by both experimental and computational approaches. The roughness element is a small circular cylinder which is submerged in the boundary layer on a flat plate. The Reynolds number based on the uniform velocity and the roughness height is 700. The 3D Navier-Stokes equations are solved by the finite difference method. The Cartesian grid is overlaid on the cylindrical grid to get finer space resolution in the wake region. The experiment is conducted with a small wind tunnel. The longitudinal velocity component was measured using a hot-wire anemometer. The initial evolution of disturbed region is clearly depicted by the two methods. We found that the inflectional instability plays an essential role in the transition process behind the isolated roughness element.

## Introduction

Transition process from laminar to turbulent flows is initiated by instability of the flow. For small 2D disturbances, the linear stability theory is useful tool to predict the features of the disturbances. Disturbances in actual flow fields, however, have finite amplitude and 3D structure, then the experiment and the direct numerical simulation(DNS) are the only means available to clarify the process.

The instability induced by high shear layers generated around a roughness element reminds us of fundamental issues of the instability; the evolution of velocity fluctuation and the intrusion of disturbed region into the surrounding laminar fluid. In particular, 3D isolated roughness stimulates the surrounding boundary layer and creates an interesting interaction between the roughness wake and the background boundary layer. Gregory and Walker(1951) found vortex systems around the roughness element by smoke-wire visualization and the china clay technique. Mochizuki(1961) confirmed the vortical structure around a spherical roughness element. Recently, Klebanoff et al.(1992) made an experiment on the evolution of a turbulent

boundary layer started by a semi-spherical element and concluded that an incipient stage of the transition is considered to be a stability governed phenomena; the inflectional profiles on the center-line is responsible for the instability and the hairpin eddy generated in the inner region. Their results, however, could not draw definite conclusion on the relation between the transition and a fully developed turbulent boundary layer downstream.

In this paper, our focus is laid on the development of turbulent regions at off-center positions and finding the mechanism of spreading in the spanwise direction.

## Numerical computation

Flowfield around and downstream the roughness element placed in the boundary layer on a flat plate is solved by applying the finite difference method to 3D Navier-Stokes equations. Computational conditions are determined from the experimental ones. All spatial derivatives except those of convection terms are approximated by the central difference. The third order upwind scheme is applied to convection terms. The Euler implicit scheme is used for the time marching except convection terms which is linearized in time. The Poisson equation for pressure is solved by SOR method. The divergence free term is added according to MAC method. For the solution near the roughness element the generalized curvilinear body-fitted grid system is applied to treat the boundary layer easily. In the wake of the roughness element, the Cartesian grid is overlaid on the body-fitted grid to improve the spatial resolution. The mesh size is  $80 \times 100 \times 75$  for the body-fitted grid and  $400 \times 414 \times 75$  for the Cartesian grid. All data displayed in this paper are limited to the numerical results and to the half of the flow field.

## Experimental setup

A small low-turbulence wind tunnel was constructed to measure the flow characteristics around an isolated roughness element. The test section is  $30\text{cm} \times 30\text{cm} \times 2\text{m}$ . The contraction



ratio of the wind tunnel is 13.4. The wind speed is controlled by the AC fan-motor from 0.5 to 14 m/s. Residual turbulence at  $U_0=5.0$  m/s is 0.08 percent of the uniform velocity. A flat plate, 26cm(width)x90cm(length)x0.5cm(thickness), is installed in the center of the test section horizontally. The leading edge of the plate is machined with 8:1 ellipse. A cylindrical roughness with 2mm diameter and 2mm height is placed 10cm behind the leading edge. The hot-wire anemometer of constant-temperature type was used to measure the velocity. The hot-wire sensor is 2.5 micron meter in diameter and 0.5mm in length and the probe of I-type is set parallel to the spanwise direction. The Reynolds number of the experiment is 700. The break-out of disturbances is so critical that disturbances appear abruptly when the uniform velocity exceeds a threshold value. The  $x$  coordinate is taken in the flow direction from the center of the roughness element, the  $y$  coordinate vertical to the plate, and the  $z$  coordinate in the spanwise direction. All coordinates are normalized by the roughness height(=diameter).

### Results and Discussion

One of adequate indicator of the development of the flow behind the roughness element is the maximum intensity (RMS value) of velocity fluctuation in the crosssection at a certain streamwise position.

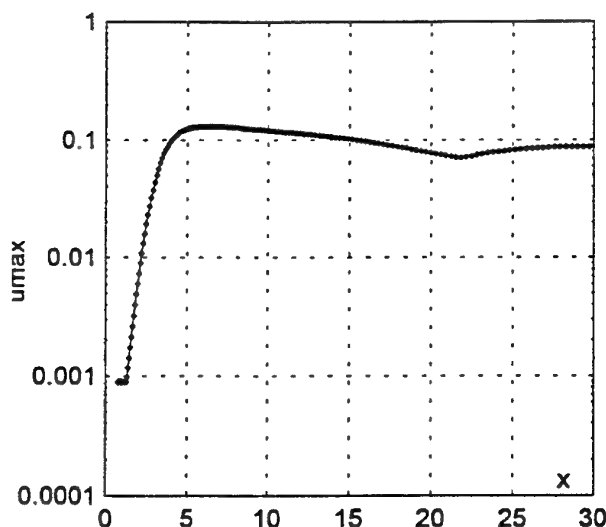


Fig.1 streamwise evolution of maximum intensity of velocity fluctuation

The maximum intensity of velocity fluctuation in the  $y$ - $z$  crosssection shows a typical streamwise evolution of velocity fluctuation in the transition region of shear flows ; a linear growth of amplitude of velocity fluctuation starts in the near wake of the roughness element. The shedding frequency of sinusoidal velocity fluctuation normalized with the displacement thickness at the roughness position and the uniform velocity is 0.073. A long nonlinear region follows the short linear region. The intensity increases up to 13 percent of the uniform velocity at  $x=6.22$  and decays slowly in the flow direction. It must be noted that there is a kink on this curve at  $x=21.9$  ; the intensity begins to rise again gradually thereafter,

suggesting a new mechanism of creating the velocity fluctuation.

Figure 2 indicates the  $z$  coordinate of the maximum intensity of velocity fluctuation in the half plane. The peak moves from the center( $z=0$ )of the wake to the off-center position( $z=-1.44$ ) at  $x=21.9$ . This dislocation of the maximum intensity means an appearance of new unstable region at the off-center position.

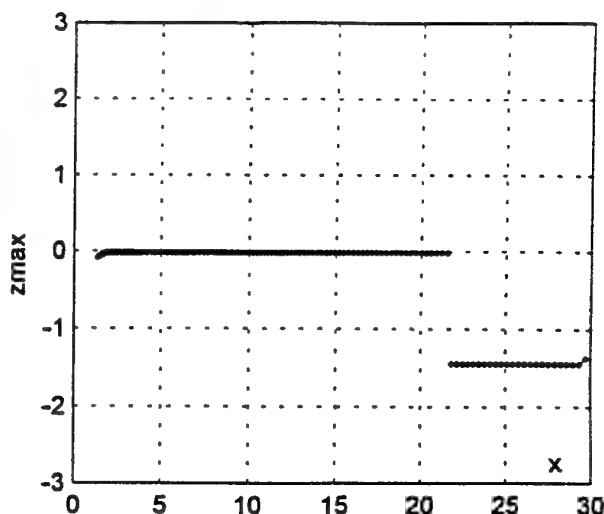


Fig.2  $z$  coordinate of maximum intensity of velocity fluctuation

Fig.3 is a slant view of the amplitude spanwise distribution at  $y=1$ . The amplitude of velocity fluctuation on the center line starts to decay at  $x=6.2$  and instead of it, a new peak turns up in the off-center position. We recognized the difference of the streamwise growth of the two peaks. The side peak has much lower amplification rate than the peak on the center-line. The cause of the new instability should be examined in detailed on the instability viewpoint.

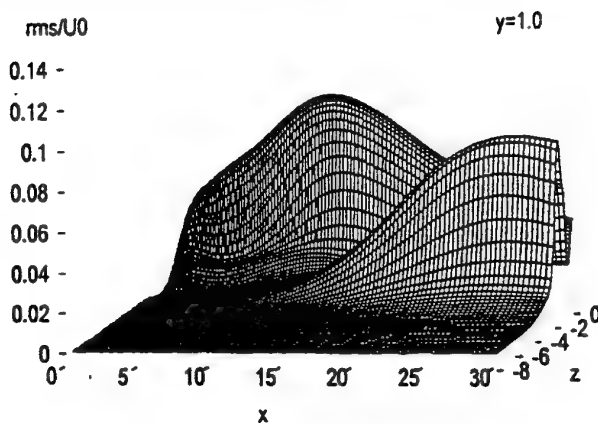


Fig.3 Variation of spanwise amplitude distribution at  $y=1$

Fig.4(a) and Fig.4(b) show the spanwise variation(half of the flow field) of mean velocity profiles of longitudinal component at  $x=7.98$ . In the vicinity of the center-line,

effect of Horseshoe vortex. The region of acceleration is sandwiched in decelerated regions. In the decelerated region, the velocity profile becomes unstable.

Horseshoe vortex makes the profile unstable. The results may give us a key to solve the issue of initial development of turbulence wedge; rapid spanwise expansion of the turbulent region.

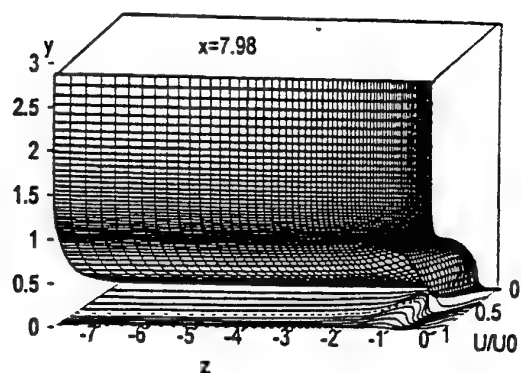


Fig.4(a) Spanwise variation of mean velocity distributions ( $x=7.98$ )

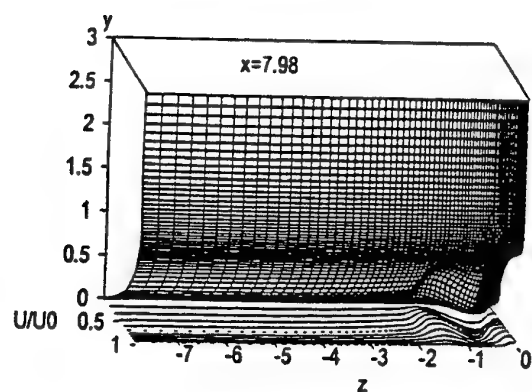


Fig.4(b) Spanwise variation of mean velocity distributions ( $x=7.98$ )

Mean velocity profiles in the vertical direction depend strongly on the spanwise location. Near the roughness element, intense acceleration occurs in the vicinity of the flat plate.

Velocity profiles at several  $z$  positions show some peculiar features as shown Fig.5(a). The  $y$  position of maximum velocity fluctuation coincides with that of inflection point. Then, it is suggested in the fact that the inviscid stability governs the phenomena. The spanwise gradient of mean velocity vanishes at  $z=-1.44$  where the intensity of fluctuation reaches the maximum (Fig.5(b)).

#### Concluding Remarks

We found two kinds of turbulent region in the wake of an isolated roughness element in a laminar boundary layer. The inflectional instability is the fundamental mechanism of disturbances in the both regions. The fluctuation on the centerline is generated by the high shear layer immediate behind the roughness element and its characteristics might show good agreement with the 2D linearised stability calculation. In the off-center turbulent region, the upwash induced by

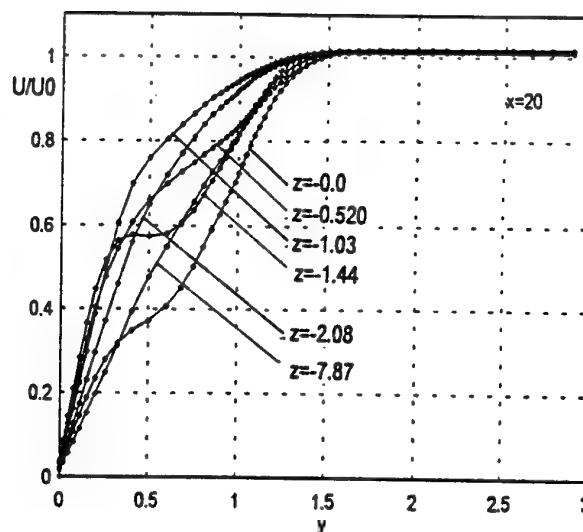


Fig.5(a) Spanwise variation of velocity distributions at  $x=20$

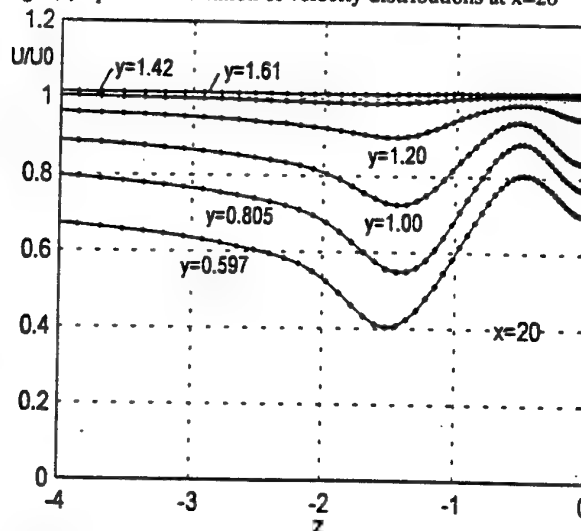


Fig.5(b) Vertical variation of spanwise velocity distribution at  $x=20$ .

#### References

- Gregory, N., and Walker, W.S., 1951, "The effect on transition of isolated surface excrescences in the boundary layer," Aero. Res. Council Reports & Memoranda No.2779.
- Klebanoff, P.S., Cleveland, Jr. W.G., and Tidstrom, K.D., 1992, "On the evolution of a turbulent boundary layer by a three dimensional roughness element," Journ. Fluid Mech., 237, pp.101-187.
- Mochizuki, M., 1961, "Smoke observation on boundary layer transition caused by a spherical roughness element," J. of Phys. Soc. Japan, 16 pp.995-1008.

## **SESSION 18 - COMBUSTION I**

# REYNOLDS STRESS CLOSURES FOR STRONGLY SWIRLING COMBUSTING JETS

Tilo Landenfeld, Anke Kremer, Egon P. Hassel, Johannes Janicka

Fachgebiet Energie- und Kraftwerkstechnik

Technische Hochschule Darmstadt

Petersenstr. 30

D-64287 Darmstadt

Germany

## ABSTRACT

This work presents computations of a strongly swirling, non-premixed methane-air diffusion flame in unconfined surrounding. Turbulence is modelled with three different linear and non-linear second order moment closures. Additionally, realizability constraints are applied to the pressure-strain correlation. Combustion is assumed to be in chemical equilibrium. Results, shown as first and second order moments of velocity, are compared with experimental data, obtained from Laser-Doppler-Velocimetry. Important properties of the flow such as the central recirculation zone are captured by all models.

## INTRODUCTION

Strongly swirling flows are widely used in technical non-premixed combustion systems, for swirl enhances mixing and stabilizes the flame. The resulting flow shows strong streamline curvature and a central recirculation zone.

Turbulence in such complex flows is mostly simulated with the  $k - \epsilon$  model (Leschziner and Rodi (1984), Dixon *et al.* (1983)) plus additional correction techniques such as Richardson number dependence.

Second order moment closures (SMC) have been applied to isothermal swirling jets (Smirnov and Chomiak (1996), Gibson and Younis (1986), Younis *et al.* (1996)) and to confined systems with density changes but without central recirculation zone (Hogg and Leschziner (1989), Jones (1994)).

In this study a strongly swirling non-premixed methane-air diffusion flame is investigated numerically and experimentally. Three second order closure models, two linear (Launder *et al.* (1975), Jones and Musonge (1988) in its revised form of Jones (1994)) and one non-linear (Speziale *et al.* (1991)), referred to as *LRR*, *JM* and *SSG* respectively, are applied and selected velocity profiles of first and second order moments are compared with experimental data. These are obtained from two-component Laser-Doppler-Velocimetry. Scalar quantities are computed with the eddy-viscosity approach. This is in contrast to the second order closure of the Reynolds stresses but gives sufficient accuracy to serve as first test, especially since the *LRR* and the *SSG* model both were not developed for flows with density gradients. Similarly, a simple combustion model with the underlying assumption of an infinitely fast reaction is chosen. It is assumed, that with this set-up the turbulence models can be compared.

## APPLIED MODELS

### Turbulence Models

Through the use of density weighted or so called Favre averages

$$\varphi_i = \widetilde{\varphi_i} + \varphi_i'' , \quad \widetilde{\varphi_i} = \frac{\overline{\rho \varphi_i}}{\bar{\rho}} \quad (1)$$

the time independent conservative equations for mass and momentum are

$$\frac{\partial(\bar{\rho} \widetilde{u_i})}{\partial x_i} = 0 , \quad (2)$$

$$\frac{\partial(\bar{\rho} \widetilde{u_i u_j})}{\partial x_j} = -\frac{\partial \bar{p}}{\partial x_i} + \bar{\rho} g_i + \frac{\partial}{\partial x_j} \left[ \bar{\rho} \left( \frac{\partial \widetilde{u_i}}{\partial x_j} + \frac{\partial \widetilde{u_j}}{\partial x_i} \right) - \bar{\rho} \widetilde{u_i'' u_j''} \right] . \quad (3)$$

The last term is known as Reynolds stress tensor and demands treatment in form of modeling.

SMC can be written in a general form

$$\begin{aligned} \frac{\partial(\bar{\rho} \widetilde{u_i'' u_j'' u_k''})}{\partial x_k} = & \bar{\rho} (\mathcal{P}_{ij} - \epsilon_{ij}) + \Pi_{ij} + \frac{\bar{\rho}' u_j''}{\bar{\rho}} \frac{\partial \bar{p}}{\partial x_i} + \frac{\bar{\rho}' u_i''}{\bar{\rho}} \frac{\partial \bar{p}}{\partial x_j} \\ & + \frac{\partial}{\partial x_k} \left( \bar{\rho} \frac{\partial(\widetilde{u_i'' u_j''})}{\partial x_k} - C_{ijk} \right) , \end{aligned} \quad (4)$$

where the symbols

$$\mathcal{P}_{ij} = - \left( \widetilde{u_i'' u_k''} \frac{\partial \widetilde{u_j}}{\partial x_k} + \widetilde{u_j'' u_k''} \frac{\partial \widetilde{u_i}}{\partial x_k} \right) \quad (5)$$

$$\epsilon_{ij} = 2 \bar{\rho} \frac{\partial \widetilde{u_i''}}{\partial x_k} \frac{\partial \widetilde{u_j''}}{\partial x_k} \quad (6)$$

$$\Pi_{ij} = \bar{\rho}' \frac{\partial \widetilde{u_i''}}{\partial x_j} + \bar{\rho}' \frac{\partial \widetilde{u_j''}}{\partial x_i} \quad (7)$$

$$C_{ijk} = \bar{\rho} \widetilde{u_i'' u_j'' u_k''} + \bar{\rho}' \widetilde{u_i''} \delta_{jk} + \bar{\rho}' \widetilde{u_j''} \delta_{ik} \quad (8)$$

Table 1: MODEL CONSTANTS FOR SMC AS THEY APPEAR IN (11), (12) and (13)

Model	$C_{\epsilon_1}$	$C_{\epsilon_2}$	$C_{\epsilon}$	$C_s$	$C_1$	$C_2$
LRR	1.44	1.90	0.15	0.22	1.5	-0.582
JM	1.40	1.90	0.18	0.22	3.0	-0.44
SSG	1.44	1.83	0.183	0.22	1.7	-0.4167
Model	$C_3$	$C_4$	$C_1^*$	$C_{nl}$		
LRR	0.764	-0.182	—	—		
JM	0.46	-0.23	—	—		
SSG	0.4125	$-0.0167 - 0.65\sqrt{b_{kl}b_{lk}}$	1.8	4.2		

represent production, dissipation, redistribution and transport, respectively.

For variable density flows an additional term with a density-velocity correlation linked to the mean pressure gradient appears in (4). Following Jones (1979) and a study by Pfuderer *et al.* (1996) it can be modelled from a truncated conservation equation as

$$\overline{\rho' u_i''} = -\frac{1}{4.3} \frac{\bar{k}}{\bar{\epsilon}} \overline{u_i'' u_j''} \frac{\partial \bar{p}}{\partial x_j} \quad (9)$$

However, it is found that in this flow the term yields no essential contribution to (4) and therefore will not be considered any further in this study.

Except for  $\mathcal{P}_{ij}$ , the terms (6) – (8) require modeling. Standard models for  $\epsilon_{ij}$  (local isotropy) and  $C_{ijk}$  (Daly and Harlow, (1970)) are

$$C_{ijk} = -C_s \frac{\bar{k}}{\bar{\epsilon}} \overline{\rho' u_i'' u_j''} \frac{\partial \overline{u_i'' u_j''}}{\partial x_l}, \quad \epsilon_{ij} = \frac{2}{3} \bar{\epsilon} \delta_{ij}, \quad (10)$$

$$\begin{aligned} \frac{\partial(\bar{\rho} \bar{\epsilon} \bar{u}_j)}{\partial x_j} = & -C_{\epsilon_1} \bar{\rho} \frac{\bar{\epsilon}}{\bar{k}} \overline{u_i'' u_j''} \frac{\partial \bar{u}_i}{\partial x_j} - C_{\epsilon_2} \bar{\rho} \frac{\bar{\epsilon}^2}{\bar{k}} + C_{\epsilon_3} \frac{\bar{\epsilon}}{\bar{k}} \frac{\partial \overline{\rho' u_i''}}{\partial x_i} \frac{\partial \bar{p}}{\partial x_j} \\ & + \frac{\partial}{\partial x_j} \left( C_{\epsilon} \bar{\rho} \frac{\bar{k}}{\bar{\epsilon}} \overline{u_i'' u_j''} \frac{\partial \bar{\epsilon}}{\partial x_k} \right). \end{aligned} \quad (11)$$

Again, the term involving the mean pressure gradient in (11) is neglected.

The pressure-strain correlation  $\Pi_{ij}$  is usually split into two parts. The return term is responsible for the return to isotropy without mean shear whereas the rapid part counteracts the production by redistributing the Reynolds stresses. Most models like LRR and JM use the formulation

$$\begin{aligned} \Pi_{ij}^{\text{lin}} = & -C_1 \bar{\rho} \bar{\epsilon} \left( \frac{\overline{u_i'' u_j''}}{\bar{k}} - \frac{2}{3} \delta_{ij} \right) + C_2 \delta_{ij} \bar{\rho} \overline{u_l'' u_m''} \frac{\partial \bar{u}_l}{\partial x_m} \\ & - C_3 \bar{\rho} \mathcal{P}_{ij} + C_4 \bar{\rho} \bar{k} \left( \frac{\partial \bar{u}_i}{\partial x_j} + \frac{\partial \bar{u}_j}{\partial x_i} \right) - \frac{2}{3} C_4 \bar{\rho} \bar{k} \frac{\partial \bar{u}_k}{\partial x_k} \delta_{ij} \\ & - \left( \frac{3}{2} C_2 + C_3 \right) \left( \bar{\rho} \overline{u_i'' u_j''} \frac{\partial \bar{u}_l}{\partial x_i} + \bar{\rho} \overline{u_l'' u_i''} \frac{\partial \bar{u}_l}{\partial x_j} \right). \end{aligned} \quad (12)$$

They are linear in terms of the mean strain and Reynolds stresses. However, the constants proposed by LRR and JM are derived with different strategies.

A nonlinear extension to (12), namely with terms quadratic in  $\overline{u_i'' u_j''}$ , has been published by Speziale *et al.* (1991) to give the SSG model

$$\Pi_{ij}^{\text{SSG}} = \Pi_{ij}^{\text{lin}} + C_{nl} \bar{\rho} \bar{\epsilon} \left[ b_{ik} b_{kj} - \frac{b_{kl} b_{kl}}{3} \delta_{ij} \right] - C_1^* \bar{\rho} \mathcal{P} b_{ij}, \quad (13)$$

where the anisotropy tensor  $b_{ij} = \overline{u_i'' u_j''} / (2\bar{k}) - 1/3 \delta_{ij}$  has been used and  $\mathcal{P} = 1/2 \mathcal{P}_{kk}$ .

All model constants are summarized in table 1.

## Realizability

In regions of strong streamline curvature, which occur in the area where entrainment and jet flow meet and are mixed, the turbulence models seem to predict unrealizable states. Thus, special care must be taken to suppress such behavior. Based on the analysis of Durbin and Speziale (1994), coefficients of the redistribution term are modified when the limit  $F = 1 + 9(III - 1/2II) = 0$  is reached, which corresponds to the upper edge in the Lumley invariant triangle. Here,  $II = b_{kl} b_{lk}$  and  $III = b_{kl} b_{lm} b_{mk}$  represent second and third invariants of anisotropy tensor  $b_{ij}$  respectively. Following this study, the LRR model is modified by

$$C_1 = \max \left[ C_1, 1 + \frac{3}{2} C_2 \frac{\mathcal{P}}{\bar{\epsilon}} - 3 C_4 \lambda_1 \right], \quad (14)$$

where  $\lambda_1$  is the largest eigenvalue of the matrix

$$\frac{\bar{k}}{2\bar{\epsilon}} \left( \frac{\partial \bar{u}_i}{\partial x_j} + \frac{\partial \bar{u}_j}{\partial x_i} \right). \quad (15)$$

The nonlinear SSG model alters to

$$\begin{aligned} C_1 = & \max \left[ C_1, 1 - \frac{1}{2} \left( C_1^* \frac{\mathcal{P}}{\bar{\epsilon}} + \frac{C_{nl}}{3} \right) \right. \\ & \left. + \frac{3}{2} C_2 \frac{\mathcal{P}}{\bar{\epsilon}} + \frac{C_{nl}}{2} II - 3 C_4 \lambda_1 \right]. \end{aligned} \quad (16)$$

For the JM model, Alvarez and Jones (1993) have concluded, that realizable solutions are obtained by adjusting the coefficients  $C_2$  and  $C_4$  of the rapid part as

$$\begin{aligned} C_2 = & C_2 \min \left[ \max \left[ 5F, 0 \right], 1 \right], \\ C_4 = & C_4 \min \left[ \max \left[ 5F, 0 \right], 1 \right]. \end{aligned} \quad (17)$$

## Chemical and Mixing Model

The combustion process is described under the assumption of chemical equilibrium. The infinitely fast reactions do not account for extinction effects, but are supposed to give a good representation of the density and temperature profiles. Since the calculations do not aim to give accurate predictions of species concentrations but rather address to estimate the applicability of second order turbulence closure models to complex flows, this approach seems legitimate.

The eddy-viscosity approach is applied to model scalar fluxes. The resulting transport equations for mean mixture fraction  $\bar{f}$  and its variance  $f''^2$  are

$$\frac{\partial \bar{\rho} \bar{u}_i \bar{f}}{\partial x_i} = \frac{\partial}{\partial x_i} \left[ \bar{\rho} \left( \nu + \frac{\nu_t}{\sigma_f} \right) \frac{\partial \bar{f}}{\partial x_i} \right], \quad (18)$$

$$\begin{aligned} \frac{\partial \bar{\rho} \bar{u}_i f''^2}{\partial x_i} = & \frac{\partial}{\partial x_i} \left[ \bar{\rho} \left( \nu + \frac{\nu_t}{\sigma_{f''^2}} \right) \frac{\partial f''^2}{\partial x_i} \right] + 2 \bar{\rho} \frac{\nu_t}{\sigma_f} \left( \frac{\partial \bar{f}}{\partial x_i} \right)^2 \\ & - 2 \bar{\rho} \frac{\bar{\epsilon}}{\bar{k}} f''^2, \end{aligned} \quad (19)$$

with  $\sigma_f = \sigma_{f''^2} = 0.7$ . Turbulent viscosity is computed from  $\nu_t = C_\mu \bar{k}^2 / \bar{\epsilon}$ ,  $C_\mu$  being 0.09. The integration of a presumed probability density function ( $\beta$ -function) yields mean density and viscosity.

## EXPERIMENTAL SYSTEM

The velocity field of the strongly swirling methane flame with a thermal load of 150 kW is investigated experimentally with a two-component fiberoptic Laser-Doppler-Anemometer. The laser beam of a 4 W Ar-Ion-Laser is divided by means of a Bragg cell into a beam pair of the wavelengths 514.5 nm (green) and 488

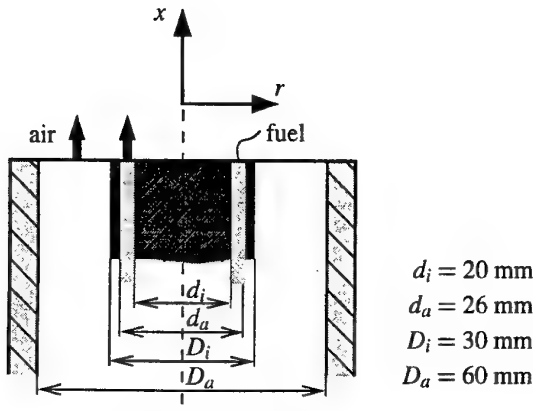


Figure 1: BURNER GEOMETRY

nm. The laser beams are collimated in a measurement volume of  $780 \mu\text{m} \times 94 \mu\text{m}$  with a front lens of 600 mm focal length.

Statistical averaging is transit time weighted to minimize velocity bias. An estimate of the statistical error concerning mean velocity is 6%, whereas fluctuations are accurate within 8%.

Geometry is explained in Fig. 1. The theoretical swirl number of 2 results in an effective swirl number of

$$S = \frac{\int_0^{R_a} \bar{u} \bar{w} r^2 dr}{R_a \int_0^{R_a} \bar{u}^2 r dr} = 0.95. \quad (20)$$

The fuel/air ratio of 1.2 corresponds to volumetric streams of 15 and  $180 \text{ m}^3/\text{h}$  and Reynolds numbers of 8000 and 42900 for fuel and air, respectively.

For a more detailed description of the burner and the experimental setup see Kremer *et al.* (1997).

## NUMERICAL SETUP

All equations are formulated in cylindrical coordinates and solved on a staggered orthogonal grid. The computational domain ranges from zero to  $L = 1.2 \text{ m}$  axially and  $W = 0.9 \text{ m}$  radially with a resolution of  $60 \times 50$  points and a grid stretching of  $\alpha_x = 1.08$  and  $\alpha_r = 1.12$ , thus giving the highest resolution at burners exit.

The SIMPLE method introduced by Patankar and Spalding (1972) ensures conservation of mass and momentum through the use of a pressure-correction equation. All convective terms are discretized with the QUICK scheme of Leonhard (1979).

Zero gradient boundary conditions are applied at the outlet plane ( $x = L$ ). Entrainment at  $r = W$  is obtained from the solution of a discrete continuity equation for each control volume. At the inlet plane ( $x = 0$ ) first and second order velocity moments except  $\overline{v''w''}$  are extracted from the experiment. The dissipation rate is calculated from the well known mixing length formula  $\bar{\epsilon} = C_\mu^{3/4} \bar{k}^{3/2} / L$ ,  $L$  being 20 % of the width of the annulus.

## RESULTS AND DISCUSSION

All models succeed to predict a recirculation zone and, as to be seen in Fig. 2, the first stagnation point lies very close to the nozzle. This is well captured by all models. The negative extremum of the velocity on the axis occurs at  $x = 45 \text{ mm}$  with  $u_{\min} = -17 \text{ m/s}$ , and is under-predicted by the *JM* model. Both, the *LRR* and the *SSG* model over-predict this value. Discrepancy is found for the prediction of the second stagnation point at approximately  $x = 150 \text{ mm}$  where the *SSG* and the *LRR* models fail, i.e. they tend to enlarge the length of the recirculation zone, see Fig. 3. The *JM* model shows good accordance concerning the recirculation zone.

The distribution of the turbulent kinetic energy along the axis is similar for all models, which predict a maximum at  $x = 40 \text{ mm}$ ,

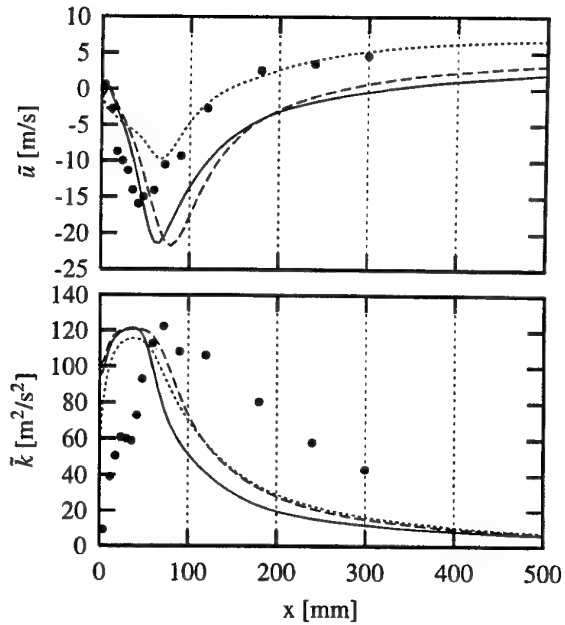


Figure 2: STREAMWISE DISTRIBUTION OF MEAN VELOCITY AND MEAN TURBULENT KINETIC ENERGY: SSG —, LRR ----, JM ·····, Exp. •

the experiment giving  $x = 80 \text{ mm}$ . The shift of the maximum towards the nozzle is probably due to a misrepresentation of the near wall turbulence, where fluctuations normal to the wall are damped. The backward flow in this region is comparable to an impinging jet. This effect would have to be accounted for through wall functions, which are not used in this work. Likewise improved chemical and scalar models are to be incorporated.

Radial profiles of  $\bar{u}$  and  $\bar{w}$  are reflected in Fig. 4. Away from the axis of symmetry the model predictions are far more similar to each other than their streamwise values. The *SSG* model is slightly superior over the linear formulations. Especially in the region behind the second stagnation point the quadratic pressure-strain model shows good accordance with the measured swirl velocity component. Overall agreement is encouraging.

In Fig. 5 the important Reynolds-stress component  $\overline{u''v''}$  and turbulent kinetic energy  $\bar{k}$  are plotted and compared with experimental data. All models correctly predict tendency and change of sign for  $\overline{u''v''}$ . Within the recirculation zone the maximum of the shear stress is over-predicted.

Again, close to the nozzle the profiles of turbulent kinetic energy are, as discussed above and seen in Fig. 2, not in good agreement with experiments. Outside the recirculation zone they predict the expected, measured contours.

## CONCLUSIONS

The flow in a strongly swirling combustor natural gas flame was studied with three different Reynolds stress closures. The first and second order moments of the velocity field were compared with experimental data and revealed overall acceptable agreement with respect to the fairly simple chemical and scalar model assumptions. The correct prediction of the second stagnation point turned out to be a sensitive test for all models. Improvements of model predictions near the exit of the burner are necessary. However, the non-linear *SSG* model seems to have superseded the linear approaches, except for deficiencies in the recirculation zone.

**Acknowledgements:** This work was supported by the BMBF/TECFLAM and Land Hessen.

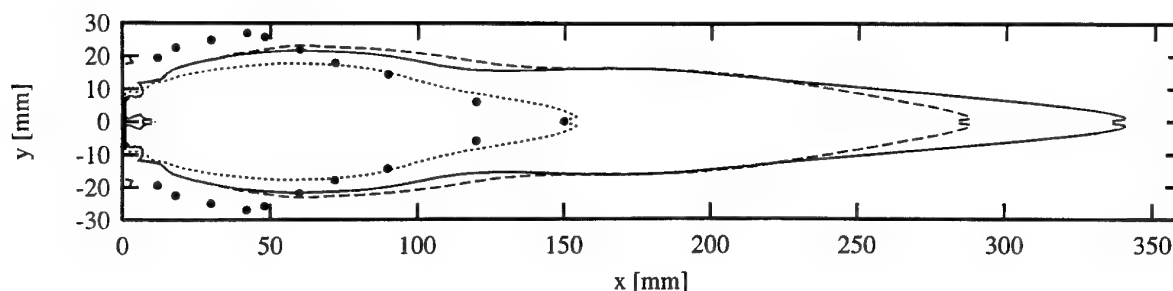


Figure 3: CONTOURS OF ZERO AXIAL VELOCITY  $\bar{u}$   
SSG —, LRR ----, JM ·····, Exp. •

## REFERENCES

- J. Alvarez and W.P. Jones, 1993, "Computation of a jet discharging into a cross-flow with a second-moment turbulence closure and a low-diffusive convection-discretisation scheme", In *Proceedings of the 2nd Int. Symp. on Turb. Mod. and Exp.*, pp. 239–250.
- B.J. Daly and F.H. Harlow, 1970, "Transport equations in turbulence", *Phys. Fluids*, Vol. 13 (11), pp. 2634–2649.
- T.F. Dixon, J.S. Truelove, and T.F. Wall, 1983, "Aerodynamic studies on swirled coaxial jets from nozzles with divergent quarls", *Journal of Fluids Engineering*, Vol. 105, pp. 197–203.
- P.A. Durbin and C.G. Speziale, 1994, "Realizability of Second Moment Closures by Stochastic Analysis", *J. Fluid Mech.*, Vol. 280, pp. 395–407.
- M.M. Gibson and B.A. Younis, 1986, "Calculation of swirling jets with a reynolds stress closure", *Phys. Fluids*, Vol. 29 (1), pp. 38–48.
- S. Hogg and M.A. Leschziner, 1989, "Second-moment-closure calculation of strongly swirling confined flow with large density gradients", *Int. J. Heat and Fluid Flow*, Vol. 10 (1), pp. 16–27.
- W.P. Jones, 1979, "Von Karman Lecture Series", Von Karman Institute for Fluid Dynamics, 1979-02, Belgium.
- W.P. Jones, 1994, "Turbulence modelling and numerical solution methods for variable density and combusting flows", In P. A. Libby and F. A. Williams, editors, *Turbulent Reacting Flows*, pp. 309–374. Academic Press, London, San Diego, New York.
- W.P. Jones and P. Musonge, 1988, "Closure of the Reynolds stress and scalar flux equations", *Phys. Fluids*, Vol. 31 (12), pp. 3589–3604.
- A. Kremer, E.P. Hassel and J. Janicka, 1997, "Velocity measurements in a strongly swirling natural gas flame", *submitted to VDI Engineering Research*.
- B.P. Leonhard, 1979, "A stable and accurate convective modeling procedure based on quadratic upstream interpolation", *Comp. Meths. Appl. Mech. Eng.*, Vol. 19, pp. 59–98.
- M.A. Leschziner and W. Rodi, 1984, "Computation of strongly swirling axisymmetric free jets", *AIAA Journal*, Vol. 22, pp. 1742–1747.
- B.E. Launder, G.J. Reece, and W. Rodi, 1975, "Progress in the development of a reynolds-stress turbulence closure", *J. Fluid Mech.*, Vol. 68, pp. 537–566.
- D.G. Pfuderer, A.A. Neuber, G. Früchtel, E.P. Hassel, and J. Janicka, 1996, "Turbulence modulation in jet diffusion flames: Modeling and Experiments", *Combustion and Flame*, Vol. 106, pp. 301–317.
- S.V. Patankar and D.B. Spalding, 1972 "A calculation procedure for heat, mass and momentum transfer in three-dimensional parabolic flows", *Int. J. Heat Mass Trans.*, Vol. 15, pp. 1787–1806.
- A.V. Smirnov and J. Chomiak, 1996, "Predictions of recirculation zones in turbulent swirl flows", In W. Rodi and G. Bergeles, editors, *Engineering Turbulence Modelling and Experiments*, Vol. 3, pp. 309–318.
- C.G. Speziale, S. Sarkar, and T.B. Gatski, 1991, "Modeling the pressure-strain correlation of turbulence", *J. Fluid Mech.*, Vol. 227, pp. 245–272.
- B.A. Younis, T.B. Gatski, and C.G. Speziale, 1994, "On the prediction of free turbulent jets with swirl using a quadratic pressure-strain model", *Journal of Fluids Engineering*, Vol. 118, pp. 800–809.

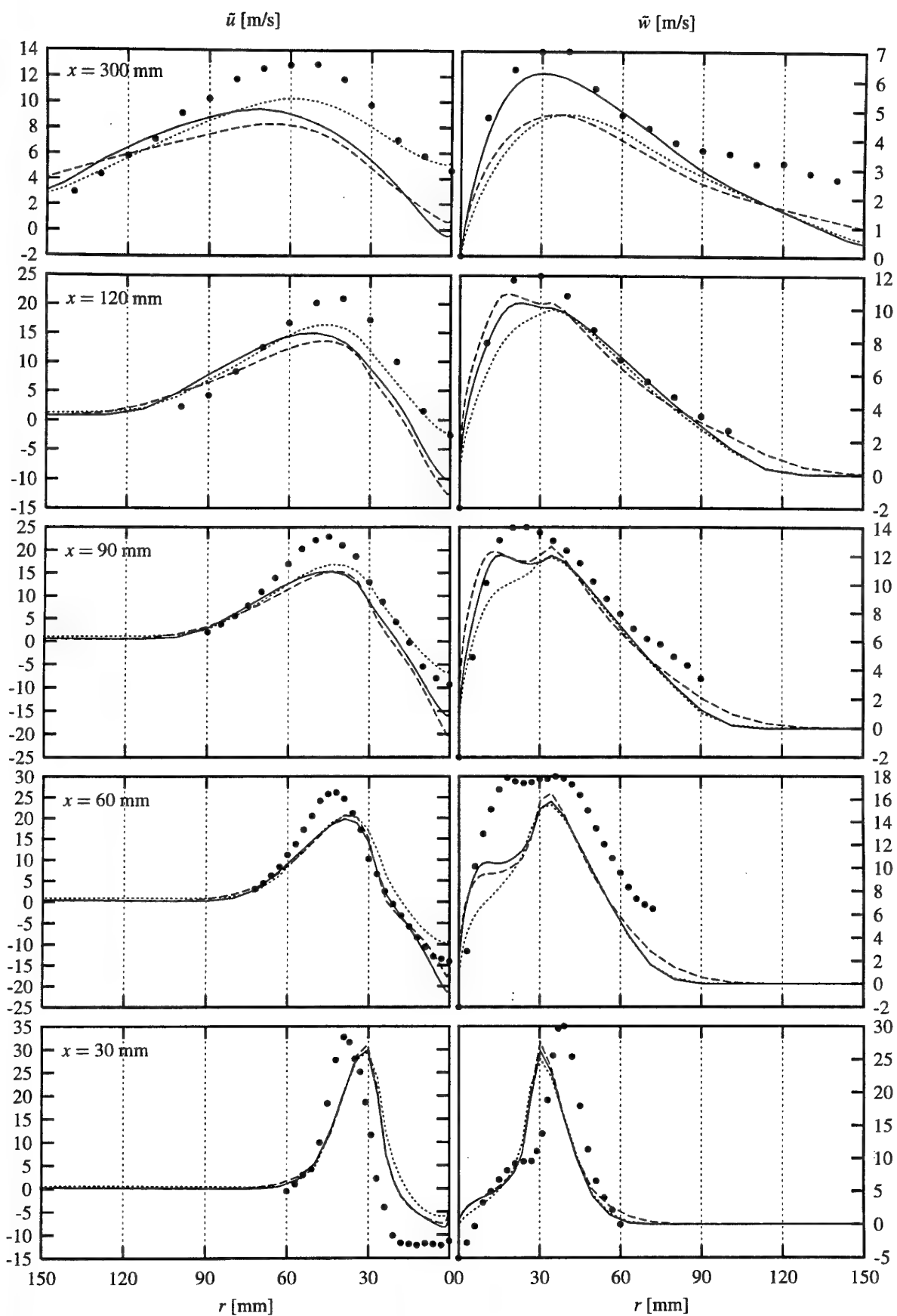


Figure 4: CROSSWISE DISTRIBUTION OF MEAN AXIAL VELOCITY  $\tilde{u}$  AND SWIRL VELOCITY  $\tilde{w}$ :  
SSG —, LRR ----, JM ·····, Exp. •



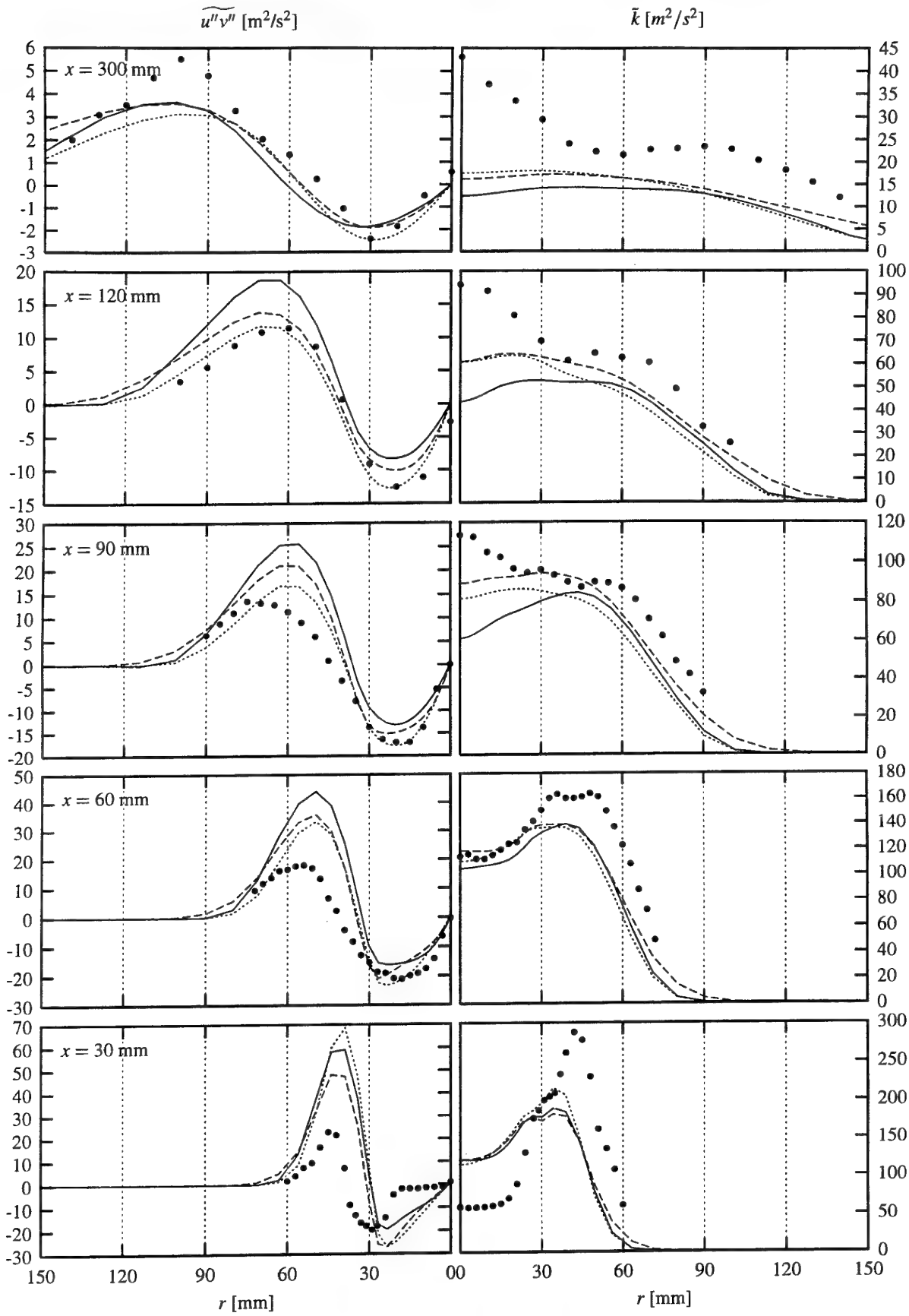


Figure 5: CROSSWISE DISTRIBUTION OF REYNOLDS STRESS COMPONENT  $\widetilde{u''v''}$  AND TURBULENT KINETIC ENERGY  $\bar{k}$ :  
SSG —, LRR ---, JM ·····, Exp. •

# A MULTI-SCALAR PDF METHOD FOR SI ENGINE COMBUSTION SIMULATION

**Reinhard M. Tatschl**

Advanced Simulation Technologies  
AVL LIST GmbH  
Kleiststrasse 48  
A-8020 Graz  
Austria

## ABSTRACT

A scalar pdf method has been implemented into the multi-purpose CFD code FIRE in order to simulate three-dimensional inhomogeneous-charge SI engine combustion. The probability method adopted solves the multi-scalar pdf transport equation for the thermochemical variables required to describe the reactive system. In the present case of a single-step global reaction, the pdf transport equation involves the scalar quantities mixture fraction, reaction progress variable and enthalpy. Numerical solution of the pdf transport equation is enabled by using a Monte-Carlo particle method.

In order to assess the ability of the method to reflect the characteristic features of premixed flame propagation in engines, different aspects of the SI engine combustion process have been numerically studied in the disc-shaped combustion chamber of a two-valve engine configuration under varying operating conditions. The results comprise data on flame propagation characteristics as well as data on heat release and on flame front propagation velocity for variations in engine speed, load, fuel to air equivalence ratio and residual gas mass fraction. Finally, the application of the method to stratified-charge SI engine combustion is presented and discussed.

## INTRODUCTION

The flame front propagation characteristic during SI engine combustion is determined by the structure and intensity of the pre-combustion in-cylinder flow field and by the contribution of the volumetric expansion of the hot combustion products to the overall flame propagation velocity. The flame speed is governed by the chemical reaction kinetics and the turbulent velocity and concentration fluctuations acting on the flame and leading to a convoluted structure of the reaction zone. The turbulent fluctuations in the flame result in intensified mixing of the cold reactants with the hot combustion products and lead to an increased rate of mean fuel conversion.

The local chemistry / turbulence interaction that eventually expresses itself in different combustion regimes is determined by the ratio of the instantaneous chemical reaction rates and the intensity of the stochastic fluctuations of the flow variables, hence by the ratio of the time scales of the chemical and physical processes. Additionally, in the case of stratified-charge combustion, turbulent flame propagation may occur under premixed, partially premixed and diffusion flame

conditions where the fuel to air equivalence ratio in the reaction zone may considerably deviate from stoichiometry resulting in local flame quenching and the formation of unburnt hydrocarbons. In order to numerically capture the relevant features of flame propagation under the above described conditions, it is of significant importance to accurately model the simultaneous effects of finite-rate chemistry and turbulent mixing in the reaction zone.

Modelling the turbulence / chemistry interaction during hydrocarbon oxidation is the major challenge in simulating turbulent reacting flows (Borghi, Cant and Bray, El Tahry, Meneveau and Poinot, Pope). The intimate coupling of the chemistry and the flow field quantities stems from the high nonlinearities of the chemical reaction rates in combination with the local stochastic fluctuations of the flow and composition fields. Since the complete spectrum of time and length scales of these fluctuations cannot be resolved within present numerical methods, the common practice adopts an averaging procedure replacing the instantaneous flow field quantities by its mean and fluctuating components.

This procedure, however, leads to a significant loss of information. Mathematically this results in the appearance of terms in the conservation equations which contain statistical correlations of fluctuating components that have to be expressed by means of known mean flow quantities. The most important term in the context of chemically reacting flows is the one determining the mean rate of fuel conversion and hence heat release. In the past, different models of various levels of complexity and partly involving severe assumptions concerning the combustion regime have been proposed in order to model this term in the relevant conservation equations.

One modelling methodology adopted in the past (Ramos and Sirignano, Ryn and Asanuma) assumes that the mean rate of chemical reaction is purely determined by chemical kinetic effects and that the influence of turbulence on combustion only enters via the effect of turbulent diffusion. Another class of models is based on the assumption that the mean rate of reaction is independent of the details of the reaction kinetics and hence the reaction progress is solely determined by intermixing of cold reactants with hot combustion products (Ahmadi-Befrui et al.). Although very helpful in providing a qualitative picture of premixed SI engine combustion, these models show very limited applicability to situations where

finite-rate chemistry effects play an important role during turbulent flame propagation in engines.

Models have been proposed that are based upon solving transport equations for the mean and variance of a reaction product mass fraction and adopting a presumed pdf distribution in order to account for the turbulence / chemistry interaction in the flame (Bray and Moss, Borghi and Moreau). Although superior to the previously mentioned models, it appeared to be impossible to adequately describe all possible shapes of the pdf which might occur during transient flame propagation in engines by just taking into account the first two moments. Moreover, the effort required to extend this approach to partially premixed flames or to complex reaction systems is prohibitive.

The most promising methods in this respect are based upon solving a full pdf transport equation for the relevant flow and combustion quantities under consideration (Dopazo, Pope, O'Brian, Janicka et al.). These transported pdf models do not rely on the assumption of infinitely fast chemical reaction, the presence of thin reaction sheets or on a presumed shape of the probability density function distribution. Hence, they are well suited for application to inhomogeneously premixed and stratified-charge combustion, where the fuel to air equivalence ratio might show large spatial and / or temporal variations. Moreover, the transported pdf method enables simultaneous treatment of premixed, partially premixed and fully non-premixed combustion situations and offers the unique opportunity of straightforward implementation of arbitrarily complex chemistry.

It is the aim of the present paper to describe the implementation of a transported multi-scalar pdf combustion model into the commercial CFD code FIRE, to present some selected results of the verification studies that have been performed and finally to demonstrate the applicability of the model to stratified-charge SI engine combustion simulation.

## MATHEMATICAL MODEL

### Gas Motion

The CFD method applied in the present work is the thermofluids analysis software package FIRE (Tatschl et al.).

FIRE solves the density-weighted, ensemble-averaged conservation equations of total mixture mass, momentum and enthalpy, and the transport equations of the  $k$ - $\epsilon$  turbulence model. Additional species mass fraction transport equations are solved in order to capture species mixing processes during intake and compression.

The governing equations are recast into the curvilinear non-orthogonal form and transformed to a contracting / expanding co-ordinate system, so to enable their solution on body-fitted computational grids with moving boundaries. The partial differential / transport equations are discretised on the basis of a finite-volume method. The temporal discretisation is Euler implicit, in order to ensure unconditional numerical stability, for approximation of the spatial derivatives a hybrid central / upwind or optional higher order differencing schemes are used. These practices lead to coupled algebraic equation systems solved iteratively based on a pressure-velocity coupling procedure. The solution of each algebraic equation system is effected using the ILU preconditioned conjugate gradient method for unsymmetric problems, ORTHOMIN.

### Thermochemistry

In the present study the hydrocarbon oxidation process is expressed by a single-step irreversible combustion reaction, in which fuel and oxygen are converted into the stable combustion products carbon-dioxide and water. In the calculations performed, octane is used for representation of the

hydrocarbon fuel, with the Arrhenius rate coefficients for the global reaction step based upon those given by Westbrook and Dryer. These had been shown to predict the variation of laminar burning velocity reasonably well for a wide range of equivalence ratio.

In order to represent the reactive system two non-dimensionalised variables, namely a mixture fraction 'f' and a reaction progress variable 'c' are adopted. The mixture fraction is equivalent to the total (burnt plus unburnt) fuel mass fraction and thus a measure of the mixing between the air and the fuel, irrespective of the combustion process. The reaction progress variable is equivalent to the reaction product mass fraction that occurs such that either all the fuel or all the oxidant is depleted (or both for stoichiometric mixtures). The reaction progress variable is bounded by the values of zero and unity corresponding to the unburnt and burnt states, respectively, regardless of the equivalence ratio.

### Combustion Model

The well known closure problem of turbulent reacting flows does not appear if the flow quantities are treated as random variables, and their joint probability density function is evaluated at each point of the flow field. Therefore, in the present study a transported multi-scalar pdf model has been adopted (Pope). The solution of the pdf transport equation provides a complete statistical description of the spatial and temporal probability distribution evolution of the scalars mixture fraction, reaction progress variable and enthalpy. The pdf model accounts for the simultaneous effects of turbulent mixing and chemical kinetics in the reaction zone, obviating the need for any prior assumptions as to whether one or the other of the two processes governs the mean rate of reaction.

The modelled form of the pdf transport equation used in the present study can be written as

$$\frac{\partial \tilde{f}(\underline{\psi}; \underline{x}, t)}{\partial t} + \sum_{i=1}^m \tilde{U}_i \frac{\partial \tilde{f}(\underline{\psi}; \underline{x}, t)}{\partial x_i} + \sum_{\alpha=1}^m \frac{\partial}{\partial \psi_{\alpha}} (\tilde{f}(\underline{\psi}; \underline{x}, t) S_{\alpha}(\underline{\psi})) = \sum_{i=1}^m \frac{1}{\rho} \frac{\partial}{\partial x_i} \Gamma_T(\underline{x}, t) \frac{\partial \tilde{f}(\underline{\psi}; \underline{x}, t)}{\partial x_i} + 2\sigma\omega \int \tilde{f}(\underline{\psi}; \underline{x}, t + \underline{\psi}'; \underline{x}, t) d\underline{\psi}' - \omega \tilde{f}(\underline{\psi}; \underline{x}, t)$$

In the above  $\tilde{f}(\underline{\psi}; \underline{x}, t)$  denotes the probability density function of the scalar variables,  $U_i(\underline{x}, t)$  represents the velocity in  $x_i$ -direction,  $\rho(\underline{x}, t)$  is the density,  $\Gamma_T(\underline{x}, t)$  is the diffusion coefficient, which in the present case is based upon the solution of the  $k$ - $\epsilon$  equations.  $S_{\alpha}(\underline{x}, t)$  represents the effect of chemical reaction calculated based upon the global reaction step described above and  $\omega$  is the turbulent mixing frequency obtained from the solution of the two equation  $k$ - $\epsilon$  turbulence model as  $\omega = \epsilon/k$ . Closure of the unknown terms in the pdf transport equation was achieved by adopting a gradient diffusion approximation and a stochastic mixing model (Curl) for modelling turbulent convection in physical and molecular mixing in composition space, respectively.

The pdf transport equation is solved adopting a Monte Carlo simulation approach (Pope), in which the continuous probability density function is represented by an ensemble of notional elements located at the cell centres of the finite volume computational grid. In order to advance the pdf in time, the notional elements are transported across physical and composition space according to the processes of convection, diffusion, chemical reaction and mixing, which are simulated sequentially by means of an operator splitting technique.

The solution of the coupled finite-volume mean flow method with the Monte Carlo pdf simulation algorithm is performed in a time marching method, with the mean velocity, pressure and

scalar fields iteratively updated according to the solution of the Monte Carlo algorithm, until full convergence of the set of equations is obtained.

## APPLICATION DETAILS

In order to assess the ability of the adopted pdf combustion model to reflect the characteristic features of flame propagation in engines, different aspects of premixed SI engine combustion have been studied numerically in the disc-shaped combustion chamber of a two-valve research engine configuration for different homogeneous-charge operating conditions. The cylinder bore and stroke were 85 mm and 94 mm, respectively, the compression ratio was 10:1. For all test cases under consideration the engine was run at 1000 rpm with the spark timing at 33 degrees crank-angle before top dead centre (TDC).

The in-cylinder flow and charge mixture composition evolution prior to combustion were obtained through simulation of the complete gas exchange and compression strokes. An unsteady gas dynamic and cycle calculation method was used to provide the initial and boundary conditions for the multidimensional simulation under the operating conditions of interest. This procedure enabled incorporation of all data pertinent to the operating engine, including the pressure wave oscillations in the intake system.

The calculations started at inlet valve opening and were continued until complete combustion of the cylinder charge. A computational time-step equivalent to 1/10 degree crank-angle was used throughout the calculations. The total number of Monte Carlo particles taken for representation of the pdf distribution during combustion was chosen to be 0.9 million. Spark ignition was simulated through prescription of the temporal variation of the reaction progress variable in a block of computational cells at the spark location, representing the very early, initially laminar flame kernel formation phase (Tatschl).

Model verification was achieved by comparison of the calculated results with the corresponding experimental data obtained in the optically accessed combustion chamber of a single cylinder research engine (Tatschl et al., Winklhofer et al.).

In order to demonstrate the applicability of the method to stratified-charge combustion, the processes of internal mixture formation and combustion were simulated for an engine configuration adopting AVL's Direct Mixture Injection technology. With DMI, fuel-stratification is obtained by injecting premixed fuel / air charge from a small prechamber volume into the main combustion chamber just before spark timing by means of an externally actuated valve. For the present study the engine was run at 1000 rpm and 1.1 bar mean effective pressure without inlet throttling, spark ignition was at 16 degrees crank-angle before TDC.

The calculations started at inlet valve closure with zero mean velocity and were continued until quenching of the heat releasing reactions. A computational time-step equivalent to 1/10 degree crank-angle was used throughout the calculations. For the engine configuration studied the computational grid during mixture formation and combustion comprised of approximately 70,000 cells. The total number of Monte Carlo particles taken for representation of the pdf distribution during combustion was chosen to be 7.0 million.

## RESULTS

Fig. 1 depicts the calculated results of the SI engine combustion process together with the corresponding experimental data in two perpendicular cross-sections. The sequence of pictures shows how the flame starts at the ignition location, grows into all directions until it reaches the piston

surface and then further propagates radially outward. The experiments show the probability distribution of the flame size, obtained by averaging of single shots; the calculated results also represent an averaged combustion process. It is evident that the early flame kernel growth process which is mainly determined by chemical kinetic effects as well as the increasing influence of turbulence, finally leading to a fully developed turbulent flame are well captured by the probability method adopted.

Besides a qualitative assessment of the combustion process, the quantification of the impact of engine speed, load and mixture composition with respect to clearly defined characteristic parameters is of major interest. The local flame front velocity represents a possible assessment quantity that can also be obtained from measurements. In SI engines the flame front velocity is determined by both the flame speed and the volumetric expansion of the hot combustion products behind the flame front.

Due to the density change of the charge as it undergoes combustion, the flame acts as a volumetric source, an effect that is intimately coupled with the local rate of heat release. The volumetric expansion of the hot combustion products behind the reaction zone and hence the local rate of heat release can be made visible by tracing the temporal evolution of the flow velocity at a fixed monitoring point under the influence of the approaching flame front. Fig. 2 shows such a velocity variation at a monitoring location on the axis of the disc-shaped combustion chamber, 5 mm below the cylinder head. The velocity course clearly shows the flow acceleration due to the approaching flame front and the subsequent deceleration and flow reversal after the flame has passed the monitoring point.

The flame speed together with the volumetric expansion velocity determine the overall flame propagation velocity. Both are linked to the thermodynamic quantities temperature and pressure, the mixture composition and to the intensity of the local turbulent velocity and scalar fluctuations.

The calculated dependence of the flame front velocity on engine speed, load and air excess ratio are shown in Fig. 3, together with the measured values. The results show that the flame front velocity scales nearly linearly with engine speed and hence turbulence intensity. An increase in volumetric efficiency and hence the pressure and temperature level also results in an increase of the flame front velocity. For a variation of the air excess ratio a maximum in the flame propagation velocity can be observed near  $\lambda=1$ . For all conditions under investigation the calculated results are well in between the range of the experimental data.

In the context of SI engine development, the ability of a combustion model to reflect the impact of fuel to air equivalence ratio and residual gas mass fraction on the overall engine performance is of vital interest, specifically in the context of SI engines adopting internal mixture formation technology. Fig. 4 shows calculated global heat release curves for variations in fuel to air equivalence ratio and different residual gas mass fractions, together with the corresponding global values derived from in-cylinder pressure measurements. It is evident that for an equivalence ratio of 0.8 a self sustaining flame front could not be established. It is, however, clear to the authors that prediction of the detailed mechanisms of flame quenching would require adoption of multi-step chemical kinetics.

The space and time resolved mixture preparation behaviour for the DMI engine configuration is shown in Fig. 5 for a cut across the symmetry plane. The depicted iso-levels represent the local fuel to air equivalence ratio distribution. Bright areas indicate fuel rich regions, whereas dark regions characterise

low fuel concentration. The propagation behaviour of the fuel vapour cloud is determined by the interaction of the in-cylinder flow field generated during the compression stroke and the flow pattern induced by the outflow of fuel vapour from the prechamber which is located at the upper left hand side of the combustion chamber. The velocity field generated by the prechamber flow leads to a strong convective motion of the fuel vapour cloud away from the prechamber region towards the spark plug.

Fig. 6 shows the temporal evolution of the mixture fraction at spark location. The first non-zero fuel concentration appears approximately 20 degrees crank-angle before TDC. With the ongoing mixture preparation process the local fuel concentration increases, attains its maximum and decreases as the fuel vapour cloud passes by. It is interesting to note, that the fuel concentration exhibits remarkable fluctuations, a fact that is of quite significant importance with respect to the ignition behaviour of SI engines with internal mixture formation technology.

The evolution of the temperature field is shown in Fig. 7 for three different instants in time, here expressed in terms of degrees crank-angle. Starting from the location of the spark the region of high temperature grows preferentially in areas with local fuel concentration near stoichiometric. It can be clearly seen that the temperature iso-levels nearly coincide in shape with the fuel concentration iso-levels. No considerable rise in temperature and hence fuel consumption can be observed in the fuel lean areas identified in Fig. 5, indicating a considerable amount of fuel to be left unburnt.

## SUMMARY AND CONCLUSIONS

A multi-scalar probability density function method for turbulent reacting flows has been implemented into the commercial CFD code FIRE in order to enable three-dimensional homogeneous and inhomogeneous-charge SI engine combustion simulation.

Model verification was achieved by comparison of the calculated results with the corresponding experimental data obtained in a single-cylinder research engine. The results clearly show the ability of the present method to reflect the characteristic features of premixed SI engine combustion and to capture the influence of engine operation and mixture composition on flame front velocity and heat release. Good agreement between the numerical and experimental results was obtained for the operating conditions considered.

The study further demonstrates the applicability of the present method to stratified-charge SI engine combustion where finite-rate chemistry effects play an important role in the overall combustion performance.

## REFERENCES

- Ahmadi-Befrui, B., Kratochwill, H., "Multidimensional Calculation of Combustion in a Loop-Scavenged Two-Stroke Cycle Engine", *Proceedings of COMODIA 90 - Int. Symposium on Diagnostics and Modelling of Combustion Engines*, pp. 465-474, Kyoto, 1990.
- Borghi, R., Moreau, P., "Turbulent Combustion in a Premixed Flow", *Acta Astronautica*, 4, pp. 321 - 341, 1977.
- Borghi, R., "Turbulent Combustion Modelling", *Prog. Energy Combust. Sci.*, Vol. 14, pp. 245-292, 1988.
- Bray, K.N.C., Moss, J.B., "A Unified Statistical Model of the Premixed Turbulent Flame", *Acta Astronautica*, 4, pp. 291-319, 1977.
- Cant, R.S., Bray, K.N.C., "A Theoretical Model of Premixed Turbulent Combustion in Closed Vessels", *Comb. Flame*, Vol. 76, pp. 243-263, 1989.
- Curl, R.L., "Dispersed Phase Mixing: 1. Theory and Effects in Simple Reactors", *AIChE Journal*, Vol. 9, pp. 175-181, 1963.
- Dopazo, C.A., "A Probabilistic Approach to Turbulent Flame Theory", *Acta Astronautica*, 3, pp. 853 - 878, 1976.
- El Tahry, S.H., "A Turbulent Combustion Model for Homogeneous-Charge Engines", *Comb. Flame*, Vol. 79, pp. 122-140, 1990.
- Janicka, J., Kolbe, W., Kollmann, W., "Closure of the Transport Equation for the Probability Density Function of Turbulent Scalar Fields", *Journal of Non-Equilibrium Thermodynamics*, 4, pp. 47 - 66, 1979.
- Meneveau, C., Poinso, T., "Stretching and Quenching of Flamelets in Premixed Turbulent Combustion", *Comb. Flame*, Vol. 86, pp. 311-332, 1991.
- O'Brien, E.E., "The Probability Density Function (PDF) Approach to Reacting Turbulent Flows", *Turbulent Reacting Flows*, Springer, pp. 185 - 218, 1980.
- Pope, S.B., "The Statistical Theorie of Turbulent Flames", *Phil. Trans. R. Soc. London*, 291, pp. 529 - 568, 1979.
- Pope, S.B., "A Monte Carlo Method for the PDF Equations of Turbulent Flow", MIT-EL 80-012, 1980.
- Pope, S.B., "PDF Methods for Turbulent Reactive Flows", *Prog. Energy Combust. Sci.*, Vol. 11, pp. 119-192, 1995.
- Ramos, J.I., Sirignano, W.A., "Turbulent Flow Field in Homogeneous-Charge, Spark-Ignition Engines", *Eighteenth Symposium (Int.) on Combustion*, pp.1825 - 1835, 1980.
- Ryn, H., Asanuma, T., "Numerical Simulation of Two-Dimensional Combustion Process on a Spark Ignition Engine with a Prechamber Using k-ε Turbulence Model", SAE 890669, 1989.
- Tatschl, R., "Multidimensional Simulation of Spark Flame Initiation Phenomena with a Generic Chemical Kinetic Reaction Scheme", PhD Thesis University of Technology Graz, 1991.
- Tatschl, R., Brandstätter, W., "Multidimensional Calculation of Spark Flame Initiation by Adopting a Generic Hydrocarbon Kinetic Scheme", *Computational Methods in Applied Sciences*, pp. 283-293, Elsevier Science Publishers, 1992.
- Tatschl, R., Wieser, K., Reitbauer, R., "Multidimensional Simulation of Flow Evolution, Mixture Preparation and Combustion in a 4-Valve Gasoline Engine", *Proceedings of COMODIA 94 - Int. Symposium on Diagnostics and Modelling of Combustion Engines*, pp. 139-149, Yokohama, 1994.
- Tatschl, R., Fuchs, H., Brandstätter, W., "Experimentally Validated Multi-dimensional Simulation of Mixture Formation and Combustion in Gasoline Engines", IMechE C499/050/96, 1996.
- Tatschl, R., Riediger, R. and Fuchs, H., "A Multi-Scalar PDF Method for Inhomogeneous-Charge SI Engine Combustion", *Proceedings of the International Colloquium on Advanced Computation & Analysis of Combustion*, Moscow, 1997.
- Westbrook, C.K., Dryer, F.L., "Chemical Kinetic Modeling of Hydrocarbon Combustion", *Prog. Energy Combust. Sci.*, Vol. 10, pp. 1-57, 1984.
- Winklhofer, E., Fraidl, G., Tatschl, R., "Flame Visualisation in Gasoline Engines - New Tools in Engine Development", SAE Japan 9530850, 1995.

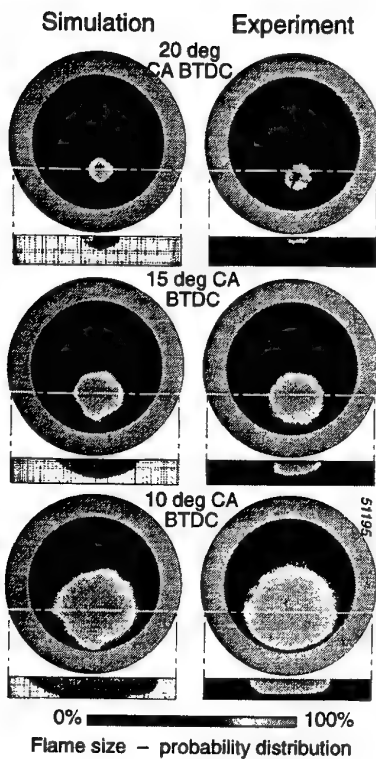


Fig. 1  
Flame Propagation;  
Calculated Results and  
Cycle-Averaged  
Experimental Data

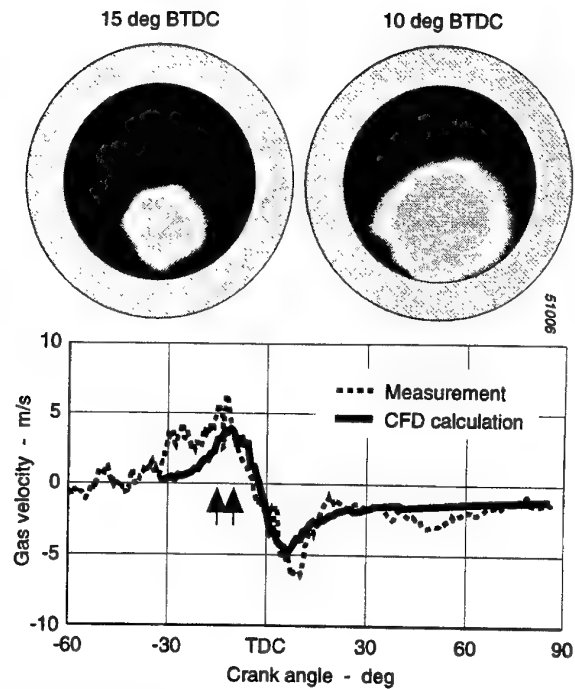


Fig. 2  
2-Valve Research Engine  
Local Gas Velocity under the Influence of Flame Propagation

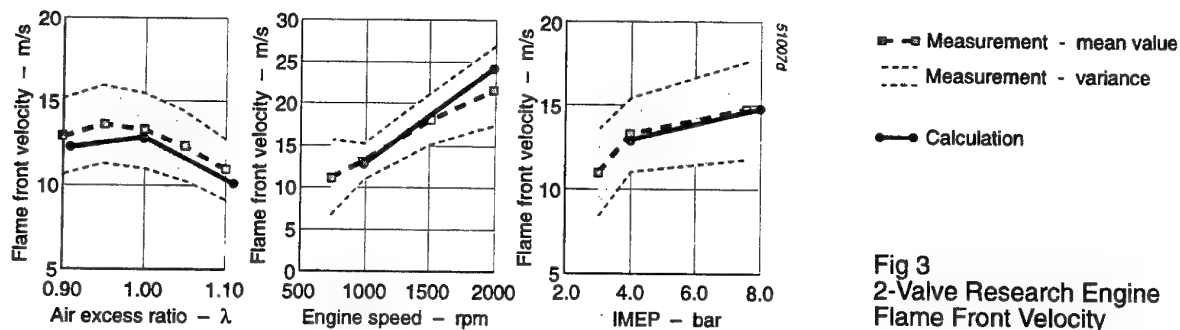


Fig 3  
2-Valve Research Engine  
Flame Front Velocity

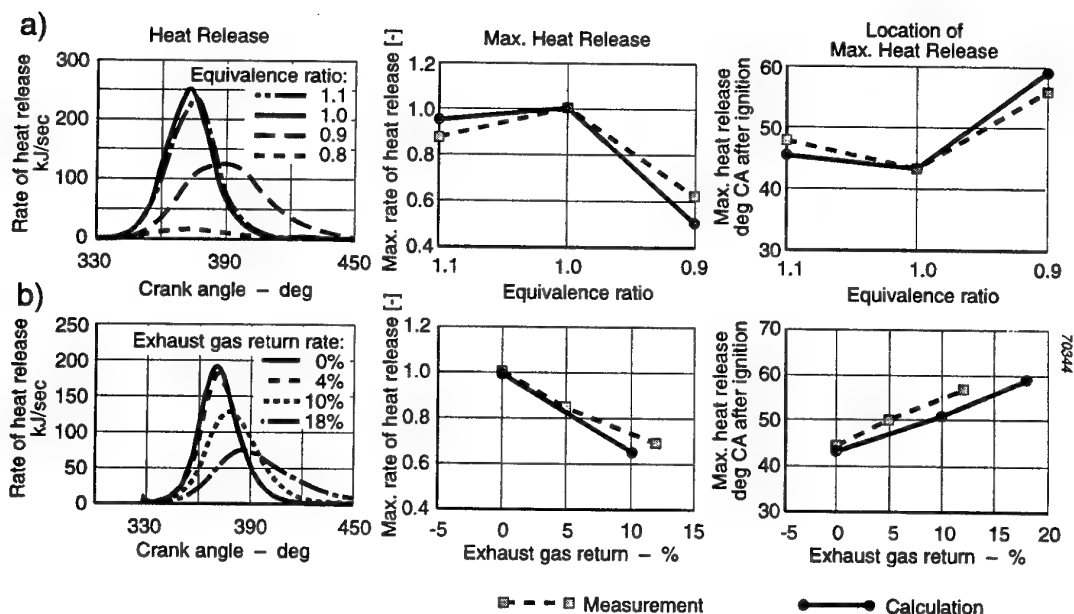


Fig. 4: Heat Release Data  
a) Variation of Fuel/Air Equivalence Ratio  
b) Variation of External Exhaust Gas Return

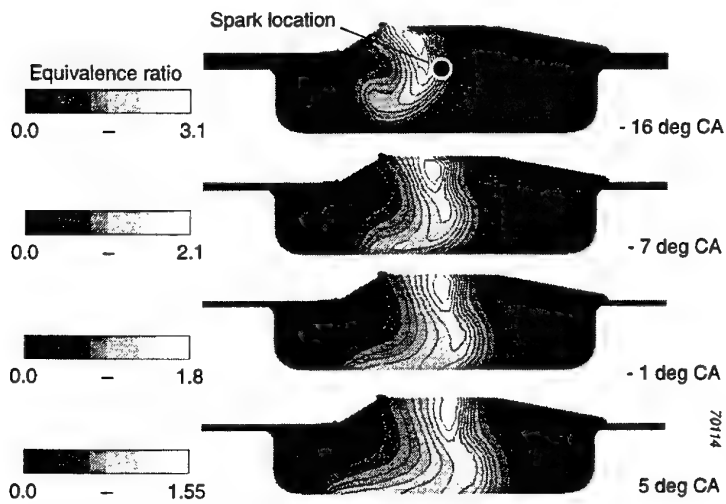


Fig. 5  
AVL DMI  
Total Fuel Concentration Field Evolution

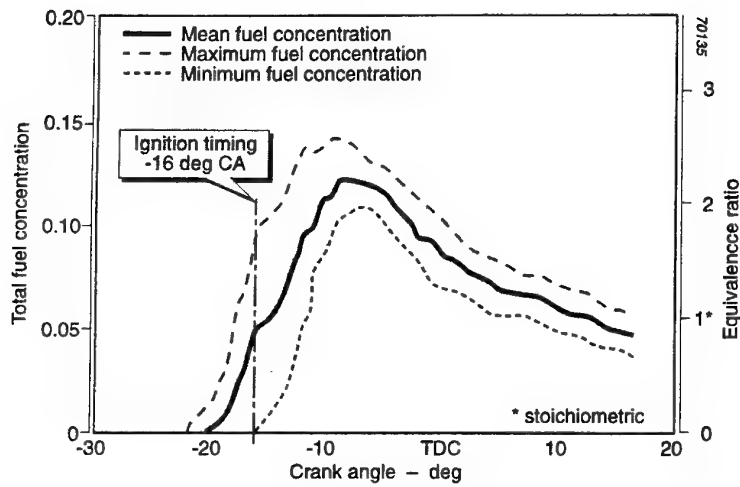


Fig. 6  
AVL DMI  
Total Fuel Concentration Evolution at  
Spark Location

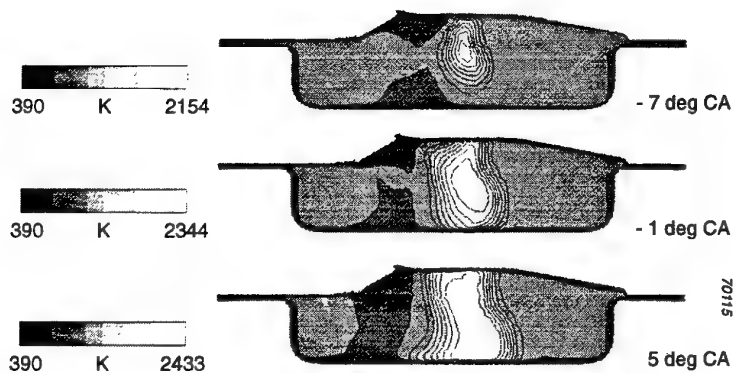


Fig. 7  
AVL DMI  
Temperature Field Evolution



# TURBULENCE STATISTICS AND SCALAR TRANSPORT IN HIGHLY-SHEARED PREMIXED FLAMES

by

D. Duarte, P. Ferrão and M. V. Heitor

Department of Mechanical Engineering  
Instituto Superior Técnico  
Av. Rovisco Pais  
1096 Lisboa Codex  
Portugal

## ABSTRACT

This paper describes recent progress in the analysis of the nature of turbulent premixed flames stabilised behind an axisymmetric baffle, which are of fundamental interest in the development of new and cleaner combustion systems. The work includes the use of laser-based diagnostics for velocity and temperature measurements, which are extended to the analysis of turbulence statistics, including the energy spectrum and typical length scales in a reacting shear layer. The results provided experimental evidence of the extension of the flamelet regime beyond the Klimov-Wiliams criterion. Arguments based on the shape of the weighted joint probability distributions of axial velocity and temperature fluctuations show that the counter-gradient nature of heat flux is derived from large departures from the local mean values.

## INTRODUCTION

In previous papers we have discussed the occurrence of non-gradient scalar fluxes in turbulent recirculating premixed flames stabilised downstream of baffles, which appear to be particularly influenced by the magnitude of the mean pressure gradients associated with the streamline curvature and are associated with the acceleration of gases across the flame front, Heitor et al. (1987), Ferrão and Heitor (1995), Duarte et al. (1996). Most of the analysis which has been presented in flames with practical interest (eg. Takagi et al., 1984, Takagi and Okamoto, 1987, Fernandes et al. 1996) may be considered to represent reacting regimes statistically equivalent to distributed reaction zones and/or well-stirred flames, but the extent to which the time-resolved nature of the flames affect their propagation remains to be understood. Also, the experimental evidence of the transition between the various combustion regimes remains to be shown, for flames of practical relevance.

As noted by Poinso et al. (1996), the time-averaged integral scales are unable to represent the multiscale nature of the interaction process between the combustion process and the turbulent flow field. In fact, the turbulent flow features a complex combination of vortices with scales ranging from the integral scale to the Kolmogorov scale. Each of these may be

characterised by a length scale and a velocity fluctuation. To described turbulence/combustion interactions, one has to take into account the existence of these various scales in the flow and, accordingly, build a spectral diagram for each point of the integral combustion diagram. The experimental validation of the combustion regimes and the related difference on the flame structure requires in-flame measurement of length scales and the associated turbulent intensities, which is the main motivation of the present paper. The work includes the analysis of counter gradient diffusion of turbulent heat flux, as reported by Ferrão and Heitor (1995), and correlates its concurrence in practical flames with the shape of weighted joint probability density functions of axial velocity and temperature fluctuations, as described by Hardalupas et al. (1996). The ultimate objective is to provide new insight into the nature of turbulent premixed flames and to provide new data for model development. The practical implication in the context of combustion devices is that the retardation of mixing, which is associated with the occurrence of counter-gradient heat flux, may be technically desirable.

It is important to make clear that in our previous works the occurrence of counter-gradient heat flux has been identified from the analysis of the terms in the conservation equations of the scalar fluxes, which clearly identify the reacting shear layer as the zone where the interaction between the mean pressure gradients and density fluctuations are important (e.g., Ferrão and Heitor, 1995).

The main purposes of this paper is to show that even in the regions of the reacting shear layer where there is no evidence of counter-gradient diffusion, the underlying driving mechanism remains important and, therefore, the so-called second moment closures must be used to calculate the flame. To achieve this objective, the method of analysis is that previously used by Cheng and Ng (1985) and, more recently, by Hardalupas et al. (1996) making use of quadrant analysis.

The next section describes the experimental method and give details of the extend to which the laser Rayleigh scattering can be used in the presented propane-air flames. The third section presents and discusses sample results, and the last section provides the main conclusions of the work.



## THE EXPERIMENTAL METHOD AND ACCURACY

### The Flames Studied

The experiments reported in this paper were conducted in unconfined non-swirling premixed flames of air and propane, stabilised on a disk with  $D=56$  mm in diameter, which is located at the exit section of a contraction with 80mm in diameter.

The annular bulk velocity is in the range  $10 < U_o(\text{m/s}) < 42$ , resulting in a Reynolds number, based on a disk diameter, up to  $1.5 \times 10^5$ . The equivalence ratio was varied between 0.53 and 1, although most of the results characterised in this paper correspond to lean flames, with  $\phi = 0.55$ . Table 1 characterises the three mean experimental conditions used throughout the work, which are identified as flame A, B and C.

Table 1 - Characterisation of experimental conditions.

Flame	$U_o$ (m/s)	Re	$\phi$	$S_L$ (cm/s)	$l_F$ (mm)
A	10	35 700	0.64	12	0.6
B	20	71 400	0.64	12	0.6
C	42	150 000	0.64	12	0.6

### The Experimental Technique

The instrumentation used throughout this work consists on a combined LDV/LRS system, which was based on a single laser light source (5W argon-ion laser). The system has derived from that described by Duarte et al. (1995) and Almeida et al. (1996), as the main data acquisition system includes a 16 bits analogue/digital converter, in place of the 12 bits data acquisition board previously used.

The velocimeter was based on the green light (514.5nm) of the laser and was operated in the dual-beam, forward-scatter mode with sensitivity to the flow direction provided by a rotating diffraction grating. The calculated dimensions of the measuring volume at the  $e^{-2}$  intensity locations were 606 $\mu\text{m}$  in length and 44 $\mu\text{m}$  in diameter.

The Rayleigh scattering system was operated from the blue line of the same laser source, which was made to pass through a 5:1 beam expander. The light converged in a beam waist of 50 $\mu\text{m}$  diameter was collected at 90° from the laser beam direction with a magnification of 1, and passed through a slit of 1 mm length. The collected light was filtered by a 1nm bandwidth interface filter and a polariser, in order to optimise the signal-to-noise ratio.

The signal was amplified and low pass filtered at 10KHz before digitalisation. The temporal resolution of the system depends on the integration time associated with this filter, which is quantified to be 50 $\mu\text{s}$ . This value, associated with the typical flow velocities, give rise to path lengths of about 1mm and, therefore, smaller than the integral length scales in the reaction shear layer. The resolution of the system was confirmed by the measured temperature distributions, which include instantaneous values close to either adiabatic or room temperature, confirming that the system is capable of resolving the temperature fluctuations associated with the premixed flames analysed in this work.

The details associated with the accuracy of the experimental method used, and in particular of the laser Rayleigh scattering,

has been discussed by Caldas et al. (1997) and is not reported here.

## RESULTS AND DISCUSSION

The most salient features of the mean flow characteristics of the flames studied through this work can be inferred from the measured velocity vectors and isocontours of mean temperature represented in figure 1 for flame C. The results are similar to those found in other baffle-stabilised recirculating flames, in that they exhibit a recirculation region extending up to  $L_r = 125\text{mm}$ , where the fluid has a large and fairly uniform mean temperature, surrounded by an annular region of highly sheared fluid where gradients of mean temperature are large. The length of the recirculation zone decreases when the Reynolds number is decreased, with the rear stagnation point located at  $L_r/D=1.8$  for  $Re=0.7 \times 10^5$  (Flame B).

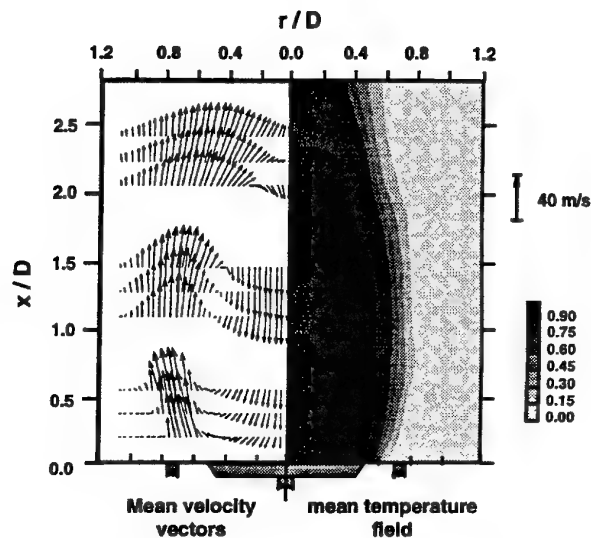


FIG. 1. DISTRIBUTION OF MEAN VELOCITY VECTORS AND ISOTHERMS ALONG A VERTICAL PLANE OF SYMMETRY FOR FLAME C.

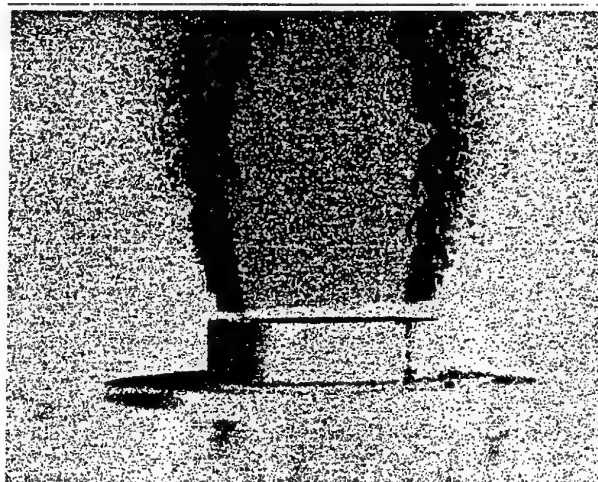


FIG. 2 - INSTANTANEOUS FLAME (B) VISUALISATION DURING A 9 NS ND-YAG LASER PULSE.

The isotherms are highly curved for the three conditions studied and reveal non-planar flames oblique to the oncoming reactants. For these conditions, the analysis of the photography of figure 2 shows that reaction occurs along a thin shear layer located between the locus of maximum axial velocity and the locus of the mean separation streamline, which is curved along its length. This curvature varies with the Reynolds number considered and imposes mean velocity effects on the turbulence field in a way which depends on the level of interaction between the gradients of mean pressure typical of the present flames and the associated density fluctuations.

Analysis has shown that along the reacting shear layer turbulence is mainly generated by the interaction between shear strain and shear stress, giving rise to a strongly anisotropic turbulent field with comparatively large axial velocity fluctuations. As the stagnation region is approached, the cross-stream turbulent components increase as a result of the increased importance of the interaction between normal strains and normal stresses in the conservation of turbulent kinetic energy as in other recirculating flows with free stagnation points.

The detailed velocity and scalar characteristics obtained along the present flames are presented elsewhere. Here, attention is focused on the zone which characterises the maximum width of the recirculation zone of the flames considered and Figure 3a) shows the related radial profiles of mean temperature, while Figure 3b) shows the temporal distributions of Eulerian time correlations for three distinct points across the reacting shear layer. Together with the power spectra of the temperature velocity fluctuations of figure 3c), the results are typical of well-behaved turbulent shear flows and suggest that the integral time scale, as defined by Hinze (1975), is as large as 1ms. This scale is a measure of the average time life of the large eddies that are mainly responsible for turbulent transport and the results confirm the suitability of the measurement technique described before to address the nature of turbulent heat flux in the present flames. Figure 4 compares the results with those obtained for lower Reynolds numbers, which agrees with the observation that the main frequency of interest in the energy spectra increases with the Reynolds number, namely between 3KHz for Flame A and 4KHz for Flame C.

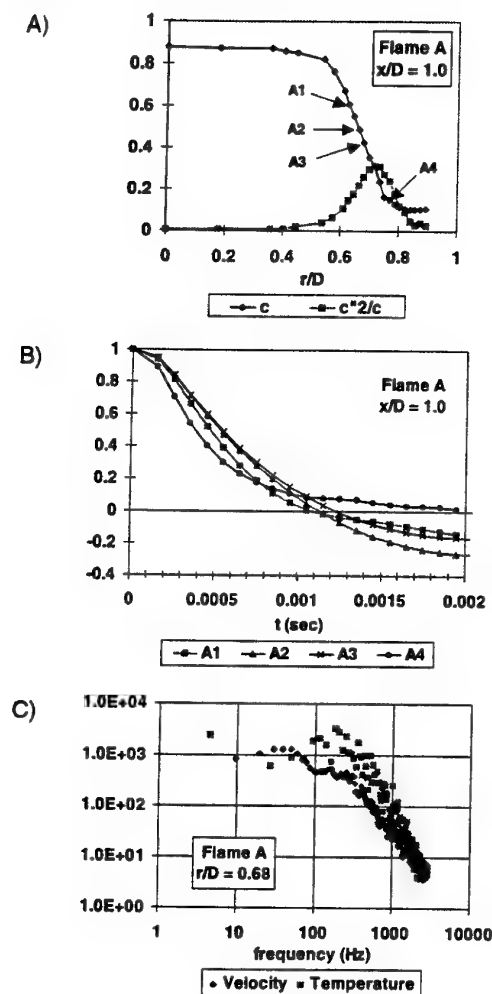


FIG. 3. ANALYSIS OF THE REACTING SHEAR LAYER OF FLAME A:  
A) MEAN TEMPERATURE PROFILE AT  $x/D = 1.0$ .  
B) EULERIAN TIME CORRELATIONS ACROSS THE REACTING SHEAR LAYER (FOR THE POINT MARKED IN A)).  
C) POWER SPECTRA OF VELOCITY AND TEMPERATURE FOR  $x/D = 1.0$  AND  $r/D = 0.68$  (POINT A3 IN A)).

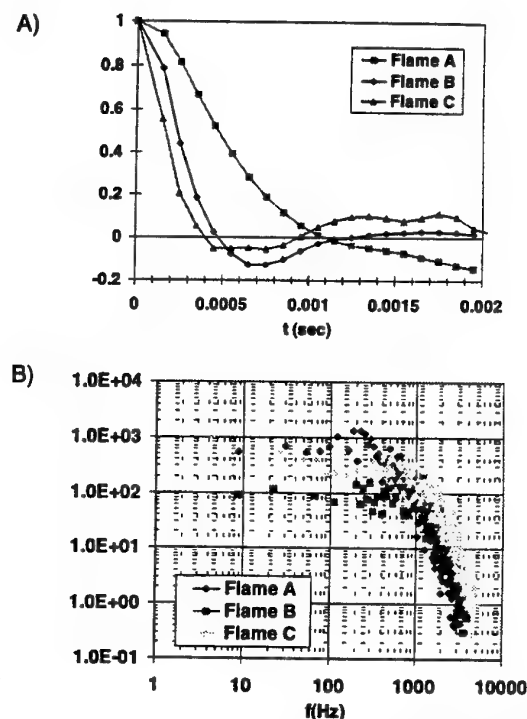


FIG. 4. ANALYSIS OF THE FLAME CHARACTERISTICS AS A FUNCTION OF THE REYNOLDS NUMBER, FOR  $X/L_R = 0.5$ :

A) EULERIAN TIME CORRELATIONS: FLAME A AT  $R/D = 0.63$ ; FLAME B AT  $R/D = 0.61$ ; FLAME C AT  $R/D = 0.64$   
B) POWER SPECTRA FOR THE SAME LOCATIONS AS IN A).

Although the radial distributions of time-averaged temperature for the three conditions studied here are qualitatively similar, the analysis above suggests that the temporal structure of the flames is different and the related experimental evidence is provided by the probability-density functions of temperature of Figure 5. While Flame A is characterised by near bimodal temperature distributions across the reacting shear layer with

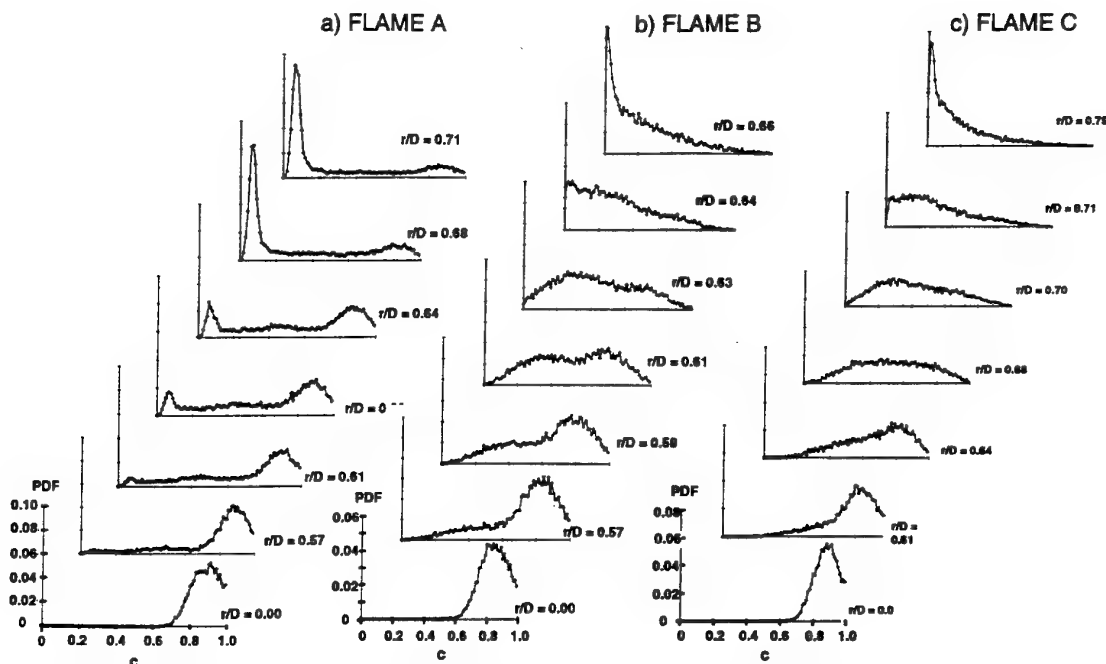


FIG. 5. RADIAL DISTRIBUTION OF THE PROBABILITY DENSITY FUNCTION OF TEMPERATURE FLUCTUATIONS, ACROSS THE REACTING SHEAR LAYER

significant probability for intermediate products, the distributions obtained for Flame C exhibit typically the near-Gaussian form characteristic of the distributed reaction combustion regime. It is clear that the absolute values of the probability distributions are influenced by the shot noise characteristics of the photomultiplier used for the Rayleigh scattering measurements, but the qualitative trends shown in Figure 5 are not affected by experimental accuracy. The burning conditions associated with Flame A are characteristic of a regime where the flame fronts become thick and bigger than the Kolmogorov length scale. Following Poinot et al (1991) the construction of the turbulent combustion diagram is straightforward, as in figure 6.

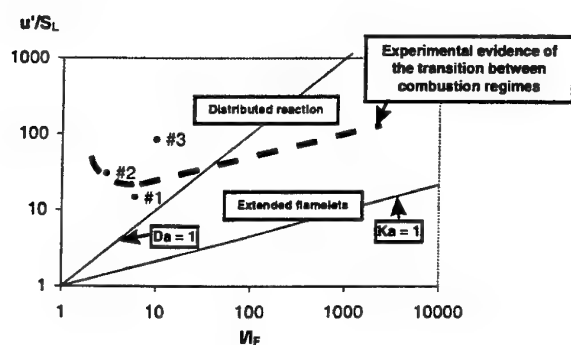


FIG. 6 - DIAGRAM FOR TURBULENT PREMIXED COMBUSTION (POINTS AS DEFINED IN THE TEXT).

The position in the reacting shear layer of flame A where a bimodal temperature distribution was identified (i.e.,  $x/D = 1.0$ ,  $r/D = 0.64$ ; #1 in figure 6) is characterised by turbulent scales which act on the flame front in two different ways. First, eddies

whose sizes are between the Kolmogorov scale and a "cut-off" scale will be inefficient and will not affect the flame front. Second, vortices larger than the "cut-off" scale will be able to affect the flame front, to wrinkle it or to form pockets but be unable to induce local quenching. Point #1 corresponds therefore to the extended flamelet regime of Poinot et al (1991).

The other locations identified in figure 6 (namely, #2 for flame B at  $x/D = 0.71$  and  $r/D = 0.61$ ; and #3 for flame C at  $x/D = 1.27$  and  $r/D = 0.68$ ) are associated with scales that are capable of locally quenching the flame front. These scales are larger and faster than the Kolmogorov scale and correspond to the distributed reaction regime of turbulent combustion. It should be noted that the near-Gaussian distributions of Figure 5 associated with flame locations #2 and #3 exhibit values between ambient ( $C=0$ ) and adiabatic ( $C=1$ ) temperatures and, therefore, are not expected to be influenced by lack of temporal resolutions of the Rayleigh system.

Figure 7 shows measured values of turbulent axial heat fluxes, which are restricted to the thin zone along the shear layer where the radial gradients of mean temperature are large. These quantities represent the exchange rate of reactants responsible for the phenomena of flame stabilisation and previous results have shown that the turbulent heat transfer is essentially directed along the isotherms, rather than normal to them, as would be expected from gradient-transport models of the kind used in non-reacting flows. It should be noted that the radial fluxes are always positive, as expected in a recirculating flame. The flame is then established by the heat transfer between the hot products and the cold reactants with the sign of the radial heat flux in qualitative agreement with gradient-transport models. Similar behaviour has been observed in other turbulent premixed flames (Heitor et al., 1987) and has also been predicted analytically (Bray et al., 1985), and is expected to be due to the interaction between the gradients of mean

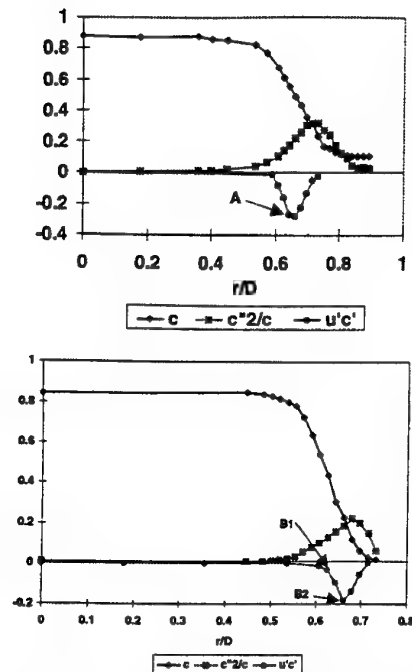


FIG. 7. RADIAL PROFILE OF TEMPERATURE AND TURBULENT HEAT FLUX CHARACTERISTICS:  
A) FOR FLAME A AT  $X/D = 1.0$ .  
B) FOR FLAME B, AT  $X/D = 0.71$ .

pressure typical of the present flow and the large density fluctuations that occur in the flames.

The analysis above explains the process of "counter-gradient" heat transport in terms of the preferential deceleration of the products of combustion, relatively to the cold reactants (see Caldas et al., 1997 for further details). This can be easily observed through the joint probability distribution of velocity and temperature fluctuations and here the analysis follows the methodology of Cheng and Ng (1985) and Hardalupas et al. (1990), making use of weighted probability distributions. The corresponding plots should be analysed based on the relative importance of the entries in the four quadrants of figure 8, with gradients 1 and 3 dominating the case of gradient diffusion. The entries in quadrants 2 and 4 arise when velocity fluctuations, which are respectively smaller and larger than the local mean, are associated with values of temperature fluctuations which are greater and smaller, respectively, than the mean value. Typical examples are shown in figure 9 to 11, which clearly show that even when the entries in the "counter-gradient" quadrants are smaller and, consequently, the time-averaged heat flux may be qualitatively represented by gradient diffusion, the absolute value of the heat flux is influenced by the source terms which drive counter diffusion. A similar observation has been made by Hardalupas et al. (1996) for non-premixed flames and confirms that it is unreasonable to expect that calculations based on effective viscosity hypothesis are accurate to represent recirculating flames. The present results bring new experimental evidence of the magnitude of turbulence/combustion interactions in strongly sheared premixed flames and permits insight into the scale of the fluctuations of temperature and velocity, which gives rise to counter-gradient diffusion of heat.

## CONCLUSIONS

Simultaneous measurements of time-resolved velocity and temperature have been obtained by laser-Doppler velocimetry and laser-Rayleigh scattering in the near wake of premixed recirculating flames of propane and air. The experiments encompass three flow conditions associated with different combustion regimes and Reynolds numbers. The results bring new insight into the fluctuations that occur in these flames, which are expressed in terms of the shape of the weighted joint probability distributions of axial velocity and temperature fluctuations. These observations are related to the streamline curvature and are shown to occur even for a flame structure characterised by near-Gaussian probability distributions of the temperature fluctuations. In addition, the characterisation of the local length scales and turbulence intensities provide experimental evidence of the extension of the flamelet regime beyond the Klimov-Williams criterion.

## ACKNOWLEDGEMENTS

The assistance of Mr. Carlos Carvalho in the preparation of this paper is gratefully appreciated. Financial support has been provided by the BRITE/EURAM programme of the DGXII of the Commission of the European Communities, under the contracts CT/95-0106.

## REFERENCES

- Almeida, P., Ferrão, P. and Heitor, M.V. 1995. The effect of swirl on the interaction between pressure gradients and density fluctuations in baffle-stabilised flames. *Proc. of 10th Symposium on Turbulent Shear Flows*. Vol. 2, pp. 16-7 to 16-12
- Caldas, F. D. Duarte, Ferrão, P., Heitor, M.V. and Pope, C. 1997. On the use of laser Rayleigh scattering to study the aerothermochemistry of recirculating premixed flames. In: *Developments in Laser Techniques and Fluid Mechanics*. Eds. Adrian et al., Springer Verlag.
- Cheng, R.K. and Ng, T.T. 1985. Conditional Reynolds stress in a strongly heated turbulent boundary layer with premixed combustion, *Phys. Fluids*, **28**, pp. 473-488.
- Duarte, D., Ferrão, P. and Heitor, M.V. 1996. Flame structure characterisation based on Rayleigh thermometry and two-point laser Doppler measurements. In: *Developments in Laser Techniques and Application to Fluid Mechanics*. Eds. Adrian et al., Springer Verlag, 185-200.
- Fernandes, E.C., Ferrão, Heitor, M.V. and Moreira, A.L.N.-1994. Velocity temperature correlation in recirculating flames with and without swirl, *9*, pp. 241-249.
- Ferrão, P. and Heitor, M.V. 1995. Turbulent mixing and non-gradient diffusion in baffl-stabilised flames. In: *Turbulent Shear Flows - 9*, Eds. Durst et al., Springer Verlag, pp. 427-437.
- Hardalupas, Y., Tagawa, M. and Taylor, A.M.K.P., 1996. Characteristics of counter-gradient heat transfer in a non-premixed swirling flame. In: *Developments in Laser Techniques and Applications to Fluid mechanics*, ed Durst et al., Springer Verlag, pp. 159-184.
- Heitor, M.V., Taylor, A.M.K.P. and Whitelaw, J.H., 1987. The interaction of turbulence and pressure gradients in baffle-stabilised premixed flames. *J. Mechanics*, **181**, pp. 387-413.

Poinsot, T., Candel, and Trouvi, A. (1996). Applications of direct numerical simulation to premixed turbulent combustion. *Prog. Energy Combust. Sci.*, **21**, pp. 531-576.

Poinsot, T., Veynante, D. and Candel, S. (1991). Quenching process and premixed turbulent combustion diagrams. *J. Fluid Mech.*, **228**, pp. 561-606.

Takagi, T., Okamoto, T., Taji, M. and Nakasuji, Y., 1984. Retardation of mixing and counter-gradient diffusions in a swirling flame. *Proc. 20th Symposium (Intl.) on Combustion*, pp. 251-258. The Combustion Institute, Pittsburgh.

Takagi, T., Okamoto, T., 1987. Direct measurement of the turbulent transport of momentum and heat in the swirling flame. In: *Laser Diagnostic and Modelling of Combustion*, Eds. Linuma, K. et al., pp. 273-280, Springer Verlag, Berlin.

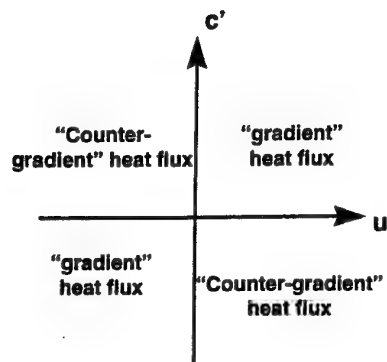


FIG. 8. PHYSICAL SIGNIFICANCE OF THE NATURE OF THE TURBULENT HEAT FLUXES, AS DERIVED FROM THE JOINT VELOCITY TEMPERATURE CORRELATIONS.

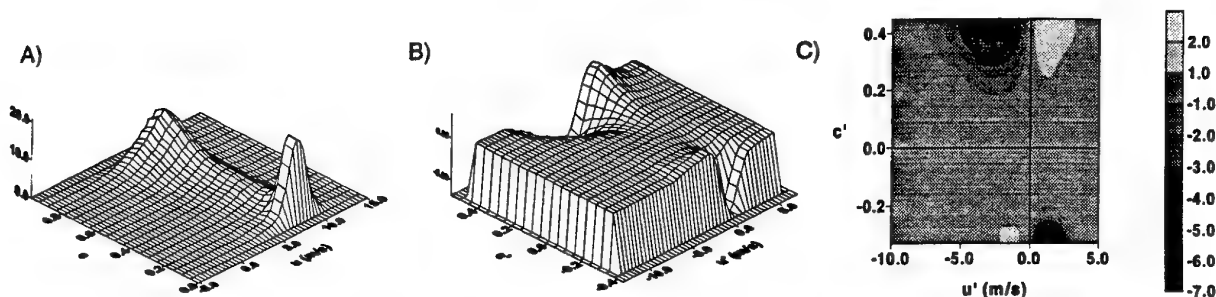


FIG. 9. ANALYSIS OF JOINT VELOCITY AND TEMPERATURE FLUCTUATIONS FOR FLAME A AT  $X/D = 1.0$  AND  $R/D = 0.64$ .

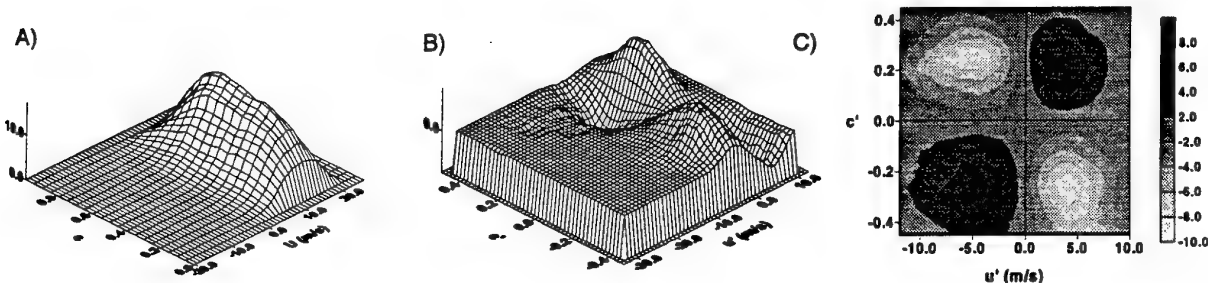


FIG. 10. ANALYSIS OF JOINT VELOCITY AND TEMPERATURE FLUCTUATIONS FOR FLAME B AT  $X/D = 0.71$  AND  $R/D = 0.63$ .

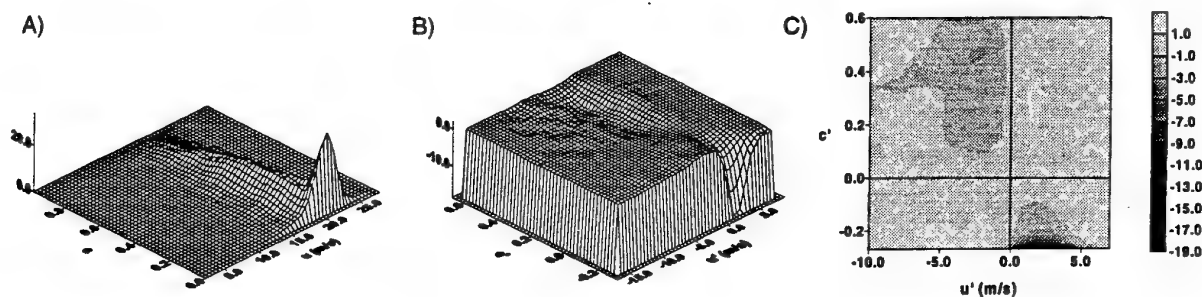


FIGURE 11. ANALYSIS OF JOINT VELOCITY AND TEMPERATURE FLUCTUATIONS FOR FLAME B AT  $X/D = 0.71$  AND  $R/D = 0.66$ .

- A) JOINT PROBABILITY DENSITY FUNCTION (PDF).
- B) 3D REPRESENTATION OF THE WEIGHTED PDF :  $U'C'P(U',C')$ .
- C) ISOCONTOURS OF THE WEIGHTED PDF REPRESENTED IN B).

# AN EXPERIMENTAL STUDY ON THE CONSECUTIVE AND COMPETING REACTION IN A TURBULENT LIQUID JET BY THE LIGHT ABSORPTION SPECTROMETRIC METHOD

Y.Sakai<sup>(1)</sup>, I.Nakamura<sup>(1)</sup>, T.Kubo<sup>(2)</sup>

<sup>(1)</sup> Department of Mechano-Informatics & Systems  
Nagoya University  
Furo-cho, Chikusa-ku, Nagoya 464-01  
Japan

<sup>(2)</sup> Graduate School of Mechano-Informatics & Systems  
Nagoya University  
Japan

## INTRODUCTION

The diffusion and mixing phenomena of matter accompanying the chemical reaction are practically important in connection with many engineering and environmental problems. The present study focuses the spotlight of attention on the chemical reaction in the liquid since the high Schmidt number matter is more available in liquid than in the gaseous phase and the turbulence plays more important role on the mixing process of such high Schmidt number matter.

Several important studies have been made in the past on the chemical reactions in the turbulent liquid flow; for example, mixing and chemical reactions in the plane turbulent mixing layer by Breidenthal(1981) and Koochesfahani and Dimotakis(1986), the competing reaction in grid-turbulence by Mehta and Tarbell(1987), the second-order reaction in grid-turbulence by Bannani *et al.*(1985), the shear-free mixing layer in grid-turbulence with a second-order reactions by Komori *et al.*(1994). However, there are still very few reports on the simultaneous measurements of the concentrations of reactants or products in the turbulent shear flows; except for the following only two reports, i.e. the mixing layer between two different velocity streams in grid-turbulence by Komori *et al.*(1994) and the competing reaction in a turbulent jet by Sakai *et al.*(1995). For the future development of the practical computational model useful to the turbulent reactive flows, the systematic experimental studies in the various shear flows are keenly expected.

The purpose of this study is to clarify the relation between the turbulent mixing and the chemical reaction in the axisymmetric turbulent jet. The chemical reaction treated in this study is the following parallel-consecutive and competing reaction(see Bourne *et al.*, 1985),



where A, B, R and S are 1-naphthol, diazotised sulphanilic acid, monoazo dye (red) and bisazo dye (purple), respectively. The aqueous solution of species B is issued from the

nozzle into the main stream including species A, and the simultaneous measurements of concentration of species R and S were performed by the novel light absorption spectrometric method(see Sakai *et al.*, 1990). The main stream is the flow of alkaline-buffered aqueous solution of Na<sub>2</sub>CO<sub>3</sub> and NaHCO<sub>3</sub> (pH=10, each concentration is 10 mol/m<sup>3</sup>), where the chemical reaction proceeds.

The similar experiments have been challenged in the past by Sakai *et al.*(1995). However in their work, the initial concentration ratio of species B to species A,  $\beta = \Gamma_{B0}/\Gamma_{A0}$  was less than 10, so that the produced amount of species S was quite small and there still remained some questions on the reliability of its concentration statistics. In the present work, to overcome the above problem, we chose the larger values of  $\beta$ (=10, 20, 40) and also tried to use the improved light probe with the larger diameter of glass fiber to obtain the more reliable data of concentration statistics of species S. In this paper, new data on the concentration fluctuation field of species R and S will be given.

## CHEMICAL REACTION

The first reaction (1) is a rapid reaction; the reaction rate coefficient  $k_1$  is estimated to be 12000 m<sup>3</sup>/(mol · sec). The second reaction rate has a temperature dependency; its coefficient  $k_2 = 1.148 \text{ m}^3/(\text{mol} \cdot \text{sec})$  at 13 °C (see Bourne *et al.*, 1985, in detail). Such a big difference between the reaction rate coefficient of reaction (1) and (2) is a distinctive feature of consecutive, competing reaction treated in this study.

## EXPERIMENTAL EQUIPMENT

Figure 1 shows the chemical reactor and coordinate system. The main stream around the nozzle has a small mean velocity 0.4 cm/sec to discharge the chemical products. The diameter of jet nozzle  $d$  is 2 mm and the issuing mean velocity at the nozzle exit  $U_N = 1.6 \text{ m/sec}$ . So the Reynolds number of the jet  $Re_J$  is about 2600. A cylindrical coordinate system is used to present the experimental data with the nozzle exit as the origin. The axial and radial coordinate are denoted by  $x$  and  $r$ , respectively.



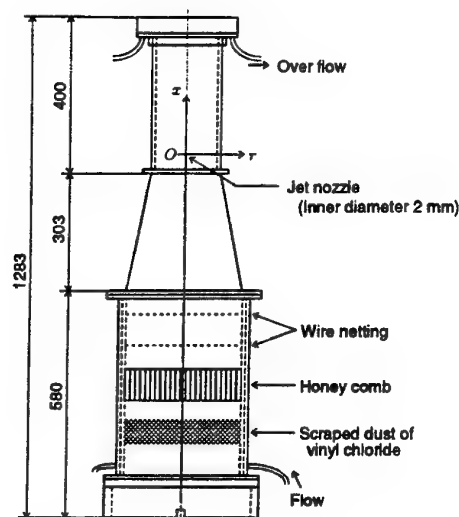


Figure 1: Chemical reactor and coordinate system.

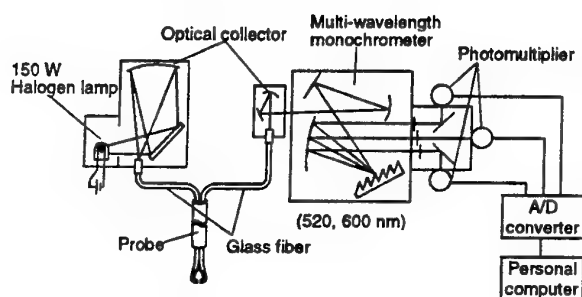


Figure 2: Schematic diagram of the measuring system.

The concentration measuring system by the light absorption spectrometric method has been developed by Sakai *et al.* (1990). This system makes it possible to take the simultaneous measurements of the instantaneous concentrations of at most three light absorptive species. A schematic diagram of the concentration measuring system is shown in figure 2. The light emitted from the halogen lamp is introduced into a sampling part through the light guide after being collected by the optical condensing system. The light modified according to the concentration fluctuations of multiple species passes again through the light guide, and then divided into three monochromatic lights (half-width of spectrum band of three lights are all about 15 nm). The intensity of each light is converted to a voltage output by the photomultiplier. Finally, the output is digitally processed by the personal computer through the 12 bit A/D converter.

Figure 3 shows the schematic sketch of the light probe. The diameter of fiber bundle is 0.5 mm, the sampling length is about 0.8 mm, so that the sampling volume is approximately  $1.6 \times 10^{-4}$  cc. In the previous experiments by Sakai *et al.* (1995), the core diameter of fiber is 0.1 mm, the sampling length is about 0.7 mm, so that the sampling volume is about  $4.4 \times 10^{-6}$  cc. Thus the present sampling volume is 36 times as large as the previous one. However it should be emphasized that the ratio of noise to signal reduced to 1/13. It seems that the improvement of the SN ratio is preferable than the spatial resolution in the present experiment. The resolution of the present probe is consid-

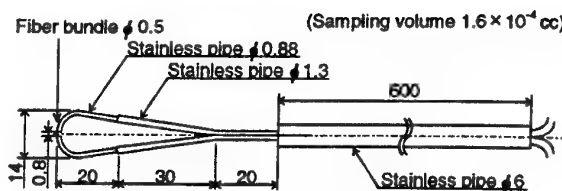


Figure 3: Schematic sketch of the light probe.

ered to be 0.8 mm, which is between Kolmogorov scale and Taylor's microscale at  $x/d > 20$ . That is 5~20 times as large as Kolmogorov scale.

## EXPERIMENTAL RESULTS

### Velocity Field

The axial ( $x$ -direction) velocity of the jet was measured by a cylinder type of hot-film probe (KNOMAX MODEL 1210-60W; the diameter and length of the sensing part are  $152 \mu\text{m}$  and 2 mm, respectively) in conjunction with a constant-temperature velocity anemometer (HAYAKAWA, Model HC-30). Here, the details are not described, but radial profiles of mean velocity  $U$  indicate a self-preservation at  $x/d > 15$ , which is almost Gaussian. The half-width of the radial profiles of mean velocity increases linearly over the self-preserving region. The radial profiles of the velocity fluctuation r.m.s. value  $u'$  show the self-preservation at  $x/d > 40$ . That profile has double peaks apart from the jet axis. From the above results, it seems that the present jet has standard characteristics of the axisymmetric turbulent jet although the Reynolds number is relatively small.

### Non-reactive Concentration Field

Before the experiments of the reactive flow, we checked the features of the non-reactive concentration field. As the diffusion matter, a direct dye "Rhoduline Red B" was used. This dye has the absorbance spectrum similar to the one of monoazo dye R.

Figure 4 shows the radial profiles of the mean concentration  $\Gamma$ , where  $\Gamma$  on the ordinate and radial distance  $r$  on the abscissa are normalized by the value on the jet axis  $\Gamma_C$  and the half-width  $b_r$ , respectively. From the figure, it is found that the mean concentration profiles show the good self-preservation in the region  $x/d > 12.5$ , which is well approximated by the Gaussian profile (solid line in the figure). We have investigated also the downstream variation of  $\Gamma_C$  and  $b_r$ . Although the figures are not shown here, we found that in the self-preserving region,  $\Gamma_C$  and  $b_r$  can be approximated by

$$\frac{\Gamma_N}{\Gamma_C} = 0.247 \left( \frac{x}{d} + 0.606 \right), \quad (3)$$

$$\frac{b_r}{d} = 0.113 \left( \frac{x}{d} + 1.42 \right), \quad (4)$$

where  $\Gamma_N$  is the concentration at the nozzle exit.

Figure 5 shows the radial profiles of the concentration r.m.s. value  $\gamma'$ . In the figure,  $\gamma'$  on the ordinate is normalized by the value on the jet axis  $\gamma'_C$ . From the figure, it is found that the r.m.s. profiles show the good self-preservation and have double peaks similar to the velocity fluctuation r.m.s. value  $u'$ . In the figure, the experimental profile obtained by Sakai (1984) is also given by the solid line. It has been already ascertained that the Sakai's profile coincides with other data (for example, the oil smoke jet by Becker *et al.* (1967), the methane gas jet by Birch *et al.* (1978)). From the figure, we can observe a very good

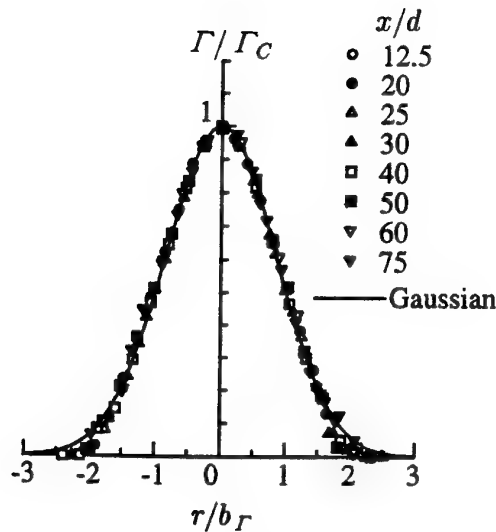


Figure 4: Radial profiles of the mean concentration.

agreement between the present data and Sakai's profile. We also found that the downstream variation of  $\gamma'_C$  can be approximated by

$$\frac{\Gamma_N}{\gamma'_C} = 0.820 \left( \frac{x}{d} + 11.75 \right). \quad (5)$$

Furthermore, it was ascertained that the values and profiles of the skewness and kurtosis factors of the probability density function of the concentration also show good agreements with other data by Becker *et al.* (1967) and Birch *et al.* (1978). Therefore, we concluded that the concentration fluctuation statistics of single species could be measured accurately by the present light probe.

#### Conserved Scalar Field

To check an accuracy of the simultaneous concentration measurement in this study, we made a comparison between the results of non-reactive concentration field given in the previous section and ones of conserved scalar field (for example, see Bilger *et al.*, 1991, in detail). For this purpose, we dealt with only the second reaction (2) here. The aqueous solution of species R was issued from the nozzle into the main stream including species B, and the simultaneous measurements of concentration of species R and S were performed. The initial concentration of species B in the main stream  $\Gamma_{B0}$  is 0.3 mol/m<sup>3</sup>, and the initial concentration of the species R in the jet  $\Gamma_{R0}$  is 2.7 mol/m<sup>3</sup>. In this case, the conserved scalar  $\tilde{F}$  is defined by

$$\tilde{F} = \frac{\tilde{\Gamma}_R + \tilde{\Gamma}_S}{\Gamma_{R0}}, \quad (6)$$

where  $\tilde{\Gamma}_R$  and  $\tilde{\Gamma}_S$  are instantaneous concentration of species R and S, respectively, and  $\tilde{F}$  is also called mixture fraction.

Here, the details are not shown, but radial profiles of mean value and r.m.s. value of the mixture fraction,  $\tilde{F}$  and  $\tilde{f}$  show good agreements with ones in the non-reactive case. Furthermore, it was also ascertained that the downstream variations of  $\tilde{F}$  and  $\tilde{f}$  show good agreements with ones in the non-reacting case. From these results, it can be concluded that the simultaneous measurement of concentration fluctuations could be performed accurately by the present light probe and measuring system. The detail

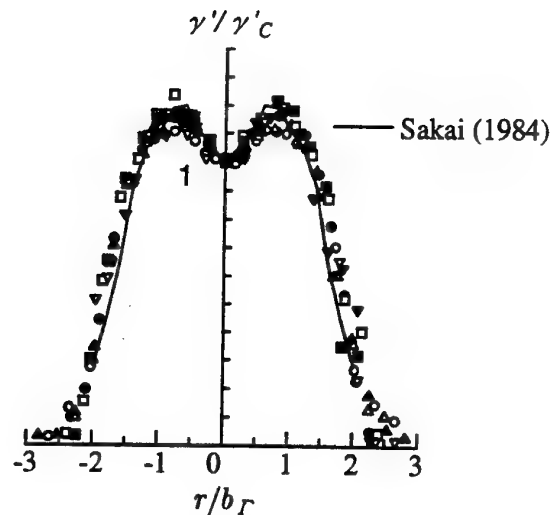


Figure 5: Radial profiles of the concentration fluctuation r.m.s. value. For symbols, see Figure 4.

statistics of the conserved scalar field will be presented in the near future.

#### Reactive Concentration Field

In this section, we will show the results concerning the consecutive and competing reaction. The initial concentration of species A in the main stream is fixed to  $\Gamma_{A0} = 0.4$  mol/m<sup>3</sup>, and the initial concentration of species B in the jet was adjusted to be  $\Gamma_{B0} = 4, 8$  and 16 mol/m<sup>3</sup>, so that in the present experiment three different initial concentration ratios of two species  $\beta = \Gamma_{B0}/\Gamma_{A0} = 10, 20$  and 40 are chosen.

Figure 6 shows the downstream variations of the mean concentration  $\Gamma_R, \Gamma_S$  of species R and S along the jet axis. The mean concentration of species R increases in the neighborhood of the jet because of the very large reaction rate coefficient of the first reaction (1). After this region, it reaches the peak value, then decreases in the downstream direction by the effect of turbulent diffusion. The production of species S becomes predominant at  $x/d > 20$ . In particular, the production of species S in the case of  $\beta = 40$  is remarkable. We notice further that the mean concentration of species R in the case of  $\beta = 40$  shows the smaller values than ones in other cases. This is because the species R produced by the first reaction (1) was consumed by the second reaction (2).

The radial profiles of the mean concentration of species R and S in the case of  $\beta = 20$  is shown in figure 7. At  $x/d = 12.5$ , the mean concentrations of both species show the peaks apart from the jet axis. This is because this position is still in the developing region of the jet, so that chemical products R and S are produced effectively in the mixing layer off the jet axis, which has the large velocity fluctuation. In further downstream region, both  $\Gamma_R$  and  $\Gamma_S$  show the peaks on the jet axis.

Figure 8 shows the downstream variations of the concentration fluctuation r.m.s. value  $\gamma'_R, \gamma'_S$  of species R and S. The r.m.s. values  $\gamma'_R$  of species R increase in the developing region of the jet ( $x/d < 10$ ) and reach the peaks. After that, they decrease to the minimums around  $x/d = 20$ , then increase again in the downstream direction gradually. The r.m.s. value  $\gamma'_S$  of species S increase monotonously in the downstream direction. Since the r.m.s. value of the



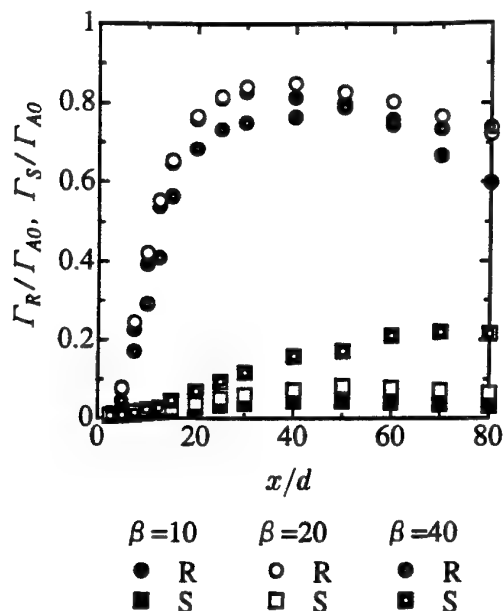
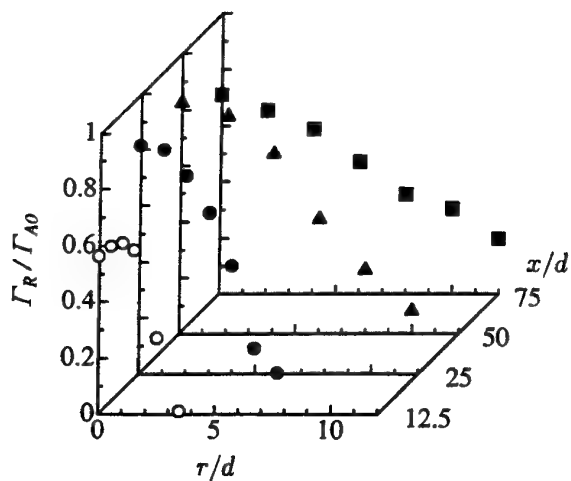


Figure 6: Downstream variations of the mean concentrations of species R and S on the jet axis.

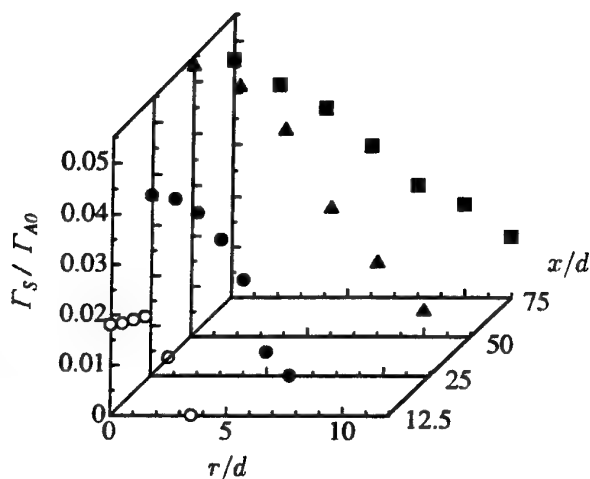
non-reactive species must decrease monotonously in the self-preserving region (at  $x/d > 12.5$  in the present experiments), the above increases of  $\gamma'_R$  and  $\gamma'_S$  can be attributed to the productions of species by chemical reactions.

Figure 9 shows the downstream variations of the probability density function (p.d.f.)  $p_R$ ,  $p_S$  of the concentration of species R and S in the case of  $\beta = 20$ . In general, it can be expected that the effect of chemical reaction appears from the lower concentration to the higher concentration. So the production of species by the chemical reaction acts to let the p.d.f. skews negatively (the negative skewness means the p.d.f. profile with the long tail in the lower concentration side). On the other hand, if the chemical production is small, the molecular diffusion enhanced by the turbulent mixing is effectively at work to make the skewness of the p.d.f. smaller. Considering the above, we can easily understand the downstream progressions of chemical production and the turbulent diffusion of species R and S from the changes of these p.d.f.s. From Fig.9(a), it is found that the skewness of p.d.f.  $p_R$  of species R is always negative at  $x/d > 20$ . The p.d.f. of species S in Fig.9(b) has also the negative skewness at  $x/d < 60$  like the p.d.f. of species R. These definitely negative skewnesses indicate that the productions of species R and S are proceeding in the region shown in the above. However, at  $x/d = 80$  in Fig.9(b), the p.d.f. looks almost Gaussian. This is because at  $x/d = 80$  the diffusion effect is superior to the production of species S.

Figure 10 shows the downstream variations of the skewness  $S_R$ ,  $S_S$  of species R and S on the jet axis. It is found that the variations of  $S_R$  and  $S_S$  show the similar tendency for all  $\beta$ , i.e., the skewness  $S_R$  and  $S_S$  have the negative values in the almost whole measurement region except near the nozzle exit, and show the minimum, maximum, minimum value in turns in the downstream direction, then they increase gradually toward about zero. These variations of skewness are explained as follows. The skewness decreases in the region  $x/d < 15$  because of the production of species in the developing region of the jet. Once the jet becomes fully developed, the diffusion effect by turbulent mixing is superior to that of chemical reaction, then the



(a) Species R.



(b) Species S.

Figure 7: Radial profiles of the mean concentration of species R and S ( $\beta = 20$ ).

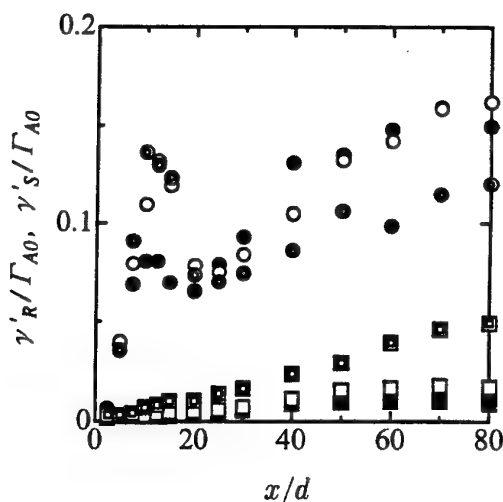
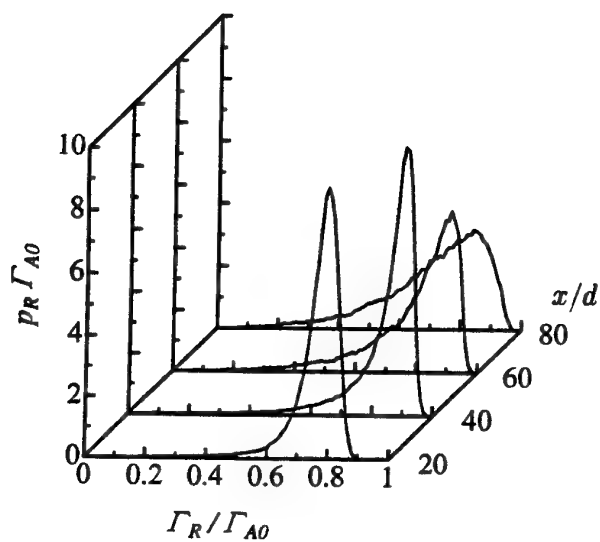
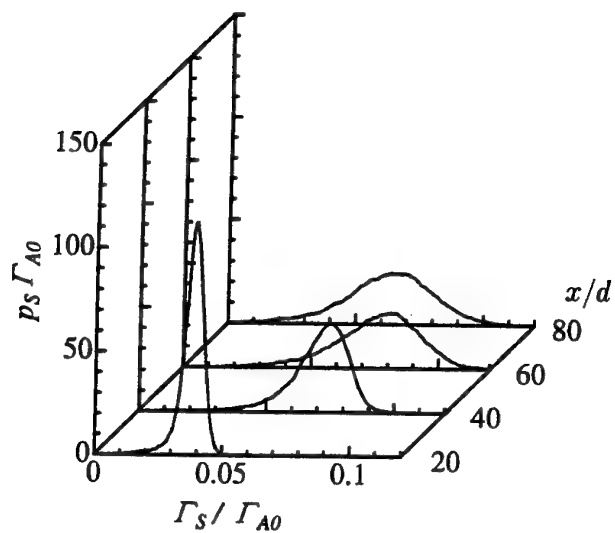


Figure 8: Downstream variations of concentration fluctuation r.m.s. value of species R and S on the jet axis. For symbols, see Figure.6.

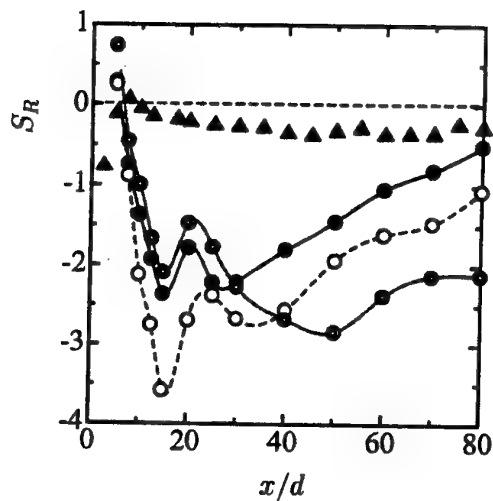


(a) Species R.

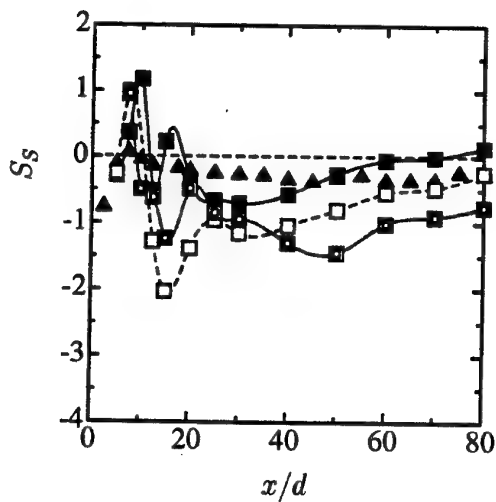


(b) Species S.

Figure 9: Downstream changes of the p.d.f. of concentration of species R and S on the jet axis ( $\beta = 20$ ).



(a) Species R.



(b) Species S.

Figure 10: Downstream variations of the skewness of species R and S on the jet axis.  $\blacktriangle$ : Non-reactive case. For other symbols, see Figure 6.

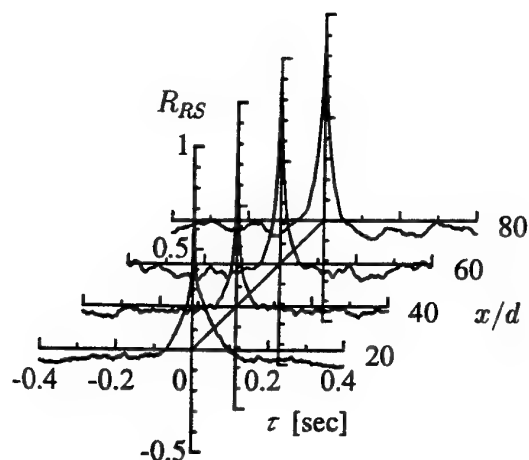


Figure 11: Downstream changes of concentration cross-correlation coefficient of species R and S on the jet axis ( $\beta = 20$ ).

skewness increases and reaches the maximum value. After that, the effect of chemical reaction becomes again superior by proceeding of turbulent mixing, then the skewness decreases and takes the second minimum value. In further downstream, the diffusion effect of turbulence becomes predominant so that the skewness increases gradually and the p.d.f. becomes like the Gaussian distribution.

Figure 11 shows the downstream changes of the concentration cross-correlation coefficient  $R_{RS}$  of species R and S. The cross-correlations show the positive values at the small time lag  $\tau$ . These positive values mean that the production of species R by the first reaction (1) is superior to the consumption of species R by the second reaction (2).

## CONCLUDING REMARKS

The consecutive and competing reaction ( $A + B \rightarrow R$ ,  $R + B \rightarrow S$ ) in the turbulent jet was investigated experimentally. The instantaneous concentration of two chemical products R and S have been measured simultaneously by the optical probe on the basis of the light absorption spectrometric method. Main conclusions are summarized as follows.

- (1) The species R starts to be produced efficiently from the neighborhood of the nozzle exit (which corresponds to the transition region of the jet), then its mean concentration reaches the peak around  $x/d = 40$ . In the further downstream region, the effect of turbulent diffusion becomes predominant so that the mean concentration decreases.
- (2) The species S is mainly produced in the fully developed turbulent region of the jet ( $x/d > 20$ ), so that its mean concentration increases gradually in the downstream direction. The balance between the chemical production and the turbulent diffusion decides the position of the peak of mean concentration. In the region where the turbulent diffusion becomes predominant, the mean concentration decreases in the downstream direction.
- (3) The skewness of the concentration p.d.f. of species R and S shows the negative value in the region where the chemical production is superior to the diffusion effect.

## REFERENCES

- Becker, H.A., Hottel, H.C. and Williams, G.C., 1967, "The nozzle fluid concentration field of the round turbulent free jet", *J. Fluid. Mech.*, Vol.30, Part 2, pp.285-303.
- Bennani, A., Gence, J.N. and Mathieu, J., 1985, "The influence of a grid-generated turbulence on the development of chemical reactions", *AIChE J.*, Vol.31, pp.1157-1166.
- Bilger, R.W., Saetran, L.R. and Krishnamoorthy, L.V., 1991, "Reaction in a scalar mixing layer" *J. Fluid. Mech.*, Vol.233, pp.211-242.
- Birch, A.D., Brown, D.R., Dodson, M.G. and Thomas, J.K., 1978, "The turbulent concentration field of a methane jet", *J. Fluid. Mech.*, Vol.188, Part 3, pp.431-449.
- Bourne, J.R., Hilber, C. and Tovstiga, G., 1985, "Kinetics of the azo coupling reactions between 1-naphthol and diazotised sulphanilic acid", *Chem. Eng. Commun.*, Vol.37, pp.293-314.
- Breidenthal, R., 1981, "Structure in turbulent mixing layers and wakes using a chemical reaction", *J. Fluid. Mech.*, Vol.109, pp.1-24.
- Komori, S., Kanzaki, T. and Murakami, Y., 1994, "Concentration correlation in a turbulent mixing layer with chemical reactions", *J. Chem. Eng. of Japan*, Vol.27, pp.742-748.
- Koochesfahani, M.M. and Dimotakis, P.E., 1986, "Mixing and chemical reactions in a turbulent liquid mixing layer", *J. Fluid. Mech.*, Vol.170, pp.83-112.
- Mehta, R.V. and Tarbell, J.M., 1987, "An experimental study of the effect of turbulent mixing on the selectivity of competing reactions", *AIChE J.*, Vol.33, pp.1089-1101.
- Sakai, Y., Ph.D. dissertation, 1984, "Experimental study on the turbulent diffusion by the light absorption method", School of Engineering of Nagoya University, (in Japanese). Also see, Nakamura, I., Sakai, Y., Tsunoda, H. and Liu, S., 1994, "Diffusion of turbulent plume around the sphere", *Memoirs of the School of Engineering, Nagoya University*, Vol.45, pp.135-184.
- Sakai, Y., Nakamura, I., Tsunoda, H. and Kushida, T., 1990, "Development of an optical fiber type of fluctuation concentration measuring system of multiple species by the light absorption spectrometric method", *Trans. of JSME (Series B)*, Vol.56-522, pp.518-522. (in Japanese)
- Sakai, Y., Nakamura, I. and Sato, R., 1995, "A study on the effect of the turbulent jet mixing on the competitive reaction in liquid", *Proc. of the 2nd Int. Conf. on Multiphase Flow '95-Kyoto*, Vol.1, pp.CO-33-CO-38.

# EXTENDED SELF-SIMILARITY AND INTERMITTENCY IN TURBULENT COMBUSTION

D. Queiros-Conde

Institut de Recherche sur les Phénomènes Hors-Equilibre  
Université de Provence  
Centre de St-Jérôme, service 252  
13397 Marseille  
FRANCE

## ABSTRACT

We evidence the existence of an extended self-similarity for a geometrical structure function analogous to that studied for turbulent flows. It gives the possibility to measure the scaling exponents  $\zeta_p$  characterizing roughness statistics. We find that the  $\zeta_p$  exponents are very close to the ones measured for turbulent flows by velocity measurements. It means that intermittency can be visualized on turbulent fronts by a geometrical approach.

A turbulent flame is characterized by the ratio  $U'/U_L$  where  $U'$  is the turbulent intensity and  $U_L$  the laminar velocity of the flame. By the tomography laser technique, we have photographed turbulent flames (propane-air-nitrogen mixture) for different values of  $U'/U_L$ . The resulting image is binarized in order to visualize the front (Fig. 1). Burnt areas are black parts. We interest on the geometry of this front and, more particularly, on its roughness fluctuations. It can be observed in Figure 2 the evolution of the roughness along the front for balls of size  $L_I/2$  where  $L_I$  is the integral scale ( $L_I=5.2\text{mm}$ ). The roughness fluctuations  $\Sigma_r$  present important variations if we compare them to the average  $\langle \Sigma_r \rangle$ . The main idea of our work is to show that this geometrical signal contains intermittency.

Our experimental procedure is the following: the front is covered by balls of size  $r$  (Fig. 3). For each ball, the local roughness  $\lambda_r=L/L_p$  is measured where  $L$  is the length of the front portion in the ball and  $L_p$  its projected length in the mean direction of propagation; the latter is determined by fitting linearly the same portion and by taking the orthogonal direction to this fit.  $\lambda_r$  being a linear roughness, to obtain the corresponding surfacic roughness  $\Sigma_r$ , an approximated formula  $\Sigma_r^2=2\lambda_r^2-1$  derived from homogeneity and isotropy arguments is used. This roughness  $\Sigma_r$  results from the action on the front of the flow scales equal or smaller than  $r$ .

In a recent study (Pocheau and Queiros-Conde, 1996; Queiros-Conde, 1996), the following scale invariant law has been proposed :

$$\Sigma_r^2 = 1 + \beta \left( \frac{U'_r}{U_L} \right)^2 \quad (1)$$

where  $U'_r$  is the r.m.s. of the flow for the scales equal or smaller than  $r$  and  $\beta=O(1)$  is a constant which depends on the equivalent ratio of the mixture. This law has been tested by direct measurements on a set of turbulent flames for different values of  $U'/U_L$  and for different scales  $r$ . The validity of (1) does not depend on the front size: if we reduce it to small size, the law is conserved and (1) is, thus, valid in each ball of size  $r$  defined on the front. This relation gives a link between roughness fluctuations and turbulent intensity. However, it is known that the turbulent flow via Darrieus-Landau instability is modified by the presence of the flame. For this reason our aim is not to use the relation (1) for quantitative purposes but to show that intermittency, despite this influence of combustion on turbulence, can appear by this geometrical procedure.

So,  $\Sigma_r$  is measured in each ball, then extracting  $U'_r$  by (1), a statistical study of  $U'_r$  fluctuations becomes possible. The following geometrical structure functions are defined:

$$S_{g,p}(r) = \left\langle \left( U_L \sqrt{\frac{\Sigma_r^2 - 1}{\beta}} \right)^p \right\rangle \quad (2)$$

We look for a scaling behavior  $S_{g,p}(r) \sim r^{\zeta_p}$ . In a log-log representation, no linear zone really appears showing that our turbulent flames result from scales between dissipative and inertial range (Fig. 4 for  $p=2$ ,  $p=3$  and  $p=5$ ). However, we evidence the existence of a power law when we represent any structure function  $S_{g,p}(r)$  as a function of another any structure function  $S_{g,q}(r)$  (Fig. 5 a) for  $p=2$ ,  $q=3$  and Fig. 5 b)

for  $p=6$ ,  $q=5$ ). This is exactly the result of Benzi *et al.* (1993) called extended self-similarity and established for turbulent flows and that holds too for low Reynolds number or scales belonging to the dissipative range. This property has allowed the determination of the relative scaling exponents  $\zeta_p/\zeta_q$ . These ones are different from the linear value  $p/q$  that they would have if  $U'r$  statistics was really gaussian. This deviation from linear behavior is called intermittency (Kolmogorov, 1962). By using the exact result  $\zeta_3=1$  of Kolmogorov (1941), the absolute exponents  $\zeta_p$  can be calculated and represented in Figure 6. We find that these values are very close to the ones obtained from velocity increments measurements on turbulent flows (Anselmet *et al.*, 1984; Benzi *et al.*, 1993).

To conclude: the evidence of extended self-similarity and intermittency on turbulent fronts suggests that some problems of turbulence could be studied by a geometrical way.

## REFERENCES

- Anselmet, F., Gagne, Y., Hopfinger, E.J., and Antonia, R.A., 1984, "High Order Velocity Functions in Turbulent Shear Flows", *J. Fluid Mech.*, Vol. 140, pp. 63-89.
- Benzi, R., Ciliberto, S., Tripiccone, R., Baudet, C., Massaioli, F., and Succi, S., 1993, "Extended Self-Similarity in Turbulent Flows", *Phys.Rev. E RC*, Vol. 48, R29.
- Kolmogorov, A.N., 1941, "Dissipation of Energy in Locally Isotropic Turbulence", *Dokl. Akad. Nauk. SSSR*, Vol. 32, p.16.
- Kolmogorov, A.N., 1962, "A refinement of previous hypothesis concerning the local structure of turbulence in a viscous fluid at high Reynolds numbers", *J. Fluid Mech.*, Vol. 13, p. 83.
- Pocheau, A. and Queiros-Conde, D., 1996, "Scale Covariance of the Wrinkling Law of Turbulent Propagating Interfaces", *Phys. Rev. Lett.*, Vol. 76, pp. 3352-3355.
- Queiros-Conde, D., 1996, "Covariance d'Echelle et Surface de Flamme en Combustion Turbulente", Ph.D Thesis, Université de Provence, France.

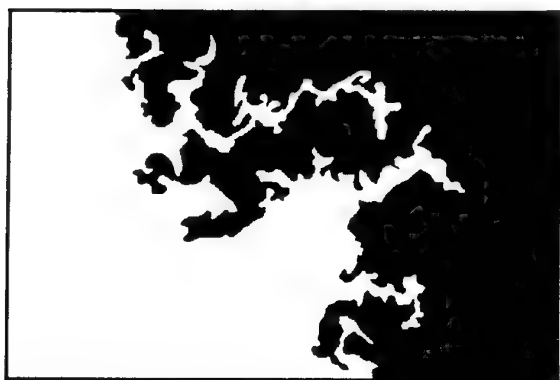


FIG. 1. TURBULENT FLAME FOR  $U/U_L=2.2$  WITH  $U_L=0.4$ . THE HEIGHT OF PICTURE REPRESENTS  $12 L_l$ .

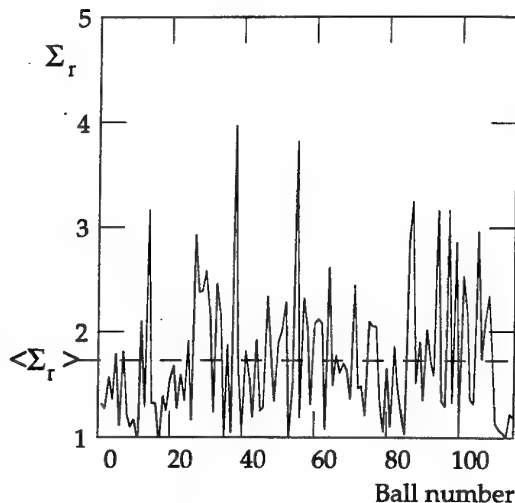


FIG. 2. ROUGHNESS FLUCTUATIONS ALONG THE FRONT FOR BALLS OF SIZE  $L_l/2$ .

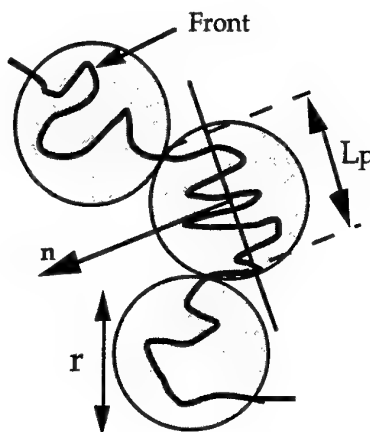


FIG. 3. METHOD TO MEASURE ROUGHNESS FLUCTUATIONS.  $n$  INDICATES THE MEAN DIRECTION OF THE FRONT IN THE BALL.

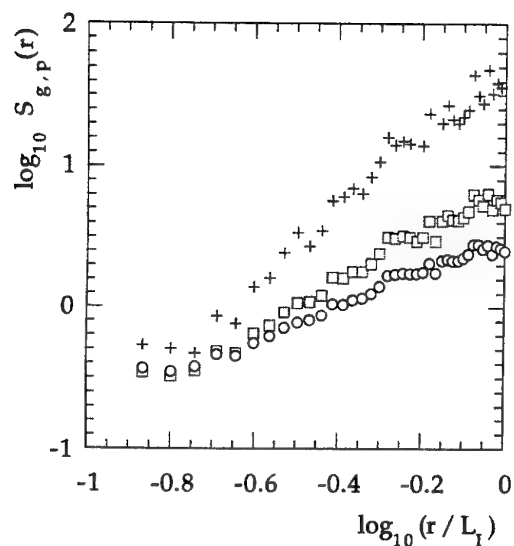


FIG. 4. LOG-LOG PLOT OF  $S_{g,2}(r)$  (CIRCLES),  $S_{g,3}(r)$  (SQUARES) AND  $S_{g,5}(r)$  (CROSSES).

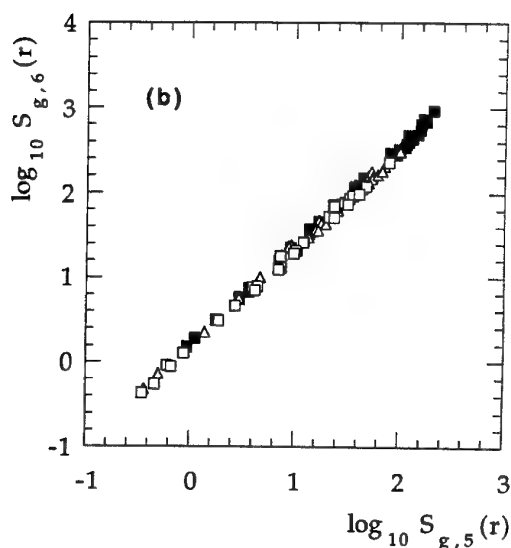


FIG. 5 (b) LOG-LOG PLOT OF  $S_{g,6}(r)$  VS.  $S_{g,5}(r)$  FOR THE SAME VALUES OF  $U/U_L$ . THE SLOPE OBTAINED BY LINEAR FITTING IS 1.15.

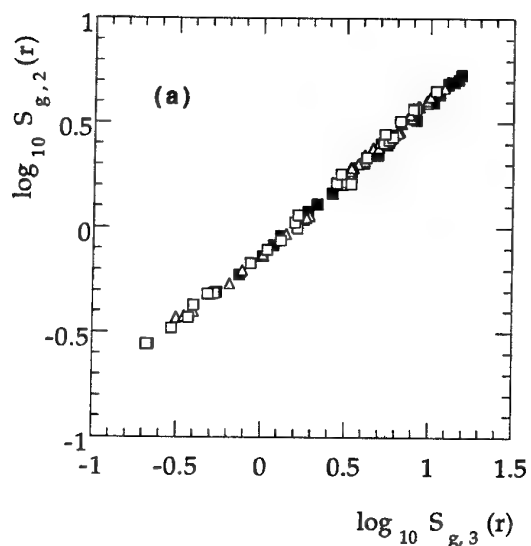


FIG. 5 (a) LOG-LOG PLOT OF  $S_{g,2}(r)$  VS.  $S_{g,3}(r)$  FOR DIFFERENT VALUES OF  $U/U_L$ : 1.4 (SQUARES), 1.7 (TRIANGLES), AND 2.2 (FULL SQUARES). THE FIT GIVES A SLOPE OF 0.71.

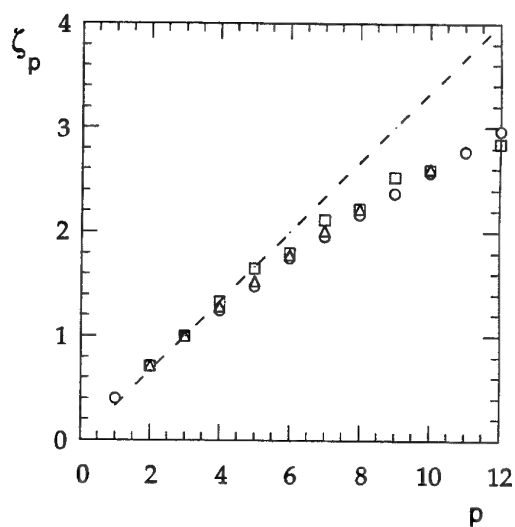


FIG. 6. EXPONENTS  $\zeta_p$  VS.  $p$  FOR  $U/U_L = 2.2$  (CIRCLES). THE TRIANGLES REPRESENT THE RESULTS OF BENZI *ET AL.*, AND THE SQUARES THE VALUES OF ANSELMETTI *ET AL.*. THE STRAIGHT LINE INDICATES THE KOLMOGOROV SCALING  $p/3$ .

## **SESSION 19 - APPLICATIONS II**

VORTEX FORMATION PROCESSES IN OPEN CHANNEL FLOWS  
WITH A SIDE DISCHARGE  
BY USING THE NON - LINEAR  $k - \epsilon$  MODEL

Takashi Hosoda and Yoshio Muramoto  
Department of Civil Engineering, Kyoto University,  
Sakyo - ku, Kyoto 606 - 01, JAPAN

Ichiro Kimura  
Department of Civil Engineering,  
Wakayama National College of Technology,  
77 Nada - Noshima, Goboh 644, JAPAN

ABSTRACT

The fundamental characteristics of the open channel flows with a side discharge are investigated experimentally and numerically. It is shown through the examination of the laboratory tests that the vortex formation processes generated by the shear instability can be seen in the downstream of an influx. The depth averaged 2-D flow model with both the simple eddy viscosity model and the non-linear  $k - \epsilon$  turbulence model are applied to reproduce the flow behaviour numerically. It is shown by the considerations of numerical results that the plane 2-D model with the simple eddy viscosity is applicable to the flow, though the model refinement is needed to improve the time averaged velocity distribution. The results of test simulations also reveal that the standard  $k - \epsilon$  model has no ability to calculate the flow induced by the shear instability, and the effect of the strain parameter on  $c_\mu$  should be included in the model.

INTRODUCTION

The open channel flow with a side discharge can be seen at the confluence point of two large and small rivers, near the outlet of the hydropower station, etc. It is necessary to know the flow structure in the downstream of an influx to predict the river bed configuration, the local scour and the bank erosion near the opposite bank of an influx.

The flow with a side discharge is characterized by the vortex formation processes, which are generated by the shear instability, in the downstream of the influx as shown in Photo. 1. As these vortices induce the large temporal velocity variations with the relatively long period in comparison with the

turbulence, it is important to reproduce the unsteady flow behaviour with vortices.

The plane 2-D unsteady flow equations with the simple eddy viscosity evaluated by  $ah u_*$  ( $a$ : constant,  $h$ : depth,  $u_*$ : friction velocity) are firstly used to calculate the flow behaviour under the condition of the laboratory tests, because the applicability of the model to the shear instability has been verified by using the linear stability analysis and the numerical tests [1,2,3]. It is shown through the comparison between the numerical and experimental results that the characteristics of the temporal velocity variations can be simulated by the numerical model to a certain extent.

From the point of view of the model refinement, the turbulence model based on the  $k - \epsilon$  model is introduced to the numerical model. It is pointed out that the standard  $k - \epsilon$  model is not applicable to the vortex generated by the shear instability as well as the Karman vortex pointed out by Franke-Rodi [4] and Kato-Launder [5] and the further refinement such as the introduction of the strain parameter is needed.

OUTLINE OF LABORATORY TESTS

The laboratory test was carried out in the Research Center of Chugoku Electric Company Ltd. by using the open channel with rectangular cross section (width  $B = 1.0$  (m), length  $L = 8.25$  (m), slope  $\sin \theta = 6/1000$ ) to investigate the influence of an efflux from the hydropower station on the river flow. The small guide channel for a side discharge is attached to the main channel at an angle to the side wall of main channel as shown in Fig.1. Hydraulic variables of laboratory test are





(a) Small vortices near the inlet



(b) Large vortices after pairing and merging

Photo 1 Flow visualization by dye for Run A-0

listed in Table 1.

The temporal velocity variations were measured at a few points in both the depth-wise and the transverse direction of several cross-sections by the electro-magnetic current meter. The flow in the downstream of an influx was visualised by dye. The small vortices in the vicinity of the inlet and the large vortices formed by the pairing and merging processes in the downstream of the inlet can be seen in Photo 1 (a) and (b).

#### NUMERICAL MODEL AND CONSIDERATIONS OF CALCULATED RESULTS

##### Basic Equations of Plane 2-D Model

The basic equations are composed of the depth-averaged continuity equation and momentum equations in the x- and y- directions expressed by Eq.(1) to Eq.(3),

$$\frac{\partial h}{\partial t} + \frac{\partial M}{\partial x} + \frac{\partial N}{\partial y} = 0 \quad (1)$$

$$\begin{aligned} \frac{\partial M}{\partial t} + \frac{\partial uM}{\partial x} + \frac{\partial vM}{\partial y} + gh \frac{\partial h}{\partial x} &= gh \sin \theta - \frac{f}{2} u \sqrt{u^2 + v^2} \\ &+ \frac{\partial -\overline{u'^2}h}{\partial x} + \frac{\partial -\overline{u'v'}h}{\partial y} + \nu \left( \frac{\partial}{\partial x} \left( h \frac{\partial u}{\partial x} \right) + \frac{\partial}{\partial y} \left( h \frac{\partial u}{\partial y} \right) \right) \end{aligned} \quad (2)$$

$$\begin{aligned} \frac{\partial N}{\partial t} + \frac{\partial uN}{\partial x} + \frac{\partial vN}{\partial y} + gh \frac{\partial h}{\partial y} &= -\frac{f}{2} v \sqrt{u^2 + v^2} \\ &+ \frac{\partial -\overline{u'v'}h}{\partial x} + \frac{\partial -\overline{v'^2}h}{\partial y} + \nu \left( \frac{\partial}{\partial x} \left( h \frac{\partial v}{\partial x} \right) + \frac{\partial}{\partial y} \left( h \frac{\partial v}{\partial y} \right) \right) \end{aligned} \quad (3)$$

where  $h$ : the water depth,  $(u, v)$ : the depth-averaged velocity vectors,  $(M, N)$ : the discharge flux vector defined as  $M \equiv hu$ ,  $N \equiv hv$ ,  $-\overline{u'_i u'_j}$ : the depth-averaged Reynolds stress tensors ( $u'_1 = u'$ ,  $u'_2 = v'$ ),  $f$ : the bottom friction factor relating to the local Reynolds number,  $\nu$ : the molecular dynamic viscosity,  $\theta$ : the bottom slope of open channel.

##### Numerical Method and Conditions of Calculation

The finite volume method with QUICK scheme for the convective inertia term is adopted as the numerical method. The Adams-Bashforth method with 2nd order accuracy is used for the time integration.

The initial and boundary conditions of calculation are illustrated in Fig. 1. The wall shear stresses are evaluated by the log-law, using the velocity in the x-direction defined at the cell adjacent to the wall.

##### Simple Eddy Viscosity Model and Its Results

The simple modeling expressed in Eq. (4) is used for the evaluation of the depth averaged Reynolds stress tensors.

$$-\overline{u'_i u'_j} = D \left( \frac{\partial u_i}{\partial x_j} + \frac{\partial u_j}{\partial x_i} \right) - \frac{2}{3} k \delta_{ij}, \quad D = \alpha h u_* \quad (4)$$

where  $u_*$ : the local friction velocity ( $= \sqrt{f(u^2 + v^2)/2}$ ),  $k$ : the depth averaged turbulent kinetic energy evaluated by the empirical formula by Nezu [6]

Table 1 Hydraulic variables of laboratory tests

	B (m)	W (m)	B/W	$\alpha$ (deg)	Q (l/s)	Q <sub>in</sub> (l/s)	h <sub>e</sub> (cm)	sin $\theta$	Re
Run A-0	1.0	0.2	5.0	40	1.98	8.89	13.11	6/1000	8300
Run A-1	1.0	0.6	1.67	40	1.98	8.89	13.11	6/1000	8300
Run A-2	1.0	0.8	1.25	40	1.98	8.89	13.17	6/1000	8300
Run A-3	1.0	1.2	0.83	40	1.98	8.89	13.11	6/1000	8300
Run B-0	1.0	0.6	1.67	90	1.98	8.89	13.04	6/1000	8300
Run B-1	1.0	0.6	1.67	75	1.98	8.89	13.02	6/1000	8300
Run B-2	1.0	0.6	1.67	25	1.98	8.89	13.0	6/1000	8300
Run C-0	1.0	0.6	1.67	40	3.95	6.92	13.10	6/1000	8300
Run C-1	1.0	0.6	1.67	40	5.93	4.94	13.09	6/1000	8300
Run C-2	1.0	0.6	1.67	40	6.92	3.95	13.13	6/1000	8300
Run C-3	1.0	0.6	1.67	40	8.89	2.96	13.25	6/1000	9060

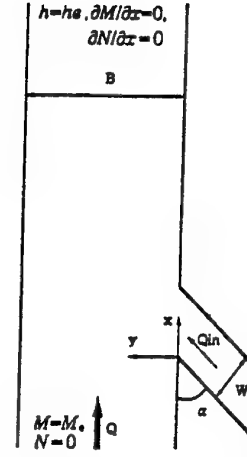


Fig. 1 Schematic illustration of laboratory test and coordinate system

as  $2.07 u_*^2$ .

The calculated flow patterns of Run A-0 with  $\alpha = 0.3$  are shown at every 5 seconds in Fig. 2. The large vortex formation and merging shown in Photo 1 (b) can be seen in the figure, but the small vortices in the vicinity of the influx shown in Photo 1 (a) is not reproduced precisely. Further investigation will be carried out by using the fine grid system.

The temporal velocity variations at the point A indicated in Fig. 2 are shown in Fig. 3. The calculated velocity variations are not periodic but chaotic, and the oscillation with the time period nearly 5 seconds, which seems to be generated by the vortex formation, can be seen in the long (20-40 sec.) periodic oscillation due to the pairing and merging of vortices. The similar feature is detected in the measured velocity variations, though the turbulence is superimposed on the velocity variations with the long period. The amplitude of the calculated velocity variations is in good agreement with the amplitude of the observed ones.

Fig. 4 shows the time averaged velocity distribution in the transverse direction of Run A-0. The model refinement seems to be required because the calculated velocity distributions with the 0-equation model are more diffused than the observed ones and the discrepancy near the side wall is large.

#### Model Refinement

From the point of view of the model refinement, the turbulence model based on the  $k-\epsilon$  model is introduced and the model performance is investigated, paying attention to the applicability to the vortex formation.

The  $k-\epsilon$  model is composed of Eq.(1) - (3) and the  $k-\epsilon$  equations given by Eq.(5) and (6) [7].

$$\frac{\partial h k}{\partial t} + \frac{\partial u h k}{\partial x} + \frac{\partial v h k}{\partial y} = \frac{\partial}{\partial x} \left( \frac{D}{\sigma_k} h \frac{\partial k}{\partial x} \right) + \frac{\partial}{\partial y} \left( \frac{D}{\sigma_k} h \frac{\partial k}{\partial y} \right) + Pro + c_k u_*^3 - h \epsilon \quad (5)$$

$$\frac{\partial h \epsilon}{\partial t} + \frac{\partial u h \epsilon}{\partial x} + \frac{\partial v h \epsilon}{\partial y} = \frac{\partial}{\partial x} \left( \frac{D}{\sigma_\epsilon} h \frac{\partial \epsilon}{\partial x} \right) + \frac{\partial}{\partial y} \left( \frac{D}{\sigma_\epsilon} h \frac{\partial \epsilon}{\partial y} \right) + c_{\epsilon_1} h \frac{\epsilon}{k} Pro + c_\epsilon \frac{u_*^4}{h} - c_{\epsilon_2} h \frac{\epsilon^2}{k} \quad (6)$$

$$Pro = D \left[ 2 \left( \frac{\partial u}{\partial x} \right)^2 + 2 \left( \frac{\partial v}{\partial y} \right)^2 + \left( \frac{\partial u}{\partial y} + \frac{\partial v}{\partial x} \right)^2 \right],$$

$$c_k = 1/\sqrt{f/2}, c_\epsilon = 3.6 c_{\epsilon_2} \sqrt{c_\mu / (f/2)}^{3/4}$$

where  $D$ : the eddy viscosity defined by Eq.(7).

#### Standard $k-\epsilon$ Model

The Reynolds stresses are evaluated by Eq.(7) in the standard  $k-\epsilon$  model.

$$-\overline{u_i u_j} = D S_{ij} - \frac{2}{3} k \delta_{ij}, D = c_\mu \frac{k^2}{\epsilon}, S_{ij} = \frac{\partial u_i}{\partial x_j} + \frac{\partial u_j}{\partial x_i} \quad (7)$$

The flow pattern of Run A-0 calculated with Eq.(7) is shown in Fig. 5. There is one steady circulation without the continuous vortex generation in the downstream of the influx.

#### Non-linear $k-\epsilon$ Model

A few types of higher order  $k-\epsilon$  models have been proposed to improve the ability of  $k-\epsilon$  model [8,9,10,11]. The second order term is only included in the non-linear  $k-\epsilon$  model as expressed in Eq.(8).

$$-\overline{u_i u_j} = c_\mu \frac{k^2}{\epsilon} S_{ij} - \frac{2}{3} k \delta_{ij} - c_\mu \frac{k^3}{\epsilon^2} \sum_{\beta=1}^3 c_\beta (S_{\beta ij} - \frac{1}{3} S_{\beta \alpha \alpha} \delta_{ij}), \quad (i,j=1,2) \quad (8)$$

$$S_{1ij} = \frac{\partial u_i}{\partial x_r} \frac{\partial u_j}{\partial x_r}, S_{2ij} = \frac{1}{2} \left( \frac{\partial u_r}{\partial x_i} \frac{\partial u_j}{\partial x_r} + \frac{\partial u_r}{\partial x_j} \frac{\partial u_i}{\partial x_r} \right), S_{3ij} = \frac{\partial u_i}{\partial x_r} \frac{\partial u_j}{\partial x_r}$$

As for the second order term, the expression based on the principle of material frame indifference (the objectivity), which was proposed by Pope [9] and Gatski-Speziale [10], is considered to be equivalent

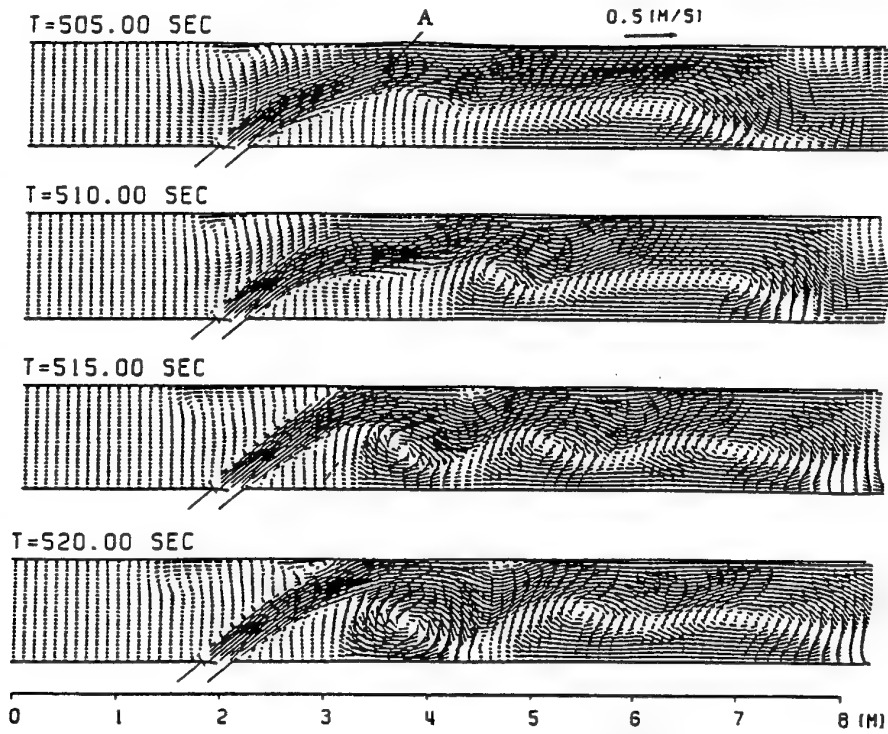
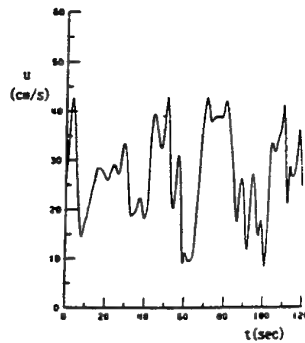
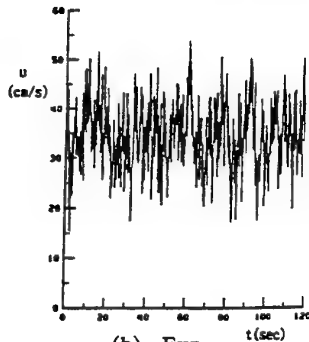


Fig. 2 Calculated results of vortex formation processes in Run A-0



(a) Cal. ( $\alpha = 0.3$ )



(b) Exp.

Fig.3 Temporal velocity variations  
(Run A-0, Point A)

to Eq.(8) if the model constants are adjusted. As the model constants,  $c_1=0.6$ ,  $c_2=0$ ,  $c_3=-0.15$  are used.

Fig. 6 shows that the steady circulation is elongated in the longitudinal direction compared with the flow pattern of  $k-\epsilon$  model, but the vortex is not shed yet.

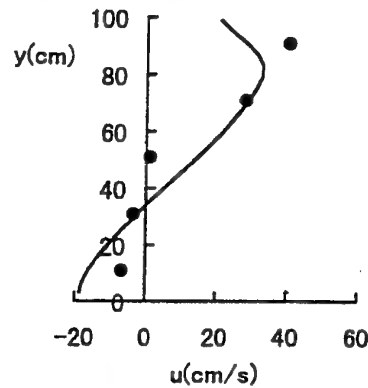


Fig.4 Transverse distribution of time-averaged  
velocity in the longitudinal direction  
(Run A-0)

#### Standard $k-\epsilon$ Model With $c_\mu$ Relating to The Strain Parameter

As the objectivity also predicts  $c_\mu$  relating to the strain parameter,  $S$ , and the rotation parameter,  $\Omega$ , defined as Eq.(9-a) and (9-b), respectively, the standard  $k-\epsilon$  model is again tested with the relation between  $c_\mu$  and the strain parameter proposed by Kato-Launder [5]. Run S-1 and S-4 listed in Table 2 are chosen as the model constants of Eq.(10). Fig.7 shows the dependency of  $c_\mu$  on the strain parameter.

$$S = \frac{k}{\epsilon} \sqrt{\frac{1}{2} S_{ij}^2} \quad (9-a)$$

$$\Omega = \frac{k}{\epsilon} \sqrt{\frac{1}{2} \Omega_{ij}^2}, \quad \Omega_{ij} = \frac{\partial u_i}{\partial x_j} - \frac{\partial u_j}{\partial x_i} \quad (9-b)$$

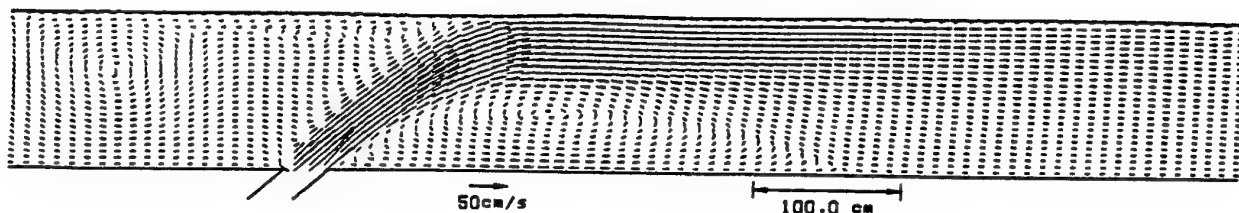


Fig.5 Plane flow pattern by standard  $k-\epsilon$  model (Run A-0)

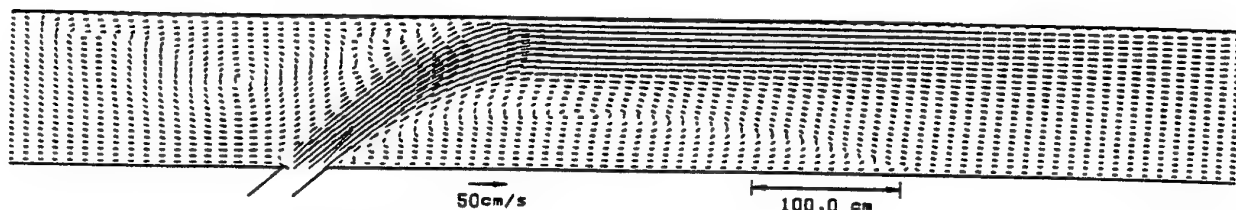


Fig.6 Plane flow pattern by non-linear standard  $k-\epsilon$  model (Run A-0,  $c_1=0.6$ ,  $c_2=0$ ,  $c_3=-0.15$ )

Table 2 Constants used in the relation between  $c_\mu$  and strain parameter

	$A_1$	$A_2$
Run S-1	0.35	0.3
Run S-2	0.35	0.2
Run S-3	0.35	0.1
Run S-4	0.7	0.3
Run S-5	1.0	0.3

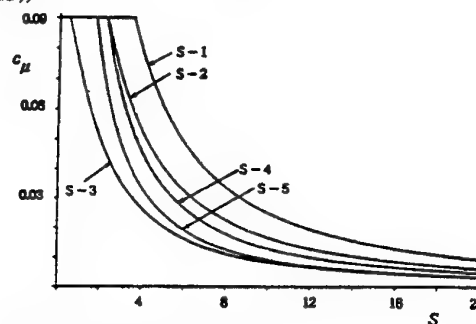


Fig.7 Relation between  $c_\mu$  and strain parameter

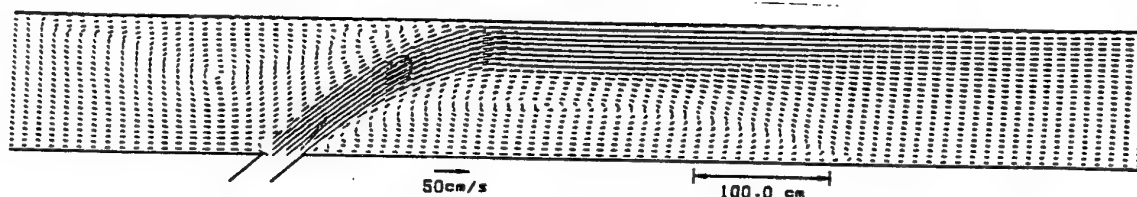


Fig.8 Calculated results of flow pattern in Run A-0 by  $k-\epsilon$  model with the effect of strain parameter on eddy viscosity (Run S-1)

$$c_\mu(S) = \min \left[ 0.09, \frac{A_2}{1 + A_1 (\min(20, S))^{1.5}} \right] \quad (10)$$

The flow patterns of Run A-0 under the conditions of Run S-1 and S-4 are shown in Figs. 8 and 9. The vortex formation processes are reproduced by using the condition of Run S-4 in Fig. 9. The time averaged velocity distributions in the transverse direction are in good agreement with the laboratory tests as shown in Fig.10 (c). Temporal velocity variations of Run S-4 are also shown in Fig.11.

## CONCLUSIONS

The results obtained in this paper are summarized as follows:

(1) It is shown by the laboratory test that the

vortex formation processes generated by the shear instability, which induce the large temporal velocity variations, are observed in the downstream flow of a side discharge.

(2) The unsteady flow with vortices can be reproduced numerically by using the plane 2-D flow model with the simple turbulence model, though the model refinement is needed to improve the time averaged flow pattern.

(3) Test simulations by the use of the turbulence model based on the  $k-\epsilon$  model reveal that the standard  $k-\epsilon$  model has no ability to calculate the flow induced by the shear instability and  $c_\mu$  relating to the strain parameter deduced by the principle of material frame indifference should be considered in the model.

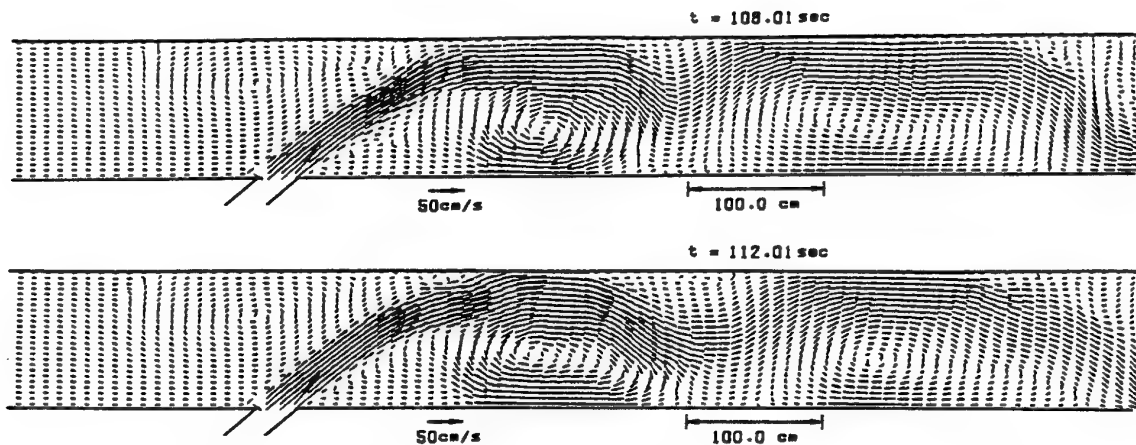


Fig. 9 Calculated results of vortex formation processes in Run A-0 by  $k-\epsilon$  model with the effect of strain parameter on eddy viscosity (Run S-4)

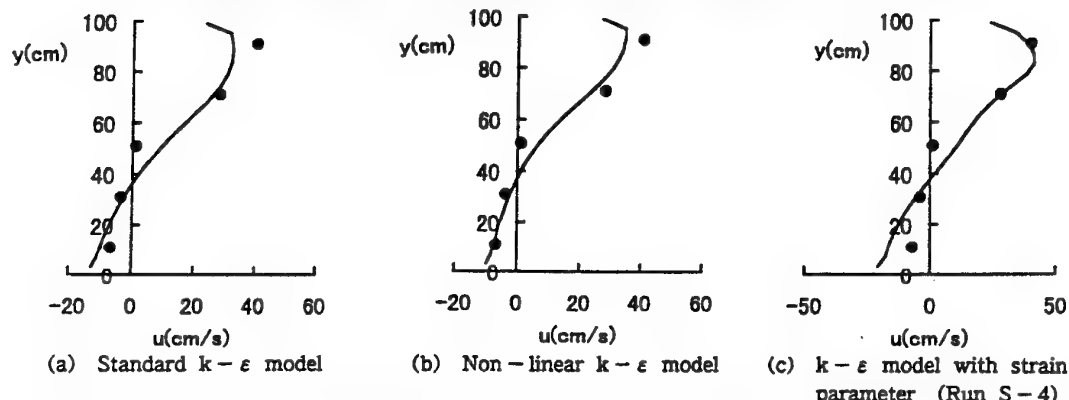


Fig.10 Transverse distribution of time-averaged velocity in the longitudinal direction (Run A-0)

#### REFERENCES

- [1] Hosoda, T. and Kimura, I.: Vortex formation with free surface variation in shear layer of plane - 2D open channel flows, Proc. 9th Symp. on Turbulent Shear Flows, Vol.1 P112, 1-4, 1993.
- [2] Nadaoka, K. and Yagi, H.: Horizontal large-eddy computation of river flow with transverse shear by SDS & 2DH model, J. of Hydraulic, Coastal and Environmental Eng., JSCE, No.473/II-24, pp. 35-44, 1993 (in Japanese).
- [3] Kimura, I., Hosoda, T. and Tomochika, H.: Characteristics of spatially growing disturbances in a mixing shear layer of open channel flows, J. of Hydraulic, Coastal and Environmental Eng., JSCE, No.509/II-30, pp.99-109, 1995 (in Japanese).
- [4] Franke, R. and Rodi, W.: Calculation of vortex shedding past a square cylinder with various turbulence models, Turbulent Shear Flows 8, pp.189-204, 1991.
- [5] Kato, M. and Launder, B.E.: The modelling of turbulent flow around stationary and vibrating square cylinders, Proc. 9th Symp. on Turbulent Shear Flows, Kyoto, Vol.1, 10-4-1~10-4-6, 1993.
- [6] Nezu, I. and Nakagawa, H.: Turbulence in open channel flows, IAHR Monograph, Balkema, 1993.
- [7] Rastogi, A. and Rodi, W.: Predictions of heat and mass transfer in open channels, J. Hydr. Div., ASCE, Vol.103 (3), pp.397-420, 1978.

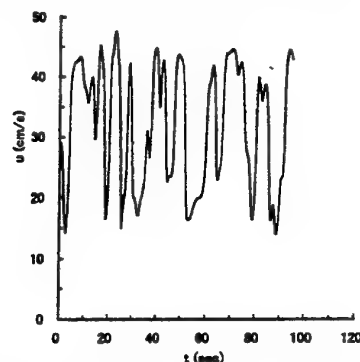


Fig.11 Temporal velocity distributions with the effect of S (Run S-4)

- [8] Yoshizawa, A.: Statistical analysis of the deviation of the Reynolds stress from its eddy viscosity representation, Phys. Fluids Vol.27, pp.1377-1387, 1984.
- [9] Rubinstein, R. and Barton, J.M.: Nonlinear Reynolds stress models and the renormalization group, Phys. Fluids A 2, pp.1472-1476, 1990.
- [10] Pope, S.B.: A more general effective viscosity hypothesis, J. Fluid Mech., Vol.72, pp.331-340, 1975.
- [11] Gatski, T.B. and Speziale C.G.: On explicit algebraic stress models for complex turbulent flows, J. Fluid Mech., Vol.254, pp.59-78, 1993.

# NUMERICAL SIMULATION AND EXPERIMENTAL VALIDATION OF THE TURBULENT COMBUSTION AND PERLITE EXPANSION PROCESSES IN AN INDUSTRIAL PERLITE EXPANSION FURNACE

A. Klipfel and M. Founti  
Mechanical Engineering Department  
Thermal Engineering Section  
National Technical University of Athens  
Patission 42, Athens 10682  
Greece

K. Zähringer, J.P.Martin and J.P.Petit  
C.N.R.S. - Laboratoire EM2C.UPR 288  
Ecole Centrale de Paris  
Grande Voie des Vignes  
92295 Châtenay - Malabry Cedex  
France

## ABSTRACT

A computational code has been developed to simulate the expansion process of perlite. A Eulerian - Lagrangian approach has been applied to model the combustion and the motion of the perlite particles in a vertical expansion furnace. The expansion of a single particle, which takes place during its motion in the furnace, has been modelled by taking into account the perlite chemical composition and the gradual variation of the temperature distribution inside the grain. Experiments, performed in a perlite expansion plant, have been used to validate the computational results.

The good agreement between measurements and predictions indicates that the developed computational tool can be used to optimise the industrial process.

## INTRODUCTION

Perlite is a volcanic mineral (70-72% SiO<sub>2</sub>), which in its expanded form has very good thermal and sound insulating properties. When granulated raw perlite is heated up in a furnace configuration to around 800-1100 °C, the combined water (2% to 6%) present in the mineral structure vaporises and reforms the softened particle shape. Steam escape creates a mineral "pop-corn" in which the original gas pockets within the rock are greatly expanded, increasing the porosity of the structure and decreasing the original density. Thus, perlite can expand 10 to 15 times its original volume.

At present, the expansion process of perlite is not optimised in industry with regard to the raw material properties and expanded product quality. For building and construction material applications, expanded perlite of uniform density, increased hardness and well controlled size distribution is required and can not be produced without optimisation of the expansion process. A computational code capable of predicting the combustion, expansion process and particle trajectories can serve in improving the quality of the final expanded product and in optimising the energy consumption inside the furnace by regulating the combustion parameters.

There are few publications treating furnace design in relation to the expansion process. Murdock and Stein (1950) provided a technical description of existing furnace concepts. Papanastassiou (1979) presented a simplified mathematical analysis of the expansion in a vertical furnace. He determined

upper and lower velocity limits for the combustion gases by estimating the distance and time needed by an expanded particle to fall in the furnace and deduced guidelines for furnace design and process control. Founti et al. (1992) and Founti and Klipfel (1995) first applied a Eulerian - Lagrangian approach, developed for the prediction of turbulent combusting flows and particle characteristics in gas-solid two-phase flows, to the prediction of the expanded perlite particle trajectories in a vertical expansion furnace. In these works the combustion and burner design have not been modelled in detail, the expansion of each perlite particle has been based on empirical correlations and the heat transfer between particles and the surrounding gases has not been taken into account.

In order to optimise the production process much more accurate models are needed, which justifies the development of a new simulation tool.

## COMPUTATIONAL APPROACH

The main features of the developed code are:

- Solution of the combustion gases flow field inside the furnace for various types of fuel.
- Tracking of the perlite particle trajectories inside the furnace with simulation of particle-wall collisions and graphical representation of the perlite trajectories via a Computer Aided Design system.
- Simulation of the expansion process and correlation to the tracking of the trajectories

## Modelling of the two-phase flow field

The combustion gases and the solid perlite particles are considered a continuous and a discrete phase respectively. The equations of the continuous phase transport are solved using a Eulerian treatment and the calculation of the perlite particle trajectories is performed using a Lagrangian formulation.

Assuming a steady, incompressible, turbulent, axisymmetric and swirling combusting flow, the time averaged equations of transfer for the gas phase have been solved:

$$\frac{\partial(\rho U \Phi)}{\partial x} + \frac{1}{r} \frac{\partial(r \rho V \Phi)}{\partial r} = \frac{\partial}{\partial x} \left( \Gamma_{\Phi} \frac{\partial \Phi}{\partial x} \right) + \frac{1}{r} \frac{\partial}{\partial r} \left( r \Gamma_{\Phi} \frac{\partial \Phi}{\partial r} \right) + S_{\Phi}$$

where according to the value of  $\Phi$  the above general equation

TABLE 1  
SOURCE TERMS OF THE GENERAL TRANSFER EQUATION

$\Phi$	$\Gamma_\Phi$	$S_\Phi$
1	0	0
u	$\mu_{eff}$	$-\frac{\partial p}{\partial x} + \frac{\partial}{\partial x} \left( \mu_{eff} \frac{\partial u}{\partial x} \right) + \frac{1}{r} \cdot \frac{\partial}{\partial r} \left( r \mu_{eff} \frac{\partial v}{\partial x} \right)$
v	$\mu_{eff}$	$-\frac{\partial p}{\partial r} + \frac{\partial}{\partial x} \left( \mu_{eff} \frac{\partial u}{\partial r} \right) + \frac{1}{r} \cdot \frac{\partial}{\partial r} \left( r \mu_{eff} \frac{\partial v}{\partial r} \right) - 2 \mu_{eff} \cdot \frac{v}{r^2} + \frac{\rho w^2}{r}$
w	$\mu_{eff}$	$-\frac{\rho v w}{r} - \frac{w}{r^2} \cdot \frac{\partial}{\partial r} (r \mu_{eff})$
k	$\mu_{eff}/\sigma_k$	$G - \rho \cdot \epsilon$
$\epsilon$	$\mu_{eff}/\sigma_\epsilon$	$\frac{\epsilon}{k} \cdot (C_1 \cdot G - C_2 \cdot \rho \cdot \epsilon)$
h	$\mu_{eff}/\sigma_h$	$H_u \cdot R_{fu}$
$m_{ox}$	$\mu_{eff}/\sigma_{ox}$	$-s \cdot R_{fu}$
$m_{fu}$	$\mu_{eff}/\sigma_{fu}$	$-R_{fu}$
$m_{CO_2}$	$\mu_{eff}/\sigma_{CO_2}$	$(1+s) \cdot R_{fu} \cdot X_{CO_2}$
$m_{H_2O}$	$\mu_{eff}/\sigma_{H_2O}$	$(1+s) \cdot R_{fu} \cdot X_{H_2O}$
$G = \mu_{eff} \left\{ 2 \cdot \left[ \left( \frac{\partial u}{\partial x} \right)^2 + \left( \frac{\partial v}{\partial r} \right)^2 + \left( \frac{v}{r} \right)^2 \right] + \left( \frac{\partial w}{\partial x} \right)^2 + \left[ r \cdot \frac{\partial}{\partial r} \left( \frac{w}{r} \right) \right]^2 + \left( \frac{\partial u}{\partial r} + \frac{\partial v}{\partial x} \right)^2 \right\}$ $\mu_{eff} = \mu + C_\mu \cdot \rho \cdot \frac{k^2}{\epsilon}$		

$$C_\mu = 0.09, C_1 = 1.44, C_2 = 1.92, \sigma_k = 1.00, \sigma_\epsilon = 1.00$$

can describe the continuity, the momentum transfer in the three major directions (axial, radial and azimuthal), the k- $\epsilon$  turbulence model, the transfer of enthalpy and the transfer of species concentration (fuel, oxygen, carbon dioxide and water vapour). The source terms  $S_\Phi$  and the effective viscosity  $\Gamma_\Phi$  are shown in Table 1.

The effects of radiation have been modelled by solving the Radiative Transfer Equation (RTE) according to the Reverse Monte Carlo method which features the definition of the complete path-lengths of the bundles inside the computational domain and the solution of the RTE on the above-defined complete path-lengths (Papapavlou et al. 1994). Furthermore, the solution of the RTE provided source/sink terms which have been incorporated in the enthalpy transfer equation.

The combustion process has been modelled considering a two step reaction mechanism where production and combustion of carbon monoxide have been taken into account. A volumetric reaction rate for the combustion of fuel and carbon monoxide has been calculated. In the mixing controlled regime, the reaction rate  $R_{mix}$  has been calculated using the Eddy Break-Up law with the empirical constant A set to 1., while in the kinetically controlled regime the reaction rate  $R_{kin}$  has been calculated according to an Arrhenius formula. For each computational cell the reaction rate has been set as the  $\min\{R_{mix}, R_{kin}\}$ .

The combustion gas has been assumed to be a mixture of oxygen, nitrogen, carbon dioxide, water vapor and gas fuel. The gas temperature has been derived from the enthalpy as  $\theta = h/C_p$  where the specific heat  $C_p$  is calculated as a weighted

sum of the individual  $C_p$  of the mixture components. The combustion gas density has been evaluated from the equation of state:

$$\rho = \frac{p}{RT \sum_{i=1}^n \frac{m_i}{M_i}}$$

Only convective heat transfer has been considered in the near wall region.

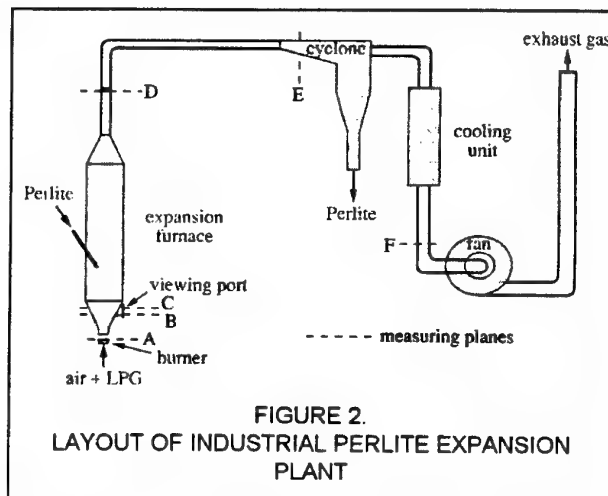
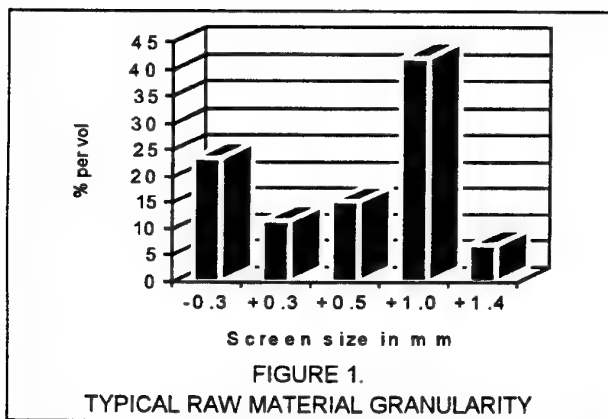
The resulting system of equations has been solved via a finite difference method based on a staggered grid arrangement, using the SIMPLE algorithm, Patankar (1980), the upwind differencing discretization scheme, and the Tri-Diagonal Matrix Algorithm.

The perlite particle trajectories have been calculated by solving the instantaneous particle motion (momentum) equation which take into account the effects of drag, shear lift (modified according to Mei, 1992, valid for flows with particle Re number larger than one), rotational lift (extended to include the relative motion between the particle and the fluid, Sommerfeld and Zivkovic, 1992) and of gravity.

The perlite particles are assumed spherical with a drag coefficient calculated using values according to Morsi and Alexander (1972), which closely simulate experimental data.

The particle dispersion due to the fluid turbulence is simulated by considering that the instantaneous fluid velocity comprises a mean and a fluctuating component. Fluid fluctuations are modelled as random numbers following a Gaussian distribution with zero mean value and standard





deviation set from  $U_{rms} = (2/3k)^{0.5}$  considering local turbulence isotropy. The particle-to-eddy interaction time is determined by the eddy life time and the crossing trajectories effect. Thereafter, it is considered that the particle starts to interact with a new eddy and a new fluctuation component is sampled from the Gaussian distribution function. The sampling is performed for the three velocity components and the fluctuations are temporally and spatially uncorrelated.

The model of Matsumoto and Saito (1970) is used to obtain the particle translational and rotational velocities after a particle-wall collision. The model distinguishes and takes account of two types of collision: a collision with and without sliding. The empirical restitution coefficients are provided by the work of Tabakoff et al. (1987). For the calculations the particles have been simulated as glass with the rest of the properties being those of quartz-sand and the pipe walls were assumed to be 2024-Al alloy.

The modulation of the gas phase turbulence due to the particles and particle-to-particle collisions are not taken into account due to the low concentration, size and density of the expanded perlite particles inside the furnace.

#### Modelling of expansion procedure

The model used for the calculation of the expansion

procedure of each perlite particle is based on calculations of the variation of the temperature and viscosity of the particle. It is assumed that expansion takes place when the softening viscosity (Shaw, 1972) of the material is attained.

The heating of perlite is calculated via a non-isothermal heat conduction model which solves the one dimensional heat conduction equation. The boundary conditions (combustion gas temperature and velocity) at each trajectory location are provided by the combustion code. The model takes into account the radiative heat flux to the perlite grain, using a Stefan-Boltzmann type of expression, considering that the perlite particles are surrounded by a black-body.

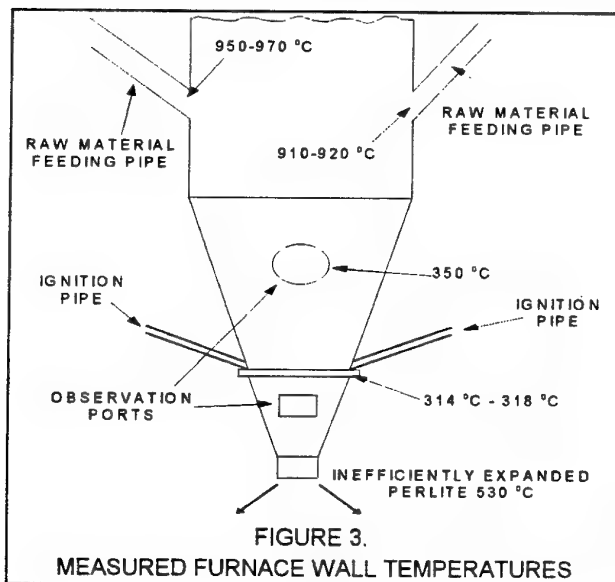
The combustion code provides the temperature and velocity fields inside the furnace. As each perlite trajectory is tracked, the temperature of the ambient gas in the particle location is calculated and the residence time of perlite in each temperature region is recorded.

Since the physical properties of perlite change during the expansion process, the developed one-dimensional, implicit, upwind numerical "perlite expansion" subroutine first calculates the temperature distribution using the properties of raw perlite. When the expansion conditions (viscosity, temperature) are attained, the concerned parts of the grain expand according to an empirical expansion ratio (about three times) and their properties change to those of expanded perlite. The expansion procedure begins at the surface of the grain and according to the heating rate, proceeds continuously towards the centre of the particle. Thus, during a certain time the perlite particle consists of an unexpanded raw perlite core, decreasing with time and surrounded by a crust of expanded material.

The tracking of the particle trajectory continues at the end of the time step, calculated by the Lagrangian code, with the new particle properties, diameter and density. If the temperature of the grain increases above 1250 °C, the melting point is reached and the trajectory is stopped.

A statistical procedure allows the tracking and evaluation of a large number (e.g. 10000) of particle trajectories. Thus for a given raw material size distribution, the final expanded material size distribution and the proportion of melted and unexpanded particles can be determined.

A typical raw material granularity, expressed in terms of volume percentage of each size fraction, is shown in Figure 1.





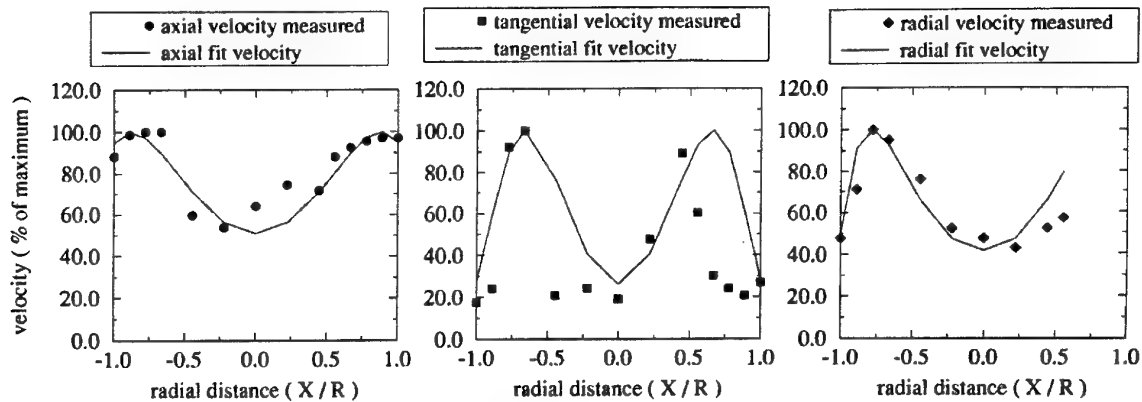


FIGURE 4.

#### MEASURED VELOCITY COMPONENTS AT FURNACE INLET

By assuming that each size fraction  $i$  ( $i = 1, n$ ) is represented by a characteristic spherical particle diameter  $D_c(i)$ , e.g. for the size fraction 0 - 300  $\mu\text{m}$  ( $i=1$ ) the characteristic diameter is  $D_c(1)=150\mu\text{m}$ , it is possible to calculate the percentage number of particles  $N_p(i)$  which corresponds to that size fraction:

$$N_p(i) = \frac{V_{FR}(i)}{P/6 D_c^3(i)}$$

where  $V_{FR}(i)$  is the percentage volume of the size fraction  $i$ . In order to obtain the initial diameter of each simulated particle, a

random number RN with uniform Probability Density Function (PDF) within the range 0 - 1 is sampled and compared to the cumulative percentage number of particles  $C(j)$  for each size fraction:

$$C(i) = \sum_j^i N_p(j), \quad i=1, n$$

Furthermore, the initial diameter of the simulated particle is set equal to the  $D_c(i)$  of the size fraction  $i$  which satisfies:

$$C(i-1) \leq RN \leq C(i)$$

#### INDUSTRIAL EXPERIMENTS

The main components of the examined perlitic expansion plant are presented schematically in Figure 2. The vertical axis-symmetric furnace is about 7 m in height and 0.6 m in diameter, it is made of steel without any radiative shield. It is driven with LPG (80% butane, 20% propane) and the burner creates a premixed swirl flame. The raw material is injected in the lower third of the furnace from two opposing ducts (Fig. 3).

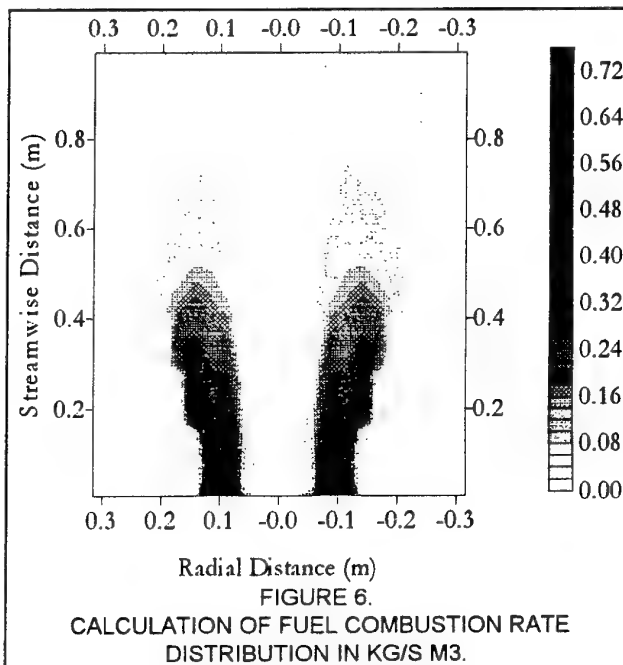


FIGURE 6.

CALCULATION OF FUEL COMBUSTION RATE DISTRIBUTION IN KG/S M3.

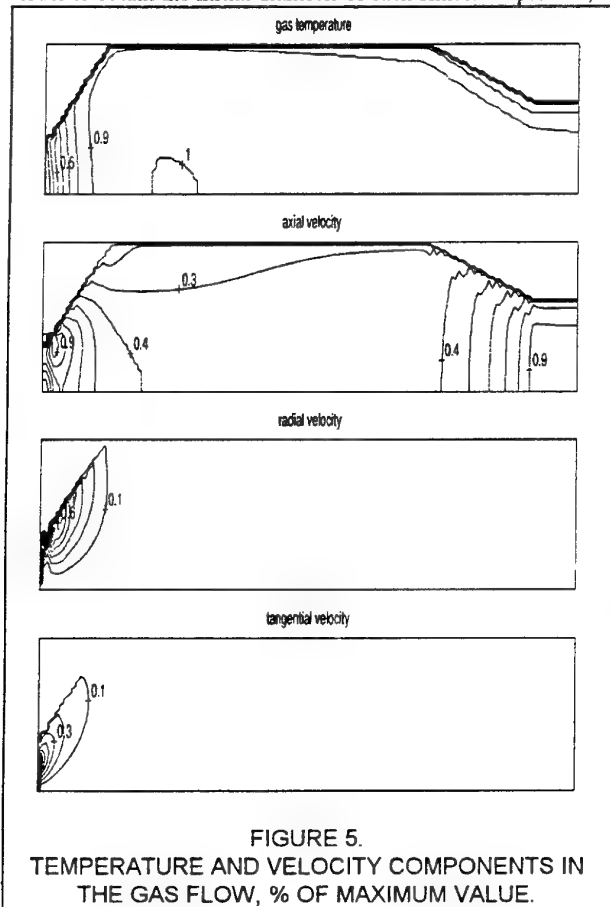
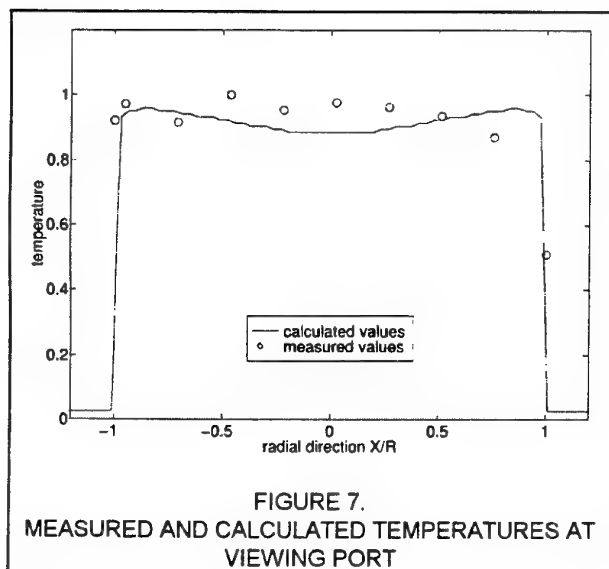


FIGURE 5.

TEMPERATURE AND VELOCITY COMPONENTS IN THE GAS FLOW, % OF MAXIMUM VALUE.



It is expanded in the furnace and the lightweight particles are conveyed out of the furnace together with the exhaust gases.

The expanded perlite is separated from the gas flow in a cyclone after passing a cooling chain. The combustion gases leave the chimney after passing through an aspiration fan.

Figure 2 also shows the planes where velocity and temperature profiles and mass flow rate measurements have been obtained, in hot and cold conditions.

Specially designed 1.5 m long thermocouples (type K and W5) with and without ceramic coating have been employed for the flame temperature measurements inside the furnace. Furnace wall temperatures have been measured with the use of optical pyrometers, which could be focused on the different measuring locations shown in Figs. 3 and 8.

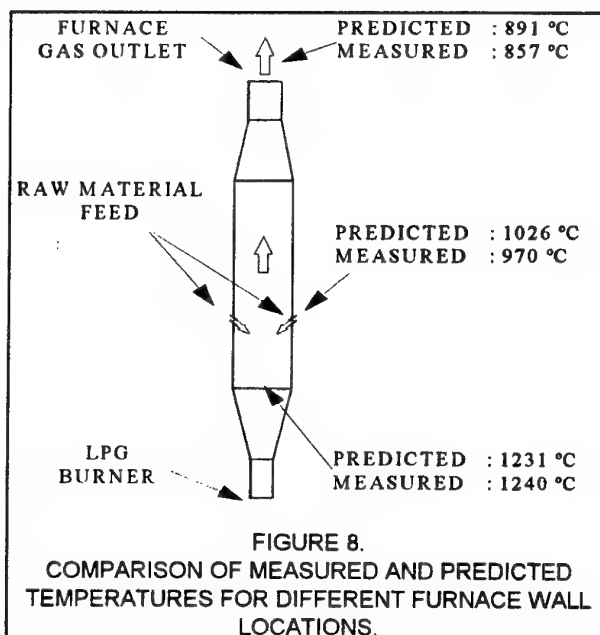
The three velocity components have been measured at the burner outlet (plane A in Fig. 2) under cold flow conditions with a hot wire anemometer. Under operational conditions, a Prandtl-tube designed to withstand high temperatures has been used to measure the temperature distribution at the lower side of the viewing port (plane C in Fig. 2).

Velocity measurements obtained at the furnace outlet and before the chimney fan have been compared to volumetric air flow rate measurements obtained with a turbine type anemometer at the aspiration side of the blowing fan. They allowed the determination of the inlet air flow rate.

During the industrial experiments (Zähringer et al., 1997) raw perlite of size distribution 0 to 1.4 mm has been expanded to yield particles in the size range between 0 to 5 mm.

### COMPUTATIONAL RESULTS

Figure 4 presents the measured velocity components at the furnace inlet, under isothermal conditions, together with the derived fitted profiles which have been used as inlet conditions to the code. The profiles demonstrate the symmetry of the flow. The axial velocity component attains high values close to the furnace walls. At  $x/R \approx 5$  the tangential component reaches nearly the same value as the axial velocity, indicating a strong swirling motion induced by the burner configuration. The same trend is observed for the radial velocity component which could not be measured over the whole furnace diameter. Non-



systematic axial velocity measurements performed with the Prandtl-tube under operating conditions showed good reproducibility with mean values of the axial velocity around 20 m/s.

Predictions have been performed in a Pentium PC (133 MHz, 32 Mbytes memory), with an unevenly distributed grid of 145 x 46 nodes in the axial and radial directions, respectively.

Figure 5 shows the predicted temperature and velocity contours for a fuel flow rate equal to 135 kg/h and air to fuel ratio equal to 17.3. The radial and tangential velocity isotachs indicate the swirling motion of the flame whereas the temperature iso-contours demonstrate, as a result of the swirling motion, relatively flat temperature distribution in the central part of the furnace, with strong gradients close to the furnace walls. The predictions are based on field calculation of the fuel combustion rate as shown in Figure 6.

In Figure 7 computed temperatures are compared to measurements performed at the level of the furnace viewing port, with very good agreement. In Figure 8 indicative measured and predicted temperatures are shown for different furnace wall locations. Maximum temperatures measured and predicted in the centre of the furnace during the expansion reached 1000 to 1100 °C. Without perlite maximum temperatures were 70 - 100 °C higher than before. When perlite is injected in the furnace it absorbs and consumes heat for its expansion, with consequent lowering of the temperatures in the furnace. Overall, the predicted temperatures in the furnace and along the walls differ from the measured values less than 10%. At the furnace outlet the difference between the measured and predicted temperatures is of the order of 20%. This is due to increased cooling of the outlet of the industrial furnace associated to the weather conditions.

The measured axial velocities at the viewing port (17 m/s) and at the furnace outlet (25 m/s) have been also predicted by the code quite accurately.

Figures 9 and 10 present estimates of expanded perlite granularity for different feeding heights and angles of the raw

material. It is shown that the expanded perlite granularity can be improved when these conditions are modified. The figures also demonstrate how the developed computational tool can be used for the optimisation of the expansion process and the improvement of the quality of the expanded perlite.

## CONCLUSIONS

A computational approach developed for the prediction of turbulent combusting flows and particle characteristics in gas-solid two-phase flows has been applied to the industrial process of perlite expansion and compared to flow rate, temperature measurements performed in a vertical perlite expansion furnace. The achieved good agreement in the results allows the improvement and control of the expansion process of perlite taking into account the expansion furnace conditions (geometry and operating parameters) as well as the raw material properties.

## ACKNOWLEDGEMENTS

The authors would like to acknowledge the support of PERLITE HELLAS S.A where the measurements have been performed. The work is being financed by the European Community within the frame of the BRITE EURAM program (project BE-7087, Optimisation of perlite processing for utilisation in new building materials) and the support is also gratefully acknowledged.

## REFERENCES

- Founti, M., Berdi, T., Kakaras, Em., Klipfel A. and Nturos Z., 1992, "On the expansion processes of industrial minerals", *Proc. of the International Conference on Energy Efficiency in Process Technology*, Ed. P.A. Pilavachi, A Conference organised by the EEC, Athens, pp. 827-833.
- Founti, M. and Klipfel, A., 1995: "Prediction of perlite-particle trajectories in vertical expansion furnaces", *2nd International Conference on Multiphase Flow*, Kyoto, Ja., Vol. 3 IA2, pp. 7 - 13.
- Matsumoto, S. and Saito, S., 1970, "Monte Carlo simulation of horizontal pneumatic conveying based on the rough wall model", *J. Chem. Engng. Ja.*, Vol. 3, pp. 223-230.
- Mei, R., 1992, "An Approximate Expression For The Shear Lift Force On Spherical Particle At Finite Reynolds Number," *International Journal of Multiphase Flow*, Vol. 18, pp. 145-147.
- Morsi, S.A. and Alexander, A.J., 1972, "An investigation of particle trajectories in two-phase flow systems", *J. Fluid Mech.*, Vol. 55, part 2, pp. 193-208.
- Murdock, J.B. and Stein, H.A., 1950, "Comparative furnace designs for the expansion of perlite", *Trans. of AIIME*, Vol. 187, pp. 111-118.
- Papapavlou, C., Marakis, J. and Kakaras, E., 1994, "Radiative heat transfer in cylindrical coal-fired furnaces using the P1 approximation and the Monte Carlo method", Eurotherm Seminar No. 37, Heat Trans. in Radiating and Combusting Systems/2, Sallugia, Italy.
- Patankar, S.V., 1980, "Numerical heat transfer and fluid flow", Hemisphere Publis. Co.
- Papanastassiou, D. J., 1979, "Perlite expansion in a vertical furnace - a simplified theoretical analysis", *Perlite Institute Annual Proceedings, Dubrovnik*, pp. 67 -71.
- Shaw, H., 1972, "Viscosities of magmatic silicate liquids: an empirical method of prediction", *Amer. J. of Science.*, Vol. 272, pp. 870-876.
- Sommerfeld, M. and Zivkovic, G., 1992, "Recent advances in the numerical simulation of pneumatic conveying through pipe systems", *Computational Methods in Applied Sciences*, Elsevier Science Publishers, pp. 201-212.
- Tabakoff, W., Malak, M.F. and Hamed, A., 1987, "Laser measurements of solid-particle rebound parameters impacting on 2024 Aluminium and 6Al-4V Titanium alloys", *AIAA - Journal*, Vol. 25, 5, pp. 721-726.
- Zähringer, K., Klipfel, A., Martin, J.P., Petit, J.P. and Founti, M., 1997, Experimental and computational investigation of vertical perlite expansion furnaces, *Proc. 4<sup>th</sup> European conference on Industrial boilers and Furnaces*, Portugal.

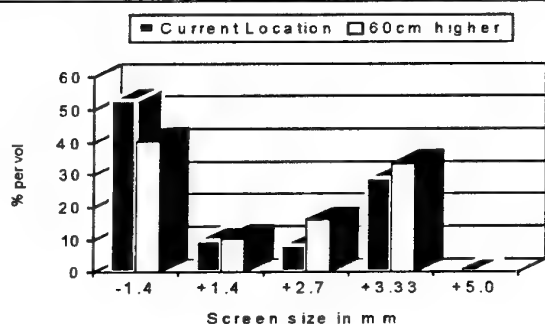


FIGURE 9.  
EFFECTS OF THE RAW MATERIAL FEEDING  
LOCATION ON THE EXPANDED PERLITE  
GRANULARITY

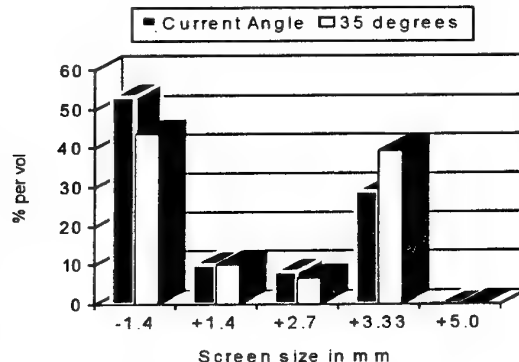


FIGURE 10.  
EFFECTS OF THE RAW MATERIAL FEEDING ANGLE  
ON THE EXPANDED PERLITE GRANULARITY

# GENERATION OF LONGITUDINAL VORTICES IN INTERNAL FLOWS WITH AN INCLINED IMPINGING JET AND ENHANCEMENT OF TARGET PLATE HEAT TRANSFER

K. Suzuki, K. Nakabe, K. Inaoka, A. Higashio, J.S. Acton and W. Chen

Department of Mechanical Engineering  
Kyoto University  
Kyoto 606-01  
Japan

## ABSTRACT

Flow velocity measurements and heat transfer experiments were carried out for a jet obliquely discharged into a crossflow in a duct. Flow measurements were made with a fiber laser Doppler velocimetry and heat transfer experiments were made by making use of a thermochromic liquid crystal. The obtained data reveal that the inclined jet is effective in generating longitudinal vortices in the crossflow. It is demonstrated to be effective in enhancing the impinging jet target plate heat transfer. Therefore, it is promising as a means to cool the inner surface of high temperature gas turbine vanes. The obtained heat transfer data are discussed in detail in terms of the measured flow field and turbulence data.

## INTRODUCTION

Generation of longitudinal vortices is an effective way to control the characteristics of near-wall flow and therefore to enhance the wall heat transfer [Suzuki, 1996]. Its effectiveness in enhancing turbulent heat transfer has been well demonstrated both for the case where vortex generators are directly attached to a heat transfer surface [Eibeck, et al., 1987 and Fiebig, et al., 1995] and for the case where they are attached to a Large Eddy Break-Up manipulator mounted in a position detached from a heat transfer surface [Inaoka, et al., 1992 and 1995]. However, in some practical cases, coolant

passages are not large enough in size to mount such vortex generators, such as in the case of the inside of a gas turbine vane. The width of the coolant air passage, between the insert and the inner surface of the turbine vane, is normally less than one millimeter. Therefore, it is valuable to find a way to generate longitudinal vortices without mounting any vortex generators.

In the case of gas turbine vanes, impinging jets issued from the multiple holes drilled in the insert are normally used as a means for the cooling of their inner surface. Thus, a study was initiated to investigate the possibility of generating the longitudinal vortices by making use of the jets themselves.

A similar attempt was made by Johnston and Nishi [1990], but they aimed at using the generated vortices as a means to suppress flow separation from the nozzle-installed surface. In the present study, it is desired to have the generated longitudinal vortices situated as close as possible to the target plate opposite to the nozzle-installed surface.

## EXPERIMENTAL APPARATUS, METHODS AND CONDITIONS

Figure 1 shows a schematic view of the experimental apparatus used in the present study. The working fluid was water driven by the head difference between the constant head tank 1 and the outlet of the test section 9. The flow coming

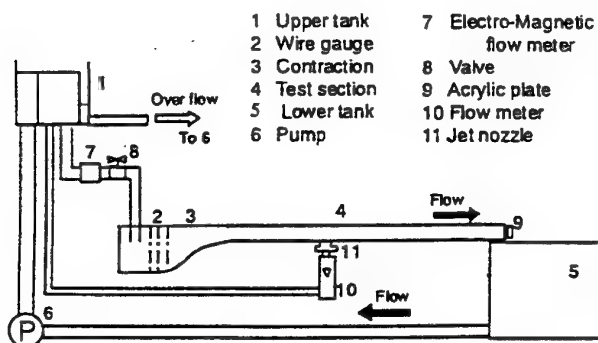


FIG.1 EXPERIMENTAL APPARATUS.

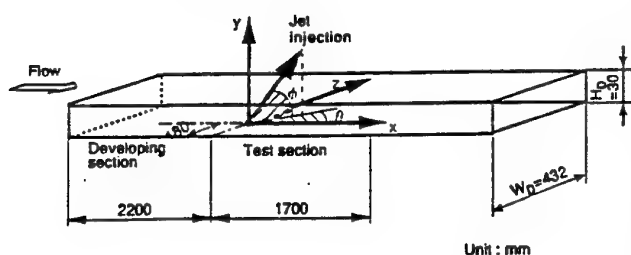


FIG.2 TEST SECTION.

into the test section 4 from the contraction 3 serves as a crossflow for an impinging jet. A circular impinging jet nozzle 11 was mounted flush with the bottom plate of the test section.

Dimensions of the test section are illustrated in Fig. 2 together with some geometric parameters, the jet nozzle arrangement and the coordinate system to be used in the present study. The origin of the coordinate system is located at the center of the open end of the jet nozzle, and  $x$ ,  $y$  and  $z$  are, respectively, the streamwise, normal and spanwise coordinates. The jet discharged from the nozzle impinges obliquely onto the ceiling of the test section. The direction of the jet is characterized by two angles; one is the pitch angle  $\phi$  raised from the floor of the test section and the other the skew angle  $\theta$  measured in a horizontal plane from the streamwise coordinate axis,  $x$ .  $\phi$  and  $\theta$  were fixed at 45 degrees and 90 degrees, respectively, in the present experiments. The nozzle center is located offset from the center line of the channel floor so as to give more space in a cross-section on the jet-directed side.

The duct was 432mm wide and 30mm high, and its aspect ratio was 14.4. The jet nozzle diameter was 6mm. Thus, the channel space is five times the nozzle diameter, which is normally regarded to be optimum in the gas turbine vane

cooling practice with perpendicularly impinging jets [Sparrow, et al., 1975]. The developing section, 2.2m long, provided 36 hydraulic diameters for the flow to develop. The channel Reynolds number was kept constant equal to 5,000 and the jet to crossflow velocity ratio,  $VR$ , was changed in three steps, i.e. 3, 5 and 7.

As has been reported previously [Nakabe, et al., 1996], flow visualization was first made to establish a general picture of the flow patterns to be formed in the channel and to see if longitudinal vortices can be generated. For this purpose, particle tracking velocimetry was applied to the sequent photographs taken by a CCD video camera mounted so as to view the test section from the downstream end of the channel. Secondary flow velocity vector distributions were constructed at several streamwise locations different in the distance from the nozzle. This part of the study was carried out for the cases at a reduced crossflow velocity but at the above mentioned values of  $VR$ . Some of the obtained results will be cited in the following discussions.

Quantitative flow and turbulence measurements were made in more detail in the present study with a two-color, three-beam fiber laser Doppler velocimeter. 1.5W Ar<sup>+</sup> laser was used as a beam source. In the adopted back-scatter type LDV optical system, a measuring control volume was set to be of the size of 115  $\mu$ m in diameter and 1.44mm in length. The scattered beam signals detected by photomultipliers were converted to velocity signals by making use of a DISA phase-locked loop frequency tracker system. Bragg-cell was used to give frequency shift in order to make the measurement of backward flow velocity. Frequency shift down to obtain actual velocity was done electronically in signal processing.

In addition to these flow measurements, heat transfer experiments were also made. The channel ceiling was used as the jet target plate or as the heat transfer surface and its surface was almost entirely covered by smoothly glued thin stainless steel strips of 5cm wide and 20  $\mu$ m thick. These were heated by passing alternating electric current. The surface temperature of the jet target plate was measured by making use of thermochromic liquid crystal. Photographs of the colored liquid crystal sheets sandwiched between the channel ceiling surface and stainless steel strips were taken from the outside with a CCD camera and the color images of the liquid crystal sheets were stored in the color frame buffer

memory of an engineering workstation. Hierarchy neural network [Kimura, 1992] was applied to convert the color images to temperature distribution. This method is much superior, both in the spatial resolution and in the surface area to be covered, to the previous one in which the surface temperature was measured with many thermocouples allocated to contact with the back surface of the heated stainless steel strips [Nakabe, et al., 1996 and Acton, et al., 1997]. Detail of the method will be reported elsewhere, but the inaccuracy (standard deviation) of the method was 0.18K at most over such a wide range of temperature from 26.5°C to 43.5°C.

The heat transfer coefficient  $\alpha$  and Nusselt number  $Nu$  based on hydraulic diameter are defined as follows:

$$Nu = \frac{\alpha(2H_D)}{\lambda}, \quad \alpha = \frac{q_w}{(T_w - T_{in})} \quad (1)$$

$T_w$  and  $T_{in}$  are, respectively, the local heat transfer surface temperature and the inlet flow temperature.  $\lambda$  and  $H_D$  are the thermal conductivity of water and the height of the test section, respectively. The wall heat flux  $q_w$  was calculated from the electric power input as mentioned above. Heat conduction loss from the heat transfer surface toward the back side of the target plate was evaluated to be less than 3% of the total heat flux so

that it was neglected. Radiative heat loss from the heat transfer surface was neglected as well.

## RESULTS AND DISCUSSION

### Nusselt Number Distributions

Figure 3 shows examples of the contours of the local Nusselt number measured on the whole area ranging from  $x/d = -5$  to 45 and from  $z/d = -10$  to 20 for the cases of (a)  $VR = 3$  and (b)  $VR = 5$  at the crossflow Reynolds number,  $Re = 5,000$ . Here,  $d$  is the jet nozzle diameter. It can be seen in Fig. 3(a) that the conspicuously enhanced region of heat transfer, defined as the region where the Nusselt number takes a value larger than one hundred, lies almost parallel to the  $x$ -axis. The maximum Nusselt number is found to appear at a position around  $(x/d, z/d) = (9.0, 4.0)$ . It indicates that the jet stagnation point is shifted downstream affected by the crossflow and off the centerline due to the oblique impingement of the jet.

For a higher  $VR$  value case shown in Fig. 3(b), the conspicuously enhanced region of heat transfer expands in spanwise direction and covers the region ranging from a bit below the centerline of the test section,  $z/d = -0.9$  to  $z/d = 13$ . The peak position of local Nusselt number is shifted back toward upstream to a position around  $(x/d, z/d) = (6.0, 4.0)$ , if compared with the counter part of the lower  $VR$  value case,

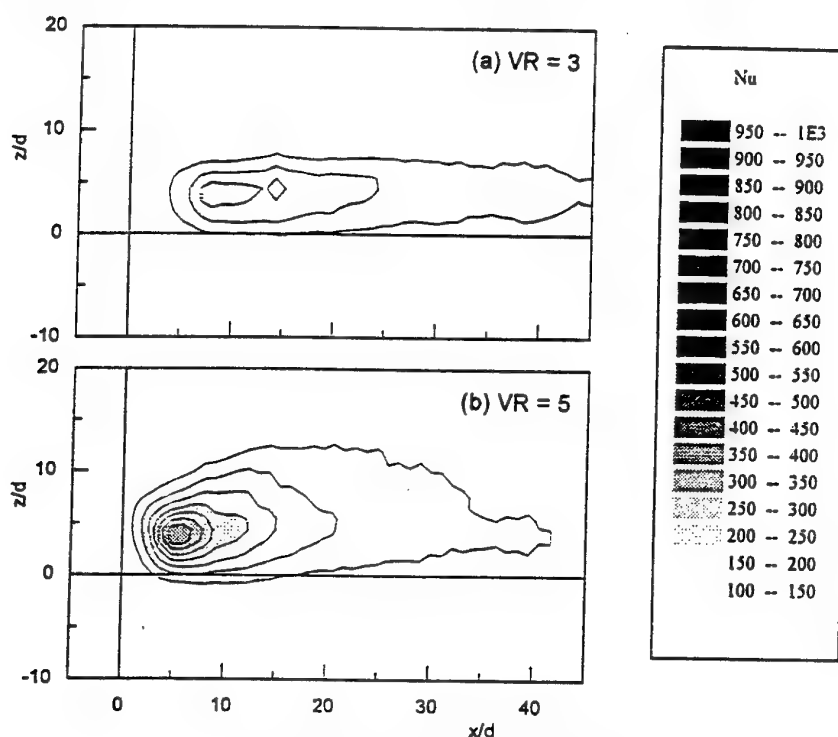


FIG.3 Nu CONTOURS ( $Re = 5,000$ ).

although its spanwise position was scarcely changed. This may reflect the decrease of the streamwise position shift of the jet stagnation point downstream from  $x/d = 0$  with an increase of VR value.

Although the supporting figures for the case of  $VR = 7$  are omitted here to save space, further spatial expansion of the conspicuously enhanced region of heat transfer and increase of peak Nusselt number was confirmed to occur with a further increase of the VR value.

### Velocity Distributions

Figure 4 shows an example of the contours of the time-averaged y-direction velocity,  $V$ , measured in the middle plane between the ceiling and floor of the test section for an experimental condition corresponding to the one of Fig. 3(b), i.e. the case of  $VR = 5$  and at  $Re = 5,000$ . The dark gray and black parts in the figure represent an upwash flow or a flow toward the target plate, while the light gray and white parts represent a downwash flow or a flow toward the nozzle-installed floor of the test section. As seen in this figure, both of upwash and downwash flows appear both in the one half and another half of the illustrated area of the middle plane. Therefore, it obviously reveals that a pair of long longitudinal vortices are generated in the test section.

The distribution of RMS turbulence intensity of y-direction fluctuating velocity,  $V'$ , in the middle plane between the ceiling and floor of the test section is also shown in Fig. 4. High turbulence intensity region observed in the figure corresponds to the upwash flow region induced by the inclined jet or in between a pair of counter rotating vortices. This high intensity turbulence may affect the time-averaged velocity field and as a consequence affect the enhancement pattern of target plate heat transfer.

### Relation between flow field characteristics and heat transfer enhancement from the target plate

Figure 5 shows the spanwise distributions of Nusselt number obtained at  $x/d = 20$  for three values of VR in comparison with the secondary flow velocity vector map for each corresponding case of different value of VR. All velocity maps were drawn as mentioned before based on the photographs taken from the downstream end of the test section and, therefore, show upstream view of the secondary flow in

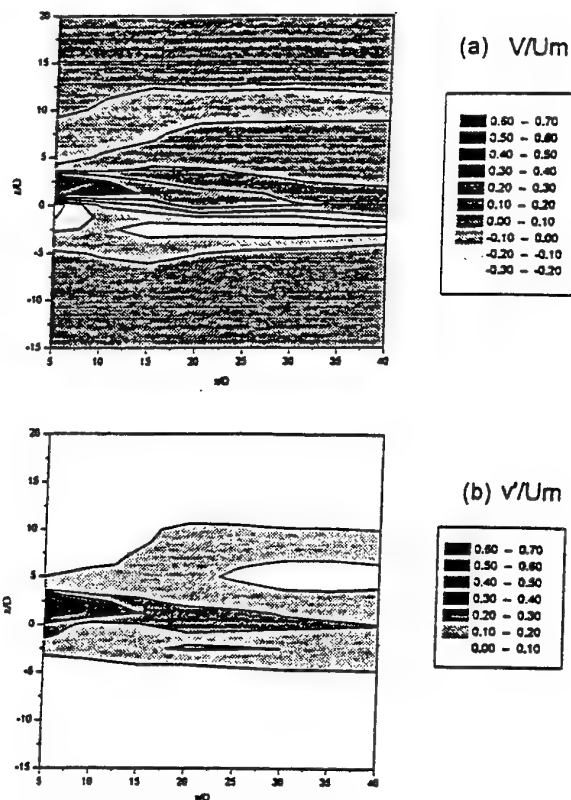


FIG.4 V AND V' CONTOURS ( $y/d = 2.5$ ,  $VR = 5$  AND  $Re = 5,000$ ).

the cross-section. A longitudinal vortex with anti-clockwise rotation is situated at an almost same position around  $z/d = 0$  in all the cases. This may have the same origin as the one previously pointed out by Johnston and Nishi [1990] near the nozzle-installed channel floor of the test section having larger y-direction space. In addition to this, another vortex having the clockwise rotation is clearly observed around  $z/d = 10$  for the case of  $VR = 5$  and around  $z/d = 7$  for the case  $VR = 7$ . Its position moves away from the nozzle position in z-direction as the VR value is increased. This vortex induces strong spanwise velocity sweeping the ceiling surface of the test section.

The spanwise position of the peak Nusselt number, noticeably observed in the case of  $VR = 3$ , is located around  $z/d = 0$  where as discussed just above corresponds to the region of upwash flow induced by the anti-clockwise vortex. This upwash flow supplies fresh fluid or cooler fluid near the target plate and enhances the heat transfer from the target plate. Studying the peak position of Nusselt number in a little more detailed manner, it is found to move a little toward the right

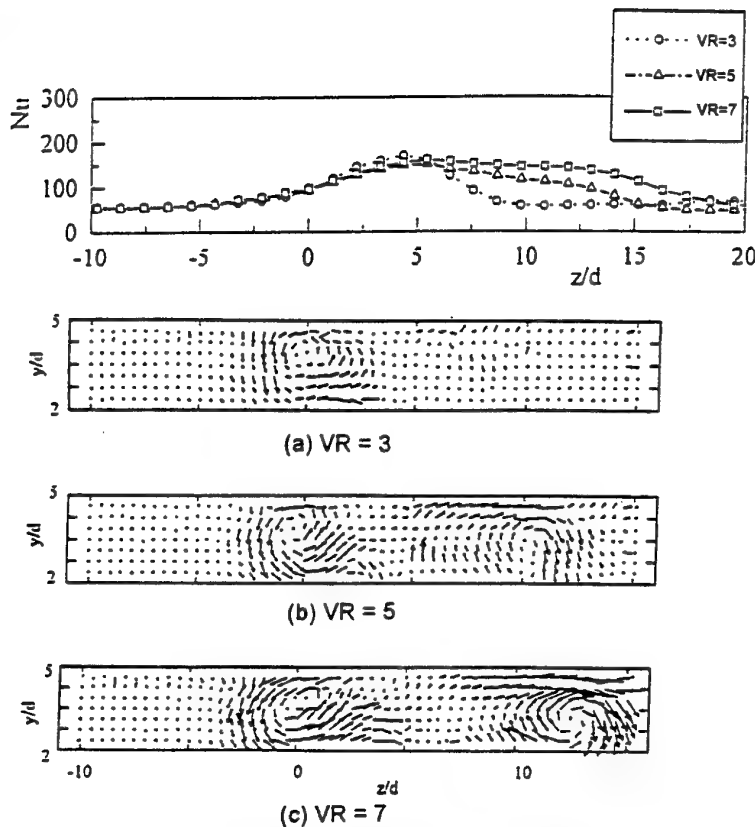


FIG.5 Nu CONTOURS AND VELOCITY VECTOR DISTRIBUTIONS ( $x/d = 20$ ,  $VR = 5$  AND  $Re = 5,000$ ).

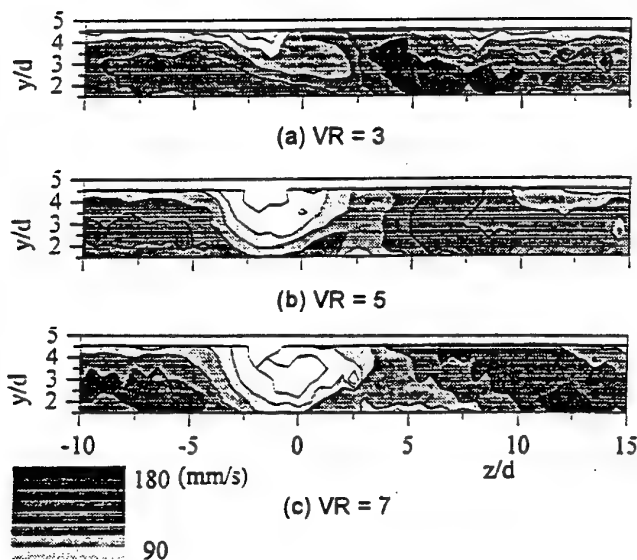


FIG.6 U CONTOURS ( $x/d = 20$ ,  $VR = 5$  AND  $Re = 5,000$ ).

end of the channel with an increase in the VR value. This will be discussed below again.

The right hand down-slope of Nusselt number distribution becomes less steep at  $VR = 5$  and, when  $VR = 7$ , the Nu distribution exhibits a shape almost like a plateau in the range of spanwise position from  $z/d = 0$  to  $z/d = 13$ . This part of the Nu distribution corresponds to the region where flow sweeping the target plate surface appears accompanied with the generation of the clockwise vortex.

Figure 6 shows the contours of the streamwise time-averaged velocity,  $U$ , for the three cases of  $VR = 3, 5$  and  $7$ . In the case of  $VR = 3$ , a small low velocity region appears near the channel ceiling just on the left side of  $z/d = 0$ . The low velocity region expands wider as the value of  $VR$  is increased. The lower streamwise velocity in this region is caused by the jet itself. It acts like a fence to the approaching flow and velocity defect produced in its wake lasts over a long distance. Similar velocity deficit accompanying the discharged jet was also observed by Compton and Johnston [1992]. Slight movement of the peak Nusselt number position with an increase in the VR value pointed out in the above may be related with this expansion of the low velocity region with an increase in VR. Low streamwise velocity near the heat transfer surface suppresses the wall heat transfer. Then, the left side of the peak of Nusselt number distribution becomes a little lower so that the peak Nusselt number position looks apparently moving in the right hand direction.

More important point observed in this figure is that high streamwise velocity region exists just on the left side of the clockwise longitudinal vortex. This high velocity region extends very near the channel ceiling so that this should be related to the increase of Nu on the right side of its peak; less steep slope on the right side of the peak Nu in the case of  $VR = 5$  and the plateau-like shape of Nu distribution in the case of  $VR = 7$ . Strong spanwise flow observed near the top wall in Fig. 5(c) sweeps the top wall with this high streamwise velocity. This should be the main cause of the heat transfer enhancement on the right hand side region of the peak Nusselt number.



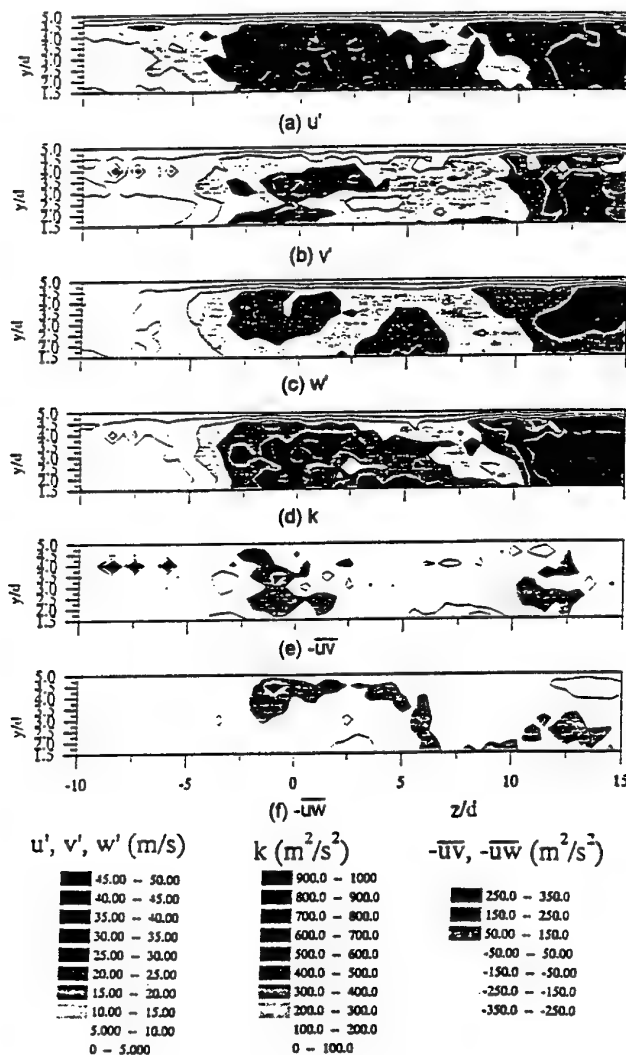


FIG. 7 CONTOURS OF TURBULENCE COMPONENTS  
( $x/d = 20$ ,  $VR = 5$  AND  $Re = 5,000$ ).

Figure 7 shows an example of the turbulence intensity distributions of  $u'$ ,  $v'$ ,  $w'$ ,  $k$ ,  $-u'v'$  and  $-u'w'$  for the case that  $Re = 5,000$  and  $VR = 7$ . These turbulence data should serve as a good data base to test a numerical computation of the presently discussed longitudinal vortices generated with an obliquely discharged jet into a turbulent crossflow.

## CONCLUSIONS

Flow measurements and heat transfer experiments were made for an obliquely impinging jet with a turbulent crossflow of channel Reynolds number,  $Re$ , equal to 5,000 in three cases of jet to crossflow velocity ratio,  $VR$ , equal to 3, 5 and 7. The main results obtained in this study are as follows:

1. Generation of a pair of counter rotating vortices was clearly observed; one having anti-clockwise rotation situated constantly around  $z/d = 0$  regardless of the  $VR$  value and the

other having clockwise rotation moving away from the nozzle position in the  $z$ -direction with an increase in  $VR$ .

2. Heat transfer enhancement can be attained over wider spanwise region when the  $VR$  value is increased. This expansion of the high Nusselt number region is caused by the high streamwise velocity flow spanwisely sweeping the target plate, which is produced by the clockwise rotating vortex.

3. The peak Nusselt number appears around  $z/d = 0$  constantly, regardless of the  $VR$  value. This is caused by the upwash region supplying fresh fluid near the target plate surface.

## ACKNOWLEDGMENT

This research was partially supported by the Grant-in-Aid of Scientific Research, Ministry of Education, Science and Culture, Japan. The authors wish to express their gratitude to Messrs. Ai, T. and Hada, S., students of Kyoto University, for their cooperation in experiments.

## REFERENCES

- Acton, J.S., Higashio, A., Inaoka, K., Nakabe, K. and Suzuki, K., 1997, *Proceedings of 1st Symposium on Flow Visualization and Image Processing*, Vol. 2, 457-462.
- Compton, D.A. and Johnston, J.P., 1992, *AIAA J.*, Vol. 32, 640-646.
- Eibeck, P.A. and Eaton, J.K., 1987, *ASME J. Heat Transfer*, Vol. 109, 16-24.
- Fiebig, M., 1995, *J. Enhanced Heat Transfer*, Vol. 2, 16-24.
- Inaoka, K., Suzuki, K., Hagiwara, Y., Suzuki, K. and Suzuki, H., 1992, *Heat Transfer - Japanese Research*, Vol. 21, 721-735.
- Inaoka, K. and Suzuki, K., 1995, *Turbulent Shear Flows* (Ed. Durst, F. et al.), Vol. 9, 365-382, Springer-Verlag.
- Johnston, J.P. and Nishi, 1990, M., *AIAA J.*, Vol. 30, 989-994.
- Kimura, 1992, *J. Visualization*, 12-Suppl. 1, 7-10 (in Japanese).
- Nakabe, K., Inaoka, K., Ai, T. and Suzuki, K., 1996, *Proceedings of 3rd KSME-JSME Thermal Conference*, Vol. 3, 59-64.
- Sparrow, E.M., Goldstein, R.J. and Rouf, M.A., 1975, *ASME J. Heat Transfer*, Vol. 97, 528-533.
- Suzuki, K., 1996, *Proceedings of Symposium on Vortices and Heat Transfer*, Bochum, (in printing).

# PHYSICAL AND NUMERICAL MODELING OF TURBULENT FLOW OVER COMPLEX TOPOGRAPHY

A. Nakayama and H. Noda

Division of Global Environmental Sciences  
Graduate school of Science and Engineering  
Kobe University  
Rokkodai, Nada-ku, Kobe 657  
Japan

## ABSTRACT

A numerical simulation using a large-eddy simulation technique and a physical simulation using a large wind tunnel model have been conducted for flow over a real topography. The region modeled is the neighborhood of a planned site for a commuter airport in a mountainous region with mild ridges and valleys with moderate vegetation. Both models cover the area of about 3.5km by 2.0km around the proposed runway strip of length 1.2km. On-site field measurements of mean wind profiles were also conducted to provide basis for the simulation. Simulations were for neutral stratification and the mean velocity and turbulent stresses were obtained by both methods and detailed comparisons are made. Particular emphasis is placed on the effects of spatial resolution of the numerical model on the simulation results, and numerical simulations using different grid size are performed. A systematic way of modeling the effects of unresolved small-scale geometry is proposed.

## INTRODUCTION

Although much progress is being made in developing large-eddy simulation techniques (LES) to compute turbulent flows of various kinds, its application to real flows in natural environment is not easy or straight-forward (eg. Mason, 1994.) Other than the fact that the boundaries are three dimensional and complex, small-scale irregularities and details of ground cover such as vegetation cannot be represented by the coordinate system and the numerical grid that can be implemented on the presently available computers. Boundaries with uniform irregularities may be considered rough boundary. In such a case simple methods based on the Reynolds-averaged equations are extended with modifications to the mixing-length due to arbitrary roughness (eg. Granville, 1985). Also low-Reynolds-number models for two-equation turbulence models have been adapted to rough boundaries (Wilcox, 1993 and Zang, 1996). These generalized roughness models have not been validated and its general applicability to complex natural topography is doubted. Furthermore, terrain with tall-tree canopies

cannot only be represented exactly nor is it practical and rough boundary and tree canopy need to be modeled in the equations (eg. Wilson and Shaw (1977), Yamada (1982).) A modeling of atmosphere-vegetation interface has been tried using a large-eddy simulation method by Hino et al. (1992). We try to approach this rough and complex boundary problem as a numerical resolution problem due to filtering effects by insufficient grid resolution and formulate more systematically. We make use of the volume fraction technique and start with the basic equations of motion that are applicable for porous flow region. This method requires the definition and information on the volume and area porosities of the medium but it can describe complex and porous boundaries without explicitly specifying the position of the boundary. Furthermore, insufficient numerical grid resolution to represent small irregularities of the boundary can be treated as a smoothing or spatial filtering of these

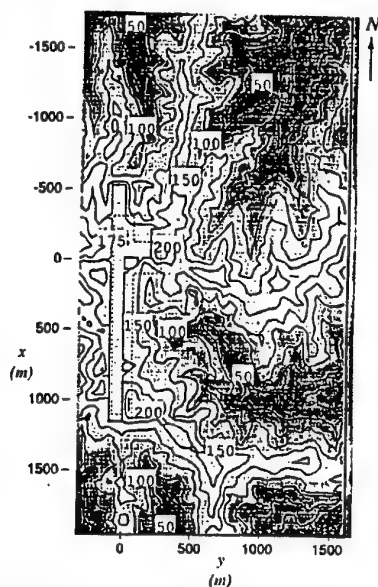


Fig.1 Map of the region to be modeled.

field quantities, porosities. For the present work, we use a low-order representation in rectangular grid, but consideration to use higher-order method which improves boundary representation is made.

### TOPOGRAPHY TO BE MODELED

Present simulation was performed as a part of evaluation of the environmental effects of alteration of a natural topography by a construction of an airstrip in the middle of a mountainous region. Much efforts were spent in the development of the method of computing the turbulent wind field and the present paper is a summary of the basic part of this study. Fig.1 is the map of the local area to be studied. The area is 50 to 200m above sea level and the narrow strip near the left edge of the map is the runway at 175m above sea level. Within about 15km to the north there are few ridges of about 300 to 400m that create some wake effects. For the purpose of computation we take positive  $x$  direction to be southward along the runway,  $y$  direction eastward from the reference position on the centerline of the runway as shown in the map.  $z$  direction vertically up from the sea level. The field measurement of the vertical wind profile by a pibal tracing indicated it is close to the 1/4th power law.

### WIND TUNNEL SIMULATION

The wind tunnel used is a 2.5m by 2.0m by 12m blower-type environmental low-speed wind-tunnel. The wind tunnel model as shown in Fig.2 has been constructed. It is an undistorted 1/900 scale model and was generated from the 1/500 map of the region and covers the area of 3.5 km by 2.0 km and the vertical distance of 1.5 km. The terrain contours were modeled with accuracy of 1m and the irregularities smaller than this scale and the roughness due to ground surface and vegetation were modeled by sand paper, fabrics and sponges. The approach flow was generated by spires and block roughness laid in the upstream 8m stretch of the test section. The generated vertical wind profile was matched the measured vertical wind profile at the upstream end of the modeled area. Mapping of the three dimensional flow was obtained using a triple-sensor hot-wire probe and detailed measurements near ground were obtained by an X-wire probe for several approach-flow directions for a fixed approach-flow speed of 10m/s.

### NUMERICAL SIMULATION USING LES TECHNIQUE LES Equations for Complex Boundary

We represent the complex boundaries including porous objects such as trees using the volume fraction method of Hirt(1993). For the purpose of deriving governing equations we use the suffix notation so that coordinates  $(x_i, x_j, x_k)$  correspond to  $(x, y, z)$  and the velocity components  $(u_i, u_j, u_k)$  to  $(u, v, w)$ . If the volume fraction occupied by fluid, or the volume porosity of the flow region at point  $(x_i, x_j, x_k)$  is  $\phi$ , and if the fraction of area, or the area porosity in a cross section perpendicular to the  $x_i$  direction is  $A_i$ , the equation of fluid motion following the FAVOR method(Hirt, 1992) is

$$\phi \rho \frac{\partial \tilde{u}_i}{\partial t} + \rho \tilde{A}_{ij} \tilde{u}_j \frac{\partial \tilde{u}_i}{\partial x_j} = -\phi \frac{\partial \tilde{p}}{\partial x_i} + \frac{\partial}{\partial x_j} \tilde{A}_{ij} \tilde{\tau}_{ij} \quad (1)$$

where  $\tau_{ij} = \mu(\partial u_i / \partial x_j + \partial u_j / \partial x_i)$  is the viscous stress and the tilde  $\sim$  denotes the instantaneous and local value. The indexes in parentheses do not follow the usual summation convention and is not summed. The continuity equation is

(a) Wind tunnel model



(b) Numerical representation

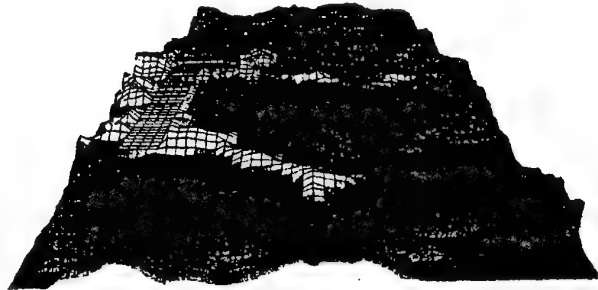


Fig.2 Wind tunnel and numerical models.

$$\frac{\partial}{\partial x_i} \tilde{A}_{ij} \tilde{u}_j = \frac{\partial \tilde{q}_i}{\partial x_i} = 0 \quad (2)$$

Here  $\tilde{q}_i \equiv \tilde{A}_{ij} \tilde{u}_j$  is the volume flux through the cross section perpendicular to the  $x_i$  direction. The location of the boundary is determined by the values of  $\phi$  and  $A_i$  and is the surface enclosing the region  $\phi > 0$ .

In order to obtain the LES equations, we take the spacial average of the above equations. If we use  $\langle \rangle$  to denote the spacial average and  $\langle' \rangle$  to denote the deviation from this average, i.e. the subgrid fluctuation, the averaged continuity equation is

$$\frac{\partial}{\partial x_i} \langle A_{ij} \rangle \langle u_j \rangle = - \frac{\partial}{\partial x_i} \langle A'_{ij} u'_j \rangle \quad (3)$$

and the average of the momentum equations are

$$\begin{aligned} \langle \phi \rangle \frac{\partial \langle u_i \rangle}{\partial t} + \langle A_{ij} \rangle \langle u_j \rangle \frac{\partial \langle u_i \rangle}{\partial x_j} \\ = - \frac{\langle \phi \rangle}{\rho} \frac{\partial \langle p \rangle}{\partial x_i} - \left\langle \frac{\phi'}{\rho} \frac{\partial p'}{\partial x_i} \right\rangle \\ + \frac{\partial}{\partial x_j} \left( \langle A_{ij} \rangle \langle \tau_{ij} \rangle + \langle A'_{ij} \tau'_{ij} \rangle + R_{ij} \right) \end{aligned} \quad (4)$$

where

$$\begin{aligned}
 R_{ij} &= -(\langle u_i q_j \rangle - \langle u_i \rangle \langle q_j \rangle) \\
 &= -(\langle u_i' q_j' \rangle + \langle u_i \rangle \langle q_j' \rangle \\
 &\quad - \langle u_i' q_j' \rangle - \langle u_i' \rangle \langle q_j' \rangle) - \langle u_i' q_j' \rangle \\
 &= -(\langle A_{ij} u_i' u_j' \rangle + \langle A_{ij} u_i' \rangle \langle u_j' \rangle \\
 &\quad - \langle A_{ij} u_i' u_j' \rangle - \langle A_{ij} u_i' \rangle \langle u_j' \rangle) - \langle A_{ij} u_i' u_j' \rangle
 \end{aligned} \quad (5)$$

is the Reynolds stress due to subgrid fluctuations. We notice that both continuity and momentum equations and even the Reynolds stresses contain correlations involving the spacial variations of the geometric parameters  $\phi$  and  $A$ , and the flow quantities. These correlation terms need to be modeled.

### Modeling of Subgrid Correlation Terms

First we notice that the present Reynolds stress is an effective momentum flux through porous section, we use the usual eddy-viscosity model with the factor of  $A_{in}$  to take into account the porosity. So, we write

$$R_{ij} = A_{in} \left( -\frac{2}{3} k_G \delta_{ij} + \nu_T \left( \frac{\partial \langle u_i \rangle}{\partial x_j} + \frac{\partial \langle u_j \rangle}{\partial x_i} \right) \right) \quad (6)$$

where  $k_G$  is the turbulent kinetic energy of the subgrid-scale motion  $k_G = 3/2 \langle u_i' u_i' \rangle$  and  $\nu_T$  is the eddy viscosity due to subgrid turbulence, for which we apply the Smagorinsky model.

$$\begin{aligned}
 \nu_T &= (C_s \Delta)^2 \sqrt{2D} \\
 D &= \left( \frac{1}{2} \right)^2 \left( \frac{\partial \langle u_i \rangle}{\partial x_j} + \frac{\partial \langle u_j \rangle}{\partial x_i} \right) \left( \frac{\partial \langle u_i \rangle}{\partial x_j} + \frac{\partial \langle u_j \rangle}{\partial x_i} \right) \\
 \Delta &= \min((\Delta_1 \Delta_2 \Delta_3)^{1/3}, \Delta_3)
 \end{aligned} \quad (7)$$

$\Delta_1$ ,  $\Delta_2$  and  $\Delta_3$  are the grid size in  $x$ ,  $y$ , and  $z$  directions respectively. Length scale like mixing length is reduced by roughness and it is probable that the length scale  $\Delta$  may have to be modified for the region very close to ground but we avoided to make special allowance.

For the correlation between the porosity and the pressure gradient, we follow Wilson and Shaw(1977) and use the formula for a form drag due to rough obstacles.

$$\left\langle \frac{\phi'}{\rho} \frac{\partial p'}{\partial x_i} \right\rangle = C_d (1 - A_{in}) f(z) \langle u_i \rangle \sqrt{\langle u_i' u_i' \rangle} \quad (8)$$

where  $C_d$  is a model constant and is the drag coefficient for the boundary which is regarded more like resistance,  $f(z)$  is a kind of damping function and in the present work we used

$$f(z) = C_1 e^{-C_2 z} \quad (9)$$

The correlation involving the viscous stress and the boundary surface, we ignored it in the present work. Also the correlation between the volume porosity and the velocity, that appears in the continuity, is ignored.

### Numerical Method

Although the present equations of motion, Eqs.(3) and (4) for the filtered quantities are somewhat different from the conventional ones with clear boundary, we can adapt conventional numerical techniques. We used a method based on HSMAC iteration method for pressure. The convergence is now to make the divergence of the flux vector  $q$  zero in stead of the actual velocity. The basic method itself has been verified for flows over simpler geometry(Noda and

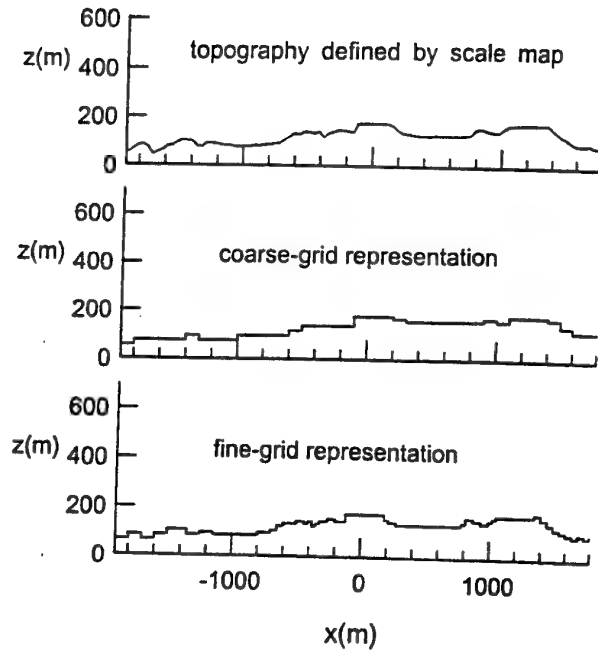


Fig.3 Low-order representation of topography using two different grids.

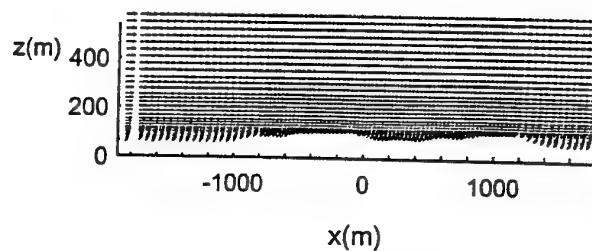


Fig.4 Typical computed instantaneous velocity distribution in a vertical cross section.

Nakayama, 1996). Rectangular mesh of variable interval was used. Boundary conditions are applied at the grid points where  $\phi$  becomes zero, which in the rectangular mesh, are made up of straight lines and is considered to be a smoothing of the original shape.

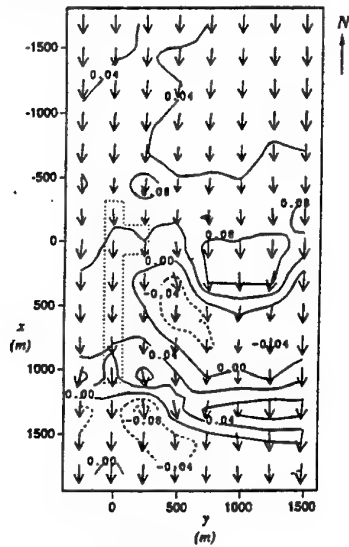
As to the computational grid and determination of the geometric quantities  $\phi$  and  $A$ , 1/500 terrain map of the region was used. The geometry thus determined is shown in Fig.1 and a cross section is shown in Fig.3(a).  $\phi$  for the actual computational grids were calculated from these.

For the present calculation,  $\phi$  has been determined from the map but  $A$  was set either equal to 0 or 1. A typical velocity distribution of the instantaneous filtered velocity vector in a vertical plane as computed by the present model is shown in Fig.4.

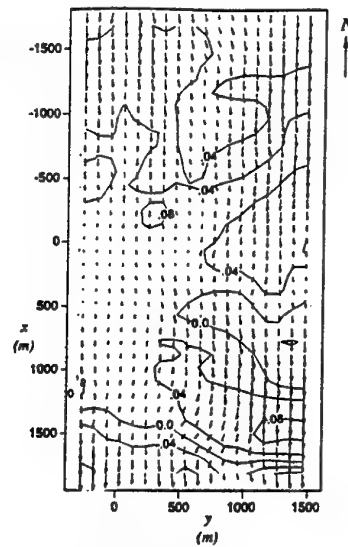
### RESULTS OF NUMERICAL SIMULATION AND COMPARISON WITH WIND TUNNEL SIMULATION

Numerical computation was carried out using two grids generated from the same numerical database of the area,

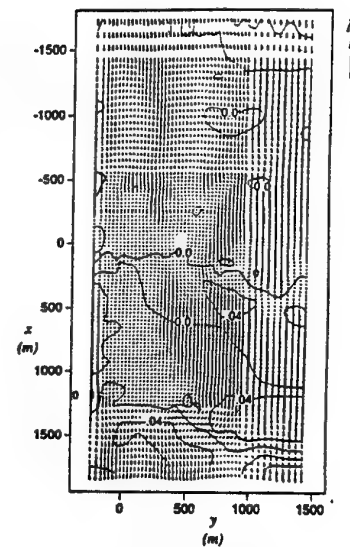
(a)  $z=195m$



Experimental

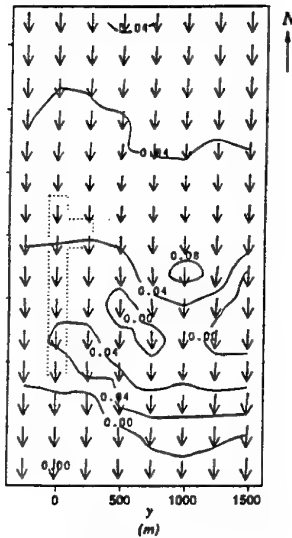


Coarse grid results

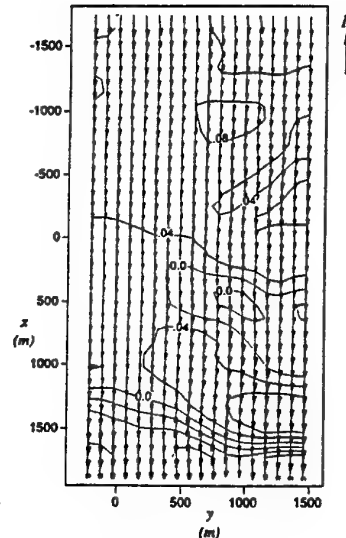


Fine grid results

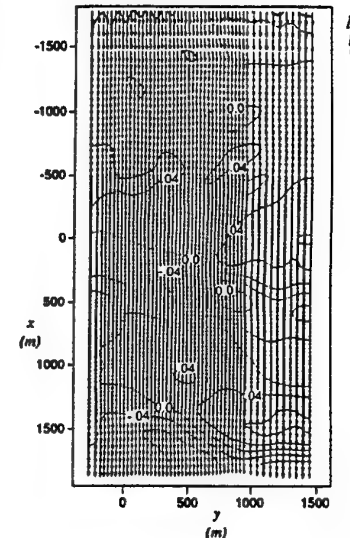
(b)  $z=275m$



Experimental



Coarse grid results



Fine grid results

Fig.5 Mean-velocity results.

shown in Fig.2. filtering with different spacial resolution for the case when the general wind is from north to south. The mean wind profile at the upstream end was assumed to take the power law as measured by the on-site survey. Random fluctuations with prescribed shear correlation superposed on this mean velocities. Turbulence were inputted upstream of the settling section placed upstream of the modeled region.

In the presentation of the results, we use the usual notation of overbars  $\bar{\quad}$  for time averages and the upper case letters for the time mean velocities so that  $U = \bar{u}_1$  and  $V = \bar{u}_2$  etc., and the lower case letters for fluctuations

from the time mean,  $u = u_1 - \bar{u}_1$ . Fig.5 shows the mean-velocity results of the computations using two grids and the experimental results at the elevations of  $z=195m$  and  $275m$ . The first one is  $20m$  from the runway surface and there are places that are very close to the ground. The second plane is at  $100m$  above runway and is higher than the location of the highest turbulence intensity. The velocity components in the horizontal plane are shown as vectors and the vertical component is indicated by the contours. Generally good agreement is seen for both grid results. The computed mean velocity more variations in the flow direction flow and areas of very low velocity than the wind-tunnel results. This may be due to too large drag coefficient for the pressure-porosity correlation.

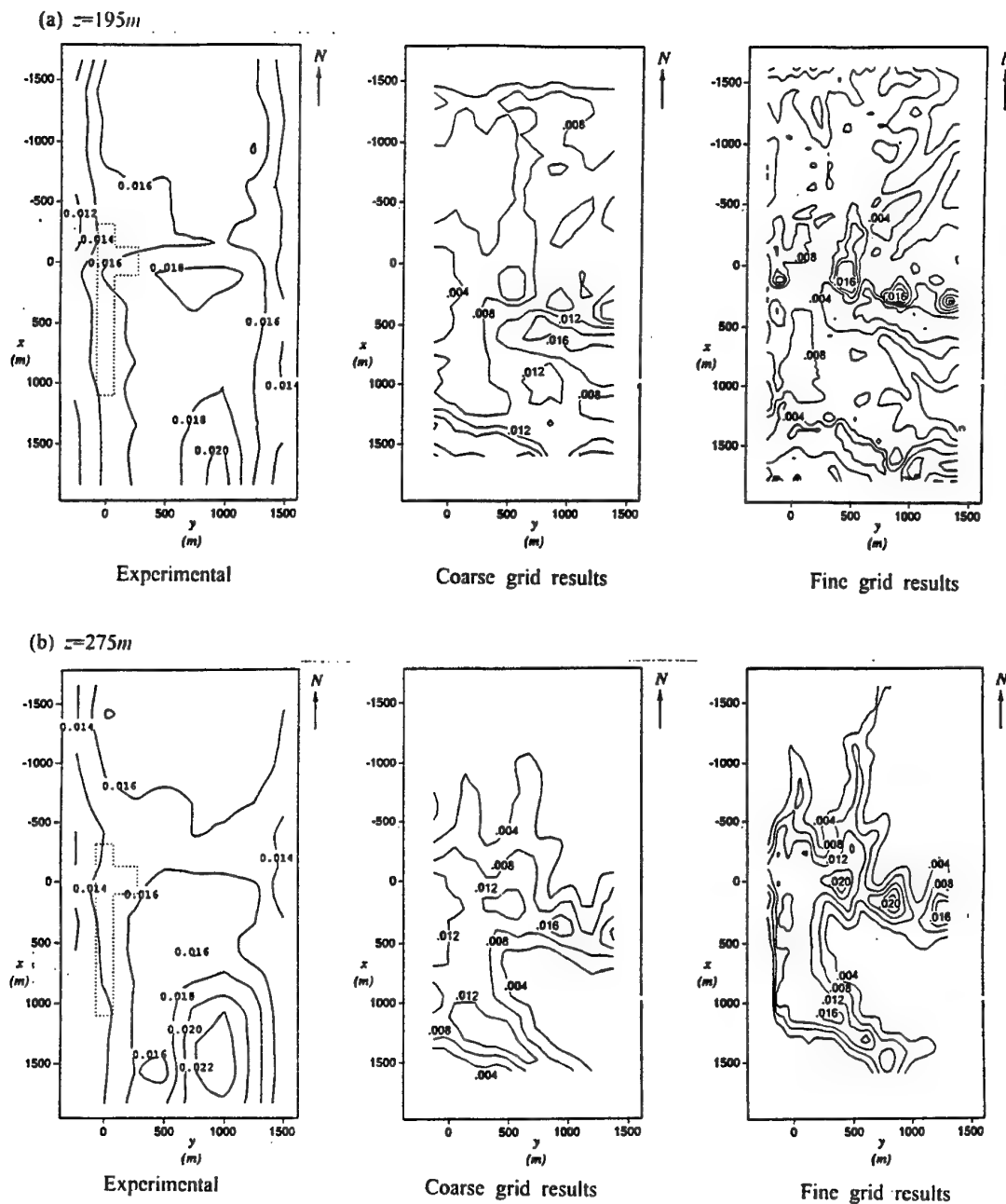


Fig.6 Turbulent-energy results.

Fig.6 shows the turbulence kinetic energy from the computations and the experiment. The computation does not include the subgrid fluctuation  $k_G$  and appears smaller than measured. The trend implied by the computation is in agreement with experiment except the experimental results of turbulence intensity at both ends are high. This is thought to be the effects of the side-wall boundary layer that existed in the wind tunnel. Also the computational results at higher elevation is not as good as near the ground. Contours of constant shear stress in the vertical plane along the runway centerline is shown in Fig.7. The shear for both signs are seen and flow is not as simple as those on flatter terrain. The overall indications are that the computations made here give good results for the mean velocity and qualitatively satisfactory results for the turbulence.

## CONCLUSIONS

A Large-eddy simulation method was applied to compute the flow over a complex topography with particular emphasis on the effects of smoothing of the boundary. Using the volume fraction method developed for porous flow, basic LES equations were derived for complex boundaries of which small-scale irregularities are not represented. This formulation models the effects of smoothing of the boundary irregularities due to finite-numerical resolution. The numerical calculation results are compared with more conventional wind-tunnel measurements. They compare favorably at least qualitatively and the computational model appears plausible, but details are not only grid-density dependent but also disagree with the measurements and more

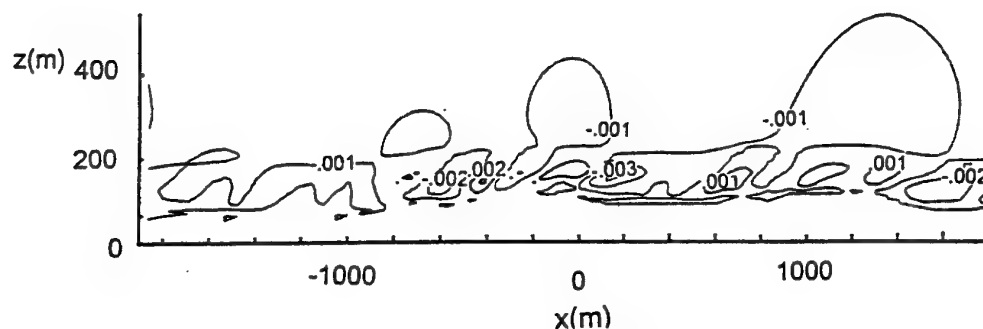


Fig.7 Turbulent shear stress distribution.

refinement is needed. For better definition of the boundary shape and roughness, the volume and area porosities need to be defined at much smaller scales than the grid scale. For general improvement of the model, the correlations between the geometric parameters and flow quantities will have to be validated with some bench-mark test cases in idealized situations.

#### REFERENCES

- Mason, P.J., 1994, "Large-eddy Simulation, A Critical Review of the Technique," *Quart. J. Roy. Meteorol. Soc.* Vol. 120, pp. 117-162.
- Hirt, C.W., 1992, "Volume-fraction Techniques: Powerful Tools for Wind Engineering," *Proc. First Int. Symp. on Comp. Wind Eng.*, pp. 333-344.
- Hino, M. Kanda, M. and Inagaki, S., 1992, "Numerical Experiment on the Momentum Transfer at the Air-Plant Interface," *Proc. Hydraulic Engineering, JSCE*, Vol. 36, pp. 689-692.
- Granville, P.S., 1985, "Mixing-length Formulations for Turbulent Boundary Layers over Arbitrary Rough Surfaces," *J. Ship Res.* Vol. 29, pp. 223-233.
- Noda, H. and Nakayama, A., 1996, "LES Simulation around Bluff Body with Splitter Plate," *Proc. 7th Symp. on Comp. Fluid Mech.*, pp. 259-260 (in Japanese.)
- Wilcox, D.C., 1993, *Turbulence Modeling for CFD*, DCW Industries, Inc., La Canada.
- Wilson, N.R. and Shaw, R. H., 1977, "A higher Order Closure Model for Canopy Flow," *J. Appl. Meteor.*, Vol. 16, 1197-1205.
- Yamada, T., 1982, "A Numerical Model Study of Turbulent Airflow in and above a forest canopy," *J. Meteor. Soc. Japan*, Vol. 60, pp. 439-454.
- Zang, H., Faghri, M. and White, F.M., 1996, "A new Low-Reynolds Number  $k$ - $\epsilon$  model for Turbulent Flow over Smooth and Rough Surfaces," *J. Fluids. Eng.*, Vol. 118, pp. 255-259.

# Experimental Investigation of Flow Near Friction Screens

P. Sullivan \* T. Oshinowo † D.C.S. Kuhn ‡ and Z. Huang §

University of Toronto  
Toronto, Ontario M5S 3G8  
Canada

May 2, 1997

## Abstract

This work investigates the flow near expanded metal screens oriented parallel to the flow, friction screens, with flow visualization and hotwire anemometry. A preliminary identification of a coherent structure has been made with flow visualization and hotwire measurements. A friction screen acts as a series of wake generators, and horseshoe-like vortices are shed. The vortices interact thus creating a low-speed layer between the screen and the undisturbed fluid.

## 1 Introduction

In pulverized coal-fired utility boilers the replacement of eroded convection tube surfaces and other metal surfaces results in expensive regular maintenance costs and lost production time. The fly ash generated in the combustion zone flows with the hot gases through the boiler then contacts and erodes tube and other metal surfaces. Due to the boiler geometry, flows with skewed velocity distributions develop and lead to high velocities and channeling in different sections of the boiler. This channeled flow contains a higher concentration of the fly ash leading to erosion problems in those areas. Local erosion protection and flue gas flow modification are the two basic approaches that have been taken to control fly ash erosion (Kratina and McMillan [3]).

Erosion shields are one of the most commonly used local erosion protection methods and act only to protect a surface without modifying the erosion conditions. Erosion shields are sacrificial surfaces and must be replaced regularly. Typically, screens are used to modify fluid flow and ash concentration, *i.e.*, modify the main erosion factors, by creating or eliminating large scale velocity or pressure non-uniformities and for the production or for the

reduction of turbulence. Expanded metal screens are of two basic types depending on their orientation to the flow and placement. Friction screens are expanded metal screens oriented parallel to the flow and are typically located between superheater tube banks and the rear water wall.

Extensive work has examined flow through simple uniform square screens in wind tunnels, *e.g.*, Batchelor [1], Naudascher and Farell [4] and reviewed recently by Idelchik [2], but this work has limited application to the complex screen types used in boilers. A numerical model of turbulent flow through expanded metal screens has been developed (Oshinowo, Kuhn and Charles [5, 6]) that compares well with corresponding experimental wind tunnel results with some weakness in predicting secondary flows at the wall. The model proved to be effective at predicting general flow features modified by the screens. No experimental work on flow around friction screens has been presented in the literature.

\*Mechanical and Industrial Engineering

†Chemical Engineering and Applied Chemistry

‡Chemical Engineering and Applied Chemistry

§Chemical Engineering and Applied Chemistry



## 2 Experimental Methods

### 2.1 Flow Visualization

Initial flow visualization experiments have been performed in a horizontal glass-walled water flume 235mm wide. The depth of flow was controlled to keep the aspect ratio of flow well above unity in all the runs. Reynolds numbers ranging from 1360 through 5970 (based on hydraulic radius) were investigated. Honeycomb flow straighteners were located at the entrance of the flume. Dramex carbon steel expanded screens of various sizes and solidity were used in the study. Detailed dimensions of the screens for the flow visualization and hotwire measurements are shown in table 1, refer to figure 1 for the notation used.

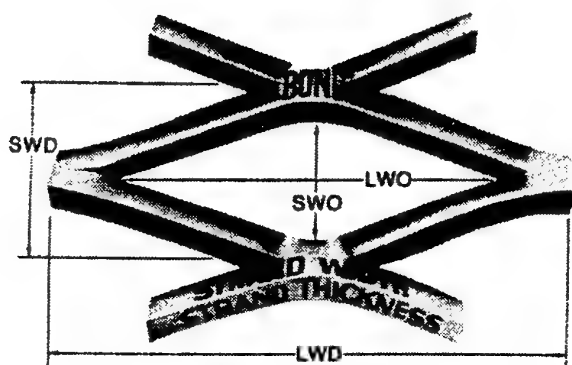
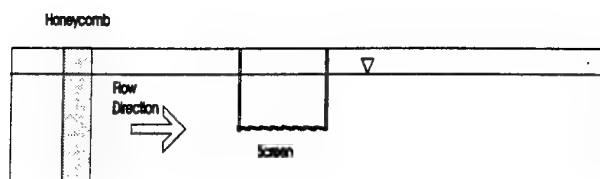


Figure 1: Schematic of a screen cell, from Dramex catalog.

A



B



Figure 2: (A) Side view of flow visualization experiment, (B) Close-up view of dye injection

The screen was positioned at 100mm from the bottom of the flume (well outside the boundary

layer). The orientation of the screen was such that the direction of its expansion was the same as the flow.

The dye (both food coloring and fluorescein) was injected at a junction of two individual screen cells (where the flow was stagnant, figure 2B) and at a number of different locations on the screen (downstream direction). The images were videotaped with a CCD camera for later analysis.

### 2.2 Hotwire Measurements

The experiments for quantitative investigation of flow around the expanded screen were carried out in a low turbulence ( $\frac{u'}{U} \ll 0.05\%$ ), recirculating wind tunnel. The tunnel has a test section 4.5m long (streamwise x-axis) and a cross-section of 0.91m (spanwise y-axis) by 1.52m (vertical z-axis) with a maximum velocity of 15m/s. The screen was mounted horizontally in the centre plane of the tunnel with its expansion in the same direction as that of the flow. The origin of the Cartesian coordinate system is at the leading edge of the first cell (of which there are thirteen on the screen) through which the tunnel centreline x-y plane passes. The x-z plane at  $y=0$ , regarded as the screen "surface", passes through the loci of the bond crests (shown in the side view of the screen in Figure 2A).

Velocity measurements were obtained with five DANTEC 55 P11 normal hot-wire probes in conjunction with a DANTEC 56C01 constant temperature anemometer system. The anemometer signals were amplified, low-passed filtered and digitized with a 12-bit A/D converter at a sampling rate of 1 kHz per channel. The hotwire calibrations were performed *in situ*.

## 3 Results

### 3.1 Flow Visualization

The flow visualization was performed at several Reynolds numbers (based on hydraulic radius of the channel). Information for all flow visualization experiments are shown in table 2.

The preliminary results show identifiable structures within the flowfield. As a vortex is shed from a bond crest, it is convected downstream where concurrent vortices are generated at crests downstream (See figure 3). These vortices interact

	Screen 1 (Flow Visualization)	Screen 2 (Wind Tunnel)
SWD	25.4 mm	23.5 mm
LWD	57.5 mm	51.0 mm
SWO	20.5 mm	17.8 mm
LWO	41.2 mm	38.5 mm
Strand Width	4.3 mm	3.75 mm
Strand Thickness	3.05 mm	2.90 mm
Strand Hydraulic Diameter	3.57 mm	3.27 mm
Solidity	25 %	32 %
Expansion Angle	27°	27°
Length x Width	180 mm x 200 mm	310 mm x 190 mm

Table 1: Details of the screen used for the experiment

Run	Aspect Ratio	Hydraulic Radius (mm)	Flowrate ( $\frac{m^3}{s}$ )	$Re_H$
1	1.430	68.5	12.15	5,970
2	1.156	74.5	5.03	2,170
3	1.253	72.2	11.05	5,020
4	1.147	74.7	10.13	4,380
5	1.287	71.5	2.95	1,360
6	1.389	74.9	10.86	1,460

Table 2: Details of the flow visualization

as they are convected downstream and is an important mechanism of growth of the layer next to the wall is the engulfment of downstream vortices (vortex B, figure 3) by vortices upstream (vortex A, figure 3). The flow visualization indicates that there is little or no interaction across the screen, thus the screen acts to isolate the two halves of the flow.

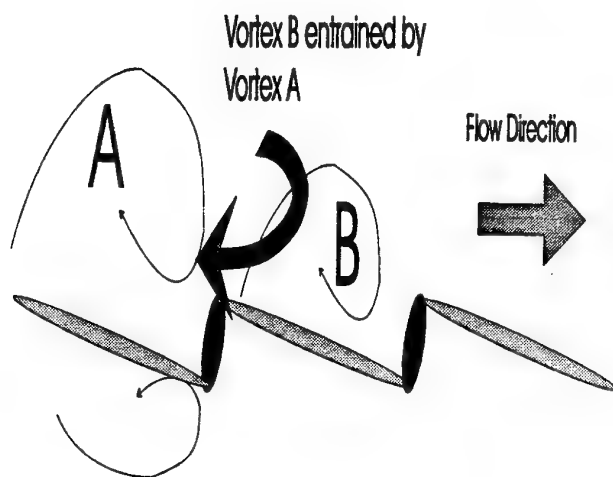


Figure 3: Interaction of vortices with friction screens at central plane.

The screen elements act to redirect the flow upward, and thus a low speed region is created at the friction screen. This is postulated to be the mechanism responsible for erosion minimization next to the wall of the boiler, and thus the screens do not act as sacrificial erosion surfaces but as flow redirection devices.

### 3.2 Hotwire Measurements

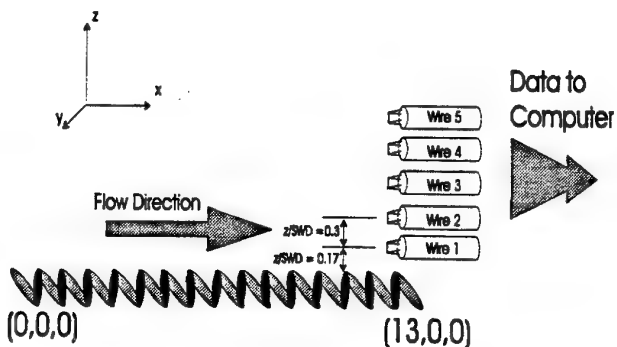


Figure 4: Conventions used in the hotwire measurements, note positions are normalized by SWD.

The measurements have been completed with rakes of 5 normal hotwires positioned vertically

(z-direction). Figure 4 defines the conventions used in this study.

### 3.2.1 Velocity Profiles

Contours of mean velocity and turbulence velocities are presented in figures 5 and 6 respectively. The mean velocity contours show some similarity to that of a flat plate; the turbulence velocities show that there is a strong discontinuity at the plate edge, where the vortical structures from either side of the plate interact. The highest turbulence intensities occur over the last cell of the screen.

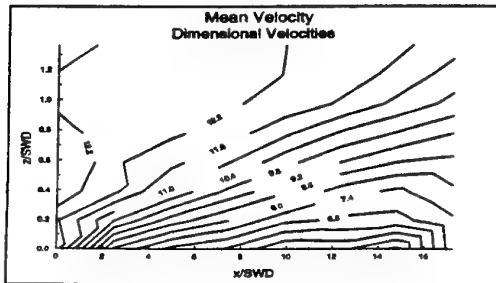


Figure 5: Mean velocity contours for the screen.

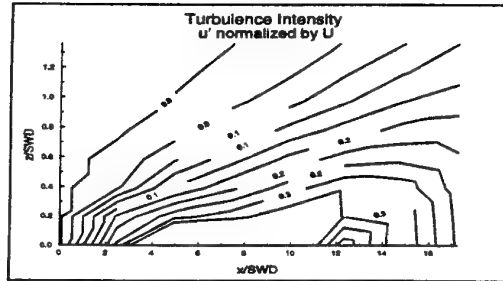


Figure 6: Turbulence velocity contours for the screen. Velocities normalized by local mean.

### 3.2.2 Power Spectral Densities

Figure 7 shows the Power Spectral Densities (PSDs) calculated for the leading edge of a cell located just before the trailing edge of the screen. The results show a prominent bulge at  $\approx 100\text{Hz}$ . Measurements made at a location upstream of the

leading edge of the screen do not show this frequency bulge indicating this is an effect of the screen. The location of the frequency peaks for wire positions 4-5, correspond to the approximate locations of the shear layer. The frequency peak does not appear at the measurement positions of wires 1-3.

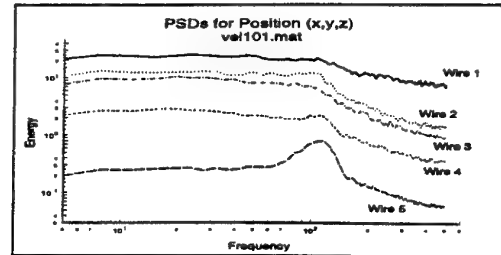


Figure 7: Power Spectral Densities at  $(\frac{x}{SWD}, \frac{y}{SWD}, \frac{z}{SWD}) = (12, 0, 0.13)$ , leading edge of last screen cell.

Figure 8 shows the PSDs at a location past the trailing edge of the screen (note that the screen ends at  $\frac{x}{SWD} = 13$ . The peaks in the PSDs at 100 Hz are noted at all measurement positions (wires 1-5). The results suggest that the influence of the outer region structure has propagated through the entire field. This confirms the results seen in the flow visualization. As noted in the flow visualization experiments, the screen acts to isolate the two halves of the flow (upper and lower regions) and allows little or no interaction across the porous body.

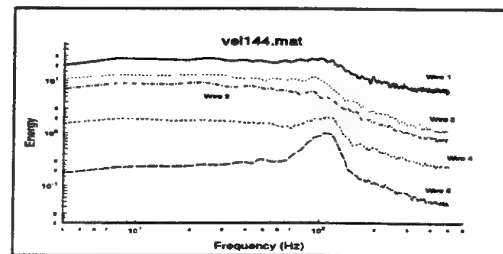


Figure 8: Power Spectral Densities at  $(\frac{x}{SWD}, \frac{y}{SWD}, \frac{z}{SWD}) = (14, 0, 0.4)$ , in the wake region.

The events captured by the flow visualization and the hotwire measurements are too large to pass through the screen cells. From the flow visualization, it is noted that the scale of the screen generated events are of the scale  $\frac{x}{SWD} = 2-3$ .

## 4 Conclusions

This work is continuing and the initial results are very encouraging. The friction screens act to isolate the flow from one side of the screen to the other. A coherent structure within the flow has been identified with flow visualization and a mechanism for the minimization of erosion proposed. The hotwire results confirm the existence of this strong frequency component; further work is being done with simultaneously sampled hotwires.

## 5 Acknowledgments

The authors gratefully acknowledge the support of the Natural Sciences and Engineering Research Council (NSERC) and Asea Brown Boveri (ABB) of this work.

## References

- [1] G. K. Batchelor. *The Theory of Homogeneous Turbulence*. Cambridge University Press, 1959.
- [2] I. Idelchik. *Fluid Dynamics of Industrial Equipment Flow Distribution Design Methods*. Hemisphere Publishing, 1991.
- [3] P. Kratina and J. McMillan. Flyash erosion in utility boilers-prediction and protection. Presented at Canadian Electrical Association Conference, Regina, Saskatchewan.
- [4] E. Naudascher and C. Farell. Unified analysis of grid turbulence. *Journal of the Engineering Mechanics Division*, EM 2:121-141, 1970.
- [5] L. Oshinowo, D.C.S. Kuhn, and M.E. Charles. A numerical and experimental study of turbulence downstream of an expanded metal screen, 1997. Submitted for publication in the *Journal of Fluids Engineering*.
- [6] L. Oshinowo, D.C.S. Kuhn, and M.E. Charles. Turbulence decay behind expanded metal screens, 1997. Submitted for publication in the *Journal of Fluids Engineering*.

## **SESSION 20 - STRATIFIED FLOWS**

# The effects of stable density stratification on the dynamics of turbulent channel flow

Oaki Iida<sup>1</sup>, Nobuhide Kasagi<sup>2</sup> and Yasutaka Nagano<sup>1</sup>

<sup>1</sup> Department of Mechanical Engineering, Nagoya Institute of Technology  
Gokiso-cho, Showa-ku, Nagoya 466, JAPAN

<sup>2</sup> Department of Mechanical Engineering, The University of Tokyo  
Bunkyo-ku, hongo, Tokyo 113, JAPAN

## ABSTRACT

Direct numerical simulations are performed for a fully-developed horizontal turbulent channel flow under stable density stratification. Internal gravity waves are found to be built up in the core region, where turbulent heat flux deteriorates drastically and a so-called thermocline results. The streamwise vortices are generated by Kelvin-Helmholtz instability and concentrated in the elongated regions between the internal gravity waves and the solid wall. Through the pressure diffusion term, the internal gravity waves interact with shear-induced turbulence. It is also found that both the skin friction and Nusselt number decrease greatly without suppression of near-wall turbulence. These decreases should be due to the suppression of energy containing eddies in the logarithmic region. When stratification becomes larger, the flow on one side of the walls becomes laminar although it is still turbulent on the other side. Relaminarization of stably stratified boundary layer is surprisingly similar to that observed in a minimal channel flow.

## 1 INTRODUCTION

In many important engineering and geophysical flows, turbulent heat transport occurs in the presence of thermal (or density) stratification. Relevant direct numerical simulations (DNS) are recently carried out for stably stratified homogeneous turbulence (Gerz et al., 1989; Holt et al., 1992). However, DNS has been rarely performed to study wall turbulent shear flows under density stratification.

The balance between mechanical generation of turbulence and damping by stability varies from case to case, creating stable boundary layers that range from being well mixed to non turbulent. The observations of the ocean and the atmosphere show that strong stable stratification

in a turbulent boundary layer induces a steeper mean velocity gradient which generates the intermittent turbulent regions due to Kelvin-Helmholtz instability (Turner, 1973; Tritton, 1988). On the other hand, in the region where the mean shear rate is small and the mean temperature gradient is large, turbulence is significantly suppressed and internal gravity waves are generated. There should be a significant interaction between the turbulent regions and the internal gravity waves in a turbulent boundary layer. There is a study (Stull, 1988) which guesses that a pressure correlation term not only acts to redistribute turbulent kinetic energy, but it can also drain energy out of the boundary layer through internal gravity wave. In short, through the pressure correlation term, they may interact with each other. However, static pressure fluctuations are exceedingly difficult to measure both in the atmosphere and laboratory experiment. Thus, accurate numerical simulations are required.

When density stratification becomes very large, the flow field might become relaminarized. The mechanism of laminarization under stable stratification is also an unknown problem. Reverse transition from turbulent to laminar flow has been studied by many investigators, since it not only has a very complex nature but also gives a fundamental insight into how to control turbulence and to reduce the drag (Narashimha et al., 1979). However, the general principles governing the relaminarization are not established, which may be useful for turbulence control.

Recently, studies using DNS have shown another kinds of relaminarization which can hardly be realized by the experiments. Choi et al. (1994) shows that significant drag reduction is achieved when the surface boundary condition is modified to suppress sweep events. Their study is very similar to a flow accompanied by drag reduction with dilute polymer addition (Pereira et al., 1994). In all

of these cases, a departure from the logarithmic law and an associated increase of the viscous sublayer are definitely observed. It will give us a fruitful conclusion to compare relaminarization of stable stratified boundary layer with typical drag-reducing flows.

Under stable density stratification, the analogy between heat and momentum transfer should not hold any longer. There are many studies which indicate that turbulent heat transfer is more deteriorated than momentum transfer and thus, turbulent Prandtl number does increase under stable density stratification. Almost all of these results are at sufficiently large Richardson numbers to suppress turbulence and generate internal gravity waves. In the dynamically unstable region due to Kelvin-Helmholtz instability, the effect of stable stratification on turbulent heat and momentum transfer should be different.

In this study, direct numerical simulations are performed to study turbulent channel flow under stable density stratification. The occurrence of internal gravity waves is ascertained in the core region. The mechanisms of interaction between gravity waves and turbulence are investigated in detail. Especially, the budget of Reynolds normal stress has been calculated to identify the pressure effect on their interaction. The features of turbulent heat and momentum transfer are also explained in detail. For example, the drag reduction mechanism due to stable density stratification is discussed in reference to that of typical drag-reducing flows. The effect of density stratification on the turbulent Prandtl number, on the other hand, is studied by systematically comparing the results of both stable and unstable stratification.

## Nomenclature

$C_f$	friction coefficient, $2\tau_w/\rho U_b^2$
$Gr$	Grashof number, $g\beta(T_t - T_b)(2\delta)^3/\nu^2$
$g$	gravitational acceleration
$Nu$	Nusselt number, $2\delta q_w/\lambda\Delta T$
$Pr, Pr_t$	molecular and turbulent Prandtl numbers
$q_w$	total heat flux at the wall
$Re_b$	bulk mean Reynolds number, $2U_b\delta/\nu$
$Re_\tau$	Reynolds number, $u_\tau\delta/\nu$
$Ri_g$	gradient Richardson number
$Ri_c$	critical Richardson number
$Ri_t$	terminal Richardson number
$T$	temperature
$T_b, T_t$	temperatures at bottom and top walls
$U$	mean velocity in $x$ -direction
$U_b$	bulk mean velocity, $\int_{-\delta}^{\delta} U dy/2\delta$
$u, v, w$	fluctuating velocity components in $x$ -, $y$ - and $z$ -directions
$u_\tau$	friction velocity, $\sqrt{\tau_w/\rho}$
$x, y, z$	streamwise, wall-normal and spanwise directions
$\beta$	volumetric expansion coefficient
$\Delta T$	temperature difference, $T_t - T_b$
$\delta$	channel half width
$\Theta$	mean temperature difference, $\bar{T} - T_b$
$\theta$	fluctuating component of $\Theta$
$\theta_\tau$	friction temperature
$\nu$	kinematic viscosity
$\rho$	density
$\tau_w$	wall shear stress

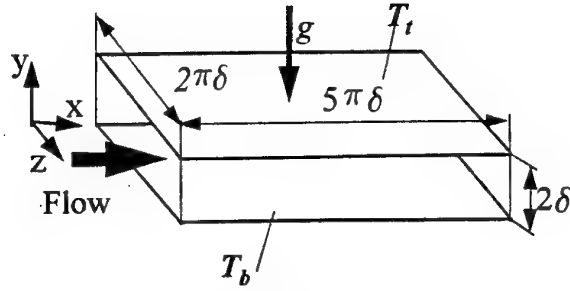


Figure 1: Coordinate system and flow conditions.

$( )_0$	value at $Gr = 0$ and $Pr = 0.71$
$( )$	ensemble average
$( )^+$	non-dimensionalized by wall variables, $u_\tau$ and $\nu$

## 2 COMPUTATIONAL CONDITIONS OF DNS

The flow geometry and the coordinate system are shown in Fig. 1. The flow field is driven by a constant mean pressure gradient in the  $x$ -direction. The flow and thermal fields are assumed to be fully developed, so that periodic boundary conditions are imposed in the  $x$ - and  $z$ -directions, respectively. The no-slip boundary condition is imposed on the velocity components on the two walls, which are heated at different, but uniform temperatures. As a result, there is a constant positive temperature difference  $\Delta T \equiv (T_b - T_t)$  between the bottom and top walls. The gravitational acceleration  $g$  is in the  $y$ -direction to cause a stable buoyancy effect.

The governing equations are the standard set of hydrodynamic equations with the Boussinesq approximation. The Reynolds number (based on the friction velocity  $u_\tau$  and channel half width  $\delta$ ) and Prandtl number are set at  $Re_\tau = 150$  and  $Pr = 0.71$  respectively. The resultant bulk Reynolds number  $Re_b (= 2U_b\delta/\nu)$  is 4580 in the case without buoyancy (see Kasagi et al. 1992). The Grashof number  $Gr (= g\beta\Delta T(2\delta)^3/\nu^2)$  is varied from 0 to  $2 \times 10^7$ .

Referring to Kim et al. (1987), a fourth-order partial differential equation for  $v$ , a second-order partial differential equation for the wall-normal component of vorticity, and the continuity equation were solved to get the instantaneous flow field. A spectral method is used to obtain the solutions with Fourier series in the  $x$ - and  $z$ -directions and a Chebyshev polynomial expansion in the  $y$ -direction.

Almost all the calculations are carried out with  $64 \times 49 \times 64$  ( $x$ -,  $y$ - and  $z$ -directions) grid system. In order to assess the numerical accuracy, finer  $128 \times 128$  Fourier modes and Chebyshev polynomials up to the 96th order in wave-number space are used for the typical case of  $Gr = 4.4 \times 10^6$ . In all cases, the spanwise period of the computational box is  $2\pi\delta$ , while the streamwise period is  $5\pi\delta$ . The results of coarse-grid calculation are in reasonable agreement with those of fine-grid one. Thus the relative comparison of present results should be valid and deserves the in-depth discussion.

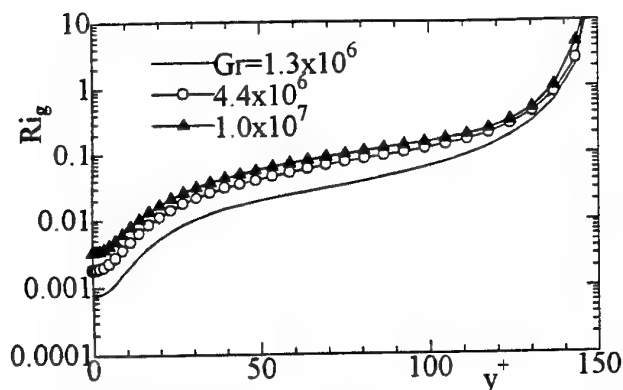


Figure 2: Distribution of Gradient Richardson number

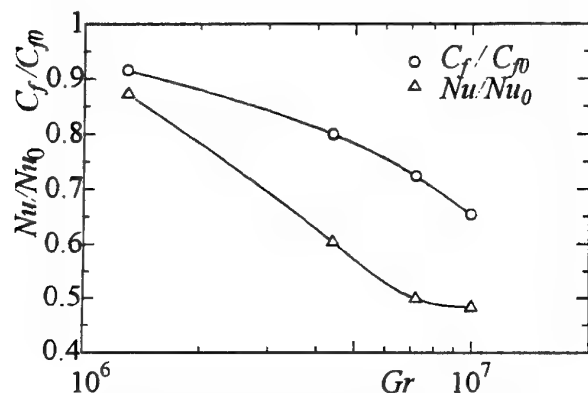


Figure 3: Distributions of  $C_f$  and  $Nu$

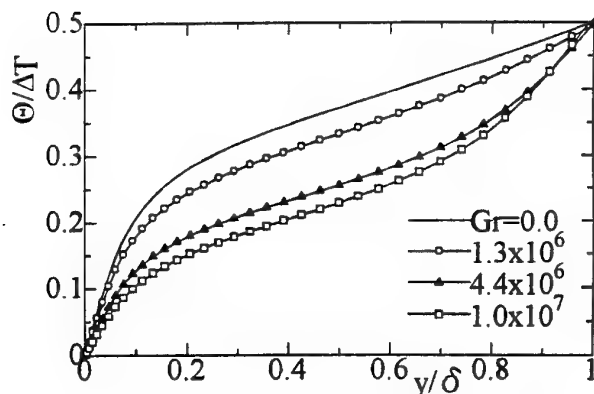


Figure 4: Mean temperature profiles  $\Theta/\Delta T$

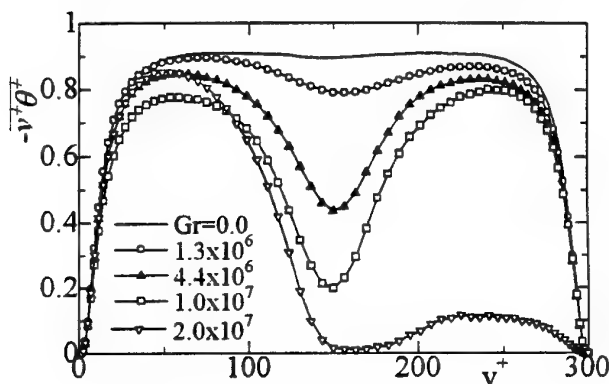


Figure 5: Distributions of turbulent heat flux  $\overline{v\theta}$

### 3 RESULTS AND DISCUSSION

The distribution of the gradient Richardson number is shown in Fig. 2. The gradient Richardson number  $Ri_g$  becomes the criterion for the status of a flow. Under stable density stratification, flows are statically stable, but there is the small range of  $0 < Ri_g < Ri_c$  where flows are dynamically unstable and nonturbulent flows may become turbulent due to Kelvin-Helmholtz instability. The experimental results show that  $Ri_c$  is almost equal to 0.25 (Stull, 1988). When  $Ri_g$  becomes larger than  $Ri_c$ , a turbulent flow should ultimately become laminar. In almost all cases of our study,  $Ri_g$  is below  $Ri_c$  in the region  $y^+ < 120$ , while it exceeds the  $Ri_c \approx 1$  in the central region of a channel.

Figure 3 shows the changes in the friction coefficient and the Nusselt number normalized by the respective values for  $Gr = 0$ , i.e.,  $C_f/C_{f0}$  and  $Nu/Nu_0$ , with the Grashof number. Both the friction coefficient and Nusselt number decrease markedly with increasing Grashof numbers, thus indicating that the flow is going to be laminar. However, the drag-reduction mechanism of stable density stratification is completely different from that observed in conventional drag reducing flows, as will be discussed later in detail.

Figure 4 shows the mean temperature profiles, and the corresponding distributions of turbulent heat flux are presented in Fig. 5. The mean temperature profile is non-dimensionalized by the temperature difference between two walls. As the Grashof number increases, the mean tem-

perature gradient becomes steeper and a so-called thermocline is generated in the channel central region where the turbulent heat flux markedly decreases. At  $Gr = 2.0 \times 10^7$ , turbulent heat flux is seen to become almost zero on one side of the wall. However, in the region  $y^+ < 120$  where  $Ri_g$  is still below  $Ri_c$ , there exists the well-mixed layer and the turbulent heat flux takes a large value.

Figures 6 (a) and (b) show the coherency and the phase between the wall-normal velocity and the temperature fluctuation at  $Gr = 0$  and  $1.0 \times 10^7$ . Under stable density stratification, the coherency takes a large value at wave numbers where the phase angle becomes  $\pi/2$ . In the case without buoyancy, the phase angle is nearly zero over all wave numbers. The definite phase angle of  $\pi/2$  at the intensive coherency regions indicates that internal gravity waves become the dominant flow structure. Thus, the remarkable decrease of the turbulent heat flux and the associated increase of the mean temperature gradient should be due to the occurrence of internal gravity waves and the suppression of turbulence.

Figures 7(a) and (b) show the iso-surfaces of the non-dimensional temperature  $(T - T_b)/\Delta T = 0.5$  under neutral and stable density stratification, respectively. There is a significant qualitative difference observed between them. In the case without buoyancy, the iso-surface of the temperature is violently torn up, indicating that the temperature should be effectively well mixed by turbulent motions. On the other hand, under stable stratification, the undulations of the iso-surfaces become smaller, indicating



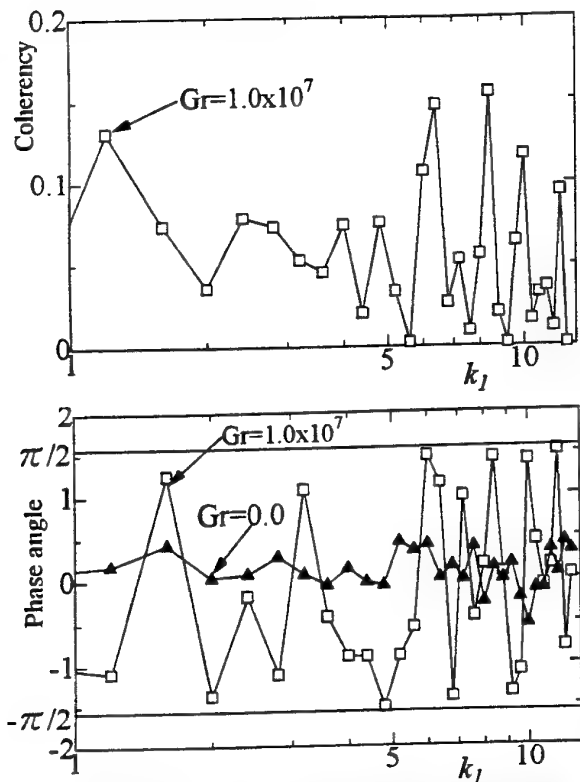


Figure 6: Coherency and phase angle between  $v^+$  and  $\theta^+$  at the center of a channel.

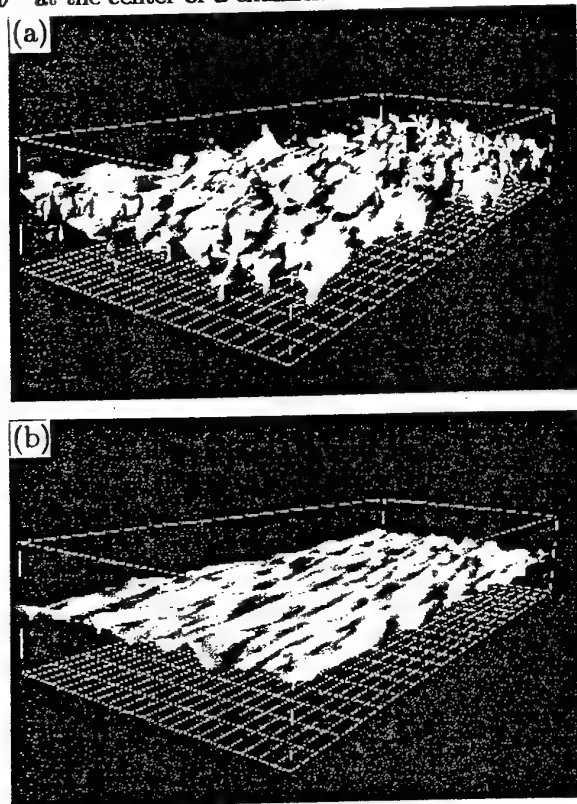


Figure 7: Iso-surfaces of non-dimensional temperature  $(T - T_b)/\Delta T = 0.5$ ; (a)  $Gr = 0.0$ , (b)  $Gr = 1.0 \times 10^7$

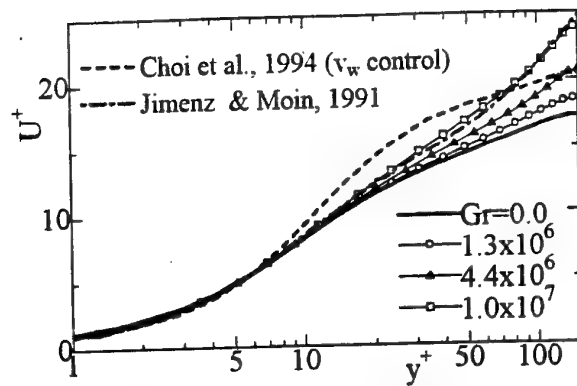


Figure 8: Mean velocity profiles  $U^+$

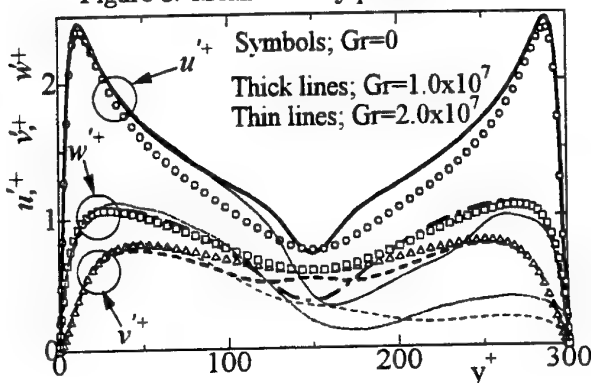


Figure 9: Rms velocity fluctuations at  $Gr = 0$ ,  $1.0 \times 10^7$  and  $2.0 \times 10^7$ .

that mixing of the temperature due to turbulence is significantly suppressed

The logarithmic plot of the mean velocity  $U^+$  is shown in Fig. 8. The result of interactive wall turbulence control by Choi et al. (1994) is also included for comparison. The mean velocity tends to increase in the region  $y^+ > 10$ . Interestingly, the logarithmic region of mean velocity profile disappears and the buffer region increases. The increased buffer region is also assured by the turbulent Prandtl number as discussed later. In the viscous sublayer  $y^+ < 10$ ,  $U^+$  coincides well with that of the neutral flow with  $Gr = 0$  in all cases. This is quite different from the result of Choi et al., where the viscous sublayer does increase with suppressing the bursting phenomena and turbulence is attenuated in the near-wall region although the turbulent structure in the logarithmic region is not so much changed.

The rms velocity fluctuations are shown in Fig. 9. In the near-wall region  $y^+ < 50$  where the gradient Richardson number is below 0.1, the distributions of rms velocity fluctuations are not significantly changed and near-wall turbulence should be maintained. In the logarithmic region, the decrease of  $v_{rms}^+$  is definitely observed, while  $u_{rms}^+$  increases due to the steeper mean velocity gradient. In the central region, as the Grashof number increases, both  $u_{rms}^+$  and  $w_{rms}^+$  decrease markedly. Also one may note that  $w_{rms}^+$  takes a minimum value smaller than that of the neutral flow at the center of a channel, while  $v_{rms}^+$  takes a maximum value, which cannot be observed in the neu-

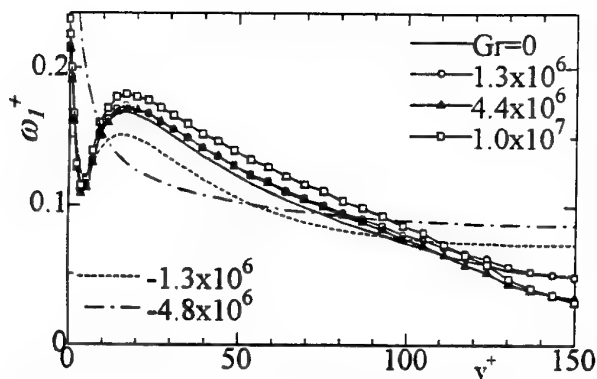


Figure 10: Distributions of rms vorticity fluctuations.

tral flow and must be associated with the occurrence of internal gravity waves.

When the Grashof number further increases to  $2.0 \times 10^7$ , there occurs a stable state in which the turbulent flow exists only on one side of the walls, although the flow sometimes becomes turbulent along both walls. These results are similar to those seen in a minimal channel flow (Jimenez and Moin, 1991), i.e., the logarithmic region of the mean velocity profile disappeared when the flow became one-sided turbulent. The disappearance of the logarithmic region is also observed in the present result (see Fig. 8). Thus, stable density stratification has apparently the same effect as narrowing the computational box.

The rms values of the streamwise component of vorticity are shown in Fig. 10. The result of unstable density stratification (Iida and Kasagi, 1997) is also included for comparison. In the region  $y^+ < 120$ , the streamwise vorticity increases, indicating that the small-scale turbulence is augmented by Kelvin-Helmholtz instability. Under unstable density stratification, the rms intensity of the streamwise vorticity decreases in the logarithmic region although all components of velocity fluctuations increase significantly there (not shown here). Thus, unstable stratification enhances the large-scale vortices with small vorticity, while under stable density stratification the larger scale eddies are suppressed, leaving small-scale eddies with large vorticity.

Figure 11 shows the budget of  $\overline{v'^2}$  for  $Gr = 4.4 \times 10^6$ . It is noted that the pressure-strain term increases over most of the channel section and the intercomponent energy transfer should be activated. The normal stress  $\overline{v'^2}$  generated by the pressure-strain term is dissipated by the buoyancy dissipation term. Thus, the turbulent structure associated with the pressure-strain term should contribute to generating the potential energy. The distributions of the diffusion terms, i.e., the pressure and turbulent diffusion terms, significantly change in the channel central region. It can be seen that through the pressure-diffusion term, kinetic energy is transported from the near-wall region to the channel central region where internal gravity waves are dominant turbulent structures. The turbulent diffusion term decreases and becomes nearly zero in the central region of a channel.

Work in linear gravity wave theory shows that  $\overline{p^+ v^+}$  is equal to the upward flux of wave energy for a vertically propagating internal gravity wave in a statically sta-

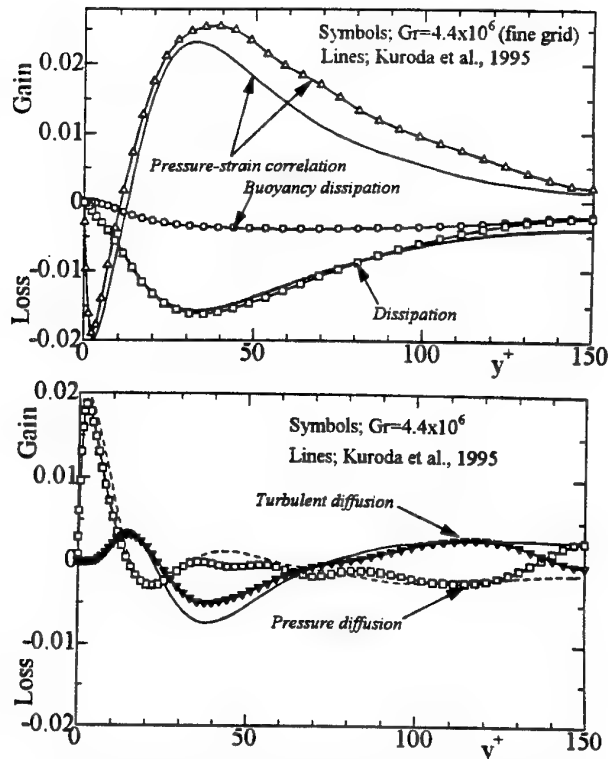


Figure 11: Budget of  $\overline{v'^2}$  at  $Gr = 0, 4.4 \times 10^6$ .

ble environment (Stull, 1988). This theory and our results suggest that turbulence energy in the wall region of stable boundary layers can be transferred to activate internal gravity waves through the pressure diffusion term.

Figure 12 shows the typical example of the velocity vectors in the  $x$ - $y$  plane in the case of  $Gr = 1.0 \times 10^7$ . In the channel central region, wave-like motions are clearly observed, as suggested by the marked decrease of  $\overline{v^+ \theta^+}$ . Moreover it should be noted that the elongated low-pressure regions are generated between the wall and the crest of internal waves. These low pressure regions correspond to the streamwise vortices which reach down to the wall and enter into the crest of the waves (not shown here). Figure 12 clearly shows the interaction between gravity

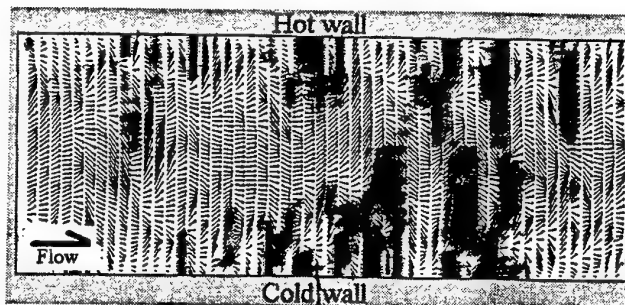


Figure 12: Instantaneous distributions of velocity vectors ( $U + u, v \times 12$ ) and pressure fluctuations in  $x$ - $y$  plane. Black to white,  $p^+ = -4$  to  $0$ ,  $Gr = 1.0 \times 10^7$

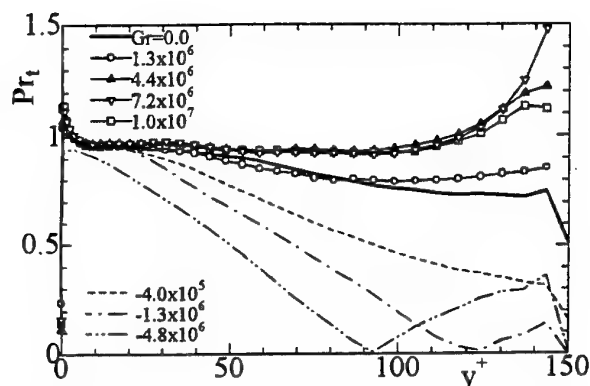


Figure 13: Distributions of turbulent Prandtl number  $Pr_t$

wave and near-wall turbulence through the pressure.

Finally, the analogy between heat and momentum transfer is discussed. Figure 13 shows the distribution of the turbulent Prandtl number. For comparison, the cases of unstable stratification are also included. Under unstable density stratification,  $Pr_t$  significantly decreases, indicating that the turbulent heat transfer is more enhanced in comparison to the momentum transfer. When stable density stratification is imposed, the turbulent heat transfer is deteriorated greatly in the channel central region, which should be due to internal gravity waves. However, in the region  $y^+ < 120$ , the decrease of  $Pr_t$  is not so remarkable as in the channel central region and  $Pr_t$  takes the same value as that in the buffer region. Profiles of the mean velocity and the turbulent Prandtl number indicate that in a stably stratified boundary layer, the buffer region does increase and the logarithmic region decreases. Considering the results of unstable stratification, it could be said that larger vortices in the logarithmic region tend to transport heat more effectively than momentum, while small-scale eddies observed in a stable boundary layer contribute equally to both heat and momentum transfer.

#### 4 CONCLUSIONS

Direct numerical simulations are performed for a fully-developed horizontal turbulent channel flow under stable density stratification. The following conclusions are obtained.

(1) In the core region where the local gradient Richardson number exceeds the critical Richardson number, turbulence is significantly suppressed and internal gravity waves become dominant flow structures. Thus, the turbulent heat flux decreases markedly and the steep mean temperature gradient (i.e., thermocline) results. In the region  $y^+ < 120$  where the Richardson number is still below the critical value, small-scale turbulence associated with the streamwise vorticity is enhanced. Instantaneous turbulent structure shows that the streamwise vortices are concentrated in the elongated regions between the internal gravity waves and the solid wall. From the result of the budget equation for  $\overline{v'^2}$ , it is found that through the pressure diffusion term, the internal gravity wave should be interacted with turbulence. When stratification becomes larger, the flow on one side of the walls becomes laminar although it

is still turbulent on the other side.

(2) Under stable density stratification, the buffer region increases and the logarithmic region disappears, which results in the significant decreases of both the Nusselt number and skin friction coefficient without suppression of near-wall turbulence. Thus, the drag reduction mechanism due to stable density stratification is completely different from that observed in the typical drag-reducing flows such as dilute polymer addition. It is also found that turbulent heat transfer is significantly deteriorated and the turbulent Prandtl number increases. From the results of both stable and unstable stratification, it can be said that as the length scale of turbulence becomes larger, heat is transported more effectively than momentum, while the small-scale eddies observed in stable boundary layers contribute equally to both heat and momentum transfer.

#### References

- [1] Choi, H., Moin, P. and Kim, J., "Active turbulence control for drag reduction in wall-bounded flows," *J. Fluid Mech.*, **262**, pp. 75-110, (1994).
- [2] Gerz, T., Schumann, U., and Elghobashi, S. E., "Direct numerical simulation of stratified homogeneous turbulent shear flows," *J. Fluid Mech.*, **200**, pp. 563-594, (1989).
- [3] Holt, S. E., Koseff, J. R., and Ferziger, J. H., "A numerical study of the evolution and structure of homogeneous stably stratified turbulence," *J. Fluid Mech.*, **237**, pp. 499-539, (1992).
- [4] Iida, O. and Kasagi, N., "Direct numerical simulation of unstably stratified turbulent channel flow," *ASME J. Heat Trans.*, **119**, pp. 53-61, (1997).
- [5] Jimenez, J. and Moin, P., "The minimal flow unit in near-wall turbulence," *J. Fluid Mech.*, **213**, pp. 213-241, (1991).
- [6] Kim, J., Moin, P., and Moser, R., "Turbulence statistics in fully developed channel flow at low Reynolds number," *J. Fluid Mech.*, **177**, pp. 133-166, (1987).
- [7] Kuroda, A., and Kasagi, N., and Hirata, M., *Turbulent Shear Flows 9*, F. Durst, N. Kasagi, B. E. Launder, F. W. Schmit, K. Suzuki and J. H. Whitelaw, Eds., Springer-Verlag, Berlin, pp. 241-257, (1995).
- [8] Narashimha, R. and Sreenivasan, K. R., "Relaminarization of fluid flows," *Adv. Appl. Mech.*, **19**, pp. 221-309, (1979).
- [9] Pereira, A. Su, and Pinho, F. T., 1994, "Turbulent pipe flow characteristics of low molecular weight polymer solutions," *J. Non-Newtonian Fluid Mech.*, **55**, pp. 321-344, (1994).
- [10] Stull, R. B., *An Introduction to Boundary Layer Meteorology*, Kluwer Academic Publishers, (1988).
- [11] Tritton, D. J., *Physical Fluid Dynamics*, The Oxford University Press, (1988).
- [12] Turner, J. S., *Buoyancy Effects in Fluids*, The Cambridge Univ. Press, (1973).

# HEAT TRANSFER IN A STABLY STRATIFIED SHEAR FLOW

Takao Kanzaki and Yoichi Ichikawa

Department of Atmospheric Science

Central Research Institute of Electric Power Industry

Komae, Tokyo, 201

Japan

## ABSTRACT

The effects of mean shear on the countergradient transfer of heat and momentum in stably stratified grid-generated turbulence in a wind tunnel are experimentally investigated. Measurements are conducted in three kinds of sheared air flows with stable stratification. Streamwise and vertical velocities and temperature are simultaneously measured. Turbulent quantities between the velocity fluctuations and temperature fluctuations are evaluated. The results show that mean shear diminishes the countergradient heat transfer. The cospectral data suggest that small-scale motions contribute to countergradient heat transfer in stratified air flows with strong shear.

## INTRODUCTION

Thermally stratified shear flows occur in the atmospheric boundary layer and the ocean. The conditions of stratification and shear affect scalar transfers of heat and air pollutants. In such a flow, scalar transfer is controlled by buoyancy forces and turbulent motion which is generated by shear. It is well known that countergradient scalar transfer occurs in a turbulent flow with strongly stable stratification. In the last two decades, countergradient scalar and momentum transfer have been extensively studied experimentally and numerically, after Komori et al. (1983) identified these phenomena in a thermally stratified open-channel water flow. Therefore, the fundamental mechanism of countergradient transfer has been largely elucidated. In wind tunnel experiments, Lienhard & Van Atta (1990), Yoon & Warhaft (1991) and Kanzaki & Ichikawa (1996) have shown that the countergradient heat transfer occurs by large-scale motion in strongly stratified air flows without shear. On the other hand, Komori & Nagata (1996) recently investigated the effects of changes in Prandtl and Schmidt numbers on countergradient transfer in water tank experiments. They concluded that countergradient transfer was initiated by

small-scale motions and then observed it at large scales in stratified water flows with high Prandtl number. They also suggested that countergradient transfer might occur at small scale even in stratified air flows where small scale turbulent motion would be stronger. Gerz & Schumann (1996) explained the countergradient transfer mechanism at small scale based on their conceptual model. They suggested that the countergradient fluxes always occur at small scale, independent of the Prandtl number. However, it remains to be determined experimentally and numerically whether small-scale countergradient heat transfer could occur in stratified air flows at a low Prandtl number. It is of great interest to investigate countergradient heat and momentum transfer in stratified air flows with shear.

The purpose of the present work is to investigate experimentally the effect of mean shear on countergradient heat transfer mechanism and the contribution of large- and small-scale motion to countergradient heat transfer in sheared air flow with stable stratification.

## EXPERIMENTS

The experiments were conducted in a new wind tunnel. Figure 1 shows the experimental setup and the measurement system. The test section of the tunnel was 7 m long and  $0.5\text{m} \times 0.5\text{m}$  in cross section. Turbulence-generating grids were installed at the entrance of the tunnel and were single-biplanar construction. The mesh size ( $M$ ) was 0.05 m and the diameter of the rods ( $d$ ) was 0.01 m. An adjustable heater and gate section were set before the turbulence grids. They were vertically separated into ten sections and each section was individually controlled to produce the initial vertical temperature step and velocity profile as desired. Stable stratification was achieved by setting of the temperature step  $\Delta T (=T_1 - T_2)$  between the upper and lower streams at 25 K. For investigation of the effect of mean shear on countergradient heat transfer, measurements

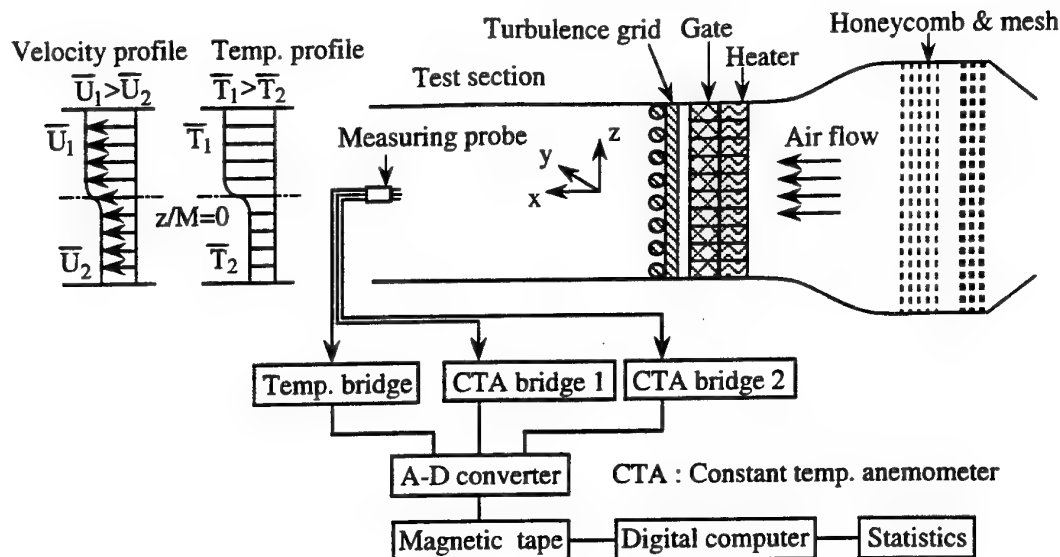


FIGURE 1. EXPERIMENTAL SETUP AND MEASUREMENT SYSTEM.

were performed in shear-free flow and in two kinds of sheared flows. In shear-free flow, the mean velocities of the upper and lower layers were set to the same value of 2.5 m/s. For the two sheared flows, turbulent mixing layers were generated by setting of the differences in the velocities  $\Delta \bar{U}$  ( $=\bar{U}_1 - \bar{U}_2$ ) between the upper layer and lower layer at 0.18 m/s and 0.47 m/s, respectively. The mean velocity of the two turbulent mixing layers was consistent with the value in the shear-free flow condition. The Reynolds number based on the mesh size was 7000 and the Brunt-Väisälä frequency,  $N=[g\beta(\partial\bar{T}/\partial z)]^{1/2}$ , was  $3.2\text{ s}^{-1}$  at  $x/M=10$  where  $\beta$  is the constant volumetric expansion coefficient. The gradient Richardson numbers of the two turbulent mixing layers were estimated as 0.62 and 0.12, respectively. The streamwise and vertical velocities and temperature were measured using an X-wire in conjunction with a cold wire. The cold wire was set within 0.001 m upstream of the X-wire. The signals of velocities from hot-wires were corrected using temperatures simultaneously measured from the cold-wire. Therefore, these probes enabled us to measure the instantaneous velocities and temperature simultaneously. The calibration of the probes was conducted at different flow velocities and temperatures before and after measurements. The measurements were mainly conducted at the centerline of the wind tunnel in the range of  $4 \leq x/M \leq 60$ . Three channels data on the instantaneous temperature and velocities were sampled at a rate of 0.001 s and digitized. The temperature fluctuations and velocity fluctuations were analyzed statistically.

## RESULTS AND DISCUSSION

Figure 2 shows the vertical turbulent heat flux correlation coefficients,  $Rw\theta = \overline{w'\theta'}/\overline{w'}\overline{\theta'}$ , for three stratified flows as functions of the buoyancy time,  $Nt$ , where  $w'$  and  $\theta'$  represent the rms values of the vertical velocity fluctuations and the temperature fluctuations. In the shear-free case, the heat flux

correlation coefficient is about -0.65 in the initial region. Stable stratification produce a positive mean temperature gradient in the vertical direction. Therefore, a negative coefficient means that the turbulent heat flux occurs down the gradient. The initial value of about -0.65 agrees with the experimental results of Lienhard & Van Atta (1990) and Yoon & Warhaft (1991) for unshaired air flow. Heat flux collapses with increasing  $Nt$  and the sign of the coefficient changes from negative to positive in the region of  $Nt > 2.2$ . This means that countergradient heat transfer occurs in this region. The positive peak value of the vertical heat flux correlation coefficient is 0.1. In the case of  $\Delta\bar{U}=0.18\text{ m/s}$ , the profile of the heat flux is similar to that on the shear-free condition. The countergradient heat transfer occurs at  $Nt > 2.3$ , though the peak value decreases. On the other hand, the behavior of the vertical heat flux in the strong shear case of  $\Delta\bar{U}=0.47\text{ m/s}$  is different from that on the other two conditions. The correlation coefficient increases with increasing  $Nt$  but remains negative at all the measurement points. Thus, the profiles of the vertical heat flux suggest that mean shear affects the heat transfer mechanism and prevents countergradient heat transfer.

The mechanism of the countergradient heat transfer can be explained in terms of the conversion of vertical kinetic energy of flow to available potential energy. Therefore, the ratio of the vertical kinetic energy (VKE) to the potential energy (PE) of the stratified air flow is estimated. Here, the kinetic energy and the potential energy are defined by  $VKE = \overline{w'^2}/2$  and  $PE = g\beta\overline{\theta'^2}/2(\partial\bar{T}/\partial z)$ , respectively. The profiles of the ratio for three flows are shown in Figure 3. In the initial region of small  $Nt$ , turbulent motion generated by grids installed at the entrance of the test section is vigorous so that the kinetic energy is considerably larger than the potential energy. In the shear-free case, according to decay of turbulence, the ratio decreases to 1 and the potential energy becomes comparable to the kinetic energy. Finally, the ratio reaches values of less than 1.0.

Comparison between the heat flux correlation coefficient and this ratio distinctly reveals that countergradient heat transfer occurs where the potential energy becomes larger than the vertical kinetic energy. This corroborates the observation that the conversion of the vertical kinetic energy to potential energy causes the heat transfer against the mean temperature gradient. The behavior of the ratio of weakly sheared flow is very similar to that of shear-free flow. In the strong shear case, the turbulent kinetic energy is generated by intense mean shear even in the downstream region, so that the ratio remains larger

than for the other two cases and never reaches one.

For investigation of the scales of motion which dominate countergradient heat transfer, cospectra between vertical velocity fluctuations and temperature fluctuations were estimated. Figure 4 shows the evolution of the cospectra,  $Co$ , for the three stratified flows. A negative value of the cospectra means down-gradient heat transfer and a positive one means countergradient heat transfer. Therefore, the behavior of the cospectra suggests the scale of motion contributing to vertical heat transfer. The vertical position of the cospectra for two

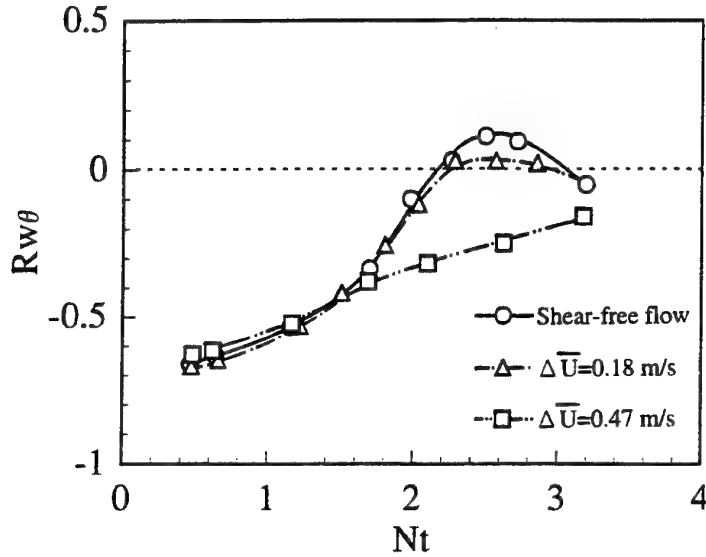


FIGURE 2. PROFILES OF VERTICAL TURBULENT HEAT FLUX CORRELATION COEFFICIENT.

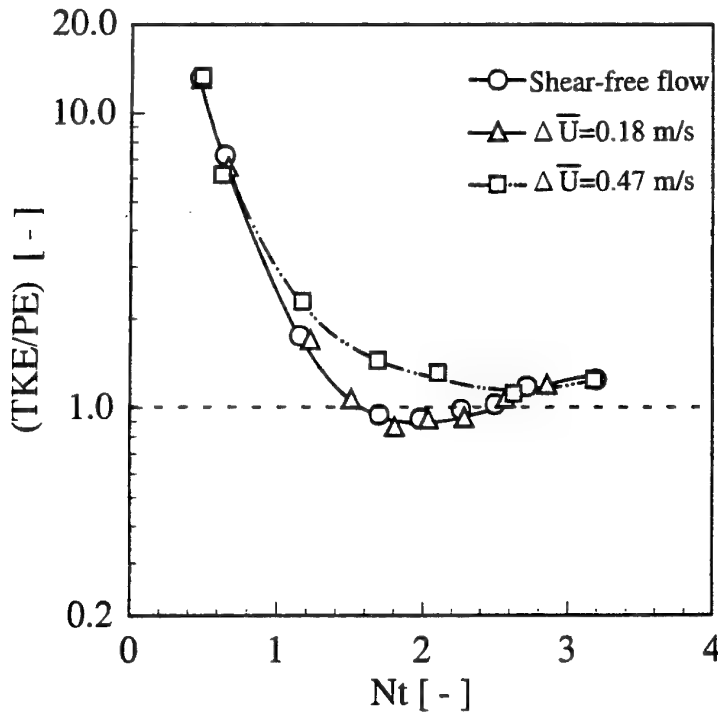


FIGURE 3. COSPECTRA OF VERTICAL TURBULENT HEAT FLUX.

large  $Nt$  are shifted -0.5 and -1.0 relative to 0, respectively. For the shear-free case, the cospectrum for  $Nt=1.70$  gives a negative value for the whole frequency region. At  $Nt=1.98$  the cospectrum indicates a positive value in the low frequency region. The region of positive values then spreads to the higher frequency side at  $Nt=2.57$ . With increasing  $Nt$ , the peak of the cospectrum decreases. For the weakly sheared flow at  $\Delta \bar{U}=0.18$  m/s, the behavior of the cospectrum is very similar to

that for shear-free flow. This means that large-scale motions contribute to counter-gradient heat transfer in both shear-free and weakly sheared air flow. This result agrees well with the results of the wind tunnel experiments by Lienhard & Van Atta (1990) and Yoon & Warhaft (1991). However, for the strongly sheared flow at  $\Delta \bar{U}=0.47$  m/s, the cospectrum is different from that in the above two cases. The cospectra reverse in sign only in the high frequency region. This behavior shows that

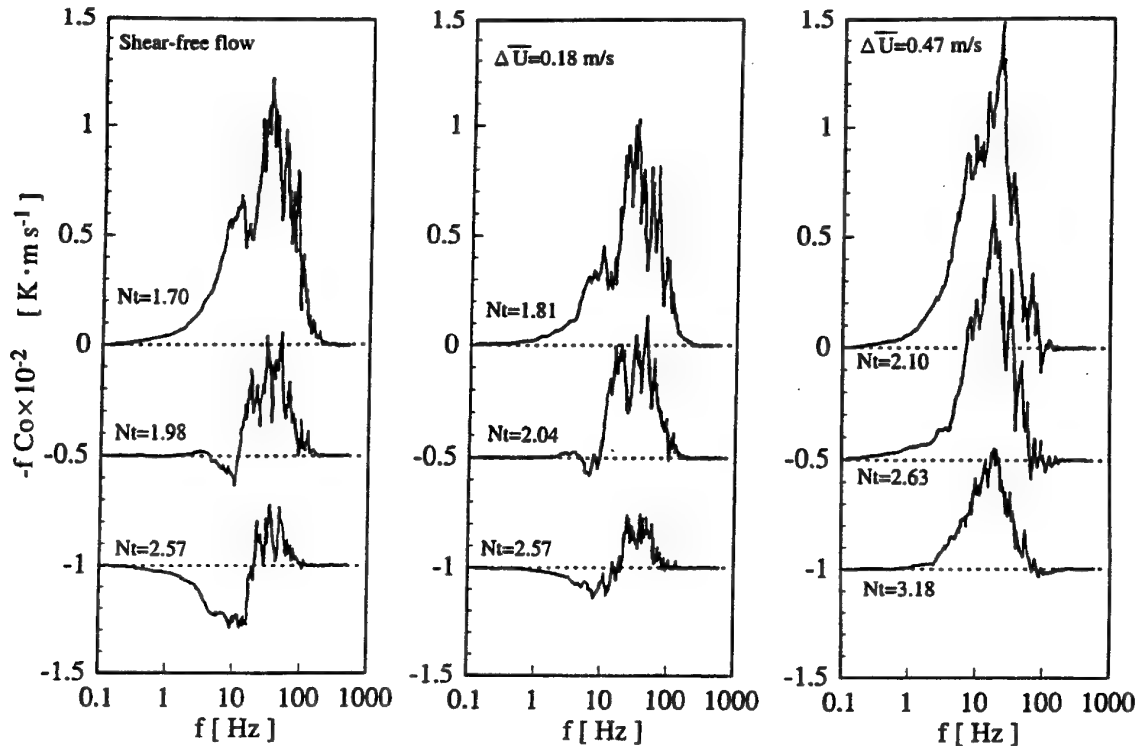


FIGURE 4. RATIO OF VERTICAL KINETIC ENERGY TO POTENTIAL ENERGY.

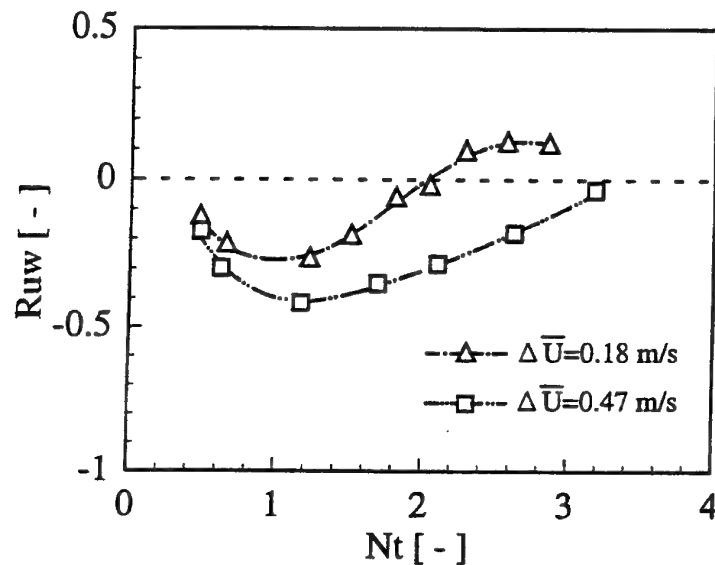


FIGURE 5. PROFILES OF MOMENTUM FLUX CORRELATION COEFFICIENT.

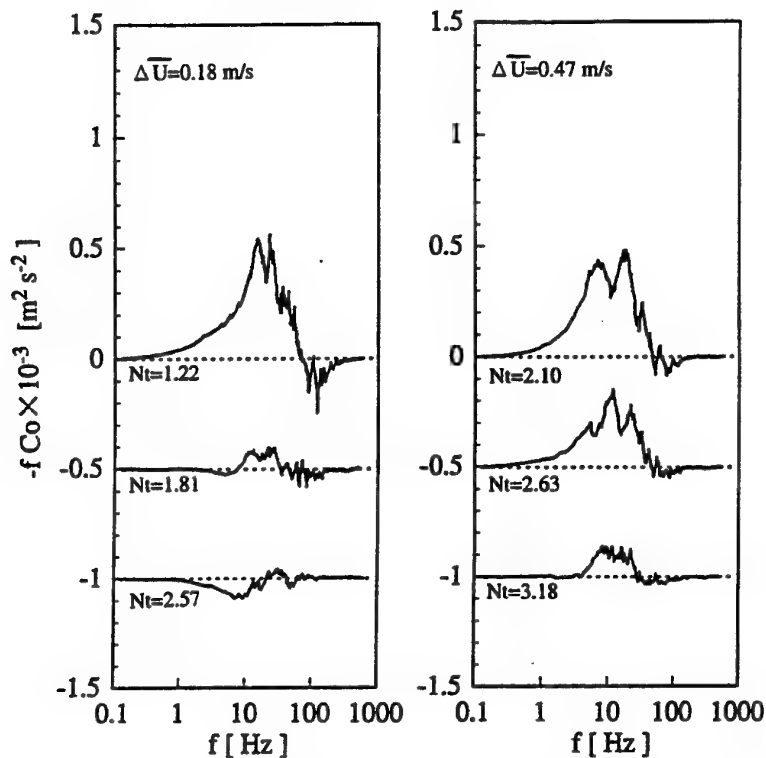


FIGURE 6. COSPECTRA OF MOMENTUM FLUX.

small-scale motions contribute to the countergradient heat flux even in air flow with a low Prandtl number. Komori & Nagata (1996) observed that countergradient heat flux was initially generated by small-scale motions in stratified water flows. It is of great interest to estimate cospectra for larger  $Nt$ , but the restrictions of the present experimental apparatus prevented these measurements.

The momentum flux correlation coefficients,  $R_{uw} = \overline{uw}/u'w'$ , for two sheared flows are plotted against  $Nt$  in Figure 5. For these sheared flows, the velocity of the upper layer is higher than that of the lower layer. Therefore, a positive mean velocity gradient is formed in the center of the wind tunnel. The direction of down gradient transfer of momentum flux coincides with that of the heat flux. The momentum flux value is negative in the initial region of small  $Nt$  and approaches zero as the turbulent motion decays in the downstream region. For the weakly sheared flow, the sign of the momentum flux changes from negative to positive at  $Nt=2.0$  and countergradient momentum transfer also occurs at that point. However, the momentum flux remains negative for strongly sheared flow. Thus, mean shear also influences momentum transfer to reduce countergradient transfer.

Cospectra between the vertical velocity fluctuations and streamwise velocity fluctuations are shown in Figure 6. For weakly sheared flow, the cospectrum of momentum flux indicates that countergradient momentum transfer occurs at high frequencies in the initial region of  $Nt=1.22$ . It then collapses and the region of countergradient transfer spreads to the low

frequency side at larger  $Nt$ . This means that, in weakly sheared flow, the small-scale motions initially contribute to the countergradient momentum transfer and then the large-scale motions also contribute to it. Such a mechanism is quite similar to that of countergradient heat transfer in water flows with high Prandtl number. The cospectrum of the strongly sheared flow shows the contribution of small-scale motions in the measurement region. These results suggest that the powerful motions generated by strong shear give rise to small-scale countergradient heat transfer in stratified air flows.

## CONCLUSION

The effects of mean shear on countergradient heat transfer in stably stratified air flows were experimentally studied. The findings of this study are summarized as follows. In strongly stratified air flow with shear, heat and momentum are transferred against the mean temperature and velocity gradients. Mean shear greatly affects the heat and momentum transfer mechanism and inhibits countergradient heat and momentum transfer. Strong turbulent motions generated by shear cause the small-scale countergradient heat transfer even in stratified air flows with low Prandtl number.

## REFERENCES

- Gerz, T., and Schumann, U., 1996, "A Possible Explanation of Countergradient Fluxes in Homogeneous Turbulence," *Theor. Comput. Fluid Dyn.*, Vol. 8, pp.169-181
- Kanzaki, T., and Ichikawa, Y., 1996, "Heat Transfer in a



Stably Stratified Grid-Generated Flow," *Advances in Turbulence VI*, S.Gavrilakis et al. ed., Kluwer, pp. 185-186.

Komori, S., Ueda, H., Ogino, F., and Mizushima, T., 1983, "Turbulence Structure in Stably Stratified Open-Channel Flow," *J. Fluid Mech.*, Vol. 130, pp. 13-26.

Komori, S., and Nagata, K., 1996, " Effects of Molecular Diffusivities on Counter-Gradient Scalar and Momentum Transfer in Strongly Stable Stratification," *J. Fluid Mech.*, Vol. 326, pp. 205-237.

Lienhard, V. J. H., and Van Atta, C. W., 1990, "The Decay of Turbulence in Thermally Stratified Flow," *J. Fluid Mech.*, Vol. 210, pp. 57-112.

Yoon, K. and Warhaft, Z., 1991, "Turbulent Mixing and Transport in a Thermally Stratified Interfacial Layer in Decaying Grid Turbulence," *Phys. Fluids A* , Vol. 3, pp. 1143-1155.

# IMPORTANCE OF THIRD-MOMENT MODELLING IN HORIZONTAL, STABLY-STRATIFIED FLOWS

T. J. Craft, J.W. Kidger and B.E. Launder  
Department of Mechanical Engineering  
UMIST, Manchester, UK

## ABSTRACT

The paper examines the computational modelling of the stably stratified mixing layer with particular emphasis being placed on the approximation of the triple moments which act as the agencies for diffusing the stresses and heat fluxes. As the turbulent second-moments decay (along with their generative agencies) their local level is increasingly dependent on the triple moments and, thus, on the strategies for modelling these processes. The most successful route we have found adopts transport closures broadly analogous to (but more complete than) those of Dekeyser and Launder (1983). An important element is the adaptation of Millionshtchikov's (1942) proposal for eliminating the fourth moments by including a further gradient-transport term as proposed by Kawamura et al (1995).

A much simpler strategy based on transport equations for stresses but adopting a gradient-diffusion hypothesis for the turbulent heat fluxes also shows promising results.

## 1. INTRODUCTION

While second-moment closures have now established themselves as a level of modelling that can adequately mimic transport processes in a range of complex flows, most of the attention in developing models of the component processes has been given to the pressure-strain and dissipation processes (or their counterparts in the scalar flux equations). By contrast, diffusive transport of the second moments, involving gradients of triple-moment products, has generally been modelled more with an eye to numerical stability and simplicity than to accuracy. In most engineering flows this emphasis makes sense because the resulting prediction of the mean-field quantities is rarely sensitive to the triple-moment modelling, especially in flow near walls.

In stratified flows, however, the situation changes because buoyant effects on at least some of the triple moments (effects which are neglected in simple 'gradient-diffusion' approximation) may become quite crucial to mimicking the flow's evolution correctly, André et al (1979); Lumley et al (1978). This appears to be especially the case under strong *stable* stratification for then buoyant effects oppose the action of mean velocity and (in the scalar flux equations) mean

temperature gradients and the local level of the second-moments then becomes far more sensitive to their diffusive transport.

The present contribution reports our experiences in computing the salinity-stratified mixing layer of Uittenbogaard (1988). This experiment has been the subject of a number of modelling studies (Uittenbogaard & Baron, 1989; Craft et al, 1996) and at least one European turbulence modelling workshop (Scheuerer, 1989). The closure levels adopted here range from partially second moment (transport equations for the stresses; gradient diffusion for the salinity fluxes) to partially third moment (in which *some* of the third-moments are obtained via transport equations, others via gradient-diffusion models). The object has been to ascertain the level of closure required for making reliable risk assessments in various flows where safety is in question. In many such practical cases the motion is three dimensional (unlike the nominally two-dimensional case considered here) so there is a strong incentive to keep the model relatively simple.

## 2. CLOSURE MODELLING

In the interests of space, the second-moment equations for Reynolds stress ( $\overline{u_i u_j}$ ) and salinity flux ( $\overline{u_i \theta}$ ) are written symbolically as:

$$\frac{D\overline{u_i u_j}}{Dt} = P_{ij} + G_{ij} + \phi_{ij} - \epsilon_{ij} + d_{ij} \quad (2.1)$$

$$\frac{D\overline{u_i \theta}}{Dt} = P_{i\theta} + G_{i\theta} + \phi_{i\theta} - \epsilon_{i\theta} + d_{i\theta} \quad (2.2)$$

where 'P' denotes generation by mean velocity gradients,  $\partial U_p / \partial x_q$  and, in the case of  $\overline{u_i \theta}$ , mean salinity gradients,  $\partial \Theta / \partial x_q$ . The G terms denote corresponding gravitational generation terms which, in the case of  $\overline{u_i \theta}$  contain the mean square salinity variance  $\overline{\theta^2}$ ; this too is obtained from a transport equation:

$$\frac{D\overline{\theta^2}}{Dt} = P_{\theta\theta} - \epsilon_{\theta\theta} + d_{\theta\theta} \quad (2.3)$$

there being no buoyant generation since velocity fluctuations do not appear in the dependent variable.

The processes denoted 'd' are diffusive transport and their approximation, forming the principal research enquiry of this paper, appears in Section 3. Here we report briefly on the models adopted for dissipation ( $\epsilon$ ) and non-dispersive pressure interactions ( $\phi$ )

Local isotropy is assumed for the dissipation processes

$$\epsilon_{ij} = \frac{2}{3} \delta_{ij} \epsilon; \quad \epsilon_{i\theta} = 0 \quad (2.4)$$

while the scalar dissipation is approximated via the kinematic dissipation  $\epsilon$  as :

$$\epsilon_{\theta\theta} = R \overline{\theta^2} \frac{\epsilon}{k} \quad (2.5)$$

where  $k$  is the turbulent kinetic energy,  $\overline{u_i^2}/2$  and the time-scale ratio  $R$  is (following Haroutunian and Launder, 1989) taken as :

$$R = \frac{3}{2} (1 + A_{2\theta}) \quad \text{where} \quad A_{2\theta} = \overline{(u_i \theta)^2} / k \overline{\theta^2} \quad (2.6)$$

Finally,  $\epsilon$  is obtained from its usual transport equation :

$$\frac{D\epsilon}{Dt} = \frac{C_{\epsilon 1}}{2} (P_{kk} + G_{kk}) \frac{\epsilon}{k} - C_{\epsilon 2} \frac{\epsilon^2}{k} + d_\epsilon \quad (2.7)$$

where  $C_{\epsilon 1} = 1.45$  and  $C_{\epsilon 2} = 1.90$ .

The diffusive transport of  $\epsilon$ ,  $d_\epsilon$ , is approximated via the *generalised gradient diffusion hypothesis* (GGDH) as :

$$d_\epsilon = C_\epsilon \frac{\partial}{\partial x_k} \left( \overline{u_j u_k} \frac{k}{\epsilon} \frac{\partial \epsilon}{\partial x_j} \right) \quad (2.8)$$

where  $C_\epsilon = 0.16$ .

Some may point out that (2.8) is an inconsistently crude approximation for transport compared with the strategies adopted in Section 3. However, with regard to closing the *second-moment* equations, the term is formally no more prominent than the diffusive transport terms in the third-moment equations for which a strictly analogous model will be adopted.

Equations (2.4) - (2.8) form part of what is often termed the 'Basic Model' used by CFD workers for more than 20 years. It is a model that has been extensively applied to shear-driven and buoyancy affected flows (Launder 1989), but which does not, with regard to  $\epsilon_{ij}$  and  $\epsilon_{i\theta}$ , satisfy the limiting kinematic requirements when, in a very strong stable stratification, vertical fluctuations tend to zero and turbulence thus approaches a 2-component state (Lumley 1978; Craft et al. 1996)

The corresponding models for the  $\phi$  processes are :

$$\begin{aligned} \phi_{ij} = & -C_1 \frac{\epsilon}{k} \left( \overline{u_i u_j} - \frac{2}{3} \delta_{ij} k \right) - C_2 \left( P_{ij} + G_{ij} - \frac{1}{3} \delta_{ij} [P_{kk} + G_{kk}] \right) \\ & + 0.5 \frac{\epsilon}{k} \left( \overline{u_i u_m} \cdot n_l n_m \delta_{ij} - \frac{3}{2} \overline{u_i u_l} \cdot n_j n_l - \frac{3}{2} \overline{u_j u_l} \cdot n_i n_l \right) \left( \frac{\ell}{1.4y} \right) \\ & - 0.08 \frac{\partial U_l}{\partial x_m} \overline{u_i u_m} (\delta_{ij} - 3n_i n_j) \left( \frac{\ell}{1.4y} \right) \\ & - 0.1ka_{lm} \left( \frac{\partial U_k}{\partial x_m} n_l n_k \delta_{ij} - \frac{3}{2} \frac{\partial U_i}{\partial x_m} n_l n_j - \frac{3}{2} \frac{\partial U_j}{\partial x_m} n_l n_i \right) \left( \frac{\ell}{1.4y} \right) \\ & + 0.4k \frac{\partial U_l}{\partial x_m} n_l n_m \left( n_i n_j - \frac{1}{3} \delta_{ij} \right) \left( \frac{\ell}{1.4y} \right) \end{aligned} \quad (2.9)$$

$$\phi_{i\theta} = -C_{1\theta} \frac{\epsilon}{k} \overline{u_i \theta} - C_{2\theta} [P_{i\theta} + G_{i\theta}] \quad (2.10)$$

where  $C_1 = 1.8$ ;  $C_2 = 0.6$ ;  $C_{1\theta} = 3.0$  and  $C_{2\theta} = 0.5$ .

All but the first line in the model for  $\phi_{ij}$  are 'wall-reflection' terms (due to Craft & Launder, 1992), the symbol  $n_k$  denoting the unit vector normal to the wall, and  $\ell$  the turbulent length scale,  $k^{1/2} \nu^{1/2} / \epsilon$ . In this study, because the flow has a *free* surface, wall-reflection terms have been applied to that surface, too, a practice whose merit has been conclusively established by Reece (1977) and McGuirk & Papadimitriou (1985)<sup>1</sup>. No wall-reflection agency has been applied to  $\phi_{i\theta}$  in conformity with long-established experience and practice, Launder (1976).

Results for an alternative, simpler modelling of  $\overline{u_i \theta}$  are also presented in Section 4 in which the GGDH is invoked :

$$\overline{u_i \theta} = -C_\theta \overline{u_k u_i} \frac{k}{\epsilon} \frac{\partial \theta}{\partial x_k} \quad (2.11)$$

with  $C_\theta = 0.30$ . Using this approximation,  $\overline{\theta^2}$  does not appear as an unknown so neither (2.2) nor (2.3) are solved. This is referred to as Model 1.

### 3. MODELLING THE DIFFUSION OF SECOND MOMENTS

The simplest strategy adopted here (Model 2) is to apply GGDH to all terms:

$$-\overline{u_k \alpha \beta} = -C_k \frac{k}{\epsilon} \overline{u_k u_l} \frac{\partial \alpha \beta}{\partial x_l} \quad (3.1)$$

where  $C_k = 0.22$  for  $\overline{u_i u_j u_k}$ , else  $C_k = 0.18$ .

<sup>1</sup> In fact, while the physical basis for wall reflection is long established (Chou, 1945), there is reason to suppose that Eq (2.9) greatly exaggerates it merely because of the inadequacies in the first line of Eq (2.9) near a surface or interface where turbulence goes to a two-component state. Indeed, recent work at UMIST, using far more elaborate models for  $\phi_{ij}$  that comply with the two-component limit (Launder & Li, 1994; Craft & Launder, 1996) adopt no wall reflection corrections of the type adopted in Eq (2.9). Nevertheless (2.9) and (2.10) are retained here partly because the region on which Section 4 focuses is well removed from the wall or free surface and partly because, with the Basic Model being so widely adopted, it seemed the most appropriate level at which to focus this initial enquiry.

In the above,  $\alpha$  and  $\beta$  may denote a velocity component or salinity fluctuation. This is the 'basic' second-moment closure. This level of approximation is not adequate in very stably stratified flows since, despite buoyant damping of the second moments, too much mixing still results. Our first studies of this problem adopted obvious algebraic elaborations of (3.1) bringing in gravitational effects, Craft et al (1996). The present more extensive study has found that such algebraic forms tend to provoke convergence problems and so here attention is directed at solving transport equations for some of the triple moments.

But which ones? The number of non-zero triple moments depends greatly on the meaning of  $\alpha$  and  $\beta$  on the left side of Eq (3.1). If  $\alpha$  and  $\beta$  both denote  $\theta$ , there are, for a two-dimensional flow, just two:  $\overline{u_1\theta^2}$  and  $\overline{u_2\theta^2}$  ( $x_3$  being the direction of spatial uniformity); if they denote velocity fluctuations, there are 6 (or 10 for an entirely general flow). Accordingly, our practice has been to retain Eq (3.1) for  $\overline{u_i u_j u_k}$  and to solve transport equations for all other third moments (Model 3). Among these is included the equation for  $\overline{\theta^3}$  which appears in the buoyant term of the equation for  $\overline{u_k \theta^2}$ . The triple moment equations in question may be written:

$$\frac{D\overline{u_k u_j \theta}}{Dt} = P_{kj\theta}^1 + P_{kj\theta}^2 + G_{kj\theta} + \phi_{kj\theta} - \epsilon_{kj\theta} + d_{jk\theta} \quad (3.2)$$

$$\frac{D\overline{u_k \theta^2}}{Dt} = P_{k\theta\theta}^1 + P_{k\theta\theta}^2 + G_{k\theta\theta} + \phi_{k\theta\theta} - \epsilon_{k\theta\theta} + d_{k\theta\theta} \quad (3.3)$$

$$\frac{D\overline{\theta^3}}{Dt} = P_{\theta\theta\theta}^1 + P_{\theta\theta\theta}^2 - \epsilon_{\theta\theta\theta} + d_{\theta\theta\theta} \quad (3.4)$$

where, in all equations, the  $P^1$ 's denote production by second-moment gradients,  $P^2$ 's arise from mean-velocity and/or salinity gradients, the  $G$ 's denote direct buoyant contributions,  $\phi$ 's are pressure-interaction terms,  $\epsilon$ 's denote molecular dissipation effects and  $d$ 's represent triple-moment diffusion due to fourth moments and (for  $\overline{u_k u_j \theta}$  and  $\overline{u_k \theta^2}$ ) pressure fluctuations.

No approximations are needed for the  $P^1$ ,  $P^2$  or  $G$  processes in any of the equations. We adopt closure models for the remaining terms that are consistent with those made in the second-moment equations. The action of the non-dispersive pressure correlations,  $\phi$ , is assumed to comprise 'return-to-isotropy' and 'destruction of production' parts. Thus

$$\phi_{k\theta\alpha} = -C_{1\alpha} \frac{\epsilon}{k} \overline{\theta u_k \alpha} - C_{2\alpha} (P_{k\theta\alpha}^1 + P_{k\theta\alpha}^2 + G_{k\theta\alpha}) \quad (3.5)$$

where  $C_{1\alpha} = 1/0.075$ ,  $C_{2\alpha} = 0.5$ , and  $\alpha$  on the right-hand side denotes either  $u_j$  or  $\theta$ .

Concerning dissipative processes, the proposals advocated by Dekeyser & Launder (1985), hereafter referred to as 'DL', are retained for  $\epsilon_{kj\theta}$  and  $\epsilon_{k\theta\theta}$ :

$$\epsilon_{jk\theta} = -C_{3\epsilon} \frac{k}{\epsilon} \overline{\theta u_j} \frac{\partial \epsilon}{\partial x_k} \delta_{jk} \quad (3.6)$$

$$\epsilon_{k\theta\theta} = -3C_{3\epsilon} \frac{k}{\epsilon} \overline{u_k u_j} \frac{\partial \epsilon}{\partial x_j} \quad (3.7)$$

where  $C_{3\epsilon} = 0.1$ , following DL. For  $\epsilon_{\theta\theta\theta}$  (a process not considered by DL) the usual approximation:

$$\epsilon_{\theta\theta\theta} = 3 \left( 2R \frac{\overline{\theta^3}}{\overline{\theta^2}} \epsilon_{\theta} \right) \quad (3.8)$$

is adopted with the coefficient  $R$  chosen as in Eq (2.6).

In earlier closure proposals for the diffusion of 3<sup>rd</sup> moments, the usual route has been to express the fourth rank products in terms of products of the constituent quantities taken two at a time (Millionshtchikov, 1942):

$$\overline{\alpha\beta\gamma\delta} = \overline{\alpha\beta} \cdot \overline{\gamma\delta} + \overline{\alpha\gamma} \cdot \overline{\beta\delta} + \overline{\alpha\delta} \cdot \overline{\beta\gamma} \quad (3.9)$$

An argument against using such a form is that the Gaussian distribution of the fluctuations on which the approximation, Eq (3.9), rests will be least accurate in regions where quadruple products are most influential, i.e. where the turbulence is strongly inhomogeneous. Possibly with such thoughts in mind, Kawamura et al (1995) proposed that, to model  $\overline{u_i u_j u_k u_m}$ , departures from Eq (3.9) should be accounted for by a gradient transport model. We apply this idea to all the quadruple products as follows:

$$\begin{aligned} d_{jk\theta} &= -\frac{\partial}{\partial x_m} \left[ \overline{u_m u_j u_k \theta} \right] \\ &= \left\{ -\frac{\partial}{\partial x_m} \left[ \overline{u_m u_j u_k \theta} - (\overline{u_m u_j} \cdot \overline{u_k \theta} + \overline{u_m u_k} \cdot \overline{u_j \theta} + \overline{u_m \theta} \cdot \overline{u_j u_k}) \right] \right\} \\ &= \left\{ -\frac{\partial}{\partial x_m} \left[ \overline{u_m u_j} \cdot \overline{u_k \theta} + \overline{u_m u_k} \cdot \overline{u_j \theta} + \overline{u_m \theta} \cdot \overline{u_j u_k} \right] \right\} \\ &= \left\{ C_{3d1} \frac{\partial}{\partial x_m} \left[ \overline{u_m u_n} \frac{k}{\epsilon} \frac{\partial}{\partial x_n} \overline{u_j u_k \theta} \right] \right. \\ &\quad \left. - \frac{\partial}{\partial x_m} \left[ \overline{u_m u_j} \cdot \overline{u_k \theta} + \overline{u_m u_k} \cdot \overline{u_j \theta} + \overline{u_m \theta} \cdot \overline{u_j u_k} \right] \right\} \end{aligned} \quad (3.10)$$

and likewise:

$$\begin{aligned} d_{k\theta\theta} &= C_{3d2} \frac{\partial}{\partial x_m} \left[ \overline{u_m u_n} \frac{k}{\epsilon} \frac{\partial}{\partial x_n} \overline{u_k \theta^2} \right] \\ &\quad - \frac{\partial}{\partial x_m} \left[ \overline{u_m u_k} \cdot \overline{\theta^2} + 2\overline{u_m \theta} \cdot \overline{u_k \theta} \right] \end{aligned} \quad (3.11)$$

$$d_{\theta\theta\theta} = C_{3d3} \frac{\partial}{\partial x_m} \left[ \overline{u_m u_n} \frac{k}{\epsilon} \frac{\partial}{\partial x_n} \overline{\theta^3} \right] - \frac{\partial}{\partial x_m} \left[ 3\overline{u_m \theta} \cdot \overline{\theta^2} \right] \quad (3.12)$$

where  $C_{3d1} = C_{3d2} = C_{3d3} = 0.1$ . Introduction of the Kawamura modification in modelling the above processes significantly improved the behaviour of Model 3.

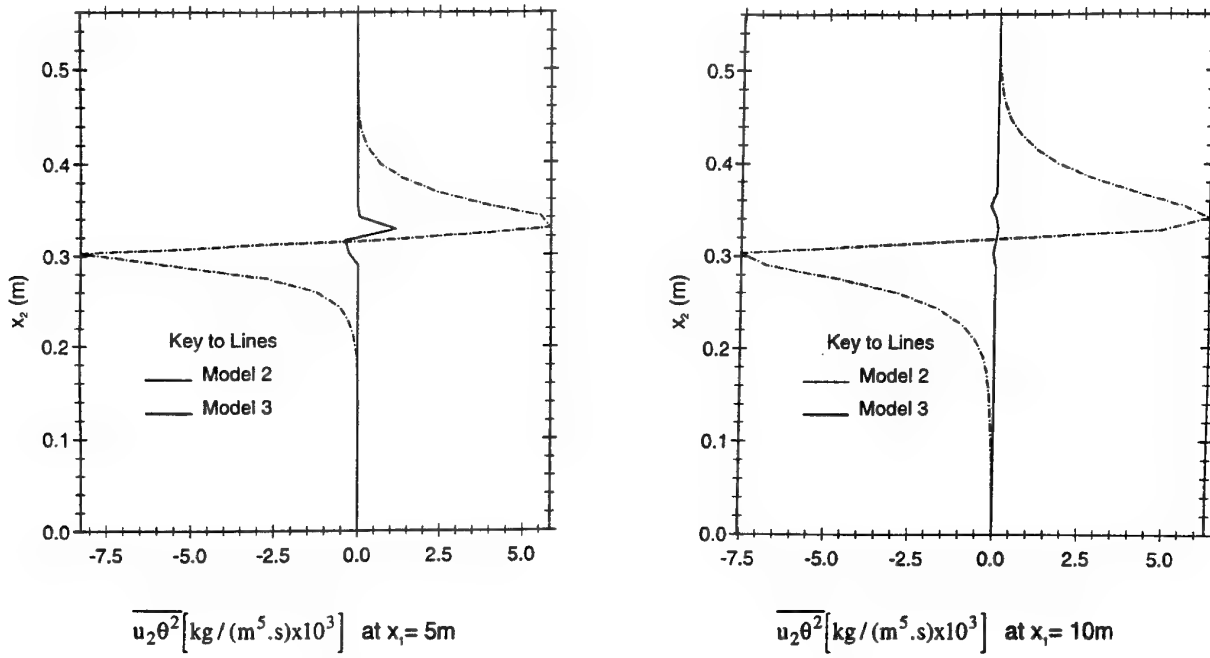


Fig 1 The variation of  $\overline{u_2 \theta^2}$  from the GGDH (Model 2) compared with that from a transport equation, (Model 3).

#### 4. PRESENTATION AND DISCUSSION OF RESULTS

Discussion of the results begins with computations of  $\overline{u_2 \theta^2}$  (with  $x_2$  vertical). In the early phases of development, Fig 1a, both the GGDH (Model 2) and transport-equation models of this process (Model 3) show a similar shape across the flow, albeit with a very different magnitude, but, by 10m, Fig 1b, the shape itself is quite different. The underlying reason for this may be seen in Fig 2, the transport-equation budget. The nearly antisymmetric profiles of  $\overline{u_2 \theta^2}$  given by the GGDH would also have been generated by the transport equation if the dominant terms in the latter had been a balance between  $(P_{k\theta\theta}^1 + d_{k\theta\theta})$  on the one hand, and the corresponding model of the pressure-containing correlations  $(-C_{1\theta} \frac{\epsilon}{k} \overline{\theta^2 u_k} - C_{2\theta} P_{k\theta\theta}^1)$  on the other. (viz. equations (3.3) and (3.5)). From solving the transport equation, however, one finds that many other processes are influential including, in particular, the dissipation process modelled by Eq(3.7).

Fig 2 shows a partial budget of  $\overline{u_2 \theta^2}$  at the 40m station where it is seen that  $\epsilon_{k\theta\theta}$  acts in direct opposition to the pressure terms. This brief paper does not provide an opportunity for examining more closely how the triple-moment equations should be closed. However, it is shown that decisions taken at this level may very substantially affect both the second-moment and the mean profiles. For example, as a result of this much-reduced diffusion of  $\overline{\theta^2}$ , the density-variance profiles are appreciably narrower and peakier, Fig 3. This difference, in turn, helps produce a strikingly different density flux profile shown in Fig 4. Although the experimental data show substantial scatter, it is plainly evident that Model 3 is far more

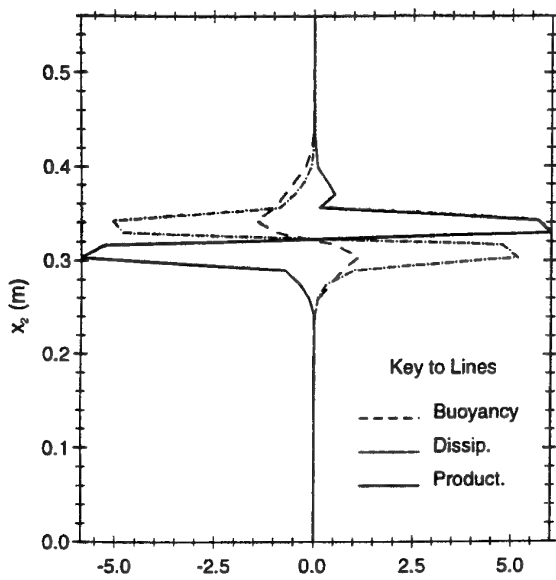
successful at capturing their variation than Model 2. However, a surprising feature is that, if the GGDH is applied to the *mean* density profile to obtain the  $\overline{u_2 \theta}$  profile directly (Model 1), then the profile of the density flux at  $x_1 = 10\text{m}$  is captured at least as well as with the most complex treatment (Model 3).

The consequent effects on the mean salinity profile is, in fact, very small at  $x_1 = 10\text{m}$ . More significant differences are evident at 40m however, shown in Fig 5. Again Models 1 and 3 give very similar results while the conventional second-moment closure leads to much more rapid mixing. The measured salinity profile exhibits a variation that appears to be intermediate between these two patterns of mixing.

Finally, concerning the dynamic field, Models 1 and 3 evidently capture the variation of turbulent shear stress (Fig 7) better than Model 2 (especially Model 1 which predicts a complete collapse of turbulent momentum transport in the upper half of the channel) but, strangely, the mean velocity profile (Fig 6), even allowing for the probable secondary motion in the data, is reproduced better with Model 2.

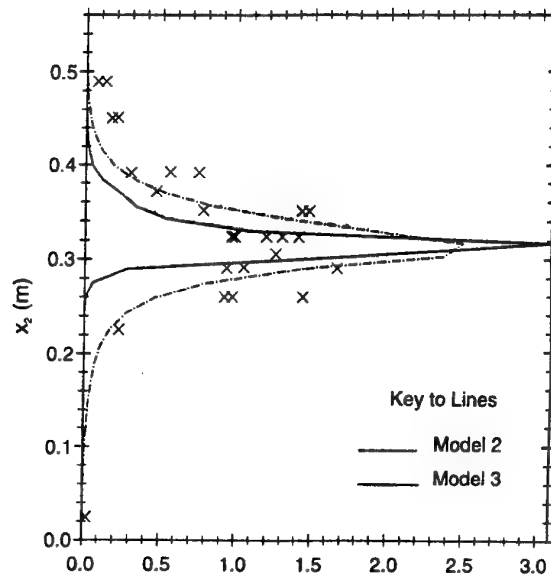
#### 5. CONCLUSION

Evidently, for problems where far-field dispersal of pollutants in stably stratified conditions is the central issue, a good deal more attention must be given to how the diffusion of second moments should be modelled. While the present research has not yet offered a clear-cut, optimum closure strategy, it is of considerable interest that applying the GGDH directly to obtain the density fluxes (Model 1) produces nearly the same results as the far more complex (partial) 3<sup>rd</sup>-moment closure, Model 3.



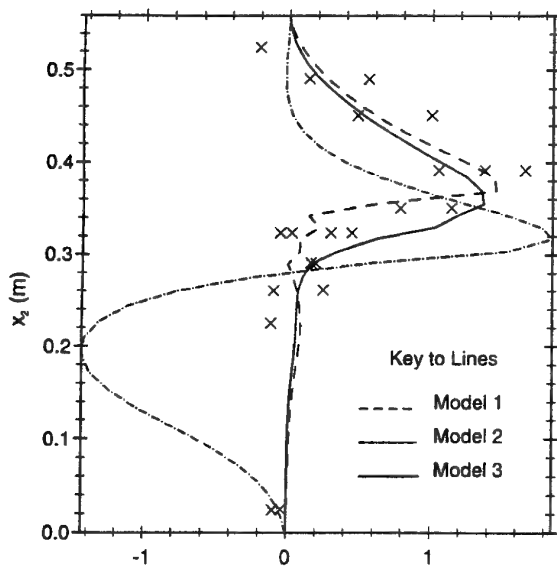
Relative budget for  $\overline{u_2\theta^2}$  at  $x_1 = 40m$

**Fig 2** The relative importance of the 3 most significant terms in the  $\overline{u_2\theta^2}$  budget



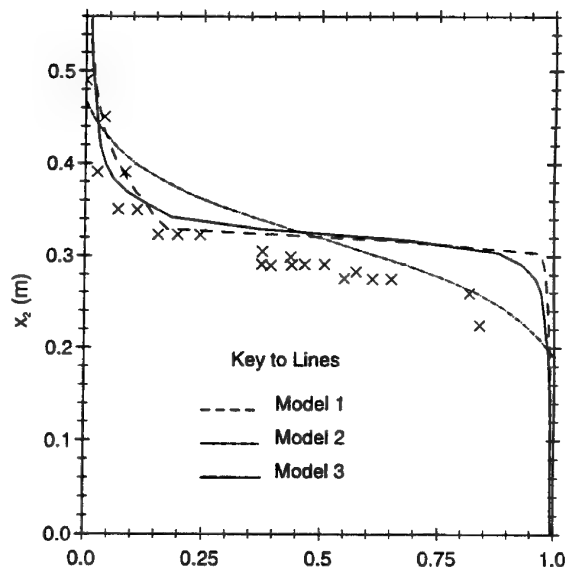
$\overline{\theta^2} [kg^2/m^2]$  at  $x_1 = 10m$

**Fig 3** The variation of  $\overline{\theta^2}$  from the 2nd and 3rd moment closures



$\overline{u_2\theta} [kg/(m^2.s) \times 10^3]$  at  $x_1 = 10m$

**Fig 4** The vertical density flux variation from the different models



$\frac{\Theta - \Theta_{min}}{\Theta_{max} - \Theta_{min}}$  at  $x_1 = 40m$

**Fig 5** The variation of relative density from the different models

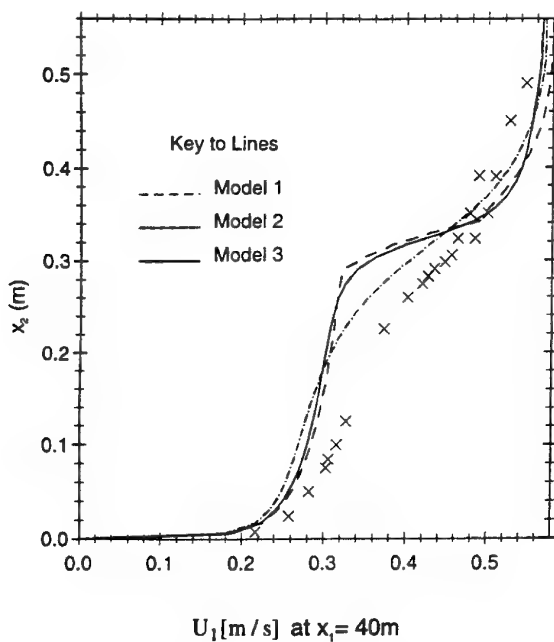


Fig 6 The streamwise velocity distribution

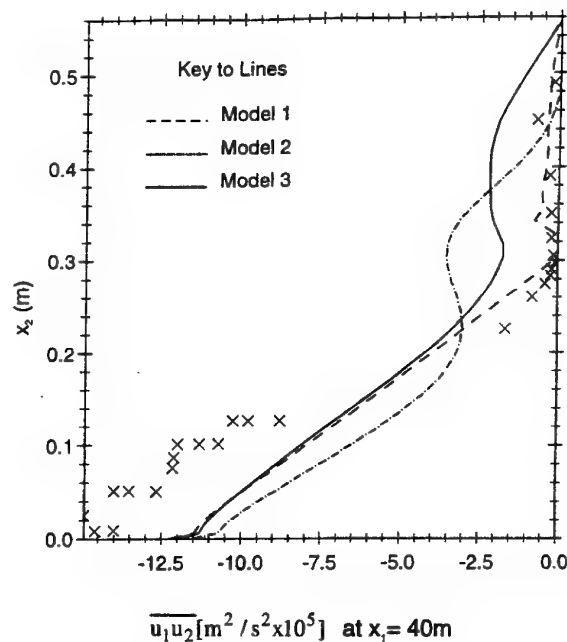


Fig 7 The shear stress distribution

## 6. ACKNOWLEDGMENTS

T J Craft's contribution has been made through the support of a Royal Society University Research Fellowship while J Kidger acknowledges with thanks an EPSRC Research Studentship. Dr N Z Ince greatly assisted progress through several personal interactions and making software available. Authors' names appear alphabetically.

## REFERENCES

- André J. C., et al., 1979, "The Clipping Approximation and Inhomogeneous Turbulence Simulations", *Turb. Shear Flows 1*, pp 307-318, ed. F. Durst et al. Springer, Berlin
- Chou P.Y., 1945, "On Velocity Correlation and Solution of the Equation of Turbulent Fluctuation", *Quart. App. Math.*, **3**, p31
- Craft T.J., Launder B.E., 1992, "New Wall-Reflection Model Applied to the Turbulent Impinging Jet" *AIAA J.*, **30**, p2970
- Craft T. J., Ince N.Z., Launder B.E., 1996, "Recent Developments in Second-Moment Closure for Buoyancy-Affected Flows", *Dynamics of Atmospheres and Oceans*, **23**, pp99-114
- Daly B.J., Harlow F.H., 1970, "Transport Equations in Turbulence" *Phys. Fluids*, **13**, p2634
- Dekeyser I., Launder B.E., 1983, "A Comparison of Triple-Moment Temperature-Velocity Correlations in the Asymmetric Heated Jet with Alternative Closure Models", *Turb. Shear Flows 4*, pp 102-117, ed. L.J.S. Bradbury et al., Springer, Berlin
- Hanjalic K., Launder B.E., 1971, "A Reynolds Stress Model of Turbulence and its Application to Thin Shear Flows", *J. Fluid Mech.*, **52**, pp609-638
- Haroutunian V., Launder B.E., 1986, "Second Moment Modelling of Turbulent Buoyant Shear Flows with an Elliptic Solver", *ASME Winter Annual Meeting, Anaheim, California*, December 1986
- Kawamura H., Sasaki J., Kobayashi K., 1995, "Budget and Modelling of Triple-Moment Velocity Correlations in a Turbulent Channel Flow based on DNS", *10th Int. Sym. on Turbulent Shear Flows*, Pennsylvania State University
- Launder B.E., 1976, "On the Effects of a Gravitational Field On the Turbulent Transport of Heat and Momentum", *J. Fluid Mech.*, **67**, pp569-581
- Launder B.E., 1989, "The Prediction of Force-Field Effects on Turbulent Shear Flows via Second-Moment Closure", *Adv. In Turbulence 2* (ed. H.H.Fernholz and H.E. Fiedler) pp338-358, Springer, Berlin
- Launder B.E., Li S-P., "On the Elimination of Wall Topography Parameters from Second-Moment Closure", 1994, *Phys. Fluids*, **6**, p999
- Lumley J.L., 1978, "Computational Modelling of Turbulent Flows", *Adv. Applied Mech.*, **18**, p123
- Lumley J.L., Zeman O., Siess J., 1978, "The Influence of Buoyancy on Turbulent Transport", *J. Fluid Mech.*, **84**, pp. 581-597
- McGuirk J, Papadimitriou C., 1985, "Buoyant Surface Layers Under Fully Entraining and Internal Hydraulic Jump Conditions", *Proc. 5th Sym. Turb. Shear Flows*, Cornell University pp 22.33 - 22.41
- Millionshtchikov M.D., 1941, "On the role of the Third Moments in Isotropic Turbulence", *C.R. Acad. Sci. SSSR*, **32**, p619
- Reece, 1977, PhD Thesis, Faculty of Engineering, University of London.
- Scheuerer G., 1989, 14th Meeting of the IAHR Working Group on Refined Flow Modelling, Gesellschaft für Reaktorsicherheit, Garching.
- Uittenbogaard R.E., 1988, "Measurement of Turbulence Fluxes in a Steady, Stratified, Mixing Layer", *3rd Int. Sym. on Refined Flow Modelling and Turb. Meas.*, Tokyo pp725-732
- Uittenbogaard R.E. and Baron F., "A Proposal : Extension of the  $q^2$ - $\epsilon$  Model for Stably Stratified Flows with Transport of Internal Wave Energy", Paper 18-4, 7<sup>th</sup> Sym. Turbulent Shear Flows, Stanford University, 1989.
- Wyngaard J.C., Sundarajan A., 1979, "The Temperature Skewness Budget in the Lower Atmosphere and its Implications for Turbulence Modelling" *Turb. Shear Flows 1*, ed. F. Durst et al., Springer, Berlin

# MODELING OF TURBULENT TRANSPORT IN PBL WITH THIRD-ORDER MOMENTS

**Boris B. Ilyushin and Albert F. Kurbatskii**  
Novosibirsk State University  
Institute of Theoretical and Applied Mechanics  
Novosibirsk, 630090  
Russia

## ABSTRACT

The results on modeling processes of vertical turbulent transport in the planetary boundary layer (PBL) by the new triple correlation model are presented. The vertical flux of the horizontal turbulent kinetic energy and correlations  $\langle w^3 \rangle$ ,  $\langle w^2 \theta \rangle$  are calculated from the differential transport equations, whereas other triple correlations necessary for closure are found from algebraic expressions. Computed profiles of vertical flux of the horizontal turbulent kinetic energy and skewness factor of turbulent vertical velocity fluctuations  $S_w = \langle w^3 \rangle / \langle w^2 \rangle^{3/2}$  are in agreement with observed and experimental data: positive across the whole width of the convective PBL including the surface layer. This result follows from the completely algebraic models for the triple correlations  $\langle w^3 \rangle$ ,  $\langle w^2 \theta \rangle$ ,  $\langle w \theta^2 \rangle$  and  $\langle w e'_h \rangle$  derived from analysis of the triple correlations  $\langle w^3 \rangle$  and  $\langle w^2 \theta \rangle$  budget.

## INTRODUCTION

In modeling pollutant dispersion in the convective PBL it is necessary to describe correctly the skewness factor of turbulent vertical velocity fluctuations (Lamb, 1981). The third-order moment models (Andre et al., 1978; Canuto et al., 1994; Ilyushin and Kurbatskii, 1996) used at present can not describe in agreement with experimental data behavior of both the skewness factor  $S_w = \langle w^3 \rangle / \langle w^2 \rangle^{3/2}$  ( $w$  is a vertical velocity fluctuation) and the vertical flux of the turbulent kinetic energy  $\langle w E' \rangle$  ( $E' = 1/2(u^2 + v^2 + w^2)$  and  $u, v$  are turbulent fluctuations of horizontal wind velocity components) across the whole width of the PBL, from the ground up to the upper boundary. Moreover, in the surface layer the calculated skewness factor is negative in contrast with the observed data of Lenschow et al. (1980).

In the new suggested model, turbulent vertical momentum and heat transport emphasizes. The turbulent vertical velocity variance  $\langle w^2 \rangle$  and the triple correlations  $\langle w^3 \rangle$ ,  $\langle w^2 \theta \rangle$ ,  $\langle w e'_h \rangle$  ( $e'_h = 1/2(u^2 + v^2)$ ) are calculated from the

differential transport equations, whereas other triple correlations necessary for closure are found from algebraic expressions. In the transport equations for the triple correlations  $\langle w^3 \rangle$  and  $\langle w^2 \theta \rangle$ , the cumulants  $C_{4w} = \langle w^4 \rangle - 3\langle w^2 \rangle^2$  and  $C_{4\theta} = \langle w^3 \theta \rangle - 3\langle w^2 \rangle \langle w \theta \rangle$  are not equal zero as it follows from Millionshchikov's quasinormality hypothesis, but found from the algebraic equations.

## BASIC DIFFERENTIAL EQUATIONS FOR VERTICAL TURBULENT TRANSPORT

The model of turbulent transport in the PBL homogeneous in the horizontal plates (Ilyushin and Kurbatskii, 1996) includes equations for the mean wind components  $U$  and  $V$ , mean potential temperature  $\theta$ , its dispersion  $\langle \theta^2 \rangle$ , vertical  $\langle w^2 \rangle$  and horizontal  $e_h$  ( $e_h = \langle e'_h \rangle$ ) components of the turbulent kinetic energy, and its dissipation  $\epsilon$ . The shear components of the Reynolds stress tensor  $\langle u_i u_j \rangle$ , horizontal components of the turbulent kinetic energy  $\langle u^2 \rangle$  and  $\langle v^2 \rangle$  as well as heat flux  $\langle u_i \theta \rangle$  are calculated by the gradient transport models (GTM) taking into account both anisotropy of turbulent transport and dependence of the turbulence time scale on the Brunt - Väisälä frequency  $N$  ( $N^2 = \beta g \partial \theta / \partial z$ ). The use of the GTM for moments  $\langle w^3 \rangle$  and  $\langle w E' \rangle$  results, as it is shown by Ilyushin and Kurbatskii (1996), in their qualitatively incorrect behavior in the surface layer, whereas for the correlation  $\langle w \theta^2 \rangle$  it gives adequate results (Ilyushin and Kurbatskii, 1996; Lenschow et al., 1980; Moeng and Wyngaard, 1989). In the new model there are used for calculating the correlations  $\langle w \theta^2 \rangle$  and  $\langle \theta^3 \rangle$  the GTMs derived from the corresponding differential transport equations in the stationary case:

$$\begin{aligned} \langle w \theta^2 \rangle = & -\frac{\tau}{c_7} \left[ \langle w^2 \rangle \frac{\partial \langle \theta^2 \rangle}{\partial z} + 2 \langle w \theta \rangle \frac{\partial \langle w \theta \rangle}{\partial z} \right. \\ & \left. + 2 \langle w^2 \theta \rangle \frac{\partial \theta}{\partial z} - \beta g \langle \theta^3 \rangle \right], \end{aligned} \quad (1)$$



$$\langle \theta^3 \rangle = -\frac{3\tau}{c_{10}} \left[ \langle w\theta \rangle \frac{\partial \langle \theta^2 \rangle}{\partial z} + \langle w\theta^2 \rangle \frac{\partial \Theta}{\partial z} \right],$$

where  $\tau = E/\varepsilon$  is the turbulence (decay) time scale,  $\beta$  is the mean coefficient of thermal expansion,  $g$  is the acceleration of gravity,  $c_7$  and  $c_{10}$  are the model constants. Eliminating  $\langle \theta^3 \rangle$  from set (1), the equation for  $\langle w\theta^2 \rangle$  can be written as

$$\langle w\theta^2 \rangle = -\frac{\tilde{\tau}_3}{c_7} \left[ \left( \langle w^2 \rangle + \frac{3}{c_{10}} \beta g \tau \langle w\theta \rangle \right) \frac{\partial \langle \theta^2 \rangle}{\partial z} + 2 \langle w\theta \rangle \frac{\partial \langle w\theta \rangle}{\partial z} + 2 \langle w^2 \theta \rangle \frac{\partial \Theta}{\partial z} \right] \quad (2)$$

$$\text{where } \tilde{\tau}_3 = \frac{\tau}{1 + 3\tau^2 N^2 / (c_7 c_{10})}.$$

The time scale  $\tilde{\tau}_3$  in (2) takes account of turbulent fluctuation damping in the stable stratified area of the PBL (Weinstock, 1989).

The correlations  $\langle e'_h w \rangle$ ,  $\langle w^3 \rangle$ , and  $\langle w^2 \theta \rangle$  are calculated from the transport equations:

$$\begin{aligned} \frac{\partial \langle e'_h w \rangle}{\partial t} = & -\langle u w^2 \rangle \frac{\partial U}{\partial z} - \langle v w^2 \rangle \frac{\partial V}{\partial z} - \langle w^2 \rangle \frac{\partial e_h}{\partial z} - \langle u w \rangle \frac{\partial \langle u w \rangle}{\partial z} \\ & - \langle v w \rangle \frac{\partial \langle v w \rangle}{\partial z} + \beta g \langle e'_h \theta \rangle - c_7 \frac{\langle e'_h w \rangle}{\tau_3}, \end{aligned}$$

$$\frac{\partial \langle w^3 \rangle}{\partial t} = -\frac{\partial C_{4w}}{\partial z} - 3 \langle w^2 \rangle \frac{\partial \langle w^2 \rangle}{\partial z} + 3 \beta g \langle w^2 \theta \rangle - c_7 \frac{\langle w^3 \rangle}{\tau_3}, \quad (3)$$

$$\begin{aligned} \frac{\partial \langle w^2 \theta \rangle}{\partial t} = & -\frac{\partial C_{4\theta}}{\partial z} - 2 \langle w^2 \rangle \frac{\partial \langle w\theta \rangle}{\partial z} - \langle w\theta \rangle \frac{\partial \langle w^2 \rangle}{\partial z} - \langle w^3 \rangle \frac{\partial \Theta}{\partial z} \\ & + 2 \beta g \langle w\theta^2 \rangle - c_7 \frac{\langle w^2 \theta \rangle}{\tau_3}, \end{aligned}$$

where  $\tau_3$  is the "return-to-isotropy" time scale. The triple pressure containing correlations are modeled as "return-to-isotropy" terms. The equation for  $\langle e'_h w \rangle$  is written with using Millionshchikov's quasinormality hypothesis to express the fourth-order moments through the second-order ones. The correlations  $\langle u w^2 \rangle$ ,  $\langle v w^2 \rangle$ ,  $\langle e'_h w \rangle$ ,  $\langle u w \theta \rangle$ , and  $\langle v w \theta \rangle$  are calculated by the GTM:

$$\langle u w^2 \rangle = -\frac{\tau}{c_7} \left[ \langle w^3 \rangle \frac{\partial U}{\partial z} + \langle u w \rangle \frac{\partial \langle w^2 \rangle}{\partial z} + 2 \langle w^2 \rangle \frac{\partial \langle u w \rangle}{\partial z} \right],$$

$$\langle v w^2 \rangle = -\frac{\tau}{c_7} \left[ \langle w^3 \rangle \frac{\partial V}{\partial z} + \langle v w \rangle \frac{\partial \langle w^2 \rangle}{\partial z} + 2 \langle w^2 \rangle \frac{\partial \langle v w \rangle}{\partial z} \right],$$

$$\begin{aligned} \langle e'_h \theta \rangle = & -\frac{\tau}{c_7} \left[ \langle e'_h w \rangle \frac{\partial \Theta}{\partial z} + \langle w\theta \rangle \frac{\partial e_h}{\partial z} + \langle u w \theta \rangle \frac{\partial U}{\partial z} \right. \\ & \left. + \langle v w \theta \rangle \frac{\partial V}{\partial z} + \langle u w \rangle \frac{\partial \langle u \theta \rangle}{\partial z} + \langle v w \rangle \frac{\partial \langle v \theta \rangle}{\partial z} \right], \end{aligned}$$

$$\begin{aligned} \langle u w \theta \rangle = & -\frac{\tau}{c_7} \left[ \langle u w^2 \rangle \frac{\partial \Theta}{\partial z} + \langle w^2 \theta \rangle \frac{\partial U}{\partial z} + \langle u w \rangle \frac{\partial \langle w\theta \rangle}{\partial z} \right. \\ & \left. + \langle w\theta \rangle \frac{\partial \langle u w \rangle}{\partial z} + \langle w^2 \rangle \frac{\partial \langle u \theta \rangle}{\partial z} \right], \end{aligned} \quad (4)$$

$$\begin{aligned} \langle v w \theta \rangle = & -\frac{\tau}{c_7} \left[ \langle v w^2 \rangle \frac{\partial \Theta}{\partial z} + \langle w^2 \theta \rangle \frac{\partial V}{\partial z} + \langle u w \rangle \frac{\partial \langle w\theta \rangle}{\partial z} \right. \\ & \left. + \langle w\theta \rangle \frac{\partial \langle v w \rangle}{\partial z} + \langle w^2 \rangle \frac{\partial \langle v \theta \rangle}{\partial z} \right] \end{aligned}$$

In correct description of the triple correlation behavior in the stable stratified area of the PBL, the relaxation time scale  $\tau_3$  calculated taking into account the Kolmogorov spectra of turbulent fluctuations depends, as it is shown by Weinstock (1989), on the Brunt - Väisälä frequency as:

$$\tau_3 = \frac{\tau}{1 + H(N^2) \frac{\pi}{18} \tau^2 N^2}, \quad H(N^2) = \begin{cases} 0 & \text{when } N^2 < 0 \\ 1 & \text{when } N^2 \geq 0 \end{cases} \quad (5)$$

For coordinated triple correlations damping in the stable stratified area of the PBL, the condition  $\tilde{\tau}_3 = \tau_3$  at  $N^2 \geq 0$  must be satisfied. From this condition, the relation  $c_{10} = 54/(\pi c_7)$  between the coefficients follows. The value of coefficient  $c_7$  used in papers of different authors changes from 5 to 12. In the present work, it is taken  $c_7 = 6.5$  as the result of numerical optimization of the model: the profiles of  $\langle E'w \rangle$  and  $\langle w^3 \rangle$  calculated by the new model were compared with the observed data.

The use of Millionshchikov's quasinormality hypothesis for closing the triple correlation transport equations does not yield physically correct description of the correlation behavior in the PBL as well as in modeling the pollutant dispersion from the point sources in homogeneous turbulence (Deardorff, 1978). To develop necessary mechanism for the triple correlations damping, it was suggested by Deardorff (1978) to modify the cumulantless approximation by adding the diffusion term "to downgradient" to the common model quasinormal expression for the quadruple correlation. That idea was used in this work also, with the differential transport equations for  $\langle w^2 \rangle$  and  $\langle w^4 \rangle$  being solved. In the transport equation for  $\langle w^4 \rangle$ , the fifth-order moment is expressed through the second- and third-order ones by the relation  $\langle w^5 \rangle = 10 \langle w^2 \rangle \langle w^3 \rangle$  following from Gram-Charlier series expansion of the probability density function of the turbulent velocity field and their following truncation on the fourth-order terms. The series convergence for the probability density function of the turbulent velocity field in the boundary layer under a plane was shown by Jovanovic et al. (1993). Thus, the equation for the cumulant  $C_{4w}$  in the high Reynolds number approximation and buoyancy effect disregard can be written as

$$\begin{aligned} \frac{\partial C_{4w}}{\partial t} = & \frac{4}{\rho} \left\{ \left\langle w^3 \frac{\partial p}{\partial z} \right\rangle - 3 \langle w^2 \rangle \left\langle w \frac{\partial p}{\partial z} \right\rangle \right\} \\ & - 4 \langle w^2 \rangle \frac{\partial \langle w^3 \rangle}{\partial z} - 6 \langle w^3 \rangle \frac{\partial \langle w^2 \rangle}{\partial z}. \end{aligned} \quad (6)$$

With the relaxation model applying to the cumulant of the pressure containing correlation (the terms in the braces), it is possible to derive from (6) the algebraic model for the cumulant  $C_{4w}$  in the stationary case:

$$C_{4w} = -\frac{\tau}{c_k} \left[ 6 \langle w^3 \rangle \frac{\partial \langle w^2 \rangle}{\partial z} + 4 \langle w^2 \rangle \frac{\partial \langle w^3 \rangle}{\partial z} \right] \quad (7)$$

In the same way, the model for the mixed cumulant  $C_{4\theta}$  is derived:

$$C_{4\theta} = -\frac{\tau}{c_k} \left[ 3 \langle w^3 \rangle \frac{\partial \langle w\theta \rangle}{\partial z} + \langle w\theta \rangle \frac{\partial \langle w^3 \rangle}{\partial z} + 3 \langle w^2 \theta \rangle \frac{\partial \langle w^2 \rangle}{\partial z} + 3 \langle w^2 \rangle \frac{\partial \langle w^2 \theta \rangle}{\partial z} \right] \quad (8)$$

Equations (7) and (8) close set (3). Testing models (7) and (8) showed that buoyancy effects do not influence noticeably on the calculated profiles of the correlations  $\langle w^3 \rangle$  and  $\langle w^2 \theta \rangle$  if the correlations  $\langle w\theta^2 \rangle$  and  $\langle \theta^3 \rangle$  are calculated from the differential transport equations and the correlations  $\langle w^3 \rangle$  and  $\langle w^2 \theta \rangle$  are found by the GTM, as it is suggested in the new triple correlation model.

The realizability conditions derived from generalized Schwarz' inequalities for the triple covariance of the vertical turbulent velocity is the following (Andre et al., 1976):

$$\langle w^4 \rangle \geq \langle w^3 \rangle^2 / \langle w^2 \rangle + \langle w^2 \rangle^2. \quad (9)$$

Necessary relaxation of the correlation  $\langle w^3 \rangle$  by Andre et al. (1976, 1978) is achieved by clipping its value ("clipping approximation") with the use of inequality (9) in which  $\langle w^4 \rangle = 3 \langle w^2 \rangle^2$  (the quasnormality hypothesis) is assumed. It is possible to note, that such procedure is not physically correct. Taking into account (9), more strong the inequality for the cumulant can be written:

$$C_{4w} \geq \langle w^3 \rangle^2 / \langle w^2 \rangle \quad (10)$$

Condition (10) is used to estimate the value of the coefficient  $c_k$  in (7) and (8). For this, there is considered decay of homogeneous turbulence satisfying the following relations:

$$\begin{aligned} \langle w^2 \rangle &= \langle w^2 \rangle_0 \exp(-t^*) \\ \langle w^3 \rangle &= \langle w^3 \rangle_0 \exp(-c_7 t^*), \\ C_{4w} &= C_{4w0} \exp(-c_k t^*), \end{aligned} \quad (11)$$

where  $t^*$  is transformed time ( $dt^* = dt/\tau$ ). Then, it follows from (10) taking into account (11) that  $c_k \leq 2c_7 - 1$ . From the Gram - Charlier series convergence, the additional condition for the coefficients run out  $1 < c_7 < c_k$ . Estimate for  $c_k$  is written as  $c_7 < c_k \leq 2c_7 - 1$ . In calculations the upper value of this estimate  $c_k = 2c_7 - 1$  is used. Decreasing the coefficient  $c_k$  value causes decreasing maximum values of the correlations  $\langle w^3 \rangle$  and  $\langle wE' \rangle$ .

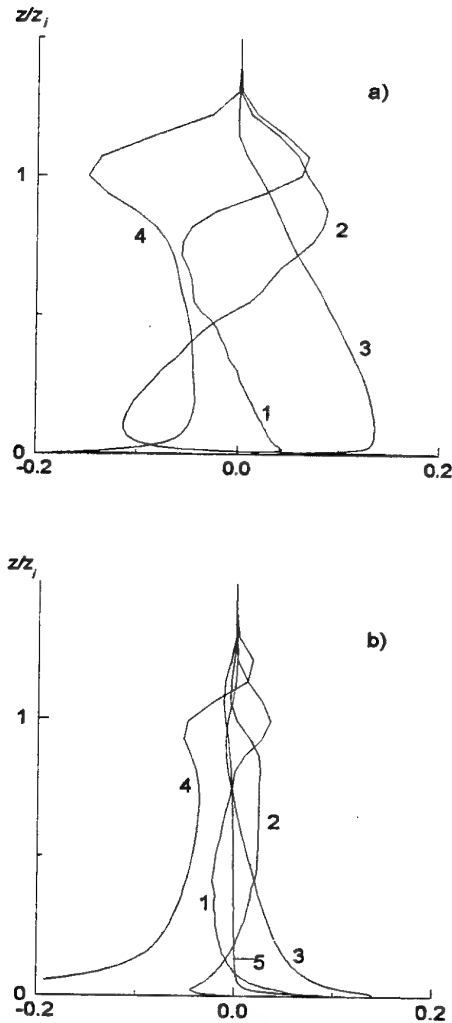


Fig. 1. The normalized budget of  $\langle w^3 \rangle$  - equation (a) and  $\langle w^2 \theta \rangle$  - equation (b): 1 - turbulent diffusion  $\partial C_4 / \partial z$ , 2 - second-order moment gradient production, 3 - buoyant production, 4 - pressure-correlation effects, 5 - temperature gradient production.

#### ALGEBRAIC MODEL FOR TRIPLE CORRELATIONS

Model (1)-(5) for the third-order moments in which vertical transport is emphasized, i.e., triple correlations  $\langle w^3 \rangle$ ,  $\langle E'w \rangle$  and  $\langle w^2 \theta \rangle$  are calculated from the differential transport equations, is more simple than the model of Andre et al. (1978) in which all triple correlations are calculated from the transport equations. However, model (1)-(5) also needs large computer time to calculate evolution of the PBL. For practical applications, for example, modeling of pollutant dispersion in the PBL, the completely algebraic model possessing main properties of model (1)-(5) in accuracy of prediction of the third-order moments over the whole PBL thickness, from the ground to the upper boundary, would be more preferable.

Analyzing behavior of the calculated balance terms (Fig. 1 a,b) in the equations  $\langle w^3 \rangle$  and  $\langle w^2 \theta \rangle$  in (3), the following local balance relations can be written:

$$-c_7 \frac{\langle w^3 \rangle}{\tau_3} - 3 \langle w^2 \rangle \frac{\partial \langle w^2 \rangle}{\partial z} + 3\beta g \langle w^2 \theta \rangle = 0, \quad (12)$$

$$-c_8 \frac{\langle w^2 \theta \rangle}{\tau_3} + 2\beta g \langle w \theta^2 \rangle = 0. \quad (13)$$

As shown by Lenschow et al.(1980), the correlation  $\langle w \theta^2 \rangle$  is calculated correctly by the gradient-type diffusion model. However, it overpredicts near the inversion layer:

$$-\langle w \theta^2 \rangle = \frac{\tau_3}{c_7} \left[ \langle w^2 \rangle \frac{\partial \langle \theta^2 \rangle}{\partial z} + 2 \langle w \theta \rangle \frac{\partial \langle w \theta \rangle}{\partial z} + 2 \langle w^2 \theta \rangle \frac{\partial \theta}{\partial z} \right]. \quad (14)$$

To correct this failure, the relaxation time scale must be taken in form (5) to damp turbulence in the inversion layer area (Weinstock,1989). From (12) and (13), the following expressions for  $\langle w^2 \theta \rangle$  and  $\langle w^3 \rangle$  are derived:

$$\langle w^2 \theta \rangle = \frac{2\tau_3}{c_8} \beta g \langle w \theta^2 \rangle, \quad (15)$$

$$\langle w^3 \rangle = -\frac{3\tau_3}{c_7} \left[ \langle w^2 \rangle \frac{\partial \langle w^2 \rangle}{\partial z} - \beta g \langle w^2 \theta \rangle \right], \quad (16)$$

where  $\tau_3$  is determined from (5). Substitution of (14) in (15) yields the algebraic expression to calculate the correlation  $\langle w^2 \theta \rangle$ :

$$\langle w^2 \theta \rangle = -\frac{2\beta g}{c_7 c_8} \tau_3 \tilde{\tau}_3' \left[ \langle w^2 \rangle \frac{\partial \langle \theta^2 \rangle}{\partial z} + 2 \langle w \theta \rangle \frac{\partial \langle w \theta \rangle}{\partial z} \right], \quad (17)$$

$$\text{where } \tilde{\tau}_3' = \frac{\tau_3}{1 + \frac{4}{c_7 c_8} \tau_3^2 N^2}. \quad (18)$$

As test have shown, to calculate correctly the correlation  $\langle w^2 \theta \rangle$  over the whole PBL thickness, behavior of time scale  $\tilde{\tau}_3'$  and  $\tau_3$  must be compatible:

$$\frac{4}{c_7 c_8} = \frac{\pi}{18}. \quad (19)$$

The value of the coefficient  $c_8 = 72/(\pi c_7) \approx 2.5$  is determined from condition (19) ( $c_7 = 6.5$  as in model (1)-(5)). Assuming  $c_7 = c_8 = 8.0$  (Andre et al.,1978), behavior of  $\tilde{\tau}_3'$  proves to be in disagreement with that of  $\tau_3$ , and, as consequence, the profile  $\langle w^2 \theta \rangle$  is calculated incorrectly.

To calculate a vertical flux of the horizontal turbulent kinetic energy  $\langle w e_h' \rangle$ , the simple gradient-type diffusion model can be used:

$$\langle w e_h' \rangle = -0.25 \tau_3 E \frac{\partial e_h}{\partial z}. \quad (20)$$

Equations (14),(16),(17) and (20) form the algebraic model for the third-order moments of vertical turbulent transport.

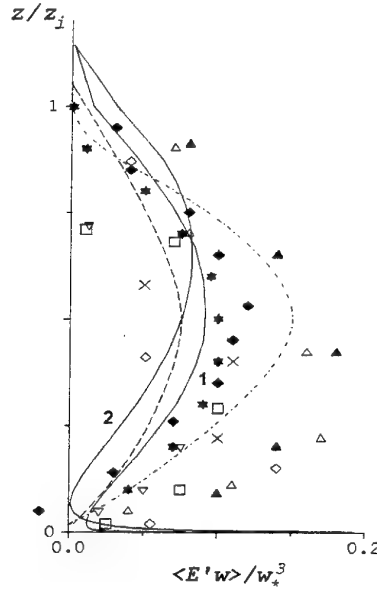


Fig. 2. The profiles of turbulent kinetic energy vertical flux: solid line - calculated by the model presented in this work (1 - the differential model and 2 - the algebraic model), dashed line - calculated by Andre et al.(1978), dash-dotted line - LES data of Moeng and Wyngaard (1989),  $\diamond$  - experimental data of Willis and Deardorff (1974),  $\star$ ,  $\triangle$ ,  $\times$ ,  $\square$ ,  $\circ$ ,  $\nabla$ ,  $\triangle$  - observed data of Lenschow et al.(1980).

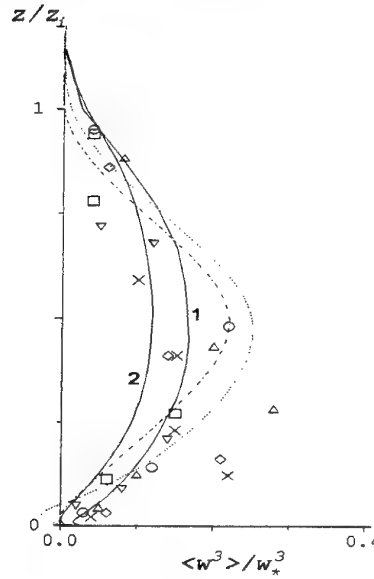


Fig. 3. The profiles of correlation  $\langle w^3 \rangle$ , lines and symbols as fig. 2; dotted line - calculated by Canuto et al.(1994).

## RESULTS OF CALCULATION

The calculated profiles of the vertical turbulence energy flux  $\langle E'w \rangle$  and the triple velocity correlation  $\langle w^3 \rangle$  ( $w_* = (\beta g z_i Q_0)^{1/3}$  - is the velocity scale in the PBL,  $Q_0$  is turbulent heat flux on the surface,  $z_i$  is the height of the inversion layer) across the whole width of the PBL are shown in Figs. 2-3 by solid lines (1 - the differential model and 2 - the algebraic model). Calculations correspond to 4

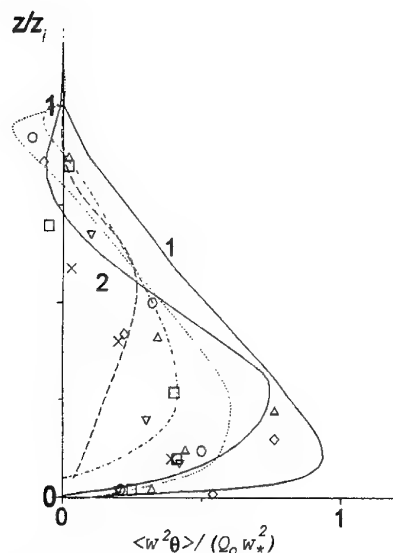


Fig. 4. Profile of the vertical flux of turbulent convective flux, lines and symbols as fig.2. Dashed line: calculated by Sun and Ogura (1980).

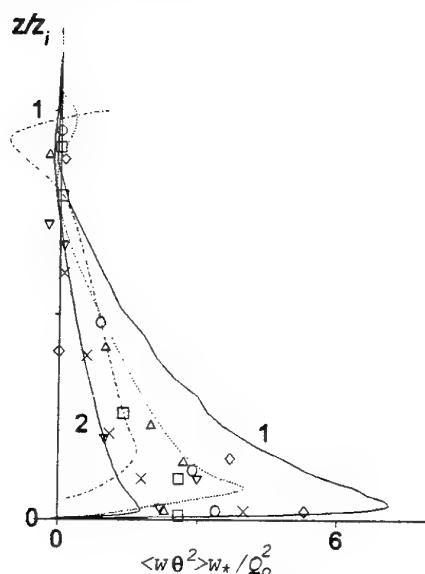


Fig. 5. The profile of correlation  $\langle w\theta^2 \rangle$ , lines and symbols as fig. 4.

p.m. (the developed the PBL). The dots of different configurations show the observed data as well as the experimental ones. Moreover, the vertical profile of  $\langle E'w \rangle$  calculated by Andre et al.(1978) is given by dashed line. It is seen, that the triple correlation profiles calculated by the new model are positive across the whole PBL including the surface layer. The observed data of Lenschow et al.(1980) lie in large range and the experimental data of Willis and Deardorff (1974) correspond to the PBL without mean wind. Differences between the profiles of  $\langle E'w \rangle$  calculated by the new model and the one suggested by Andre et al.(1978), when all correlations up to the triple ones were found from the prognostic differential transport equations, are negligible.

The profiles of the triple correlations  $\langle w^2\theta \rangle$  and  $\langle w\theta^2 \rangle$  across the layer height which were calculated by models (2) and (3) as well as the observed data of Lenschow et al.(1980) are shown in Figs. 4-5. It is possible to note that in the lower part of the mixed layer behavior of  $\langle w^2\theta \rangle$  calculated by the new model correspond qualitatively correctly to the observed data, because in the equation for  $\langle w\theta \rangle$  in (3) there is the term  $\langle w^3 \rangle \partial \theta / \partial z$ . To ignore this term (Sun and Ogura, 1980) leads to qualitatively incorrect behavior of  $\langle w^2\theta \rangle$  in the lower part of the PBL (dotted line in Fig. 4). For comparison on Figs.2-5 there are shown also LES data of Moeng and Wyngaard (1989) and on Fig.3 the profile  $\langle w^3 \rangle$  calculated by Canuto et al.(1994) in the shearless convective PBL. One can see, the profile  $\langle w^3 \rangle$  in area of the surface layer is negative. It should be noted that there is difference in behavior of the vertical flux  $\langle wE' \rangle$  near ground when it is calculated by model (1)-(5) and by algebraic one (Fig.2). Model (20) does not take into account the influence of mean wind gradient explicitly. However, the results obtained by both models (Figs. 2-5) do not differ significantly and, therefore, the new algebraic model for the third-order moments  $\langle w^3 \rangle$ ,  $\langle w^2\theta \rangle$ ,  $\langle w\theta^2 \rangle$  and  $\langle wE' \rangle$  allows us to parametrize vertical turbulent transport with satisfactory accuracy: the calculated correlation  $\langle w^3 \rangle$  and  $\langle wE' \rangle$  are positive over the whole PBL thickness, including the surface layer. In comparison with differential model, the algebraic model has high computational efficiency.

## CONCLUSIONS

Thus, the new model for the triple correlations gives the profiles  $\langle w^3 \rangle$  and  $\langle E'w \rangle$  positive in the whole width of the PBL including the surface layer without using physically incorrect procedure of "clipping approximation" (Andre et al., 1976, 1978) for the triple correlation values. Computing efficiency of the new model is achieved by means of minimized calculation of the triple correlations from the differential transport equations. To physically correct description of vertical transport, it is necessary to solve three transport equations for the triple correlations  $\langle w^3 \rangle$ ,  $\langle w^2\theta \rangle$ , and  $\langle e'_h w \rangle$ . All other triple correlations necessary to closure are calculated by the GTM. New algebraic model for the triple correlations of vertical turbulent transport in the PBL predicts with satisfactory accuracy the positive profiles of  $\langle w^3 \rangle$  and  $\langle wE' \rangle$  over the whole PBL thickness, including the surface layer, and can be used for parametrization.

This work was financially supported by the Russian Foundation for Basic Research (Grant N 96-05-64007).

## REFERENCES

- Andre, J.C., De Moor, G., Lacarrere, P. and Du Vachat, R., 1976, "Turbulence approximation for inhomogeneous flow: Part 1. The clipping approximation," *J. Atmos. Sci.*, Vol.33, pp.476-481.
- Andre, J.C., De Moor, G., Lacarrere, P., Therry, G., du Vachat, R., 1978, "Modeling the 24-hour evolution of the mean and temperature structures of the planetary boundary layer," *J. Atmos. Sci.*, Vol.35, pp.1861-1883.
- Canuto, V.M., Minotti, F., Ronchi, C., Ypma, R.M., Zeman, O., 1994, "Second-order closure PBL model with new third-order moments: comparison with LES data," *J. Atmos. Sci.*, Vol.51, pp.1605-1618.

Deardorff, J.W., 1978, "Closure of second- and third-moment rate equations for diffusion in homogeneous turbulence," *Phys.Fluids*, Vol.21, pp.525-530.

Ilyushin, B.B. and Kurbatskii, A.F., 1996, "Modeling of Contaminant Dispersion in the Atmospheric Convective Boundary Layer," *Izv. RAN. Fizika Atmos. and Okeana*, Vol.32, pp.307-322.

Jovanovic, J., Durst, F., 1993, "Statistical analysis of dynamic equations for higher-order moments in turbulent wall bounded flows," *Phys.Fluids A*, Vol.5, pp.2886-2900.

Lamb, R.G., 1981, "The dispersion of pollutant in convective boundary layer. In Atmospheric Turbulence and Air Pollution Modelling (ed. F.T.M. Nieuwstadt and H. Van Dop). (1981). Dordrecht: Holland / Boston: U.S.A. / London: England.

Lenschow, D.H., Wyngaard, J.C., Pennel, W.T., 1980, "Mean-field and second-moment budgets in a baroclinic, convective boundary layer," *J.Atmos.Sci.*, Vol.37, pp.1313-1326.

Moeng, C.-H. and Wyngaard, J. C., 1989, "Evaluation of turbulent transport and dissipation closures in Second-order modeling," *American Meteorological Society*, Vol.46, pp.2311-2330.

Sun, W.-Y. and Ogura, Y., 1980, "Modeling the evolution of the convective planetary boundary layer," *J.Atmos.Sci.*, Vol.37, pp.1558-1572.

Weinstock, J. A., 1989, "Theory of turbulent transport," *J.Fluid Mech.*, Vol.202, pp.319-338.

Willis, G.E., Deardorff, J.W., 1974, "A laboratory model of the unstable planetary boundary layer," *J.Atmos.Sci.*, Vol.31, pp.1297-1307.

# MIXING IN A STABLY-STRATIFIED SHEAR LAYER

C. Staquet

Laboratoire de Physique  
Ecole normale supérieure de Lyon  
46 allée d'Italie  
69364 Lyon cdx 07  
France

K.B. Winters

Applied Physics Laboratory  
University of Washington  
Henderson Hall HN-10  
Seattle WA 98105-6698  
USA

## ABSTRACT

The analysis of mixing in stably-stratified fluids proposed by Winters *et al.* (1995) has been applied to high resolution direct numerical simulations of a shear layer performed by Staquet (1994, 1995). Winters *et al.* proposed to define the mixing efficiency from the *diffusive* flux across the isopycnals, for which they derive an analytical expression, instead of using the *advective* buoyancy flux (as this is usually done in oceanography). Both definitions are compared in the present work. These definitions become close during the later stage of the flow only, when the dynamics are weakly nonlinear. The value of mixing efficiency then compares very well with that found in the oceanic thermocline. When the flow dynamics are strongly nonlinear by contrast, only the definition based upon the diffusive flux is able to provide an instantaneous estimate of mixing efficiency, as it remains strictly positive.

## INTRODUCTION

In a stably-stratified fluid, mixing ultimately involves the smallest scales of the flow, at which molecular processes are acting. A precise and direct measurement of vertical mixing seems to be difficult in laboratory experiments for instance. Even in the academic situation of mixing across a sharp density interface between two fluids, respectively at rest and perturbed by an oscillating grid, no conclusion can be drawn for the entrainment law, which characterizes the rate of mixing (Fernando 1991). One reason is very likely that mixing, though occurring at dissipative scales, is controlled by large scale processes. More generally, the relation between flow dynamics and mixing is an open question and most studies of mixing first aim at estimating whether mixing is weak or strong compared to molecular diffusion. This will also be the purpose in the present study.

We shall first present a new definition of mixing efficiency, based upon previous works by Lorenz (1955), Thorpe (1977) and Winters *et al.* (1995). The work by Winters *et al.* contains the key for such a definition, in providing an analytical expression for the diffusive flux of scalar. This work will next be applied to a shear layer sub-

jected to a strong stratification, whereof dynamics have been obtained by two-dimensional direct numerical simulations of high resolution (Staquet 1994, 1995).

## DIFFUSIVE VERSUS ADVECTIVE FLUX OF DENSITY

The analysis of mixing we shall use is based upon a few fundamental ideas.

In a stably-stratified fluid, energy is required to mix the fluid: kinetic energy is required to raise heavy fluid, thus producing potential energy.

Only a part of this potential energy is used to mix the fluid. The other part is reversibly converted into vertical kinetic energy, and is usually referred to as the available potential energy,  $E_a$ . The part of potential energy associated with mixing, the background potential energy  $E_b$ , is the minimum potential energy of the fluid. Indeed, let us consider a turbulent flow subjected to a stable stratification. When all fluctuations have ceased, for instance by viscous dissipation or because these fluctuations were associated with internal waves that have propagated away, the fluid has returned to rest and its potential energy is  $E_b$ . It is minimum in the sense that any density fluctuation will make it increase. It is not available in the sense that any fluid particle has reached its minimum level and cannot be displaced further downwards.

In general,  $E_b$  is not simply the potential energy of a horizontally averaged density profile. Rather,  $E_b$  is the potential energy of a "sorted" density profile. These ideas go back to Lorenz (1955) and have been applied to one-dimensional experimental density profiles by Thorpe (1977). In the latter case, the sorted profile is obtained by sorting the fluid parcels so that the heaviest one has the lowest altitude and the lightest one occupies the highest altitude. Thus, the sorted profile is stable. Winters *et al.* (1995) and Winters & d'Asaro (1996) have provided a mathematical framework to extend these ideas to three dimensions.

Their analysis provides an analytical expression for the

rate of change of the background potential energy:

$$\frac{dE_b}{dt} = \Phi_d \quad (1)$$

with

$$\Phi_d = \kappa g \left\langle \frac{|\nabla \rho|^2}{-\frac{d\rho}{dz}} \right\rangle, \quad (2)$$

where  $\langle \rangle$  denotes a volume average.  $\Phi_d$  is the *diffusive* flux of density (more generally, of scalar). This flux can only occur across the isopycnals (or constant density surfaces) and is thus a diapycnal diffusive flux.  $d\rho/dz_*$  is the vertical gradient of the sorted density profile  $\rho(z_*)$ , with  $z_*(x, y, z)$  denoting the position in the sorted profile of the fluid parcel located at position  $(x, y, z)$ .  $\kappa$  and  $g$  respectively refer to the diffusion coefficient for density changes and to the acceleration of gravity. Since the sorted profile is stable, equation (2) implies that  $\Phi_d$  is strictly positive. Hence, the potential energy associated with mixing can only increase from equation (1), which is physically correct.

The importance of the diapycnal diffusive flux stems from the fact that, in the ocean, the diapycnal flux is usually estimated by  $g\langle \rho'w' \rangle$  that is, by the downgradient *advective* flux of density (e.g. Gregg 1987). This flux being unknown, one model proposed by Osborn & Cox (1972) assumes that, for a homogeneous and steady flow, the downgradient advective flux is balanced by the dissipation rate of density fluctuations, which can be estimated from microstructure measurements. This balance writes:

$$\langle \rho'w' \rangle = \kappa \left\langle \frac{|\nabla \rho'|^2}{-\frac{d\rho}{dz}} \right\rangle. \quad (3)$$

In such a model, the vertical gradient of the mean density profile  $-\frac{d\rho}{dz}$  is assumed to be larger than the vertical scale at which turbulent motions occur and is thus constant. As investigated by Davis (1994) for instance, this balance is approximate. Also,  $d\rho/dz$  can be of either sign so that  $\langle \rho'w' \rangle$  is not strictly positive.

Mixing is usually characterized by a mixing efficiency coefficient. This coefficient is defined by the total diapycnal flux (i.e. the rate of increase of potential energy associated with mixing) relative to the rate of input of energy to the fluid. When the flow is not forced, the dissipation rate of kinetic energy is rather used. In the ocean, the mixing efficiency is defined by

$$\gamma_a = \frac{\langle \rho'w' \rangle}{\epsilon}, \quad (4)$$

$\langle \rho'w' \rangle$  being estimated by the model of Osborn & Cox. We propose to rather define this coefficient as:

$$\gamma_d = \frac{\Phi_d - \Phi_{lam}}{\epsilon}, \quad (5)$$

$\Phi_{lam}$  being the diffusive flux due to molecular effects only, in the absence of density fluctuations: this flux corresponds to a laminar diffusive flux. Thus,  $\Phi_d - \Phi_{lam}$  represents the diffusive flux due to density fluctuations only and corresponds to the diapycnal *turbulent* diffusive flux. Since  $\Phi_d - \Phi_{lam}$  is strictly positive,  $\gamma_d$  is also positive. Thus, in addition to provide a physically more consistent definition of mixing efficiency, (5) also provides an instantaneous estimate for this efficiency.

## DIRECT NUMERICAL SIMULATIONS OF A TWO-DIMENSIONAL STABLY-STRATIFIED SHEAR LAYER: NUMERICAL MODEL AND FLOW DYNAMICS

### Equations of motions and numerical method

Let  $(x, y, z)$  be a Cartesian coordinate system where  $x$  is in the direction of the mean flow,  $y$  in the spanwise

direction and  $z$  points upwards. We study a temporal shear layer, that is, a flow which is statistically uniform in the horizontal plane and develops in time. We assume that the fluid motion is described by the two-dimensional Navier-Stokes equations in the Boussinesq approximation:

$$\frac{\partial \omega}{\partial t} + Jac(\omega, \psi) = \frac{g}{\rho_0} \frac{\partial \rho}{\partial x} + \nu \nabla^2 \omega \quad (6)$$

$$\frac{\partial \rho}{\partial t} + Jac(\rho, \psi) = \kappa \nabla^2 \rho.$$

$\psi$  is a stream function related to the velocity field by  $u = -\partial\psi/\partial z$ ,  $w = \partial\psi/\partial x$ . The vorticity field has only one component in this two-dimensional situation, along the spanwise direction, and is related to  $\psi$  by  $\omega = -\Delta\psi$ . As well, the baroclinic torque, which only involves density gradients in the Boussinesq approximation, is simply proportional to the streamwise gradient of the density field  $\rho$ .  $Jac$  denotes the Jacobian function and  $\nu$  is the kinematic viscosity.

We decompose  $\rho$  as  $\rho(x, z, t) = \rho_0 + \bar{\rho}(z, t) + \rho'(x, z, t)$ , where  $\rho_0$  is a constant density reference,  $\bar{\rho}(z, t)$  is the mean (horizontally averaged) density and  $\rho'$  is the deviation from the mean. The initial mean velocity and mean density profiles are similarity solutions of the viscous Boussinesq equations:

$$\bar{U}_i(z) = U \operatorname{erf}\left(\frac{\sqrt{\pi}}{2} \frac{z}{\delta_i}\right) \quad (7)$$

$$\bar{\rho}_i(z) = -\frac{\Delta\rho}{2} \operatorname{erf}\left(\frac{\sqrt{\pi}}{2} \frac{z}{\delta_i/\sqrt{Pr}}\right).$$

No density perturbation is superposed initially upon the mean density profile. By contrast, a two-dimensional perturbation is superimposed upon the mean velocity field at  $t = 0$ , in order to promote the development of the Kelvin-Helmholtz instability. For boundary conditions, we assume that the flow is periodic in the streamwise direction, and at the horizontally oriented boundaries take free slip conditions on the velocity.

Equations (6) have been solved numerically in dimensionless form. The length and velocity scales are  $\delta_i$  and  $U$  respectively and time is made dimensionless using the advective time scale  $\delta_i/U$ . The density is scaled by  $\Delta\rho/2$ . With this scaling, the dimensionless parameters which come into play in the equations are:  $Re$ , the Reynolds number, initially equal to  $U\delta_i/\nu$ ; the minimum Richardson number, whose expression at  $t=0$  is

$$J = g \frac{\Delta\rho}{\rho_0} \frac{\sqrt{Pr}}{2} \frac{\delta_i}{U^2} \quad (8)$$

and the Prandtl number  $Pr = \nu/\kappa$  (which has the constant value of 0.7). Three calculations will be presented, with values of the set of parameters  $(J, Re)$  equal to

- run R1:  $(J, Re) = (0.083, 1000)$
- run R2:  $(J, Re) = (0.167, 1000)$
- run R3:  $(J, Re) = (0.167, 2000)$ .

Equations (6) have been solved using a pseudo-spectral method (e.g. Canuto et al. 1988): the spatial derivatives are computed in Fourier space while the nonlinear terms are computed in physical space. Along the vertical direction where free slip boundary conditions are imposed, the use of Fourier transforms is made possible by symmetrizing the velocity components and the density field about the  $z$ -boundary (Orszag 1971, Appendix II): On the doubled domain,  $u$  is expanded in a cosine series in  $z$  and  $w$  and  $\rho$  in a sine series in  $z$ , which enforces the boundary conditions.

### Overall flow dynamics

The detailed evolution of the three runs mentioned above has been described in Staquet (1994, 1995) and only the

stages of interest for the study of mixing will be recalled here.

The shear layer is strongly stratified (especially for  $J = 0.167$ ) but still unstable. The Kelvin-Helmholtz instability thus grows but yields Kelvin-Helmholtz vortices of weaker circulation than in the unstratified case. This instability saturates at about  $t = 50$ . The strong stratification yields thin layers associated with sharp vertical gradients of density and velocity, located in between the Kelvin-Helmholtz vortices. These layers, referred to as 'baroclinic layers' in Staquet (1995), may become unstable, in particular through secondary small scale Kelvin-Helmholtz instabilities (at  $t \approx 85$ ). In the three calculations we present in this paper, only in run R3 do these secondary instabilities develop (figure 1a). For the purpose of mixing study, these calculations have been pursued over a much longer time (more than 300 time units), up the time the small scale fluctuations have been weakened by diffusion (figures 1b and 1c).

## DIRECT NUMERICAL SIMULATIONS OF A TWO-DIMENSIONAL STABLY-STRATIFIED SHEAR LAYER: ANALYSIS OF MIXING

### Sorted versus horizontally averaged density profile

The analysis of mixing proposed by Winters et al. (1995) and Winters & d'Asaro (1996) relies on a sorted density profile  $\rho(z_*)$ , whereof potential energy is minimum. The sorted profile for run R3 is compared to the horizontally averaged density profile  $\bar{\rho}(z)$  in figure 2a, at the times figures 1a and 1b are plotted. At  $t = 85$ , the two profiles strongly differ: the sorted profile is stable, par construction, while the mean profile displays a strong overturning about the center of the layer. Thus its vertical gradient is not one-signed. At  $t = 360$ , the mean profile has also become stable (figure 2b). However, it does not account for the mixing of density about the center of the layer. Only the sorted profile accounts for this behavior.

### Quantitative estimate of the diapycnal diffusive flux

The total diffusive flux  $\Phi_d$  is compared to the laminar diffusive flux  $\Phi_{lam}$  in figure 3. No density fluctuations is present at  $t = 0$  so that  $\Phi_d/\Phi_{lam}$  is equal to 1 initially. This ratio next increases and displays a first maximum about  $t = 50$ , when the Kelvin-Helmholtz instability saturates. This maximum has the greatest value for the weakest stratified flow, because the vertical extent of the Kelvin-Helmholtz vortex is the highest then. Thus, the larger the vertical scale of the instability, the higher the (instantaneous) diapycnal flux is. This point is reinforced by the fact that, for a given value of  $J$ , a higher Reynolds number (and thus a lower viscosity but a larger vertical extent of the instability) promotes a higher value of  $\Phi_d/\Phi_{lam}$ . For run R1,  $\Phi_d/\Phi_{lam}$  next decreases down to a value slightly greater than 1. By contrast, this ratio for run R3 keeps increasing beyond the first maximum at  $t = 50$ , because of secondary small scale instability. No such instability occurs in run R2, and the maximum value reached by  $\Phi_d/\Phi_{lam}$  is the smallest in this calculation. In all three calculations,  $\Phi_d/\Phi_{lam}$  eventually decays smoothly, reaching a value slightly larger than 1. This attests of the presence of weak density fluctuations compared to the background density.

### Diffusive and advective density fluxes: comparison

The turbulent diffusive flux of density  $\Phi_d - \Phi_{lam}$  is compared to the advective flux of density  $\langle \rho w \rangle$  in figure 4, for run R3 only. An analogous behavior is observed for runs R1 and R2.

As expected from an advective flux,  $\langle \rho w \rangle$  displays oscillations of large amplitude about zero. By contrast, the turbulent diffusive flux is one-signed, by construction. It is interesting to note that, when density fluctuations have weakened at the end of the calculation, both quantities become of the same order. Only at the end of the calculations, therefore, do  $\gamma_a$  and  $\gamma_d$ , respectively defined by (4) and (5), become close.

### Instantaneous mixing efficiency

$\gamma_d$  defined by (5) is plotted for runs R1, R2 and R3 in figure 5. This coefficient starts from zero, because  $\Phi_d = \Phi_{lam}$  at initial time, and strongly increases next, as the Kelvin-Helmholtz instability develops.  $\gamma_d$  reaches an absolute maximum value for run R1 at  $t \approx 50$ , which is the highest value of the three runs because the vertical extent of the instability is the largest, as noted above. For runs R2 and R3, which only differ by the value of the Reynolds number,  $\gamma_d$  reaches the same value when the Kelvin-Helmholtz instability saturates, at  $t \approx 50$ . This value is three times lower than for run R1. The occurrence of secondary instabilities in run R3 is next responsible for a further increase of  $\gamma_d$  but the level reached for run R1 is not attained.

As the small scale instabilities are progressively weakened by diffusion,  $\gamma_d$  decays. An asymptotic value seems to be reached in all three runs, close to 0.2. As we showed in figure 4, the definitions of mixing efficiency based upon the advective and diffusive flux of density become close at the later stage of flow. It is then noteworthy to recall that the value of mixing efficiency in the oceanic thermocline, where shear instability processes occur as well, is of order 0.2. One wonders then whether the simple structure of the flow associated with the asymptotic value of  $\gamma_d$  in our calculations, is not generic of those at which mixing occurs in the ocean (figures 1b and 1c). Further work is required to examine this important point.

We should comment about the high value we find for mixing efficiency maxima. In laboratory experiments, mixing efficiency values are at most 0.4, which is one order of magnitude less than values found in our simulations. We think that the two-dimensional character of our calculations is responsible for this behaviour. In two dimensions, the vorticity is conserved by nonlinear terms, which prevents energy from being transferred toward small scales (but note that vorticity can locally increase beyond its maximum value through linear -stratification- effects). The fact that no cascade of energy is allowed toward small scales very likely yields an anomalously small (compared to a three-dimensional situation) value of the dissipation rate of kinetic energy. We think that this accounts for the large value of mixing efficiency that we find. Three-dimensional effects would mostly yield smaller scale instabilities, such as buoyancy induced instabilities (e.g. Schowalter et al. 1994), and enhanced kinetic energy dissipation. However, as time elapses, diffusion should damp all small scale motions, whether two- and three-dimensional. We therefore think that the later stage of the flow, and associated mixing efficiency, should be independent upon the flow dimensionality.

## CONCLUSIONS

We have applied a new mathematical formalism developed by Winters et al. (1995) to analyse mixing in stably-stratified inhomogeneous flows. This formalism provides an analytical expression for the rate of increase of the potential energy associated with mixing, that is, for the diffusive flux of density. This permits to propose a new definition of mixing efficiency, defined by the ratio of the total turbulent diffusive flux of density over the dissipation rate of kinetic energy. Such mixing efficiency can be defined



instantaneously, as opposed to previous definition used in the ocean.

For the case of a two-dimensional stably-stratified shear layer, we find two main results: the efficiency of mixing is strongly sensitive to whether turbulence occurs through large or small scale instabilities (being greater in the former case than in the latter); as the small scale fluctuations become damped by diffusion, the mixing efficiency tends toward an asymptotic value, whatever the initial value of the Richardson and Reynolds numbers. This value is of order 0.2, which is the common value measured for mixing efficiency in the oceanic thermocline. Further work remains however to be done to determine whether the associated structure of the flow could be generic of those at which mixing occurs in the ocean.

#### ACKNOWLEDGEMENTS

This work has been initiated during a visit of KBW at ENS Lyon, thanks to a CNRS Associate Researcher position. Calculations have been performed on the Cray C98 of IDRIS (CNRS computer center).

#### REFERENCES

- Canuto, C., Hussaini, M.Y., Quarteroni, A., and Zang, T.A., 1988, "Spectral methods in fluid dynamics, *Springer series in computational physics*, Springer Verlag, Berlin.
- Davis, R. E., 1994, "Diapycnal mixing in the ocean: the Osborn-Cox model", *J. Phys. Oceanogr.*, Vol. 24, pp. 2560-2576.
- Fernando, H. J. S., 1991, "Turbulent mixing in stratified fluids", *Ann. Rev. Fluid Mech.*, Vol. 23, pp. 455-493.
- Gregg, M. C., 1987, Diapycnal mixing in the thermocline: a review, *J. Geophys. Res.*, Vol. 92-C5, pp. 5249-5286.
- Lorenz, E. N., 1955, "Available potential energy and the maintenance of the general circulation", *Tellus*, Vol. 7, pp. 157-167.
- Orszag, S. A., 1971, "Numerical simulation of incompressible flows within simple boundaries. I. Galerkin (spectral) representation", *Studies Applied Maths*, Vol. 50(4), pp. 293-327.
- Osborn, T. R., and Cox, C. S., 1972, "Oceanic fine structure", *Geophys. Fluid Dyn.*, Vol. 3, pp. 321-345.
- Schowalter, D. G., Lasheras, J. C., & van Atta, C. W., 1994, "A study of streamwise vortex structure in a stratified shear layer", *J. Fluid Mech.*, Vol. 281, pp. 247-291.
- Staquet, C., 1994, "A numerical study of vorticity layers in a two-dimensional stratified shear flow", *Meccanica*, (Special Issue on Vortex Dynamics, E.J. Hopfinger & P. Orlandi eds), Vol. 20 (4), pp. 489-506.
- Staquet, C., 1995, "Two-dimensional secondary instabilities in a strongly stratified shear layer", *J. Fluid Mech.*, Vol. 296, pp. 73-126.
- Thorpe, S. A., 1977, "Turbulence and mixing in a Scottish Loch", *Phil. Trans. R. Soc. Lond.*, Vol. A 286, pp. 125-181.
- Winters, K. B., Lombard, P. N., Riley, J.J., and d'Asaro, E. A., 1995, "Available potential energy and mixing in density-stratified fluids", *J. Fluid Mech.*, Vol. 289, pp. 115-128.
- Winters, K. B., and d'Asaro, E. A., 1996, "Diascalar flux and the rate of fluid mixing", *J. Fluid Mech.*, Vol. 317, pp. 179-193.

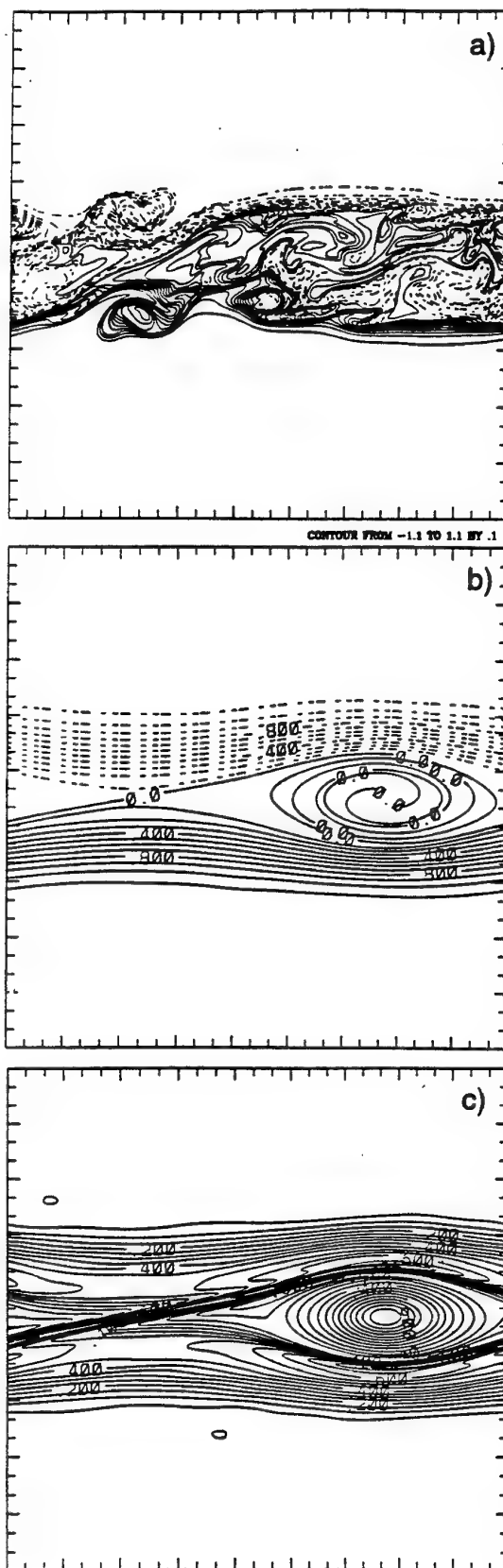


Figure 1: Constant contours of the density field for run R3 at different times. (a)  $t=85$ ; (b)  $t=360$ . (c) Vorticity field at  $t=360$ .

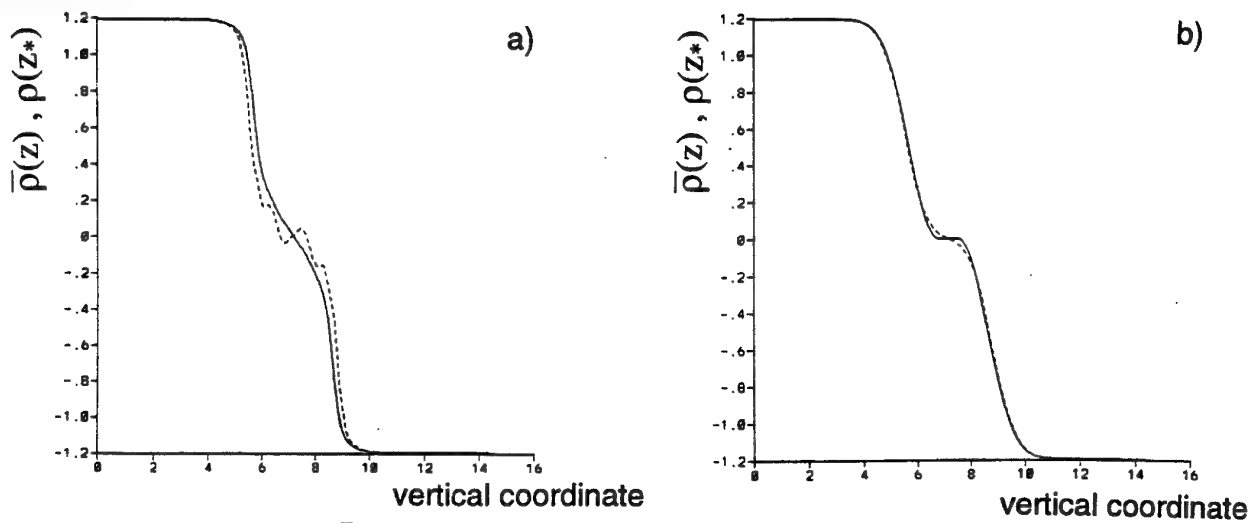


Figure 2: Comparison of the horizontally averaged density profile (dash line) with the sorted density profile (full line) at different times. (a)  $t=85$ ; (b)  $t=360$ .

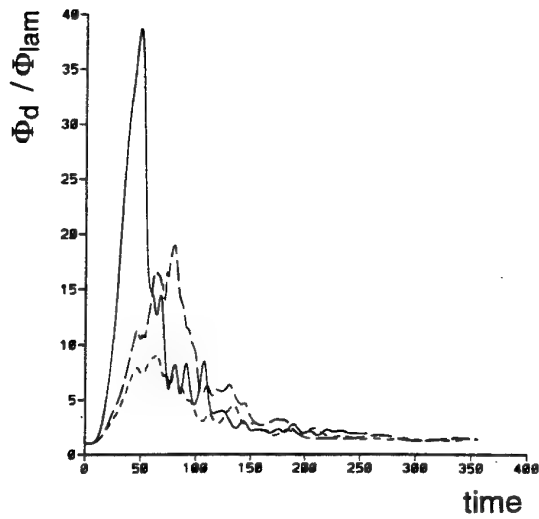


Figure 3: Temporal evolution of the diffusif flux of density  $\Phi_d$  normalized by the laminar diffusive flux of density  $\Phi_{lam}$  for runs R1 (full line), R2 (small dash line) and R3 (long dash line).

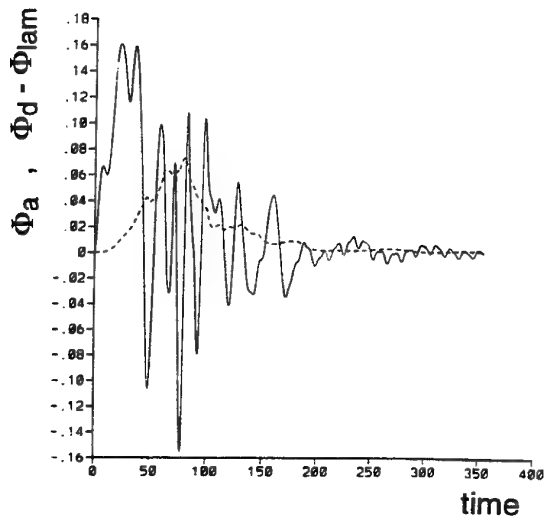


Figure 4: Temporal evolutions of the turbulent diffusive flux of the density  $\Phi_d - \Phi_{lam}$  and the advective flux of density  $\langle \rho w \rangle$  for run R3.

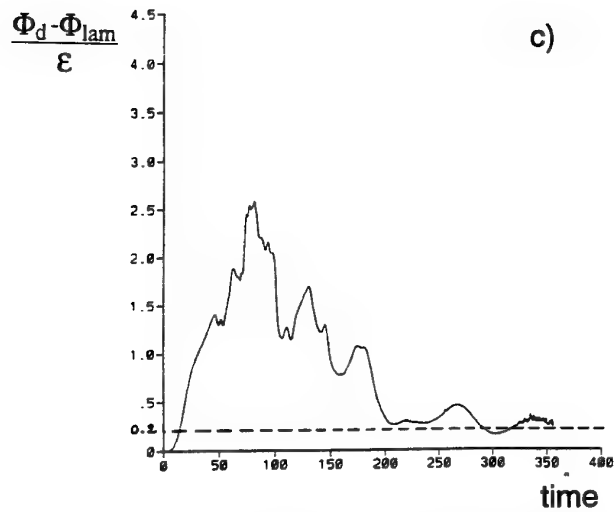
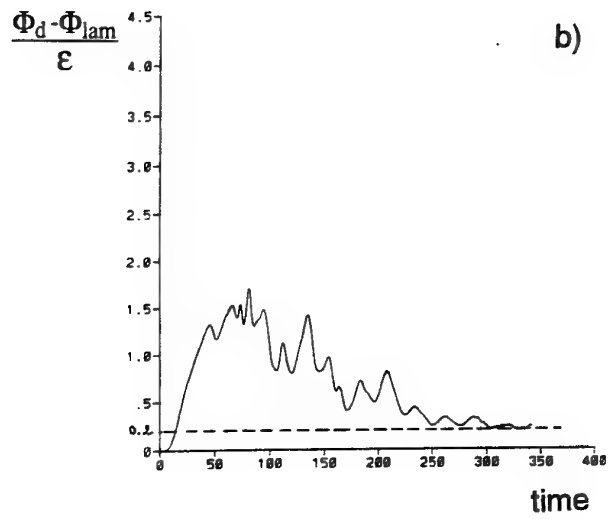
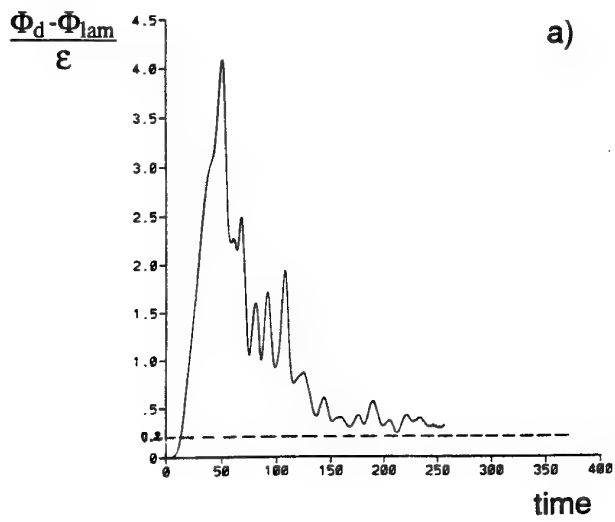


Figure 5: Temporal evolution of the mixing efficiency  $\gamma_d$  defined by (5) for runs R1 (a), R2 (b) and R3 (c). The 0.2 value is indicated by a dotted line.

## **SESSION 21 - COMBUSTION II**

# LARGE EDDY SIMULATION OF A TURBULENT NON-PREMIXED FLAME

N. Branley and W. P. Jones

Department of Chemical Engineering and Chemical Technology  
Imperial College of Science, Technology and Medicine  
London SW7 2BY  
United Kingdom

## ABSTRACT

A hydrogen jet diffusion flame has been simulated using Large Eddy Simulation. The effect of heat release has been included via a conserved scalar type combustion model. A standard Smagorinsky model was used to represent the subgrid scale stresses and scalar flux. Equilibrium chemistry data was used to relate the mixture fraction to the thermodynamic variables of density, temperature and species concentrations. The probability density function of the subgrid scale fluctuations of mixture fraction was presumed to take the form of a  $\beta$ -function. The results obtained are in reasonable accord with measured data.

## INTRODUCTION

Large eddy simulation (LES) has been applied in the past to a number of complex isothermal flows, such as backward facing steps (Akselvoll & Moin, 1993), flows over hemispheres (Manhart & Wengle, 1993) and jets in cross-flows (Jones & Wille, 1995; Jones & Wille, 1996a; Jones & Wille, 1996b). Whilst the use of Reynolds averaged methods in the calculation of turbulent reacting flows has been the focus of much work over the past two decades, the extension of LES to reacting flows is a recent development (see for example Cook *et al.*, 1997 and the references therein). LES offers the possibility of improving predictive capabilities in turbulent combustion by providing a means by which the effects of such phenomena as the stabilising/de-stabilizing effects of swirling motions and buoyancy forces, for example, can be included with the minimum of modelling assumptions. The aim of the present work is to investigate the use of LES in variable density, turbulent reacting flows with the view of advancing the use of LES in practical engineering problems.

A hydrogen jet diffusion flame issuing into a coflowing stream of air has been simulated. This flow has been investigated extensively by Bilger and his coworkers (Kent & Bilger, 1973; Glass & Bilger, 1978; Kennedy & Kent, 1981) and a detailed set of experimental data is available for validation of the method.

## GOVERNING EQUATIONS AND MODELLING

The equations describing the motions of the large scale structures of a turbulent flow are obtained by applying a spatial filter to the continuity and Navier-Stokes equations. If the spatial filter commutes with time and space differentiation then the filtered equations take the same form as the original equations. The resulting equations can be written as:

$$\frac{\partial \bar{p}}{\partial t} + \frac{\partial \bar{p} \tilde{u}_i}{\partial x_i} = 0, \quad (1)$$

and

$$\frac{\partial \bar{p} \tilde{u}_i}{\partial t} + \frac{\partial \bar{p} \tilde{u}_i \tilde{u}_j}{\partial x_j} = -\frac{\partial \bar{p}}{\partial x_i} + \frac{\partial}{\partial x_j} \left\{ \mu \left( \frac{\partial \tilde{u}_i}{\partial x_j} + \frac{\partial \tilde{u}_j}{\partial x_i} \right) \right\}. \quad (2)$$

Here  $\rho$  is the density,  $u_i$  is the velocity component in the  $x_i$  direction,  $p$  is the pressure and  $\mu$  is the molecular viscosity, which is assumed constant. The overbar denotes the application of the spatial filter; the tilde denotes that the filtered quantity is density weighted, i.e. for a quantity  $f$ ,  $\tilde{f} \equiv \overline{\rho f} / \bar{\rho}$ . The term  $\tilde{u}_i \tilde{u}_j$  is unknown and the substitution

$$\bar{p} \tilde{u}_i \tilde{u}_j = \bar{p} \tilde{u}_i \tilde{u}_j + \tau_{ij}, \quad (3)$$

where  $\tau_{ij}$  is the modelled subgrid stress, is required for closure. In this work a variable density (see for example Moin *et al.*, 1991) form of the Smagorinsky model (Smagorinsky, 1963) has been used for the subgrid stress such that

$$\tau_{ij} = \underbrace{(C_s \Delta)^2 \bar{\rho} \sqrt{2} |\tilde{S}_{ij}|}_{\mu_t} \tilde{S}_{ij}, \quad (4)$$

where  $\mu_t$  is the eddy viscosity,  $\tilde{S}_{ij}$  is the strain rate, and  $\Delta$  the characteristic length scale for the smallest resolved motion,

$$\Delta = (\delta x_1 \delta x_2 \delta x_3)^{\frac{1}{3}}, \quad (5)$$

where  $\delta x_i$  are the local mesh spacings. The Smagorinsky parameter  $C_s$  was assumed constant and equal to 0.1. In

the constant density case equation 4 reduces to the standard Smagorinsky model.

The evaluation of the density requires a description of the combustion process. In this work a conserved scalar formulation has been adopted (see Jones & Kakhi, 1996 for a review of the method). A brief description now follows.

The use of a single diffusion coefficient for all species present in the flow implies that a single transport equation can be used to express the conservation of each element mass fraction,  $z_\alpha$ . If the Prandtl and Schmidt numbers are equal then the same equation will also describe the conservation of enthalpy. In non-premixed combustion the fuel and oxidant enter the domain in separate feeds, and the element mass fractions can be normalised to yield identical boundary conditions for each (Bilger, 1976) according to

$$\xi_\alpha = \frac{z_\alpha(x_i, t) - z_{\alpha,2}(x_i, t)}{z_{\alpha,1}(x_i, t) - z_{\alpha,2}(x_i, t)}, \quad (6)$$

where  $z_{\alpha,1}$  is the mass fraction of element  $\alpha$  in the fuel stream and  $z_{\alpha,2}$  its value in the air stream. The value of  $\xi_\alpha$  is independent of the element  $\alpha$  used in equation 6, and the subscript can be dropped. The resulting quantity  $\xi$  is strictly conserved and referred to as the mixture fraction.

A thermochemical model is needed to relate  $\xi$  to the concentration fields of the reactive species, temperature and density. In the present work the chemical equilibrium approach has been adopted.

The spatially filtered transport equation for the conserved scalar,  $\xi$  is written

$$\frac{\partial \bar{\rho} \tilde{\xi}}{\partial t} + \frac{\partial \bar{\rho} u_i \tilde{\xi}}{\partial x_i} = \frac{\partial}{\partial x_i} \left\{ \frac{\mu}{\sigma} \frac{\partial \tilde{\xi}}{\partial x_i} \right\}, \quad (7)$$

where  $\sigma$  is the Prandtl number. Closure is obtained by the introduction of a subgrid scalar flux

$$J_i = \bar{\rho} \tilde{u}_i \tilde{\xi} - \bar{\rho} u_i \tilde{\xi} \quad (8)$$

into equation 7. The subgrid scalar flux is modelled by

$$J_i = -\frac{\mu_t}{\sigma_t} \frac{\partial \tilde{\xi}}{\partial x_i}, \quad (9)$$

where  $\sigma_t$  is the turbulent Prandtl number, the value of which was taken as 0.7.

It is well known that because of the strong nonlinearity of the relationship between the mixture fraction and the thermodynamic variables, it is not sufficient to use the filtered mixture fraction alone in the determination of the state of the flow. Some account must be taken of the subgrid fluctuations in the mixture fraction. Following the approach widely used in conventional turbulent combustion modelling (Jones & Whitelaw, 1982), these fluctuations are described by a presumed-shape density weighted probability density function (pdf),  $P(\xi, x_i)$ . Then for any quantity  $f$  which is uniquely related to the mixture fraction,

$$\bar{f} = \bar{\rho} \int_0^1 \frac{f(\xi)}{\bar{\rho}(\xi)} P(\xi, x_i) d\xi, \quad (10)$$

so that if  $f = 1$  then

$$\bar{\rho} = \left\{ \int_0^1 \frac{P(\xi, x_i)}{\bar{\rho}(\xi)} d\xi \right\}^{-1}. \quad (11)$$

The pdf was assumed to take the form of a  $\beta$  function,

$$P(\xi, x_i) = \frac{\xi^{a-1} (1-\xi)^{b-1}}{\int_0^1 \xi^{a-1} (1-\xi)^{b-1} d\xi}, \quad 0 < \xi < 1, \quad (12)$$

where  $a$  and  $b$  are determined from the filtered value  $\tilde{\xi}$  and its subgrid variance  $\tilde{\xi}''^2$ . In this work  $\tilde{\xi}''^2$  is determined directly from the resolved scalar field by

$$\tilde{\xi}''^2 = C \Delta^2 \left( \frac{\partial \tilde{\xi}}{\partial x_i} \right)^2, \quad (13)$$

$C$  being a constant dependent on parameters appearing in the modelled transport equation for  $\tilde{\xi}''^2$  (Jones, 1993), and equal to 0.13.

## CALCULATION METHOD

The spatially averaged transport equations are discretised using finite volume methodology. A co-located mesh structure is employed whereby velocities, pressure, mixture fraction and density are defined at cell centres. The formulation is fully implicit, and an approximate factorisation technique is adopted to determine the pressure.

For the momentum equations, spatial derivatives are evaluated using second order energy conserving central differences. For time derivatives a second order three point backward difference scheme is used giving

$$\left[ \rho \frac{\partial \phi}{\partial t} \right]_i^{n+1} \approx \rho_i^{n+1} \left\{ \frac{3}{2} \frac{\phi_i^{n+1} - \phi_i^n}{\delta t} - \frac{1}{2} \frac{\phi_i^n - \phi_i^{n-1}}{\delta t} \right\} + O(\delta t^2), \quad (14)$$

where  $\phi_i^n$  denotes the discrete value any filtered variable  $\phi$  at location  $i$  and time level  $n$ . The density at time level  $n+1$  required in equation 14 is obtained through the use of the two-step method described in detail in Jones & Wille, 1996a. The resulting method is formally second order accurate in space and time.

For the scalar transport equation a different approach to the convection terms is adopted. Whilst central difference schemes have been seen to work well for the momentum equations in LES (Ferziger & Peric, 1996), their use in the scalar transport equation leads to difficulties. Since the scalar field plays an active role in the flow, via the density, it must remain bounded by its physical limits if unrealistic values of the density are to be avoided. It is well known that central differences do not guarantee that this requirement will be met (Roache, 1971), and the resulting scalar field may require clipping to enforce  $0 \leq \xi \leq 1$  throughout the domain. In the present work, however, the use of clipping was ineffective and an alternative approach was therefore adopted to keep the scalar field bounded. This involved use of a TVD type scheme (see for example Jones, 1993) based upon a central difference approximation limited so that the scalar bounds were not violated. Whilst it is known that TVD type schemes may result in excessive numerical dissipation unless the mesh spacings are small (Boris *et al.*, 1992), their use, or some similar approach, seems essential for scalar quantities in reacting-flow LES.

To illustrate the approach adopted, the one-dimensional case with positive convection velocity,  $u$ , is considered. In this case the convection term is approximated by

$$u \frac{\partial \phi}{\partial x} \approx u \frac{\phi_{i+\frac{1}{2}} - \phi_{i-\frac{1}{2}}}{\delta x} \quad (15)$$

and the cell face values  $\phi_{i+\frac{1}{2}}$  and  $\phi_{i-\frac{1}{2}}$  are obtained from

$$\phi_{i+\frac{1}{2}} = \phi_i + \frac{\Psi_{i+\frac{1}{2}}}{2} (\phi_{i+1} - \phi_i) \quad (16)$$

$$\phi_{i-\frac{1}{2}} = \phi_{i-1} + \frac{\Psi_{i-\frac{1}{2}}}{2} (\phi_i - \phi_{i-1}). \quad (17)$$

The limiter  $\Psi$  is defined as

$$\Psi_{i\pm\frac{1}{2}} = \max(0, \min(\lambda r_{i\pm\frac{1}{2}}, 1)) \quad (18)$$

where

$$r_{i+\frac{1}{2}} = \frac{(\phi_i - \phi_{i-1})(x_{i+1} - x_i)}{(\phi_{i+1} - \phi_i)(x_i - x_{i-1})}, \quad (19)$$

and

$$r_{i-\frac{1}{2}} = \frac{(\phi_{i-1} - \phi_{i-2})(x_i - x_{i-1})}{(\phi_i - \phi_{i-1})(x_{i-1} - x_{i-2})}, \quad (20)$$

with  $\lambda = 2$ . While other forms of limiter are possible (see for example Sweby, 1984), the present aim is to minimise the numerical dissipation and consequently central differences should be used as far as possible. The limiter defined by equation 18 results in upwinding for  $r_{i\pm\frac{1}{2}} \leq 0$  and central differencing for  $0.5 \leq r_{i\pm\frac{1}{2}} \leq \infty$ . The cut-off point corresponding to  $r_{i\pm\frac{1}{2}} = 0.5$  is somewhat arbitrary and beneficial results may be obtained by reducing this value further, i.e., by increasing the value of  $\lambda$  in equation 18.

## COMPUTATIONAL PARAMETERS

The flow configuration studied in this work consists of a jet of hydrogen issuing at a velocity of  $u_{jet} = 151.1 \text{ ms}^{-1}$  from a nozzle of diameter  $D = 7.62 \text{ mm}$  with a coflowing stream of air with velocity  $u_c = 15.1 \text{ ms}^{-1}$ . The Reynolds number based on the bulk velocity of the jet and the nozzle diameter is  $Re = 10730$ . The effect of buoyancy was neglected since the Froude number,  $Fr = \frac{u^2}{gD}$ , is approximately  $3 \times 10^5$ .

Calculations were performed on a rectangular domain of dimension  $28D \times 28D \times 50D$ . A mesh consisting of 100 grid nodes in the streamwise ( $x_1$ ) direction and  $79 \times 79$  grid nodes in the planes normal to the streamwise direction was employed. The total number of grid nodes was constrained by the availability of computing resources. The grid lines in the  $x_2$  and  $x_3$  directions were expanded smoothly from the jet centreline, with an expansion ratio of 1.06 at the inflow boundary, falling to unity with distance downstream. The grid lines in the  $x_1$  direction were also expanded smoothly with an expansion ratio of 1.01.

## BOUNDARY CONDITIONS

The instantaneous velocity  $\tilde{u}_i$  at the inflow is generated by adding a fluctuating component  $\tilde{u}'_i$  to a specified mean profile  $\langle \tilde{u}_i \rangle$ . The instantaneous component is supplied by scaling a Gaussian deviate  $G(x_i, t)$  (Press *et al.*, 1992) (a random number with a Gaussian distribution) with a specified profile of turbulent intensity, so that for the  $\tilde{u}_1$  component for example, the instantaneous velocity at the inflow is  $\tilde{u}_1 = \langle \tilde{u}_1 \rangle + G_1 \sqrt{\langle \tilde{u}_1'^2 \rangle}$ . The Gaussian distribution has zero mean and unit variance ensuring that the profiles of mean velocity and turbulent intensity computed during the simulation at the inflow match those used to specify the inlet condition. This approach yields an incorrect shear stress at the inlet and is to some extent physically unrealistic; velocities at different and adjacent time levels are presumed uncorrelated. However, the consequence of this are unlikely to be important in the present flow. The turbulence levels in the inflow are negligibly small compared with those generated by the shear layers around the jet. A more precise description of the inflow turbulence seems unwarranted at this stage.

Constant velocity profiles of  $\langle \tilde{u}_1 \rangle = 151.1 \text{ ms}^{-1}$  in the jet and  $\langle \tilde{u}_1 \rangle = 15.1 \text{ ms}^{-1}$  in the coflow were used, with  $\langle \tilde{u}_2 \rangle = \langle \tilde{u}_3 \rangle = 0$  across the inlet. Turbulent intensities were 0.3% in the jet and 3% in the coflow. The mixture fraction inlet conditions were  $\tilde{\xi} = 1$  in the jet and zero elsewhere. The mixture fraction variance was zero across the whole of the inflow boundary. At the outflow a zero

gradient non-reflecting condition was applied for  $\tilde{u}_i$ ,  $\tilde{\xi}$  and  $\tilde{\xi}''^2$ .

On all remaining boundaries a zero normal velocity was enforced, with a zero gradient condition being used for the wall-parallel component. The mixture fraction and its sub-grid variance were also treated using a zero gradient condition.

## RESULTS

The jet was impulsively started at time  $t = 0$ . In the early stages of the calculation the flow experienced a rapid expansion which caused the Courant numbers to increase dramatically with each time step. To maintain temporal accuracy and to prevent the calculation from becoming unstable, the maximum Courant number was kept at 0.3. This necessitated the use of a variable time step. In the later stages of the flow it was found unnecessary to recompute the time step to keep the Courant numbers within an acceptable range of 0.3.

The combustion model is not accurate in the near nozzle region due to the importance of non-equilibrium effects. Its use in this region lead to instabilities which may be attributed to the rapid expansion of the flow in this area coupled with insufficient mesh refinement. To prevent these instabilities from arising, combustion was suppressed in the region  $x_1 \leq D$  and the density was evaluated from the equation of state for an ideal gas.

The equations were integrated over a time interval corresponding to approximately 40 mean residence times,  $\tau_{res} = u_j/L$ , where  $L$  is the length of the computational domain. To obtain statistics the flow variables were then averaged as necessary over the last 20 residence times. For the radial profiles of rms turbulence intensities the results were also spatially averaged in the toroidal direction in which the flow is homogeneous.

A snapshot of the flow is shown in figure 8, which depicts the toroidal component of vorticity on a plane cutting through the axis of the jet. The simulation is seen to give a qualitatively realistic picture of the flows behaviour.

The predicted centreline variation of axial velocity is shown in figure 1. In the near nozzle region the suppression of combustion results in an under-prediction of the velocity. The point at which combustion commences sees a rapid increase in velocity, though the peak value is under-predicted. Further downstream the agreement between measurement and simulation is good. The slight lack of smoothness displayed in the computed profile is due to the finite sample size used to calculate the averages.

The axial velocity profile obtained from the simulation at  $x_1/D = 40$  is shown in figure 2. The computed and measured profiles are in good agreement though the predicted velocities exceed measured values at all radial positions. The discrepancy is greatest at the edge of the jet where a difference of 17% exists between measurement and simulation. To some extent this can be attributed to adverse effects from the boundary condition on the walls parallel to the main flow direction, which restricts the expansion of the jet and hence causes some small artificial acceleration of the flow in this vicinity.

Axial turbulence intensity predictions are shown in figure 3. The level of agreement is reasonable though the simulation is seen to produce a higher level of turbulence intensity than found in the measurements, possibly arising from the use of too low a value for the Smagorinsky parameter. The predictions show a peak in intensity away from the centreline in the shear layer, which agrees qualitatively with the measured data.

The mean mixture fraction centreline variation is shown in figure 4. The measured data consists of Favre and conventional averages, along with probe-sampled composition measurements of mixture fraction obtained by Kent & Bil-

ger, 1973. Agreement is poor in the near nozzle region but improves with distance downstream. The centreline mixture fraction is over-predicted throughout, though the radial variation shown in figure 5 exhibits tolerable agreement away from the centreline.

Temperature and species mole fractions on a wet basis are shown in figures 6 and 7 respectively. The predicted temperature shows only qualitative agreement with experiment, the centreline temperature and maximum temperature being over predicted by around 300C and 150C respectively. The predicted species mole fractions however show better agreement. The centreline value for hydrogen is only very slightly under-predicted, and the general trend is quantitatively correct. For water, the centreline value is again slightly under-predicted, as is the maximum value, which occurs in the simulations closer to the centreline than in the measured data. The simulation also correctly reproduces the overlapping of hydrogen and oxygen profiles, a typical feature of turbulent diffusion flames. The presence of oxygen is predicted closer to the centreline than measured values, though agreement improves further out from the flame centre. Overall, however, the level of agreement is very good.

## CONCLUSIONS

Large Eddy Simulation has been applied to the computation of a turbulent jet diffusion flame burning hydrogen in air. Density fluctuations have been accounted for through the use of density weighted filtering and a standard Smagorinsky model was used for the subgrid stresses. For combustion a conserved scalar formulation has been applied in conjunction with a presumed shape  $\beta$ -pdf and a simple gradient model for the subgrid fluctuations. Overall the results of the computations are in good agreement with measured mean and fluctuating components of velocity and with the mean concentration profiles. Some discrepancies exist, however, particularly with regard to the mean temperature profile. While it is possible that some of the differences between computation and measurement are related to the simplified description of combustion, it is likely that the use of a finer computational grid would lead to improved predictions. The implementation of a dynamic model (Piomelli & Liu, 1995) is also likely to lead to improved closure for the sub-grid stresses, the scalar flux and the scalar variance.

## ACKNOWLEDGEMENTS

The authors gratefully acknowledge the support of British Gas plc. The simulations were performed on the Cray T3D at EPCC, funded by EPSRC under grant number GR/K41601.

## REFERENCES

- Akselvoll, K., & Moin, P. 1993. Large eddy simulation of a backward facing step flow. *Pages 303-313 of: Rodi, W., & Martelli, F. (eds), Engineering Turbulence Modelling and Experiments 2.*
- Bilger, R.W. 1976. Turbulent Diffusion Flames. *Progress in Energy and Combustion Science*, 1, 87-109.
- Boris, J., Grinstein, F., Oran, E., & Kolbe, R. 1992. New insights into large eddy simulation. *Fluid Dynamics Research*, 10, 199-228.
- Cook, A.W., Riley, J.J., & Kosaly, G. 1997. A laminar flamelet approach to subgrid-scale chemistry in turbulent flows. *Combustion and Flame*, 109, 332-341.
- Ferziger, J.H., & Peric, M. 1996. *Computational Methods for Fluid Dynamics*. Berlin, Heidelberg: Springer-Verlag.
- Glass, M., & Bilger, R.W. 1978. The turbulent jet diffusion flame in a co-flowing stream - Some velocity measurements. *Combustion Science and Technology*, 18, 165-177.
- Jones, W.P. 1993. Turbulence Modelling and numerical solution methods for variable density and combusting flows. *Chap. 6, pages 309-374 of: Libby, P.A., & Williams, F.A. (eds), Turbulent Reacting Flow*. Academic Press.
- Jones, W.P., & Kakhi, M. 1996. Mathematical modelling of Turbulent flames. *Chap. 16, pages 411-491 of: Unsteady Combustion*. Kluwer Academic Publishing. Nato ASI Series, Vol 306. Series E: Applied Sciences.
- Jones, W.P., & Whitelaw, J.H. 1982. Calculation Methods for Reacting Turbulent Flows: A Review. *Combustion and Flame*, 48, 1-26.
- Jones, W.P., & Wille, M. 1995. Large Eddy Simulation of a jet in a cross flow. *Tenth Symposium on Turbulent Shear Flows*, 4.1-4.6.
- Jones, W.P., & Wille, M. 1996a. Large Eddy simulation of a plane jet in a cross-flow. *International Journal of Heat and Fluid Flow*, 17(3), 296-306.
- Jones, W.P., & Wille, M. 1996b. Large Eddy Simulation of a Round Jet in a Cross-flow. *In: Bergeles, G., & Rodi, W. (eds), Engineering Turbulence Modelling and Measurements*. Elsevier.
- Kennedy, M., & Kent, J.H. 1981. Scalar Measurements in a Co-flowing turbulent diffusion flame. *Combustion Science and Technology*, 25, 109-119.
- Kent, J.H., & Bilger, R.W. 1973. Turbulent Diffusion Flames. *Pages 615-625 of: Fourteenth Symposium (International) on Combustion*. The Combustion Institute, Pittsburgh.
- Manhart, M., & Wengle, H. 1993. A spatiotemporal decomposition of a fully inhomogeneous turbulent flow field. *Theoretical and Computational Fluid Dynamics*, 5, 223-242.
- Moin, P., Squires, W., Cabot, W., & Lee, S. 1991. A dynamic subgrid-scale model for compressible turbulence and scalar transport. *Physics of Fluids A*, 11, 2746-2757.
- Piomelli, U., & Liu, J. 1995. Large eddy simulation of rotating channel flows using a localized dynamic model. *Physics of Fluids*, 7(4), 839-848.
- Press, W.H., Teukolsky, S.A., Vetterling, W.T., & Flannery, B.P. 1992. *Numerical Recipes in FORTRAN*. Second edn. Cambridge University Press, UK.
- Roache, P. 1971. *Computational Fluid Dynamics*. Albuquerque, New Mexico: Hermosa Press.
- Smagorinsky, J. 1963. General circulation experiments with the primitive equations. I. The basic experiment. *Monthly Weather Review*, 91, 99-164.
- Sweby, P.K. 1984. High Resolution Schemes Using Flux Limiters for Hyperbolic Conservation Laws. *SIAM Journal for Numerical Analysis*, 21(5), 995-1011.



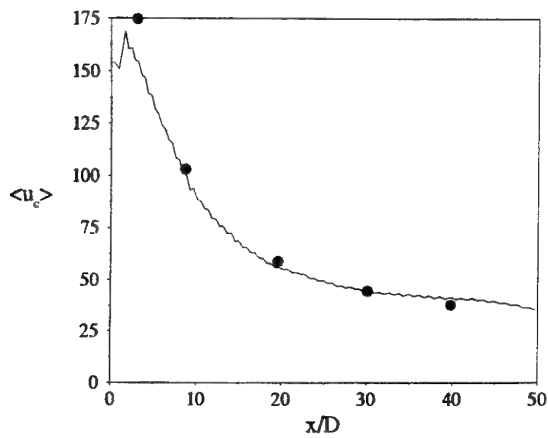


Figure 1: Mean axial velocity on the centreline; — predictions, • Glass and Bilger.

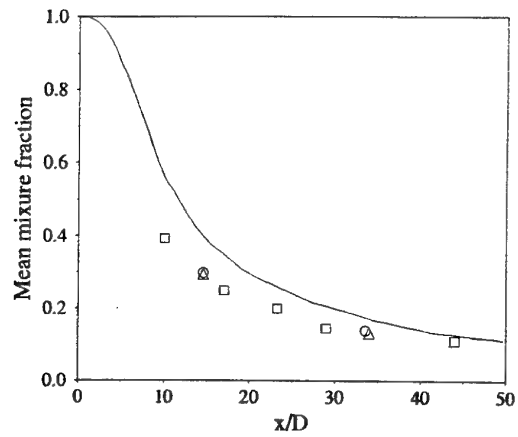


Figure 4: Mean mixture fraction on the centreline; — predictions; • conventional mean,  $\Delta$  Favre mean, Kennedy and Kent;  $\square$  Kent and Bilger.

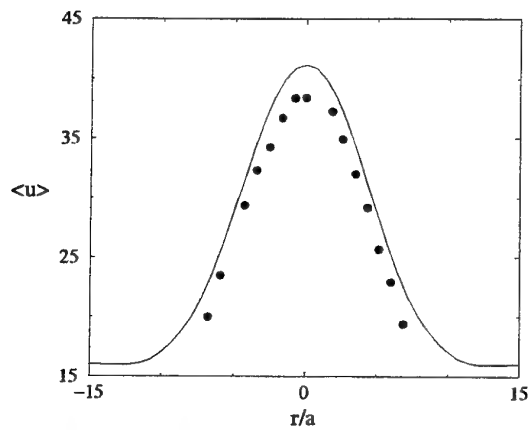


Figure 2: Mean axial velocity,  $x_1/D = 40$ ; — predictions, • Glass and Bilger.

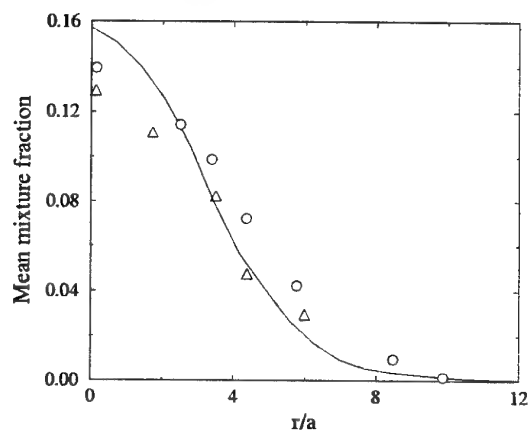


Figure 5: Mean mixture fraction,  $x_1/D = 34$ ; — predictions; • conventional mean,  $\Delta$  Favre mean, Kennedy and Kent.

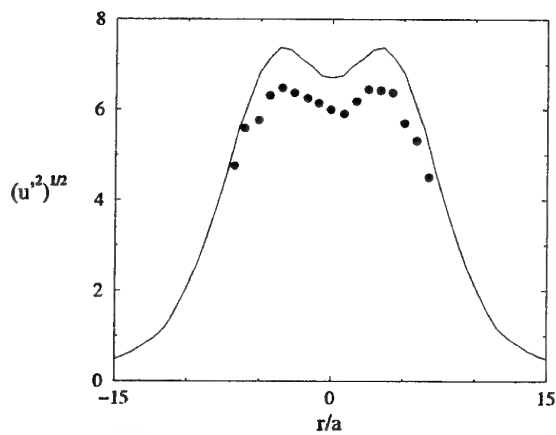


Figure 3: Axial turbulence intensity;  $x_1/D = 40$ ; — predictions, • Glass and Bilger.

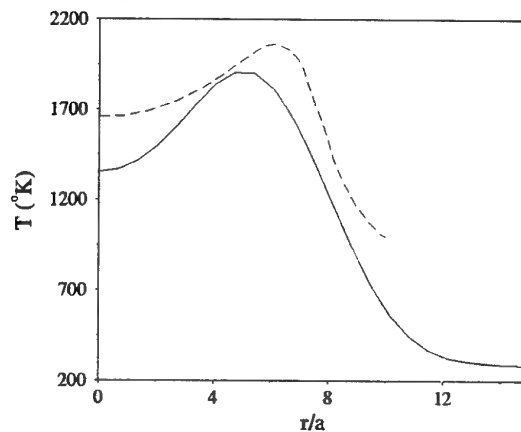


Figure 6: Mean temperature (Kelvin)  $x_1/D = 40$ ; — predictions; --- Kent and Bilger.

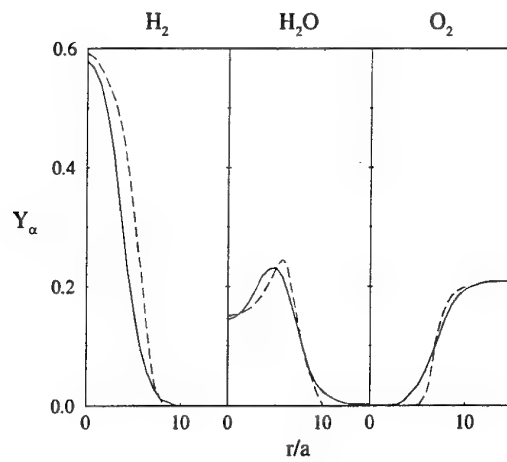


Figure 7: Mean mole fractions  $x_1/D = 40$ ; — predictions; - - - Kent and Bilger.

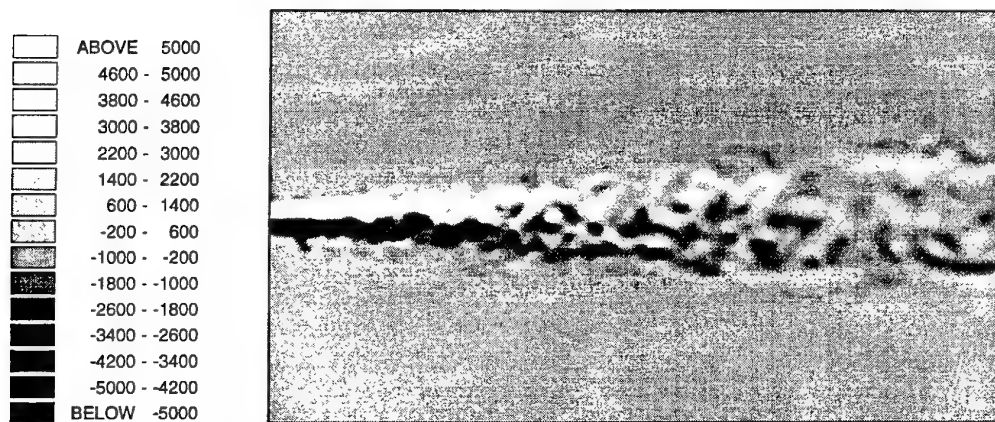


Figure 8: Toroidal component of instantaneous vorticity on a plane intersecting the jet axis.

# ANALYSIS OF FLAME SURFACE DENSITY CONCEPTS IN NON-PREMIXED TURBULENT COMBUSTION USING DIRECT NUMERICAL SIMULATIONS

E. van Kalmthout, D. Veynante

CENTRE DE RECHERCHE SUR LA COMBUSTION TURBULENTE

Laboratoire E.M2.C.

Ecole Centrale Paris

92295 Châtenay-Malabry Cedex

France

## INTRODUCTION

Flame surface density models are now widely used in turbulent combustion both to describe premixed and non-premixed situations. In this approach, the flame is assumed to be a collection of thin laminar flame elements and the mean reaction rate of the species  $k$  is modeled as:

$$\bar{\omega}_k = V_k \bar{\Sigma} \quad (1)$$

where  $\bar{\Sigma}$  is the available flame surface per unit volume (flame surface density) and  $V_k$  the local consumption rate of the species  $k$  per unit of flame area. The main advantage of this formulation is to decouple the chemical problem, described by the local reaction rate  $V_k$  and estimated from laminar flame studies, from the interaction between flame surface and turbulent flow field. The flame surface density  $\bar{\Sigma}$  may be estimated from an algebraic expression or as a solution of a balance equation.

In non-premixed combustion, a modeled transport equation for the flame surface density  $\bar{\Sigma}$  was first derived from phenomenological considerations by Marble and Broadwell (1977). Such a concept yields to suitable descriptions of practical situations (Veynante et al. 1986; Lacas et al. 1987; Fichot et al. 1994). Recently, Van Kalmthout et al. (1996b), extending the theoretical work developed by Vervisch et al. (1995), have proposed an exact, but unclosed, transport equation for the flame surface density  $\bar{\Sigma}$ . In this approach, the flame is described as the surface corresponding to the stoichiometric value,  $Z_{st}$  of the mixture fraction  $Z$ .

In this work, flame surface density  $\bar{\Sigma}$  and terms in  $\bar{\Sigma}$  equation are analyzed using direct numerical simulations of a two dimensional turbulent mixing layer.

## THEORETICAL BACKGROUND

The standard theory of non-premixed combustion is based on the conserved scalar description of the flow field (Bilger 1976; Libby and Williams 1980). Under certain restrictions (equal diffusivities of all species, unity Lewis number), the chemical reaction



may be described in terms of a mixture fraction  $Z$  defined as:

$$Z = \frac{\phi \frac{Y_F}{Y_F^\infty} - \frac{Y_O}{Y_O^\infty} + 1}{\phi + 1} \quad (2)$$

where  $s$  is the mass stoichiometric ratio and  $\phi = sY_F^\infty/Y_O^\infty$  is the equivalence ratio,  $Y_F^\infty$  (respectively  $Y_O^\infty$ ) denotes the value of the fuel mass fraction  $Y_F$  (oxidizer mass fraction  $Y_O$ ) in the pure fuel (oxidizer) stream.  $Z = 1$  is the pure fuel stream and  $Z = 0$  in the oxidizer stream.

The scalar  $Z$  is governed by a convection-diffusion transport equation:

$$\frac{\partial Z}{\partial t} + \mathbf{u} \cdot \nabla Z = \frac{1}{\rho} \nabla \cdot (\rho D \nabla Z) = w |\nabla Z| \quad (3)$$

where  $\rho$  is the density and  $D$  is the mass diffusivity. Other variables such as mass fractions, reaction rates or temperature may be directly expressed as functions of  $Z$ . A displacement speed  $w$  of the iso- $Z$  surface has been introduced in equation (3). The displacement speed  $w$  may be split in a normal and a curvature related component:

$$w = \frac{\nabla \cdot (\rho D \nabla Z)}{\rho |\nabla Z|} = -\frac{1}{\rho |\nabla Z|} \mathbf{n} \cdot \nabla [\rho D |\nabla Z|] - D \nabla \cdot \mathbf{n} \quad (4)$$

where  $\mathbf{n} = -\nabla Z/|\nabla Z|$  is the normal vector to the iso- $Z$  surface chosen pointing towards the oxidizer.  $\nabla \cdot \mathbf{n}$  denotes the curvature of the flame front.

Under the assumption of a fast chemistry, the flame is described as laminar thin flame elements lying on the iso-level  $Z = Z_{st} = 1/(\phi + 1)$  surface where  $Z_{st}$  is the stoichiometric value of the mixture fraction  $Z$  (Peters 1986). Then, following Pope (1988) or Vervisch et al. (1995), the flame surface density is defined by:

$$\bar{\Sigma} = \overline{|\nabla Z| \delta(Z - Z_{st})} = \langle |\nabla Z| | Z = Z_{st} \rangle p(Z = Z_{st}) \quad (5)$$

where  $\delta$  is the Dirac-function and overbar denotes ensemble averaging.  $p(Z = Z_{st})$  is the probability that  $Z = Z_{st}$  and  $\langle Q | Z = Z_{st} \rangle$  is the conditional averaging of  $Q$  for  $Z = Z_{st}$ .

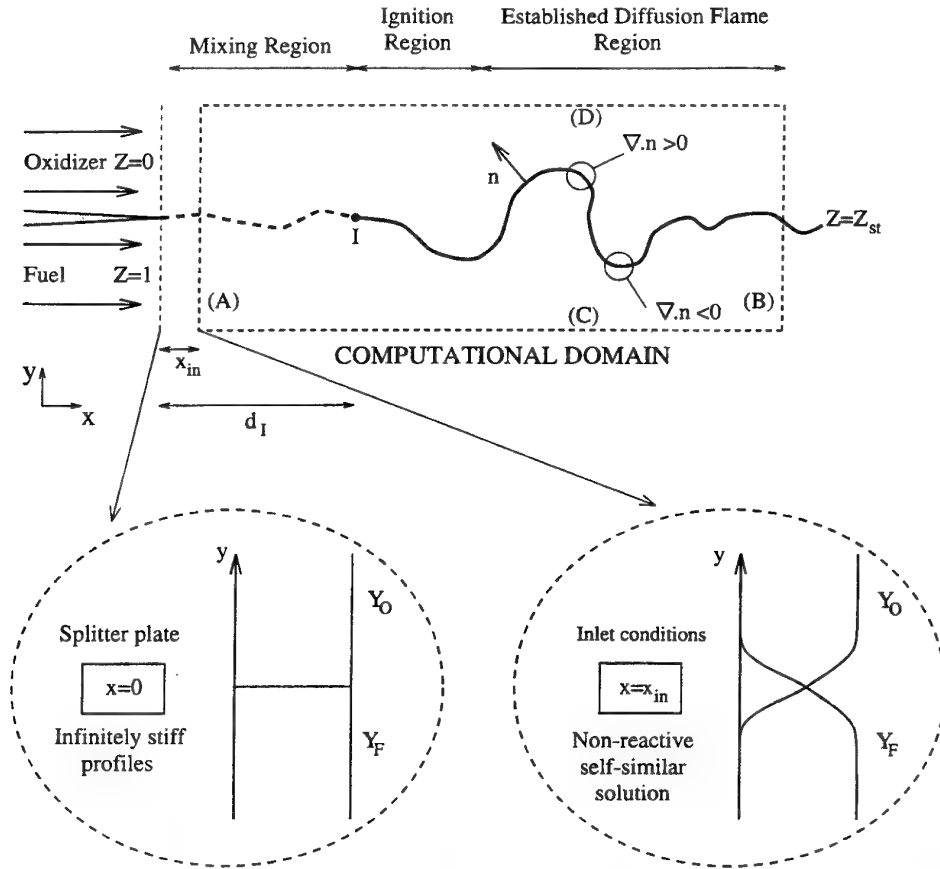


Figure 1: Computational domain. Boundaries are referred by uppercase letters. Vector  $\mathbf{n}$  designates the flame normal (pointing towards the oxidizer region). The curvature  $\nabla \cdot \mathbf{n}$  is positive when the flame is convex towards the oxidizer. The parameter  $x_{in}$  measures the distance from the splitter plate to the inlet of the computational domain. The self-similar non-reactive solution of the Navier-Stokes equations is imposed at the inlet boundary (A). An homogeneous and isotropic turbulent velocity field, with a Von Kármán - Pao energy spectrum, is injected at the inlet of the computational domain (A).

Then, combining Eq. (3) and (5), an exact balance equation for  $\bar{\Sigma}$  may be derived (Van Kalmthout et al. 1996b):

$$\underbrace{\frac{\partial \bar{\Sigma}}{\partial t}}_I + \underbrace{\nabla \cdot (\bar{u} \bar{\Sigma})}_{II} + \underbrace{\nabla \cdot (\langle u' \rangle_s \bar{\Sigma})}_{III} = \underbrace{\langle \nabla \cdot \mathbf{u} - \mathbf{n} \mathbf{n} : \nabla \mathbf{u} \rangle_s \bar{\Sigma}}_{IV} + \underbrace{\langle w \nabla \cdot \mathbf{n} \rangle_s \bar{\Sigma}}_V - \underbrace{\nabla \cdot [\langle w \mathbf{n} \rangle_s \bar{\Sigma}]}_{VI} \quad (6)$$

where  $\langle \rangle_s$  denotes averaging along the iso-level surface, defined for any quantity  $Q$  as:

$$\langle Q \rangle_s = \frac{Q |\nabla Z| \delta(Z - Z_{st})}{|\nabla Z| \delta(Z - Z_{st})} = \frac{Q \bar{\Sigma}}{\bar{\Sigma}} \quad (7)$$

Terms composing Eq. (6) correspond respectively to unsteady effects (I), mean convection (II), turbulent transport (III), strain rate (IV) acting on the flame front. Terms (V) and (VI) combine surface displacement relatively to flow and curvature effects. Terms (III) to (VI) in Eq. (6) are unclosed and require modeling.

## NUMERICAL SIMULATIONS

The direct simulation code NTMIX (Haworth and Poinot 1992) is used to solve the complete 2D Navier-Stokes equations. Spatial derivatives are calculated with high order compact finite difference scheme ( $O(\Delta x^6)$ ) while

temporal integration is performed by a third order Runge-Kutta method ( $O(\Delta t^3)$ ). An homogeneous and isotropic turbulent velocity field, with a Von Kármán - Pao energy spectrum (Hinze 1975) is injected at the inlet of the computational domain (Van Kalmthout et al., 1996a; 1996b). A chemically reacting two dimensional mixing layer with thermal expansion (equivalence ratio  $\phi = 1$ ) is computed (Fig. 1) for three different turbulence Reynolds number  $Re_T$  (105, 201 and 310). In a first step, oxidizer and fuel streams have the same inlet mean velocity (no mean shear). Numerical parameters are summarized in Table 1. An example of the flow field is displayed on figure 2.

All quantities intervening in the previous equations may be extracted from DNS for each location  $(x, y)$  and averaged over time (Van Kalmthout et al. 1996b).

## RESULTS AND DISCUSSION

### Global properties

The total reaction rate integrated across the flame brush,  $\int \bar{\omega}_F dy$ , is plotted as a function of the downstream location  $x$  on figure 3 for the laminar case and the three turbulent cases A, B and C. As expected, the total reaction rate starts from zero in the initial region and increases dramatically when the ignition occurs. Then, as the well established mixing layer is developing, the total reaction rate decreases.  $\int \bar{\omega}_F dy$  is also found to increase with the turbulence Reynolds number  $Re_T$ . The same integrated

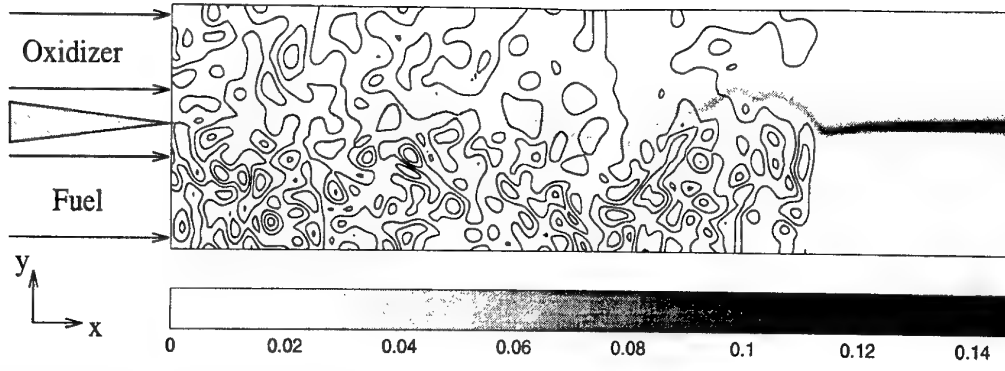


Figure 2: Interaction of an homogeneous and isotropic turbulence with a non-premixed flame (intermediate time: the injected turbulence has not reached the outflow boundary on the right of the computational domain) in a spatially developing mixing layer. Grayscale of reaction rate and vorticity contours are represented.

Case	$N_x$	$N_y$	$u'$	$\varepsilon$	$Re_T$	$l_t$	$\varepsilon/k$
A	501	121	$2.61 \cdot 10^{-2}$	$4.11 \cdot 10^{-5}$	105	0.40	0.04
B	501	121	$5.43 \cdot 10^{-2}$	$4.13 \cdot 10^{-4}$	201	0.37	0.09
C	1001	121	$8.65 \cdot 10^{-2}$	$1.74 \cdot 10^{-3}$	310	0.36	0.16

Table 1: Numerical simulation parameters (divided by their reference value). RMS velocity  $u'$  and its dissipation  $\varepsilon$ , integral length scale  $l_t$ , turbulence Reynolds number  $Re_T = k^{1/2} l_t / \nu$ . The numerical grid size is  $N_x \times N_y$ .

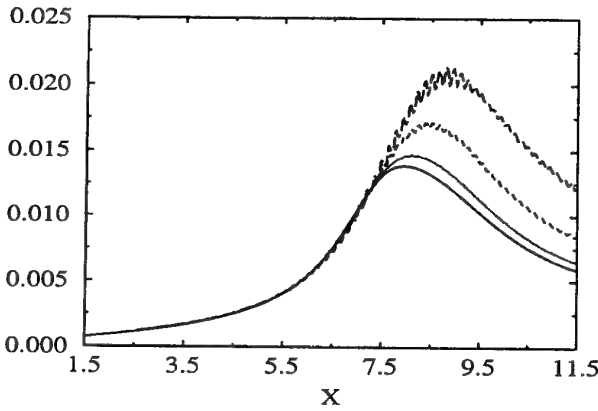


Figure 3: The total fuel consumption rate, integrated across the flame brush,  $\int \bar{\omega}_F dy$  (normalized by  $\rho_{ref} L_{ref} Y_{F\infty} t_{ref}^{-1}$ ) is plotted as a function of the downstream location  $x/L_{ref}$ . Laminar values —, Case A ( $Re_T = 105$ ) ·····, Case B ( $Re_T = 201$ ) ----, Case C ( $Re_T = 310$ ) -.-.-.

mean fuel consumption rate,  $\int \bar{\omega}_F dy$ , is now plotted normalized by its value in the corresponding laminar mixing layer on figure 4 as a function of the downstream location  $x$  for the three cases A – C. Then, a constant level, depending on the turbulence intensity, is reached, corresponding to the well established mixing layer. Compared to case A, the total reaction rate is increased by about 40 % in case B and 110 % in case C.

Following Eq. (1), this increase of the total reaction rate with the turbulence level may be explained both by an increase of the total available flame surface density  $\bar{\Sigma}$  or an increase of the local reaction rate  $V_F$ .

The total available flame surface increases with the Reynolds number as shown on Fig. 5 where the integrated flame surface density  $I_\Sigma = \int \bar{\Sigma} dy$  is plotted as a function of

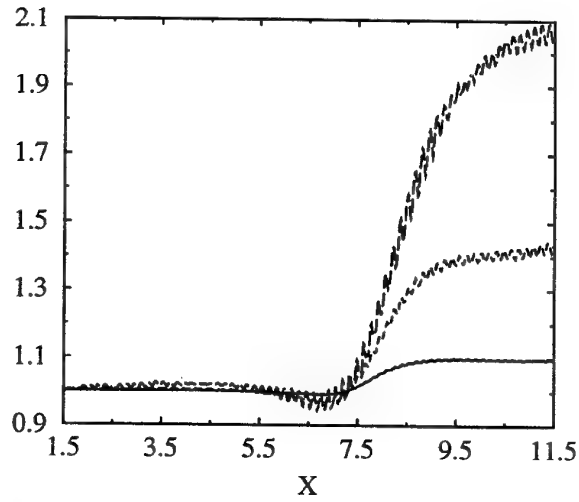


Figure 4: Total turbulent consumption rate  $\int \bar{\omega}_F dy$  (normalized by its laminar value). Case A ( $Re_T = 105$ ) —, Case B ( $Re_T = 201$ ) ----, Case C ( $Re_T = 310$ ) -.-.-. Quantities are plotted versus  $x/L_{ref}$ . The laminar ignition occurs at the location  $x/L_{ref} \approx 7.7$

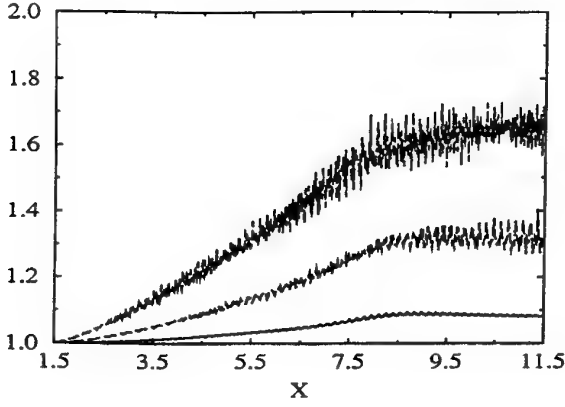


Figure 5: Integrated flame surface density  $I_\Sigma = \int \bar{\Sigma} dy$  (normalized by its laminar value). Case A ( $Re_T = 105$ ) —, Case B ( $Re_T = 201$ ) ----, Case C ( $Re_T = 310$ ) ——. Quantities are plotted versus  $x/L_{ref}$ . The laminar ignition occurs at the location  $x/L_{ref} \approx 7.7$ .

the downstream location  $x$ . In the well established flame zone, the total flame surface in case B ( $Re_T = 201$ ) is about 30 % higher than in case A ( $Re_T = 105$ ). In case C ( $Re_T = 310$ ), the flame surface is increased by about 70 % compared to case A.

Flame surface density  $\bar{\Sigma}$  profiles in the established diffusion flame region are plotted in Fig. 6 as a function of the transverse location  $y$  for the three values of the turbulence Reynolds number  $Re_T$ . All profiles are almost symmetric and look as a gaussian function. As the turbulence Reynolds number  $Re_T$  increases, the maximum value of the flame surface density  $\bar{\Sigma}$  decreases but the flame brush becomes larger and the total available flame surface increases as noticed on figure 5.

On the other hand, the mean scalar dissipation rate conditioned for the mixture fraction  $Z = Z_{st}$ ,  $\langle \chi | Z = Z_{st} \rangle$  is also found to increase with the turbulence Reynolds number  $Re_T$  as shown on figure 7. As shown by Peters (1983) or Williams (1985), the local flame structure is controlled by the local scalar dissipation  $\chi$  of the mixture fraction  $Z$  and the local reaction rate, assuming a steady-state laminar flame, is found to increase with  $\chi$ . Then, an increase of the conditional scalar dissipation corresponds to an increase of the local reaction rate  $V_F$ .

The increase of the total reaction rate,  $\int \bar{\omega}_F dy$ , with the turbulence Reynolds number combines (Eq. 1):

- an increase of the available flame surface area due to the wrinkling of the flame front induced by turbulence motions.
- an increase of the local fuel consumption rate  $V_F$  explained by an increase of the local scalar dissipation  $\chi$  at the flame front according to non premixed laminar flame theory and confirmed by DNS results.

These results are summarized and quantified in Table 2

### Flame surface density balance equation

All terms in the flame surface density balance equation (6) may be extracted from direct numerical simulations. In the following, we will focus our attention on the right hand side terms in the  $\bar{\Sigma}$  equation. An example of numerical results is displayed on figure 8 for case B. The main flame surface area source term is the strain rate term  $(\nabla \cdot \mathbf{u} - \mathbf{nn} : \nabla \mathbf{u})_s$  (term IV in Eq. 6). The normal displacement term (VI) is positive in the center of the mixing

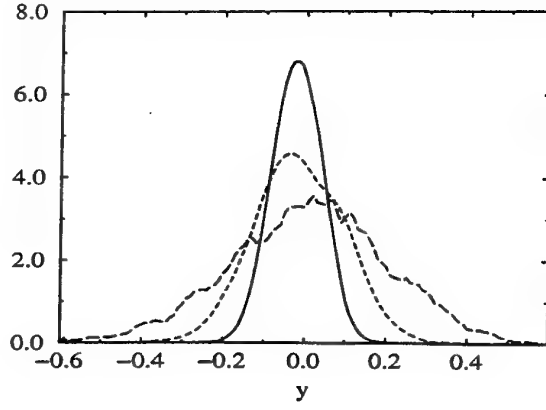


Figure 6: Flame surface density  $\bar{\Sigma}$  (normalized by  $L_{ref}^{-1}$ ) plotted versus  $y$ . Case A ( $Re_T = 105$ ) —, Case B ( $Re_T = 201$ ) ----, Case C ( $Re_T = 310$ ) ——.

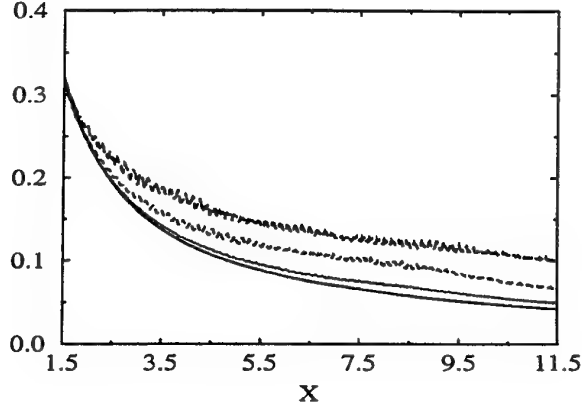


Figure 7: Conditional scalar dissipation rate  $\langle \chi | Z = Z_{st} \rangle$  (normalized by  $t_{ref}^{-1}$ ) plotted as a function of the downstream location  $x/L_{ref}$ . Laminar values —, Case A ( $Re_T = 105$ ) ·····, Case B ( $Re_T = 201$ ) ----, Case C ( $Re_T = 310$ ) ——.

Case	laminar	A	B	C
$Re_T$	-	105	201	310
$\int \bar{\omega}_F dy$	1.0	1.1	1.4	2.1
$\int \bar{\Sigma} dy$	1.0	1.08	1.3	1.7
$\langle \chi   Z = Z_{st} \rangle$	1.0	1.2	1.7	2.5

Table 2: Comparison of the evolution of the integrated reaction rate  $\int \bar{\omega}_F dy$ , the integrated flame surface density  $\int \bar{\Sigma} dy$  and the conditional scalar dissipation  $\langle \chi | Z = Z_{st} \rangle$  with the turbulence Reynolds number  $Re_T$ . All data are normalized by comparison with the laminar case.

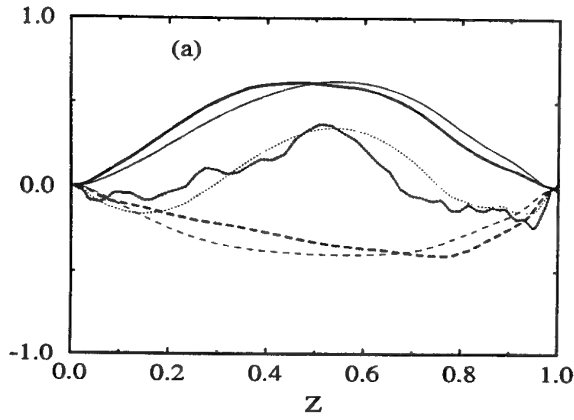


Figure 8: Right hand side terms in the balance equation for the flame surface density (Eq. 6) plotted as a function of  $\bar{Z}$ . Bold lines correspond to DNS results, normal lines refer to model (discussed in Van Kalmthout and Veynante, 1997): strain rate  $\langle \nabla \cdot \mathbf{u} - \mathbf{nn} : \nabla \mathbf{u} \rangle_s \bar{\Sigma}$  —, normal displacement  $-\nabla \cdot [\langle w \mathbf{n} \rangle_s \bar{\Sigma}]$  ..... , displacement/curvature  $\langle w \nabla \cdot \mathbf{n} \rangle_s \bar{\Sigma}$  ---- . Quantities are normalized by  $L_{ref}^{-2} a_{ref}$ . Case B.

layer and becomes negative at the boundaries. In fact, this term is a convective term corresponding to a displacement of the flame front relatively to the flow field and does not contribute to increase or decrease the total available flame surface. The curvature/displacement term (V) is always a sink term. This finding is easily explained because, when the equivalence ratio  $\phi = 1$ , the normal component of the displacement  $w$  is almost equal to zero (Van Kalmthout and Veynante 1997). Then, from Eq. (4):

$$\langle w \nabla \cdot \mathbf{n} \rangle_s \bar{\Sigma} \approx -\langle D(\nabla \cdot \mathbf{n})^2 \rangle_s \bar{\Sigma} \quad (8)$$

which is clearly negative.

The increase in flame surface area when the turbulence Reynolds number  $Re_T$  increases is mainly due to the increase of the strain rate term  $\langle \nabla \cdot \mathbf{u} - \mathbf{nn} : \nabla \mathbf{u} \rangle_s$  in the  $\bar{\Sigma}$ -equation (Eq. 6) as displayed on Fig. 9 where the strain rate is plotted as a function of the mean passive scalar value  $\bar{Z}$  for the three turbulence Reynolds number  $Re_T$ . In classical modeling, this term is closed as the inverse of the integral scale turbulence time:

$$\langle \nabla \cdot \mathbf{u} - \mathbf{nn} : \nabla \mathbf{u} \rangle_s = \alpha \frac{\varepsilon}{k} \quad (9)$$

where  $k$  is the turbulent kinetic energy and  $\varepsilon$  its dissipation.  $\alpha$  is a model constant. This modeled expression is quite well verified in our data (see Fig. 8) where  $\alpha$  is found to be about  $\alpha \approx 3$ .

Surface averaged curvatures  $\langle \nabla \cdot \mathbf{n} \rangle_s$  and square-curvatures  $\langle (\nabla \cdot \mathbf{n})^2 \rangle_s$  are displayed on figure 10 for case B. The surface averaged curvature,  $\langle \nabla \cdot \mathbf{n} \rangle_s$ , is a linear function of the mean mixture fraction  $\bar{Z}$  and is positive (respectively negative) at the oxidizer (fuel) stream side of the reaction zone. The flame front is mainly convex towards the oxidizer for  $\bar{Z} \rightarrow 0$  (positive curvature) and mainly convex towards the fuel stream for  $\bar{Z} \rightarrow 1$  (negative curvature). On the other hand, for  $\bar{Z} \approx 0.5$ , the mean curvature is closed to zero but large fluctuations are observed, denoted by the value of the square curvature  $\langle (\nabla \cdot \mathbf{n})^2 \rangle_s$ . From this simple analysis and introducing a wrinkling length scale  $L_f$  of

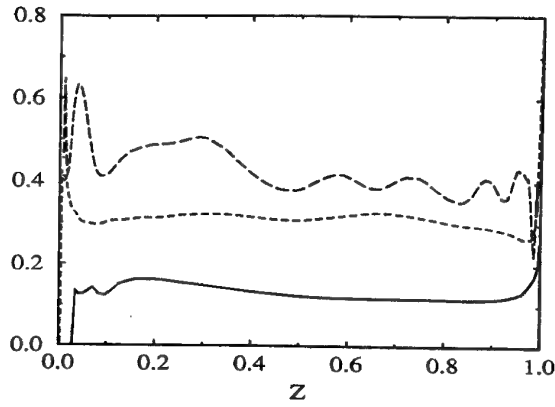


Figure 9: Profiles of the surface averaged strain rate,  $\langle \nabla \cdot \mathbf{u} - \mathbf{nn} : \nabla \mathbf{u} \rangle_s$ , plotted as a function of the mean mixture fraction  $\bar{Z}$  for a given downstream location and three turbulence levels. Case A ( $Re_T = 105$ ) —, Case B ( $Re_T = 201$ ) ----, Case C ( $Re_T = 310$ ) - · - ·. Quantities are normalized by  $t_{ref}^{-1}$ .

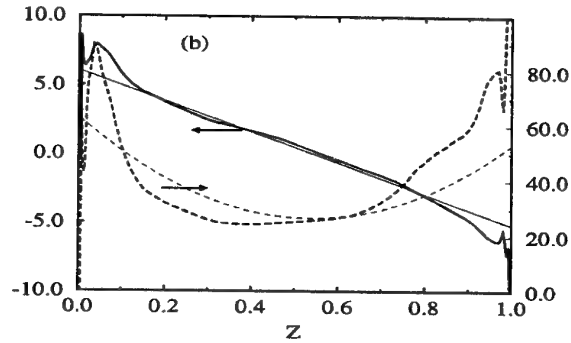


Figure 10: Transverse profiles of the surface averaged curvature  $\langle \nabla \cdot \mathbf{n} \rangle_s$  — and square curvature  $\langle (\nabla \cdot \mathbf{n})^2 \rangle_s$  ----, plotted as a function of  $\bar{Z}$ . Bold lines correspond to DNS data, normal lines refer to model. Curvature is normalized by  $L_{ref}^{-1}$ , square curvature is normalized by  $L_{ref}^{-2}$ . Case B.

the flame front (similar to the one proposed by Bray et al. 1987 for turbulent premixed combustion), we have:

$$\langle \nabla \cdot \mathbf{n} \rangle_s|_{\bar{Z}=0} \propto \frac{1}{L_f} ; \quad \langle \nabla \cdot \mathbf{n} \rangle_s|_{\bar{Z}=1} \propto -\frac{1}{L_f} \quad (10)$$

Assuming a constant molecular diffusivity  $D$  and neglecting the normal contribution in  $w$  (equivalence ratio  $\phi = 1$ ), a linear estimate for  $\langle \nabla \cdot \mathbf{n} \rangle_s$  leads to (Van Kalmthout et al. 1996b):

$$\langle w \rangle_s \approx -D \langle \nabla \cdot \mathbf{n} \rangle_s \approx -D \frac{Z^* - \bar{Z}}{L_f} \quad (11)$$

where  $Z^*$  is a constant estimated as  $Z^* = Z_{st} = 0.5$ .

This analysis is well sustained from DNS data as shown on figure 11 where the surface averaged displacement speed  $\langle w \rangle_s$  is displayed as a function of the mean mixture fraction  $\bar{Z}$  for the three cases A - C.  $\langle w \rangle_s$  is found to be a linear function of  $\bar{Z}$  with a slope slightly increasing with the Reynolds number. Following this analysis, The flame wrinkling length  $L_f$  decreases slightly when the turbulence

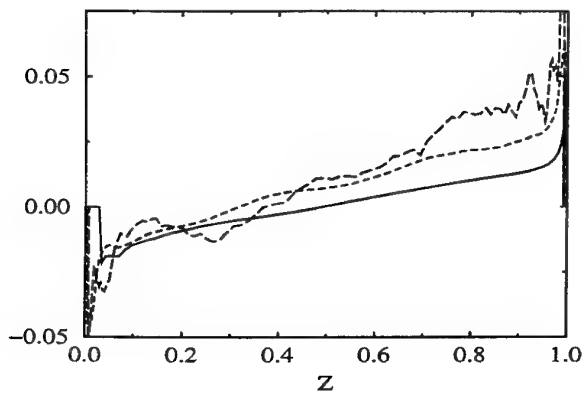


Figure 11: Surface averaged displacement speed  $\langle w \rangle_s$  versus  $\bar{Z}$ . Case A ( $Re_T = 105$ ) —, Case B ( $Re_T = 201$ ) ----, Case C ( $Re_T = 310$ ) ——. Quantities are normalized by  $a_{ref}$ .

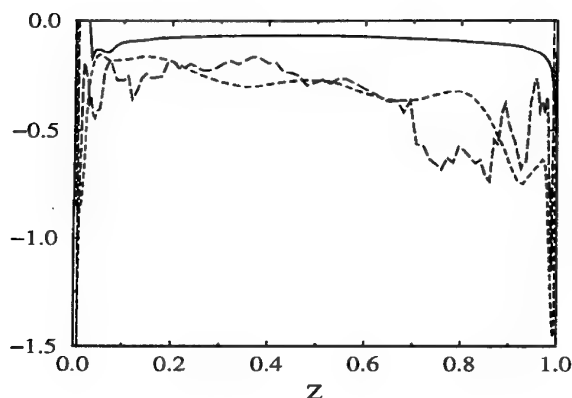


Figure 12: Displacement/curvature term  $\langle w \nabla \cdot \mathbf{n} \rangle_s$  versus  $\bar{Z}$ . Case A ( $Re_T = 105$ ) —, Case B ( $Re_T = 201$ ) ----, Case C ( $Re_T = 310$ ) ——. Quantities are normalized by  $a_{ref} L_{ref}^{-1}$ .

Reynolds number  $Re_T$  increases, corresponding to an increase of the flame front wrinkling and of the total flame surface area (Fig. 5).

The displacement/curvature term  $\langle w \nabla \cdot \mathbf{n} \rangle_s$  is plotted as a function of  $\bar{Z}$  on figure 12. This term is always a sink term in the  $\bar{\Sigma}$ -equation and slightly increases with the turbulence Reynolds number  $Re_T$  because of the higher values of  $\langle (\nabla \cdot \mathbf{n})^2 \rangle_s$  (Eq. 8).

## CONCLUSIONS

The influence of the turbulence Reynolds number on a spatially developing diffusion flame is analyzed by direct numerical simulations. Mean reaction rates, flame surface densities  $\bar{\Sigma}$  and some terms of an exact  $\bar{\Sigma}$ -equation are extracted from DNS data. The global reaction rate is found to increase with the turbulence Reynolds number. This increase is due both to the increase of the local reaction rate  $V_F$  (increase of the local scalar dissipation) and of the total flame area  $\bar{\Sigma}$  because of the strain rate term in the  $\bar{\Sigma}$ -equation. As the Reynolds number increases, the maximum value of the flame surface density  $\bar{\Sigma}$  decreases but the spatial extension of the flame brush is increased

and the flame front is more wrinkled.

**Acknowledgements :** Direct simulations were performed on a Cray C90 computer made available by IDRIS, Orsay, France. E. van Kalmthout has been supported by an European TMR fellowship.

## References

- Bilger, R. (1976). Turbulent jet diffusion flames. *Prog. Energ. Combust. Sci.* 1(87), 109–130.
- Bray, K., M. Champion, and P. Libby (1987). The turbulent premixed boundary layer with enthalpy. *Combust. Sci. Technol.* 55.
- Fichot, F., B. Delhay, D. Veynante, and S. Candel (1994). Strain rate modelling for a flame surface density equation with application to non-premixed turbulent combustion. In *25th Symposium (International) on Combustion*. The Combustion Institute.
- Haworth, D. and T. Poinso (1992). Numerical simulations of Lewis number effects in turbulent premixed flames. *J. Fluid Mech.* 244, 405–436.
- Hinze, J. (1975). *Turbulence*. McGraw-Hill.
- Lacas, F., S. Zikrikout, and S. Candel (1987). A comparison between calculated and experimental mean source terms in non premixed turbulent combustion. In *23rd Joint Propulsion Conference*, Volume 87-1782. AIAA.
- Libby, P. and F. Williams (1980). *Turbulent reacting flows*. New York: Springer Verlag.
- Marble, F. and J. Broadwell (1977). The coherent flame model of non-premixed turbulent combustion. Project Squid TRW-9-PU, Project Squid Headquarters, Chaffee Hall, Purdue University.
- Peters, N. (1983). Local quenching due to flame stretch and non-premixed combustion. *Combust. Sci. Technol.* 30, 1–17.
- Peters, N. (1986). Laminar flamelet concepts in turbulent combustion. In *Twenty-first Symposium (International) on Combustion*, pp. 1231–1250. The Combustion Institute.
- Pope, S. (1988). The evolution of surfaces in turbulence. *Int. J. Eng. Sci.* 26(5), 445–469.
- Van Kalmthout, E., T. Poinso, and S. Candel (1996a). Direct simulation of flame stabilization processes. In *Sixth International Conference on Numerical Combustion*, New Orleans.
- Van Kalmthout, E., D. Veynante, and S. Candel (1996b). Direct numerical simulation analysis of flame surface density equation in non-premixed turbulent combustion. In *26th Symposium (International) on Combustion*. The Combustion Institute.
- Van Kalmthout, E. and D. Veynante (1997). Direct numerical simulations analysis of flame surface density models for non-premixed turbulent combustion. *In preparation*.
- Vervisch, L., E. Bidaux, K. Bray, and W. Kollmann (1995). Surface density function in premixed turbulent combustion modeling, similarities between probability density function and flame surface approach. *Phys. Fluids A* 7(10), 2496 – 2503.
- Veynante, D., S. Candel, and J. Martin (1986). Coherent flame modeling of chemical reactions in a turbulent mixing layer. In *2nd Workshop on Modelling of Chemical Reaction System, Heidelberg*, pp. 386–398. Springer-Verlag.
- Williams, F. (1985). *Combustion Theory* (2 ed.). Addison-Wesley.



# LARGE EDDY SIMULATIONS OF TURBULENT PREMIXED FLAMES BASED ON THE G-EQUATION AND A FLAME FRONT WRINKLING DESCRIPTION

J. Piana<sup>(1)</sup>, F. Ducros<sup>(2)</sup>, D. Veynante<sup>(1)</sup>

CENTRE DE RECHERCHE SUR LA COMBUSTION TURBULENTE

<sup>(1)</sup> Laboratoire E.M2.C.  
Ecole Centrale Paris  
92295 Chatenay-Malabry Cedex  
France

<sup>(2)</sup> CERFACS  
42, Av. G. Coriolis  
31057 Toulouse Cedex  
France

## INTRODUCTION

As most combusting flows exhibit large scale coherent structures (Coats 1996), large eddy simulations (LES) is a very promising tool for their numerical simulations. In this approach, large coherent structures are explicitly computed whereas the effects of the smallest turbulent scales are modelled.

For example, LES could be a powerful approach for numerical simulations of combustion instabilities (Menon and Jou 1991). These instabilities, due to a coupling between heat release, hydrodynamic flow field and acoustic waves, are characterized by large coherent structures and have to be avoided because they induce noise, variations of the system characteristics, large heat transfers and may lead to the system destruction. Then, LES seems to be a well adapted approach to predict the occurrence of such instabilities and to numerically test passive or active control methods.

Large eddy simulations could also allow a better description of the turbulence / combustion interactions because, in LES, large structures are explicitly computed and instantaneous fresh and burnt gases zones, where turbulence characteristics may be quite different, are clearly identified.

Unfortunately, a large range of characteristic times and length scales are involved in combustion phenomena and development of subgrid scale models is a difficult task. The thickness  $\delta_L$  of a premixed flame, about 0.1 to 1 mm, is generally smaller than LES mesh size  $\Delta$ . Species mass fractions and temperature are very stiff variables and the flame structure cannot be resolved in the computation. Two approaches have been proposed to overcome this difficulty:

- *Artificially thickened flame* (Butler and O'Rourke 1977). In this approach, the thickness of the flame front is increased, keeping constant the laminar flame speed. Then, the structure of the thickened flame is resolved on the LES computational mesh and complex chemistry schemes may be easily incorporated. Nevertheless, lengths and time scale ratios, comparing turbulence and combustion characteristics are affected in an unpredictable way.
- *Flame front tracking technique (G-equation)*. The flame is assumed to be a thin interface separating fresh

and burnt gases ("flamelet") and is described as the iso-surface  $G^*$  of a field variable  $G$ . This approach is retained in the present work.

Under the widely used flamelet concept, the flame surface is described as an infinitely thin propagating surface. The key idea of the  $G$ -equation approach is to track the position of the flame front using a field variable  $G$ . The flame surface is associated with the  $G = G^*$  iso-level surface (Kerstein et al. 1988). The  $G$ -field does not have to follow the gradients of the progress variable  $c$  and can be smoothed out to be resolved on the LES mesh. The  $G$ -equation is written:

$$\frac{\partial G}{\partial t} + \vec{u} \cdot \vec{\nabla} G = w |\vec{\nabla} G| \quad (1)$$

where  $w$  is the local displacement speed of the iso-surface  $G$ , relative to the flow velocity  $\vec{u}$ . Nevertheless, this kinematic description of the combusting flow field leads to various difficulties for non constant density flows (Piana et al. 1996). First, the flame front displacement speed  $w$  is affected by thermal expansion and should be corrected for density variation. A coupling is also needed between the  $G$ -equation and the species or energy balance equations. In fact, the  $G$ -equation corresponds to a kinematic description of the flame front and involves its displacement speed  $w$ . On the other hand, the reactant consumption and the heat release rate are controlled by the consumption speed  $S_c$ . Of course,  $w$  and  $S_c$  are related but may be quite different, especially in high flame front curvature zones as pointed out by Poinso et al. (1991). The displacement speed  $w$  may also be quite different from the laminar flame speed  $S_L$ .

In a LES context (Moser 1996; Menon 1996), the  $G$ -equation is generally used to describe the filtered  $\bar{G}$  field as:

$$\frac{\partial \bar{G}}{\partial t} + \vec{u} \cdot \vec{\nabla} \bar{G} = \bar{S}_T |\vec{\nabla} \bar{G}| \quad (2)$$

where a subgrid scale turbulent flame speed  $\bar{S}_T$  is introduced. Overbar denotes LES-filtered quantities:

$$\bar{Q}(x) = \int Q(x') F(x - x') dx' \quad (3)$$

where  $F$  is the LES filter in the physical space and  $\mathbf{x}$  the spatial location. The turbulent flame speed  $\bar{S}_T$  is generally modeled extending experimental fits of the mean turbulent flame speed in Reynolds averaging context:

$$\frac{\bar{S}_T}{S_L} = 1 + \alpha \left( \frac{\bar{u}'}{S_L} \right)^n \quad (4)$$

where  $\bar{u}'$  is the rms of the subgrid scale velocity fluctuations and  $\alpha$  and  $n$  two constants. Unfortunately, the turbulent flame speed is not a well defined quantity (Gouldin 1996) and the scatter of experimental data is very large. Then, no universal model is available for  $\bar{S}_T$ .

The objective of the present work is to propose a refined closure of the  $G$ -equation based on flame surface density and flame front wrinkling concepts.

## THEORETICAL ANALYSIS

The application of a Favre-LES filter to the  $G$ -equation (1) leads to:

$$\begin{aligned} \frac{\partial \bar{\rho} \tilde{G}}{\partial t} + \nabla \cdot \bar{\rho} \tilde{\mathbf{u}} \tilde{G} = & - \underbrace{\nabla \cdot (\bar{\rho} [\tilde{G} \tilde{\mathbf{u}} - \tilde{G} \tilde{\mathbf{u}}])}_{\text{unresolved transport}} \\ & + \underbrace{\bar{\rho} w |\tilde{\nabla} G|}_{\text{front displacement}} \end{aligned} \quad (5)$$

where the Favre filter  $\tilde{Q}$  is defined by:

$$\bar{\rho} \tilde{Q} = \int \rho Q(\mathbf{x}') F(\mathbf{x} - \mathbf{x}') d\mathbf{x}' \quad (6)$$

Two unclosed terms, corresponding respectively to unresolved transport and to front displacement, are found in Eq. (5) and have to be modeled.

### Unresolved transport

In the present simulations, the unresolved transport terms in  $G$ -equation, as in other filtered transport equations, is closed using a classical gradient assumption (as for a passive scalar):

$$\bar{\rho} [\tilde{G} \tilde{\mathbf{u}} - \tilde{G} \tilde{\mathbf{u}}] = - \frac{\mu_t}{S_c^G} \tilde{\nabla} \tilde{G} \quad (7)$$

where  $S_c^G$  is a Schmidt number assumed to be constant. The subgrid scale turbulent viscosity  $\mu_t$  is determined from a filtered structure function (Ducros et al. 1996):

$$\mu_t = 0.00084 \bar{\rho} \Delta \sqrt{\tilde{F}_2} \quad (8)$$

where the filtered structure function  $\tilde{F}_2$ :

$$\tilde{F}_2 = [\tilde{\mathbf{u}}(\bar{\mathbf{x}} + \bar{\Delta}) - \tilde{\mathbf{u}}(\bar{\mathbf{x}})]^2 \quad (9)$$

is estimated at the location  $\bar{\mathbf{x}}(i, j, k)$  from the six adjacent points  $(i+1, j, k)$ ,  $(i-1, j, k)$ ,  $(i, j+1, k)$ ,  $(i, j-1, k)$ ,  $(i, j, k+1)$  and  $(i, j, k-1)$ , using a three iterated Laplacien filter (Ducros et al. 1996).

### Flame front displacement

The front displacement term is rewritten as:

$$\begin{aligned} \bar{\rho} w |\tilde{\nabla} G| &= \int \rho w |\tilde{\nabla} G| F(\mathbf{x} - \mathbf{x}') d\mathbf{x}' \\ &= \int \int_0^1 \rho w |\tilde{\nabla} G| \delta(G - G') F(\mathbf{x} - \mathbf{x}') dG' d\mathbf{x}' \\ &= \int_0^1 \langle \rho w \rangle_s^{G'} \Sigma^{G'} dG' = \langle \rho w \rangle_s \Sigma \end{aligned} \quad (10)$$

where  $\delta$  is the Dirac delta function.  $\Sigma^{G'}$  is the subgrid surface density of the iso-surface  $G = G'$  and  $\langle w \rangle_s^{G'}$  is the averaged displacement speed  $w$  averaged along the surface  $G = G'$  at the subgrid level. These quantities are defined by:

$$\Sigma^{G'} = \int |\tilde{\nabla} G| \delta(G - G') F(\mathbf{x} - \mathbf{x}') d\mathbf{x}' \quad (11)$$

and

$$\langle \rho w \rangle_s^{G'} \Sigma^{G'} = \int \rho w |\tilde{\nabla} G| \delta(G - G') F(\mathbf{x} - \mathbf{x}') d\mathbf{x}' \quad (12)$$

$\Sigma$  and  $\langle w \rangle_s$ , introduced in Eq. (10), may be viewed as generalized subgrid flame surface density and surface averaged flame displacement speed, defined as:

$$\begin{aligned} \Sigma &= \int_0^1 \Sigma^{G'} dG' \\ &= \int_0^1 \int |\tilde{\nabla} G| \delta(G - G') F(\mathbf{x} - \mathbf{x}') d\mathbf{x}' dG' \\ &= |\tilde{\nabla} G| \end{aligned} \quad (13)$$

and

$$\begin{aligned} \langle \rho w \rangle_s &= \frac{\int_0^1 \langle \rho w \rangle_s^{G'} \Sigma^{G'} dG'}{\Sigma} \\ &= \frac{\int_0^1 \int \rho w |\tilde{\nabla} G| \delta(G - G') F(\mathbf{x} - \mathbf{x}') d\mathbf{x}' dG'}{\Sigma} \\ &= \frac{\bar{\rho} w |\tilde{\nabla} G|}{|\tilde{\nabla} G|} \end{aligned} \quad (14)$$

Quantities such as  $\Sigma^{G'}$ ,  $\langle \rho w \rangle_s^{G'}$ ,  $\Sigma$  and  $\langle \rho w \rangle_s$  have now to be modelled. Averaged displacement speed along the flame front may be estimated from the laminar flame speed  $S_L$  and the fresh gases density  $\rho_0$  as:

$$\langle \rho w \rangle_s = \langle \rho w \rangle_s^{G'} = \rho_0 S_L \quad (15)$$

Subgrid scale surface densities  $\Sigma^{G'}$  and  $\Sigma$  may be described from algebraic expressions or by a balance equation. Starting from equation (1) and definitions (11) and (13), there is no theoretical difficulties to derive exact, but unclosed, balance equations for  $\Sigma^{G'}$  or  $\Sigma$ . From equation (1), one easily obtains a balance equation for  $|\tilde{\nabla} G|$ :

$$\begin{aligned} \frac{\partial |\tilde{\nabla} G|}{\partial t} + \nabla \cdot [\tilde{\mathbf{u}} |\tilde{\nabla} G|] &= (\nabla \cdot \tilde{\mathbf{u}} - \tilde{\mathbf{n}} \tilde{\mathbf{n}} : \tilde{\nabla} \mathbf{u}) |\tilde{\nabla} G| \\ &- \nabla \cdot [w \tilde{\mathbf{n}} |\tilde{\nabla} G|] + w \nabla \cdot \tilde{\mathbf{n}} |\tilde{\nabla} G| \end{aligned} \quad (16)$$

where  $\tilde{\mathbf{n}}$  is the unit vector normal to the iso- $G$  surface, defined by:

$$\tilde{\mathbf{n}} = - \frac{\tilde{\nabla} G}{|\tilde{\nabla} G|} \quad (17)$$

and  $\nabla \cdot \tilde{\mathbf{n}}$  is the iso-surface curvature. Eq. (16) becomes, after filtering and using the previous definitions:

$$\begin{aligned} \frac{\partial \Sigma}{\partial t} + \nabla \cdot [\langle \tilde{\mathbf{u}} \rangle_s \Sigma] &= \langle \nabla \cdot \tilde{\mathbf{u}} - \tilde{\mathbf{n}} \tilde{\mathbf{n}} : \tilde{\nabla} \mathbf{u} \rangle_s \Sigma \\ &- \nabla \cdot [\langle w \tilde{\mathbf{n}} \rangle_s \Sigma] + \langle w \nabla \cdot \tilde{\mathbf{n}} \rangle_s \Sigma \end{aligned} \quad (18)$$

The two first terms in the right hand side correspond respectively to the strain rate acting on the  $G$ -isosurface and to the normal front displacement. The last term combines

propagation and curvature effects. In fact, this equation is formally identical to the balance equation for flame surface density widely used in Reynolds averaged equations (Trouné and Poinso 1994; Vervisch et al. 1995).

An alternative formulation is to recast surface densities in terms of surface wrinkling. The subgrid scale wrinkling of the  $G'$ -iso-surface (i.e. the subgrid scale  $G'$ -iso-surface divided by the projection of this surface in the resolved propagating direction) may be defined by:

$$\Xi^{G'} = \frac{\int |\vec{\nabla} G| \delta(G - G') F(x - x') dx'}{\bar{n}_p \cdot \int \bar{n} |\vec{\nabla} G| \delta(G - G') F(x - x') dx'} \quad (19)$$

where  $\bar{n}$  is the unit vector normal to the  $G'$ -surface and  $\bar{n}_p$  is the unit vector normal to the resolved propagating direction. They are defined by:

$$\bar{n} = -\frac{\vec{\nabla} G}{|\vec{\nabla} G|} \quad \text{and} \quad \bar{n}_p = -\frac{\vec{\nabla} \bar{G}}{|\vec{\nabla} \bar{G}|} \quad (20)$$

Assuming that the  $G$ -field is large compared to the  $F$ -filter size (i.e. the filtered conditioned  $G$ -gradient may be estimated from the filtered  $G$ -gradient) leads to the following estimate:

$$\Xi^{G'} = \bar{\Xi} \approx \frac{|\vec{\nabla} G|}{|\vec{\nabla} \bar{G}|} \quad (21)$$

In the  $G$ -equation framework, only the  $G^*$ -iso-level surface, denoting the flame position, has to be precisely tracked. Then, combining Eq. (14) and (21) and introducing the flame front wrinkling factor  $\Xi = \Xi^{G^*}$ , the front displacement term in Eq. (5) is written:

$$\overline{\rho w |\vec{\nabla} G|} \approx \langle \rho w \rangle_s \Xi |\vec{\nabla} \bar{G}| \approx \rho_0 S_L \Xi |\vec{\nabla} \bar{G}| \quad (22)$$

where  $\langle \rho w \rangle_s$  is estimated from the laminar flame speed  $S_L$  and the density of fresh gases,  $\rho_0$ . A transport equation, formally identical to the one proposed by Weller (1993) in a Reynolds average context, may also be derived for  $\Xi$ , replacing  $\Sigma$  by  $\Xi |\vec{\nabla} \bar{G}|$  in Eq. (18).

To solve a balance equation for the subgrid scale flame surface density  $\Sigma$  or the subgrid flame front wrinkling  $\Xi$  is probably a promising approach. But, in a first step, a simple algebraic expression is proposed to describe the flame front wrinkling  $\Xi$  in order to close the front displacement term in Eq. (5).

### ESTIMATION OF THE FLAME FRONT WRINKLING FACTOR $\Xi$

Veynante et al. (1994, 1996) have performed instantaneous flame front visualizations in a turbulent V-shaped premixed flame (Fig. 1). In this experiment, a laser sheet is used to visualize the flow field seeded with oil droplets. As the droplets burn at the flame front, the interface between illuminated and dark areas on the images corresponds to the flame front. Then a statistical analysis may be conducted to extract flame front characteristics such as flame surface densities (in a Reynolds averaging context), vectors normal to the flame front or front curvatures.

The instantaneous images may also be processed in a LES-context to extract the subgrid scale flame surface density  $\Sigma$  or the flame front wrinkling  $\Xi$ . An example of experimental results is displayed on Fig. 2 where  $\Xi$  is plotted as a function of the size  $\Delta$  of the square box filter. As expected, the wrinkling factor increases from 1 (no wrinkling at the subgrid scale level) to a constant value  $\Xi_{max}$ , depending on turbulence characteristics and chemical equivalence ratio,

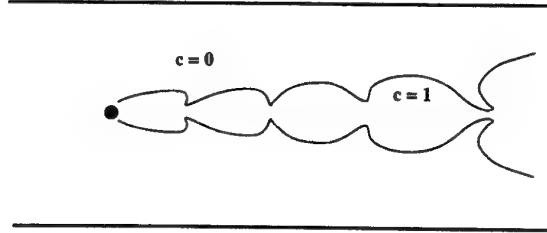


Figure 1: Experimental configuration of Veynante et al. (1994, 1996). A turbulent premixed propane-air flame is stabilized behind a small rod. A V-shape flame is observed. As the flow is seeded with oil droplets burning at the flame front, the instantaneous flame front, separating fresh gases ( $c = 0$ ) from burnt gases ( $c = 1$ ) is visualized using a laser sheet.

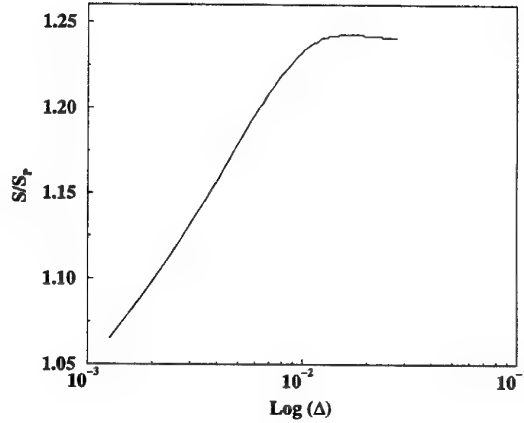


Figure 2: Experimental measurements of the subgrid scale flame front wrinkling  $\Xi$  plotted as a function of the LES mesh size  $\Delta$  (in m). Data extracted from the flame front visualizations made by Veynante et al. (1994, 1996). Input flow speed: 8 m/s; turbulence level: 10 %, equivalence ratio: 0.78.

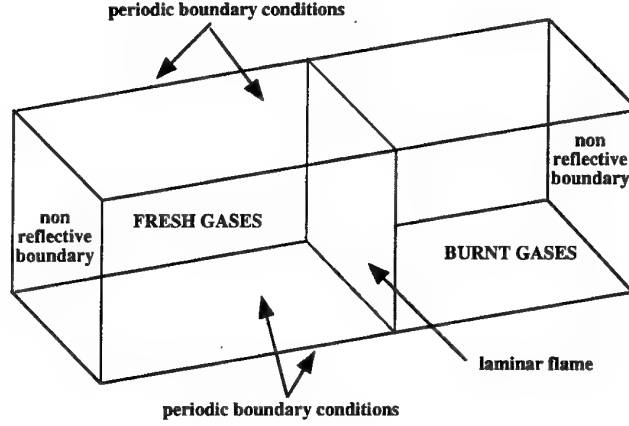


Figure 3: Numerical configuration

when the filter size exceeds the outer cut-off scale  $L_{out}$  (i.e. the larger wrinkling scale) of the flame front. A simple fit may be proposed to describe  $\Xi$ :

$$\Xi = 1 + (\Xi_{max} - 1) \left[ 1 - \exp \left( -\beta \frac{\Delta}{L_{out}} \right) \right] \quad (23)$$

where  $\Xi_{max}$  and  $L_{out}$  have to be modeled, for example using fractal or Bray-Moss-Libby theories.

Classical expressions for turbulent flames speed  $\bar{S}_T$  (Eq. 4) may be easily recovered. Assuming that  $\Xi_{max}$  is inversely proportional to the flame wrinkling length scale  $L_y$  introduced by Bray et al. (1987),  $\Xi_{max}$  may be estimated as:

$$\Xi_{max} - 1 \approx a \frac{L_{out}}{L_y} \quad (24)$$

where the outer cut-off scale  $L_{out}$  is used as a scaling factor.  $a$  is a model constant. When the wrinkling length  $L_y$  is large,  $\Xi_{max} \approx 1$  corresponding, as expected, to no flame front wrinkling at the subgrid scale level. Estimating the outer cut-off scale  $L_{out}$  using the turbulence integral length scale  $l_t$  and replacing  $L_y$  by the expression proposed by Bray et al. (1987), leads to:

$$\Xi_{max} - 1 = a \frac{l_t}{C l_t \left( \frac{S_L}{u'} \right)^n} = \frac{a}{C} \left( \frac{u'}{S_L} \right)^n \quad (25)$$

where  $C$  and  $n$  are two constants. Then:

$$\Xi_{max} = \frac{\bar{S}_T^{max}}{S_L} \approx 1 + \frac{a}{C} \left( \frac{u'}{S_L} \right)^n \quad (26)$$

which corresponds to Eq. (4). A similar result may also be achieved from fractal theory.

The proposed approach is quite attractive: in its simplest forms, expressions proposed to model the subgrid turbulent flame speed  $\bar{S}_T^{max}$  are recovered but the formulation could be easily refined, using an algebraic expression or a balance equation for the flame surface density  $\Sigma$  or the flame front wrinkling  $\Xi$ .

## NUMERICAL TESTS

A premixed flame propagating in a turbulent flow field is simulated using a LES version of the DNS code NTMIX-3D (Stoessel 1995). An homogeneous and isotropic turbulence, decreasing with time, is initialized, according to a Von Karman - Pao turbulence spectrum (Hinze 1975), in a rectangular box (Fig. 3). The computational grid is  $128 \times 32 \times 32$ . A plane laminar flame is superimposed to the flowfield at time  $t = 0$ , separating fresh reactants on the left-hand side ( $x < 0$ ) from burnt products on the right ( $x > 0$ ). The left- and the right- sides of the computational domain are inflow and outflow boundaries (non-reflecting conditions) while periodic conditions are applied at lateral boundaries. The problem is statistically one-dimensional. After the initial time  $t = 0$ , the flame front is wrinkled by turbulent motions.

Unresolved transport terms are modeled using a filtered structure function to estimate the subgrid turbulent viscosity  $\mu_t$  (Eqs. 7 and 8). Turbulent Prandtl and Schmidt numbers for temperature and scalar diffusion are chosen constant and equal to 0.6. In a first step, a constant value of the subgrid scale factor  $\Xi$  is assumed.

The first computation is conducted with a low turbulence level. The turbulence Reynolds number  $Re_t$ , based on the integral length scale  $l_t$ , the velocity fluctuation  $u'$  and the viscosity of fresh gases  $\nu$ , is  $Re_t = u' l_t / \nu = 200$ . An instantaneous snapshot of the flame front, described with the  $G = 0.5$ -isosurface, is plotted on Fig. 4 together with cuts

of the vorticity field at the boundaries. The wrinkling of the flame surface remains low and, because of viscous effects induced by the higher temperature, the turbulence structures have almost disappeared in the burnt gases. In fact, this computation is closed to a direct numerical simulation and subgrid scale models are not predominant.

On the other hand, when the turbulence Reynolds number is increased to  $Re_t = 5000$  (Fig. 5), the resolved flame front is clearly more wrinkled and turbulence structures remain in the burnt gases side. Such a computation cannot be conducted by DNS.

## CONCLUSIONS

A new LES subgrid scale model for reacting flow field is proposed in the  $G$ -equation framework. This approach is based on a subgrid flame surface density, or subgrid flame front wrinkling, description. This concept is very attractive because, in its simplest form, classical expressions for the subgrid turbulence flame speed  $\bar{S}_T$  are recovered but this analysis may be easily refined using algebraic expressions or solving transport equations for the flame surface density  $\Sigma$  or the flame front wrinkling factor  $\Xi$ .

Two preliminary tests have been presented. When the initial turbulence Reynolds number,  $Re_t$ , is low ( $Re_t = 200$ ), the wrinkling of the flame front remain low and the turbulence structures disappears in the burnt products because of viscous effects. This simulation could be conducted using direct numerical simulation. But, the second test case with a higher turbulence Reynolds number ( $Re_t = 5000$ ) clearly shows that numerical simulations of high Reynolds numbers reacting flows are possible with our approach. In this case, the resolved flame front is clearly wrinkled and turbulence structures are not dissipated in the burnt products.

These preliminary results have now to be validated to show the ability of this  $G$ -equation formulation to provide quantitative informations on the structure on a highly turbulent reacting flow. The proposed model should also be improved. In a first step, algebraic expressions for the subgrid scale wrinkling of the flame front,  $\Xi$ , or for the subgrid flame surface density,  $\Sigma$ , will be tested. Dynamic formulations of these algebraic expressions are also under developments.

**Acknowledgements :** Computations were carried out at IDRIS (Institut du Développement et des Ressources en Informatique Scientifique, Orsay - France).

## References

- Bray, K., M. Champion, and P. Libby (1987). The turbulent premixed boundary layer with enthalpy. *Combust. Sci. Technol.* 55.
- Butler, T. and P. O'Rourke (1977). A numerical method for two dimensional unsteady reacting flows. In *Proceedings of the 16th Symposium (Int.) on Combustion*. The Combustion Institute, Pittsburgh.
- Coats, C. (1996). Coherent structures in combustion. *Prog. Energ. Combust. Sci.* 22, 427-509.
- Ducros, F., P. Comte, and M. Lesieur (1996). Large-eddy simulation of transition to turbulence in a boundary layer developing spatially over a flat plate. *J. Fluid Mech.* 326, 1-36.
- Gouldin, F. (1996). Combustion intensity and burning rate integral of premixed flame. In *Proceedings of the 26th Symposium (Int.) on Combustion*. The Combustion Institute, Pittsburgh.
- Hinze, J. (1975). *Turbulence*. McGraw-Hill.
- Kerstein, A., W. Ashurst, and F. Williams (1988). Field equation for interface propagation in an unsteady homogeneous flow field. *Phys. Rev. A* 37(7), 2728-2731.
- Menon, S. (1996). Large-eddy simulation of combustion instabilities. In *Proceedings of the Sixth International Conference on Numerical Combustion*, New Orleans, Louisiana, March 4-6.
- Menon, S. and W. Jou (1991). Large-eddy simulations of combustion instability in an axisymmetric ramjet combustor. *Combust. Sci. Technol.* 75, 53.
- Moser, V. (1996). Large-eddy simulations of turbulent premixed flames using a capturing/tracking hybrid approach. In *Proceedings of the Sixth International Conference on Numerical Combustion*, New Orleans, Louisiana, March 4-6.
- Piana, J., D. Veynante, S. Candel, and T. Poinso (1996). Direct numerical simulation analysis of the  $g$ -equation in premixed combustion. In *Proceedings of the second ERCOFTAC workshop on Direct and Large Eddy Simulation*, Septembre 16-19, Grenoble, France.
- Poinso, T., T. Echekki, and M. Mungal (1991). A study of the laminar flame tip and implications for premixed turbulent combustion. *Combust. Sci. Technol.* 81(1-3), 45.
- Stoessel, A. (1995). An efficient tool for the study of 3d turbulent combustion phenomena on mpp computers. In *Proceedings of the HPCN 95 Conference*, Milan (Italy). Springer Verlag.
- Trounev, A. and T. Poinso (1994). The evolution equation for the flame surface density. *J. Fluid Mech.* 278, 1-31.
- Vervisch, L., E. Bidaux, K. Bray, and W. Kollmann (1995). Surface density function in premixed turbulent combustion modeling, similarities between probability density function and flame surface approach. *Phys. Fluids A* 7(10), 2496 - 2503.
- Veynante, D., J. Duclos, and J. Piana (1994). Experimental analysis of flamelet models for premixed turbulent combustion. In *Twenty-fifth Symposium (International) on Combustion*. The Combustion Institute.
- Veynante, D., J. Piana, J. Duclos, and C. Martel (1996). Experimental analysis of flame surface density models for premixed turbulent combustion. In *Proceedings of the 26th Symposium (Int.) on Combustion*. The Combustion Institute, Pittsburgh.
- Weller, H. (1993). The development of a new flame area combustion model using conditional averaging. Technical Report TF/9307, Dept. of Mech. Eng., Imperial College, London.

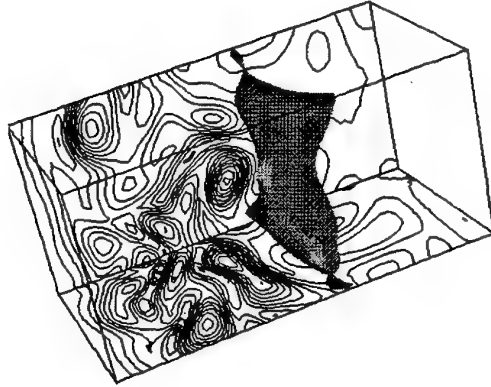


Figure 4: Instantaneous snapshot of a premixed flame propagating in a turbulent flow. The flame front, corresponding to  $G^* = 0.5$ -iso-level, is displayed with cuts of the vorticity field. The flame separates fresh reactants on the left side of the figure from burnt products at the right side. The turbulence Reynolds number is  $Re_t = u' l_t / \nu = 200$  where  $l_t$  is the integral length scale,  $u'$  the initial turbulence level in the fresh gases and  $\nu$  the kinematic viscosity of fresh gases.

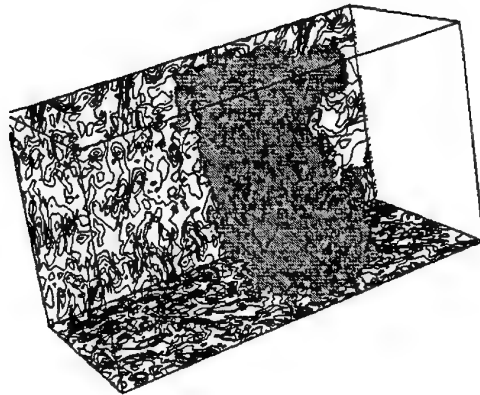


Figure 5: Instantaneous snapshot of a premixed flame propagating in a turbulent flow. The flame front, corresponding to  $G^* = 0.5$ -iso-level, is displayed with cuts of the vorticity field. The flame separates fresh reactants on the left side of the figure from burnt products at the right side. The turbulence Reynolds number is  $Re_t = u' l_t / \nu = 5000$  where  $l_t$  is the integral length scale,  $u'$  the initial turbulence level in the fresh gases and  $\nu$  the kinematic viscosity of fresh gases.

# MODELLING OF TURBULENT CONVECTION IN JOINT PDF EQUATION. APPLICATIONS TO TURBULENT PREMIXED COMBUSTION

F. Galzin - T. Mantel : Renault-Research Division  
9-11 Avenue du 18 juin 1940  
92500 Rueil Mailmaison - France

R. Borghi : IRPHE - UMR 138 CNRS  
ESM2 - IMT  
Tech. de Château Gombert  
13451 Marseille Cedex 20 - France

## ABSTRACT

The fuel concentration and enthalpy joint pdf approach is considered here in order to simulate the propagation of a turbulent premixed flame in a closed vessel, like in S.I. engines. A Lagrangian-Eulerian Monte Carlo method is used to solve the corresponding pdf transport equation. In this equation, although the reaction term needs no modelling except the kinetic scheme, two terms have to be modelled, namely the micromixing term which represents the transport in composition space due to molecular effects, and the turbulent convection term which characterizes the turbulent dispersion in the physical space. This paper focus on the modelling of this last term. The turbulent convection transport of the stochastic particles in the physical space is represented by two different models. The first one assumes the classical gradient-diffusion transport while the second one, which is a generalization to reacting flows of the Random Flight Model of Durbin (1980), is based on the Lagrangian description of the turbulence and evolves the turbulent velocities of the particles. The models are presented and tested in various situations, namely simple one dimensional simulations with frozen turbulence during the ignition and the flame propagation, and two-dimensional simulation of a premixed flame in a closed vessel. The importance of the turbulent convective transport modelling is thus emphasized and the effect of the model on the ignition, the flame propagation and the turbulent flame characteristics is clearly shown.

## 1 INTRODUCTION

To calculate the properties of turbulent reactive flow fields, the probability density function (pdf) approach (Pope 1985, Dopazo 1994) is especially suited because the

reaction rate is directly calculated in the governing equations. The method considered here consists of solving the transport equation for the joint pdf of the compositions, namely the fuel mass fraction and the mass enthalpy including the heat of formation of the species involved, and to calculate the velocity field using an external Eulerian code. In this pdf equation, the transport in physical space due to turbulent velocity fluctuations has to be modelled. Although conventional gradient transport models have been proposed (Janicka *et al.* 1979, Pope 1985), gradient transport hypothesis is questionable in reactive flows (Libby and Bray 1981), especially for low turbulence and high values of the heat release factor (Veynante *et al.* 1997).

In this paper, the effects of the turbulent diffusion of concentration and energy on the ignition and propagation of premixed flames in a closed vessel are investigated. Since the traditional finite-difference or finite-volume techniques are not efficient, a Monte Carlo method is used here to solve the scalars joint pdf. Two different turbulent convection models are then tested: a model based on a gradient transport assumption (Pope, 1985) and a stochastic process for the particles velocity based on a Lagrangian description of inhomogeneous turbulent dispersion for inert flows (Durbin 1980) and adapted here to reactive flows. This paper is organized as follows. In section 2, the various models of turbulent dispersion are both presented and the generalized Durbin's model is tested and validated in simple one-dimensional inert configuration. Section 3 presents the results of one-dimensional and two-dimensional simulations of the turbulent flame propagation in a closed vessel, and is devoted to studying the effects of the model on the turbulent flame characteristics.

## 2 TURBULENT CONVECTIVE TRANSPORT MODELLING

To study inhomogeneous variable-density flows, it is more suitable to use the mass density function (mdf) (Pope 1985) :  $\mathcal{F}(\underline{\psi}) = \rho(\underline{\psi})f(\underline{\psi}) = \bar{\rho}\tilde{f}(\underline{\psi})$  where  $f(\underline{\psi})$  is the joint pdf of the scalars represented by  $\underline{\psi}$ . The transport equation for the joint mdf is :

$$\begin{aligned} \frac{\partial \mathcal{F}(\underline{\psi})}{\partial t} + \frac{\partial}{\partial x_i} (\tilde{U}_i \mathcal{F}(\underline{\psi})) &= \frac{\partial}{\partial x_i} \left( \bar{\rho} d \frac{\partial}{\partial x_i} \left( \frac{\mathcal{F}(\underline{\psi})}{\bar{\rho}} \right) \right) \\ (I) \quad (II) \quad (III) \\ - \frac{\partial}{\partial x_i} \left( \langle u'_i | \underline{\phi} = \underline{\psi} \rangle \mathcal{F}(\underline{\psi}) \right) &- \frac{\partial}{\partial \psi_1} \left( \dot{w}_F(\underline{\psi}) \mathcal{F}(\underline{\psi}) \right) \\ (IV) \quad (V) \\ - \frac{\partial}{\partial \psi_2} \left( \left[ \left\langle \frac{Dp}{Dt} | \underline{\psi} \right\rangle + \langle \tau_{ij} \frac{\partial U_j}{\partial x_i} | \underline{\psi} \right] \frac{\mathcal{F}(\underline{\psi})}{\rho(\underline{\psi})} \right) \\ (VI) \quad (VII) \\ - \sum_{\alpha=1}^2 \sum_{\beta=1}^2 \frac{\partial}{\partial \psi_\alpha} \frac{\partial}{\partial \psi_\beta} \left( \langle d \frac{\partial \phi_\alpha}{\partial x_i} \frac{\partial \phi_\beta}{\partial x_i} | \underline{\psi} \rangle \mathcal{F}(\underline{\psi}) \right) \quad (1) \\ (VIII) \end{aligned}$$

where  $\underline{\phi}$  represents the couple of physical variables ( $Y, h$ ) and  $\underline{\psi}$  represents the corresponding couple of probabilistic variables associated to  $\underline{\phi}$ . The overbars and the  $\tilde{\cdot}$  denote Reynolds averaged quantities and Favre averaged quantities respectively. The primes denote fluctuations. The quantities within angular brackets are conditional expectations : for any function  $R$ ,  $\langle R | \underline{\psi} \rangle$  written for  $\langle R(\underline{x}, t) | \underline{\phi}(\underline{x}, t) = \underline{\psi} \rangle$  is the conditional expectation of  $R$  given that  $\underline{\phi} = \underline{\psi}$ .

The pdf considered here is an Eulerian one. Indeed, it is the pdf of fluid properties at a given spatial location. Following Pope (1985), the approach used for solving equation (1) is a mixed Lagrangian-Eulerian Monte Carlo method. Within a device of volume  $V$  with a corresponding mass  $M$ , the initial mdf is represented by a large number  $N$  of stochastic particles, each representing a mass  $\Delta m = M/N$ . In order to contribute at each point  $\underline{x}$  and each time  $t$  to the discrete representation of the mdf, these particles evolve in physical and composition spaces according to adapted stochastic processes. Let us divide the volume  $V$  into  $c$  cells. The average mass density  $\bar{\rho}_k$  in cell number  $k$  of volume  $v_k$  is calculated by the relation (see Pope 1985) :

$$\bar{\rho}_k = \Delta m \frac{N_k}{v_k}$$

where  $N_k$  denotes the number of particles in the considered cell. The Favre average of any property  $Q(\underline{\phi})$  in cell  $k$  is determined using :

$$\tilde{Q}_k \sim \frac{1}{N_k} \sum_{N_k} Q(\underline{\phi}^n)$$

where  $\underline{\phi}^n = (\phi_1^n, \phi_2^n)$  represents the properties of particle number  $n$  located in cell  $k$ . Thus, the ensemble average over the particles in the cell  $k$  approximates the density-weighted average.

The problem is then to find stochastic processes that govern the particles evolution and so that the pdf of these

particles evolves in the same way as the pdf of fluid particles. For the closed terms (II, III, V) of equation (1) these processes are very simple (Pope, 1985). The modelling of terms (VI) and (VII) which are due to pressure and to viscous effects is presented in Galzin (1996). The micromixing (VIII) which is a crucial point of the pdf approach is often represented by one of the two classical models proposed by Dopazo O'Brien (1974) or Curl (1963).

Here, we focus our attention on term (IV) which represents the transport in physical space due to turbulent velocity fluctuations. By just considering the transport in physical space and assuming a given turbulence with no mean flow, the mdf equation (1) can be simply written :

$$\frac{\partial \mathcal{F}(\underline{\psi})}{\partial t} = - \frac{\partial}{\partial x_i} \left( \langle u'_i | \underline{\phi} = \underline{\psi} \rangle \mathcal{F}(\underline{\psi}) \right) \quad (2)$$

The joint scalars pdf contains no information about the velocity and thus, the expectation  $\langle u'_i | \underline{\psi} \rangle$  has to be modelled.

### 2.1 The Pope's model (1985)

Using the gradient diffusion assumption for the pdf  $f(\underline{\psi})$ , equation (2) can be written as follows (Pope, 1985) :

$$\frac{\partial \mathcal{F}(\underline{\psi})}{\partial t} = \frac{\partial}{\partial x_i} \left( \bar{\rho} d_f \frac{\partial}{\partial x_i} \left( \frac{\mathcal{F}(\underline{\psi})}{\bar{\rho}} \right) \right) \quad (3)$$

where the turbulent diffusion coefficient is  $d_f = \nu_t / Sc_f$ ;  $\nu_t$  is the turbulent diffusivity coefficient defined by  $\nu_t = c_\mu k^2 / \epsilon$  and  $Sc_f$  is a turbulent Schmidt number.  $k$  and  $\epsilon$  represent the turbulent energy and the corresponding dissipation respectively.

The stochastic process for the location  $x_i$  ( $i = 1, 2, 3$ ) of the stochastic particles corresponding to (3) is (Pope 1985) :

$$x_i(t + \delta t) - x_i(t) = \frac{1}{\bar{\rho}} \frac{\partial (\bar{\rho} d_f)}{\partial x_i} \delta t + \sqrt{2 d_f} \Delta_{\delta t} W_t \quad (4)$$

where  $\Delta_{\delta t} W_t$  represents a Gaussian white-noise process defined by  $\Delta_{\delta t} W_t = \sqrt{\delta t} \xi_i$ . The variable  $\xi$  denotes an independant standardized Gaussian random variable with zero mean and variance equal to 1.

### 2.2 The Durbin's model (1980)

Following the theory of Taylor (1921) for the homogeneous cases, Durbin proposed a model, which takes into account the temporal correlations of the particles velocity, adapted to variable Lagrangian time scale situations. The model is presented firstly here for homogeneous flows in finite difference form (in the  $y$  direction): the subscript  $n$  denotes a value at the  $n^{th}$  time step

$$\begin{cases} v_n = a v_{n-1} + b \xi_n \\ y_n = y_{n-1} + \frac{v_n + v_{n-1}}{2} \Delta t \end{cases} \quad (5)$$

where

$$\begin{aligned} a &= 1 - \frac{\Delta t}{T_L} \\ b &= \sigma_v \sqrt{1 - a^2} \end{aligned} \quad (6)$$



and with the initial condition

$$v_0 = \sigma_v \xi_0 \quad (7)$$

As previously,  $(\xi)$  is a set of independant Gaussian random numbers with zero mean and variance equal to 1. For homogeneous flows,  $\sigma_v$  represents the variance of the particle velocity and  $T_L$  is the Lagrangian time scale. This model clearly tends to recover the properties of the turbulent motion of fluid particles that are :

- The velocity fluctuations are nearly random Gaussian variables, according to observed turbulent fluctuations.
- The fluid particles keep the memory of their past states during a finite time.

For inhomogeneous flows<sup>1</sup>, two different situations have to be considered :

- $\Delta t < T_L$ : The homogeneous process (5-6) is used with a two steps predictor-corrector method. Indeed, the parameters  $a$  and  $b$  (see relation (6)) are evaluated at  $y_{n+1/2}$ .
- $\Delta t > T_L$ : The system (5-6) is no longer valid and Durbin proposes intuitively a process which recovers the Pope's model for inhomogeneous inert flows. Thus, he introduces the following drift velocity for the particles :

$$V_D = \sigma_v^2 \frac{\partial T_L}{\partial y}$$

Indeed, a particle moving in a direction of increasing  $T_L$  persists in its motion longer than an other particle moving in a direction of decreasing  $T_L$ .

For homogeneous flow, the model parameters  $\sigma_v$  and  $T_L$  can be estimated from the Eulerian quantities, namely the turbulence intensity and the turbulent integral time scale (Hinze 1975). It can be shown as well that the asymptotic limit ( $t \gg T_L$ ) of the Durbin's or Taylor's dispersion model corresponds to a classical diffusion process with a turbulent diffusion coefficient  $d^*$  defined by :

$$d^* = \sigma_v^2 T_L \quad (8)$$

In order to recover, in the limit  $t \gg T_L$ , the turbulent diffusion coefficient prescribed by the classical  $k-\varepsilon$  model, namely  $d^* = C_\mu k \tau_t$  ( $C_\mu = 0.09$ ), the Lagrangian time scale  $T_L$  and the variance  $\sigma_v$  are evaluated in the following way :

$$\frac{\sigma_v^2}{k} = \frac{C_\mu}{C_0} \quad (9)$$

$$\frac{T_L}{\tau_t} = C_0 \quad (10)$$

The constant  $C_0$  is not universal. Berlemont (1981) picked  $C_0 = 0.2$  while Picart *et al.* (1986) adopted  $C_0 = 0.14$ . According to Hinze (1975), the constant  $C_0$  ranges from 0.2 to 0.6. In the following,  $C_0 = 0.3$ .

### 2.3 The generalized Durbin's model

The Durbin stochastic process for the turbulent velocity  $u_i$  of a particle can be written equivalently as follows (here  $u_i = u_i'$  since the mean velocity is assumed to be equal to zero) :

$$u_i(t + \delta t) - u_i(t) = -u_i \frac{\delta t}{T_L} + \sigma_v \sqrt{1 - a^2} \xi_i \quad (11)$$

where  $(\xi)$  always represents a set of independant standardized Gaussian random variables. Obviously, the particles are moving in the physical space according to the classical process :

$$x_i(t + \delta t) - x_i(t) = u_i \delta t \quad (12)$$

This process is here generalized in order to deal with turbulent reacting flows (with variable density and turbulent energy profiles). The Eulerian equation for the particle velocity corresponding to (11) can be expressed by :

$$\rho Du_i = -\frac{\rho u_i}{T_L} \delta t + \rho \sigma_v \sqrt{1 - a^2} \xi_i \quad (13)$$

where  $Du_i$  denotes the particular derivation of the velocity  $u_i$ .

Developing the LHS of (13) and averaging the new expression, assuming the mean velocity equal to zero, the following result can be deduced :

$$\tilde{\xi} = \frac{1}{\bar{\rho} \sigma_v} \frac{\Delta t}{\sqrt{1 - a^2}} \frac{\partial(\bar{\rho} \sigma_v^2)}{\partial y} \quad (14)$$

Finally, the system (5-6) simply has to be used with (14). The variance property is still valid.

### 2.4 Test and validation of the new model in a simple inert case

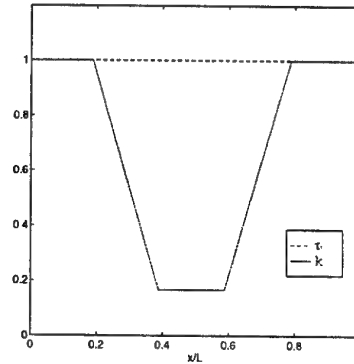


Figure 1: turbulent profiles across the domain

Turbulent dispersion of particles has been simulated in a one dimensional bounded domain of length  $L$  ( $\Delta x = 1/40 L$ ). Initially, the particles are distributed in a uniform manner, namely 500 particles per cell. Two cases are investigated : firstly, a inhomogeneous stationary turbulent energy profile with constant density is assumed (see Figure 1) and secondly, a variable density profile is postulated in a steady homogeneous turbulence (see Figure 2). This last profile is very similar to that encountered in flames. In both cases, the mean velocity field is zero. The Fig-

<sup>1</sup>The feature which characterizes inhomogeneous turbulence in Durbin's model (1980) is the spatial variability of the Lagrangian time scale

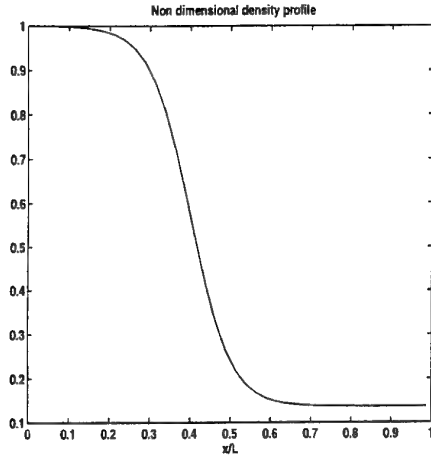


Figure 2: density profile across the domain

ures 3 and 4 present the evolution of the spatial distribution of the particles in the whole domain. As clearly shown by these pictures, the original Durbin model does not implicitly take into account the drift velocity due to the inhomogeneity of  $k$  and  $\bar{\rho}$ .

The necessary improvement of the Durbin's process using our modifications (called Durbin bis) for both cases studied is clearly demonstrated, in order to verify the conservation of stochastic particles in computational cells and consequently the mass conservation. The original Durbin's model is actually not adapted to such situations (see Figures 3 and 4).

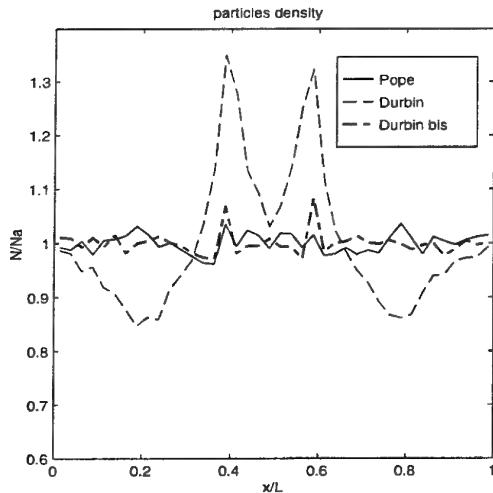


Figure 3: distribution of stochastic particles in the domain -  $N_a$  represents the initial particle density (inhomogeneous turbulent intensity assumption)

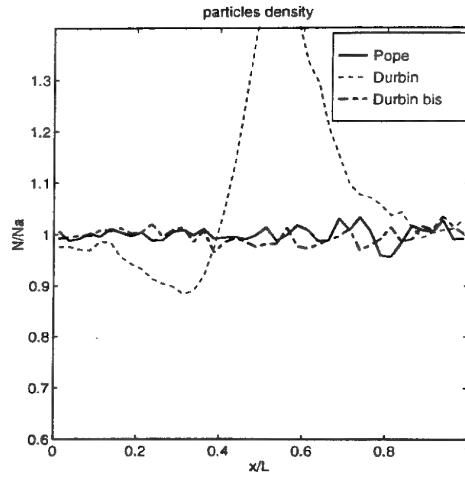


Figure 4: distribution of stochastic particles in the domain (variable density assumption)

### 3 APPLICATION TO TURBULENT REACTIVE FLOWS

#### 3.1 One dimensional configuration

Lagrangian-Eulerian Monte Carlo simulations are performed in order to simulate a 1D turbulent premixed flame propagation in a closed vessel of 200 mm length. The mixture is a propane-air one with equivalence ratio equal to 0.9. Calculations are performed in half geometry, and combustion is initiated on the right side of the computational domain, by introducing a localized source term ( $E_{ign} = 3 \text{ mJ} - \Delta t_{ign} = 1 \text{ ms}$ ) for the enthalpy in the pdf equation. The energy released during ignition is assumed to decrease linearly with time and to vary spatially with an exponential profile as well. An idealised steady homogeneous turbulence is assumed for simplicity ( $u' = 0.8 \text{ m/s}$  and integral length scale  $l_t = 5.4 \text{ mm}$ ). The initial thermodynamic conditions of the simulations are as follows :  $\bar{T}_0 = 300 \text{ K}$  and  $\bar{P}_0 = 3 \text{ bar}$ . All the unknown information required by the various stochastic processes of the Lagrangian Monte Carlo method are provided by the Eulerian Kiva2 code from Los Alamos (Amsden *et al.* 1989). The particles density is initially equal to 500 particles per cell.

Figure 5 presents the evolution of the temperature 600 K in the domain during the ignition period, using the gradient-diffusion model and the generalized Durbin model. The fresh gases velocity is plotted as well. A very simple regular grid of cell size  $\Delta x/l_t = 4.610^{-2}$  is used for this simulation. The micromixing (see term (VIII) in equation 1) is here represented by the well-known deterministic LMSE model (Dopazo & O'Brien 1974).

The crucial effect of the turbulent dispersion of concentration and temperature on early flame growth is clearly illustrated on that picture. The energy released by the spark in the ignition zone is diffusing more slowly with the Durbin type model. Consequently, the flame kernel is growing faster. Moreover, since the energy is more concentrated in the ignition volume using Durbin generalized model, the unburned gases expansion is more intense than using the gradient-diffusion type Pope process. This, the

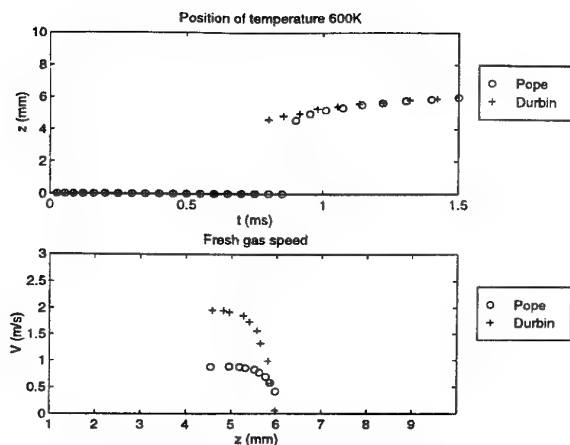


Figure 5: position of the temperature 600 K (mm) versus time (ms) and fresh gas velocity (m/s) versus position - LMSE model - ignition phase

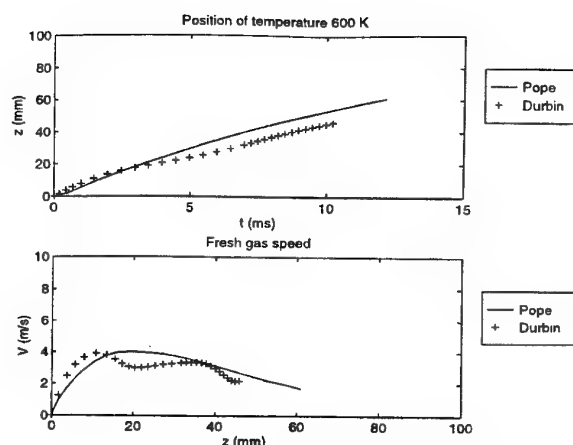


Figure 6: position of the temperature 600 K (mm) versus time (ms) and fresh gas velocity (m/s) versus position - new mixing model

flame propagates faster. The behaviour of the two turbulent convective transport models is quite different. The new Durbin type model is more realistic since it does not consider the gradient-diffusion assumption which is questionable for reactive flows but also, especially in this simulation, since it can take into account the unsteadiness of the ignition period.

Figure 6 presents the results corresponding to the fully-developed flame propagation. Here, the cell size of the grid is such that  $\Delta x/l_t = 0.18$ . The micromixing is modelled in a different way as previously mentioned. Improving the idea of Pope and Anand (1984), a new model for micromixing (VIII) has been proposed (Galzin 1996). It considers the different combustion regimes and takes into account the eventual presence of flamelets which can be more or less perturbed by small scale turbulence. A parameter based on the ratio of the Kolmogorov length scale and the laminar flame thickness controls this perturbation in the concentration space. The characteristic mixing time scale is calculated by solving (using the Kiva2 code) the transport equation for the scalar dissipation modelled by Mantel & Borghi (1994) in the case of fast chemistry and generalized to distributed combustion regimes by Galzin & Borghi (see Galzin 1996). The turbulent flame propagates faster using the gradient-diffusion process. Nevertheless the fresh gas speed behaviour is quite similar with the two models. In a view to understand these results, Figure 7 presents the temporal evolution of the non dimensionalized turbulent flame speed and thickness, respectively reduced by  $u'$  and  $l_t$ . An important effect of turbulent dispersion on the turbulent flame characteristics is shown. The flame looks thinner with the generalized Durbin model and the corresponding turbulent flame speed is smaller. This can be explained by the slower diffusion process with Durbin type model.

### 3.2 Two dimensional simulation

The combustion chamber is a parallelepipedal constant volume ( $100 \times 60 \times 60 \text{ mm}^3$ ). It has been studied experimentally by Floch (1990) and can reproduce aerodynamic

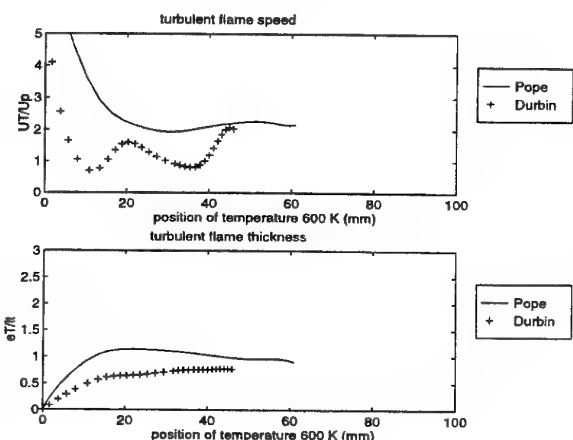


Figure 7: reduced turbulent flame speed and thickness versus position of temperature 600 K (mm)

conditions that occur in S.I engines. The flame propagates in a propane-air mixture with equivalence ratio 0.9. Combustion is ignited by an energy supply ( $E_{ign} = 7 \text{ mJ}$ ,  $\Delta t_{ign} = 1 \text{ ms}$ ). At this time, the turbulence is assumed to be homogeneous and isotropic. The temporal evolution of the turbulent flow field is calculated by a  $k - \epsilon$  turbulence model introduced in the Kiva2 code. Initial turbulence conditions at ignition time are  $u' = 0.8 \text{ m/s}$  and  $\epsilon = 150 \text{ m}^2/\text{s}^3$ . These conditions do not exactly correspond to the experimental data given by Floch (1990). Indeed, the turbulent energy is experimentally calculated including the contribution due to cycle to cycle variations. According to the symmetry of the geometry, a simple two-dimensional rectangular mesh composed of  $30 \times 100$  cells is used. Initially, the particles are uniformly distributed, namely 500 particles per cell.

The new perturbed flamelet mixing model is used in this simulation. Wall heat transfer is also considered by introducing a specific stochastic process for the enthalpy variable (see Galzin 1996).

The Figure 8 presents the temporal evolution of the temperature 600 K on the symmetry axis of the chamber and

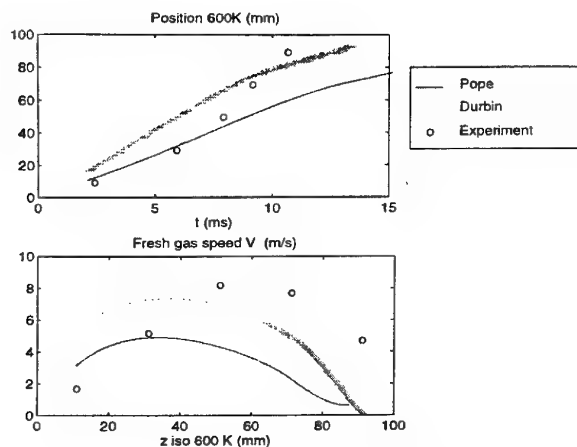


Figure 8: position of the temperature 600 K (mm) versus time (ms) and fresh gas velocity (m/s) versus position

of the corresponding fresh gas speed using the various turbulent convective transport processes. It shows the effect of the diffusion turbulent term modelling on the flame propagation in the 2D combustion chamber and on the fresh gas velocity due to thermal expansion as well. The behaviour of the models is different compared to 1D calculation. Indeed, the Durbin's model leads to a faster propagation than the Pope's model, which seems to be in better agreement with the experimental data<sup>2</sup>. The difference between the two models can partially be explained by the fact that the Durbin's model generates a thinner flame leading to higher velocity gradients and then to a higher production of turbulent kinetic energy. This last phenomenon was not taken into account in the 1D simulation since the turbulence was frozen. In this two-dimensional simulation, the unsteadiness of the turbulence interacting with combustion seems to play an important role. Nevertheless, the  $k - \epsilon$  model used here probably fails to correctly model this interaction. Consequently, it is quite difficult to validate a turbulent diffusion model rather than another.

## 4 CONCLUDING REMARKS

Durbin's model has been generalized in order to study turbulent reacting flows. The comparison with a gradient diffusion model (Pope 1985) clearly shows the important role of the turbulent diffusion on ignition, premixed flame propagation and turbulent flame characteristics.

Comparison between these two models on the two-dimensional configuration is very delicate. The interaction between the flame and the turbulence is extremely complex and is certainly not taken into account in the classical  $k - \epsilon$  model used in this study.

<sup>2</sup>The flame propagation in the second part of the combustion chamber can hardly be simulated due to the turbulence generating perforated grid (Floch 1990) which cannot be described by the modelling.

## References

- AMSDEN A.A, O'ROURKE P.J AND BUTLER T.D, 1989 Kiva2: a computer program for chemically reactive flows with sprays. Report LA-11560-MS. Los Alamos National Laboratories.
- BERLEMONT A., . *Modélisation et prédiction du comportement de particules discrètes dans un écoulement turbulent*. PhD thesis Université de Rouen 1981.
- CURL R. L., 1963 Dispersed phase mixing : I. theory and effects in simple reactors. *A.I.Ch.E Journal* **9**, 175-181.
- DOPAZO C., 1994 Recent developments in pdf methods. In *Turbulent Reacting Flows* , pp. 375-474. Academic Press.
- DOPAZO C. AND O'BRIEN E.E, 1974 An approach to the autoignition of a turbulent mixture. *Acta Astronautica* **1**, 1239-1266.
- DURBIN P.A, 1980 A random flight model of inhomogeneous turbulent dispersion. *The Physics of Fluids* **23**, 2151-2153.
- FLOCH A., . *Etude de la turbulence instationnaire dans une chambre de combustion à volume constant, interaction avec la propagation d'une flamme allumée par étincelle*. PhD thesis Université de Rouen 1990.
- GALZIN F., . *Contribution à la modélisation de la combustion dans les moteurs à allumage commandé*. PhD thesis Université de Rouen 1996.
- HINZE J.O., 1975 *Turbulence*. McGraw-Hill - New York.
- JANICKA J., KOLBE W. AND KOLLMANN W., 1979 Closure of the transport equation for the probability density function of turbulent scalar fields. *J. Nonequil. Thermodyn.* **4**, 47-66.
- LIBBY P.A AND BRAY K.N.C, 1981 Implications of the laminar flamelet model in premixed turbulent combustion. *Combustion and Flame* **39**, 33-41.
- MANTEL T. AND BORCHI R., 1994 A new model of premixed wrinkled flame propagation based on a scalar dissipation equation. *Combustion and Flame* **96**, 443-457.
- PICART A, BERLEMONT A. AND GOUSSET G., 1986 Modelling and predicting turbulence fields and the dispersion of discrete particles transported by turbulent flows. *Int.J.Multiphase Flow* **12-2**, 237-261.
- POPE S.B, 1985 PDF methods for turbulent reactive flows. *Prog. Energy Combust. Sci* **11**, 119-192.
- POPE S.B. AND ANAND M.S., 1984. Flamelet and distributed combustion in premixed turbulent flames. In *Twentieth Symposium (International) on Combustion* pages 403-410. The Combustion Institute.
- TAYLOR G.I, 1921 Diffusion by continuous movements. *Proc. London Math. Soc.* **20**, 196.
- VEYNANTE D., TROUVÉ A., BRAY K.N.C AND MANTEL T., 1997 Gradient and counter-gradient scalar transport in turbulent premixed flames. *Journal of Fluid Mechanics* **332**, 263-293.

# EFFECTS OF UNSTABLE STRATIFICATION AND MEAN SHEAR ON THE CHEMICAL REACTION IN GRID-GENERATED TURBULENCE

S. Komori, K. Nagata

Department of Chemical engineering

Kyushu University

Hakozaki, Fukuoka 812-81

Japan

## ABSTRACT

The effects of unstable thermal stratification and mean shear on chemical reaction and turbulent mixing were experimentally investigated in a liquid mixing layer downstream of turbulence-generating grids with and without a rapid chemical reaction. The results show that the turbulent mixing is enhanced at both large- and small-scales by buoyancy in unstably-stratified conditions and that the chemical reaction is intensively promoted. The mean shear also acts to enhance the turbulent mixing mainly at large-scales but the chemical reaction rate is not so large compared to in the unstably-stratified case. The unstable stratification without mean shear is proposed as a good technology to attain mild mixing.

## INTRODUCTION

When two reactants are introduced into a turbulent flow, turbulent mixing plays an important role on the progress of the chemical reaction until two species are perfectly mixed up to the minimum scale of turbulence. The effect of turbulent mixing on the mean reaction rate is very significant for higher-order reactions, which often appear in industrial reactors or in environmental flows. The mean fluid shear is used in general to promote the turbulent mixing and chemical reaction. However, it is often required to promote the turbulent mixing and chemical reaction in very weakly sheared conditions. For example, some of biochemical-reactors or polymerization-reactors need to mildly mix the fluids without damaging cells or polymers. It is, therefore, of practical importance to develop an unsheared mixing technology.

The purpose of this short paper is to propose a method based on the utilization of unstable stratification which can promote the chemical reaction and turbulent mixing under unsheared conditions. The effects of both unstable thermal-stratification and mean shear on the chemical reaction and turbulent mixing are experimentally investigated in a liquid mixing-layer downstream of turbulence-generating grids, and both the effects are compared.

## EXPERIMENTS

Experiments were carried out in three flows; an unsheared neutrally-stratified flow, an unsheared unstably-stratified flow and a sheared neutrally-stratified flow. A rapid chemical reaction between an acid and a base was used (Komori et al. 1993). The unstably-stratified flow and sheared flow were obtained by changing the initial temperature or velocity between upper and lower layers as shown in Figure 1. The initial temperature and velocity differences were set to get the almost same values of the turbulent kinetic energy in both developed flows behind the grids. The initial temperature difference was 10K for an unstably-stratified flow and the velocity difference was 3cm/s for a sheared flow. The cross-sectional mean velocity was set to the same value of 12.5cm/s in both sheared and unsheared flows and the Reynolds number based on the mesh size of a turbulence-generating grid and the cross-sectional mean velocity was 2500. Instantaneous velocity and concentration were simultaneously measured using a two-component laser Doppler velocimeter and a laser induced fluorescence technique (Komori and Nagata 1996). The turbulence quantities such as the intensities and power spectra of velocity fluctuations, the turbulent mass fluxes and the Reynolds stress were measured. Furthermore the total amount of the reaction product was estimated from the vertical (transverse) profiles of mean concentration of chemical product.

## RESULTS AND DISCUSSION

Figures 2a, b and c show the vertical (transverse) profiles of the mean concentrations,  $C_A$  and  $C_P$ , of chemical species A and chemical product P in unsheared neutrally-stratified, unsheared unstably-stratified and sheared neutrally-stratified flows. When the mean concentrations of chemical species A are compared between reacting and non-reacting cases, the progress of chemical reaction can clearly be noticed. When the mean concentration of the product  $C_P$  is integrated in the vertical direction, it is found that the chemical reaction is surprisingly promoted by unstable stratification compared to the effect of the mean shear. The ratio of the integrated value of  $C_P$  in the unsheared unstably-stratified flow to that in

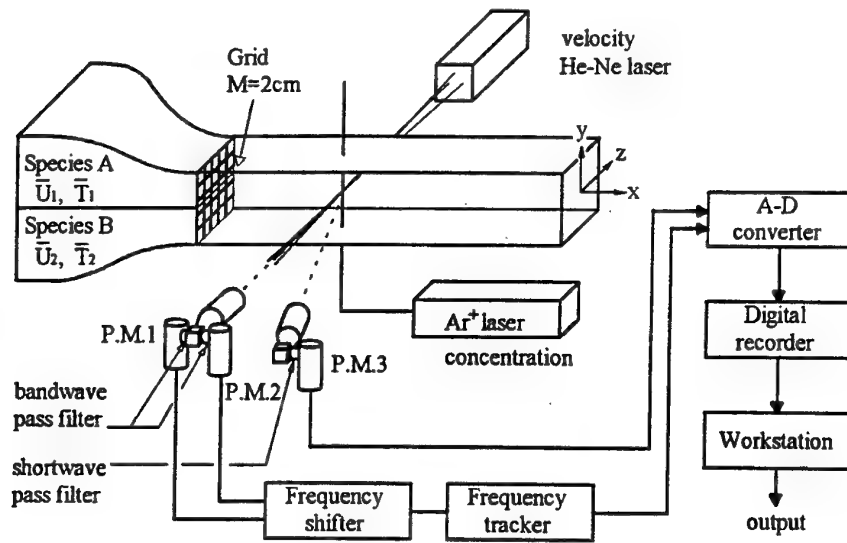


Figure 1: Experimental apparatus.

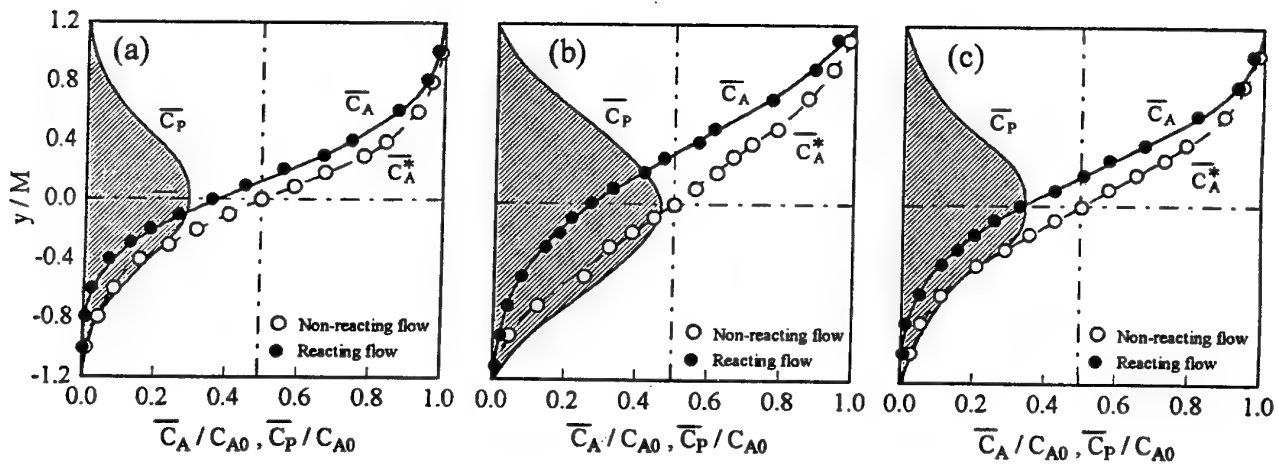


Figure 2: Vertical distributions of mean concentrations of chemical species A and product P: (a) in an unshowered neutrally-stratified flow, (b) in an unshowered unstably-stratified flow, (c) in a sheared neutrally-stratified flow.

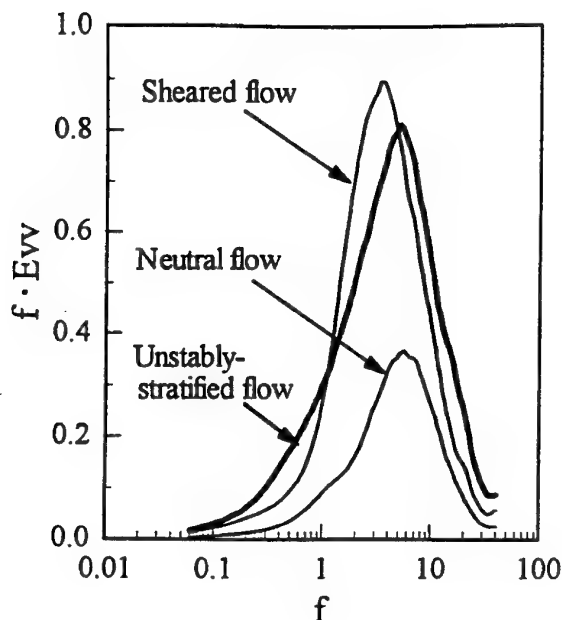


Figure 3: Power spectra of the vertical velocity fluctuation.

the sheared neutrally-stratified flow reaches 1.55. The intense promotion of chemical reaction in unstably-stratified conditions can be understood with turbulent mixing by buoyancy.

Figure 3 shows the power spectra of the vertical velocity fluctuation  $v$  in the three flows. The turbulent mixing is enhanced at both large- and small-scales by buoyancy under unstably-stratified conditions. Whereas the mean shear acts to enhance the turbulent mixing mainly at large-scales. The difference in turbulent mixing at small-scales results in the intense promotion of chemical reaction in the unstably-stratified flow.

Figure 4 shows the vertical profiles of the Reynolds stress in the correlation coefficient form for both unsheared unstably-stratified and sheared neutrally-stratified flows. The Reynolds stress in the unstably-stratified flow is certainly close to zero compared to large values in the sheared neutrally-stratified flow. The result suggests that the unstable stratification is a good tool to attain the promotion of chemical reaction and turbulent mixing under unsheared conditions, since the shearing stress acting on the fluid is much weaker in an unsheared unstably-stratified flow than in a sheared neutrally-stratified flow. The mild buoyancy-mixing technology may be useful for designing biochemical- and polymerization-reactors.

## CONCLUSIONS

The effects of unstable thermal stratification and mean shear on chemical reaction and turbulent mixing were experimentally investigated in a liquid mixing layer with and without a rapid chemical reaction. The main results from this study can be summarized as follows:

- (1) The chemical reaction is intensively promoted by buoyancy in unstably stratified conditions, since the turbulent mixing is enhanced at both large- and small-scales by buoyancy.
- (2) When the turbulence kinetic energy is set to the same value in both unsheared unstably-stratified and sheared neutrally-stratified flows, the chemical reaction rate be-

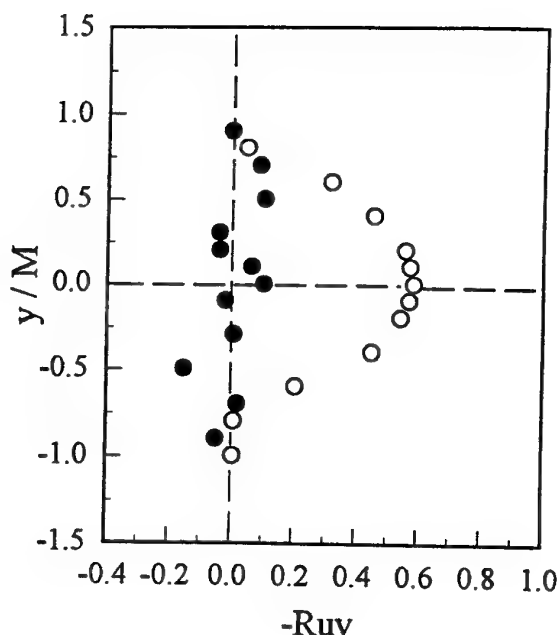


Figure 4: Vertical distributions of the Reynolds stress in unsheared unstably-stratified and sheared neutrally-stratified flows: ●, in an unsheared unstably-stratified flow; ○, in a sheared neutrally-stratified flow.

comes larger in unstably-stratified conditions than in sheared neutrally-stratified conditions. The difference is attributed to that the mean shear acts to enhance the turbulent mixing mainly at large-scales and that the mixing at small-scales is weaker than in unstably-stratified conditions.

(3) The unstable stratification may be useful for practical application to a mild mixing technology without shear.

## REFERENCES

- Komori, S., Nagata, K., Kanzaki, T. and Murakami, Y., 1993, "Measurements of mass flux in a turbulent liquid flow with a chemical reaction", *AIChE J.*, Vol. 39, pp. 1611-1620.
- Komori, S., and Nagata, K., 1996, "Effects of molecular diffusivities on counter-gradient scalar and momentum transfer in strong stable stratification", *J. Fluid Mech.*, Vol. 326, pp. 205-237.

## **SESSION 22 - JETS I**



# MEASURED REYNOLDS STRESS DISTRIBUTIONS AND ENERGY BUDGETS OF FULLY PULSED ROUND FREE JETS AND COMPARISONS WITH $k-\epsilon$ MODEL PREDICTIONS

Klaus Bremhorst and Peter J. Gehrke  
Department of Mechanical Engineering  
The University of Queensland  
Brisbane Queensland 4072  
Australia

Shuisheng He  
The Manchester School of Engineering  
The University of Manchester  
Manchester M13 9PL  
United Kingdom

## ABSTRACT

A detailed experimental examination of the turbulent kinetic energy budgets in a fully pulsed air jet exhausting into still air is made. Through the pulse hot-wire anemometer measurements were used to obtain estimates of all measurable terms in the energy budget of the intrinsic or phase averaged turbulent kinetic energy. These estimates are compared with those produced by the standard and a modified  $k-\epsilon$  model of turbulence. While the modified model reproduces bulk features of the velocity field, neither the standard model nor the modified model reproduces the budgets through the pulse correctly due to the existence of negative production of turbulent kinetic energy.

## INTRODUCTION

Measurements in fully pulsed round air jets by Bremhorst and Harch (1979) and Bremhorst and Hollis (1990) showed significant increases in entrainment over steady jets of the same mass flow rate. Reynolds shear stress measurements indicated an increase for the pulsed case but when normalised on jet momentum, the two were similar. In the present context, fully pulsed means that the mass flow varies from no flow to maximum flow during the pulsing cycle.

Graham and Bremhorst (1993) showed that the standard  $k-\epsilon$  model even with round jet modifications, could not predict correctly the decay of centre line velocity. For a fully pulsed jet, the latter has a characteristic change in slope when the inverse of centre line velocity is plotted against downstream distance while the steady jet has a near constant slope after the jet exit region. Modification of  $C_{2\epsilon}$  at a downstream point in the jet where it changes from pulse domination to steady behaviour, was necessary and was the only constant the adjustment of which gave correct predictions.

This leads to the conclusion that dissipation behaviour is likely to be modelled incorrectly by the standard model and provided the motivation for a more detailed investigation of

Reynolds stress distributions and energy budgets through the pulse. The region of greatest interest is that leading from pulse domination to steady jet behaviour and it is in this region that the measurements to be reported were taken.

## DEFINITIONS AND BASIC EQUATIONS

Fig.1 defines the flow velocities for the axial component. The instantaneous velocity,  $U_\tau$  at time  $\tau$  from the start of the pulse, consists of a time mean velocity,  $\bar{U}$ , a periodic component,  $U_{p,\tau}$  and a stochastic component termed the intrinsic turbulence,  $u_{i,\tau}$ . The sum of the intrinsic and periodic components of velocity is the aggregate turbulence velocity,  $u_{a,\tau}$ . Eqs 1(a)-(c) define these interrelationships. The period of the pulse is  $t_p$ .

$$U_\tau = \bar{U} + u_{p,\tau} + u_{i,\tau} \quad (1a)$$

$$= U_{p,\tau} + u_{i,\tau} \quad (1b)$$

$$= \bar{U} + u_{a,\tau} \quad (1c)$$

The turbulent kinetic energy budget for a steady jet case is given in Panchapakesan and Lumley (1993). The pulsed jet form for incompressible, axisymmetric, non-swirling flow is shown in Appendix A and differs from the steady case through the additional time dependent terms. In the limit for no pulsing, phase averaging represented by  $\langle \rangle$  replaces time averaging with all pulsed components vanishing.

## JET FACILITY AND INSTRUMENTATION

The jet investigated was produced by a pair of geared rotating rollers as shown in Fig. 2. This is the same facility that was used in the earlier work reported by Bremhorst and Harch (1979) and Bremhorst and Hollis (1990) with the exception that the exit diameter was halved and a smoothing section with rounded contraction was fitted to achieve this reduction, details

of which are not included in Fig.2. The jet exit diameter was 12.77 mm and the bulk mean jet exit velocity was kept at 36.6 m/s. Flow was pulsed at 10 Hz with a 1:2 ratio of time on to time off.

Disa 55M01 main unit with 55M11 constant temperature hot-wire anemometer adaptors were used to measure the various velocity components. X-wire configurations were used for  $v$  and  $w$  measurements while two single wires spatially separated but with the wires parallel and slightly offset to avoid thermal wake interference, were used for spatial derivatives of longitudinal velocity components. The Kolmogorov length scale was estimated from measurements to be of the order of 0.1 mm. 5µm Wollaston wire was used with active lengths of 0.5-0.6 mm in order to give adequate spatial resolution and for the X-probe, wire separation was no more than 0.3 mm.

### HOT-WIRE TECHNIQUES AND DATA ANALYSIS

Prior to measurements in the pulsed jet, all measurement techniques were tested in a steady jet and results compared with those of Panchapakesan and Lumley (1993) with excellent agreement in most cases, Gehrke (1997). The method of Panchapakesan and Lumley (1993) of X-array hot-wire calibration and data conversion by means of transformed variables was used but with two important differences. The first relates to the cooling law used to fit calibration data of voltage and velocity pairs. Panchapakesan and Lumley (1993) used a King's law based expression. For the larger velocity range needed in the present work, this led to bias errors in the higher order velocity products. These authors also used a curve of best fit to relate transformed variables to actual variables. This led to further bias as seen in the higher products of velocities.

In the present work, the Siddall and Davies (1972) quadratic equation for voltage as a function of velocity was used while spline functions were used for fitting actual data to transformed data. These two measures removed the observed bias from higher order products. Linear interpolation was used to convert voltages which fell between points in the lookup table generated from the calibration data.

Data processing was by conversion of analogue signals to digital form with a DASH 16F 12 bit analogue converter with a Metrabyte SSH-4 sample hold module to remove phase shifts during sampling. Resolution was optimised by filtering and amplification of the analogue signal. Subsequent data reduction was by DOS and Unix based systems with programs written in the C language.

Pulsed jet signals were processed to yield mean, periodic and intrinsic velocity components. A phase averaged form of the turbulent energy budget was developed in order to identify the relevant terms in the budget, Eq. (A1).

Phase averaging (denoted by  $\langle \rangle$ ) with respect to a timing mark on the rollers yielded distributions of Reynolds stresses and energy components through the pulse. The intrinsic shear stress,  $uv_{i,t}$ , was evaluated from Eq. (2) where the summation is over  $N_t$  values of the signal at time  $\tau$  from the moment of valve opening. Other phase averaged quantities were evaluated similarly.

$$uv_{i,t} = \langle uv_{i,t} \rangle = \frac{1}{N_t} \sum_{i=1}^{N_t} (U_{i,t} - U_{p,t}) (V_{i,t} - V_{p,t}) / N_t \quad (2)$$

$\langle vw^2 \rangle$  was not measured but set to  $0.5 \langle u^2 v \rangle$  based on the observation by Browne, Antonia and Shah (1987) that for a steady jet,  $\overline{vw^2}$  distributions are similar to those of  $\overline{u^2 v}$ . Only

the longitudinal velocity fluctuation related components of dissipation were measured using temporal derivatives or spatially separated wires as appropriate, Gehrke (1997). The remaining mean squared terms of spatial derivatives were found by the ratio method of Wygnanski and Fiedler (1969). The cross products of spatial derivatives were found by the averaging method of Browne, et al (1987).

Since periodic and intrinsic velocity fluctuations are uncorrelated, Eqs. (3) hold.

$$\overline{u_a^2} = \overline{u_p^2} + \overline{u_i^2} \quad \overline{v_a^2} = \overline{v_p^2} + \overline{v_i^2} \quad \overline{w_a^2} = \overline{w_p^2} + \overline{w_i^2} \quad (3)$$

### EXPERIMENTAL RESULTS

Decay of the centre line mean velocity,  $U_0$ , is different for steady and fully pulsed jets. For the  $x/d$  region of interest, this and the relevant half velocity radii are shown in Figs. 3(a) and (b) where  $x$  is the distance from the jet exit,  $d$  is the nozzle exit diameter,  $U_e$  is the mean jet exit velocity and  $r_{1/2}$  is the half velocity radius. Another noticeable difference is seen in the intrinsic turbulence level of the axial turbulence velocity levels, Fig.4, which for the pulsed jet is significantly higher than for a steady jet even when the pulsed component has become insignificant at  $x/d = 75$ . The turbulent kinetic energy is given in Fig. 5 where the intrinsic component for the pulsed jet is significantly above that for a steady jet.

Cross-products and triple products of intrinsic turbulence components are strongly dependent on the time through the pulse, Fig.6 and 7 thus giving large spatial and time derivatives relevant to the turbulent kinetic energy budget. Similarly, root-mean-squares of space derivatives of intrinsic velocity fluctuations required for the kinetic energy budget vary strongly throughout the pulse, Fig.8.

Fig.9 typifies the intrinsic turbulent kinetic energy budgets obtained from the measurements. In the figure,  $k_{Trans}$  denotes each transport component of the budget and  $k_0$  denotes the total intrinsic component of turbulent kinetic energy. A dominant feature of these results is the presence of the acceleration term which is balanced to a large degree by the advection term with the others playing a smaller role to give closure of the energy equation. For modelling purposes the most interesting term is production, Fig.10, which clearly illustrates significant regions through the pulse of negative production.

An examination of the terms making up the production of turbulence, Eq. A1, shows that this is attributable to the high spatial gradients of the periodic velocity component. In a steady jet, these components are absent which is consistent with the rapid decay of negative production with increasing  $x/d$  as seen in Fig. 10.

### COMPARISON WITH COMPUTATIONAL RESULTS

The results of Fig.9 can now be compared with budgets obtained with the standard  $k-\epsilon$  model and the model of Graham and Bremhorst (1993) with the modified  $C_{2\epsilon}$ . The effect of the change in  $C_{2\epsilon}$  is to stop the excessively rapid decay of intrinsic turbulent kinetic energy with increasing downstream distance. This in turn yields a change in the decay of the axial velocity and leads to good agreement with experimental results. From the computed through the pulse turbulent kinetic energy budgets of Figs.11(a) and (b), it is seen that this model falls short in dealing with the negative production of turbulence.

## CONCLUSIONS

Phase averaged measurements in a fully pulsed jet highlight differences between it and a steady jet in important aspects such as level of intrinsic or stochastic turbulent stresses through the pulse, presence of a large acceleration component in the energy budget, and most importantly, a significant negative production of turbulent energy for part of the pulse. Modelling of the flow with the standard and modified k-ε models fails to account for this aspect even though bulk features of the flow are predicted correctly by the modified model.

The conclusion initially drawn from modelling based on the standard k-ε model that the problem lies in the dissipation term of the dissipation equation is not substantiated by the above work but rather highlights the possible cause as being the negative production of turbulence which is modelled incorrectly by both models.

## ACKNOWLEDGMENTS

The Australian Research Council assisted financially with various stages of the project. The generous assistance provided by Professor J.D. Jackson of The University of Manchester in providing the opportunity to carry out the energy budget computations was invaluable.

## REFERENCES

Bremhorst, K. and Harch, W.H., 1979, "Near field velocity measurements in a fully pulsed subsonic air jet." *Turbulent*

*Shear Flows I*, ed. Durst, F., Launder, B.E., Schmidt, F.W. and Whitelaw, J.H., Springer Verlag, Berlin, pp. 37-54.

Bremhorst K. and Hollis, P.G. 1990, "Velocity field in an axisymmetric pulsed subsonic air jet." *ALAA Journal*, Vol. 28, 12, pp. 2043-2049.

Browne, L.W.B., Antonia, R.A. and Shah, D.A., 1987, "Turbulent energy dissipation in a wake." *Journal of Fluid Mechanics*, Vol. 179, pp. 307-326.

Gehrke, P.J., 1997, "The turbulent kinetic energy balance of a fully pulsed axisymmetric jet." Ph.D. Thesis, The University of Queensland, Brisbane, Queensland, Australia.

Graham, L.J.W. and Bremhorst, K. 1993, "Application of the k-ε turbulence model to the simulation of a fully pulsed free air jet." *ASME, Journal of Fluids Engineering*, Vol. 115, 71, pp. 70-74.

Panchapakesan, N.R. and Lumley, J.L., 1993, "Turbulence measurements in axisymmetric jets of air and helium, Part: I air jet." *Journal of Fluid Mechanics*, Vol. 246, pp. 197-223.

Siddall, R.G. and Davies, T.W. (1972), "An improved response equation for hot-wire anemometry." *International Journal of Heat and Mass Transfer*, Vol. 15, pp. 367-368.

Wyganski, I. and Fiedler, H., 1969, "Some measurements in the self-preserving jet." *Journal of Fluid Mechanics*, Vol. 38, pp. 577-612.

## APPENDIX A - THROUGH THE PULSE OR PHASE AVERAGED TURBULENT KINETIC ENERGY BUDGET

$$-\left[ \langle v_I^2 \rangle \frac{\partial (\bar{v} + \langle v_p \rangle)}{\partial r} + \langle w_I^2 \rangle \frac{(\bar{v} + \langle v_p \rangle)}{r} + \langle u_I^2 \rangle \frac{\partial (\bar{u} + \langle u_p \rangle)}{\partial x} + \langle uv_I \rangle \left( \frac{\partial (\bar{v} + \langle v_p \rangle)}{\partial x} + \frac{\partial (\bar{u} + \langle u_p \rangle)}{\partial r} \right) \right]$$

production

$$-\frac{1}{2} \left[ (\bar{v} + \langle v_p \rangle) \frac{\partial \langle v_I^2 \rangle}{\partial r} + (\bar{u} + \langle u_p \rangle) \frac{\partial \langle v_I^2 \rangle}{\partial x} + (\bar{v} + \langle v_p \rangle) \frac{\partial \langle w_I^2 \rangle}{\partial r} + (\bar{u} + \langle u_p \rangle) \frac{\partial \langle w_I^2 \rangle}{\partial x} \right. \\ \left. + (\bar{v} + \langle v_p \rangle) \frac{\partial \langle u_I^2 \rangle}{\partial r} + (\bar{u} + \langle u_p \rangle) \frac{\partial \langle u_I^2 \rangle}{\partial x} \right]$$

advection

$$-\frac{1}{2} \left[ \frac{\partial \langle v_I^3 \rangle}{\partial r} + \frac{\partial \langle u^2 v_I \rangle}{\partial r} + \frac{\partial \langle w^2 v_I \rangle}{\partial r} + \frac{\langle v_I^3 \rangle}{r} + \frac{\langle u^2 v_I \rangle}{r} + \frac{\langle w^2 v_I \rangle}{r} + \frac{\partial \langle u_I^3 \rangle}{\partial x} + \frac{\partial \langle uv_I^2 \rangle}{\partial x} + \frac{\partial \langle uw_I^2 \rangle}{\partial x} \right]$$

diffusion

$$-\frac{1}{2} \left[ \frac{\partial \langle v_I^2 \rangle}{\partial t} + \frac{\partial \langle u_I^2 \rangle}{\partial t} + \frac{\partial \langle w_I^2 \rangle}{\partial t} \right] - \frac{1}{\rho} \left[ \langle w_I \frac{\partial p_I}{\partial x} \rangle + \langle v_I \frac{\partial p_I}{\partial r} \rangle + \langle \frac{w_I}{r} \frac{\partial p_I}{\partial \theta} \rangle \right] - \text{dissipation} = 0 \quad (A1)$$

time

pressure transport

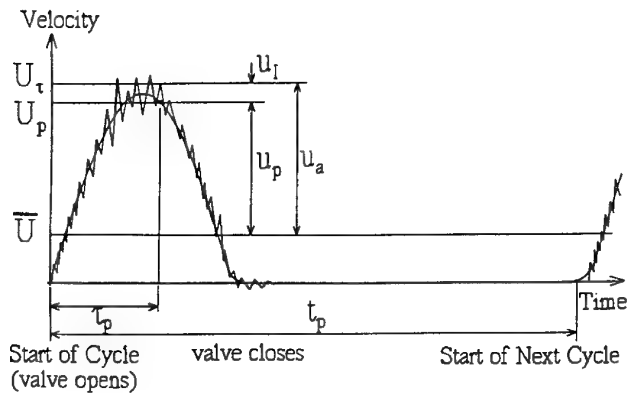


FIG. 1 - PULSED FLOW TERMINOLOGY

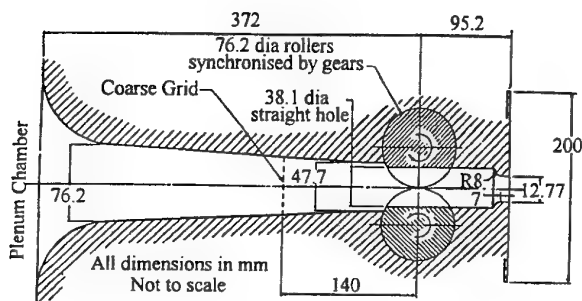


FIG. 2 - PULSED JET VALVE

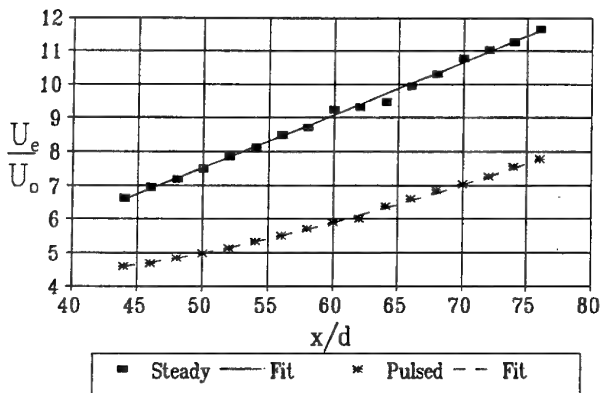


FIG. 3A - STEADY AND PULSED JET CENTRELINE VELOCITY DECAY (INVERSE OF VELOCITY NORMALIZED ON JET EXIT VELOCITY)

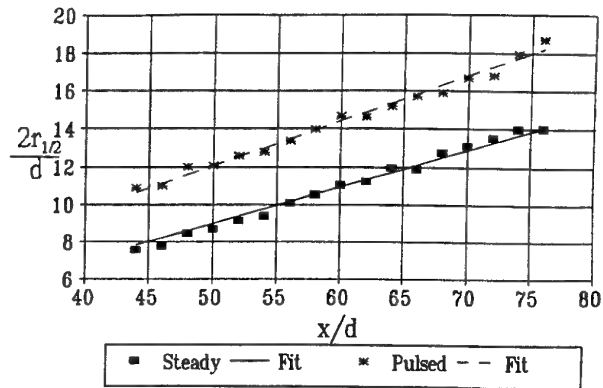


FIG. 3B - STEADY AND PULSED JET HALF RADIUS GROWTH

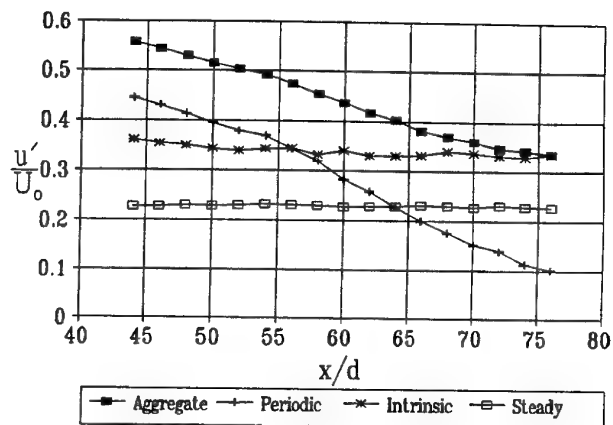


FIG. 4 - VARIATION OF AXIAL TURBULENCE VELOCITY ALONG JET CENTRELINE

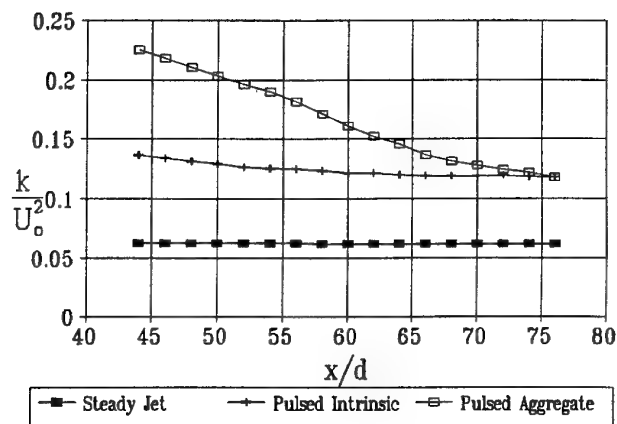


FIG. 5 VARIATION OF TURBULENT KINETIC ENERGY ALONG JET CENTRELINE

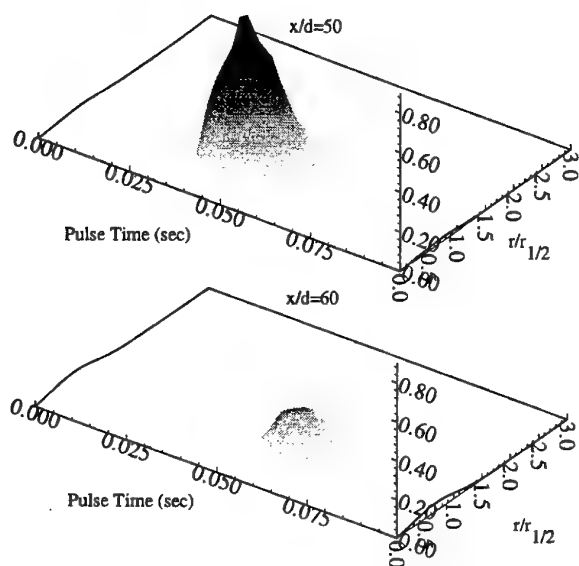


FIG.6 - VARIATION OF INTRINSIC REYNOLDS SHEAR STRESS

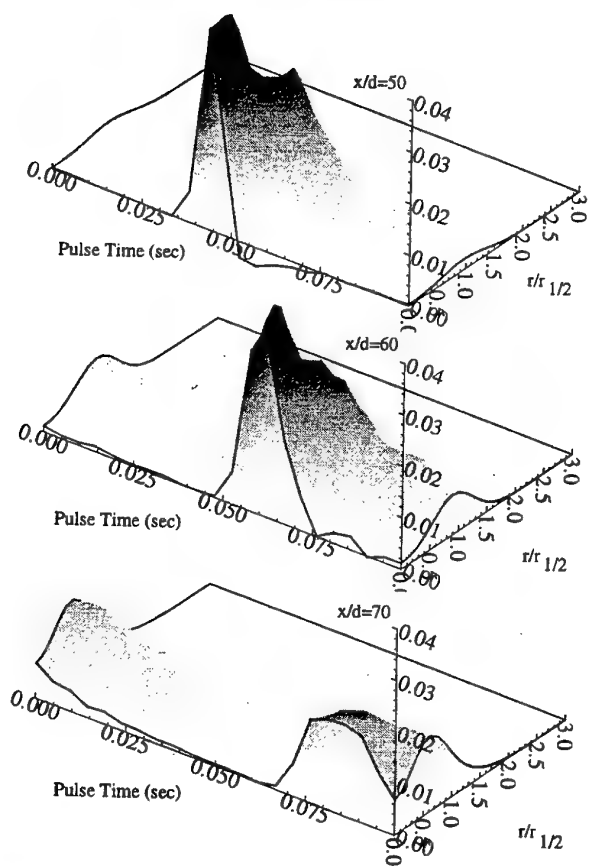


FIG.7 - VARIATION OF RADIAL DIFFUSION OF INTRINSIC UV PRODUCT,  $\langle uv^2 \rangle$

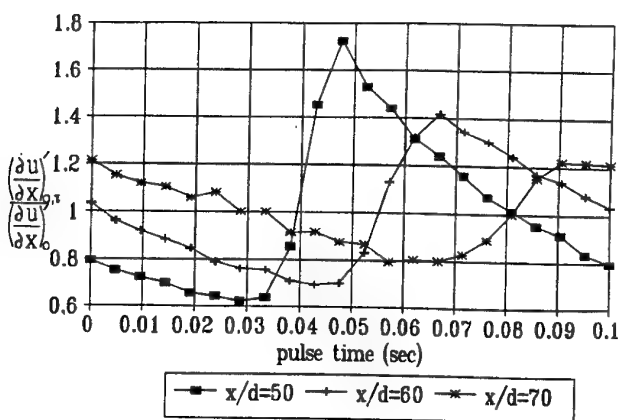


FIG.8 - ROOT-MEAN-SQUARE OF GRADIENT OF AXIAL VELOCITY FLUCTUATION THROUGH THE PULSE

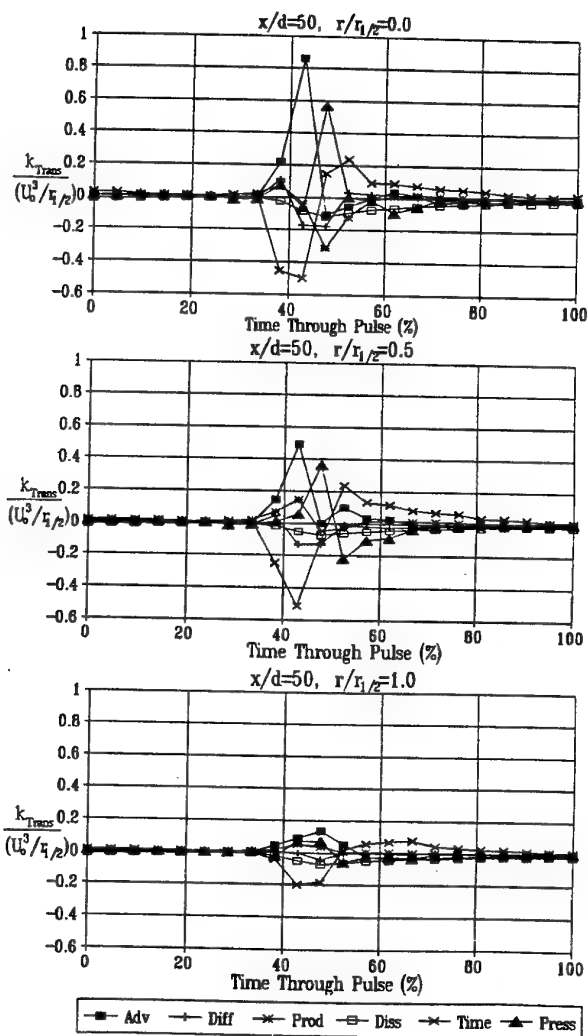


FIG.9 - THROUGH PULSE KINETIC ENERGY BUDGETS AT X/D = 50

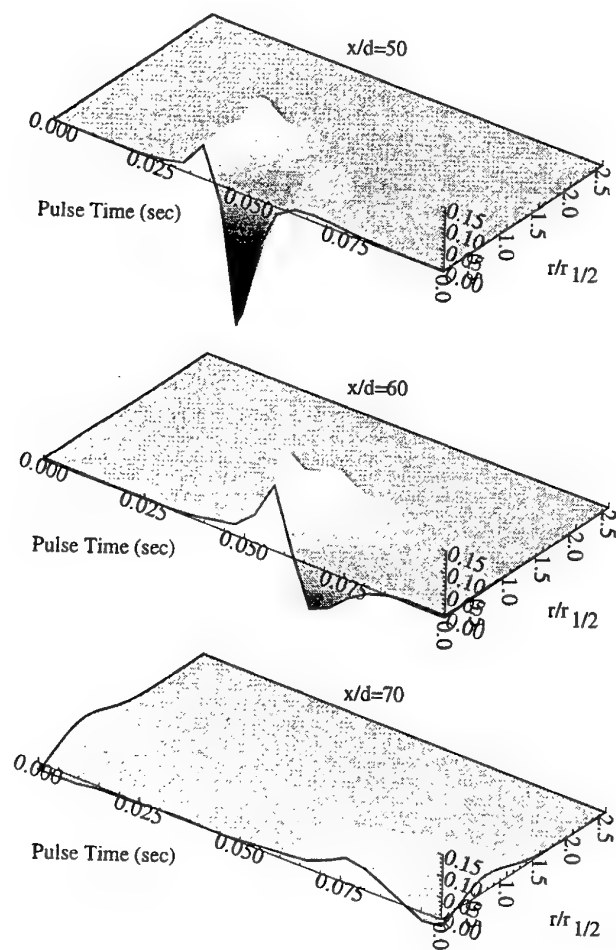


FIG.10 - TURBULENCE PRODUCTION THROUGH THE PULSE

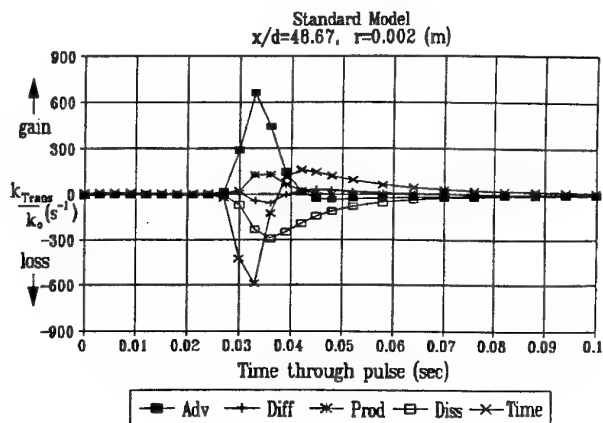


FIG.11A - THROUGH PULSE MODELLED KINETIC ENERGY BUDGETS NEAR CENTRELINE AND X/D = 48.7, STANDARD  $k-\epsilon$  MODEL

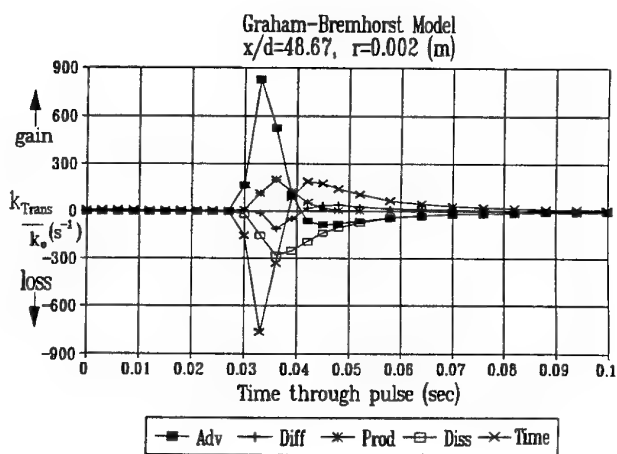


FIG.11B - THROUGH PULSE MODELLED KINETIC ENERGY BUDGETS NEAR CENTRELINE AND X/D = 48.7, GRAHAM-BREMHORST (1993) MODEL

# VORTICAL STRUCTURE OF AN ACOUSTICALLY FORCED PLANE JET: BI-ORTHOGONAL EDDIES vs. PHYSICAL EDDIES

D. Faghani, A. Sévrain, H.-C. Boisson

Institut de Mécanique des Fluides de Toulouse  
UMR CNRS/INP-UPS 5502  
Av. du Prof. C. SOULA  
31400 TOULOUSE  
FRANCE

## ABSTRACT

Phase locked X-probe hot wire measurements were made in the near field of a forced plane jet at Reynolds number 5600. They revealed leap frog pairings during which the trailing eddy's convection velocity grew up to 1.2 times the exit velocity. Bi-orthogonal decomposition of the velocity field yielded spatial (*topos*) and temporal (*chronos*) eigenfunctions which were compared to aforementioned eddies. It appeared that at least two pairs of eigenfunctions were required for a satisfactory reconstruction and that, more generally, orthogonal decomposition was quite dependent on the considered flow domain. Further one-dimensional decomposition showed the possibility of eddy detection in a coherent structure eduction scheme.

## NOMENCLATURE

$H, Z$	Exit slot width and height
$\mathcal{D}$	Measurement domain at slot's mid height
$U_0$	Jet exit velocity
$Re$	Reynolds number $U_0 H / \nu$
$\delta_0$	Initial boundary layer thickness
$\delta_{\omega 0}$	Initial vorticity thickness
$\theta_0$	Initial momentum thickness
$U_i(x, y, t)$	Instantaneous velocity vector
$\bar{U}$	Temporal mean value
$u$	Temporal fluctuation
$u'$	Temporal rms value
$f_0$	Initial instab. & eddy roll-up freq.
$S_{\theta 0}$	Sthroual number $f_0 \theta_0 / U_0$
$\psi_n, \varphi_n$	$n^{\text{th}}$ chronos and topos
$a_n^2$	$n^{\text{th}}$ BOD eigenvalue
$\varepsilon_n$	$n^{\text{th}}$ mode energy fraction $a_n^2 / \sum a_n^2$
$h$	BOD entropy $-\frac{1}{\ln N} \sum \varepsilon_n \ln \varepsilon_n$
$\varphi_p$	Phase relatively to forced flow period $T$

## INTRODUCTION

After an early introduction of Proper Orthogonal Decomposition (POD) in atmospheric turbulence by Fukuoka (1951) and Lorenz (1956), Lumley (1970) formalized its

use in turbulence theory as an objective means of discriminating between random turbulence and organized motion. Since late 80s, POD has known a fast growing popularity among experimental and numerical turbulence research community. Concerning turbulent flow analysis, coherent structures (CS) have been tracked through POD eigenfunctions in various turbulent situations. Both experimental (Herzog 1986) and numerical (Moin & Moser 1989) wall-bounded flow data were used to capture POD based CSs. Free shear layers were also extensively studied by Bonnet et al. (1993), Delville (1995) and Glauser & George (1987) through hot-wire measurements. Other investigations by Sirovich and coworkers are to be reported on jets (Sirovich et al. 1990) and Rayleigh-Bénard convection (Sirovich & Park 1990).

Apart from CS eduction, more and more effort has also been devoted to finding low dimensional POD based dynamical systems for numerical simulations. Early attempts relied on mixed Fourier-POD decompositions to cope with homogeneous directions and/or statistical time stationarity. In order to keep difficulty level low enough, only a few (often one!) Fourier modes were considered along with several POD modes. To further avoid phase recovery problems for temporal Fourier modes, focus was put on space-time separation yielding Sirovich's (1990) Snapshot POD and, in a deterministic frame of work, Aubry et al.'s (1991) bi-orthogonal decomposition (BOD). Low-dimensional dynamical systems were so defined for a turbulent boundary layer by Aubry et al. (1987) and for a turbulent free shear layer by Rajaei et al. (1994) and Cordier (1996).

One of the major issues in turbulent research via POD analysis is the relation between eigenfunctions and physical CSs as observed in visualizations. In this paper, we address this matter through experimental results in a plane jet at moderate Reynolds number. To clarify the situation in a rigorous deterministic frame of work, bi-orthogonal decomposition was performed in the near field of the jet under acoustical forcing. Phase locked measurements permitted to compare the instantaneous 2D velocity and vorticity fields with those reconstructed by BOD. The intricate phase relation between calculated eigenfunctions ensuring a physically acceptable image of CSs was examined.

Table 1: INITIAL FLOW CHARACTERISTICS

$Re$	5600
$H$ (mm)	10
$H/Z$	1/150
$u'/U_0$ (%)	0.8
$\theta_0/H$	0.028
$\delta_{\omega 0}/H$	0.12
$\delta_0/H$	0.2
$\delta_{\omega 0}/\theta_0$	4.3
$S_{\theta 0}$	0.0086

Further 1D results are also presented at fixed downstream stations to show the reliability of BOD in eddy description and detection.

## EXPERIMENTAL SETUP

Measurements were carried out in a low-speed open-return wind tunnel facility (fig.1) providing a clean plane jet at a moderate Reynolds number ( $Re=5600$ ). Exit velocity had a flat top profile with maximum fluctuation rms  $0.008U_0$ . Compared to Meyer et al.'s (1989) experimental set up, the exit nozzle was stretched to produce thicker boundary layers. Meanwhile,  $\theta_0/H = 0.0028$  was small

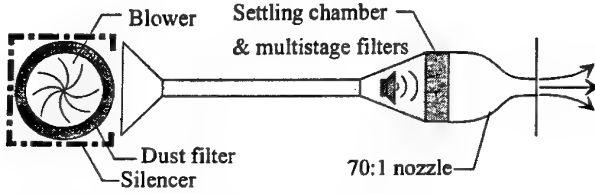


Figure 1: SCHEMATIC OF AIR-JET FACILITY

enough to produce varicose (symmetric) eddy roll-up at mean frequency  $S_{\theta 0}=0.0086$  in the non excited "natural" jet. This instability frequency (half the theoretical value predicted by Michalke (1965) for the hyperbolic tangent profile) was present in the initial mixing layers with a very low rms magnitude (less than  $0.001U_0$ ).

Acoustic forcing was applied with a loudspeaker placed before the settling chamber (fig.1) with non detectable aerodynamic perturbation on the flow. The frequency  $f_0$  was chosen to meet  $S_{\theta 0}$ . The rms magnitude of the induced fluctuations at this frequency was  $u'/U_0 = 0.35\%$ . Mean profiles presented no alterations: all boundary layer thicknesses and global velocity fluctuations remained the same as in the "natural" case as listed in table 1. But, instantaneous organization was severely altered exhibiting periodic eddy roll-up and pairing taking place at fixed locations as described by Faghani (1996).

Velocity data were gathered by hot wire X-probe using a numerical scheme based on modified cosine law. The over all precision on velocity measurements was evaluated to be 2% for  $U$  and 8% for  $V$ . The hot wire probe was positioned with high accuracy ( $\pm 0.05H$ ) on a predefined grid  $\mathcal{D}$  at mid height stretching laterally from  $-H$  to  $H$  and reaching as far as  $5.3H$  longitudinally to cover the first pairing. The mesh size was  $0.2H$  for  $X$  and  $0.1H$  for  $Y$ . Data acquisition was triggered by loudspeakers's driving signal enabling a posteriori phase alignment between signals. Special care was taken to minimize quarter and half period uncertainties which might arise from frequency halving entailed by near field subharmonic cascade. The sampling frequency  $f_s = 5000\text{Hz}$  was far above Nyquist limit. Data were acquired sequentially at each position and processed to obtain phase-aligned velocity fields (snapshots) before calculating instantaneous vorticity field and

two-dimensional BOD eigenfunctions. Velocity data base so gathered was formed of 75 temporal  $25 \times 21 = 525$ -point snapshots.

## FLOW DESCRIPTION

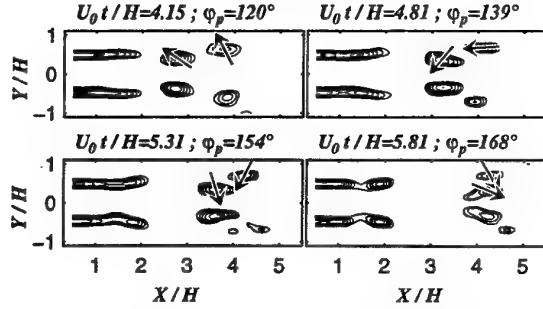


Figure 2: CONDITIONALLY MEASURED VORTICITY FIELD  $\omega_z$

To highlight eddy interactions, vorticity fields  $\omega_z$  were calculated as shown on fig.2.  $\varphi_p$  is the flow phase relatively to its period  $T$  (during which two pairings take place at  $X \approx 4.3H$ ). Detailed study of eddy kinematics based on these figures helped to explain mean velocity, rms and Reynolds stress  $\overline{uv}$  profiles. A typical leap frog pairing sequence can be followed on fig.2. The resulting vortex nutation, as described by Ho and Huerre (1984), was accompanied by  $\overline{uv}$  cancellation at  $X \approx 4.3H$  where pairing was complete. Convection velocity calculations revealed that the leading eddy travelled at a roughly constant velocity  $0.4U_0$  while the trailing eddy speeded up continuously to reach  $1.2U_0$  once pairing was complete ( $\varphi_p = 168^\circ$ ). This eddy kinematics information was used as a basis to be compared to BOD eigenfunctions and reconstructed velocity fields.

## JET FLOW TOPOS AND CHRONOS

Aubry et al. (1991) presented the bi-orthogonal decomposition or BOD as a deterministic analysis tool for complex spatio-temporal signals. Since the excited jet almost behaved like a deterministic flow, this technique was chosen to analyze the velocity field. A complete 2D decomposition was first performed before applying a more restrictive but experimentally more accessible 1D decomposition at fixed  $X$  positions.

### 2D Decomposition

Taking advantage of the comprehensive velocity database available from the conditional sampling described above, a complete 2D decomposition was performed in the same manner as Rajaei et al. (1994) did (though they preferred to call their decomposition a snapshot POD). Following Carrion (1993), spatial and temporal kernels were respectively defined as:

$$l_{ij}(x, x', y, y') = \int_0^T U_i(x, y, t) U_j(x', y', t) dt \quad (1)$$

$$s(t, t') = \iint_{\mathcal{D}} U_i(x, y, t) U_i(x, y, t') dx dy \quad (2)$$

2D spatial eigenfunctions *topos*  $\varphi_{i,n}(x, y)$  and related scalar temporal eigenfunctions *chronos*  $\psi_n(t)$  were then respectively computed for these kernels:

$$\iint_{\mathcal{D}} l_{ij}(x, x', y, y') \varphi_{j,n}(x', y') dx' dy' = a_n^2 \varphi_{i,n}(x, y) \quad (3)$$



$$\int_0^T s(t, t') \psi_n(t') dt' = a_n^2 \psi_n(t) \quad (4)$$

so that the velocity field could be evaluated at each time step by:

$$U_i(x, y, t) = \sum_n a_n \psi_n(t) \varphi_{i,n}(x, y) \quad (5)$$

Since the flow was known to be symmetric about the jet axis (see fig.2), calculations were only performed for negative  $Y$ . Numerical resolution of eq.4 led to a  $75 \times 75$  matrix eigenvalue problem yielding the chronos. Topos were then computed by projecting velocity fields on the chronos rather than by resolving eq.3 which would have led to a huge matrix eigenvalue problem of order  $500 \times 500$ !

BOD's space-time separation resulted in pairs of quasi-sinusoidal eigenfunctions with  $\pi/2$  time and space lags as shown in figure 3. At this cost, a correct mimic of eddy

$$\int s^x(t, t') \psi_n^x(t') dt' = a_n^{x2} \psi_n^x(t) \quad (9)$$

where the longitudinal coordinate  $X$  is a parameter on which kernels, topos and chronos depend. Again, velocity vector could be reconstructed by summing up topos and chronos:

$$U_i(x; y, t) = \bar{U}_i(x; y) + \sum_n a_n^x \psi_n^x(t) \varphi_{i,n}^x(y) \quad (10)$$

$U_i(x; y, t)$  could be identified with eddies' signature as they convected past a fixed  $X$  position. From an energetic point of view, at each  $X$  station, three eigenfunctions gathered over 90% of the fluctuating energy. Calculation of BOD-based entropy  $h$  showed its capability to outline characteristic vortical interactions such as eddy roll-up, growth and pairing. Figure 4 shows that entropy's growth rate de-

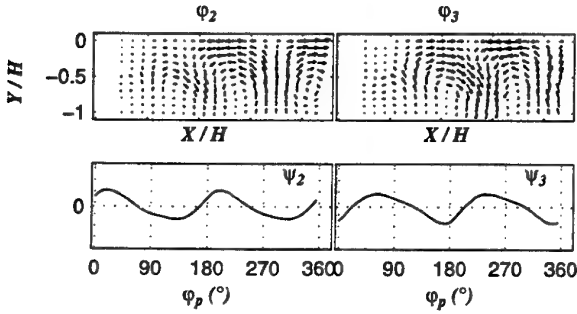


Figure 3: FIRST 2D TOPOS & CHRONOS

convection by spatially fixed topos was obtained as will be shown later (see fig.6). Such spatio-temporal separations, even from a stochastic point of view as in snapshot POD, require at least two eigenfunctions and their particular phase relation to describe any physical eddy and its convection.

As it can be seen from eq.1 and 2, the decomposition was applied to the full velocity field since, according to Aubry et al. (1991), the time-average is not, a priori, an eigenfunction and should not be subtracted. In fact, results showed that for the  $U$  component, the first topos almost coincided with the time-average  $\bar{U}$  and that the temporal fluctuations of its corresponding chronos were negligible. To further investigate this point, BOD was also applied to the sole fluctuating field and showed small differences with the former case. Meanwhile, it was clear that  $\bar{V}$  was not an eigenfunction and needed several topos to be recovered.

### 1D Decomposition

Though more limited than the two-dimensional decomposition, the one-dimensional version is often more accessible to experimental investigation. Given that for the 2D decomposition no significant differences between full velocity BOD and fluctuating velocity BOD were detected, here, only the fluctuating velocity field was decomposed. At each longitudinal position,  $X$ -dependent spatial and temporal kernels were evaluated by:

$$l_{ij}^x(y, y') = \int u_i(x; y, t) u_j(x; y', t) dt \quad (6)$$

$$s^x(t, t') = \int u_i(x; y, t) u_j(x; y, t') dy \quad (7)$$

as well as their eigenfunctions:

$$\int l_{ij}^x(y, y') \varphi_{j,n}^x(y') dy' = a_n^{x2} \varphi_{i,n}^x(y) \quad (8)$$

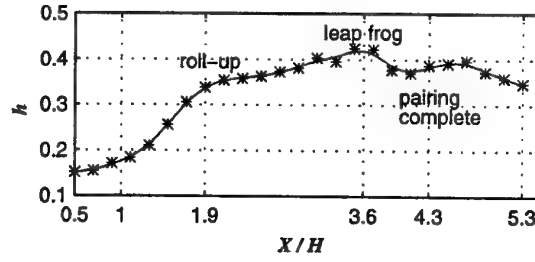


Figure 4: 1D BOD ENTROPY

creases at  $X \approx 1.9H$  where eddy roll-up puts an end to the initial instability amplification (see fig.2). A local entropy maximum can be seen at  $X \approx 3.6H$  where competition between eigenmodes ends up with an energy transfer from higher order topos and chronos to the first two ones yielding a global entropy decrease<sup>1</sup> until pairing is complete at  $X \approx 4.3H$  (see also fig.2). The entropy decrease could be explained by the simpler velocity fluctuation signature of coalesced eddies.

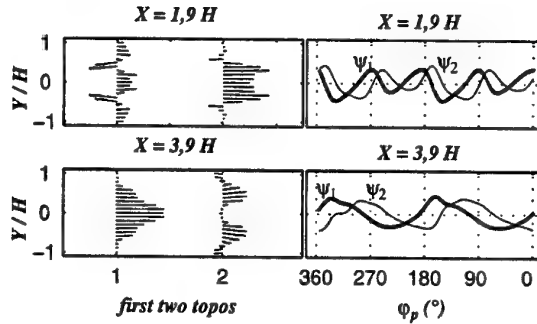


Figure 5: 1D TOPOS AND CHRONOS

Examination of eigenmodes showed high  $X$ -dependence for one-dimensional topos while related chronos maintained quarter-period time lags and exhibited frequency halving with increasing  $X$  according to the subharmonic cascade entailed by pairing (fig.5). These special features were used, as will be explained later, as eddy detection criteria.

<sup>1</sup>Entropy is maximum when energy is equally distributed between eigenmodes.

## EDDY ANALYSIS VIA BOD

### 2D eddy reconstruction

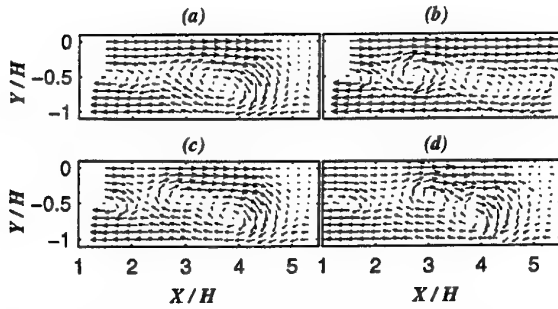


Figure 6: MEASURED vs 2D BOD RECONSTRUCTED VELOCITY FIELD IN CONVECTED FRAME ( $U_c = 0.6U_0$ )

The 2D BOD eigenvalue spectrum revealed that over 80% of fluctuating energy was contained in only two pairs of eigenfunctions. A more detailed study showed that a good description of the eddies required both pairs of eigenfunctions. Any other limited reconstruction based only on one pair resulted in non physical eddies. Therefore, even in such a simple case, several eigenfunctions and their complex phase relations are required in order to capture the eddies. Figure 6 shows reconstructed velocity fields based on modes 1, 2 and 3 (a); 1, 4 and 5 (b) and on the first five modes (c) which are to be compared to measured velocity (d). The most energetic topes and chronos were related to large scale features of the flow (fig.6(a)) while the less energetic fourth and fifth eigenmodes (fig.6(b)) represented smaller scales. These results were consistent with physical characteristics of the flow since  $u'$  increased downstream while time and space scales of the jet increased through pairings. It is obvious (and was indeed verified) that if only the left half of the grid was decomposed, energetic topes would represent small topes along with high frequency ( $\approx f_0$ ) chronos corresponding to single eddies right after roll-up. On the other hand, a right half-grid BOD would produce bigger energetic topes with lower frequency chronos ( $\approx f_0/2$ ) reflecting eddy pairing. The analysis domain dependance of eigenmodes is a logical result in space expanding flows such as moderate Reynolds number shear flows and could pose some difficulties in eigenvector based dynamical system simulations. This matter will be discussed in the last section.

### Eddy detection

1D BOD decomposition allowed eddy time-space signature reconstruction at each  $X$  station with only one pair of topes and their related chronos (not presented). The fast convergence of orthogonal decomposition was expected to provide a few and simple eddy detection criteria. Figure 7 shows how both eddies and saddle points were detected thanks to the first two chronos. Detection criteria were reasonably simple and did not rely on thresholds since only zero crossings and local extrema were used. The reliability of BOD in eddy eduction may prove more interesting in the non excited jet which exhibits intermittency. There the idea would be to project the instantaneous time-space measurements on several pairs of spatial eigenfunctions which are known to correspond to special eddy events such as roll-up or pairing. These could be chosen between natural jet's eigenmodes thanks to the knowledge acquired from the excited jet. For instance, spatial eigenfunctions similar to those of the excited jet at  $X = 1.9H$  would finger out

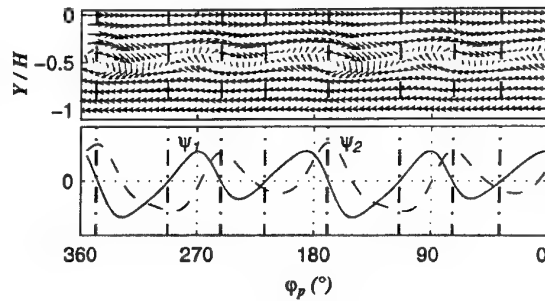


Figure 7: EDDY DETECTION WITH 1D BOD AT  $X = 1.9H$

newly formed eddies right after roll-up while those rather similar to excited jet's topes at  $X = 4.3H$  would educe pairs of coalesced eddies. Our results show significant similarities between excited topes and natural spatial eigenfunctions (though at different abscissae) suggesting direct use of excited topes even in the natural jet.

## DISCUSSION AND CONCLUDING REMARKS

In this attempt to understand the connection between POD type decompositions and physical coherent motion, it appears that several eigenfunctions have to be combined to recover vorticity based eddies. Relevant modes were naturally chosen among the most energetic ones. Their blind combination, especially regardless of their temporal phase relation, can end up in non physical structures. In this deterministic work frame, we simply recovered this information thanks to the chronos. In non periodic situations of more interest, mode selection is again based on energetic considerations. Phase information can be obtained either via third order moments as performed by Moin and Moser (1989) (a priori statistics) or by projecting the instantaneous velocity field on eigenfunctions before performing a posteriori conditional statistics. This remark, along with the fact that eigenmodes may show strong dependance on the considered flow domain, should be kept in mind when any dynamical system is to be based on orthogonal eigenfunctions.

Another point which deserves attention is the fact that the most energetic orthogonal eigenmodes exhibited rather large scales and low frequencies. In our case, this was a natural consequence of the jet flow as discussed above. On the other hand, it is often claimed that in fully turbulent flows, CSs are not necessarily very energetic though possessing spatial expansions comparable to flow dimensions. Capturing not very energetic but highly correlated CSs by POD remains an open issue to be investigated.

This leads to another important question which is the validity of our results in non excited and more turbulent shear flows. Attempts to detect CSs in more turbulent flows with 1D BOD has indeed proved more difficult though possible to implement. Applied to a highly turbulent separated flow, 1D BOD chronos did not exhibit features as sharp as in the present case. There, random eddy size and trajectory did not allow simple detection criteria. Meanwhile, eddy detection was successfully applied to a higher Reynolds number plane jet ( $Re=15000$ ) as mentioned by Faghani (1996). Besides, some Reynolds number invariance for topes and chronos was observed though some rescaling seemed necessary.

As far as flow control is concerned, eigenmodes invariance is also of prime interest. The problem is to know whether eigenmodes remain unaltered under flow manipulation. If this is not the case, during control phases while energy is fed to (or pumped from) the flow, eigenmodes may greatly change. Any dynamical system used in an ac-

tive control loop and based on "natural" flow eigenmodes would then prove inadequate<sup>2</sup>. Our plane jet results show, however, some invariance between "natural" and excited topes and chronos.

## Acknowledgements

We gratefully acknowledge Professor J.-P. Bonnet, Dr. J. Delville and their coworkers for the many helpful discussions we had as well as for the interest they showed in our work during its progress. We also wish to thank all members of electronics laboratory at IMFT for their technical support in the realization of our data acquisition equipment.

## REFERENCES

- Aubry N., Guyonnet R. and Lima R., 1991, "Spatio-temporal Analysis of Complex Signals: Theory and Application," *Journal of Statistical Physics*, Vol. 64, No. 3/4, pp. 683-739.
- Bonnet J.-P. and coworkers, 1993, "Etude Expérimentale de la Structure d'une Couche de Mélange Plane Turbulente en Fluide Incompressible. Application de la Décomposition Orthogonale aux Valeurs Propres," DRET Contract No. 90-171, LEA, CEAT, Poitiers, France.
- Carrión S., 1993, "Reliability of Bi-orthogonal Decomposition Applied to a Rotating Disk Boundary Layer," *Experiments in Fluids*, Vol. 14, pp. 59-64.
- Cordier L., 1996, "Etude des Systèmes Dynamiques Basés sur la Décomposition Orthogonale aux Valeurs Propres (POD). Application à la Couche de Mélange Turbulente et à l'écoulement entre deux Disques Contrarotatifs," *Thèse de l'Université de Poitiers*, France.
- Delville J., 1995, "La Décomposition Orthogonale aux Valeurs Propres et l'Analyse de l'Organisation Tridimensionnelle des Écoulements Turbulents Cisaillés Libres," *Thèse de l'Université de Poitiers*, France.
- Faghani D., 1996, "Etude des Structures Tourbillonnaires de la Zone Proche d'un Jet Plan: Approche non Stationnaire Multidimensionnelle," *Thèse de l'I.N.P. Toulouse*, France.
- Fukuoka A. A., 1951, "A Study on 10-day Forecast (a Synthetic Report)," *Geophysics Magazine*, Vol. 177.
- Glauser M. N., and George W. K., 1987, "An Orthogonal Decomposition of the Axisymmetric Jet Mixing Layer Utilizing Cross-wire Velocity Measurements," *6<sup>th</sup> Symposium on Turbulent Shear Flow*, Toulouse, France.
- Herzog S., 1986, "The Large Scale Structure in the Near Wall Region of a Turbulent Pipe Flow," *PhD Thesis*, Cornell University.
- Ho Ch.-M. and Huerre P., 1984, "Perturbed Free Shear Layers," *Annual Review of Fluid Mechanics*, Vol. 16, pp. 365-424.
- Lorenz E. N., 1956, "Empirical Orthogonal Functions and Statistical Weather Prediction," Scientific Report No. 1, Statistical Forecasting Project, Department of Meteorology, MIT.
- Lumley J. L., 1970, "Stochastic Tools in Turbulence," Academic Press.
- Meyer J., 1989, "Structures Organisées et Transition dans la Zone Proche du Jet Plan: Synthèse d'Analyse Expérimentale, Visuelle et Numérique," *Thèse de l'I.N.P. Toulouse*, France.
- Michalke A., 1965, "On Spatially Growing Disturbances in an Inviscid Shear Layer," *Jour. Fluid Mech.*, Vol. 23, pp. 521-544.
- Moin P. and Moser M., 1989, "Characteristic-eddy Decomposition of Turbulence in a Channel," *Jour. Fluid Mech.*, Vol. 200, pp. 471-509.
- Rajae M., Karlsson S. K. F. and Sirovich L., 1994, "Low-dimensional Description of Free-shear-flow Coherent Structures and Their Dynamical Behaviour," *Jour. Fluid Mech.*, Vol. 258, pp. 1-29.
- Sirovich L., 1990, "Turbulence and the Dynamics of Coherent Structures, Parts I, II and III," *Quarterly of Applied Mathematics*, Vol. XLV, No. 3, pp. 561-582.
- Sirovich L., Kirby M. and Winter M., 1990, "An Eigenfunction Approach to Large Scale Transition Structures in Jet Flow," *Phys. of Fluids*, Vol. A2 (2), pp. 127-136.
- Sirovich L. and Park H., 1990, "Turbulent Thermal Convection in a Finite Domain: Part I. Theory," *Phys. of Fluids*, Vol. A2 (9), pp. 1649-58.

<sup>2</sup>POD based dynamical systems for turbulent plane and round free shear flows have been investigated by Cordier (1996).

# ENTRAINMENT AND MIXING PATTERNS IN COFLOWING FORCED JETS SUBJECTED TO AXIAL AND AZIMUTHAL FORCING

K. Prestridge and J.C. Lasheras

Department of Applied Mechanics and Engineering Sciences

University of California, San Diego

9500 Gilman Drive

La Jolla, California 92093-0411

U.S.A.

## ABSTRACT

Phase-averaged Particle Imaging Velocimetry (PIV) measurements of an axially and azimuthally forced coflowing, turbulent jet are used to investigate changes in the entrainment and mixing of the jet. It is shown that, for a downstream distance less than  $7D_j$ , the time-averaged entrainment of the jet at  $Re = 4700$  remains unchanged by the forcing. Visualizations and phase-averaged measurements of the velocity and vorticity fields of the jet at a Reynolds number of 1550 subjected to high amplitude axial forcing showed evidence of lateral ejections similar to those observed in heated and low density jets. These ejections appear to be the result of instabilities in the vortex rings developing from the strong axial forcing.

## INTRODUCTION

Axisymmetric turbulent jets have a fundamental flow geometry with wide application to many designs. Under certain conditions, i.e. in heated and low-density turbulent jets, lateral ejections of jet fluid have been observed, Monkewitz *et al.* (1990), Sreenivasan *et al.* (1989), and many others. These lateral ejections appear to contribute to an increase in the entrainment and mixing of the jet. Their appearance has been identified with the jet's transition from convective to absolute instability, Monkewitz *et al.* (1990), however, to date, no detailed description of the mechanisms responsible for their formation has been fully identified. From flow visualization experiments and vortex dynamics simulations of low Reynolds number forced jets, Lasheras *et al.* (1991) have attributed the appearance of these ejections to the growth of the instabilities of the large-scale vortex rings forming in the jet. By forcing the ring instability with the use of corrugated nozzles, Lasheras *et al.* showed that the induction between the large-scale vortex rings and the streamwise vortices forming in the braids may lead to several modes of lateral ejections. In all modes identified in their experiments, the laterally ejected jet fluid was found to be the result of the amplification of the vortex ring instabilities, which caused the formation and pinching-off of vortex loops that, under their own induction, were propelled sideways. Furthermore, their experiments showed that the lateral ejections occur only when

the jet is strongly forced in the axial mode, a result consistent with the unforced experiments of heated or variable density jets, which formed lateral ejections only when the jet was in the absolutely unstable (i.e. self-excited) mode. Experiments with heated and forced cold jets by Monkewitz *et al.* (1990) have led to the proposal of another model for the side ejections which is also based upon the instability of the primary vortex rings. They proposed that the primary vortex rings undergo a Widnall type of instability, and the resulting waviness and tilting of the rings in the streamwise direction causes the fluid from inside the jet to be propelled laterally by induction. They also observed similar lateral ejections in strongly forced cold jets. Direct numerical simulations by Brancher *et al.* (1994) have also examined the lateral ejections. They observed a local strengthening of the braid vorticity that connects the periodic vortex ring structures. They proposed that this localized strengthening is caused by the instability of the primary vortex ring, causing the magnitude of the braid vorticity to become large enough to induce a velocity on the internal fluid of the jet, propelling it laterally away from the center of the jet. The actual origin of the fluid which is ejected laterally and the mechanism which causes the lateral ejections remain unresolved despite the many visualizations of the phenomena, largely due to the lack of quantitative information about the velocity, and hence vorticity, field of the jet.

Other experimental and numerical investigations have provided evidence of lateral ejections of a similar nature, caused by various forcing methods used to alter the mixing and entrainment of the jet. These experiments usually focused on the effect of the nozzle's geometry, with the ultimate goal of manipulating the vortex dynamics such that mixing is enhanced. Examples of these investigations include, but are not limited to experiments with tabbed nozzles: Bradbury and Khadem (1975), Zaman *et al.* (1994), lobed nozzles: Prestridge and Lasheras (1996), Grinstein *et al.* (1996), Lasheras *et al.* (1991), and Martin and Meiburg (1991), nozzles with other geometric configurations, such as square and elliptic nozzles: Grinstein *et al.* (1995), and Ho and Gutmark (1987). Although these experimental and numerical investigations have shed some light on the vortex dynamics of forced jets, they have not

conclusively identified the mechanism responsible for the onset of side jets.

In order to fully understand the mechanisms responsible for the formation of these side jets, we are conducting a set of controlled experiments where, for each jet velocity (i.e. Reynolds number), we vary the frequency and amplitude of the axial forcing, as well as the azimuthal wavenumber. We would like to reconstruct the three-dimensional evolution of the vorticity in the jet, and for that purpose, PIV techniques are used. Instantaneous planar velocity measurements, which are made using PIV, make it possible to calculate the vorticity component perpendicular to the imaging plane. By taking advantage of the periodicity resulting from the axial forcing, through the use of phase-averaging techniques, we can measure the evolution of the three-dimensional vortex dynamics of the jet. The vorticity field of a large volume of the jet flow can be completely reconstructed by combining measurements taken by varying the location of the measurement plane so that enough points are measured to resolve the velocity field. In this paper, we present preliminary measurements of a region very close to the nozzle of the jet ( $z/D_j < 7$ ), and our discussion will concentrate only on measurements taken along an axial plane. This will demonstrate the feasibility of our methodology for the purpose of measuring the evolution of the vorticity field of the forced jet and isolating the mechanism responsible for the formation of side jets.

## EXPERIMENTAL SET-UP

### Coflowing Jet Facility

The experimental facility consists of a water jet which issues along the central axis of a coflowing water channel. The jet flows through a 25 mm diameter PVC pipe into the water channel. The recirculating water channel provides a low-speed, laminar coflow for the jet, with variable velocity and a test section measuring 61 cm wide by 74 cm high by 175 cm long. The jet flow is supplied using a constant-head gravity-fed supply tank, which prevents contamination of the jet by the pumping mechanism. In our facility, the jet velocity can be varied up to 70 cm/s. In the study reported here, most of the investigation took place at one jet velocity, with a centerline velocity of  $U_{CL} = 39$  cm/s, a mean velocity of  $\bar{U} = 25.7$  cm/s, and a coflow velocity of  $U_\infty = 7$  cm/s. The jet exit velocity profiles are shown in Figure 1. It is clear from the measured exit velocity profiles that the conditions at the jet exit correspond to fully-developed, turbulent pipe flow. There is little difference between the measured exit velocity profiles of all of the nozzles. In addition, another set of restricted measurements will be made at a lower jet velocity of  $\bar{U} = 12$  cm/s. The purpose of this second set of measurements is to determine the effects of a lower convection velocity on the development of instabilities in the primary vortex structures, thus allowing the study of the various instabilities in a restricted observation window.

For the first set of measurements, at the higher mean velocity, the momentum thickness of the round jet is 0.25 cm, with  $Re_\theta = \frac{(\bar{U} - U_\infty)\theta}{\nu} \approx 400$ . The diameter of the round jet is 30 mm, and the resulting Reynolds number,  $Re = \frac{(\bar{U} - U_\infty) D_j}{\nu}$ , is approximately 4700. For the second set of measurements, the Reynolds number is 1550.

### Axial and Azimuthal Forcing

The jet is forced using both static and dynamic perturbations. The static perturbation is in the form of corrugated nozzles with amplitudes of the corrugations equal to  $0.1 D_j$ . Since this perturbation is of the same order of magnitude as the momentum thickness of the jet, it can be considered a large-amplitude perturbation. The number and types of

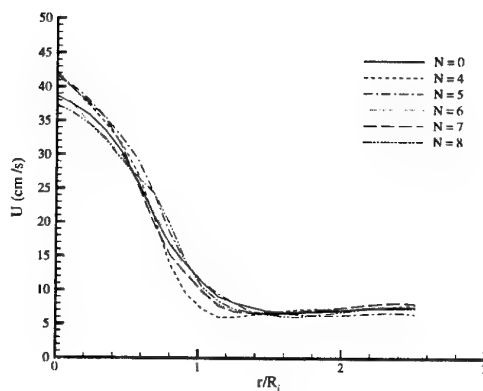


Figure 1: Exit velocity profiles of axially unforced jets.

azimuthal forcing are defined by the number of lobes or peaks in the azimuthal direction. The round nozzle is referred to as  $N = 0$ , while the wavenumber,  $N$ , (number of corrugations) is varied from 4 to 8. The dynamic perturbation is achieved by applying axial forcing to the jet flow far upstream of the exit using a plunger mechanism. The result is a sinusoidal, axisymmetric forcing of the axial velocity at the nozzle exit. The frequency of the axial forcing can be varied using a variable-speed motor which actuates the plunger. In order to isolate the various effects, only two axial forcing frequencies will be examined here: 3 Hz and 5.6 Hz, corresponding to Strouhal numbers ( $St = \frac{f D_j}{\bar{U} - U_\infty}$ ) of 0.5 and 0.95, respectively, for the  $Re = 4700$  jet. The amplitude of the axial perturbation is approximately 30% of the mean exit velocity.

### Measurement Technique

Particle Imaging Velocimetry is used to determine the velocity information at different planes near the exit of the jet. The cross-correlation method is implemented, and two separate digital images are interrogated to determine the distance travelled by each particle. The PIV facility consists of two 30 Hz Nd:YAG lasers, the relative timing of which is controlled using a custom-built timing device synchronized by a Sony CCD camera (resolution of  $640 \times 480$  pixels). The lasers are aligned on a common path using a polarizing beamsplitter cube, and a light sheet of approximately 3 mm thickness is projected through the bottom of the test section using a cylindrical lens. The flow is seeded with Potters Industries' silver-coated hollow glass spheres, with a mean diameter of  $10 \mu m$ . Instantaneous images of the flow field are collected using a Nikon 50 mm lens attached to the CCD camera. Image capture is done digitally using a Pentium 133 MHz personal computer and a Matrox Meteor frame grabbing board. The time separation of the lasers can be varied between 0.5 ms and 66 ms in order to grab at 30 frames per second. Cross-correlation is performed using VisiFlow software, commercially available from AEA Technology. The correlation peak search is optimized using a Gaussian fit, and the interrogation box size is 64 pixels on each side with a 75% overlap. This interrogation box size was used to minimize the error associated with the high-speed part of the flow. The laser pulse separation time used is 5 ms. Phase-averaging is also performed by marking a predetermined phase position on the images using an LED which is synchronized with the motor driving the axial forcing.

By examining the potential core region of the jet in detail, we optimize the resolution of the PIV technique and

are able to see the coherent structures clearly. A zoomed-in region near the exit of the jet, measuring  $6.8\text{ cm} \times 5.3\text{ cm}$ , was used to characterize the nozzle exit flow with the smallest resolution possible at this Reynolds number. For an interrogation box of  $64 \times 64\text{ pixels}$ , this provides a spatial resolution of approximately  $6.8\text{ mm}$ , which is small enough to resolve the exit characteristics.

A larger region of the flow ( $116\text{ mm} \times 88\text{ mm}$ ) was also examined to capture the vortex dynamics downstream and along the jet centerline. This region gives a resolution of  $11\text{ mm}$  per  $64\text{ pixels}$  and corresponds to approximately 3.5 jet diameters downstream. The image focused on the lower half of the jet in order to optimize the resolution, and all of the nozzles were positioned so that the peaks of their lobes intersected the measurement plane at the bottom of the nozzle. The time- and phase- averaged velocity fields that are presented in Figure 2 are actually the composite of two images acquired separately. The first image corresponds to  $0 \leq z/D_j \leq 3.5$ , while the second image is located from  $3.5 \leq z/D_j \leq 7$ . The images of forced jets were phase-averaged, while the unforced jets were time-averaged. No instantaneous data is presented. The two averaged images were patched together with two columns of overlapping vectors removed. None of the final images were smoothed, and the result is a field of  $70 \times 25$  vectors. For clarity, only alternate vectors are plotted in Figure 2.

## RESULTS

The results presented here are of a restricted set of measurements performed in a two-dimensional axial plane perpendicular to the jet exit and intersecting its center. As mentioned in the previous section, the spatial measurement, spanning from  $z/D_j = 0$  to  $z/D_j = 7$ , is obtained by patching together the measurements of two smaller planes, thereby increasing the downstream distance along which we can study the evolution of the jet while preserving a desired spatial resolution, sufficient to capture the phenomena of interest.

### Effect of Azimuthal Perturbation

Let us start by presenting the effects of changing the nozzle lip through the addition of sinusoidal, azimuthal perturbations in the form of lobed nozzles. In Figure 2, the time-averaged velocity field of the unforced, round jet is pictured, along with the time-averaged streamlines, which illustrate the lateral entrainment of the jet. From the measurements of the mean velocity, a quantification of the entrainment of the jet was made by calculating the mass flow rate through each jet's cross-section. For each downstream location, a volumetric flow rate (per unit width),  $Q$ , can be defined as:

$$Q(z) = \int_0^\infty [U(r/R_j) - U_\infty] d(r/R_j) \quad (1)$$

Therefore, the amount of fluid entrainment at each downstream location can be measured, and a comparison made for all of the cases studied.

A comparison of the entrainment rates for each of the different azimuthal wavenumbers is shown in Figure 3. Observe that, although the early effects of the lobed nozzles on the entrainment can be clearly seen, there is only a small increase in the entrainment of the jet in the near field for all of the lobed nozzles, as compared to the round nozzle. We believe that this is the case primarily because, for the sake of comparison, the nozzles were all positioned with their outward lobes pointing downward. At this Reynolds number this result is to be expected due to the high convection velocity of the jet, combined with the fact that the region we were examining is very close to the nozzle. Based on flow visualizations and past experiments (Lasheras *et al.*, 1991),

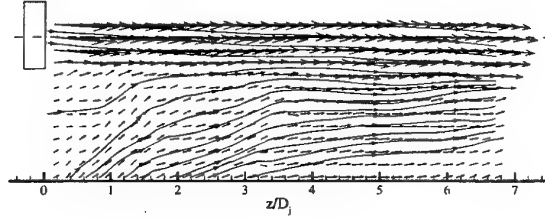


Figure 2: Time-averaged streamlines and velocity vectors of unforced round jet. Approximate nozzle location is pictured for clarity. Dashed line is jet centerline, and only the lower portion of the jet is shown.

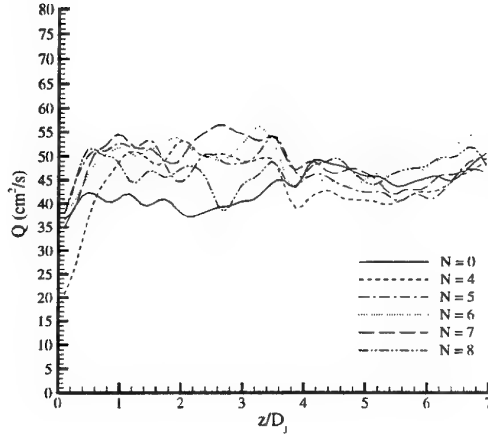


Figure 3: Volumetric entrainment (per unit width) of the time-averaged unforced jets.

we foresee that any effect that may be felt by the azimuthal perturbation will probably occur further downstream.

These results are consistent with previously published entrainment rates for round jets. The variation of mass flow rate with downstream location was measured by Crow and Champagne (1971) for round jets. They found that,

$$\frac{dQ}{dz} = \begin{cases} 0.136Q_e/D & (z/D \leq 2) \\ 0.292Q_e/D & (z/D \geq 6), \end{cases} \quad (2)$$

where  $Q_e$  is the mass flow rate at the exit plane,  $D$  is the diameter of the jet, and  $z$  is downstream position. In Figure 3, our measurements show that the mass flow rate for  $z/D < 6$  changes with  $z$  as  $0.11Q_e/D$ , while the rate of change is  $0.26Q_e/D$  for  $z/D > 6$ . Both of these measured values are in good agreement with the steady growth rates measured by Crow and Champagne. This agreement leads us to conclude that, in the first seven jet diameters downstream, no noticeable modification of the jet entrainment results from the azimuthal perturbation.

The initial instability of the jet can also be seen in the small fluctuations in the jet's entrainment shown in Figure 3, where the natural frequency of the instability can





The averaged vorticity fields for the round jet are shown in Figure 8 for the unforced case as well as for the two different forcing frequencies. These images are phase-averaged, thereby capturing the vortex structures at several locations. Positive vorticity is indicated by the solid line, while negative vorticity is shown by the dotted line. The jet centerline is shown by a dashed line for clarity, along with the location of the nozzle, shown as a rectangle at the left of the plot. In the unforced case, the development and spreading of the jet is clearly visible. In the second case, where  $St = 0.5$ , the concentrated vortex ring structures show the coherency of the flow. The location of the vortex rings corresponds to the waviness in the streamlines observed in Figure 4. The periodic increase in entrainment pictured in Figure 5 is also the result of this forcing. At the highest Strouhal number, Figure 8(c), the vortex rings form in the near field, but their coherency appears to break down as they are convected downstream. This results in the periodic increase in the near field entrainment, with a leveling off after  $(z/D_j > 4)$ , as shown in Figure 6.

The vorticity field for the 8-lobed jet is pictured in Figure 9. This nozzle was chosen because of the increased entrainment observed with it at  $St = 0.5$  near the nozzle exit, as shown in Figure 5. The region of vorticity at the

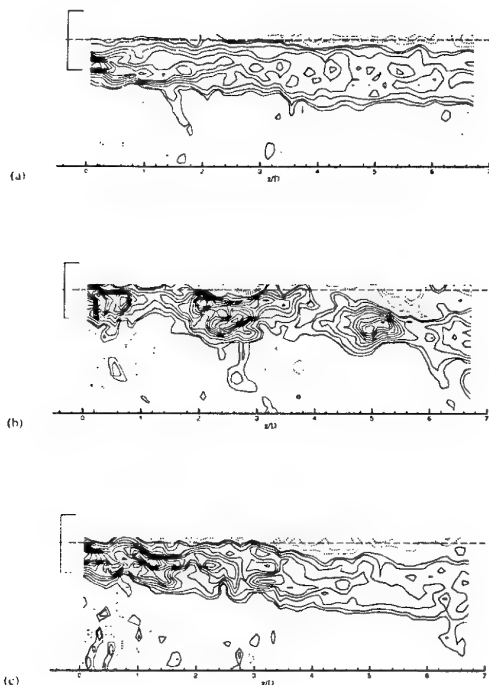


Figure 8: Vorticity distribution in round jet. (a) Unforced, (b)  $St = 0.5$ , (c)  $St = 0.95$ . Dashed line indicates jet centerline.

lip of the unforced, 8-lobed jet (Figure 9(a)) is thicker than the same region in the round nozzle (Figure 8(a)). This effect is limited to the near field, however, and there seems to be little difference between the overall breakup of the vortex structures downstream of the nozzle.

#### Effect of the Amplitude of the Axial Forcing

The above experiments have shown little or no effect of the azimuthal forcing on the entrainment of the jet in a downstream distance less than or equal to seven jet diameters. As mentioned above, this could be due to the limited time which our restricted measuring window allows for

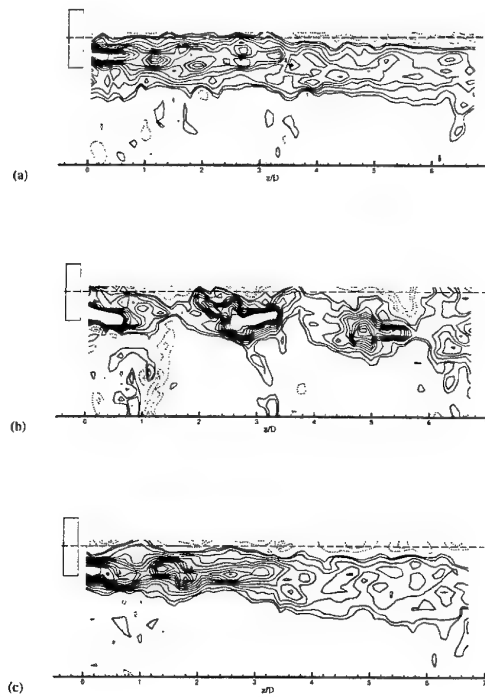


Figure 9: Vorticity distribution in 8-lobed jet. (a) Unforced, (b)  $St = 0.5$ , (c)  $St = 0.95$ . Dashed line indicates jet centerline.

the growth of the various instabilities. Thus, in order to increase the observation time, the jet velocity was lowered to  $\bar{U} = 12 \text{ cm/s}$ . The corresponding Reynolds number of the jet was  $Re = 1550$ . The only axial forcing frequency tested was  $3 \text{ Hz}$ , which is the frequency that corresponded to  $St = 0.5$  previously. Now, the corresponding Strouhal number is  $St = 1.5$  due to the lower jet velocity. The amplitude of the axial forcing was also increased to approximately 60% of the mean exit velocity. At this Reynolds number, a smaller resolution could be used, since lower velocities were involved. The interrogation box size was reduced to  $32 \times 32 \text{ pixels}$ , and the time separation of the laser pulses was kept at  $5 \text{ ms}$ . Due to the small size of the lateral ejections, the smallest spatial resolution was used, and the region examined measured  $75 \text{ mm} \times 58 \text{ mm}$ , which resulted in a spatial resolution of  $3.8 \text{ mm}$ . The images of the jet's central axis span along  $0 \leq z/D_j \leq 2.5$ .

When the higher amplitude axial forcing was applied to the jet, the vortex dynamics of the jet appeared to be altered significantly, as shown in Figure 10, where an instantaneous image of the particles in the jet is shown. The flow is from left to right, and only the lower half of the jet is shown in the picture, with the centerline indicated by a dashed line. The jet fluid is more densely seeded with particles than the coflow in order to aid in visualization. This picture is an instantaneous image taken at the same phase ( $\phi = 0$ ) as the phase-averaged vorticity shown in Figure 11. The primary rollup of vorticity is indicated by the arrow labeled "I" in Figure 10. This event is captured in the vorticity field of Figure 11 at  $z/D_j = 1$ , but the fine features of the rollup cannot be captured due to the resolution resulting from the phase averaging. Another interesting feature shown in Figure 10 is the ejection of jet fluid marked by the arrow labeled "II." This event is not fully captured in the phase averaging either, possibly due to jitter in the location of the event. However, visualiza-



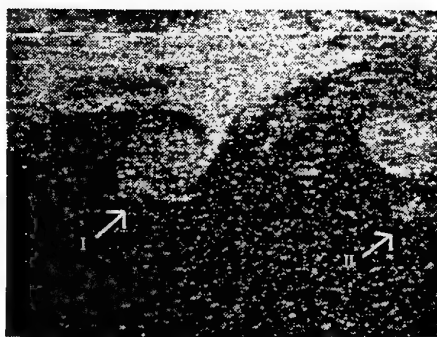


Figure 10: Instantaneous image of particles in forced jet,  $N = 4$ ,  $St = 1.5$ . Jet centerline is indicated by the dashed line.

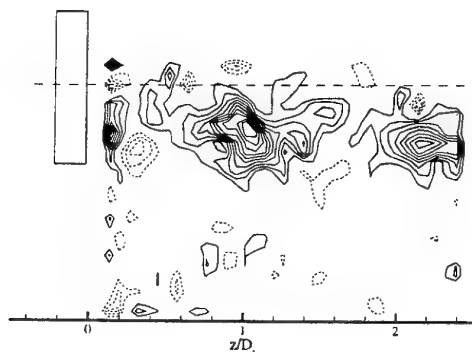


Figure 11: Phase-averaged vorticity field of jet,  $N = 4$ ,  $St = 1.5$ .

tions indicate that the event occurs regularly downstream of this observation window. Measurements further downstream should be able to capture this event as it grows.

The effect of the high amplitude forcing on the entrainment of the jet is shown in Figure 12, where small localized increases in entrainment are observed in the regions of the vortex rollup. The effect of the azimuthal perturbation cannot be seen in the small downstream region that we are examining here ( $z/D_j < 2.5$ ).

## CONCLUSION

The combined use of planar PIV measurements of a turbulent, coflowing jet subjected to axial and azimuthal forcing have shown that the time-averaged entrainment of the jet remains unchanged down to axial distances of  $7D_j$ . Lowering of the jet Reynolds number and increasing the amplitude of the axial forcing was found to lead to the appearance of lateral ejections similar to the ones encountered in heated and low-density jets. The measurements as well as flow visualizations appear to indicate that the lateral ejection of jet fluid is the result of the amplification of the ring instability resulting in the pinching off of vortex loops. Further studies are underway to apply these techniques to produce a phase-averaged three-dimensional reconstruction of the vorticity field in a region spanning  $15D_j$ . Based on the preliminary results presented here, it is foreseen that these measurements will reveal the necessary information to study the mechanism of these side ejections.

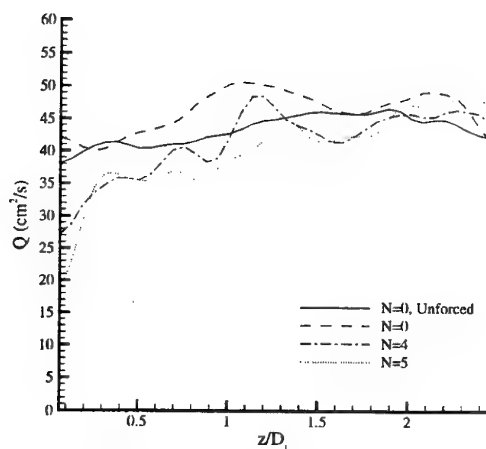


Figure 12: Volumetric entrainment of the  $Re = 1500$  jet.

## REFERENCES

- Bradbury, L. J. S. and Khadem, A. H., 1975, "The distortion of a jet by tabs." *J. Fluid Mech.*, Vol. 70, pp. 180-183.
- Brancher, P., Chomaz, J. M., and Huerre, P., 1994, "Direct numerical simulations of round jets: Vortex induction and side jets." *Phys. Fluids*, Vol. 6, pp. 1768-1774.
- Crow, S. C. and Champagne, F. H., 1971, "Orderly structure in jet turbulence." *J. Fluid Mech.*, Vol. 48, pp. 547-591.
- Grinstein, F. F., Gutmark, E. and Parr, T., 1995, "Near field dynamics of subsonic free square jets: A computational and experimental study." *Phys. Fluids*, Vol. 7, pp. 1483-1497.
- Grinstein, F. F., Gutmark, E. J., Parr, T. P., Hanson-Parr, D. M. and Obeysekare, U., 1996, "Streamwise and spanwise vortex interaction in an axisymmetric jet." *Phys. Fluids*, Vol. 8, pp. 1515-1524.
- Ho, C. M. and Gutmark, E., 1987, "Vortex induction and mass entrainment in a small-aspect-ratio elliptic jet." *J. Fluid Mech.* Vol. 179, pp. 383-405.
- Lasheras, J. C., Lécuna, A. and Rodriguez, P., 1991, "Three-dimensional vorticity dynamics in the near field of coflowing forced jets." *Lect. in Appl. Math.*, Vol. 28, pp. 403-422.
- Martin, J. E. and Meiburg, E., 1991, "Numerical investigation of three-dimensionally evolving jets subject to axisymmetric and azimuthal perturbations." *J. Fluid Mech.*, Vol. 230, pp. 271-318.
- Michalke, A. and Hermann, G., 1982, "On the inviscid instability of a circular jet with external flow." *J. Fluid Mech.*, Vol. 114, pp. 343-359.
- Monkewitz, P. A., Bechert, D. W., Barsikow, B. and Lehmann, B., 1990, "Self-excited oscillations and mixing in a heated round jet." *J. Fluid Mech.*, Vol. 213, pp. 611-639.
- Prestridge, K. and Lasheras, J. C., 1996, "Three-dimensional vorticity dynamics in a coflowing, turbulent jet subjected to axial and azimuthal perturbations." *European Series in Applied and Industrial Mathematics. Proceedings.* ([www.emath.fr/Maths/Proc/Vol.1/prestrid.htm](http://www.emath.fr/Maths/Proc/Vol.1/prestrid.htm)), Vol. 1, pp. 553-564.
- Sreenivasan, K. R., Raghu, S. and Kyle, D., 1989, "Absolute instability in variable density round jets." *Exp. in Fluids*, Vol. 7, pp. 309-317.
- Zaman, K. B. M. Q., Reeder, M. F. and Samimy, M., 1994, "Control of an axisymmetric jet using vortex generators." *Phys. Fluids*, Vol. 6, pp. 778-793.

## SENSITIVITY OF IMPINGING TURBULENT JETS TO THE EXTERNAL DISTURBANCES

Sergey V. Alekseenko, Artur V. Bilsky,  
Dmitriy M. Markovich, Vladimir I. Semenov  
Institute of Thermophysics, Siberian Branch of RAS,  
Acad. Lavrentyev ave., 1  
Novosibirsk, 630090  
Russia

### ABSTRACT

The results of experimental study of submerged impinging jet flow are presented for the condition of external forcing with low amplitudes. The regularities of flow development are found to be sufficiently sensitive to the Reynolds number. At high Reynolds numbers the effect of forcing is negligible for the mean and spectral characteristics of flow, though the main harmonic and subharmonic develop by the resonance way. This fact is explained by their low intensity and greater influence of the random turbulence. In the case of moderate and low Reynolds numbers, a forcing of flow at frequencies from the range of the greatest sensitivity gives a strong effect on the flow characteristics: significant drag reduction, sharp growth of pulsation's level, enhancement or suppression of broad band turbulence depending on the conditions. An intrinsic role of subharmonic resonance in development of instabilities was confirmed for such types of flow as impinging jet. The pure subharmonic excitation and joint excitation of subharmonic with the small contribution of fundamental give a more weak effect on the flow structure than forcing at the most probable frequencies even with extremely low amplitudes.

### INTRODUCTION

The classical interpretation of the turbulence implicates the statistical description of flow which is considered as sufficiently random process and can be adequately described with dividing the flow characteristics to the average and pulsating components. Another approach is based on the suggestion that the quasi-determined vortex structures are the basic structural elements of turbulent shear layers. This second assumption was repeatedly confirmed during last three decades. Crow and Champagne (1971) studied the response of a round jet to the controlled axisymmetric excitation and found that the jet shear layer was able to maintain and amplify the organized structures. Later, Brown and Roshko (1974) confirmed that the large-scale vortex structures are actually connected with the turbulent mixing layers at high values of the Reynolds number.

Moreover, as was shown in the experiments by Winant and Browand (1974), the spreading of the mixing layer was due primarily to pairing (co-rotation and merging) of these spanwise vortices.

The use of periodical excitation of shear flow is one of the ways to study the development of instabilities with certain initial parameters: frequencies, phases and modes. Some of the works are devoted to the investigation of instability wave dynamics in the free shear flows such as mixing layers and jets. One of the recent studies is the work by Paschereit et al. (1995) where authors generated resonant subharmonic interaction between the two axisymmetric traveling waves in the jet shear layer and observed the strong influence of the initial phase difference between the subharmonic and fundamental during external excitation of the flow.

Contrary to free jet flows, the coherent structures in confined mixing layers and, particularly, attaching jets and their role in transfer processes are not adequately explored. Only a few studies were conducted in order to analyze the large-scale structures in impinging round jets. A structural image of the impingement region was statistically derived by means of analysis of the surface-pressure fluctuations in the work by Kataoka et al. (1985). Kataoka et al. (1987)

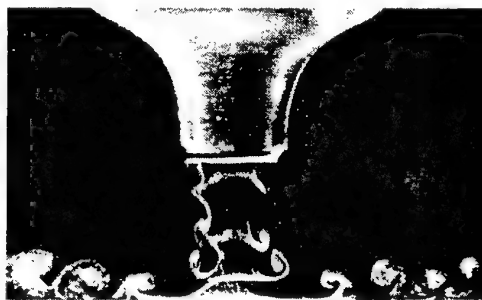


FIGURE 1. PHOTOGRAPH OF IMPINGING JET  
FLOW.  $Re=1000$ ,  $H/d=2$

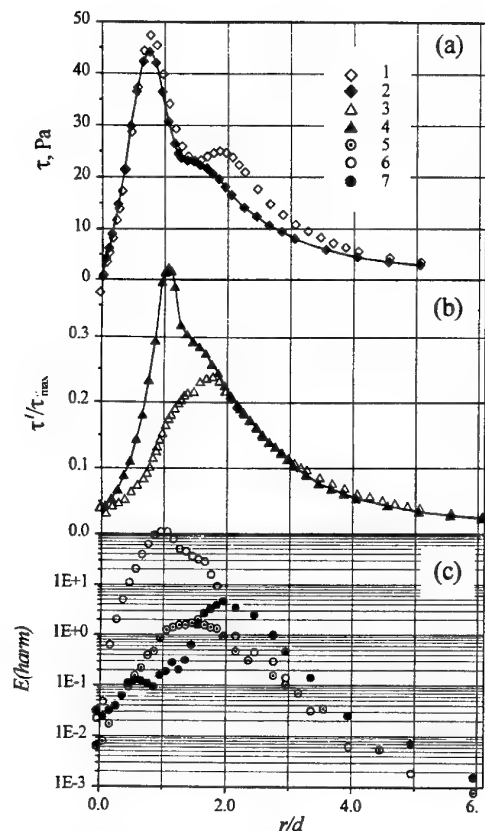


FIGURE 2. DISTRIBUTIONS OF MEAN SKIN FRICTION, ITS RMS. PULSATIONS AND INTENSITY OF HARMONICS.  $Re=25200$ .

associated the heat transfer intensification near the stagnation point with the periodical renewal of the surface by large-scale vortex structures penetrating into this region. Ho and Nasseir (1981) supposed that the decrease of vortices frequency occurred as a result of the collective interaction of large-scale structures in the near-wall region of high speed impinging air jet. Their work is one of few where the instability analysis was made for confined mixing layers. The unsteady separations of radial wall jet flow in the vicinity of an impingement region were observed by Didden and Ho (1985) and Ozdemir and Whitelaw (1992). The first measurements of instant velocity field in the round impinging jet were made by Landreth and Adrian (1990) with use of PIV technique which, however, have not been provided with high spatial resolution. The recent work by Meola et al. (1995) shows the presence equidistant azimuthal structures which appear in impinging nonisothermal round jet.

This work is devoted to the study of development of instabilities in the impinging round jet under the periodical forcing. The main results are obtained with the aid of electrodiffusion method for measuring velocity and wall shear stress.

#### DESCRIPTION OF EXPERIMENT

The experimental set-up consisted of a test section which represented the rectangular channel, made of Plexiglas, with the dimensions of  $86 \times 162 \times 1600$  mm<sup>3</sup>, the system of pumps and flow meters, a reservoir, connecting tubes and apparatus for measurements. A well-profiled round nozzle was inserted through the side wall of a channel. The submerged round jet issuing from the nozzle impinging normally on the opposite

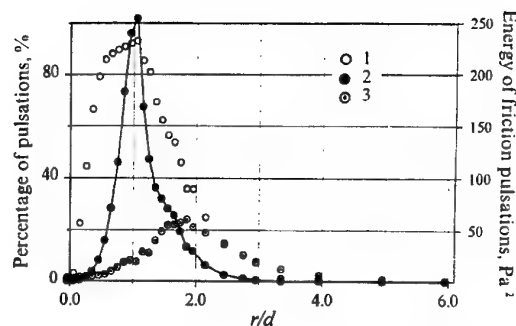


FIGURE 3. COHERENT AND BROAD-BAND COMPONENTS OF SKIN FRICTION PULSATIONS.  $Re=25200$ .

wall (measuring plate) of the channel. The skin friction probes were placed at the measuring plate which could be shifted and this allowed for changing the radial position of each probe with an accuracy of 0.1 mm.

To measure the wall shear stress and liquid velocities the electrodiffusion method was applied. The details of this technique are described in the author's work (Alekseenko and Markovich, 1994). The electrical signals from the probes passed to the a.d. transformer through the d.c. amplifiers. A complete data processing was accomplished by a personal IBM computer. The computer program allowed us to determine the mean values of the velocity and skin friction, its rms. pulsations, spectral density of the velocity and friction pulsations and the time of existence of the flow with the given direction. For the spectral density estimation the Fast Fourier Transform technique was applied. Each array of the experimental data, which was processed by FFT, consisted of about 100 segments of 2048 points.

The flow pattern is shown in Fig.1 for the Reynolds number equal to 1000. The visualization was performed with the aid of hydrogen bubbles which were produced on the surface of platinum wire during water hydrolysis.

The excitation of flow was provided by a standard electrodynamic vibration exciter ESE 201 connected by the instrumentality of the silphone with the plenum chamber. The sinusoidal excitant signals destined from the generator through the power amplifier to the exciter. The initial oscillations of flow involved axisymmetric mode ( $m=0$ ) and

their rms. value changed from  $\bar{u}/U_0 = \sqrt{\bar{u}_2}/U_0 = 0.0001$  to 0.001 depending on the experimental conditions. The forcing frequency,  $f_f$ , was characterized by the Strouhal number,  $Sh_d = f_f \cdot d/U_0$ . The velocity measurements near the nozzle exit have showed that the imposed oscillations of level mentioned above do not influence on the initial flow characteristics. The degree of natural turbulence measured in the vicinity of nozzle was in the range of

$u'/U_0 = \sqrt{u'^2}/U_0 = 0.005 \div 0.008$  at the nozzle axis and  $0.05 \div 0.06$  at the center of shear layer. The value of momentum thickness  $\theta$  at the nozzle exit, obtained from the velocity profile equals  $\theta \approx 0.1$  mm.

During the experiments, three values of Reynolds number were tested:  $Re = 12700$ ,  $25200$  and  $46200$ . Besides, the visualization experiments for lowest  $Re = 1000$  were fulfilled. Here  $Re = U_0 \cdot d/\nu$ ,  $U_0$  is the mean flow rate velocity at the nozzle exit,  $d$  is the nozzle diameter equal to 10 mm and  $\nu$  is the kinematic viscosity of solution equal to  $1.04 \cdot 10^{-6}$  m<sup>2</sup>/s. The distance  $H$  between the edge of a

nozzle and plate did not change in the most experiments and was equal to 20 mm ( $H/d = 2$ ).

## EXPERIMENTAL RESULTS

### Intermediate Reynolds number, $Re=25200$

In Fig.2,a,b the distributions of wall shear stress and its rms. pulsations for the axisymmetric jet impingement are shown. The destinations are the following: symbols 1,2 and 3,4 are  $\tau$  and  $\tau'/\tau_m$  for unforced and forced jets correspondingly. Forcing is carried out at the frequency  $f_f = 150$  Hz ( $Sh_d = 0.57$ ) and amplitude  $\tilde{u}/U_0 = 0.0002$ . 5 - intensity of pulsations for most probable frequency  $f_{mp}$  in unforced jet; 6, 7 - intensities of main harmonic  $f_r$  and

subharmonic  $f_r/2$  for the forced jet. Here  $\tau' \equiv \sqrt{\tau'^2}$ . In the absence of forcing such distributions are typical for small values of  $H$  when the barrier is placed within the length of the initial region of the free axisymmetric jet. In the vicinity of the stagnation point the mean friction grows linearly with increase of radial coordinate  $r$ . With the aid of double electrochemical probe it was possible to measure the skin friction values in the close vicinity of stagnation point where flow direction changes its sign in time. At  $r/d = 0.75 \div 0.8$  a local maximum of wall shear stress is attained. The behaviour of friction distributions at larger distances  $r$  depends essentially on the jet Reynolds number. At low  $Re$  the mean friction decreases monotonically and the point of maximum of rms. pulsations (turbulence intensity) is placed more closely to the stagnation point than for larger  $Re$  (see Fig. 7). For Reynolds numbers of the same order and higher the second local maximum of  $\tau$  appears at  $r/d \approx 2$ . For  $Re > 4 \cdot 10^4$  the distributions of mean friction become self-similar relative to the Reynolds number. In this case the position of maximum turbulence intensity coincides practically with the point of the second maximum of friction.

Figure 2,c demonstrates the development of instability waves along the impingement surface. The data were obtained from the measured spectra of wall shear stress pulsations. Both the intensity of harmonic with most probable frequency for the unforced jet and the intensity of main harmonic for the forced jet develop similar to the rms. friction pulsations. The most probable (preferable) frequency  $f_{mp}$  corresponds to the maximum of power spectrum of skin friction pulsations in the absence of forcing (Fig.4,c, line I). If the forcing frequencies lie in a certain range near  $f_{mp}$  ( $120 < f_f < 210$  Hz, or  $0.45 < Sh_d < 0.8$  for  $Re = 25200$ ), one can observe a sharp amplification of pulsations at response frequency  $f_r$  (which is equal to the forcing frequency  $f_f = f_r = 150$  Hz, see Fig.2) and its harmonics,  $2f_r$ ,  $3f_r$ , etc. The growth of higher harmonics occurs similar to the main one but their intensity is lesser (see power spectrum in Fig.4,c). The subharmonic,  $f_r/2$ , develops by the other way. It achieves its maximum value at  $r/d \approx 2$ , and this fact demonstrates that at this point the first vortex merging occurs. At distance  $r/d \approx 1$  the intensity of subharmonic has a small plateau and as is seen from Fig.2,c, its position coincides with the coordinate of main harmonic's maximum. With increasing radial distance from  $r/d \approx 1$  to  $r/d \approx 2$  the sharp growth of subharmonic's intensity takes place. According to Ho and Huerre (1984), this is manifestation of subharmonic resonance phenomena. One of the conditions of its existence is the local equilibrium of the main harmonic.

Also the effect of the reduction of wall shear stress is observed for the considered frequencies range. The mean

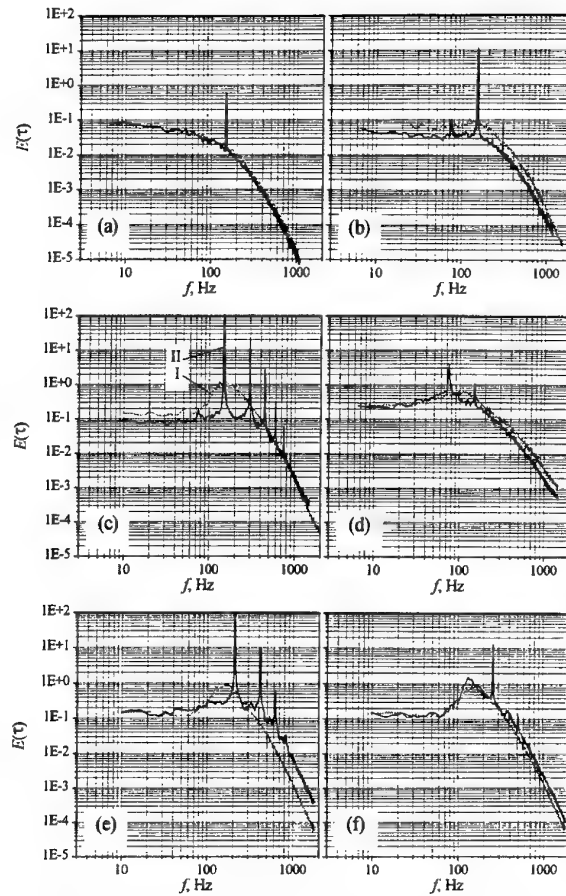


FIGURE 4. POWER SPECTRA OF WALL SHEAR STRESS PULSATIONS.  $Re=25200$ .

friction in the region  $1.5 < r/d < 3$  may reduce by 20-30% in comparison with the case of an unforced jet. The second maximum of friction disappears (Fig. 2,a). A minor drop in friction is also observed at the point of first maximum ( $r/d \approx 0.8$ ).

Analysis of power spectra of turbulent pulsations allows to split the pulsation's energy onto the coherent and broad-band components. Figure 3 demonstrates this disjunction for the conditions coinciding with Fig.2. The destinations are: 1 - the percentage of coherent component, 2,3 - coherent and broad-band energy correspondingly. The coherent percentage achieves 90% in the region where the large-scale structures penetrate intensively ( $r/d = 0.5 \div 1.2$ ). Outside this region the coherent part of pulsations becomes lesser.

An other important effect which has been observed in the forced impinging jet at some conditions is the broad-band turbulence suppression. In Fig.4 the power spectra of wall shear stress pulsations are presented for the following conditions:  $Re = 25200$ ; (a)-  $f_f = 150$  Hz ( $Sh_d = 0.57$ ),  $\tilde{u}/U_0 = 0.0002$ ,  $r/d = 0.2$ ; (b) -  $r/d = 0.5$ ; (c) -  $r/d = 1.1$ ; (d) -  $r/d = 2.2$ ; (e) -  $f_f = 210$  Hz ( $Sh_d = 0.8$ ),  $\tilde{u}/U_0 = 0.00015$ ,  $r/d = 1.0$ ; (f) -  $f_f = 260$  Hz ( $Sh_d = 1.0$ ),  $\tilde{u}/U_0 = 0.0001$ ,  $r/d = 1.0$ . Line I corresponds to the impinging jet without forcing, line II - forced jet.

Figure 4 reveals that the reduction of wall shear stress pulsations energy takes place over wide frequency range if Reynolds numbers are moderate, the condition  $f_r = f_f$  is

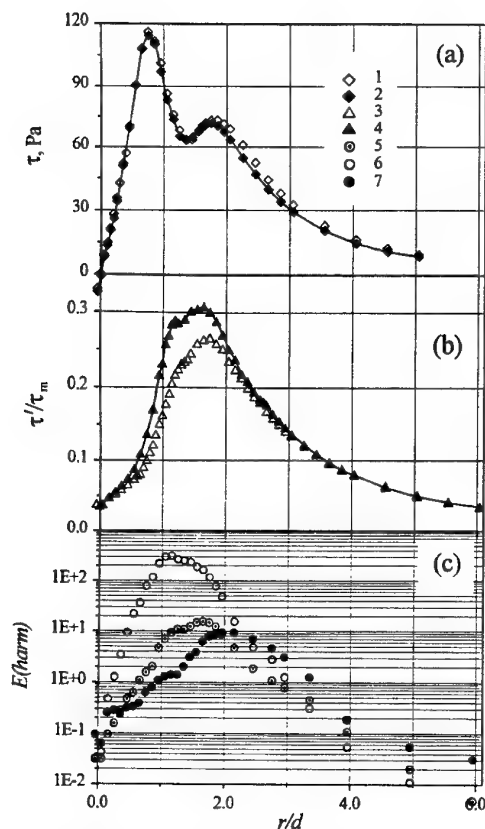


FIGURE 5. DISTRIBUTIONS OF MEAN SKIN FRICTION, ITS RMS. PULSATIONS AND INTENSITY OF HARMONICS.  $Re=46200$ .

valid and radial distances are in the range  $0.5 < r/d < 2.0$ . The similar effect of turbulence suppression in the forced free shear layers was obtained by Zaman & Hussain (1981), however, that effect was found for high Strouhal numbers  $Sh_d = 1.2 \div 2.4$  and the maximum suppression occurred for the value of  $Sh_0 = 0.017$  which corresponded to the prediction of the linear stability theory. These values of frequencies were not tested in our experiments. However at relatively high forcing frequencies,  $f_f = 180$  Hz and  $f_f = 210$  Hz, on the contrary, the enhancement of turbulence at the high frequency area of spectra was observed (see Fig. 4,e). At larger frequencies  $f_f = 260$  Hz ( $Sh_d = 1.0$ ) this effect disappears (Fig. 4,f).

The forcing frequency  $f_f = 180$  Hz ( $Sh_d = 0.68$ ) also satisfies the conditions of subharmonic resonance and development of subharmonic is similar to shown in Fig.2,c.

The jet is markedly sensitive only to the mentioned neighbourhood of the most probable frequency. At the boundaries of this range,  $f_f = 130$  Hz ( $Sh_d = 0.49$ ) and  $f_f = 210$  Hz ( $Sh_d = 0.8$ ), the amplification of main harmonic takes place also but the development of subharmonic occurs without resonance phenomena and its growth occurs monotonically. At larger frequencies, the structure of flow does not change significantly in comparison with the case of unforced impinging jet.

However, the determined range of external frequencies which exert the most pronounced influence on the impinging jet flow structure differs from the literature data for free jet flows. Thus, Ho and Huerre (1984) noted that in most known experiments the preferable frequencies lie in the range of  $0.25 < Sh_d < 0.5$ .

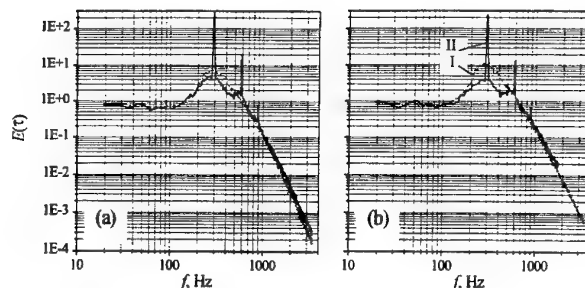


FIGURE 6. POWER SPECTRA OF WALL SHEAR STRESS PULSATIONS.  $Re=46200$ .

#### High Reynolds number, $Re=46200$

In our previous work (Alekseenko and Markovich, 1996) it was noted that at large  $Re$  ( $Re > 4 \cdot 10^4$ ) the impinging jet flow become self-similar and conservative to the change of parameters. It concerns the external excitation also. For the forcing frequency coinciding with the most probable frequency ( $f_{mp} = 290 \div 300$  Hz for  $Re = 46200$ ) it is impossible to observe the significant changes. The distributions of mean skin friction remain almost the same (Fig.5,a) and the level of rms. friction pulsations changes weakly (Fig.5,b). However, the behavior of main harmonic and subharmonic occurs similar to the case described above ( $Re = 25200$ ) including the presence of subharmonic resonance (Fig.5,c). The development of these waves does not influence essentially on the flow structure and mean characteristics because of their low intensity. In Fig. 6 the power spectra are shown for two values of radial coordinate. One can conclude that the regular part of flow pulsations is much more weak in comparison with the case of low  $Re$ . A suppression of turbulence is also negligible and is observed only in the vicinity of forcing frequency. The flow conditions for Figs 5 and 6 are the following:  $Re=46200$ ,  $H/d=2$ , Forcing frequency  $f_f = 295$  Hz ( $Sh_d = 0.61$ ) and amplitude  $\tilde{u}/U_0 = 0.0001$ . The destinations in Fig.5 correspond to the Fig. 2. In Fig.6: (a) -  $r/d=1.1$ , (b) -  $1.3$ . Line I corresponds to the impinging jet without forcing, line II - forced jet.

#### Low Reynolds numbers

Figure 7 presents the dynamics of mean wall shear stress, its rms. pulsations and intensity of main harmonics for the low Reynolds number. The main regularities remain similar to ones observed for moderate Reynolds numbers. Only exception is the fact that in the absence of forcing at low  $Re = 12700$  the second maximum of mean skin friction does not take place. However, during the forcing of the jet at frequencies from the range of sensitivity ( $f_f \approx f_{mp} = 65$  Hz in the case of Fig.7) we also can observe the reduction of friction over whole range of radial distances up to  $r/d = 4$ . Total degree of drag reduction in such resonant regimes may achieve 30%. Rms. pulsations of friction also sharply grow (Fig.7, b) and their maximum shifts to the point  $r/d \approx 1$  similar to the case of intermediate Reynolds numbers. The development of harmonics occurs according to the regularities described for intermediate Reynolds numbers (Fig.7,c). The flow conditions for Fig.7 are:  $Re = 12700$ ,  $f_f = 65$  Hz ( $Sh_d = 0.53$ ) and amplitude  $\tilde{u}/U_0 = 0.0004$ . The destinations correspond to Figs 2 and 5.

If we will excite jet flow by two frequencies simultaneously, at  $f_f = 65$  Hz - main harmonic and at  $f_f/2 = 32.5$  Hz - subharmonic, the development of flow characteristics will strongly depend on the amplitude ratio,

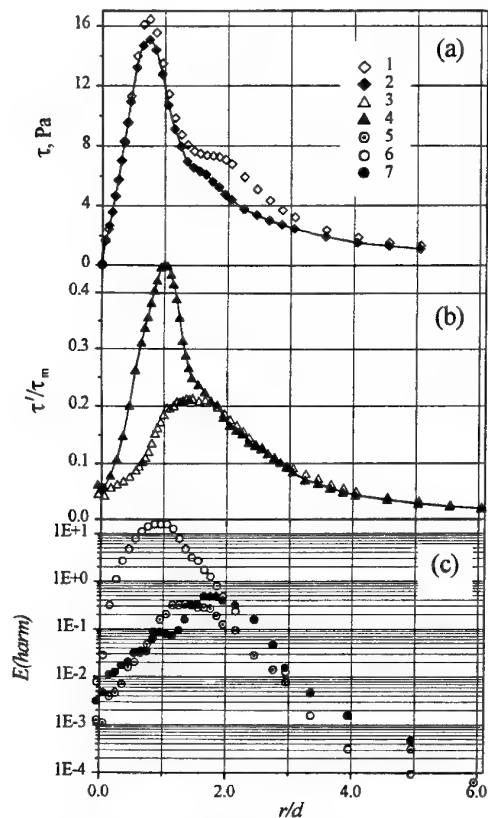


FIGURE 7. DISTRIBUTIONS OF MEAN SKIN FRICTION, ITS RMS. PULSATIONS AND INTENSITY OF HARMONICS.  $Re=12700$ .

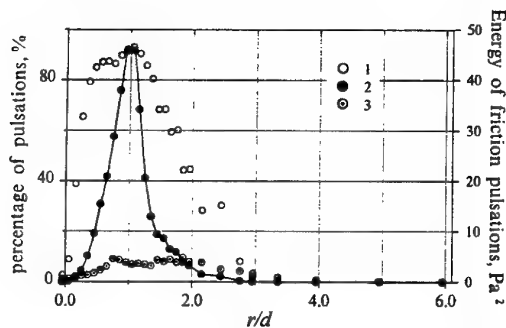


FIGURE 8. COHERENT AND BROAD-BAND COMPONENTS OF SKIN FRICTION PULSATIONS.  $Re=12700$ .

$\gamma = A_{sub}/A_{fun}$ . At relatively small intensities of subharmonic, the result is weakly changed from the pure excitation at the frequency close to the  $f_{mp}$ . The distributions of main flow characteristics is close to the case of single-frequency excitation.

If  $\gamma$  is sufficiently large ( $\gamma = 7$ ) the development of excited disturbances at  $f_r = 65$  Hz and  $f_r/2 = 32.5$  Hz occurs by the same way as for  $\gamma = 2$ . However, the hard suppression of the second harmonic,  $2 \cdot f_r$ , is observed due to harmonic  $3f_r/2$ , which grows strongly.

The interesting fact was obtained when the forcing of flow was made at the frequency which was close to studied subharmonic, but at the same time, multiples of which lie in

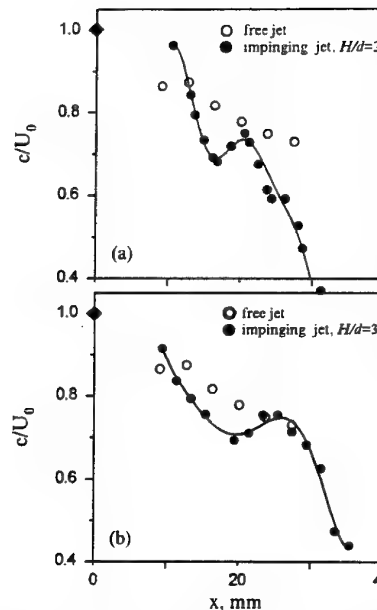


FIGURE 9. PHASE VELOCITY OF COHERENT STRUCTURES IN IMPINGING JET.  $Re=1000$   
(a) -  $H/d=2$ , (b) - 3.

the range of sensitivity  $f_r = 2f_f$ ,  $f_r = 3f_f$ . Such a frequency was  $f_f = 40$  Hz for  $Re=12700$ , i.e. pure subharmonic excitation was applied. In this case both intensities of response frequencies ( $f_r = 2f_f$  and  $f_r = 3f_f$ ) change almost equivalent, however, they do not achieve very high level. For this reason, the changes in mean flow parameters, such as mean skin friction and rms. friction pulsations, are not remarkable in comparison with the case of unforced flow.

The behaviour of coherent and broad-band components of pulsation's energy (Fig.8) is similar to the case of intermediate Reynolds numbers (Fig.3). The destinations in Fig. 8 are the same that in Fig. 3.

Both the suppression and enhancement of broad band turbulence were observed at low Reynolds numbers in dependence on different conditions: frequency and amplitude of excitation and radial coordinate  $r/d$ . The tendency keeps similar for most of tested conditions: in the vicinity of stagnation point the changes in spectra are negligible, at moderate  $r/d$  ( $0.5 < r/d < 1.5$ ) the enhancement of turbulence occurs and the turbulence suppression is observed for large values of  $r/d$ . Such a behaviour of flow requires an explanation and further studying.

The dependences of phase velocity of vortex structures in impinging jet, obtained with the aid of computer processing of flow videimages are shown in Fig.9. These data are presented for Reynolds number equal to 1000. The  $x$ -axis corresponds here to the distance along the jet trajectory. The tendency of vortices motion is demonstrated by the graphs. The velocity of coherent structures has a local minimum when they come near the wall. At increasing  $x$  their velocity grows up to some level and then decrease with the distance. For comparison the dependences of structures velocity for free jet are shown in the plots. In this case the decrease of velocity occurs monotonically.

## CONCLUSIONS

The experimental investigation of impinging jet flow was fulfilled under the condition of external forcing with low amplitudes. The regularities of flow development are found to be sufficiently sensitive to the Reynolds number.



At high Reynolds numbers the influence of forcing is negligible for the mean and spectral characteristics of flow, though the main harmonic and subharmonic develop by the resonance way. This fact is explained by their low intensity and greater influence of random turbulence.

At moderate and low Reynolds numbers, the forcing of flow at frequencies within the range of greatest sensitivity gives the strong effect on flow characteristics: significant drag reduction, sharp growth of pulsation's level, enhancement or suppression of broad band turbulence depending on the conditions. An intrinsic role of subharmonic resonance in development of instabilities was confirmed for such types of flow as impinging jet. The pure subharmonic excitation or joint excitation of subharmonic with the small contribution of fundamental give a more weak effect on the flow structure than forcing at the most probable frequency even with extremely low amplitudes.

The nonmonotonical changing of phase velocity of coherent structures in the near-critical-point region was demonstrated.

## REFERENCES

- Alekseenko S.V. and Markovich D.M., 1994, Electrodiffusion Diagnostic of Wall Shear Stresses in Impinging Jets. *J. Appl. Electrochemistry*, Vol. 24, pp.626-631.
- Alekseenko S.V., Markovich D.M. and Semenov V.I., 1996, Resonance Effects in an Impinging Round Jet, in C.-J.Chen, C. Shih, J. Lienau and R.J. Kung (eds), *Flow Modelling and Turbulence Measurements VI*, pp.109-116, A.A.Balkema Publishers, Rotterdam.
- Brown G.L. and Roshko A., 1974, On Density Effects and Large Scale Structure in Turbulent Mixing Layer, *J.Fluid Mech*, Vol. 64, pp.775-816.
- Crow S.C. and Champagne F.H., 1971, Orderly Structure in Jet Turbulence, *J.Fluid Mech*, Vol. 48, pp.547-591.
- Didden N. and Ho C.-M., 1985, Unsteady Separation in a Boundary Layer Produced by an Impinging Jet, *J. Fluid Mech*, Vol. 160, pp.235-256.
- Hanratty T.J. and Campbell J.A., 1983, Measurements of Wall Shear Stress, in *Fluid Mechanics Measurements*, pp. 559-615, Washington, Hemisphere.
- Ho C.M. and Huang L.S., 1982, Subharmonics and Vortex Merging in Mixing Layers, *J.Fluid Mech*, Vol. 119, pp. 443-473.
- Ho C.M. and Huerre P., 1984, Perturbed Free Shear Layers, *Ann. Rev. Fluid Mech.*, Vol. 16, pp. 365-424.
- Ho C.M. and Nosseir N.S., 1981, Dynamics of an Impinging Jet. Part I. The Feedback Phenomenon, *J. Fluid Mech*, Vol. 105, pp. 119-142.
- Kataoka K., Kamiyama Y., Hashimoto S. and Komai T., 1985, Mass Transfer Between a Plane Surface and an Impinging Turbulent Jet: the Influence of Surface-Pressure Fluctuations, *J. Fluid Mech*, Vol. 119, pp. 91-105.
- Kataoka K., Suguro M., Degawa H., Maruo K. and Mihata I., 1987, The Effect of Surface Renewal due to Large-Scale Eddies on Jet Impingement Heat Transfer, *Int. J. Heat Mass Transfer*, Vol. 30, pp. 559-567.
- Landreth C.C. and Adrian R.J., 1990, Impingement of a Low Reynolds Number Turbulent Circular Jet onto a Flat Plate at Normal Incidence, *Experiments in Fluids*, Vol. 9, pp. 74-84.
- Meola C., de Luca L. and Carlomagno G.M., 1995, Azimutal Instability in an Impinging Jet: Adiabatic Wall Temperature Distribution, *Experiments in Fluids*, Vol. 18, pp. 303-310.
- Ozdemir I.B. and Whitelaw J.H., 1992, Impingement of an Axisymmetric Jet on Unheated and Heated Flat Plates, *J. Fluid Mech*, Vol. 240, pp. 503-532.
- Paschereit C.O., Wygnanski I. and Fiedler H.E., 1995, Experimental Investigation of Subharmonic Resonance in an Axisymmetric Jet, *J. Fluid Mech*, Vol. 283, pp. 365-407.
- Winant C.D. and Browand F.K., 1974, Vortex Pairing, the Mechanism of Turbulent Mixing-Layer Growth at Moderate Reynolds Number, *J.Fluid Mech*, Vol. 63, pp. 237-255.
- Zaman K.B.M.Q. and Hussain A.K.M.F., 1981, Turbulence Suppression in Free Shear Flows by Controlled Excitation, *J. Fluid Mech.*, Vol. 103, pp. 133-159.

# LARGE EDDY SIMULATION OF PLANE IMPINGING JETS

Makoto Tsubokura, Toshio Kobayashi, and Nobuyuki Taniguchi

Institute of Industrial Science, University of Tokyo  
22-1, Roppongi 7chome, Minatoku  
Tokyo 106  
Japan

## ABSTRACT

Numerical investigation of a turbulent plane impinging jet at  $Re=6,000$  was conducted using a Large Eddy Simulation (LES). Instead of Smagorinsky's model, two eddy viscosity types of SGS models were used which had been derived without assuming the balance of SGS energy production and dissipation rates. The model coefficients are dynamically solved as proposed by Germano et al. To solve the numerical instability induced by the negative coefficients in the dynamic procedure, we adopted Lagrangian type averaging technique developed by Meneveau et al. The simulation results were compared with experimental data measured by LDV. Overall agreements with the experiments were good in both models even though the model dependency was observed in predicting turbulent intensities. The turbulent energy transfer mechanism of the impinging zone was also investigated by examining the GS turbulent energy budget and the normal Reynolds stress budget.

## INTRODUCTION

The impinging jet is often used in various industrial applications such as heating, cooling or drying the materials. In addition, its physics is theoretically interesting because it contains many typical turbulent features such as a transition, a free shear layer, a wall shear layer, and a stagnation. The impinging jet consists of three characteristic regions: the free jet region, the stagnation region, and the wall jet region. In the free jet region, a transition from the laminar to the turbulence is observed with large coherent structures of twin vortices, which break down downstream. In the stagnation region, stretching of the eddies whose axis are parallel to the streamline of wall jet cause fully three dimensional structures and lead to sufficiently high increase in heat and mass transfer rates.

The most important mechanism, however, is the redistribution of the turbulent energy among three normal Reynolds stresses by the pressure velocity correlation in the stagnation region. Despite its importance, not many researchers have investigated its transfer mechanism in the stagnation region (for example, Gutmark et al., 1978). It is difficult to predict the statistics numerically by the Reynolds averaged turbulence model due to insufficient modeling of the wall reflection term in the pressure strain correlation term. On the contrary, the LES is suitable to solve this type of a flow because it simulates three dimensional eddy structures instantaneously by modeling only smaller scale of isotropic eddies. Thus, the objective of our research is to investigate the turbulence energy transfer mechanism of the plane impinging jet by using a modified SGS model, which is considered to be more advantageous in simulating a complicated turbulent flow. The paper has examined the grid-scale (GS) turbulent energy budget and the normal Reynolds stress budget as well as the mean velocity and the turbulent intensities. In the study, we use two eddy viscosity types of subgrid-scale (SGS) models instead of Smagorinsky's model. These model are derived without assuming the balance of SGS energy production and dissipation rates. The model coefficients are dynamically solved as proposed by Germano et al. (1991). The dynamic procedure tends to become numerically unstable due to the negative eddy viscosity. To solve this problem, we have adopted Lagrangian type averaging technique developed by Meneveau et al. (1996). This technique is more appropriate for a complicated flow geometry than an ordinarily averaging method in which average is taken over the statistically homogeneous directions. The LDV measurements conducted by the authors will also briefly presented.



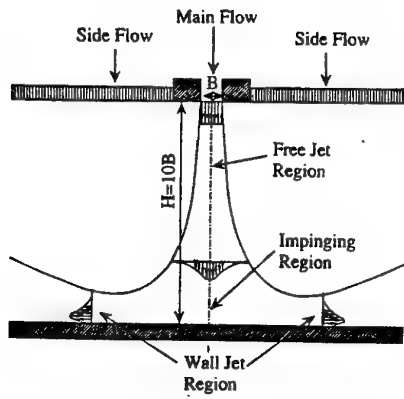


FIGURE 1: PLANE IMPINGING JET

## ANALYSIS MODEL

The plane impinging jet analyzed in this study is shown in fig. 1. The length from the nozzle exit to the impinging plate is given by  $H=10B$  in this study where  $B$  is the nozzle width. We assume that the velocity profile at the nozzle exit is a top-hat shape with lower turbulent intensities because an inlet flow are assumed to come through a confined nozzle. In this study, we impose a 5% side flow on both sides of a main flow considering entrainment of the free jet. This side flow also prevents the reverse flow at the outflow boundary. Hereafter, the streamwise direction of the plane jet is denoted as  $y$  or  $x_2$ , that of the wall jet is  $x$  or  $x_1$ , and the spanwise direction of the plane jet is as  $z$  or  $x_3$ .

## NUMERICAL METHOD

### Governing equations

The fluid is assumed to be incompressible and Newtonian in this study. The governing equations can be obtained by operating a spatial filter to the continuity equation and the Navier-Stokes equations, which are finally given as follows:

$$\frac{\partial \bar{u}_i}{\partial x_i} = 0 \quad (1)$$

$$\frac{\partial \bar{u}_i}{\partial t} + \frac{\partial (\bar{u}_i \bar{u}_j)}{\partial x_j} = -\frac{1}{\rho} \frac{\partial \bar{p}}{\partial x_i} + \nu \frac{\partial^2 \bar{u}_i}{\partial x_j \partial x_j} - \frac{\partial}{\partial x_j} \tau_{ij} \quad (2)$$

The SGS stress term appearing in eq.(2) is given as  $\tau_{ij} = \bar{u}_i \bar{u}_j - \bar{u}_i \bar{u}_j$ , which must be modeled. Hereafter the space filtered and the ensemble averaged velocities are given as  $\bar{u}_i$  and  $[\bar{u}_i]$  respectively. The difference between the raw value and the space filtered value is given by  $u'_i$  and that of the ensemble averaged case is given by  $\bar{u}'_i$ . Accordingly, raw velocity are denoted as  $u_i = [\bar{u}_i] + u'_i$  and  $\bar{u}_i = \bar{u}_i + \bar{u}'_i$ .

### SGS Models

Smagorinsky's eddy viscosity model has been the most

frequently used one among SGS models in the engineering problems. This model was derived from the local equilibrium hypothesis, which is valid for excessively high Reynolds number. However, it is doubtful to apply this model to a low Reynolds number flow. In fact, the eddy viscosity never become zero unless the GS strain rate tensor  $\dot{S}_{ij} = 1/2 (\bar{u}_i / x_j + \bar{u}_j / x_i)$  is zero. In other words, the eddy viscosity may exist even when flow is in a laminar state. One of the solution to this problem is certainly the dynamic SGS model proposed by Germano et al. in 1991. The validity of the dynamic SGS model in the transition flow has been already presented in its original paper. In this case, model coefficient would be zero when a flow field become laminar. But it is rather reasonable to develop the eddy viscosity representation free from the SGS equilibrium assumption. In this study we have used the following an isotropic and an anisotropic eddy viscosity models.

#### ● Isotropic eddy viscosity model

$$\tau_{ij} - \frac{1}{3} \delta_{ij} \tau_{kk} = -2 C \bar{\Delta} \sqrt{(\bar{u}_k - \bar{u}_k)(\bar{u}_k - \bar{u}_k)} \dot{S}_{ij} \quad (3)$$

#### ● Anisotropic eddy viscosity model

$$\begin{aligned} \tau_{ij} - \frac{1}{3} \delta_{ij} \tau_{kk} = & -\nu_{jk} \frac{\partial \bar{u}_i}{\partial x_k} - \nu_{ik} \frac{\partial \bar{u}_j}{\partial x_k} \\ & + \frac{1}{3} \delta_{ij} \left( \nu_{ik} \frac{\partial \bar{u}_l}{\partial x_k} + \nu_{lk} \frac{\partial \bar{u}_l}{\partial x_k} \right) \end{aligned} \quad (4)$$

with the eddy viscosity tensor  $\nu_{ij}$  given as

$$\nu_{ij} = C \bar{\Delta} \frac{(\bar{u}_i - \bar{u}_i)(\bar{u}_j - \bar{u}_j)}{\sqrt{(\bar{u}_k - \bar{u}_k)(\bar{u}_k - \bar{u}_k)}} \quad (5)$$

Here  $C$  is a model coefficient and  $\bar{\Delta}$  is the length scale of

the model which is given by  $\bar{\Delta} = \sqrt{\Delta_1 \Delta_2 \Delta_3}$  where  $\Delta_i$  is the filter width for the  $i$  direction. These models can be derived such that SGS stress tensor is proportional to the product of the SGS stress's production rate and the proper time scale. The isotropic model in eq.(3) is derived under the assumption of the weak anisotropy of the SGS field (see Yoshizawa et al. (1996)), while the anisotropic model in eqs.(4) and (5) is derived without the weak anisotropic assumption. It should be noted that the final representation of the anisotropic model in eq.(4) is in fact a kind of the Generalized Normal Stress(GNS) model, which had been already proposed by Horiuti in 1993 (see also Durbin (1991)). The validity of these models coupled with dynamic procedure with the comparison with the dynamic Smagorinsky's model has been already shown for simple turbulent channel flow by the authors (to appear). One of the drawbacks of the original dynamic procedure is numerical instability induced by the negative coefficient. In case of a simple turbulence such as a channel flow, the solution to this problem is to perform an averaging operation for statistically homogeneous direction during the derivation of the model coefficient(see Germano et al. (1991)). Because of this averaging operation, the dynamic procedure cannot be

applied to practical engineering problems. To overcome this problem, in this study we adopted the Lagrangian dynamic SGS model proposed by Meneveau et al. in 1996. The Lagrangian dynamic model conducts averaging operation along the particle trajectories so that no statistically steady direction is required. Thus, this model makes it possible to apply dynamic procedure to the engineering flow problems with complicated geometry or the drastic changes in the mean velocity direction. Furthermore a model coefficient can be determined locally as a function of time and space.

### Discretization Method

Governing equations in eqs.(1) and (2) are discretized based on the finite volume method with the staggered grid and Cartesian velocity components. The 2nd order finite difference method is utilized to discretize the space derivatives and no artificial viscosity is considered for the convective term. Time integration is conducted based on the 2nd order Adams-Bashforth method and all terms are treated explicitly with a relatively small time step  $\Delta t=0.0045$  normalized by the nozzle exit velocity  $V_0$  and the nozzle width  $B$ . MAC method is used to couple the pressure field with the velocity. The pressure Poisson equation is solved by ICCG method.

### Mesh Configuration and Boundary Condition

The size of computational domain is  $50B \times 10B \times 3.9B$  with  $300 \times 96 \times 34$  nodes in the  $x, y, z$  direction respectively. Consequently the analysis domain consists of 979,200 nodes. Mesh configuration on the  $x$ - $y$  plane used in this study is shown in fig. 2. The mesh width near the wall is sufficiently fine ( $0.013B$ ) so that no artificial or *ad hoc* boundary condition such as the damping function for the wall is considered and the velocity does not slip on the wall. Reynolds number is set to 6,000 which is normalized by nozzle width  $B$  and the inlet velocity  $V_0$ .

For an inlet boundary at the nozzle exit, the following velocity profile is given

$$V_0 = -30 \left\{ 1 - \left( \frac{x/B}{0.5} \right)^{10} + v'_0 \right\} \quad (6)$$

where  $x$  is the distance from the center line of the free jet and  $v'_0$  is a time dependent velocity perturbation. Three values of Strouhal number 0.34, 0.46 and 0.52 are given as a perturbation, which is observed in the experiment of Thomas et al. in 1986. A convective boundary condition is used for the outflow velocity boundary condition.

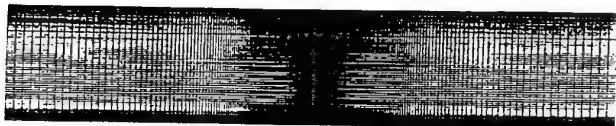


FIGURE 2: MESH CONFIGURATION

## EXPERIMENTS

The experiments were conducted in a closed watercourse. The inlet slot jet was coming out through the confined nozzle with a size of  $B=20$  mm and the spanwise length of 200mm, and was impinging orthogonally onto the flat surface located at 200mm from the nozzle exit. Turbulent statistics such as the mean velocity and the turbulent intensities were measured by two channel LDV system on the central  $x$ - $y$  plane at  $z/B=1.95$ . Measured turbulence on the center of the jet at the nozzle exit was about 3% of the mean velocity.

## RESULTS

Hereafter the isotropic eddy viscosity model given in eq.(3) and the anisotropic model given in eqs. (4) and (5) are represented by DI (Dynamic Isotropic) and DA (Dynamic Anisotropic) respectively. All figures are non-dimensionalized by the nozzle width  $B$  and the inlet velocity  $V_0$ . The value  $y/B$  denotes the non-dimensionalized distance from the impinging plate.

### Turbulent Statistics in the free jet region

The streamwise mean velocity and the turbulent intensity profiles of the free jet are shown in figs. 3 and 4 respectively. Both DI and DA model simulate mean velocity very well and difference of the models is very little. The streamwise mean velocity profile is nearly the top-hat shape at  $y/B=9$ , and develops downstream along the jet center line. It was found that the profile, if normalized by the center line velocity  $V_c$  and the half width  $b$  of  $V_c$ , follows the Gaussian distribution of  $V/V_c = \exp \{ -0.693 (x/b)^2 \}$  around  $y/B=5$  (figure not shown). This distribution was known as the profile at the self preserving region of the plane jet by the experiment conducted by Dracos et al. in 1992. On the other hand, some differences between the models are observed in the turbulent intensity profile. At  $y/B=5$  and  $y/B=3$  two peaks due to the free shear layer can be clearly simulated by DA model while DI model predicts moderate peaks at the center of the jet, which couldn't be observed in the experiment.

### Turbulent Statistics in the wall jet region

The streamwise mean velocity and the turbulent intensity profiles of the wall jet are indicated in figs. 5 and 6 respectively. At this region, both models also predict the mean velocity profiles very well. At  $x/B=2$ , the turbulent intensity of DA model is underestimated compared to that of the experimental data while DI model correlates well with the experiments. However, underestimation by DA model gradually becomes smaller away from the stagnation point to the streamwise direction, and DA model comes to show better agreement with the experiments than DI model at  $x/B=7$ .

### Turbulent Statistics in the Stagnation Region

Fig. 7 indicates the turbulent statistics of DI and DA model in the stagnation region. The mean velocity profiles for normal wall direction show good agreement with experimental data in both DI and DA models in this region.

Both models also predict the turbulent intensities qualitatively well but compared to the DI model, DA model underestimates those statistics around this region.

### GS Turbulent Energy Budget

In the stagnation region, the mean velocity of the free jet normal to the impinging plate slows down abruptly due to the plate, and changes the direction from normal to the wall to along the wall and speeds up. Accordingly among strain rate tensor, the normal components such as  $[\tilde{u}_1]/x_1$  by acceleration and  $[\tilde{u}_2]/x_2$  by deceleration is important in this region, and it is completely different from the shear flows.

Fig. 9 indicates the budget of the GS turbulent energy ( $k = 1/2 \{ [\tilde{u}_i \tilde{u}_i] - [\tilde{u}_i][\tilde{u}_i] \}$ ) predicted by DI model along the center line of the plane jet. The peak of the production term that is given by  $P_{kk} = -([\tilde{u}_2 \tilde{u}_2] - [\tilde{u}_2][\tilde{u}_2]) \partial[\tilde{u}_2]/\partial x_2$  can be observed around  $y/B=0.4$ , which would be the results of the rapid deceleration of the mean flow along the jet center line. But due to strong damping of the perturbation for the normal wall direction as wall approaching then  $[\tilde{u}_1 \tilde{u}_1]$  having the same level as  $[\tilde{u}_2 \tilde{u}_2]$  just the vicinity of the wall, the production term is not dominant near the wall.

This tendency is completely different from that of the round impinging jet observed by Nishino et al. in 1995. According to Nishino's experiment, strong negative production was observed in the near wall region where the excess in the radial turbulent intensity was found. Instead of the negative production, the dissipation and the molecular diffusion terms are dominant as loss terms in the plane impinging jet.

It should be noted here that diffusion due to the SGS stress and dissipation due to the SGS stress are included in the turbulent diffusion and the dissipation terms respectively. Fig. 10 shows the effect of the SGS model in these terms. From this figure, we have found that the effect of SGS model in the turbulent diffusion is trivial while SGS model is dominant in the dissipation term except the near wall region where viscous dissipation is large.

### Normal Reynolds Stress Budget

As we have pointed out at the previous section, the normal components of the strain rate tensor is dominant in the stagnation region. In other words, one can say that stretch and contraction of the fluid motions are dominant in the impinging region. Consequently redistribution of the turbulent energy among the normal Reynolds stress due to the pressure strain term will play an important role in the energy transfer mechanism of the turbulence in this region.

Fig. 11 indicates the budgets of the normal Reynolds stress  $R_{11}$ ,  $R_{22}$  and  $R_{33}$  for  $x_1$ ,  $x_2$  and  $x_3$  direction respectively along the center line of the plane jet. Here  $R_{aa} = [\tilde{u}_a \tilde{u}_a] - [\tilde{u}_a][\tilde{u}_a]$  ('a' is not summed up). These budgets were estimated from the results of DI model.

This figure implies that as the free jet decelerates, the major gain of the turbulence energy from the main flow field

is obtained by the production term of the  $R_{22}$  around  $y/B=1.5$ . While just near the wall,  $R_{22}$  gains the energy from the pressure diffusion term that is balanced with the pressure strain term.

As the figure indicates, the pressure strain term of the  $R_{22}$  redistributes the energy to the  $R_{11}$  and the  $R_{33}$  where these terms work as the gain. It is worth noting that redistribution to  $R_{11}$  and  $R_{33}$  is at the ratio of one and four in this case. In  $R_{11}$ , redistributed energy balances with the negative production term except at the vicinity of the wall. This negative production would be caused by the acceleration of the mean flow along the wall. That is, the turbulent energy is consumed and is recurred to the mean flow field. On the other hand, redistributed energy in  $R_{33}$  is mainly dissipated by molecular and SGS viscosity. According to these figures, it is clear that the dissipation of the GS turbulent energy indicated in fig. 6 is mostly coming from the dissipation of  $R_{33}$ .

### CONCLUSION

The GS turbulence energy budget and the normal Reynolds stress budget as well as the mean velocity and the turbulent intensities were calculated by LES. The modified SGS model was employed for the complicated turbulence with the transition and the stagnation. Distribution of the mean velocity and the turbulent intensities were correlated well with the experimental data obtained by LDV. The GS turbulence energy budget revealed that negative production was not dominant near the impinging plate in contrary with the round impinging jet. From the normal Reynolds stress budget, transfer mechanism of the turbulent energy was presented such that pressure strain term played an important role in redistributing turbulence energy of  $R_{22}$  to  $R_{11}$  and  $R_{33}$  at the rate of about 1 and 4 in our case.

Finally it can be said that our LES with modified SGS model predicted the properties of the turbulent impinging jet well enough to estimate the transfer mechanism of turbulent energy.

### REFERENCES

- T. Dracos, M. Giger and G. H. Jirka, *J. Fluid Mech.* 241 (1992), pp.587-614
- P. A. Durbin, *Theor. Comp. Fluid Dynamics* 3 (1991), pp.1-13
- E. Gutmark, M. Wolfstein and I. Wygnanski, *J. Fluid Mech.* 88-4 (1978), pp.737-756
- M. Germano, U. Piomelli, P. Moin and W. H. Cabot, *Phys. Fluids A* 3(1991), pp.1760-1765
- K. Horiuti, *Phys. Fluids A* 5(1993), pp.146-157
- C. Meneveau, T. S. Lund and W. Cabot, *J. Fluid Mech.* 319 (1996), pp.353-385
- K. Nishino, M. Samada, K. Kasuya and K. Torii, *Proc. of the 10th Symp. on Turb. Shear Flow* (1995), pp.12-13~12-18
- F. O. Thomas and V. W. Goldschmidt, *J. Fluid Mech.* 163 (1986), pp.227-256
- A. Yoshizawa, M. Tsubokura, T. Kobayashi and N. Taniguchi, *Phys. Fluids.* 8 (1996), pp.2254-2256

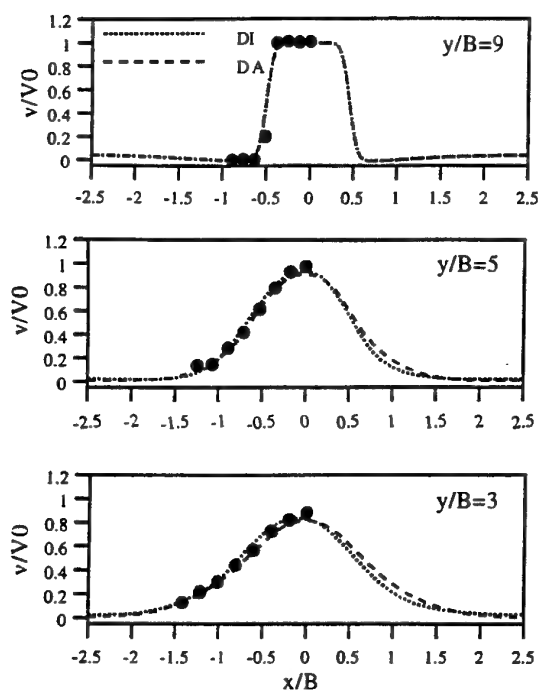


FIG.3: STREAMWISE MEAN VELOCITY OF THE FREE JET (symbol; exp.)

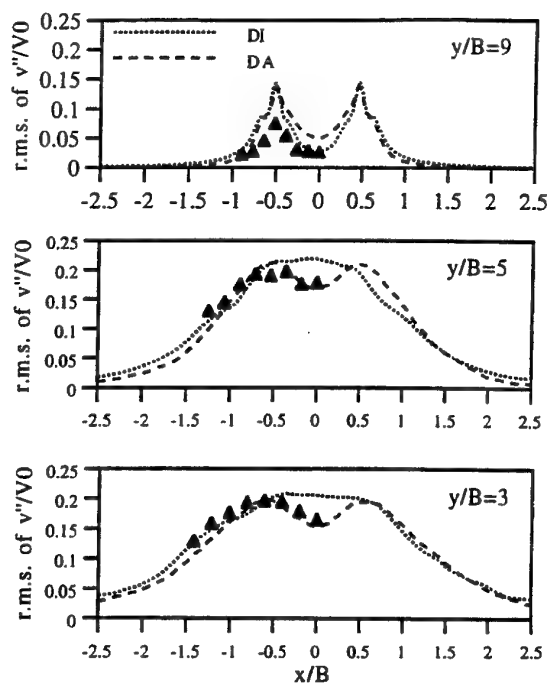


FIG.4: STREAMWISE TURBULENT INTENSITY OF THE FREE JET (symbol; exp.)

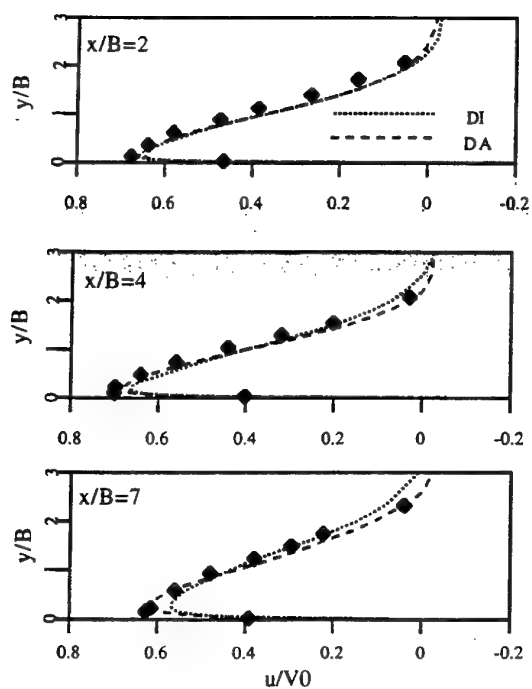


FIG.5: STREAMWISE MEAN VELOCITY OF THE WALL JET (symbol; exp.)

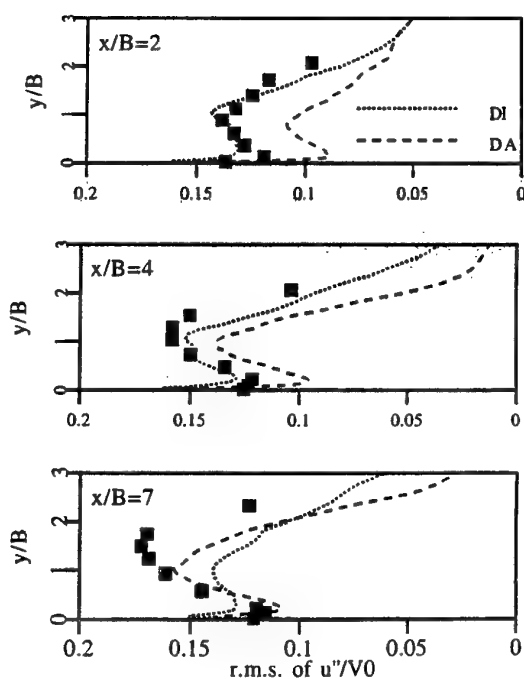


FIG.6: STREAMWISE TURBULENT INTENSITY OF THE WALL JET (symbol; exp.)

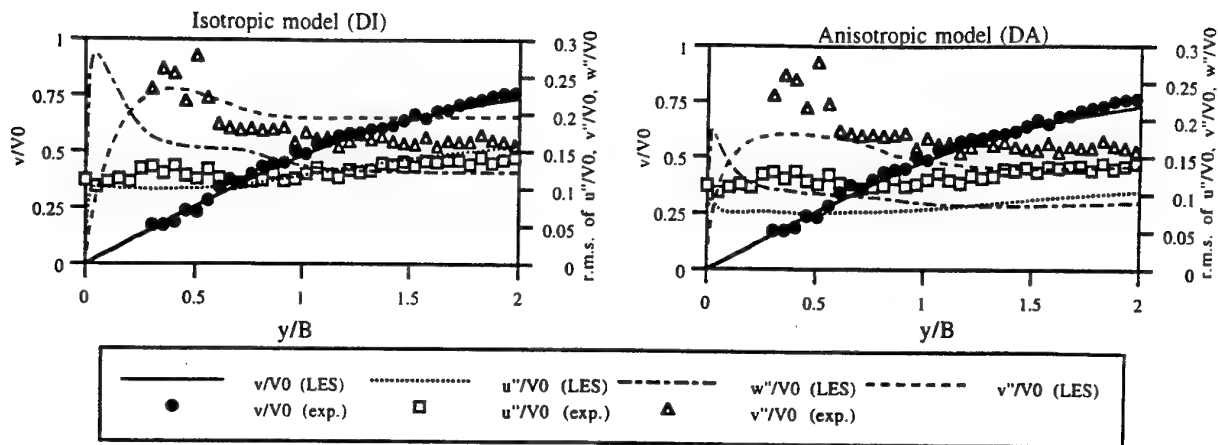


FIG.7: TURBULENT STATISTICS IN THE STAGNATION REGION

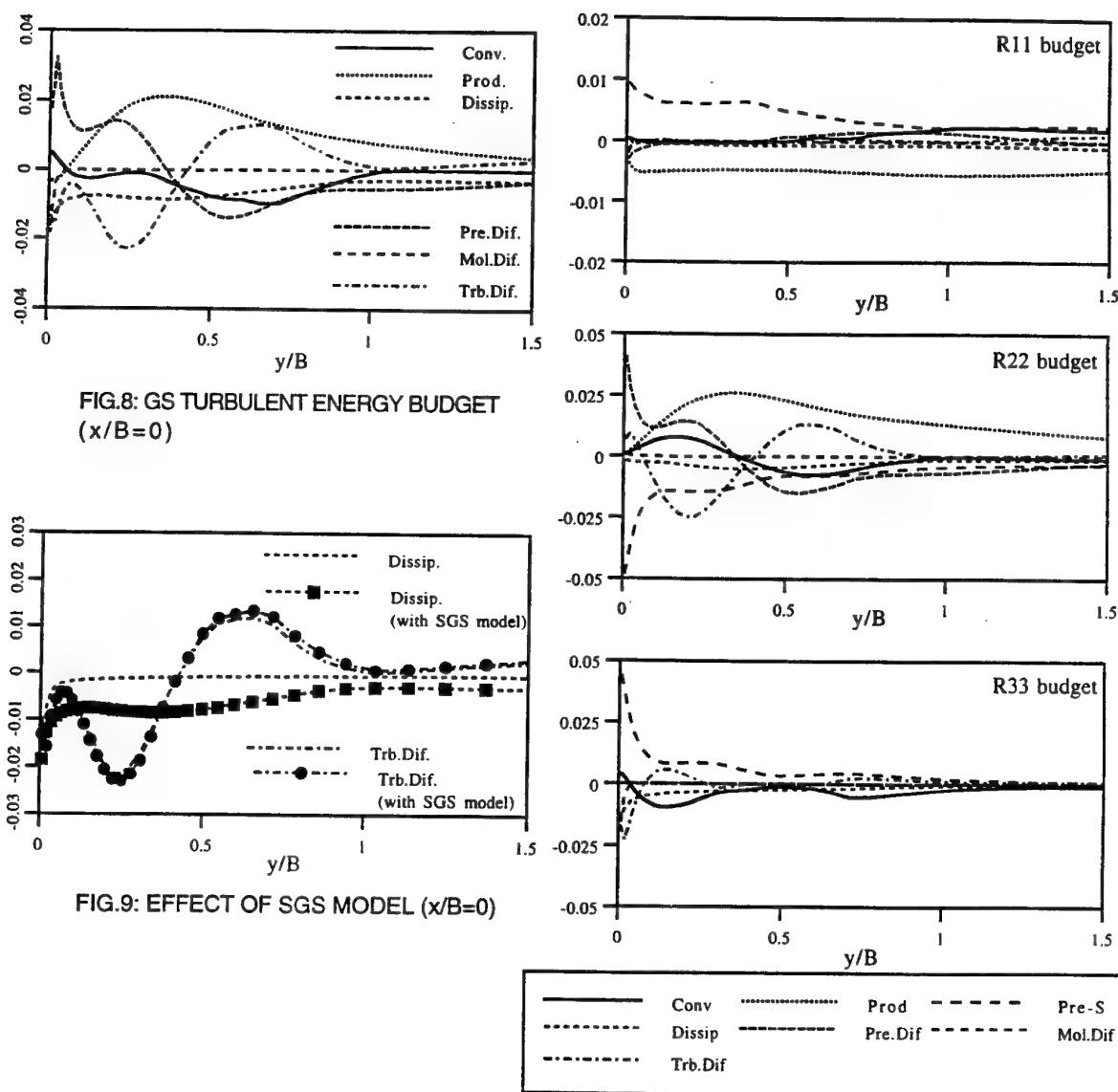


FIG.10: GS REYNOLDS STRESS BUDGET ( $x/B=0$ )

## **POSTER SESSION - 2**

# New First-Order Closure Models For Stably Stratified Flows

B. Abart and J.-F. Sini  
Laboratoire de Mécanique des Fluides UMR n° 6598  
Ecole Centrale de Nantes  
BP 92101  
F-44321 Nantes cedex 3

## ABSTRACT

The paper considers stratification complex phenomena. Two new first-order turbulence models presented here are designed to simulate stably stratified flows. In order to test them, before atmospheric applications, those models are evaluated on flows of rather simple configuration with «active» stratification (constant temperature gradient and shear or thermal mixing layer experiment and DNS data) and compared with second-order closure simulations. For weak stratification, a simple extension of  $k$ - $\epsilon$  standard model, namely  $k$ - $\epsilon$ - $Ri$  model, provides rather good results with low CPU time consumption. For high stratification, a five equation model is proposed which simulates quite well the strong interaction of dynamic and thermal mechanisms.

## INTRODUCTION

The effect of stable stratification (density decrease with height at faster rate than the adiabatic one) is of major importance in geophysical flows. The density decrease (increase of potential temperature with height) frequently diminishes turbulence which becomes more anisotropic and can strongly reduce effective vertical diffusivity. Those stratification effects are due to some exchanges between turbulent kinetic energy ( $k$ ) and potential energy:

$$E_{pot} = \frac{g}{\theta_0} \frac{\overline{\theta'^2}}{2} \quad (1)$$

by means of the thermal vertical flux ( $\overline{w'\theta'}$ ). Clearly, accurate prediction and control of pollution concentrations largely depend on our understanding of turbulence dynamics for these conditions.

Complex dynamical, physical and chemical phenomena and their interactions occur in the lower atmosphere. However, limitation to first-order closure is imposed for computational cost and applicability reasons. Previous first-order models are

not able to simulate kinetic/potential energy exchanges and, sometimes great, diffusion effects. Indeed, usually, those models use simple gradient modelling for the vertical heat flux, underestimate or ignore turbulence anisotropy due to stratification.

Then, two new types of first-order closure adapted for stratified flows are proposed. The first model is a simple extension of the standard  $k$ - $\epsilon$  model introducing the turbulence Richardson number in order to take into account turbulence anisotropy caused by weak stratification (thermal turbulent diffusion is neglected). The second and third models presented here solve five equations (second first-order closure type) issuing from second-order closures (Gibson and Launder, 1978 -GL- and Craft and Launder, 1991-CL) for turbulent kinetic energy ( $k$ ), its dissipation rate ( $\epsilon$ ), vertical turbulent kinetic energy ( $\overline{w'^2}$ ), vertical thermal flux ( $\overline{w'\theta'}$ ) and temperature variance ( $\overline{\theta'^2}$ ). These more elaborate models allow stronger stratified flow simulation than the first model with more realistic representation of phenomena.

## $k$ - $\epsilon$ - $Ri$ MODEL

This first model, extension of the standard  $k$ - $\epsilon$  model, is based on a turbulence anisotropy parameterization for free shear part of turbulent normal stresses ( $-2/3k$  in standard  $k$ - $\epsilon$  model) in terms of the horizontal turbulence Richardson number  $Ri_u$  (3).

In free shear stably stratified flows, evolution equations of the vertical and horizontal parts of turbulent kinetic energy are:

$$\begin{cases} U \frac{\partial \overline{u'^2}/2}{\partial x} = -\overline{v' \frac{\partial u'}{\partial x_i}} - \frac{\partial}{\partial x_i} (\overline{u'_i u'^2}) - \frac{1}{\rho_0} \overline{u' \frac{\partial p'}{\partial x}} \\ U \frac{\partial \overline{w'^2}/2}{\partial x} = \frac{g}{\theta_0} \overline{w'\theta'} - \overline{v' \frac{\partial w'}{\partial x_i}} - \frac{\partial}{\partial x_i} (\overline{u'_i w'^2}) - \frac{1}{\rho_0} \overline{w' \frac{\partial p'}{\partial x}} \end{cases} \quad (2)$$

$\overline{w'^2}$  is directly reduced by buoyancy (if  $\overline{w'\theta'} < 0$ ) and  $\overline{u'^2}$  is indirectly modified by redistribution energy phenomena. So, we can identify in all Reynolds stresses equations three contributions: first, pure Reynolds stresses coupling (by means of pressure-strain terms), second, buoyancy contribution (direct for  $\overline{w'^2}$ , indirect for others) and third, shear terms (not written in (2)).

Consequently, for the  $k$ - $\epsilon$ - $Ri$  model, in order to reproduce these three parts,  $\overline{w'^2}$  is separated in the free shear part,  $\overline{w'^2}_{FS}$  - sum of purely turbulent and direct thermal parts- and the shear one. In the same way,  $\overline{u'^2}_{FS}$  denotes the free shear part of  $\overline{u'^2}$  (representing turbulent and indirect thermal contributions).

We will present first the free shear part modelling and next, the shear one.

### Free Shear Part

An experimental correlation based on free shear grid turbulence decay affected by constant temperature gradient (Yoon and Warhaft, 1989's and Lienhard and Van Atta, 1989's experiments) is built to provide a relation between the vertical turbulent Froude number  $Fr_t$  and the horizontal turbulent Richardson number  $Ri_u$ :

$$Fr_t = c Ri_u^{-n} \text{ with } \begin{cases} Fr_t = \overline{w'^2}^{0.5} / NL_u \\ Ri_u = (NL_u)^2 / \overline{u'^2} \end{cases} \quad (3)$$

where  $N$  is the Brünt Väisälä frequency  $-N^2 = (g/\theta_0) \partial\theta/\partial z$ ,  $L_u = \overline{u'^2}^{1.5} / \epsilon$  the horizontal turbulence lengthscale and  $c$  and  $n$  are some simple functions of  $Ri_u$ .

In the experiments,  $Ri_u$  range from 0.0 to 70.0. Four zones can be approximately identified (fig. 1):

- turbulence isotropy for  $Ri_u \leq 0.1$  («passive» flow).
- anisotropy increasing for  $0.1 \leq Ri_u \leq 1.0$ .
- return to isotropy for  $1.0 \leq Ri_u \leq 30.0$ .
- oscillations for  $Ri_u$  higher than 30.0; but, because of the too high complexity of oscillatory wave phenomenon at this closure level, these oscillations are not taken into account in the  $k$ - $\epsilon$ - $Ri$  model and turbulence isotropy is imposed ( $\overline{u'^2}_{FS} = 2/3k$ ).

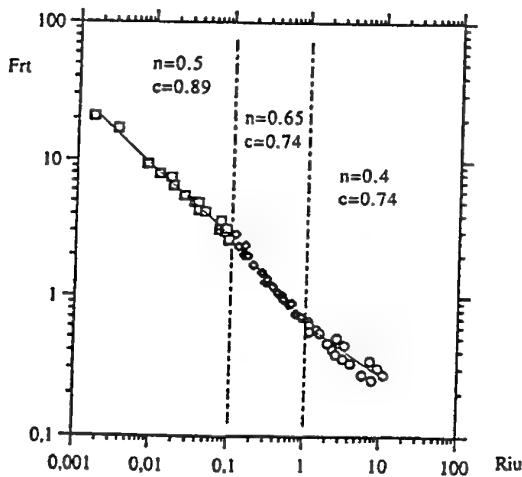


Fig. 1:  $Ri_u$  fonction of  $Fr_t$  for experiments and correlation (3).

By using evident relation  $\overline{w'^2}/\overline{u'^2} = Ri_u Fr_t^2$  based on number definition (3), the anisotropic parameterization is obtained:

$$\begin{cases} \overline{w'^2}_{FS} / \overline{u'^2}_{FS} = c^2 Ri_u^{-2n+1} \\ \overline{u'^2}_{FS} = \overline{v'^2}_{FS} \text{ (assuming horizontal isotropy)} \\ 2k = \overline{u'^2} + \overline{v'^2} + \overline{w'^2} = 2\overline{u'^2}_{FS} + \overline{w'^2}_{FS} \end{cases} \quad (4)$$

In fact, system (4) is a simple anisotropic modelling for the first oscillatory wave (represented by the three first zones) of the kinetic/potential energy exchange phenomenon. So, thermal stratification has a direct influence on  $\overline{u'^2}_i$ .

### Shear Part

Supposing cross derivatives preponderance, homogeneity hypothesis applied on  $\overline{u'w'}$  second-order GL's transport equation gives:

$$\overline{u'w'} = -3/2 C_\mu \frac{k}{\epsilon} \left( \overline{u'^2} \frac{\partial W}{\partial x} + \overline{w'^2} \frac{\partial U}{\partial z} \right); C_\mu = 0.09 \quad (5)$$

Generalization of (5) for shear part,  $\overline{u'_i u'_j s}$ , is adopted (no sum on  $i$  and  $j$ ):

$$\overline{u'_i u'_j s} = -3/2 C_\mu \frac{k}{\epsilon} \left( \overline{u'^2}_i \frac{\partial U_j}{\partial x_i} + \overline{u'^2}_j \frac{\partial U_i}{\partial x_j} \right) + C_\mu \frac{k}{\epsilon} \overline{u'^2}_k \frac{\partial U_k}{\partial x_k} \delta_{ij} \quad (6)$$

As anisotropy of  $\overline{u'^2}_i$  normal stresses due to stratification is taken into account by means of (4), we see that equation (6) sensiblize all the Reynolds stresses to stratification. Reminding that, in the standard  $k$ - $\epsilon$  model,  $\overline{u'_i u'_j s} = -C_\mu k^2 / \epsilon S_{ij}$  where  $S_{ij}$  is the strain rate tensor, the major improvement of this formulation is that it limits the over-estimation of turbulent kinetic energy production by shear in stably stratified flows.

Indeed, reduction of  $\overline{w'^2}$  by stratification (equation (4)) impose reduction of  $\overline{u'w'}$  and so of shear production.

Using (6), supposing weak anisotropy, anisotropic turbulent viscosity is:

$$\nu_{Tij} = 3/2 C_\mu \frac{k}{\epsilon} \frac{\overline{u'^2}_i + \overline{u'^2}_j}{2} \quad (7)$$

### Heat Fluxes

Modelling for vertical heat flux results from  $\overline{w'\theta'}$  GL's transport equation using Rodi, 1985's type of hypotheses (applied on convection, diffusion and shear production terms). Then,  $\overline{w'\theta'}$  depends on vertical turbulence anisotropy:

$$g/\theta_0 \overline{w'\theta'} = \frac{(C_1 - 1)\epsilon/k(\overline{w'^2} - 2/3k)}{\overline{w'^2}/k - 2 + 4/3C_3} \quad (8)$$

Equation (8) allows an estimation of turbulent Prandtl number  $Pr_t$  to calculate horizontal heat fluxes by means of usual gradient formulation with anisotropic turbulent viscosity (7):

$$\begin{cases} Pr_t = -\frac{\nu_{T33}}{\overline{w'\theta'}} \frac{\partial\theta}{\partial z} \\ \overline{u'_i \theta'} = -\frac{\nu_{Tij}}{Pr_t} \frac{\partial\theta}{\partial x_i} \quad (i = 1 \text{ or } 2) \end{cases} \quad (9)$$



## k and ε equations

k and ε modelled equations are extensions of Chen and Kim, 1987's model for stratified flows: time scale  $(P_k + C_{\epsilon 3} G_k)/k$  is used instead of  $P_k/k$  with  $C_{\epsilon 3} = 0 - 0.2$  (Rodi, 1985).

$$\begin{cases} \frac{Dk}{Dt} = P_k + G_k - \epsilon + \text{Dif}_k \\ \frac{D\epsilon}{Dt} = C_{\epsilon 1} \frac{\epsilon}{k} (P_k + C_{\epsilon 3} G_k) + C_{\epsilon 4} \frac{(P_k + C_{\epsilon 3} G_k)^2}{k} - C_{\epsilon 2} \frac{\epsilon^2}{k} + \text{Dif}_\epsilon \end{cases} \quad (10)$$

with  $P_k$  is shear production,  $G_k$  buoyancy production and  $\text{Dif}$  diffusion term.

To end, Launder and Sharma, 1974 low Reynolds number extensions are introduced.

## FIVE EQUATION MODELS

Anisotropisation by stratification is due to kinetic/potential energy exchanges by means of vertical heat flux. Indeed, assuming vertical homogeneity and stationarity, the equations for vertical turbulent kinetic energy, vertical heat flux and temperature variance reduce to (Yoon and Warhaft, 1989):

$$\begin{cases} U \frac{\partial \overline{w'^2}/2}{\partial x} = \frac{g}{\theta_0} \overline{w'\theta'} - \overline{w'\theta'} \frac{\partial \overline{w'}}{\partial x_i} - \frac{1}{\rho_0} \overline{w'} \frac{\partial p'}{\partial x} \\ U \frac{\partial \overline{w'\theta'}}{\partial x} = -\overline{w'^2} \frac{\partial \theta}{\partial z} + \frac{g}{\theta_0} \overline{\theta'^2} - \frac{1}{\rho_0} \overline{\theta'} \frac{\partial p'}{\partial x} \\ U \frac{\partial \overline{\theta'^2}/2}{\partial x} = -\overline{w'\theta'} \frac{\partial \theta}{\partial z} - \epsilon_\theta \end{cases} \quad (11)$$

In order to take into account energy exchanges and turbulent diffusion (terms not written in (11) which have to be modelled) due to stratification, two five equation models are based on explicit resolution of the three further transport equation for  $\overline{w'^2}$ ,  $\overline{w'\theta'}$  and  $\overline{\theta'^2}$  of two second-order models. Indeed, second-order closure is usually regarded as being the best level of wide applicability. Basic second-order model for thermal flows (GL) is known to have limitations (especially in non-local equilibrium -i.e.  $P_k + G_k \neq \epsilon$ ) so we consider also nonlinear Craft and Launder, 1991's realizable model (CL) which have quadratic pressure-strain expression and moreover does not seem to need empirical «wall-reflexion» terms (Craft et al, 1996). The two five equation models will be denoted here by 5GL and 5CL, respectively issued from GL and CL.

Other unknown Reynolds stresses are estimated by:

$$\begin{aligned} \overline{u'_i u'_j} &= \left( k - 1/2 \overline{w'^2} \right) \delta_{ij} - 3/2 C_\mu \frac{k}{\epsilon} \left( \overline{u'_i^2} \frac{\partial U}{\partial x_i} + \overline{u'_j^2} \frac{\partial U}{\partial x_j} \right) \\ &+ 3/2 C_\mu \frac{k}{\epsilon} \left( \overline{u'^2} \frac{\partial U}{\partial x} + \overline{v'^2} \frac{\partial V}{\partial y} \right) \delta_{ij} \quad (\text{no sum on } i \text{ and } j) \end{aligned} \quad (12)$$

Equation (12), with the same shear part that of the k-ε-Ri model (6), allows vanishing into two component turbulence (extinction of  $\overline{w'^2}$ ,  $\overline{w'\theta'}$  and  $\overline{u'w'}$ ). Indeed, in a simple shear flow with strong stable stratification, extinction of  $\overline{w'^2}$  by buoyancy imposes extinction of  $\overline{u'w'}$  in (12).

k and ε transport equations are the same as used in the k-ε-Ri model.

## TEST CASES AND ANALYSIS

In order to determine the three models (k-ε-Ri model, 5GL and 5CL) applicability range in terms of Richardson number, two free-shear and one shear stably stratified test cases are selected.

The three flows show active thermal behaviour: the thermal lengthscale affects that of the velocity field. So, if these test case configurations seem to be numerically rather simple, the physics is complex because of this interaction between dynamic lengthscale of both turbulence and stratification in these unconfined flows.

5GL and 5CL converge more slowly than the k-ε-Ri model: at least twice as many iterations are needed to obtain the same numerical convergence on the three test cases. This is evidently due to the strongest coupling associated with the three additional transport equations.

### Case 1

Case 1 is a grid turbulence decay with initial «passive» vertical flux (13) affected by a constant vertical gradient of temperature (Yoon and Warhaft, 1989's experiment with high Brünt Väisälä frequency  $N = 1.3 \text{ s}^{-1}$  and grid Reynolds number  $Re_M = UM/\nu = 4000$ ).

$$\rho_0 \overline{w'\theta'} = \overline{w'\theta'} / (\overline{w'^2} \overline{\theta'^2})^{0.5} = -0.7 \quad (13)$$

This experiment allows assesment of models about anisotropisation by stratification. This test is particularly important for the k-ε-Ri model because its construction is partly based on this type of flow (correlation (4)).

For the k-ε-Ri model, anisotropisation is effectively well predicted (fig. 2).

Despite their further equations, five equation and second-order models are less accurate than the k-ε-Ri model (fig. 3). Indeed, this test case reveals that linear models (GL and 5GL) delay the initial evolution of potential energy, turbulence anisotropy and vertical flux partly due to rapid pressure-strain part. With their non-linear pressure-strain modelling, CL and 5CL show a slightly better behaviour than linear models though not perfect (vertical heat flux minimum is between that of the k-ε-Ri model and of linear ones).

### Case 2

Case 2 is a grid turbulence decay submitted to a thermal mixing layer. It is a stably stratified mixing layer sandwiched between regions of neutral turbulence (Jayesh, Yoon and Warhaft, 1990's experiment with  $\Delta\theta = 20\text{K}$  and Brünt Väisälä

frequency on the centre line  $N_c = 2.68\text{s}^{-1}$ ). This test case is an extension from the experiments of Yoon and Warhaft, 1989 with a vertical inhomogeneity which fundamentally changes the nature of the flow. In this strongly stratified situation, after an initial growth ( $x/M \leq 40$ ), the mixing layer thickness diminishes with fetch and on the centre line, heat flux and turbulent kinetic energy are reduced comparing with their level in the rest of the flow because of potential energy production.

Case 2 allows first validation of present models for flows where diffusion plays an important role (for example, inversion layer in atmosphere) and second, it shows the superiority of non-linear pressure-strain modelling issued from Craft and Launder, 1991.

First, the weak decrease rate of potential temperature half width is predicted by all models except the standard k-ε model which provides a growth rate comparable with that of «passive» step

case  $\Delta\theta = 4K$  of Ma and Warhaft, 1986 (half width not shown here).

On the centre line, as the  $k-\epsilon$ -Ri model by construction does not simulate turbulence and heat diffusion effects on Reynolds stresses and heat fluxes, turbulence anisotropy is underestimated (here,  $Ri_u$  is in «return to isotropy» range although experiment shows anisotropy growth); but, vertical heat flux shows an acceptable evolution compared with experiment and more elaborate models (fig. 4), partly because  $w'\theta'$  behaviour is less dependent on diffusion than on equilibrium state between  $k$  and  $Epot$  (we point out that in the  $k-\epsilon$ -Ri model, this exchange phenomenon is implicitly represented by the anisotropisation correlation (3)). Five equation and second-order models achieve rather good agreement for  $w'\theta'$  except the unpredicted weak center-gradient flux (fig. 4).

Vertical evolution of  $\overline{w'^2}/\overline{w'^2}_0$ , vertical velocity variance divided by its value outside the layer, and of  $\rho_{w\theta}$  (13) show a far better overall agreement for second-order models than for five equation ones (only  $\rho_{w\theta}$  at  $x/M=180$  shown in fig. 5). This discrepancy is partly due to evaluation of  $\overline{u'w'}$  which plays a role in Reynolds stresses redistribution (pressure-strain rapid part modelling) and potential energy vertical diffusion. Indeed, in second-order models,  $\overline{u'w'}$  is obtained by an evolution equation and so:

$$\rho_{uw} = \overline{u'w'}/(\overline{u'^2}\overline{w'^2})^{0.5} = 0-0.2 \quad (14)$$

(confirmed by Jayesh et al., 1991). This is not the case in first-order models where  $\overline{u'w'}$  only depends on shear (so, here,  $\overline{u'w'} = 0$ ).

The experimentally observed heat flux decreasing and relative minimum near the centre line<sup>1</sup> is only predicted by CL and qualitatively reproduced by 5CL and the  $k-\epsilon$ -Ri model (fig.6). We can see here the importance to first analyse absolute values (i.e. dimensional profiles) before relative ones. This discrepancy between GL's and CL's models is due to delayed heat flux behaviour prediction of GL, yet revealed with Case 1.

So, for this flow with strong diffusion, despite only qualitative results on turbulence and heat correlations, the  $k-\epsilon$ -Ri model allows good predictions of mean variables ( $U_i, \theta$ ) and turbulent kinetic energy ( $k$ ). More physical behaviour is found with CL and 5CL than with GL and 5GL. Lastly, CL shows, not surprisingly, better agreement with experiment than its new first-order version.

### Case 3

Case 3 is a stably stratified and sheared homogeneous turbulence (Large Eddy Simulations and Direct Numerical Simulations of Kaltenbach et al., 1994 and Holt et al., 1992).

The gradient Richardson number is defined by:

$$Ri = \frac{g}{\theta_0} \frac{\partial\theta}{\partial z} / \left( \frac{\partial U}{\partial z} \right)^2 \quad (15)$$

Two tests are conducted: one for  $Ri=0.13$  where local equilibrium (i.e.  $P_k + G_k = \epsilon$ ) is nearly satisfied and another for  $Ri=0.5$  where stratification imposes turbulence decay.

This low Reynolds number flow is simulated using low Reynolds versions of models. Launder and Sharma, 1974's

model is used as basic first-order model named here Low Reynolds Model. At all Richardson number, DNS showed huge impact of stratification on turbulent kinetic energy production by shear  $P_k$ .

$k$  behaviour of standard  $k-\epsilon$  and low Reynolds models is far from equilibrium state ( $Ri=0.13$ ) or decrease ( $Ri=0.5$ ) predicted by DNS (fig. 7 and 8). For  $Ri=0.13$ , the  $k-\epsilon$ -Ri model achieves globally good agreement on  $k$  evolution even if  $P_k/\epsilon$  is 20%

over-estimated (not shown) because of simple modelling of  $\overline{w'^2}$  and  $\overline{u'w'}$  (equations (3) and (4)).  $Ri=0.5$  case  $Ri_u$  range is obviously out of this model range applicability ( $Ri_u$  is between 25 and 50): the  $k-\epsilon$ -Ri model behaviour is nearly the same than the standard  $k-\epsilon$  and low Reynolds model ones.

On the other hand, if  $k$  prediction is accurate for the five equation models (fig. 7 and 8), 5CL captures the experimental behaviour of potential energy quite well in the two  $Ri$  cases contrary to 5GL which fails to give the correct evolution (partly due to  $\epsilon_\theta$  estimation made with constant time-scale ratio  $R$ ). Furthermore, 5CL even provides  $Epot/k$  mean level and first oscillation period showed by DNS with very good accuracy (period over-estimated by 5%) (fig. 9).

### CONCLUSION

The following conclusions can be drawn from this evaluation of the two new types of first-order closure presented here in comparison with second-order models by means of experiments and DNS data:

- the  $k-\epsilon$ -Ri model, extension of standard  $k-\epsilon$  one, is widely better in capturing stratification effects than this latter and shows good results for weak  $Ri_u$  ( $\leq 30$ ).
- Craft and Launder, 1991's second-order closure model with nonlinear pressure-strain performs better and shows more physical behaviour than the basic model of Gibson and Launder, 1978. Its five equation version is recommended for stably stratified atmospheric flow studies.

In order to validate these two models in their respective stratification applicability range, atmospheric type flows will be used with and without complex orography effects (heated wall, hill).

### ACKNOWLEDGEMENTS

The numerical calculations were carried out on the CRAY C90 supercomputers of the CNRS national computing centre. Complete computer support was given by the Scientific Council of Institut de Développement et de Recherche pour l'Informatique Scientifique -IDRIS- (CNRS), Orsay, France.

### REFERENCES

- Chen, Y.S., and Kim, S.-W., 1987, "Computation of turbulent flows using an extended  $k-\epsilon$  turbulence closure model." NASA Report, 27p.
- Craft, T.J., and Launder, B.E., 1991, "Computation of impinging flows using second-moment closures." *Proceedings, Eight Turbulent Shear Flows*, pp 8-5-1,8-5-6.
- Craft, T.J., Ince, N.Z., and Launder, B.E., 1996, "Recent developments in second-moment closure for buoyancy-affected flows." *Dynamics of Atmospheres and Oceans*, Vol. 23, pp 99-114.
- Gibson, M.M., and Launder, B.E., 1978, "Ground effects on pressure fluctuations in the atmospheric boundary layer." *J. Fluid Mechanics*, Vol. 86, pp. 491-511.

<sup>1</sup> Unfortunately, Jayesh et al., 1991's paper does not show vertical profile of vertical heat flux. Its behaviour can be deduced by analysis of  $\rho_{w\theta}$ ,  $\overline{w'^2}$  and  $\theta'^2$  vertical profiles. Only one precise value is known on the centre line (fig. 6).

Holt, S.E., Koseff, J.R., and Ferziger, J.H., 1992, "A numerical study of evolution and structure of homogeneous stably stratified sheared turbulence." *J. Fluid Mechanics*, Vol. 237, pp. 499-539.

Jayesh, Yoon, K., and Warhaft, Z., 1991, "Turbulent mixing and transport in a thermally stratified interfacial layer in decaying grid turbulence." *Physics of Fluids*, Vol. A.3, pp 1143-1155.

Kaltenbach, T., Gerz, T., and Shumann, U., 1994, "Large-eddy simulation of homogeneous turbulence and diffusion in stably stratified shear flow." *J. Fluid Mechanics*, Vol. 280, pp. 1-40.

Launder, B.E., and Sharma, 1974, "Application of the energy-dissipation model of turbulence to the calculation of flow near a spinning disk." *Lett. Heat and Mass Transfer*, Vol. 1, pp 131-138.

Lienhard, J.H., and Van Atta, C.W., 1990, "The decay of turbulence thermally stratified flow." *J. Fluid Mechanics*, Vol. 210, pp. 57-112.

Ma, B.K., and Warhaft, Z., 1986, *Phys. Fluids*, Vol. 29, p 3114.

Rodi, W., 1985, "Calculation of stably stratified shear layer flows with a buoyancy-extended k-ε turbulence model." *Turbulence and Diffusion in Stable Environment*, ed. J.H. Hunt, Oxford University Press, New York, pp 111-143.

Yoon, K., and Warhaft, Z., 1990, "The evolution of grid-generated turbulence under conditions of stable thermal stratification." *J. Fluid Mechanics*, Vol. 215, pp 601-638.

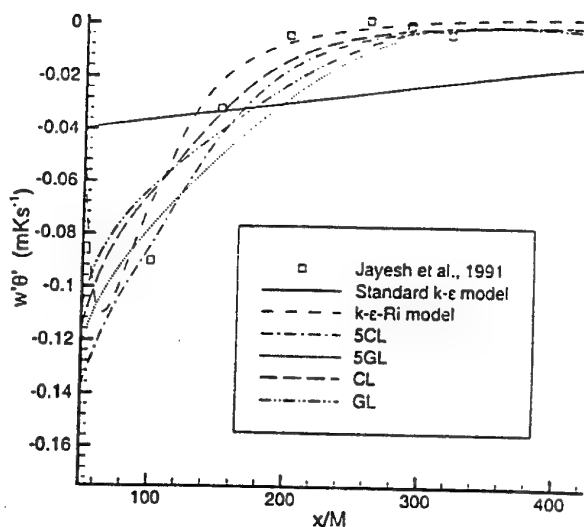


Fig. 4 Vertical heat flux on the centre line.

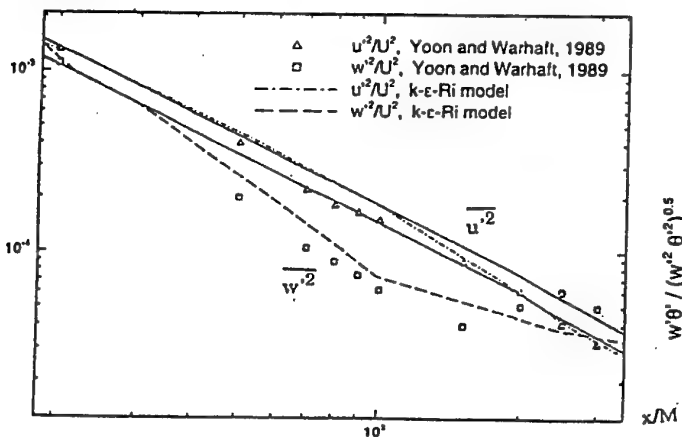


Fig. 2 Turbulence anisotropy for k-ε-Ri model.

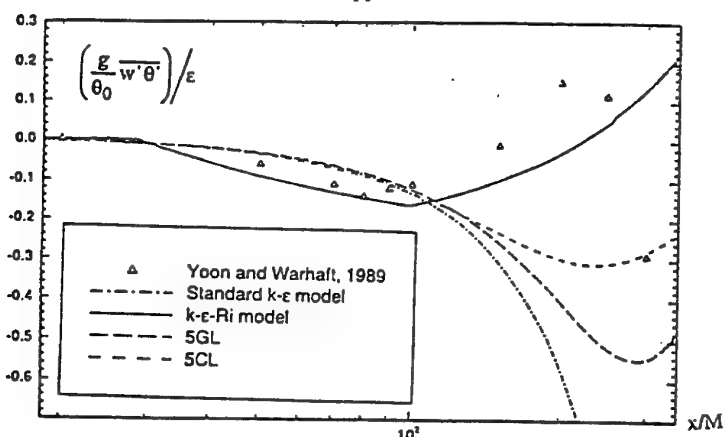


Fig. 3 Buoyancy over turbulent kinetic energy dissipation.

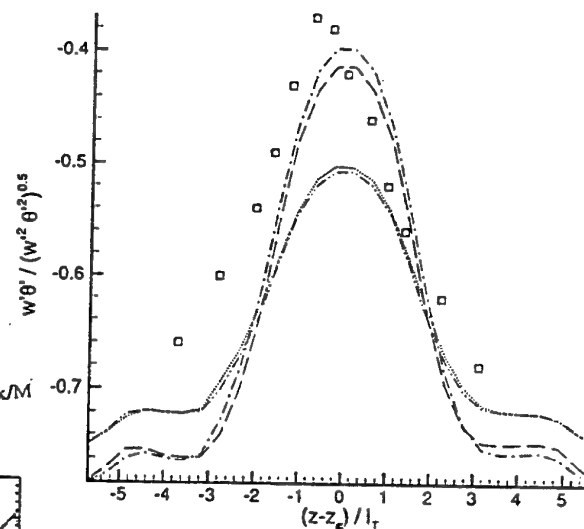


Fig. 5 Vertical profile of  $\rho w\theta$  ( $z_c$  is centre line height and  $l_T$  is the potential temperature half width).

Caption on fig. 4.

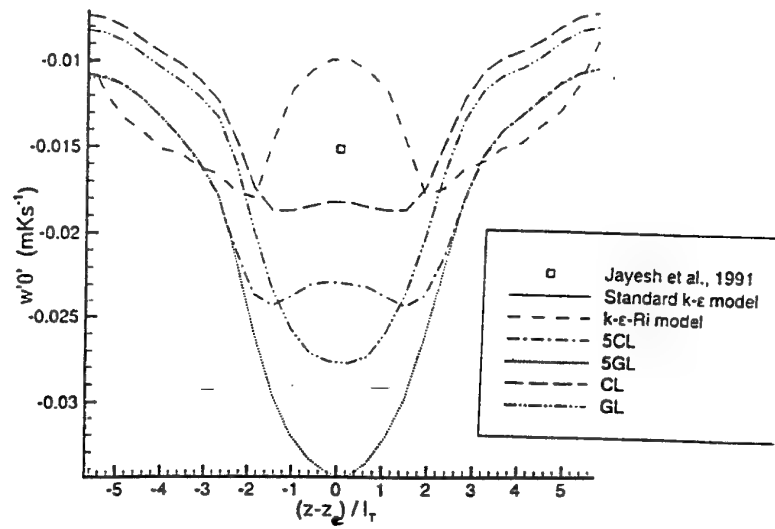


Fig. 6 Vertical profile of vertical heat flux.

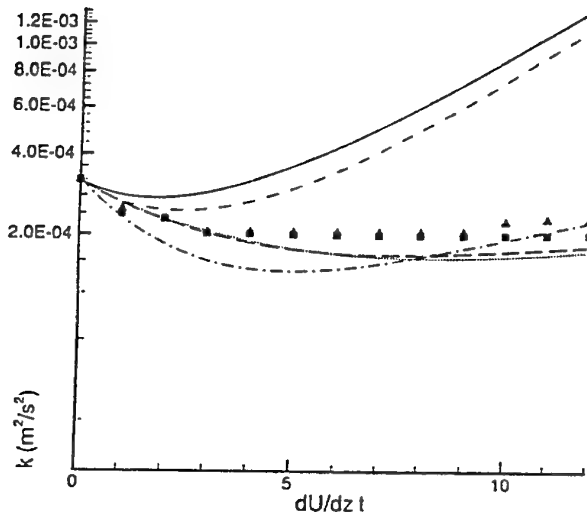


Fig. 7 Time evolution of  $k$  for  $Ri=0.13$ . Caption is below.

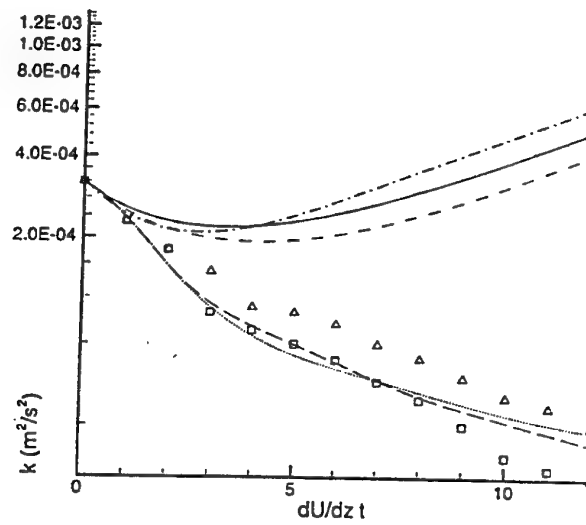


Fig. 8 Time evolution of  $k$  for  $Ri=0.5$ . Caption is below.

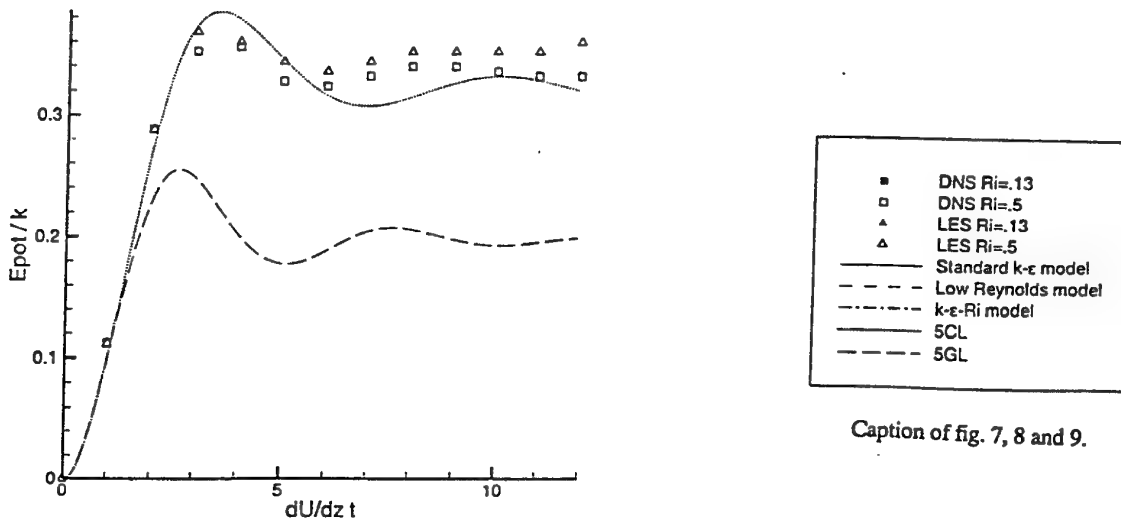


Fig. 9 Time evolution of  $E_{pot}/k$  for  $Ri=0.5$ . Caption is below.

Caption of fig. 7, 8 and 9.

# NUMERICAL SIMULATION OF DIURNAL ATMOSPHERIC FLOW VARIATIONS IN A COASTAL COMPLEX TERRAIN AREA AND COMPARISON OF RESULTS WITH FIELD OBSERVATIONS

K. Sada, Y. Ichikawa, K. Asakura

Atmospheric Science Department

Central Research Institute of Electric Power Industry

2-11-1 Iwado Kita, Komae-shi, Tokyo 201

JAPAN

## ABSTRACT

Application of a second moment closure turbulence model to computations of mesoscale atmospheric flows over coastal complex terrain is described. The boundary layer approximation and the hydrostatic assumption were used in this numerical simulation. The turbulence was first treated using the Reynolds stress model, and then the advection and diffusion terms of Reynolds stress and heat flux transport equations were approximated for obtaining algebraic equations for Reynolds stresses and heat fluxes. Furthermore, unsteady flow variations measured in the atmosphere were included in this model by means of consideration of the heat budget at the ground surface and a four-dimensional data assimilation method at wind velocities. The model calculation results reproduce well the field measurement results; i.e., the calculation results for unsteady variations of wind velocities and mixing layer development over the land area agree well with the results of field experiments.

## INTRODUCTION

Terrain conditions around power plants in Japan are usually complex and the influences of these terrain conditions on airflow and stack gas diffusion are significant. Because the stack gas diffusion phenomena are also governed to a large extent by turbulence, it is necessary to estimate turbulence when accurate prediction is made. In this work, a numerical simulation method that can be used to estimate the turbulence was developed for prediction of mesoscale atmospheric flows under complex terrain conditions around a power plant. The effects caused by temperature nonuniformity, such as the ground surface temperature variations due to changes in the intensity of solar radiation, are not negligible in the atmosphere, because turbulence increases and decreases when unstable and stable layers are formed, respectively. Furthermore, the influences of large-scale inflows into the area are also not negligible, because airflow directions vary according to the inflow patterns. For these reasons, it is necessary to take into consideration not only the turbulence but also the unsteady effects, such as changes in ground surface temperature and

unsteady large-scale inflows, when more accurate airflow and stack gas diffusion predictions are to be made. To simulate airflows in the atmosphere, the ground temperature was estimated by means of heat budget consideration including solar radiation intensity variations. Unsteady wind variations were incorporated into the model by a four-dimensional data assimilation method. The performance of the developed numerical simulation method under complex terrain and thermally non-neutral conditions was demonstrated and its accuracy is discussed based on comparison of field measurement results.

## FIELD OBSERVATION

Field observations, for collecting data for comparison with the calculation results, were conducted during the daytime for about one week in the summer of 1994. This observation period was selected because the weather was often fine and sea breezes often occurred then and it was not difficult to conduct field observations and collect data under such weather conditions. The hourly variations in wind velocity and temperature at up to 2000 m above the ground were measured using rawinsondes at four points within the field observation area; i.e., the power station was located at Point A and the west-east and south-north distances were both zero (Fig. 1), Point B was about 4 km north northwest of the power station, Point C was about 9 km north northeast of the power station and point D was about 6 km north northwest of the power station. Points A and C were located beside the coastline, at altitudes above mean sea level of nearly zero. Points B and D were located inland and about 5 km from the coastline, at altitudes above mean sea level of about 100 m. The rawinsondes were released from 10 a.m. to the afternoon at one-hour intervals. Data for a given day were selected for comparison with the calculated unsteady flow field; i.e., a sea breeze occurred at around noon and unstable mixing layers developed over the land area on that day.

## SIMULATION MODEL

A numerical simulation method based on turbulence closure

techniques was developed for prediction of mesoscale atmospheric flows. This numerical simulation method is based on the so-called  $z^*$  coordinate system. When this coordinate system is used, only vertical linear interpolations are necessary at grid generations. The physical coordinates ( $x, y, z$ ) are transformed to calculation coordinates ( $\xi, \eta, \zeta$ ) using

$$\xi = x, \quad \eta = y, \quad \zeta = \bar{H} \frac{z - z_s(x, y)}{H - z_s(x, y)}, \quad (1)$$

where  $z_s$  is the altitude of the terrain above mean sea level and  $H$  and  $\bar{H}$  are the heights of the physical and calculation domains, respectively (e.g. Sada et al., 1996). Then the boundary layer approximation is performed; i.e., horizontal but not vertical gradients of turbulence quantities are eliminated. Furthermore, the vertical component of wind motion is treated under the hydrostatic assumption in this numerical method. Finally, the wind velocity transport equations of the two horizontal components,  $U$  and  $V$ ,

$$\begin{aligned} \frac{D^*U}{D^*t} = fV + \zeta_z \frac{\partial}{\partial \zeta} (-\overline{uw}) \\ - \left\{ 1 - \beta(\Theta - \langle \Theta \rangle) \right\} \Theta \left\{ \frac{\partial \pi(\bar{H})}{\partial \xi} + g \frac{\partial}{\partial \xi} \left( \frac{1}{\zeta_z} \int_{\zeta}^{\bar{H}} \frac{1}{\Theta} d\zeta' \right) - \frac{\zeta_x}{\zeta_z} \frac{g}{\Theta} \right\} \\ + G_u \frac{\sum_{k=1}^N w_k^2 (U_{ok} - \hat{U}_k)}{\sum_{k=1}^N w_k}, \end{aligned} \quad (2)$$

$$\begin{aligned} \frac{D^*V}{D^*t} = -fU + \zeta_z \frac{\partial}{\partial \zeta} (-\overline{vw}) \\ - \left\{ 1 - \beta(\Theta - \langle \Theta \rangle) \right\} \Theta \left\{ \frac{\partial \pi(\bar{H})}{\partial \eta} + g \frac{\partial}{\partial \eta} \left( \frac{1}{\zeta_z} \int_{\zeta}^{\bar{H}} \frac{1}{\Theta} d\zeta' \right) - \frac{\zeta_y}{\zeta_z} \frac{g}{\Theta} \right\} \\ + G_v \frac{\sum_{k=1}^N w_k^2 (V_{ok} - \hat{V}_k)}{\sum_{k=1}^N w_k}, \end{aligned} \quad (3)$$

are derived. The right-hand sides of the above two equations indicate the substantial derivatives of  $U$  and  $V$ , respectively.  $f$ ,  $\Theta$ ,  $\beta$  and  $g$  are the Coriolis parameter, potential temperature, thermal expansion coefficient and gravity parameter, respectively.  $\langle \Theta \rangle$  is the horizontally averaged potential temperature and  $\pi(\bar{H})$  is modified pressure at  $\bar{H}$ .

The lowercase letters  $u, v$  and  $w$  are the fluctuation components of velocity where  $w$  is a vertical component.

In this report, because unsteady atmospheric flows in a coastal area with complex topographic conditions are simulated and the obtained simulation results are compared with measured wind and temperature profiles, a four-dimensional data assimilation (FDDA) scheme developed by Benjamin and Seaman (1985) and Stauffer and Seaman (1990), based on Newtonian relaxation or "nudging," is incorporated into the velocity transport equations for the two horizontal wind components. The nudging terms, the fourth terms on the right-hand sides of equations (2) and (3), are based on the correction term of a successive-correction objective analysis technique, which gives accurate results for regions of low data density.  $G_u$  and  $G_v$  are the nudging factors and determine the relative weight of nudging. A four-dimensional weighting function,  $w$

in the last terms on the right-hand sides of equations (2) and (3), is a function of horizontal, vertical and temporal effects between the calculation and measurement values.  $N$  is the number of measurements and the subscript  $ok$  indicates measurement values.  $\hat{U}_k$  and  $\hat{V}_k$  are predicted  $U$  and  $V$  values, respectively. In these calculations carried out using the FDDA technique, the velocity profiles obtained by rawinsondes within the calculation domain are used as individual objective profiles.

The values of the vertical mean wind velocity component ( $\bar{W}$ ) and potential temperature are obtained from the continuity equation and transport equation of potential temperature, respectively,

$$\frac{\partial JU}{\partial \xi} + \frac{\partial JV}{\partial \eta} + \frac{\partial JW}{\partial \zeta} = 0, \quad (4)$$

$$\frac{D^*\Theta}{D^*t} = \zeta_z \frac{\partial}{\partial \zeta} (-\overline{w\Theta}), \quad (5)$$

where  $J$  is the Jacobian of the coordinate transformation.  $\Theta$  is the fluctuation component of potential temperature.

Next it is necessary to determine the Reynolds stresses  $\overline{uw}$  and  $\overline{vw}$  and heat flux  $\overline{w\Theta}$ . The turbulence closure model based on the Reynolds stress model proposed by Gibson and Launder (1978) and Launder (1988) is applied first. For avoiding extensive calculation and use of large amounts of computer resources, the advection and diffusion terms in the Reynolds stress and heat flux equations are simplified according to the suggestions of Rodi (1976), and finally the Reynolds stresses and heat fluxes are expressed in terms of algebraic equations, for example,

$$\begin{aligned} \overline{uw} = \frac{k}{P_k + G_k - \left(1 - C_1 - \frac{3}{2} C_1^* f\right) \epsilon} \\ \times \left\{ - \left(1 - C_1 + \frac{3}{2} C_1^* C_1^* f\right) \overline{w^2} \zeta_z \frac{\partial U}{\partial \zeta} \right. \\ \left. + \left(1 - C_1 + \frac{3}{2} C_1^* C_1^* f\right) \beta g u \Theta \right\}, \end{aligned} \quad (6)$$

$$\begin{aligned} \overline{w\Theta} = \frac{1}{2k} \left\{ P_k + G_k - \left(1 - 2C_{10} - 2C_{10}^* f\right) \epsilon \right\} + \frac{1}{2\theta^2} (P_\theta - 2\epsilon_\theta) \\ \times \left\{ - \overline{w^2} \zeta_z \frac{\partial \Theta}{\partial \zeta} + \left(1 - C_{10} + C_{10}^* C_{10}^* f\right) \beta g \Theta \right\}, \end{aligned} \quad (7)$$

where the model constants are indicated by  $C$  and distinguished by use of subscripts and a superscript. The conventionally used model constants are taken from the work of Launder (1988).  $P_k$  and  $G_k$  are the production and buoyancy terms of the turbulent kinetic energy ( $k$ ) transport equation and  $\epsilon$  is the dissipation rate of turbulent kinetic energy.  $P_\theta$  and  $G_\theta$  are the production and buoyancy terms of the temperature variance transport equation and  $\epsilon_\theta$  is the dissipation rate of temperature variance. The turbulent kinetic energy transport equation, its dissipation transport equation and temperature variance transport equation are also solved for the turbulence closure. These equations are solved in finite-difference forms by use of the algorithm of the SMAC method. The initial velocity and turbulence quantities are set from the observation results collected at 10 a.m. The wall function methods are applied for velocity and turbulence quantities including the stratification effects described by Yaglom (1977).

Furthermore, the heat budget at the ground surface is taken

into account for determining the unsteady ground surface temperature (Kondo, 1990, Stull, 1991, Mannouji, 1982). In this heat budget, radiation (including longwave and shortwave components), latent heat exchange, sensible heat exchange and heat transfer into the ground are considered.

The calculation domain has dimensions of about 37 km in both the south-north and east-west directions and 3 km in the vertical direction as shown in Fig. 1. The eastern third of the calculation domain is an area of sea containing islands. The western two-thirds of the calculation domain is land, which includes mountains higher than 1000 m. Rivers and lakes are also located in this land area. The numbers of grid points are 80, 64 and 40 in the south-north, east-west and vertical directions, respectively. The grid lengths in the vertical direction are increased at elevated positions.

## RESULTS AND DISCUSSION

Calculation results for wind velocity are compared with field observation results in Figs. 2, 3, 4 and 5. The comparisons between the calculation and measurement results are made for four positions at which rawinsonde observations were made. The solar radiation was relatively weak and the ground surface temperature started to increase at around 11 a.m. For these reasons, though a sea breeze, i.e. negative values of west-east velocity,  $U$ , occurred near the ground, the sea breeze was detected at relatively low heights, for instance, about 100 m from the ground at Point C. Some discrepancies between the observation and calculation results are identified; viz., the calculated sea breeze velocity is lower than the velocity of sea breeze detected at Point D at a height above the ground of less than about 600 m. However, the calculated profile and the values of  $U$  agree well with those determined in the observations. Namely, a sea breeze is calculated to occur near the ground, and a wind blowing in the direction opposite that of sea breeze, i.e. positive values of  $U$ , was calculated to occur at elevated positions. Due to the increase in the intensity of solar radiation, i.e. maximum solar radiation occurred at around 1 p.m. on the observation day, and the fact that the ground surface temperature increased much more than the sea surface

temperature, the air tended to flow more from the sea to the land area at 1 p.m. than at 11 a.m. For these reasons, the measured velocity components of the sea breeze near the ground increased at 1 p.m.; i.e., the absolute values of negative  $U$  increased at Point C up to around 3 m/s as indicated in Fig. 3. Furthermore, the sea breeze was also detected at higher positions at 1 p.m., i.e. at about 500 m above the ground at Point C. These features of the sea breeze, viz. the increment in sea breeze velocity components and its measured height above the ground, are also reproduced by the calculation results for all four positions in Fig. 3 and good agreement between the results of the observations and calculations is obtained. Measured west-east velocity components at an elevated position at 1 p.m. were positive values as at 11 a.m. and these features of  $U$  are also reproduced by the calculation results. Though positive values continue throughout daytime for both numerical simulation and observations, negative values of  $U$  are obtained, i.e., a sea breeze is detected, near the ground. According to these opposite directional winds, a sea breeze is considered to be the local airflow there, and these phenomena are reproduced by calculation results.

South wind components, positive values of  $V$ , continued in the daytime when observations were performed as indicated in Figs. 4 and 5. Disagreement between the calculated and measured south-north velocity components is observed for regions in which the spatial variations of the measurement values are large and when the temporal variations of the measurement values are large. For instance, the measured south-north velocities at Point A at 11 a.m. near the ground were low compared with those at other observation points at 11 a.m., and a small disagreement between calculated and measured south-north velocity components is observed for Point A near the ground. Furthermore, measured south-north velocities at Point B at 1 p.m. at around  $z=1000$  m are small as compared with those at other observation points at 1 p.m. and those at 11 a.m., and some disagreement between calculated and measured south-north velocity components is observed for Point B at around  $z=1000$  m. These disagreements demonstrate the difficulty of simulating rapid and spatially large variations,

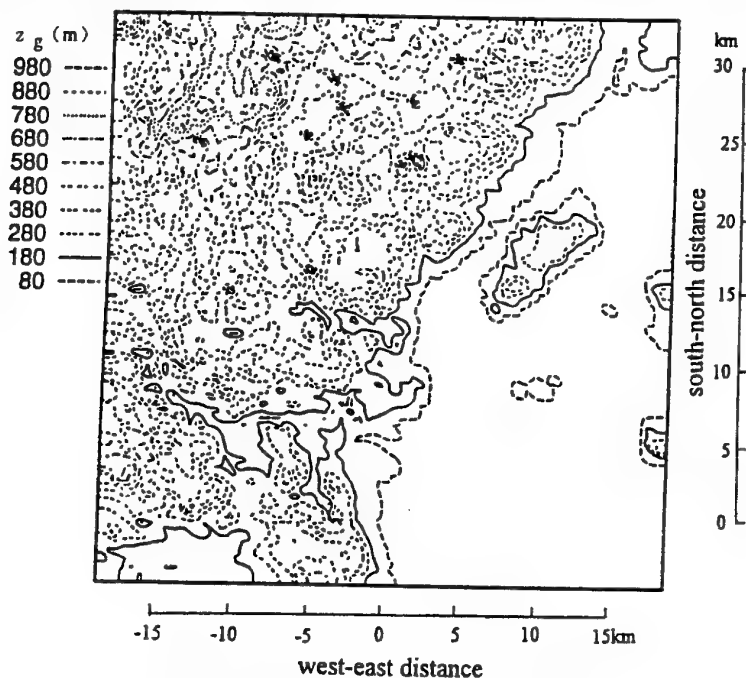


Fig. 1 Calculation domain and terrain altitude.



even when a four-dimensional data assimilation scheme is used. The disagreements are due to the fact that the numerical simulations are performed satisfying a physical process, for instance continuity conditions and other conservation conditions, and consequently the calculation results obtained tend to vary smoothly with time and space. For this reason, the calculated south-north velocity components at Point B at 1 p.m. vary smoothly with height, and some discrepancies are obtained at around  $z=1000$  m. However, the regions in and times at which disagreements are obtained are limited and otherwise good agreement is obtained.

Calculated potential temperature profiles at Point A, located beside the coastline, are shown in Fig. 6 in comparison with observation results. The measured potential temperature at 11 a.m. decreased with the height above the ground, due to stable stratification at an elevated position. However, the vertical gradient of the measured potential temperature was almost constant with change in height when the height was lower than 300 m, due to the beginning of the increment of the ground surface temperature at 11 a.m. These features of potential temperature are reproduced by the calculation results, and good agreement between the observation and calculation results is obtained. Due to the increase in the intensity of solar radiation, the ground surface temperature continued to increase until 1 p.m., at which time the measured potential temperatures were also larger than those at 11 a.m. Furthermore, an almost

constant measured potential temperature region extended vertically up to about 1000 m at 1 p.m. This almost constant measured potential temperature region corresponds to the mixing layer, in which active turbulent mixing occurs in the vertical direction. The calculated ground surface temperature increment at 1 p.m. is smaller than that determined in the observation, and discrepancies of several degrees Celsius between calculated and measured potential temperature are observed for heights of less than about 700 m. Though some discrepancies between calculated and measured potential temperature are observed, increments of potential temperature and an almost constant measured potential temperature region are identified by calculation for 1 p.m. and good agreement between calculation and observation results is obtained.

Contour lines of calculated potential temperature are shown in Fig. 7 for the west-east cross-section in which Point A is included and the south-north distance is equal to zero. Positive and negative values of west-east distance in Fig. 7 correspond to the land and sea areas, respectively. The ratios of contour line intervals at elevated positions are equally varied with west-east distance between the ground and the top of the calculation domain, viz.  $z=3$  km. These features of contour lines at an elevated position indicate stable stratification as shown in Fig. 6. On the other hand, the contour lines over the land and near the ground, i.e. in the regions of negative west-east distance and at heights lower than about 1000 m, are sparse.

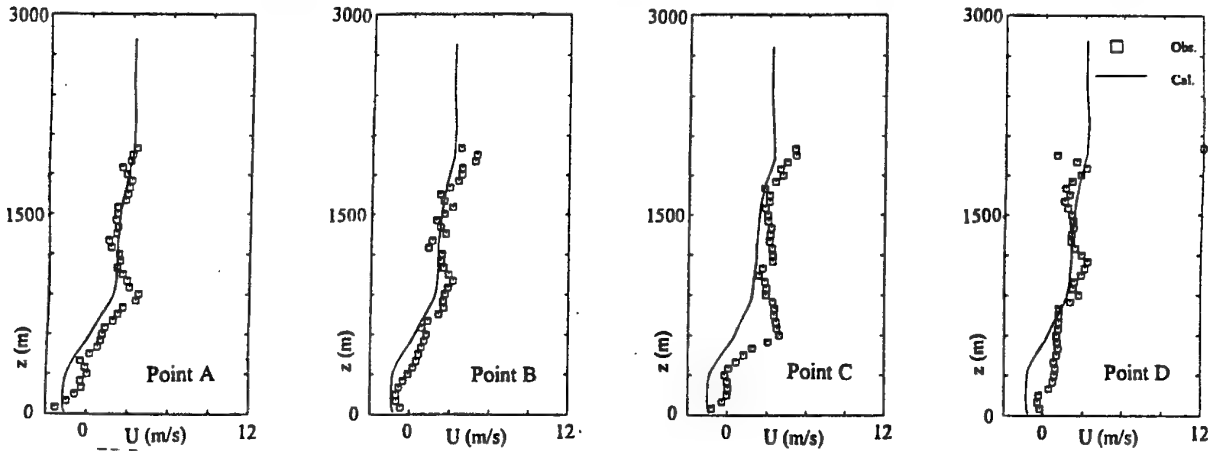


Fig. 2 West-east components of velocity,  $U$ , at 11 a.m. The negative and positive values indicate east and west winds, respectively.

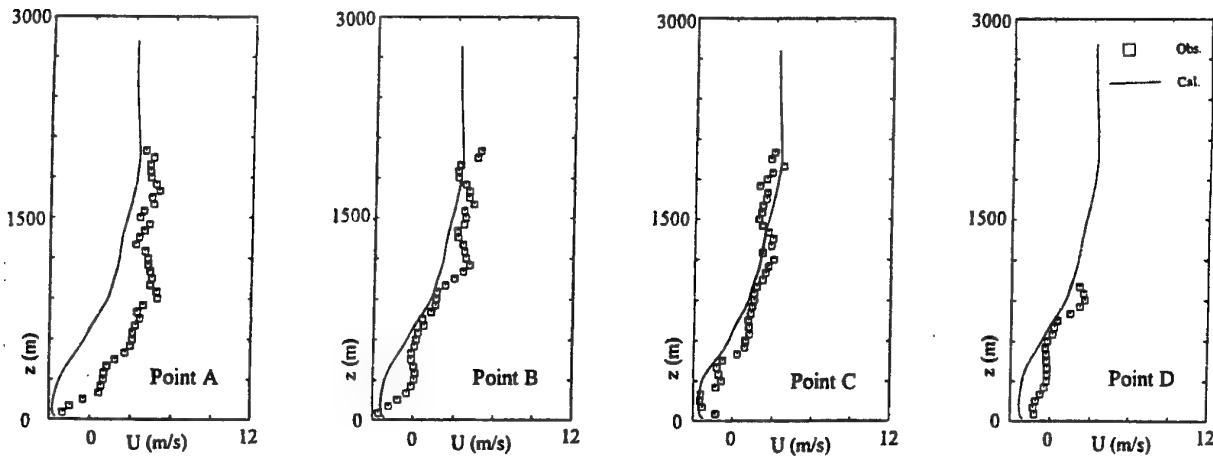


Fig. 3 West-east components of velocity at 1 p.m.



These features of contour lines near the ground are typical at 3 p.m. and indicate the development of a mixing layer over the land. These regions in which the contour lines are not obtained correspond to the constant potential temperature regions as indicated in Fig. 6.

Contour lines of calculated turbulent kinetic energy are shown in Fig. 8 for the same cross-section as for Fig. 7. Densely distributed contour lines are on the land area at negative west-east distances, and sparse contour lines are on the sea at positive west-east distances. These densely distributed contour lines show the increments in turbulent kinetic energy on the land area. As regards the time variations of turbulent kinetic energy, densely distributed contour lines are located near the ground at 11 a.m.; this indicates that the production of turbulent kinetic energy occurs near the ground. Approaching 1 p.m., i.e. with increasing intensity of solar radiation and ground surface temperature, contour lines obtained heights and the number of contour lines increase. This indicates that the production of turbulent kinetic energy is enhanced by a buoyancy effect and the calculated turbulent kinetic energy increases not only near the ground but also at elevated positions. Though the solar radiation weakened approaching 3 p.m., these features of the calculated turbulent kinetic energy at 1 p.m. are also observed for 3 p.m. They are due to the large heat capacity of the ground soil, and the decrement of the ground surface temperature is small in spite of the solar radiation intensity decrement at 3

p.m. The features of the turbulent kinetic energy mentioned above, its increment at around the noon for instance, indicate the unsteady development of the mixing layer on land corresponding to constant potential temperature profiles up to about 700 m as indicated in Fig. 6.

## CONCLUSIONS

Unsteady airflows over coastal complex terrain were calculated by a simulation method. This numerical simulation method based on turbulence closure techniques and complex terrain is treated by use of a so-called  $z^*$  coordinate system. In this report, because unsteady atmospheric flows were simulated and the simulation results obtained were compared with measured wind and temperature profiles, a four-dimensional data assimilation scheme was incorporated into the velocity transport equations for the two horizontal wind components, and the heat budget was taken into consideration for varying ground surface temperature. The profiles of wind velocity versus height obtained by calculation are similar to those determined by field observation except in some regions in which the spatial variations of the measurement values were large. Furthermore, development of sea breezes and the mixing layer was well reproduced. Namely, the calculated turbulent kinetic energy increases at elevated positions, where the calculated potential temperature is almost constant with height, at around noon. Furthermore, the increment in sea wind

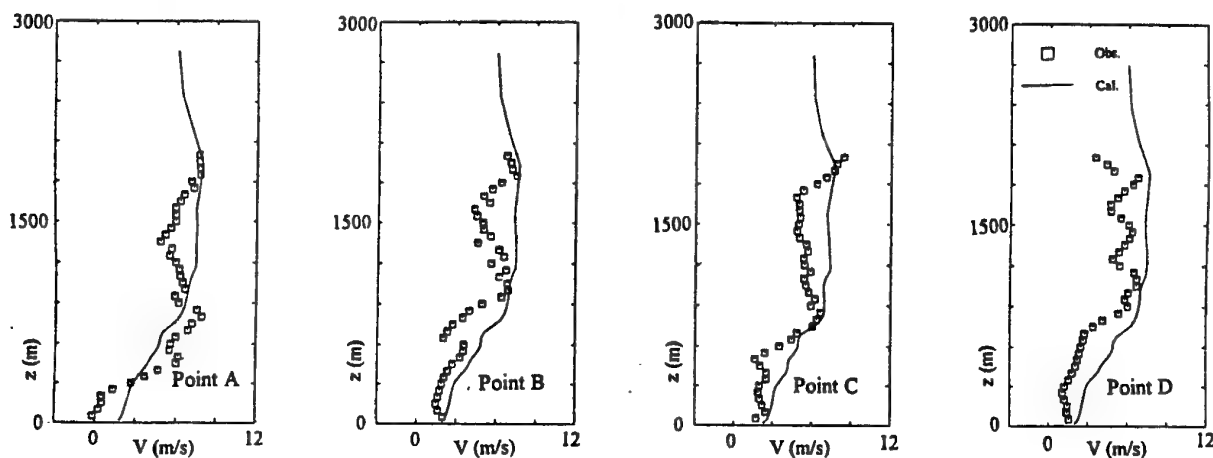


Fig. 4 South-north components of velocity,  $V$ , at 11 a.m. The negative and positive values indicate north and south winds, respectively.

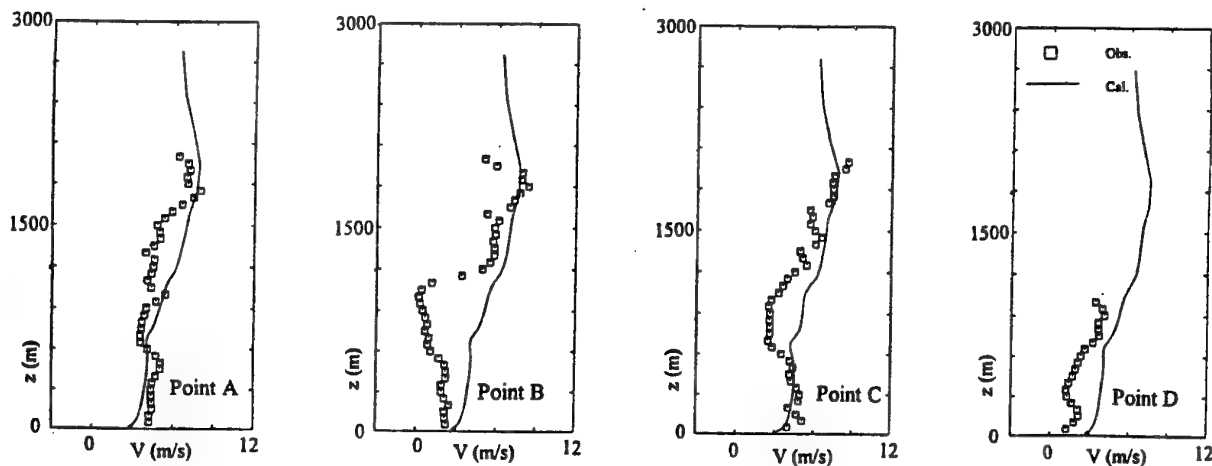


Fig. 5 South-north components of velocity at 1 p.m.

velocity at around noon, i.e., negative values of  $U$ , is well reproduced by calculation results and good agreement between the calculation and observation results is obtained.

## ACKNOWLEDGMENTS

This research was commissioned by the Agency of Natural Resources and Energy, of the Ministry of International Trade and Industry of Japan.

## REFERENCES

- Benjamin, S. G., and Seaman, N. L., 1985, "A Simple Scheme for Objective Analysis in Curved Flow", *Monthly Weather Review*, Vol. 113, pp. 1184-1198.
- Gibson, M. M., and Launder, B. E., 1978, "Ground Effects on Pressure Fluctuations in the Atmospheric Boundary Layer", *Journal of Fluid Mechanics*, Vol. 86, Part.3, pp. 491-511.
- Kondo, H., 1990, "A Numerical Experiment of the Extended Sea Breeze over Kanto Plain", *Journal of the Meteorological Society of Japan*, Vol. 68, No. 4, pp.419-434.
- Launder, B. E., 1988, "On the Computation of Convective Heat Transfer in Complex Turbulent Flows", *ASME Journal of Heat Transfer*, Vol. 110, pp. 1112-1128.
- Mannouji, N., 1982, "A Numerical Experiment on the Mountain and Valley Winds", *Journal of the Meteorological Society of Japan*, Vol. 60, No. 5, pp.1085-1105.
- Rodi, W., 1976, "A New Algebraic Relation for Calculating the Reynolds Stresses", *ZAMM* 56, T219-221.
- Sada, K., Ichikawa, Y., and Asakura, K., 1996, "Numerical Simulation Using the Turbulence Closure Model for Atmospheric Flow under Complex Terrain Conditions", *Proceedings of the 6th International Symposium on Flow*

Modeling and Turbulence Measurements, Chen, C.-J. et al., ed., A. A. Balkema Publishers, Rotterdam, pp. 607-614.

Stauffer, D. R., and Seaman, N. L., 1990, "Use of Four-Dimensional Data Assimilation in a Limited-Area Mesoscale Model. Part : Experiments with Synoptic-Scale Data", *Monthly Weather Review*, Vol. 118, pp. 1250-1277.

Stull, R. B., 1991, "An Introduction to Boundary Layer Meteorology", Kluwer Academic Publishers.

Yaglom, A. M., 1977, "Comments on Wind and Temperature Flux-Profiles Relationship", *Boundary-Layer Meteorology*, Vol. 11, pp. 899-102.

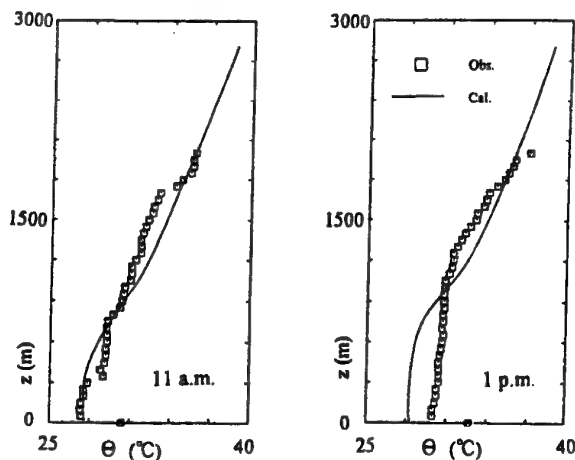


Fig. 6 Potential temperature at Point A.

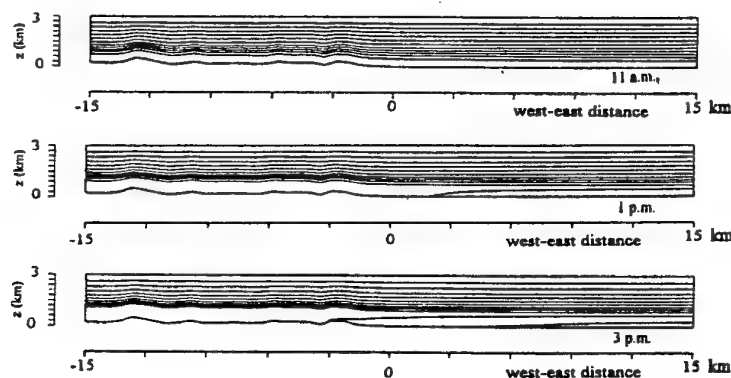


Fig. 7 Contour lines of potential temperature at the cross-section of south-north distance 0km.

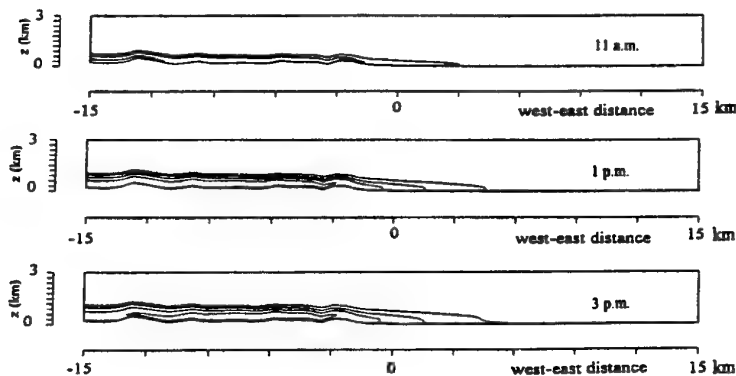


Fig. 8 Contour lines of turbulent kinetic energy at the same cross-section as for Fig. 7.

# EXPERIMENTAL STUDY OF INTERNAL WAVES IN THE STRATIFIED SHEAR FLOW BETWEEN TWO IMMISCIBLE LAYERS

Markus Keicher and Alexander M. K. P. Taylor  
Mechanical Engineering Department  
Imperial College of Science, Technology and Medicine  
Exhibition Road  
London SW7 2BX  
United Kingdom

## ABSTRACT

Quarter-scale experiments in a mould of a width of  $L = 457$  mm simulating the continuous casting of steel beneath a floating slag layer, by using olive oil floating on water, were conducted in order to gain insight into the transient effects such as internal waves in the flow pattern in the mould leading to entrainment of the floating layer. Water was injected through a model of a submerged bifurcated entry nozzle into the mould model at a range of jet Reynolds numbers from 10500 to 17500. The associated range of Froude numbers amounted from 1.50 to 2.60. Mean and rms internal wave heights at the simulated steel meniscus between the two immiscible layers were quantified as a function of volume flow rate in the feed pipe, referred to as casting speed, between 16 and 28 l/min and the immersion depth of the submerged nozzle varying from 50 mm to 150 mm. Conditions which induced the start of entrainment of the floating layer into the lower flow are identified. A digital image processing system was employed to measure interfacial mean, and the corresponding rms, wave heights which were complemented by laser-Doppler anemometer measurements to simultaneously determine the associated horizontal velocity component, called wave pushing velocity, just upstream of an internal wave trough. The normalised magnitude of internal mean wave heights decreased by about 0.3 with increasing casting speed and by about 0.15 with increasing immersion depth of the bifurcated nozzle. Corresponding rms values decreased by 0.2 over the range of casting speeds and by about 0.1 as the immersion depth increased. With increasing casting speed, the influence of the immersion depth decreased by about 0.1 in mean as well as in rms wave heights. The position of minimum internal wave height coincided with the region of the maximum of the corresponding rms value and coincided with locations where entrainment was most likely to occur. A critical value of a dimensionless Weber number,  $We_c = \rho u_s^2 h / \sigma$ , of about 21 is suggested, based on instantaneous wave heights and associated simultaneously obtained wave pushing velocities, above which slag entrainment will occur.

## INTRODUCTION

In the mould of the continuous casting process in steel production, the liquid steel is injected through a submerged bifurcated entry nozzle (SEN) which is below the interface formed by the floating semi-molten layer of slag. The flow of molten steel within the mould is fully turbulent and the flow pattern above the exit of the submerged entry nozzle, near the surface, consists of a pair of vortices (see Figure 1) on either side of the vertical symmetry plane and their transient motion induces unsteady internal waves at the steel meniscus between the denser steel and the lighter slag. Figure 2 shows a quarter-scale laboratory experiment, simulating the slag/molten steel interface by olive oil floating on water, and was obtained by means of the digital image processing system which is described in the following section. In production, the casting speed is limited in part by the fact that these waves ultimately become sufficiently strong to result in the intermittent entrainment of the slag into the steel which leads to undesirable inclusions in the final product. These must be minimised. The interfacial wave heights as well as the start of entrainment depend on the strength of the vortices which can be controlled by changing the flow rate in the feed pipe and the immersion depth of the submerged entry nozzle. Hence, this paper focuses on the fluid dynamic point of view by physical modelling of the steel meniscus within the continuous casting mould, rather than on the point of view of metallurgy, and at the same time data of interfacial wave is provided to assist the development and testing of simulation the flow through the application of computational fluid dynamics (CFD) models.

Interfacial waves in the mould are generated as a result of the interaction between the transient motion of the upper pair of vortices and the steel meniscus and in the worst case, in terms of steel production, lead to slag entrainment. The classical theoretical study of *rising* vortices in *potential* flow was performed by Lamb (1932), who calculated the paths and the speed of vortices approaching a solid flat lid. Numerical potential flow solutions for two counter-rotating vortices

approaching the free surface illustrated that vortices with large circulation elevate the mean free surface level. By the time the vortices turn to move outward, away from the vertical plane of symmetry, rather than upward, the high surface curvature suggested that so-called 'surface breaking' was impending (Telste 1989). A *viscous* solution was provided by Ohring and Lugt (1991) who presented the decay of the primary vortices and the generation of surface vorticity as well as secondary vortices. The introduction of surface tension tends to flatten the surface curvature. At low Froude number<sup>1</sup> the free surface acts as a stiff wall whereas the surface can be easily deformed at high Froude number. In a combination of theoretical and experimental studies, cylinders were circulated at a *fixed* distance below the surface by Jeong and Moffat (1992) in contrast to vortices *approaching* the free surface. After exceeding a critical angular velocity,  $\Omega_c$ , of the cylinders, the free surface dips downwards and forms a standing wave, a so-called 'cusp' or 'scar', where surface tension has been taken into account but gravity has been neglected. It is believed, based on studies which investigated the interaction of vortices with a free surface, that globules of a layer floating on the surface can be stripped from such a cusp (scar) into the area of low pressure of the lower liquid due to streamline compression at the trough of the standing wave.

Despite the importance of knowing interfacial behaviour under the influence of the transient motion of vortices to various industrial applications, such as the continuous casting process, relatively little effort has been made to quantify internal waves or to characterise the propensity of entrainment of the floating layer into the lower layer. Critical conditions and the mechanism of the removal of droplets from a liquid surface by a parallel air flow resulting from a Kelvin-Helmholtz instability were studied by Woodmansee and Hanratty (1969). The purpose of this work is to quantify and thus to improve the understanding and description of internal waves in a stratified shear flow between two immiscible layers under the influence of transient vortices and to identify a critical criterion above which entrainment takes place by physical modelling.

The flow configuration and experimental techniques are described in the following section. The results are then presented and discussed, and the conclusions are given in the closing section.

## FLOW CONFIGURATION AND EXPERIMENTAL TECHNIQUES

### Flow Configuration

It has become common practice to use water to simulate the molten steel flow since the kinematic viscosities,  $\nu$ , of water and molten steel are similar. A layer of olive oil of 2 cm thickness was employed as a slag simulant as it is immiscible with and lighter than water, easy to procure, easy to dispose, and causes no damage to the Perspex mould model. This led to a density ratio of  $\rho_{\text{slag}}/\rho_{\text{steel}} = 0.92$  in comparison with 0.43 in the real plant thus, due to the greater ratio, permitting waves with higher amplitudes at the interface to be generated. The present quarter scale configuration was based upon the dimensions of existing physical moulds at British Steel plc in order to aid comparisons and the interpretation of gained data. A schematic of the

experimental arrangement is shown in Figure 1. Water was circulated, driven by a centrifugal pump, between the storage sump, where a cooling circuit was incorporated to maintain constant water temperature, and the transparent Perspex model of the mould, thus allowing optical access. It was 457 mm in width,  $L$ , had a depth,  $W$ , of 59 mm, i.e. normal to the plane of the paper, and a height,  $H$ , of 686 mm. In order to promote a uniform outflow at the bottom of the test section, a stainless steel baffle plate with 427 holes of diameter 5 mm was installed, with the holes distributed uniformly (7 by 61) across the cross-section. The flow of steel was simulated by injecting water through a Perspex model of a submerged bifurcated entry nozzle (SEN), seen in Figure 3, into the mould. The fluid inlet, marked as station A in Figures 1 and 3, was about 80 inner diameters,  $D = 19.5$  mm, above the stainless steel feed pipe of the bifurcated nozzle to assure a fully developed flow just upstream of the bifurcated nozzle to assist future numerical simulation of the flow using CFD. At the same time, station A depicts the exit of the contraction of the honeycomb which was installed to ensure a swirl free flow approaching the SEN. The honeycomb, with hexagonal cells of nominal passage diameter of 6 mm and a length of 85 mm, was installed in order to remove any swirling component of velocity. The two outlet ports of the nozzle were identical within manufacturing tolerance and 180 degrees apart, drilled with a circular cross-section of 17.5 mm diameter. The ports' axes were inclined at 20 degrees below the horizontal and the immersion depth (ID) of the nozzle was defined as the distance from the meniscus to the top of the nozzle port. The casting rate was simulated by varying the water flow rate by controlling the volume flow rate through the flowmeter in the supply pipe. The two exit pipes, connecting the mould with the storage tank, were equipped with one flowmeter each and the flows were adjusted to be the same in each. To accomplish steady flow conditions, the entire system had to be free of air bubbles, which was achieved by using a running time of 1.5 hours before starting measurements.

In a typical steel production plant the bulk velocity in the feed pipe,  $v_{b, \text{pipe}}$ , is ranging from 0.9 to 1.56 m/s and velocity scaling was used to provide similarity between a real configuration and the constructed tank: in other words, the same casting speed was used where the casting speed is here defined as the volume flow rate of water through the mould divided by the cross-sectional area of the caster, namely  $59 \times 457 \text{ mm}^2$ . This constitutes a compromise between Reynolds number similarity and Froude number similarity for surface phenomena. The range of jet Reynolds numbers leaving each port was between 42000 and 70000 in the real plant, and consequently 10500 and 17500 in the quarter scale model where the port cross-section diameter represents the characteristic length. This corresponds to a range of volume flow rates,  $Q$ , in the feed pipe of the model of 16 to 28 l/min where the lower value is at the limit of a Reynolds number independent flow. The Froude number was defined as follows:

$$Fr = \frac{v_{b, \text{pipe}}}{\sqrt{(1 - \frac{\rho_{\text{slag}}}{\rho_{\text{steel}}})gL}} \quad (1)$$

which results in a range from 0.28 to 0.49 in the real plant and from 1.50 to 2.60 in the mould model. The immersion depth (ID) of the submerged entry nozzle was varied for the model between 50, 100, and 150 mm following values which represent appropriate values of the real plant and which also ensured the required bulk velocity range in the feed pipe without causing

<sup>1</sup>the Froude number was defined as the ratio between the translational velocity of the vortex pair and the square root of the product between gravity and the distance between the vortex centres.

permanent entrainment of the floating olive oil layer into the water flow.

### Measurement Techniques and Uncertainties

The entire flow facility was enclosed in a dark room and a 500 W lamp was positioned below the Perspex tank to illuminate the flow. The interfaces between air/olive oil and olive oil/water were visualised as bright lines, i.e. as intensity maxima in brightness, and recorded on a video tape by a charge coupled device (CCD) camera (JVC - GR 323) at a rate of 25 frames per second which was located perpendicular to the transparent test section. The S-VHS video tape recorder (Panasonic AG - 7350) was equipped with an RS - 232C interface board to enable off-line control via personal computer where an eight bit black and white image grabber (Matrox IP - 8) with on-board memory buffers (2x1024x1024 pixels) was built in. In the interface board a time code generator/reader (AG - IA232TC) was incorporated and the time code information was embedded in one of the available audio tracks of the video tape. Thus, in principle, any particular frame could be retrieved and converted into 256 ( $2^8$ ) shades of grey, representing a brightness resolution, by means of the eight bit A/D converter of the installed image grabber. Images, typically with a resolution of 768x512 pixels, were then stored onto the hard disk of the computer and the interfaces air/olive oil and olive oil/water of each frame could be detected using the intensity maxima. Subsequently, the number of pixels depicting the olive oil layer across the test section could be converted into interfacial wave heights where one pixel corresponded to 0.6 mm in the sub-scale model. In order to determine mean and rms interfacial wave heights typically a number of 1000 arbitrarily sampled (over a duration of 25 minutes of the recorded video tape) frames was considered.

The dual-beam laser-Doppler anemometer operated in forward scatter and made use of a 30 mW He-Ne laser at a wavelength of 632.8 nm, a diffraction grating and associated optics, and a custom-built frequency counter for the processing of the Doppler signals. Thus, horizontal (u) mean and rms velocity components, called wave pushing velocities, were measured at a position  $x/(L/2) = -0.72$  and at a distance of about  $y/(L/2) = 0.02$  below the calm meniscus according to the investigated immersion depth of the submerged entry nozzle, as indicated in Figure 2. Thus, the x-co-ordinate was constant for the investigated flow configurations and it was ensured that velocity measurements were taken just upstream of the internal scar as suggested by Woodmansee and Hanratty (1969) to identify a critical condition above which entrainment might occur.

The synchronisation of interfacial wave height measurements and the determination of the associated wave pushing velocity was realised by means of a bar-code number, seen in Figure 2, which was superimposed on the right top side of each video field, Sakakibara *et al.* (1993), and the embedded time code on the video tape. The laser beam was switched on at an arbitrary time whilst the CCD camera was recording the interfacial flow pattern of the considered flow configuration and to identify the frame in which the laser beam became visible for the first time, and thus indicating the start of collection of time dependent laser-Doppler velocity measurements and the reference time zero, the bar-code number used. Subsequently, consecutive frames were transferred to the hard disk for postprocessing as described above. The velocity measurements were sorted into temporal bins with duration of 1/25 s, and hence each frame could be related to the corresponding velocity bin.

The instrumentation and experimental technique are described in more detail by Keicher (1997), together with estimates of uncertainties of the measured quantities. In brief, the errors in determining interfacial wave heights are of the order of 6 % of the actual value. These uncertainties stem in the first place from the inaccuracy in detecting the interfaces which had various sources. One of the main sources was the location of the interface air/olive oil which could be determined within an accuracy of  $\pm 1$  pixel as it was represented by a wide, say about 3 pixels, bright line across the tank. Another source was owing to the depth of the tank, i.e. normal to the plane of the paper, because the interfacial waves observed were three dimensional with a maximum effect for the highest casting speed. However, in obtaining the wave heights, only the two dimensional projection of the interface was considered. Uncertainties in measuring velocities were estimated to be less than 3 % of the bulk velocity and the inaccuracy in synchronising both techniques amounted to about 1/25 s.

### RESULTS AND DISCUSSION

The interfacial characteristics as a function of casting speed and immersion depth of the SEN are shown in Figures 4 - 9 and are a representative sample of the measurements obtained. The propensity of olive oil entrainment is revealed in Figure 10 and was defined as the stripping away of an olive oil globule into the water flow, established during observation of the recorded video. Detailed results including flow visualisation and velocity characteristics of the flow pattern in mould are available in the report by Keicher (1997).

The velocity measurements, although not presented here, revealed a asymmetry of less than 6 % in the velocity profiles, for both horizontal and vertical (u, v) components, measured to the left and to the right of the nozzle ports' exit plane. A discrete frequency of fluctuating (u, v) velocities of about 0.1 Hz was detected and, from the recorded video of the flow pattern, entrainment occurred at positions where the highest mean velocities as well as the highest mean velocity gradients in horizontal (u) direction were measured which was about half way between the narrow wall and the feed pipe of the nozzle. Flow reversal in horizontal direction behind a free surface depression was perceptible by means of flow visualisation as well as laser-Doppler anemometry, which indicates the generation of counter rotating vortices drawing the scar between them and eventually promoting entrainment as confirmed by means of evaluating the recorded video tape.

In Figure 2, a video frame with a typical olive oil/water interface wave pattern can be seen together with the *flat* air/olive oil interface. Note that the latter interface was always flat. For the description of interfacial wave heights, the origin of the xy-co-ordinate system was situated on the symmetry plane of the mould at the calm meniscus, seen in Figure 2. The unsteady distance between the air/olive oil and olive oil/water interfaces was defined as the instantaneous wave height, H, and to acquire the relative, i. e. with respect to the calm meniscus, wave height, h, the thickness of the olive oil layer was subtracted. Measurements were taken at ten equidistant positions across the tank, every 3.75 cm, starting at  $\pm 4.7$  cm with respect to the symmetry axis, and shall be referred to below as Pos -5 to Pos 5. For the presented results, distances were normalised by half of the mould width, L/2, and wave heights by the velocity height,  $v_{b, pipe}^2 / 2g$ .

In Figure 4 the normalised mean wave heights are shown as a function of casting speed for an immersion depth of the submerged entry nozzle of 50 mm. The feed pipe as well as the above designation for the positions of measurement are also illustrated. The graphs are close to symmetric about the y-axis. Large mean wave heights occurred close to the narrow walls ( $x/(L/2) = \pm 1$ ) and the minimum was found at a position of about mid way between the narrow wall and the feed pipe on either side of the nozzle. An increase of the casting speed led to a decrease in the magnitude of normalised mean wave heights by about 0.3. Figure 5 shows the corresponding rms values and depicts a peak for each casting speed on either side of the nozzle at the location Pos -2 and Pos 2, respectively. The magnitude of normalised wave height fluctuations also decreased by about 0.2 with increasing casting speed. Figures 6 to 9 complement the above findings and in addition illustrate the influence of the immersion depth (ID) of the nozzle on the interfacial characteristics for two representative casting speeds, 16 l/min and 24 l/min, which correspond to bulk velocities in the feed pipe of  $v_{h, pipe} = 0.9$  and 1.34 m/s, respectively. As expected, the smaller the immersion depth the greater the magnitude of normalised mean wave heights, say by about 0.15, where for ID = 100 mm the minimum occurred closer to the feed pipe of the nozzle than for the other two presented immersion depths. For both casting speeds considered, the corresponding normalised rms profiles show the highest values for an immersion depth of ID = 100 mm and decrease by about 0.1 as the immersion depth increased. With increasing casting speed, the influence of the immersion depth decreases by about 0.1 in mean as well as in rms wave heights.

As mentioned above, waves may become sufficiently strong to result in the intermittent entrainment of the olive oil into the water and a critical criterion above which entrainment will occur shall be quantified. One dimensionless group which yields such a criterion in an appropriate way seems to be the Weber number, as proposed by Woodmansee and Hanratty (1969) for the mechanism of droplet atomisation for a parallel air and liquid flow. In this work the propagational speed of the wave was supposed to be zero which yields a standing wave. The Weber number represents the ratio between inertia and surface tension force and can then be written as follows:

$$We = \frac{\rho u_s^2 h}{\sigma} \quad (2)$$

where  $\rho$  denotes the density of olive oil (918 kg/m<sup>3</sup>),  $u_s$  stands for the wave pushing velocity in horizontal (x) direction, as marked in Figure 2 just upstream of the internal scar, and  $\sigma$  is the surface tension between olive oil and water (0.02 N/m). The instantaneous relative wave height,  $h$ , as well as the corresponding simultaneously measured instantaneous wave pushing velocity,  $u_s$ , were determined as described above where the normalised mean wave pushing velocity, i. e. divided by the corresponding  $v_{h, pipe}$ , was about 0.08. The calculated instantaneous relative wave height at Pos -3 was considered to be appropriate to acquire the Weber number, because it was the position where the lowest wave heights occurred and where entrainment was observed to happen. Figure 10 presents the number of entrainment events for an observation period of 90 seconds of the recorded video against the instantaneous We number for the 12 different flow configurations considered in

this work. When no entrainment was observed the highest value of the We number for the particular flow configuration is shown in the graph; when an entrainment event was identified by observing the video, the corresponding frame and thus the corresponding instantaneous We number could be identified and is plotted. The position of entrainment coincided with the region of the maximum of the corresponding rms levels for internal wave heights. Over the range observed, an increase in the casting speed had a stronger influence than a decrease in the immersion depth of the nozzle on the event of entrainment. Figure 10 shows a tendency for entrainment to increase with We and a critical Weber number,  $We_c$ , of about 21 exists beyond which entrainment is expected. Some of the entrained globules float up directly towards the meniscus due to buoyancy, others become incorporated into the water flow and emulsify.

The turbulent water flow in the mould, in particular the vortices beneath the meniscus, induces internal waves and the boundary condition at the interface that velocity is continuous requires that the more viscous, here olive oil, must speed up on the disturbed interface while the less viscous layer must slow down relative to the undisturbed shear of the respective fluids. On the other hand, strong vortices beneath the interface olive oil/water elevate the meniscus and induce countervortices drawing an internal scar between them. The water flowing below the olive oil encounters a pressure decrease at the scar (trough) due to the contraction of streamlines and the corresponding high velocities and their high rms values. Inevitably, a suction will result which increases the deeper the internal wave. The curved interface yields a stabilising pressure drop across the meniscus because of surface tension. However, it is believed that the stripping away of olive oil globules, i. e. entrainment of the upper fluid into the lower layer, occurs from an internal scar due to high shear stresses at the interface and if the suction below the trough is greater than the pressure drop due to surface tension and streamline separation takes place. Consequently olive oil globules become carried away into the area of low pressure.

## CONCLUSIONS

The continuous casting process was studied by means of quarter-scale laboratory experiments simulating the mould. Olive oil was employed as a slag simulant floating on water and multi point internal wave height measurements complemented with simultaneous wave pushing velocity measurements were quantified as a function of casting speed and immersion depth of the bifurcated submerged entry nozzle.

The graphs show that the normalised magnitude of internal mean wave heights and their rms values decreased with increasing casting speed and increasing immersion depth of the submerged entry nozzle by about 0.2. At higher casting speed the influence of the immersion depth decreased by about 0.1.

Entrainment was observed at the position of minimum wave height which coincided with the region of the maximum of the corresponding rms levels and the event of entrainment is far more sensitive towards an increase in the casting speed than towards a decrease in the immersion depth over the range considered here. To identify the propensity of entrainment a critical dimensionless Weber number,  $We_c$ , of about 21 was found, above which entrainment is expected. The number is based on instantaneous wave heights and associated simultaneously obtained wave pushing horizontal velocities upstream of the trough.



## ACKNOWLEDGEMENTS

The authors are glad to acknowledge the support of the colleagues within the Thermofluids Section at Imperial College, in particular Drs. Y. Hardalupas and J. M. Nouri and Messrs. A. Grispos and J. Christoyannis, as well as financial support from British Steel plc and the European Coal and Steel Community, ECSC.

## REFERENCES

- Jeong, J. T., and Moffatt, H. K., 1992, "Free-Surface Cusps Associated with Flow at Low Reynolds Number," *J. Fluid Mech.*, Vol. 241, pp. 1 - 22.
- Keicher, M., 1997, "Physical Modelling of the Continuous Casting Process," Technical Report TF 97/06, MED, Imperial College, University of London.
- Lamb, H., 1932, "Hydrodynamics," 6th Edition, Cambridge University Press.
- Ohring, S., and Lugt, H. J., 1991, "Interaction of a Viscous Vortex Pair with a Free Surface," *J. Fluid Mech.*, Vol. 227, pp. 47 - 70.
- Sakakibara, J., Hishida, K., and Maeda, M., 1993, "Measurements of Thermally Stratified Pipe-Flow Using Image Processing," *Exp. in Fluids*, Vol. 16, pp. 82 - 96.
- Telste, J. G., 1989, "Potential Flow about Two Counter-Rotating Vortices Approaching a Free Surface," *J. Fluid Mech.*, Vol. 201, pp. 259 - 278.
- Woodmansee, D. E., and Hanratty, T. J., 1967, "Mechanism for the Removal of Droplets from a Liquid Surface by a Parallel Air Flow," *Chem. Eng. Sci.*, Vol. 24, pp. 299 - 307.

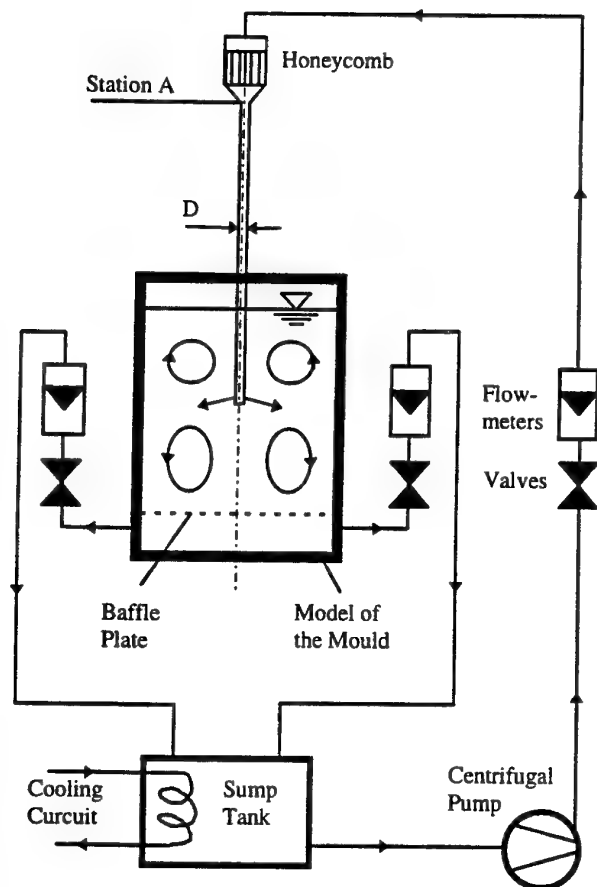


FIGURE 1: SCHEMATIC OF THE FLOW FACILITY.

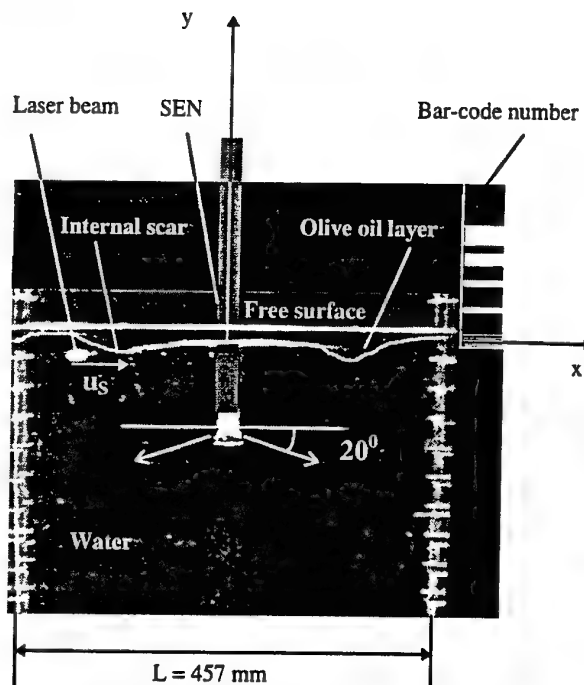


FIGURE 2: TYPICAL INTERNAL WAVE PATTERN.

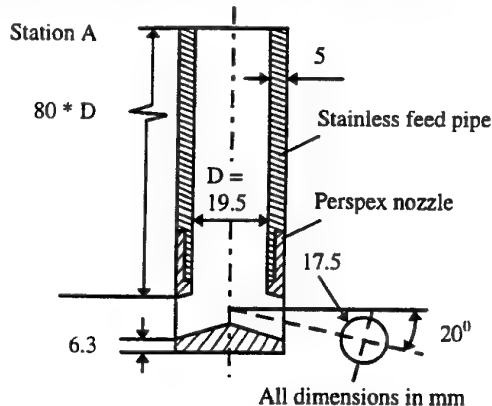


FIGURE 3: SCHEMATIC OF THE SUBMERGED ENTRY NOZZLE.

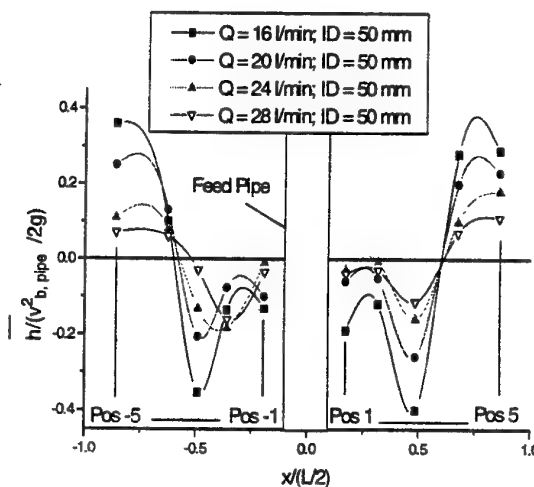


FIGURE 4: NORMALISED MEAN WAVE HEIGHTS AS A FUNCTION OF CASTING SPEED (ID = 50 mm).

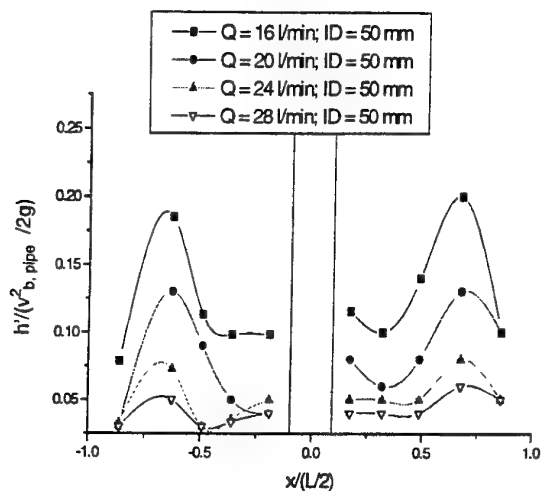


FIGURE 5: NORMALISED RMS WAVE HEIGHTS AS A FUNCTION OF CASTING SPEED (ID = 50 mm).

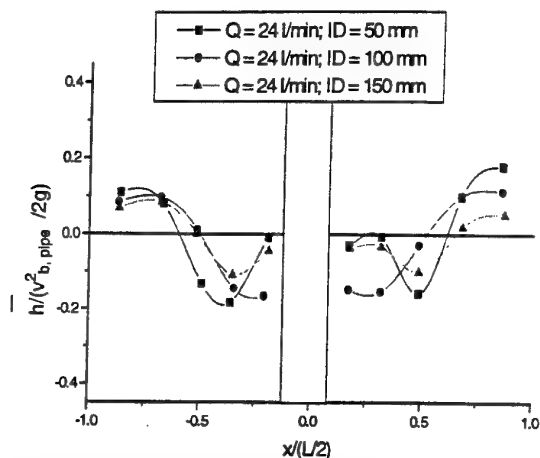


FIGURE 8: NORMALISED MEAN WAVE HEIGHTS AS A FUNCTION OF IMMERSION DEPTH (Q = 24 l/min).

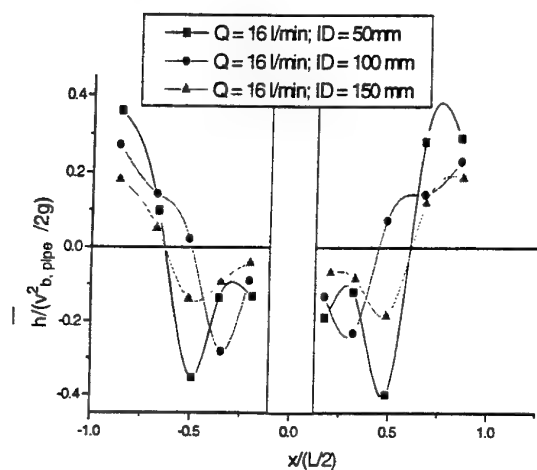


FIGURE 6: NORMALISED MEAN WAVE HEIGHTS AS A FUNCTION OF IMMERSION DEPTH (Q = 16 l/min).

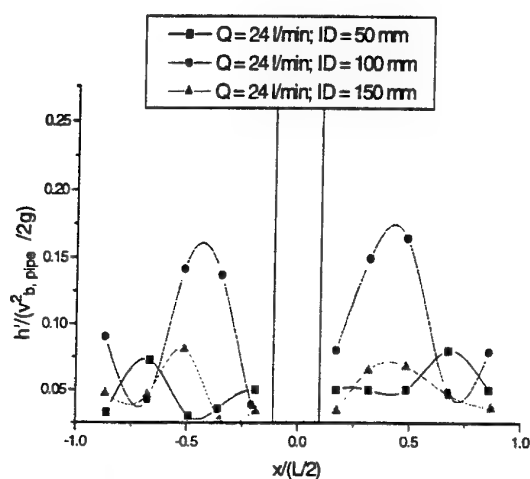


FIGURE 9: NORMALISED RMS WAVE HEIGHTS AS A FUNCTION OF IMMERSION DEPTH (Q = 24 l/min).

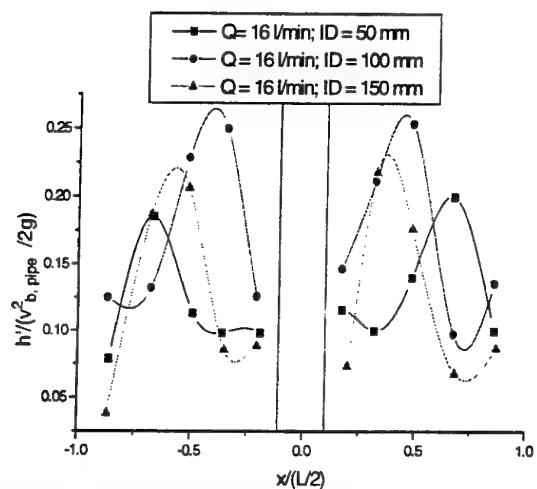


FIGURE 7: NORMALISED RMS WAVE HEIGHTS AS A FUNCTION OF IMMERSION DEPTH (Q = 16 l/min).

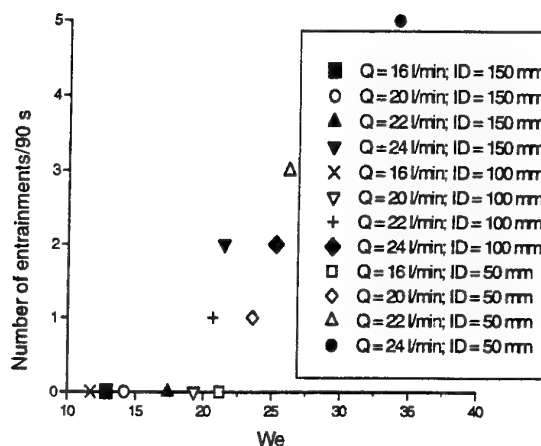


FIGURE 10: NUMBER OF ENTRAINMENTS AGAINST WEBER NUMBER,  $We = \rho u_s^2 h / \sigma$ .



# NUMERICAL PREDICTION OF PERFORMANCE OF ANNULAR JET PUMP

Norikazu Namiki

Toyo Seikan Corporation

1-3-1, Uchisaiwai-cho, Chiyoda-ku,  
Tokyo, 100, Japan

Osamu Kitamura and Makoto Yamamoto

Department of Mechanical Engineering

Science University of Tokyo

1-3, Kagurazaka, Shinjuku-ku,  
Tokyo, 162, Japan

## ABSTRACT

Jet pumps are used in a great number of engineering applications. However, no numerical method for determining the performance has been established yet. In the present study, focusing on turbulence models, a numerical method for predicting the performance of an annular jet pump is investigated. The flow fields are simulated by solving Reynolds and continuity equations with standard  $k-\epsilon$  and Reynolds stress models at different Reynolds numbers. Performance parameters (i.e. flow ratio, head ratio, efficiency, and pressure coefficient) are computed using the calculated flow fields, and compared with the experimental data. It is shown that a recirculation in the mixing chamber is formed at relatively low Reynolds number, and that a standard  $k-\epsilon$  model always underestimates the head ratio and the efficiency because of the excessive turbulent mixing, whereas a standard Reynolds stress model can satisfactorily predict them.

## 1. INTRODUCTION

Jet pumps have been used for a great number of engineering applications in chemical plants, nuclear power stations, food industries and so on. Many theoretical, experimental and/or numerical investigations have been reported, and some handbooks have already been published (for example, Karassik, 1976). It is well known that the efficiency of a jet pump is generally low, because the driving principle is based on turbulent mixing between the high-speed jet and the low-speed suction fluid. For the purpose of predicting and raising the efficiency, Sanger(1970) and Yano et al.(1990) proposed methods to determine the efficiency theoretically. However, their methods are lack of universality, and thus cannot be applied to different types of jet pumps. On the other hand, although it is expected that numerical simulations play an important role to improve the efficiency, no numerical method to obtain the performance correctly has been established yet.

In the present study, a numerical method for predicting the performance of an annular jet pump is investigated, fo-

cusing on turbulence models. The flow fields are simulated by solving Reynolds and continuity equations with high-Reynolds-number type  $k-\epsilon$  (Launder and Spalding, 1974) and Reynolds stress (Gibson and Launder, 1978) models at a wide variety of Reynolds number ( $5.48 \sim 7.67 \times 10^5$ ). Performance parameters such as flow ratio, head ratio, efficiency, and mean pressure coefficient are computed using the calculated flow fields with each turbulence model, and compared with the corresponding experimental data. We adopted the experiment for annular jet pumps measured by Shimizu et al.(1985) due to the abundance of data on the performances. It is shown that a large recirculation in the mixing chamber is formed at relatively low Reynolds number, and that a standard  $k-\epsilon$  model always underestimates the head ratio and the efficiency because of the overestimation of turbulent mixing, whereas a Reynolds stress model can satisfactorily predict them.

## 2. ANNULAR JET PUMP

Jet pumps are commonly classified into three types (i.e. central, annular, and bend types) by the geometry. In the present study, an annular jet pump is investigated. This pump uses a high-speed annular jet to entrain a low-speed flow from the central pipe. It is well known that an annular jet pump is advantageous for applications involving hydraulic transport of large solids such as fish, capsules, whole potatoes and onions, because of the little pumping damage to solids. An annular jet pump has been experimentally studied by some researchers such as Shimizu et al.(1985,1987) and Elger et al.(1991). In the present study, we calculated the flow fields in the annular jet pump investigated by Shimizu et al.(1985). They measured the performances under various conditions without solid particles.

Fig.1 shows the schematic of an annular jet pump. The definitions and the dimensions for the symbols are listed in Table 1. Fig.2 shows the computational domain and the cylindrical coordinate system used in this study. The inlet boundaries of the driving jet and the suction flow ("BJ"

and "BS" in Fig.2) were set  $D_0$  upstream from the suction exit ("SE"). Therefore, the length of the computed region is  $D_0 + L$ . And we refer to the nozzle and throat section shaded in the figure as "Mixing Chamber".

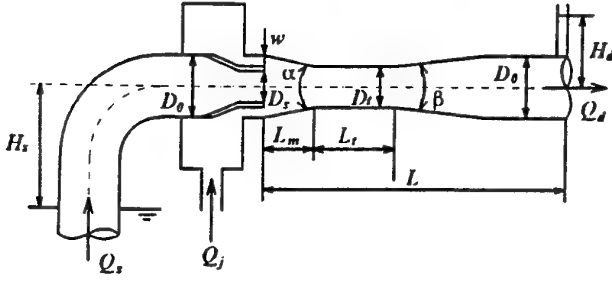


Fig.1 Schematic of Annular Jet Pump

Table 1 Definitions and Dimensions of Symbols

Symbol	Definition	Dimension
$D_0$	Diameter of driving flow pipe	55.0 [mm]
$D_s$	Diameter of suction flow pipe	43.0 [mm]
$D_t$	Diameter of throat	38.0 [mm]
$L_m$	Length of nozzle	31.7 [mm]
$L_t$	Length of throat	102.3 [mm]
$L$	Total length	429.0 [mm]
$w$	Annular height of driving jet	4.0 [mm]
$\alpha$	Convergent angle of nozzle	30.0 [deg]
$\beta$	Divergent angle of diffuser	5.8 [deg]
$H_s$	Head of suction flow	1.00 [m]
$H_d$	Head of exit flow	1.48 [m]

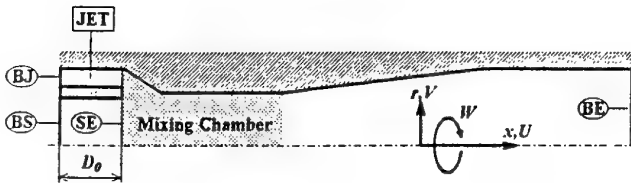


Fig.2 Computational Domain and Coordinate System

### 3. NUMERICAL PROCEDURES

#### 3.1 Governing Equations

We assumed that the flow field in the jet pump is incompressible and fully turbulent. Therefore, the governing equations are expressed in a tensorial form by following equations.

[Continuity Equation]

$$\frac{\partial U_i}{\partial x_i} = 0 \quad (1)$$

where  $U_i$  stands for mean velocity component, and  $x_i$  is Cartesian coordinate.

[Reynolds Equation]

$$\frac{\partial U_i}{\partial t} + U_j \frac{\partial U_i}{\partial x_j} = -\frac{1}{\rho} \frac{\partial P}{\partial x_i} + \frac{\partial}{\partial x_j} \left( \nu \frac{\partial U_i}{\partial x_j} - \overline{u_i u_j} \right) \quad (2)$$

where  $t$  denotes time,  $\rho$  density,  $P$  mean pressure, and  $\overline{u_i u_j}$  Reynolds stress. Reynolds stress  $\overline{u_i u_j}$  is calculated using any turbulence model. In the present study, standard high-Reynolds-number type  $k - \epsilon$  and Reynolds stress models were adopted. They are expressed as follows.

[ $k - \epsilon$  Model (Launder and Spalding, 1974)]

$$\frac{\partial k}{\partial t} + U_j \frac{\partial k}{\partial x_j} = P_k + \frac{\partial}{\partial x_j} \left( \frac{\partial \nu_t}{\partial x_k} \frac{\partial k}{\partial x_j} \right) - \epsilon \quad (3)$$

$$\frac{\partial \epsilon}{\partial t} + U_j \frac{\partial \epsilon}{\partial x_j} = C_{\epsilon 1} \frac{\epsilon}{k} P_k + \frac{\partial}{\partial x_j} \left( \frac{\partial \nu_t}{\partial x_k} \frac{\partial \epsilon}{\partial x_j} \right) - C_{\epsilon 2} \frac{\epsilon^2}{k} \quad (4)$$

$$\overline{u_i u_j} = -\nu_t \left( \frac{\partial U_i}{\partial x_j} + \frac{\partial U_j}{\partial x_i} \right) + \frac{2}{3} k \delta_{ij} \quad (5)$$

$$\nu_t = C_\mu \frac{k^2}{\epsilon} \quad (6)$$

$$P_k = -\overline{u_i u_j} \frac{\partial U_i}{\partial x_j} \quad (7)$$

$$C_\mu = 0.09, \sigma_k = 1.0, \sigma_\epsilon = 1.3, C_{\epsilon 1} = 1.44, C_{\epsilon 2} = 1.92 \quad (8)$$

where  $k$  is turbulent kinetic energy,  $\epsilon$  its dissipation rate,  $\nu_t$  eddy viscosity, and  $P_k$  production rate of turbulent kinetic energy  $k$ .

[Reynolds Stress Model (Gibson and Launder, 1978)]

$$\frac{\partial \overline{u_i u_j}}{\partial t} + U_m \frac{\partial \overline{u_i u_j}}{\partial x_m} = P_{ij} + \Phi_{ij} + \frac{\partial}{\partial x_m} \left( C_\epsilon \overline{u_i u_m} \frac{k}{\epsilon} \frac{\partial \overline{u_i u_j}}{\partial x_l} \right) - \frac{2}{3} \epsilon \delta_{ij} \quad (9)$$

$$\frac{\partial \epsilon}{\partial t} + U_m \frac{\partial \epsilon}{\partial x_m} = C_{\epsilon 1} \frac{\epsilon}{k} P_k + \frac{\partial}{\partial x_m} \left( C_\epsilon \overline{u_i u_m} \frac{k}{\epsilon} \frac{\partial \epsilon}{\partial x_l} \right) - C_{\epsilon 2} \frac{\epsilon^2}{k} \quad (10)$$

$$P_{ij} = -\overline{u_i u_k} \frac{\partial U_j}{\partial x_k} - \overline{u_j u_k} \frac{\partial U_i}{\partial x_k} \quad (11)$$

$$\Phi_{ij} = \Phi_{ij(1)} + \Phi_{ij(2)} + \Phi_{ij(1)}^w + \Phi_{ij(2)}^w \quad (12)$$

$$\Phi_{ij(1)} = -C_1 \frac{\epsilon}{k} \left( \overline{u_i u_j} - \frac{2}{3} k \delta_{ij} \right) \quad (13)$$

$$\Phi_{ij(2)} = -C_2 \left( P_{ij} - \frac{2}{3} P_k \delta_{ij} \right) \quad (14)$$

$$\Phi_{ij(1)}^w = C_1' \frac{\epsilon}{k} \left( \overline{u_k u_m} n_k n_m \delta_{ij} - \frac{3}{2} \overline{u_k u_i} n_k n_j - \frac{3}{2} \overline{u_k u_j} n_k n_i \right) f_w \quad (15)$$

$$\Phi_{ij(2)}^w = C_2' \left( \Phi_{km(2)} n_k n_m \delta_{ij} - \frac{3}{2} \Phi_{ik(2)} n_k n_j - \frac{3}{2} \Phi_{jk(2)} n_k n_i \right) f_w \quad (16)$$

$$f_w = \frac{k^{1.5}}{C_l \epsilon x_l} \quad (17)$$

$$C_1 = 1.8, C_2 = 0.6, C_1' = 0.5, C_2' = 0.3,$$

$$C_s = 0.22, C_e = 0.18, C_{\epsilon 1} = 1.44, C_{\epsilon 2} = 1.92,$$

$$C_l = 2.5 \quad (18)$$

where  $P_{ij}$  means production rate of each Reynolds stress component,  $\Phi_{ij}$  redistribution of Reynolds stresses, and  $x_l$  normal distance from a wall.

### 3.2 Numerical Method

MAC method was adopted in this study. Although a staggered grid system is generally used in MAC method, we employed a regular grid system because of the easy utilization in a generalized coordinate system. Forward Euler scheme was applied to all temporal terms, 3rd order upwind scheme (Kawamura and Kuwahara, 1985) to convec-

tive terms, and 2nd order central differencing scheme to remaining terms.

In order to simulate the performance of the annular jet pump, five Reynolds numbers, based on the maximum velocity of a driving jet  $U_j^{max}$  and the diameter of a driving flow pipe  $D_0$ , were selected. Table 2 lists the maximum velocities and Reynolds numbers used in this study. Since we used two turbulence models, 10 cases were computed.

After checking the grid independence of the solutions, we decided to employ 148 grid points in the axial direction and 80 in the radial direction, respectively. A large amount of grid points were clustered near the walls and the inlet boundaries.

Boundary conditions are listed in Table 3. Most of them are commonly utilized in the studies of computational fluid dynamics. Some special cases considered are explained below (shaded columns in Table 3).

Inlet boundary of a driving jet ("BJ" in Fig.2): After calculating a fully developed turbulent flow in a coaxial pipe, the solutions were fixed as this boundary condition.

Inlet boundary of a secondary flow ("BS" in Fig.2): The mean velocity profile was extrapolated from the inner region. And the mean pressure was given, using Bernoulli's law;

$$P_{atm} = \frac{1}{2} \rho U_s^2 + P_s + \rho g H_s \quad (19)$$

where subscript s denotes the inlet of the suction pipe and all physical quantities are averaged over the cross section. Atmospheric pressure  $P_{atm}$  and suction head  $H_s$  were fixed in all computations.

Exit boundary ("BE" in Fig.2): Similar to the inlet of a secondary flow, the velocity profile was extrapolated and the pressure was calculated by applying Bernoulli's law;

$$P_d = P_{atm} + \rho g H_d \quad (20)$$

where head  $H_d$  was fixed again.

Wall boundaries: Wall function was employed along each streamline, since high-Reynolds-number type turbulence models were used in this study. It should be noted that the shear component of Reynolds stresses was fixed to be 0 on the wall to suppress numerical oscillations.

Table 2 Reynolds Numbers and Maximum Jet Velocities

$Re$ Number $[\times 10^5]$	$U_j^{max}$ [m/s]
5.48	10.0
6.03	11.0
6.58	12.0
7.12	13.0
7.67	14.0

Table 3 Boundary Conditions used in This Study

Boundary	Velocity (U, V)	Pressure (P)	Turbulent kinetic energy (k) Dissipation rate ( $\epsilon$ )	Reynolds stresses (Normal: $\overline{u_i u_i}$ , Shear: $\overline{u_i u_j}$ )
Inlet of driving flow (BJ)	Fixed by computational results for coaxial pipe flow*	$\partial P / \partial x = 0$	Fixed by computational results for coaxial pipe flow*	Fixed by computational results for coaxial pipe flow*
Inlet of suction flow (BS)	$\partial U / \partial x = \partial V / \partial x = 0$	Given by Eq.(19)*	$\partial k / \partial x = \partial \epsilon / \partial x = 0$	$\partial \overline{u_i u_i} / \partial x = 0$ , $\partial \overline{u_i u_j} / \partial x = 0$
Exit (BE)	$\partial U / \partial x = \partial V / \partial x = 0$	Fixed by Eq.(20)*	$\partial k / \partial x = \partial \epsilon / \partial x = 0$	$\partial \overline{u_i u_i} / \partial x = 0$ , $\partial \overline{u_i u_j} / \partial x = 0$
Wall	$U = V = 0$	$\partial P / \partial n = 0$	$\partial k / \partial n = \partial \epsilon / \partial n = 0$	$\partial \overline{u_i u_i} / \partial n = 0$ ; $\overline{u_i u_j} = 0$ *
Axis	$\partial U / \partial r = 0$ , $V = 0$	$\partial P / \partial r = 0$	$\partial k / \partial r = \partial \epsilon / \partial r = 0$	$\partial \overline{u_i u_i} / \partial r = 0$ , $\overline{u_i u_j} = 0$

### 3.3 Performance Parameters

To estimate the performance of a jet pump, mass flow ratio  $M$ , head ratio  $N$ , efficiency  $\eta$  and mean pressure coefficient  $C_P$  were calculated, using the converged solutions for the flow fields. These parameters can be expressed by following equations;

$$M = \frac{Q_s}{Q_j} \quad (21)$$

$$N = \frac{(K_K - K_P)U_d^2/2g + P_d/\rho g - U_s^2/2g - P_s/\rho g}{U_j^2/2g + P_j/\rho g - (K_K - K_P)U_d^2/2g - P_d/\rho g} \quad (22)$$

$$\eta = MN \quad (23)$$

$$C_P = \frac{P/\rho g - P_s/\rho g}{U_j^2/2g} \quad (24)$$

where  $Q$  stands for mass flow rate,  $U$  mean axial velocity,  $P$  mean pressure over the cross section, and subscripts  $j, s, d$  denote driving jet, suction flow and exit flow, respectively.  $K_K$  and  $K_P$  are mean correction factors for kinetic energy and pressure energy. They are obtained by the next equations;

$$K_K = \frac{(\rho/2) \int_0^r 2\pi(U^2 + W^2)U r dr}{(\rho/2)U_d^2(Q_j + Q_s)} \quad (25)$$

$$K_P = \frac{\int_0^r 2\pi U r \rho \int_r^W (W^2/r) dr dr}{(\rho/2)U_d^2(Q_j + Q_s)} \quad (26)$$

where  $U$  is mean axial velocity component and  $W$  mean circumferential velocity one,  $r$  radial distance from the pump axis (see Fig.2).

It should be noted that mean values such as  $U_j, Q_s, P_s$  and so forth were estimated by approximating the discrete data on the grid points with 2nd order interpolation and then integrating them.

## 4. RESULTS AND DISCUSSION

### 4.1 Flow Field in Mixing Chamber

Fig.3 shows the mean velocity in the axial direction and the turbulent kinetic energy profiles in the mixing chamber at different Reynolds numbers. It is found that a large recirculation is formed, when Reynolds number is small

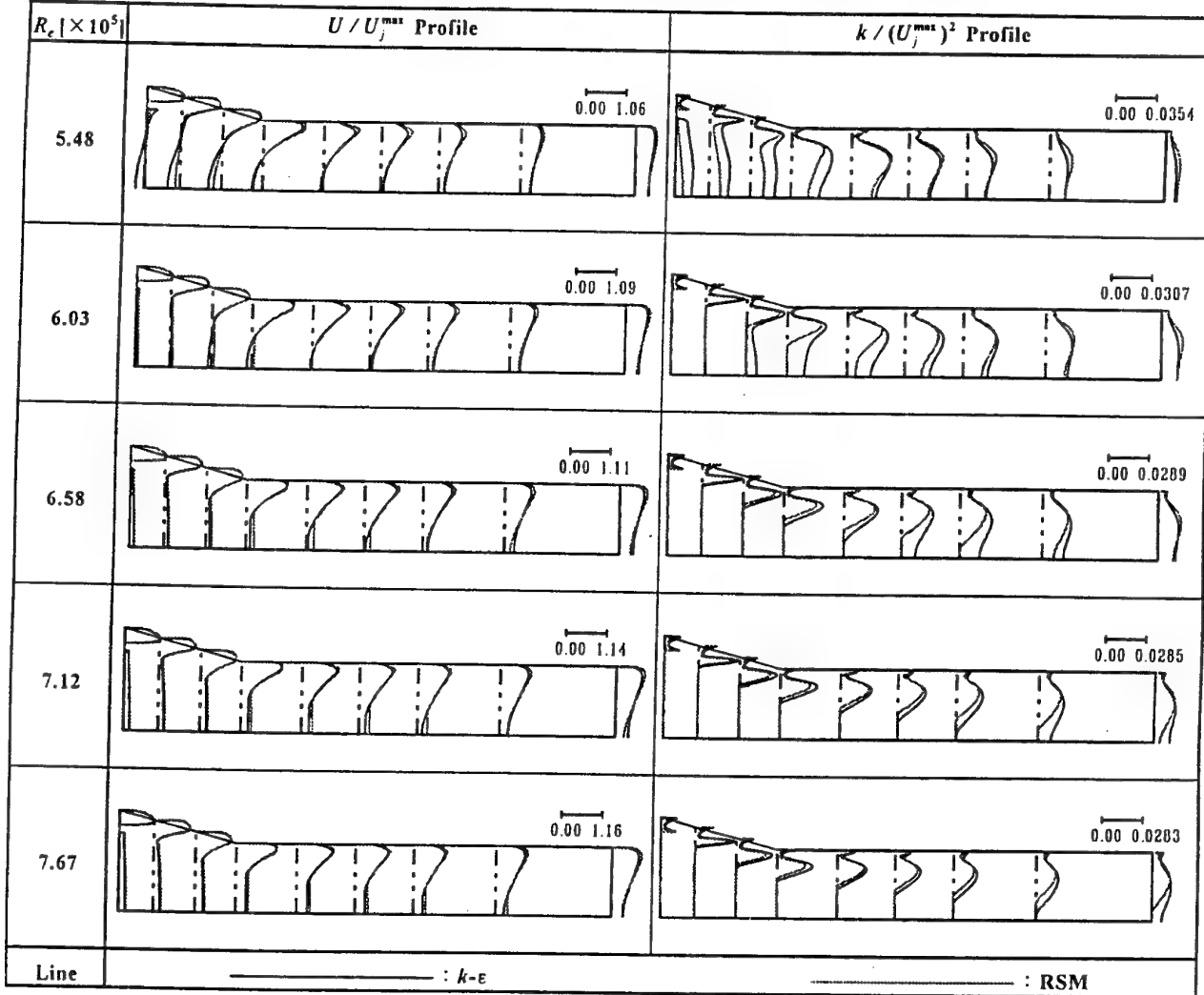


Fig.3 Numerical Results of Mean Axial Velocity and Turbulent Kinetic Energy Profiles

(consequently, mass flow ratio is low), and it disappears as Reynolds number increases. Although this trend can be reproduced by a  $k-\epsilon$  model and a Reynolds stress model (referred to "RSM" in the figures), the recirculation predicted by a  $k-\epsilon$  model is stronger than that by a Reynolds stress model. In addition, it is clear that the turbulent kinetic energy within the throat region calculated by a  $k-\epsilon$  model is larger than that by a Reynolds stress model. This is probably caused by the overprediction of eddy viscosity and thus excessive production of turbulence. This point will be described later.

#### 4.2 Prediction of Performances

The performance parameters estimated from each converged solution (Fig.3) are depicted and discussed in this section.

Fig.4 plots the mass flow ratio  $M$  for various Reynolds numbers. It is apparent that mass flow ratio increases with the increase of Reynolds number. This trend is reproduced by both models, but mass flow ratios estimated by a Reynolds stress model are always about 1.2 times higher than those by a  $k-\epsilon$  model. This fact reflects that the mass flow rate entrained from the suction pipe is small in the computations with a  $k-\epsilon$  model.

Fig.5 depicts the head ratio  $N$  for mass flow ratio  $M$ . The numerical results are also compared with the corresponding experimental data. It is easily found that a Reynolds stress model can predict head ratio more reasonably, especially at relatively high Reynolds number.

Fig.6 shows the efficiency  $\eta$  for mass flow ratio  $M$ . The predicted data are compared with experiments again. We can see that the efficiency obtained by a Reynolds stress model is in good agreement with the experimental data over a whole range of the calculated mass flow ratio. And it is clear that the efficiency calculated by a  $k-\epsilon$  model is always underpredicted, especially at high mass flow ratio.

These results suggest that a Reynolds stress model is more suitable than a  $k-\epsilon$  model to calculate the flow field and the performance of annular jet pumps.

#### 4.3 Cause of Discrepancies

In this section, we consider the reason why the difference described above occurs.

Fig.7 depicts the separating streamlines and the mean pressure coefficient predicted by each model at Reynolds number of  $6.58 \times 10^5$ . Separating streamline is defined as the streamline passing through the upper lip of the inner pipe (closed star symbol in Fig.7). From this figure, it is seen that, comparing the results by two models, the separating streamline calculated by a  $k-\epsilon$  model penetrates more deeply in the mixing chamber, and the mean pressure coefficient (i.e. mean pressure) obtained by a  $k-\epsilon$  model is higher than that by a Reynolds stress model, and recovers more quickly. This suggests that a  $k-\epsilon$  model overestimates eddy viscosity, and thus excessive turbulent mixing takes place in the mixing chamber. On the contrary, the pressure calculated by a Reynolds stress model is kept to be low, and this low pressure contributes the large mass flow rate entrained from the suction pipe and the higher efficiency. This tendency also suggests that to

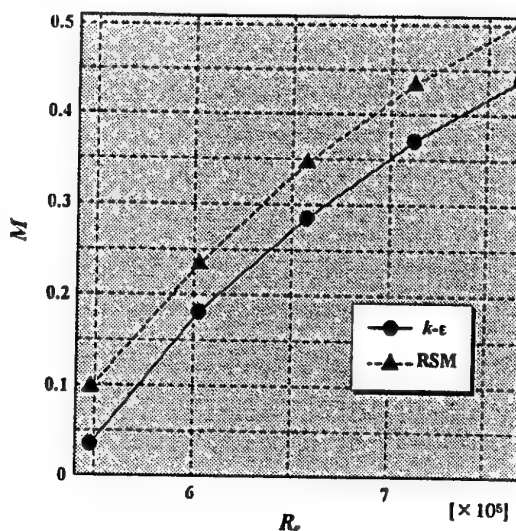


Fig.4 Predicted Mass Flow Ratio for Reynolds Number

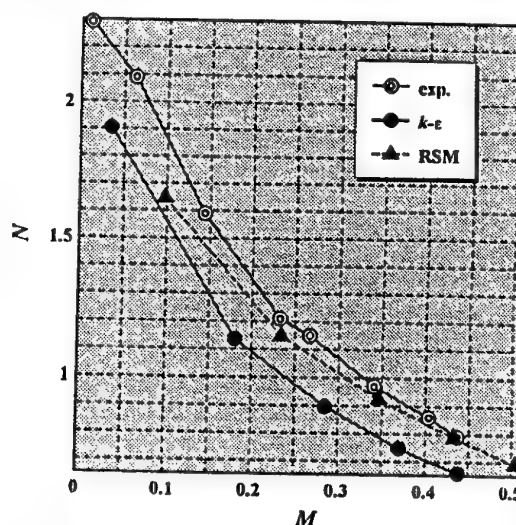


Fig.5 Relation between Mass Flow Ratio and Head Ratio

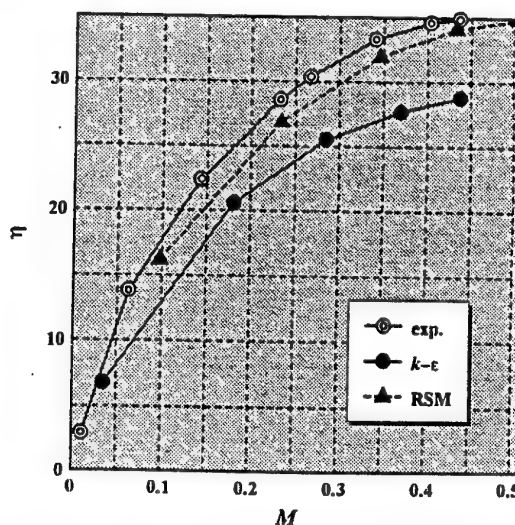


Fig.6 Relation between Mass Flow Ratio and Efficiency

keep low pressure in the mixing chamber is preferable to the performance of an annular jet pump.

Fig.8 plots the height of separating streamlines  $H_b$  at different Reynolds numbers. As shown in Fig.7, the height of a separating streamline is defined as the distance between the pump axis and the separating streamline at the exit of the nozzle section. It is found that a  $k-\epsilon$  model underestimates the height all over the Reynolds number calculated. Therefore, it is apparent that the excessive turbulent mixing is always resulted in by a  $k-\epsilon$  model. Moreover, we can see that at low Reynolds number a  $k-\epsilon$  model predicts the too small height. This would be caused by the very large recirculation which exists in the mixing chamber.

Although we did not investigate the streamline curvature effect in the mixing chamber, the excessive turbulent mixing by a  $k-\epsilon$  model is probably contributed from the effect. Further investigations on this point will be needed.

## 5. SUMMARY

We investigated the predictability of the performance of an annular jet pump. The flow field was computed by standard high-Reynolds-number type  $k-\epsilon$  and Reynolds stress turbulence models, and the performance parameters of the jet pump was estimated with use of the converged solutions. Comparing the results with the experimental data, followings conclusions were obtained.

- (1) At low mass flow ratio, a large recirculation is formed in the mixing chamber. This recirculation is reproduced by both models qualitatively. However, a  $k-\epsilon$  model tends to predict a larger and stronger recirculation.
- (2) A  $k-\epsilon$  model underpredicts the mass flow ratio, head ratio, and efficiency because of the excessive turbulent mixing in the mixing chamber, while a Reynolds stress model is able to predict them more reasonably.
- (3) The numerical results suggests that to keep low pressure in the mixing chamber is preferable to the performance of an annular jet pump.
- (4) It is still needed to investigate different configurations and other types of jet pumps in order to establish a numerical method to determining the performance of jet pumps.

## ACKNOWLEDGMENT

This research has partly been supported through the Kurata Research Grant by the Kurata Foundation.

## REFERENCES

- Elger, D.F. et al., "A New Way to Represent Jet Pump Performance", Trans. ASME, J. Fluids Eng., Vol.113, (1991), pp.439-444
- Gibson, M.M. and Launder, B.E., "Ground Effects on Pressure Fluctuations in the Atmospheric Boundary Layer", J. Fluid Mech., Vol.86, (1978), pp.491-511
- Karassik, I.J. et al. edited, Pump Handbook, McGraw-Hill, (1976), pp.231-247
- Kawamura, T. and Kuwahara, K., "Direct Simulation of a Turbulent Inner Flow by Finite-Difference Method", AIAA Paper 85-376, (1985), 1-10
- Launder, B.E. and Spalding, D.B., "The Numerical Computation of Turbulent Flows", Comp. Meth. Appl. Mech. Eng., Vol.3, (1974), pp.269-289

Razinsky, E. and Brighton, J.A., "Confined Jet Mixing for Nonseparating Condition", Trans. ASME, J. Basic Eng., Vol.93-3, D, (1971), pp.333-349

Sanger, N.L., "An Experimental Investigation of Several Low-Area-Ratio Water Jet Pumps", Trans. ASME, J. Basic Eng., Vol.92-1, D, (1970), pp.11-20

Shimizu, Y. et al., "On Annular Jet Pumps", Turbomachinery, Vol.13-6, (1985), pp.40-49 (in Japanese)

Shimizu, Y. et al., "Studies of the Configuration and Performance of Annular Type Jet Pumps", Trans. ASME, J. Fluids Eng., Vol.109, (1987), pp.205-212

Yano, H. et al., "Performance of a New Type of Water Jet Pump", Trans. ASME, J. Eng. Ind., Vol.112, (1990), pp.172-174

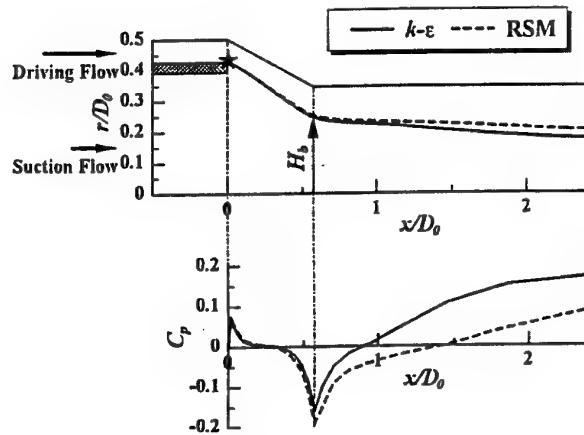


Fig.7 Separating Streamline and Mean Pressure Coefficient in Mixing Chamber

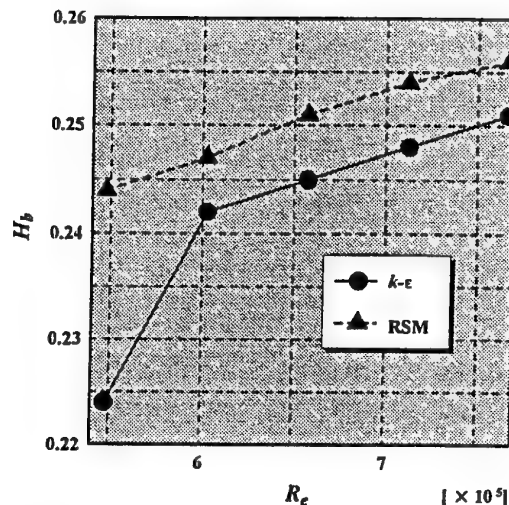


Fig.8 Height of Separating Streamline at Different Reynolds Numbers

# FUEL -AIR RATIO INFLUENCE ON MIXING PROCESSES IN TURBULENT PREMIXED ACETYLENE FLAME

Vukman V. Bakić, Simeon N. Oka, Aleksandra A. Ačanski, Miša M. Stefanović  
Laboratory for Thermal Engineering and Energy Research,  
"Vinča" Institute of Nuclear Sciences  
P.O.Box 522, 11001 Belgrade, Yugoslavia

## ABSTRACT

In this paper, the mean velocity, turbulence intensity and temperature profiles in a different cross-sections of premixed acetylene flame and for different acetylene-air ratios are given. For velocity measurements laser Doppler anemometer was used, while the temperature field measurements were performed by Pt-PtRh 10% thermocouple. LDA measurements and conditional and unconditional statistics of the velocity fluctuations produced by combustion products and surrounding air, can give more detailed data about the character and intensity of turbulent mixing in the flame. Through comparative analysis of the obtained mean velocity and temperature profiles, length and width of a characteristic regions in the premixed acetylene flame and their characteristics properties were established for different fuel-air ratio. With the increase of acetylene content in mixture, velocity and temperature fields are considerably changing.

length and width of characteristics regions and characteristic properties of the flow field is analyzed. Intensity of turbulent mixing in different flame regions, was also discussed.

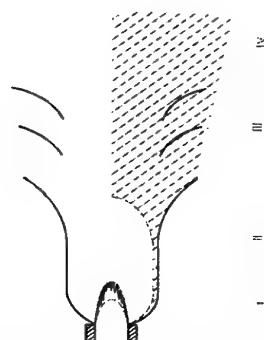


FIG.1. SCHEMATIC PICTURE OF PREMIXED AXISYMMETRIC FLAME FLOW FIELD.

## INTRODUCTION

Premixed acetylene flames are widely used in the industrial processes such as welding, metal cutting etc. This has motivated several experimental studies of such flames, Gaydon and Wolfhard (1960), Hargave and others (1987), etc., providing both mean velocity and temperature profiles together with a photographic records of the overall flame structure. Experimental investigations have been mostly performed with the industrial burners using laser-Doppler anemometry for velocity measurements and thermocouples for temperature measurements, with the aim to reduce noise and to increase combustion efficiently. In earlier experiments Matović, Oka and Durst (1994), according to the LDA-velocity information, different regions in the flow field of the premixed acetylene/air flame have been established: the region of the flame front (I), the region of constant flame width (II), the developing region (III) and the fully developed jet flow region (IV), Fig.1. In this paper, the influence of different acetylene/air ratios on the

## EXPERIMENTAL EQUIPMENT AND FLOW CONDITION

The experimental apparatus in this study has been the same as in Oka and Bakić (1996). Uniform acetylene/air mixture with different acetylene/air volume flow ratio,  $Q_{ac}:Q_a=1:12, 1:9.5, 1:7.5$ , was supplied to the burner with 8mm inner diameter. At the exit of the burner, fully developed turbulent velocity profiles were formed. Velocity measurements have been carried out using one-component laser Doppler system consisting of a 15mW helium-neon laser, a conventional transmission optics including a beam splitter and a double Bragg cell. All measurements have been carried out with a frequency shift of 5MHz with long time stability of  $10e^{-7}$  Hz.

The premixed acetylene/air mixture and surrounding air were seeded with  $Al_2O_3$  particles with mean diameter of  $2\mu m$ . Using the estimates given in Durst, Melling and Whitelaw (1976), it can be shown that  $2\mu m$  particles can follow the frequency



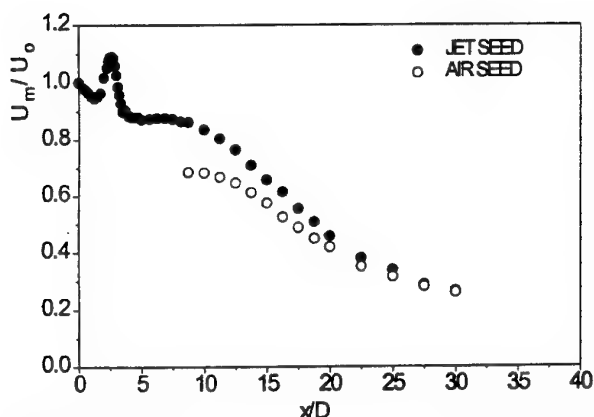


FIG.2. MEAN VELOCITY ALONG THE FLAME AXIS FOR CONDITIONAL SEEDING.

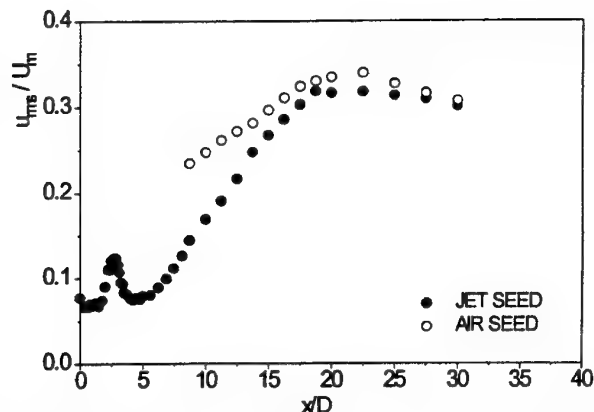


FIG.3. TURBULENCE INTENSITY ALONG THE FLAME AXIS FOR CONDITIONAL SEEDING.

up to 3 kHz. Uncoated thermocouple of Pt-Pt/Rh 10%, with a diameter of  $100\mu\text{m}$  was used. The thermocouple was about 80 diameters long to minimize heat conduction. Radiation correction was performed according to Bradley, Matthews (1968) and Stroomer (1995).

## EXPERIMENTAL RESULTS

### Mixing in Different Regions of the Premixed Acetylene/air Flame

Results of the mean velocity measurements along the flame axis, for the acetylene/air volume ratio 1:12 and for conditional statistics are shown in Fig.2. The axial velocity is normalized by exit velocity at the jet axis  $U_0=17.83\text{m/sec}$ . Fig.2. clearly shows characteristic regions in the premixed acetylene flame: region of flame front, region of constant axial velocity, developing region and fully developed jet flow region.

The region of flame front ends approximately 3 diameters downstream of the burner exit. This region is characterized by sharp increase in axial velocity followed by axial velocity decrease. Rapid temperature increase caused by combustion brings a stream flow relaminarisation beyond the flame front and a formation of the constant velocity region. Adiabatic temperature of the premixed acetylene/air flame is about  $2950\text{K}$ . The region of constant velocity ends 8.5 diameters downstream of the burner exit, where fluid originating from the air penetrates to the flame centerline. Measurements conditioned on the surrounding air could not be carried out for axial distances  $x/D \leq 8.5$ . In this region, fluid originating from the surrounding air did not penetrate to the flame axis.

For axial distance  $x/D=8.5$  the mean axial velocity of fluid originating from the jet is considerably higher than the mean axial velocity of fluid originating from the surrounding air. Large eddies of entrained cold air have much higher density and thus greater inertia than the eddies of combustion products. The eddies in the flow are continually breaking down into the smaller eddies, while diffusion is taking place, at molecular level, at all eddy boundaries. The jet becomes fully turbulent in the region of sharply increasing turbulence, while the eddies of surrounding air continue to be engulfed into flame, further

reducing velocity.

Turbulence intensity distribution along flame axis for conditional seeding, shown in Fig.3., has been normalized using local mean velocity at the axis. Just downstream the burner exit, turbulence intensity is approximately constant, until the flame front is reached. At the flame front, the maximum turbulence intensity occurs at the same point where the mean velocity at the flame axis has maximum value. After the increase of turbulence intensity at the flame front, it considerably decreases in the constant velocity region.

Rapid downstream increase of turbulence intensity at the flame axis corresponds to the point where the eddies of air entrained from the flame surroundings have finally reached the flame centerline. Intensive mixing process between combustion products and surrounding air starts at this cross section. Obviously, large density difference delays the mixing process, with downstream increase of turbulence intensity and intensification of mixing process.

Axial mean velocity in cross-section  $x/D=5$ , for conditional seeding is shown in Fig. 4. The mean axial velocity for conditional jet seeding have constant values for radial distance  $0 \leq y \leq 6\text{mm}$ .

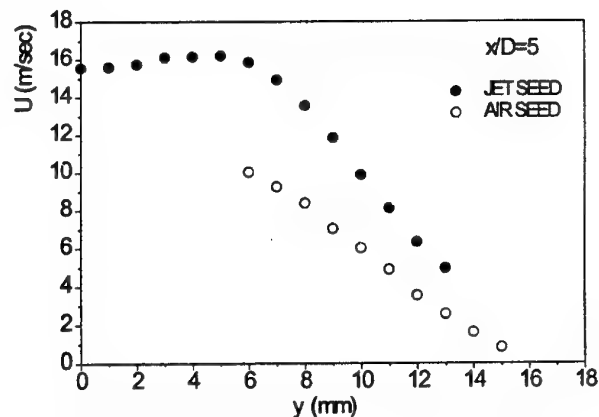


FIG.4. PROFILES OF AXIAL MEAN VELOCITY FOR CONDITIONAL SEEDING AT AXIAL LOCATIONS  $x/D=5$ .



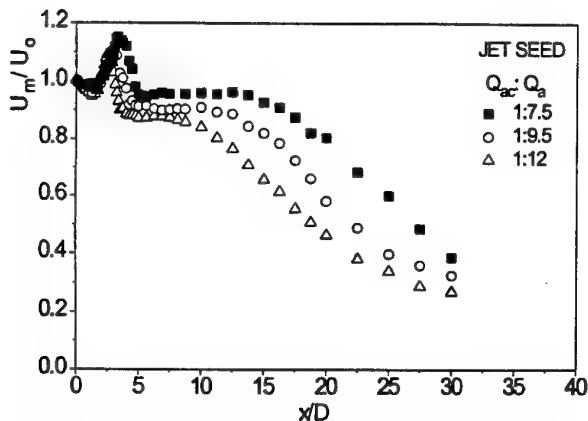


FIG.5. MEAN VELOCITY ALONG THE FLAME AXIS FOR DIFFERENT ACETYLENE/AIR VOLUME RATE.

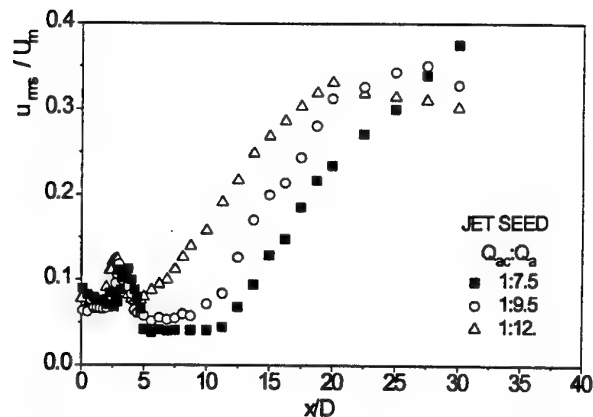


FIG.6. TURBULENCE INTENSITY ALONG THE FLAME AXIS FOR DIFFERENT ACETYLENE/AIR RATE.

In this region there is no mixing between combustion products and surrounding air. This cross section is in the region of constant velocity. Decrease of the mean axial velocity in cross-section  $x/D=5$ , for conditional jet seeding starts at the point where the mixing process begins. Similar behavior was established in other cross sections in the region of the constant velocity.

#### Axial Mean Velocity, Turbulence Intensity and Isotherms for Different Acetylene/Air Ratios

Results of the mean velocity and turbulence intensity along the flame axis, for the three different acetylene/air volume ratios are shown in Fig.5. and Fig.6.

With the increase of acetylene share in the mixture above the acetylene share for stoichiometric conditions, velocity maximum that corresponds to the outer edges of the flame front

is moving downstream and the height of the "flame brush" is increasing. This was also noticed by visual observations visualization. Downstream of the flame front the velocity in the flame axis increases with the increase of acetylene content in the mixture. For the stoichiometric acetylene/air ratio  $Q_{AC}:Q_A=1:12$ , theoretically complete combustion of reactants can be obtained. The increase of velocity in the region of the constant velocity can be explained by the fact that the excess of acetylene that has not been burned in the flame front, ultimately burns up at the flow edges causing the increase of the temperature in this region and decrease of the mixing intensity between the flame and surrounding air. This is clearly shown on temperature and mean velocity profiles. Length of the constant velocity region is increasing with the share of acetylene in the mixture. For the volume ratio  $Q_{AC}:Q_A=1:12$  the constant velocity region is ending on  $x/D=8.5$  distance, while for the ratio  $Q_{AC}:Q_A=1:7.5$ , this region is ending on  $x/D=12$  distance.

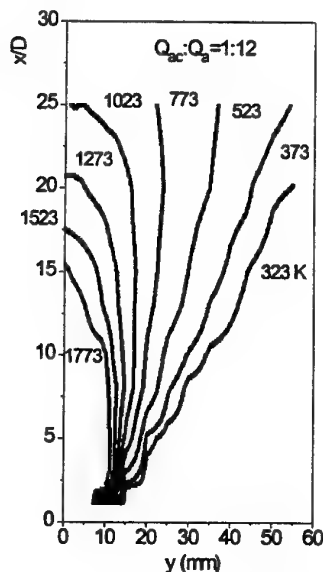


FIG.7. ISOTHERMS FOR ACETYLENE/AIR VOLUME RATIOS 1:12 AND 1:7.5.

With the larger share of acetylene in the mixture, the high temperature region is extending on the larger axial distance along the flame axis. Flame with a larger share of acetylene is not expanding so fast as the flame with a smaller share of acetylene. This is noticeable on Fig.7., where the flame isotherms for the stoichiometric acetylene/air ratio and for larger share of acetylene are given.

Because of the significant increase in combustion products temperature in this region and corresponding decrease of density, volume flow rate through the cross-sections of the flame is increased. At the same time, decrease of mixing intensity does not lead to rise in flow expansion, but the width of the jet stays the same or become smaller. This is also the reason for the increase velocity.

#### **Radial Profiles of the Axial Mean Velocity and Temperature for Different Acetylene/Air Ratios**

Fig.8. compares the mean axial velocity and temperature radial profiles on  $x/D=5, 8, 10$  and  $15$  distances for a different acetylene/air ratios in the mixture.

In the same cross-sections and for different acetylene/air ratios in the mixture, radial profiles of axial mean velocity are considerably different. On  $x/D=5$  distance, increase of velocity

from the flame axis to the flame edges is noticeable. For stoichiometric ratio,  $Q_{ac}:Q_a=1:12$ , mean axial velocity profile is nearly flattened up to  $y=6$  mm distance, because of the lack of mixing process between jet and surrounding air in this region. Increase of the acetylene content in the mixture leads to incomplete burning of acetylene in the flame front. The excess of the acetylene is burning further at the point where jet and surrounding air are starting to mix, which cause temperature increase in this area. Surrounding air serves as an oxidant for burning of the excess of acetylene at the flame edges. Temperature increase causes a velocity increase, and leads to occurrence of maximum velocity at the flame edges. In this area temperatures were above thermocouple measuring range. Increase of the acetylene content in the mixture causes increase of mean temperature radial profiles gradient. At the  $x/D=8$  distance, there is no more velocity maximum, because the greatest part of the acetylene is burned until this cross-section. Constant velocity region spreads with the increase of the acetylene content in a mixture. At the  $x/D=10$  distance, constant velocity region in radial profile for  $Q_{ac}:Q_a=1:12$  and  $1:9.5$  volume ratios doesn't exist more, while for  $Q_{ac}:Q_a=1:7.5$  volume ratio in this region is still noticeable. Mean velocity at the  $x/D=15$  distance don't show existence of a constant velocity region for all three acetylene/air ratios.

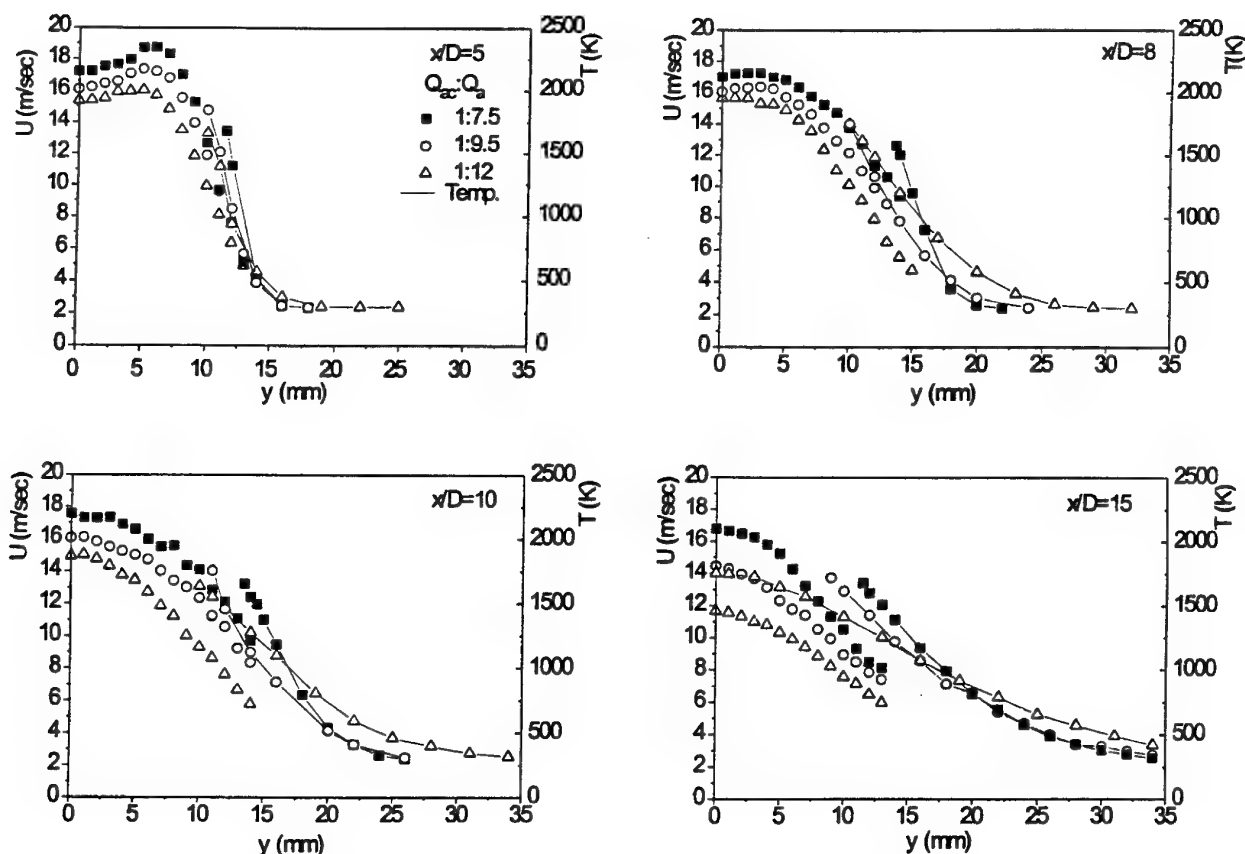


FIG.8. RADIAL PROFILES OF MEAN AXIAL VELOCITY AND TEMPERATURE AT THE  $x/D=5, 8, 10$  AND  $15$  DISTANCES.

## CONCLUSIONS

Temperature and velocity field measurements in the acetylene premixed flame for a different acetylene/air ratios showed that with the increase of acetylene content in the mixture, velocity and temperature fields considerably changing. Velocity values in the flame front and in the whole flow field are increasing with the increase of acetylene content in the mixture.

Length of the constant velocity region increases with the increase of the acetylene content in the mixture. Temperature measurements with thermocouple showed that the temperature in flame increases with the increase of acetylene content in mixture ratio. Existence of velocity maximum, in the area where mixing process between combustion products and surrounding air is starting, is a result of acetylene excess burning at that place. This temperature increase also cause a decrease of the intensity of the mixing process between surrounding air and combustion products.

## REFERENCES

- Bradley, D. and Matthews, K.J., 1968, "Measurement of high gas temperatures with fine wire thermocouples", *Journal of Mechanical Engineering Science*, Vol.10., pp. 299-305.
- Firestorm, R.M. and Westenberg, A.A., 1965, "Flame Structure", McGraw-Hill, N.Y.
- Gaydon, A.G. and Wolfhard, H.G., 1960, "Flames and their Structure, Radiation and Temperature", Chapman & Hall, London.
- Hargave, G., Fairweather, M. and Kilham, K., 1987, "Forced Convective Heat Transfer From Premixed Flames", *Journal of Heat and Fluid Flow*, pp.55-63.
- Matović, M., Oka, S. and Durst, F., 1994, "Structure of the Mean Velocity and Turbulence in Premixed Axisymmetric Flame", *ASME Journal of Fluids Engineering*, Vol.116, pp.631-636.
- Oka, S. and Bakić, V., 1996, "Investigation of Turbulent Field in Premixed Acetylene Flame Using Conditional and Unconditional LDA Statistics", *Proceedings, 3rd International Symposium of Engineering Turbulence Modeling and Experiments*, Crete, Greece, pp. 807-816.
- Stroomer, P., 1995, "Turbulence and OH Structures in Flames", Ph.D. Thesis, Technical University Delft, Holland.

# ROLE OF MEAN STRAIN AND TURBULENT DIFFUSION IN EARLY TURBULENT PREMIXED FLAME GROWTH

T. Mantel - F. Galzin : Renault-Research Division  
9-11 Avenue du 18 juin 1940  
92500 Rueil Mailmaison - France

R. Borghi : IRPHE - UMR 138 CNRS  
ESM2 - IMT  
Tech. de Château Gombert  
13451 Marseille Cedex 20 - France

## ABSTRACT

The role of mean strain and turbulent diffusion on the propagation of the early stages of a premixed turbulent flame is investigated. In order to well describe the early flame growth, turbulent combustion models have to carefully model these two effects. In the present study, a new model for the mean strain based on its decomposition into an isotropic and anisotropic part is proposed. The turbulent diffusion fluxes of species and enthalpy are modeled using a lagrangian approach which take into account the memory effect of turbulence via a lagrangian time scale. The turbulent combustion model utilized here is based on the presumed pdf approach coupled with a transport equation for the scalar dissipation. Application of these models to the propagation of a spherical flame ignited in a point is presented.

## 1 INTRODUCTION

In the modeling of turbulent premixed combustion, both chemical reactions and turbulent transport have to be carefully treated. In the limit of high Damköhler number ( $Da = \tau_t/\tau_c$ ,  $\tau_t$  and  $\tau_c$  being respectively a turbulent and chemical time scales), it is commonly assumed that chemistry can be represented by a single step reaction. In such a limit, flamelet models and presumed pdf (probability density function) approaches can be used to model the mean reaction rate  $\bar{\dot{w}}$  and describe the propagation of turbulent premixed flames. Concerning the turbulent fluxes  $\overline{\rho u_i'' c''}$  of the progress variable  $c$  ( $c = 0$  in the fresh gases and  $c = 1$  in the fully burnt gases), most of the models consider a first gradient assumption. However, both theoretical studies (Bray *et al.* 1981) and numerical data (Veynante *et al.* 1997) show that gradient diffusion assumption is no valid in some premixed combustion regime

especially for low  $u'/S_L$  ratio where  $u'$  represents the rms velocity fluctuations and  $S_L$  the laminar burning velocity.

This ongoing work presents recent developments concerning modeling of turbulent premixed combustion using a presumed pdf (probability density function) approach coupled with a transport equation for the scalar dissipation (Mantel & Borghi 1994). During the early flame growth ignited by a spark, the respective roles of strain produced by the mean velocity field on the flame and turbulent diffusion of concentration and energy are crucial. These different aspects are numerically investigated and new models for these two contributions are proposed.

## 2 ROLE OF STRAIN

### 2.1 Introduction

As presented in the review paper of Peters (1986), the stretch  $K$  is determinant in premixed turbulent combustion because it is responsible for flame surface area production but can also be responsible for local extinction when  $K$  exceeds a critical value especially for flames near the flammability limits.  $K$  can be expressed in term of flame strain and flame curvature (Matalon 1983, Candel & Poinot 1990)

$$K = -\mathbf{n} \otimes \mathbf{n} \odot \vec{\nabla} \mathbf{U} + \vec{\nabla} \cdot \mathbf{U} + S_d \mathbf{n} \nabla \mathbf{n} \quad (1)$$

where  $\mathbf{n}$  represents the vector normal to a flame element ( $\mathbf{n} = \vec{\nabla} c / |\vec{\nabla} c|$ ) and  $S_d$  is the propagation velocity of the flame. The total stretch can also be expressed as the relative increase of a flame surface element  $\delta A$  (Karlovitz *et al.* 1953)

$$K = \frac{1}{\delta A} \frac{d(\delta A)}{dt} \quad (2)$$

Here, our attention will focus on the stretch of the scalar field by the flow, represented by  $\mathbf{n} \otimes \mathbf{n} \odot \vec{\nabla} \mathbf{U}$  (or  $n_i n_j \partial U_i / \partial x_j$ ) in Eq. 1. This term appears explicitly in most of the turbulent combustion models using a transport equation for a scalar related to the mean reaction rate. This is the case of the transport equation for the flame surface density  $\Sigma$  (Candel & Poinso 1990), for the variance of the scalar  $G$  investigated by Peters (1992) or for the scalar dissipation  $\bar{\epsilon}_c$  (Mantel & Borghi 1994). In the transport equation for  $\bar{\epsilon}_c$ , this term is expressed by  $\overline{dc_{i,k} \frac{\partial U_i}{\partial x_k}}$  and is decomposed into two contributions having different physical meanings and related to different length and time scales namely

$$-\overline{dc_{i,k} \frac{\partial U_i}{\partial x_k}} = S_t + s_t \quad (3)$$

where

$$S_t = -\overline{dc'_{i,k} c'_{j,k} \frac{\partial U_i}{\partial x_k}}$$

$$s_t = -\overline{dc'_{i,k} c'_{j,k} \frac{\partial u'_i}{\partial x_k}}$$

Here  $c_{i,k}$  represents the spatial derivative of  $c$  in the  $x_i$  direction.

The first term  $S_t$  corresponds to the stretching of the scalar field by mean velocity gradients and the second term  $s_t$  represents the stretching of the scalar field by the turbulent velocity field. According to a classical order of magnitude analysis based on scale relations, (see Tennekes & Lumley 1972, Mantel & Borghi 1994), one can show that,  $s_t$  is related to the small scales of turbulence and is greater than  $S_t$  by a factor  $\mathcal{O}(Re_t^{1/2})$ . This result has been partly illustrated by Antonia & Browne (1983) who have measured these two terms by studying the destruction of temperature fluctuations in a turbulent plane jet. More precisely, their measurements did not clearly show that  $\overline{c'_{i,k} c'_{j,k}} \neq 0$  is  $\mathcal{O}(Re_t^{-1/2})$  indicating that  $S_t$  cannot be systematically neglected.

However, this order of magnitude analysis is valid for a steady flow like the propagation of a premixed planar flame in a infinite medium and can be put into question for a strongly unsteady situation such as the ignition of a turbulent medium by a spark where gas expansion due to the heat release provokes high velocity gradients. In that case, we will see later that  $S_t$  can become as large as  $s_t$  and its modeling needs to be considered with great care.

## 2.2 Effect of $S_t$ on turbulent premixed flames

The mean strain  $S_t$  has been principally investigated in the case of the dissipation of an inert scalar in presence of a mean velocity gradient such as in a turbulent mixing layer (Jones & Musson 1988, Tulapurkara *et al.* 1989). By extension, the case of turbulent reacting flows has been also treated using the same models (Borghi & Duttoya 1978, Cant *et al.* 1990, Candel & Poinso 1990, Mantel & Borghi 1994). However, in reacting flows, a significant contribution of the mean shear comes from thermal expansion across the turbulent flame brush. This is especially the case during the growth of a spherical kernel where radial velocity gradients are very strong.

Very few results exist concerning the estimation of  $S_t$  in turbulent flows. We can cite the work of Antonia &

Browne (1983) for a non reactive turbulent plane jet and the recent numerical study of Trouvé (1994) and experimental investigation of Veynante *et al.* (1996) concerning turbulent premixed flames.

Although it is commonly accepted that  $S_t$  plays the role of a production of  $\bar{\epsilon}_c$ , the experimental results of Antonia & Browne (1983) exhibit production or destruction of  $\bar{\epsilon}_c$  depending the position in the jet. This is also observed by Veynante *et al.* (1994) who have measured positive and negative contributions in  $S_t$ .

The experiment of Veynante *et al.* (1994) is concerned with a two-dimensional turbulent premixed V-shape flame stabilized on a cylindrical rod. Mean velocity gradients and orientation factors  $\langle n_i n_k \rangle_s$  are measured using laser velocimetry and tomographic visualizations. They conclude that the strain rate cannot be only related to the mean shear but have also to thermal expansion and orientation factors (the subscript  $s$  indicates an area weighted ensemble average,  $\langle f \rangle_s = \bar{f} \Sigma / \Sigma$ ). This analysis is confirmed by Trouvé (1994) in direct numerical simulation of a turbulent premixed flame submitted to a constant shear flow  $\partial \bar{U}_1 / \partial x_2$ . It appears that  $\langle S_t \rangle_s$  can be approximated by

$$\langle S_t \rangle_s = \alpha \frac{\partial \bar{U}_2}{\partial x_2} + \beta \frac{\partial \bar{U}_1}{\partial x_2} \quad (4)$$

where  $\alpha$  and  $\beta$  are constant. For all the cases studied by Trouvé, it is found that these two contributions are of the same order of magnitude. It is worth mentioning that the tensor  $\langle n_i n_k \rangle_s$  is found strongly dissymmetric in the experiment of Veynante *et al.* (1996). Moreover, both in Veynante *et al.* (1994) and in Trouvé (1994),  $S_t$  is found smaller than  $s_t$  by one order of magnitude and can even be neglected in the models.

## 2.3 Existing models for $S_t$

In order to propose and to validate a new model, two basic turbulent flows are considered (i) the of a spherical front propagation in a turbulent premixed medium and (ii) a two-dimensional turbulent mixing layer.

### Propagation of a spherical front in a turbulent premixed medium

In the case of the propagation of a spherical front in a turbulent medium, the expression for  $S_t$  can be directly obtained. Moreover, by considering local isotropy for the scalar field,  $S_t$  reduces to (see Appendix for details)

$$S_t = -\frac{1}{3} \bar{\epsilon}_c \vec{\nabla} \cdot \vec{U} = -\frac{1}{3} \bar{\epsilon}_c \left( \frac{\partial \bar{U}_r}{\partial r} + 2 \frac{\bar{U}_r}{r} \right) \quad (5)$$

In this particular case, both expansion and compression occur. Thus,  $S_t$  can be both production and dissipation of  $\bar{\epsilon}_c$  (or  $\Sigma$ ) across the turbulent flame brush. It actually produces (dissipates)  $\Sigma$  in the leading (trailing) edge of the flame.

### A two-dimensional turbulent mixing layer

In this kind of flow, it is well known that mean strain tends to increase the surface of mixing. Analogy can be made for the case of a premixed flame submitted to a mean shear flow. This case has been studied using direct numerical

simulation by Trouvé (1994) for different value of the strain rate. In all the treated cases, the flame surface tends to increase due to the strain.

### The model of Jones & Mussonge (1988)

Jones & Mussonge (1988) propose a modeling for  $S_t$  in the configuration of a turbulent mixing layer. This model is expressed by

$$S_t = -C_{JM} \bar{\epsilon} \frac{\overline{u_i u_k}}{2k} \frac{\partial \overline{U_i}}{\partial x_k} \quad (6)$$

From Eq. 6,  $S_t$  is calculated for the case of a spherical flame ignited in a point and propagating in a premixed turbulent medium. After some algebra, Eq. 6 is written (see Appendix)

$$S_t = -C_{p_s} \frac{\bar{\epsilon}}{2k} (\overline{u_r^2} \frac{\partial \overline{U_r}}{\partial r} + \frac{\overline{U_r}}{r} (\overline{u_\theta^2} + \overline{u_\phi^2})) \quad (7)$$

Here, we consider  $(\overline{u_i u_k})_{i \neq k} = 0$  and  $\frac{\partial \overline{U_r}}{\partial \theta} = \frac{\partial \overline{U_r}}{\partial \phi} = \overline{U_\theta} = \overline{U_\phi} = 0$ . Assuming isotropic turbulence ( $\overline{u_r^2} = \overline{u_\theta^2} = \overline{u_\phi^2} = 2k/3$ ) is the only possibility to recover the definition of  $S_t$  given by Eq. 5.

### The model of Jones & Mussonge using an eddy viscosity closure

In the Jones & Mussonge model, the Reynolds stress tensor is used to relate the anisotropy of the scalar field to the anisotropy of the turbulent flow field (Tulapurkara *et al.* 1989, Mantel & Borghi 1994). In the case where the Boussinesq approximation is used to close the Reynolds stress tensor, the model of Jones & Mussonge writes

$$S_t = C_{JM} \frac{\bar{\epsilon}}{2k} \left\{ \nu_t \left[ \frac{1}{2} \left( \frac{\partial \overline{U_i}}{\partial x_k} + \frac{\partial \overline{U_k}}{\partial x_i} \right) - \frac{2}{3} \frac{\partial \overline{U_i}}{\partial x_l} \delta_{ik} \right] - \frac{2}{3} k \delta_{ik} \right\} \frac{\partial \overline{U_i}}{\partial x_k} \quad (8)$$

And in the case of the spherical flame

$$S_t = C_{JM} \frac{\bar{\epsilon}}{6k} \left\{ \nu_t \left[ \left( \frac{\partial \overline{U_r}}{\partial r} \right)^2 - 2 \frac{\overline{U_r^2}}{r^2} - 8 \frac{\partial \overline{U_r}}{\partial r} \frac{\overline{U_r}}{r} \right] - 2k \left( \frac{\partial \overline{U_r}}{\partial r} + \frac{\overline{U_r}}{r} \right) \right\} \quad (9)$$

During the early spherical flame growth ( $r \approx 0$ ), the term  $(\overline{U_r}/r)^2$  in Eq. 9 is positive and becomes very large leading to a tremendous production of  $\bar{\epsilon}$ . The consequences of this behaviour on the flame growth are very critical and numerically leads to a supersonic flame velocity.

However, in the case of the mixing layer,  $S_t$  given by Eq. 9 is always negative and corresponds to a production of  $\bar{\epsilon}$  which is consistent with common observations.

### 2.4 A new model for $S_t$

Here, we present a model which satisfy the two cases cited above. The idea consists of separating  $S_t$  in an isotropic and an anisotropic contribution namely

$$S_t = -C_{p_i} \frac{\bar{\epsilon}}{3} \frac{\partial \overline{U_j}}{\partial x_j} - \frac{\partial \overline{U_i}}{\partial x_k} \quad (10)$$

The problem is to find a model for the tensor  $\overline{\gamma_{ik}}$  representing the anisotropy of the scalar field. In order to satisfy the two test flows, the terms of the main diagonal must be zero and  $\overline{\gamma_{ik}} \partial \overline{U_i} / \partial x_k$  must be always positive. A possible tensor for  $\overline{\gamma_{ik}}$  satisfying these two conditions is the deformation tensor (rotational for the velocity)

$$\overline{\gamma_{ik}} = \frac{C_{p_s}}{2} \frac{\nu_t}{k} \bar{\epsilon} \left( \frac{\partial \overline{U_i}}{\partial x_k} - \frac{\partial \overline{U_k}}{\partial x_i} \right) \frac{\partial \overline{U_i}}{\partial x_k} \quad (11)$$

Here, the anisotropy of the scalar field is still related to the deformation of the mean velocity field like in previous models, but  $\overline{\gamma_{ik}}$  given by Eq. 11 allows to describe the early flame growth and a mixing layer. Finally, the model for  $S_t$  writes

$$S_t = -C_{p_i} \frac{\bar{\epsilon}}{3} \frac{\partial \overline{U_j}}{\partial x_j} - \frac{C_{p_s}}{2} \frac{\nu_t}{k} \bar{\epsilon} \left( \frac{\partial \overline{U_i}}{\partial x_k} - \frac{\partial \overline{U_k}}{\partial x_i} \right) \frac{\partial \overline{U_i}}{\partial x_k} \quad (12)$$

where  $C_{p_i}$  and  $C_{p_s}$  are constant;  $C_{p_i} = 1$  in order to recover the spherical flame growth and  $C_{p_s} < 0$  in order to produce flame surface in the mixing layer configuration.

## 3 APPLICATION TO THE EARLY FLAME GROWTH

### 3.1 The ignition model

Concerning the ignition model, infinitely fast reaction are considered. Moreover, the energy transferred to the medium is integrally transformed in chemical energy. Following Fruchard & Borghi (1994), the ignition rate is

$$\tilde{w}_{ign} = \frac{E_{ign}}{\Delta t_{ign} Y_f^u (-\Delta H)} (1 - \bar{\epsilon}) \quad (13)$$

where  $E_{ign}$ ,  $\Delta t_{ign}$ ,  $Y_f^u$ ,  $(-\Delta H)$  represent the ignition energy, the duration of the spark, the concentration of fuel in the fresh reactants and the energy released by the chemical reactions (Fruchard & Borghi 1994).

### 3.2 The turbulent combustion model

For the turbulent combustion model, a presumed pdf approach based on the transport equation for the scalar dissipation  $\bar{\epsilon}$  is used (Mantel & Borghi 1994). This equation for constant density and constant diffusivity writes:

$$\begin{aligned} \frac{\partial \bar{\epsilon}}{\partial t} + \overline{U_k} \frac{\partial \bar{\epsilon}}{\partial x_k} = & - \frac{\partial \overline{u'_i \epsilon_c}}{\partial x_k} + d \frac{\partial^2 \bar{\epsilon}}{\partial x_k^2} - 2 d c'_{,k} c'_{,i} \frac{\partial \overline{U_k}}{\partial x_i} \\ & - 2 d c'_{,k} c'_{,i} \frac{\partial \overline{u'_k}}{\partial x_i} - 2 d u'_k c'_{,i} \frac{\partial \bar{\epsilon}}{\partial x_k} \\ & - 2 d c'_{,k} c'_{,i} \frac{\partial \overline{u'_k}}{\partial x_i} - 2 d^2 \frac{\partial c'_{,i} \partial c'_{,i}}{\partial x_k \partial x_k} - 2 d c'_{,i} \frac{\partial \bar{w}}{\partial x_i} \end{aligned} \quad (14)$$

The modeled equation used in the present study is the same as in Mantel & Borghi (1994) except for production of  $\bar{\epsilon}$  due to mean velocity gradients  $S_t = d c'_{,i} c'_{,k} \frac{\partial \overline{U_k}}{\partial x_i}$  for which the new model proposed here (see § 2.4) is used. Finally, the modeled equation for  $\bar{\epsilon}$  used here is:

$$\begin{aligned} \frac{\partial \bar{\epsilon}}{\partial t} + \overline{U_k} \frac{\partial \bar{\epsilon}}{\partial x_k} = & \frac{\partial}{\partial x_k} \left( \frac{\nu_t}{\sigma_{\epsilon_c}} \frac{\partial \bar{\epsilon}}{\partial x_k} \right) - (C_{p_i} \frac{\bar{\epsilon}}{3} \frac{\partial \overline{U_j}}{\partial x_j} + \overline{\gamma_{ik}} \frac{\partial \overline{U_i}}{\partial x_k}) \bar{\epsilon} \\ & + C_{p_s} \frac{\epsilon}{k} \frac{\nu_t}{\sigma_{\epsilon_c}} \frac{\partial \bar{\epsilon}}{\partial x_k} \frac{\partial \bar{\epsilon}}{\partial x_k} + \alpha_0 Re_t^{1/2} \frac{\epsilon}{\bar{\epsilon} k} \\ & - \beta_0 Re_t^{1/2} \frac{\bar{\epsilon}^2}{c'^2} (1 + C_u \frac{S_L}{u'})^{-2\gamma} \end{aligned} \quad (15)$$

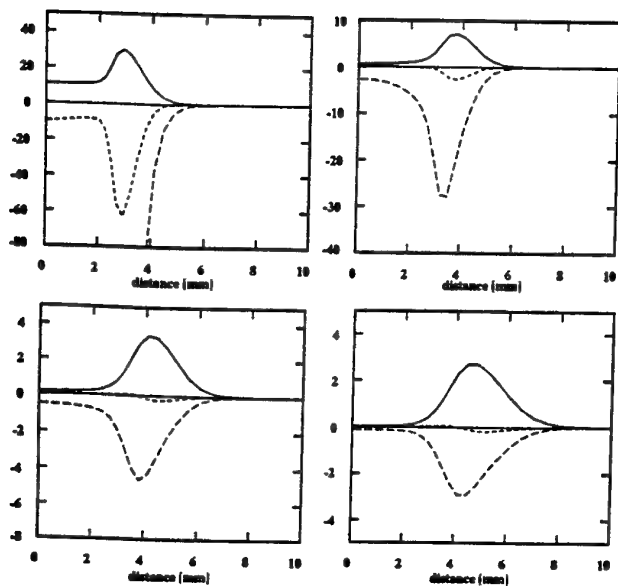


Figure 1: Profiles of: ——— turbulent stretch, ----- mean strain, - - - - - dissipation of  $\epsilon_c$  across the flame front at different time

The constants appearing in Eq.(16) are given in detail in Mantel & Borghi (1994). In order to solve the modeled transport equation for  $c^2$ , a presumed pdf approach is used. The shape of the pdf is presumed using the ideas of Borghi (1988) in order to take into account the presence of laminar flamelets in the turbulent flow field.

### 3.3 The turbulent diffusion model

An improvement to classical gradient modeling is proposed for turbulent fluxes of species and energy. Here, the turbulent dispersion model is based on the pioneering work of Taylor (1921). This model is based on the description of the turbulent motion by following the random trajectory of particles. It consists of modeling the eddy diffusivity using a memory effect of the turbulence via a lagrangian time scale. Thus, the eddy diffusivity is corrected with a damping function and writes:

$$\nu_t = C_\mu \frac{k^2}{\epsilon} (1 - \exp(-t^*/\tau_{lag})) \quad (16)$$

where  $\tau_{lag} = c_{lag} l_t / u'$  ( $l_t, u'$  and  $c_{lag}$  being the turbulence integral length scale, the rms turbulence intensity and a constant). The constant  $c_{lag}$  varies from 0.2 to 0.6 (Hinze 1975). The time  $t^*$  represents the time at which the memory effect of turbulence is taken into account by the flame. In our calculation,  $t^*$  is defined when a small amount of burnt gases (here  $t^* = t_{c=0.01}$ ) is present in the computational cell.

These different models are implemented in a computer code for reacting flows with variable density.

## 4 CONFIGURATION

The configuration studied here is concerned with the propagation of a turbulent premixed propane-air flame in a closed vessel. The flame is ignited by a spark in a decaying homogeneous and isotropic turbulence. The characteristics of the turbulence at the ignition timing are

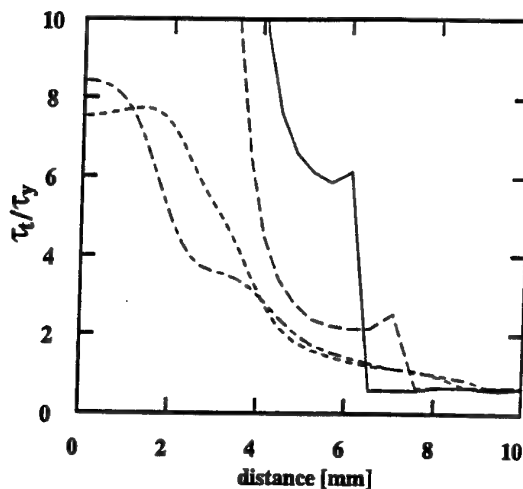


Figure 2: Profiles of ratio  $\tau_t/\tau_y$  across the flame front at different time: ———  $t = 0.1ms$ , -----  $t = 0.2ms$ , - - - - -  $t = 0.5ms$ , - . - . -  $t = 1.7ms$

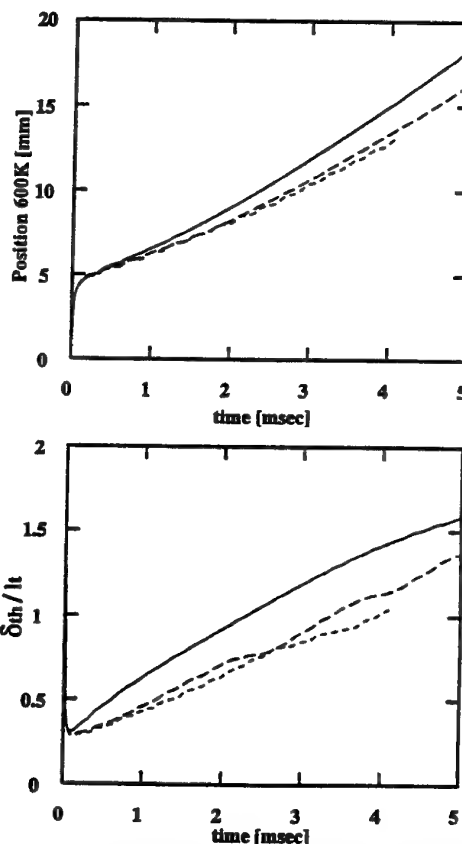


Figure 3: Time evolution of the iso-temperature 600K and of the turbulent flame thickness for different values of  $c_{lag}$ : ———  $c_{lag} = 0$ , -----  $c_{lag} = 0.2$ , - . - . -  $c_{lag} = 0.4$  at different time

$u' = 1.1m/s$ ,  $l_t = 6mm$ . Concerning the ignition, we specify  $E_{ign} = 3mJ$  and  $\Delta t_{ign} = 120\mu s$ .

## 5 RESULTS

Unlike the classical models, the strain due to mean velocity gradients leads to a dissipation of  $\overline{\epsilon_c}$  (or  $\overline{\Sigma}$ ) in the case of a spherical expanding flow. Figure 1 shows the crucial role of this term on early flame growth. At very early time ( $t = 0.1ms$ ), we can observe that the contribution of this term is of the same order of magnitude as the one for the stretching due to small scale turbulence (here, the dissipation is very high and goes out of the figure). As the time goes on, the contribution of  $S_t$  rapidly decreases and becomes one order of magnitude smaller than the predominant term of Eq. 16 (stretching due to small scale turbulence and dissipation). We can also notice that the model of Jones & Mussonge (1988) for  $S_t$  applied to this configuration leads to a tremendous production of  $\epsilon_c$  and to an unrealistic propagation of the flame front leading to a complete failure of the code. Figure 2 also shows the profile of the ratio  $\tau_t/\tau_c$  across the flame front at different times (here  $\tau_c = \overline{c'^2}/\overline{\epsilon_c}$ ). One can observe that this ratio is not constant and significantly varies from the fully burnt gases to the fresh reactants. The discontinuity of the curve at  $t = 0.1ms$  (in the leading edge of the flame) corresponds to a region of the flame where both  $\overline{c'^2}$  and  $\overline{\epsilon_c}$  tend to zero. Thus,  $\tau_c = \overline{c'^2}/\overline{\epsilon_c}$  is not well defined and the condition  $\tau_c = \tau_t$  is chosen to avoid this numerical problem.

A second important result of this study concerns the effect of the turbulent diffusion model on the characteristics of the turbulent flame brush thickness  $\delta_{th}$ . The Fig. 3 presents the time evolution of the iso-temperature  $600K$  and of the turbulent flame thickness for different values of the constant  $c_{lag}$ . We notice a significant influence of the eddy diffusivity model on the flame propagation and on the turbulent flame thickness  $\delta_{th}$  based on the maximum gradient of  $\tilde{c}$ .

## 6 CONCLUSIONS

This paper presents a new modeling for the effect of strain due to the mean velocity field on  $\overline{\epsilon_c}$  (and consequently  $\overline{\Sigma}$ ). The influence of this effect on the propagation of a spherical flame ignited by a spark in a decaying isotropic turbulence seems to be crucial and has to be treated carefully. The modeling of the turbulent diffusion fluxes has also a significant impact on the behaviour of flame propagation and its structure.

## APPENDIX

### Determination of $S_t$ in spherical coordinates

The term  $S_t = -d\overline{c'^2}/c',k \partial \overline{U_i}/\partial U_k$  can be rewritten using tensorial notation

$$S_t = -d\overline{c'^2}/c',k \partial \overline{U_i}/\partial U_k = -d \overline{\nabla c'} \otimes \overline{\nabla c'} \odot \overline{\nabla U} \quad (1)$$

Here, the operators  $\otimes$  and  $\odot$  represent respectively the tensorial product and the contracted product.

The tensor  $\overline{\nabla c'} \otimes \overline{\nabla c'}$  is expressed

$$\overline{\nabla c'} \otimes \overline{\nabla c'} = \begin{pmatrix} \frac{\partial c'}{\partial r} \\ \frac{1}{r} \frac{\partial c'}{\partial \theta} \\ \frac{1}{r \sin \theta} \frac{\partial c'}{\partial \phi} \end{pmatrix} \otimes \begin{pmatrix} \frac{\partial c'}{\partial r} \\ \frac{1}{r} \frac{\partial c'}{\partial \theta} \\ \frac{1}{r \sin \theta} \frac{\partial c'}{\partial \phi} \end{pmatrix} = \begin{pmatrix} \left(\frac{\partial c'}{\partial r}\right)^2 & 0 & 0 \\ 0 & \frac{1}{r^2} \left(\frac{\partial c'}{\partial \theta}\right)^2 & 0 \\ 0 & 0 & \frac{1}{r^2 \sin^2 \theta} \left(\frac{\partial c'}{\partial \phi}\right)^2 \end{pmatrix}$$

Thus,  $S_t$  is

$$S_t = \begin{pmatrix} \left(\frac{\partial c'}{\partial r}\right)^2 & 0 & 0 \\ 0 & \frac{1}{r^2} \left(\frac{\partial c'}{\partial \theta}\right)^2 & 0 \\ 0 & 0 & \frac{1}{r^2 \sin^2 \theta} \left(\frac{\partial c'}{\partial \phi}\right)^2 \end{pmatrix} \odot \begin{pmatrix} \frac{\partial \overline{U_r}}{\partial r} & 0 & 0 \\ 0 & \frac{\overline{U_r}}{r} & 0 \\ 0 & 0 & \frac{\overline{U_r}}{r} \end{pmatrix}$$

and finally,

$$S_t = -d \frac{\partial c'}{\partial r} \frac{\partial c'}{\partial r} \frac{\partial \overline{U_r}}{\partial r} - d \frac{\partial c'}{\partial \theta} \frac{\partial c'}{\partial \theta} \frac{\overline{U_r}}{r^3} - d \frac{\partial c'}{\partial \phi} \frac{\partial c'}{\partial \phi} \frac{\overline{U_r}}{r^3 \sin \theta} \quad (2)$$

Since

$$\overline{\epsilon_c} = d(\overline{\nabla c'})^2 = d \frac{\partial c'}{\partial r} \frac{\partial c'}{\partial r} + d \frac{\partial c'}{\partial \theta} \frac{\partial c'}{\partial \theta} \frac{1}{r^2} + d \frac{\partial c'}{\partial \phi} \frac{\partial c'}{\partial \phi} \frac{1}{r^2 \sin \theta} \quad (3)$$

$S_t$  is expressed by

$$S_t = -d \frac{\partial c'}{\partial r} \frac{\partial c'}{\partial r} \left( \frac{\partial \overline{U_r}}{\partial r} - \frac{\overline{U_r}}{r} \right) - \overline{\epsilon_c} \frac{\overline{U_r}}{r} \quad (4)$$

If we consider local isotropy ( $\overline{c_i c_k} |_{i \neq k} = \overline{c_i^2} = \overline{c_k^2} = \frac{1}{3} \overline{\epsilon_c}$ ) for the scalar field (in average), we have

$$S_t = -\frac{\overline{\epsilon_c}}{3} \left( \frac{\partial \overline{U_r}}{\partial r} + 2 \frac{\overline{U_r}}{r} \right) = -\frac{1}{3} \overline{\epsilon_c} \overline{\nabla} \cdot \overline{U} \quad (5)$$

### The model of Jones & Mussonge

The model of Jones & Mussonge writes

$$S_t = -C_{JM} \overline{\epsilon_c} \frac{\overline{u_i u_k}}{2k} \frac{\partial \overline{U_i}}{\partial x_k} = -C_{JM} \overline{\epsilon_c} \frac{\overline{\epsilon_c}}{2k} \overline{u'} \otimes \overline{u'} \odot \overline{\nabla U} \quad (6)$$

Considering  $\overline{u_i u_k} = 0$  for  $i \neq k$

$$\overline{u'} \otimes \overline{u'} \odot \overline{\nabla U} = \begin{pmatrix} \frac{\partial \overline{U_r}}{\partial r} & 0 & 0 \\ 0 & \frac{\overline{U_r}}{r} & 0 \\ 0 & 0 & \frac{\overline{U_r}}{r} \end{pmatrix} \odot \begin{pmatrix} \overline{u_r^2} & 0 & 0 \\ 0 & \overline{u_\theta^2} & 0 \\ 0 & 0 & \overline{u_\phi^2} \end{pmatrix}$$



and

$$\overline{\mathbf{u}' \otimes \mathbf{u}'} \odot \vec{\nabla} \bar{\mathbf{U}} = \overline{u_r^2} \frac{\partial \bar{\mathbf{U}}_r}{\partial r} + (\overline{u_\theta^2} + \overline{u_\phi^2}) \frac{\bar{\mathbf{U}}_r}{r} \quad (7)$$

Thus,

$$S_t = -C_{JM} \frac{\bar{\epsilon}_c}{2k} \left( \overline{u_r^2} \frac{\partial \bar{\mathbf{U}}_r}{\partial r} + (\overline{u_\theta^2} + \overline{u_\phi^2}) \frac{\bar{\mathbf{U}}_r}{r} \right) \quad (8)$$

### The model of Jones & Mussonge using an eddy viscosity model

In the Jones & Mussonge model, the Reynolds stress tensor is used to relate the anisotropy of the scalar field to the anisotropy of the turbulent flow field. In the case where the Boussinesq approximation is used to close Reynolds stress tensor, the model of Jones & Mussonge writes

$$\begin{aligned} S_t &= C_{JM} \frac{\bar{\epsilon}_c}{2k} \left\{ \nu_t \left[ \left( \frac{\partial \bar{\mathbf{U}}_i}{\partial x_k} + \frac{\partial \bar{\mathbf{U}}_k}{\partial x_i} \right) - \frac{2}{3} \frac{\partial \bar{\mathbf{U}}_i}{\partial x_i} \delta_{ik} \right] - \right. \\ &\quad \left. - \frac{2}{3} k \delta_{ik} \right\} \frac{\partial \bar{\mathbf{U}}_i}{\partial x_k} \\ &= C_{JM} \frac{\bar{\epsilon}_c}{2k} \left[ \nu_t (2\bar{\mathbf{S}} - \frac{2}{3} \vec{\nabla} \cdot \bar{\mathbf{U}} \bar{\mathbf{I}}) - \frac{2}{3} k \bar{\mathbf{I}} \right] \odot \vec{\nabla} \bar{\mathbf{U}} \end{aligned} \quad (9)$$

where

$$\bar{\mathbf{S}} = \frac{1}{2} (\vec{\nabla} \bar{\mathbf{U}} + (\vec{\nabla} \bar{\mathbf{U}})^T) \quad (10)$$

We have

$$\begin{aligned} S_t &= C_{JM} \frac{\bar{\epsilon}_c}{2k} \left\{ \nu_t \left( \begin{pmatrix} \frac{\partial \bar{\mathbf{U}}_r}{\partial r} & 0 & 0 \\ 0 & \frac{\bar{\mathbf{U}}_r}{r} & 0 \\ 0 & 0 & \frac{\bar{\mathbf{U}}_r}{r} \end{pmatrix} \odot \begin{pmatrix} \frac{\partial \bar{\mathbf{U}}_r}{\partial r} & 0 & 0 \\ 0 & \frac{\bar{\mathbf{U}}_r}{r} & 0 \\ 0 & 0 & \frac{\bar{\mathbf{U}}_r}{r} \end{pmatrix} \right) \right. \\ &\quad \left. - \frac{2}{3} \left[ \nu_t \left( \frac{\partial \bar{\mathbf{U}}_r}{\partial r} + 2 \frac{\bar{\mathbf{U}}_r}{r} \right) + k \right] \left( \frac{\partial \bar{\mathbf{U}}_r}{\partial r} + 2 \frac{\bar{\mathbf{U}}_r}{r} \right) \right\} \end{aligned}$$

Finally,  $S_t$  writes

$$\begin{aligned} S_t &= C_{JM} \frac{\bar{\epsilon}_c}{6k} \left\{ \nu_t \left[ \left( \frac{\partial \bar{\mathbf{U}}_r}{\partial r} \right)^2 - 2 \frac{\bar{\mathbf{U}}_r^2}{r^2} - 8 \frac{\partial \bar{\mathbf{U}}_r}{\partial r} \frac{\bar{\mathbf{U}}_r}{r} \right] \right. \\ &\quad \left. - 2k \left( \frac{\partial \bar{\mathbf{U}}_r}{\partial r} + \frac{\bar{\mathbf{U}}_r}{r} \right) \right\} \end{aligned} \quad (11)$$

### Closure using the rotational vector

$$S_t = C_{P_s} \frac{\bar{\epsilon}_c}{3} \frac{\partial \bar{\mathbf{U}}_j}{\partial x_j} + \frac{C'_{P_s}}{2} \frac{\nu_t}{k} \bar{\epsilon}_c \left( \frac{\partial \bar{\mathbf{U}}_i}{\partial x_k} - \frac{\partial \bar{\mathbf{U}}_k}{\partial x_i} \right) \frac{\partial \bar{\mathbf{U}}_i}{\partial x_k} \quad (12)$$

$$= C_{P_s} \bar{\epsilon}_c \vec{\nabla} \cdot \bar{\mathbf{U}} - C'_{P_s} \frac{\bar{\epsilon}_c}{2k} \nu_t (\vec{\nabla} \wedge \bar{\mathbf{U}}) \odot \vec{\nabla} \bar{\mathbf{U}} \quad (13)$$

### References

ANTONIA, R.A. & BROWNE, L.W.R. 1991 The destruction of temperature fluctuations in a turbulent plane jet. *J. Fluid Mech.* **228**, 581-606.

BORGHI, R. 1988 Turbulent combustion modelling. *Progress in Energy and Combust. Science* **14**, 245-292.

BORGHI, R. & DUTOYA, D. 1978. On the scales of the fluctuations in turbulent combustion. In *Seventeenth Sym. (Int.) on Combustion* pages 235-244. The Combustion Institute.

BRAY, K.N.C., LIBBY, P.A., MASUYA, G., & MOSS, J.B. 1981 Turbulence production in premixed turbulent flames. *Combust. Sci. Tech.* **25**, 127-140.

CANDEL, S.B. & POINSOT, T.J. 1990 Flame stretch and the balance equation for the flame area. *Combust. Sci. and Tech.* **70**, 1-15.

CANT, R.S., POPE, S.B., & BRAY, K.N.C. 1990. Modelling of flamelet surface-to-volume ratio in turbulent premixed combustion. In *Twenty-Third Symposium (International) on Combustion* pages 809-815. The Combustion Institute.

FRUCHARD, N. & BORGHI, R. 1994. In *Zel'dovich Memorial Symposium*.

HINZE, J.O. 1975 *Turbulence*. Mc Graw Hill New-York.

JONES, W.P. & MUSSONGE, P. 1988 Closure of the reynolds stress and scalar flux equations. *Phys. Fluids* **31**, 3589-3604.

KARLOVITZ, B., DENNISTON, D.W., KNAPSCHAEFER, D.H., & WELLS, F.H. 1953. Studies on turbulent flames. In *Fourth Symposium (International) on Combustion* pages 613-. The Combustion Institute.

MANTEL, T. & BORGHI, R. 1994 A new model of premixed wrinkled flame based on a scalar dissipation equation. *Combust. and Flame* **96**, 443-457.

MATALON, M. 1983 On flame stretch. *Combust. Sci. and Tech.* **31**, 169-181.

PETERS, N. 1986. Laminar flamelet concepts in turbulent combustion. In *Twenty-first Symposium (International) on Combustion* pages 1231-1250. The Combustion Institute.

PETERS, N. 1992 A spectral closure for premixed turbulent combustion in the flamelet regime. *J. of Fluid Mech.* **242**, 611-629.

TAYLOR, G.I. 1921 Diffusion by continuous movements. *Proc. London Math. Soc.* **20**, 196.

TENNEKES, H. & LUMLEY, J.L. 1972 *A First Course in Turbulence*. The MIT Press.

TROUVÉ, A. 1994 The production of premixed flame surface area in turbulent shear flow. *Comb. and Flame* **99**, 687.

TULAPURKARA, E.G., ANTONIA, R.A., & BROWNE, L.W.R. 1989. Optimisation of a  $\bar{\theta}^2 - \bar{\epsilon}_\theta$  model for a turbulent far-wake. In *Seventh Symp. Turb. Shear Flows* pages 2921-2926.

VEYNANTE, D., DUCLOS, J.-M., & PIANA, J. 1994. Experimental analysis of flamelet models for premixed turbulent combustion. In *Twenty-Fifth Symposium (International) on Combustion* pages 1249-1256. The Combustion Institute.

VEYNANTE, D., DUCLOS, J.-M., & PIANA, J. 1996 Experimental and theoretical analysis of flame surface density modelling for premixed turbulent combustion. In *CRCT - Rapport 1993-94*. Eds Technip.

VEYNANTE, D., TROUVÉ, A., BRAY, K.N.C., & MANTEL, T. 1997 Gradient and counter-gradient scalar transport in turbulent premixed flames. *J. Fluid Mech.* **332**, 263-293.

# MODELLING OF VARIABLE DENSITY EFFECTS IN THE SECOND MOMENT AND DISSIPATION EQUATIONS IN TURBULENT PREMIXED FLAMES

R. P. Lindstedt and E. M. Váos  
Mechanical Engineering Department  
Imperial College  
London SW7 2BX  
UK

## INTRODUCTION

Moment closure methods have long provided the base for theoretical models used for computations of turbulent reacting flows in geometries of practical interest. Within the latter context closures are primarily required for the turbulent transport of momentum and scalar(s), the Reynolds stresses and turbulent scalar fluxes and the mean reaction rate(s). To date most reported research efforts have mainly focused on the closure of the latter (e.g. Bray 1990; Duclos *et al.* 1993) adopting, invariably, gradient diffusion type approximations for turbulent transport. However, theoretical studies, (e.g. Bray & Libby 1994; Lindstedt & Váos 1996a), have shown the considerable impact of turbulence transport modelling on global flame characteristics such as the turbulent burning velocity and the flame brush thickness and evidently the evolution of mean and turbulent quantities. A closure at the second moment level has been found to be *essential* in this respect, an argument also supported by earlier application of transported *pdf* methods (e.g. Húlek & Lindstedt 1996a) and strongly indicated by experimental and DNS studies (e.g. Heitor *et al.* 1987; Rutland & Cant 1994).

Perhaps the most critical closure aspects in second moment methods concern the redistribution/scrambling and dissipation terms in the Reynolds stress and scalar flux equations. Considerable progress in this area has been made in the context of isothermal flows (e.g. Launder 1996). In variable density flows the prevalent approach features a recasting of models derived on a constant density basis in a density weighted form. The closure of such terms and the significance of the involved assumptions in flows with *reacting* scalars has been recently examined by Lindstedt and Váos (1996a; 1996b). The present contribution extends the latter work by consideration of possible extended variable density model forms for the turbulent kinetic energy dissipation rate. The resulting model equations are subsequently applied to the simulation of turbulent premixed flames in the flamelet regime of combustion featuring realistic levels of heat release.

## CLOSURE CONSIDERATIONS

The pressure correlation terms in the Reynolds stress

equations can be decomposed into redistributive and isotropic parts (Lumley 1978). The latter may be further split into pressure transport and pressure dilatation terms. Similarly pressure correlation terms in the scalar flux equations can be split into pressure "scrambling" and pressure transport terms.

Because of the above decomposition and the resulting traceless forms, redistribution terms are invariably modelled by recasting closures derived on a constant density basis in a density weighted form. A similar procedure is also applied to the pressure scrambling terms. The latter approach has been found to be adequate in flows featuring *conserved* scalars, i.e. mixing problems and diffusion flames (e.g. Jones 1993). By contrast, Lindstedt & Váos (1996a) have found that in flows involving reacting scalars the above approach remains insufficient irrespective of specific model formulations. Regrettably, an analytical treatment of exact unclosed terms provides little information for modelling purposes. Lindstedt & Váos (1996a) have thus proposed extended variable density forms based on the following physical considerations.

Turbulence production in premixed flames at practical rates of heat release evolves as a fine balance between strain and preferential acceleration related effects. In particular strain effects feature a prevalence of normal strain components which invariably lead to reduction of turbulence levels, i.e. "dilatation". Preferential acceleration effects arise due to a self-induced pressure drop within the flame and are thus exerted through the mean pressure gradient terms in the respective second moment equations. The latter type of effects invariably lead to turbulence production and non-gradient turbulent scalar fluxes (e.g. Libby & Bray 1981). Experimental (e.g. Ferrão 1993) and DNS studies (e.g. Trouvé *et al.* 1994; Rutland & Cant 1994) suggest that at realistic rates of heat release the contributions of mean pressure gradient terms are dominant and essentially determine the turbulent kinetic energy levels, the levels of anisotropy and the magnitude and alignment of the scalar flux vector.

On the other hand, models derived on a constant density basis feature a scaling of redistribution solely on mean strain. Hence, the rate at which energy is trans-

ferred between components, i.e. the rate of minimisation of anisotropy, regardless of specific model forms, will be substantially lower than the rate at which anisotropy is produced. It is thus suggested that model formulations should explicitly include an *additional* part representing preferential acceleration effects. The methodology and modelling approximations are thus analogous to those adopted in strongly stratified flows with force field effects (Launder 1975). Indeed the evolution of turbulence under such circumstances is affected in a similar manner and therefore the resulting scaling of the models should be identical. The latter observation is of considerable importance. While the formulation of such acceleration redistribution/scrambling terms using invariant methods is straightforward, calibration of constants and evaluation of different model forms in the context of inhomogeneous combustions flows would raise insurmountable difficulties.

In the present work "slow" and "strain" redistribution is obtained by a model based on the Generalised Langevin model of Haworth & Pope (1987) which yields corresponding scrambling terms for the scalar flux equations (Pope 1994). A simple Isotropisation of Production type model (Gibson & Launder 1976) is adopted for the acceleration redistribution/scrambling parts.

The most commonly employed model equation for the turbulent kinetic energy dissipation rate, assuming a generalised gradient diffusion model for the turbulent transport of dissipation, takes the following well known form,

$$\frac{\partial \bar{\rho} \tilde{\varepsilon}}{\partial t} + \frac{\partial \bar{\rho} \tilde{u}_i \tilde{\varepsilon}}{\partial x_i} = \frac{\partial}{\partial x_k} \left[ C_{\varepsilon_1} \bar{\rho} \tilde{\varepsilon} \frac{\partial \tilde{u}_k}{\partial x_i} \right] - C_{\varepsilon_2} \bar{\rho} \tilde{\varepsilon} \frac{\partial \tilde{u}_k}{\partial x_i} - C_{\varepsilon_3} \bar{\rho} \tilde{\varepsilon} \frac{\partial \tilde{u}_k}{\partial x_i} \quad (1)$$

where  $C_{\varepsilon_1}$  and  $C_{\varepsilon_2}$  are assigned the values of 1.44 and 1.92, while a reasonable value for  $C_{\varepsilon_3}$  is approximately 0.18 (Jones 1980). The above equation is almost entirely derived on empirical principles — the exact transport equation for the dissipation rate proves to be of little help for modelling purposes.

Some support, however, is provided by the analyses of Lumley (1992; 1996), which based on energy cascade principles, suggest that the generation term for the turbulence dissipation rate corresponds to the rate at which energy is fed to the lower wavenumber end of the spectrum. Within the "standard" model of equation (1) the "dissipation feeding rate" is essentially identified with the (scaled) production term of the turbulent kinetic energy. However, while this modelling approach is arguably sufficient in isothermal shear driven flows, variable density flows may feature a prevalence of normal strain components, due to dilatation, and/or counter-gradient shear stresses, due to preferential acceleration effects. The "generation" term will thus, invariably, amount to a *negative* contribution. In order to provide compensation for such effects, various terms have been proposed in past work and include, for example, the contribution of mean density gradients or mean pressure gradients or the mean velocity divergence (cf. Jones 1980). The inclusion of any single or any combination of the latter terms from this point of view is largely heuristic and the calibration of relevant modelling constants becomes uncertain.

This ambiguity, however, may be partly resolved by the phenomenological approach presented above and thus related to the modelling of the redistribution/scrambling terms. Hence, relevant model forms should directly incorporate both strain and preferential acceleration related terms. The present authors have thus performed calculations of turbulent premixed flames including a mean pressure gradient term in the turbulent dissipation equation

(Lindstedt & Váos 1996a).

$$\frac{\partial \bar{\rho} \tilde{\varepsilon}}{\partial t} + \frac{\partial \bar{\rho} \tilde{u}_i \tilde{\varepsilon}}{\partial x_i} = \frac{\partial}{\partial x_k} \left[ C_{\varepsilon_1} \bar{\rho} \tilde{\varepsilon} \frac{\partial \tilde{u}_k}{\partial x_i} \right] - C_{\varepsilon_2} \bar{\rho} \tilde{\varepsilon} \frac{\partial \tilde{u}_k}{\partial x_i} - C_{\varepsilon_3} \bar{\rho} \tilde{\varepsilon} \frac{\partial \tilde{u}_k}{\partial x_i} \quad (2)$$

In the context of strongly stratified flows the corresponding modelling constant  $C_{\varepsilon_3}$  is assigned values in the region 0.95–1.2 (e.g. Jones 1993; Launder 1996). On the other hand, it has been found (Lindstedt & Váos 1996a) that in turbulent premixed flames the latter constant has to be assigned a relatively high value ( $C_{\varepsilon_3} = 1.4$ ). The discrepancy may primarily be attributed to the assumed form of the strain related production term. As noted above, in turbulent premixed flames the latter will result in negative rather than positive contributions. Therefore, a higher  $C_{\varepsilon_3}$  value is required to provide compensation. An alternative general form is thus considered here.

$$\frac{\partial \bar{\rho} \tilde{\varepsilon}}{\partial t} + \frac{\partial \bar{\rho} \tilde{u}_i \tilde{\varepsilon}}{\partial x_i} = \frac{\partial}{\partial x_k} \left[ C_{\varepsilon_1} \bar{\rho} \tilde{\varepsilon} \frac{\partial \tilde{u}_k}{\partial x_i} \right] - \bar{\rho} \tilde{\varepsilon} \mathcal{P} \quad (3)$$

$$\mathcal{P} = (C_1 \delta_{ij} + C_2 b_{ij} + C_3 b_{ij}^2) \tilde{k} S_{ij} + C_4 \mathcal{G} + C_5 \tilde{\varepsilon} \quad (3)$$

$$\mathcal{G} = \tilde{u}_i' \frac{1}{\bar{\rho}} \frac{\partial \bar{\rho}}{\partial x_i} \quad S_{ij} = \frac{1}{2} \left[ \frac{\partial \tilde{u}_i}{\partial x_j} + \frac{\partial \tilde{u}_j}{\partial x_i} \right]$$

$$b_{ij} = \frac{\tilde{u}_i' \tilde{u}_j'}{\tilde{k}} - \frac{2}{3} \delta_{ij} \quad b_{ij}^2 = b_{ij} b_{ij}$$

In equation (3)  $C_1$ – $C_5$  are constants although general formulations as functions of anisotropy or strain invariants (e.g. Launder 1996) are also possible. For the present purposes the second order term is omitted ( $C_3 = 0$ ) and thus equation (3) reduces to the "standard" model of equation (1) at the zero-heat release limit. In the latter case the constants  $C_2$  and  $C_5$  of equation (3) can be identified with  $C_{\varepsilon_1}$  and  $C_{\varepsilon_2}$  of equation (1) and are thus here assigned the "standard" values of 1.44 and 1.92 respectively.  $C_1$  is assigned here the value of 0.5 hence a positive velocity divergence will result in a positive contribution. The latter fact allows the mean pressure gradient term constant  $C_4$  ( $C_{\varepsilon_3}$ ) to be assigned the value of 1.2 — in better agreement with corresponding values in strongly stratified flows.

Closures for the remaining terms are as outlined by Lindstedt & Váos (1996a). The triple moment and pressure transport terms are approximated using the generalised gradient diffusion model of Daly & Harlow (1970). Models for the pressure dilatation term have been suggested by Zhang & Rutland (1995) and Húlek & Lindstedt (1996b). On the evidence of calculations however, it has been found that such models lead to considerable over-predictions of turbulence intensities. The pressure dilatation term is thus here ignored. It should be noted, however, that the contribution of this term is potentially important for flames characterised by turbulence intensities which are low compared to the laminar burning velocity.

Flames in the flamelet regime of combustion are considered here and closures for the velocity-reaction rate correlations in the scalar flux equations and the scalar variance/time scale have thus been obtained following Bray (1980) and Bray *et al.* (1985). For the present purposes the mean reaction rate is obtained by an algebraic model, derived on the assumption that the flame surface geometry is fractal (Gouldin 1987; Lindstedt & Váos 1996b),

$$\bar{S}_c = C_R \rho_u \frac{u_L}{V_K} \tilde{\varepsilon} \tilde{c} (1 - \tilde{c}) \quad (4)$$

where  $C_R$  is a constant,  $u_L$  the *unstrained* laminar burning velocity and  $V_K$  is the Kolmogorov velocity. The reaction rate constant  $C_R$  has been calibrated to the value of 2.6 — the latter value has been found to be relatively insensitive to changes in the dissipation model.

## APPLICATION OF THE MODEL

The second moment model described above, is here applied to the simulation of two turbulent premixed flames stabilised in stagnation point flow geometries. The simulations are fully two-dimensional and transient — the governing equations are integrated in time until a steady state is reached. The numerical procedure is described elsewhere (Lindstedt & Váos 1996a). Results from simulations with a gradient diffusion closure for the turbulent scalar fluxes, while retaining a second moment closure for the Reynolds stresses, are also presented. In the latter cases the “standard” dissipation equation model is used as the effect of the mean pressure gradient terms in the second moment equations has to be omitted.

The first case considered here features a slightly lean methane flame ( $\phi = 0.9$ ) stabilised between two opposed jets of reactants. Experimental data are provided by Mastorakos (1993). Inspection of Figure 1 reveals significant differences between predictions using a gradient diffusion and a transport equation based closure for the turbulent scalar fluxes. Using a gradient diffusion closure neither the flame stabilisation point nor the flame brush thickness is accurately predicted. The observed differences thus signify the overwhelming importance of the modelling of turbulent transport. Clearly, gradient diffusion closures lead to under-predictions of the latter and thus of the turbulent burning velocity (Bray 1990). Some compensation may be provided by increasing the reaction rate constant — the value of  $C_R = 4.5$  is used here for illustration purposes. In the latter case the flame stabilisation point is accurately predicted, however, further significant discrepancies in the evolution of mean and turbulence quantities can be observed (Figures 1–5).

On the other hand, observed differences in predictions between the two dissipation production models using a full second moment closure do not appear significant with the notable exception of Figure 5. Predictions for the progress variable and mean velocity profiles (Figures 1 and 2) are in excellent agreement with experiment and slightly in favour of the extended dissipation model. The predicted turbulence intensity profiles are in reasonable agreement with experiment (Figures 3 and 4) with the minor exception of the axial turbulence intensity close to the leading edge of the flame. However, it appears difficult to explain the measured peak at this location.

The second case features a stoichiometric ethylene flame stabilised in the stagnation point flow created by an impinging jet on a plate. Experimental data for the latter case are provided by Cheng & Shepherd (1991). The flame examined here is stabilised sufficiently far from the stagnation plane so that the solid-boundary conditions at the plate have been found to have little influence on mean and turbulent quantities in the area of interest. Using a gradient diffusion closure, observed differences between predictions and experimental data for both mean and turbulence quantities (Figures 6–9) are more pronounced compared to the previous case. By contrast, predictions of the mean axial velocity and scalar profiles using a full second moment closure are in good agreement with experiment and clearly in favour of the extended dissipation model (Figures 6 and 7). The predictions of the axial and radial turbulence intensities reveal an essential feature of turbulent premixed flames, i.e. flame induced turbulence production. However, while post-flame values are in reasonable agreement with experiment the respective peak values appear somewhat under-predicted (Figures 8 and 9). The measured peaks for

the present case are located very close to the trailing edge of the flame. As noted above, the omission of a pressure dilatation model may also prove significant in this respect.

The area where significant differences have been observed between the dissipation models of equations (2) and (3) is in the evolution of the integral length scale through the flame (Figures 5 and 10). Using equation (3) the evolution of the integral length scale seems to follow that of other turbulence quantities, e.g. the turbulence intensities, while equation (2) yields a continual length scale increase through the flame. In the absence of detailed experimental measurements and/or relevant DNS data, however, no further comment can be made.

## CONCLUSIONS

The present work comprises a modelling study of turbulent premixed flames using second moment closures. The accurate representation of variable density effects in the second moment and dissipation equations — in particular the redistribution/scrambling and dissipation production terms — is given considerable attention. The effects amount to dilatation induced by enhanced normal strain components and pressure gradient related production through preferential acceleration. Regrettably, an analytical or semi-analytical treatment of the exact unclosed terms provides little information for modelling purposes. Closure difficulties are partly resolved here by adoption of a phenomenological approach and model formulations have been obtained by consideration of suitable invariant forms. The modelling approach proposed is general and combustion regime independent. Significantly, the noted evident similarity with strongly stratified flows permits additional model terms to be developed/calibrated separately from other elements of closure and partly subjected to exact constraints.

Clearly, further work is required related to the modelling of the turbulent transport of second moments (triple moments and pressure transport), the pressure dilatation and reaction related terms. However, the present model compares well with detailed experimental data and appears to provide a sound basis for further improvements also in these areas.

## ACKNOWLEDGEMENT

The authors wish to express their gratitude to the CEC for its financial support through contract EV5V-CT93-0274 (EMERGE).

## REFERENCES

- Bray, K. N. C., 1980, “Turbulent Flows with Premixed Reactants,” In P. Libby and F. Williams, ed., *Turbulent Reacting Flows, Topics in Applied Physics*, Vol. 44, Springer-Verlag.
- Bray, K. N. C., 1990, “Studies of the Turbulent Burning Velocity,” *Proceedings of the Royal Society of London A*, Vol. 431, No. 1882, pp. 315–335.
- Bray, K. N. C., and Libby, P. A., 1994, “Recent Developments in the BML Model of Premixed Turbulent Combustion,” In P. A. Libby and F. A. Williams, ed., *Turbulent Reacting Flows*, Chapter 3, pp. 115–151, Academic Press.
- Bray, K. N. C., Libby, P. A., and Moss, J. B., 1985, “Unified Modelling Approach for Premixed Turbulent Combustion — Part I: General Formulation,” *Combustion and Flame*, Vol. 61, pp. 87–102.
- Cheng, R. K., and Shepherd, I. G., 1991, “The influence of burner geometry on Premixed Turbulent flame propagation,” *Combustion and Flame*, Vol. 85, pp. 7–26.
- Daly, B. J., and Harlow, F. H., 1970, “Transport Equations in Turbulence,” *Physics of Fluids*, Vol. 13, pp. 2634.
- Duclos, J. M., Veynante, D., and Poinot, T., 1993,

"A comparison of flamelet models for Premixed Turbulent Combustion," *Combustion and Flame*, Vol. 95, pp. 101-117.

Ferrão, P. M. C., 1993, *Análise Experimental de Chamas Turbulentas com Recirculação*, Ph. D. thesis, Universidade Técnica de Lisboa.

Gibson, M. M., and Launder, B. E., 1976, "On the Calculation of Horizontal, Turbulent, Free Shear Flows under Gravitational Influences," *ASME Journal of Heat Transfer*, Vol. 129C, pp. 81.

Gouldin, F. C., 1987, "An application of Fractals to the modelling of premixed turbulent flames," *Combustion and Flame*, Vol. 68, pp. 249-266.

Hülek, T., and Lindstedt, R. P., 1996a, "Computations of steady-state and transient premixed turbulent flames using pdf methods," *Combustion and Flame*, Vol. 104, pp. 481-504.

Hülek, T., and Lindstedt, R. P., 1996b, "Modelling of Unclosed Non-Linear Terms in a pdf Closure for Turbulent Flames," *Mathematical and Computer Modelling*, Vol. 24, No. 8, pp. 137-147.

Haworth, D. C., and Pope, S. B., 1987, "A pdf Modeling Study of Self-similar Turbulent Free Shear Flows," *Physics of Fluids A*, Vol. 30, No. 4, pp. 1026-1044.

Heitor, M. V., Taylor, A. M. K. P., and Whitelaw, J. H., 1987, "The interaction of turbulence and pressure gradients in a baffle-stabilized premixed flame," *Journal of Fluid Mechanics*, Vol. 181, pp. 387-413.

Jones, W. P., 1980, "Models for Turbulent Flows with Variable Density and Combustion," In *Prediction Methods for Turbulent Flows*, VKI-Lecture Series, Hemisphere.

Jones, W. P., 1993, "Turbulence Modelling and Numerical Solution Methods for Variable Density and Combusting Flows," In *Turbulent Reacting Flows*, Chapter 6, pp. 309-374, Academic Press.

Launder, B. E., 1975, "On the effects of a gravitational field on the turbulent transport of heat and momentum," *Journal of Fluid Mechanics*, Vol. 67, No. 3, pp. 569-581.

Launder, B. E., 1996, "An Introduction to Single-Point Closure Methodology," In T. B. Gatski, M. Y. Hussaini, and J. L. Lumley, ed., *Simulation and Modeling of Turbulent Flows*, Chapter 6, pp. 243-310, Oxford University Press.

Libby, P. A., and Bray, K. N. C., 1981, "Countergradient Diffusion in Premixed Turbulent Flames," *AIAA Journal*, Vol. 19, No. 2, pp. 205-213.

Lindstedt, R. P., and Váos, E. M., 1996a, "Modelling of premixed turbulent flames with second moment methods," Paper submitted for publication in *Combustion and Flame*.

Lindstedt, R. P., and Váos, E. M., 1996b, "Closure of Second Moment Equations for Turbulent Premixed Flames in the Flamelet Regime," Technical Report TF/96/04, Mechanical Engineering Department, Imperial College of Science, Technology and Medicine, London.

Lumley, J. L., 1978, "Computational Modelling of Turbulent Flows," *Advances in Applied Mechanics*, Vol. 18, pp. 123-176.

Lumley, J. L., 1992, "Some comments on turbulence," *Physics of Fluids A*, Vol. 4, No. 2, pp. 203-211.

Lumley, J. L., 1996, "Fundamental Aspects of Incompressible and Compressible Turbulent Flows," In T. B. Gatski, M. Y. Hussaini, and J. L. Lumley, ed., *Simulation and Modeling of Turbulent Flows*, Chapter 1, pp. 5-78, Oxford University Press.

Mastorakos, E., 1993, *Turbulent Combustion in Opposed Jet Flows*, Ph. D. thesis, University of London.

Pope, S. B., 1994, "On the Relationship between Stochastic Lagrangian Models of Turbulence and Second Moment Closures," *Physics of Fluids*, Vol. 6, No. 2, pp. 973-985.

Rutland, C. J., and Cant, R. S., 1994, "Turbulent Transport in Premixed Flames," In *Proceedings of the Summer*

*Program*, Center for Turbulence Research, Stanford.

Trounev, A., Veynante, D., Bray, K. N. C., and Mantel, T., 1994, "The coupling between flame surface dynamics and species mass conservation in premixed turbulent combustion," In *Proceedings of the Summer Program*, Center for Turbulence Research, Stanford.

Zhang, S., and Rutland, C. J., 1995, "Premixed Flame Effects on Turbulence and Pressure-Related Terms," *Combustion and Flame*, Vol. 102, pp. 447-461.

## FIGURES

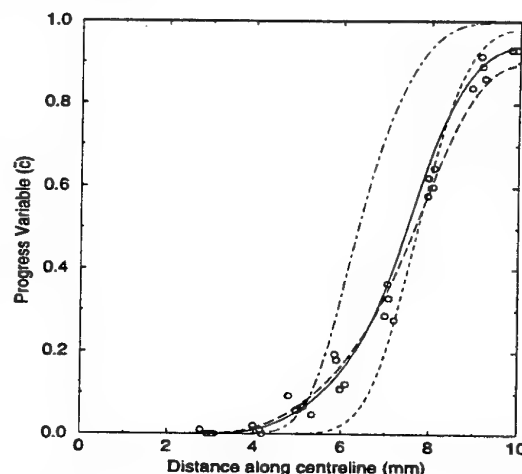


Figure 1: Predicted and measured (Mastorakos 1993) reaction progress variable predictions along the centreline. Symbols ( $\circ$ ) experiment. Lines : (---) gradient diffusion closure for turbulent scalar fluxes with  $C_R = 2.6$ ; (- · -) gradient diffusion closure with  $C_R = 4.5$ ; (- - -) second moment closure with standard dissipation equation; (—) second moment closure with extended dissipation equation.

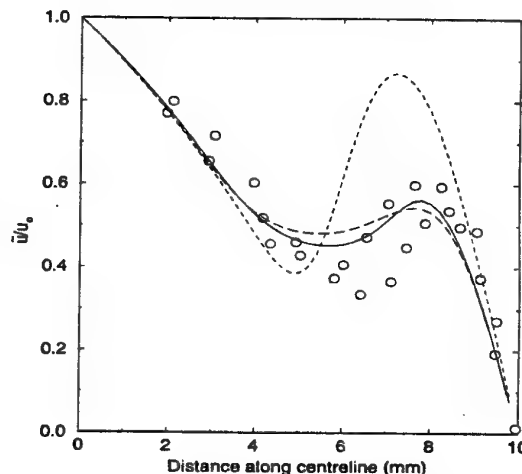


Figure 2: Predicted and measured (Mastorakos 1993) axial velocity profiles along the centreline. Velocity is normalised by the burner exit velocity on the centreline ( $u_0$ ). Symbols ( $\circ$ ) experiment. Lines : (---) gradient diffusion closure for turbulent scalar fluxes with  $C_R = 4.5$ ; (- - -) second moment closure with standard dissipation equation; (—) second moment closure with extended dissipation equation.

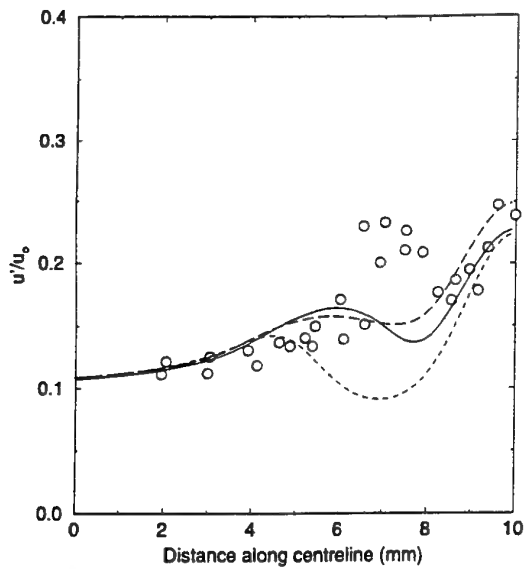


Figure 3: Predicted and measured (Mastorakos 1993) axial intensity profiles on centreline. Symbols, lines and normalisation as in Figure 2.

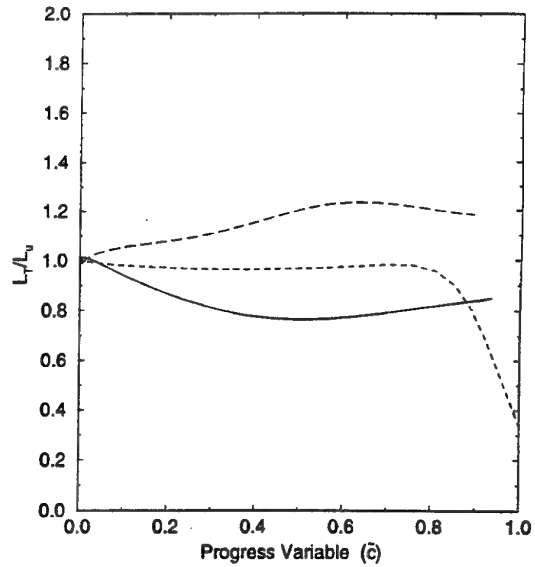


Figure 5: Length scale evolution in progress variable space, on the centreline for the flame of Mastorakos (1993). Lines as in Figure 2.

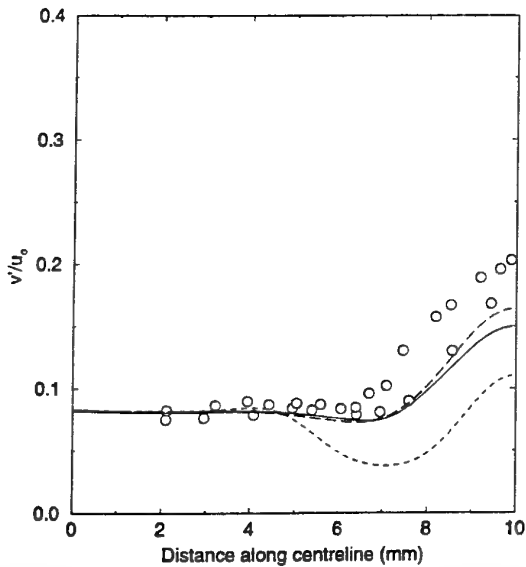


Figure 4: Predicted and measured (Mastorakos 1993) radial intensity profiles on centreline. Symbols, lines and normalisation as in Figure 2.

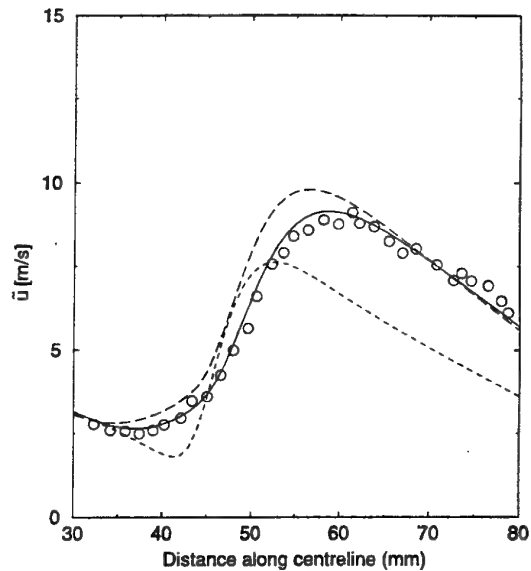


Figure 6: Predicted and measured (Cheng & Shepherd 1991) axial velocity profiles along the centreline. Symbols and lines as in Figure 2.

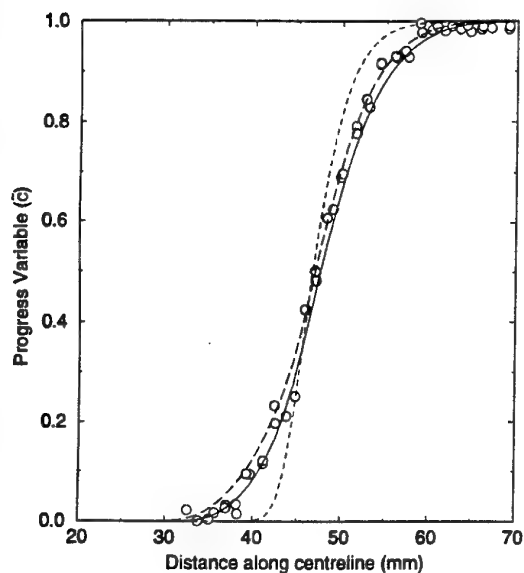


Figure 7: Predicted and measured (Cheng & Shepherd 1991) reaction progress variable profiles along the centreline. Symbols and lines as in Figure 2.

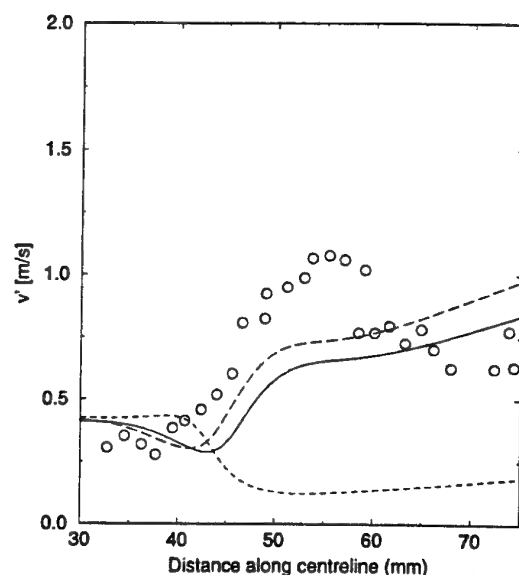


Figure 9: Predicted and measured (Cheng & Shepherd 1991) radial intensity profiles on centreline. Symbols, lines and normalisation as in Figure 2.

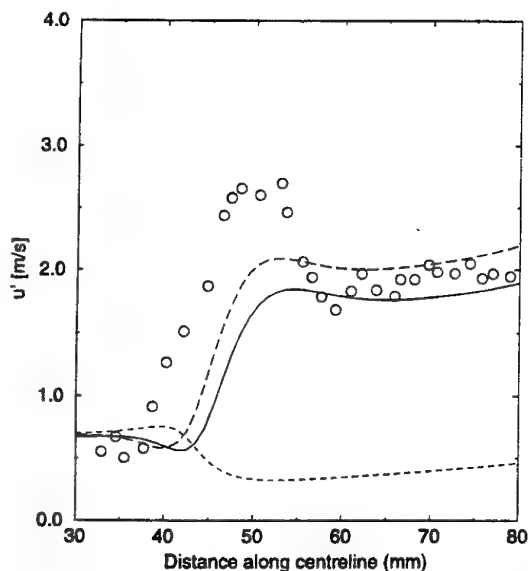


Figure 8: Predicted and measured (Cheng & Shepherd 1991) axial intensity profiles on centreline. Symbols, lines and normalisation as in Figure 2.

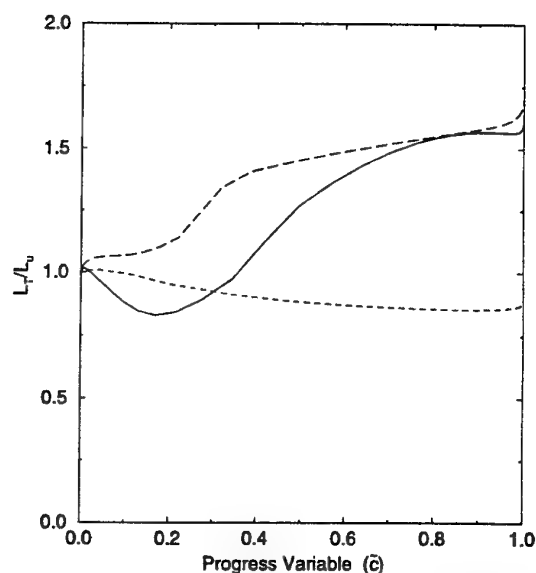


Figure 10: Length scale evolution in progress variable space, on the centreline for the flame of Cheng & Shepherd (1991). Lines as in Figure 2.

**DIRECT NUMERICAL SIMULATION OF 2-D COMPRESSIBLE CHEMICALLY  
REACTING MIXING LAYER WITH COMPACT DIFFERENCE SCHEME**

**G. Cai, F. Zhuang, D. Fu**

Fluid Mechanics Institute  
Beijing Univ. of Aero. and Astro.  
Beijing 100083  
China

See late papers



# TWO-POINT VELOCITY MEASUREMENTS IN NON REACTING AND REACTING TURBULENT STAGNATION FLOWS

E. Bourguignon, Y. Michou, I. Gökalp

Laboratoire de Combustion et des Systèmes Réactifs  
Centre National de la Recherche Scientifique  
1c, avenue de la recherche scientifique  
45071 Orléans cedex 2, France

## ABSTRACT

Two-point velocity measurements have been made in opposed jet and stagnation plate configurations, both in reacting and non-reactive flows. The evolution of the turbulence characteristics for the two flow configurations has been determined in the non-reactive case, but only for the opposed jet configuration for the reacting case. The validity of the Taylor hypothesis for large turbulent scales has been checked. It is concluded that the Taylor hypothesis is not appropriate for the opposed jet configuration due to the intrinsic instability of the stagnation plane in this configuration. In the reacting case, the flame front behaves like a stagnation plane and influences the variation of turbulence scales.

## INTRODUCTION

The spatial correlation function of flow velocity provides information about the length scales of turbulent fluctuations. Laser Doppler velocimetry performed simultaneously in two points of the flow field allows determination of both longitudinal and transversal spatial correlations. It is also possible to obtain these correlation functions from the time correlation (or auto-correlation) by invoking the Taylor hypothesis (Taylor, 1938). This hypothesis is valid under the condition of isotropic turbulence for a steady turbulent flow field exhibiting a dominant mean velocity. However, for certain flow configurations the limits of its validity are not clear. The stagnation point flow configuration studied here is one example where the Taylor hypothesis has to be tested. This flow configuration is of interest in turbulent combustion studies (Cho et al., 1988, Kostiuk et al., 1991; Mounaïm-Rousselle, 1993) for the particular flame characteristics it allows (Mounaïm-Rousselle and Gökalp, 1994). Up to now, the turbulent flow conditions (turbulence intensities and the integral length scales obtained via the Taylor hypothesis) at the exit of the burner have been taken as the reference conditions to characterise the turbulent flame regimes in this configuration. However, due to the divergence of the stagnation

point flow, turbulence characteristics are supposedly changing when approaching the flame stabilised in the vicinity of the stagnation plane. The aim of this study is to characterise the evolution of the turbulence characteristics in the stagnation point flow and to determine the validity limits of Taylor hypothesis in this flow configuration (Bourguignon, 1997).

## EXPERIMENTAL SET-UP

Figure 1 shows the experimental set-up. Two geometrically identical burners (30 mm diameter) are mounted on a computer controlled two-axes traverse system. The upper burner is water-cooled. The burners are supplied with identical premixed methane/air mixtures. The nozzles are placed such that the generated opposed jet flow field produces an axisymmetric free stagnation plane. The jets are surrounded by a co-flow of air (exit section 50 mm) that homogenises the turbulence and reduces the low frequency bouncing of the flames (Mounaïm and Gökalp, 1993). Thus, a uniform velocity profile for large radial distances is preserved. A perforated plate, placed at 40 mm upstream of the nozzle exit generates the turbulence. The perforated plates have 3 mm holes and a blockage ratio of 50%. The turbulence intensity at the exit of the nozzle is 10% with an integral length scale of 3.5 mm.

The flow velocities are measured by laser Doppler velocimetry operated in the one-component mode, where only the axial mean and fluctuating velocities are measured. A 1.5 Watts green (514.5 nm) beam from an argon-ion laser is focused in an optical fibre. The green beam is separated into two beams; one is frequency shifted by a Bragg cell and a differential frequency of 5 MHz is used to remove the directional ambiguity.

The probe volume arrangement for two point measurements is inspired from Pfeifer (1986). The first probe volume is formed by the incoming two laser beams. Light scattered out from this probe volume is collected by a lens and focused onto the first photo-multiplier. The second probe volume is produced by imaging the first probe volume with a spherical mirror. Light scattered from the second probe volume is directed onto the

second photo-multiplier. The distance separating the probe volumes may be varied from zero to 30 mm by turning the spherical mirror and by displacing the second probe volume and the second collection optics.

Doppler bursts are collected by two photo-multipliers placed in the forward scattering direction for each probe volume at approximately  $15^\circ$  from the optical axis. The signals (low passed at 10 MHz, and high passed at 1 MHz) are analysed by a TSI processor IFA 755 to determine the local flow velocity. The signals from the LDV processor are amplified before computer storage for post-processing. The data are analysed to obtain the mean and rms fluctuations of the velocity. Seeding is provided by oil droplets with mean size less than  $1\text{ }\mu\text{m}$  introduced into the flow by an atomiser.

The figure 2 shows the measurement arrangement. One-component velocity measurements are made along the axial direction. The first step for the measurement consists in making the two probe volumes merged. The second step is to separate progressively the second volume from the first one which is fixed. The velocity measurements are made simultaneously for the two probe volumes by using the coincidence mode acquisition and a coincidence time window of  $10\text{ }\mu\text{s}$ .

## EXPERIMENTAL RESULTS

### Non reactive flows

Experiments were conducted on two stagnation point flow configurations : the stagnation plate stabilised flow (configuration A) and the opposed jet flows (configuration B). Earlier studies of Mounaïm-Rousselle (1993) have shown that in the opposed jet configuration, the stagnation plane is unstable and generates perturbations at low frequencies in the flow field. This issue can be pointed out by comparing the auto-correlation functions obtained for the two configurations coefficients of the configuration B are higher for larger time

(figure 3 and figure 4), at the same position in the flow and for the same exit conditions. They show that the auto-correlation delays than for the configuration A. The low frequency movements of the flow in configuration B, due to the stagnation plane instabilities, induce an increase of the auto-correlation coefficients for high time delays. Consequently, the determination of the integral time scale from the auto-correlation functions will be affected. Indeed, one can apply two usual methods to determine the integral time scale from the auto-correlation function : first, by integrating the auto-correlation function from zero time delay to the time delay for which the auto-correlation coefficient is equal to 0, or, second, by equating it to the time delay for the auto-correlation coefficient equal to  $1/e$ . These two methods are used here for the two configurations, between the exit of the burner ( $Z/D = 1$ ), with  $D$  the diameter of the burner, and the axial position  $Z/D = 0.2$  near the stagnation plane. For the configuration A (figure 5), the two methods give the same results. In this case, the auto-correlation function can be approximated by an exponential function. On the other hand, the results obtained for configuration B are different (figure 6); the auto-correlation function here can not be represented entirely by an exponential function, because of its behaviour at long time delays. This is an important point because of its influence on the determination of the integral length scales via the Taylor hypothesis. In order to verify the validity of the Taylor hypothesis for the two stagnation point flow configurations, we performed a comparison between the integral length scale obtained via the Taylor hypothesis and the one directly determined by using the two-point LDV measurements. This technique allows us to determine the space-time correlation between the two probe volumes. From these space time correlation functions, the spatial correlation function is obtained for zero time delay, which then allows us to determine the integral length scale.

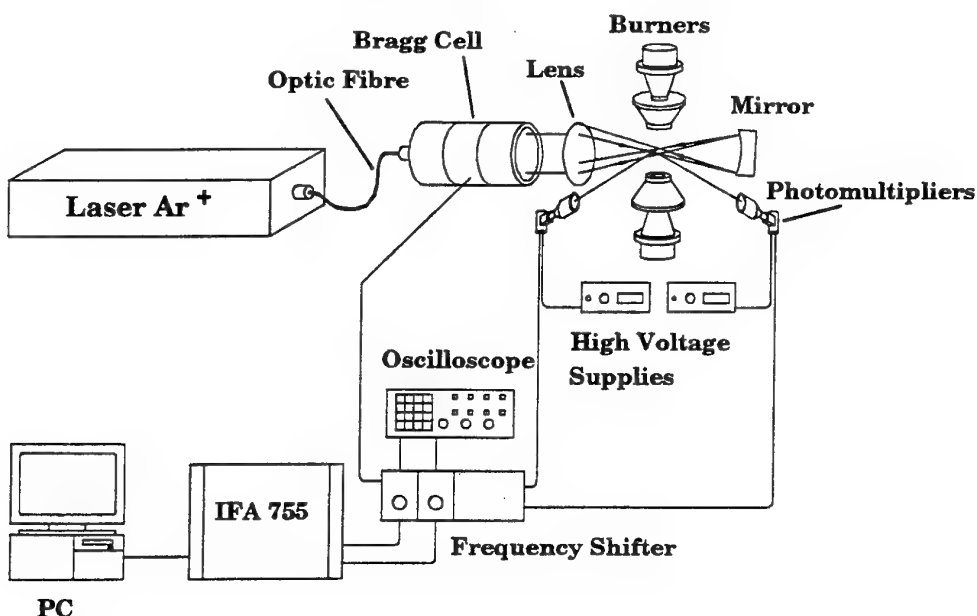


FIGURE 1 - SCHEMATIC REPRESENTATION OF THE EXPERIMENTAL SET-UP

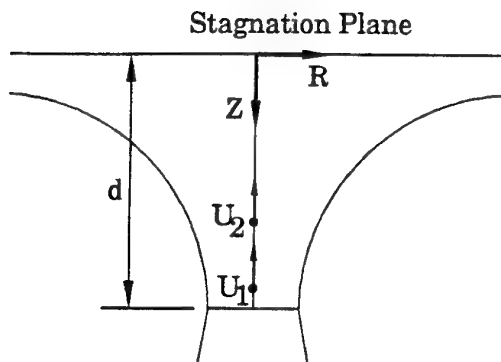


FIGURE 2 - EXPERIMENTAL CONFIGURATION FOR VELOCITY MEASUREMENTS

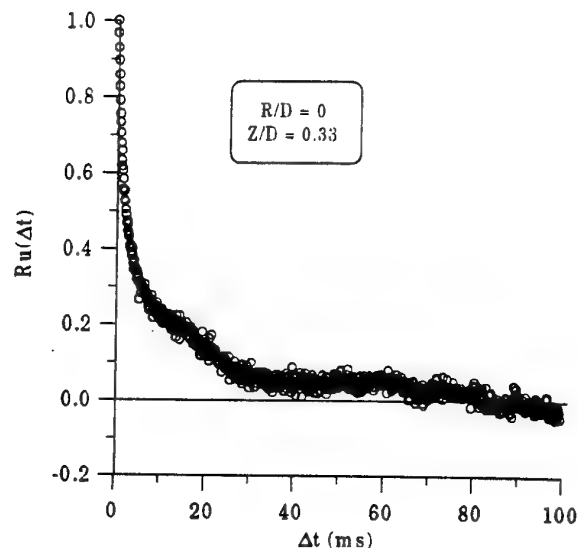


FIGURE 4 - AUTO-CORRELATION FUNCTION  $R_u(\Delta t)$  FOR CONFIGURATION B

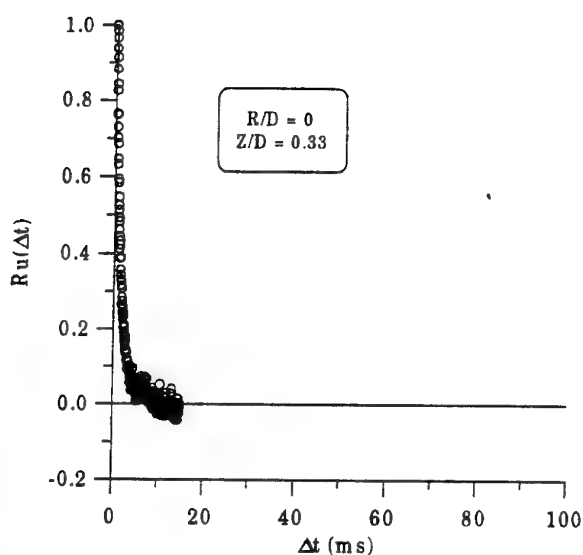


FIGURE 3 - AUTO-CORRELATION FUNCTION  $R_u(\Delta t)$  FOR CONFIGURATION A

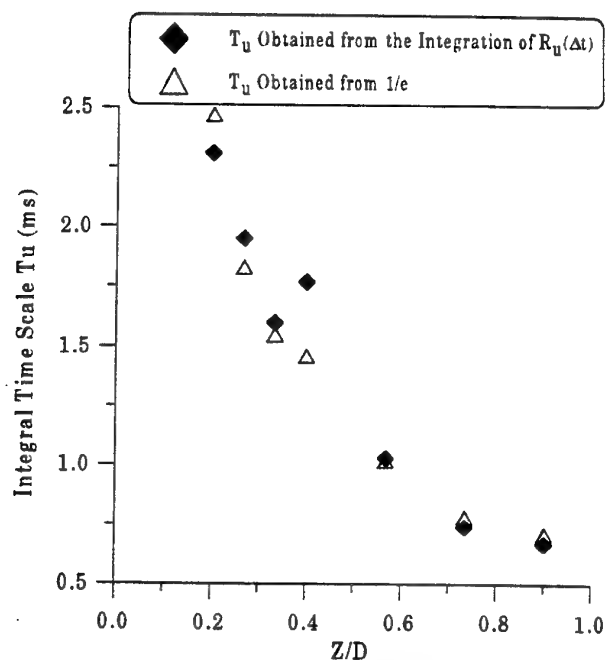


FIGURE 5 - VARIATION OF THE INTEGRAL TIME SCALE FOR CONFIGURATION A

There is then two possibilities (figure 7). If the two probe volumes can be separated enough to obtain a spatial correlation coefficient between the two points equal to zero (which is the case for measurement positions close to the burner exit section,  $Z_1 = -27$  mm on figure 7), then the spatial correlation function is entirely determined. However, if the two probe volumes can not be separated enough, because of the presence of the stagnation plane (which is the case for measurement points in the vicinity of the stagnation plane,  $Z_1 = -6$  mm on figure 7), then the spatial correlation function is truncated. In order to find a general method to determine the integral length scales in

all cases, we compare here the two methods to determine the integral length scale (integration of the spatial correlation function or the value of the separation between the probe volumes for a spatial correlation coefficient equal to  $1/e$ ). Figure 8 shows the determination of the integral length scale by using the two methods when the spatial correlation function is entirely determined. The results are identical in this case. Therefore, concerning the truncated spatial correlation functions, we use the method at  $1/e$  to estimate the integral length scale.

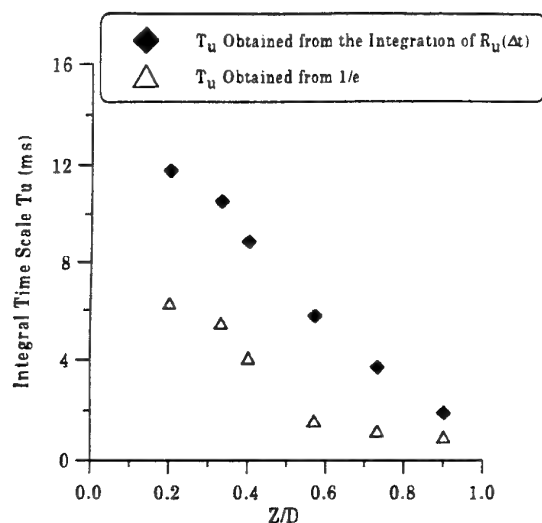


FIGURE 6 - VARIATION OF THE INTEGRAL TIME SCALE FOR CONFIGURATION B

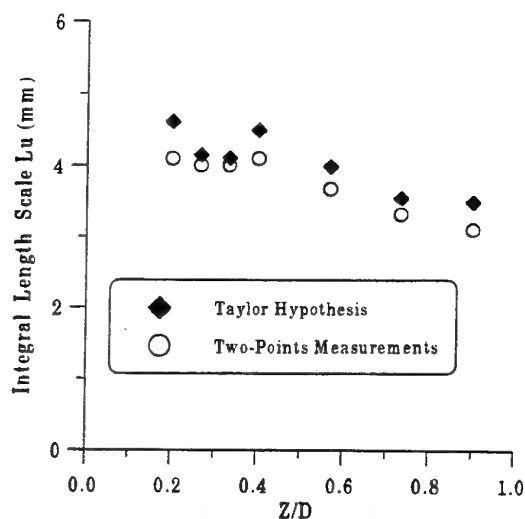


FIGURE 9 - AXIAL VARIATION OF THE INTEGRAL LENGTH SCALE FOR CONFIGURATION A

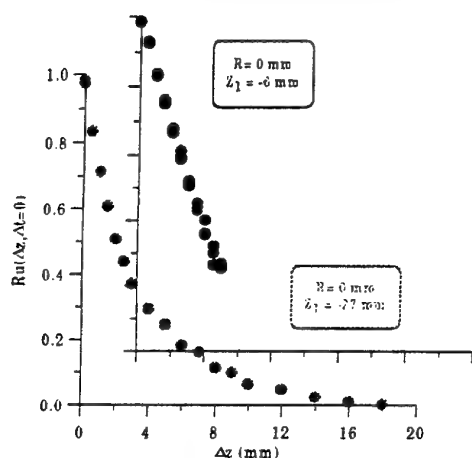


FIGURE 7 - SPATIAL CORRELATION FUNCTIONS FOR CONFIGURATION A

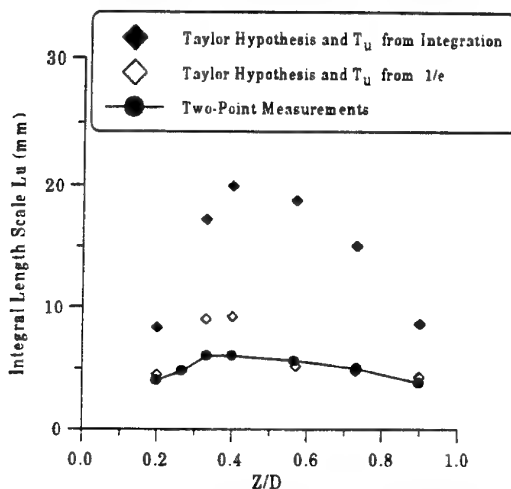


FIGURE 10 - AXIAL VARIATION OF THE INTEGRAL LENGTH SCALE FOR CONFIGURATION B

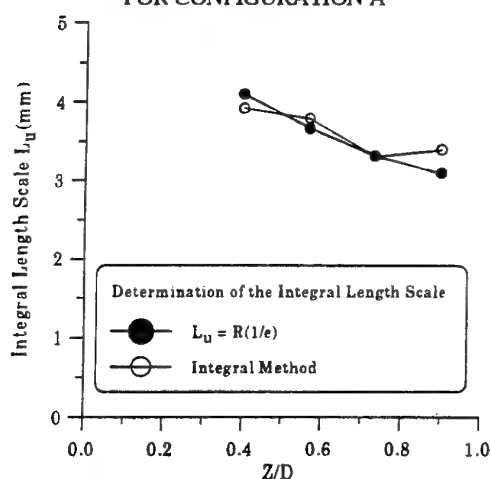


FIGURE 8 - COMPARISON BETWEEN THE TWO METHODS FOR THE DETERMINATION OF THE INTEGRAL LENGTH SCALE

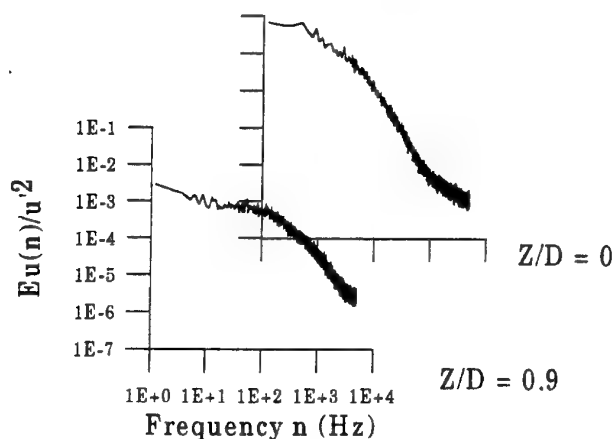


FIGURE 11 - SPECTRAL DENSITY FUNCTIONS FOR CONFIGURATION B

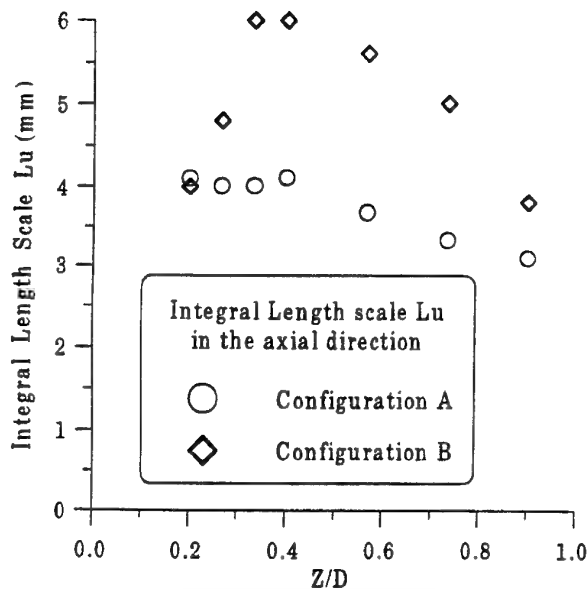


FIGURE 12 - VARIATION OF THE INTEGRAL LENGTH SCALE IN THE AXIAL DIRECTION FOR CONFIGURATIONS A AND B

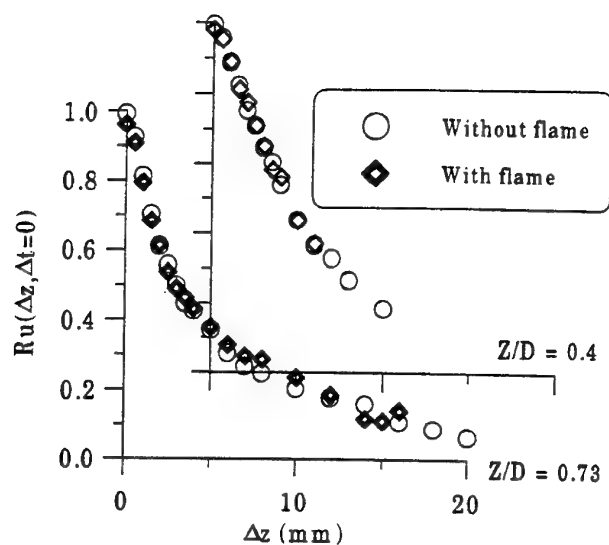


FIGURE 14 - LONGITUDINAL SPACE CORRELATION FUNCTIONS IN REACTING AND NON-REACTING FLOWS FOR CONFIGURATION B

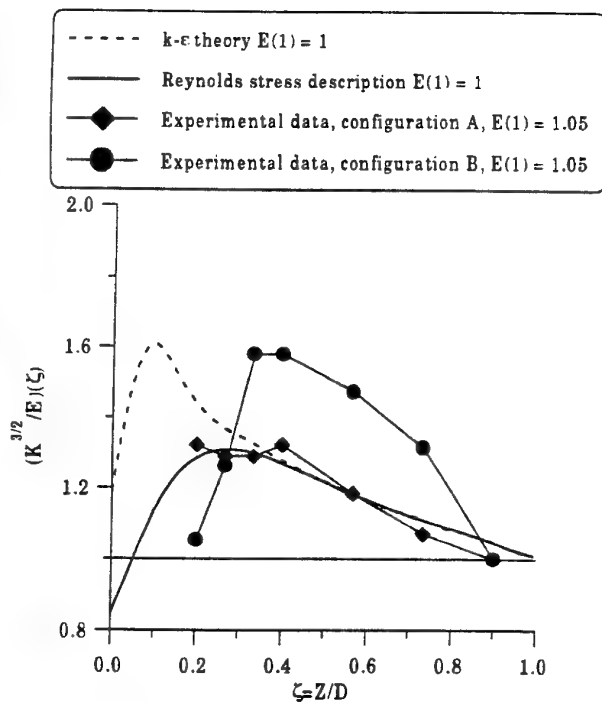


FIGURE 13 - COMPARISON BETWEEN EXPERIMENTAL DATA AND MODEL PREDICTIONS

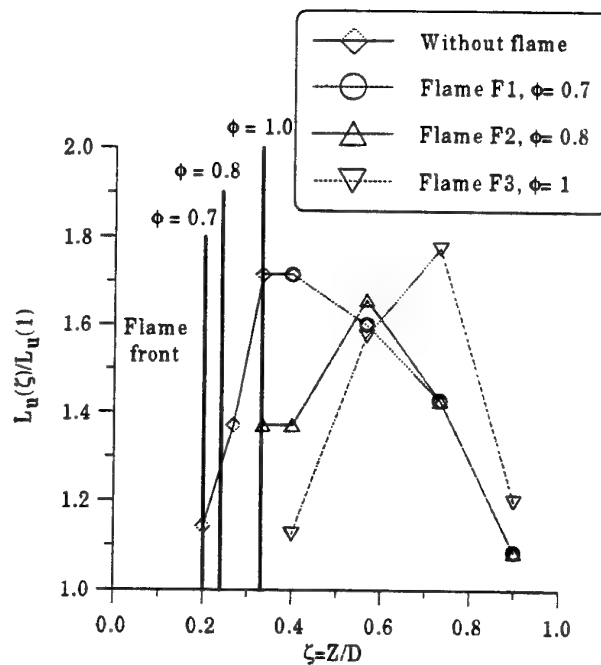


FIGURE 15 - INFLUENCE OF THE TURBULENT FLAME FRONT ON THE EVOLUTION OF THE INTEGRAL LENGTH SCALE

We can now determine the variation of the integral length scale for the two configurations (figure 9 and figure 10) and compare with the results obtained with the Taylor hypothesis. We can see that the two methods are in agreement in the case of configuration A. for measurements between  $0.2 < Z/D < 1$ . In the case of the measurements made in the configuration B

(figure 10), the results obtained via the Taylor hypothesis lead to an overestimation of the integral length scale compared to two-point measurements. In the case of configuration B (figure 4), due to the instability of the stagnation plane, an important fraction of the turbulent kinetic energy is concentrated at low frequencies, as shown by the spectra on figure 11, between 0

and 100 Hz. These low frequencies affect the auto-correlation functions so that we can not use them to evaluate the integral time scale (and consequently the integral length scale).

If we compare the results obtained directly by two-point measurements (figure 12), we also note a difference of the evolution of the integral length scale between the two configurations.

### Comparison with the model predictions

The experimental results for configurations A and B are compared with two models (figure 13). The first one is for opposed jets, with a  $k-\epsilon$  turbulence model by Bray et al. (1994); the second one is a Reynolds stress model by Champion and Libby (1993). To proceed, they introduced a dimensionless turbulent kinetic energy  $K(\zeta) \equiv k(\zeta)/k_0$  and a dimensionless mean viscous dissipation rate  $E(\zeta) \equiv \epsilon(\zeta)d/k_0U_0$ , with  $k_0$  and  $U_0$ , the turbulent kinetic energy and the mean axial velocity at the exit of the burner, respectively and  $\zeta = Z/d$ , a dimensionless axial position in the flow. A definition of the integral length scale at the exit of the burner is given by  $L = k_0^{3/2}/\epsilon_0$ , and in the flow by  $L(\zeta) = k(\zeta)^{3/2}/\epsilon(\zeta)$  (Champion and Libby, 1993). They show that the evolution of the turbulence from the exit to the neighbourhood of the stagnation plane is subject to initial conditions, at the exit of the burner ( $\zeta = 1$ ). These initial conditions can be grouped as  $E(1) = k_1^{1/2}d/L_0U_0$ . Figure 13 shows the distribution of a dimensionless measure of the turbulent length scale  $K(\zeta)^{3/2}/E(\zeta) = L(\zeta)/L_0E(1)$  for a value of  $E(1) = 1$ . The experimental conditions are here very close to those of the model with  $E(1) = 1.05$ . The qualitative evolution of the integral length scale is found to be in agreement with the distribution given by the model predictions. However, quantitatively, the Reynolds stress model give better results. The evolution of the turbulent length scale for configuration A is well represented. In the case of configuration B, the evolution of the integral length scale is underestimated by the Reynolds stress model. This seems to be due to the fact that the model does not into account take the influence of the hydrodynamic instability of the stagnation plane on the global evolution of the turbulent structure of the flow.

### REACTIVE OPPOSED JET FLOWS

Figure 14 shows the spatial correlation functions at two different axial locations of the fixed measurement volume, for the reacting case with the opposed jet configuration. The equivalence ratio of the flame is 0.7, and this lean flame is very close to extinction. For both measurement locations, the spatial correlation functions in the reacting and non-reacting cases are identical, indicating that the lean flame is not enough energetic to modify the turbulence structure in the upstream flow and non-reacting turbulence characteristics can be used for predicting flame extinction conditions. If we observe now the influence of richer flames (figure 15), farther from extinction limits, we note that the flame front has an effect on the upstream flow. The turbulent structures are then perceptively modified from the exit of the burner to the flame front. The global evolution of the integral length scale is the same as the non reactive case but the flame front acts as a stagnation plane and force the turbulence scale to be modified.

### CONCLUSION

Two-point velocity measurements have been made in opposed jet flow and stagnation plate configurations. The Taylor hypothesis is valid in a flow stabilised by a plate for the large scale of the turbulence when  $Z/D > 0.2$ , but can not be used to evaluate the integral length scale of the turbulence in an opposed jet flow due to the influence of the hydrodynamic instability of the stagnation plane and its consequence on the auto-correlation function. The integral length scales are compared with the model predictions. The second order (i.e. Reynolds stress) model can predict the global evolution of the integral length scale in a turbulent impinging jet. In the reactive case, the flame front is found to behave like a stagnation plane and able to modify perceptively the turbulent structure in the upstream flow

### ACKNOWLEDGMENTS

This work is supported by the CNRS and the Conseil Régional du Centre.

### REFERENCES

- Bourguignon, E., 1997, Etude expérimentale de la combustion turbulente de prémélange dans un écoulement à jets opposés, *PhD thesis*, University of Orléans.
- Bray, K.N.C., Champion, M., and Libby, P.A., 1992, "Premixed Flames in Stagnating Turbulence: Part III- The  $\bar{k} - \bar{\epsilon}$  Theory for Reactants Impinging on a Wall", *Combustion and Flame*, vol. 91, pp 165-186.
- Bray, K.N.C., Champion, M., and Libby, p.a., 1994, "Flames in Stagnating Turbulence", *Turbulent Reactive Flows* (Eds PA Libby et FA Williams), Academic Press, pp 573-607.
- Champion, M., and Libby, P.A., 1993, "Reynold Stress Description of Opposed and Impinging Turbulent Jets. Part I: Closely Spaced Opposed Jets", *Physics of Fluids*, A 5 (1), pp 203-216.
- Champion, M., and Libby, P.A., 1994, "Reynold Stress Description of Opposed and Impinging Turbulent Jets. Part II: Axisymmetric Jets Impinging on Nearby Walls"- *Physics of fluids*, A 6 (5), pp 1805-1819.
- Cho, P., Law, C.K., Cheng, R.K., and Shepherd, I.G., 1988, "Velocity and Scalar Fields of Turbulent Premixed Flames in Stagnation Flow", *Twenty-Second Symposium (Int.) on Combustion*, pp 739-745.
- Kostiuk, L.W., 1993, "Experimental Study of Premixed Turbulent Combustion in Opposed Streams. Part I and II". *Combustion and Flame*, vol 92, pp 377-409.
- Mounaïm-Rousselle, C., 1993, "Combustion Turbulente Prémélangée dans un Ecoulement à Jets Opposés", *PhD thesis*, University of Orléans.
- Mounaïm-Rousselle, C. and Gökalp, I., 1994, "Strain Effects on the Structure of Counterflowing Turbulent Premixed Flames", *Twenty-Fifth Symposium (Int.) on Combustion*, pp 1199-1205.
- Pfeifer, H.J., 1986, "Correlation and Spectral Density measurements by LDA", ISL rapport.
- Taylor, J.T., 1938, "The Spectrum of Turbulence", *Proc. Roy. Soc. A* 164, p 476

# CHARACTERISTICS OF THE TURBULENT FLOW IN PIPES WITH HELICAL TURBULENCE PROMOTERS

Karen F. F. Vicari and Sergio V. Möller

Programa de Pós-Graduação em Engenharia Mecânica - PROMEC  
Universidade Federal do Rio Grande do Sul - UFRGS  
Rua Sarmiento Leite, 425  
90050-170 - Porto Alegre, RS, Brazil

## ABSTRACT

This paper presents the results of the experimental study of the turbulent flow of air in a circular pipe with helical type internal turbulence promoters. A Pitot tube and hot wires were applied for the measurements of velocity, velocity fluctuations and Reynolds stresses. Statistical functions of the velocity fluctuations, as Auto-Spectral Density Functions and Auto-Correlations, were also determined. Results show that, in general, turbulence characteristics in the pipes with helical turbulence promoters have similar behavior as in the smooth pipe, with higher values. Velocity distribution is affected by the presence of an azimuthal velocity component which gives an helical behavior to the flow in this geometry.

## INTRODUCTION

Heat transfer enhancing devices, like fins or turbulence promoters, are found in heat exchange equipments in the nuclear and process industries. They are used with the purpose of increasing the heat removal ratios from a surface to a coolant. Thermal hydraulic analysis of these equipments must lead to the correct prediction of heat exchange ratios and temperature distribution, which is necessary for the subsequent structural analysis, leading to safe and reliable operating conditions of the equipments.

Thermal hydraulic analysis is made by the solution of balance equations for mass, momentum and energy. In turbulent flows, these equations become more complicated due to the presence of the Reynolds stresses, leading to the so called closure problem of turbulence (Hinze, 1975). Experimental studies for the determination of turbulence characteristics are necessary for the development and validation of models or methods for the solution of these equations.

Studies of flow and heat transfer in ducts or channels with artificial roughness or turbulence promoters, and their consequences, have being subject of the interest of many authors, starting with Nikuradse (1950), the experiment of Rehme (1978) in roughened rod bundles, Chiou (1987) and Kim and Webb (1993) and, more recently, the results of

Blanco (1996) in a heated circular pipe with helical turbulence promoters. By means of the analysis of temperature fluctuations, Blanco (1996) and Blanco and Möller (1996) show that the structure of the turbulent flow is strongly affected by this type of turbulence promoters. In general, these works show the characteristics of flow and/or heat transfer parameters, like pressure drop, velocity and turbulence characteristics distribution, heat transfer coefficient, etc., and confirm the fact that the insertion of artificial roughness or turbulence promoters increases momentum exchange and, in heated channels, the heat exchange ratio. The use of turbulence promoters is, therefore, attractive, and must be considered in applications where the heat transfer must be enhanced.

The purpose of this paper is to describe results of measurements of turbulence characteristics in a circular pipe with helical type internal turbulence promoters, as described in more detail in Vicari (1996).

## EXPERIMENTAL PROCEDURE

A scheme of the test section is shown in Figure 1. Measurements of air flow velocity and velocity fluctuations were performed radially, at three axial positions before the outlet of a 6.0 m long PVC pipe with 65 mm internal diameter. In a length of 1.2 m of the pipe, corresponding to the region of the outlet, turbulence promoters, obtained by the insertion of helical springs made of copper wires of two different diameters, and a fixed pitch of about 30 mm, were inserted. Position 1 is about 30 mm of the outlet. The probes in this case were placed close to the spring for the beginning of the radial traverse. Position 2 corresponds to a traverse in the intermediate positions between two turns of the spring. Position 3 is similar to 1. It was chosen with the purpose of investigating if the flow was developed. Radial position was measured by means of a micrometer and a contact sensor, with a total accuracy of 0.02 mm. Table 1 lists geometry and flow conditions investigated.

Velocity was measured by means of Pitot tubes with 1.3 mm external diameter connected to a Hartmann & Braun ARA 500 pressure transmitter. Velocity and velocity fluctuations for the measurements of Reynolds normal

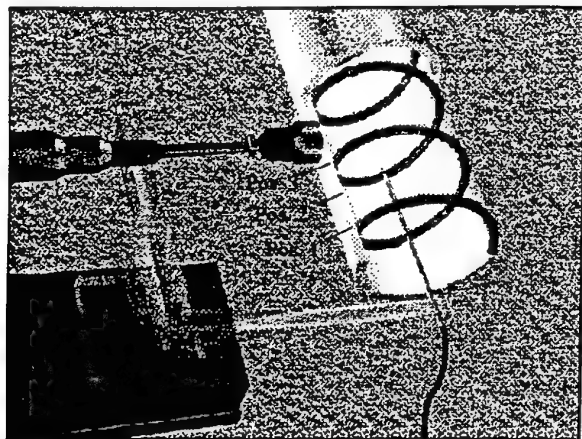


Figure 1: Schematic view of the test section (outlet).

(turbulence intensities) and shear stresses were obtained by means of a DANTEC 55M hot wire anemometer. Axial velocity and its fluctuations were measured with a hot wire probe, with a single wire perpendicular to the direction of the main flow (called "straight" wire probe). Radial and azimuthal velocity components, as well as turbulence intensities and Reynolds shear stresses in these directions, were obtained by means of a single wire probe, having the wire 45° inclined with respect to the main flow direction (called "slant" wire probe) and the results of the measurements with the "straight" wire probe using Collis relations (Collis and Williams, 1959) and the method proposed by Hooper (Hooper, 1980; Vosáhl, 1984; Möller 1988), adapted for this research work.

Data acquisition was carried out with help of a Keithley DAS-58 A/D converter board connected to a personal computer. Velocity and Reynolds stresses measurements, were performed with a sampling frequency of 1 kHz and a time record of 10 seconds. For spectral analysis a sampling frequency of 50 kHz was used and the hot wire output signals were high pass filtered at 1 Hz while a low pass filter set at 20 kHz was also applied. In both cases hot wire output signals were amplified 10.7 times.

Before inserting the turbulence promoters, measurements were performed in the smooth pipe with the purpose of verifying the adequacy of measurement and evaluation techniques. Results of the measurements in the smooth pipe, compared to the literature, showed no significant discrepancies for the velocity and Reynolds stresses distributions.

Analysis of uncertainties in the results shows a contribution of 1.4 % from the measurement equipments (including hot wire, pressure transducer and A/D converter).

## RESULTS

### Velocity Field

Figure 2 shows the dimensionless velocity profile, obtained with all measurements techniques applied. For comparison, as a continuous line, is shown also Nikuradse's "Law of the Wall" (Nikuradse, 1932) distribution of the time-averaged velocity  $\bar{U}$  of the turbulent isothermal flow in a smooth pipe, scaled with the friction velocity  $u^*$ , given, in dimensionless form by

$$u^+ = 2.5 \ln y^+ + 5.5 \quad (1)$$

TABLE 1: Flow conditions.

Probe	Smooth	$a/R=0.086$	$a/R=0.101$
$T (^{\circ}\text{C})$	20.00	19.20	22.40
$P(\text{mmHg})$	759.0	762.4	765.0
$U_m (\text{m/s})$	12.48	11.77	11.85
$Re$	53674	51250	50642
$u^* (\text{m/s})$	0.655	1.755	2.062

In general, the curves have a behavior similar to the "Law of the Wall" with slightly increasing slopes but very lower values.

Overbars will denote, henceforth, time averaged quantities.

The same comparison can be made to Nikuradse's law for the rough pipe (Nikuradse, 1950),

$$u^+ = 2.5 \ln(y/a) + 8.48 \quad (2)$$

where  $a$  is the height of roughness elements (sand in Nikuradse's work). In the present work,  $a$  represents the diameter of the turbulent promoters. A similar behavior for the pipes with turbulence promoters observed in Figure 2 can be found in Figure 3. The lower values of dimensionless axial velocity profiles in the pipes with helical turbulence promoters, shown in both figures 2 and 3, can be immediately attributed to the raise in the friction velocity by the action of the turbulence promoters which increases mean wall shear stress.

This behavior can be associated also to the presence of a radial and an azimuthal components of the mean velocity vector, shown in Figures 4 and 5, respectively  $\bar{V}$  and  $\bar{W}$ , scaled with the velocity at the center of the pipe  $U_{\max}$ . Near the wall the azimuthal component have values that reach about 10% of  $U_{\max}$ , decreasing to zero in the center of the pipe, showing the helical behavior of the flow, reflected also in the radial component, responsible for the flow redistribution.

### Turbulence Measurements

The normal components of the Reynolds stress tensor are usually presented in form of turbulence intensities, i.e. the square root of the mean square value of the component of the velocity fluctuation in axial, radial and azimuthal directions, respectively, scaled with the friction velocity.

The analysis of the turbulence intensity in axial direction, Figure 6, shows, for the pipe with the smaller  $a/R$  ratio, magnitudes similar to those obtained in the smooth pipe. By increasing the  $a/R$  ratio, the values of dimensionless axial turbulence intensities decrease, although their actual values are higher than in the smooth pipe or in the pipe with the smallest  $a/R$  ratio, due to the raise of the flow resistance and of the friction velocity due to the helicoids.

An interesting feature of this component is the presence of an inflection in the largest  $a/R$  ratio. The resulting distribution has almost constant values for  $y/R$  less than 0.4 and greater than 0.8. This behavior can be attributed to the azimuthal component of the velocity and to the helicoidal motion induced by the turbulence promoters.

The other two components, presented in Figures 7 and 8, show, in general, lower values as in the smooth pipe. Only the measurements performed at Position 1 in the largest  $a/R$  ratio are slightly higher than the values in the smooth pipe. The values of the azimuthal and radial turbulence intensities in the presence of the turbulence promoters are higher in the pipe with the largest  $a/R$  ratio.



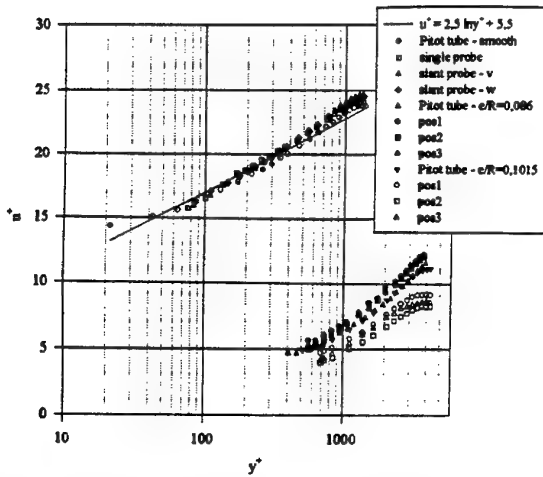


Figure 2: Dimensionless axial velocity profiles in the smooth pipe and in the pipes with turbulence promoters.

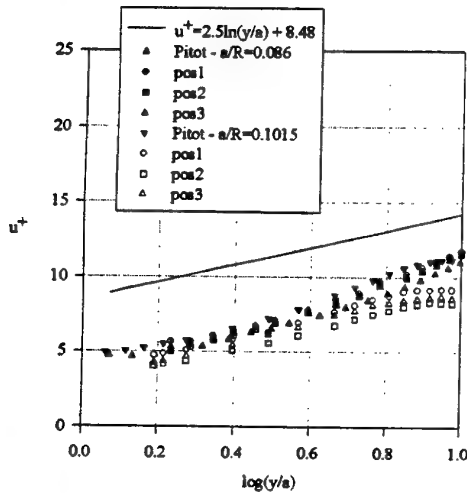


Figure 3: Dimensionless axial velocity profiles in the pipes with helical turbulence promoters.

This behavior is reflected in the plot of the turbulence kinetic energy, Fig. 9, defined as

$$k' = \frac{1}{2} (\overline{u'^2} + \overline{v'^2} + \overline{w'^2}) \quad (3)$$

In Fig. 9, the values of  $k'$ , scaled with the square of the friction velocity  $u^*$ , in the presence of the turbulence promoters are lower than in the smooth pipe, due to the raise in the friction velocity, but the pipe with the largest  $a/R$  ratio presents higher values of the scaled kinetic energy. Helical turbulence promoters, therefore, increase the turbulence intensities in radial and azimuthal directions, rather than axial direction.

The dispersion observed in the results of radial turbulence intensity is attributed to the velocity gradient along the probe wire, to uncertainties in the axial positioning of the probe, and to the fact that, with the present technique the probe must be rotated  $180^\circ$  to perform the measurements.

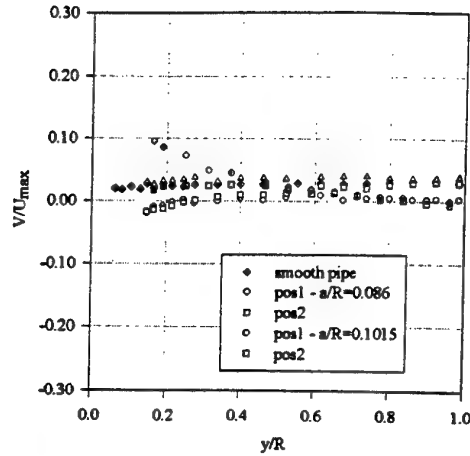


Figure 5: Dimensionless radial velocity profiles in the pipes with helical turbulence promoters.

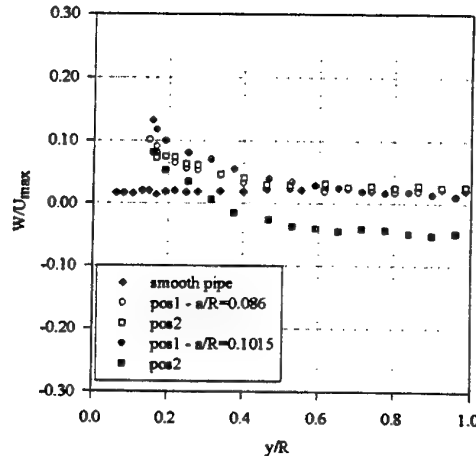


Figure 5: Dimensionless azimuthal velocity profiles in the pipes with helical turbulence promoters.

### Spectral Analysis

The Fourier Analysis is a valuable tool for the study of random phenomena, being widely applied to turbulence studies. Usually, random data are presented in form of time series, representing a continuous (analog) function of time, sampled for digital analysis with a frequency  $f$  as a sequence of numbers at regular time intervals.

The autospectral density function (or power spectrum) represents the rate of change of the mean square value of a certain time function with the frequency  $f$  (Bendat and Piersol, 1986) for an adequate integration (observation) time  $\theta$ . In the Fourier space, the autospectral density function will be defined as the Fourier transform of the autocorrelation function, defined as the mean value of the product of this function at a time  $t$ , with its value at a time  $t+\tau$ .

By defining an one dimensional wave number

$$k_1 = 2\pi f / \bar{U} \quad (4)$$

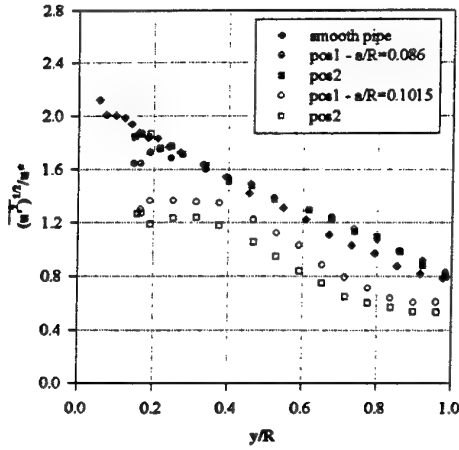


Figure 6: Axial turbulence intensity distribution.

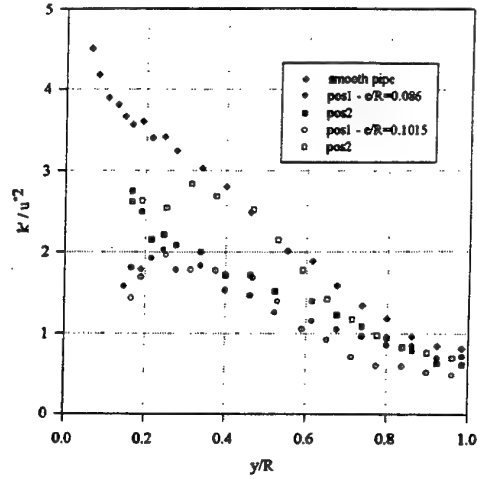


Figure 9: Kinetic energy of turbulence.

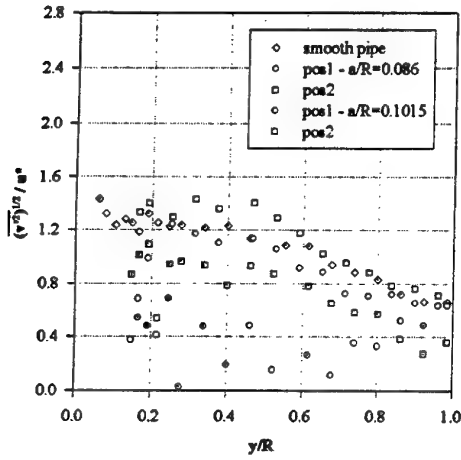


Figure 7: Radial turbulence intensity distribution.

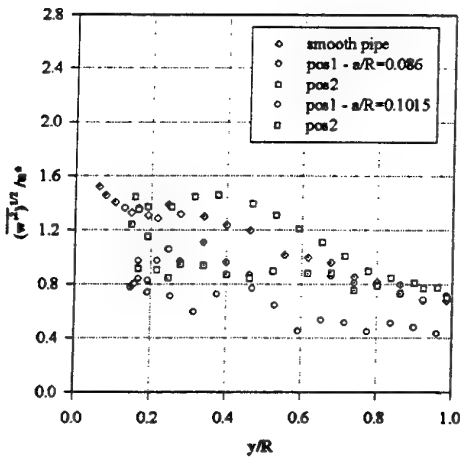


Figure 8: Azimuthal turbulence intensity distribution.

the wave number spectrum of a component  $u'$  of the fluctuating velocity will be given by

$$\phi_{u'u'}(k_1) = \frac{\bar{U}}{2\pi} \phi_{u'u'}(f) \quad (5)$$

Equations (6) and (7) can be rewritten in dimensionless form as

$$k_1^* = k_1 D \quad (6)$$

and

$$\phi_{u'u'}^*(k_1^*) = \frac{\phi_{u'u'}(k_1)}{U_m^2 D} \quad (7)$$

Figures 10 to 12 present the autospectral density of velocity fluctuation on the axial direction of the flow, in the three geometries investigated. The autospectral densities are higher when the turbulence promoters are inserted, however there must exist an optimized ratio for  $e/R$ , for maximum production of energy since the values are higher for  $e/R=0.086$  than for  $e/R=0.1015$ .

In general there is a reduction of the production range ( $-1$ ) as the distance to the wall is increased, but the extension of this range is reduced with increasing  $a/R$  ratio. In this case, it is also noticed that the region with  $-5/3$  exponent is increased, indicating that the production range becomes shorter (as the  $-5/3$  exponent in the spectra appears for smaller wave numbers) and that the diffusion of energy increases. At high wave numbers, the spectra start to assume a  $-7$  exponent. The several narrow peaks at the end of the curves were produced by the high pass filter, without any meaning in this analysis.

It is useful to define an auto correlation coefficient function  $C_{u'u'}$ , obtained by scaling the autocorrelation by the mean square values of  $u'$ . The results of  $C_{u'u'}$ , presented in Figs. 13, show that, as the probe is moved to the center of the pipe,  $C_{u'u'}$  tends more rapidly to zero. This occurs also by including turbulence promoters and increasing  $a/R$  ratio. Although turbulence intensities increase due to the turbulence promoters, time scales are reduced, even in the regions near

the walls, confirming the reduction in the production (-1 range) in the spectra and the enhancement of the turbulent diffusion.

## CONCLUDING REMARKS

This paper presents the experimental result of the temperature fluctuations in a pipe with internal helical turbulence promoters.

The presence of this type of turbulence promoters influences the velocity distribution law, but still having a behavior similar to Nikuradse's "Law of the Wall" for the smooth pipe with lower values as the  $a/R$  ratio is increased. The same was observed when the comparison was made with Nikuradse's law for the rough pipe. This is attributed to the raise in the friction velocity by the action of the turbulence promoters and by the presence of an azimuthal component of the main velocity which gives an helicoidal behavior to the main flow.

Turbulence intensities are also influenced by the helicoidal flow, with higher values than in a smooth pipe, although this fact is not shown in the dimensionless representations, due to the higher values of the friction velocity.

The main feature of the flow in pipes with helical turbulence promoters will be the reduction in the production range of kinetic energy and high turbulence diffusion.

Future investigations will map the entire flow field in a cross section of the pipe, to explain more clearly the presence and effects of the radial and azimuthal velocity components. Double wire probes will be used for spectrum measurements. The search for a friction law (including pressure drop and wall shear stress distribution) is also necessary.

## ACKNOWLEDGMENTS

The support of FAPERGS - Research Foundation of the State of Rio Grande do Sul, through the grant 90.1549-0 and of CNPq - Brazilian Scientific and Technological Council, through the grant 400180/92-8, are gratefully acknowledged.

Karen Vicari thanks also the CNPq for granting her a fellowship.

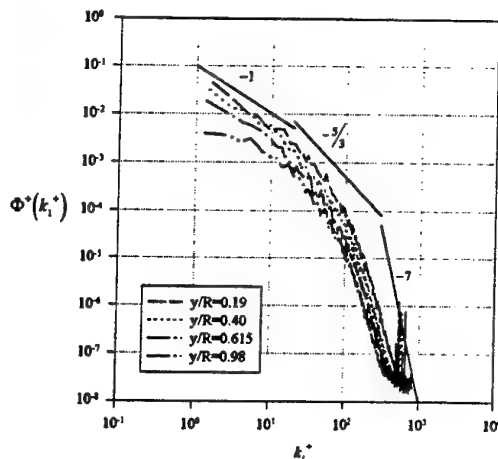


Figure 10: Autospectral Density of Axial Velocity Fluctuations in the smooth pipe.

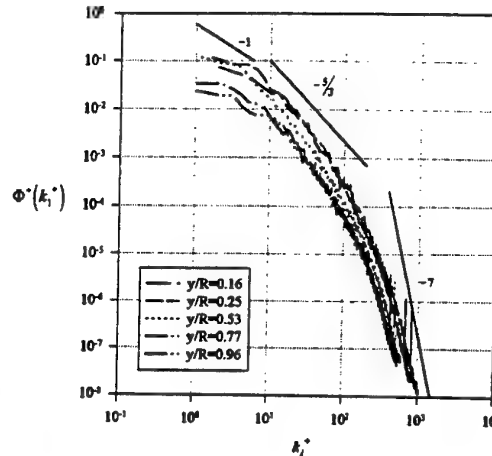


Figure 11: Autospectral Density of Axial Velocity Fluctuations in the pipe with turbulence promoters ( $a/R=0.086$ ) Pos. 1.

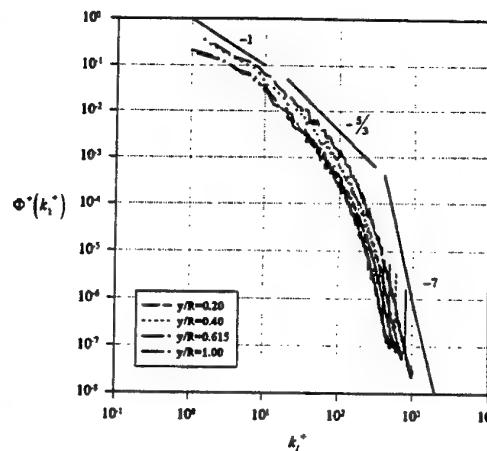


Figure 12: Autospectral Density of Axial Velocity Fluctuations in the pipe with turbulence promoters ( $a/R=0.101$ ) Pos. 1.

## LIST OF SYMBOLS

$a$	Height of turbulence promoter - m.
$A_t$	Cross section area - $m^2$ .
$C_{u'u'}$	Cross correlation coefficient function.
$D$	Pipe diameter - m.
$k_1$	Wave number - $m^{-1}$ .
$k_1^+$	Dimensionless wave number ( $k_1 D$ ).
$r$	Radial coordinate - m.
$R$	Pipe radius - m.
$Re$	Reynolds number ( $U_m D / \nu$ ).
$t$	Time - s.
$\bar{U}$	Axial velocity - m/s.
$u'$	Axial velocity fluctuation - m/s.
$U_m$	Mean axial velocity - m/s.
$U_{max}$	Maximal axial velocity - m/s.
$u^*$	Friction velocity ( $\tau_w / \rho$ ) <sup>1/2</sup> - m/s.

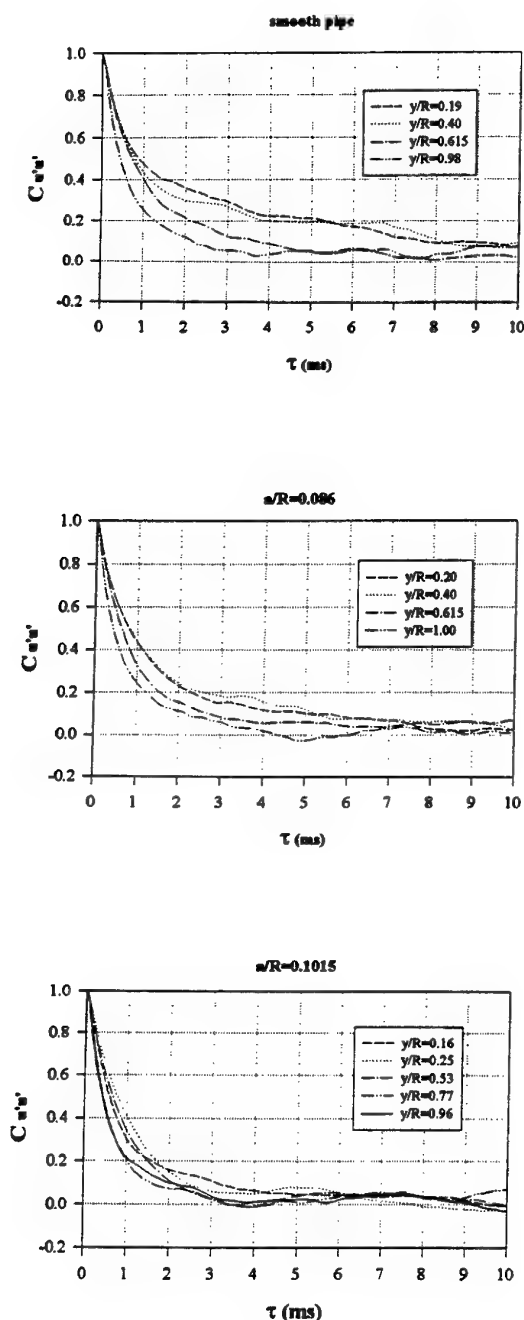


Figure 13: Autocorrelation coefficient functions at several locations in the smooth pipe and in the pipes with turbulence promoters with  $a/R=0.086$  and  $a/R=0.1015$ .

$\bar{V}$	Radial velocity - m/s.
$v'$	Radial velocity fluctuation - m/s.
$\bar{W}$	Azimuthal velocity - m/s.
$w'$	Azimuthal velocity fluctuation - m/s.
$y$	Distance to pipe wall - m.
$y^+$	Dimensionless wall distance ( $y u^* / \nu$ ).
$u^+$	Dimensionless velocity ( $\bar{U} / u^*$ ).

$\phi_{u'u'}$	Autospectral density function ( $m^2/s^2 Hz$ ).
$\phi_{u'u'}^+$	Dimensionless autospectral density function.
$\nu$	Kinematic viscosity - $m^2/s$ .
$\rho$	Density - $kg/m^3$ .
$\tau_w$	Wall shear stress - Pa.

## REFERENCES

- Bendat, J. S. and Piersol, A. G., 1986, "Random Data: analysis and measurement procedures", John Wiley & Sons, New York.
- Blanco, R. L. D. and Möller, S. V., 1995, "Spectral analysis of temperature fluctuations in the turbulent flow through pipes with internal roughness" (in Portuguese), *Proc. X ENFIR, 10th Brazilian Meeting on Reactor Physics and Thermal-Hydraulics*, pp. 196-201, Águas de Lindóia.
- Blanco, R. L. D., 1996, "Experimental study of temperature fluctuations in a heated pipe with internal helical turbulence promoters" (in Portuguese), Dr. Eng. Thesis, PROMEC, Federal University of Rio Grande do Sul - UFRGS, Porto Alegre, Brazil.
- Blanco, R. L. D. and Möller, S. V., 1996, "Experimental study of temperature variance in pipes with internal helical turbulence promoters" (in Portuguese), *Proc. ENCIT/LATCIM 96, 6th Brazilian Congress of Engineering and Thermal Sciences and 6th Latin American Congress of Heat and Mass Transfer*, Vol. 2, pp. 663-668, Florianópolis.
- Chiou, J. P., 1987, "Experimental Investigation of the Augmentation of Forced Convection Heat Transfer in a Circular Tube Using Spiral Spring Inserts", *Transactions of the ASME*, Vol. 109.
- Collis, D. C. and Williams, M. J., 1959, "Two-Dimensional Convection from Heated Wires at Low Reynolds Numbers", *Journal of Fluid Mechanics*, v. 6, pp. 357-384.
- Hinze, O., 1975, "Turbulence", McGraw-Hill, New York.
- Hooper, J. D., 1980, "Fully developed turbulent flow through a rod cluster", Ph. D. Thesis, University of New South Wales.
- Kim, N. H., Webb, R. L., 1993, "Analytic Prediction of the Function and Heat Transfer for Turbulent Flow in Axial Internal Fin Tubes", *Journal of Heat Transfer*, pp. 553-559, Vol. 115.
- Möller, S. V., 1988, "Experimentelle Untersuchung der Vorgänge in engen Spalten zwischen den Unterkanälen von Stabbündeln bei turbulenter Strömung", Dr.-Ing. Dissertation, Universität Karlsruhe (TH), Karlsruhe (also: KfK 4501, 1989).
- Nikuradse, J., 1932, "Gesetzmässigkeit der turbulenten Strömung in glatten Röhren", *VDI, Forschungsheft* 356.
- Nikuradse, J., 1950, "Laws of Flow in Rough Pipes", NASA Technical Memorandum 1292, pp. 1-26, USA.
- Rehme, K., 1978, "The Structure of Turbulent Flow through a Wall Subchannel of a Rod Bundle with Roughened Rods", KfK 2716, Kernforschungszentrum - Karlsruhe, Karlsruhe.
- Vicari, K. F. F., 1996, "Experimental study of the turbulent flow in a pipe with internal helical turbulence promoters" (in Portuguese), M. Eng. Dissertation, PROMEC, Federal University of Rio Grande do Sul - UFRGS, Porto Alegre, Brazil.
- Vosáhlo, L., 1984, "Computer programs for evaluation of turbulent characteristics from hot-wire measurements", KfK 3743, Kernforschungszentrum Karlsruhe, Karlsruhe.

# TURBULENT STRUCTURE OF AN INTERMITTENT REGION OF THE TURBULENT BOUNDARY LAYER INTERACTING WITH CONTROLLED LONGITUDINAL VORTEX ARRAYS

Chiharu FUKUSHIMA  
Dept. of Mechanical Engineering  
Gifu University  
Yanagido 1-1, Gifu 501-11  
Japan

Hideo OSAKA and Gabriela NEDELCU  
Dept. of Mechanical Engineering  
Yamaguchi University  
Tokiwadai 2557, Ube 755  
Japan

## ABSTRACT

Conditional averaged patterns on the outer layer of a turbulent boundary layer has been investigated for further understanding of the developing process of the boundary layer interacting with the spanwise periodic longitudinal vortex arrays which is artificially generated in a free stream. Two parameters, namely, spanwise periodicity of the longitudinal vortex arrays  $L/S$  and the arrangement height of airfoil arrays, were independently varied for five cases. Intermittency factor profiles revealed the effect of pairs of counterrotating secondary flows which showed the downwash flow at the midspan of the airfoil, and conversely, the upwash flow for the center slice of neighboring airfoils. Intermittency factors are remarkably affected by the spacing between neighboring airfoils. The value of the intermittency factor becomes smaller in the inner layer with increasing values of  $L/S$  at the midspan of the airfoil.

## INTRODUCTION

In our previous papers (Osaka and Fukushima 1992, 1996), a flowfield in which the spanwise periodic longitudinal vortex arrays generated in the free stream, moving downstream, interact with the turbulent boundary layer were investigated experimentally. In those studies, it was found that the upwash and downwash secondary flows are caused within the boundary layer due to the longitudinal vortices, and then the turbulence quantities reveal spanwise periodic or aperiodic variations depending on the value of  $L/S$  ( $L$  denotes the spanwise distance between neighboring airfoils,  $S$  the airfoil span). However, in order to understand the relationship between the behavior of the longitudinal vortex arrays, and the modification of the spatial structure in the turbulent boundary layer, it is necessary to discuss the process of the longitudinal vortex arrays breaking into the turbulent boundary layer, considering the modification of turbulent/non-turbulent motions in the outer layer.

There have been few papers discussing the development of the turbulent boundary layer interacting with the longitudinal

vortex arrays generated in the free stream excluding our papers (Furuya et al. 1975a~1979, Osaka et al. 1977, and Nakamura et al. 1987a). Nakamura et al. (1987b) examined the intermittent motions in the outer region of the turbulent boundary layer in the case of  $L/S=1$ . They found that the longitudinal vortex arrays cause the spanwise variation of the intermittency factor profiles; which differ at relative spanwise positions of the arrangement of the airfoil arrays. Cutler and Bradshaw (1993a, 1993b) suggested that the existence of the separation line, which is formed outboard of the vortex, is significant for the development of the turbulent boundary layer interacting with a pair of longitudinal vortex, generated from the delta wing attached at two different heights in the free stream. It can be assumed that the results of the irregular behavior of the longitudinal vortex, such as the vortex wandering, affect the boundary layer properties.

From the results of these studies, it can be understood that the strength of the extra strain rate, due to the longitudinal vortex arrays is significant to manage the turbulent properties of the boundary layer. The examination in these flowfields may raise some interesting issues such as spatial instability (Nishioka 1989) of the turbulent boundary layer, chaotic behavior (Kaneko 1989) (e.g. bifurcation of vortex filament, interchange between coherent and chaotic motion), and the relationship between the steady longitudinal vortices and such unsteady phenomena as; large eddy motion (turbulent bulge) in the outer layer, and bursting phenomenon in the near-wall region.

In the present study, the turbulent structure of an intermittent region (i.e. entrainment process) of the turbulent boundary layer, interacting with the spanwise periodic longitudinal vortex arrays generated in the free stream, was investigated taking the following two aspects into consideration; how the longitudinal vortices are accepted into the boundary layer depending on the value of  $L/S$ , and how they contribute to the variation of the zone averaged patterns of turbulent/non-turbulent motions in the turbulent boundary layer.



boundary layer. When  $L/S=1.07$  (Case 2), the contours are significantly distorted in the spanwise direction at  $x'/\delta_0 \approx 40$ . The intermittent regions are distanced from the wall in the upwash regions of the secondary flow, while they close to the wall in the downwash regions of the secondary flow. The longitudinal vortices seem embedded in the boundary layer, in comparison with the spanwise averaged boundary layer thickness  $\delta_m$ . Although the secondary flows affect the boundary layer, the longitudinal vortices have not embedded within the boundary layer in this section, considering the development of the local (at each spanwise sliced section) boundary layer thickness  $\delta$ . In the cases where  $L/S=4$  (Cases 3 and 5), the longitudinal vortices have embedded deeply within the boundary layer at  $x'/\delta_0 \approx 40$ . The contours then exhibit the spanwise periodic variation, which clearly corresponds to the spanwise arrangement of the airfoils. In these cases (Cases 3 and 5), the intermittent regions are concentrated near the wall at the midspan of the airfoil, and are extended beyond  $\delta_m$  between neighboring airfoils. However, around  $z = \pm 70\text{mm}$  (in the region between neighboring airfoils), the distributions of the contours are not significantly affected by the secondary flows, and almost agree with those of the present two-dimensional turbulent boundary layer. Those regions of the contours are not exactly specified at  $x'/\delta_0 \approx 150$ , since the vorticity of the induced longitudinal vortices diffuse within the whole boundary layer in the streamwise direction.

**Intermittency factor profiles at representative spanwise sliced section.** Figure 3 shows the intermittency factor profiles for five cases at three representative spanwise sliced sections (the midspan of the airfoil, the spanwise edge of the airfoil, and the center between neighboring airfoils) at  $x'/\delta_0 \approx 70$ . In this figure, dotted lines show the two-dimensional turbulent boundary layer profile in the present experiments. The normal distance  $y$  is normalized

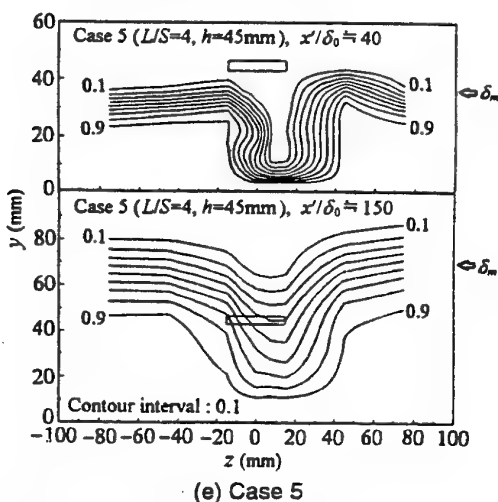
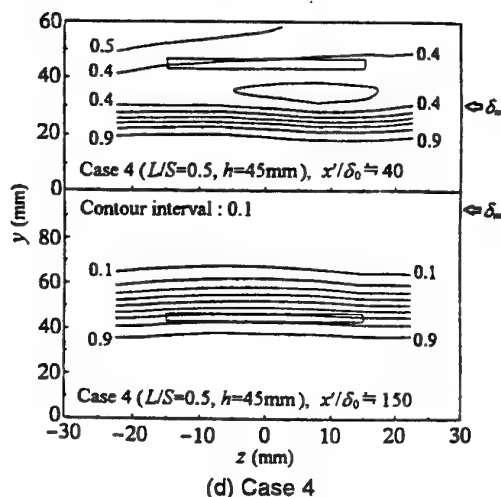
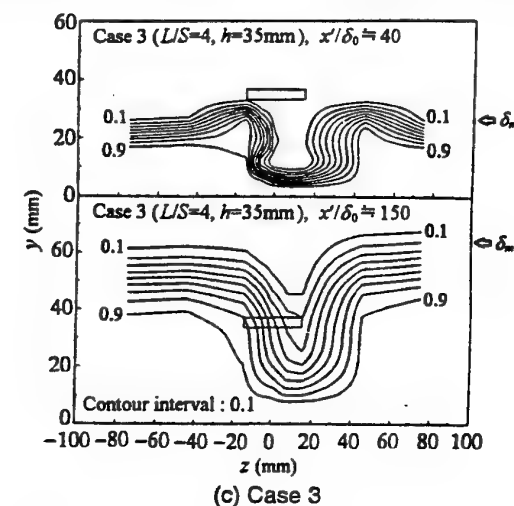
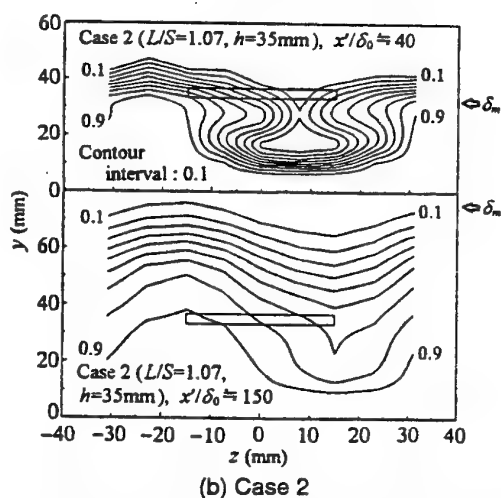
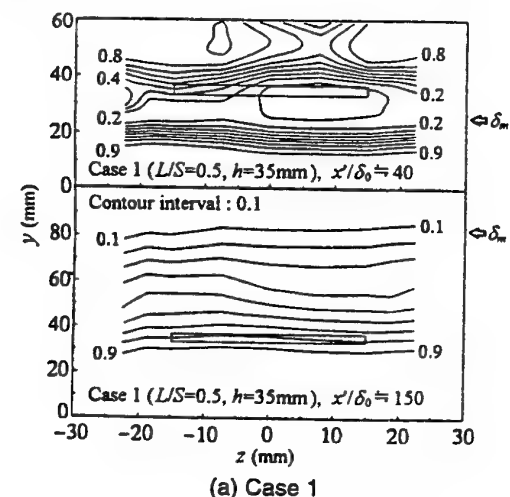


FIGURE 2 CONTOURS OF INTERMITTENCY FACTOR FOR 5 CASES AT  $x'/\delta_0 \approx 40$  AND 150.



with the spanwise averaged boundary layer thickness  $\delta_m$  in each case. In Cases 1 and 4, the variation of the intermittency factor profiles depending on the spanwise sliced sections are not observed in each case. The difference between Cases 1 and 4 is the difference of the relative value of  $\gamma$  to the two-dimensional flow. The values of the  $\gamma$  only in Case 4 are larger than those in the two-dimensional flow even in the boundary layer. One of the reasons of these results, can be explained by the fact that the induced longitudinal vortices in Case 4 trace more upper trajectories, than those in Case 1, due to the effect of the arrangement height of the airfoils. The intermittency factor profiles, in cases where  $L/S \geq 1$  (Cases 2, 3, and 5), exhibit significant spanwise variation which is closely related to the behavior of the induced longitudinal vortices within the boundary layer. In Case 2, the intermittency factor profiles are affected by the secondary flows. Comparing the  $\gamma$  profiles at the three representative slices, it can be seen that there is a difference in scale of  $0.2\delta_m$  at the same value of  $\gamma$ ; that is, the intermittency factor profile at the spanwise edge of the airfoil is larger than that at the other two representative spanwise sliced sections, since the longitudinal vortices, whose origin is the spanwise edge of the airfoil element, gradually drift toward the positive spanwise side while the vortex size increases in the streamwise direction. In Cases 3 and 5, the value of the  $\gamma$  profiles at the midspan of the airfoil is extremely small even in the inner layer of the boundary layer, due to the downwash secondary flow. At the spanwise edge of the airfoil, in Case 3, the profile is affected by the upwash secondary flow (as observed in Case 2), due to the lateral drift of the longitudinal vortices and the downwash secondary flow being restricted to the near wall region due to the embedding of the longitudinal vortices within the inner layer. On the other hand, in Case 5, the profile is smaller than the two-dimensional flow profile in the range of  $y/\delta_m \leq 0.65$ , and is larger in the range of  $y/\delta_m > 0.65$ . This means that there is no upwash/downwash interface in this sliced section owing to the deformation of the secondary flow.

From the results, it can be found that the spanwise periodicity of the longitudinal vortices  $L/S$  control the decaying of the streamwise vorticity and the paths of the longitudinal vortices resulting from the difference of the degree in the interaction between neighboring vortices. Therefore, the  $\gamma$  profiles at the representative spanwise sliced section reveal significant deformation depending on the value of  $L/S$ . The deformed  $\gamma$  profiles owing to the downwash secondary flow

becomes significant behind the midspan of the airfoil with the increasing value of  $L/S$ , and is maintained even in the far downstream section.

As to the effect of the arrangement height of the airfoil, the variation of the intermittency factor profile is described in relation to the behavior of the longitudinal vortices and the secondary flows, mentioned above, independent of the arrangement height. The only difference is that as the boundary layer thickness nominally changes, so does the relative normal position of the deformed  $\gamma$  profile. Therefore, the effect of the arrangement height is recognized to be the effect of the local Reynolds number, as mentioned in the previous work (Osaka and Fukushima 1992, 1996).

#### Large eddy time scales for the intermittent motion

**Turbulent bulge crossing frequency.** Figure 4 shows the turbulent bulge crossing frequency  $f$  ( $s^{-1}$ ) in the representative spanwise sliced sections at  $x'/\delta_0 \approx 70$ . The results are given in the three cases, Case 1 ( $L/S=0.5$ ), Case 2 ( $L/S=1.07$ ), and Case 3 ( $L/S=4$ ). In Case 1, the turbulent bulge crossing frequency  $f$  exhibit similar distributions in each spanwise sliced section. In Case 2, each profile of  $f$ , except at the spanwise edge of the airfoil, has two peak values, although these two values are different. Looking at these peaks, it is thought that the left hand side and the right hand side peak correspond to the influence of the downwash and upwash flows of the secondary flow, respectively. Therefore, two peaks of  $f$  suggest the existence of the distinct downwash/upwash interface of the fluids in these sections. The upwash secondary flow transport high-turbulence fluid from the wall. Whereas, the downwash secondary flow deform, or divide the large eddy (turbulent bulge) to pieces due to the entrainment of the low-turbulence fluid toward the wall; i.e. decrease the large eddy scale. In Case 3, the profile of the bulge crossing frequency between neighboring airfoils almost agrees with that of the two-dimensional flow. Behind the spanwise edge of the airfoil, the profile has two-peak values as observed in Case 2. At the midspan of the airfoil, the value of  $f$  is significantly larger than that of two-dimensional flow profile, due to the effect of the downwash secondary flow. These secondary flows (in Cases 2 and 3), eventually, increase the occurrence of the turbulence zones, and consequently control the level of the peak value. In Cases 4 and 5 (not shown here), distributions of  $f$  exhibit similar variations to those in Cases 1 and 3 respectively.

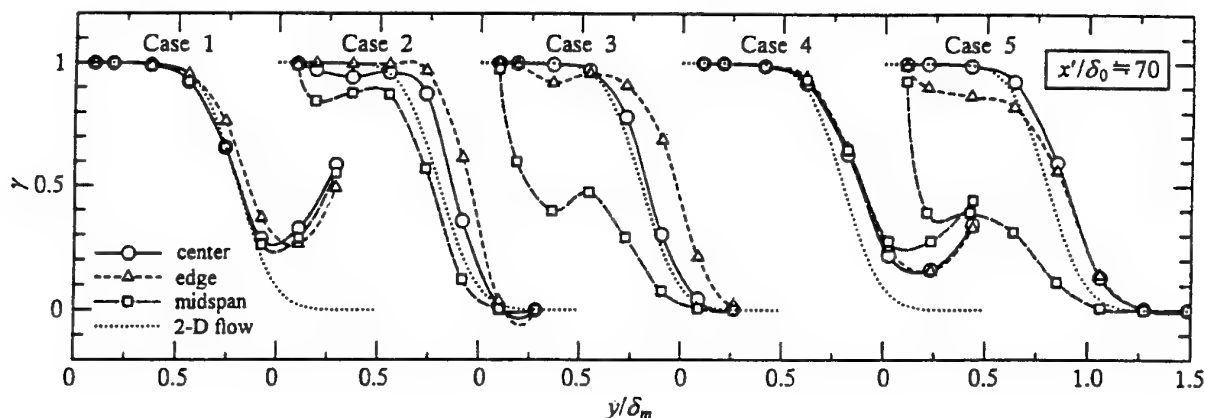


FIGURE 3 INTERMITTENCY FACTOR PROFILES FOR 3 REPRESENTATIVE SLICED SECTIONS AT  $x'/\delta_0 \approx 70$ .



### On/off period of turbulence and non-turbulence.

Figures 5 and 6 shows the zone averages of on/off period of turbulence  $\langle T_m \rangle_T$  and non-turbulence  $\langle T_m \rangle_N$ , respectively. The results are given in the three representative cases. In Case 1, the profiles of  $\langle T_m \rangle_T$  and  $\langle T_m \rangle_N$  almost agree with that of two-dimensional flow within the boundary layer. In cases where  $L/S \geq 1$  (Cases 2, 3, and 5), comparing with the results of the intermittency factor  $\gamma$ , it can be found that the upwash secondary flow, which lift the high-turbulence fluid near the wall, decrease and increase the scale of the non-turbulent and turbulent zones, respectively. On the contrary, the downwash secondary flow, which transports the low-turbulence fluid, decrease and increase the scale of the turbulent and non-turbulent zones, respectively. That is, in Case 2, the profile of  $\langle T_m \rangle_T$  at the spanwise edge of the airfoil is larger than that of the other two representative slices, and the profile at the midspan of the airfoil is smaller than the other two cases. Whereas, the profiles of  $\langle T_m \rangle_N$  are vice versa. In Case 3, at the spanwise edge of the airfoil, on/off period of turbulence  $\langle T_m \rangle_T$  is small in the range of  $y/\delta_m \leq 0.6$ , and that of non-turbulence  $\langle T_m \rangle_N$  is large in the same range. Behind the midspan of the airfoil,  $\langle T_m \rangle_T$  is smaller than that in the two-dimensional flow within the whole layer, and then  $\langle T_m \rangle_N$  becomes large. In comparison with the results (in Case 3) obtained at  $x'/\delta_0 \approx 40$  (not shown here), it can be understood that these features of the  $\langle T_m \rangle_T$  and  $\langle T_m \rangle_N$  profiles correspond to the spanwise paths of the longitudinal vortices which move apart in the streamwise direction. The profiles of  $\langle T_m \rangle_T$  and  $\langle T_m \rangle_N$  in Cases 4 and 5 (not shown here) exhibit similar variations to those observed in Cases 1 and 3, respectively.

### Zone average of streamwise velocity

Figure 7 shows the distributions of zone average and conventional time average of the streamwise velocity component for representative three cases at  $x'/\delta_0 \approx 70$ . The profiles in Case 1 almost agree with the two-dimensional flow profiles in each sliced section. That is, the profiles of the turbulent zone average  $\langle U \rangle_T/U_1$  agrees with the conventional time average  $\bar{U}/U_1$  in the range of  $y/\delta_m \leq 0.6$ , and those of the non-turbulent zone  $\langle U \rangle_N/U_1$  are larger than the other two averages, since non-turbulent fluids are entrained into the whole outer layer. In Cases 2 and 3, the discussion are given in each sliced section. At the center slice between

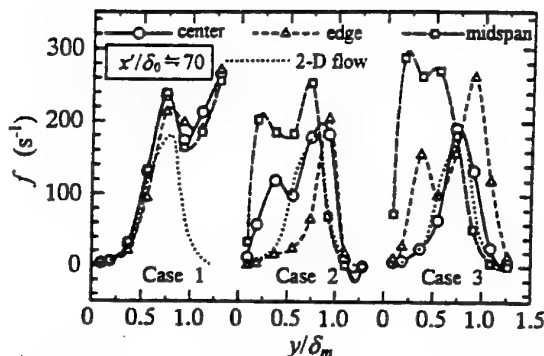


FIGURE 4 FREQUENCY OF OCCURRENCE OF TURBULENCE AND NON-TURBULENCE.

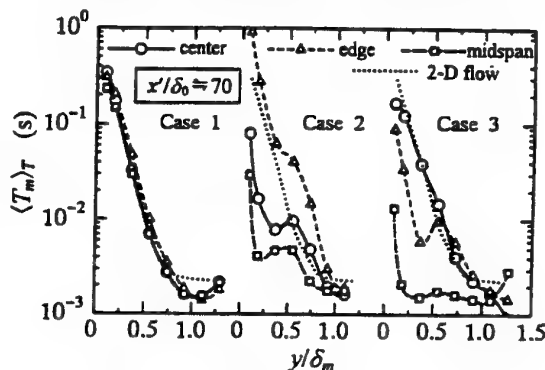


FIGURE 5 ON/OFF PERIOD OF TURBULENCE.

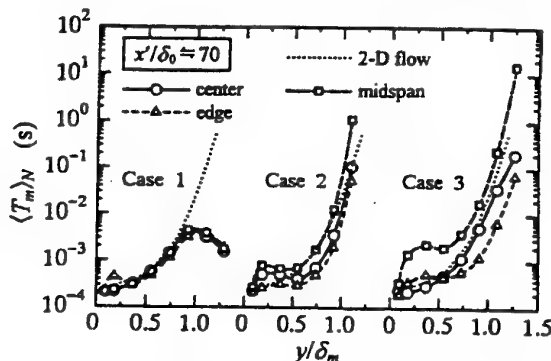


FIGURE 6 ON/OFF PERIOD OF NON-TURBULENCE.

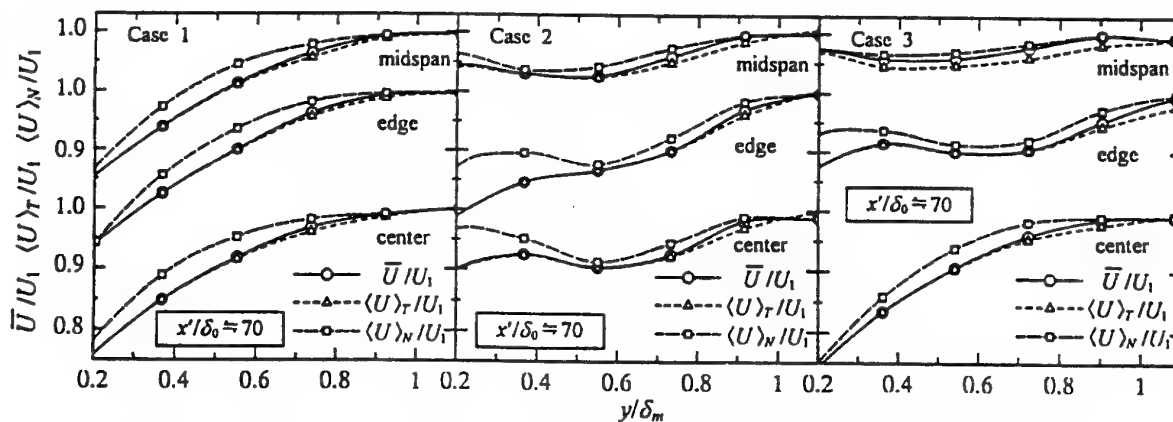


FIGURE 7 ZONE AVERAGE AND CONVENTIONAL TIME AVERAGE OF THE STREAMWISE VELOCITY COMPONENT FOR 3 CASES AT  $x'/\delta_0 \approx 70$ .

neighboring airfoils, the value of  $\bar{U}/U_1$  in Case 2 increase in the range of  $y/\delta_m \leq 0.5$ , and the value of  $\langle U \rangle_N/U_1$  is considerably large in the same range due to the downwash secondary flow. The value of  $\bar{U}/U_1$ , on the other hand, decrease in the range of  $y/\delta_m > 0.5$  in which the effect of the upwash secondary flow appears. In Case 3, all the profiles approximately agree with the two-dimensional flow profile. At the spanwise edge of the airfoil, only non-turbulent zone average  $\langle U \rangle_N/U_1$  in Case 2 increases in the range of  $y/\delta_m < 0.5$ . In this sliced section, the turbulent bulge crossing frequency had markedly decreased, as mentioned above. In the range between  $y/\delta_m = 0.5 \sim 0.8$ , the  $\bar{U}/U_1$  profile decreases and agrees with the  $\langle U \rangle_T/U_1$  due to the upwash secondary flow. In Case 3, the increase of  $\bar{U}/U_1$  below  $y/\delta_m = 0.5$ , and decrease above  $y/\delta_m = 0.5$  is due to the downwash and upwash secondary flows respectively. At the midspan of the airfoil, the value of  $\bar{U}/U_1$  in both Cases 2 and 3 increases due to the downwash secondary flow, however, the profile in Case 3 does not agree with the  $\langle U \rangle_T/U_1$  profile, and furthermore, the  $\langle U \rangle_N/U_1$  does not deviate remarkably from the  $\bar{U}/U_1$  profile. Therefore, the effect of the downwash secondary flow apparent in Case 3 is more significant than that in Case 2. From the results, it can be found that the upwash and downwash secondary flows distort not only the conventional time average of the streamwise velocity component, but also the zone average of the streamwise mean velocity component; the upwash secondary flow decrease both the value of  $\bar{U}/U_1$  and  $\langle U \rangle_T/U_1$ , conversely, the downwash secondary flow increase both the value of  $\bar{U}/U_1$  and  $\langle U \rangle_N/U_1$ .

## CONCLUSIONS

In order to examine the turbulent structure of the boundary layer interacting with the longitudinal vortex arrays generated in the free stream, conditional averaged patterns of the outer layer were experimentally investigated for the five cases of airfoil arrangement. As for the results, spacing between the airfoil ( $L/S$ ) play a significant role in the modification of the intermittent motions. In cases where  $L/S \geq 1$  (Case 2, 3, and 5), the contours of intermittency factor  $\gamma$  reveal spanwise periodic variation corresponding to the spanwise arrangement of the airfoils owing to the downwash and upwash secondary flows. The effect of the spanwise periodicity  $L/S$  is most significant at the midspan of the airfoil, i.e. the value of the  $\gamma$  decrease with the increasing value of  $L/S$ , and is consistently maintained in the far downstream region. The turbulent bulge crossing frequency  $f$ , zone average of on/off period of turbulence  $\langle T_m \rangle_T$  and non-turbulence  $\langle T_m \rangle_N$  are also modified depending on the value of  $L/S$ . In the case of  $L/S = 0.5$ , the value of  $f$ ,  $\langle T_m \rangle_T$ , and  $\langle T_m \rangle_N$  almost agree with those of the two-dimensional flow. On the other hand, in cases where  $L/S \geq 1$ , in the downwash region of the secondary flow,  $f$  have the peak value, and  $\langle T_m \rangle_T$  increase, while in the upwash region of the secondary flow,  $f$  have the peak value and  $\langle T_m \rangle_T$  decrease. Furthermore, these modifications of each property are closely related to the behavior of the induced longitudinal vortices within the boundary layer. Therefore, the variations of the conventional time average and the zone average of the streamwise velocity component, which depend on the relative spanwise slices, can be explained. The effect of the arrangement height of the airfoils  $h$  does not contribute to the spanwise variation of the conditional averaged properties in the outer layer, however, it appears as the local Reynolds number effect.

## REFERENCES

- Cutler, A.D., and Bradshaw, P., 1993a, "Strong Vortex/ Boundary Layer Interactions, Part 1. Vortices High," *Exp. in Fluids*, Vol. 14, pp. 321-332.
- Cutler, A.D., and Bradshaw, P., 1993b, "Strong Vortex/ Boundary Layer Interactions, Part 2. Vortices Low," *Exp. in Fluids*, Vol. 14, pp. 393-401.
- Furuya, Y. and Osaka, H., 1975a, "The Spanwise Non-Uniformity of Nominally Two-Dimensional Turbulent Boundary Layer (1st Report, Characteristics of Spanwise Velocity Distribution)," *Bulletin of the Jpn. Soc. Mech. Eng.*, Vol. 18, No. 121, pp. 664-672.
- Furuya, Y., Nakamura, I., Osaka, H. and Honda, H., 1975b, "The Spanwise Non-Uniformity of Nominally Two-Dimensional Turbulent Boundary Layer (2nd Report, Wall Shear Stress and Flow Field)," *Bulletin of the Jpn. Soc. Mech. Eng.*, Vol. 18, No. 121, pp. 673-680.
- Furuya, Y., Nakamura, I., Osaka, H. and Shimizu, T., 1976, "The Spanwise Non-Uniformity of Nominally Two-Dimensional Turbulent Boundary Layer (3rd Report, Influence of the Streamwise Vortices Arising from the Protrusion)," *Bulletin of the Jpn. Soc. Mech. Eng.*, Vol. 19, No. 134, pp. 922-929.
- Furuya, Y., Nakamura, I., Osaka, H. and Shimizu, T., 1979, "Effects of the Streamwise Vortex Row on Turbulent Boundary Layer (1st Report, Properties of the Streamwise Vortex Row and Mean Velocity Field of Turbulent Boundary Layer)," *Trans. Jpn. Soc. Mech. Eng.*, (in Japanese) Vol. 45, No. 393, pp. 618-627.
- Hedley, T.B., and Keffer, J., 1974, "Turbulent/Non-Turbulent Decisions in an Intermittent Flow," *J. Fluid Mech.*, Vol. 64, Part 4, pp. 625-644.
- Kaneko, K., 1989, "Pattern Dynamics in Spatiotemporal Chaos (Pattern Selection, Diffusion of Defect and Pattern Competition Intermittency)," *Physica*, D 34, pp. 1-41.
- Kovaszny, L.S.G., Kibens, V., and Blackwelder, R.F., 1970, "Large-Scale Motion in the Intermittent Region of a Turbulent Boundary Layer," *J. Fluid Mech.*, Vol. 41, Part 2, pp. 283-325.
- Nakamura, I., Osaka, H., Kushida, T. and Ohkubo, N., 1987a, "A Study on the Interaction Between Longitudinal Vortices and a Turbulent Boundary Layer," *Trans. Jpn. Soc. Mech. Eng.*, (in Japanese), Vol. 53, No. 492, pp. 2340-2347.
- Nakamura, I., Kushida, T., Osaka, H., and Okamoto, H., 1987b, "An Experimental Study on the Effect of Interaction of Longitudinal Vortices and a Turbulent Boundary Layer on the Intermittent Region," *Fluid & Heat Eng. Reseach*, (in Japanese), Vol. 22, No. 2, pp. 33-42.
- Nishioka, M., 1989, "Evolution of Tollmien-Schlichting Waves into Wall Turbulence," *J. Jpn. Soc. Aeronautical and Space Science*, (in Japanese), Vol. 37, No. 421, pp. 9-17.
- Osaka, H., Shimizu, T., Nakamura, I. and Furuya, Y., 1977, "The Spanwise Non-Uniformity of Nominally Two-Dimensional Turbulent Boundary Layer (4th Report, Uniformization of Flow Field and Comparison of Various Flows)," *Bulletin of the Jpn. Soc. Mech. Eng.*, Vol. 20, No. 141, pp. 307-314.
- Osaka, H. and Fukushima, C., 1992, "Effect of Controlled Longitudinal Vortex Arrays on the Development of a Turbulent Boundary Layer," *Experimental Thermal and Fluid Science*, Vol. 5, No. 3, pp. 290-298.
- Osaka, H. and Fukushima, C., 1996, "Spanwise Variation of Turbulent Flowfield for the Turbulent Boundary Layer Interacting with Controlled Longitudinal Vortex Arrays," *JSME Int. Journal*, Series B, Vol. 39, No. 1, pp. 10-18.
- Tennekes, H., and Lumley, J.L., 1972, "A First Course in Turbulence," The MIT Press, p. 19.

# EFFECT OF LOCAL BLOWING ON THE INSTABILITY OF CHANNEL FLOW

Yong Mann CHUNG and Hyung Jin SUNG

Department of Mechanical Engineering  
Korea Advanced Institute of Science and Technology  
373-1 Kusong-dong, Yusong-ku, Taejeon, 305-701  
Korea

Andrey V. BOIKO

Department of Theoretical and Applied Mechanics  
Russian Academy of Sciences, Siberian Branch  
630090 Novosibirsk  
Russia

## ABSTRACT

A direct numerical simulation was made of the instability in a spatially-evolving channel flow. A local surface suction/blowing was imposed at the upper wall ( $x/h = 20$ ). A Tollmien-Schlichting wave was superimposed on the laminar channel flow at the inflow. At the outflow, the buffer domain technique was applied to suppress the reflection of outgoing waves. The influence of the local suction/blowing on the linear and nonlinear instabilities of the flow was examined. It was found that the local suction/blowing increases the disturbance energy significantly in the interaction zone. The effects of the blowing strength ( $0 \leq A_S \leq 0.1$ ) on the subcritical channel flow were scrutinized. Two regimes of the wave/flow interaction were found by varying  $A_S$ , i.e., 'monotonic' and 'vortex splitting' regimes.

## INTRODUCTION

Laminar-turbulent transition is one of the challenging problems in fluid mechanics. It is significant not only from a fundamental point of view but also for the improvement of vehicle performance and maneuverability as well as for the effective control of further turbulent events (Morkovin and Reshotko, 1990; Kachanov, 1994). The main obstacle in studying it arises due to a large variety of mechanisms that can lead to the transition. The process of laminar-turbulent transition in two-dimensional flows at a low level of environmental disturbances is usually initiated by the amplification of unstable instability waves, called Tollmien-Schlichting (T-S) waves, through receptivity to the environmental disturbances (Kachanov, 1994). At a large initial intensity of incoming disturbances, other, usually initially three-dimensional, mechanism could prevail (Boiko *et al.*, 1994). The stability of parallel laminar flow to two-dimensional small disturbance can be described by the primary linear stability theory (Drazin and Reid, 1981). Here the term 'linear' means the applicability of superposition principle, which presumes the absence of mutual influence of several waves to each other and amplitude independence of their development.

When the primary unstable wave is amplified up to a critical threshold, nonlinear effects set up or the flow becomes unstable to three-dimensional disturbances as a result of secondary instabilities (Herbert, 1988). At later stages of the transition in a plane channel or boundary layer flow, these new mechanisms produce three-dimensional vortex structures, which lead to K-type

or N-type breakdowns, depending on the amplitude of the initial disturbances and the background noise characteristics (Herbert, 1988; Kachanov, 1994). In the transitional flow, linear secondary growth of the primary wave and nonlinear effects with three-dimensional character, once they are initiated, become violent and lead rapidly to turbulence; as a consequence, in particular, it is much more difficult to control the flow field effectively.

The need to create energy-saving technologies for laminar flow control (LFC) is the background of the research for understanding the physics of linear instability and finding possible ways to control the flow instability in the (near-) linear range. A literature survey reveals that there have been many attempts to control or lessen the unfavorable behavior associated with laminar-turbulent transition. To date, several methods have been employed, e.g., near-wall fluid suction and blowing or cooling and heating, surface modifications in the form of humps and dips, flow streamlining by favorable pressure gradients, and others (for more detail, see Morkovin and Reshotko (1990) and references therein).

In the transition simulations of shear flows, such as channel flows, boundary layers, free shear layers, jets, wakes, etc., there are two different points of view: temporal and spatial approaches which differ in treating the process development in time or space respectively (Kleiser and Zang, 1991). In closed systems, such as Bénard convection and Taylor Couette flow, the transition evolves in time not in space, making the temporal approach the proper one. Most of engineering flows are, on the contrary, spatially unstable, the transition being spatially-evolving. Consequently, in the latter open systems, the spatial method should be generally used to investigate the characteristics of transition process (Fasel, 1990).

In the linear approach a transformation theorem is known by Gaster (1962), which is strictly applicable only to almost neutral waves of *two dimensional parallel flows*. The theorem allows one to use the results of temporal theory, which is easier to solve numerically, to predict behavior of spatially-evolving flow (Gaster, 1962; Fasel, 1990). In more complicated flows, such a theorem is generally absent or is not so straightforward. Consequently, it is natural to simulate this process with the spatial approach, as transition of shear flows in open systems evolves spatially in the streamwise direction.

Nevertheless, during the past decade, despite the limitation of the underlying physics, many unsteady transition problems have

been analyzed by the temporal approach, mainly due to simplicity and natural restrictions on computer power. Recently, as the computer industry develops, the spatial approach has been receiving ever-increasing interest in the transitional numerical simulations. In the present study, spatial simulation has been employed to scrutinize the instability characteristics of spatially-evolving channel flow. A discussion of various aspects of spatial simulations is found in Fasel (1990) together with a summary of previous results.

Previous research covering numerical simulations may be categorized as follows, according to their underlying principles: (i) the primary linear stability theory; (ii) the asymptotical analysis of Navier-Stokes equations at very-high Reynolds numbers; (iii) the direct numerical simulation of the full Navier-Stokes equations. The book by Drazin and Reid (1981) is dedicated to the linear stability theory. For more details on (ii), a comprehensive review of triple-deck methods by Nayfeh (1991) is currently available. In the present work, direct numerical simulations were done to investigate the linear and nonlinear characteristics of transitional channel flows. Direct numerical simulations have been reviewed recently by Kleiser and Zang (1991).

For theoretical investigations of flow transition due to traveling T-S wave instabilities, the plane Poiseuille flow can be regarded as a prototype case. The base flow is strictly parallel and is an exact solution of the Navier-Stokes equations unlike the Blasius boundary layer flow (Kleiser and Zang, 1991). It is known that plane channel flow is linearly stable up to  $Re_{cr} = 5772$  based on the half channel width and center-line velocity (Orszag, 1971). From this point of view, the flows at  $Re < Re_{cr}$  are subcritical in contrast to supercritical, or linearly unstable flows at  $Re > Re_{cr}$ . Since the possible growth rate of a T-S wave in a plane channel flow is small by magnitude ( $O \approx 10^{-2}$ ), its sign is very sensitive to the geometric perturbations and mean velocity distributions (Ghaddar *et al.* 1986). For periodic disturbances in the streamwise direction, such as grooved channels (Ghaddar *et al.*, 1986; Amon and Patera, 1989), baffled channels (Roberts, 1994), and a periodic array of cylindrical objects (Karniadakis *et al.*, 1988), several temporal stability studies have been made by using the periodic boundary condition in the mean flow direction.

Apart from the geometric modifications, the method of local surface suction/blowing has attracted considerable interest from researchers. This is a well-known and much-explored method of controlling transition of wall-bounded shear flows, because it provides a powerful and simple means to control laminar to turbulent transition locally (Biringen, 1984; Danabasoglu *et al.*, 1991). In addition, it is relatively easy to control the strengths of surface suction/blowing rather than to change pressure gradients or geometric configurations of the flow. It is well known that for wall-bounded flows even small changes in mean velocity field applied appropriately can lead to strong changes of transition behavior. Therefore, local wall suction/blowing has been considered as a promising method towards active transitional flow control (Joslin *et al.*, 1995). Suction/blowing influences the stability of laminar shear flows through local changes of mean velocity profiles, that, in their turn, affect both T-S wave amplification and dispersion properties as well as the flow receptivity to external or upstream disturbances. It was found that active control by periodic suction/blowing was very effective in reducing the T-S wave amplitudes as well as the nonlinear disturbances, which results in substantial amplitude attenuation (Danabasoglu *et al.*, 1991).

In the present study, a direct numerical simulation has been made to scrutinize the influence of local surface suction/blowing on the linear and nonlinear instability of spatially-evolving channel flow. As transition evolves in the streamwise direction with strong upstream influence, a proper spatially-evolving approach was required to allow the disturbance to modify the mean flow field. The main aim of this work is to depict the T-S wave interaction with the planar channel flow perturbed by the local steady suction/blowing. The influence of the blowing strength was examined.

In Section 2, we briefly introduce the numerical method used in this study; the numerical results and discussion for spatial in-

stability of the channel are presented in Section 3, followed by a summary in Section 4.

## NUMERICAL METHOD

### Governing Equations

We consider a two-dimensional incompressible viscous fluid between two parallel plates located at  $y = 0$  and  $y = 2h$ , respectively. The incompressible Navier-Stokes equations in primitive variables may be written as follows:

$$\frac{\partial u_i}{\partial t} + \frac{\partial}{\partial x_j} (u_i u_j) = -\frac{\partial p}{\partial x_i} + \frac{1}{Re} \frac{\partial^2 u_i}{\partial x_j \partial x_j}, \quad (1)$$

$$\frac{\partial u_i}{\partial x_i} = 0,$$

where  $u_i (= U_i + u'_i)$  is the velocity component and  $p$  the pressure. All quantities are non-dimensionalized using the center-line velocity  $U_c$  and the channel half-height  $h$ . The Reynolds number is defined as  $Re = U_c h / \nu$ , where  $\nu$  is the kinematic viscosity.

A local steady surface suction/blowing was applied through a port located at the upper wall to perturb the transitional channel flow. The effect of the surface suction/blowing was represented by the boundary condition at the upper wall,

$$u = 0, v = -A_S H(x) \quad \text{at } y = 2h, \quad (2)$$

$$H(x) = e^{-(x-x_S)^2/\sigma^2}, \quad (3)$$

where  $x_S$  is the streamwise location of the center of the suction/blowing port at the upper wall.  $H(x)$  represents a Gaussian distribution of the velocity profile across the port. The small parameter  $A_S$  corresponds to the maximum velocity of the surface suction/blowing and  $A_S > 0$  for blowing. In these calculations,  $\sigma$  was set to be unity and the location of the port was fixed at  $x_S = 20h$ . For the present configuration, the consequent volume flux through the port is  $\sqrt{\pi}\sigma A_S$ .

### Boundary Conditions

For the stability computation, a two-dimensional T-S wave was superimposed on the laminar parabolic profile at the inflow boundary:

$$u'_i(x=0, y, t) = A_{TS} \Re[\hat{u}_i(y) e^{-i\omega_R t}], \quad (4)$$

where  $A_{TS}$  is the amplitude of the inflow perturbations and  $\hat{u}_i(y)$  is the complex velocity vector calculated from the spatial eigenfunctions of the Orr-Sommerfeld equation corresponding to the real frequency  $\omega_R$ . Also,  $i = \sqrt{-1}$  and  $\Re$  represents the real part of a complex number.

At the outflow, the buffer domain technique of Streett and Macaraeg (1989) was used to suppress the reflection of outgoing waves. In the buffer domain, the governing equations must be modified to have strictly outgoing waves. For this purpose, the streamwise viscous terms are reduced to zero using a smooth coefficient function.

### Linear Stability Theory

The governing equation for the linear stability of parallel shear flow can be obtained by assuming a wave-like solution of the form:

$$u'_i(x, y, t) = \Re[\hat{u}_i(y) e^{\alpha x - i\omega_R t}]. \quad (5)$$

Here,  $\alpha$  is the complex wave number defined as  $\alpha = \alpha_R + i\alpha_I$ . After linearization with respect to  $(U, V)$ , the resulting Orr-Sommerfeld equation can be written as:

$$\left[ (U_0 - \omega_R/\alpha)Q - \frac{d^2}{dy^2} U_0 + \frac{i}{\alpha Re} Q^2 \right] \hat{v} = 0. \quad (6)$$

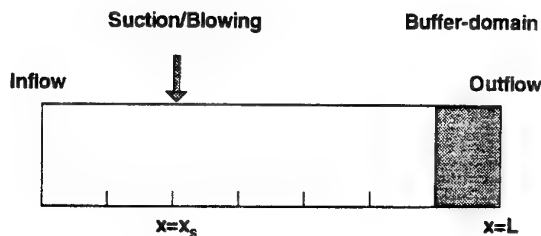


Figure 1: Flow configuration and definition of coordinate system.

Here,  $Q = d^2/dy^2 - \alpha^2$  and  $U_0$  is the base flow of the form  $U_0(y) = y(2 - y)$ . After obtaining  $\hat{v}$  from Eqn. 6,  $\hat{u}$  can be easily calculated from the continuity equation,  $\hat{u} = i\hat{v}_y/\alpha$ .

After solving Eqn. 1, the perturbation field ( $u'$ ,  $v'$ ) can be extracted by subtracting the initial unperturbed flow from the perturbed one:

$$u'_i = u_i - U_i. \quad (7)$$

This approach differs from the usual approach to the stability studies where the equations for an infinitesimal perturbation are solved independently (e.g., Ghaddar *et al.*, 1986). These linear perturbation equations are obtained by substituting Eqn. 7 into the flow equations (Eqn. 1), assuming that the perturbation is so small that the higher powers of the perturbation can be neglected, and using the fact that  $(U, V)$  is also a solution of the Navier-Stokes equations. Unlike the linear stability theory (Ghaddar *et al.*, 1986), the approach used in the present study is not limited to linear perturbations, as large nonlinear perturbations can also be studied.

### Numerical Method

A fractional-step method was employed to solve the unsteady Navier-Stokes equations. This is based on a time-splitting method in conjunction with the approximate factorization technique (Kim and Moin, 1985). For more details, the readers may refer to the paper of Le and Moin (1991).

Based on the time-splitting method, the solution procedure consists of semi-implicit approach with a three step Runge-Kutta method for the nonlinear convective terms and the Crank-Nicholson method for the viscous terms. This method is second-order accurate in time for the viscous terms and third-order accurate in time for the convective terms. The resulting Poisson equation for the pressure correction in the fractional step method was solved in wave-number space by the transformation of variables into a one-dimensional discrete Fourier series. All numerical computations were carried out on a CRAY-YMP-C90.

## RESULTS AND DISCUSSION

### Numerical Parameters

In the present study, we consider a two-dimensional laminar channel flow between two parallel plates located at  $y = 0$  and  $y = 2h$ , with a local steady suction/blowing through a port ( $x/h = 20$ ) at the upper wall. A configuration of the flow and the relevant coordinate definitions are illustrated in Fig. 1. The streamwise distance of the computational domain is  $120h$  from the inflow, which is equivalent to approximately 20 times the T-S wave length at  $Re = 5000$ . At the outlet, the buffer domain holds  $10h$  ( $110 \leq x/h \leq 120$ ).

In order to establish the accuracy of the time dependence of the simulation, the growth rate and wave number ( $\alpha_R, \alpha_I$ ) for two-dimensional T-S wave were calculated. This was then compared with the numerical solution for linear Orr-Sommerfeld equation at Reynolds number  $Re = 5000$ . For both steady and unsteady

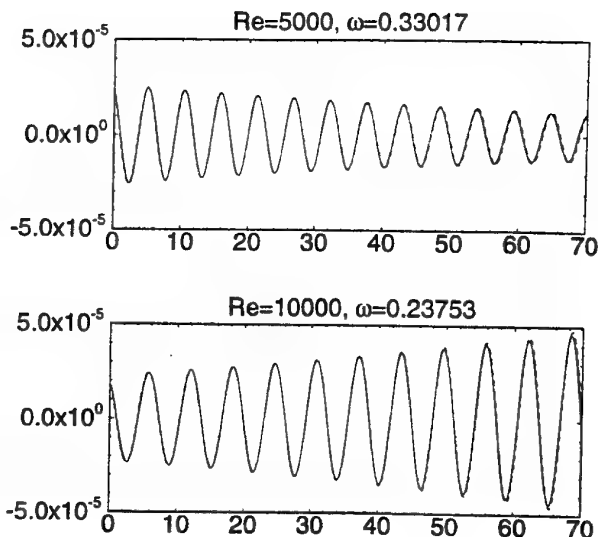


Figure 2: Comparison of the present simulation with the theoretical solution: —, present calculation; ---, linear solution.

flows, the observed streamlines were unchanged for grids with more than  $(1024 \times 129)$ . In the latter case, the difference between the eigenvalues obtained from the simulation and from the linear Orr-Sommerfeld solution was less than 1%. Several trial calculations were repeated to monitor the sensitivity of the results to the grid size. Based on these preliminary calculations, most of simulations reported here employed the  $(1024 \times 129)$  mesh system to give numerical stability without excessive computation time.

The length of the time step  $\Delta t$  was chosen to be adequate not only to retain numerical stability of the method (based on CFL number), but also to represent the instability characteristics of the flow properly. A constant time-step, equal to  $1/256$  of one T-S period ( $T_{TS}$ ), was adopted for the three-stage Runge-Kutta method, which never exceeds one half of the limiting value allowed by the numerical method.

Before proceeding further, it is important to ascertain the reliability and accuracy of the present simulation. Toward this end, the plane Poiseuille flow ( $A_S = 0$ ) was selected as a test case for the employed numerical techniques since the stability characteristics are well understood and documented in the literature (Orszag, 1971). Two Reynolds numbers were tested, which are subcritical ( $Re = 5000$ ) and supercritical ( $Re = 10,000$ ). In the subcritical case, the frequency for the least stable eigenmode is  $\omega_R = 0.33017$ . For these parameters, the Orr-Sommerfeld solution gives  $\alpha = 1.1557 + i0.0106$ . In the supercritical case, the eigenvalue is  $\alpha = 1.0006 - i0.0109$  for  $\omega_R = 0.23753$ . The frequency  $\omega_R$ , which corresponds to the least stable mode at each Reynolds number, was chosen to ensure the rapid decay of all other frequencies.

In Fig. 2, a typical comparison was made for the normal perturbation velocity  $v'$  for both cases with a small value of  $AT_S$ , i.e.,  $AT_S \ll 1$ . The disturbance amplitude was defined as the rms magnitude of  $u$  component of the T-S wave, which was set as  $AT_S = 10^{-4}$  to exclude the possibility of the subcritical transition due to the high amplitude of initial T-S wave. Figure 2 shows the disturbance velocity at the centerline along the streamwise direction. As shown in Fig. 2, the results from the present simulation and the linear Orr-Sommerfeld solution are in excellent agreement for both cases. The disturbance kinetic energy was found to decay exponentially with a growth rate  $\alpha_I = 0.0106$  at  $Re = 5000$ . The wave number of the perturbation ( $\alpha_R$ ) can also be obtained by observing the behavior of the perturbation velocity  $v'$  at a constant  $y$ . The wave number of the perturbation ( $\alpha_R$ )



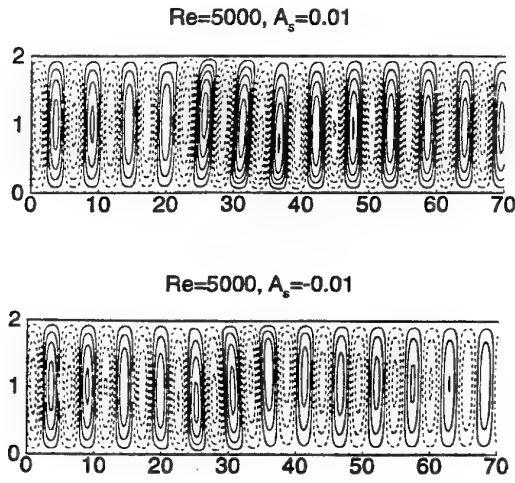


Figure 3: Disturbance streamfunction contours.

was also found to be very close to the accurate value from the Orr-Sommerfeld solution ( $\alpha_R = 1.1557$ ). These observations indicate that the present transition simulations are adequate for the spatially-evolving transition flows.

#### Effect of suction/blowing on T-S wave stability

In order to demonstrate the effect of the small-intensity suction/blowing on the streamwise development of a T-S wave, computations were performed for subcritical ( $Re = 5000$ ) channel flows. As mentioned earlier, the local suction/blowing was applied at the upper wall ( $x_S = 20h$ ). Note that since some extra amount of fluid ( $\sqrt{\pi\sigma A_S}$ ) is supplied (taken out) through the blowing (suction) port, the consequent effective Reynolds number is increased (decreased).

The disturbance streamfunction contours of T-S waves with blowing ( $A_S = 0.01$ ) and suction ( $A_S = -0.01$ ) are illustrated in Fig. 3 for subcritical case. Quasi-steady, time-periodic behavior of the disturbed flow has been established after a transient period of  $32T_{TS}$ , which corresponds to approximately 8000 time steps. Downstream of the suction/blowing port, which is located at  $x_S = 20h$ , the wave grows in both cases in the streamwise direction up to a certain high amplitude and then the disturbance remains apparently constant in amplitude downstream, exhibiting considerable distortions from previous cases. Note that in the blowing case the consequent effective Reynolds number increases, since some extra amount of fluid which corresponds to  $\sqrt{\pi\sigma A_S}$  is supplied into the channel through the port (see Section 2.1). Due to the suction/blowing, the T-S waves are observed to be no longer symmetric with respect to the channel centerline ( $y = h$ ). The wave near the blowing port leads the wave of the centerline, while the wave in the opposite side of the blowing port lags. On the contrary, a reversed trend is observed in the suction case. The difference could also be seen in the wave propagation velocity, which is primarily attributed to changes in Reynolds number modification due to flow injection/removing. In the supercritical case, the phase difference is more significant compared to the subcritical case (not shown here).

Variations of the  $u'_{rms}$ -profiles by the local suction/blowing are exhibited in Fig. 4. Upstream the suction/blowing port, the typical channel flow  $u'_{rms}$ -profiles are displayed, exhibiting one maximum near the channel wall. However, the  $u'_{rms}$ -profiles are significantly changed at the downstream of the port. Two peaks in the blowing side and one peak in the opposite side are detected near the blowing port. In particular, the increase of peak value in the opposite side is appreciable. This is due to the enhanced shear near the wall by the continuity constraint (Drazin and Reid, 1981). The third peak value observed in the blowing side increases with

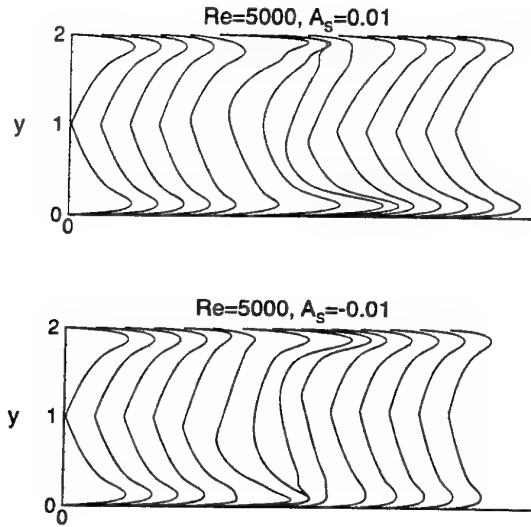


Figure 4: Variation of the  $u'$ -profile.

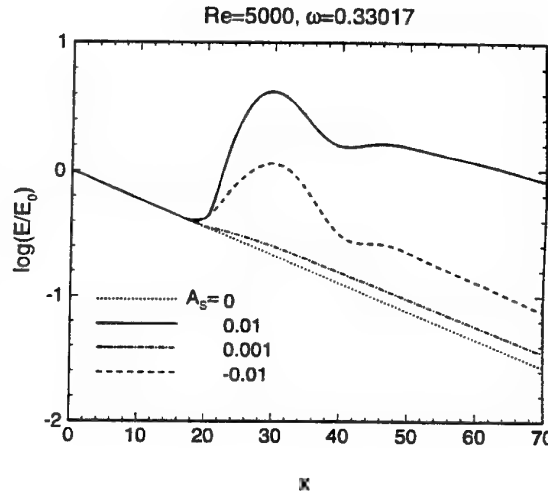


Figure 5: Streamwise variation of the amplification factor.

the distance from the suction/blowing port, and then decreases slowly, returning to the  $u'_{rms}$ -profile of the channel flow. The appearance of a third maximum in the  $u'_{rms}$ -profile is a typical feature with an inflection point in the mean flow profile (Nayfeh *et al.*, 1988). For supercritical case, these features (a third peak near the wall and increased disturbance amplitude in the opposite side) are more evident (not shown here).

To describe the effect of suction/blowing quantitatively, it is useful to measure the spatial growth of the disturbances. It appears that the spatial-growth behavior of disturbances can be affected by the criteria which we choose (Kachanov, 1994). Several different criteria for measuring the disturbance amplitude have been devised in the literature: for more details, see Fasel and Konzelmann (1990),

- 1  $u'_{rms}$ : centerline value of  $u'$  amplitude distribution.
- 2  $v'_{rms}$ : centerline value of  $v'$  amplitude distribution.
- 3  $\sqrt{\int_0^2 u'^2(x) dy}$ :  $u'$ - component to the kinetic energy distribution.

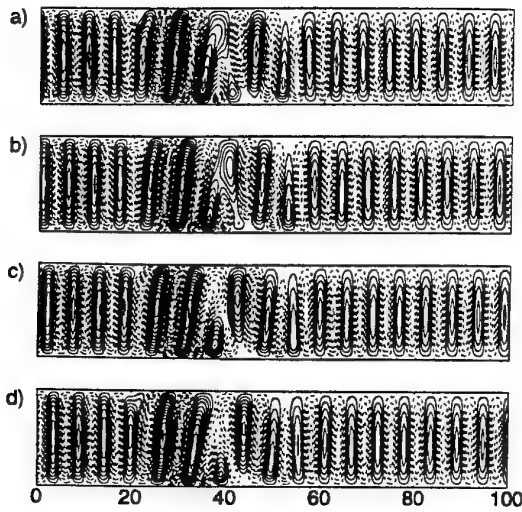


Figure 6: Instantaneous disturbance streamlines for 4 equally-spaced time intervals over one period at  $A_S = 0.03$ .

$$4 \int_0^2 \bar{v}'^2(x) dy : v' \text{- component to the kinetic energy distribution.}$$

$$5 \int_0^2 (\bar{u}'^2(x) + \bar{v}'^2(x)) dy : \text{kinetic energy distribution.}$$

Variations of the amplification factor  $\log(E(x)/E_0)$  are displayed in Fig. 5 for subcritical cases. Here, the disturbance amplitude  $E(x)$  at a given streamwise station was expressed in terms of the integral of disturbance kinetic energy across the channel height (similar to criterion 5),

$$E^2(x) = \frac{1}{2} \int_0^2 (\bar{u}'^2(x) + \bar{v}'^2(x)) dy. \quad (8)$$

For no suction/blowing ( $A_S = 0$ ),  $E(x)$  changes exponentially in the downstream direction as  $e^{-\alpha_1 x}$ , where the amplification factor shows a straight line in a log plot with the slope of  $-\alpha_1$ .

A small surface suction/blowing ( $|A_S| \leq 0.01$ ) is likely to have a very strong effect on the behavior of the growth rate. Inside the interaction zone ( $20 \leq x/h \leq 50$ ), it is seen that the surface suction/blowing increases the amplification factor significantly in both suction and blowing cases, i.e.,  $|A_S| = 0.01$ . Downstream of the interaction zone ( $x/h \geq 50$ ), the growth rates return smoothly to those of plane channel flow showing the locality of the wave/flow interaction close to the control port. In the subcritical case, blowing is found to have more significant effect on the downstream disturbance behavior than suction. Based on the above calculation, blowing was found to have more significant effect on the downstream disturbance behavior in subcritical case (see Fig. 5). In what follows we consider the effects of increasing the magnitude of the blowing strength.

### Effect of blowing strength

All the computations for subcritical blowing cases ( $\omega = 0.33017$  at  $A_{TS} = 10^{-4}$ ) are summarized in Table 1. The blowing strength ( $A_S$ ) was increased up to 0.1 to investigate its effect on the instability characteristics.

Figure 6 displays the instantaneous disturbance streamlines for four equally-spaced time instants over one complete cycle of the flow at  $A_S = 0.03$ . The general feature of the flow patterns is qualitatively different from that of the moderate amplitude blowing ( $A_S = 0.01$ ) of Fig. 3(a). A small vortex near the lower wall is observed in Fig. 6(a) at three T-S wave lengths downstream ( $x = 40h$ ). The small vortex is then merged with the upstream large vortex. The resulting combined vortex is splitted

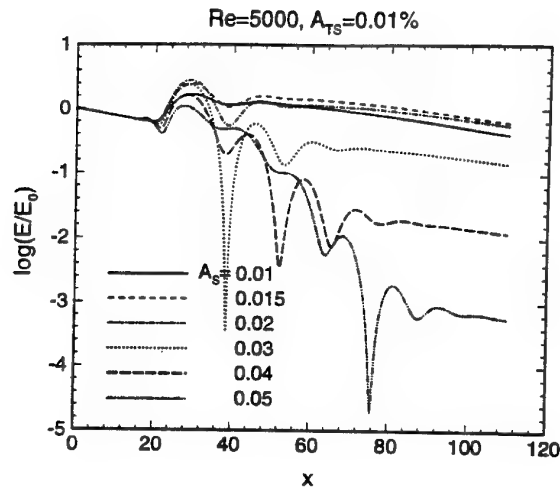


Figure 7: Streamwise variation of the amplification factor  $\log(E(x)/E_0)$  of the fundamental wave component.

into two children-vortices: one is near the upstream lower wall, the other near the downstream upper wall, as shown in Fig. 6(b). The upstream children-vortex shrinks in strength as it flows, while the downstream one recovers its strength across the whole channel (Fig. 6(c)). The small upstream children-vortex will decay as it goes downstream and be merged with the upstream vortex (Fig. 6(d)). This forms one complete cycle of 'vortex splitting'. The disturbance streamfunctions of  $A_S = 0.04$  and  $A_S = 0.05$  were seen to be similar to those of  $A_S = 0.03$ , indicating the appearance of a new developed regime of the wave/flow interaction, termed 'vortex splitting' regime.

Streamwise variations of the amplification factor  $\log(E(x)/E_0)$  of the fundamental wave component are presented in Fig. 7. Here,  $E(x)$  is defined by the centerline value of  $v'$  amplitude distribution, i.e.,  $E(x) = v'_{rms}$ , instead of criteria 5 used in Fig. 5. As can be seen, the response of the flow to the surface blowing is systematic up to  $A_S = 0.02$  (called 'monotonic' regime). Beyond this threshold value, a new 'vortex splitting' regime is observed, in which spike-like peaks appear in the distribution. For example, the peak occurs at about  $x = 40h$  for  $A_S = 0.03$ . These locations are related to the vortex splitting observed in Fig. 6. The location of the peak goes downstream as  $A_S$  increases. So, for  $A_S = 0.04$ , peak locates at  $x = 50h$  and for  $A_S = 0.05$ , at  $x = 75h$ .

Figure 8 represents the growth rate of the fundamental wave at various blowing strengths. For large blowing strengths ( $A_S \geq 0.03$ ), the value  $\alpha_1$  decreases dramatically to a negative extreme and then abruptly changes the sign, which decays to an ordinary

Table 1: Summary of the computation cases.

Cases	$A_{TS}$ (%)	$A_S$	$L$	Grid system
Case1	0.01	0.	120	1024×128
Case2	0.01	0.005	120	1024×128
Case3	0.01	0.01	120	1024×128
Case4	0.01	0.015	120	1024×128
Case5	0.01	0.02	120	1024×128
Case6	0.01	0.025	120	1024×128
Case7	0.01	0.03	120	1024×128
Case8	0.01	0.04	120	1024×128
Case9	0.01	0.05	120	1024×128
Case10	0.01	0.1	120	1024×128

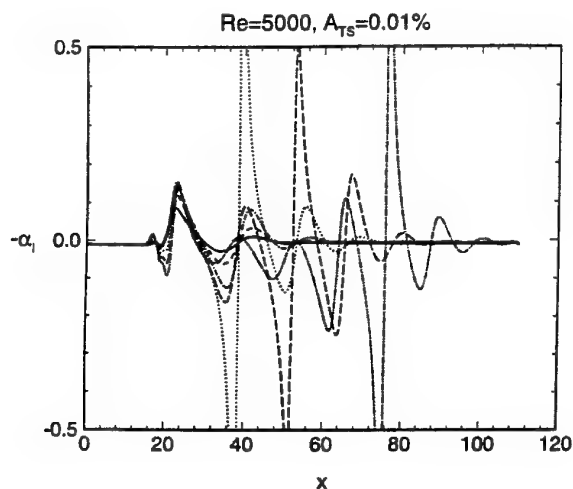


Figure 8: Growth rate of the fundamental wave at various blowing strengths.

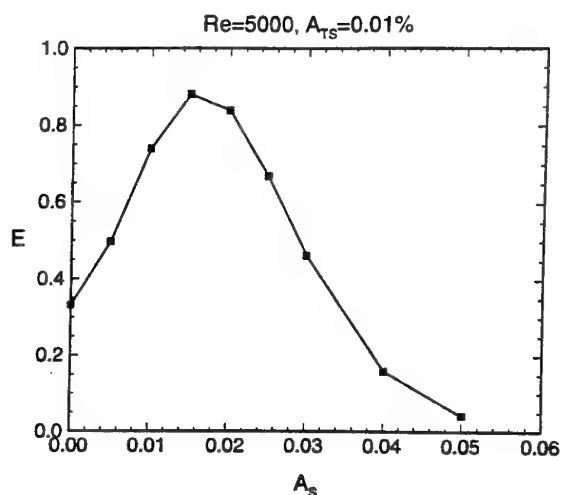


Figure 9: Disturbance energy of the fundamental component at  $x = 100h$ .

value. Note that the locations of the peaks and the abrupt change of the sign are consistent with those of the vortex splitting and the spike-like peaks observed in the Figs. 6 and 7. Figure 9 shows the fundamental component of the disturbance energy at  $x = 100h$ . This can be calculated from Fig. 7. The disturbance energy has a maximum at  $A_S = 0.015$  and then decreases as  $A_S$  increases.

## CONCLUDING REMARKS

A direct numerical simulation was done to study the spatial stability of the channel flow in the presence of a local surface suction/blowing. Inside the interaction zone, the surface suction/blowing was found to increase the amplification factor significantly in the subcritical case. A threshold value of the blowing was found, above which the wave development changed its behavior, i.e., the spikes and the corresponding vortex splitting appeared in the streamwise amplitude distribution. A new developed regime of the wave/flow interaction was observed, which is termed 'vortex splitting' regime. The locations of the peaks and the abrupt change of the sign of  $\alpha$  were consistent with those of the vortex splitting and the spike-like peaks. In a global point of view, the present work is also connected with the receptivity problem, in which the flow response on some external disturbances is main concern. In that case, we may consider the T-S wave as an 'external' disturbance.

## REFERENCES

- Amon, C. H. and Patera, A. T., 1989, "Numerical calculation of stable three-dimensional tertiary states in grooved-channel flow," *Phys. Fluids A*, Vol. 1 (12), pp. 2005–2009.
- Biringen, S., 1984, "Active control of transition by periodic suction-blowing," *Phys. Fluids*, Vol. 27 (6), pp. 1345–1347.
- Boiko, A. V., Westin, K. J. A., Klingmann, B. G. B., Kozlov, V. V., and Alfredsson, P. H., 1994, "Experiments in a boundary layer subjected to free stream turbulence. Part 2: The role of T-S waves in the transition process," *J. Fluid Mech.*, Vol. 281, pp. 219–245.
- Danabasoglu, G., Biringen, S., and Streett, C. L., 1991, "Spatial simulation of instability control by periodic suction blowing," *Phys. Fluids A*, Vol. 3, pp. 2138–2147.
- Drazin, P. G. and Reid, W. H., 1981, *Hydrodynamic stability*, first edition Cambridge University Press.
- Fasel, H. F., 1990, "Numerical simulation of instability and transition in boundary layer flows," in *Laminar-Turbulent Transition*, IUTAM Symposium, Toulouse/France, D. Arnal and R. Michel, eds., Springer-Verlag, pp. 587–597.
- Fasel, H. F. and Konzelmann, U., 1990, "Non-parallel stability of a flat-plate boundary layer Navier-Stokes equations," *J. Fluid Mech.*, Vol. 221, pp. 311–347.
- Ghaddar, N. K., Korczak, K. Z., Mikic, B. B., and Patera, A. T., 1986, "Numerical investigation of incompressible flow in grooved channels. Part 1: Stability and self-sustained oscillations," *J. Fluid Mech.*, Vol. 163, pp. 99–127.
- Herbert, Th., 1988, "Secondary instability of boundary layers," *Annu. Rev. Fluid Mech.*, Vol. 20, pp. 487–526.
- Joslin, R. D., Nicolaides, R. A., Erlebacher, G., Hussaini, M. Y., and Gunzburger, M. D., 1995, "Active control of boundary-layer instabilities: Use of sensor and spectral controller," *AIAA J.*, Vol. 33 (8), pp. 1521–1523.
- Kachanov, Y. S., 1994, "Physical mechanisms of laminar-boundary-layer transition," *Annu. Rev. Fluid Mech.*, Vol. 26, pp. 411–482.
- Karniadakis, G. E., Mikic, B. B., and Patera, A. T., 1988, "Minimum-dissipation transport enhancement by flow destabilization: Reynolds' analogy revisited," *J. Fluid Mech.*, Vol. 192, pp. 365–391.
- Kim, J. and Moin, P., 1985, "Application of a fractional-step method to incompressible Navier-Stokes equations," *J. Comput. Phys.*, Vol. 59, pp. 308–323.
- Kleiser, L. and Zang, T. A., 1991, "Numerical simulation of transition in wall-bounded shear flows," *Annu. Rev. Fluid Mech.*, Vol. 23, pp. 495–537.
- Le, H. and Moin, P., 1991, "An improvement of fractional step methods for the incompressible Navier-Stokes equations," *J. Comput. Phys.*, Vol. 92, pp. 369–379.
- Morkovin, M. V. and Reshotko, E., 1990, "Dialogue on progress and issues in stability and transition research," in *Laminar-Turbulent Transition*, IUTAM Symposium, Toulouse/France, D. Arnal and R. Michel, eds., Springer-Verlag, pp. 3–29.
- Nayfeh, A. H., 1991, "Triple-deck structure," *Computers Fluids*, Vol. 20 (3), pp. 269–292.
- Nayfeh, A. H., Ragab, S. A., and Al-Maaith, A. A., 1988, "Effects of bulges on the stability of boundary layers," *Phys. Fluids*, Vol. 31 (4), pp. 796–806.
- Orszag, S. A., 1971, "Accurate solution of the Orr-Sommerfeld stability equation," *J. Fluid Mech.*, Vol. 50, pp. 689–703.
- Roberts, E. P. L., 1994, "A numerical and experimental study of transition processes in an obstructed channel flow," *J. Fluid Mech.*, Vol. 260, pp. 185–209.
- Streett, C. L. and Macaraeg, M. G., 1989, "Spectral multi-domain for large-scale fluid dynamic simulations," *Applied Numerical Mathematics*, Vol. 6, pp. 123–139.



# TURBULENT VELOCITY PROFILES IN GRAVEL BED RIVERS

G.M. Smart

National Institute of Water & Atmospheric Research  
P.O. Box 8602  
Christchurch  
New Zealand

## ABSTRACT

Field measurements made at high and low flows with electronic Pitot tubes show logarithmic velocity profiles to fit over much of the flow depth in high relative roughness, gravel bed rivers. Under mobile bed conditions, a direct relation between bed material size and hydraulic roughness was not evident but a linear relation between hydraulic roughness and bed shear stress was identified.

The ratio of mobile bed shear stress to hydraulic roughness may depend on turbulent kinetic energy per unit depth.

## INTRODUCTION

Analysis of vertical profiles of streamwise velocity measured in gravel bed rivers, requires careful re-appraisal of factors often taken for granted in laboratory flume studies.

A primary problem is to define where the actual river bed lies. This becomes more difficult:

- (i) when the bed material becomes larger in relation to flow depth,
- (ii) when the bed becomes mobile and entrained in the flow, and
- (iii) where bed forms (sometimes moving) are superposed on the bed.

A second problem is to define a representative roughness size for the material forming the bed. This becomes more difficult as the range in particle size of bed material increases and under conditions (ii) and (iii) above.

Thirdly, most formulae for predicting flow depth and velocity have been verified under controlled conditions and rely on knowledge of local energy grade. Under flood conditions in gravel bed rivers, it is difficult to accurately measure local water surface slope.

In order to analyse New Zealand gravel-bed river data measured under a combination of the above conditions, it was necessary to adopt some unambiguous definitions for reference levels and roughness size.

The river data were therefore plotted with vertical coordinate,  $z = h_{\max} - h + E$  where  $h$  is the hydrostatic depth below the water surface at which a velocity was measured and  $h_{\max}$  is the maximum hydrostatic depth reading during lowering and raising the velocity meter. The adjustment  $E$  is introduced to cover velocity profile origin displacement and because it was usually unknown whether the velocity meter came to rest ( $h = h_{\max}$ ) on top of a large boulder or in a hole in the river bed.  $E$  was incremented, or decremented, by a few millimeters at a time, until the best fit of the logarithmic profile was found:

$$u = (U^*/\kappa) \ln(z) - (U^*/\kappa) \ln(Z_0) \quad (1)$$

where Von Karman's  $\kappa$  is assumed to have a constant value of 0.4 and shear velocity  $U^*$ , and hydraulic roughness  $Z_0$ , are parameters of the fitted profile. The "optimum" value of  $E$  was used with the corresponding value of  $Z_0$  to define the flow depth:

$$H = h_{\max} + E - Z_0 \quad (2)$$

The channel bed is thus defined to be where a log-profile representation of local time averaged velocity vanishes when extrapolated into the bed. Thus  $u = 0$  at elevation  $z = Z_0$  above the datum  $z = 0$ . This gives a realistic position for the bed when the meter comes to rest on a rock protruding above general bed level as shown in the lower left profile of Fig. 1.

Where a logarithmic velocity profile cannot statistically be rejected, this technique fixes the location of the bed and gives an unambiguous method for calculation of flow depth,  $H$ , when the bed is irregular or moving.

## DATA COLLECTION

"Instantaneous" turbulent velocities were measured by a weighted, electronic Pitot tube (NIWA POEM 1000) lowered on a cable or rod into a river. A ring of holes surrounding the Pitot tube, with the holes perpendicular to

the flow direction, indicated the static head of water above the instrument. The static head port and neighboring forward-facing Pitot tube port were connected to opposite sides of the diaphragm of a rapid response differential pressure transducer located behind the Pitot tube. In this way the velocity fluctuations in the flow were separated from pressure fluctuations by the transducer. Static head and dynamic velocity head data were recorded 24 times per second as the instrument was slowly lowered to the river bed and slowly raised again, so that a vertical profile of turbulent velocity versus depth was obtained. More detailed description of the instrumentation is given by Smart (1991, 1994) and Smart & Carter (1995).

A typical vertical profile of longitudinal velocities comprised around 4000 depth and velocity pairs recorded over 3 - 4 minutes. Descriptions of gravel bed river sections investigated are given by Nikora and Smart (1997).

### DATA ANALYSIS

For rough, non-mobile beds at high Reynolds numbers, the hydraulic roughness is related to a sediment size parameter (e.g. Van Rijn, 1982). Under mobile bed conditions in the gravel bed rivers, no such relationship could be identified. This could indicate that the sampled bed grain size,  $d_{50}$ , is not representative of hydraulic roughness in these rivers or that local  $d_{50}$  could not be determined with sufficient accuracy to reveal any pattern, or a combination of both. However, analysis of the data indicated that under mobile bed conditions there appears to be a relationship between  $Z_0$  and bed shear stress ( $\rho U_*^2$ ) as shown in Fig. 2.

Chamberlain (1983) showed that atmospheric  $Z_0$  is proportional to  $U_*^2 / 2g$  with sand, snow and the surface of the ocean forming the boundary roughness.

For the gravel-bed river data the empirical relation:

$$Z_0 = m U_*^2 / 2g \quad \text{for mobile bed} \quad (3)$$

appears to break down under conditions when the flow velocities were not sufficient to move bed material (Figure 2).

This may be compared with relations of type:

$$Z_0 = 0.14 \nu / U_* \quad \text{for hydraulically smooth bed} \quad (4)$$

where kinematic viscosity,  $\nu$ , is constant over the flow depth. Equations (3) and (4) are equivalent if we replace  $\nu$  in (4) by  $\nu_m$  where:

$$\nu_m = (m / (0.28 g)) U_*^3 \quad \text{turbulent, mobile bed} \quad (5)$$

and assume  $\nu_m$  to be the depth averaged value. According to Nezu & Nakagawa (1993), eddy viscosity,  $\nu_t$ , can be given approximately by:

$$\nu_t = (H / \text{k.e.}) U_*^3 \quad (6)$$

where k.e. is the flow turbulent kinetic energy. Equations (5) and (6) imply that  $m$  depends inversely on the turbulent kinetic energy per unit depth.

This relation is investigated in Fig. 3 where the variance in turbulent velocity measurements over a vertical profile is taken to represent turbulent kinetic energy.

### CONCLUSIONS

Iterative adjustment of the origin offset was successfully used to achieve a statistically significant logarithmic velocity profile fit in rivers with high relative boundary roughness. The criteria of best fit of the velocity profile to the measured data was used to determine values of logarithmic profile parameters which can vary depending on the position chosen for the origin of the profile  $z = 0$ .

With bed shear stress and hydraulic roughness determined in this way a linear relation between these parameters was evident when the channel bed was mobile.

The ratio of mobile bed shear stress to hydraulic roughness appears to depend on turbulent kinetic energy per unit depth.

### ACKNOWLEDGEMENT

The research was carried out under contract CO1614 from the Foundation for Research, Science and Technology (New Zealand).

### REFERENCES

- Chamberlain, A.C. 1983 "Roughness length of sea, sand, and snow." *Boundary-Layer Meteorology* 25, 405-409.
- Nezu, I. and Nakagawa, H. 1993 *Turbulence in open channel flows*. A.A. Balkema, Rotterdam.
- Nikora, V.I. and Smart, G.M. 1997 "Some turbulence characteristics of New Zealand gravel bed rivers". *J. Hydr. Engrg.*, ASCE, in print.
- Smart, G.M. 1991. "A P.O.E.M. on the Waiho (electronic gauging of rivers)." *Journal of Hydrology (NZ)*, vol 30, No. 1, 37-44.
- Smart, G.M. 1994. "Turbulent velocities in a mountain river." *Hydraulic Engrg.* '94, Proc. ASCE Nat. Conf. on Hydraulic Engrg., Buffalo (NY), 844-848.
- Smart, G.M. and Carter, G.S. 1995. "Measuring river turbulence intensity with coarse-gravel bedload." *Proc. HYDRA 2000*, 26 IAHR Congress, vol. 1, London, 486-491.
- van Rijn, L.C., 1982. "Equivalent roughness of alluvial bed." *J. Hydr. Engrg.*, ASCE, 108 (HY10), 1215-1218.

### NOTATION

- $d_{50}$  = grain size for which 90% of a sample of bed material is finer;
- $E$  = offset correction to vertical axis to optimise fit of Eq. 1;
- $g$  = gravitational force per unit mass;
- $h_{max}$  = maximum hydrostatic depth measured during lowering and raising meter;
- $H$  = flow depth ( $= h_{max} + E - Z_0$ );
- $m$  = ratio of hydraulic roughness to shear velocity head;
- $u$  = local "instantaneous" streamwise velocity;
- $u$  = local, time averaged streamwise velocity;
- $U_*$  = friction velocity,  $= \sqrt{\tau_o / \rho}$ ;
- $z$  = distance from the origin of vertical profile of velocity;

$Z_0$  = hydraulic roughness parameter;  
 $\kappa$  = universal von Karman constant ( $\kappa \approx 0.40$ );  
 $\nu$  = kinematic viscosity of water;  
 $\nu_m$  = depth averaged eddy viscosity with mobile bed;

$\rho$  = density of water;  
 $\tau_0$  = shear stress on channel bed;

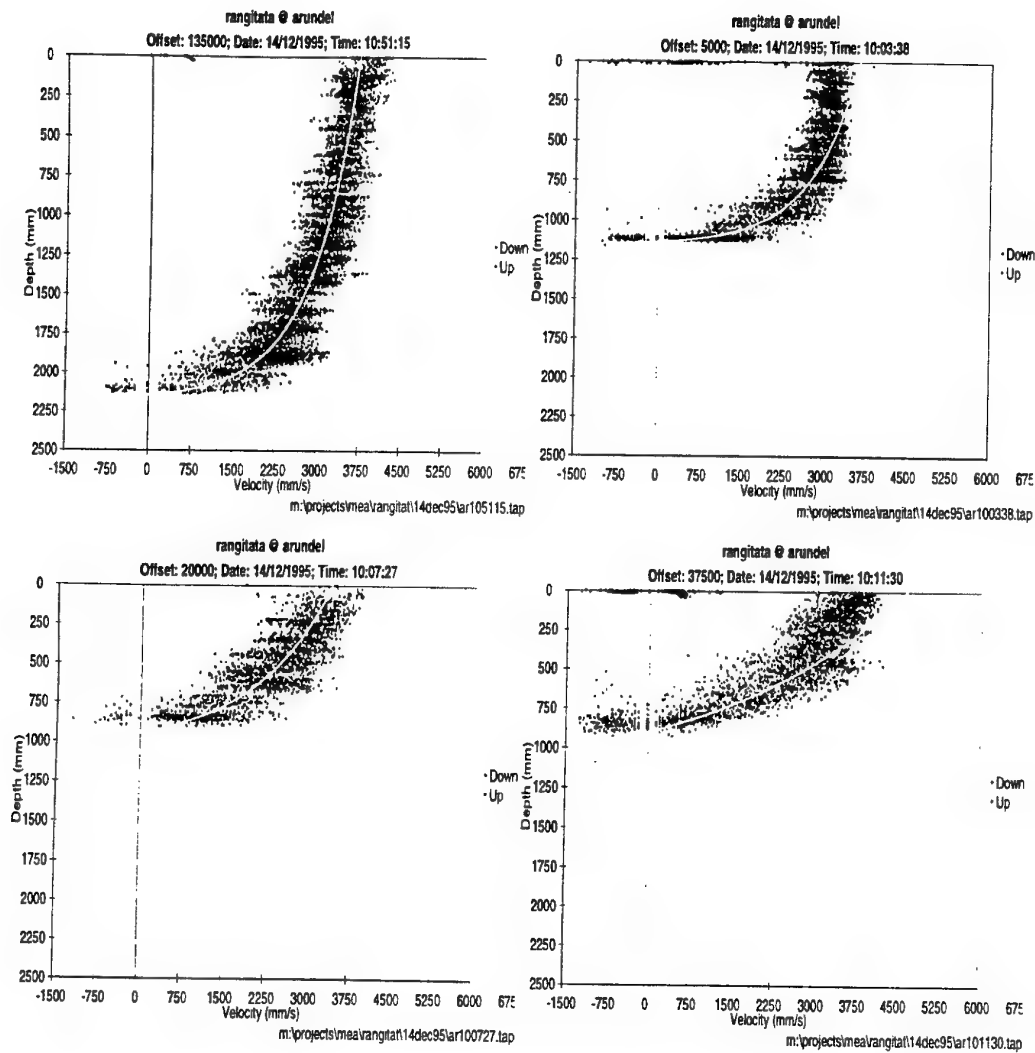


Fig 1 Profiles of downstream river velocity with  $U^* = 0.33, 0.34, 0.56$  and  $1.45$  m/s respectively.

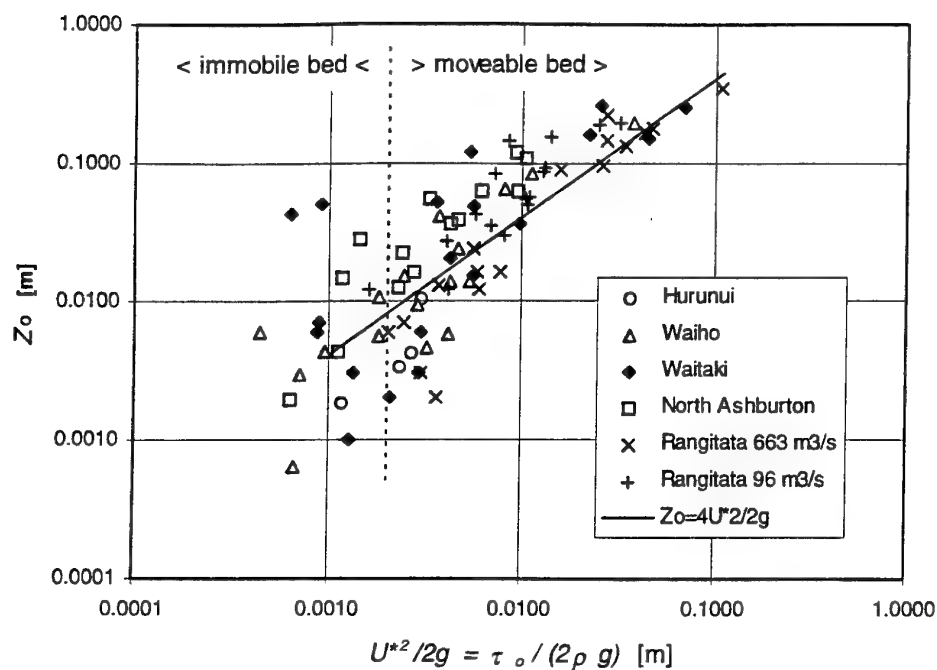


Fig. 2 Relation between bed shear and hydraulic roughness in gravel bed rivers.

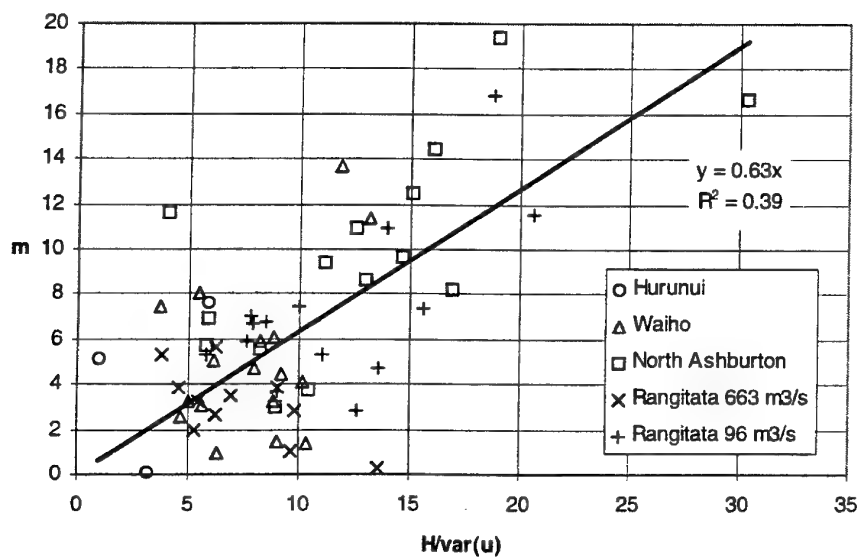


Fig. 3 Ratio of hydraulic roughness to bed shear stress as an inverse function of turbulent kinetic energy per unit depth.

# COMPUTATION WITH THE $k$ - $\epsilon$ MODEL WITH TURBULENT MASS TRANSFER IN THE WALL-REGION

Chaouat Bruno

Energetics Department  
Office National d'Etudes et de Recherches Aéronautiques (ONERA)  
92320 Châtillon  
France

## ABSTRACT

Numerical flow field simulations inside a permeable walled duct with an impermeable diverging area are obtained by solving the Navier-Stokes equations with an appropriate  $k$ - $\epsilon$  turbulence model. For these simulations, turbulence is injected at the wall, according to experimental studies of the fluid mechanics associated with porous walls. In the present case, the turbulent kinetic energy at the wall is considered as a parameter. In order to take into account the mass transfer at the wall, an asymptotic analysis of the  $k$ - $\epsilon$  turbulence model is carried out and indicates that a high Reynolds number  $k$ - $\epsilon$  formulation is required to perform the simulations. A Couette flow model is also proposed with the aim of investigating mean flow properties at the blowing wall. Some interesting features of the flow are also presented. A transition phenomenon from the laminar to the turbulent flow regime is observed in the duct. The average mean velocity and the Reynolds stress tensor are compared with experimental data. The wall layer in presence of turbulent mass transfer is investigated in detail. Of interest is the absence or diminished influence of the viscous sublayer.

## INTRODUCTION

The objective of this work is to investigate the flow field characteristics in presence of turbulent mass transfer at the wall. In practical applications, blowing wall is encountered in solid propellant rocket motors, (Chaouat, 1997). The injected gas flow at the wall is generated by the solid propellant combustion. This type of application presents great physical interest because the turbulence structure in this flow is quite different from that in pipe or boundary layer flow with impermeable wall. The fluid mechanics associated with turbulent mass transfer from porous walls has recently been investigated by Avalon (1991), Ramachandran *et al.* (1992). Ramachandran remarked that the flow exiting from a porous walls presents turbulence intensity at the wall which is proportional to the filter rating (pore size) and increases linearly with the mean flow intensity. Twenty

percent turbulence intensity magnitude is measured near the wall from the 100 microns sample. These results of interest indicate that turbulence is introduced by the porous wall. However, the measurements cannot be achieved in the region very close to the wall (some dimensionless unit distance) because the probe is located a few millimeters away from the porous wall. In this work, we propose to perform numerical simulations with refined meshes near the wall ( $0.3 \mu\text{m}$ ) in order to obtain a high resolution of the turbulent flow field. Some appropriate  $k$ - $\epsilon$  damping functions are chosen according to the results of the asymptotic analysis of the  $k$ - $\epsilon$  turbulence model, based on the Taylor series expansions in space for the velocity and pressure fluctuations. This approach, deduced from the formalism of Hinze (1975), was applied by Speziale *et al.* (1992) to  $k$ - $\epsilon$  turbulence modeling for an impermeable wall.

A Couette model is also proposed for investigating the mean flow properties in presence of mass transfer at the wall. In the past, similar works were conducted by Stevenson (1965), Launder and Spalding (1972) and recently by Bizot, (1995). In this study, the Couette equations are solved by taking into account the pressure gradient term and turbulence injection at the wall.

## TURBULENCE FLUCTUATIONS AT THE WALL

The theoretical approach, usually used to analyse the turbulent flow in the wall region, is based on the Taylor series expansions in space for the velocity components and the pressure fluctuations. In this study, this approach is extended to the case of a blowing wall. A cartesian frame of reference  $x_1, x_2, x_3$  is considered with the direction  $x_2$ , along the mean flow velocity, normal to the wall. The characteristic of the blowing wall is to introduce some fluctuations at the wall ( $x_2=0$ ) which must be related to the mean injected velocity. Above a certain threshold of the mass flow rate, the injected flow becomes turbulent. The Taylor series expansions of the velocity

fluctuations  $u'$  and the pressure fluctuations  $p'$  are given by a local expansion in space with respect to the coordinate  $x_2$ .

These expressions are as follows :

$$u'_i(x_1, x_2, x_3, t) = u'_i(x_1, 0, x_3, t) + \sum_{j=1}^{\infty} \frac{x_2^j}{j!} \frac{\partial^j u'_i}{\partial x_2^j}(x_1, 0, x_3, t). \quad (1)$$

$$p'(x_1, x_2, x_3, t) = p'(x_1, 0, x_3, t) + \sum_{j=1}^{\infty} \frac{x_2^j}{j!} \frac{\partial^j p'}{\partial x_2^j}(x_1, 0, x_3, t). \quad (2)$$

No particular assumptions have been made regarding the fluctuation intensities  $u'_1, u'_2$  and  $u'_3$  at the wall associated with the directions  $x_1, x_2$  and  $x_3$ , although the mean injected velocity is along the direction  $x_2$ . By introducing the new functions:

$$a_{ij}(x_1, x_3, t) = \frac{1}{j!} \frac{\partial^j u'_i}{\partial x_2^j}(x_1, 0, x_3, t), \quad (3)$$

$$\alpha_j(x_1, x_3, t) = \frac{1}{j!} \frac{\partial^j p'}{\partial x_2^j}(x_1, 0, x_3, t), \quad (4)$$

the fluctuations  $u'_i$  and  $p'$  can be rewritten in a simpler compact form as:

$$u'_i(x_1, x_2, x_3, t) = \sum_{j=0}^{\infty} a_{ij}(x_1, x_3, t) x_2^j, \quad (5)$$

$$p'(x_1, x_2, x_3, t) = \sum_{j=0}^{\infty} \alpha_j(x_1, x_3, t) x_2^j, \quad (6)$$

where  $a_{i0} = u'_i(x_1, 0, x_3, t)$  and  $\alpha_0 = p'(x_1, 0, x_3, t)$ . For an impermeable wall, the coefficients  $a_{i0}$  are zero. This theoretical formulation is convenient in describing the turbulent process near the wall. For instance, by using the Reynolds average, one can easily obtain the following exact expression of the turbulent kinetic energy :

$$k = \frac{1}{2} (a_{10}^2 + a_{20}^2 + a_{30}^2) \quad (7)$$

$$+ (a_{10}a_{11} + a_{20}a_{21} + a_{30}a_{31}) x_2 + O(x_2^2).$$

As can be expected, this expression shows that  $k$  presents a linear variation near the wall ( $x_2=0$ ). The first square correlation term represents the contribution of the injected turbulence at the wall. For impermeable wall, only some fluctuation correlations of the coefficients  $a_{ij}$  have been obtained by Kim *et al.* (1988) for a flow field in a plane channel. In the same way, turbulent processes such as the production, the destruction and the diffusion of the  $k$  and  $\epsilon$  transport equations, can be calculated by this formalism. For instance, the diffusion of the turbulent kinetic energy generated by the velocity fluctuations.

$$\phi(k) = -\frac{1}{2} \frac{\partial}{\partial x_2} [\overline{u'_i u'_i u'_j}] , \quad (8)$$

takes the form as :

$$\phi(k) = -\frac{1}{4} \frac{(a_{10}^2 + a_{20}^2 + a_{30}^2) a_{21}}{(a_{10}a_{11} + a_{20}a_{21} + a_{30}a_{31}) a_{20}} + O(x_2). \quad (9)$$

## ASYMPTOTIC ANALYSIS OF THE $k$ - $\epsilon$ MODEL

Numerical simulations using the standard  $k$ - $\epsilon$  turbulence model (Jones and Launder, 1972) require the knowledge of damping functions which have been only calibrated for impermeable walls. These functions  $f_1, f_2$  and  $f_\mu$  appear in the  $k$ - $\epsilon$  model equations in the following way:

$$\frac{\partial k}{\partial t} + \bar{u}_j \frac{\partial k}{\partial x_j} =$$

$$-\frac{\partial}{\partial x_j} \left[ \left( v + \frac{v_i}{\sigma_k} \right) \frac{\partial k}{\partial x_j} \right] - \overline{u'_i u'_j} \frac{\partial \bar{u}_j}{\partial x_i} - \epsilon, \quad (10)$$

$$\frac{\partial \epsilon}{\partial t} + \bar{u}_j \frac{\partial \epsilon}{\partial x_j} =$$

$$-\frac{\partial}{\partial x_j} \left[ \left( v + \frac{v_i}{\sigma_\epsilon} \right) \frac{\partial \epsilon}{\partial x_j} \right] - c_1 f_1 \overline{u'_i u'_j} \frac{\partial \bar{u}_j}{\partial x_i} + c_2 f_2 \frac{\epsilon^2}{k}, \quad (11)$$

where the turbulent eddy viscosity  $\nu_t$  is evaluated as :

$$\nu_t = c_\mu f_\mu \frac{k^2}{\epsilon}, \quad (12)$$

and the double velocities correlation  $\overline{u'_i u'_j}$  is modeled by the well-known Boussinesq hypothesis. In (10), (11), (12),  $c_1, c_2, c_\mu, \sigma_k$  and  $\sigma_\epsilon$  are constant coefficients. The asymptotic analysis of the  $k$ - $\epsilon$  equations consists in comparing the order of magnitude of the exact expressions of the diffusion, production and destruction terms of the exact  $k$ - $\epsilon$  transport equations with the modeled diffusion, production and destruction terms of equations (10) and (11). Since the Taylor series expansions of the exact diffusion, production and destruction terms calculated by using (5) and (6) are  $O(1)$  at the wall with turbulent mass transfer, this analysis indicates that the damping functions must be  $O(1)$ , (Chaouat, 1994). The matching conditions with the core flow require that these functions are equal to one in the outer region of the wall zone. For practical applications, these functions are taken to unity. The interpretation of this result is that a wall with turbulent mass transfer should be considered as a virtual wall for the numerical simulations.

For the impermeable wall, the following damping functions, which satisfy the asymptotic conditions for the  $k$ - $\epsilon$  turbulence model (Speziale *et al.*, 1992)  $f_1 = O(1)$ ,  $f_2 = O(x_2^2)$ ,  $f_\mu = O(1/x_2)$ , are proposed as defined recently by Myong and Kasagi, (1992) :

$$f_1 = 1 - a_1 e^{-\frac{R_t^2}{a_2}}, \quad (13)$$

$$f_2 = \left( 1 - e^{-\frac{x_2^+}{a_3}} \right)^2, \quad (14)$$

and :

$$f_\mu = \left[ 1 + \frac{a_4}{\sqrt{R_t^2}} \right]^2 \tanh \left( \frac{x_2^+}{a_5} \right), \quad (15)$$

where  $R_t = k^2 / \nu \epsilon$  is the turbulent Reynolds number and  $x_2^+$  is the dimensionless variable. The numerical values are the following:  $a_1 = 2/9$ ,  $a_2 = 36$ ,  $a_3 = 4.9$ ,  $a_4 = 3.45$ ,  $a_5 = 70$ .

## COUETTE FLOW ANALYSIS

A useful theoretical approach in determining the mean flow characteristics near a blowing wall consists in making the Couette assumptions in the Navier-Stokes equations. In this situation, by using the Reynolds average in order to decompose each instantaneous variable into mean and fluctuating part, the steady momentum equation in the longitudinal direction  $x_1$  is written as follows (Cebeci and Smith, 1974) :

$$m \frac{\partial \bar{u}_1}{\partial x_2} = -\frac{\partial \bar{p}}{\partial x_1} + \mu \frac{\partial^2 \bar{u}_1}{\partial x_2^2} - \rho \frac{\partial}{\partial x_2} (\overline{u'_1 u'_2}). \quad (16)$$

where  $m$  is the injected mass flow rate defined as  $m = \rho u_2$ . The steady momentum equation in the normal direction  $x_2$  reduces to  $\partial \bar{p} / \partial x_2 = 0$ . For the Couette analysis, it is more convenient to introduce the dimensionless variables defined as:

$$x_1^* = \frac{x_1 u_\tau}{\nu}, u_1^* = \frac{u_1}{u_\tau}, p^* = \frac{p}{\rho u_\tau^2}, \quad (17)$$

$$m^* = \frac{m}{\rho u_\tau}, \tau^* = \frac{\tau}{\rho u_\tau},$$

where  $u_\tau$  is the friction velocity. By using these variables, a first integration of equation (16) can be rewritten in the dimensionless form as :

$$1 + m^* \bar{u}_1^* + x_2^* \frac{\partial \bar{p}^*}{\partial x_1^*} = \frac{\partial \bar{u}_1^*}{\partial x_2^*} - \bar{u}_1^* \bar{u}_2^*. \quad (18)$$

In the general case, this equation cannot be solved theoretically. If we consider the regime where the flow injected at the wall is laminar, the turbulence contribution in the viscous sublayer vanishes. By using the boundary condition of the shear stress, equation (18) can be integrated and the velocity profile takes the form as :

$$u_1^*(x_2^*) = \frac{1}{m^*} \left( 1 + \frac{1}{m^*} \frac{\partial \bar{p}^*}{\partial x_1^*} \right) (e^{m^* x_2^*} - 1) - \frac{1}{m^*} \frac{\partial \bar{p}^*}{\partial x_1^*} x_2^*. \quad (19)$$

Expression (19) shows that the dimensionless velocity profile presents an exponential variation versus the dimensionless distance. However, for a particular value of the dimensionless pressure gradient given by  $\partial \bar{p}^* / \partial x_1^* = -m^*$  which implies that the shear stress at the wall  $\tau_w = -(\mu / m) \partial \bar{p} / \partial x_1$ , one finds again the standard velocity profile  $u_1^* = x_2^*$  in the viscous sublayer ( $x_2^* \leq 3$ ). Above a certain threshold of the injected mass flow rate, the turbulence contribution cannot be neglected at the wall. In this case, equation (18) cannot be solved theoretically. However, a Taylor series expansions in space of the dimensionless velocity profile can be made. One can obtain :

$$\bar{u}_1^*(x_2^*) = (1 + \bar{u}_1^* \bar{u}_2^*)_{(x_2^*=0)} x_2^* + [m^* (1 + \bar{u}_1^* \bar{u}_2^*) + \frac{\partial \bar{p}^*}{\partial x_1^*} + \frac{\partial}{\partial x_2^*} (\bar{u}_1^* \bar{u}_2^*)]_{(x_2^*=0)} \frac{x_2^{*2}}{2} + O(x_2^{*3}). \quad (20)$$

This expression, written in the general form with the dimensionless Reynolds stress tensor, indicates that the linear profile is no longer valid because of the turbulence effects. It is shown that the dimensionless velocity profile is governed by

the turbulence injection introduced at the wall, the mass flow rate and the pressure gradient.

## BOUNDARY CONDITIONS OF COMPUTATIONAL DOMAIN

Figure 1 shows the experimental apparatus and corresponds to a nozzleless solid rocket motor using a porous-walled duct with an impermeable-walled diverging area. The duct length  $L$  is 48 cm and the height  $h$  is 1 cm. A refined grid has been defined for the simulations. The space discretization requires  $171 \times 120$  meshes in the directions  $x_1$  and  $x_2$ . The thickness  $\Delta x_2$  between two consecutives grid points is taken as  $0.3 \mu\text{m}$ .

so that the dimensionless thickness near the wall region,  $\Delta x_2^*$ , is of a magnitude of 0.1 wall unit. The cold flow characteristics for the computations are:

- Air molecular weight:  $M = 29 \cdot 10^{-3} \text{ kg/mole}$  ;
- Specific heat ratio:  $\gamma = 1.4$  ;
- Mean static pressure: 3 bars ;
- Injection temperature: 260 K ;
- Injected mass flow rate:  $13 \text{ kg/m}^2 \cdot \text{s}$ .

Boundary conditions for the permeable wall are applied to the computational domain. The turbulent kinetic energy at the wall is considered as a parameter. In order to see the influence of the turbulence at the wall, the first simulation is made without injected turbulence intensity, whereas the second simulation is performed with turbulence intensity, equals to 75 % of the injected mean square velocity. Regarding the boundary conditions of the dissipation rate  $\epsilon$  in the case of turbulent injection, the hypothesis of universal spectrum of turbulence in the inertial sub-range has been made. According to this consideration, the dissipation rate is obtained by:

$$\epsilon = c_\mu^{\frac{3}{4}} \frac{k^{\frac{3}{2}}}{l}, \quad (21)$$

where the turbulence length scale  $l$  is assumed to be of the same order of that of the wall porosity ( $100 \mu\text{m}$ ). For the impermeable wall, the turbulent kinetic energy at the wall ( $x_2=0$ ) is zero and the dissipation rate is obtained by the well known relation :

$$\epsilon = 2 \nu \left[ \frac{\partial \sqrt{k}}{\partial x_2} \right]^2 + O(x_2^2). \quad (22)$$

## NUMERICAL RESULTS

In this section, numerical flow field simulations are presented. The numerical results are compared with experimental data obtained by Traineau *et al.*, (1986) at ONERA. The accuracy of the numerical scheme is of the second order in time and space. Figure 2 shows the pressure contours of the flow. It can be seen that the pressure is constant along the direction normal to the wall. The evolution of the integral momentum flux coefficient introduced by Huesmann and Eckert (1968) defined by :

$$\beta = \frac{\rho h \int_0^h \rho \bar{u}_1^2 dx_2}{\left( \int_0^h \rho \bar{u}_1 dx_2 \right)^2}, \quad (23)$$

which provides a criterion for the transition velocity profile, is plotted in figure 3. It can be observed by the rapid drop in the coefficient  $\beta$  that the numerical calculations predicts a transition

regime which occurs respectively at  $x_1=0.10$  cm and 0.15 cm for the simulations performed with and without turbulence injection. These results are quite close to the experimental prediction observed for  $x_1=18$  cm. Figure 4 shows the evolution of the normalized mean velocity profiles  $u_1^*=u_1/u_{1c}$  (where  $u_{1c}$  is the center velocity) and the turbulent Reynolds stress tensor

$u_1'u_1'$  corresponding to the duct cross-sections located at different axial distances.  $x_1=11.1$  cm; 24.1 cm; 40.6 cm. One can notice that the velocity profiles are in very good agreement with the experimental data. The flattening of the velocity curves is attributed to the effects of turbulence. For the first section, it can be noted that the Reynolds stress profiles, deduced from the simulation performed with some turbulence intensity at the wall, show a better agreement with experimental data. Figure 5 shows the profile of the dimensionless velocity  $u_1^*=u_1/u_\tau$  near the wall region with the normal dimensionless distance to the wall  $x_2^*=x_2 u_\tau/\nu$  for  $x_2^* \leq 10$ . As it could be expected by the previous Couette analysis, the slope coefficient of the dimensionless mean velocity gradient at the wall is equal to unity for the simulation performed without turbulence injection. Numerical data indicate that  $\partial p^*/\partial x_1^* = -m^*$  which implies that the linear velocity law is the physical solution of equation (18) in the viscous sublayer. For the other simulation performed with turbulence injection, the slope coefficient is approximately 1/40 which is in good agreement with the prediction of expression (20) rewritten with the  $k-\epsilon$  turbulence model. As it was expected in this case, the linear profile is no longer valid because of the turbulent effects.

Figure 6 shows the dimensionless evolutions of the turbulent kinetic energy  $k^*=k/u_\tau^2$  and dissipation rate  $\epsilon^*=\epsilon\nu/u_\tau^4$  in a duct cross-section located at  $x_1=24.1$  cm. It can be observed that these turbulent terms vary on a very large dimensionless distance ( $x_2^*=5000$  or  $x_2=h/2$ ) to be completely described.

## CONCLUSION

Numerical flow field simulations induced by wall injection, have been presented. These investigations allow one to improve the fluid mechanics understanding of this type of flow. The computed velocity profiles indicate very good agreement with the experimental profiles and the transition phenomenon from laminar to turbulent regime is correctly predicted. The wall region in presence of mass transfer has been investigated in details. Particular interesting is the absence of the viscous sublayer in the case of turbulence injection at the wall. The second order closure model (Launder *et al.*, 1975, Speziale, 1991) which requires transport equations for each components of the Reynolds stress tensor could be an alternative for investigating this type of flow.

## REFERENCES

- Avalon, G., 1991, "Aérodynamique Interne des Propulseurs à Propergol Solide," *Technical report ONERA n°4/2486 EY*.
- Bizot, A., 1995, "Turbulent Boundary Layer with Mass Transfer and Pressure Gradient in Solid Propellant Rocket Motors," *AIAA Paper* 2708.
- Chaouat, B., 1994, "Modélisation et Simulation des Ecoulements Turbulents dans les Propulseurs à Propergol Solide," Ph.D. Thesis, University of Paris VI, France.
- Chaouat, B., 1997, "Flow Analysis of a Solid Propellant Rocket Motor with Aft Fins," *Journal of Propulsion and power*, Vol. 13, n° 2., pp.194-196.
- Cebeci, T. and Smith, A. M. O., 1974, "Analysis of Turbulent Boundary Layers," *Academic Press*, Inc.
- Hinze, J. O., 1975, *Turbulence*, *Mc Graw-Hill*, Publishing Company.
- Huesmann, K. and Eckert, E., 1968, "Studies of the Laminar Flow and the Transition to Turbulence in Porous Tubes Uniform Injection Through the Tube Wall," *Warme und Stoffübertragung*, Vol. 1, pp. 1-9.
- Jones, W. P. and Launder, B. E., 1972, "The Prediction of Laminarization with a Two-equation Model of Turbulence," *Int. Journal Heat Mass Transfer*, Vol. 15, pp. 301-314.
- Kim, J. P., Moin, P. and Mansour, R., 1988, "Reynolds-stress and Dissipation-rate Budgets in a Turbulent Channel Flow Region," *J. Fluid Mech.*, Vol. 194, n° 15.
- Launder, B. E. and Spalding, D. B., 1972, "Mathematical Models of Turbulence," *Academic Press London and New York*.
- Launder, B. E., Reece, G. J. and Rodi, W., 1975, "Progress in the Development of a Reynolds-stress Turbulence Closure," *J. Fluid Mech.*, Vol. 68, pp. 537-566.
- Myong, H. and Kasagi, N., 1990, "A New Approach to the Improvement of  $k-\epsilon$  Turbulence Model for Wall-Bounded Shear flows," *JSME international*, Vol. 33, pp. 63-72.
- Ramachandran, N., J. Heaman, J. and Smith, A., 1992, "An Experimental Study of the Fluid Mechanics Associated with Porous Wall," *AIAA Paper* 0769.
- Speziale, C. G., Abid, R. and Anderson, E., 1990, "Critical Evaluation of Two-Equation Models for Near-Wall Turbulence," *AIAA Journal*, Vol 30, pp.324-331.
- Speziale, C. G., 1991, "Analytical Method for the Development of Reynolds-Stress Closures in Turbulence," *J. Fluid Mech.*, Vol.23, pp.107-157.
- Stevenson, T. N., 1963, "A Law of the Wall for Turbulent Boundary Layers with Suction or Injection," *The college of Aeronautics, Cranfield Rep. Aero.*, Vol. 166.
- Traineau, J. C., Hervat, P. and Kuentzmann, P., 1986, "Cold Flow Simulation of a Two-Dimensional Nozzleless Solid Rocket Motor," *AIAA Paper* 1447.



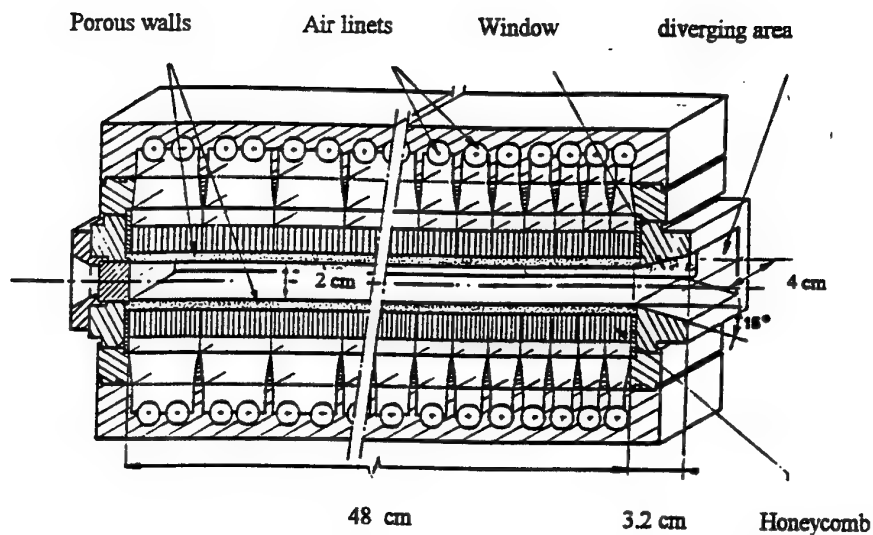


FIGURE 1. SCHEMATIC OF EXPERIMENTAL APPARATUS.



FIGURE 2. PRESSURE CONTOURS IN THE PERMEABLE WALLED-DUCT  
 $\Delta p = 0.05$  bar.

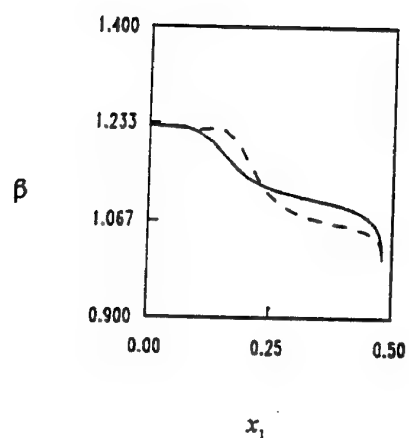


FIGURE 3 : EVOLUTION OF THE MOMENTUM COEFFICIENT  $\beta$  :  
 — zero turbulence intensity; — 75% turbulence intensity.

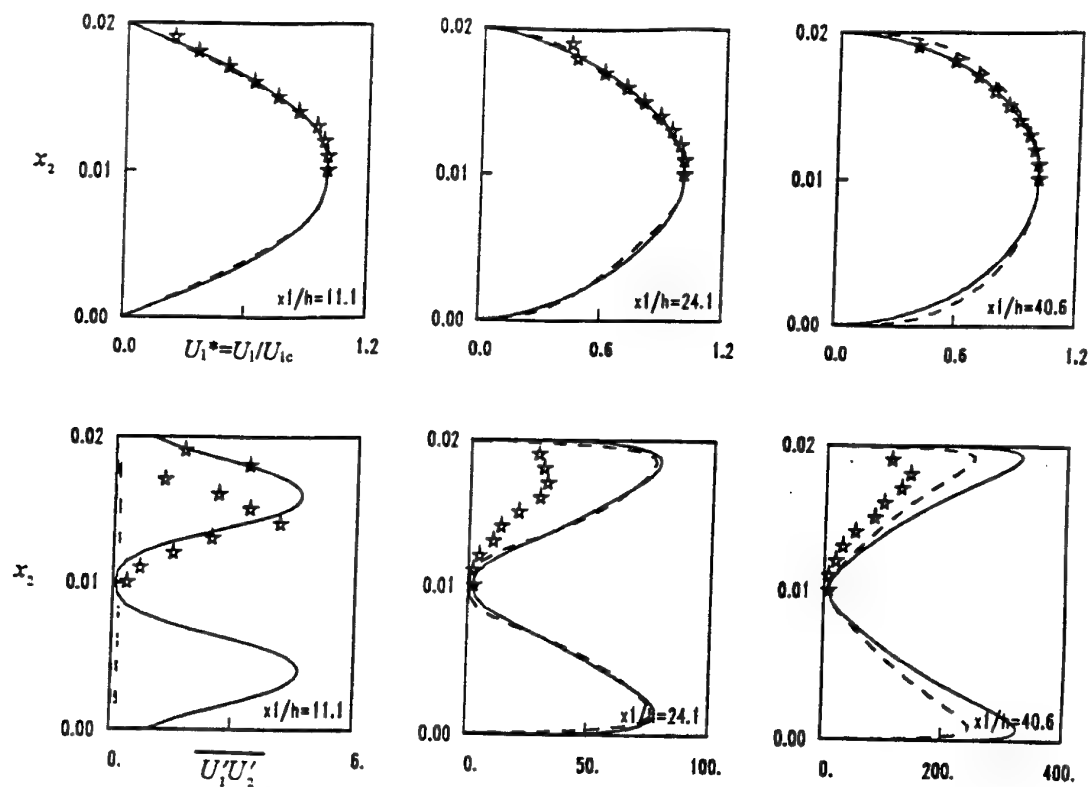


FIGURE 4. COMPARISON OF THE EXPERIMENTAL AND NUMERICAL PROFILES FOR THE NORMALIZED MEAN VELOCITY  $U_1^* = U_1/U_{1c}$  AND REYNOLDS STRESS  $\overline{U_1'U_2'}$  IN VARIOUS CROSS-SECTIONS OF THE DUCT :  
 \*\*\* experimental data; - - 0% turbulence intensity; — 75 % turbulence intensity.

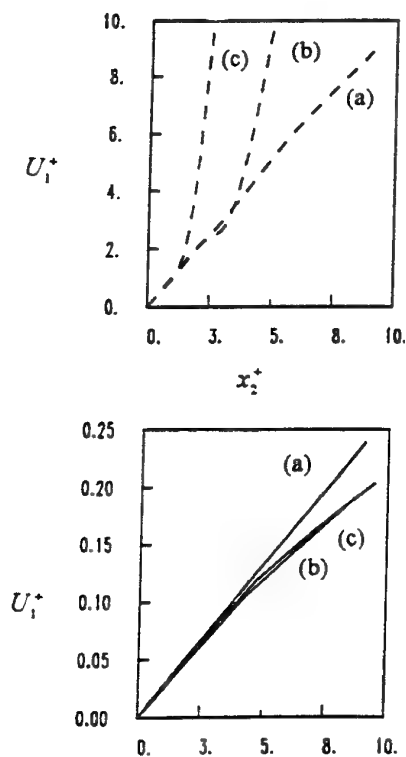


FIGURE 5. EVOLUTION OF THE DIMENSIONLESS VELOCITY PROFILE : - - 0% turbulence intensity; — 75% turbulence intensity ; (a)  $x_1 = 11.1$  cm; (b)  $x_1 = 24.1$  cm; (c)  $x_1 = 40.6$  cm.

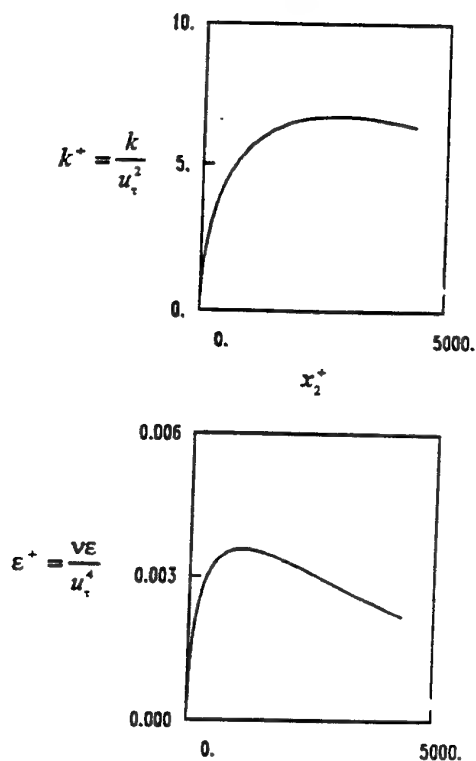


FIGURE 6. EVOLUTION OF THE DIMENSIONLESS TURBULENT KINETIC ENERGY AND DISSIPATION RATE ;  $x_1 = 24.1$  cm — 75% turbulence intensity.

# INVESTIGATION OF THE BURSTING PHENOMENON IN TRANSITIONAL BOUNDARY LAYERS

Václav Uruba, Pavel Jonáš, Oton Mazur

Department of Fluid Mechanics

Institute of Thermomechanics

Academy of Sciences of the Czech Republic

Dolejšková 5

182 00 Praha 8

Czech Republic

## ABSTRACT

The bursting phenomenon within the by-pass transition on the flat plate was experimentally investigated. The outer stream was disturbed by various grid turbulence generators to study the influence of length scale conserving the intensity of turbulence on the leading edge.

The pattern recognition technique to detect the burst was used.

Dramatic changes of bursting phenomenon parameters during the transition were found out. The dependence on the length scale of outer stream was not approved.

## INTRODUCTION

### Motivation

The concept of the universality of the bursting phenomenon in the wall bounded shear flows is generally accepted. The coherent motions called the bursting phenomenon, a couple of two events - sweep and ejection, play a fundamental role in the turbulent energy and turbulent shear production in every turbulent boundary layer. They manifest themselves the interaction between inner and outer parts of turbulent boundary layer. Turbulent boundary layer is the final stage of the laminar/turbulent transition of a boundary layer. Thus the characteristics of bursts could be a good indicator of the evolution of transition process particularly in the by-pass transition turbulent boundary layer since the effect of outer stream turbulence on bursts in a turbulent boundary layer has been observed. The aim of presented study is therefore to clarify the role of the bursting phenomenon in by-pass transition.

### By-pass Transition

The process of „natural“ boundary layer transition to turbulence can be characterise by several stages. In the first stage the laminar boundary layer develops linear 2D oscillations, Tollmien-Schlichting waves. Then the amplitude of waves increase, spanwise distortions of vortical structures

develop and grow in an increasingly 3D and non-linear manner. They are eventually converted into turbulent spots (intermittent region). Finally the fully turbulent boundary layer originates.

By-pass transition occurs when the formation and amplification process of 2D Tollmien-Schlichting waves in natural transition is „bypassed“ due to presence of forced disturbances of sufficient amplitude. Sources of such disturbances include higher free-stream turbulence. In this mode of transition, Tollmien-Schlichting waves and the above described cause of transition are less evident. They support the action of the forced disturbances. The first indication of transition may be the direct formation of turbulent spots. The by-pass transition significantly reduces the length of unstable laminar flow and promote earlier transition. The by-pass transition has significant practical importance.

### Bursting Phenomenon

An important discovery in recent years is that the most active dynamical processes take place in a region very close to the wall, in region  $5 < y^+ < 70$ , which at high Reynolds numbers may constitute a very small portion of the boundary layer, often less than 1% of the boundary layer thickness. That there is strong activity in the near-wall region was shown already by Townsend 1956, but the crucial role this region plays in the turbulence dynamics was first conclusively demonstrated by Kline et al. 1967. They used hydrogen bubbles generated by an electric wire to visualize the low-speed water channel. This technique revealed the presence of low-speed streaks of fairly regular spanwise spacing. Intermittently, the streaks begin to oscillate and they break up in a fairly violent motion, a „burst“. Kline et al. 1967 proposed a conceptual model for bursting. In this model the fundamental dynamical mechanisms sorted out are the lift-up of low-speed streak and stretching of spanwise vorticity producing a thin shear layer that is inflectionally unstable. The breakdown of this shear layer, possibly caused by

Kelvin-Helmholtz type instability, would therefore constitute the main source of small-scale turbulence.

Further visual studies e.g. by Corino and Brodkey 1969 showed that there were two kinds of stress-producing motions: ejections involving rapid outflow of low-speed fluid from the wall region and sweeps characterized by inflow of high-speed fluid toward the wall. Both of these processes contribute about 70% of the total Reynolds stress. The balance is made up of wallward and outward interactions giving negative stress contributions. The ejections could sometimes involve moderately small scale structures. The stress-producing motions are highly intermittent, occurring maybe about 25% of the total time.

## EXPERIMENTAL SETUP

### Experimental Apparatus

The investigated boundary layer develops on a wooden flat plate in the close circuit wind tunnel (0.5m x 0.9m). The mean velocity of the outer stream is 5 m/s. The turbulence level of the flow is controlled by means of turbulence generating plane grids or screens of various geometry. Every grid is placed across the flow in the proper distance upstream from the leading edge of the plate. Thus, there has been achieved homogeneous turbulence with the turbulence level 3% and with the dissipative length scales between 6 and 35 mm at the leading edge plane (COST/ERCOFTAC SIG on Transition Test Case T3A+).

Three grid generators of turbulence differing by geometry were used to disturb the outer stream (GT 1, GT 3, GT 5). In all cases the structure of the turbulence of outer stream in the position of leading edge was homogenous and close to isotropy. The mean velocity  $U_e = (5,00 \pm 0,05)$  m/s, the intensity of turbulence  $Iu_e = (3,00 \pm 0,03)\%$  and the dissipative length scale  $L_e = 6,8$  mm for GT 1,  $L_e = 16,3$  mm for GT 3 and  $L_e = 34,5$  mm for GT 5. Definitions of intensity of turbulence  $Iu_e$  and dissipative length scale  $L_e$ :

$$Iu_e = \frac{\sqrt{u^2}}{U_e} \quad L_e = \frac{\left(\overline{u^2}\right)^{3/2}}{U_e \frac{d}{dx} \left(\overline{u^2}\right)} \quad (1)$$

where

$u$  is instantaneous longitudinal fluctuation velocity component,

$U_e$  is mean velocity of outer stream.

The hot wire technique with the single wire probe (DISA 55P01) indicating the longitudinal component of the local velocity was used. The DISA CTA measurement system 55M indicated the velocity. The single-hot-wire technique is applied with the wire parallel to the wall and perpendicular to the main stream direction due to the small boundary layer thickness.

The useful signals from anemometer were of frequencies up to 3 kHz.

The anemometry system is connected to a PC equipped with the data acquisition system (National Instruments) controlled by the software LabVIEW. The data were digitally evaluated. The sampling frequency of 25 kHz was chosen as to be able to reconstruct the signal in details. In all measured points the record of 750 000 samples corresponding to 30 seconds was taken and saved on hard disk of computer to process afterwards.

The experimental set-up has been described in details in Jonáš et al. 1996.

## Procedures

Adapted pattern recognition method proposed by Wallace et al. 1977 has been employed. This technique can detect and obtain the ensemble averages of simple wave forms that are related to bursting phenomenon.

Only the  $u$ -signal patterns are recognized using a simple criteria. The validity of the method was proved by simultaneous processing of  $v$ - and  $w$ -signals as well as  $uv$ - or  $uw$ - together with  $u$ -signal. It is found that simple signal shapes describe the turbulence structures on the average. The  $u$ -signal consists of a gradual deceleration from a local maximum followed by a strong acceleration. The  $v$ -signal is found to be approximately  $180^\circ$  out of phase with  $u$ -signal. These signal shapes can be easily associated with the coherent structures that have been observed visually.

On the basis of this technique the computer algorithm was created:

1. The  $u$ -velocity voltage data from anemometer are acquired.
2. The voltage data are transformed into velocity.
3. The time series is smoothed by smoothing window of appropriate length.
4. The derivative of time series is calculated.
5. The maxima of derivative are explored, its locations define the limits of events.
6. In each event the minimum of derivative is looking for.
7. The events are sorted following the criterion if the absolute value of derivative maximum is greater then the absolute value of minimum. If the criterion is accomplished, the event is consider to be a BURST.

8. The characteristics of burst events (and also non-burst events) are calculated and statistically processed (temporal average, central moments, lengths, period of occurrence).

This algorithm slightly differs from the Wallace one.

## RESULTS

The investigation of bursting phenomenon has been executed in several positions downstream from the leading edge within the transitional boundary layer.

Certain dependence of the bursts characteristics on the distance from the wall has been observed by several researchers.

Hence the investigation has been executed in the exactly defined distance from the wall  $y_B$ , where the skewness factor of velocity fluctuations changes its sign. This choice of the position is physically justified in a turbulent boundary layer as there the Reynolds stress and the turbulence production have their maximum while the bursting phenomenon is very considerably responsible for these production. Thus it is promising to observe bursts in this position (see Jonáš 1992). In the fully developed turbulent boundary layer the position  $y_B$  corresponds to  $y^+ \approx 12$ .

To describe the evolution of the transition process the measurements in the distance  $y_B$  from the wall was chosen. It is possible to carry out repeatable observations without any important distortion in the distance  $y_B$  using the chosen experimental technique. In the figure 1 the  $y_B$  vs.  $Re_x$  (the Reynolds number defined as customary) courses are shown.

To define the outer stream quality the position outside the boundary layer were investigated (in the distance of 70mm from the wall).

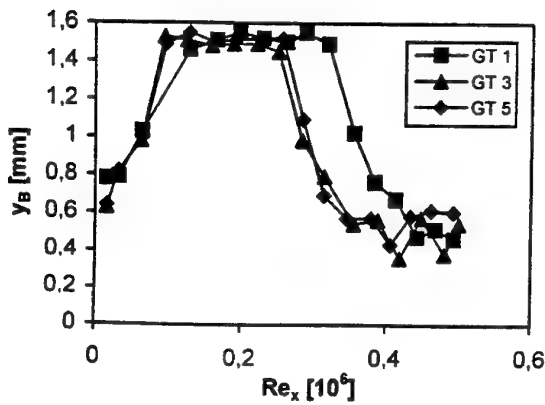


FIG. 1 - THE DISTANCE FROM THE WALL FOR THE BURST INVESTIGATION.

The profiles of bursting phenomenon characteristics were evaluated in four  $x$ -positions. The first position I ( $Re_x \approx 3,1 \cdot 10^4$ ) corresponds to the laminar region characterized by Blasius-like mean velocity profile in boundary layer. The second position II ( $Re_x \approx 1,3 \cdot 10^5$ ) corresponds to the beginning of the transition, whereas the position III ( $Re_x \approx 3,1 \cdot 10^5$ ) corresponds to the late stage of the transition process. The last position IV ( $Re_x \approx 4,8 \cdot 10^5$ ) is located in turbulent boundary layer region. In the figure 2 the courses of skin friction coefficient are shown ( $C_f$  vs.  $Re_x$ ). The skin friction coefficient is very good indicator of transition. Hence the transition stages and chosen longitudinal positions can be clearly seen in this figure.

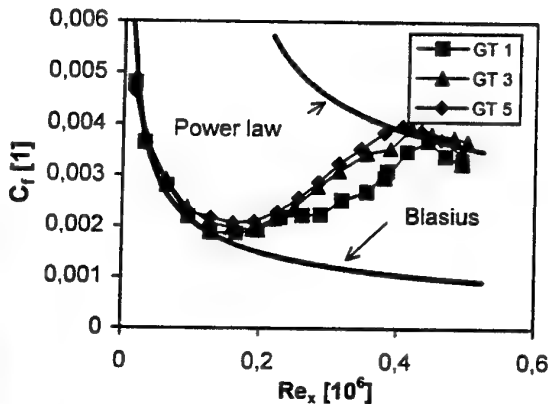


FIG. 2 - SKIN FRICTION COEFFICIENT.

The non-dimensional quantities characterising the length and period of occurrence of the bursts using both inner (index +) and outer (index e) boundary layer parameters have been defined as follows. The non-dimensional mean period of burst occurrence (non-dimensionalised by inner and outer flow parameters):

$$T_p^+ = \bar{T}_p \frac{u_\tau}{\delta_1} \quad (2)$$

$$T_p^e = \bar{T}_p \frac{U_e}{\delta_1} \quad (3)$$

where:

$\bar{T}_p$  is the mean period of bursting events,

$U_e$  is the mean outer stream velocity,

$u_\tau$  is the local skin friction velocity,

$\delta_1$  is the local displacement boundary layer thickness.

The non-dimensional mean burst durations:

$$T_B^+ = \bar{T}_B \frac{u_\tau^2}{\nu} \quad (4)$$

$$T_B^e = \bar{T}_B \frac{U_e^2}{\nu} \quad (5)$$

where:

$\bar{T}_B$  is the mean duration of bursting events,

$\nu$  is the kinematics viscosity.

The length of smoothing window was tested. In the figure 3 the dependence of the evaluated burst period  $T_p^e$  on the smoothing windows length  $\tau_s$  is plotted (GT 1,  $y_B$ ,  $Re_x = 4,8 \cdot 10^5$ ). It is seen that the evaluated  $T_p^e$  is approximately independent on windows length for  $\tau_s > 0,01s$ . The value 0,012s of  $\tau_s$  (the rectangle) was taken for all following evaluations.

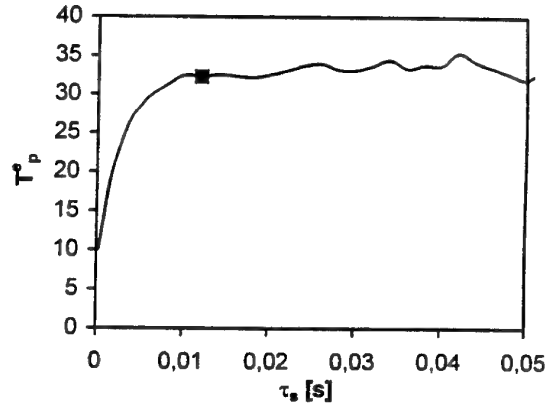


FIG. 3 - SMOOTHING WINDOWS TESTING.

The most detailed analysis of bursting phenomenon was performed in the  $y_B$  distance from the wall. In the figures 4 and 5 the courses of  $T_p^+$  and  $T_B^+$  vs.  $Re_x$  for the three turbulence generators are compared. The inner non-dimensional parameters were chosen in this case. Any systematic influence of outer stream length-scales on period of occurrence and duration of bursts was not find out.

In fully developed boundary layer the bursting phenomenon in  $y_B$  position is characterised by following constant values of nondimensional parameters (Jonáš 1992):  $T_p^e = 30 \div 32$  and  $T_B^e = 1,94 \cdot (1 \pm 0,065) \cdot 10^4$ .

Our results of outer parameters non-dimensionalised periods and durations of bursts presented in the figures 6 and 7 get near those values for higher  $Re$ , although the fully turbulent boundary layer has not been achieved yet.

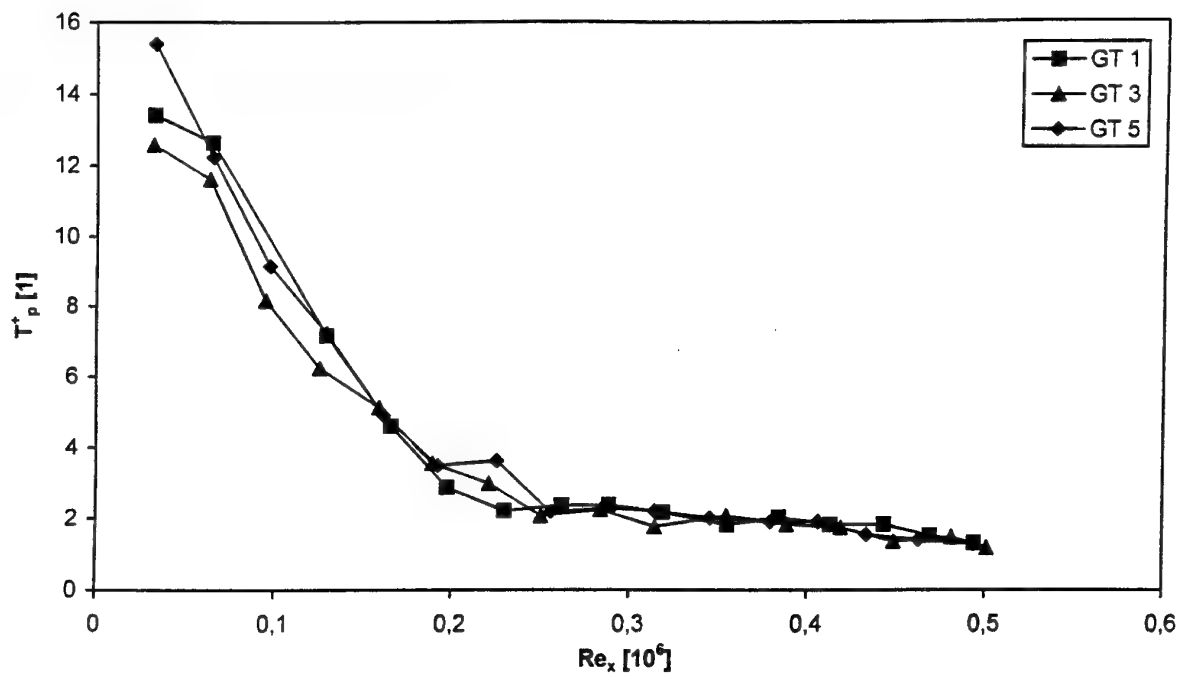


FIG.4 - NON-DIMENSIONED (BY INNER PARAMETERS) MEAN PERIOD OF BURST OCCURRENCE.

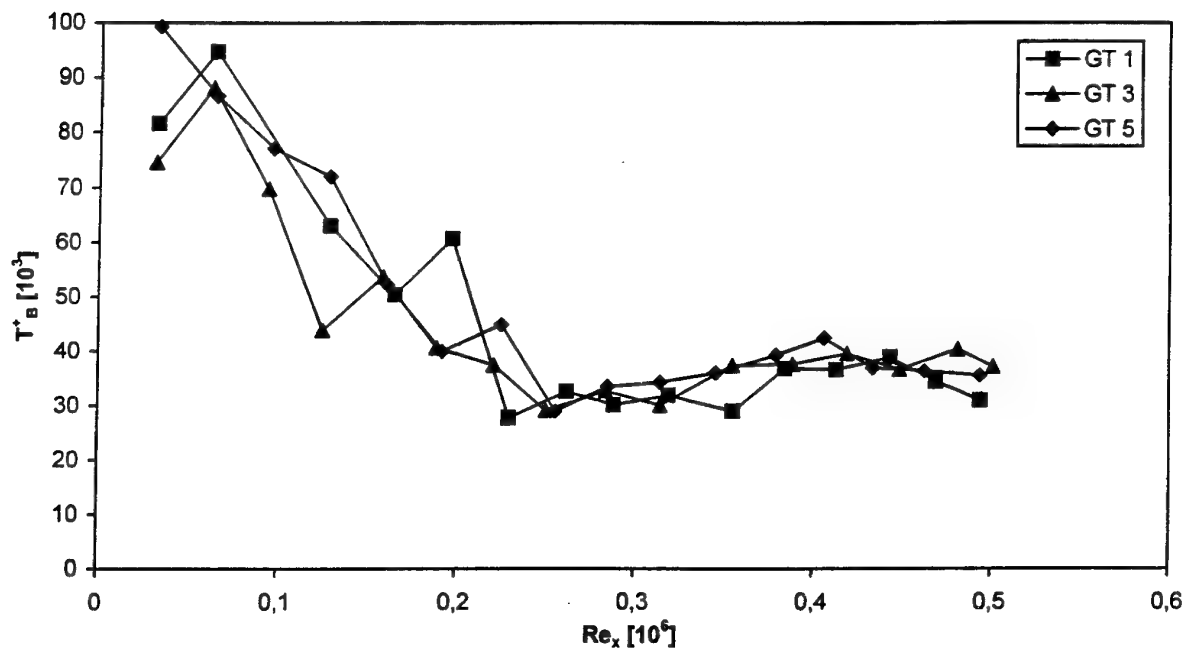


FIG.5 - NON-DIMENSIONED (BY INNER PARAMETERS) MEAN BURST DURATION.

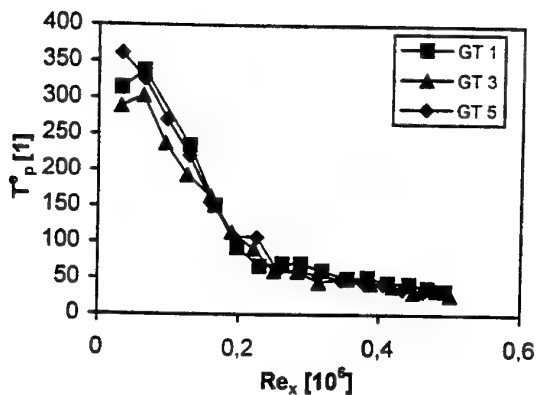


FIG.6 - NON-DIMENSIONED (BY OUTER PARAMETERS) MEAN PERIOD OF BURST OCCURRENCE.

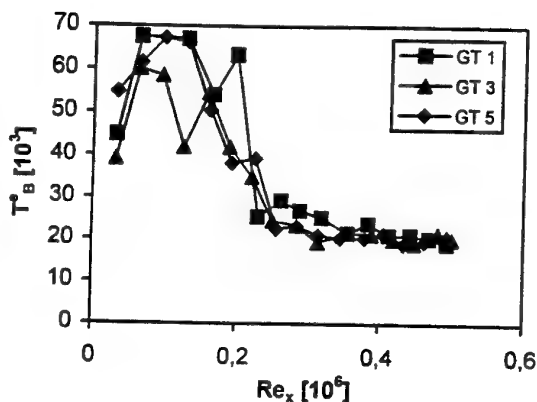


FIG.7 - NON-DIMENSIONED (BY OUTER PARAMETERS) MEAN BURST DURATION.

Many other statistical characteristics of the investigated events have been evaluated e.g. ensemble-averaged patterns in bursts, statistics of fluctuations inside and outside of the classified events etc.

Figure 8 shows the typical interpreted probability density

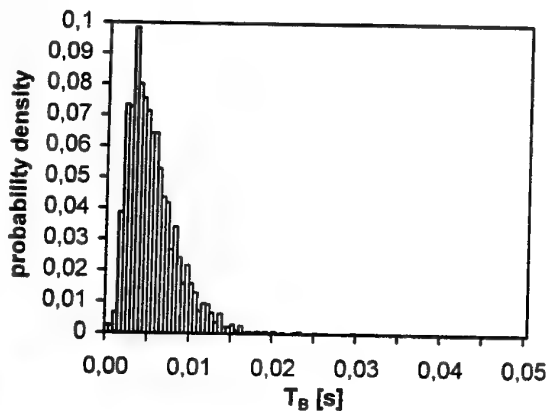


FIG.8 - EXAMPLE OF PROBABILITY DENSITY DISTRIBUTION OF BURST DURATION.

distribution of burst duration  $T_B$  (for the case of GT 1,  $Re_x = 4.8 \cdot 10^5$  and distance from the wall  $y_B$ ). This distribution is very close to lognormal one. The distribution is quite narrow, indicating the small range of scales in the flow. The highest amplitude for beginning of transition can be recognised.

In figure 9, the normalised (by event length) and ensemble averaged patterns are seen. The presented case of GT 1, distance  $y_B$  from the wall, for various positions along the transitional boundary layer. The maximal amplitude of the mean burst was evaluated in the beginning of transition region (position II).

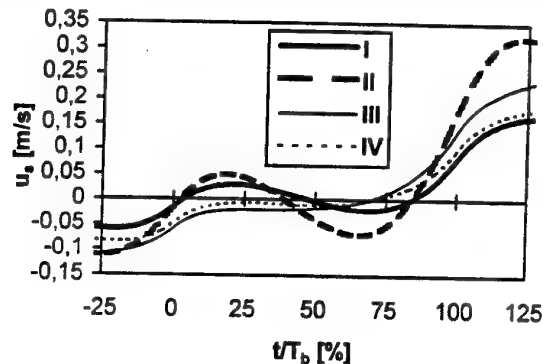


FIG.9 - EXAMPLE OF ENSEMBLE-AVERAGED BURST PATTERNS.

Item, the bursting phenomenon outside the boundary layer was investigated. The results are informative because the used technique was developed for identification of the bursts inside the boundary layer. In the figure 10 the non-dimensional mean burst period  $T_p^+$  vs.  $Re_x$  is plotted. The value of  $T_p^+$  is strongly influenced by length scale of the outer stream. The longer length scale of outer stream the longer period of bursting phenomenon.

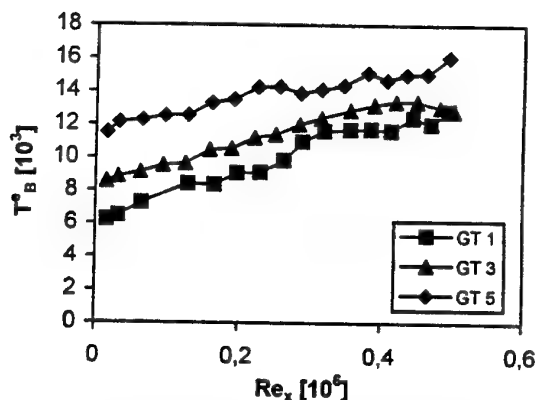


FIG.10 - THE PERIOD OF BURST OCCURRENCE OUTSIDE THE BOUNDARY LAYER.

Comparison of the profiles of the non-dimensional mean burst period  $T_p^+$  vs. non-dimensional distance from the wall (normalised by impulse thickness of boundary layer) for various  $Re_x$  is given in the figure 11 and 12 respectively. Presented case was evaluated for GT 1, the other cases were qualitatively

similar. The bursting periods are shortened along the transition region. Maxima are still lower and closer to the wall.

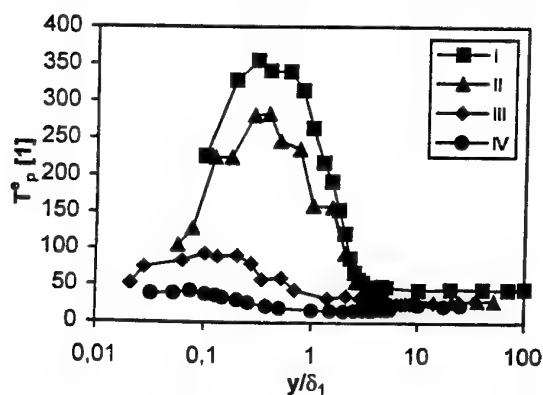


FIG.11 - THE PROFILES OF THE PERIODS OF BURST OCCURRENCE.

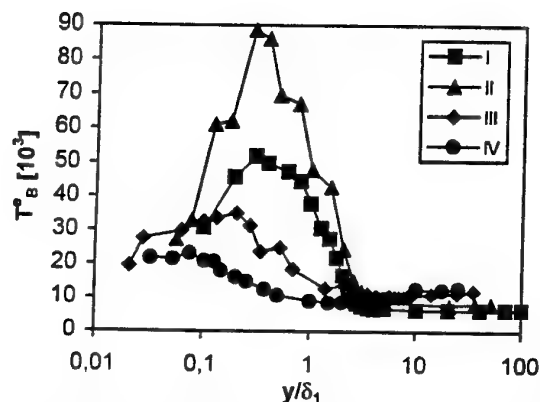


FIG.12 - THE PROFILES OF THE BURST DURATIONS.

Note, that while the period of bursts grows for increasing  $Re_x$ , the burst duration is of highest value for the beginning of transition (position II). It could be the evidence of amplified burst activity in this region.

## CONCLUSIONS

There are dramatic changes of the bursting phenomenon parameters along the transitional boundary layer. The energy of bursts is increasing along the transitional boundary layer.

The systematic influence of the length scale of the outer stream on the bursting phenomenon inside the transitional boundary layer was not observed although there are differences of the bursting process outside the boundary layer.

After the first information presented in Uruba et al. 1995 the experimental apparatus as well as the procedures have been improved. So far all planned measurements (behind five grid-generators) are not completed.

## AKNOLDIGEMENT

This work was funded by the grants from budged of the Czech Republic by means of ministry of Education, Youth and Physical Training of CR (project No. OC F1.10 and OC F1.60) and from the Grant Agency of the Czech Republic (project No.

101/96/1696) and from the Grant Agency of the Academy of Sciences of the Czech Republic (project No. A2076602).

## REFERENCES

- Corino, E.R. and Brodkey, R.S. 1969. „A Visual Investigation of the Wall Region in Turbulent Flow,” *J.Fluid Mech.* 37, pp.1-30.
- Jonáš, P., 1992, „On Turbulent Boundary Layer Perturbed by Outer Flow Turbulence,” *Power Engineering*, Lithuanian Acad. of Sciences, No.3, pp.69-80.
- Jonáš, P., Mazur, O., Uruba, V., 1996, „On the Boundary Layer Transition in Turbulent Flows with Various Length Scales,” In: *Advances in Turbulence VI*, S.Gavrilakis, L.Machiels and P.A.Monkewitz (Eds.), Kluwer, pp.345-346.
- Kline, S.J., Reynolds, W.C., Schraub, F.A. and Runstadler, P.W., 1967, „The Structure of Turbulent Boundary Layers,” *J.Fluid Mech.*, 30, pp.741-773.
- Townsend, A.A., 1956, „The Structure of Turbulent Shear Flow,” *Cambridge University Press*, Cambridge.
- Uruba, V., Jonáš, P., Mazur, O., 1995, „A Contribution to the Study of the Bursting Phenomenon in a Transitional Boundary Layer,” *EUROMECH Colloquium 330*, pp.57-58.
- Wallace J.M., Brodkey R.S., Eckelmann H., 1977, „Pattern-Recognised Structures in Bounded Turbulent Shear Flows,” *J.Fluid Mech.*, 83, pp.673-693.



# Computation of Turbulent Flows using Upwind-Bias 5th-Order Schemes

P. G. Huang  
Department of Mechanical Engineering  
University of Kentucky  
Lexington, KY 40506  
USA

## Abstract

Two conservative, 5th-order upwind-biased finite difference schemes for the solution of Navier-Stokes equations will be presented. The schemes are based on a high-order multi-dimensional reconstruction of the integral form of the governing equations. An implicit delta form of the iterative solution technique has been introduced to stabilize the overall algorithm. The method is coupled with a 6th-order SIMPLE pressure-Poisson solver in a collocated mesh. Very accurate solutions can be obtained using only a relatively small number of grid points.

## Introduction

With the arrival of large-scale CFD solvers, our expectation in the scale and magnitude of the problems CFD can handle has grown. In the aerospace and automobile industries, the application of CFD tools as part of the prototype design process has now become routine. This type of calculation frequently involves complex 3-D geometries but due to the low accuracy of the numerical schemes employed in most application codes, a large number of grid points are generally required to achieve grid-independent solutions. The computer storage and time needed for such a computation are generally beyond what current workstations can handle. As a result, the improvement of numerical schemes, which may reduce the number of grid points needed, thus reducing computer memory usage and execution time, is still a pacing item of the overall CFD development.

On the other hand, the era of using large eddy simulation in practical applications has arrived; at least for simple flow configurations. Such a flow simulation generally involves time-dependent 3-D calculation of the Navier-Stokes equations. Hence, one of the major difficulties in applying the large eddy simulation to practical situations is to maintain reasonable numerical accuracy with an affordable number of grid points. Such a demand also requires the improvement of numerical schemes.

The present paper presents two conservative, 5th-order upwind-biased finite difference schemes for the solution of the Navier-Stokes equations. The schemes are essentially improved versions of the original Rai and Moin's scheme

[1991]. The major differences between the current approach and the original Rai's scheme are twofold. First, the current approach uses a *conservative* upwind-bias approach. Second, the current high order approximation is applied in a multi-dimensional sense. This is done by applying an accurate multi-dimensional reconstruction process to the integral form of the governing equations. The method is more akin to the recent proposal of Rai and Chakravarthy [1993].

The 6th-order central difference scheme was used for the diffusion and the pressure gradient terms. In addition, a modified version of Rhie and Chow method [1983] was employed in a collocated grid arrangement to avoid the checkerboard-type of pressure oscillation. This greatly reduced the computing effort and memory storage requirements associated with the use of the staggered grid system. Modifications have been made to the method to ensure a 6th-order accuracy of the pressure-Poisson solver.

Overall, the method has been demonstrated to achieve accurate solution for flows with separation using a reasonable number of grid points.

## Integral Form of the Governing Equations

The integral form of the governing equations can be written as:

$$\oint_A \rho u_i n_i dA = 0 \quad (1)$$

$$\oint_A \rho u_m u_i n_i dA = \oint_A \tau_{im} n_i dA - \oint_A P n_m dA \quad (2)$$

where  $A$  is the surface of the control volume and  $n_i$  is the vector element of the outwardly directed normal unit vector,  $\vec{n} = n_1 \vec{i} + n_2 \vec{j} + n_3 \vec{k}$ , on the surface element,  $dA$ .

## Discretization

As shown in figure 1, an interface A-B-C-D is located between nodal points P and E, where points A, B, C, and D

are assumed to be co-planar. The mass flux across interface A-B-C-D can be evaluated by

$$\dot{m} = \int_{A_{ABCD}} \rho u_i n_i dA \approx \bar{\rho} \bar{u}_i A_{i,ABCD} \quad (3)$$

where  $A_{i,ABCD}$  is the vector element of the outwardly directed area vector,

$$\bar{A}_{ABCD} = \frac{1}{2}(\bar{x}_{AC} \times \bar{x}_{BD}); \quad (4)$$

the overbar symbol,  $\bar{\cdot}$ , denotes that the value is a 6th-order symmetrical mean across the interface A-B-C-D. The value of  $\bar{\rho}$  is obtained below, but the evaluation of  $\bar{u}_i$  is somewhat more tedious (due to the use of Rhie and Chow method) and will be discussed in equation (20).

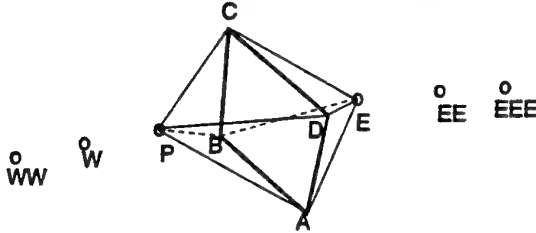


Figure 1: Calculation of fluxes across the control volume face, ABCD

To find a 6th-order symmetric mean of any quantity  $\phi$ , at interface A-B-C-D, one first fits a 6th-order Lagrange polynomial constructed from the values of  $\phi$ 's at WW, W, P, E, EE and EEE in order to find the value of  $\phi$  at the center of the plane, A-B-C-D. Next, the mean value of  $\phi$  at the interface is obtained from

$$\bar{\phi} = \frac{1}{A_{ABCD}} \int_{A_{ABCD}} \phi dA. \quad (5)$$

In practice, the integration of equation (5) is done by using the 6th-order Gaussian rule, which involves the sum of the products of the Gaussian weightings,  $w$ 's and the values of  $\phi$ 's, at 9 assigned positions inside plane A-B-C-D,

$$\bar{\phi} \approx \sum_{i=1}^3 \sum_{j=1}^3 w_i w_j \phi_{ij} \quad (\text{no sum on } i \text{ and } j) \quad (6)$$

where the indices  $i$  and  $j$  denote the positions of Gaussian points. The values of  $\phi_{ij}$  at Gaussian points were evaluated using the 6th-order Lagrange interpolation of the neighboring cell face values of  $\phi$  in the direction formed by the plane, A-B-C-D.

The convection term of the  $u_m$ -momentum equation across interface A-B-C-D is evaluated by

$$F_C = \int_{A_{ABCD}} \rho u_m u_i n_i dA \approx \hat{m} \hat{u}_m \quad (7)$$

where  $\hat{m}$  is evaluated from equation (3); the hat symbol,  $\hat{\cdot}$ , denotes that it is the 5th-order upwind-biased mean value across the plane A-B-C-D. The value of  $\hat{u}_m$  is obtained by first evaluating the cell face value of  $u_m$  using the 5th-order Lagrange interpolation either from points WW, W, P, E and EE or from points W, P, E, EE and EEE, depending on positive or negative sign, respectively, of  $\hat{m}$ . Then the 6th-order Gaussian integration, equation (6), is applied to find the mean value across the plane A-B-C-D.

The evaluation of the diffusion term is less straightforward, however. The diffusion flux for the  $u_m$ -momentum equation across the plane A-B-C-D can be shown to be

$$F_D = \int_{A_{ABCD}} \tau_{im} n_i dA \approx \bar{\tau}_{im} A_{i,ABCD}. \quad (8)$$

where  $\bar{\tau}_{im}$  is the 6th-order symmetrical mean of the stresses whose values involve the evaluation of the 6th-order symmetrical mean of strain tensor,  $\partial u_m / \partial x_i$ ,

$$S_{im} = \frac{1}{2} \left( \frac{\partial u_i}{\partial x_m} + \frac{\partial u_m}{\partial x_i} \right) - \frac{1}{3} \delta_{im} \left( \frac{\partial u_k}{\partial x_k} \right). \quad (9)$$

The 6th-order symmetrical mean gradient of any quantity,  $\partial \phi / \partial x_i$ , at the interface A-B-C-D can be obtained from the divergence theorem,

$$\begin{aligned} \frac{\partial \phi}{\partial x_i} &= \frac{1}{\Omega_{P-ABCD-E}} \oint_{\Omega_{P-ABCD-E}} \frac{\partial \phi}{\partial x_i} dV \\ &= \frac{1}{\Omega_{P-ABCD-E}} \oint_A \phi n_i dA \\ &\approx \frac{1}{\Omega_{P-ABCD-E}} \sum_{\text{all surfaces}} \bar{\phi} \Delta_i \end{aligned} \quad (10)$$

where  $\Omega$  represents the volume of the geometry P-ABCD-E,  $V$  is the volume,  $\Delta_i$  denotes the vector element of the outwardly directed area vector of triangles on the surface of the shape P-ABCD-E, and  $\bar{\phi}$  is the averaged value on the surface of the desired triangle.

The vector element component of the pressure force acting on the plane ABCD in the  $m$  direction is then approximated by

$$\int_{A_{ABCD}} P n_m dA \approx \bar{P} A_{m,ABCD} \quad (11)$$

where  $\bar{P}$  denotes the 6th-order symmetric mean of the pressure value on the plane ABCD. Similar to the way mean density was evaluated, the central value of  $P$  is first interpolated by the Lagrange polynomial using the values of  $P$ 's at WW, W, P, E, EE and EEE; the Gaussian rule, (6), is then used to find the mean value of  $P$  on the plane.

## Numerical Algorithm

Once all the terms in equations (1) and (2) have been evaluated, they are moved to the RHS of the solution matrix. The 1st order, upwind  $\Delta$ -form, deferred-correction method is used to solve the discretized equations. The goal is to drive the RHS to zero, therefore the accuracy of the final solution (5th-order one) would not be affected by the upwind nature of the LHS treatments. This, of course, requires in-step iterations that will be performed in conjunction with the in-step iterative solution procedure of the fully implicit SIMPLE algorithm.

The advantage of the  $\Delta$ -form solution procedure is that it is very robust for its stability and is not affected by the instability associated with the use of high order schemes, which generally give rise to negative values of discretization coefficients (or perhaps worse, zero diagonal). For example, for the solution of the following equation,

$$\frac{\partial \phi}{\partial x} = 0, \quad (12)$$

the 2nd-order central differencing of equation (12) yields,

$$\frac{1}{2\Delta x} (\phi_{i+1} - \phi_{i-1}) = 0. \quad (13)$$

As can be seen from (13), there is no diagonal term and, therefore, the solution of this equation becomes impossible when an iterative method is used. On the other hand, with the current method we rewrote (12) in

$$\frac{\partial \Delta \phi}{\partial x} = - \left( \frac{\partial \phi}{\partial x} \right)^n \quad (14)$$

where

$$\Delta \phi = \phi^{n+1} - \phi^n \quad (15)$$

is the correction to  $\phi^n$  to an improved solution,  $\phi^{n+1}$ . From (14), it can be seen that if one treats the LHS and RHS identically, the discretized equation will be reduced to (13). However, this is exactly what one wants to avoid since the original equation is unstable. The current approach proposes to use the first-order, upwind difference scheme for the LHS, while the fifth-order upwind-biased scheme is applied to the RHS side. For example, in order to achieve the 2nd order central differencing, the discretized equation yields

$$\frac{1}{\Delta x} (\Delta \phi_i - \Delta \phi_{i-1}) = \frac{1}{2\Delta x} (\phi_{i+1}^n - \phi_{i-1}^n) \quad (16)$$

This system of equations is stable since the diagonal is dominant. When the solution converges,  $\Delta \phi$  becomes zero and the equation (16) reduces to equation (13). It should be noted, that since the RHS is evaluated explicitly, one can easily replace the discretization schemes with any other scheme without altering the solution algorithm.

Tests have shown that this approach is very robust. Due to the diagonal dominance of the matrix system, residuals of the in-step iterations drop monotonically and the overall rate of convergence is not much affected by the splitting procedure.

### Pressure Solution Algorithm

The coupling between the momentum and the continuity equations will be handled through the SIMPLE approach. To eliminate the checkerboard-type of oscillation in pressure, the Rhie and Chow treatment is adapted in a collocated grid system. The method is modified slightly in the current code to accommodate the use of a 6th-order pressure scheme in conjunction with the  $\Delta$ -form solution procedure.

A pseudo-velocity vector,  $\tilde{u}_m$ , is first proposed;

$$\tilde{u}_m = u_m + \frac{\partial p}{\partial x_m} \frac{V_{ijk}}{a_{ijk}} \quad (17)$$

where  $u_m$  is an intermediate solution obtained from the solution of the momentum equations, and  $a_{ijk}$  is the diagonal coefficient of the discretized equation for  $\Delta u_m$ -equation at the  $ijk$ -point. The symmetrical, 6th-order Lagrange formula is then employed to interpolate the value of  $\tilde{u}_m$  to the center of plane ABCD. The 6th-order symmetrical mean of  $\tilde{u}_m$ ,  $\bar{\tilde{u}}_m$ , across the plane, is then obtained by using the Gaussian rule (6).

Once the 6th-order mean value of the pseudo-velocity,  $\bar{\tilde{u}}_m$ , is obtained at the interface ABCD, a mean velocity  $\bar{u}_m$  is recovered by the following approximation:

$$\bar{u}_m = \bar{\tilde{u}}_m - \frac{\partial p}{\partial x_m} \frac{V_{ijk}}{a_{ijk}} \quad (18)$$

where  $\bar{u}_m$  represents a second intermediate solution extracted from the momentum equations,  $\partial p / \partial x_m$  is the 6th-order symmetrical mean pressure gradient evaluated at the interfacial plane ABCD according to (10), and  $V_{ijk} / a_{ijk}$  is the 6th-order symmetrical mean value at the plane ABCD ( $V_{ijk} / a_{ijk}$  and can be interpolated from points WW, W,

P, E, EE and EEE and then integrated in the ABCD plane using the Gaussian rule (6)).

The interpolating scheme illustrated by equations (17) and (18) is the essence of the Rhie and Chow method [1983]. By substituting (17) into (18) one can show that the error introduced by this approximation is of the 7th-order.

To ensure the mass flux across ABCD to satisfying the continuity equation, a correction to the second intermediate velocity,  $\bar{u}_m$ , is approximated by:

$$u_m' = - \frac{\partial p'}{\partial x_m} \frac{V_{ijk}}{a_{ijk}} \quad (19)$$

such that

$$\bar{u}_m = \bar{u}_m + u_m' \quad (20)$$

By substituting the corrected velocity appearing in (20) into (3), and summing the mass fluxes over all control volume faces, one can obtain a Poisson equation for  $p'$ , which can be solved by the 2nd order central difference scheme. Once again, because this equation is of a  $\Delta$ -form, a low-order treatment in the LHS of the equation should not affect the final higher-order solution represented by the RHS. This approach is, in essence, the SIMPLE algorithm.

### Results

So far we have tested the proposed method for three different flows – flat plate turbulent boundary layer, laminar wall driven cavity flows and boundary layer flow separation caused by strong adverse pressure gradients. All results showed a large reduction of grid points needed for grid independent results can be achieved using the proposed high order schemes. To demonstrate the effects of the new schemes, the results of the calculations of an axial flow along an axisymmetric cylinder with a superimposed adverse pressure gradient separation [Driver, 1983], are shown. Boundary layer suction was applied through slots on the wind tunnel walls, and this mass flow removal (about 10% of the incoming tunnel mass flow), produced an adverse pressure gradient associated with the negative displacement effect of suction. Experimental data, including velocity and Reynolds Stress profiles, have been measured in several locations. Since the flow separation has been observed experimentally, a full Navier-Stokes prediction method is recommended. It requires the specification of an outer boundary, such as a streamline far away from the body. The experimental velocity profiles have been integrated to obtain stream function, thus defining a surface of constant stream-function or stream-line. From a computational point of view, this allows the flow to be treated as an internal flow in a duct where one boundary is the surface of the cylinder (no-slip condition), and the other surface is a streamline (slip condition).

The inlet profile is a good match to a equilibrium boundary layer with  $Re_\theta = 2760$ , and can be obtained by matching the calculated momentum thickness with the experimental value using the results obtained from the calculation of a spatial evolving boundary layer (using the same N-S or a boundary layer code).

A standard solution has been obtained using the QUICK schemes on a  $300 \times 200$  mesh. The grids in the streamwise direction are uniform and expand in the y direction exponentially with the first  $y^+$  less than 0.1. It has been found that for, a second-order scheme, typically at least 60 grids points are needed in the direction normal to the wall to achieve a good solution [Bardina et al., 1996, Huang, 1997]. Figures 2 and 3 show the comparison of results using various numerical schemes on a  $20 \times 15$  mesh. As can be seen from the results, the two new 5th-order schemes, one with the Gaussian surface-averaging and one without, match

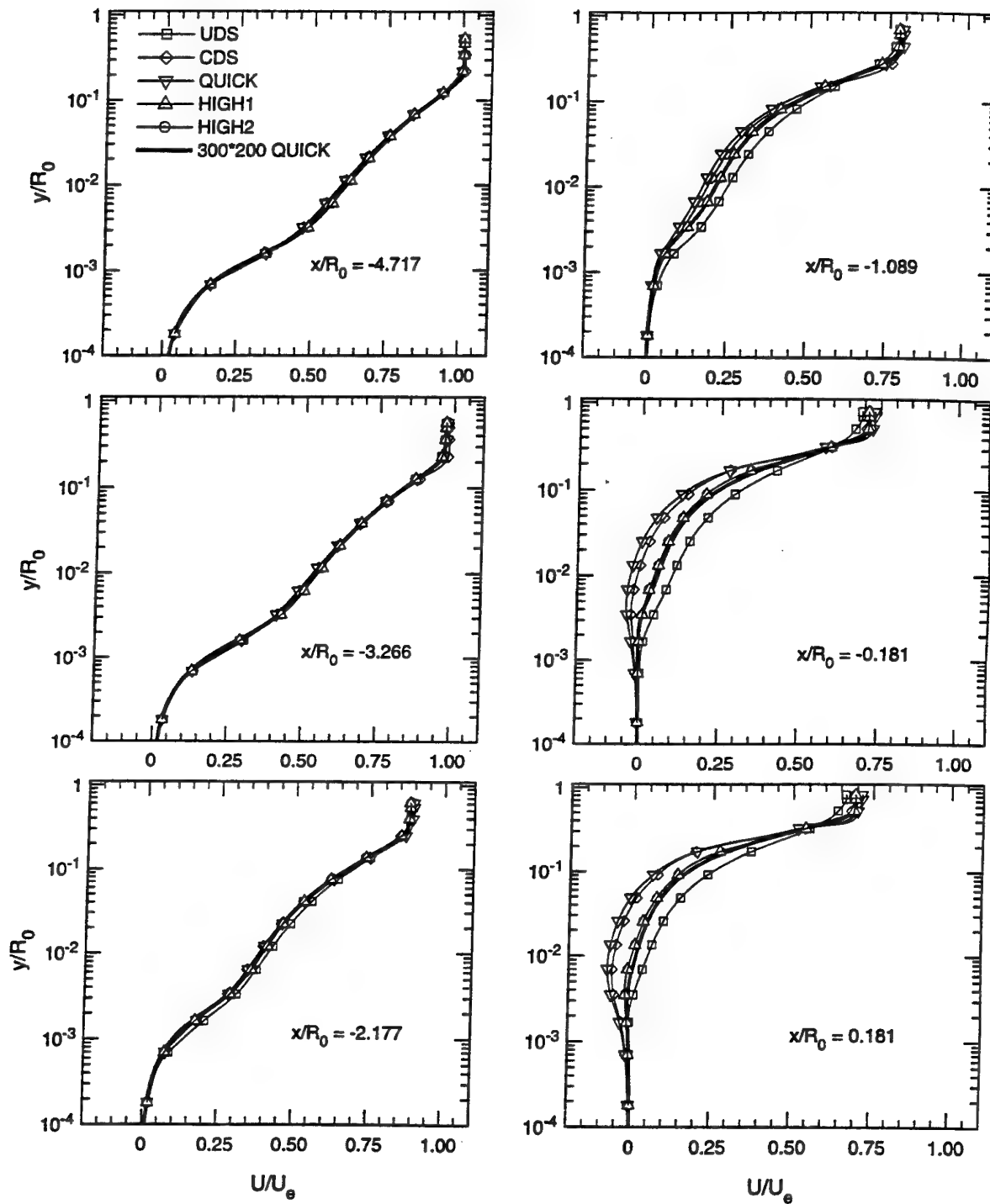


Figure 2: Comparison of the velocity profiles - part 1.

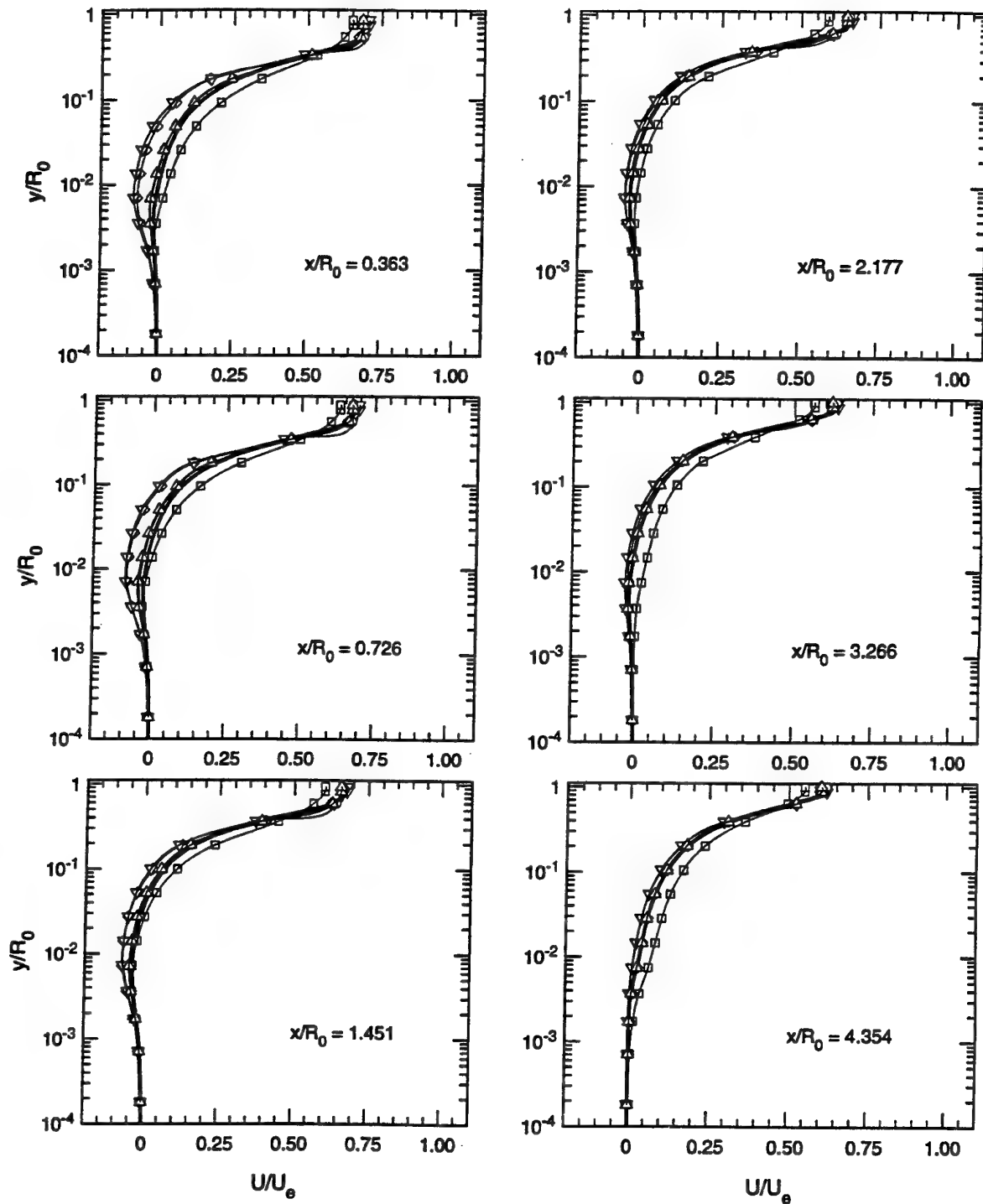


Figure 3: Comparison of the velocity profiles - part 2.

the standard solution very well. The remarkable agreement with the fine grid solution using the QUICK scheme demonstrates the usefulness of the high-order schemes.

### Concluding Remarks

The current paper demonstrates that a large reduction of computational grid points is possible by employing high-order numerical schemes. The method also shows that the use of the delta form deferred-correction solution procedure can avoid numerical instability problems associated with the use of high order schemes.

The solution algorithm described in the paper can be summarized to have the following form:

$$\text{NUMERICS}(\Delta\phi) = \text{PHYSICS}(\phi) \quad (21)$$

where  $\phi$  is any variable the solution is required. The left hand side, NUMERICS, is a stabilizing numerical method, aiming to drive the right hand side, PHYSICS, to zero. Note that the solution of  $\phi$  is governed by PHYSICS and NUMERICS is only a mean to get to the desired solution. Therefore NUMERICS has to be stable but does not necessarily have to be accurate. This strategy is analogous to the pressure solution method used in the SIMPLE algorithm.

The arrangement given by (21) makes the coding very easy. Since the right side, PHYSICS, is explicit, the numerical implementation is straightforward. Here, a 5th-order multi-dimensional reconstruction of the integral form of the governing equations is recommended. The first order upwind differencing scheme is suggested to treat the left hand side, NUMERICS. The method has been applied together with a 6th-order approximation of the Poisson equation for pressure in a collocated grid arrangement. Overall, the method has been demonstrated to achieve a large reduction of grid points required to achieve grid independent solutions.

### REFERENCES

- Bardina, J. E., Huang P. G. and Coakley, T. J. "Turbulence Modeling Validation, Testing and Development," NASA-TM 110446, 1997.
- Driver, D. M., "Axial flow along an Axisymmetric Cylinder with superimposed Adverse Pressure Gradient Separation," AIAA 91-1781, 1991.
- Huang P. G. "Validation of Turbulence Models - Uncertainties and Measures to Reduce Them", 1997 ASME Fluids Engineering Conference, Vancouver, BC, Canada, June 22-26, 1997.
- Rai, M. M. and Moin, P., "Direct simulation of turbulent flow using finite-difference schemes," Journal of Computational Physics, 96, pp. 15-53, 1991.
- Rai, M. M. and Chakravarthy, S., "Conservative high-order-accurate finite-difference methods for curvilinear grids," AIAA-93-3380-CP, 1993.
- Rhie, C. M. and Chow, W. L., "Numerical study of the turbulent flow past an airfoil with trailing edge separation," AIAA J, 21, pp. 1525-1532, 1983.

# DEVELOPMENT OF A NON-LINEAR, STRAIN-SENSITIVE $k$ - $\omega$ TURBULENCE MODEL

Dimitrios Sofialidis and Panayotis Prinos  
Hydraulics Lab., Department of Civil Engineering  
Aristotle University of Thessaloniki  
Thessaloniki, 54006  
Greece

## ABSTRACT

A new low-Reynolds eddy viscosity model (EVM) of the  $k$ - $\omega$  type is presented having the following characteristics. a) The Cross Diffusion Term (CDT) that appears in the exact  $\omega$ -equation is included while it has been omitted in the previous  $k$ - $\omega$  models. The term requires no modelling and is essential for the correct near-wall variation of the flow variables. b) The Non-Linear Stress-Strain Relation (NLSSR) of Craft et al. (1993) is employed to express the Reynolds stress field. Its coefficients are allowed to vary with the mean deformation of the flow instead of being constants, leading to much improved results. c) Strain and vorticity invariants are used to prescribe the turbulence damping in a more physical manner than empirical damping functions. The model is validated in simple homogeneous flows, smooth and rough fully developed channel flow and fully developed square duct flow. Computations are compared against available experimental, empirical and Direct Numerical Simulation (DNS) data.

## INTRODUCTION

Recently, significant amount of effort was invested in the elaboration of the EVM's in order to approach the precision of the full Reynolds stress closures. Although, in principal, the latter describe the physics of turbulent flow in a higher degree, are still expensive in computer resources for routine engineering applications. A main drawback of the standard EVM's is their incapability to capture the normal Reynolds stress anisotropy which, in many cases, results in overall failure of the model. A solution, in the framework of an EVM, is to expand the linear relation that links the turbulent stresses with the mean deformation of the flow to include quadratic and higher order terms. Such a relation is applied in the present model (hereafter referred to as SP model). Another elaboration, also included in the SP model, is the damping of turbulence caused by strong straining of the mean flow, as observed in experiments and DNS calculations. The above improvements, combined with the correct near-wall asymptotic behaviour and the satisfactory application to various, different in nature, turbulent flow fields is expected to result in a useful prediction tool for engineers.

The most popular EVM is the  $k$ - $\epsilon$  scheme, where  $k$  is the turbulent kinetic energy and  $\epsilon$  its dissipation rate, on which much effort and research has been invested. However, the accumulated experience from its application revealed certain intrinsic weaknesses such as the lack of a natural boundary condition for  $\epsilon$  at the wall and the numerically stiff second-order-derivative terms of the mean velocity which frequently appear in the  $\epsilon$ -equation in order to improve the near-wall predictions (e.g. Craft et al., 1993). For this reason there have been several alternative proposals for the second variable that describes the turbulent length scale. One of them is the  $k$ - $\omega$  model which is adopted in the present study and  $\omega$  is simply equal to  $(\epsilon/k)$ . One basic advantage over the  $k$ - $\epsilon$  model is the natural boundary condition for  $\omega$  at the wall that emerges from its exact transport equation.

The exact  $\omega$ -equation can easily be derived from the exact  $\epsilon$ -equation (Speziale et al., 1992) and features the CDT which is included "as is" in the SP model. The term has been ignored in previous  $k$ - $\omega$  models (e.g. Wilcox, 1988) although is necessary for the correct near-wall asymptotic behaviour of the model. In addition, the SP model is anisotropic due to the expansion of the linear Boussinesq relation to include quadratic and cubic terms of the mean strain and vorticity tensors (Craft et al., (1993). Finally, the model is strain-sensitive in order to simulate in a more physical way the turbulence damping. This effect is incorporated in the eddy viscosity relation. The calibration procedure for the model constants and functions is given in the subsequent paragraphs.

## MODEL EQUATIONS

The time-averaged Navier-Stokes equations and the continuity equation are coupled with the transport equations for the two turbulent variables,  $k$  and  $\omega$ . The transport equations for the latter quantities are:

$$U_j \frac{\partial k}{\partial x_j} = P_k + \frac{\partial}{\partial x_j} \left[ \left( \nu + \frac{\nu_t}{\sigma_k} \right) \frac{\partial k}{\partial x_j} \right] - k\omega \quad (1)$$

where  $U_j$ =mean velocity component in the  $x_j$  direction,  $P_k$ =production rate due to shear,  $\nu$ =fluid's kinematic viscosity,  $\nu_t$ =eddy viscosity,  $\sigma_k=1.2$  and

$$U_j \frac{\partial \omega}{\partial x_j} = c_{\omega 1} \frac{\omega}{k} P_k + \frac{\partial}{\partial x_j} \left[ \left( \nu + \frac{\nu_t}{\sigma_\omega} \right) \frac{\partial \omega}{\partial x_j} \right] - c_{\omega 2} \omega^2 + \frac{2\nu}{k} \frac{\partial k}{\partial x_j} \frac{\partial \omega}{\partial x_j} \quad (2)$$

where  $c_{\omega 1}=0.39(Rt^{0.4}+9)/(Rt^{0.4}+1)$ ,  $c_{\omega 2}=(11/6)(1-\exp[-Rt^{-0.25}])^2-1$ ,  $c_\omega=1.45$ , and the last term in Eq. 2 is the CDT.

The eddy viscosity is given by  $\nu_t=f_\mu c_\mu(k/\omega)$ , where  $f_\mu=(1+2/Rt)(1-\exp[1-0.02Rt^{0.75}])$  is a damping function and  $Rt=k/(\nu\omega)$  is the local turbulent Reynolds number. The influence of  $f_\mu$  is restricted in the near-wall region. The parameter  $c_\mu$  is a function of  $M=\max(S, \Omega)$ , where  $S=(1/\omega)(0.5S_{ij}S_{ij})^{1/2}$  and  $\Omega=(1/\omega)(0.5\Omega_{ij}\Omega_{ij})^{1/2}$  are a strain and a vorticity invariant respectively and  $S_{ij}=(\partial U_i/\partial x_j + \partial U_j/\partial x_i)$  is the mean strain and  $\Omega_{ij}=(\partial U_i/\partial x_j - \partial U_j/\partial x_i)$  is the mean vorticity tensor. The model sensitivity to the straining of the flow is achieved through the variation of  $c_\mu$  with  $M$ , instead of being equal to 0.09 as in most of the EVM's. Nevertheless, additional turbulence damping is required, hence the use of  $f_\mu$ . The expression for  $c_\mu$  is similar to that of the CLS model:

$$c_\mu = \frac{0.3}{1 + 0.3M^{1.5}} \left\{ 1 - \exp \left[ \frac{-0.36}{\exp(-0.9M)} \right] \right\} \times \left\{ 1 - \exp \left[ \frac{-15}{(M^{0.6} + 0.01)} \right] \right\} \quad (3)$$

except the last term which is activated for large values of  $M$ .

The Reynolds stresses that appear in the momentum equations of mean motion and in  $P_k$  are explicitly described by the NLSSR of Craft et al. (1993):

$$\begin{aligned} \overline{u_i u_j} = & \left( -\nu_t S_{ij} + \frac{2}{3} \delta_{ij} k \right) + \\ & + c_1 \frac{\nu_t}{\omega} \left( S_{ik} S_{kj} - \frac{1}{3} S_{kq} S_{kq} \delta_{ij} \right) + c_2 \frac{\nu_t}{\omega} \left( \Omega_{ik} S_{kj} + \Omega_{jk} S_{ki} \right) + \\ & + c_3 \frac{\nu_t}{\omega} \left( \Omega_{ik} \Omega_{jk} - \frac{1}{3} \Omega_{qk} \Omega_{qk} \delta_{ij} \right) + \\ & + c_4 \frac{c_\mu^2 \nu_t}{\omega^2} \left( S_{ki} \Omega_{qj} + S_{kj} \Omega_{qi} \right) S_{kq} + \\ & + c_5 \frac{c_\mu^2 \nu_t}{\omega^2} \left( \Omega_{iq} \Omega_{qm} S_{mj} + S_{iq} \Omega_{qm} S_{mj} - \frac{2}{3} S_{qm} \Omega_{mn} \Omega_{nq} \right) + \\ & + c_6 \frac{c_\mu^2 \nu_t}{\omega^2} S_{ij} S_{kq} S_{kq} + c_7 \frac{c_\mu^2 \nu_t}{\omega^2} S_{ij} \Omega_{kq} \Omega_{kq} \end{aligned} \quad (4)$$

where the first bracket is the linear Boussinesq term and  $\delta_{ij}$  is the Kronecker delta. The coefficients  $c_1$ - $c_7$  are functions of the strain and vorticity invariants and are given below.

$$c_1 = - \left[ 0.035 \left( 1 + \frac{200M}{1000 + M^{2.5}} \right) + \frac{5M}{10 + M^3} \right] \left( \frac{M^3}{450 + M^3} \right) w_{1,3}$$

$$c_2 = 0.075 \left( 156 - 0.56 \frac{M^2}{600 + M^2} \right) w_2$$

$$c_3 = (0.15 w_{1,3} - c_1) \left( \frac{M^3}{450 + M^3} \right) \frac{S}{0.5(S + \Omega)}$$

$$c_6 = - \frac{M}{c_\mu} \left[ 0.0049 \left( 1 + \frac{200M}{7 + M^4} \right) + \frac{M^{0.5}}{8000 + 0.9M^{2.5}} \right] \quad (5)$$

$$c_4 = -10, \quad c_5 = 0, \quad c_7 = -c_6$$

$$w_{1,3} = \frac{Rt^{0.8} + 25}{Rt^{0.8}}, \quad w_2 = \frac{Rt^{0.75} + 50}{Rt^{0.75}}$$

The values of  $c_1$ - $c_7$  in the CLS model are constants and equal to -0.1, 0.1, 0.26, -10, 0, -5, and 5 respectively. The calibration of the coefficients will be briefly discussed in the next section.

## APPLICATION OF THE MODEL

The SP model is compared with the non-linear, strain-sensitive  $k$ - $\epsilon$  model of Craft et al. (1993), as improved by Suga (1995) (hereafter referred to as CLS model), against experimental measurements and DNS data. The cases examined are simple homogeneous strain fields (homogeneous shear, axisymmetric contraction and expansion and plane strain), smooth and rough fully developed channel flow and fully developed square duct flow.

### Simple homogeneous flows

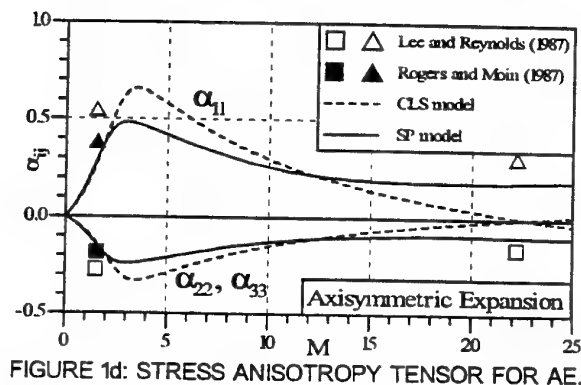
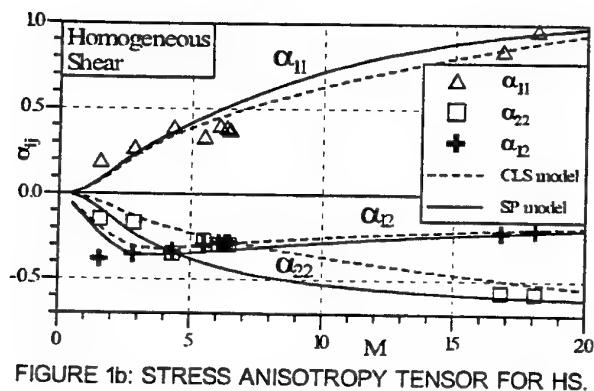
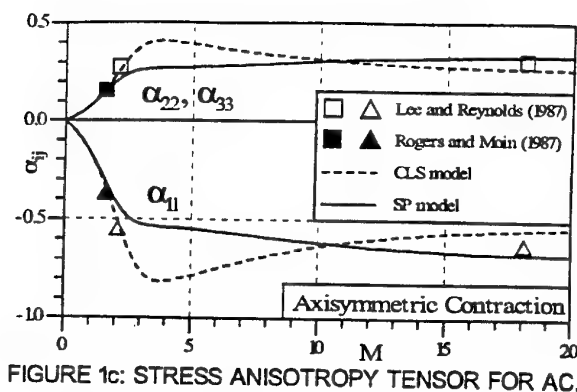
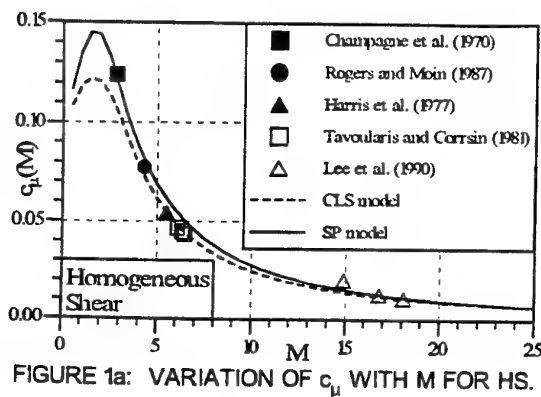
**Homogeneous shear (HS).** Experimental and DNS data have revealed that the strong straining of the flow causes the damping of turbulence in a similar way as by the existence of a solid boundary (Lee et al., 1990). In HS the only non-zero mean velocity gradient is  $(dU_1/dx_2)$  which is uniform, where  $U_1$ =mean streamwise velocity and  $x_2$ =vertical direction. The strain parameter,  $S$ , is equal to  $(1/\omega)(dU_1/dy_2)$  and the anisotropy components, extracted from the NLSSR, are:

$$\begin{aligned} \alpha_{11} = c_\mu S^2 \left[ \frac{1}{3}(c_1 + c_3) + 2c_2 \right], \quad \alpha_{33} = c_\mu S^2 \left[ -\frac{2}{3}(c_1 + c_3) \right] \\ \alpha_{22} = c_\mu S^2 \left[ \frac{1}{3}(c_1 + c_3) - 2c_2 \right] \end{aligned} \quad (6)$$

$$\alpha_{12} = -c_\mu S + c_\mu S^3 [2(-c_5 + c_6 + c_7)], \quad \alpha_{13} = \alpha_{23} = 0$$

where  $\alpha_{ij}=(\overline{u_i u_j})/(k-2/3\delta_{ij})$ . By setting  $c_5=0$  and  $c_6=-c_7$  it is more convenient to calibrate  $c_\mu$  with reference to  $\alpha_{12}$  as a function of  $S$  in order to depress  $\nu_t$  and consequently turbulence for large strain rates. For reasons of generality  $S$  may be substituted by  $M$  to account for flows where  $\Omega$  has locally a higher value than  $S$ . Figs (1a) and (1b) show the variation of  $c_\mu$  and  $\alpha_{12}$  respectively with  $M$  for CLS and SP models against the experimental data of Tavoularis and Corrsin (1981) for  $S=6.1, 6.3$  and  $6.5$ , Harris et al. (1977) for  $S=5.5$ , Champagne et al. (1970) for  $S=2.8$  and the DNS results of Lee et al. (1990) for  $S=14.9, 16.8$  and  $18.1$  and Rogers and Moin (1987) for  $S=1.6$  and  $4.3$ . The normal anisotropy components  $\alpha_{11}$ ,  $\alpha_{22}$  and  $\alpha_{33}$  offer a means of calibrating  $(c_1+c_3)$  and  $c_2$  through Eq. 6. The results are given in Fig. (1b) where  $\alpha_{33}$  is not plotted since by definition  $\alpha_{11}+\alpha_{22}+\alpha_{33}=0$ .





**Axisymmetric contraction (AC)/expansion (AE) and plane strain (PS).** For the sake of brevity the strain and anisotropy fields of these homogeneous flows are omitted but can be found elsewhere (Lee and Reynolds, 1987 and Suga, 1995). These flows are irrotational, hence non-diagonal components of  $\alpha_{ij}$  are zero, and the diagonal components, as expressed by Eq. 4, exhibit  $c_1$  and  $c_3$  only. The results from the calibration of the two coefficients are given in Figs (1c), (1d) and (1e) for AC, AE and PS respectively. DNS data of Lee and Reynolds (1987) for  $S=2.1$  and 18.1, 1.5 and 22.2 and 1.6 and 32.5 for AC, AE and PS respectively, as well as from Rogers and Moin (1987) for  $S=1.6$ , 1.6 and 1.9 for AC, AE and PS respectively are used for comparison purposes. The calibration of  $c_1$  for AC, AE and PS allows  $c_3$  to be decoupled from the expression of  $(c_1+c_3)$  adopted from the calibration in HS.

The distinction made between  $S$  and  $\Omega$  in the  $c_3$  coefficient emerges from the Rapid Distortion Theory, a strainless field where all anisotropy components should be zero and  $c_3$  is the only coefficient that appears in the non-zero components they are expressed from Eq. 4. Therefore, in order for  $c_3$  to become zero, it is necessary to be multiplied with  $S$  which is zero. The term does not alter the predictions for HS since  $S=\Omega$ , neither for AC, AE and PS since  $\Omega=0$ . The calibration procedure leaves  $c_4$  free to choose for its value. Suga (1995) calibrated  $c_4$  with reference to fully developed swirling shear flow, therefore the proposed value was retained.

Finally, the functions  $w_{1,3}$  and  $w_2$  do not take effect for the above flows but are intended to enhance the stress anisotropy near solid boundaries, where  $Rt$  takes low values.

In general, the SP model performs better than the CLS model (due to the different coefficients in Eq. 4). Also, Lee (1989) discusses the asymptotic limit of  $\alpha_{ij}$  for AC and AE (as  $S$  tends to  $\infty$ ), where for example in AE  $\alpha_{11}$  tends to  $1/3$  and  $\alpha_{22}$  to  $-1/6$ . Fig. (1d) shows that SP model abides with this restriction while in CLS model  $\alpha_{11}$  and  $\alpha_{22}$  change sign at  $M=22$ .

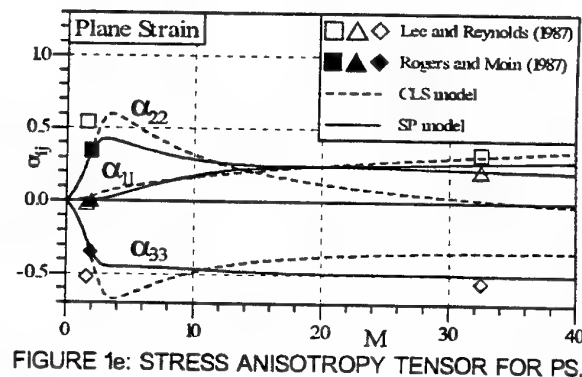


FIGURE 1e: STRESS ANISOTROPY TENSOR FOR PS.

### Smooth fully developed channel flow (SCF)

**Asymptotic analysis.** The Taylor series expansion method is employed to assess the near-wall asymptotic behaviour of the various flow and model parameters (a detailed description of the method can be found in Mansour et al. (1988)). The expansion of the mean velocity components (the same applies to the instantaneous values as well as to the fluctuations) and continuity considerations at the wall ( $y=0$ ) gives that  $U=\mathcal{O}(y)$ ,  $V=\mathcal{O}(y^2)$  and  $W=\mathcal{O}(y)$ , where  $U$ ,  $V$  and  $W$  are the streamwise, normal and horizontal mean velocity components,  $y$  is the normal distance from the wall and " $\mathcal{O}$ " denotes order of magnitude. It follows that  $k=\mathcal{O}(y^2)$ ,  $\epsilon=\mathcal{O}(1)$ , hence  $\omega=(\epsilon/k)=\mathcal{O}(y^{-2})$ ,  $\partial U/\partial y=\mathcal{O}(1)$ , and  $S=\mathcal{O}(y^2)$ . The eddy viscosity is defined as  $-\overline{uv}/(\partial U/\partial y)$  and since  $uv=\mathcal{O}(y^3)$  it follows that  $\nu_t=\mathcal{O}(y^3)$  which in turn gives the condition  $c_\mu f_\mu=\mathcal{O}(y^{-1})$  for the model. It is easy to derive that  $c_\mu=\mathcal{O}(1)$  and hence  $f_\mu$  should vary as  $\mathcal{O}(y^{-1})$  which is satisfied since  $Rt=k/(\nu\omega)=\mathcal{O}(y^4)$ .

Speziale et al. (1992) describe a detailed order-of-magnitude analysis for the exact terms in the  $k$  and  $\omega$  equations in

comparison to the corresponding modelled terms in order to derive the desired asymptotic variation of the model coefficients. Near the wall the exact  $\omega$ -equation writes:

$$\frac{2\nu}{k} \frac{\partial k}{\partial y} \frac{\partial \omega}{\partial y} + \nu \frac{\partial^2 \omega}{\partial y^2} + \omega^2 = 0 \quad (7)$$

where the first term is the CDT and it is obvious that its omission returns a variation for  $k$  different than the desired quadratic one (e.g.  $O(y^{3.23})$  for the model of Wilcox, 1988). Speziale et al. (1992) conclude that the dissipation term coefficient,  $c_{\omega 2}$  should be of the form  $(11/6f_2-1)$  and  $f_2=O(y^2)$ . Also, the coefficient of the production term,  $c_{\omega 1}$ , should vary as  $O(1)$ . Both conditions are satisfied in SP model. The solution of Eq. 7 is  $\omega=2\nu/y^2$ , which is used as a boundary condition in the first grid node adjacent to the wall, provided that it is located near the wall, well inside the viscous sublayer.

Results computed with SP model are compared against DNS data of Kim (1989) and the CLS model for a Reynolds number of 13750 based on the mean velocity and channel width. Fig. (2a) shows the velocity profiles normalized with the shear velocity,  $U_\tau$ , in wall coordinates ( $y^+=yU_\tau/\nu$ ) along with the observed logarithmic law. SP model returns a better value for the von-Karman constant,  $\kappa$ , than CLS model. In Fig. (2b) the normalized  $k$  profiles show that SP model captures better the near-wall peak.

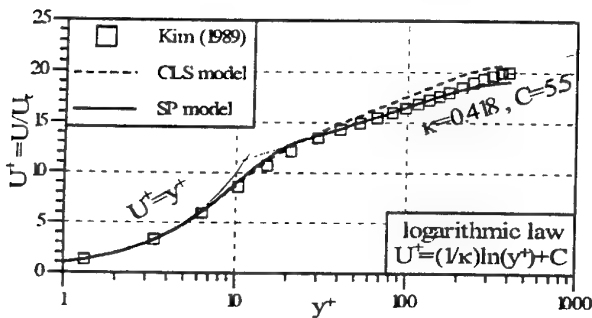


FIGURE 2a: VELOCITY PROFILES FOR SCF.

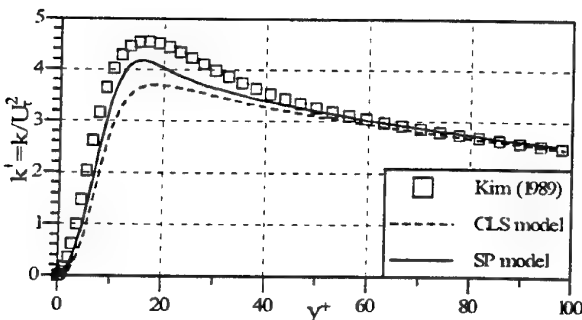


FIGURE 2b: PROFILES OF  $k^+$  FOR SCF.

The normalized  $\epsilon$  profiles are given in Fig. (2c). SP model simulates qualitatively the near-wall variation producing a local minimum and a local maximum while CLS model features only a local maximum. Also, the value of  $\epsilon^+$  at the wall is better captured by SP model. In Fig. (2d), where the normalized turbulent shear stress is plotted, SP model slightly overestimates the peak value while CLS model follows almost perfectly the DNS data. In Fig. (2e) the profiles of the turbulent intensities show the superiority of the SP over the CLS model. The allowance of the coefficients in the NLSSR to vary with  $M$  and the near-wall correction functions  $w_{1,3}$  and  $w_2$  produce a reasonable stress field. The strain parameter  $S$  is displayed in Fig.

(2f), where the SP model is found to produce a better variation near the wall than the CLS model. Finally, Fig. (2g) shows the damping parameter ( $c_\mu f_\mu/0.09$ ) for the SP model and its near-wall distribution is found in excellent agreement with the DNS data.

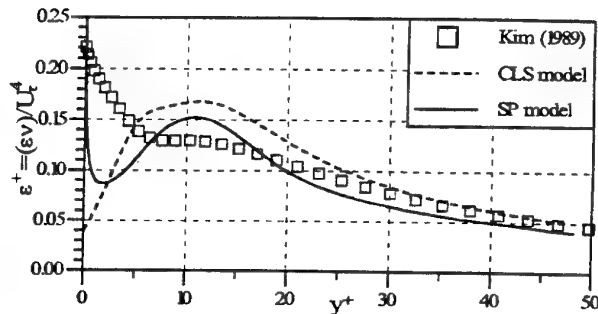


FIGURE 2c: PROFILES OF  $\epsilon^+$  FOR SCF.

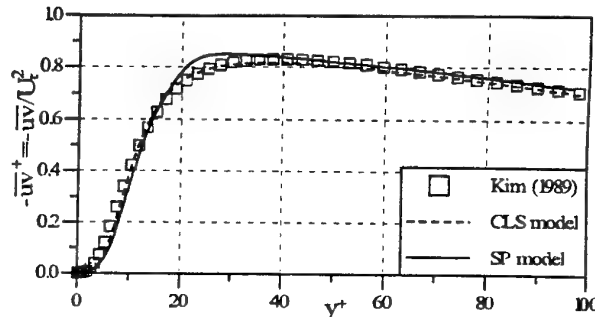


FIGURE 2d: TURBULENT SHEAR STRESS FOR SCF.

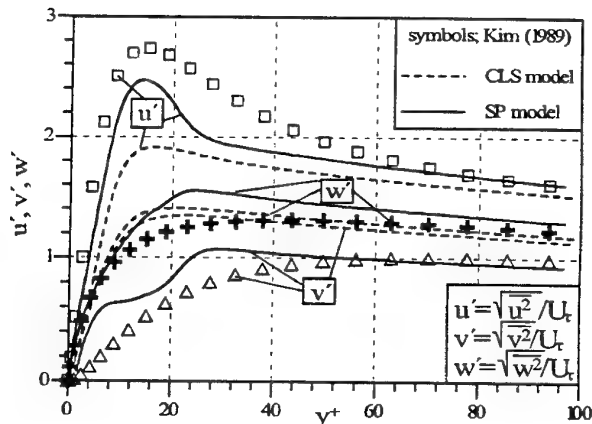


FIGURE 2e: TURBULENT INTENSITIES FOR SCF.

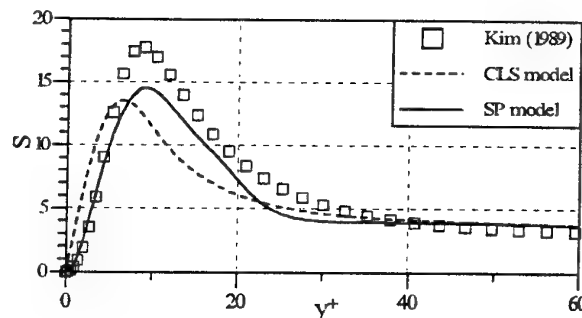


FIGURE 2f: STRAIN PARAMETER FOR SCF.

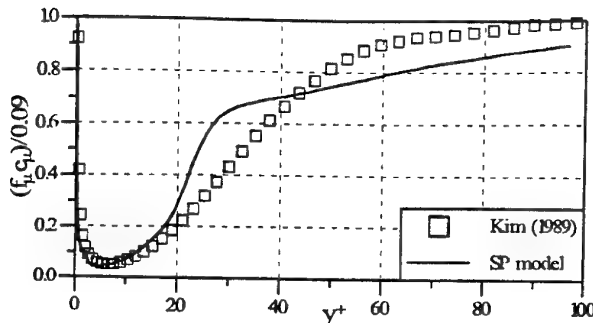


FIGURE 2g: DAMPING PARAMETER FOR SCF.

#### Rough fully developed channel flow (RCF)

Flow over a rough surface produces higher drag than over a smooth one and the constant  $C$  of the logarithmic law of the wall is shifted by  $\Delta C$ , while  $\kappa$  retains its value:

$$U^+ = \frac{1}{\kappa} \ln y^+ + C - \Delta C \quad (8)$$

Cebeci and Bradshaw (1977) proposed the following correlation for sandgrain roughness:

$$\Delta C = \left[ C - 8.5 + \frac{1}{\kappa} \ln k_s^+ \right] \times \sin[0.4258(\ln k_s^+ - 0.811)] \quad (9)$$

valid for  $2.25 < k_s^+ < 90$ , where  $k_s^+ = k_s U_\tau / \nu$ ,  $C = 5.2$ ,  $\kappa = 0.42$  and  $k_s$  is the height of the sandgrain. For values of normalized roughness height higher than 90 Eq. 9 is valid without the sin term.

The effect of roughness in the SP model is achieved solely by the adjustment of the boundary condition for  $\omega$  without any other modifications in the governing equations. Following the suggestion of Wilcox (1988) based on dimensional considerations,  $\omega$  is prescribed explicitly as:

$$\omega = \frac{U_\tau^2}{\nu} S_R \quad (10)$$

and is applied at the top of the roughness. All the remaining variables are expressed at the same point as in the case of a smooth boundary. The term  $S_R$  was calibrated for various roughness heights and is given by the following expressions:

$$\begin{aligned} S_R &= \frac{1800}{(k_s^+)^3} & k_s^+ < 20 \\ S_R &= \frac{2.02}{(k_s^+)^{0.7}} - 0.25 & 20 \leq k_s^+ < 50 \\ S_R &= \frac{0.89}{(k_s^+)^{0.55}} + 0.05 & 50 \leq k_s^+ < 200 \\ S_R &= \frac{0.63}{(k_s^+)^{0.4}} - 0.25 & 200 \leq k_s^+ < 1000 \end{aligned} \quad (11)$$

The results of the above adjustments in the SP model are given in Fig. (3a) in terms of the shift  $\Delta C$  against Eq. 9. Also, in Fig. (3b) the normalized velocity profiles for the SP model are plotted

against the logarithmic law extracted from Eq. 9 for three roughness heights. The agreement is satisfactory for the whole range of roughness height that SP model was applied.

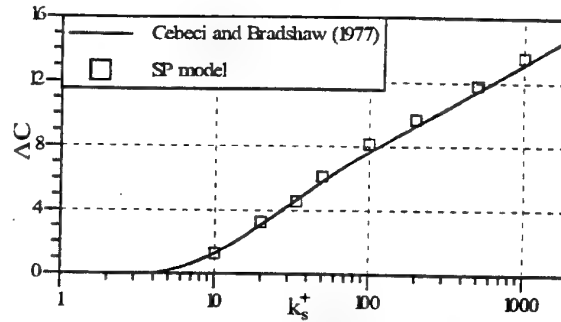


FIGURE 3a: ROUGHNESS SHIFT  $\Delta C$ .

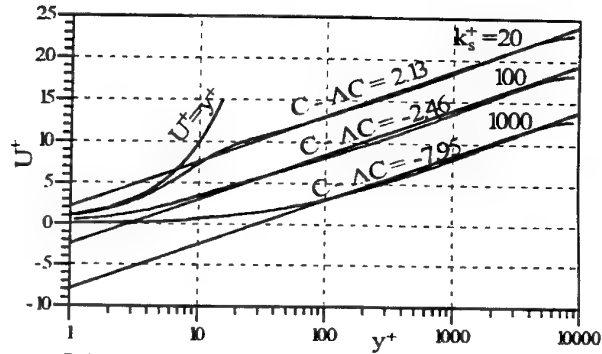


FIGURE 3b: VELOCITY PROFILES FOR RCF.

#### Fully developed square duct flow (SDF)

Fully developed flow in a straight duct of square cross section is a typical example in which turbulence-driven secondary currents at the cross section occur. Although the secondary motion is only a small percentage of the main flow (2-3% of the bulk streamwise velocity  $U_b$ ), it affects significantly the flow characteristics and in particular the skin friction and the heat transfer at the walls. It is well established that turbulence models can simulate the secondary motion only if they are capable of capturing the normal stress anisotropy.

The SP model is again compared to the CLS model against DNS data of Gavrilakis (1992) for a Reynolds number of 4410 based on the mean streamwise velocity and the duct width  $2h$ . The streamwise, normal and horizontal velocity components are  $U$ ,  $V$  and  $W$  respectively and the corresponding directions are  $x$ ,  $y$  and  $z$ .

Fig. (4a) shows the wall shear stress  $\tau_w$  normalized with the mean value  $\tau_{w,m}$ . The SP model reproduces the local minimum (observed even in higher Reynolds numbers) in contrast to the CLS model. Fig. (4b) shows the mean streamwise velocity profiles at the wall bisector, in wall coordinates, where SP is found to perform marginally better than CLS model.

Finally, in Fig. (4c) the normalized horizontal velocity is presented at two verticals. The superiority of the SP model is obvious producing much stronger secondary currents than CLS model. The reason lies in the calibration of the coefficients in the NLSSR that results in an improved normal stress anisotropy field (see Fig. (2e)).

Similar conclusions were reached from the performance of the two models for a higher Reynolds number (10320) against the results from the Direct Numerical Simulation of Huser and Biringen (1993).

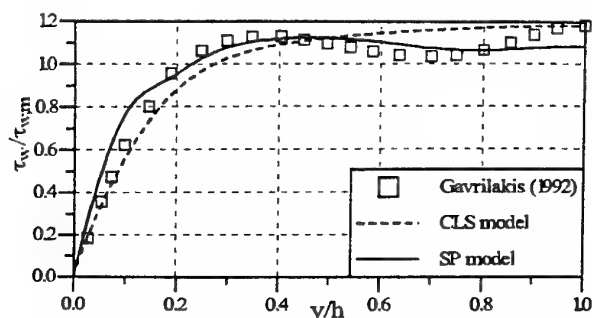


FIGURE 4a: VARIATION OF WALL SHEAR STRESS.

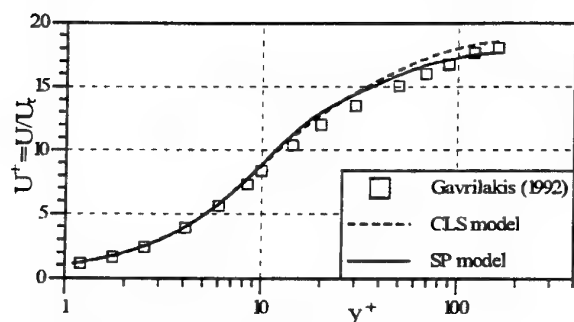


FIGURE 4b: VELOCITY PROFILES FOR SDF.

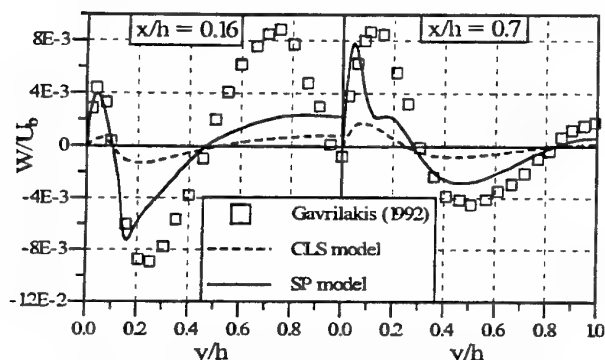


FIGURE 4c: SECONDARY VELOCITIES FOR SDF.

## CONCLUSIONS

A new low-Reynolds model of the  $k-\omega$  type is presented. The model is strain-sensitive in order to simulate the turbulence damping occurring at high mean strain rates and employs a non-linear relation for the prescription of the turbulent stresses in terms of the mean strain and vorticity tensors.

The coefficients of the non-linear stress-strain relation are calibrated with reference to simple homogeneous flows and are expressed as functions of the strain/vorticity invariant of the mean flow, in contrast to the model of Craft et al. (1993) where they are constants.

The Cross-Diffusion Term, which appears in the exact  $\omega$ -equation, is included without modifications since it is essential for the correct near-wall asymptotic behaviour of the model. The coefficients of the modelled transport equation for  $\omega$  are determined with reference to DNS data of smooth fully developed channel flow and satisfy the order-of-magnitude analysis of Speziale et al. (1992) and the near-wall behaviour that is recovered from the Taylor series expansion method.

The model is successfully applied to smooth fully developed channel flow and a simple adjustment of the boundary condition for  $\omega$  enables its application for flows over rough surfaces. The

model is also validated for fully developed square duct flow and it is proved much better than the CLS model in the simulation of turbulence-driven secondary currents.

## REFERENCES

- Cebeci, T., and Bradshaw, P., 1977, "Momentum transfer in boundary layers," Hemisphere, Publishing Corporation.
- Champagne, F. H., Harris, V. G., and Corrsin, S., 1970, "Experiments on nearly homogeneous turbulent shear flow," *Journal of Fluid Mechanics*, Vol. 41, Part 1, pp. 81-139.
- Craft, T. J., Launder, B. E., and Suga, K., 1993, "Extending the applicability of eddy viscosity models through the use of deformation invariants and non-linear elements," *Proceedings, 5th International Symposium on Refined Flow Modelling and Turbulence Measurements*, Paris, pp. 125-132.
- Gavrilakis, S., 1992, "Numerical simulation of low-Reynolds-number turbulent flow through a straight square duct," *Journal of Fluid Mechanics*, Vol. 244, pp. 101-129.
- Harris, V. G., Graham, J. A. H., and Corrsin, S., 1977, "Further experiments in nearly homogeneous turbulent shear flow," *Journal of Fluid Mechanics*, Vol. 81, Part 4, pp. 657-687.
- Huser, A., and Biringen, S., 1993, "Direct numerical simulation of turbulent flow in a square duct," *Journal of Fluid Mechanics*, Vol. 257, pp. 65-95.
- Kim, J., 1989, Unpublished data provided by Dr K. Suga.
- Lee, M. J., 1989, "Distortion of homogeneous turbulence by axisymmetric strain and dilatation," *Physics of Fluids*, A1(9), pp. 1541-1557.
- Lee, M. J., Kim, L., and Moin, P., 1990, "Structure of turbulence at high shear rate," *Journal of Fluid Mechanics*, Vol. 216, pp. 561-583.
- Lee, M. J., and Reynolds, W. C., 1987, "On the structure of homogeneous turbulence," *Turbulent Shear Flows 5*, F. Durst et al., ed., Springer-Verlag Berlin Heidelberg, pp. 54-66.
- Mansour, N. N., Kim, J., and Moin, P., 1988, "Reynolds-stress and dissipation rate budgets in a turbulent channel flow," *Journal of Fluid Mechanics*, Vol. 94, pp. 15-44.
- Rogers, M. M., and Moin, P., 1987, "The structure of the vorticity field in homogeneous turbulent flows," *Journal of Fluid Mechanics*, Vol. 176, pp. 33-66.
- Speziale, C. G., Abid, R., and Anderson, E. C., 1992, "Critical evaluation of two-equation models for near-wall turbulence," *AIAA Journal*, Vol. 30, No 2, pp. 324-331.
- Suga, K., 1995, "Development and application of a non-linear eddy viscosity model sensitized to stress and strain invariants," Ph.D. Thesis, UMIST, Manchester, UK.
- Tavoularis, T., and Corrsin, S., 1981, "Experiments in nearly homogeneous turbulent shear flow with a uniform mean temperature gradient. Part 1," *Journal of Fluid Mechanics*, Vol. 104, pp. 311-347.
- Wilcox, C. D., 1988, "Reassessment of the scale-determining equation for advanced turbulence models," *AIAA Journal*, Vol. 26, No 11, pp. 1299-1310.

# Proposal of a Low-Reynolds-Number Two-Equation Model to Predict Dynamic and Thermal Field

C. B. Hwang and C. A. Lin  
Department of Power Mechanical Engineering  
National Tsing Hua University  
Hsinchu, TAIWAN 30043

## Abstract

An improved low Reynolds-Number  $k - \tilde{\epsilon}$  and  $k_\theta - \tilde{\epsilon}_\theta$  turbulence model is proposed. The model is designed to conform with the near-wall characteristics obtained with direct numerical simulation data, but also to possess correct asymptotic behaviour in the vicinity of the wall. Key features of the  $k - \tilde{\epsilon}$  model are the adoption of Taylor microscale in the damping function and the inclusions of the pressure diffusion terms in both  $k$  and  $\tilde{\epsilon}$  equations. The asymptotic limits of the  $k_\theta$  and  $\tilde{\epsilon}_\theta$  equations are also satisfied by incorporation of the viscous dissipation related terms. Predicted results compared with the DNS data of the parallel Couette flows, indicate that the proposed model reproduces correctly the near-wall turbulent properties. Regarding the thermal field, simulations contrast with the DNS data of channel flows show the capability of the proposed model to mimic the variations of the temperature field at various Prandtl numbers.

## Introduction

To model correctly the turbulence transport processes and the heat transfer characteristics in the vicinity of the wall, the developments of low-Reynolds-number models are vigorously pursued in recent decades. Based on direct numerical simulation data, a simplified form of low-Reynolds-number two-equation turbulence model was proposed[1]. The proposed dynamic model was shown to be able to predict accurately the channel and reattaching flows[1].

Apart from the dynamic field, intensive efforts are concentrated on the the modelling of the scalar field, which is particularly important in thermal field and reacting flows. Within the framework of two-equation turbulence model,

scalar variance( $k_\theta$ ) and scalar variance dissipation rate( $\epsilon_\theta$ ) are frequently adopted to model the eddy diffusivity of the scalar field, without the explicit prescription of the turbulent Prandtl number,  $Pr_t$ . In the present paper, a  $k_\theta$  and  $\tilde{\epsilon}_\theta$  model is proposed to model the thermal field. The proposed  $k_\theta$  and  $\tilde{\epsilon}_\theta$  equations are designed to satisfy the asymptotic limits by incorporation of the viscous dissipation related terms.

## Near-Wall Modelling

### $k - \tilde{\epsilon}$ model for dynamic field

The governing equations for momentum, turbulent kinetic energy and turbulent dissipation rate are,

$$\frac{\partial U_j U_i}{\partial x_j} = -\frac{1}{\rho} \frac{\partial P}{\partial x_i} + \frac{\partial}{\partial x_j} \left[ \nu \left( \frac{\partial U_i}{\partial x_j} + \frac{\partial U_j}{\partial x_i} \right) - \overline{u_i u_j} \right] \quad (1)$$

$$\underbrace{\frac{\partial U_j k}{\partial x_j}}_{c_k} = \underbrace{\frac{\partial}{\partial x_j} \left[ \nu \frac{\partial k}{\partial x_j} \right]}_{D_k} + \underbrace{\frac{\partial}{\partial x_j} \left[ \frac{\nu_t}{\sigma_k} \frac{\partial k}{\partial x_j} \right]}_{T_k} - \underbrace{\frac{1}{2} \nu \frac{\partial}{\partial y} \left[ \frac{k}{\epsilon} \frac{\partial \tilde{\epsilon}}{\partial y} \right]}_{\Pi_k} - \underbrace{\overline{u_i u_j} \frac{\partial U_i}{\partial x_j}}_{P_k} - \underbrace{(\tilde{\epsilon} + \hat{\epsilon})}_{\epsilon} \quad (2)$$

$$\underbrace{\frac{\partial U_j \tilde{\epsilon}}{\partial x_j}}_{c_{\tilde{\epsilon}}} = \underbrace{\frac{\partial}{\partial x_j} \left[ \nu \frac{\partial \tilde{\epsilon}}{\partial x_j} \right]}_{D_{\tilde{\epsilon}}} + \underbrace{\frac{\partial}{\partial x_j} \left[ \frac{\nu_t}{\sigma_{\tilde{\epsilon}}} \frac{\partial \tilde{\epsilon}}{\partial x_j} \right]}_{T_{\tilde{\epsilon}}} - \underbrace{\nu \frac{\partial}{\partial y} \left[ \frac{\tilde{\epsilon}}{k} \frac{\partial k}{\partial y} \right]}_{\Pi_{\tilde{\epsilon}}} - \underbrace{1.44 \overline{u_i u_j} \frac{\partial U_i}{\partial x_j} \frac{\tilde{\epsilon}}{k}}_{P_{\tilde{\epsilon}}} - \underbrace{1.92 \frac{\tilde{\epsilon}^2}{k}}_{\epsilon_{\tilde{\epsilon}}} \quad (3)$$

$$-\overline{u_i u_j} = \nu_t \left( \frac{\partial U_i}{\partial x_j} + \frac{\partial U_j}{\partial x_i} \right) - \frac{2}{3} \delta_{ij} k \quad \nu_t = 0.09 f_\mu (y_\lambda) \frac{k^2}{\tilde{\epsilon}}$$

where  $y_\lambda = y/\sqrt{\nu k/\tilde{\epsilon}}$  and  $\sqrt{\nu k/\tilde{\epsilon}}$  is the Taylor microscale. The damping functions of the model are,

$$f_\mu = 1 - \exp(-0.01 y_\lambda - 0.008 y_\lambda^3)$$

$$\sigma_k = 1.4 - 1.1 \exp\left(-\frac{y_\lambda}{10}\right)$$

$$\sigma_\varepsilon = 1.3 - 1.0 \exp\left(-\frac{y_\lambda}{10}\right)$$

The functions are chosen to retain the high-Reynolds-number form away from solid boundaries. The asymptotic values of turbulent Prandtl number  $\sigma_k$  and  $\sigma_\varepsilon$  are adopted as 0.3 to obtain sufficient dissipation rate in the vicinity of the wall. In the core region of the flow,  $\sigma_k > \sigma_\varepsilon$  is chosen to eliminate the common drawback that turbulent diffusion of  $k$  overwhelms that of  $\varepsilon$  [2].

In the present approach, the dissipation rate is decomposed into two parts, i.e.,  $\varepsilon = \bar{\varepsilon} + \hat{\varepsilon}$ , and adopting  $\bar{\varepsilon}$  as the dependent variable. The advantage of this approach is that  $\bar{\varepsilon}$  reaches zero at the wall,  $\varepsilon_w = \hat{\varepsilon}_w = 2\nu(\frac{\partial\sqrt{k}}{\partial y})_w^2$ , and  $\bar{\varepsilon}$  equals to  $\varepsilon$  at about  $y^+ > 15$ .

The inclusion of the pressure diffusion terms,  $\Pi[1]$ , in both  $k$  and  $\bar{\varepsilon}$  equations enable the asymptotic limits to be satisfied. The adopted form of  $f_\mu$  reproduces correctly the asymptotic limit, i.e.  $f_\mu \propto y$  and hence  $-\overline{u'v'} \propto y^3$  towards the wall. The adoption of  $y_\lambda$  avoids the obvious defect, i.e. the singularity occurring at the reattaching point by adopting  $y^+ = u_\tau y/\nu$ . The modelled  $\Pi_\varepsilon$  also generates the extra source for  $\bar{\varepsilon}$  in the buffer zone, completely replacing the commonly adopted function,  $2\nu\nu_t(U_{i,jk})^2$ .

### $k_\theta - \bar{\varepsilon}_\theta$ model for thermal field

The incompressible temperature equation can be written as,

$$\frac{\partial U_j \Theta}{\partial x_j} = \frac{\partial}{\partial x_j} \left[ \alpha \frac{\partial \Theta}{\partial x_j} - \overline{u_j \theta} \right] + \frac{1}{\rho C_p} (S_\theta + \bar{S}_\theta) \quad (4)$$

$$-\overline{u_j \theta} = \alpha_t \frac{\partial \Theta}{\partial x_j}$$

where  $S_\theta = \mu(\frac{\partial U_i}{\partial x_j} + \frac{\partial U_j}{\partial x_i}) \frac{\partial U_i}{\partial x_j}$  and  $\bar{S}_\theta = \mu(\frac{\partial \bar{u}_i}{\partial x_j} + \frac{\partial \bar{u}_j}{\partial x_i}) \frac{\partial \bar{u}_i}{\partial x_j} = \rho \varepsilon$  denote the viscous dissipation terms.

Hence the exact  $k_\theta = \bar{\theta}^2/2$  equation takes the form,

$$\underbrace{\frac{\partial U_j k_\theta}{\partial x_j}}_{C_{k_\theta}} = \underbrace{\frac{\partial}{\partial x_j} \left[ \alpha \frac{\partial k_\theta}{\partial x_j} \right]}_{D_{k_\theta}} + \underbrace{\frac{\partial}{\partial x_j} \left[ \frac{\alpha_t}{\sigma_h} \frac{\partial k_\theta}{\partial x_j} \right]}_{T_{k_\theta}} + \underbrace{\frac{1}{\rho C_p} \bar{\theta} S_\theta}_{\Pi_{k_\theta}} - \underbrace{\overline{u_j \theta} \frac{\partial \Theta}{\partial x_j}}_{P_{k_\theta}} - \underbrace{(\bar{\varepsilon}_\theta + \hat{\varepsilon}_\theta)}_{\varepsilon_\theta} \quad (5)$$

Before examining the asymptotic behaviour of the above equation, it is beneficial to look into the asymptotic values of the instantaneous components,

$$\theta = b_4 y + c_4 y^2 + d_4 y^3 + \dots$$

$$k_\theta \equiv \frac{\bar{\theta}^2}{2} = \frac{1}{2} \bar{b}_4^2 y^2 + \bar{b}_4 c_4 y^3 + \dots$$

$$= \frac{1}{2} b_\theta y^2 + c_\theta y^3 + d_\theta y^4 + \dots$$

$$\varepsilon_\theta \equiv \alpha \left( \frac{\partial \theta}{\partial y} \right)^2 = \alpha b_\theta + 4\alpha c_\theta y + d_\phi y^2 + \dots$$

$$\hat{\varepsilon}_\theta = 2\alpha \left( \frac{\partial \sqrt{k_\theta}}{\partial y} \right)^2 = \alpha b_\theta + 4\alpha c_\theta y + d'_\phi y^2 + \dots$$

$$\tilde{\varepsilon}_\theta = \varepsilon_\theta - \hat{\varepsilon}_\theta = (d_\phi - d'_\phi) y^2 + \dots$$

By inserting the  $y$  dependent quantities into the  $k_\theta$  equation, it can be observed that the dominant terms in the vicinity of the wall are  $D_{k_\theta}$ ,  $\varepsilon_\theta$  and  $\Pi_{k_\theta}$ . To keep the asymptotic limits balanced up to the first order term, the viscous dissipation function term is modelled as,

$$\frac{1}{\rho C_p} \bar{\theta} S_\theta = -\frac{1}{2} \alpha \frac{\partial}{\partial y} \left[ \frac{k_\theta}{\varepsilon_\theta} \frac{\partial \hat{\varepsilon}_\theta}{\partial y} \right] \quad (6)$$

As in the case of the turbulent dissipation rate equation, the  $\varepsilon_\theta$  is decomposed into two terms, i.e.  $\varepsilon_\theta = \bar{\varepsilon}_\theta + \hat{\varepsilon}_\theta$ . Here, the  $\bar{\varepsilon}_\theta$  equation is adopted and the modelled equation takes the form,

$$\underbrace{\frac{\partial U_j \bar{\varepsilon}_\theta}{\partial x_j}}_{C_{\bar{\varepsilon}_\theta}} = \underbrace{\frac{\partial}{\partial x_j} \left[ \alpha \frac{\partial \bar{\varepsilon}_\theta}{\partial x_j} \right]}_{D_{\bar{\varepsilon}_\theta}} + \underbrace{\frac{\partial}{\partial x_j} \left[ \frac{\alpha_t}{\sigma_\phi} \frac{\partial \bar{\varepsilon}_\theta}{\partial x_j} \right]}_{T_{\bar{\varepsilon}_\theta}} - \underbrace{\alpha \frac{\partial}{\partial y} \left[ \frac{\bar{\varepsilon}_\theta}{k_\theta} \frac{\partial k_\theta}{\partial y} \right]}_{\Pi_{\bar{\varepsilon}_\theta}} - \underbrace{C_{P_1} f_{P_1} \frac{\bar{\varepsilon}_\theta}{2k_\theta} \overline{u_j \theta} \frac{\partial \Theta}{\partial x_j} - C_{P_2} f_{P_2} \frac{\bar{\varepsilon}_\theta}{k} \overline{u_i u_j} \frac{\partial U_i}{\partial x_j}}_{P_{\bar{\varepsilon}_\theta}} - \underbrace{C_{D_1} f_{D_1} \frac{\bar{\varepsilon}_\theta^2}{2k_\theta} - C_{D_2} f_{D_2} \frac{\bar{\varepsilon}_\theta \tilde{\varepsilon}_\theta}{k}}_{\varepsilon_{\bar{\varepsilon}_\theta}} \quad (7)$$

The inclusion of the  $\Pi_{\bar{\varepsilon}_\theta}$  term renders the satisfaction of the asymptotic limits in the vicinity of the wall.

The eddy diffusivity of temperature,  $\alpha_t$ , is generally expressed as a function of velocity scale ( $k^{\frac{1}{2}}$ ), the characteristic length scale ( $L_m$ ) or the mixing time-scale ( $\tau_m$ ) [3, 4],

$$\alpha_t = C_\lambda f_\lambda k^{\frac{1}{2}} L_m = C_\lambda f_\lambda k^{\frac{1}{2}} k^{\frac{1}{2}} \tau_m \quad (8)$$

where the form of  $\tau_m$  varies, but usually is deemed to be a function of  $R = \frac{k_\theta}{\varepsilon_\theta} / \frac{k}{\varepsilon}$ , which is the ratio

of the thermal and mechanical time-scale. In the present approach, the form of the time scale adopted is  $\tau_m = \frac{k}{\varepsilon} \sqrt{\frac{Pr}{2R}}$ , which is designed to reproduce the DNS data in the core region[5]. The coefficients and the damping functions adopted are,

$$\begin{aligned} C_\lambda &= 0.116 & f_\lambda &= f_\mu \\ C_{P1} &= 1.8 & f_{P1} &= 1 - \exp(-\frac{y_\lambda}{20}) \\ C_{P2} &= 1.4 + 17\exp(-4.5Pr) & f_{P2} &= 1 \\ C_{D1} &= 2.7 - 0.5\exp(-\frac{R_t}{60}) & f_{D1} &= 1 \\ C_{D2} &= 0.8 & f_{D2} &= 1 \\ \sigma_h &= \sigma_k & \sigma_\phi &= \sigma_\varepsilon \end{aligned}$$

where the turbulent Reynolds number is defined as,  $R_t = \frac{k^2}{\nu \varepsilon}$ .

## Numerical Procedure

The present numerical procedure[6] solves discretised versions of all equations over a staggered finite-volume arrangement. The principle of mass-flux continuity is imposed indirectly via the solution of pressure-correction equations according to the SIMPLE algorithm[7]. The flow-property values at volume faces contained in the convective fluxes which arise from the finite-volume integration process are approximated by the quadratic upstream-weighted interpolation scheme(QUICK)[8].

It was found that the employment of the third order approximation of the surface derivatives arising from the viscous and pressure diffusion processes is essential in reproducing the correct flow near-wall asymptotic behaviour, by ensuring that the derivative is evaluated right at the surface.

The computed solution is assumed to have converged to its steady-state when the magnitude of the absolute residual sources of mass and momentum, normalized by the respective inlet fluxes, falls below 0.01%.

## Results and Discussions

### Turbulent plane Couette-Poiseuille flow

The performance of the proposed model is further contrasted with the DNS data of the fully developed plane Couette-Poiseuille flow[9]. The schematic picture of the flow is shown in Figure 1, where the top wall is at rest and the bottom wall is moving at a constant speed,  $U_w$ . The Reynolds number based on the channel half width  $\delta$  and

the bottom wall velocity, is 1800. Grid densities of sizes 60 and 100 in the direction normal to the wall were used to check the grid independence and the 60 grid was found adequate. The first grid node near the wall was placed at  $y^+ \approx 0.1$ , to ensure the adequate resolution of the viscous sub-layer.

The influence of the moving wall on the flow can be seen by the asymmetric axial velocity distribution across the channel, shown in Figure 2, where the location of the maximum axial velocity is observed to shift towards the moving wall. When examining the velocity log-law plots, shown in Figures 3 and 4, the velocity distribution at the top wall side is similar to that obtained from the fully developed channel flow. However, a marked different profile is observed at the moving bottom wall region and the velocity distribution is well predicted by the proposed model.

Due to the reduction of the shear stress at the moving wall, the turbulent kinetic energy level adjacent to the bottom wall is severely damped, as can be seen in Figure 5, compared to the  $k$  level at the top wall side. However, at the bottom wall, the  $k$  level predicted by the LS model[10] decays monotonically, which is inconsistent with the DNS data distribution.

As observed in the fully developed channel flows, the local maximum of the  $\varepsilon$ , shown in Figure 6, locates at the wall near the stationary side. At the region  $y_b^+ < 20$  on the moving wall side, the local maximum of the  $\varepsilon$  is again found at the wall, shown in Figure 7, and this is reproduced correctly by the proposed model. The CH[11] prediction shows a rise to its local maximum, then decays monotonically towards the wall. However, the LS prediction decays monotonically towards the wall at  $y_b^+ < 20$ . Finally, the performance of the proposed model can be ascertained by observing the turbulent kinetic energy budgets near the fixed and moving walls, shown in Figures 8 to 9.

### Channel flows with internal heat source

The performance of the proposed model is then contrasted with the DNS data of channel flows with internal heat source at  $Re_\tau = 180$ [12]. The overall performance of the model is evaluated by examining the turbulence quantities in thermal fields, shown in Figures 10 to 12. Good agreements with the DNS data can be seen from the figures and the Prandtl number



dependence of the temperature field is adequately captured. Notably the proposed model is with an unsophisticated form and the success is partly attributed to the correct asymptotic near-wall behaviours.

## Conclusion

An improved and simplified low-Reynolds-Number two-equation turbulence model is proposed. The model is designed not only to conform with the near-wall characteristics obtained with direct numerical simulation data, but also to possess correct asymptotic behaviour in the vicinity of the wall. The performance of the proposed model is contrast with the DNS data of the turbulent plane Couette-Poiseuille flow and channel flow with internal heat source. The results indicate that the present model reproduces reasonably the near-wall turbulence and consequently heat transfer behaviours.

## Acknowledgements

This research work was supported by the National Science Council of Taiwan under grant NSC-85-2212-E-007-057 and the computational facilities were provided by the National Centre for High-Performance Computing of Taiwan which the authors gratefully acknowledge.

## References

- [1] Hwang, C. B. and Lin, C. A., 1997, "An Improved Low-Reynolds-Number  $k - \tilde{\epsilon}$  Model based on Direct Numerical Simulation Data". 35th Aerospace Sciences Meeting & Exhibit, Jan. 6-10, Reno, N.V.
- [2] Nagano, T. and Tagawa, M., 1990, "An Improved  $k - \epsilon$  Model for Boundary Layer Flows", J. of Fluids Engng., Vol. 112: pp. 33-39.
- [3] Nagano, T. and Kim, C., 1988, "A Two-Equation Model for Heat Transport in Wall Turbulent Shear Flows", J. of Heat Transfer, Vol. 110: pp. 583-589.
- [4] Youssef, M. S., Nagano, Y. and Tagawa, M., 1992, "A Two-equation Heat Transfer Model for Predicting Turbulent Thermal Fields under Arbitrary Wall Thermal Conditions", Int. J. Heat Mass Transfer, Vol. 35, Vol. 11: pp. 3095-3104.
- [5] Horiuti, K., 1992, "Assessment of Two-Equation Models of Turbulent Passive-Scalar Diffusion in Channel Flow", J. Fluid Mech., Vol. 238: pp. 405-433.
- [6] Lin, C. A. and Leschziner, M. A., 1993, "Three-Dimensional Computation of Transient Interaction Between Radially Injected Jet and Swirling Cross-Flow Using Second-Moment Closure," Computational Fluid Dynamics Journal, Vol. 1., No. 4, pp. 423-432.
- [7] Patankar, S. V., 1980, "Numerical Heat Transfer and Fluid Flow", Hemisphere Publishing Corporation.
- [8] Leonard, B. P., 1979, "A Stable and Accurate Convective Modelling procedure Based on Quadratic Upstream Interpolation," Computer Methods in Applied Mechanics and Engineering, Vol. 19, June, pp. 59-98.
- [9] Kuroda, A., Kasagi, N., and Hirata, M., 1993, "Direct Numerical Simulation of Turbulent Plane Couette-Poiseuille Flows: Effect of Mean Shear on the Near Wall Turbulence Structure", Proceeding of the 9th Symposium on Turbulent Shear Flow, Kyoto University, Kyoto, Japan, August 16-18, pp. 8.4.1-8.4.6.
- [10] Jones, W. P., and Launder, B. E., 1973, "The Calculation of Low-Reynolds-Number Phenomena with a Two-Equation Model of Turbulence," International Journal of Heat and Mass Transfer, Vol. 16, pp. 1119-1130.
- [11] Chien, K. Y., 1982, "Predictions of Channel and Boundary Layer Flows with a Low-Reynolds-Number Turbulence Model," AIAA Journal, Vol. 20, No. 1, pp. 33-38.
- [12] Kim, J. and P. Moin, 1989, "Transport of Passive Scalars in a Turbulent Channel Flow", in *Turbulent Shear Flows 6*, pp. 85-96.



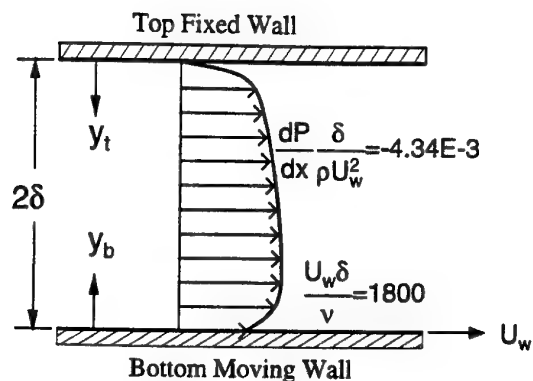


Figure 1: The schematic of the plane Couette-Poiseuille flow

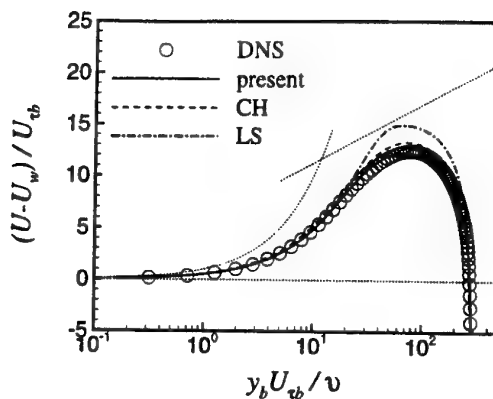


Figure 4: Mean velocity plotted from the moving wall

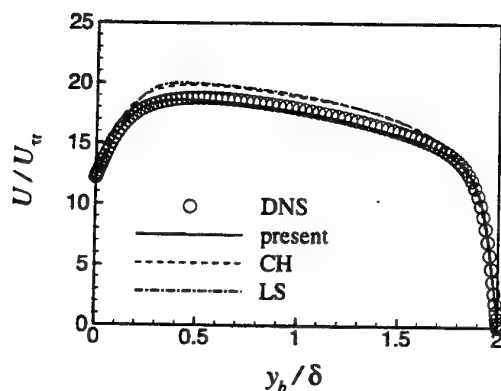


Figure 2: Mean velocity profile

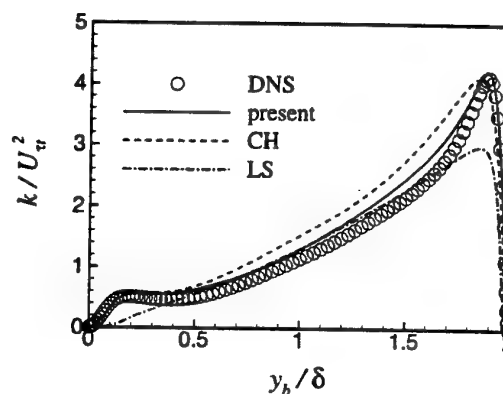


Figure 5: Turbulent kinetic energy distribution

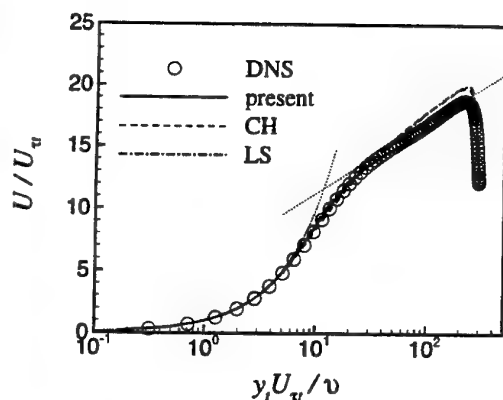


Figure 3: Mean velocity plotted from the fixed wall

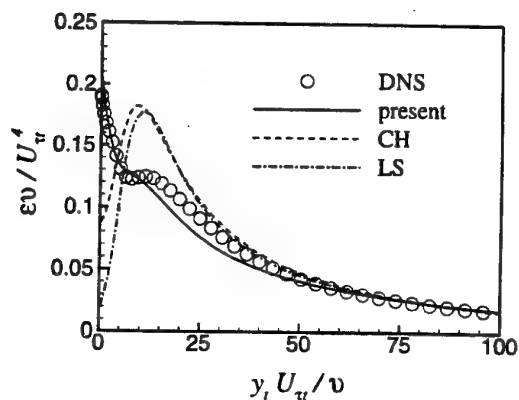


Figure 6: Turbulence dissipation rate distribution at fixed wall

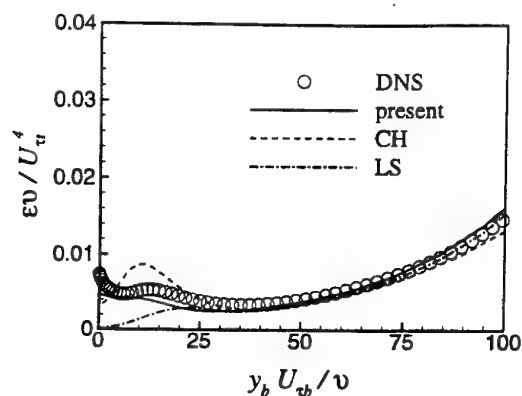


Figure 7: Turbulence dissipation rate distribution at moving wall

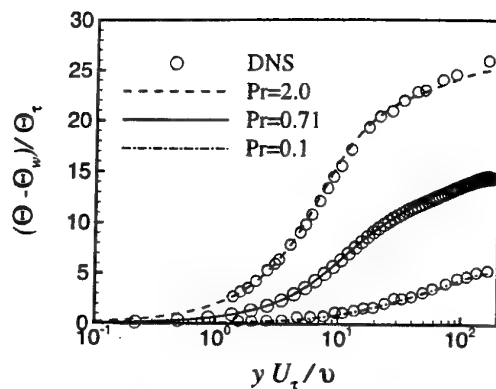


Figure 10: Mean temperature distributions with various Prandtl numbers

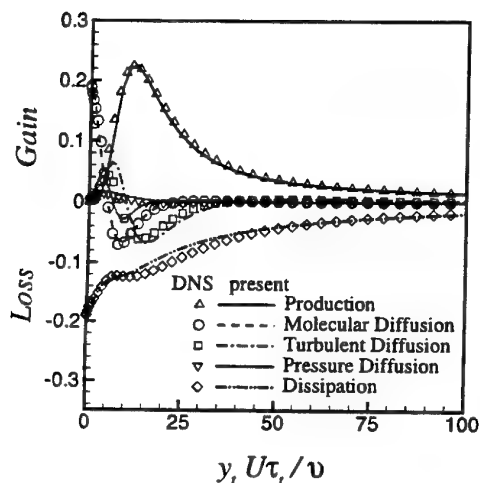


Figure 8:  $K$  budgets of at the fixed wall

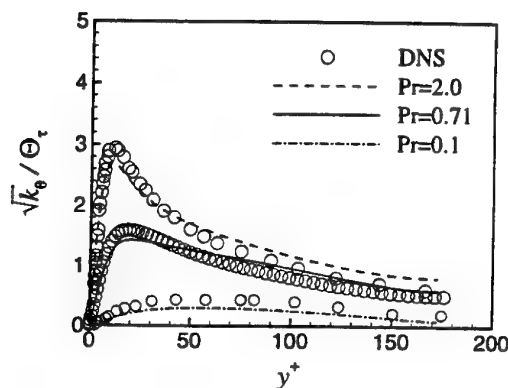


Figure 11: Temperature fluctuation intensities with various Prandtl numbers

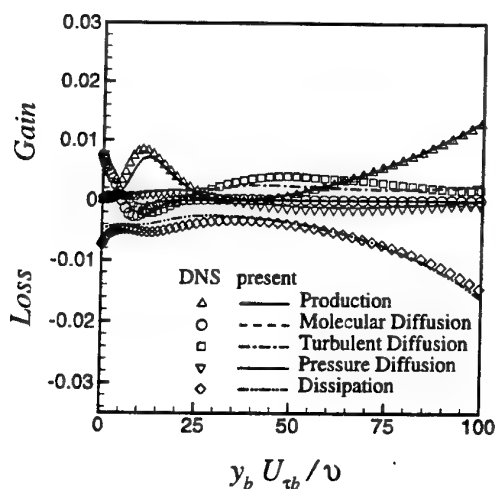


Figure 9:  $k$  budgets of at the moving wall

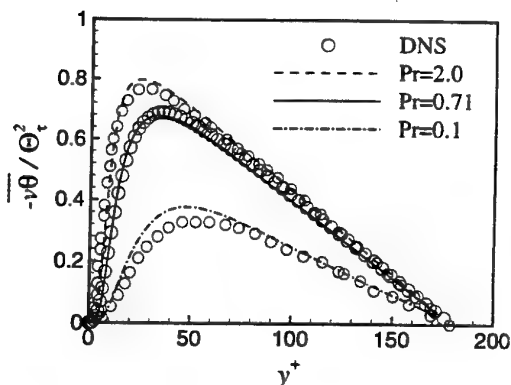


Figure 12: Turbulent heat flux with various Prandtl numbers

# NEAR-WALL MODELIZATION FOR DISSIPATION EQUATION IN SECOND-MOMENT TURBULENCE CLOSURES

G.B. Deng and M. Visonneau

Division de Modélisation Numérique

Laboratoire de Mécanique des Fluides, CNRS UMR 6598

Ecole Centrale de Nantes

B.P. 92101

44321 Nantes Cedex 3

France

## ABSTRACT

This paper is devoted to the near-wall modelization of the turbulent dissipation-rate equation. A critical analysis of common approach used for the dissipation-rate equation near-wall closure both for two-equation model as for Reynolds-stress model is given first. Based on this analysis, two original near-wall models are proposed. The first one is based on a blending approach in which an algebraic model is used to determine the turbulent dissipation-rate near the wall. In the second approach, turbulent frequency  $\omega$  is solved instead of turbulent dissipation-rate  $\epsilon$ . They allow the low-Reynolds-number model proposed by Shima for the Reynolds-stress transport equation to be applied to several complex three-dimensional flows even though the wall-limiting behaviour of the Reynolds-stress is not correct.

## INTRODUCTION

Based on our own experience, memory occupation and CPU per point per iteration required by a second-moment closure are only about twice as much as that needed by a two-equations model. Thus, modern computers should allow second-moment closures to be applied to a wide range of applications. However, the age of application of second-moment closure does not seem to have come yet. Few results have been presented for practical applications. This unusual contrast in CFD raises interrogations on the orientation in second-moment closure development where the preference is often given to model accuracy and universality to the detriment of efficiency. In this paper, we try to focus on this issue by considering low-Reynolds-number second-moment closures.

Near-wall turbulence modeling is a key issue in wall shear flow computations. Because of the frequent strong three-dimensionality of the velocity field near the wall, we cannot rely on a wall function approach for three-dimensional complex flow. A low-Reynolds-number model must be used instead. Such a model can be constructed by introducing appropriate damping functions and additional terms. Launder & Shima (1989) have proposed a very simple model that allows the Gibson & Laun-

der model to be integrated down to the wall. Further modifications were made by Shima (1993) who presented several applications for boundary-layer flows. Recent developments in near-wall second-moment closures are mainly focused on accuracy and universality by taking into account physical constraints and mathematical formalism. For example, Launder & Tselepidakis (1991) attempt to improve accuracy by developing a realizable nonlinear pressure-strain model. Craft & Launder (1995) tried to construct a more universal model by replacing wall normal distance and wall normal vector by Reynolds-stress invariants.

Besides accuracy and universality, efficiency is also an important issue in model development. By efficiency, we mean here the capability for a model to provide a realistic solution with minimum computational resources. Contradictions between the model complexity induced by physical and mathematical constraints and its efficiency have been addressed by S. Jakirlić & K. Hanjalić (1995). One of the most annoying problems for wall-flow computations with second-moment closures concerns unphysical laminarization. It is not unusual that complex model constraints are so difficult to satisfy that we can only converge towards a laminar flow which is a possible solution of the second-moment closure with given boundary conditions. Attention must be paid to model development and implementation in order to avoid such unphysical laminarization.

Undesirable laminarization may occur in complex flow configuration such as non-equilibrium flow in separation zone. It may also be simply of numerical origin. Strong space and/or time variation, insufficient grid points distribution, impossibility to ensure theoretical limiting behavior of the solution on general curvilinear grid, etc. are likely causes leading to unphysical laminarization. The aim of the present paper is the improvement of second-moment closure efficiency.

The work presented in this paper was conducted after the failure to implement the Shima model (1993) in our code for solving Reynolds-Averaged Navier-Stokes equations on general three-dimensional curvilinear grids. Details of implementation can be found in Deng & Visonneau (1996). After a very careful check-

ing that ensures that the code was bug-free, we were very disappointed to find out that a solution could be obtained only for very simple developed wall-flows such as fully developed channel flow, flat plane boundary-layer flow, etc... For all the other tested configurations that do not pose any problem to two-equation models, even as simple as two-dimensional backward step flow, we often experienced with flow laminarization, leading to unphysical unsteady solution or divergence. Detailed analyses presented below show that the problems originate from the dissipation equation. These problems are not specific to Shima model. They are also present in many other second-moment closures. Consequently, instead of trying to revise the dissipation equation, two new approaches are proposed, namely, a blending  $R_{ij} - \epsilon$  model and a  $R_{ij} - \omega$  model. Both retain Shima's near-wall low-Reynolds formulation for the Reynolds-stress transport equations but differ through the turbulent dissipation transport equation in the near-wall region.

By using the two new approaches, the Shima model for the Reynolds-stresses can be applied to complex wall shear flows such as flows around the HSVA tanker and flows inside a rectangular curved duct without any other modifications. Results are presented in the following sections.

### NEAR-WALL CLOSURE

Unlike in second-moment closure, near-wall closure for the turbulent dissipation equation in two-equation model is at least a numerically well-solved problem. It seems to be straightforward to extend a near-wall closure in two-equation model to Reynolds-stress model. However, to our knowledge, none of existing dissipation equation for near-wall two-equation models can be directly applied to second-moment closure by simply changing the turbulent transport model. Except the turbulent transport model, the turbulent dissipation equation in second-moment closure is often more complex. It usually involves several additional terms. Yet, in spite of its complexity, few of them have been proved to be able to be applied to complex geometry.

A comparison with two-equation models is worthwhile for second-moment closures. At high Reynolds number, the turbulence dissipation equation is modeled as:

$$\frac{D\epsilon}{Dt} = \text{Production} - \text{Dissipation} + \text{Diffusion} \quad (1)$$

The modelization of the production term and the dissipation term in two-equation model and in Reynolds-stress model are similar, they are often treated as:

$$\text{Production} = C_{\epsilon 1} \frac{\epsilon}{k} P_k \quad (2)$$

with  $P_k$  being defined as:

$$P_k = -\overline{u_i' u_j'} \frac{\partial u_i}{\partial x_j}$$

and

$$\text{Dissipation} = C_{\epsilon 2} \frac{\epsilon^2}{k} \quad (3)$$

The diffusion term is modeled as

$$\text{Diffusion} = \frac{\partial}{\partial x_i} \left[ \left( \nu + \frac{\nu_t}{\sigma_\epsilon} \right) \frac{\partial \epsilon}{\partial x_i} \right] \quad (4)$$

in two-equation model and

$$\text{Diffusion} = \frac{\partial}{\partial x_i} \left[ \left( \nu \delta_{ij} + C_\epsilon \overline{u_i' u_j'} \frac{k}{\epsilon} \right) \frac{\partial \epsilon}{\partial x_j} \right] \quad (5)$$

in Reynolds-stress model if the simplest form is chosen.

Different length scales are involved in the near-wall region. Even with DNS data, it is still very difficult to model the dissipation-rate equation with accuracy. Near-wall extension is often formulated by introducing ad-hoc damping functions and by adding additional terms to the high-Reynolds-number model equation such that it can be integrated down to the wall and the global features of the flow such as the skin friction coefficient and the behaviour of the law-of-wall are correctly calculated, at least for simple flow.

When equation (1) is extended to the wall, two different layers must be taken into account. In the buffer layer, the magnitude of turbulent production  $P_k$  is almost the same as the turbulent dissipation-rate  $\epsilon$ . This constraint is imposed by the turbulent kinetic energy equation. In the buffer layer, diffusion term is often negative. With  $C_{\epsilon 1} = 1.44$  and  $C_{\epsilon 2} = 1.92$ , the negative terms are much larger than the positive terms in equation (1). We must either increase the production or reduce the dissipation. The first solution is preferred, since it can be justified by the exact transport equation for  $\epsilon$ . According to the DNS results of Mansour & al. (1988), although the turbulent production term  $P_\epsilon^4$  (see Mansour & al. (1988) for the notation) is the most important production term away from the wall, the mixed production term  $P_\epsilon^1$  and the mean velocity gradient production term  $P_\epsilon^2$  become equally important in the buffer layer. As the result, it is natural to increase the production term. This solution is often adopted in second-moment closures.

The second layer that needs to be taken into account in near-wall modelization is the sublayer. Unlike in the buffer layer, near-wall model is usually formulated differently for two-equation model and Reynolds-stress model in this region. For two-equation model, it is easy to ensure the correct wall limiting behaviour of the shear-stress by introducing appropriate damping function. In this case, the order of the production term is  $O(y)$ . It is negligible compared with the diffusion term which become positive and has an order of  $O(1)$ . Equation (1) can not be in balance near the wall, since the order of the dissipation term is  $O(1/y^2)$ . The balance can be established by introducing a damping function  $f_{\epsilon 2}$  with an order of  $O(y^2)$  such that the dissipation term becomes the same order as the diffusion term. Since the order of the damping function  $f_{\epsilon 2}$  is  $O(y^2)$ , it also reduces the magnitude of the dissipation term in the buffer layer. For this reason, additional production term is not needed in two-equation model.

In second-moment closures, Reynolds-stress tensor is determined from a system of transport equation. With this approach, it is not easy to ensure the correct wall-limiting behaviour of the Reynolds-stress tensor. Attempts have been made to develop near-wall model which meets the wall-limiting behaviour. But such model is only validated in simple configuration where wall normal direction coincides with the coordinate system. Improvements still need to be made before they can be applied to complex geometry. In the present study, we prefer to use a very simple near-wall model proposed by Shima (1993). One of the drawbacks of the Shima model is that all Reynolds-stress components tend to  $O(y^2)$  at the wall. As a result, the production term becomes  $O(1)$  instead of  $O(y)$  near the wall. Such limiting behaviour is in violation with the physics and should be avoided.

In the Shima model, the dissipation term is modeled as

$$\text{Dissipation} = C_{\epsilon 2} \frac{\epsilon \tilde{\epsilon}}{k} \quad (6)$$

with

$$\tilde{\epsilon} = \epsilon - 2\nu \left( \frac{\partial \sqrt{k}}{\partial y} \right)^2 \quad (7)$$

It is commonly accepted that the quantity  $\bar{\varepsilon}$  thus defined behaves as  $O(y^2)$  near the wall. Thus, the dissipation term becomes  $O(1)$  near the wall, and can be in balance with the diffusion and the production term. The justification of such model can be traced back to K. Hanjalić and B.E. Launder (1976) who relied on an analysis of the exact wall-limiting behaviour of  $k$  and  $\varepsilon$ . Although the analysis is correct, it cannot be used to justify the wall-limiting behaviour of  $\bar{\varepsilon}$ , since the asymptotic behaviours of  $k$  and  $\varepsilon$  predicted by a numerical model are not the same as the exact wall-limiting behaviour.

In the appendix below, we show that  $\bar{\varepsilon}$  tends to  $O(y^2)$  at the wall only when a converged solution is obtained with a second or higher order discretization scheme. During the iteration, the dissipation term given by (6) may be unbounded. For these reasons, it is not surprising that unphysical laminarization occurs frequently when the dissipation term is treated as (6). This model is inappropriate in the near wall modelization.

Too many ad-hoc modifications need to be made if we want to revise the dissipation-rate equation in the Shima model. It is necessary to introduce a damping function  $f_{\varepsilon 2}$  to the dissipation term such that it tends to  $O(1)$  at the wall. It is preferable to apply another damping function  $f_{\varepsilon 1}$  to the production term such that it vanishes at the wall. Additional production terms need to be added to balance the equation in the buffer layer. Having little physical justification, such ad-hoc modifications increase the numerical stiffness. It is why we prefer to choose an other alternative. Two original solutions are proposed here, namely, a  $R_{ij} - \varepsilon$  blending model and a  $R_{ij} - \omega$  model. They are presented in the following subsections.

#### The blending approach

In the blending approach, two different values for the turbulence dissipation are calculated separately. The first one  $\varepsilon_1$  is evaluated from an algebraic expression proposed by Wolfshtein (1969):

$$\varepsilon_1 = \frac{k^{3/2}}{C_\mu^{3/4} y} \frac{1}{1 - e^{-\frac{\sqrt{k} y}{A_\varepsilon}}} \quad (8)$$

with

$$\kappa = 0.41, C_\mu = 0.09 \text{ and } A_\varepsilon = \frac{2\kappa}{C_\mu^{3/4}}$$

The second one  $\varepsilon_2$  is computed from the high Reynolds number  $\varepsilon$  equation:

$$\begin{aligned} \frac{D\varepsilon_2}{Dt} &= C_{\varepsilon 1} \frac{\varepsilon_2}{k} P_k - C_{\varepsilon 2} \frac{\varepsilon_2^2}{k} \\ &+ \frac{\partial}{\partial x_k} \left( C_\varepsilon \frac{k}{\varepsilon} \overline{u'_k u'_l} \frac{\partial \varepsilon_2}{\partial x_l} + \nu \frac{\partial \varepsilon_2}{\partial x_k} \right) \end{aligned} \quad (9)$$

with  $\varepsilon_2 = 0$  at the wall as boundary condition. That equation can be solved directly down to the wall, and, even with this unphysical boundary condition,  $\varepsilon_2$  provides a good approximation for the turbulence dissipation away from the wall. As  $\varepsilon_1$  is valid close to the wall, the turbulence dissipation  $\varepsilon$  can be determined in the following way:

$$\varepsilon = C_{wall} \varepsilon_2 + (1 - C_{wall}) \varepsilon_1 \quad (10)$$

with:

$$C_{wall} = 1 - \exp \left[ - \left( \frac{k^2}{\nu \varepsilon_2} \right)^{1/4} \right]$$

The principle of the blending approach is very similar to two-layer approach proposed by Chen & Patel (1987) which has been successfully applied to a two-equation model. But the blending approach is more efficient from the point of view of numerical computation, because there is no need to determine the matching position. Unlike the two-layer approach where even the first derivative of dissipation-rate is not continuous, the blending approach ensures a smooth solution. Compared to other dissipation-rate equation models in second-moment closures where several ad-hoc damping functions and additional terms are usually involved, only one blending function is used in the present model. Due to this simplicity, the blending approach is found to be very efficient. The Shima model for Reynolds-stress transport equation can be used with the blending approach without any modification.

#### The $R_{ij} - \omega$ model

The  $R_{ij} - \omega$  model can be considered as an extension of the Wilcox's  $k - \omega$  model to Reynolds-stress model. In second-moment closures, the transport equation for  $\omega$  can be written as:

$$\begin{aligned} \frac{D\omega}{Dt} &= \alpha \frac{\omega}{k} P_k - \beta \omega^2 \\ &+ \frac{\partial}{\partial x_k} \left( C_\varepsilon \frac{k}{\varepsilon} \overline{u'_k u'_l} \frac{\partial \omega}{\partial x_l} + \nu \frac{\partial \omega}{\partial x_k} \right) \end{aligned} \quad (11)$$

Unlike the  $\varepsilon$  equation, the  $\omega$  equation can be solved down to the wall without any damping function. However, when equation (11) is solved with the Shima's model, the slope of the law of the wall proves to be correct but the additive constant is over-predicted. Damping function may be introduced to obtain the correct behaviour, but it usually increases the numerical stiffness of the model. Authors prefer to alter the viscous diffusion term by multiplying the kinematic viscosity  $\nu$  by a factor  $C_\omega = 0.55$  chosen to give the correct additive constant of the law of the wall. Resulting model equation reads simply as

$$\begin{aligned} \frac{D\omega}{Dt} &= \alpha \frac{\omega}{k} P_k - \beta \omega^2 \\ &+ \frac{\partial}{\partial x_k} \left( C_\varepsilon \frac{k}{\varepsilon} \overline{u'_k u'_l} \frac{\partial \omega}{\partial x_l} + \nu C_\omega \frac{\partial \omega}{\partial x_k} \right) \end{aligned} \quad (12)$$

with

$$\alpha = \frac{5}{9}, \beta = \frac{3}{40} \text{ and } \varepsilon = 0.09 \omega k$$

as proposed by Wilcox in his  $k - \omega$  model, and  $C_\varepsilon = 0.18$ . We consider that the influence of the kinematic viscosity  $\nu$  outside the wall region is negligible, so  $C_\omega = 0.55$  is kept as constant in the whole field. If it is necessary, it can be replaced by a function which tends to 1 away from the wall.

Asymptotic analysis shows that the wall limiting behaviour of  $\overline{u'_i u'_j}$  and  $\omega$  given by the above model is

$$\omega = \frac{6\nu C_\omega}{\beta y^2} \quad (13)$$

and

$$\overline{u'_i u'_j} \sim y^{2.55}$$

Although the wall-limiting behaviour of Reynolds-stress given by the  $R_{ij} - \omega$  is not correct, we prefer to keep the model equation as simple as possible rather than to introduce several damping functions which bring a negligible improvement, but increase the numerical stiffness. In addition, the exact wall-limiting behaviour of  $\omega$  given by (13) cannot be obtained by any numerical method.

For example, with second-order central difference scheme, the truncation error of the second derivative at the first grid point from the wall is equal to

$$\frac{h^2}{12} \frac{\partial^4 \omega}{\partial y^4} \sim \frac{10}{h^4}$$

where  $h$  is the grid space supposed to be constant. Whatever the grid space used, the truncation error has always the same magnitude as that of the second derivative itself ( $\sim 6/h^4$  at the first grid point). The only way to obtain the exact solution of  $\omega$  near the wall is to impose that solution directly on the first few grid points near the wall, which complicates the numerical implementation.

## MODEL VALIDATION

A fully developed channel flow at high Reynolds number is chosen for calibration. The blending function and the  $C_\omega$  coefficient are chosen such that the law of wall is correctly predicted for this flow. The model thus calibrated gives prediction similar as the original model for simple flows. Figures 1 et 2 present results for a fully developed channel flow at  $Re_\tau=180$  for which Kim, Moin & Moser's direct simulation results (1987) can be used for comparison. Although the blending function and the  $C_\omega$  coefficient are not calibrated for this configuration, the accuracy of the original model is globally preserved. Predictions for the turbulent dissipation-rate are presented in figure 3. None of three models can give accurate prediction of  $\epsilon$  near the wall, but they agree well away from it.

The advantage of the two newly proposed models over the Shima model is demonstrated over complex geometries. Both models have been used to calculate the stern-flow around the HSVA tanker. The computation has been carried out on an O-O grid topology around the entire hull. Computational grid is far from orthogonal. Flow in the aft-part of the ship is quite complex. The interaction of the three-dimensional boundary layer with the longitudinal vortex results in a complex separation zone. More detail informations about this test case can be found in deng & al. (?). This is a real challenge for turbulent model accuracy and efficiency testing. We cannot prevent the computations from diverging with the Shima model. While with  $R_{ij} - \epsilon$  blending model and  $R_{ij} - \omega$  model, good prediction can be obtained. Figures 4 and 5 compare U and W velocity components respectively at the station  $X/L=0.978$  for several depths. Results obtained with the Chen-Patel  $k-\epsilon$  model and the  $k-\omega$  model of Wilcox are also presented for comparison. The most important feature of the flow is the formation of a longitudinal vortex in the aft-part of the ship. The distortion of the longitudinal velocity iso-levels shown in figure 4 indicates the influence of the longitudinal vortex. Except the  $k-\epsilon$  model, all other models can predict the distorted U velocity profiles near the center of the vortex. Both for two-equation model and for Reynolds-stress model, better result is obtained when the turbulent frequency  $\omega$  is used to determine the turbulent length scale. The width of the longitudinal vortex is better predicted with Reynolds-stress model.

The next application is the simulation of a developing turbulent flow in a 90 deg. curved duct of rectangular cross section with an aspect ratio of six ( $Re = 2.24 \cdot 10^5$ ). Measurements were carried out by Kim & Patel (1994). The geometry of this configuration is quite simple. Computation can be done on an orthogonal grid. Even so, the Shima model ends up with divergence. One of the possible reasons for the failure is the presence of a corner region in which the asymptotic analysis leading to the conclusion  $\bar{\epsilon} \sim O(y^2)$  is no longer valid. The dissipation term (6) may be

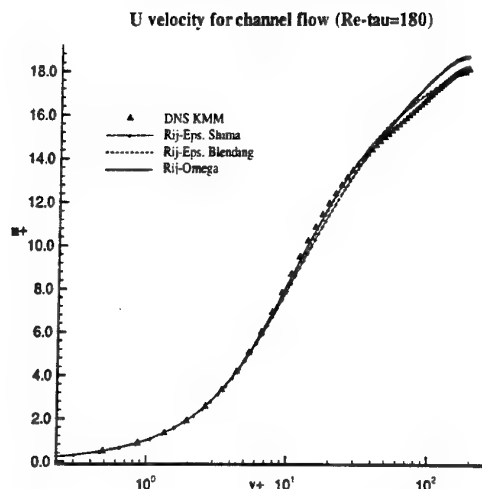


Fig. 1: U velocity profiles for the KMM channel

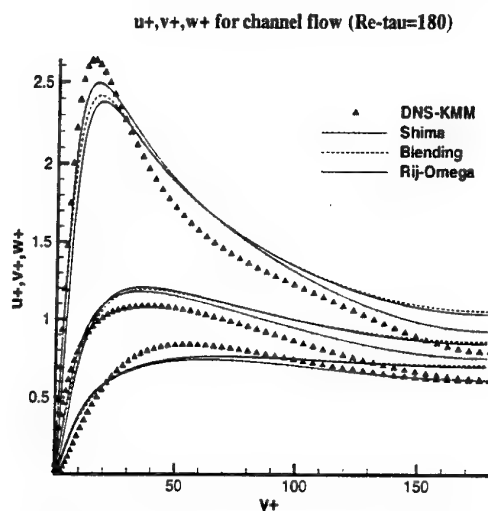


Fig. 2:  $u'$ ,  $v'$  and  $w'$  for the KMM channel

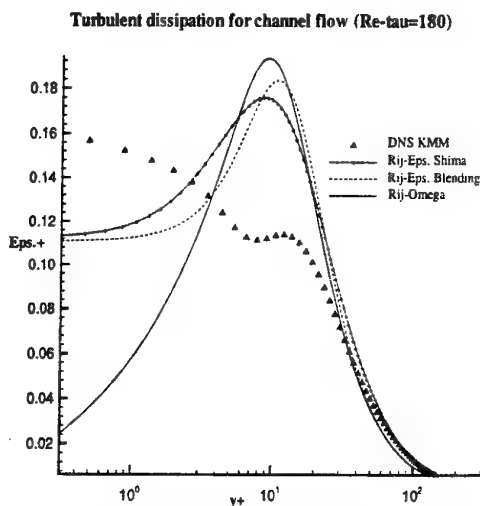


Fig. 3: Turbulent dissipation for the KMM channel

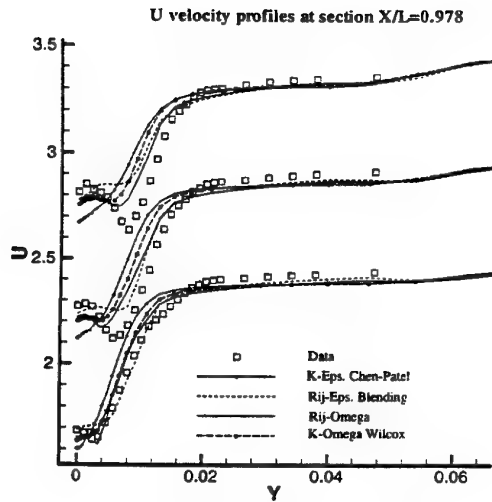


Fig. 4: U velocity profiles for the HSVA tanker

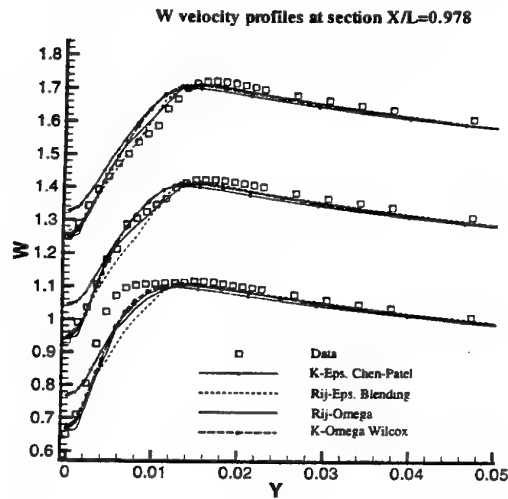


Fig. 5: W velocity profiles for the HSVA tanker

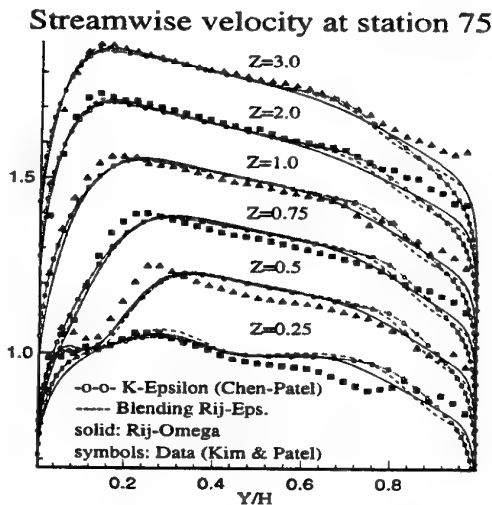


Fig. 6: Longitudinal velocity profiles at section 75 ( $Y/H=0$  is the convex wall)

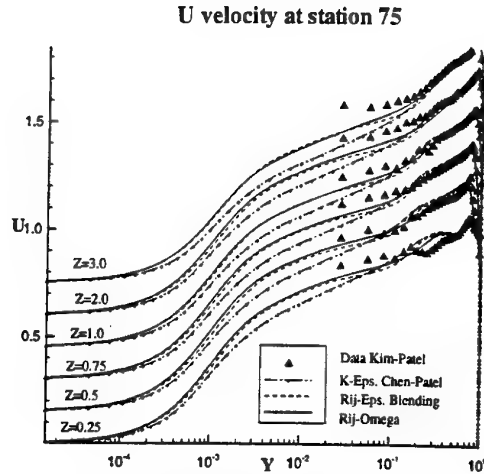


Fig. 7: Longitudinal velocity profiles at section 75 ( $Y/H=0$  is the concave wall)

unbounded. With the  $R_{ij} - \epsilon$  blending model and the  $R_{ij} - \omega$  model, computation can be carried out easily.

Figure 6 shows streamwise velocity profiles at section 75 at several depths. All turbulence models give similar prediction from the convex wall ( $Y/H=0$ ) to the center of the channel. Discrepancies with experimental data are mainly observed in the corner region. However, near the concave wall ( $Y/H=1.0$ ), results are quite different with different models. Due to curvature effect, streamwise velocity increases quickly away from the concave wall. Such effect is not captured by the  $k - \epsilon$  model. When we examine the velocity profiles near the concave wall (figure 7), we can see that the two Reynolds-stress models give similar results which are quite different from those provided by the  $k - \epsilon$  model. Compared with experimental data, Reynolds-stress models give better prediction even they are still unsatisfactory. In the previous test case, both Reynolds-stress models give nearly the same result for the outer part of the shear layer. However, in this test-case, some differences are observed near the concave wall. Shear layer is too diffused with  $R_{ij} - \omega$  model. The differences observed are probably due to model constant. We have chosen the constants proposed by Wilcox which do not correspond to the constants used in the  $R_{ij} - \epsilon$  blending model. Menter (1993) has shown that with  $C_{\epsilon 1} = 1.44$  and  $C_{\epsilon 2} = 1.92$ , the corresponding constants in the  $\omega$  equation should be  $\alpha=0.44$  and  $\beta=0.0828$ .

## CONCLUSIONS

The near-wall Reynolds-stress model proposed by Shima was found to be unsuitable for complex three-dimensional flow computations. Analysis shows that problems are mainly originated from the near-wall modelization for the dissipation term in the turbulent dissipation-rate equation. Two original near-wall models to determine the length scale for second-moment closure have been proposed. Emphasis is placed on model efficiency. Ad-hoc damping functions and additional terms are reduced to minimum. We introduce only one blending function in the first model and one ad-hoc coefficient in the second one. With our new proposals, the near-wall model proposed by Shima for the Reynolds-stress transport equation can be applied to several complex three-dimensional flows. Improvements are observed compared with two-equation model. Both models can be applied to other Reynolds-stress model.

## APPENDIX

In this appendix, a near wall asymptotic analysis is performed to determine the order of dissipation term defined by equation (6). By using the exact asymptotic behaviour of  $k$  and  $\epsilon$ , it can be shown that the order is  $O(1)$  (see K. Hanjalić and B.E. Launder (1976)). But such analysis is not valid for a turbulence model, since the wall limiting behaviour determined by the model equation with the given boundary conditions cannot be considered as the same as the exact behaviour. For instance, with  $k=0$  as boundary condition, the leading order term of  $k$  can only be considered as  $O(y)$  instead of  $O(y^2)$ . Thus, when we perform a near wall asymptotic analysis for a turbulence model, we must use the following assumption for  $k$  and  $\epsilon$  in the immediate vicinity of a wall:

$$\begin{aligned} k &= k_1 y + k_2 y^2 + k_3 y^3 + \dots \\ \epsilon &= \epsilon_0 + \epsilon_1 y + \epsilon_2 y^2 + \dots \end{aligned}$$

In most turbulent models, the pressure-transport term  $(p'(u'_j \delta_{jk} + u'_i \delta_{ik}))_{,k}$  which tends to  $O(y)$  at the wall is neglected. Thus, the following equation holds in the immediate vicinity of a wall both for two-equation model and for Reynolds-stress model

$$\epsilon = \nu \frac{\partial^2 k}{\partial y^2} + O(y^2) \quad (14)$$

From this equation, we can obtain

$$\begin{aligned} \epsilon_0 &= 2\nu k_2 \\ \epsilon_1 &= 6\nu k_3 \end{aligned}$$

To ensure the correct wall-limiting behaviour of  $k$ , the following boundary condition can be applied to  $\epsilon$  at the wall

$$\epsilon = 2\nu \left( \frac{\partial \sqrt{k}}{\partial y} \right)^2$$

With such a boundary condition, it is easy to calculate the leading order term of  $\epsilon$ :

$$\epsilon = \frac{\nu k_1^2}{2(k_1 y + k_2 y^2 + \dots)} + O(1)$$

Since  $\epsilon$  is finite at the wall,  $k_1$  must be equal to zero. As a result, in the immediate vicinity of the wall, the following expression holds

$$\epsilon = 2\nu \left( \frac{\partial \sqrt{k}}{\partial y} \right)^2 + 2\nu k_3 y + O(y^2)$$

The above analysis shows that  $\bar{\epsilon}$  defined by (7) tends to  $O(y^2)$  at the wall only when  $k_3=0$ , which is not true in general. As  $k$  tends to  $O(y^2)$  at the wall, the dissipation term calculated by (6) is unbounded when  $k_3 \neq 0$ . Consequently, when we obtain a converged solution with a model where the dissipation term in the dissipation rate transport equation is modeled as (6), the converged solution must be a solution with  $k_3=0$ . However, if the condition  $k_3=0$  can be admitted at the convergence, nothing can assure that this is also true during the iterative resolution process. Such possible unbounded term is the sources of numerical instability. This analysis is not in contradiction with that of K. Hanjalić and B.E. Launder (1976), since we base on the assumption that the pressure-transport term is neglected in the model.

For some models, this is a built-in mechanism which ensures that  $k$  tends to  $O(y^2)$  at the wall. In this case, we can use

$$\frac{\partial \epsilon}{\partial y} = 0$$

as boundary condition, which gives  $k_3=0$ . With such near-wall model,  $\bar{\epsilon}$  tends to  $O(y^2)$  at the wall theoretically. But even in this case, in order to assure that the discrete value of the dissipation term (6) is bounded during the iterative resolution process, we need to solve the  $k$  transport equation (or Reynolds-stress transport equations for second-moment closure) implicitly at least with a second-order accurate scheme and without unsteady term. Otherwise, equation (14) is not satisfied numerically. This is the principal cause of unphysical relaminarization that we have observed during our early implementation of Reynolds stress model. Consequently, model given by equation (6) is inappropriate.

## Acknowledgements

This research was supported by DRET through Contract 95.34.139.00.470.75.01, monitored by Dr. Moschetti. Thanks are due to the Scientific Committee of IDRIS and the DS/SPI for attributions of Cpu on the Cray C98 and T3E.

## REFERENCES

- Chen, H. and Patel, V., 1987, "Practical Near-Wall Turbulence Models for Complex Flow Including Separation", AIAA Paper 87-1300, AIAA Meeting.
- Craft, T. and Launder, B., 1995, "Improvements in Near-Wall Reynolds Stress Modelling for Complex Flow Geometries", 20-25, *Proceeding of 10th Symposium on Turbulent Shear Flows*, Pennsylvania.
- Deng, G. and Visonneau, M., 1996, "Evaluation of Eddy-Viscosity and Second-Moment Turbulence Closures for Steady Flows around Ships", *21st Symposium on Naval Hydrodynamics*, Trondheim.
- Hanjalić, K. and Launder, B., 1976, "Contribution towards a Reynolds-Stress Closure for Low-Reynolds-Number Turbulence", *J. Fluid Mech.*, Vol. 74, pp. 593-610.
- Jakirlić, S. and Hanjalić, K., 1995, "A Second-Moment Closure for Non-Equilibrium and Separating High- and Low-Reynolds-Number Flow", 23-25, *Proceeding of 10th Symposium on Turbulent Shear Flows*, Pennsylvania.
- Kim, W. and Patel, V., 1994, "Origin and Decay of Longitudinal Vortices in Developing Flow in a Curved Rectangular Duct", *J. of Fluids Engineering*, Vol. 116, pp. 45-52.
- Kim, J., Moin, P., and Moser, R., 1987, "Turbulence Statistics in Fully Developed Channel Flow at Low Reynolds Number", *J. Fluid Mech.*, Vol. 177, pp. 133-166.
- Launder, B. and Shima, N., 1989, "Second-Moment Closure for the Near-Wall Sublayer: Development and Application", *AIAA Journal*, Vol. 27, pp. 1319-1325.
- Launder, B. and Tselepidakis, D., 1991, "Progress and Paradoxes in Modelling Near-Wall Turbulence", 29-1, *Proceeding of 8th Symposium on Turbulent Shear Flows*, Munich.
- Mansour, N., Kim, J., and Moin, P., 1988, "Reynolds-stress and Dissipation-rate Budgets in a Turbulent Channel Flow", *J. Fluid Mech.*, Vol. 194, pp. 15-44.
- Menter, F., 1993, "Zonal Two-Equation  $k - \omega$  Turbulence Models for Aerodynamic Flows", AIAA Paper 93-2906, *AIAA 24th Fluid Dynamics Conference*, Orlando.
- Shima, N., 1993, "Prediction of Turbulent Boundary Layers with a Second Moment Closure", *J. of Fluids Engineering*, Vol. 115, pp. 56-69.
- Wolfshtein, M., 1969, "The Velocity and Temperature Distribution in One-Dimensional Flow with Turbulence Augmentation and Pressure Gradient", *J. Heat & Mass Transf.*, Vol. 12, pp. 301-318.



# CALIBRATION OF MODELS FOR THE SLOW PRESSURE-STRAIN RATE USING LES

K. Alvelius, M. Hallbäck, A.V. Johansson

Department of Mechanics

KTH

100 44 Stockholm

Sweden

## ABSTRACT

In this work large eddy simulation (LES) is used to investigate the behavior of the slow pressure-strain rate in homogeneous decaying turbulence relaxing towards isotropy. In particular the dependence on the anisotropy tensor and the turbulence Reynolds number is studied. The relation between the filtered and unfiltered quantities is studied to see whether LES may be used for calibration purposes.

## INTRODUCTION

In the Reynolds averaged Navier-Stokes (RANS) equations a large part of the flow physics is put into the Reynolds stresses. Therefore it is important to have turbulence models that can capture the flow physics. The requirement that the models should be valid for different flow cases will in general make them complicated with several model parameters. These model parameters can be calibrated against experiments, direct numerical simulations (DNS) or LES. DNS can today only be used at low Reynolds numbers whereas LES and experiments can be used at high Reynolds numbers. When LES is used the results will depend on the model for the sub-grid scale (SGS) stress tensor. The fact that LES only gives the filtered field has to be considered when calculating turbulence statistics. The Results from the LES can be checked by doing simulations with a finer resolution.

## THE LES

The governing equations in LES are the filtered Navier-Stokes and continuity equations for incompressible flow

$$\frac{\partial \bar{u}_i}{\partial t} + \bar{u}_j \frac{\partial \bar{u}_i}{\partial x_j} = -\frac{1}{\rho} \frac{\partial \bar{p}}{\partial x_i} + \nu \frac{\partial^2 \bar{u}_i}{\partial x_j \partial x_j} - \frac{\partial \tau_{ij}}{\partial x_j} \quad (1)$$

$$\frac{\partial \bar{u}_k}{\partial x_k} = 0 \quad (2)$$

where an overline ( $\bar{\phantom{x}}$ ) denotes a filtered quantity and  $\tau_{ij} = \bar{u}_i \bar{u}_j - \bar{u}_i \bar{u}_j$  is the sub-grid scale (SGS) stress tensor which has to be modelled. In the case of homogeneous turbulence the main task of the SGS model is to provide the correct energy transfer from the large scales to the sub-grid scales.

Two different models, the Smagorinsky (1963) model and the spectral model (Chollet 1984), are used in combination with spectral cut-off filters.

### The Smagorinsky model

The Smagorinsky (1963) model for the SGS stresses reads

$$\tau_{ij} = \frac{1}{3} \tau_{kk} \delta_{ij} - 2\nu_T \bar{s}_{ij} \quad (3)$$

$$\nu_T = (C_s L)^2 (2\bar{s}_{pq} \bar{s}_{pq})^{1/2} \quad (4)$$

where  $\bar{s}_{ij} = (\bar{u}_{i,j} + \bar{u}_{j,i})/2$ .  $L$  is a filter width and  $C_s$  is the Smagorinsky constant. The Smagorinsky model is implemented together with a cubic cut-off filter which in spectral space is

$$\hat{G}(\mathbf{k}) = \begin{cases} 1 & \text{if } |k_i| \leq k_c^i \quad i = 1, 2, 3 \\ 0 & \text{otherwise} \end{cases} \quad (5)$$

where a hat  $\hat{\phantom{x}}$  denotes a Fourier transformed quantity,  $\mathbf{k}$  is the wavenumber vector in the Fourier representation and  $k_c^i$  are the cut-off wave numbers in the three directions. We follow the approach by Deardorff (1970) and base the filter width on the grid volume  $L \equiv \pi/(k_c^1 k_c^2 k_c^3)^{1/3}$  which is a reasonable choice for moderately strained meshes. The trace  $\tau_{kk}$  is put into the pressure according to  $\bar{q} \equiv \bar{p}/\rho + \tau_{kk}/3$ . The modelled form of (1) is then given by

$$\frac{\partial \bar{u}_i}{\partial t} + \bar{u}_j \frac{\partial \bar{u}_i}{\partial x_j} = -\frac{\partial \bar{q}}{\partial x_i} + \nu \frac{\partial^2 \bar{u}_i}{\partial x_j \partial x_j} - \frac{\partial \tau_{ij}^a}{\partial x_j} \quad (6)$$

where  $\tau_{ij}^a \equiv \tau_{ij} - \tau_{kk} \delta_{ij}/3 = -2\nu_T \bar{s}_{ij}$ .

### The spectral model

The spectral model, Chollet (1984), for the SGS stress tensor is implemented in the spectral space

$$i k_k \hat{\tau}_{ik} = \nu_T(k) k^2 \hat{u}_i \quad (7)$$

$$\nu_T(k) = K_o^{-3/2} [0.441 + 15.2 e^{(-3.03 k_c/k)}] \sqrt{\frac{E(k_c)}{k_c}} \quad (8)$$

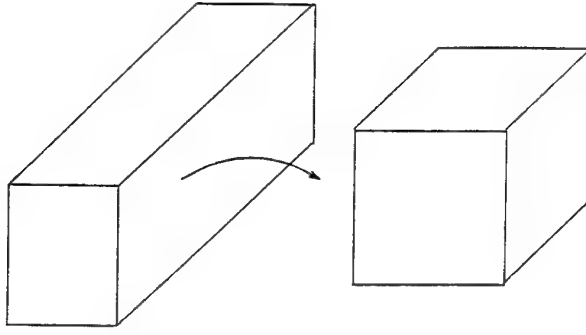


Figure 1: The computational domain before (left) and after the straining (right).

where  $K_0$  is the Kolmogorov constant and  $E$  is the kinetic energy spectrum. The derivation of the model suggests that it should be used together with a spherical cut-off filter

$$\hat{G}(k) = \begin{cases} 1 & \text{if } |k| \leq k_c \\ 0 & \text{otherwise} \end{cases} \quad (9)$$

where  $k_c$  is the cut-off wavenumber. Here the divergence of the complete SGS-stresses are modeled, not only the deviatoric part. The contribution from the SGS stresses to the pressure in the Poisson equation enters into the equation in Fourier space as  $k_i k_j \hat{\tau}_{ij}$ . This term is however zero for the spectral model which gives that it does not influence the pressure directly. The modeled form of equation (1) is here given in spectral space by.

$$\frac{d\hat{u}_i}{dt} + i k_k \hat{u}_i \hat{u}_k = -\frac{i}{\rho} k_i \hat{p} - (\nu + \nu_T(k)) k^2 \hat{u}_i \quad (10)$$

### The numerical simulation

A spectral method with a second order mixed Crank-Nicolson and Adams-Bashforth time stepping method is used to solve the modelled equations for homogeneous turbulence. A 3/2 dealiasing method is implemented in physical space where the non-linear terms are calculated. Isotropic initial velocity fields are generated with a given model energy spectrum using random phases. The model energy spectrum is

$$E = \begin{cases} Ak^a & \text{if } k \leq k_p \\ Ak_p^{a-b} k^b & \text{if } k > k_p \end{cases} \quad (11)$$

The value  $b = -1$  has been used since it gave the fastest relaxation to a desirable energy spectrum shape. This velocity field is strained irrotationally, either according to rapid distortion theory or in the simulation, and then relaxed towards isotropy. The straining is defined by the changes of the side lengths of the computational domain which goes from  $2\pi(e_1, e_2, e_3)$  to  $2\pi(1, 1, 1)$  in the  $(x_1, x_2, x_3)$  directions (figure 1). The straining with the simulation gives non-isotropic grids and is implemented only for the Smagorinsky model. The straining by the simulation can be considered as an approximation of the flow at the centerline of a contraction in a wind tunnel. The mean velocity gradients are constant throughout the whole straining. The codes have been implemented on a Cray J90 with 32 processors and on an IBM SP2 with 110 processors.

### THE SLOW PRESSURE-STRAIN RATE

In the Reynolds averaged approach the transport equation for the Reynolds stresses contain the pressure-strain

rate,  $\Pi_{ij} \equiv 2\langle p s_{ij} \rangle / \rho$ , which needs to be modelled. It can be divided into a slow part,  $\Pi_{ij}^{(s)} \equiv 2\langle p^{(s)} s_{ij} \rangle / \rho$ , which is related to the turbulence-turbulence interaction source term in the Poisson equation for the pressure, and a rapid part,  $\Pi_{ij}^{(r)} \equiv 2\langle p^{(r)} s_{ij} \rangle / \rho$ , which responds directly to changes in the gradients of the mean velocity field. In flow cases where the mean velocity field is constant only the slow pressure-strain rate remains

$$\Pi_{ij} = \Pi_{ij}^{(s)} \quad (12)$$

The quantities available for modelling  $\Pi_{ij}^{(s)}$  are the kinetic energy  $K \equiv \langle u_k u_k \rangle / 2$ , the dissipation rate of kinetic energy  $\epsilon \equiv 2\nu \langle s_{pq} s_{pq} \rangle$  and the anisotropy tensor  $a_{ij} \equiv \langle u_i u_j \rangle / K - \delta_{ij} / 3$ . Single-point models for the slow pressure-strain rate are typically of the form

$$\frac{\Pi_{ij}^{(s)}}{\epsilon} = f(Re_T) [\beta_1 (II_a, III_a) a_{ij} + \beta_2 (II_a, III_a) (a_{ik} a_{kj} - \frac{1}{3} II_a \delta_{ij})] \quad (13)$$

where  $Re_T \equiv 4K^2 / (\nu \epsilon)$  is the turbulence Reynolds number,  $II_a = a_{pk} a_{kp}$  and  $III_a = a_{pk} a_{kq} a_{qp}$  are the second and third invariants of  $a_{ij}$ . Define the mixed invariants

$$I_{ap} \equiv a_{ik} \frac{\Pi_{ik}^{(s)}}{\epsilon f}, \quad I_{aap} \equiv a_{ij} a_{jk} \frac{\Pi_{ki}^{(s)}}{\epsilon f} \quad (14)$$

From (13) we may form two scalar equations for  $I_{ap}$  and  $I_{aap}$  (Sjögren and Johansson 1997a), from which we obtain, for the non-axisymmetric case ( $II_a^3 \neq 6III_a^2$ ), expressions for the two unknown functions in (13)

$$\beta_1 = \frac{II_a^2 I_{ap} - 6III_a I_{aap}}{II_a^3 - 6III_a^2}, \quad (15)$$

$$\beta_2 = 6 \frac{II_a I_{aap} - III_a I_{ap}}{II_a^3 - 6III_a^2} \quad (16)$$

These functions are evaluated in the LES.

### EVALUATION OF LES DATA

The fact that LES produces results only for filtered quantities has to be taken into account when evaluating LES data. Thus, estimates of the relations between filtered and unfiltered  $\Pi_{ij}^{(s)}$ ,  $K$ ,  $\epsilon$  and  $a_{ij}$  are needed.

### The pressure-strain rate

The main contribution to the pressure-strain rate comes from the large scales. This implies that it is well suited for evaluation from LES computations. However, when the Smagorinsky model is used in the LES it is only possible to calculate  $\Pi_{ij}^{les} \equiv 2\langle (\bar{p}/\rho + \tau_{kk}) \bar{s}_{ij} \rangle$ . The contribution from the trace of the SGS stress tensor is investigated by defining the pressure-strain contribution at wavenumber magnitude  $k$  as

$$P_{ij}(k) \equiv 2 \int_{\Omega} \left( \frac{1}{\rho} \bar{p}^* + \hat{\tau}_{kk}^* \right) i k_j \hat{u}_i d\Omega \quad (17)$$

where the integration domain  $\Omega$  is a spherical shell of radius  $k$  in spectral space.  $P_{11}$  is calculated from a  $192^3$  velocity field and also from the same velocity field filtered down to a  $96^3$  field. The difference between them is the difference between the contribution from  $\tau_{kk}$  at the different filter levels. These two quantities are plotted in figure (2a) and it is clear that the contribution from  $\tau_{kk}$  is very small since the two curves are almost identical. The pressure-strain evaluated from a  $96^3$  simulation (figure 2b) shows

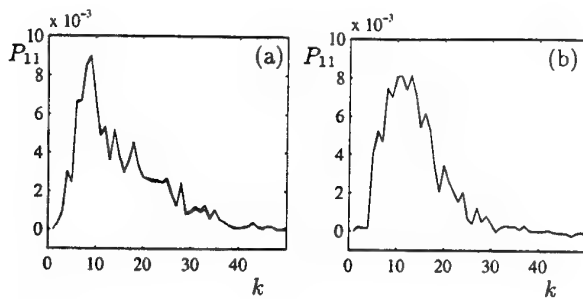


Figure 2: (a): the pressure strain distribution from a  $192^3$  LES and from the same field filtered to  $96^3$  modes. (b): the pressure strain distribution from a  $96^3$  LES.

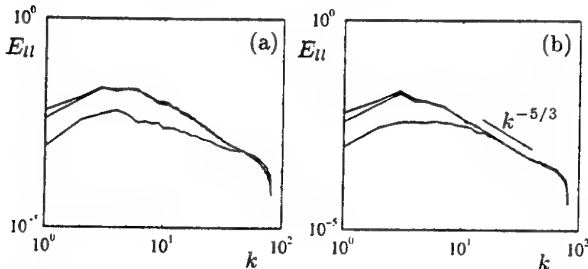


Figure 3: The energy spectrum from a  $96^3$  simulation using the Smagorinsky model. (a): at  $t = 0.17$ , (b): at  $t = 0.76$ .

that the main contribution to the pressure-strain rate in the simulation indeed is from the large scales. Hence the pressure strain rate is set equal to the pressure-strain rate calculated from the LES

$$\Pi_{ij} = \Pi_{ij}^f \quad (18)$$

where a superscript  $f$  indicates that the quantity is calculated from the filtered field.

### The anisotropy and dissipation

In decaying turbulence with isotropy on the sub-grid scales it is possible to derive correction formulas for  $a_{ij}$  and  $\epsilon$  that only depends on the spectrum shape. Assuming the energy spectrum shape in equation (11) with  $b = -5/3$  gives (Alvelius et al. 1996),

$$a_{ij} = \left(1 - \frac{3+3a}{5+3a} \left(\frac{k_p}{k_c}\right)^{2/3}\right) a_{ij}^f \quad (19)$$

$$\epsilon = \left(1 - \left(\frac{k_p}{k_c}\right)^{2/3}\right) \epsilon^f \quad (20)$$

These correction functions go to unity as the ratio between the cut-off wavenumber and the peak wavenumber of the energy spectrum  $k_c/k_p$  becomes large. The energy spectra of the different velocity components,  $E_{\alpha\alpha} = \langle u_\alpha u_\alpha \rangle / 2$  are plotted in figure (3) for a  $96^3$  simulation at the times  $t = 0.17$  and  $t = 0.76$ . It shows that the different spectra at  $t = 0.76$  are equal for the smallest resolved scales in the simulation. This supports the assumption of isotropy of the sub-grid scales.

### The limit of infinite Reynolds numbers

The turbulence Reynolds number is a measure of the ratio between the large scales ( $l$ ) and the small scales ( $\eta$ ),  $Re_T \sim (l/\eta)^{4/3}$ . An increase of  $Re_T$  will give a decrease in  $\eta$  if  $l$  is constant. If  $Re_T$  is large enough there will exist an inertial sub-range for the energy spectrum. The

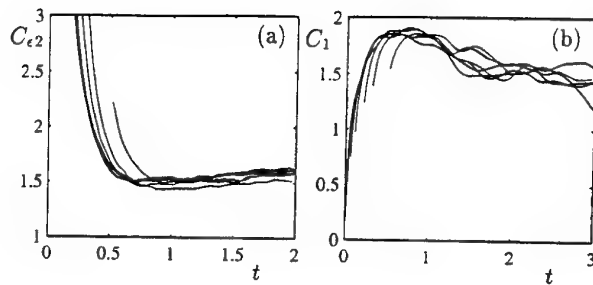


Figure 4: The Smagorinsky model relaxing  $96^3$  velocity fields strained with different  $t_{str}$ . (a): The time scale ratio  $C_{e2}$ . (b): The Rotta parameter  $C_1$ .

averaged quantities considered here becomes more or less independent of Reynolds number for values of  $Re_T$  at which the inertial sub-range starts to develop. When the inertial sub-range is increased the statistics will change marginally, due to the low energy content in the highest wave numbers, and approach an asymptotic limit. The limit of infinite  $Re_T$  is represented in the LES by an inertial sub-range all the way out to the cut-off wave number. If the cut-off wavenumber is large enough the main part of the scales are resolved to give the asymptotic behavior illustrated by the estimates in (18,19,20).

### VALIDATION OF THE LES

The results from the LES will typically depend on the SGS stress model, the resolution and in the beginning of the simulation on the initial condition. The validity of the results from the LES is checked by using the two different SGS stress models and also by doing calculations on finer grids which will make the influence from the SGS stress model weaker. The influence of the initial condition is studied by generating the strained velocity fields with rapid distortion theory or with the simulation, which then are relaxed. The ratio between the decay time scales of  $K$  and  $\epsilon$ ,  $C_{e2} \equiv (K/\dot{K})/(\epsilon/\dot{\epsilon})$ , is studied in order to see how the turbulence decays. The velocity field is considered to be relaxed from its initial state when  $C_{e2}$  is slowly varying. The prediction of  $\Pi_{ij}$  is studied by calculating the Rotta parameter,  $C_1$ , which is defined through the Rotta (1951) model for the slow pressure strain rate  $\Pi_{ij}^{(s)} = C_1 \epsilon a_{ij}$ .

### Different ways of straining

The rapid distortion straining will most likely give a less physically correct velocity field compared to a field strained in a simulation. In the latter case the turbulence has time to develop during the straining and it is plausible that the results early in the relaxation will be better compared to the first case. The drawback of the rapid distortion straining is investigated by relaxing  $96^3$  velocity fields, using the Smagorinsky model, strained with rapid distortion theory and in the simulation. The times during which straining takes place are  $t_{str} = 0.05; 0.1; 0.2; 0.3; 0.5$ . The rapid distortion is considered as the limit  $t_{str} = 0$ . Figure (4) shows that the results for  $C_1$  only differ slightly early in the simulation. The difference later in the simulation is due to statistical uncertainty.  $C_{e2}$  behaves the same in all simulations, although possibly shifted slightly in time.

### Model dependence

The dependence of the choice of SGS stress model is tested at high Reynolds number for axisymmetric  $96^3$  simulations with a  $a = 4$  initial field. In figure (5) time realizations of  $C_{e2}$  and  $C_1$  are shown for the Smagorinsky

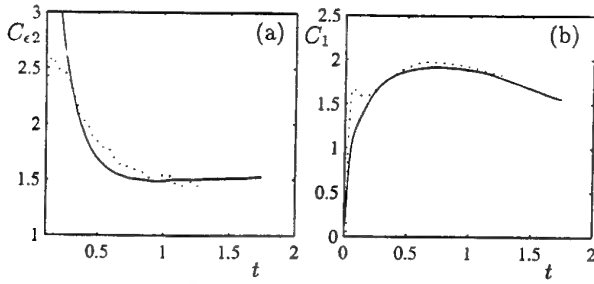


Figure 5: The Smagorinsky model (full lines) and spectral model (dotted lines) relaxing a  $96^3$  velocity field. (a): The time scale ratio  $C_{\epsilon 2}$ . (b): The Rotta parameter  $C_1$ .

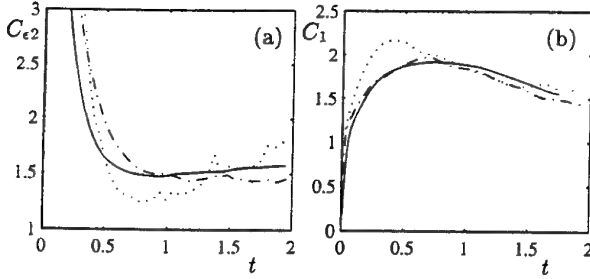


Figure 6: Relaxations on  $96^3$  grid (full lines),  $128^3$  grid (dashed dotted lines) and  $256^3$  grid (dotted lines) using the Smagorinsky model. (a): The time scale ratio  $C_{\epsilon 2}$ . (b): The Rotta parameter  $C_1$ .

model and the spectral model. The different models gives more or less the same behavior for  $C_1$  and  $C_{\epsilon 2}$  and the results are concluded to be quite insensitive to the choice of SGS stress model.

### Resolution dependence

Even though the sub-grid scales do not directly contribute to the quantities considered, they may influence them indirectly through the energy containing large scales. Therefore, in order to get a reliable result it is necessary to have a sufficiently large range of scales between the smallest energy containing scales which contribute to the result and the filter scale. The results of the LES are checked by doing simulations with different resolutions. In figure (6)  $C_{\epsilon 2}$  and  $C_1$  are plotted for  $96^3$ ,  $128^3$  and  $256^3$  simulations with  $a = 2$  initial energy spectra. The value of  $C_1$  differs slightly in the beginning of the simulations. This seems to be due to the fact that the larger simulations take longer times to reach a relaxed state from its initial conditions which is indicated by the undershoot in  $C_{\epsilon 2}$  which results in a too low value of  $\epsilon$ . When  $C_{\epsilon 2}$  has converged the results for  $C_1$  agree well for the different resolutions and we conclude that it is sufficient to do  $96^3$  simulations and that such simulations also relax faster to a physical state as compared to higher resolutions.

The  $96^3$  simulation gives values of  $C_1$  very similar to those with  $a = 4$  in figure (5). It is therefore assumed that the results are independent of the value of  $a$ .

## RESULTS

LES data has been generated with  $96^3$  simulations where ten different realizations are made for each parameter case in order to get enough statistics.

The model in equation (13) assumes that it is possible to separate the dependence on  $Re_T$  and  $a_{ij}$ . The function

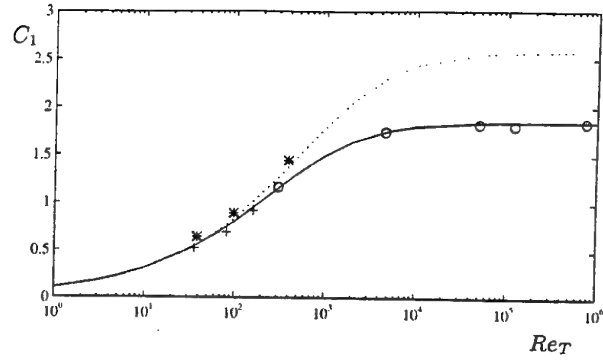


Figure 7: The Rotta parameter  $C_1$ , versus the turbulence Reynolds number at the anisotropy value  $a_{11} = -0.3$ . 'o': LES data, '\*': DNS data, '+': DNS data at  $a_{11} = -0.38$ , dotted line:  $C_{1\infty}f$  from (21) with  $C_{1\infty} = 2.58$  and  $D_1 = 1307.6$ , full line:  $C_{1\infty}f$  from (21) with  $C_{1\infty} = 1.85$  and  $D_1 = 600$ .

$f(Re_T)$  is calibrated in axisymmetric turbulence at a certain anisotropy value. The anisotropy dependence is studied at high Reynolds number for different initial anisotropic states.

### The Reynolds number dependence

The dependence on  $Re_T$  has been studied by setting  $\beta_1 = C_{1\infty}$  and  $\beta_2 = 0$  in equation (13), which essentially gives the Rotta model (1951) with  $C_1 = C_{1\infty}f$  as the Rotta parameter. The function  $f$  has been suggested by Hallbäck et al. (1993) to be

$$f = \sqrt{\frac{2Re_T}{D_1} + \left(\frac{Re_T}{D_1}\right)^2} - \frac{Re_T}{D_1} \quad (21)$$

where  $D_1$  is a constant. LES calculations have been made for relaxing axisymmetric turbulence ( $e_2 = e_3 = 1.5$ ) using the Smagorinsky model with  $C_s = 0.115$ . In the simulations  $k_c/k_p \approx 12$  which gives a negligible correction to the LES data.  $C_1$  is plotted versus  $Re_T$  for the anisotropy value  $a_{11} = -0.3$  in figure (7).  $C_{1\infty}f(Re_T)$  with  $C_{1\infty} = 1.85$  and  $D_1 = 600$  is in good agreement with the LES data. The preliminary results by Alvelius et al. (1996)  $C_{1\infty} = 2.5$  is hence lowered. Hallbäck (1993) calibrated the function at low Reynolds numbers against DNS data to get  $C_{1\infty} = 2.58$  and  $D_1 = 1307.6$ . Wind tunnel measurements by Sjögren and Johansson (1997b) gave values of  $C_1$  that are between the two calibrations. The new calibration coincides with the old for low Reynolds numbers, where the DNS data is, except at one point. In this point the value of  $C_1$  is larger than both curves, probably due to a too low value of  $C_{\epsilon 2}$ . This suggest that the new calibration may be the correct one.

### The anisotropy dependence

The anisotropy dependence has been studied at high Reynolds numbers where the dependence on  $Re_T$  asymptotically vanishes. Different types of rotation free straining are considered. The anisotropy invariant map (AIM) in figure (8) illustrates the relaxations of the different initial velocity fields. The functions  $\beta_1$  and  $\beta_2$  can be expanded in the invariants  $II_a$  and  $III_a$ . A fifth order realizable expansion can be written on the form, (Sjögren and Johansson 1997)

$$\beta_1 = c_1 F + \left(\frac{9}{8}c_1 + c_3\right)\left(\frac{8}{9}(F - 1) + 2II_a - II_a^2\right) \quad (22)$$

$$\beta_2 = c_2 F + \left(\frac{9}{8}c_1 + c_3\right)\left(\frac{1}{2}II_a + \frac{3}{2}III_a\right) \quad (23)$$

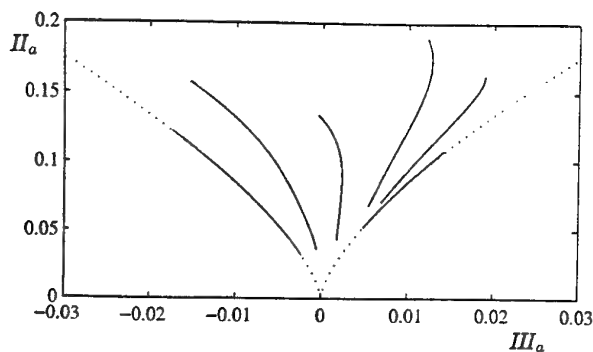


Figure 8: The anisotropy invariant map for the simulations.

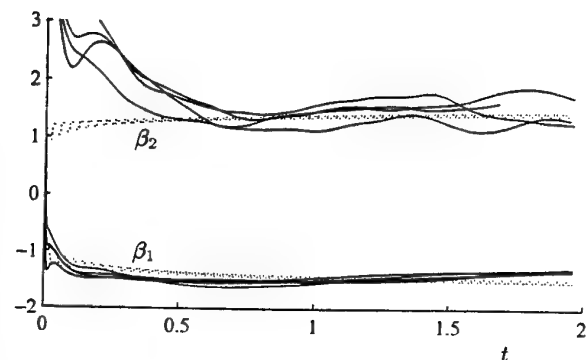


Figure 9: The functions  $\beta_1$  and  $\beta_2$  from the simulations (full lines) and the model (dotted line).

where  $F = 1 - \frac{9}{8}(II_a - III_a)$ . The constants  $c_i$  ( $i = 1, 2, 3$ ) are calibrated against the LES data, for the non-axisymmetric flows, using a least square method. This gives  $c_1 = -1.56$ ,  $c_2 = 1.61$  and  $c_3 = 1.27$ . Sjögren calibrated the constants at lower Reynolds numbers using DNS to be  $c_1 = -2.4$ ,  $c_2 = 2.2$  and  $c_3 = 1.2$ . Sjögren used the value  $D_1 = 1307.6$  in the calibration. In the range of  $Re_T$  used in the DNS the value of  $D_1$  will strongly influence the function  $f(Re_T)$ . This may be an explanation for the difference between the results from the two calibrations.

In figure (9) the functions  $\beta_1$  and  $\beta_2$  are plotted for the non axisymmetric cases. We see that after the initial phase in the simulations the functions  $\beta_1$  and  $\beta_2$  are more or less constant with values independent of the anisotropy state. The model has no problem of capturing this behaviour. From this we may conclude that it may be sufficient to take

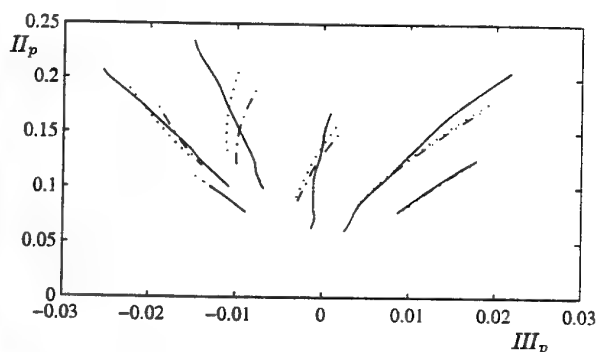


Figure 10: The relaxation paths in the pressure invariant map for the simulations (full lines), the model (dotted line) and the simplified model (dashed dotted line).

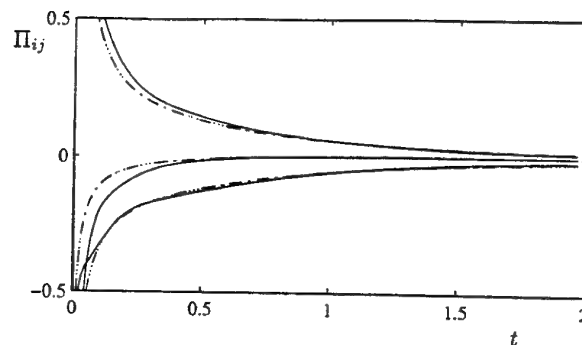


Figure 11: The pressure-strain rate  $\Pi_{ij}$  from a non-axisymmetric simulation (full lines), the model (dotted line) and the simplified model (dashed dotted line).

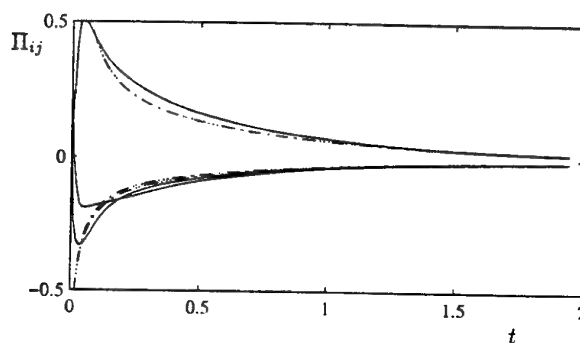


Figure 12: The pressure-strain rate  $\Pi_{ij}$  from an axisymmetric simulation (full lines), the model (dotted line) and the simplified model (dashed dotted line).

$\beta_1$  and  $\beta_2$  as constants in the model, which however will give a non-realizable model. A simpler realizable model is obtained from (22) and (23) by setting  $c_3 = -9c_1/8$  which gives that only the first term containing  $F$  is retained

$$\frac{\Pi_{ij}^{(s)}}{\epsilon} = f(Re_T)F[c_1 a_{ij} + c_2(a_{ik}a_{kj} - \frac{1}{3}II_a\delta_{ij})] \quad (24)$$

where  $c_1 = -1.56$ ,  $c_2 = 1.61$ . In figure (10) time realizations of the invariant  $II_p \equiv \Pi_{pq}\Pi_{pq}/\epsilon^2$  is plotted against the invariant  $III_p \equiv \Pi_{p[i}\Pi_{l]q}\Pi_{qp}/\epsilon^3$  for the anisotropy cases in figure (8). A curve to the left in figure (8) corresponds to a curve to the right in figure (10). The model follows the LES data well in the axisymmetric contraction and expansion case. In the middle of the figure, close to  $III_p = 0$  the agreement is worse. The simplified model gives qualitatively the same result.

A direct comparison of the pressure-strain rates from the models and the LES (figure 11,12) shows that they agree very well in both axisymmetric and non-axisymmetric flows.

## CONCLUSIONS

It is supported that LES with still a relatively low physical resolution can be used to calibrate turbulence quantities in the asymptotic limit of high  $Re_T$ . In the homogeneous flow case considered here the pressure-strain rate model performs well. It gives a good prediction over all the Reynolds number and anisotropy range. The results suggests that the simplified model (24) is sufficient to follow the LES data.

## REFERENCES

- Alvelius, K., Hallbäck, M., and Johansson, A.V., 1996 "Investigation of the self-consistency of the Smagorinsky constant and the value of the Rotta parameter at high Reynolds numbers", In *Proc. of the second ERCOFTAC Workshop on Direct and Large Eddy Simulation*, Grenoble, France
- Chollet, J.P., 1994, "Two-Point Closure Used for a Sub-Grid Scale Model in Large Eddy Simulations", in *Turbulent Shear Flow IV*, eds., F. Durst and B. Launder Springer-Verlag, Heidelberg, 62.
- Deardorff, J.W., 1970, "On the magnitude of the Subgrid scale Eddy coefficient", in *Journal of computational physics* 7, pp. 120-133 (1971).
- Hallbäck, M., Sjögren, T., and Johansson, A.V., 1993 "Modeling of intercomponent transfer in Reynolds stress closures of homogeneous turbulence." In *Proc. of Turbulent Shear Flows IX*, eds. Durst, Kasagi, Launder and Whitelaw, pp. 23.4.1-6.
- Rotta, J., 1951 "Statistische theorie nichthomogener turbulenz I", *Z. für Physik* 129, pp. 547-572.
- Smagorinsky, J., 1963. "General circulation experiments with the primitive equations", *Mon. Weather Rev.* 91, p. 99.
- Sjögren, T. and Johansson, A.V., 1997a. "Development and calibration of algebraic non-linear models for terms in the Reynolds stress transport equations", in *Doctoral thesis*, KTH, Stockholm.
- Sjögren, T. and Johansson, A.V., 1997b. "Measurement and modelling of homogeneous axisymmetric turbulence. Part 1: The return to isotropy process", in *Doctoral thesis*, KTH, Stockholm.

**L.R.N. K- $\varepsilon$  MODEL FOR PREDICTION OF TURBULENT BOUNDARY LAYERS,  
DEVELOPING UNDER STRONG PRESSURE GRADIENT CONDITIONS**

**E. V. Shishov, A. I. Leontiev, A. V. Gerasimov**

Russian Federation  
Jubileyniy prospect, d.84,kv.22  
141 400 Moscow-Khimki-10  
Russia

See late papers

# EXPERIMENTAL AND COMPUTATIONAL STUDY OF PRESSURE EFFECTS ON TURBULENT FLOW IN AN ASYMMETRIC PLANE DIFFUSER

L. Brunet<sup>(1)</sup>, J.-B. Cazalbou<sup>(1)</sup>, P. Chassaing<sup>(1)(2)</sup>, L. Jervase<sup>(1)</sup>

<sup>(1)</sup> ENSICA Département de Mécanique des Fluides  
1, place Emile Blouin  
31056 Toulouse cedex 5  
France

<sup>(2)</sup> INPT Institut de Mécanique des Fluides de Toulouse  
Allée du Professeur Camille Soula  
31500 Toulouse  
France

## ABSTRACT

An experiment is presented in which a fully developed duct flow is subjected to a strong adverse pressure gradient through a plane diffuser. An essential difference between this configuration and the widely studied adverse-pressure-gradient boundary layers lies in the structure of the outer layer which is fully turbulent in our case and intermittent in a regular boundary layer. Comparison with  $(k, \epsilon)$  model calculations are presented in an attempt to see if the known deficiency of the model in the prediction of retarded wall-bounded flows could be related to the presence of intermittency in the outer layer. The obtained results bring some support to this hypothesis, global characteristics, velocity-defect profiles and turbulent kinetic energy profiles are in good agreement while changes in the structural parameter  $-\overline{u'v'}/k$  remain unseen by the model.

## INTRODUCTION

Since the review of experimental data and prediction methods at the 1981 Stanford conference, the prediction of adverse pressure gradient wall-bounded flows remains a difficult task. With two-equation eddy-viscosity models, the problem usually manifests as an overestimation of the computed friction coefficient while the characteristic thicknesses are underestimated. These effects have been found to have their origin, as well in the inner region with an anomalous shift of the logarithmic law (Huang & Bradshaw, 1995), as in the outer region with too low values of the wake parameter ( $\Pi$ ) (Wilcox, 1988).

This study was undertaken to investigate the outer region deficiency. We start from the fact that, in opposition to the case of a plane channel flow, the eddy-viscosity constitutive relation in the  $((k, \epsilon))$  model is ill-behaved in the outer region of a turbulent boundary layer (Cazalbou & Bradshaw, 1994) and want to examine how the nature of the outer layer — whether it is intermittent as in the case of a semi-confined boundary layer or fully turbulent when the pressure gradient is imposed to a fully developed internal flow — could be related to the observed deficiencies. The case of semi-confined APG flows is well documented and experiments like those of Samuel & Joubert (1974) or Skare & Krogstad (1994), have been useful to assess the per-

formances of current turbulence models. Fully turbulent APG flows are fewer: one can mention the plane-diffuser flow of Obi et al. (1993) or the axisymmetric-diffuser flow of Arora & Azad (1980). In this paper, we present an experiment that has been designed to supplement these data: a fully established plane-channel flow is subjected to a smoothly increasing adverse pressure gradient with no separation and no curvature effect on one of the walls. Experimental data will be compared to calculation results obtained with the standard  $(k, \epsilon)$  turbulence model to see if the prediction is better in this case of fully turbulent APG flow.

## EXPERIMENT

### Experimental setup

As can be seen in figure 1, the flow is generated in a 6 cm wide channel whose aspect ratios are respectively 108 and 12.7 in the longitudinal and transverse directions. The test section is 1 m long, made up of a lower plane glass wall and a contoured ceiling whose shape has been designed to obtain the desired pressure-gradient evolution. The outlet of the test section is smoothly connected to a second constant-section duct of 15 cm width. The Reynolds number at the inlet of the test section, based on channel height and velocity in the symmetry plane, is equal to 40,000. 65 static pressure taps are distributed on each of the lower and upper walls, measurements are obtained from a differential pressure transmitter *Effa* GA76B with reference to pressure at the inlet of the diffuser. Laser-doppler measurements are possible through the lower wall and one of the side walls.  $U$  (along  $x$ ) and  $V$  (along  $y$ ) velocity components with the three associated Reynolds stress ( $\overline{u'^2}$ ,  $\overline{v'^2}$  and  $\overline{uv'}$ ) have been measured at 21 different stations along the diffuser with an IFA 750 two-components doppler-signal processor from *TSI*. The friction coefficient is evaluated at each station by fitting the velocity profile to the logarithmic law. Two-dimensionality of the flow has firstly been checked at the end of the plane channel: the maximum mean velocity varies by less than 1 % within 400 mm around the centerline of the channel. In the diffuser,



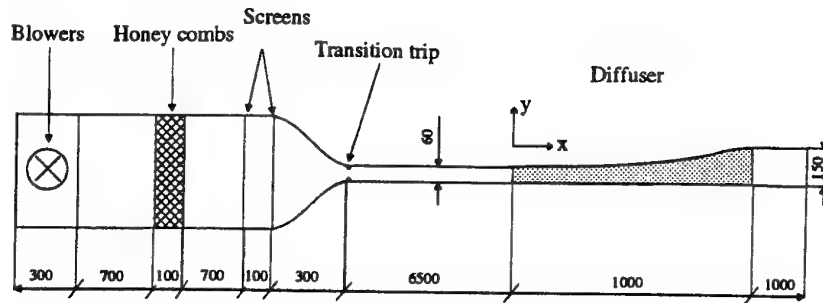


Figure 1: Sketch of the experimental facility.

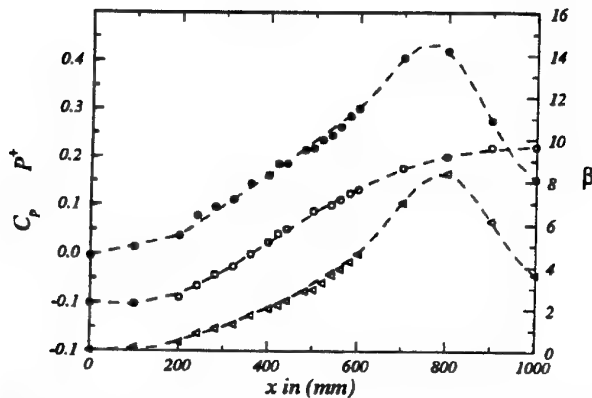


Figure 2: Longitudinal evolution of pressure coefficient and pressure gradient parameters.  $\circ$ : pressure coefficient,  $\bullet$ :  $P^+$ ,  $\triangle$ :  $\beta$ .

a momentum balance has been evaluated that appears to be satisfactory up to 700 mm from the inlet, farther away two-dimensionality and/or skin friction coefficient values will not be considered as reliable.

### Description of the flow

The flow can be characterized by the longitudinal evolution of the pressure gradient normalized by both inner and outer flow scalings. To this end, we shall consider some equivalent of a boundary layer thickness ( $\delta$ ) defined as the distance above the lower wall where the mean velocity reaches its maximum in the section ( $U_0$ ), the momentum ( $\theta$ ) and displacement ( $\delta^*$ ) thicknesses will be obtained from integrations up to  $\delta$  with velocities non-dimensionalized by  $U_0$ . The evolutions of the Clauser parameter  $\beta = \delta^* \bar{P}_{,x} / \tau_w$ , "viscous" pressure gradient  $P^+ = \nu \bar{P}_{,x} / (\rho U_d^2)$  and pressure coefficient  $(P - P_0) / \rho U_d^2$  ( $P_0$  is the inlet pressure and  $U_d$  is the bulk mean value of the velocity) are plotted in figure 2. One can see that the value of the pressure coefficient increases gradually across the diffuser, the pressure gradient reaching its maximum at approximately  $x = 420$  mm.  $\beta$  and  $P^+$  respectively peak at 8.5 and  $4.2 \cdot 10^{-2}$  at  $x = 800$  mm, their values are still as high as 7 and  $4 \cdot 10^{-2}$  at  $x = 700$ , the limit beyond which we shall not consider our data as fully reliable. In comparison with the case of a regular boundary layer, these values are well within the range where classical turbulence models fail: in the reference experiment of Samuel & Joubert,  $\beta$  increases up to 7.7 while  $P^+$  stays below  $1.1 \cdot 10^{-2}$ .

To further investigate the structure of the flow, it will be interesting to refer to the analysis of Perry *et al.* (1966). From dimensional reasoning, these authors propose a partition of the APG inner layer into two different regions, the first one is similar to that of a zero pressure gradient inner

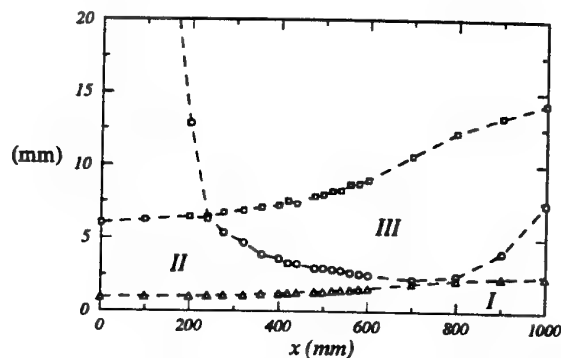


Figure 3: Location of the different regions of the inner layer,  $\square$ :  $0.2\delta$ ,  $\circ$ :  $1.41/P^+$ ,  $\triangle$ :  $y^+ = 30$ .

layer with a viscous layer and—if the pressure gradient is not too high—the familiar logarithmic layer. Farther from the wall the mean flow is supposed to depend only on the kinematic pressure gradient and the distance to the wall leading to a half-power law for the mean velocity profile. Examination of experimental data has led Perry *et al.* to propose the following half-power law:

$$\bar{U}^+ = K (P^+ y^+)^{1/2} + \frac{1}{\kappa} \ln \left( \frac{C}{P^+} \right) + A \quad (1)$$

with:  $K = 4.16$ ,  $\kappa = 0.4$  and  $A = 5.1$ . This relation is believed to be valid in the inner region for  $y^+ \geq 1.41/P^+$ . Taking the limit of the viscous region at  $y^+ = 30$ , Perry *et al.* consider that the logarithmic layer disappears when  $P^+$  becomes higher than 0.05. We have plotted in figure 3 a sketch of the different regions in our flow, the limit of the viscous region corresponds to  $y^+ = 30$ , the half-power region lies above the line corresponding to  $y^+ \geq 1.41/P^+$  and the limit of the inner region is tentatively given at  $y = 0.2\delta$ . Accordingly, the mean velocity profiles should exhibit a half-power portion for  $x$  greater than 320 mm and the presence of a logarithmic region is not warranted for the 700 and 800 mm stations.

## COMPARISON WITH MODEL CALCULATIONS

### Calculation procedure

Calculations have been performed using the two-dimensional Reynolds-averaged Navier-Stokes equations and the  $(k, \epsilon)$  eddy-viscosity model. The model is implemented in its "high Reynolds number" standard form — i.e. with values of the constants as given in Launder & Sharma (1974) — and with wall functions used to bridge the viscous region (Launder & Spalding, 1974). This approach has been adopted to limit as much as possible the incidence of an incorrect modelling of the "low Reynolds num-

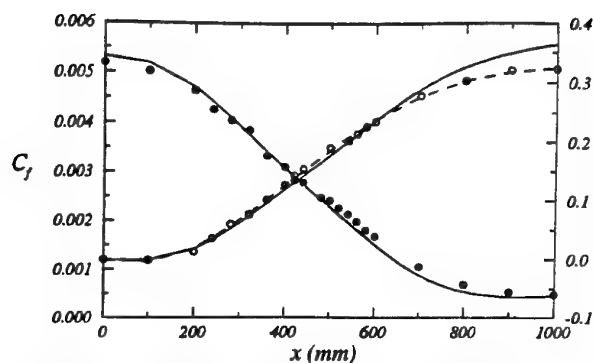


Figure 4: Evolution of pressure (o) and skin friction (•) coefficients along the diffuser, solid lines: calculations, symbols: experiment.

ber" region and to focus the discussion on the behaviour of the model in the outer region which is our primary interest here.

The calculation procedure is inspired from Kwak (1989), it is based on the artificial-compressibility method and finite-volume discretization. Time integration is explicit, space discretization is centered for the diffusion terms and uses the flux-difference-splitting method of Roe (1981) for the convection-pressure terms.

The computational domain is made up of the diffuser and two 500 mm long inlet and outlet constant-section ducts. The computational grid comprises respectively 100 and 30 points in the longitudinal ( $\xi$ ) and transverse ( $\eta$ ) direction. The constant- $\xi$  grid lines are orthogonal to both walls and the centers of the near-wall cells are located at approximately  $y^+ = 30$ .

Inflow boundary conditions are obtained from the solution of the model equations for the one-dimensional duct-flow problem except for pressure which is extrapolated from its value inside the domain assuming constant pressure gradient. At the outlet, pressure is fixed and all other variables are extrapolated with the assumption of zero gradient.

### Global characteristics

Computed pressure coefficients and friction coefficients (defined as  $C_f = 2(\bar{P} - \bar{P}_0)/\rho U_d^2$ ) are plotted against experimental data in figure 4. Pressure coefficients are in reasonably good agreement up to  $x = 700$  mm, farther away the computed results become significantly higher than the experimental data. This seems coherent with what is expected from the three-dimensional effects that we suspect to take place in this region of the flow: the thickening of the boundary layers on the side walls acts to increase the velocity in the center portion of the diffuser and thus should reduce the effective pressure gradient. Skin friction coefficients are in good agreement all along the diffuser. However, as we note in figure 3, the existence of the logarithmic layer is questionable for stations beyond  $x = 700$  mm and so for our evaluation of the wall shear stress. Therefore, we shall merely retain the good agreement between computed and experimental results up to station  $x = 600$  mm.

Integral thicknesses are plotted in figure 5, here again the agreement is fairly satisfactory up to  $x = 700$  mm. Beyond this station, the computed displacement thickness is directly affected by the overestimated pressure gradient, while the computed momentum thickness is much less affected and stays in close agreement with the experimental results all along the diffuser. We note that, in the region between  $x = 0$  and  $x = 600$  mm where we consider our results as reliable, the shape factor increases from 1.34 to 1.54, this is comparable with the values given by Samuel

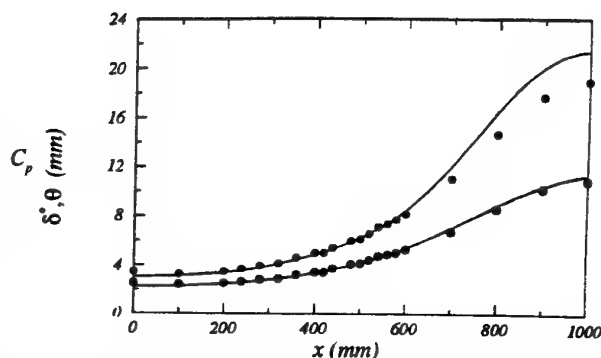


Figure 5: Evolution of displacement (upper curves) and momentum (lower curves) thicknesses along the diffuser, solid lines: calculations, symbols: experiment.

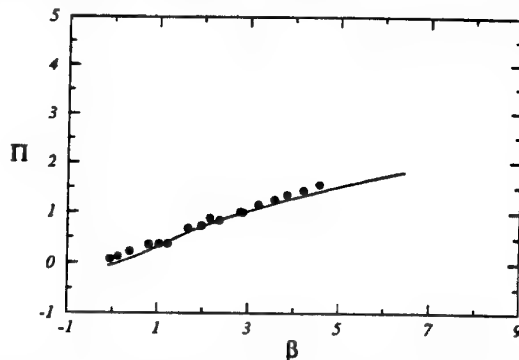


Figure 6: Evolution of the wake parameter against  $\beta$  up to  $x = 600$  mm, solid line: calculations, symbols: experiment.

& Joubert for their experiment (1.39–1.61), a case where  $(k, \epsilon)$ -model predictions show significant errors on the friction coefficient and characteristic thicknesses.

The evolution of the wake parameter  $\Pi$  (Coles, 1956) as a function of  $\beta$  is interesting since predictions with the  $(k, \epsilon)$  model systematically underestimates  $\Pi$  in a regular APG boundary layer (see Wilcox, 1988). In figure 6, the computed and experimental  $\Pi$ - $\beta$  curves are plotted for  $0 \leq x \leq 600$  mm, the range for which we expect a logarithmic layer so that Coles' formulation is meaningful. One may refer to Wilcox' (1988) figure 1-c and see that the situation is significantly improved over the case of APG boundary layers, in fact it appears that our  $(k, \epsilon)$  data are almost identical to Wilcox' as if the model could not distinguish whether or not the flow is fully confined.

### Local results

In detailed comparison, 7 stations have been selected for presentation. These stations are located between  $x = 400$  mm and  $x = 700$  mm which is the region of most intense pressure gradient for which we assume the flow to remain two-dimensional. The following table gives the detail of these stations and several characteristic parameters of interest.

$x$	$\delta$	$\theta$	$\delta^*$	$\beta$	$P^+$	$C_f$
[mm]	[mm]	[mm]	[mm]	—	$10^{-2}$	$10^{-3}$
400	36,18	3,48	5,03	1,97	1,63	3,09
440	36,83	3,77	5,47	2,36	1,86	2,77
480	39,28	4,09	6,01	2,83	2,14	2,47
520	41,08	4,41	6,58	3,21	2,34	2,25
560	43,39	4,89	7,41	3,85	2,62	1,97
600	44,87	5,30	8,19	4,57	3,00	1,66
700	53,16	6,75	11,04	6,98	4,05	1,05

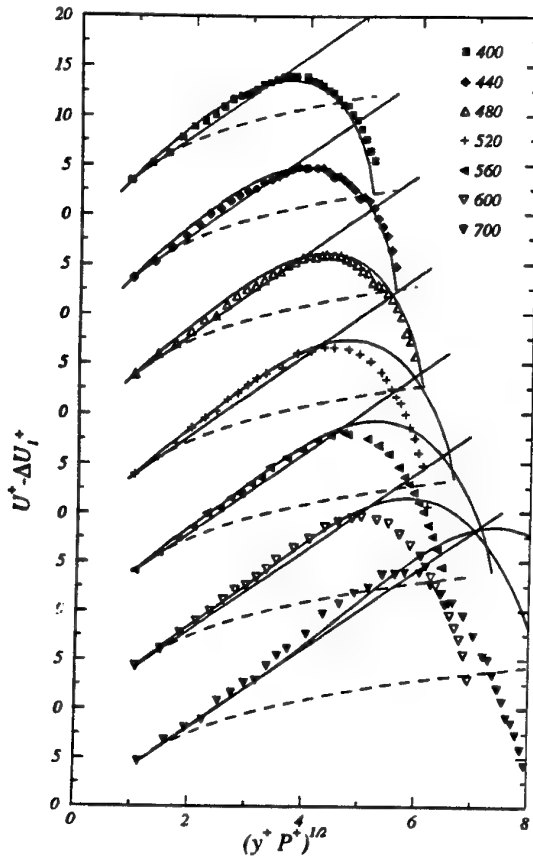


Figure 7: Velocity profiles in half-power plot, symbols: experiment, solid line: computation, solid straight line: half-power law, dashed line: log. law.

**Mean-velocity field.** In a first step we shall examine the consistency of our results with Perry *et al.* (1966) theory. Velocity profiles in the form given by equation 1 are plotted in figure 7 for the selected stations. It can be seen that, in the experiment, convincing  $y^{1/2}$  layers do not appear before  $x = 440 \sim 480$  despite the fact that, on the basis of figure 3, the half-power law is expected even before  $x = 400$ . In fact, as in Samuel & Joubert experiment, the  $y^{1/2}$  layer is not observed in the region of increasing pressure gradient. The computed profiles show the same trend, flat portions on the plots appear even later with a slope which is slightly but consistently higher than  $K = 4.16$ , except for the last station. The overall agreement between computed and experimental results is downgraded far from the lower wall as  $x$  increases because overestimation of the pressure gradient and underestimation of  $u_\tau$  cumulates in  $P^+$ .

In figure 8, the velocity profiles have been plotted in the classical velocity-defect formulation. Agreement between computation and experiment is fairly good except for the last station and confirm the good behaviour of the model in the outer region of this flow. It is obvious from the figure that no similarity holds with the  $u_\tau$ - $\delta$  scaling. Several other outer scalings can be considered in APG wall-bounded flows. We shall examine first the proposal of Perry & Schofield (1973) who seek an outer law in the form:

$$\frac{U_0 - \bar{U}}{U_s} = f\left(\frac{y}{\Delta}\right) \quad (2)$$

that connects to the wall region through a half-power overlap layer described by the law:

$$(U_0 - \bar{U})/U_s = -2K'(y/\Delta)^{1/2} + 1 \quad (3)$$

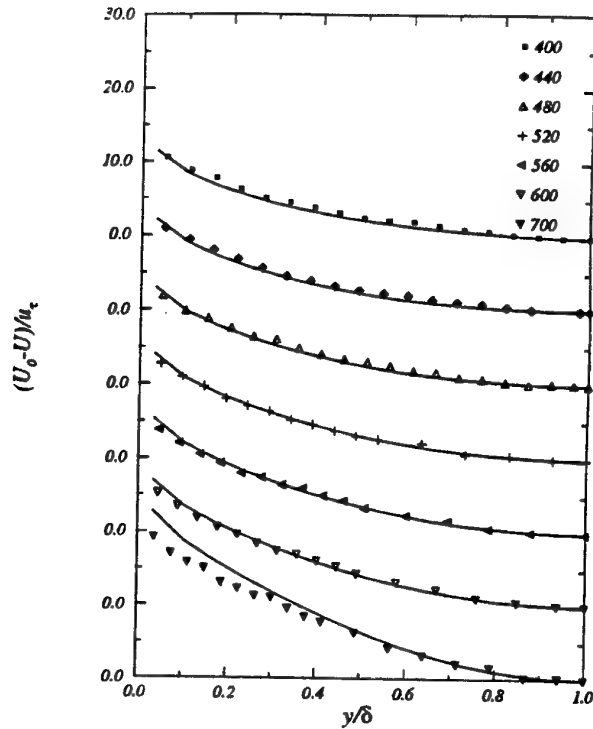


Figure 8: Velocity defect profiles in  $u_\tau$ - $\delta$  scaling, solid lines: calculations, symbols: experiment.

This last relation shows that  $U_s$  is a characteristic scale that can be deduced from the value of the intercept to 0 of the linear portion of the  $\bar{U}/U_0$  vs.  $(y/\delta^*)^{1/2}$  graph, this is what has been done here for all stations.  $\Delta$  is a length scale defined as  $\delta^* U_0 / (U_s C)$ . In figure 9 the velocity defects normalized by  $U_s$  have been plotted against  $\delta^* U_0 / U_s$ . The collapse of the graphs brings some support to the adopted scaling. Experimentally as well as numerically the curves obtained at the last station depart significantly from the others, but it could be checked that this scaling brings experiment and computation in close agreement even for this station. Another possible scaling for APG wall-bounded flows has been proposed by Kader & Yaglom (1978) in the form:

$$\frac{U_0 - \bar{U}}{u_p} = f\left(\frac{y}{\delta}\right) \quad \text{with: } u_p^2 = \delta \bar{P}_{,x} / \rho \quad (4)$$

This scaling has been adopted in figure 10. Here, the collapse of the different profiles is less convincing than with Perry & Schofield scaling. However it could be checked that this formulation brings also the experimental and computed results in close agreement.

**Turbulent field.** In this section we restrict the discussion to turbulent kinetic energy and turbulent shear stress which are of primary interest considering the level of turbulence closure that has been studied here. Measurements of  $\overline{u^2}$ ,  $\overline{v^2}$ ,  $\overline{uv}$  have been obtained at all seven stations selected here. The turbulent kinetic energy is therefore evaluated assuming that  $\overline{w^2} = 0.5(\overline{u^2} + \overline{v^2})$ . However, measurements of  $\overline{w^2}$  have been made at station  $x = 600$  mm that give some support to this approximation  $\overline{w^2}$  being almost constantly equal to  $0.45(\overline{u^2} + \overline{v^2})$ .

Turbulent kinetic energy normalized by  $u_\tau^2$  is plotted against  $y/\delta$  in figure 11. Except for the last station where the underpredicted value of  $u_\tau$  causes significant discrepancies, the agreement between experiment and computation is good. In particular, the turbulent kinetic energy level at  $\delta$ , the level and position of the maxima are satisfactory.

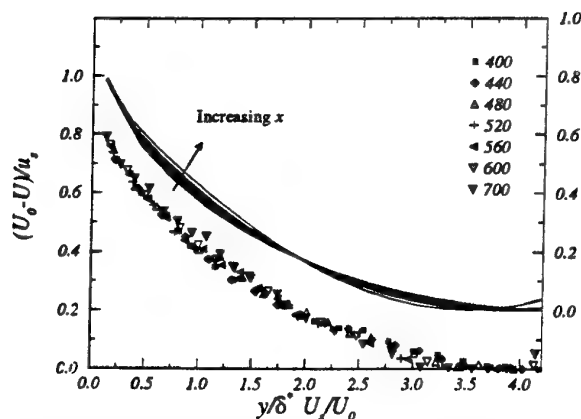


Figure 9: Velocity-defect plot according to Perry & Schofield scaling, solid lines: calculations, symbols: experiment.

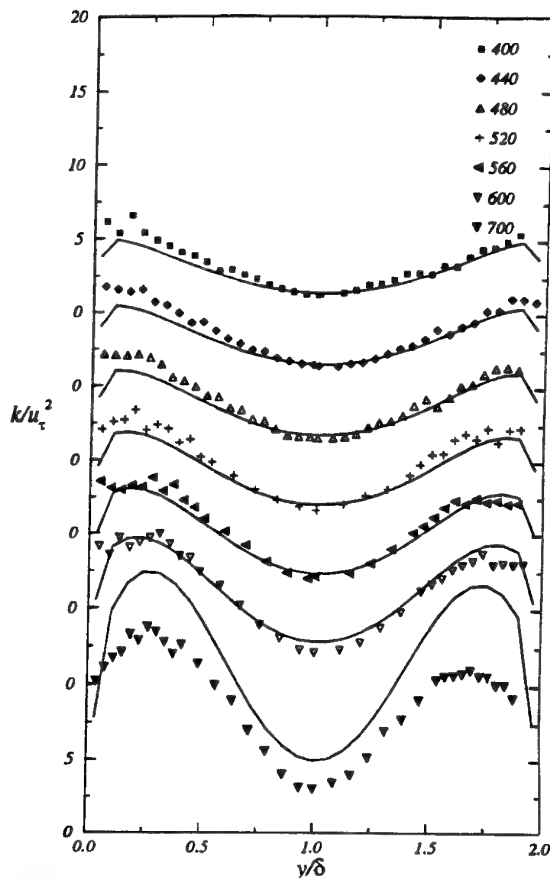


Figure 11: Turbulent kinetic energy profiles (legend as in Figure 8).

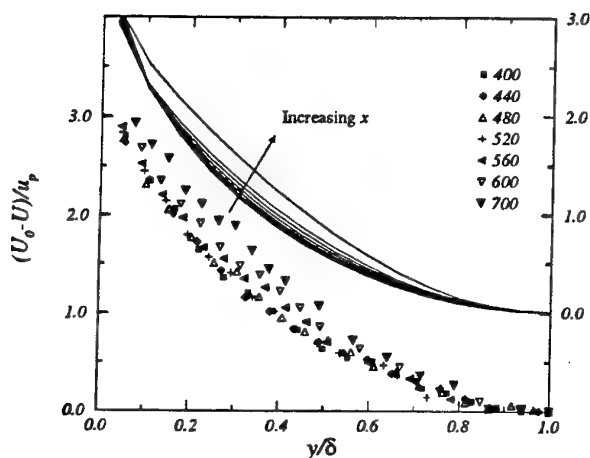


Figure 10: Velocity-defect plot according to Kader & Yaglom scaling, solid lines: calculations, symbols: experiment.

One should note the high values reached by  $k^+$  in the flow, its value peaks at about 10 for  $x = 600$  mm. Such high levels are usual in APG flows and can be favourably compared to those reached in the experiment of Nagano *et al.* (1991) for equivalent values of  $\beta$ .

The evolution of the structure parameter  $-\overline{uv}/k$  is of interest since its value is usually fairly constant outside the viscous region of wall-bounded flows, the accepted value being 0.3. Our experimental data for  $-\overline{uv}/k$  are rather noisy but have been retained for presentation for they show some interesting trends. As can be seen in figure 12, the data involve some plateau whose value appears to be consistently below 0.25 which is rather low compared to the accepted value 0.3. Spalart & Watmuff (1993) and Skåre & Krogstad (1994) also observed a drop in the values of  $-\overline{uv}/k$  for APG boundary layers but not so marked as here. Another feature that is worth to mention is a consistent shortening of the plateau as the pressure gradient increases. In any case these results need to be confirmed by new measurements with larger samples. The computed results appears to be insensitive to these structural changes, this is not surprising since a constant value of  $-\overline{uv}/k$  ( $= C_\mu^{1/2} = 0.3$ ) is intrinsically part of the definition of the  $(k, \epsilon)$  model.

## CONCLUSIONS

The results presented here seem to indicate that the predictions obtained with the  $(k, \epsilon)$  model in a fully turbulent APG wall-bounded flow do not suffer from the deficiencies observed in the intermittent outer layer of a regular boundary layer. The skin friction coefficient, characteristic thicknesses and wake parameter are well predicted and the velocity profiles in several defect formulations are in

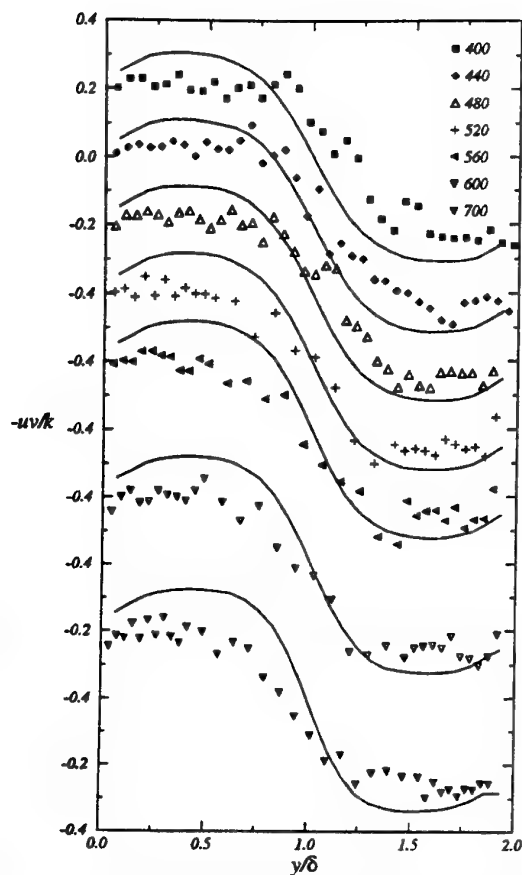


Figure 12: Structure parameter  $-\overline{uv}/k$  (legend as in Figure 8).

good agreement with measurements. As a consequence, it may be thought that sensitizing the model to the intermittency phenomenon is likely to improve model predictions in a regular boundary layer. Cho & Chung (1991) have defined such a model for free shear flows, extending its use to wall-bounded flows may help to solve the APG-flow prediction problem.

## REFERENCES

- S. C. Arora, R. S. Azad, 1980, "Turbulent Kinetic Energy Balance in a Flow with Adverse Pressure Gradient", *AIAA Paper*, No. 80-0073.
- J.-B. Cazalbou, P. Bradshaw, 1994, "Turbulent Transport in Wall-bounded Flows, Evaluation of Model Coefficients Using Direct Numerical Simulation", *Phys. Fluid A*, Vol. 5, pp. 3233-3239.
- J. R. Cho, M. K. Chung, 1991, "A  $k-\epsilon-\gamma$  Equation Turbulence Model", *J. Fluid Mech.*, Vol. 237, pp. 301-322.
- D. Coles, 1956, "The Law of the Wake in the Turbulent Boundary Layer", *J. Fluid Mech.*, Vol. 1, pp. 191-226.
- P. G. Huang, P. Bradshaw, 1995, "The Law of the Wall for Turbulent Flows in Pressure Gradients", *AIAA J.*, Vol. 33, pp. 624-632.
- D. Kwak, 1989, "Computation of Viscous Incompressible Flows", *Computational Fluid Dynamics*, V.K.I. Lecture Series 1989-4.
- B. A. Kader, A. M. Yaglom, 1978, "Similarity Treatment of Moving-equilibrium Turbulent Boundary Layers in Adverse Pressure Gradients", *J. Fluid Mech.*, Vol. 89, pp. 305-342.
- B. E. Launder, B. I. Sharma, 1974, "Application of the Energy-dissipation Model of Turbulence to the Calculation of Flow near a Spinning Disc", *Letters in heat and mass transfer*, Vol. 1, pp. 131-138.

B. E. Launder, D. B. Spalding, 1974, "The Numerical Computation of Turbulent Flows", *Comp. Methods Appl. Mech. Eng.*, Vol. 3, pp. 269-289.

Y. Nagano, M. Tagawa, T. Tsuji, 1991, "Effect of Adverse Pressure Gradient on Mean Flows and Turbulence Statistics in Boundary Layer", *Proceedings of the 8th Symposium on Turbulent Shear Flows*, Paper 2-3.

S. Obi, K. Aoki, S. Masuda, 1993, "Experimental and Computational Study of Turbulent Separating Flow in an Asymmetric Plane Diffuser", *Proceedings of the 9th Symposium on Turbulent Shear Flows*, P305.

A. E. Perry, J. B. Bell, P. N. Joubert, 1966, "Velocity and Temperature Profiles in Adverse Pressure Gradient Turbulent Boundary Layers", *J. Fluid Mech.*, Vol. 25, p. 299-320.

A. E. Perry, W. H. Schofield, 1973, "Mean Velocity and Shear Stress Distributions in Turbulent Boundary Layers", *Phys. Fluids*, Vol. 16, pp. 2068-2074.

P. L. Roe, 1981, "Approximate Riemann Solvers, Parameter Vectors and Difference Schemes", *J. Comput. Phys.*, Vol. 43, pp. 357-372.

A. E. Samuel, P. N. Joubert, 1974, "A Boundary Layer Developing in an Increasingly Adverse Pressure Gradient", *J. Fluid. Mech.*, Vol. 66, pp. 481-505.

P. E. Skåre, P.-Å. Krogstad, 1994, "A Turbulent Equilibrium Boundary Layer Near Separation", *J. Fluid Mech.*, Vol. 272, pp. 319-348.

P. R. Spalart, J. H. Watmuff, 1993, "Experimental and Computational Study of a Turbulent Boundary Layer with Pressure Gradient", *J. Fluid Mech.*, Vol. 249, pp. 337-371.

D. C. Wilcox, 1988, "Reassessment of the Scale Determining Equation for Advanced Turbulence Models", *AIAA J.*, Vol. 26, pp. 1299-1310.

# MIXING IN COAXIAL JETS WITH LARGE DENSITY DIFFERENCES

Michel Favre-Marinet<sup>1</sup>, Edith Beatriz Camano<sup>2</sup>, Jaroslav Sarboch<sup>3</sup>

<sup>1</sup>Laboratoire des Ecoulements Géophysiques et Industriels, Institut de Mécanique de Grenoble  
INPG, UJF, CNRS, B.P. 53X, 38041 Grenoble, France.

<sup>2</sup>Instituto de Pesquisas Hidráulicas, Universidade Federal de Rio Grande do Sul,  
Porto Alegre, Brasil.

<sup>3</sup>Technical University, Prague, Czech Rep.

## ABSTRACT

The paper describes an experimental investigation of coaxial jets with large density differences. Measurements by various techniques show that density effects on the flow dynamics and the mixing are taken into account to the first order by considering the specific outer to inner jet momentum flux ratio  $M$  and not separately the density and the velocity ratios. For a given value of  $M$ , however, a slight enhancement of mixing is found for density ratios much smaller than one.

## AIM OF RESEARCH

Coaxial jets are present in several practical applications, especially in the field of combustion where the mixing process is largely controlled by the flow dynamics. This has motivated numerous investigations on isothermal coaxial jets, principally in the homogeneous case (Champagne and Wygnanski 1971, Kwan and Ko 1976, Au and Ko 1987, Dahm et al 1992, Rehab et al 1997). Very few investigations have, however, considered the effects of density on these flows although large density differences may be present in industrial processes. Gladnick et al (1990) found an increase in mixing with increasing velocity ratio (limited to 2 in their study) in an axisymmetric jet flow of CFC-12 issuing into a coannular jet flow of air (density ratio : 0.26). This was attributed to the presence of annular vortex rings originating in the mixing layer between the inner jet and coannular flow.

The present research is an attempt to simulate the flow conditions of liquid propellant rocket engine injectors which are characterized by a low velocity-high density inner jet surrounded by a high velocity - low density co-annular jet. By using various gas combinations (air, helium, SF<sub>6</sub>), it is possible to reach very large density differences in the flow field near the nozzle. The objectives of the research are to investigate the effects of density variations on the flow, in particular the evolution of the density field by using thermo-anemometry in relation to the flow dynamics.

## EXPERIMENTAL SET-UP AND INSTRUMENTATION

The experimental set-up consists of a pair of concentric axisymmetric nozzles discharging into quiescent ambient air. The inner nozzle is supplied by air or SF<sub>6</sub> and consists of a tube 200mm long. The annular nozzle is supplied by air or helium (Fig. 1). The flow enters the outer nozzle radially through an annular porous cylinder (radius 38 mm) and is deviated downstream in the axial direction. The experimental conditions are :

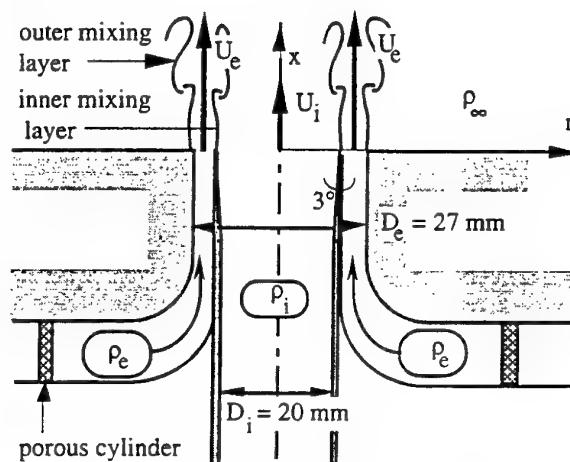


FIGURE 1: SKETCH OF THE COAXIAL JET

- \* Inner jet (i)      Diameter :  $D_i = 20$  mm  
Bulk velocity :  $U_i$       density :  $\rho_i$
- \* Outer jet (e)      Diameter :  $D_e = 27$  mm  
Bulk velocity :  $U_e$       density :  $\rho_e$
- \* Ambient fluid:      density :  $\rho_\infty$
- \* Diameter ratio       $\beta = D_e/D_i = 1.35$  (constant in this experiment)
- \* Bulk velocity ratio       $r_v = U_e/U_i$       ( $3 < r_v < 70$ )

- \* Density ratio  $S = \rho_e/\rho_i$  ( $0.028 < S < 1$ )
- \* Specific momentum flux ratio  $M = r_v^2 S$  ( $1 < M < 200$ )

The Reynolds number used is based on the hypothetical jet with outer fluid properties and a velocity such as to have the same total momentum flux. It may be expressed as :

$$Re_M = Re_{ext} [1 + (1-M)/\beta^2 M]^{1/2}, \text{ where}$$

$$Re_{ext} = \rho_e U_e D_e / \mu_e. \text{ Typical values are :}$$

- \* air/air or air/SF6 jets :  $Re_{ext} = 11000$   
 $7300 < Re_M < 7800$ ,
- \* helium/air jets :  $Re_{ext} = 3200$   
 $2100 < Re_M < 2400$

The velocity ratio  $r_v$  was varied by changing the inner velocity (inner Reynolds number  $Re_i = \rho_i U_i D_i / \mu_i$ ) and by keeping the outer velocity constant (6 m/s for air and 16 m/s for helium). In most experiments, the jet issued into ambient air. To test the effect of ambient fluid density, some measurements were made with the jet issuing into a chamber filled with helium (cross-section 0.66 m x 0.90 m).

Measurements were made with an original design of the aspirating probe used by Brown and Rebollo (1972) for the study of the inhomogeneous mixing layers. It consists of a very thin tube (I.D. 80  $\mu$ m, O.D. 300  $\mu$ m) connected to a vacuum pump. When the aspirating pressure is lower than a critical value, the mass flow is blocked in the tube and a hot-wire placed inside is then only sensitive to density but insensitive to velocity. Contrary to the arrangement of Brown and Rebollo, in the present experiment the hot-wire was located at the entrance of the suction tube in order to improve the time-response of the probe. The probe was calibrated in the inner nozzle flow with known velocity and density. It has been verified that it remains only sensitive to density variations in this configuration. The working principle of the probe requires a large local perturbation of the flow since nearly sonic conditions are maintained at the tube entrance. Fortunately, the perturbation velocity decreases very rapidly with  $r$ , the distance to the probe (as  $1/r^2$ ). The spatial resolution is estimated to be of the order of 1 mm. The time-response of the probe is about 1 ms. These probe characteristics have been checked in a helium-air mixing layer and in the far-field of a helium-air jet. In the latter flow, the measured mean density and the corresponding r.m.s fluctuation are in good agreement with the results of Pitts (1986).

Laser-sheet visualizations were performed by using a 15W copper laser pulsed at 10 kHz. The sheet thickness was estimated to be about 1mm. The air flow was seeded with encense smoke and the pictures were recorded with a video camera at 50 frames/s and at a shutter speed of 1/4000s. As a result, each frame was exposed to two laser shots separated by a time interval of 0.1 ms.

## RESULTS

### Onset of recirculation

The initial stages in the development of the flow are governed by the growth of the mixing layers, generated on both sides of the annular outer jet. An important feature of the flow is the entrainment of fluid issued from the central nozzle into the inner mixing layer surrounding the potential core. The length of the central potential core results directly from the balance between the mass flow rate of the inner fluid and the entrainment rate into the inner mixing layer. It may be expressed in terms of the normalized entrainment velocity

$v_E/U_i$ . This entrainment process results in a decrease of the mass flow rate in the central region. Consequently, the central jet velocity first decreases to a minimum value. This value is reached at the point where the inner mixing layers merge on the jet-axis.  $v_E/U_i$  increases with increasing velocity ratio  $r_v$  and it is expected that for sufficiently high values of  $r_v$ , a regime of recirculation occurs near the nozzle.

Although the present situation is more complex, the plane mixing layer is a good basis for the understanding of the influence of the parameters which characterize the coaxial jet. Effects of density have been considered by Brown and Roshko (1974) and more recently by Dimotakis (1986), who has modelled the asymmetric entrainment on the two sides of the mixing layer. Quite recently, numerical simulations of Soteriou and Ghoniem (1995) have confirmed the observed tendency to mixing enhancement when the slower stream becomes denser. In the Dimotakis model, the mixing layer growth is due to entrainment by the large-scale vortical structures present in the flow and is predicted by modelling the entrainment velocity  $v_E$  on each side of the mixing layer. On the low-speed side of the inner mixing layer (free stream velocity:  $U_i$ ),  $v_E$  is given by :

$$v_E / (U_c - U_i) = \epsilon$$

where  $\epsilon$  is roughly independent of  $r_v$  and  $S$  (at least for moderate values of  $S$ ). The convection velocity  $U_c$  of the vortical structures in the model is related to the freestream velocities and to the density ratio  $S$ , resulting in :

$$v_E / U_i = \epsilon \frac{S^{1/2}(r_v - 1)}{1 + S^{1/2}} = \epsilon \frac{M^{1/2} - S^{1/2}}{1 + S^{1/2}} \quad (1)$$

It can be seen that for high values of the velocity ratio  $r_v$ ,  $v_E/U_i$  is directly related to the momentum ratio  $M$ , and in the limit  $S \rightarrow 0$ ,  $v_E/U_i = \epsilon M^{1/2}$ . When applied to coaxial jets with high velocity ratios, this model suggests that the effects of density may be taken into account by considering the flux momentum ratio  $M$  to characterize the flow. However, when  $M$  is kept constant, a second-order effect of density is still present and Eq.1 indicates an enhancement of entrainment of the low-speed stream when the high-speed stream has lower density.

These predictions are confirmed by the present experimental investigation. It has been shown that recirculation occurs when  $r_v$  is higher than a critical value (Villermaux et al 1994, Camano and Favre-Marinet 1994). The effects of density have been explored by using various combinations of air, helium and SF6 so that  $S$  varies from 1 to values as low as 0.028. The onset of recirculation was detected by visualizations, laser-velocimetry and thermo-anemometric techniques (Camano 1996). Results obtained with different methods are in good agreement and show that effects of density are rather well taken into account by considering the flux momentum ratio  $M$  and not separately  $r_v$  and  $S$ . As a matter of fact, the separation between the two regimes may be defined in terms of a critical ratio  $M_c$ . The central jet has a potential core of length  $L$  which decreases with increasing  $M$ . When  $M$  is higher than  $M_c$  ( $\approx 50$ ), reverse flow occurs at a distance of about  $1D_i$  from the nozzle and a recirculation bubble appears in the central region of the jet. The length of this bubble increases with  $M$  in the direction of the nozzle.

### Visualizations

For air-air jets, the mixing layers consist of regular axisymmetric structures (Fig.2) similar to those observed in wa-



ter by other authors (Dahm et al 1992, Rehab et al 1997) Cross-sectional views show the development of azimuthal instabilities on both sides of the coannular jet. They correspond to longitudinal vortices as demonstrated by the typical view (Fig.2) taken at  $x/D_i=1$ . About a dozen azimuthal structures are present at this distance from the nozzle.

For  $S$  much smaller than one (SF6 as the inner fluid), the flow looks similar to the homogeneous case. It may be noted, however, that the growth of the seeded annular jet is faster than for the preceding case. This seems to be caused by the faster development of the small scale structures which are responsible of the more corrugated interface between the two jets. The recirculation regime is shown in Fig. 3 for two values of  $S$ .



FIGURE 2: VISUALIZATIONS BY LASER-SHEET.  $M=9$ ;  $U_e=6\text{m/s}$ ,  $Re_M=7730$ , left : air-air coaxial jet,  $r_v=3$ ,  $Re_i=2700$ ; right : air/SF6 coaxial jet,  $S=0.21$ ,  $r_v=6.5$ ,  $Re_i=7360$ ; top : cross-sectional views at  $x/D_i=1$ ; bottom : sideviews of the jet



FIGURE 3: VISUALIZATIONS BY LASER-SHEET.  $M=144$ ;  $U_e=6\text{m/s}$ ,  $Re_M=7280$ , left : air-air coaxial jet,  $r_v=12$ ,  $Re_i=675$ ; right : air/SF6 coaxial jet,  $S=0.21$ ,  $r_v=26$ ,  $Re_i=1840$

Visual inspection of the films gives an estimation of the length of the potential core  $L$  (Fig.4). Although the data present a rather large scatter due to experimental uncertainties, some trends may be deduced from Fig.4. For air/air jets,  $L/D_i$  follows a law in  $M^{-1/2}$  in agreement with the predictions of Rehab et al (1997). When recirculation occurs, the length of the potential core decreases faster than indicated by the pre-

ceding law. There is a significant effect of gravity for the air/SF6 jets for intermediate values of  $M$ . All the results for this gas combination indicate, however, a shortening of the potential core, even in the case of favorable gravity. This is especially true for the larger values of  $M$  for which the results obtained with the two opposite up/down directions of the nozzle are the same. The He/air jets results are close to those of the homogeneous case. Only the situation with adverse gravity was visualized. Note that the outer helium jet is strongly slowed down by the external ambient air. This corresponds to the trend of decreasing entrainment velocity and lengthening the potential core. Finally, the case of very large density differences (He/SF6,  $S=0.028$ ) gives higher values of  $L/D_i$  for the two up/down directions of the nozzle.

These results seem to indicate that the shear layer growth is increased when density ratio is small ( $S=0.2$ ). This enhancement of entrainment is in agreement with Eq.1. The opposite tendency is found, however, for coaxial jets with very large density differences ( $S=0.028$ ) for yet unexplained reasons.

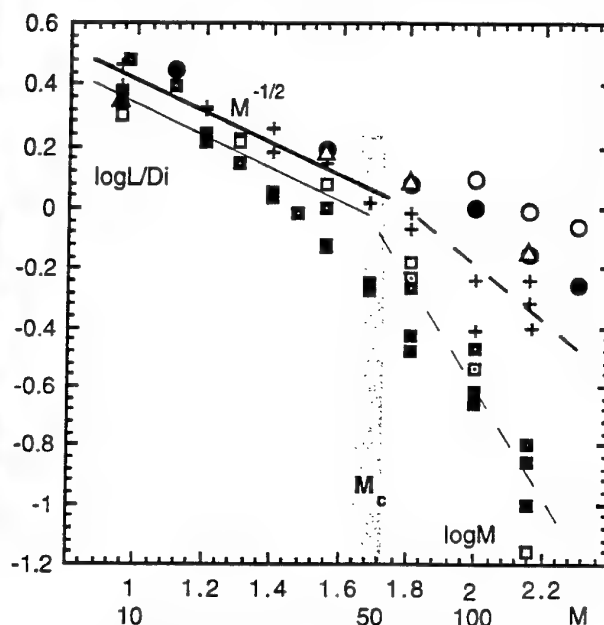


FIGURE 4: LENGTH OF THE POTENTIAL CORE DEDUCED FROM VISUALIZATIONS

+ , air/air;  $\bullet$ ,  $\circ$ , He/SF6;  $\blacksquare$ ,  $\square$ , air/SF6;  $\triangle$ , He/air. Open symbols correspond to measurements with the nozzle in the downward direction and solid symbols to measurements with the nozzle in the upward direction.

#### Mixing in coaxial jets

Density was measured by an aspirating probe in a helium-air jet flowing in the vertical upward direction. For this combination of gas, it has been verified that the results obtained in the near-field are affected neither by viscous effects, nor by gravity effects. The first point was checked by comparing measurements for  $Re_M=2520$  and 1260. On the other hand, experiments were conducted with the nozzle in the upward and in the downward direction. Quite similar results were found for the axial evolution of density in the first ten diameters in the two sets of experiments.

Density effects were tested by comparing pure helium-pure air jets ( $S=0.138$ ) to coaxial jets with a moderate value of  $S$  ( $S=0.655$ ) obtained by using an air-helium mixture as the



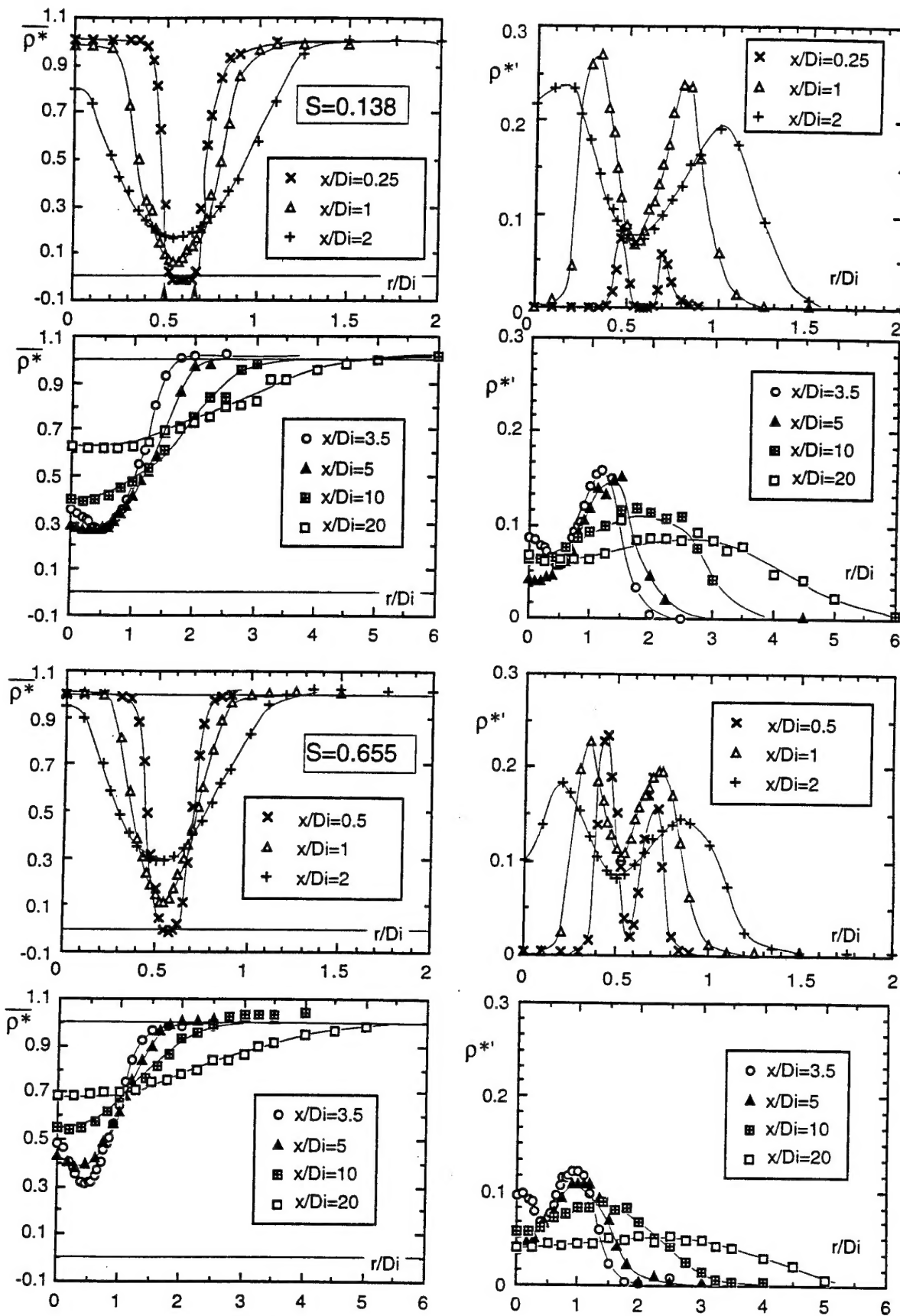


FIGURE 5 : MEAN AND R.M.S DENSITY PROFILES.  $M = 9$   
 $Rei = 2760$ . Top :  $S = 0.138$ ,  $ReM = 2590$ ; Bottom :  $S = 0.655$ ,  $ReM = 5900$

annular jet fluid ( $U_e=7.3$  m/s). The density was normalized with the values at the exit plane (here  $\rho_\infty = \rho_j$ ):

$$\rho^* = (\rho - \rho_e) / (\rho_j - \rho_e).$$

**Cross-sectional profiles** Figure 5 compares mean and r.m.s ( $\rho^{*'} = \sqrt{\rho^{*2}}$ ) density profiles across the jet for strong and moderate density ratios and for the same value of  $M$  ( $M=9$ ). Since the global features are very similar for the two sets of measurements, it clearly demonstrates that the change in density is satisfactorily taken into account by grouping  $r_v$  and  $S$  in the flux momentum ratio  $M$ .

The mixing process gives rise to shear layer growth on the inner and outer sides of the annular jet. As a result, the outer jet potential core extends to less than one diameter in this particular geometrical configuration. For this value of  $M$ , the mixing layers merge on the jet-axis at a distance of about  $1.5D_i$ .  $\rho^*$  decreases in the downstream direction in the central region whereas it is still increasing in the coannular region. As far as the mean flow is concerned, the mixing process is completed in the central region for  $x/D_i \approx 4.5$ . Further downstream, the mean and r.m.s profiles evolve toward the shapes of the round jet. A small influence of  $S$  may be observed on Fig. 5 which shows a slower mixing process for the case of moderate density ratio. For example, the deviation between the minimum and the values of  $\rho^*$  on the axis is significantly larger than in the other case at  $x/D_i \approx 3.5$ . Moreover, the normalized level of fluctuations is also lower for  $S=0.655$ .

Results on the mixing layer growth are summarized on Fig 6 which gives the position  $r_{0.9}/D_i$  of the points where  $\rho^*=0.9$  in the two experiments. The estimated value of the spatial resolution of the probe is reported in the same figure. Very near the nozzle, the high value of  $r_{0.9}/D_i$  reached on the outer side of the jet for  $S=0.138$  may be attributed partly to integration effects of the probe. It is likely that the lateral extent of the mixing layer defined by  $\rho^*=0.9$  is close to that observed in visualizations. Since the present results only take the low-speed sides of the coannular jet mixing layers into account, the half-value of the slopes of  $d\delta_{vis}/dx$  obtained by Brown and Roshko (1974) in the plane mixing layer are reported on the same graph. On the outer side of the annular jet, the mixing layer growth is in good agreement with the observations of these authors. In particular, the enhancement of diffusion for low values of  $S$  is also found in the present experiment. The observed slopes are, however, significantly larger on the inner side than on the outer side, whereas the predicted slopes have opposite trends: they should decrease by 20% between  $r_v = \infty$  and  $r_v = 8$ . This discrepancy is probably related to the confinement in the inner potential core and to the resulting adverse pressure gradient.

**Density measurements along the jet axis** The downstream evolutions of the mean density and the  $\rho^{*}$ -r.m.s are significantly affected by  $M$  (Favre-Marinet & Camano 1996). The length of the potential core  $L_p$  decreases with increasing  $M$ . Very intense fluctuations take place in the near-field region and  $\rho^{*}$  reaches a maximum value slightly downstream from the end of the potential core. These  $\rho^{*}$  fluctuations are related to the crossing of large scale structures at the end of the potential core ( $M < M_c$ ) or to large oscillations of the upstream boundary of the recirculation bubble for the highest values of  $M$  ( $M > M_c$ ), as shown by visualizations.

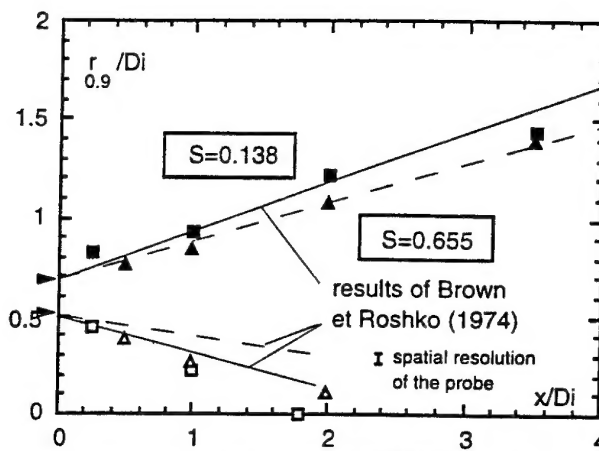


FIGURE 6: MIXING LAYER GROWTH.  $M=9$

■  $r_{out}/D_i$ , □  $r_{int}/D_i$ ,  $S=0.138$   
▲  $r_{out}/D_i$ , △  $r_{int}/D_i$ ,  $S=0.655$

**Length of the potential core** It is very important to know the length  $L$  of the potential core for optimizing the operation of rocket-engines. Figure 7 summarizes results obtained by various techniques in the homogeneous flow.  $L$  was determined by laser-anemometry (position of the minimum velocity on the jet-axis) and by laser-sheet visualizations. Complementary results were obtained by using a hot/cold wire probe, consisting of a cold wire placed very close upstream from a hot-wire (typical distance:  $20\mu m$ ). With this method,  $L$  was determined by detecting the maximum rms fluctuations of the signal given by the cold wire. All methods are in remarkable agreement and show that  $L$  follows a  $M^{-1/2}$  power-law. Moreover, the present results collapse with those of Rehab et al (1997) obtained in a geometrically similar water channel. The length of the potential core was also determined from the measurements of density with  $L_p$  defined as the distance where  $\rho^*$  departs from 1 by a given percentage (say 5%). For the moderate value of  $S$  (0.655), the behaviour of  $L_p$  is quite similar to that of  $L$ . Due to its definition,  $L_p$  is, however, much smaller than the other determinations of  $L$ .

Further measurements for different values of  $S$  show that  $L_p$  is not considerably affected by density effects when plotted vs  $M$  (Fig. 8). This is in agreement with the visualization study (Fig. 4) and with the predictions of the model of Rehab et al (1997), who calculated the length of the potential core by equating the mass flow rate issuing from the central nozzle and that entrained across the surface of the potential core. Present measurements confirm the significant role played by  $M$  in the near-field dynamics of the flow and in the resulting mixing process. Small effects of density may, however, be observed on Figure 8, especially for moderate values of  $M$ . As expected from Eq.1, entrainment of inner fluid is enhanced and  $L_p$  is reduced when  $S$  is decreased ( $S=0.138$ ). This effect is more pronounced, when the ambient and the outer jet fluids are the same (helium in this experiment). In this case, it is expected that the outer jet is slowed down less rapidly by the ambient fluid, resulting in an increase of entrainment of the central jet by the inner mixing layer.

The behaviour of He/SF<sub>6</sub> coaxial jets ( $S=0.028$ ) seems paradoxical, since when compared to the results for

$S = 0.655$ , the potential core length is slightly increased for this combination of gas. Contrary to the predictions given by Eq.1, entrainment is reduced by such further decrease of  $S$ .

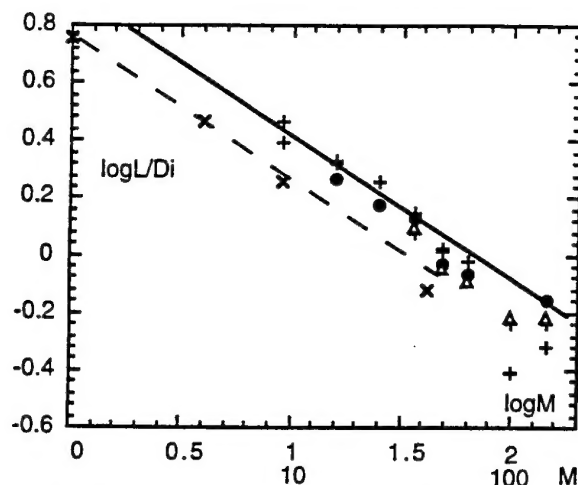


FIGURE 7 : LENGTH OF THE POTENTIAL CORE. HOMOGENEOUS FLOW

● "wake" hot/cold-wire probe; ○, laser-sheet visualizations; △, laser anemometry; × — —, aspirating probe  $S=0.655$   
—  $L/Di = 8/M^{1/2}$  Rehab et al (1996)

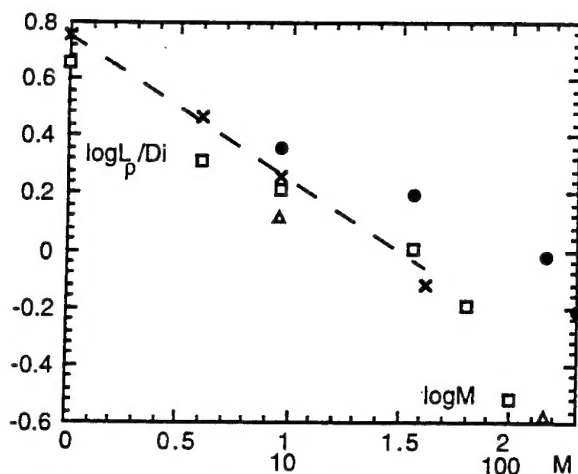


FIGURE 8 : INFLUENCE OF DENSITY ON THE LENGTH OF THE POTENTIAL CORE

— ×  $S = 0.655$  - amb. air ●  $S = 0.028$  - amb. He  
□  $S = 0.138$  - amb. air; △  $S = 0.138$  - amb. He

## SUMMARY AND CONCLUSIONS

The various experimental techniques used in the present work are in agreement and show that the dynamics of coaxial jets are essentially governed by the outer to inner jet flux momentum ratio  $M$ . The length of the potential core depends mainly on  $M$ . A regime of recirculation occurs in the near-field region when  $M$  is higher than a critical value  $M_C$  ( $\approx 50$ ).

This study shows that the new aspirating probe is well suited for mean and fluctuating density measurements in variable density flows, except perhaps in thin layers very close to the nozzle.

The concentration field of coaxial jets is strongly affected

by the dynamics of the flow; effects of density on mixing are also rather well taken into account by considering  $M$ , instead of  $r_v$  and  $S$  separately.

The length of the potential core deduced from density measurements on the jet axis varies as  $M^{-1/2}$  for moderate values of  $S$ , in agreement with simple calculations. A reduction of this length is observed for density ratio much smaller than one ( $S \approx 0.14$ ). This effect is consistent with the behaviour of the mixing layer with density differences. The opposite behaviour occurs for extremely low values of  $S$  and this unexpected result has not been explained yet.

## REFERENCES

- Au, H., and Ko, N.W.M., 1987, "Coaxial jets of different mean velocity ratios", *Journal of Sound and Vibration*, Vol. 116, 3, pp. 427-443.
- Brown, G.L., and Rebollo, M.R., 1972, "A small fast-response probe to measure composition of a binary mixture", *AIAA J.*, Vol. 10, 5, pp. 649-652.
- Brown, G.L., and Roshko, A., 1974, "On density effects and large structure in turbulent mixing layers", *Journal of Fluid Mechanics*, Vol. 64, 4, pp. 775-816.
- Camano, E.B., 1996, "Etude expérimentale des jets coaxiaux avec différences de densité". Thèse INP Grenoble.
- Camano, E.B., and Favre-Marinet, M., 1994, "On the initial region of inhomogeneous coaxial jets", *Advances in Turbulence V*, pp. 58-62, R.Benzi Ed., Kluwer Academic Publishers.
- Champagne, F.H., and Wygnanski, I.J., 1971, "An experimental investigation of coaxial jets", *Int. Journal of Heat and Mass Transfer*, Vol. 14, pp. 1445-1461.
- Dahm, W.J.A., Frieler, C.E., Tryggvason, G., 1992, "Vortex structure and dynamics in the near field of a coaxial jet", *Journal of Fluid Mechanics*, Vol. 241, pp. 371-402.
- Dimotakis, P.E., 1986, "Two-dimensional shear-layer entrainment", *AIAA Journal*, Vol. 24, 11, pp. 1791-1796.
- Favre-Marinet, M., Camano, E., 1996, "Mixing in coaxial jets with large density differences", *IUTAM Symposium on Low-speed variable density flows*, Marseille.
- Gladnick P., Enotiadis, J., LaRue J., Samuelsen, G., 1990, "Near-field characteristics of a turbulent coflowing jet", *AIAA Journal*, Vol. 28, 8, pp. 1405-1414.
- Kwan, A.S.H., and Ko, N.W.M., 1976, "Coherent structures in subsonic coaxial jets", *Journal of Sound and Vibration*, Vol. 48, 2, pp. 203-219.
- Pitts, W.M., 1986, "Effects of global density and Reynolds number variations on mixing in turbulent, axisymmetric jets", *Nat. Bur. Stand., NBSIR 86-3340*.
- Rehab, H., Villiermaux, E., Hopfinger, E.J., 1996, "Flow regimes of large velocity ratio coaxial jets", to appear in *Journal of Fluid Mechanics*.
- Soteriou, M.C. and Ghoniem, A.F., 1995, "Effects of the free-stream density ratio on free and forced spatially developing shear layers", *Phys. Fluids 7*, Vol. 8, pp. 2036-2051.
- Villiermaux, E., Rehab, H., Hopfinger E.J., 1994, "Breakup regimes and self-sustained pulsations in coaxial jets", *Meccanica*, Vol. 29, 4, pp. 393-401.

## ACKNOWLEDGMENTS

This research was supported by the Société Européenne de Propulsion. The authors would like to gratefully acknowledge the help of Prof. Drobniak for the visualization study.

**SIMULATION OF TWO-DIMENSIONAL STRUCTURES IN VARIABLE  
DENSITY COAXIAL JETS**

**P. Reynier, A. Kourta, H. Ha Minh**

Institut de Mécanique des Fluides de Toulouse  
Avenue du Professeur C. Soula  
31400 Toulouse

See late papers